Transactions of the ASME®

Transactions of the ASME, Journal of Heat Transfer (ISSN 0022-1481) is published quarterly (Feb., May, Aug., Nov.) for $155 per year by The American Society of Mechanical Engineers, 345 East 47th Street, New York, NY 10017. *Second class* postage paid at New York, NY and additional mailing offices. POSTMASTER: Send address changes to Transactions of the ASME, Journal of Heat Transfer, c/o THE AMERICAN SOCIETY OF MECHANICAL ENGINEERS, 22 Law Drive, Box 2300, Fairfield, NJ 07007-2300.
CHANGES OF ADDRESS must be received at Society headquarters seven weeks before they are to be *effective. Please send old label and new address.*
PRICES: To members, $29.00, annually; to nonmembers, $155.00. Add $15.00 for postage to countries outside the United States and Canada.
STATEMENT from By-Laws. The Society shall not be responsible for statements or opinions advanced in papers or . . . printed in its publications (B7.1, para. 3).

INDEXED by Applied Mechanics Reviews and Engineering Information, Inc.

Journal of Heat Transfer

Published Quarterly by The American Society of Mechanical Engineers

VOLUME 112 • NUMBER 2 • MAY 1990

ANNOUNCEMENTS

TECHNICAL PAPERS

TECHNICAL NOTES

(Contents Continued on p. 273)

(Contents continued)

1989 Max Jakob Memorial Award Lecture

Some Optimizing Examples in Forced Convective Heat Transfer

Y. Mori
Tokyo Institute of Technology,
Meguro, Tokyo 157, Japan

Three examples are selected as representative cases concerning the basic convective heat transfer in the heat exchanger field, each of which has a specified parameter for optimizing the individual specific condition. First, the chemical vapor deposition of a silicone layer for SiH_4 on the hot bottom wall of a horizontal rectangular furnace duct is discussed, assuming that a spatially uniform thickness of the layer is the optimal one. Second, the compact heat exchanger is studied with the insertion of a twisted strip in each channel so that the outlet temperature of the heated gas becomes uniform by changing the twist pitch appropriate to each channel. Third, a shell and helical tube heat exchanger is discussed for controlling flow-induced tube vibration by inserting separating plates between the tube arrays and optimizing the interval of the plates.

1 Introduction

Energy saving and economic incentives since the energy crisis have promoted studies of heat transfer enhancement. However, problems related to the reliability and global environmental impact of power plants or thermal systems have recently been attracting attention, together with economic improvement. In other words, recently, the need to enhance heat transfer performance or to develop more efficient thermal equipment or plants has sometimes been overshadowed by the requirement for more reliable or environmentally acceptable conditions.

In order to satisfy a specific condition or optimize the conditions, an appropriate parameter should be selected so as to meet the requirement for the said condition. Three examples are discussed as typical cases: one from the field of semiconductor production, that is, high-technology field, and two others that are associated with fossil fuel and nuclear power plants. In consideration of the thermal engineering standpoint of coping with global carbon dioxide problems, among heat exchanger problems in energy conservation and alternative energies, reliable compact plate-fin heat exchangers are discussed for the former case and improvement of the reliability and enhanced heat transfer performance of shell-and-tube high-temperature heat exchangers for gas-cooled nuclear reactors is discussed for the latter case.

In the first example, the heat transfer problem associated with the metal-organic chemical vapor deposition problem (CVD) in a horizontal and rectangular furnace duct, for producing silicon or gallium-arsenate layers from the raw gas, is discussed. In the CVD duct with a hot bottom wall and a cold top wall, the thickness of the deposit layer is required to be uniform. However, in a conventional duct with a hot bottom wall and cooled top and side walls, a pair of roll cells are known to play an essential role, as reported by Moffat and Jensen (1986). In this case, the thickness distribution of the deposit layer, shown by the hatched zone in Fig. 1(*a*), is thin in the middle and thick near the side walls. On the other hand, when the side walls are heated enough, the cells rotate in the opposite direction. Thus it is understood that the parameter that controls the thickness distribution is the temperature of the side walls.

The second example is related to a compact plate-fin regenerative heat exchanger for high-temperature uses such as in gas turbine and fuel cell plants. Only a few fully reliable units for long-term operation have been successfully developed, mainly due to large thermal stress, as reported by Mori et al. (1985). High thermal stress is often caused by undesirable temperature distributions in the hottest part of the heat exchanger, such as the region between the hot gas inlet and the heated gas outlet, as shown by point M in Fig. 1(*b*). A uniform temperature distribution at the heated gas outlet is preferable from the thermal stress standpoint. In order to satisfy this condition, twisted strips of various twist pitches are inserted in all channels. In this case, the parameter to decrease the highest outlet temperature is the twist pitch of the strips.

The third example mainly concerns the flow-induced tube-vibration problem of the shell and spiral tube high-temperature heat exchanger generally reviewed by Savkar (1986). Up to the present many studies of flow-induced tube vibration have been reported, because this is one of the most serious problems associated with shell-and-tube heat exchangers. A proposal is made in this paper to be applied to the in-line tube array construction shown in Fig. 1(*c*). It will be shown that insertion of separating plates between the in-line tube arrays, and selection of the optimal lateral pitch H of the plates, shown in Fig. 1(*d*), can control tube vibration.

2 Optimal Condition of Uniform Growth Rate of the Deposit Layer in a CVD Duct

An experimental and theoretical discussion is made of a horizontal rectangular duct with a hot bottom wall (Mori et al., 1989). The duct used for the experiments had almost the same dimensions as the actual CVD duct used for producing the silicon layer, and is 30 mm high and 60 mm wide. The duct 1 m long and is set downstream of a wind tunnel. The test portion of the duct is set 120 mm upstream of the duct exit. The flow in the test portion was fully developed. The upper wall of the duct is made of a 8-mm-thick transparent plastic plate for flow visualization. The bottom and side walls are made of 10-mm bakelite plates. 10-μm pieces of stainless

Contributed by the Heat Transfer Division and presented at the 26th National Heat Transfer Conference, Philadelphia, PA, August 6-9, 1989. Manuscript received by the Heat Transfer Division November 17, 1989; revision received February 6, 1990. Keywords: Heat Exchangers, High-Temperature Phenomena, Mixed Convection.

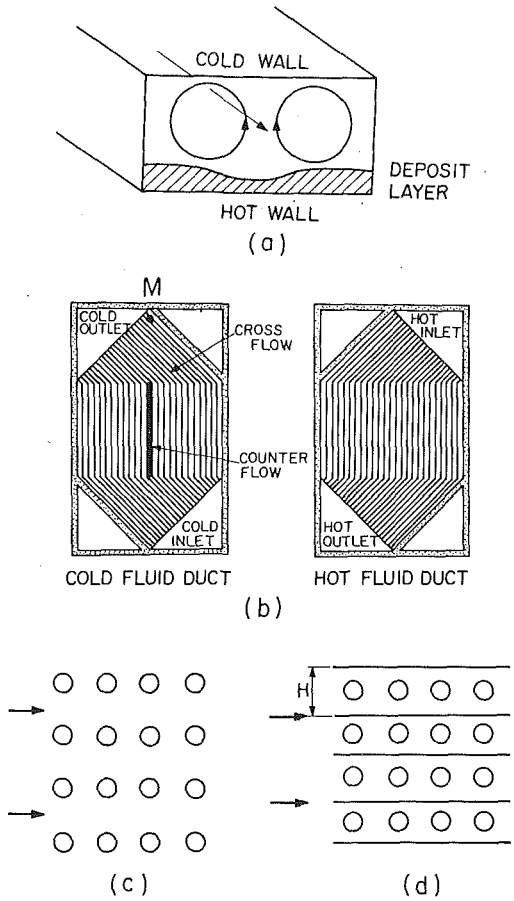

Fig. 1 Model pictures of discussed examples

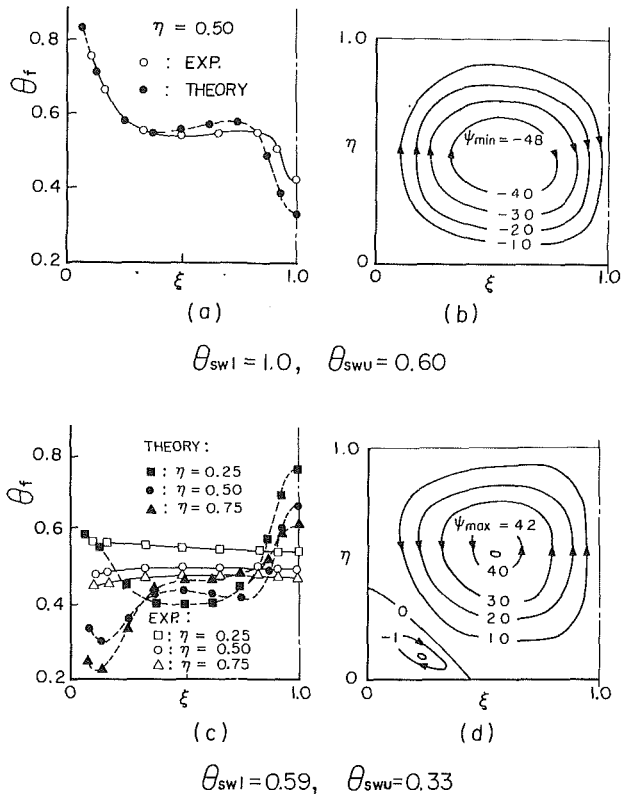

Fig. 2 Temperature and stream function distributions when the lower side wall is heated and for optimal measured temperature

steel foil are stuck on the inner surface of the cork plates covering the bakelite plate and heated by an a-c current. The side walls are divided into two parts in the middle, in order to heat them separately. Air was used as the working fluid. Experiments were chiefly performed under the condition of Reynolds number of 220 and Grashof number of 5×10^5, which are almost the same order of magnitude as a conventional CVD furnace duct for producing the silicon layer. Measured temperatures are nondimensionalized by the temperature difference between the bottom and top walls and expressed by θ. The nondimensional temperatures of the upper and lower half side walls are expressed by the subscripts *swu* and *swl*, respectively.

In the numerical analysis, the flow and temperature fields were assumed to be two dimensional, steady, laminar, and fully developed. The Boussinesq approximation was used with the assumption of the constant physical properties of fluid. The flow and temperature fields were assumed symmetric with respect to the middle vertical plane, and only the left half of the duct was analyzed by dividing it into 40 × 40 cells of equal size. An SOR numerical calculation method was used. When the side walls are not heated, the correlation between the experimental and numerical results for the temperature field is rather good, but not in complete agreement due to the slight thermal conduction to the side walls from the hot bottom wall. Figures 2(*a*) and 2(*b*) show the results when the lower half of the side wall is heated to the same temperature as that of the bottom wall. As shown in Fig. 2(*a*), the temperature correlation between theory and experiment is excellent. The rolling direction of the cell shown by the calculated stream function map in Fig. 2(*b*) is opposite to that when the side walls are not heated. In consideration of the temperature distributions in the two cases where the lower half of the side wall is not heated and heated up, and also of the fact that in the former case the

Nomenclature

C = constant
d' = width
d_e = hydraulic diameter of duct
D = tube diameter
g = gravitational acceleration
Gr = Grashof number $= g\beta\Delta T d^3/\nu^2$
H = plate distance
Nu = Nusselt number
p = pressure
Pr = Prandtl number
Re = Reynolds number $= ud_e/\nu$
T_b = bulk temperature
T_w = wall temperature
u = mean fluid velocity
x = coordinate in the horizontal direction
y = coordinate vertical to x direction in a cross section
z = coordinate in the flow direction
α = heat transfer coefficient
β = thermal expansion coefficient
Δp = pressure drop
ΔT = temperature difference
Δz = z direction distance
η = nondimensional coordinate of y
θ = nondimensional temperature difference
λ = thermal conductivity of fluid
ν = kinematic viscosity
ξ = nondimensional coordinate of x
ρ = density
Ψ_{max} = maximum value of stream function

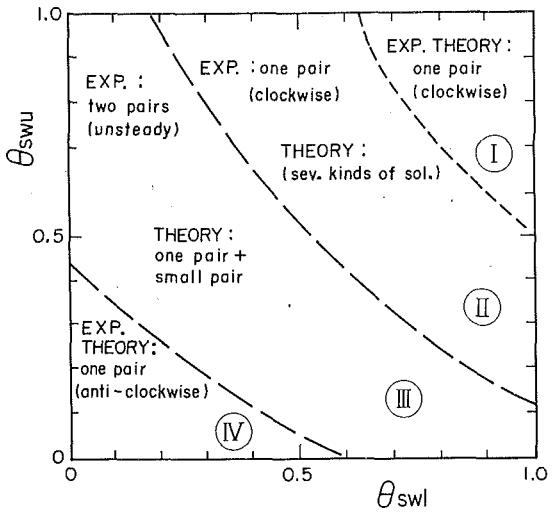

Fig. 3 Vortex cell map versus nondimensional side wall temperatures

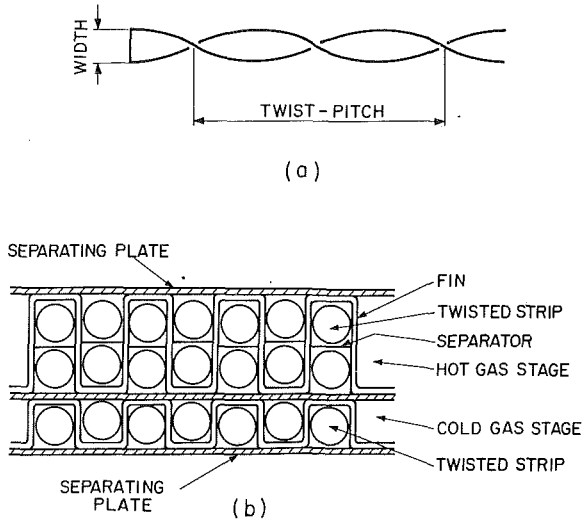

Fig. 4 Inserted twisted strip and cross section of compact plate-fin heat exchanger

maximum temperature of the fluid is at the middle section and in the latter it is near the side wall, the uniform temperature distribution on a horizontal plane cross section is considered to be attainable when the side wall is adequately heated. The resulting temperature distribution to satisfy this optimal condition, which is obtained after several trial-and-error experiments, is shown in Fig. 2(*c*) by open squares, circles, and triangles for different horizontal planes. As seen in Fig. 2(*c*), there is a big difference between the experimental results shown by solid lines and the numerical results by the broken lines. From the flow visualization experiments made under the optimal condition, the flow was found to be an oscillating one. The measured temperature distributions shown in Figs. 2(*a*) are the time-averaged values. It was also confirmed that two pairs of vortices exist unsteadily in the cross section. This unsteady flow is considered to be caused by transition instability initially due to the occurrence of an inflection point in the velocity profile of the secondary flow descending on the hot side wall.

The important points related to this unsteady second flow are, first, that the unsteady flow has predominating frequencies in the spectrum starting at 0.019 Hz. The second point is that the fluctuating motion has an amplitude large enough to make the time-averaged value of the growth rate of the layer spatially uniform. This unsteady flow might develop into a kind of chaotic flow field. Theoretical and experimental studies on the chaotic flow mainly discuss the free convection in a horizontal cubic container reviewed from the heat transfer standpoint by Yang (1989). The flow field explained above might be of a chaotic character, but to identify it exactly as a chaotic flow several experiments have to be carried out, for example, to check if whether Lyapunov index is positive as reported by Sano and Samada (1985). The experiment reported in this paper uses combined flow; few papers have discussed this kind of combined flow from the chaotic standpoint. Figure 3 shows the pattern of a grouping of the convective cells related to the temperatures of the side walls. The horizontal axis is the average temperature of the lower half wall and the vertical axis is that of the upper half. The values of Reynolds and Grashof numbers for this pattern are the same as those of Fig. 2. The expression for the circulating direction of the secondary flow is shown in the left half of the cross section. The pattern of Fig. 3 is divided into four regions. In regions I and IV, the results of experimental and numerical studies are in agreement, but in the other two regions, II and III, they are different. Region III is useful from a practical standpoint as it has the uniform time-averaged growth rate of the deposit layer on the bottom wall. The flow pattern shown in Fig. 3 may depend strongly on the Reynolds and Grashof numbers.

3 Optimal Temperature Distribution of the Heated Gas Outlet of the Compact Plate-Fin Heat Exchanger

With increasing demand for electric power and with the need for decentralized power stations, research and development of advanced gas turbine and fuel cell plants attracts the concern of utility people. One R&D problem related to these plants is the installation of power plants in densely populated urban areas, which requires the development of compact plate-fin heat exchangers for high-temperature applications, as reviewed by Bergles (1985). The plate-fin compact heat exchanger consists of many stages of hot and cold gas channels, as shown in Fig. 4(*b*). The stages lie one upon another. A stage consisting of square channels is usually used as the cold gas passage, while the hot gas channel has a rectangular cross section with an aspect ratio larger than unity. One of the important factors to consider in the study of regenerative compact plate-fin heat exchangers is enhanced reliability, particularly by relaxing thermal stresses. The insertion of twisted strips as shown in Fig. 4(*a*) in the channels for this purpose is taken up in this paper. When the shape of the channel is square for use with a cold gas flow, the twisted strip is easily inserted in the channel. However, in the case of a rectangular channel for hot gas flow, the aspect ratio of the cross section can be approximated by the integer 2 or 3 instead of the fractional number without serious problems. Experiments on flow and heat transfer performance when a twisted strip is installed in a square cross section have been reported earlier by Mori et al. (1985). In the following, the results of experiments with rectangular channels having aspect ratios of 2 and 3 are shown together with those for square channels. For the rectangular channel having aspect ratio of 2 and 3, it is proposed to insert a separator of extremely thin plate, as shown in Fig. 4(*b*). The gap between the twisted strips and the channel is within 1 mm. The effect of the twisted strips is to enhance the heat transfer performance by the induced secondary flow, but it should be noted that in addition to this effect, additional heat transfer enhancement is available at high temperatures.

Experiments on friction and heat transfer performance were performed in channels having aspect ratios of 1, 2, and 3, and with a bare duct. The kinds of twisted strip are shown in Fig. 5, where the symbols of the experimental data are also indicated. Experiments were performed at room temperature and

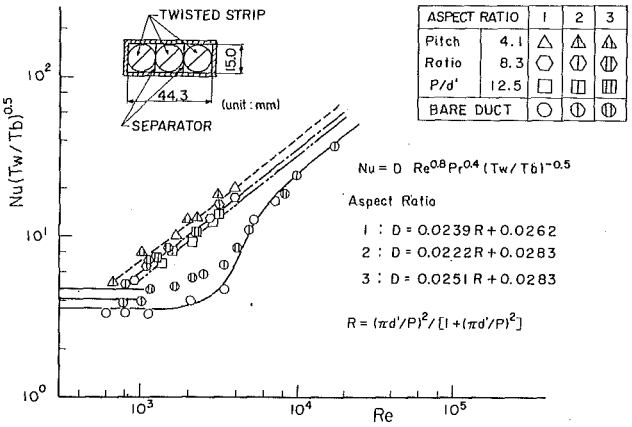

Fig. 5 Nusselt number performance for various twist-pitch conditions of strip

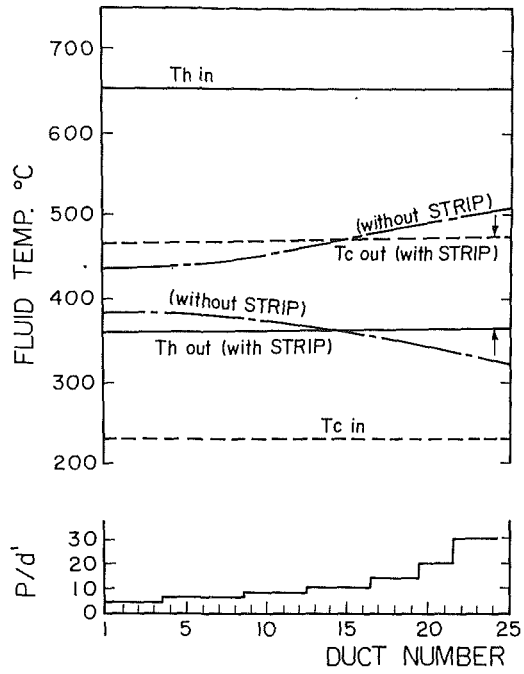

Fig. 6 Optimal temperature and twisted-pitch distributions

at several high temperatures up to 650°C. The friction coefficient f defined by $\{\Delta p/\rho u^2/2\}\cdot\{d_e/4\,\Delta z\}$, which is obtained in the experiments, is proportional to the -0.06 power of Re. The effect of the physical properties on it is dependent on the power of -0.1 of the ratio T_w/T_b in the turbulent region. This is shown in the following formula reported by Mori et al. (1976) where C is the proportionality constant and is a function of R and the ratio of strip width d' and twist pitch P.

$$\text{Square duct}: \; C = 8.70R + 2.52$$
$$\text{Rectangular duct}: \; C = 7.33R + 2.50$$

$$R = (\pi d'/P)^2/\{1+(\pi d'/P)^2\}$$

The experimental results were correlated as Nusselt numbers, defined by $\alpha d_e/\lambda$. The Nusselt number is found to be proportional to the 0.8 power of the Reynolds number in the turbulent region and to the power of -0.5 of the ratio of the wall and fluid bulk temperatures as shown in Fig. 5. The reason that the data for the aspect ratio of 3 are slightly larger than those of other aspect ratios is that in calculating Nusselt number the surface area of the separator is not taken into consideration. The construction of the conventional compact plate-fin heat exchanger is symmetric. To make a comparison of experimental and predicted results, the tested heat exchanger was not as large in size, as explained later on. However, this fact causes hardly any disadvantage in applying the results to practical compact heat exchangers. As seen from the middle right-hand picture of Fig. 1(b), the heat exchanger consists of three sections: the two crossflow sections set at each side of the counterflow section. The insertion of twisted strips in the channels of the crossflow section is not advisable, because the length of the strips varies from channel to channel and is not effective enough. Therefore, twisted strips were installed in the channels of the hot and cold gas stages of the counterflow section. For bare channels in the crossflow section, the results reported so far by Rohsenow and Hartnett (1973) are used in the calculations. In the calculations of the temperature fields of hot and cold gases, under the condition of making the pressure drop in each channel equal, the flow rate distribution in the channels with twisted strips was calculated by several trial-and-error calculations to get the optimal twist-pitch distribution of strips, until a uniform outlet temperature of the heated gas is obtained. As the twist pitch of the strip is different in each channel, the transferred heat would vary with each channel. The stage consists of 25 channels in parallel. In Fig. 6, the calculated results without strips are shown by chained lines, while those with the strips of optimal twist pitch are shown by solid and broken lines for the given total exchanged heat when the inlet temperature of the hot gas is 650°C and that of cold gas is 230°C. The counterflow section is 1000 mm long and 355 mm wide. Thirteen stages are for cold gas and 12 for hot gas flows. The heat exchanged is about 40 kW. As seen from Fig. 6, the maximum temperature of the heated gas is reduced because of the optimal twist-pitch distribution, resulting in the relaxation of the thermal stress. The distribution of the ratios of twisted pitch of the strip is shown in the lowest part of the figure by a solid line. The optimal pitch distribution changes discontinuously because the twisted strips were divided into seven groups to facilitate easy production of the twisted strips. When the twist pitch is small, the strong secondary flow induced causes remarkable heat transfer enhancement. As explained above, the parameter to optimize the outlet temperature of the heated gas by making it uniform is the twist pitch of inserted strips. The optimizing procedure is easily performed by iterative numerical calculations. The optimizing procedure developed in this paper can be applicable to the relaxation of thermal stresses when the numerical calculation method of three-dimensional stress distribution of a complicated honeycomb structure is developed.

4 Control of Tube Vibration of High-Temperature Shell and Tube Heat Exchanger by Insertion of Flat Plates at Optimal Intervals for Separating Tube Arrays

Among various kinds of heat exchangers, only the metallic shell-and-tube heat exchanger of adequate construction may be available with high reliability at about 900°C when a proper metal is used. One of the important problems in the development of the high temperature gas–gas heat exchangers of shell-and-tube type is the tube vibration caused by vortex shedding or vortex interaction. Mori et al. (1986) reported that the von Karman vortices behind tubes cause strong pressure fluctuations of a constant frequency around the upstream tubes. This is the main course of tube vibration. In consideration of the pressure fluctuation caused when von Karman vortices are the main cause of the tube vibration, in the case of the in-line tube array construction, the insertion of separating flat plates between the parallel tube arrays is discussed in order to make the distance between the plates optimal. The experimental setup for this problem has seven tubes of the in-line arrangement between the two parallel flat plates. Three tubes in the middle are elastically supported. The transverse and lateral displace-

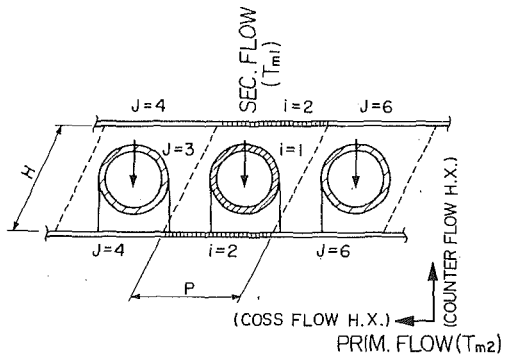

Fig. 7 Experimental rig for heat transfer enhancement performance by separating plates

ments of the three tubes were measured. The tube diameter D was fixed at 20 mm and the distance H between the separating plates was varied. The experimental results proved that when H/D was larger than 2, the transverse displacement was as large as that of a single cylinder in an open flow. By reducing the ratio H/D below 2, the transverse displacement becomes smaller. The optimal value of H/D ratio was found as 1.53. The pitch of the tubes was taken to be almost the same value as the distance between the plates. Thus the tube vibration is well controlled by optimizing the distance between the separating plates. The other important role of the plates separating in-line tube arrays is the heat transfer enhancement by surface radiative heat transfer between the plates and the tubes. Figure 7 shows a heat transfer experimental device that has almost the same configuration used for the study of tube vibration. The flow and heat transfer model shown in Fig. 7 is applicable to shell-and-tube heat exchangers of the helical and U-tube type. The heated gas flows in the tube. At high temperatures, a lot of radiative heat is expected to be transferred from the separating plates to the tube surface, and significant heat transfer enhancement is anticipated. The experimental results were reported by Mori et al. (1976). The heat transfer enhancement factor E, which is defined as the effective heat transfer coefficient divided by the purely convective heat transfer coefficient divided by the purely convective heat transfer coefficient, is about 1.1 at low temperatures and increases up to 1.7 at a temperature of 900°C. The flat thin plates inserted between the in-line tube arrays can not only control the tube vibration but also make a contribution to heat transfer enhancement (Watanabe et al., 1983).

Based on the fundamental research explained above, a high-temperature He-He heat exchanger was built and tested in Japan using funds from the Ministry of International Trade and Industry as an important component in an advanced high-temperature gas cooled nuclear reactor system, which heats He up to 950°C and will be useful not only for generation of electricity but for production of hydrogen. The heat exchanger consists of helical coil tubes and has such advantages as axially symmetric construction, acceptability of thermal elongation, feasibility of scale-up, and capability of in-service inspection. The high-temperature heat exchanger thus designed and manufactured based on experimental data described above, and shown in Fig. 8, was tested as reported by Mori (1985). In place of separating flat plates, layers of thin cylindrical shell 6 mm thick are installed between the helical tube layers. No tube vibration was observed and heat transfer enhancement by radiation was observed. Based on this success, a larger high-temperature heat exchanger of the same construction as that in Fig. 8, having helical tubes, separate cylindrical shells, and a capacity of about 10 MW exchanged heat, is now under construction in Japan for use in the thermal system of an experimental high-temperature gas-cooled nuclear reactor for

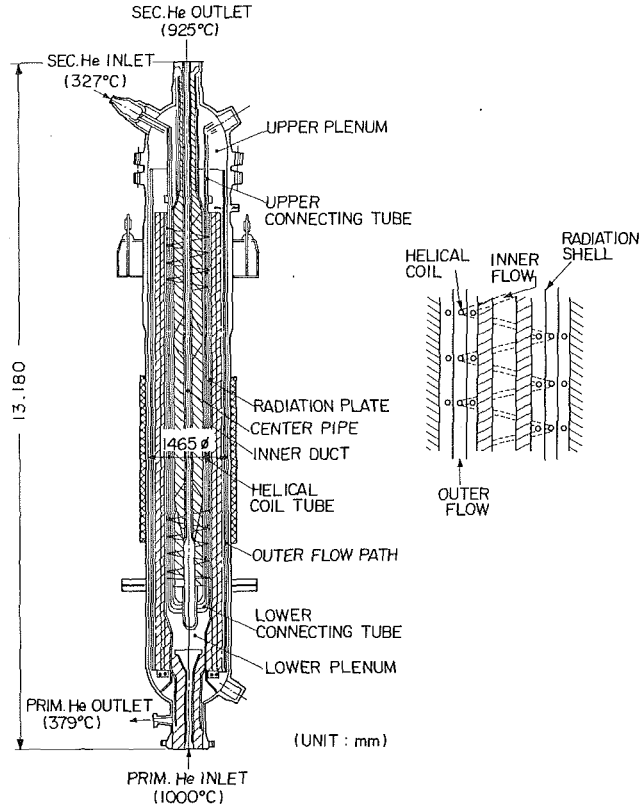

Fig. 8 High-temperature shell-spiral tube heat exchanger with separating cylindrical shells

multipurpose applications, such as for the production of hydrogen as a future clean fuel.

5 Conclusion

This paper discusses three typical problems closely related to heat transfer. The subject of the discussion is to find a parameter highly related to heat transfer and controlling the essential performance of the phenomenon, and to optimize the parameter in order to satisfy the condition required for the problems. The three topics taken up are the deposition of the semi-conductor layer in a CVD furnace as an example from the high-technology field, enhancement of reliability of a compact heat exchanger at high temperatures, and development of a shell-and-tube heat exchanger for a high-temperature gas-cooled nuclear reactor system. Based on theoretical and experimental studies, the following conclusions on the controlling parameter and optimal condition in the case of the three examples are obtained.

In the CVD furnace problem, the parameter controlling spatial uniformity of the deposit layer thickness is found to be the side wall temperature distribution and the optimal condition of the distribution is experimentally obtained. The optimal case is an unsteady flow containing two pairs of vortices and the time-averaged temperatures of the horizontal planes are uniform.

In the compact plate-fin heat exchanger study, a proposal to insert a twisted strip with twist pitch appropriate to each channel is made for the purpose of making the outlet temperature of the heated gas uniform. The optimal twist-pitch distribution is numerically calculated. The final target of development of a reliable compact plate-fin heat exchanger should be the relaxation of the maximum thermal stress of the exchanger.

In the flow-induced tube vibration problem of the shell-and-tube heat exchanger, installation of separating plates between

the in-line tube array is proposed. By setting the optimal interval between the plates, tube vibration is fully controlled and heat transfer is enhanced by radiation when used in a system such as a gas-cooled nuclear reactor.

The principle of the studies in this paper is applicable to heat transfer problems in which the optimal condition is a factor other than heat transfer enhancement, for example, enhancement of the reliability of the heat exchanger and other similar factors.

References

Bergles, A. E., 1985, "Augmented Heat Exchangers for High Temperature Application," *High Temperature Heat Exchangers*, Hemisphere, New York.

Moffat, H., and Jensen, K. F., 1986, "Complex Flow Phenomena in MOCVD Reactors," *J. Crystal Growth*, Vol. 77, pp. 108–110.

Mori, M., Mizuno, M., Ito, M., and Urabe, S., 1985, "Design and Thermal Dynamic Analysis on the Intermediate Heat Exchanger for HTGR," *High Temperature Heat Exchangers*, Hemisphere, New York.

Mori, Y., Taira, T., and Watanabe, K., 1976, "Heat Transfer Augmentation by Radiation Plates," ASME Paper No. 76-HT-3.

Mori, Y., 1985, "Future Development of High Temperature Heat Exchanger," *High Temperature Heat Exchangers*, Hemisphere, New York.

Mori, Y., Hijikata, K., and Nobuhara, T., 1986, "A Fundamental Study of Symmetrical Vortex Generation Behind a Cylinder by Wake Heating, or Splitter Plate or Mesh," *Int. J. Heat Mass Transfer*, Vol. 29, pp. 1193–1201.

Mori, Y., and Koizumi, H., 1989, "Control of Bénard Cell Performance in a Combined Flow in a Rectangular Horizontal Duct of Heated Bottom Wall," *JSME Transactions*, Series B, Vol. 55, pp. 820–827.

Rohsenow, W. M., and Hartnett, J. P., 1973, *Handbook of Heat Transfer*, McGraw-Hill, New York, pp. 7–112.

Sano, M., and Şamada, Y., 1985, "Measurement of the Lyapunov Spectrum From a Chaotic Time Series," *Phys. Rev. Let.*, Vol. 55, pp. 1082–1085.

Savkar, S. D., 1986, "Flow-Induced Vibration in Heat Exchanger—A Review," *Heat Transfer in High Technology and Power Engineering*, Hemisphere, New York.

Watanabe, K., Mori, Y., and Taira, T., 1983, "Study on Heat Transfer and Optimization of Heat Transfer," *JSME Transactions*, Series B, Vol. 55, pp. 685–694.

Yang, K. T., 1988, "Transition and Bifurcations in Laminar Buoyant Flows in Confined Enclosures," ASME JOURNAL OF HEAT TRANSFER, Vol. 110, pp. 1191–1204.

R. Shau

J. Batista

G. F. Carey

Computational Fluid Dynamics Laboratory,
Aerospace Engineering & Engineering Mechanics Dept.,
The University of Texas at Austin,
Austin, TX 78712

An Improved Algorithm for Inverse Design of Thermal Problems With Multiple Materials

An optimization scheme and matrix partitioning strategy are developed in conjunction with a boundary element solution procedure for inverse design in heat transfer. The optimal control problem is to locate interior heating or cooling passages inside a coated conducting domain to achieve a desired boundary temperature when the heat flux is specified (or vice versa). As the interior passages can be parameterized with a few variables, the optimization problem is of low dimension. the matrix partitioning scheme for the boundary element system and optimization search procedure lead to a fast computational scheme for this class of problems.

Introduction

Inverse design problems arise in many areas of engineering and typically involve an analysis calculation for temperature, stress, flow velocities, and so on, coupled to an iterative optimization scheme to achieve the design goal from an initial configuration. Examples include least-weight design for structures, shock-free design in aerodynamics, and thermal management in heat transfer problems. In the present study we consider a class of problems for inverse design in heat transfer that lead to a low-order optimization problem coupled with a large-scale analysis calculation. That is, there are relatively few control variables for the optimization, but the analysis calculation potentially may be prohibitive if many optimization steps are needed. Moreover, the design problems in question involve a natural separation of the analysis variables to subclasses that are influenced only to limiting degrees by changes in the design variables. This leads to a natural partitioning of the associated matrix problem that can be exploited in computations.

More specifically the focus of the present study deals with an improved algorithm when a boundary element method is applied for steady heat transfer calculations of optimization problems with multiple material layers. Our work is a natural extension of previous studies initiated on this class of problems by Kennon (1984), Kennon and Dulikravich (1985), Chiang (1985), and Chiang et al. (1987). The design objective in these studies is to locate interior cooling or heating passages within the domain so that a given surface temperature or flux is achieved. Related applications arise for internally cooled turbine blades and cooling of electronic equipment. Since the problems considered involve the surface field, a boundary element method for heat transfer analysis is appropriate. This is to be embedded efficiently within an optimization algorithm.

The turbine blade application has been the subject of previous experimental design studies by Hay et al. (1983), and Hannis and Smith (1983), and provides a test case for model comparison. A main distinction in the present algorithm is the form of partitioning introduced in the boundary element problem when there are multiple layers (material coatings). This new block partitioning scheme implies that the matrix calculations at each optimization step are significantly reduced when compared with previous schemes. As a result, computation time for representative calculations may be reduced by as much as an order of magnitude for problems where a moderate number of optimizations steps are required. A new search strategy and other improvements to the optimization scheme further accelerate convergence and improve the robustness of the algorithm.

Contributed by the Heat Transfer Division for publication in the JOURNAL OF HEAT TRANSFER. Manuscript received by the Heat Transfer Division June 17, 1988. Keywords: Computer Codes, Conduction, Numerical Methods.

Analysis

1 Problem Statement. Consider heat transfer in a domain with specified outer boundary temperature and containing several layers as coatings. The primary inverse problem is to determine the location and size of coolant passages in the interior to produce a desired heat flux distribution at the outer surface. Certain auxiliary constraints such as the minimum distance of approach of the coolant "holes" to the outer boundary or to one another are also specified.

If the temperature u is specified on the interior coolant boundaries and the temperature on the exterior boundary, then the associated boundary value problem can be solved to determine a flux on the outer boundary. This will, in general, differ from the design flux Q. The error $Q - q$ on the outer surface can be used to construct an objective function $E = E(Q-q)$ for the optimization problem with respect to the parameters controlling the coolant passage location and size. In the present studies the coolant passages will be circular and hence the control variables are the locations (x_i, y_i) of the circle centers and their radii r_i, $i = 1, 2, \ldots, m$. Values of v_i (x_i, y_i, r_i) may be incrementally adjusted in the optimization process to minimize E.

Evidently there are few optimization variables, so this implies a low dimensional optimization problem is to be solved. The efficiency of the method then rests largely on the cost of solving the boundary-value problem approximately at each optimization step. A direct approach to the optimization problem would be to set up and solve successive boundary element systems for each new configuration as $\mathbf{v}$ is incrementally adjusted in the optimization step. This would necessitate full system formation and solution at each step, which implies that the procedure would not be practical in those cases where a moderate or large number of optimization steps are required. Clearly, as the locations of grid points on the outer boundary and interior layers are fixed, most of the entries in the boundary element system will not change throughout the procedure. This observation motivated the approaches in the previous studies (cited in the Introduction). The current work is a further extension on this class of algorithms that leads to a more efficient scheme in the case where the domain is layered.

2 Boundary Element Formulation. Consider the multilayered domain $\Omega = \cup\Omega_i$ shown in Fig. 1 with layer Ω_i bounded by contours Γ_i, Γ_{i+1} and interior "core" Ω_0 contain-

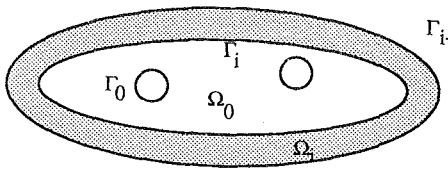

Fig. 1 Annular subdomain Ω_i bounded by Γ_i and Γ_{i+1} and containing inner passages Γ_i

ing heating or cooling passages $\Gamma_0 = \cup\gamma_j$, $j=1, 2, \ldots, J$. The subdomain Ω_i has material property k_i and fundamental solution for two-dimensional problems $u_i^* = (1/2\pi k_i)\ln(1/r)$ for diffusion operator $\nabla\cdot(k\nabla(\cdot))$.

Applying Green's third identity to a representative annular subdomain Ω_i and introducing the fundamental solution gives the integral equation for x in Ω_i.

$$\beta_i u(x) + \int_{\Gamma_i} \left(uk_i \frac{\partial u_i^*}{\partial n} - u_i^* k_i \frac{\partial u}{\partial n}\right) ds + \int_{\Gamma_{i+1}} \left(uk_i \frac{\partial u_i^*}{\partial n} - u_i^* k_i \frac{\partial u}{\partial n}\right) ds = 0 \tag{1}$$

where n denotes the outward normal direction from the respective boundaries of Ω_i, $\beta_i = \theta/2\pi$ where θ is the interior angle at x ($\theta = 2\pi$ if x is interior to Ω_i), and the integrals on Γ_i, Γ_{i+1} are oppositely directed.

In particular, equation (1) holds for x on Γ_i and Γ_{i+1} so we have a pair of boundary integral equations for Ω_i. For a continuously turning boundary contour, $\beta_i = 1/2$. Since we are dealing with a multilayered domain and Γ_{i+1} is common to Ω_i and Ω_{i+1}, it proves convenient to orient integrals in the same direction and treat contour normals similarly. Reversing the direction of integration on Γ_i and the associated normals preserves the signs in the first integral of equation (1). Setting $q_i = k_i\, \partial u/\partial n$, $q_i^* = k_i\, \partial u_i^*/\partial n$ for the normal flux components, the boundary integral equation has the form

$$\beta_i u(x) + \int_{\Gamma_i} (uq_i^* - u_i^* q_i) ds + \int_{\Gamma_{i+1}} (uq_i^* - u_i^* q_i) ds = 0 \tag{2}$$

and this is representative of the boundary integral contributions for any layer in Ω.

But Γ_{i+1} is shared by Ω_i and Ω_{i+1} so that setting $i+1$ for i in equation (2) yields a similar integral contribution on Γ_{i+1} from Ω_{i+1}. Both u and the normal flux q are continuous across Γ_{i+1} so $q_{i+1} = q_i$ here. Further, the fundamental solutions on Ω_i and Ω_{i+1} satisfy $k_i u_i^* = k_{i+1} u_{i+1}^*$, $k_i q_i^* = k_{i+1} q_{i+1}^*$ on Γ_{i+1} so that

$$\oint_{\Gamma_{i+1}} (uq_{i+1}^* - u_i^* q_{i+1}) ds = \frac{k_i}{k_{i+1}} \oint_{\Gamma_{i+1}} (uq_i^* - u_i^* q_i) ds \tag{3}$$

Hence the contribution of the second integral in equation (2) for x on Γ_{i+1} can be obtained simply by scaling the value on Γ_{i+1} from the previous layer by the factor k_i/k_{i+1}. Similarly, the value of the first integral in equation (2) for x on Γ_i would be available from the calculation on Ω_{i-1} by scaling with (k_{i-1}/k_i).

Introducing a boundary element discretization Γ_i^h, Γ_{i+1}^h and expansions u_h, q_{ih} the boundary element system corresponding to equation (2) with control point $\mathbf{x}_k$ on the boundary is defined by Brebbia (1980) or Carey and Oden (1983)

$$\beta_i u_h(\mathbf{x}_k) + \int_{\Gamma_i} (u_h q_i^* - u_i^* q_{ih}) ds + \int_{\Gamma_{i+1}} (u_h q_i^* - u_i^* q_{ih}) ds = 0 \tag{4}$$

where in the integrand $u_h = u_h(s)$, $q_h = q_h(s)$, $q_i^* = q_i^*(\mathbf{x}_k; s)$ and $u_i^* = u_i^*(\mathbf{x}_k; s)$. Setting u_h = constant in equation (4) determines β_i. Evaluating the integral contributions in equation (4) by accumulating element integrals on Γ_i and Γ_{i+1}, the boundary element equations for Ω_i with $\mathbf{x}_k$ on Γ_i can be written conveniently in block system form as

$$\mathbf{H}_{ii}^{(i)}\mathbf{u}_i + \mathbf{G}_{ii}^{(i)}\mathbf{q}_i + \mathbf{H}_{ii+1}^{(i)}\mathbf{u}_{i+1} + \mathbf{G}_{ii+1}^{(i)}\mathbf{q}_{i+1} = \mathbf{0} \tag{5}$$

where $\mathbf{H}_{ii}^{(i)}$ corresponds to the contributions from $\beta_i u_h(\mathbf{x}_k) + \oint_{\Gamma_i} u_h q_i^* ds$, $\mathbf{G}_{ii}^{(i)}$ to $-\oint_{\Gamma_i} u_i^* q_{ih} ds$, and so on. The first subscript of the block matrices in equation (5) corresponds to the contour that control point $\mathbf{x}_k$ traverses and the second subscript corresponds to the integral contour being evaluated. The superscript indicates the domain Ω_i. Note that, as usual, the diagonal entries corresponding to β_i can be determined from the appropriate boundary angle at the control point or by means of an auxiliary problem for $U = 1$. Replacing the first subscript of each matrix in equation (5) by $i+1$ gives the form of the second boundary element subsystem of Ω_i associated with $\mathbf{x}_k$ on Γ_{i+1},

$$\mathbf{H}_{i+1\,i}^{(i)}\mathbf{u}_i + \mathbf{G}_{i+1\,i}^{(i)}\mathbf{q}_i + \mathbf{H}_{i+1\,i+1}^{(i)}\mathbf{u}_{i+1} + \mathbf{G}_{i+1\,i+1}^{(i)}\mathbf{q}_{i+1} = \mathbf{0} \tag{6}$$

The block boundary element system equations (5) and (6) can be computed for each subdomain sequentially and boundary conditions specified to construct a block partitioned system for the boundary-value problem on Ω. Note also that, in view of equation (3) it follows that

$$\mathbf{G}_{i+1\,i+1}^{(i+1)} = \frac{k_i}{k_{i+1}}\mathbf{G}_{i+1\,i+1}^{(i)} \text{ and } \mathbf{H}_{i+1\,i+1}^{(i+1)} = \frac{k_i}{k_{i+1}}\hat{\mathbf{H}}_{i+1\,i+1}^{(i)} \tag{7}$$

where $\hat{\mathbf{H}}_{i+1\,i+1}^{(i)}$ agrees with $\mathbf{H}_{i+1\,i+1}^{(i)}$ except that the contribution to the diagonal due to β_{i+1} must first be scaled by the reciprocal k_{i+1}/k_i. Similar relations hold on Γ_i for the Ω_{i-1} and Ω_i contributions.

As an example, let us consider a single system ($N=2$) with $\Omega = \Omega_0 \cup \Omega_1$, and u specified on Γ_0 and Γ_2. From equations (5) and (6) the block-partitioned system is

$$\begin{bmatrix} \mathbf{H}_{00}^{(0)} & \mathbf{G}_{00}^{(0)} & \mathbf{H}_{01}^{(0)} & \mathbf{G}_{01}^{(0)} & \mathbf{0} & \mathbf{0} \\ \mathbf{H}_{10}^{(0)} & \mathbf{G}_{10}^{(0)} & \mathbf{H}_{11}^{(0)} & \mathbf{G}_{11}^{(0)} & \mathbf{0} & \mathbf{0} \\ \mathbf{0} & \mathbf{0} & \mathbf{H}_{11}^{(1)} & \mathbf{G}_{11}^{(1)} & \mathbf{H}_{12}^{(1)} & \mathbf{G}_{12}^{(1)} \\ \mathbf{0} & \mathbf{0} & \mathbf{H}_{21}^{(1)} & \mathbf{G}_{21}^{(1)} & \mathbf{H}_{22}^{(1)} & \mathbf{G}_{22}^{(1)} \end{bmatrix} \begin{bmatrix} \mathbf{u}_0 \\ \mathbf{q}_0 \\ \mathbf{u}_1 \\ \mathbf{q}_1 \\ \mathbf{u}_2 \\ \mathbf{q}_2 \end{bmatrix} = \mathbf{0} \tag{8}$$

Transposing terms involving prescribed boundary values $\mathbf{u}_0$, $\mathbf{u}_2$ and using equation (7), we have the block system

$$\begin{bmatrix} \mathbf{G}_{00}^{(0)} & \mathbf{H}_{01}^{(0)} & \mathbf{G}_{01}^{(0)} & \mathbf{0} \\ \mathbf{G}_{10}^{(0)} & \mathbf{H}_{11}^{(0)} & \mathbf{G}_{11}^{(0)} & \mathbf{0} \\ \mathbf{0} & \frac{k_0}{k_1}\hat{\mathbf{H}}_{11}^{(0)} & \frac{k_0}{k_1}\mathbf{G}_{11}^{(0)} & \mathbf{G}_{12}^{(1)} \\ \mathbf{0} & \mathbf{H}_{21}^{(1)} & \mathbf{G}_{21}^{(1)} & \mathbf{G}_{22}^{(1)} \end{bmatrix} \begin{bmatrix} \mathbf{q}_0 \\ \mathbf{u}_1 \\ \mathbf{q}_1 \\ \mathbf{q}_2 \end{bmatrix} = - \begin{bmatrix} \mathbf{H}_{00}^{(0)}\mathbf{u}_0 \\ \mathbf{H}_{10}^{(0)}\mathbf{u}_0 \\ \mathbf{H}_{12}^{(1)}\mathbf{u}_2 \\ \mathbf{H}_{22}^{(1)}\mathbf{u}_2 \end{bmatrix} \tag{9}$$

which can be solved for the unknown nodal temperature and flux values.

In the context of the present optimization problem, boundary element systems such as equation (9) are to be solved many times, and our purpose now is to develop a special partitioning scheme, so that repeated solution is highly efficient. The first

important observation is that several of the entries in equation (9) do not change during successive optimization steps and hence do not need to be recomputed. More specifically, only the location of the interior passage boundaries $\Gamma_0 = \cup \gamma_j$ are altered.

For notational convenience let us write the system equation (9) as

$$\mathbf{A}\mathbf{x} = \mathbf{f} \tag{10}$$

where $\mathbf{A}$ is naturally partitioned to blocks $\mathbf{A}_{ij}$, as shown in equation (9), with $\mathbf{A}_{14} = \mathbf{A}_{24} = \mathbf{A}_{31} = \mathbf{A}_{41} = \mathbf{0}$. The central idea is to proceed to eliminate successively $\mathbf{x}_4$, then $\mathbf{x}_3$, etc., in a manner similar to the back-substitution step of Gaussian elimination. In this way the partitioned problem leads to a set of lower dimensional matrix inversion computations that need to be done only at the first optimization step. Successive optimization steps then require elimination solution of a low dimensional problem for $\mathbf{z}_1$ (i.e., for $\mathbf{q}_0$).

Summarizing the main steps, from equation (10),

$$\mathbf{x}_N = \mathbf{A}_{NN}^{-1}\mathbf{f}_N - \mathbf{A}_{NN}^{-1}\mathbf{A}_{NN-1}\mathbf{x}_{N-1} - \mathbf{A}_{NN-2}^{-1}\mathbf{x}_{N-2} \tag{11}$$

This pre-eliminates $\mathbf{x}_N$ in favor of $\mathbf{x}_{N-1}$ and $\mathbf{x}_{N-2}$. This involves inversion of block $\mathbf{A}_{NN}$ together with block matrix multiplications. Continuing to the equation for $\mathbf{x}_{N-1}$, and using equation (11) for condensation we obtain

$$\mathbf{x}_{N-1} = (\mathbf{A}_{N-1N-1} - \mathbf{A}_{N-1N}\mathbf{A}_{NN}^{-1}\mathbf{A}_{NN-1})^{-1}[\mathbf{f}_{N-1} - \mathbf{A}_{N-1N}\mathbf{A}_{NN}^{-1}\mathbf{f}_N + (\mathbf{A}_{N-1N}\mathbf{A}_{NN}^{-1}\mathbf{A}_{NN-2} - \mathbf{A}_{N-1N-2})\mathbf{x}_{N-2}] \tag{12}$$

where requires inversion of the new composite block matrix on the right to pre-eliminate $\mathbf{x}_{N-1}$. This procedure clearly can be carried to higher levels for $\mathbf{x}_{N-2}, \mathbf{x}_{N-3}, \ldots, \mathbf{x}_2$, necessitating inversion of a composite block matrix at each step. Finally, the problem is reduced, by this condensation process, to solution of the system for $\mathbf{x}_1$ (i.e., $\mathbf{q}_0$), which must be solved at least once during each optimization step. All the prior condensation steps and matrix inversions still apply, and herein lies the efficiency of the method when a sufficiently large number optimization steps are needed.

Each block matrix inverse is of size equal to the number of nodes n_i on the interface concerned. The matrix inversion is of order $(n_i)^3$ so the operation count for inversion of $(N-1)$ blocks is $O(\Sigma_{i=1}^{N} n_i^3)$. If $n_i = O(n)$ for all $i > 0$, we have $O((N-1)n^3)$ operations. Note also that matrix multiplication requires the same number of operations as inversion so the total work estimate for the block condensation approach is $O(k(N-1)n^3)$ where $k-1$ is an estimate of the average number of new block matrix products required per row.

It is evident that this scheme is highly recursive and becomes increasingly complex as the size N of the block system increases. Moreover, it is important that matrix products from previous levels not be repeated at higher levels if k is to be kept small and optimal efficiency realized. To demonstrate these aspects of the algorithm we take the problem in equation (9) and carry out all the steps in algorithm form.

Algorithm

Row 4 Condensation (11)
Compute $\mathbf{A}_{44}^{-1}$ and overstore† $\mathbf{A}_{44}^{-1} \rightarrow \hat{\mathbf{A}}_{44}$.
Using equation (11), compute: $\mathbf{A}_{44}^{-1}\mathbf{f}_4 \rightarrow \hat{\mathbf{f}}_4$;
$\mathbf{A}_{44}^{-1}\mathbf{A}_{42} \rightarrow \hat{\mathbf{A}}_{42}$; $\mathbf{A}_{44}^{-1}\mathbf{A}_{43} \rightarrow \hat{\mathbf{A}}_{43}$
(so $\mathbf{x}_4 = \hat{\mathbf{f}}_4 - \hat{\mathbf{A}}_{42}\mathbf{x}_2 - \hat{\mathbf{A}}_{43}\mathbf{x}_3$)

Row 3 Condensation (12)
Compute $(\mathbf{A}_{33} - \mathbf{A}_{34}\hat{\mathbf{A}}_{43})^{-1} \rightarrow \hat{\mathbf{A}}_{33}$
Compute $\mathbf{f}_3 - \mathbf{A}_{34}\hat{\mathbf{f}}_4 \rightarrow \hat{\mathbf{f}}_3$
Compute $\mathbf{A}_{34}\hat{\mathbf{A}}_{42} - \mathbf{A}_{32} \rightarrow \hat{\mathbf{A}}_{32}$
Compute $\hat{\mathbf{A}}_{33}\hat{\mathbf{f}}_3 \rightarrow \hat{\mathbf{f}}_3$
Compute $\hat{\mathbf{A}}_{33}\hat{\mathbf{A}}_{32} - \hat{\mathbf{A}}_{32}$
(so $\mathbf{x}_3 = \hat{\mathbf{f}}_3 - \hat{\mathbf{A}}_{32}\mathbf{x}_2$)

Row 2 Condensation
Compute $(\mathbf{A}_{22} + \mathbf{A}_{23}\hat{\mathbf{A}}_{32}) \rightarrow \hat{\mathbf{A}}_{22}$
Compute $(\mathbf{f}_2^* - \mathbf{A}_{23}\hat{\mathbf{f}}_3) \rightarrow \hat{\mathbf{f}}_2^*$
Compute $\mathbf{A}_{22}^{-1} - \hat{\mathbf{A}}_{22}$
Compute $\hat{\mathbf{A}}_{22}\hat{\mathbf{f}}_2^* \rightarrow \hat{\mathbf{f}}_2^*$
Compute $\hat{\mathbf{A}}_{22}\mathbf{A}_{21}^* \rightarrow \hat{\mathbf{A}}_{21}^*$
(so $\mathbf{x}_2 = \hat{\mathbf{f}}_2^* - \hat{\mathbf{A}}_{21}^*\mathbf{x}_1$)

Reduced System for x_1
Compute $(\mathbf{A}_{11}^* - \mathbf{A}_{12}^*\hat{\mathbf{A}}_{21}^*) - \mathbf{A}_{13}^*\hat{\mathbf{A}}_{32}\hat{\mathbf{A}}_{21}^* \rightarrow \hat{\mathbf{A}}_{11}^*$
Compute $\mathbf{f}_1^* - \mathbf{A}_{12}^*\hat{\mathbf{f}}_2^* - \mathbf{A}_{13}^*\hat{\mathbf{f}}_3 - \mathbf{A}_{13}^*\hat{\mathbf{A}}_{32}\hat{\mathbf{f}}_2 \rightarrow \hat{\mathbf{f}}_1^*$
(so $\hat{\mathbf{A}}_{11}^* x_1 = \hat{\mathbf{f}}_1^*$ for elimination solution).

The entries with asterisks are recomputed for each optimization step. The major recalculations occur in the first row equation for $\mathbf{x}_1$ and some minor recalculations in the second row equation.

3 Constrained Optimization Algorithm. The problem to be addressed is one of constrained optimization: The position and size of the internal coolant boundaries are to be adjusted to minimize the error objective function E on the exterior boundary subject to geometric constraints to ensure that the "holes" remaining within the innermost domain Ω_0 do not approach one another too closely and have radii greater than a specified minimum level. The control variables for the optimization problem are the coordinates (x_i, y_i) of the hole centers and the hole radii r_i, as indicated in the overview of Section 1.

Several detailed features and refinements of the optimization algorithm related to the treatment of constraints, the line search strategy employed, and the gradient descent optimization procedure are now described. This scheme is employed in the numerical studies that follow in Section 4. We begin with some brief preliminaries describing the gradient optimization algorithm and then describe special features of the present constrained optimization procedure.

Gradient Method. In gradient-based optimization schemes, gradient information ∇E is computed at the current iterate $\mathbf{v}_n$ for the objective function E and used to determine a descent direction $\mathbf{d}_n$. A line search minimization procedure then gives the size α_n of the step to be taken in this direction. The sequence of iterates generated along the optimization "path" are then given by

$$\mathbf{v}_{n+1} = \mathbf{v}_n + \alpha_n \mathbf{d}_n$$

In this manner the optimization scheme reduces to successive steps in which search directions are determined and one-dimensional minimization (line search) is conducted.

As an example, the simplest strategy is the steepest descent method in which the direction is precisely $\mathbf{d}_n = -\nabla E(\mathbf{v}_n)$, so that the initial local rate of decrease of E is greatest. However, this method does not include information related to the curvature of the objective function (second derivatives) which is naturally important near the minimum. Consequently, the rate of convergence may be very slow. If a local Taylor series expansion is introduced and truncated beyond second derivatives, then minimizing this quadratic yields the well known Newton-Raphson iteration $\mathbf{v}_{n+1} = \mathbf{v}_n - \mathbf{G}_n^{-1}(\nabla E_n)$ where $\mathbf{G}_n$ is the Hessian of E evaluated at $\mathbf{v}_n$. This method can be improved by augmenting it with a line search. The method is expensive (especially in the present context) and may fail if $\mathbf{G}_n$ is not positive definite. Further, for a quadratic function

† ^ indicates array overstore of entries.

E, $\mathbf{G}=\mathbf{I}$ and the method then reverts to the steepest descent scheme. This form, together with the observation that a change of variables can accelerate the steepest descent (SD) scheme, leads naturally to the notion of preconditioning and the recursion

$$\mathbf{v}_{n+1}=\mathbf{v}_n+\alpha_n\mathbf{H}_n(\nabla E_n)$$

In the present work we employ a Davidon Fletcher Powell (DFP) scheme with periodic SD "restarts." In the DFP method the first step is by steepest descent and successive $\mathbf{H}_n$ are chosen to approximate the Hessian as a possitive definite secant update (Walsh, 1975). That is

$$\mathbf{H}_1=\mathbf{I}$$

$$\mathbf{H}_{n+1}=\mathbf{H}_n+\mathbf{A}_n+\mathbf{B}_n, \qquad n\geq 1$$

where

$$\mathbf{A}_n=\frac{\mathbf{w}_n\mathbf{w}_n^T}{\mathbf{w}_n{}^T\mathbf{u}_n}, \qquad \mathbf{B}_n=-\frac{\mathbf{H}_n\mathbf{u}_n\mathbf{u}_n^T\mathbf{H}_n}{\mathbf{u}_n^T\mathbf{H}_n\mathbf{u}_n}$$

with

$$\mathbf{w}_n=\alpha_n\mathbf{d}_n, \qquad \mathbf{d}_n=-\mathbf{H}_n(\nabla E_n)$$

and

$$\mathbf{u}_n=\nabla E_{n+1}-\nabla E_n$$

If the scheme "stagnates" and is converging too slowly, we restart with a steepest descent step.

Remark. Other optimization techniques such as the Polak-Ribiere conjugate gradient scheme may be similarly applied.

Line Search with Constraints. The basic line search procedure is to find the minimizer α_{opt} in a quadratic fit to E for three points along the line. This search must also accommodate the constraint that the "holes" lying within Ω_0 not approach one another too closely. Let us consider a typical line search, and for notational convenience drop the step index n. To accommodate the constraints better, the search direction vector $\mathbf{d}$ is first normalized to unit length. Because of the geometric nature of the constraints it is easy to calculate the maximum allowable stepsize $\alpha_{\max}$ such that $\mathbf{v}$ still remains in the "feasible" region: By simply checking the distance from the current circle centers to the nearest point on the discretized interface in the direction of search and ensuring that holes do not "overlap," the value of $\alpha_{\max}$ is obtained. This then determines the search interval.

Having determined the interval $[0, \alpha_{\max}]$, we next locate $\mathbf{v}^{(1)}=\mathbf{v}^{(0)}+\alpha^{(1)}\mathbf{d}$ such that $E^{(1)}=E(\mathbf{v}^{(1)})$ satisfies $E^{(1)}<E^{(0)}$ and then $\mathbf{v}^{(2)}=\mathbf{v}^{(0)}+\alpha^{(2)}\mathbf{d}$ such that $E^{(2)}>E^{(1)}$ with $0<\alpha^{(1)}<\alpha^{(2)}<\alpha^{\max}$. In the numerical calculations following, we first set $\alpha_1/\alpha_{\max}=c^p$ with parameters c, p specified. Early in the optimization procedure we set $p=1$ so that the first point tested is at fractional distance c from the origin point. The search continues from this point toward $\mathbf{v}^{(0)}$ until $\mathbf{v}^{(1)}$ is located. If this partial line search fails, then a full line search is made. After $\mathbf{v}^{(1)}$ is located, the interval $(\alpha^{(1)}, \alpha_{\max})$ is sampled to find $\mathbf{v}^{(2)}$ and the quadratic minimization completed.

Remarks:

1 The sampling procedure for $\alpha^{(1)}$ is modified as the optimization proceeds by increasing p. At the outset $p=1$ so the first trial for $\mathbf{v}^{(1)}$ is moderately distant from $\mathbf{v}^{(0)}$. Later in the optimization procedure p is increased so that the line search is carried out closer to the current iterate.

2 If the search for $\mathbf{v}^{(1)}$ fails due to the poor quality or properties of $\mathbf{H}$, then the method is restarted with $\mathbf{H}=\mathbf{I}$ for a steepest descent step.

3 Subspace variants of the scheme in which some control variables are not adjusted can be developed and used to accelerate the scheme. For instance, the radii may be fixed (small) for several optimization steps during which the hole centers move close to their "target" distinctions. Then the radii can be varied to complete the optimization process. This arrangement shows a great deal of improvement in computational efficiency, especially for cases with a large number of "holes." If a hole radius falls below a specified minimum value the hole can be "deleted."

4 Multiple solutions may exist corresponding to local minima. (We show an example later.) In this case the value of E determines the suitability of the computed design. Other configurations can be computed and special techniques introduced to try to determine a global minimizer. For example, initial holes can be redistributed and more holes added, but this will increase the cost of computation.

To summarize, the major steps in the algorithm are:

1. Initialize: Select starting vector $\mathbf{v}^{(0)}$, compute BEM solution, evaluate error objective function.
2. Optimization:
   For step $k=0, 1, 2, \ldots, K$
   Calculate $\nabla E(\mathbf{v}_k)$ by differencing BEM results
   Construct $\mathbf{H}$ and direction $\mathbf{d}_k$
   Calculate $\alpha_{\max}$
   Line search for α_k
   Update $\mathbf{v}_{k+1}=\mathbf{v}_k+\alpha_k\mathbf{d}_k$
   Test convergence criterion
   End.

Algorithm Performance. We begin with some performance studies for a representative problem to give an indication of the relative computational efficiency of the main procedural steps. The examples chosen correspond to heat transfer in a domain with a single layer coating and from one to three interior holes. A discretization of linear boundary elements was used in the numerical studies. The number of elements on the interface and outer boundary was doubled from 28 to 56 to 112 to assess the effect of problem size on efficiency. The number of elements per hole was also varied from 8 to 16 since this controls the size of the reduced problem. The objective function E is chosen to be the normalized discrete least-squares error in flux defined by

$$E=\left(\sum_{i=1}^{N}(Q_i-q_i)^2\Big/\sum_{i=1}^{N}Q_i^2\right)^{1/2}.$$

Results are summarized in Table 1 for the calculation and broken down as a percentage of total CPU time. We separate specifically the following: formation of $\mathbf{H}$, $\mathbf{G}$ block matrices; inversions (recall equations (11) and (12) and the associated condensation algorithm); matrix products in partition-condensation scheme; and Gaussian elimination (G.E.) for final reduced system. The results are further separated to identify those calculations that are made once only, denoted by (•), and those that are repeated at each subsequent step denoted by [•]. In most of the cases shown we see that the successive calculations that are repeated at each step are relatively inexpensive. The worst case is the first row of case 4 where there are 3 holes and 16 elements per hole. In this instance the reduced system is relatively large. At the other extreme, the fine outer mesh calculation in row 3 of case 1 demonstrates that the cost of repeated calculations is now negligible. We include also in the last column the total CPU time for the first calculation. In later case studies the rate of convergence of the optimization scheme is explored.

Remark. Note that this scheme involves a 4×4 block partitioning. Numerical studies on the smallest test problem in Table 1 indicate a savings of approximately 45 percent for the initial inversion when compared with the coarser 2×2 partition. The repeated calculations of the reduced problem are 30

Table 1 Performance of algorithm with mesh refinement and varying number of "holes" showing percent of total CPU time; (•) denotes initial calculation only, and [•] is for repeated optimization steps

Cases 1–4: # of Nodes	Formatting H and G %	Inverse %	Partition (Non Repeated) %	Partition (Repeated) %	G.E. %	Overall CPU(s) for the 1st Calculation
Outer: 28 Inter: 28 Hole: 8 # of Holes: 1	(41.1) [5.9]	23.2	31.00	[4.4]	[0.080]	12.14
Outer: 56 Inter: 56 Hole: 8 # of Holes: 1	(26.3) [2.0]	30.6	40.40	[2.6]	[0.014]	71.30
Outer: 112 Inter: 112 Hole: 8 # of Holes: 1	(15.3) [0.62]	36.0	47.20	[1.5]	[0.002]	475.50
Outer: 28 Inter: 28 Hole: 8 # of Holes: 3	(44.2) [16.9]	17.5	23.80	[12.7]	[1.200]	15.80
Outer: 56 Inter: 56 Hole: 8 # of Holes: 3	(28.1) [5.9]	27.1	36.54	[7.8]	[0.200]	78.80
Outer: 112 Inter: 112 Hole: 8 # of Holes: 3	(16.1) [1.8]	33.9	45.60	[4.2]	[0.040]	492.50
Outer: 28 Inter: 28 Hole: 8 # of Holes: 5	(45.47) [25.1]	13.1	17.60	[19.8]	[3.900]	21.40
Outer: 56 Inter: 56 Hole: 8 # of Holes: 5	(29.4) [9.6]	24.3	32.10	[13.2]	[0.900]	89.70
Outer: 112 Inter: 112 Hole: 8 # of Holes: 5	(16.6) [2.9]	32.9	43.10	[7.2]	[0.200]	520.52
Outer: 28 Inter: 28 Hole: 16 # of Holes: 3	(42.5) [27.8]	10.8	14.90	[23.0]	[5.600]	25.30
Outer: 56 Inter: 56 Hole: 16 # of Holes: 3	(29.4) [11.2]	21.9	29.70	[15.71]	[1.500]	96.90
Outer: 112 Inter: 112 Hole: 16 # of Holes: 3	(16.9) [3.5]	31.5	42.20	[8.8]	[0.300]	532.40

Table 2 Comparison of DFP, FR, and PR schemes; target (4.5, 13), $r = 0.6$

Initial Guess	OPT Scheme	# of Iterations & Error Level	# of SD Restarts
x y	DFP	12 (1.06%)	0
(8,10)	FR	13 (71.5%)	2
$r = 0.1$	PR	14 (71.5%)	2
x y	DFP	18 (1%)	0
(6,11)	FR	30 (1%)	0
$r = 0.1$	PR	30 (1%)	4

percent less than in the 2×2 partition. The efficiency increases with mesh refinement.

Comparison of Optimization Methods. In Fig. 2 we compare the Steepest Descent and Davidon Fletcher Powell algorithm performance for a typical test problem. In the DFP scheme the method was restarted every 2 steps or 4 steps, respectively.

As noted previously, other gradient optimization strategies such as the Fletcher Reeves (FR) and Polak Ribiere (PR) methods can be introduced instead of the DFP scheme. These conjugate-gradient methods are generally most suitable for large-scale optimization problems where there are many optimization variables (Fletcher, 1980). For small-scale optimization problems the DFP scheme is considered to be one of the most effective nonlinear search techniques.

A comparison of the DFP, FR, and PR methods is included in Table 2 for a turbine blade with a single hole and two different initial guesses. In the first case the starting guess is at (8, 10) with $r = 0.1$, and is far from the solution (4.5, 13) with $r = 0.6$. Both the FR and PR methods fail to reduce the error below 71 percent even with steepest descent restarts. In the second case with improved starting guess, all three methods converge, although PR requires restarting with steepest descent for the first four steps.

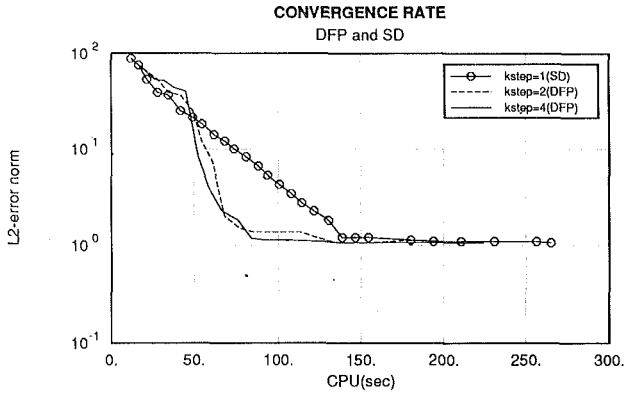

Fig. 2 Comparison between steepest descent and Davidon Fletcher Powell schemes

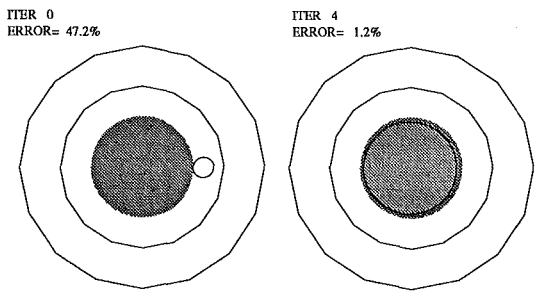

Fig. 3 Solution iterates 0, 4 for Problem 1; the shaded circle is the "target" and the open circle is the optimization iterate

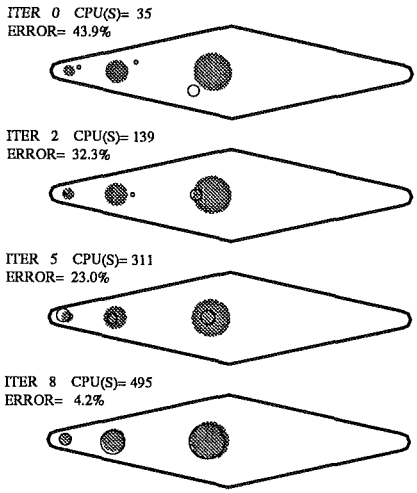

Fig. 4 Convergence history for Problem 2 at iterates 0, 2, 5, 8

Case Studies

Problem 1. The first problem is a simple test case for Laplace's equation in a "layered" annular domain between concentric circles. The analytic solution is for a concentric inner hole of radius 0.5. The interface is at $r = 0.8$ and the outer surface at $r = 1.2$. In the numerical study the inner hole is located at (0.6, 0.0) with radius 0.1.

The initial configuration and the results after four iterations are shown in Fig. 3 for calculations on the HARRIS 800 computer with discretizations of 8, 16, and 16 nodes for the inner, interface, and outer boundaries, respectively. The error objective function E starts at 47.2 percent and this decreases to 1.2 percent after four iterations. Numerical mesh refinement studies also revealed for this example the need for care in the matrix inversion step of the partition solution scheme. Full

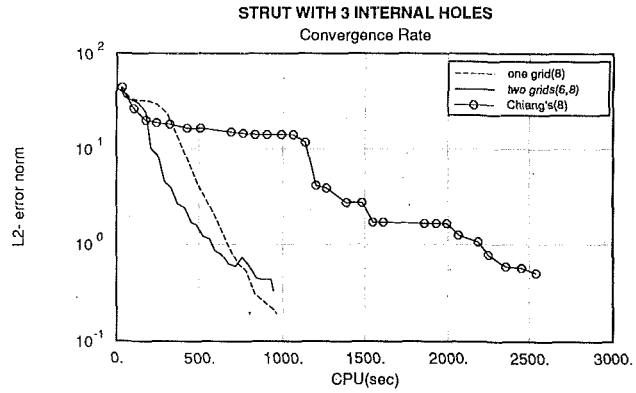

Fig. 5 Comparison of convergence rate for Problem 2

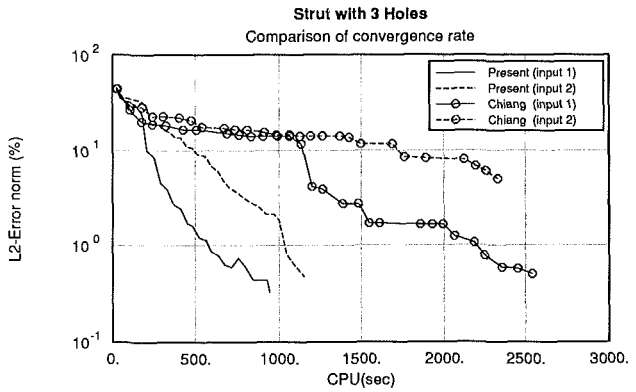

Fig. 6 Convergence comparison with inferior initial guess

pivoting was used to prevent errors due to scaling and finite precision calculations.

Problem 2. The second test problem is a strut with three holes that was also studied by Chiang (1985). The target is the configuration with three shaded holes shown in Fig. 4 and the open circles correspond to the current optimization solution step. There are 24 nodes on the interface and 24 on the exterior. Each inner hole has eight nodes. The initial configuration and solution at iterates 0, 2, 5, 8, are shown in the figure. By iteration eight the error is less than 5 percent and by iteration 16 (not shown) it is 0.2 percent. The convergence of the algorithm is graphed in Fig. 5 as a solid line and can be compared with the second solid line curve from Chiang (1985). To test the sensitivity of the schemes to the initial iterate, the problem was recomputed with the initial x coordinate of the largest hole perturbed 0.1 unit upward. The comparative results are shown in Fig. 6 as dashed lines.

Problem 3. The final test problem corresponds to internal cooling of a coated turbine blade. Here the purpose is to test the algorithm performance when the initial choice is remote. Optimization proceeds with fixed small radius for the first few steps until the target is sufficiently close and then the radius is also adjusted. The initial configuration gives E equal to 94 percent. After 18 iterates the error is of order one percent. The sequence of configuration iterates is given in Fig. 7.

The turbine blade problem was next computed for an example with five interior passages from the starting iterate shown in Fig. 8. The interesting feature of this calculation is the demonstration of nonunique solutions. By iteration 6 one of the holes has essentially disappeared and the size of one of the remaining holes increases to accommodate the boundary error better. As observed earlier, several local minima for the objective function may exist and the final solution may depend on the starting configuration, as in the present instance.

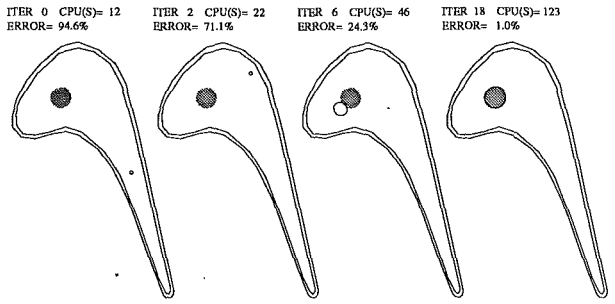

Fig. 7 Convergence history for Problem 3

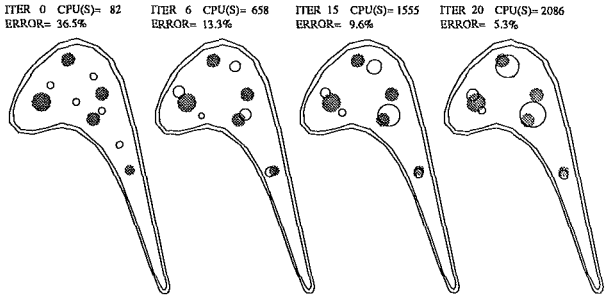

Fig. 8 Convergence history for Problem 8 exhibiting nonuniqueness

Concluding Remarks

The numerical results and performance studies indicate that for problems of practical interest involving coatings, the new partitioning scheme and algorithm are superior to previous strategies. This, in conjunction with the improved line search procedure, has been observed in some applications to improve computational efficiency by an order of magnitude.

Acknowledgments

We express our appreciation to T. L. Chiang for the use of his code in the comparison studies.

References

Brebbia, C. A., 1980, *The Boundary Element Method for Engineers*, Pentech Press.

Carey, G. F., and Oden, J. T., 1983, *Finite Elements: A Second Course*, Prentice Hall, New Jersey.

Chiang, T. L., Dulikravich, G. S., and Hayes, L. J., 1985, "Inverse Design of Coolant Flow Passages in Ceramically Coated Scram Jet Combustor Struts," in press.

Chiang, T., 1985, "Inverse Design of Composite Multi-holed Internally Cooled Turbine Blades," Master of Science Thesis, University of Texas at Austin.

Daniels, R. W., 1978, *An Introduction to Numerical Methods and Optimization Techniques*, North-Holland, New York.

Fletcher, R., 1980, *Practical Methods of Optimization*, Vol. 1, Wiley, New York.

Hannis, J. M., and Smith, M. K. D., 1983, "The Design and Testing of Air-Cooled Blading for an Industrial Gas Turbine," ASME *Journal of Engineering for Power*, Vol. 105, pp. 466-473.

Hay, N., Lampard, D., and Benmansour, S., 1983, "Effects of Crossflows on the Discharge Coefficient of Film Cooling Holes," ASME *Journal of Engineering for Power*, Vol. 105, pp. 243-248.

Kennon, S., 1984, "Novel Approaches to Grid Generation, Inverse Design and Acceleration of Iterative Schemes," Master of Science Thesis, University of Texas at Austin.

Luenberger, D. G., 1984, *Linear and Nonlinear Programming*, 2nd ed., Addison-Wesley.

Walsh, G. R., 1975, *Methods of Optimization*, Wiley, Chichester.

A Method for Analyzing Heat Conduction With High-Frequency Periodic Boundary Conditions

D. A. Caulk
Engineering Mechanics Department,
General Motors Research Laboratories,
Warren, MI 48090-9055

A special method is developed for calculating the steady periodic temperature solution in solid bodies with high-frequency boundary conditions. The numerical difficulty associated with steep gradients and rapid temperature variation near the boundary is addressed by confining all transient temperatures to a narrow boundary layer of constant depth. The depth of the layer is specified in advance and depends only on the period of the boundary disturbance and the thermal diffusivity of the material. The transient solution in the surface layer is represented by a polynomial in its transverse coordinate, with time-varying coefficients determined by a Galerkin method. This solution is coupled with the steady interior solution by imposing continuity of temperature and time-averaged heat flux at the interface. Although the method is sufficiently general to handle nonlinear boundary conditions, it turns out to be particularly useful in the important case of a time-varying heat transfer coefficient. In the latter case, it is possible to decouple the solution process and determine the solution in the transient surface layer separately from the solution in the steady interior. This reduces the effort of determining the complete steady periodic solution to little more than a routine steady analysis. Comparison with an exact solution shows that the polynomial representation for the transient solution in the surface layer converges very rapidly with increasing order. Moreover, the solution at the surface turns out to be relatively insensitive to the choice of the layer depth as long as it is greater than a certain minimum value. An application to permanent mold casting is given, illustrating both the utility and accuracy of the method in a practical context.

Introduction

The practical importance of heat conduction problems with periodic boundary conditions was discussed by Carslaw and Jaeger (1959), who cited applications in geophysics, experimental measurement of thermal diffusivity, and thermal stresses in cylinder walls of internal combustion engines. The temperature solution in these problems is usually composed of both periodic and decaying parts, while approaching a steady periodic solution in the limit of long time. The classical method for determining the steady periodic solution is to express the boundary condition in a series of harmonics and use Fourier transforms. Unfortunately, these methods are often slow to converge and only apply when the boundary conditions are linear with constant coefficients.

An alternative approach is to integrate the diffusion equation directly, using a finite difference or finite element method. Determining the long time limit with such an approach is extremely costly since the time step must be very small to avoid problems of numerically induced oscillations (Myers, 1978). To avoid these difficulties, Myers (1980) used a direct time integral of the spatially discretized equations, expressing the solution in terms of eigenvalues and eigenvectors that depend on the spatial discretization of the region. While this technique has some advantages, it is also restricted to linear boundary conditions with constant coefficients.

When the period of the boundary disturbance is small compared to the normal time scale of heat conduction in the body, the periodic transient attenuates very rapidly with depth from the surface. This situation presents new difficulties of its own (Hogge and Gerrekens, 1983). Numerical integration must now contend with widely separated time scales associated with the two transients in the problem. The diffusion equation must be integrated over the entire body, with a time step controlled by the rapid temperature variation and (frequently) high temperature gradients in a narrow region near the boundary. Such analysis is not only time consuming, but the stiff equations that result usually require special methods of numerical integration (Gear, 1971).

Problems with high-frequency periodic boundary conditions occur in cyclic manufacturing processes, such as die casting and plastic injection molding, where molten material is repeatedly injected into a mold cavity on a regular process cycle. Usually, the cycle is very short compared to the "startup" transient of the mold and it takes several cycles to reach a balance between periodic boundary heating at the cavity surface and steady internal cooling by the water lines in the mold. Once this occurs, the transient temperatures in the mold are confined to a relatively narrow region near the cavity surface and the temperatures in the bulk of the mold are essentially steady. A similar situation also occurs in internal combustion engines, where the combustion cycle is very short compared to the service transients of the engine.

Since the boundary conditions in these problems are usually expressed in terms of heat transfer coefficients that depend on time, they fall outside the scope of traditional transform methods. Updike (1984) tried to overcome this limitation in a one-dimensional analysis of transient heat conduction in the cylinder wall of an internal combustion engine. He used a Fourier decomposition of the solution and satisfied the boundary conditions by collocation in time. His solution required at least 40 modes to converge because of the high-frequency content in his boundary temperature.

Contributed by the Heat Transfer Division for publication in the JOURNAL OF HEAT TRANSFER. Manuscript received by the Heat Transfer Division April 20, 1989; revision received August 23, 1989. Keywords: Materials Processing and Manufacturing Processes, Numerical Methods, Transient and Unsteady Heat Transfer.

In this paper, we present a new method for calculating the steady periodic solution with high-frequency boundary conditions, aimed at overcoming some of the problems mentioned above. The method, which imposes a prior restriction on the domain of the transient solution, applies to a general three-dimensional body and is compatible with a variety of numerical techniques. The basic assumption is that all transient temperature variation occurs within a narrow boundary layer of constant thickness, and the solution everywhere else is steady. This assumption is similar to the transient penetration concept used by Goodman (1964), except that here the penetration distance is *constant* and specified in advance. In contrast, Goodman's penetration distance is introduced as an unknown function of time, which is determined as part of the solution. A time-varying penetration depth is normally restricted to monotonic boundary conditions. Although nonmonotonic boundary conditions can be treated by introducing multiple, independent penetration depths, this approach would be unwieldy for a periodic boundary condition. The use of a constant penetration depth for periodic boundary conditions appears to be new.

The temperature solution in the transient surface layer is represented by a polynomial expansion in the transverse coordinate, with time-varying coefficients. Heat flux is neglected in the other directions and the unknown coefficients are determined by a Galerkin method. Temperature continuity is imposed at the interface between the surface layer and the steady interior, but continuity of heat flux is enforced only in a time-averaged sense. This is another departure from the integral methods of Goodman, which impose strict continuity of heat flux. The Galerkin method is especially attractive in this context because it can handle a broad class of boundary conditions.

The effectiveness of the present approach clearly depends on how the specific choice for the constant layer thickness affects the accuracy of the solution. This question is explored for the particular case of a half-space with a sinusoidal surface flux. The accuracy of the layer solution improves as the layer depth increases, but at the cost of slower convergence in the polynomial representation. Although these general trends are not too surprising, it turns out that very good accuracy can be achieved with remarkably few terms in the polynomial representation. In the half-space example, just four terms in the polynomial representation were sufficient to reduce the error in the boundary solution to well under one percent. Each subsequent term improved the accuracy by nearly an order of magnitude.

Although the Galerkin method makes this approach especially suited to nonlinear problems, it also has advantages in the frequently occurring case of a linear boundary condition with a time-varying heat transfer coefficient. In this case it is possible to decouple the solution procedure and determine the steady interior solution separately from the surface transient.

As a practical example illustrating the usefulness of the approach, we consider a problem from permanent mold casting in Section 4. The decoupled solution procedure is applied to this problem and we show how the entire effect of the one-dimensional surface transient on the three-dimensional interior solution can be reduced to an effective steady heat transfer coefficient defined on the boundary. With only three polynomial terms, the solution compares extremely well with the results of a much more costly finite difference analysis of the same problem.

Problem and Approach

Consider a three-dimensional body subjected to a periodic thermal excitation on its boundary. Let t_p be the period of excitation and α the thermal diffusivity of the material. We consider the case when $(\alpha t_p)^{1/2}$ is small compared with the body dimension L, so that the heat conduction equation may be expressed as

$$\frac{\partial \theta}{\partial \tau} = \frac{\alpha t_p}{L^2} \nabla^2 \theta \tag{1}$$

where θ is the temperature and $\tau = t/t_p$ is nondimensional time. The periodic boundary condition may take the general form

$$f(\theta, q, x_\alpha, \tau) = f(\theta, q, x_\alpha, \tau + 1) = 0 \tag{2}$$

where q is the normal heat flux and x_α ($\alpha = 1, 2$) are curvilinear surface coordinates defined over the boundary. Since the coefficient of $\nabla^2\theta$ on the right-hand side of equation (1) is small, the solution will be nearly steady everywhere in the body except very near the boundary, where a time-varying solution is necessary to satisfy the boundary condition (2). We idealize the solution by assuming that all transient temperature variation occurs within a narrow boundary layer of constant depth d, which depends only on α and t_p. Let z be a third coordinate (Fig. 1) defined along the inward normal to the boundary surface, so that the *transient surface layer* is contained between the boundary and the interface $z = d$. The region enclosed by $z = d$ is called the *quasi-steady interior*. We assume the temperature is continuous at the interface, but only require con-

Nomenclature

a_m, b_m = constant coefficients in solution (21)
c = heat capacity per unit mass
c_c = heat capacity of the casting material per unit mass
d = depth of the transient surface layer
d_c = half-thickness of the casting
h = heat transfer coefficient between the casting and the mold
h_e = effective heat transfer coefficient for the steady interior solution
k = thermal conductivity
L = characteristic body dimension
N = number of terms in the polynomial expansion
q = heat flux
q_i = heat flux at the interface between the transient surface layer and the steady interior
q_s = heat flux at the boundary surface
t = time
t_p = time period of the boundary disturbance
x_α = curvilinear coordinates on the boundary surface
z = thickness coordinate in the surface layer
α = thermal diffusivity
ζ = nondimensional thickness coordinate in the surface layer
η = nondimensional parameter defined by equation (28)
θ = temperature
θ_a = linear coefficient in solution (14)
θ_m = coefficient functions in polynomial expansion
θ_c = casting temperature
θ_c^0 = initial casting temperature
θ_s = surface temperature
Λ = nondimensional parameter defined by equation (28)
μ = linear coefficient in solution (14)
μ_m = linear coefficient in solution (31)
ρ = mass density
ρ_c = mass density of the casting material
τ = nondimensional time
ϕ = nondimensional surface layer thickness

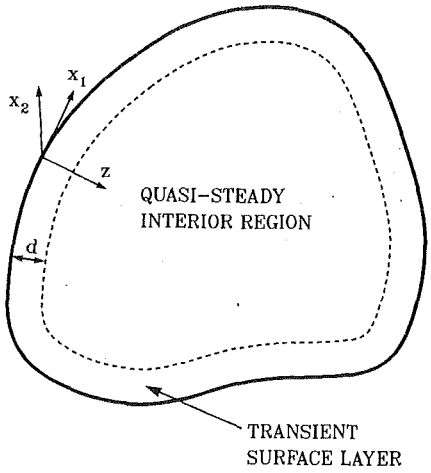

Fig. 1 Geometry and coordinates

tinuity of heat flux in a time-averaged sense. The local radius of curvature on the boundary is assumed to be large compared to d so that the effect of boundary curvature may be reasonably neglected in the calculation of the transient solution. We also assume that the boundary condition (2) varies slowly on the scale of the layer depth, so that it is reasonable to neglect the heat flux parallel to the surface in the calculation of the transient temperatures.

With reference to the coordinates in Fig. 1, we assume that the temperature solution in the surface layer may be represented by the finite polynomial

$$\theta(x_\alpha, z, t) = \theta_0(x_\alpha) + \sum_{n=1}^{N} \theta_n(x_\alpha, t)(1 - z/d)^n \tag{3}$$

where θ_0 has been taken independent of time, consistent with the assumption of temperature continuity at $z = d$. The coefficient functions $\theta_n(x_\alpha, t)$ in equation (3) are determined by neglecting the heat flux parallel to x_α and requiring that the heat conduction equation be satisfied in the following integrated sense:

$$\int_0^d \left(\rho c \frac{\partial \theta}{\partial t} + \frac{\partial q}{\partial z}\right) \zeta^n \, dz = 0 \qquad (n = 0\ 1, \ldots, N) \tag{4}$$

where ρc is the heat capacity per unit volume, q is the heat flux parallel to z, and $\zeta = 1 - z/d$. This is a form of the Galerkin method. For $n = 0$, equation (4) can be integrated directly to give

$$\rho c d \sum_{m=1}^{N} \frac{1}{m+1} \dot{\theta}_m + q_i = q_s \tag{5}$$

where q_s and q_i are values of the heat flux at the surface $z = 0$, and the interface $z = d$, respectively. For convenience, a superposd dot denotes a partial derivative with respect to time. For $n > 1$, we first integrate equation (4) by parts to obtain

$$\rho c d \sum_{m=1}^{N} \frac{1}{m+n+1} \dot{\theta}_m + n \int_0^1 q \zeta^{n-1} d\zeta = q_s \qquad (n = 1, 2, \ldots, N) \tag{6}$$

To evaluate the remaining integral in equation (6), we substitute from equation (3)

$$q = -k \frac{\partial \theta}{\partial z} = \frac{k}{d} \sum_{m=1}^{N} m \theta_m \zeta^{m-1} \tag{7}$$

and obtain

$$\rho c d \sum_{m=1}^{N} \frac{1}{m+n+1} \dot{\theta}_m + \frac{k}{d} \sum_{m=1}^{N} \frac{mn}{m+n-1} \theta_m = q_s$$

$$(n = 1, 2, \ldots, N) \tag{8}$$

where k is the thermal conductivity. Note that while equation (7) is used to compute the weighted integral of the heat flux in equation (6), it does not have to be compatible with the values of q_s and q_i determined by equations (5) and (8). The unknown functions $q_s(x_\alpha, t)$ and $\theta_n(x_\alpha, t)$ $(n = 1, 2, \ldots, N)$ are determined by the N equations (8), and the boundary condition

$$f\left(\theta_0 + \sum_{n=1}^{N} \theta_n, q_s, x_\alpha, \tau\right) = f\left(\theta_0 + \sum_{n=1}^{N} \theta_n, q_s, x_\alpha, \tau + 1\right) = 0 \tag{9}$$

which follows from equations (2) and (3). The interfacial heat flux q_i is determined from equation (5).

The surface layer solution is coupled to the steady interior solution through the interface conditions at $z = d$. Instead of imposing these conditions on each solution directly, it is more convenient to extend the interior solution to the surface of the body by identifying it with the time-averaged solution in the surface layer. This satisfies the interface conditions at $z = d$ and eliminates the need to solve the steady problem over a subregion of the body. To make this work, it is necessary to derive a consistent time-averaged boundary condition for the extended interior solution.

When the periodic boundary condition (2) is linear with constant coefficients, the time-averaged boundary condition may be obtained by integrating equation (2) directly. In this case, the transient and steady solutions decouple completely and the present approach offers no particular advantage over transform methods. Although the two solutions remain coupled when the boundary condition has time-varying coefficients, the present approach can still be used to decouple the *solution process* and solve the steady problem separately from the surface transient.

To show this, we first integrate the surface layer equations (8) over one time period to obtain

$$\bar{q}_s = \frac{k}{d} \sum_{m=1}^{N} \frac{mn}{m+n-1} \bar{\theta}_m \qquad (n = 1, 2, \ldots, N). \tag{10}$$

where an overbar designates the time-averaged value of a function and we have used the fact that the solution is periodic. The N linear equations (10) have the unique solution

$$\bar{\theta}_1 = (d/k)\bar{q}_s \tag{11}$$

$$\bar{\theta}_n = 0 \qquad (n = 2, \ldots, N) \tag{12}$$

Hence, the average temperature distribution in the surface layer is linear, as might be expected. From equations (3) and (11) the average temperature on the boundary is just

$$\bar{\theta}_s = \bar{\theta}(x_\alpha, 0, t) = \theta_0 + \sum_{m=1}^{N} \bar{\theta}_m = \theta_0 + \bar{\theta}_1 = \theta_0 + (d/k)\bar{q}_s \tag{13}$$

This relationship is true for any periodic boundary condition. Next, we solve the surface layer equations (8) for the prescribed boundary condition (9) and derive an independent relationship between θ_1 and θ_0. When the boundary condition is linear, this relationship is also linear, and since θ_0 is constant, we can simply average it over the period to obtain

$$\bar{\theta}_1 = \mu(x_\alpha)[\theta_a(x_\alpha) - \theta_0] \tag{14}$$

where the coefficient functions μ and θ_a depend only on the time-averaged surface layer solution at the point x_α. We can now eliminate θ_0 between equations (13) and (14) to get

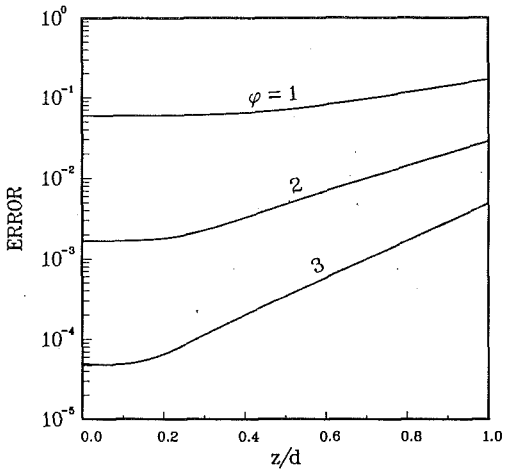

Fig. 2 Modeling error as a function of position in the layer for increasing values of the nondimensional layer depth $\phi = d/(\alpha t_p)^{1/2}$

$$\bar{q}_s = (k/d)\left(\frac{\mu}{1-\mu}\right)(\theta_a - \bar{\theta}_s) \tag{15}$$

which is the desired boundary condition on the time-averaged solution. The entire effect of the surface transient on the interior solution is embodied in the two coefficient functions μ and θ_a, which are completely independent of the interior solution. Hence, even though the two solutions remain coupled, it is not necessary to compute them simultaneously. The product

$$h_e = (k/d)\left(\frac{\mu}{1-\mu}\right) \tag{16}$$

may be interpreted in equation (15) as an effective heat transfer coefficient for the time-averaged solution, with θ_a as an effective ambient temperature.

After the steady interior solution has been determined from the boundary condition (15), the resulting values of $\bar{\theta}_s$ and $\bar{q}_s$ may then be used in equation (13) to compute the unknown interface temperature θ_0 and hence recover the explicit surface layer solution.

The foregoing result has important practical significance. In many of the applications discussed in the introduction, the periodic boundary condition is expressed through a time-varying heat transfer coefficient. The present approach makes it possible to decouple the solution procedure for these problems by first determining the solution in the surface layer as a linear function of θ_0 and then forming the boundary condition (15) for the steady interior solution. This decoupled solution process works even when the boundary condition (9) is such that the layer solution must be determined numerically.

Regardless of the form of the boundary condition, the solution clearly depends on the choice for the surface layer depth d. In the next section we use a particular example for which there is an exact solution to investigate the effect of d on the potential accuracy of the solution and the rate of convergence with the order of the polynomial representation (3).

Effect of Layer Depth

Consider a half-space $z \geq 0$ with a periodic heat flux boundary condition

$$q_s = \frac{k}{(\alpha t_p)^{1/2}} \cos(2\pi t/t_p) \tag{17}$$

and a vanishing temperature at infinity. The exact solution of this problem is

$$\theta(z,t) = \frac{1}{(2\pi)^{1/2}} \exp\left[-\left(\frac{\pi}{\alpha t_p}\right)^{1/2} z\right] \cos\left[\frac{2\pi t}{t_p} - \left(\frac{\pi}{\alpha t_p}\right)^{1/2} z - \frac{\pi}{4}\right] \tag{18}$$

In this case the surface layer equations (8) become

$$\phi^2 \sum_{m=1}^{N} \frac{1}{m+n+1}\dot{\theta}_m + \sum_{m=1}^{N} \frac{mn}{m+n-1}\theta_m = \phi\cos(2\pi t/t_p) \tag{19}$$

where

$$\phi = d/(\alpha t_p)^{1/2} \tag{20}$$

is the nondimensional layer depth and a superposed dot now designates $\partial/\partial\tau$. The solution of equation (19) has the form

$$\theta_m = a_m\cos(2\pi t/t_p) + b_m\sin(2\pi t/t_p) \tag{21}$$

where a_m and b_m are determined by the linear system

$$\begin{aligned} 2\pi\phi^2 \sum_{m=1}^{N} \frac{1}{m+n+1} b_m + \sum_{m=1}^{N} \frac{mn}{m+n-1} a_m &= \phi \\ -2\pi\phi^2 \sum_{m=1}^{N} \frac{1}{m+n+1} a_m + \sum_{m=1}^{N} \frac{mn}{m+n-1} b_m &= 0 \end{aligned} \tag{22}$$

The coefficients (21) may be substituted in the basic polynomial representation (3) to give the temperature distribution in the layer

$$\theta(z,t) = \sum_{m=1}^{N} a_m(1-z/d)^m\cos(2\pi t/t_p) + \sum_{m=1}^{N} b_m(1-z/d)^m\sin(2\pi t/t_p) \tag{23}$$

which, for specific values of ϕ and N, may be compared with the exact solution (18).

The solution (23) contains two sources of error. The first is in the physical approximation embodied in the transient surface layer assumption. For convenience, we call this the *modeling error*. The magnitude of the modeling error depends on the choice of the layer depth; as ϕ increases, the layer includes more of the region actually affected by transient temperatures, and so the potential accuracy of the layer solution increases. The second source of error is in the approximate representation (3) for the layer solution. We call this the *solution error*. Formally, we define the solution error as the magnitude of the remainder in the representation (3), after truncation to N terms. The solution error not only depends on the number of polynomial terms in (3), but it also depends on the layer depth, since the nature of the solution changes as the layer depth is increased.

Figure 2 displays the modeling error as a function of position for several values of the layer depth. The solution error has been suppressed in these results by using sufficient polynomial terms in equation (3) to guarantee solution accuracy to at least six significant figures. Since the error at any point z actually fluctuates on the same frequency as the boundary disturbance, we have plotted the amplitude of that error, corresponding to its maximum value over the period. The error values are absolute, after both solutions have been normalized such that the exact solution (18) has an amplitude of unity at $z = 0$. The modeling error decreases very rapidly as the layer depth increases. This is not too surprising since the amplitude of the exact solution (18) decreases exponentially with depth. The rate of convergence, however, is much more rapid near the surface.

Figure 3 shows the solution error as a function of layer depth. Although it varies somewhat with z, only the average

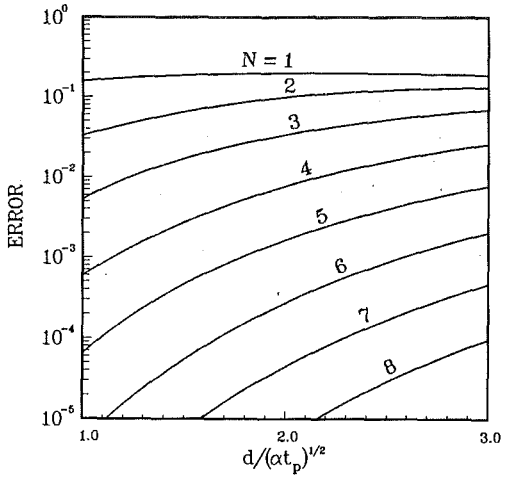

Fig. 3 Average solution error as a function of nondimensional layer depth for increasing values of N

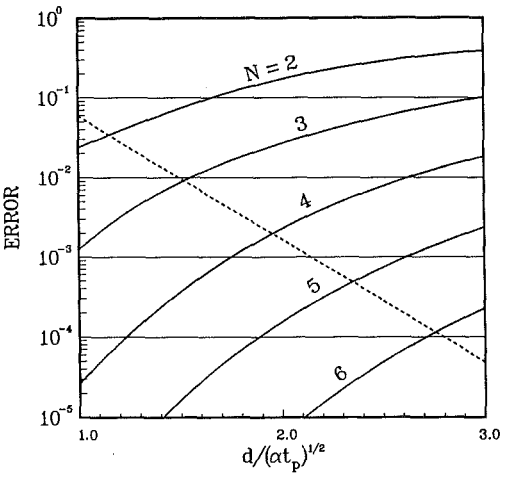

Fig. 4 Modeling error (dashed line) and solution error (solid lines) at $z=0$ as a function of nondimensional layer depth $\phi = d/(\alpha t_p)^{1/2}$

value is displayed in Fig. 3 for simplicity. It is clear from the figure that the solution error for a given layer depth may be reduced by increasing N, and that larger values of N are required to achieve the same solution accuracy as the layer depth is increased. Although a deeper layer includes more of the region actually affected by the transient, thereby increasing the potential accuracy of the solution, more polynomial terms are required to maintain a comparable solution error, and so realize that potential. Therefore, the layer must be deep enough to achieve a desired accuracy to the depth of interest, but not so deep that an excessive number of polynomial terms become necessary.

In most practical situations, the surface solution is most important, and so the layer can be thin and the number of polynomial terms small. Figure 4 shows both sources of error at the point $z=0$. The modeling error, shown by the dashed line, represents the potential accuracy in the layer solution. To achieve that potential, the solution error, represented by the solid lines, must be less than the modeling error. For example, suppose we desired a solution that was accurate at the surface to within 10^{-2}. Then ϕ would have to be at least 1.5 and N no less than 4. To avoid larger values of N, ϕ must also be less than 2.6.

In the present example, the boundary condition had a single frequency. When there is mixed frequency content, the layer thickness should be chosen based on the lowest frequency, corresponding to the greatest transient penetration. This will control the modeling error. The value of N can then be selected empirically. Based on the above results, N should increase as higher frequencies become more significant in the solution.

A Metal Casting Example

To apply this general formulation to a problem in metal casting, we consider a mold consisting of at least two separate components that fit together around an empty cavity in the shape of the desired part. Liquid metal is either poured or injected into this cavity, where it cools and solidifies before being ejected. In a cyclic casting process, the mold ultimately reaches a periodic steady state in which the heat absorbed from the casting by each mold component is balanced by the heat removed by its internal cooling lines. Since the rate and sequence of solidification in the casting depend strongly on the steady mold temperatures, it is important to be able conveniently to calculate the effect of different cooling line configurations on the steady periodic solution.

Previous treatments of this problem rely on initial value formulations. Riegger (1981), Ohtsuka et al. (1982), and Granchi et al. (1983) all assumed initial conditions based on empirical observations, carrying their time integration only as far as casting ejection. Since their solutions did not span a complete cycle, it is impossible to check how well their initial conditions simulate steady periodic conditions. Grant (1981) avoided any question of initial conditions by integrating his finite difference equations through at least ten casting cycles to approximate steady periodic conditions. This is a costly alternative, especially when the mold is large. The present method avoids the inherent difficulties of an initial value formulation by using the transient surface layer approach to calculate the steady periodic solution directly.

As an example, consider a mold for a thin casting that has a high thermal conductivity. Consistent with the assumption in the surface layer, we neglect any transient heat flux in the casting parallel to the cavity surface. We also neglect the transverse temperature gradients in the casting relative to those in the mold, so that at any point x_α the casting may be regarded as a lumped mass. Let $\theta_c(x_\alpha, t)$ denote the local temperature of the casting at the point x_α. The latent heat of solidification is reflected in an equivalent heat capacity c_c for the casting, which we assume to be constant in time. For simplicity, we consider a symmetric problem in which the mold temperatures are the same on both sides of the casting. A coating is usually applied to the cavity surface of the mold to protect it from thermal shock and act as a release agent. We assume that this coating can be represented by a heat transfer coefficient h. The casting is ejected at $\tau = r < 1$. After this we assume the heat flux at the cavity surface vanishes.

Let d_c denote the half-thickness of the casting, and ρ_c the constant casting density. Then, the normal heat flux on the cavity surface at any time during the cycle is given by

$$q_s = \begin{cases} h\left(\theta_c - \sum_{m=0}^{N} \theta_m\right), & 0 \le \tau < r \\ 0, & r < \tau \le 1 \end{cases} \tag{24}$$

With this boundary condition, the surface layer equations (8) may be written as

$$\phi^2 \sum_{m=1}^{N} \frac{1}{m+n+1}\,\dot{\theta}_m + \sum_{m=1}^{N} \left(\frac{1}{m+n-1} + \phi\Lambda\right)\theta_m = \phi\Lambda(\theta_c - \theta_0),\ 0 \le \tau < r \tag{25}$$

$$\phi^2 \sum_{m=1}^{N} \frac{1}{m+n+1}\,\dot{\theta}_m + \sum_{m=1}^{N} \frac{1}{m+n-1} + \theta_m = 0 \quad r < \tau \le 1 \tag{26}$$

and for the casting

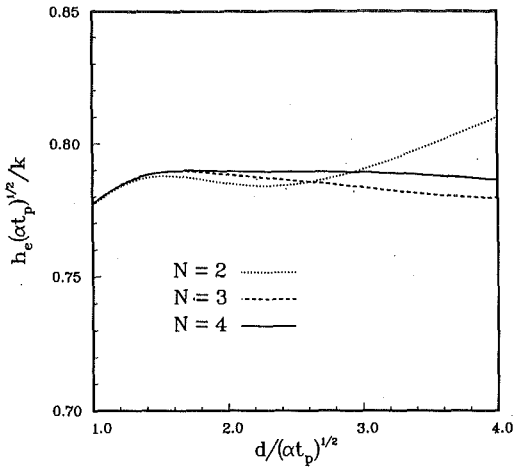

Fig. 5 Effective heat transfer coefficient as a function of nondimensional layer depth for $\Lambda = 10$, $\eta = 1$, and $r = 0.5$

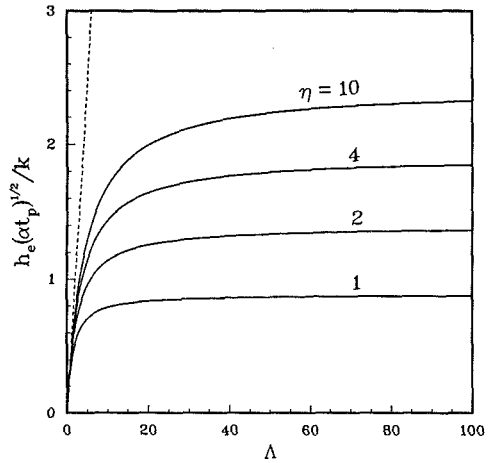

Fig. 6 Effective heat transfer coefficient as a function of Λ for different values of η; the dashed line represents the limiting case when the transient surface layer makes no contribution to h_e

$$\eta \dot{\theta}_c = -\Lambda \left(\theta_c - \theta_0 - \sum_{m=1}^{N} \theta_m \right), \quad 0 \le \tau < r \tag{27}$$

The nondimensional parameters Λ and η are defined by

$$\Lambda = \frac{h(\alpha t_p)^{1/2}}{k}, \qquad \eta = \frac{\rho_c c_c d_c}{\rho c (\alpha t_p)^{1/2}} \tag{28}$$

where η is a ratio between the thermal capacities of the casting and the transient surface layer. The physical significance of Λ will become more apparent when we look at specific results. The coefficients θ_m satisfy the periodicity conditions

$$\theta_m(\tau) = \theta_m(\tau + 1) \tag{29}$$

while the casting temperature satisfies the initial condition

$$\theta_c(0) = \theta_c^0 \tag{30}$$

This mixture of steady periodic and initial value problems is outside the scope of traditional transform methods, but it is an ideal application of the transient surface layer approach. The solution of equations (25)–(30) is a straightforward exercise in linear algebra, and so we omit the details here. We note, however, that the solution for θ_c and θ_m will be linear in the difference $(\theta_c^0 - \theta_0)$. Hence,

$$\theta_m = \mu_m(\phi, \Lambda, \eta, r, \tau)[\theta_c^0 - \theta_0] \tag{31}$$

and since $(\theta_c^0 - \theta_0)$ is independent of time, the average value of θ_m is also linear in $(\theta_c^0 - \theta_0)$, so that

$$\bar{\theta}_m = \bar{\mu}_m(\phi, \Lambda, \eta, r)[\theta_c^0 - \theta_0] \tag{32}$$

This has the same form as equation (14). Hence, from equations (15) and (16) the boundary condition on the time-averaged solution is simply

$$\bar{q}_s = h_e(\theta_c^0 - \bar{\theta}_s) \tag{33}$$

where h_e is an effective heat transfer coefficient defined by

$$h_e = (k/d)\left(\frac{\bar{\mu}_1}{1 - \bar{\mu}_1}\right) \tag{34}$$

The boundary condition (33) can now be combined with suitable boundary conditions on the other mold surfaces to compute the three-dimensional steady solution in the mold. Then the explicit transient temperature solution in the surface layer can be recovered directly from

$$\frac{\theta - \bar{\theta}_s}{\theta_c^0 - \bar{\theta}_s} = \frac{\sum_{m=1}^{N} \mu_m (1 - z/d)^m - \bar{\mu}_1}{1 - \bar{\mu}_1} \tag{35}$$

which follows from equations (3), (13), and (31).

As in the previous section, the solution to this problem also depends on the depth of the surface layer. Figure 5 displays the effective heat transfer coefficient from equation (34) as a function of the layer depth, assuming values of $\Lambda = 10$, $\eta = 1$, and $r = 0.5$, which are typical of aluminum die casting. Although the convergence rate is slower for larger values of d, the effective heat transfer coefficient h_e is nearly constant for values of $\phi > 1.5$. This is also true of the full transient solution, although we don't show the details here.

If we select $\phi = 1.5$ and consider the case when $r = 0.5$, then Fig. 6 shows how h_e depends on h, or equivalently, on Λ. The effective heat transfer coefficient increases sharply at first, and becomes less sensitive to h for larger values of Λ. This can be explained if we first understand that h_e reflects both the conductive resistance of the surface coating and the effective resistance due to the thermal inertia of the transient surface layer. Both act as a barrier to the time-averaged flow of heat from the casting to the mold interior. Smaller values of Λ correspond to more insulative surface coatings, which tend to mask the influence of the surface layer inertia on the time-averaged solution. In this case the transient surface layer solution is weakly coupled to the steady interior solution and $h_e \to rh$. This limit is represented by the dashed line in Fig. 6. As Λ increases, the inertial resistance of the transient surface layer has a greater influence on h_e and the relative importance of h diminishes. Hence, Λ represents a ratio of the inertial resistance in the transient surface layer to the conductive resistance of the surface coating, as each affects the time-averaged flow of heat from the casting to the mold interior.

The value of η also affects this relationship. When η is small, the casting cools more rapidly because of its relatively low thermal capacity. This reduces the temperature difference between the casting and the mold surface compared to the temperature drop across the transient surface layer, and so diminishes the importance of h. Hence, the curves in Fig. 6 corresponding to smaller values of η level off more quickly. The asymptotic value is smaller because h_e is defined on the basis of the *initial* casting temperature (equation (33)) and the time-averaged effect of a decreasing casting temperature is reflected in a smaller value of h_e.

For thin castings typical in die casting processes, η is usually less than 1. For the petroleum-based liquids used to coat the dies, values of Λ are usually greater than 10. In this range, variations in the heat transfer coefficient h have almost no effect on the time-averaged steady temperatures in the die. They will, however, affect the transient solution in the casting and in the surface layer.

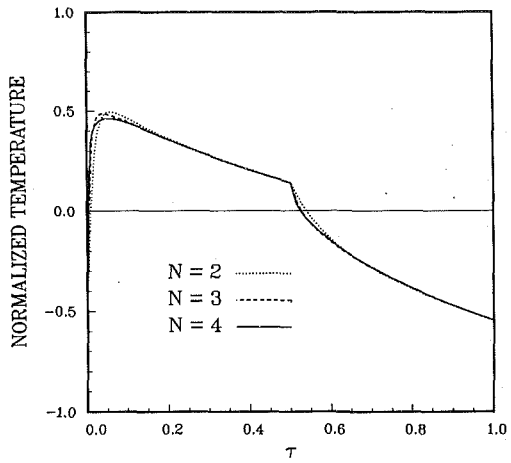

Fig. 7 Transient temperature solution at $z=0$ from equation (35) for different values of N

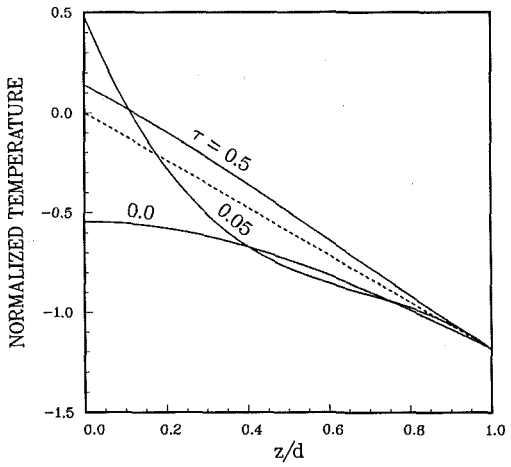

Fig. 8 Temperature distribution through the thickness of the layer at three different times during the cycle; the dashed line is the time-averaged distribution

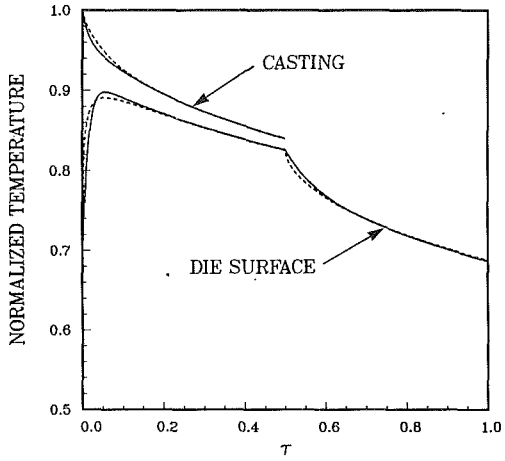

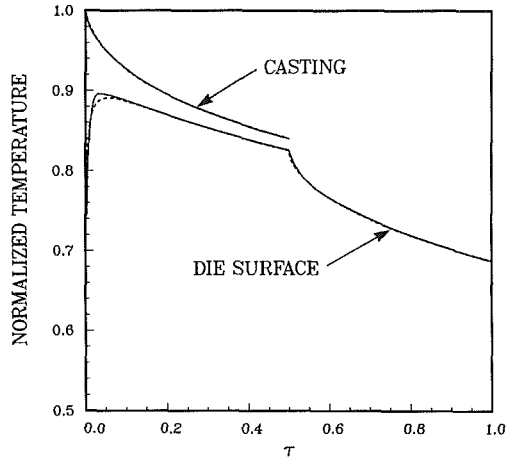

Fig. 9 Comparison of the transient surface layer solution (solid line) for (*a*) $N=2$ and (*b*) $N=3$ with corresponding results from a finite difference analysis (dashed line)

Figure 7 displays the normalized transient solution at $z=0$, calculated from equation (35) for $\Lambda=10$ and $r=0.5$. These results correspond to $\phi=1.5$, but like the time-averaged results in Fig. 5, the only effect of increasing ϕ is to slow the rate of convergence in N. In this case, practical convergence is reached with just three polynomial terms. Figure 8 shows the corresponding temperature distribution through the layer at three times during the cycle for $N=3$.

In the previous section, we assessed the accuracy of the surface layer solution by comparing it with an analytical solution. In the present example, we compare with a finite difference solution. To do this, we must specify the mold geometry and remaining boundary conditions. For simplicity, consider a one-dimensional die with a fixed temperature of zero at $z=5\ (\alpha t_p)^{1/2}$. Again, we assume values of $\Lambda=10$, $\eta=1$, and $r=0.5$, and take $\phi=1.5$. In this case, the time-averaged steady solution is linear in z and the complete temperature solution can be formed by combining it with equation (35). The corresponding finite difference solution was found by starting with a uniform mold temperature and integrating through enough casting cycles to reach steady state. In this case, at least 35 cycles are necessary to achieve a periodic solution to four significant figures. Figure 9 compares the two solutions for both the casting temperature and the temperature at the cavity surface, each normalized by the initial casting temperature. Figure 9(*a*) shows the comparison for $N=2$ and Fig. 9(*b*) shows the comparison for $N=3$. At $N=4$, the two results are virtually indistinguishable. From a practical point of view, the accuracy of the layer solution with just $N=2$ is remarkable.

Discussion

This paper provides an accurate and efficient means of analyzing heat conduction problems with high-frequency periodic boundary conditions. The principal assumption is that all transient temperatures occur within a narrow boundary layer of constant depth. As long as this layer includes most of the region actually affected by transient temperatures, the accuracy of the surface solution is not greatly affected by the specific choice of the layer depth. The transient solution in the surface layer can be represented very accurately by a low-order polynomial with time-varying coefficients determined by a Galerkin method.

The problem of determining the steady periodic solution in a three-dimensional body is reduced to a set of first-order ordinary differential equations on the boundary, combined with a three-dimensional steady solution in the interior. These two solutions can be decoupled when the boundary conditions are linear, even if the coefficients depend on time. In this case, the entire effect of the surface transient on the steady interior solution can be reduced to an effective heat transfer coefficient, which is independent of the steady interior solution. Since the layer equations depend parametrically on the surface coordinates, they are not spatially coupled. Hence, it is only necessary to solve them at a finite number of boundary nodes—the same ones used to specify boundary conditions for the numerical solution of the steady problem. This reduces the effort of determining the steady periodic solution to little more than

finding the steady solution alone. Not only is the efficiency of the solution improved, but the numerical difficulties of the full-field transient solution are avoided.

Finally, we note that the present method can be used to solve the unsteady periodic problem as well. It is only necessary to assume that the unsteady interior solution is quasi-static on the time scale of the periodic boundary disturbance. Equation (15) still serves as the appropriate boundary condition, together with initial conditions defined over the interior. After the unsteady interior solution has been determined, the complete solution involving both time scales can be formed by superposition.

Acknowledgments

The author would like to express his gratitude to Martin Barone for useful insights concerning alternative numerical methods and for helpful suggestions during the preparation of this paper.

References

Carslaw, H. S., and Jaeger, J. C., 1959, *Conduction of Heat in Solids*, Clarendon Press, Oxford, United Kingdom.

Gear, C. W., 1971, *Numerical Initial Value Problems in Ordinary Differential Equations*, Prentice Hall, Englewood Cliffs, NJ.

Goodman, T. R., 1964, "Application of Integral Methods to Transient Nonlinear Heat Transfer," *Advances in Heat Transfer*, Vol. 1, J. P. Hartnett and T. F. Irvine, eds., Academic Press, New York.

Granchi, M., Vettori, E., and Cerini, E., 1983, "Computer Thermal Analysis of Die Casting Dies," *12th International Die Casting Congress and Exposition*, Minneapolis, MN.

Grant, J. W., 1981, "Thermal Modeling of a Permanent Mold Casting Cycle," *Modeling of Casting and Welding Processes*, Metallurgical Society of AIME, Warrendale, PA, pp. 19–37.

Hogge, M., and Gerrekens, P., 1983, "Steep Gradient Modeling in Diffusion Problems," *Numerical Methods in Heat Transfer*, Vol. II, R. W. Lewis et al., eds., Wiley, New York, pp. 73–97.

Myers, G. E., 1978, "The Critical Time Step for Finite-Element Solutions to Two-Dimensional Heat-Conduction Transients," ASME JOURNAL OF HEAT TRANSFER, Vol. 100, pp. 120–127.

Myers, G. E., 1980, "Long-Time Solutions to Heat-Conduction Transients With Time-Dependent Inputs," ASME JOURNAL OF HEAT TRANSFER, Vol. 102, pp. 115–120.

Ohtsuka, Y., Mizuno, K., and Yamada, J., 1982, "Application of a Computer Simulation System to Aluminum Permanent Mold Castings," *Transactions, American Foundrymen's Society*, Vol. 90, pp. 635–645.

Riegger, O. K., 1981, "Application of a Solidification Model to the Die Casting Process," *Modeling of Casting and Welding Processes*, Metallurgical Society of AIME, Warrendale, PA, pp. 39–72.

Updike, W. A., 1984, "Computation of Surface Temperatures for Time-Dependent Periodic Convection Boundary Conditions," presented at the ASME Winter Annual Meeting, New Orleans, LA, Paper 84-WA/HT-40.

A General Method for the Comparison of Compact Heat Transfer Surfaces

T. A. Cowell
Department of Mechanical and Production Engineering,
Brighton Polytechnic,
Moulsecoomb, Brighton BN2 4GJ,
United Kingdom

This paper presents a family of methods for comparing compact heat transfer surface configurations. It is shown how measures for the relative values of required hydraulic diameter, frontal area, total volume, pumping power, and number of transfer units for different surfaces can be derived and displayed, when any two of the above five parameters are held constant. A wide range of comparisons that are independent of the particular duty can be simply made. A further development allowing comparisons, where three of the five parameters are fixed, yields very clear and compact indications of the relative merits of different surfaces.

1 Introduction

A clear and simple statement of the relative merits of different heat transfer surfaces is not easily made. It is particularly difficult to arrive at general conclusions that are valid for varying fluid properties and overall geometric sizes and shapes. The complexity of the problem is partially reduced by the use of nondimensional parameters to specify the surface characteristics—usually j-and f-factor values expressed as functions of Reynolds number. However, the final statement of "performance" of a given heat transfer surface still needs to be specified in terms of at least four interrelated characteristics: heat transfer, fluid pumping power, size, and shape. A very wide range of different methods have been proposed for facilitating comparison and these have been well reviewed and summarized by Shah (1978).

Four basic categories of comparison method were identified:

(i) Direct comparison of j and f values. These methods include the well-known "area goodness" comparison proposed by London (1964).
(ii) Comparisons of heat transfer as a function of fluid pumping power. These include the "volume goodness" factor comparison (London and Ferguson, 1949).
(iii) Comparison with a reference surface. Shah recommends the use of the methods of Bergles et al. (1974) from within this category.
(iv) A miscellaneous category including methods that are either somewhat obscure in interpretation, or only have relevance to particular applications.

Despite the wide choice of comparison methods, difficulties remain with all of them. For example, the "area goodness" factor only compares surfaces for a fixed fluid pressure drop, and even then the comparison is not completely quantitative. The "volume goodness" comparison requires hydraulic diameters to be fixed, and furthermore needs a set of representative fluid properties to be selected. While, this time, the results reveal a genuine ranking of surfaces, they do not represent a fully quantitative comparison. The use of a reference surface for comparison requires a suitable surface to be chosen, and here too, representative fluid properties must be selected. In general all methods suffer either from complexity, or from lack of clarity in interpretation, and sometimes both.

It is believed that the method of heat transfer surface comparison proposed here overcomes these shortcomings. A suite of comparison procedures is presented that allows easily interpreted quantitative comparison of the important "performance" characteristics by the consideration of a range of parameters, without reference to any particular set of fluid properties and flow rates.

Heat transfer surface comparisons range from those that at one extreme aim to give an indication of the intrinsic relative merits of different heat transfer surface geometries, independent of fluids and duty, to those at the other extreme in which comparisons between heat exchangers for particular heat transfer duties are required. In the former case a number of limiting assumptions are usually made, and these must be gradually abandoned as one moves toward the latter type of comparison. At the same time, the resulting comparisons range from the general and indicative at the one end, to the narrow but precise at the other. The former type of comparison is discussed here.

The analysis only considers the behavior of one fluid in the heat exchanger. The thermal resistance between the other fluid and its surface is assumed to be zero. In real compact surface heat exchangers with gases on the side under study and liquids on the other side, this assumption can be closely approached. A more significant assumption is that fin efficiency effects are ignored. The fin efficiency is strongly dependent upon the particular fluid properties and flow rates, and upon the heat-exchanger material and scale. This is not relevant where the surface is for use in a regenerative heat exchanger. It is assumed that the fluid properties can be identified by single values that are valid throughout the heat transfer matrix. Finally, contraction and expansion losses at the matrix inlet and outlet sections are ignored when fluid flow resistance is being considered. For detailed comparisons between heat exchangers for a particular duty, the general methods can be used as indicators in the first instance, but the effects of the limiting assumptions must then be evaluated.

2 The Heat Transfer Problem

The method depends upon the consideration of a notional heat transfer problem:

A heat exchanger is required to transfer heat from m (kg/s) of fluid at a rate of Q (W) with an available effective temperature difference of ΔT (K).

The fluid properties are density ρ (kg/m^3), specific heat capacity c_p [J/(kgK)], dynamic viscosity μ (Ns/m^2), and Prandtl number Pr.

The heat transfer requirement implies the need for the heat exchanger to have a number of heat transfer units N_{tu}, given by

Contributed by the Heat Transfer Division for publication in the JOURNAL OF HEAT TRANSFER. Manuscript received by the Heat Transfer Division December 10, 1987; revision received July 2, 1989. Keywords: Finned Surfaces, Forced Convection, Heat Exchangers.

$$N_{tu} = \frac{Q}{mc_p \Delta T} \tag{1}$$

In the first part of this paper, the assumption is made that Q and thus N_{tu} are fixed. Later sections consider the comparisons of the relative values of N_{tu} yielded by different surfaces and geometries. Where N_{tu} is fixed the symbol N_{tu}^{+} is used.

3 The Performance Calculation Equations

For any solution to the above problem, of particular interest are:

Total heat exchanger volume	V	(m^3)
Heat exchanger frontal area	A	(m^2)
Fluid pumping power	P	(W)

The heat exchanger also has length in the fluid flow direction given by $L = V/A$.

It is assumed that for any surface under consideration, values of j and f as functions of Reynolds number are available. Also needed are the hydraulic diameter d of the test surface for which the data were derived, and σ, the ratio of minimum free flow area A_c to frontal area A.

Hydraulic diameter is defined as

$$d = \frac{4A_c L}{A_s} = \frac{4\sigma AL}{A_s} = \frac{4\sigma V}{A_s} \text{ (m)} \tag{2}$$

where A_s is the total heat transfer surface area. Reynolds number is defined as

$$\mathrm{Re} = \frac{md}{A_c \mu} = \frac{md}{\sigma A \mu} \tag{3}$$

The Colburn modulus is defined as

$$j = \mathrm{St}\mathrm{Pr}^{2/3} \tag{4}$$

where the Stanton number

$$\mathrm{St} = \frac{hA_c}{mc_p} = \frac{h\sigma A}{mc_p} \tag{5}$$

and where h is heat transfer coefficient, which by rearrangement of equation (4) and equation (5) can be expressed as

$$h = \frac{j}{\mathrm{Pr}^{2/3}} \cdot \frac{mc_p}{A\sigma} \quad (\mathrm{W/m^2K}) \tag{6}$$

Remembering the assumption of zero resistance on the other fluid side, the rate of heat transfer is given by

$$Q = hA_s \Delta T \quad (W) \tag{7}$$

and the pressure drop by

$$\Delta p = \frac{2fm^2 L}{\rho A_c^2 d} = \frac{2fm^2 L}{\rho \sigma^2 A^2 d} \quad (\mathrm{N/m^2}) \tag{8}$$

The fluid pumping power is thus

$$P = \frac{\Delta p m}{\rho} = \frac{2fm^3 L}{\rho^2 A^2 \sigma^2 d} \quad (\mathrm{W}) \tag{9}$$

Equation (3) can be rearranged to give

$$A = \frac{d}{\sigma \mathrm{Re}} \cdot \frac{m}{\mu} \quad (\mathrm{m^2}) \tag{10}$$

Equation (7) can be rearranged after substitution for h from equation (6), for A_s from equation (2), for Q from equation (1), and subsequent substitution for A from equation (10) to yield

$$V = \frac{d^2}{\sigma j \mathrm{Re}} \cdot \frac{mN_{tu}^{+}\mathrm{Pr}^{2/3}}{4\mu} \quad (\mathrm{m^3}) \tag{11}$$

Remembering that $L = V/A$, and substituting for A from equation (10) and for V from equation (11), equation (9) becomes

$$P = \frac{f\mathrm{Re}^2}{jd^2} \cdot \frac{m\mu^2 N_{tu}^{+}\mathrm{Pr}^{2/3}}{2\rho^2} \quad (\mathrm{W}) \tag{12}$$

4 Comparison of Surfaces of Particular Scale

Since the performance data for a particular surface are expressed in nondimensional form, they can theoretically be applied to any surface having the same geometric proportions but at different overall scales. However, it is often of value to compare the performance of different surfaces at the particular scale for which the performance data were obtained, i.e., with the same hydraulic diameter as the test samples. This can be done by consideration of the equations presented in Section 3.

Equations (10), (11), and (12) have deliberately been written so as to separate out those parameters that are associated with the required heat transfer duty, and those that are associated with a particular solution. Thus for any heat transfer duty, the second terms remain constant and the values of the first terms are direct measures of the relative frontal area, relative volume, and relative pumping power of the particular solution. These are

$$A_d^{*} = \frac{d}{\sigma \mathrm{Re}} \quad (\mathrm{m}) \tag{13}$$

Nomenclature

A = heat exchanger frontal area, m^2
A_c = minimum free flow area, m^2
A_s = total area for heat transfer, m^2
c_p = specific heat capacity, J/(kgK)
d = hydraulic diameter, m
f = friction factor = $\Delta p \rho A_c^2 d/(2m^2 L)$
h = heat transfer coefficient, W/(m^2 K)
j = j factor = $\mathrm{St}\mathrm{Pr}^{2/3}$
L = heat exchanger length in fluid flow direction, m
m = fluid mass flow rate, kg/s
N_{tu} = number of transfer units = $hA_s/(mc_p)$
P = fluid pumping power, W
Pr = Prandtl number
Q = heat transfer rate, W
Re = Reynolds number = $md/(\mu A_c)$
Re_t = Reynolds number = $mt/(\mu A_c)$
St = Stanton number = $hA_c/(mc_p)$
t = strip width/pitch for reference surface, m
V = heat exchanger volume, m^3
Δp = pressure drop, N/m^2
ΔT = effective temperature difference, K
μ = dynamic viscosity, Ns/m^2
ρ = density, kg/m^3
σ = minimum free flow to frontal area ratio

Superscripts

* = part of parameter associated with solution
′ = part of parameter associated with problem
\+ = constant (or fixed) parameter

Subscripts

A = for constant frontal area
d = for fixed hydraulic diameter
Ntu = for constant number of transfer units
o = for reference surface
P = for constant pumping power
V = for constant heat exchanger volume

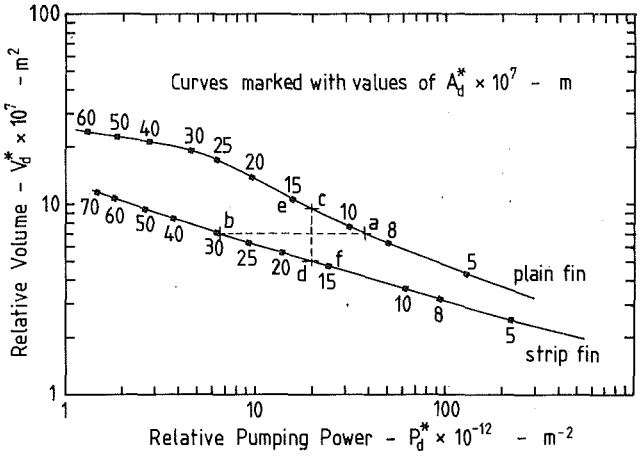

Fig. 1 Relative volume plotted against relative pumping power for surfaces at fixed scale and constant heat transfer (constant number of transfer units)

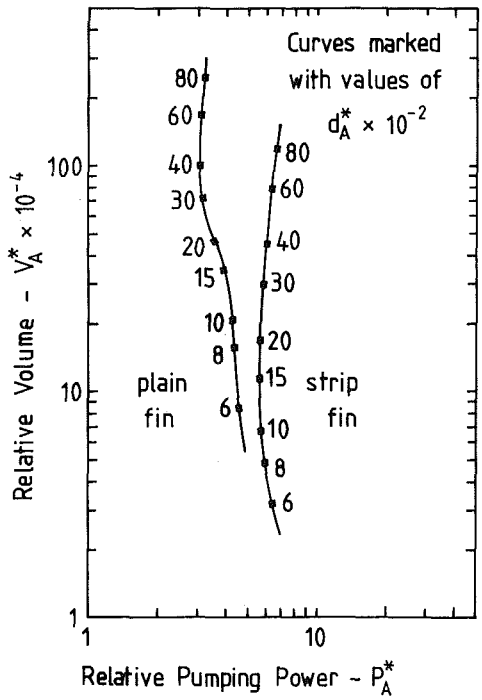

Fig. 2 Relative volume plotted against relative pumping power for constant frontal area and number of transfer units; parameters dimensionless

$$V_d^* = \frac{d^2}{\sigma j \mathrm{Re}} \quad (\mathrm{m}^2) \tag{14}$$

$$P_d^* = \frac{f\mathrm{Re}^2}{jd^2} \quad (\mathrm{m}^{-2}) \tag{15}$$

The suffix d indicates that parameters are for fixed hydraulic diameter for any particular surface and the asterisk indicates the part of the parameter associated with the particular solution.

For each of the surfaces to be compared, the "relative pumping power" P_d^* can be plotted against "relative volume" V_d^* and the curves marked with the corresponding values of "relative frontal area," A_d^*. These curves allow a wide range of comparisons to be easily made. Figure 1 shows curves plotted for two different surfaces based on performance data taken from Kays and London (1984). Both are plate fin surfaces with similar hydraulic diameter and values of σ. The one is a plain fin (surface 11.1) and the other a strip fin (surface 3/32-12.2). It can be seen that for the same total volume (e.g., $V_d^* = 7 \times 10^{-7}$) the plain fin surface will have pumping power some 38/6.4 = 5.9 times higher than the strip fin, but the frontal area will be smaller by a factor of 9/30 = 0.3 (points *a* and *b* on Fig. 1). For the two surfaces to perform the required duty with the same pumping power (e.g., for $P_d^* = 20 \times 10^{12}$) the total volumes will be in the ratio 9.4:5 = 1.9:1 with frontal areas in the ratio 14:17 = 1:1.2 (points *c* and *d* on Fig. 1). For the same frontal area (e.g., $A_d^* = 15 \times 10^{-7}$) the heat exchange volumes will be in the ratio 10.6:4.7 = 2.2:1 and the pumping powers in the ratio 16:24 = 2:3 (points *e* and *f* on Fig. 1). It can be seen that the two surfaces have different relative merits when operated under different constraints, and the curves plotted in this way allow easy identification of these relative merits.

Comparisons are often required on the basis of weight or cost. It is relatively easy to multiply the V_d^* values by the appropriate values of weight or cost per unit volume for each of the surfaces, and thus to make the required comparisons. These curves are of general application and do not depend upon the particular problem or fluid. The curves can be used to compare different surfaces or different configurations of a single surface.

Since the surface performance data are in nondimensional form, it is valid for any value of scale as characterized by the hydraulic diameter. It is therefore possible, for a single surface, to plot a complete "carpet" of curves on a graph of V^* against P^* consisting of intersecting lines of constant hydraulic diameter and constant A^*. This would allow comparisons to include the possibility of different hydraulic diameters. However the comparison task becomes quite complex with so many data on display, particularly when sets of curves for more than one surface are overlaid on each other. Specific comparisons can be more easily made by using the methods described in the following sections.

5 Comparisons for Fixed Frontal Area

The characteristics of compact heat exchangers often need to be compared under the constraint that frontal area is fixed. Application of this condition allows the comparison of heat transfer surfaces without the need for scale to be specified. If A^+ is the fixed frontal area, equation (10) can be rearranged as

$$d_A = \sigma \mathrm{Re} \cdot \frac{\mu A^+}{m} = d_A^* \cdot d_A' \quad (\mathrm{m}) \tag{16}$$

The subscript A implies the fixed frontal area condition, the asterisk implies the solution-related component, and the prime indicates the problem-related part. Since frontal area is now fixed, A^+ joins the problem-related part of the equation.

This relationship allows us to eliminate d from both equations (11) and (12) to yield

$$V_A = \frac{\sigma \mathrm{Re}}{j} \cdot \frac{\mu A^{+2} N_{tu}^+ \mathrm{Pr}^{2/3}}{4m} = V_A^* \cdot V_A' \quad (\mathrm{m}^3) \tag{17}$$

$$P_A = \frac{f}{\sigma^2 j} \cdot \frac{m^3 N_{tu}^+ \mathrm{Pr}^{2/3}}{2A^{+2}\rho^2} = P_A^* \cdot P_A' \quad (\mathrm{W}) \tag{18}$$

A plot of V_A^* against P_A^* with the curves marked with values of d_A^* allows the required comparisons to be made. Curves for the same surfaces as Fig. 1 are plotted in Fig. 2. They show that the pumping power depends little upon the scale (hydraulic diameter) of the surface. It shows the extent to which the "high-performance" strip fin can provide a solution of smaller volume (and thus smaller length L in this constant area case) within the limits of Reynolds number for which performance data are available. Any strip fin solution always has

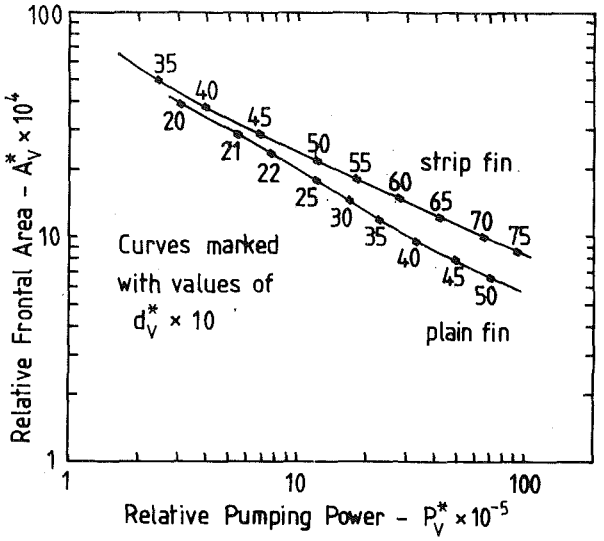

Fig. 3 Relative frontal area plotted against relative pumping power for constant volume and number of transfer units; parameters dimensionless

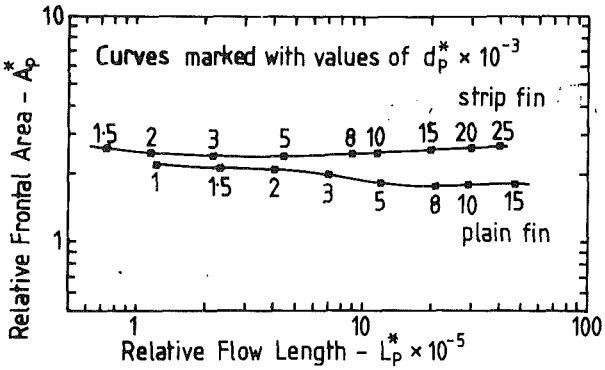

Fig. 4 Relative frontal area plotted against relative flow length for constant pumping power and number of transfer units; parameters dimensionless

a higher pumping power than any plain fin solution. Quantitative comparisons can be made as before, and it can be seen that where there are solutions of the same frontal area *and* volume for the two surfaces, the strip fin solution requires a hydraulic diameter approximately twice that of the plain fin. (For the same σ this implies half the heat transfer surface area; see equation (2).)

If comparisons of weight are wanted rather than of volume, then as before, V_A^* can be simply multiplied by the value of weight per unit volume for each surface, since this does not change with scale. However cost per unit volume is in all probability a function of scale, and simple comparisons on a cost basis are not possible.

6 Comparisons for Fixed Heat Exchanger Volume

A similar procedure can be followed if one wishes to compare the characteristics of different solutions having the same total volume V^+. We can now rearrange equation (11) and use it to eliminate d from equations (10) and (12) to yield

$$d_v = (\sigma j \mathrm{Re})^{1/2} \cdot \left[\frac{4\mu V^+}{N_{tu}^+ m \mathrm{Pr}^{2/3}}\right]^{1/2} = d_v^* \cdot d_v' \quad (\mathrm{m}) \tag{19}$$

$$A_v = \left(\frac{j}{\sigma \mathrm{Re}}\right]^{1/2} \cdot \left[\frac{4mV^+}{N_{tu}^+ \mu \mathrm{Pr}^{2/3}}\right]^{1/2} = A_v^* \cdot A_v' \quad (\mathrm{m}^2) \tag{20}$$

$$P_v = \frac{f\mathrm{Re}}{\sigma j^2} \cdot \frac{\mu \mathrm{m}^2 N_{tu}^{+2} \mathrm{Pr}^{4/3}}{8\rho^2 V^+} = P_v^* \cdot P_v' \quad (\mathrm{W}) \tag{21}$$

The corresponding curves are plotted in Fig. 3 for the same two surfaces as before. Similar quantitative comparisons can be made. In this case it can be seen that in general the strip fin is likely to have larger frontal area. The curves allow the relative frontal areas and their dependence on relative hydraulic diameter to be instantly assessed, together with the corresponding values of relative pumping power.

7 Comparisons for Fixed Pumping Power

If comparisons are now made of the different geometries that are able to deliver the required heat transfer under the constraint that pumping power has a fixed value P^+, then rearrangement of equation (12) yields the resulting expression for hydraulic diameter

$$d_p = \left[\frac{f\mathrm{Re}^2}{j}\right]^{1/2} \cdot \left[\frac{N_{tu}^+ m\mu^2 \mathrm{Pr}^{2/3}}{2\rho^2 P^+}\right]^{1/2} = d_p^* \cdot d_p' \quad (\mathrm{m}) \tag{22}$$

Substitution of this expression for d_p into equations (10) and (11) yields

$$A_p = \left[\frac{f}{j\sigma^2}\right]^{1/2} \cdot \left[\frac{N_{tu}^+ m^3 \mathrm{Pr}^{2/3}}{2\rho^2 P^+}\right]^{1/2} = A_p^* \cdot A_p' \quad (\mathrm{m}^2) \tag{23}$$

$$V_p = \frac{f\mathrm{Re}}{\sigma j^2} \cdot \frac{N_{tu}^{+2} m^2 \mu \mathrm{Pr}^{4/3}}{8\rho^2 P^+} = V_p^* \cdot V_p' \quad (\mathrm{m}^3) \tag{24}$$

In this case, the comparison can be more easily interpreted if flow length is considered rather than volume and

$$L_p = \frac{V_p}{A_p} = \left[\frac{f\mathrm{Re}^2}{j^3}\right]^{1/2} \cdot \left[\frac{N_{tu}^{+3} m\mu^2 \mathrm{Pr}^2}{32\rho^2 P^+}\right]^{1/2} = L_p^* \cdot L_p' \quad (\mathrm{m}) \tag{25}$$

Figure 4 is a plot of A_p^* against L_p^* for the same two surfaces as before, with the corresponding values of d_p^* marked on the curves. Again, a wide range of comparisons can be rapidly made between different geometric solutions using the same surface type, or between different surfaces.

8 Comparison for Fixed Frontal Area and Volume

Figures 2 and 3 both make it clear that in general it is possible to find solutions to the notional heat transfer problem using different surfaces that have both the same frontal area *and* volume. These solutions are represented by the intersections with horizontal lines on either Fig. 2 or Fig. 3. It can also be seen that for the two curves plotted, there are regions at either end of the Reynolds number ranges where there is no overlap. Where there is overlap the solution effectively relates the hydraulic diameters of the two surfaces to each other. Thus if we wish to compare the performance of surface a at some Reynolds number Re_a, with a different surface b, it is necessary to determine the Reynolds number for surface b to which this corresponds. While this can be done, it implies that the appropriate calculations need to be carried out separately for each combination of surface pairs involved in any comparison exercise. It also means that over parts of the Reynolds number ranges, no comparison can be made.

Both these problems can be overcome by designating a reference surface against which all others can be compared, which in turn also allows direct comparisons among the others. The choice of reference surface is a problem. Bergles et al. (1974) and Soland et al. (1978) have used the Dittus-Boelter equation for turbulent flow through a tube. For the surfaces under consideration here, the Reynolds number

ranges typically from 300 to 10,000, which means that at the low end, the turbulent flow equation is inappropriate. At very low values of Re, the solution for fully developed laminar duct flow (Nusselt number = const) may be appropriate, but not for very far into the range of interest here. Equations describing the transition from laminar to turbulent duct flow are available but the majority of compact surfaces do not demonstrate the traditional duct flow transition behavior, and usually both j and f change more or less monotonically with Reynolds number.

The surface configuration eventually selected as reference surface is a notional strip fin, which has infinitely small strip thickness (and thus $\sigma = 1$) and strip width equal to strip pitch. The configuration is shown schematically in Fig. 5. It is then assumed that the performance is described by the equations governing laminar flow over a flat plate

$$j_o = 0.664 \mathrm{Re}_t^{-1/2} \tag{26}$$

$$f_o = 2j_o \tag{27}$$

where Re_t is the Reynolds number based on strip width t. The suffix o indicates values for the reference surface. The hydraulic diameter of this surface is given by

$$d_o = 2t \quad \text{(m)} \tag{28}$$

Equation (26) can therefore be rewritten to express j_o as a function of Reynolds number based on hydraulic diameter

$$j_o = 0.47 \mathrm{Re}_o^{-1/2} \tag{29}$$

The equation for j_o is valid for values of Re_t up to 10^5 and therefore for Re_o values up to 5×10^4. It is thus appropriate over the whole of the Reynolds number range of interest. It is also an appropriate choice because it represents an idealization of the generic strip fin surface type, which is widely recognized as having the potential for advantageous heat transfer characteristics. The choice of strip width equal to strip pitch is arbitrary and proves to have no effect on the comparison method at the end of the day.

Equations (13) and (14) can be used to show that in the case under consideration here

$$\frac{d}{\sigma \mathrm{Re}} = \frac{d_o}{\mathrm{Re}_o} \quad \text{(m)} \tag{30}$$

and

$$\frac{d^2}{\sigma j \mathrm{Re}} = \frac{d_o^2}{j_o \mathrm{Re}_o} \quad (\mathrm{m}^2) \tag{31}$$

The hydraulic diameter can be eliminated from these equations to yield

$$\frac{j}{\sigma \mathrm{Re}} = \frac{j_o}{\mathrm{Re}_o} \tag{32}$$

Substitution for j_o from equation (29) yields the relationship between Re and Re_o

$$\mathrm{Re}_o = 0.605 \left[\frac{\sigma \mathrm{Re}}{j} \right]^{2/3} \tag{33}$$

Thus for any value of Re for the surface under comparison, the corresponding value of Re_o for the reference surface can be calculated. This allows the corresponding ratio of hydraulic diameters to be calculated from equation (30)

$$\frac{d}{d_o} = \frac{\sigma \mathrm{Re}}{\mathrm{Re}_o} = 1.654 (\sigma \mathrm{Re} j^2)^{1/3} \tag{34}$$

The other parameter of interest is the ratio of the pumping powers. From equation (15) one can write

$$\frac{P}{P_o} = \frac{f \mathrm{Re}^2}{j d^2} \Big/ \frac{f_o \mathrm{Re}_o^2}{j_o d_o^2} = \frac{f}{2j\sigma^2} \tag{35}$$

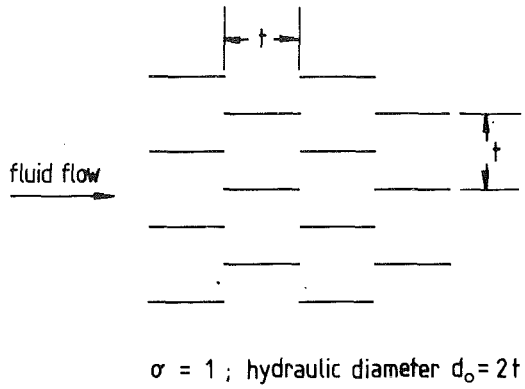

Fig. 5 Notional offset strip reference surface

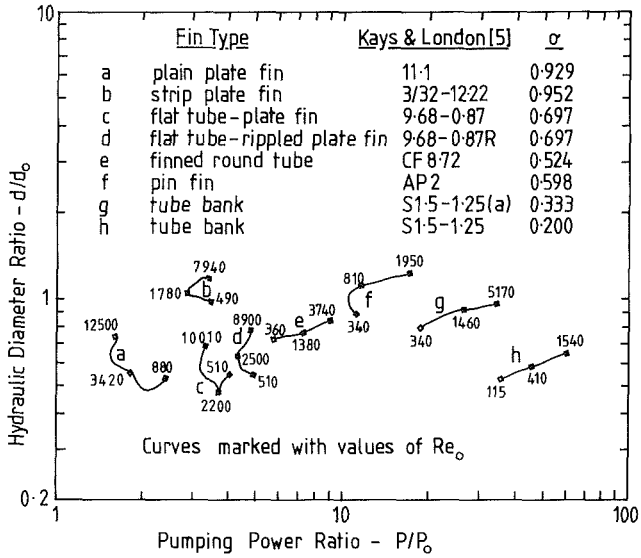

Fig. 6 Pumping power ratio plotted against hydraulic diameter ratio for constant frontal area, volume, and number of transfer units

The comparison is made by plotting d/d_o against P/P_o for the surfaces under consideration, and marking the curves with values of Re_o. Thus to compare the characteristics of different surfaces, points from the curves having the same Re_o value are considered. The pumping power and hydraulic diameter ratios for each can thus be identified and compared. For different surfaces, giving the same rate of heat transfer within the same volume and frontal area, one thus has a measure of the relative pumping power requirements and of the relative hydraulic diameters needed to perform the duty. Low pumping power is obviously advantageous.

The scale of a surface has no effect on material content if all dimensions are truly to scale, but it does have a significant influence on heat transfer surface area requirements; see equation (2). Large hydraulic diameter is thus advantageous. There can be other practical advantages of larger hydraulic diameter. As the scale of a surface is reduced to the limit, it becomes increasingly difficult to scale down the material thickness fully, simply for manufacturing reasons. The ability to use a surface of larger hydraulic diameter helps to alleviate this problem.

Curves for examples of several different generic types of surface are displayed in Fig. 6. A further advantage of the method becomes apparent. For any particular surface, the ratio values only cover relatively narrow ranges. This allows very simple statements of the relative merits of surfaces to be made.

Comparison of plain and segmented strip plate fin surfaces,

Table 1 Relative parameter values for two parameters fixed or constant

RELATIVE PARAMETER	CONSTANT OR FIXED PARAMETER: N_{tu}^+				P^+			V^+	
	d^+	A^+	V^+	P^+	d^+	A^+	V^+	d^+	A^+
d^*	—	σRe	$(\sigma j Re)^{1/2}$	$\left(\frac{f Re^2}{j}\right)^{1/2}$	—	σRe	$\left(\sigma Re^3\right)^{1/4}$	—	σRe
A^*	$\frac{d}{\sigma Re}$	—	$\left(\frac{j}{\sigma Re}\right)^{1/2}$	$\left(\frac{f}{j\sigma^2}\right)^{1/2}$	$\frac{d}{\sigma Re}$	—	$\left(\frac{f}{\sigma^2 Re}\right)^{1/4}$	$\frac{d}{\sigma Re}$	—
V^*	$\frac{d^2}{\sigma j Re}$	$\frac{\sigma Re}{j}$	—	$\frac{f Re}{\sigma j^2}$	$\frac{d^4}{\sigma f Re^3}$	$\frac{\sigma^3 Re}{f}$	—	—	—
P^*	$\frac{f Re^2}{j d^2}$	$\frac{f}{\sigma^2 j}$	$\frac{f Re}{\sigma j^2}$	—	—	—	—	$\frac{\sigma f Re^3}{d^4}$	$\frac{f}{\sigma^3 Re}$
N_{tu}^*	—	—	—	—	$\frac{j d^2}{f Re^2}$	$\frac{j\sigma^2}{f}$	$\left(\frac{\sigma j^2}{f Re}\right)^{1/2}$	$\frac{\sigma j Re}{d^2}$	$\frac{j}{\sigma Re}$

a and b, for example, shows that the strip fin surface can perform the same duty within the same size and shape, but can do so with a hydraulic diameter, double that of the plain fin.

The disadvantage, however, will be a pumping power that is between 40 and 100 percent higher, depending upon the value of the Reynolds number in the reference surface at which the comparison is made.

The very high pumping power penalties associated with pin fin and tube (or rod) bundles can be seen in the curves for surfaces f, g, and h. To make matters worse, the required hydraulic diameter ratios also come down as the value of σ decreases.

Curves c and d are both for flat-sided tube and plate fin surfaces that are identical except that in the case of d the fin is rippled. At low Reynolds numbers the rippled fin carries a 20 percent pumping power penalty with no associated advantages of scaling. At the higher Reynolds numbers, the pumping power penalty is 40 percent but a scaling advantage of between 15 and 30 percent is apparent. The poor hydraulic diameter ratios relative to the plain plate fin arise because of the lower σ values that result from the presence of the flat tubes.

9 Other Comparisons for Fixed Heat Transfer

In the previous sections, the four parameters d, A, V, and P have been considered as variables. Sections 4 to 7 have considered the implications of fixing each in turn. The only irregularity has been that comparisons have been made for constant A, V, and P, while in Section 4, each surface was considered to have its own fixed value of d.

The results are summarized in the first part of Table 1. It would have been possible to make comparisons on the basis of a single constant hydraulic diameter for all surfaces, and indeed some of the existing comparison methods do this. However, the practical value of such a comparison is not easily seen.

In section 8 the comparison procedure was based on the fixing of two of the variables A and V, and in principle it is possible to derive a further five similar comparisons by fixing any two of the four variables, and calculating the corresponding ratios for the other two.

It turns out that four of the comparisons yield curves similar in characteristics to those in Fig. 6, but none of them give such a clear physical interpretation of the relative merits of surfaces as the original. Attempts to compare surfaces transferring a given quantity of heat for the same frontal area and pumping power prove to be impossible as consideration of either Fig. 2 or Fig. 4 will show. The original comparison based on surfaces transferring the same quantity of heat within the same frontal area and volume is believed to be the most valuable.

Table 2 Parameter ratios and reference surface Reynolds number for three parameters fixed or constant

	CONSTANT OR FIXED PARAMETERS: A^+, V^+, N_{tu}^+	A^+, V^+, P^+	A^+, V^+, d^+	A^+, d^+, N_{tu}^+
Re_o	$0.6\left(\frac{\sigma Re}{j}\right)^{1/3}$	$0.96\left(\frac{\sigma^3 Re}{f}\right)^{2/3}$	$\sigma Re \frac{d_o}{d}$	$\sigma Re \frac{d_o}{d}$
$\frac{d}{d_o}$	$1.65\left(\sigma Re j^2\right)^{1/3}$	$1.04\left(\frac{Re f^2}{\sigma^3}\right)^{1/3}$	—	—
$\frac{V}{V_o}$	—	—	—	$0.47\left(\frac{d^3}{\sigma j^2 d_o^3 Re}\right)^{1/2}$
$\frac{P}{P_o}$	$\frac{f}{2\sigma^2 j}$	—	$1.06\left(\frac{f^2 d_o^3 Re}{d^3 \sigma^3}\right)^{1/2}$	$\frac{f}{2\sigma^2 j}$
$\frac{N_{tu}}{N_{tu_o}}$	—	$\frac{2\sigma^2 j}{f}$	$2.13\left(\frac{\sigma j^2 d_o^3 Re}{d^3}\right)^{1/2}$	—

10 Comparisons for Variable Heat Transfer

All comparisons so far have been for a constant heat transfer duty. Comparisons of the relative heat transfer capability of different surfaces and geometries are sometimes required. It is not possible to use the methods described here to assess the relative values of Q, the heat transferred, because Q and ΔT, the effective temperature difference, are interdependent. However comparison can be made on the basis of relative values of N_{tu}, the number of heat transfer units. If one now considers the variables of the system to be d, A, V, P, and N_{tu}, the number of possible comparison procedures of the type already described is greatly increased. All comparisons so far have been for constant N_{tu}. In principle it is possible to fix each of the others in turn and arrive at an equivalent range of comparisons. Table 1 displays the relative parameter values for all possible combinations in which two of the five parameters are fixed. It should be noted that the case of fixed A and fixed d is not presented because in this case the constraints do not adequately define the solution.

It can be seen that the value of d_A^* is always equal to (σRe), and A_d^* always equals (d/σRe). In many cases a relative parameter value is the reciprocal of another relative parameter value elsewhere in the table.

The reasons become clear when the appropriate equations are considered. Plots similar to those in Figs. 1 to 4 can be prepared from values of the three relative parameters contained in any vertical column of Table 1.

Several other comparisons of the type shown in Fig. 6 could be made by fixing any three of the five variables. In practice, not all of these will be useful. Of particular interest will be those comparisons in which A and V are held constant together with one of the other three parameters. Figure 6 presents the case where the third constant parameter is number of transfer units, and Table 2 gives the corresponding ratios for the cases where the third constant or fixed parameter is pumping power and hydraulic diameter respectively. Also shown in Table 2 are the volume and pumping power ratios for the case where d is fixed and A and N_{tu} are held constant. In this case, with fixed frontal area, the volume ratio V/V_o is identical to the flow length ratio L/L_o. The choice of a value of d_o for insertion in the comparison parameters is arbitrary. It can be set equal to unity or alternatively a value near to

those of the surfaces under investigation can be chosen. This latter approach has the advantage that the comparison ratio values themselves should lie in the region of unity.

It can be seen that the parameter $(f/\sigma^2 j)$, or its reciprocal, appears several times in Table 2. It also appears in the relative parameter expressions of Table 1, and consideration of the appropriate equations suggests why this should be so. All of the ratio parameters of Table 2 will cover a relatively small range of values for any particular surface.

11 Relationship to Previously Identified Comparison Parameters

A whole range of surface comparison parameters have been identified here, and it is not surprising that some of them are the same as, or similar to, such parameters identified by other workers.

From the first group of comparison methods as categorized by Shah (1978) (the direct comparison of j and f values), London (1964) identifies j/f as being an indicator of the required heat exchanger frontal area for fixed heat transfer and pressure drop. The larger is j/f, the smaller the required frontal area is likely to be. By taking the expressions in the first column of Table 1 (i.e., the relative values of frontal area, volume, and pumping power for constant number of transfer units and fixed hydraulic diameter), it can be shown that if pumping power is also fixed

$$A^*_{Ntu,d,P} = \frac{f}{\sigma^2 j} \tag{36}$$

where $A^*_{Ntu,d,P}$ indicates relative frontal area for constant N_{tu}, P, and fixed d.

To give a true comparison London's parameter should therefore have been $(\sigma^2 j/f)$. This is also identical to our $N^*_{tu,P,A}$ and equal to half of our $(N_{tu}/N_{tu,o})$. The reciprocal of this parameter has been suggested by Larkin (1968) except that he includes a surface effectiveness term. It is a measure of pumping power per number of transfer units for fixed frontal area. The same parameter has been presented here as $P^*_{Ntu,A}$, which clearly has the same meaning.

Bergwerk (1963) identifies the comparison parameter $(f\mathrm{Re}^2/j)$, which is identical to the expression given here for $d^*_{Ntu,P}$. He does not explain the significance of the parameter but uses it instead of Reynolds number to plot experimental surface performance data. It is a parameter that can be easily calculated from given design conditions and facilitates his comparison procedures. Consideration of his equations confirms the common origin of the parameter with $d^*_{Ntu,P}$ given here.

Dahlgren and Jenssen (1970) use a parameter that is identical to $P^*_{Ntu,d}$ given here, except that they use hydraulic radius rather than hydraulic diameter. In this case the parameter is also effectively a measure of relative pumping power for constant heat transfer and fixed hydraulic diameter, but the authors do not identify it clearly as such. A similar parameter is one of several used by Eckert and Irvine (1956). It only differs in that it uses Stanton number rather than j factor and it also includes a surface effectiveness term. It is interpreted as the pumping power per unit volume for fixed heat exchanger effectiveness, i.e., for fixed number of transfer units. This is an equivalent interpretation to that made here.

Soland et al. (1978) present a method for comparing plate fin surfaces of fixed scale, i.e., for fixed hydraulic diameter. The fixed scale allows them to take fin efficiency into account and their comparison parameters contain a surface effectiveness term. They introduce the further complication that the performance characteristics are reduced so that they relate to the surface areas of the unfinned bare plates. The two comparison parameters are measures of pumping power per unit volume and number of transfer units per unit volume, for surfaces with fixed hydraulic diameter, and these have forms identical to $P^*_{V,d}$ and $N^*_{tu,V,d}$ as identified here. Consideration of the meanings of the two sets of parameters shows that this should be so.

12 Conclusion

A large but coherent family of heat transfer surface performance comparison methods has been presented. The three parameter plots of the type shown in Figs. 1–4 allow a wide range of easily comprehensible comparisons to be made. The comparison of relative pumping powers and relative scale (hydraulic diameters) as displayed in Fig. 6 provides simple and compact statements of the relative merit of different heat transfer surfaces. The paper has also shown how several of the previously identified performance parameters are related to each other.

Acknowledgment

The author would like to acknowledge the value of discussions with Prof. Peter Heggs of Bradford University in helping to generate the ideas presented here.

References

Bergles, A. E., Blumenkrantz, A. R., and Taborek, J., 1974, "Performance Evaluation Criteria for Enhanced Heat Transfer Surfaces," *Proc. 4th Int. Heat Transfer Conf.*, Vol. 2, pp. 239–243.

Bergwerk, W., 1963, "The Utilisation of Research Data in Heat Exchanger Design," Proc. IMechE, Vol. 178.

Dahlgren, A. I., and Jenssen, S. K., 1970, "Comparison of Heat Exchange Surfaces," *Chemical and Process Engineering, Heat Transfer Survey*, pp. 31–33.

Eckert, E. R. G., and Irvine, T. F., 1956, "Selection of Optimum Configurations for a Heat Exchanger With One Dominating Film Resistance," ASME Paper No. 56-S-20.

Kays, W. M., and London, A. L., 1984, *Compact Heat Exchangers*, 3rd ed., McGraw-Hill, London.

Larkin, B. S., 1968, "Evaluation of Heat Exchanger Surfaces for Use in Gas Turbine Cycles," ASME Paper No. 68-WA/HT-23.

London, A. L., 1964, "Compact Heat Exchangers," *Mechanical Engineering*, ASME, Vol. 86, pp. 31–34.

London, A. L., and Ferguson, C. K., 1949, "Test Results of High-Performance Heat Exchanger Surfaces Used in Aircraft Intercoolers and Their Significance for Gas-Turbine Regenerator Design," *Trans. ASME*, Vol. 71, pp. 17–26.

Shah, R. K., 1978, "Compact Heat Exchanger Surface Selection Methods," *Proc. 6th Int. Heat Transfer Conf.*, Toronto, Vol. 4, pp. 193–199.

Soland, J. G., Mack, W. M., and Rohsenow, W. M., 1978, "Performance Ranking of Plate-Fin Heat Exchanger Surfaces," ASME JOURNAL OF HEAT TRANSFER, Vol. 100, pp. 514–519.

The Second Law Quality of Energy Transformation in a Heat Exchanger

D. P. Sekulic[1]
Department of Mechanical Engineering
and Materials Science,
Duke University,
Durham, NC 27706
Mem. ASME

This paper presents the entropy generation (irreversibility) concept as a convenient method for estimating the quality of the heat exchange process in heat exchanger analysis. The entropy generation caused by finite temperature differences, scaled by the maximum possible entropy generation that can exist in an open system with two fluids, is used as the quantitative measure of the quality of energy transformation (the heat exchange process). This measure is applied to a two-fluid heat exchanger of arbitrary flow arrangement. The influence of different parameters (inlet temperature ratio, fluid flow heat capacity rate ratio, flow arrangements) and the heat exchanger thermal size (number of heat transfer units) on the quality of energy transformation for different types of heat exchangers is discussed. In this analysis it is assumed that the contribution of fluid friction to entropy generation is negligible.

Introduction

For comparative evaluation of the energy transformation in heat exchangers, it is necessary to have a quantitative measure of the "quality" or "level of excellence" of performance. As is known from thermodynamics (Hatsopoulos and Keenan, 1965; Haywood, 1980), the measure of excellence of every thermal process is the reversibility of this process. The measure of the level of irreversibility is entropy generation (Bejan, 1982b) or, in other words, entropy is the scale used to determine quantitatively the quality of thermal energy transformation.

Irreversibility due to heat transfer is the principal form of quality reduction in a heat exchanger (reduction in the quality of thermal energy as it is transferred from higher to lower temperatures). Insight into recent research efforts on this subject can be found in Bejan (1987).

A heat exchanger is an inherently irreversible device and, consequently, the second law aspects of heat exchanger theory and design have been considered frequently (Bejan, 1977; London, 1982; Zubair et al., 1987; etc.). However, the general behavior of entropy generation and, consequently, the quality of energy transformation in a heat exchanger as a function of its thermal size, have not yet been completely investigated and published.

First Law of Thermodynamics and Quality of Energy Transformation. Consider a heat exchanger as an open system (Fig. 1). Let it be supposed that nothing is known about the inside structure of this system. For such a "black box" (Fig. 1*a*), it is possible to formulate the balance equations for mass and energy flow. The only information that can be drawn from the macrobalance, with respect to the quality of the heat exchange process (for such black box representation), is the so-called "thermal efficiency" or, most frequently, "heat exchanger effectiveness" (Kays and London, 1984). However, this quantity gives very limited information on the quality of energy transformation in the system. At this stage it is known that, in a real heat exchanger, one part of the thermodynamically limited maximum heat transfer rate is transferred and, therefore, another part is "lost." From the definition of heat exchanger effectiveness (macro-energy balance based on black box representation, i.e., the overall energy balance for a heat exchanger), it is impossible to conclude anything about the detailed structure of this quantity (with respect to the size—physical and thermal—of a heat exchanger).

For such analysis it is necessary to come inside the black box. In other words, the so-called micro-energy balance[2] is relevant (Fig. 1*b*). In general, it is possible to show that the heat exchanger effectiveness is explicitly dependent on: (*i*) the thermal size of the heat exchanger, (*ii*) the fluid flow heat

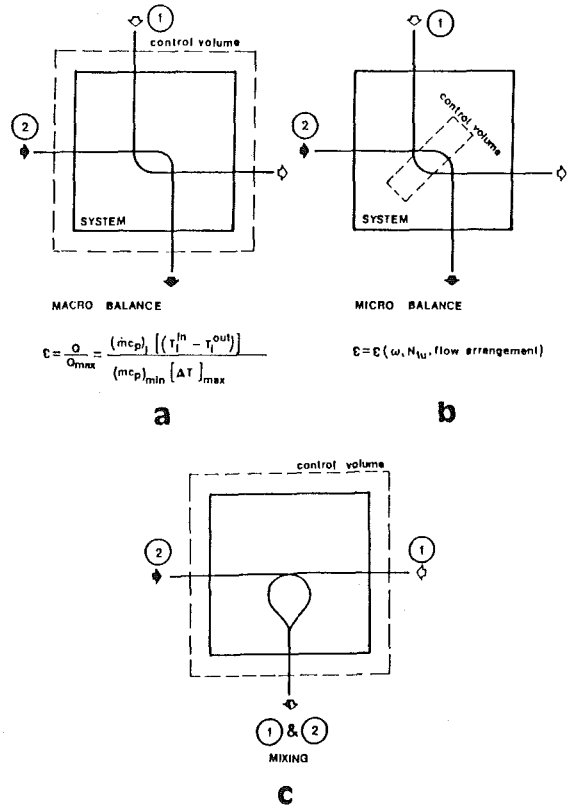

Fig. 1 Heat exchanger: (*a*) macrobalance, (*b*) microbalance, (*c*) fluid mixing

[1]Permanent address: Department of Mechanical Engineering, Faculty of Technical Sciences, University of Novi Sad, 21000 Novi Sad, Yugoslavia.

Contributed by the Heat Transfer Division for publication in the JOURNAL OF HEAT TRANSFER. Manuscript received by the Heat Transfer Division December 12, 1988. Keywords: Heat Exchangers, Thermodynamics and Second Law.

[2]This heat exchanger analysis uses microbalance in setting forth differential equations from which the macroperformance relationships have been derived (i.e., energy balance for an arbitrary differential control volume).

capacity rate ratio, and (*iii*) the flow arrangement in a heat exchanger (using the standard approximations, Kays and London, 1984).

The heat exchanger effectiveness correlation gives little insight into the quality of energy transformation. It is possible only to establish the "operating point" of the heat exchanger under consideration, i.e., it is known what quantity of energy (heat or, better, enthalpy) is transferred. Therefore, information about the quality of energy transformation must be taken from the second law of thermodynamics.

Second Law of Thermodynamics and Quality of Energy Transformation. The entropy imbalance equation or entropy generation balance (Second Law of Thermodynamics) can be applied to a control volume of the open system through a procedure similar to that used in writing the energy balances (Bejan, 1982b). It is easy to show that entropy generation in a heat exchanger for gas-to-gas application can be expressed (Bejan, 1977) as

$$\dot{S}=\dot{S}_{\Delta T}+\dot{S}_{\Delta P}=(\dot{m}c_p)_2\{\omega\ln[1+\epsilon(\tau^{-1}-1)]+\ln[1+\omega\epsilon(\tau-1)] - \omega\frac{R_1}{c_{p_1}}\ln\left(1-\frac{\Delta p_1}{p_1^{in}}\right)-\frac{R_2}{c_{p_2}}\ln\left(1-\frac{\Delta p_2}{p_2^{in}}\right)\} \quad (1)$$

Let only the finite temperature difference be considered as a source of irreversibility. For such a situation equation (1) can be expressed in a reduced form.

$$\dot{S}=\dot{S}_{\Delta T}=(\dot{m}c_p)_2\{\omega\ln[1+\epsilon(\tau^{-1}-1)]+\ln[1+\omega\epsilon(\tau-1)]\} \quad (2)$$

The level of entropy generation is the quantitative measure of the quality level of energy transformation (subsequently in the text: quality of energy transformation). Entropy generation equal to 0 corresponds the highest quality, and entropy generation greater than 0 represents poorer quality. In this way the quality of energy transformation can be expressed in a quantitative manner.

Heat Exchange Reversibility Norm

There is at least one difficulty in applying such a concept. Heat transfer is inherently an irreversible process and it is not possible to compare the quality of a real process in a heat exchanger with an ideal one. However, if it is known which process is the most disadvantageous, the concept can be easily applied:

$$\text{Quality of energy transformation} = 1-\frac{\text{Entropy generation in the real process}}{\text{Entropy generation in the most disadvantageous case}}$$

Now, the question is: Which process is the most disadvantageous in heat exchange between two fluids in a heat exchanger?

In Fig. 1, two completely different physical situations are given: In Fig. 1(*a*), a heat exchanger of arbitrary flow arrangement is presented and in Fig. 1(*c*), fluid mixing of the same two fluids is shown. Let the situation presented in Fig. 1(*c*) be considered in detail.

For an open system, as in the case of adiabatic mixing of the same two fluids, entropy generation is as follows:

$$\dot{S}=\sum_{i=1}^{2}(\dot{m}c_p)_i\ln\frac{T^{out}}{T_i^{in}} \quad (3)$$

The common outlet temperature (from the first law of thermodynamics) is

$$T^{out}=\frac{\sum_{i=1}^{2}(\dot{m}c_p)_i\,T_i^{in}}{\sum_{i=1}^{2}(\dot{m}c_p)_i} \quad (4)$$

Formally, it can be shown (Sarangy and Chowdhury, 1982; Sekulic, 1986) that $\dot{S}_{\Delta T}$, equation (2), has an extremum.

$$(\dot{S}_{\Delta T})_{\max}\ \text{at}\ \epsilon^*=\frac{1}{1+\omega} \quad (5)$$

The substitution of ϵ^* into equation (2) gives the same correlation as equation (3) (adiabatic mixing of two fluid streams). The two physical processes, although completely different, are compared only with regard to the resulting entropy generation. The entropy generation, equation (3), can be interpreted as the largest possible generation that can exist in a heat exchanger considered as an open system with two fluids (Baclic, 1983).

As it is much more convenient to talk about variables in nondimensional form, the dimensionless measure of entropy generation (irreversibility) expressed as

$$I=\omega\ln[1-\epsilon(1-\tau^{-1})]+\ln[1-\omega\epsilon(1-\tau)] \quad (6)$$

and the maximum possible dimensionless entropy generation

$$I_{\max}=\omega\ln\frac{\omega\tau+1}{(\omega+1)\tau}+\ln\frac{\omega\tau+1}{\omega+1} \quad (7)$$

are used.

Finally, from the definition of the quality of an energy transformation process in a heat exchanger, as shown above, and from equations (6) and (7) it follows that

Nomenclature

c_p = specific heat at constant pressure, J/kg K
E = constant = 0.232544, Table 3
I = dimensionless rate of thermodynamic irreversibility
$\dot{m}$ = mass flow rate, kg/s
N_{tu} = number of heat transfer units
p = pressure, Pa
$\dot{Q}$ = heat transfer rate, W
R = ideal gas constant, J/kg K
$\dot{S}$ = rate of entropy generation, W/K
T = temperature, K
Y_S = heat exchange reversibility norm
ϵ = heat exchanger effectiveness
τ = T_1/T_2, inlet temperature ratio
Φ = $N_{tu,B}/N_{tu,A}$
ω = $(mc_p)_1/(mc_p)_2 \le 1$, heat capacity rate ratio

Subscripts

A = pass A
B = pass B
max = maximal value
min = minimal value
Δp = refers to Δp
ΔT = refers to ΔT
1 = low heat capacity rate side
2 = high heat capacity rate side

Superscripts

• = per unit time
in = at exchanger inlet
out = at exchanger outlet
* = at maximal irreversibility

Acronyms

HERN = heat exchange reversibility norm, equations (8) and (9)

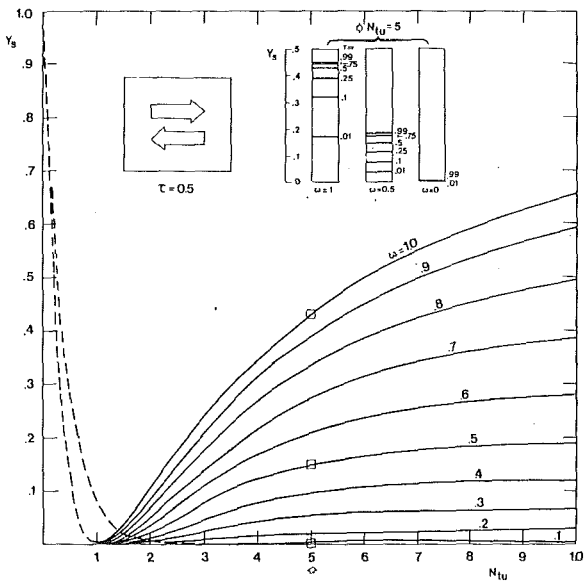

Fig. 2 Y_S **versus** N_{tu}, ω, **and** τ **of countercurrent heat exchanger**

$$Y_S = 1 - \frac{\omega \ln[1-\epsilon(1-\tau^{-1})] + \ln[1-\omega\epsilon(1-\tau)]}{\omega \ln\dfrac{\omega\tau+1}{(\omega+1)\tau} + \ln\dfrac{\omega\tau+1}{\omega+1}} \tag{8}$$

The quantity derived from equation (8) can be termed the "Heat Exchange Reversibility Norm" (HERN). Note that the complementary value $(1-Y_S)$ is the "entropy generation number" (Bejan, 1977) scaled by the maximum entropy generation number, which has the physical meaning of the "irreversibility norm" (Sekulic and Baclic, 1984) or entropy generation level.

In cases where pressure drop must be taken into account, the definition of HERN must be modified, i.e., the relations given by equations (6) and (7) need to be replaced by those including the irreversibility contribution resulting from the pressure drop (see equation (1)). However, this modification is not trivial. The definition of the pressure drop contribution corresponding to the maximum irreversibility is not straightforward. In order to do this the convention regarding reference outlet pressures must be established. General recommendations concerning reference outlet pressure do not exist and must be analyzed separately for different heat exchanger applications, along with the definition of the HERN term.

The pressure drop contribution to the entropy generation (i.e., the effect on the quality of energy transformation in a heat exchanger) could be analyzed directly from equation (1). Details of such an approach, especially valuable for thermodynamic optimization, have been discussed by Bejan (1977), Sekulic and Herman (1986), and recently by Bejan (1987).

Let the measure of the quality of energy transformation (HERN) be considered more closely. As can be seen from equation (8), the quality of the heat transfer process in a heat exchanger depends on three quantities (considering only the part of irreversibility caused by finite temperature differences): (*i*) the ratio of inlet temperatures, (*ii*) the ratio of heat capacity rates, and (*iii*) the effectiveness of the heat exchanger. However, the effectiveness of a heat exchanger is a function of heat capacity rate ratio, number of transfer units, and fluid flow arrangement. Then, the quality of energy transformation in a heat exchanger given by equation (8) is

$$\text{HERN} \sim f(\tau, \omega, N_{tu}, \text{flow arrangement}) \tag{9}$$

Thus the quality of energy transformation in a heat exchanger depends both on the characteristics of the environment in which the transformation occurs (thermal size, flow arrangement) and the characteristics of the fluids (inlet temperature ratio, heat capacity rate ratio).

Table 1 Thermal size of the heat exchanger at the maximum entropy generation

FLOW ARRANGEMENT		$\varepsilon^* = \frac{1}{1+\omega}$	N_{tu}^*
COUNTERCURRENT		$\frac{1-\exp[-N_{tu}^*(1-\omega)]}{1-\omega\exp[-N_{tu}^*(1-\omega)]}$	$\frac{1}{1-\omega}\ln(\frac{1}{\omega})$
COCURRENT		$\frac{1-\exp[-N_{tu}^*(1+\omega)]}{1+\omega}$	$+\infty$
CROSSFLOW: STRONGER FLUID MIXED		$\frac{1}{\omega}[1-\exp(-\omega[1-\exp(-N_{tu}^*)])]$	$\ln[\frac{1}{1+\frac{1}{\omega}\ln\frac{1}{1+\omega}}]$
CROSSFLOW: WEAKER FLUID MIXED		$1-\exp(-[1-\exp(-N_{tu}^*\omega)]/\omega)$	$\frac{1}{\omega}\ln\frac{1}{1+\omega\ln\frac{\omega}{1+\omega}}$
CROSSFLOW: BOTH FLUIDS MIXED		$\frac{1}{\frac{1}{1-\exp(-N_{tu}^*)}+\frac{\omega}{1-\exp(-N_{tu}^*\omega)}-\frac{1}{N_{tu}^*}}$	non explicite
CROSSFLOW: BOTH FLUIDS UNMIXED		$1-\frac{1}{\omega N_{tu}^*}\exp[-(1+\omega)N_{tu}^*]\sum_{n=1}^{\infty}\alpha\omega^{n/2}I_n(2N_{tu}^*\sqrt{\omega})$	non explicite

From equation (9), it can be concluded that the most convenient presentation of the quality of energy transformation in a heat exchanger should be the presentation of HERN as a function of thermal size of a heat exchanger. It is also possible to present the corresponding entropy generation number as a function of effectiveness (Bejan, 1982a; Sharangy and Chowdhury, 1982), but this type of diagram is not very convenient for analysis.

The general behavior of HERN (Y_S lines) for the countercurrent flow arrangement is presented in Fig. 2.

It is easy to derive that

$$\left.\begin{aligned}\frac{\partial}{\partial N_{tu}}(Y_S)=0\\ \frac{\partial^2}{\partial N_{tu}^2}(Y_S)>0\end{aligned}\right\} \tag{10}$$

for $N_{tu}=N_{tu}^*$.

At first glance, this result is not physically quite understandable (Sekulic, 1986; Bejan, 1987).[3] In addition, in reality there is no fluid mixing in a heat exchanger (see Fig. 1 and equation (5)) but, at a certain finite thermal size (for all but cocurrent flow arrangement and ω not equal to 0) the heat transfer process has the same results as fluid mixing. This means that the exit temperatures of both fluids (at a given finite thermal size) are equal.

The maximum entropy generation (i.e., the minimum HERN) separates the (Y_S, N_{tu}) region into two parts. From the standpoint of quality of energy transformation, in the region to the left of the minimum quality point (dashed lines, Fig. 2) the irreversibility of the energy transformation process increases with an increase of thermal size of a heat exchanger (τ, $\omega=$ const). In the region to the right of the minimum point, an increase of thermal size causes a decrease of irreversibility. From that point of view, the second region is preferred. Of course, both regions are of design interest.

In Table 1, calculation results of thermal size at maximum entropy generation are presented for different fluid flow arrangements. In the subsequent table (Table 2), some numerical values of N_{tu}^* for different fluid flow heat capacity rate ratios are given.

What happens when the thermal size of a heat exchanger increases to infinity? It is interesting to note that these limits are

[3] This result can be related to the "entropy generation paradox" in a heat exchanger, noted for the first time by Tribus, published later by Bejan (1982a), and discussed by Sekulic (1986).

Table 2 Thermal sizes of the heat exchanger at the maximum entropy generation for different ω values

ω	1.0	0.9	0.8	0.7	0.6	0.5	0.4	0.3	0.2	0.1
						N_{tu}^*				
ε^*	0.500	0.527	0.555	0.588	0.625	0.667	0.714	0.769	0.833	0.909
	1.000	1.054	1.116	1.189	1.277	1.368	1.527	1.720	2.012	2.558
	+ ∞									
	1.181	1.249	1.327	1.419	1.529	1.666	1.840	2.076	2.426	3.060
	1.181	1.240	1.308	1.386	1.480	1.549	1.738	1.932	2.219	2.742
	1.256	1.324	1.401	1.492	1.601	1.734	1.905	2.135	2.476	3.095
	1.118	1.176	1.246	1.327	1.423	1.540	1.689	2.889	3.184	2.721

THE THREE DECIMAL PLACES SHOWN ARE TRUNCATION FROM N_{tu}^* - VALUES CALCULATED TO 6 SIGNIFICANT FIGURES

Table 3 Heat exchanger reversibility limits (Y_S at $N_{tu} = \infty$)

FLOW ARRANGEMENT	$\omega \neq 1$ & 0	$\omega = 1$	$\omega = 0$
			$Y_S\|_{N_{tu}=\infty}$
	$1-\frac{-\omega\ln\tau+\ln[1+\omega(\tau-1)]}{(1+\omega)\ln\frac{1+\tau\omega}{1+\omega}-\omega\ln\tau}$	1	
	0	0	
	$1-\frac{\omega\ln[1+\frac{1-e^{-\omega}}{\omega}(\frac{1}{\tau}-1)]+\ln[1+(1-e^{-\omega})(\tau-1)]}{(1+\omega)\ln\frac{1+\tau\omega}{1+\omega}-\omega\ln\tau}$	$1-\frac{\ln[1+\varepsilon\frac{(\tau-1)^2}{\tau}]}{\ln\frac{(\tau+1)^2}{4\tau}}$	0
	$1-\frac{\omega\ln[1+(1-e^{-1/\omega})(\frac{1}{\tau}-1)]+\ln[1+\omega(1-e^{-1/\omega})(\tau-1)]}{(1+\omega)\ln\frac{1+\tau\omega}{1+\omega}-\omega\ln\tau}$		
	0	0	
	$1-\frac{-\omega\ln\tau+\ln[1+\omega(\tau-1)]}{(1+\omega)\ln\frac{1+\tau\omega}{1+\omega}-\omega\ln\tau}$	1	

not the same for different flow arrangements with the exception of $\omega = 0$. Calculations of these limits are presented in Table 3.

In case of a condenser or evaporator ($\omega = 0$), it can be proved that equation (8) is reduced to

$$Y_S = 1 - \frac{\ln[1+\epsilon(\tau^{-1}-1)] - \epsilon(1-\tau)}{(\tau-1)-\ln\tau} \tag{11}$$

This limiting case indicates a considerable level of entropy generation as indicated in Table 3. In addition to this, from Fig. 2 it can be recognized that, in this case, the quality of energy transformation decreases monotonically with the increase of thermal size (see also Bejan, 1977, 1987; Sarangi and Chowdhury, 1982; and Zubair et al., 1987).

Application of HERN Concept to Various Types of Heat Exchanger

It is important to determine whether a HERN analysis can be used to establish which of two competitive heat exchanger flow arrangements is better with respect to the quality of energy transformation. In Fig. 3, a comparison of the quality of energy transformation (expressed through Y_S or $1-Y_S$) in a set of the six main flow arrangements (one pass heat exchangers) is presented. It is obvious that HERN values of various flow arrangements vary between the two completely different situations: countercurrent (the best) and cocurrent (the worst), and that this criterion is very selective. As the size of a heat exchanger increases (see Fig. 4), the behavior of HERN differs dramatically in the two limiting cases (countercurrent and cocurrent). The larger the heat exchanger for the cocurrent fluid flow arrangement, the lower is the HERN, and vice versa for countercurrent flow: the larger the heat exchanger (for $N_{tu} > N_{tu}^*$), the greater is the HERN.

Another interesting result seen from Fig. 4 is that, for the arrangement with both fluids mixed, HERN comes to the local

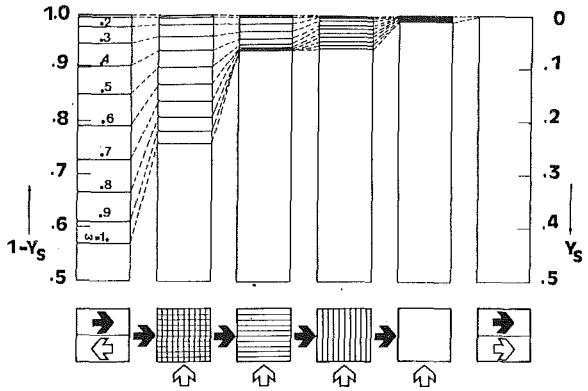

Fig. 3 Irreversibility and/or reversibility levels of heat exchangers ($N_{tu} = 5$, $\tau = 0.5$)

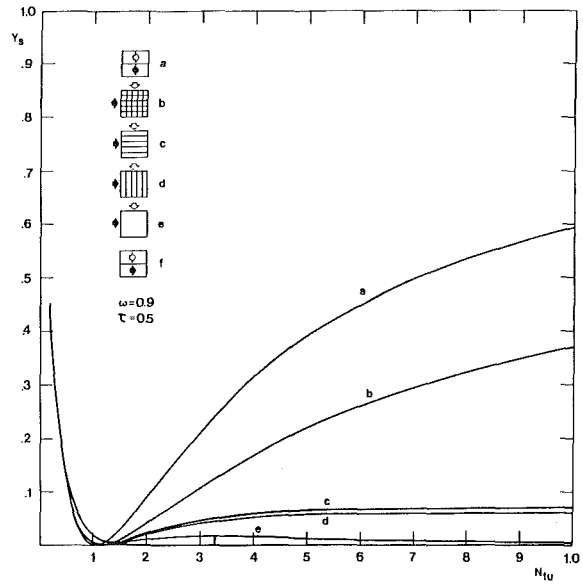

Fig. 4 Y_S for one-pass heat exchangers

maximum. This means that it is possible to find a thermal size for some real heat exchangers (heat exchangers of finite size), at which a local minimum in entropy generation exists.

Even without a study of other details of entropy generation in these six characteristic cases of one-pass heat exchangers, it can be concluded that the cocurrent flow arrangement is, of course, the least favorable, while the others are more or less favorable, although not as good as the countercurrent arrangement.

In the Fig. 5, a comparison of entropy generation levels (expressed in terms of $1-Y_S$) in three characteristic noncompact shell-and-tube heat exchangers is presented. For balanced fluid streams (the heat capacity rate ratio of fluid streams equal to 1), the flow arrangement "1-2 shell-and-tube exchanger, shell fluid mixed—TEMA E shell" is obviously the least desirable (Case a, Fig. 5).

Multipass exchangers can be analyzed in a similar way to one-pass two-fluid heat exchangers. In Fig. 6, a comparison of entropy generation level for selected two-pass arrangements is presented. As can be seen from this figure, for a complete imbalance between fluid streams there is no difference between flow arrangements under consideration, but some difference exists for ω greater than zero. It is especially obvious between the inverted and identical order flow arrangements for ω greater than 0.5.

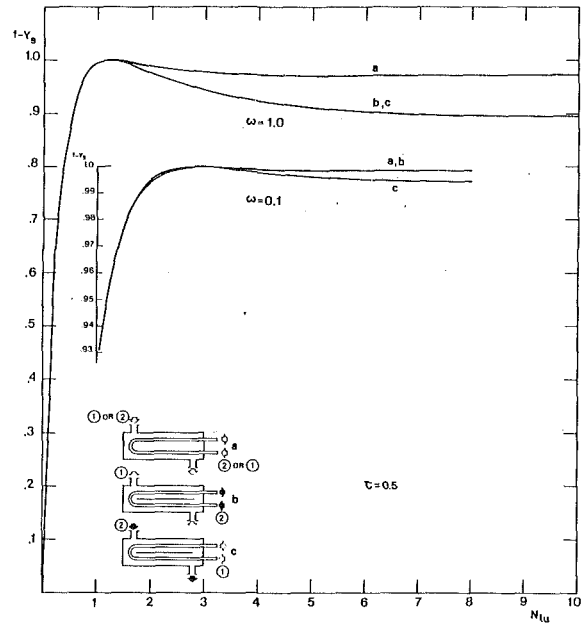

Fig. 5 Entropy generation level versus N_{tu} of shall and tube heat exchangers (a—shell fluid mixed, *b* and *c*—shell fluid unmixed)

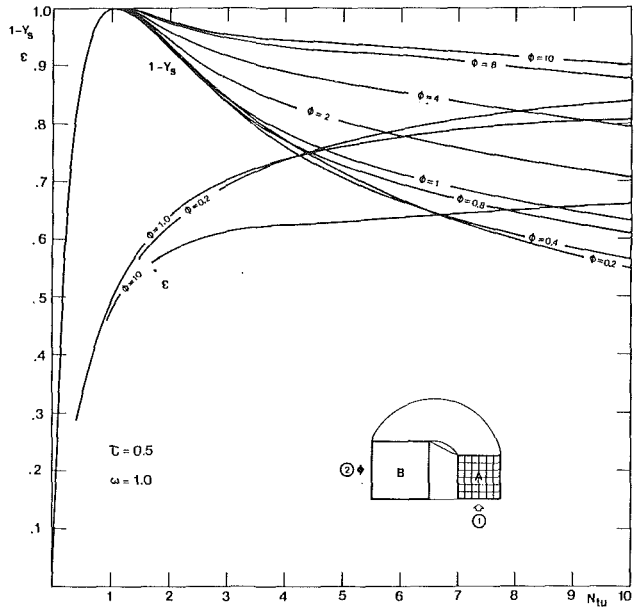

Fig. 7 Entropy generation level and ϵ versus N_{tu} of two-pass heat exchanger with unequally sized passes (pass *A* neither fluid mixed, pass *B* both fluids mixed)

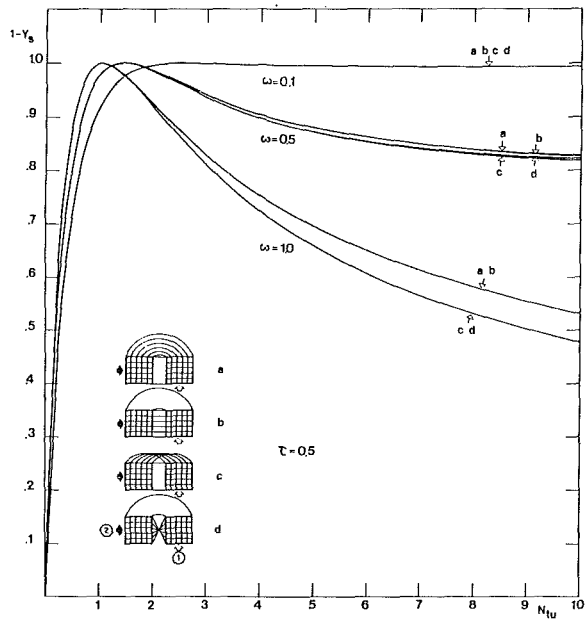

Fig. 6 Entropy generation level versus N_{tu} of two-pass crossflow heat exchangers (*a* and *b*—countercurrent coupling inverted order, *c* and *d*—countercurrent coupling identic order; *a* and *c*—weaker fluid unmixed throughout, *b* and *d*—stronger fluid unmixed throughout)

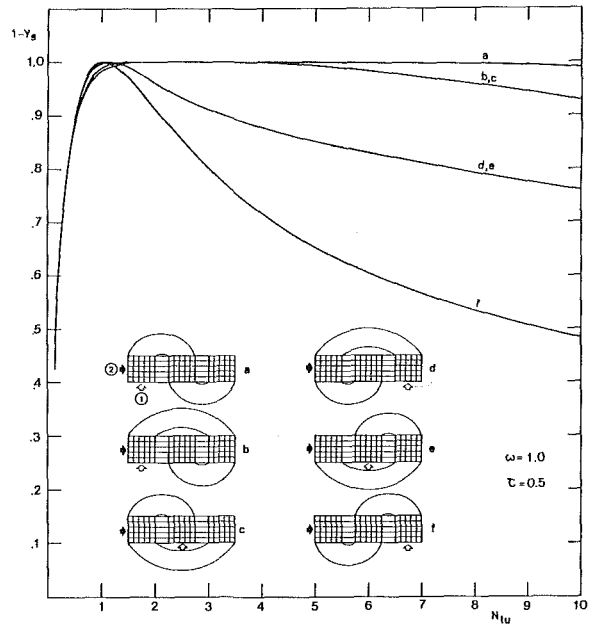

Fig. 8 Entropy generation level versus N_{tu} of three-pass heat exchangers (stronger fluid stream unmixed throughout and the weaker stream mixed between passes and unmixed in each pass)

Figure 7 shows entropy generation level $(1 - Y_S)$ and heat exchanger effectiveness of a two-pass heat exchanger with unequally sized passes as a function of the number of heat transfer units. An analysis of entropy generation, as seen in the same figure, shows that irreversibility is increased by increasing the difference between the passes (for instance, by increasing Φ above 1, i.e., the pass with poorer effectiveness is enlarged). Hence, the larger the pass B, the higher the entropy generation and the lower the effectiveness of the exchanger. On the contrary, positive effects can be achieved by reducing Φ, i.e., enlarging pass A in relation to pass B. It should be noted that for different N_{tu} values at $\Phi < 1$, effects can be either positive or negative. The analysis shows that the causes of positive or negative effects in combining unequally sized passes in two-pass crossflow heat exchangers should be sought in the level of entropy generation in a heat exchanger.

Finally, the comparison of three-pass exchangers is given in Fig. 8. It is clear that arrangement *f* (inverted order, pure countercurrent) is the best, and that arrangement *a* (inverted order, pure cocurrent flow arrangement) has the highest entropy generation level.

Operating Point Charts and Irreversibility Limits

Some further uses of the HERN approach in heat exchanger design are possible. From the first law of thermodynamics (macro and microbalances), as already shown, the operating point (N_{tu}, ω, ϵ) for a given situation can be found. Are there solutions that satisfy the set of parameters for a given

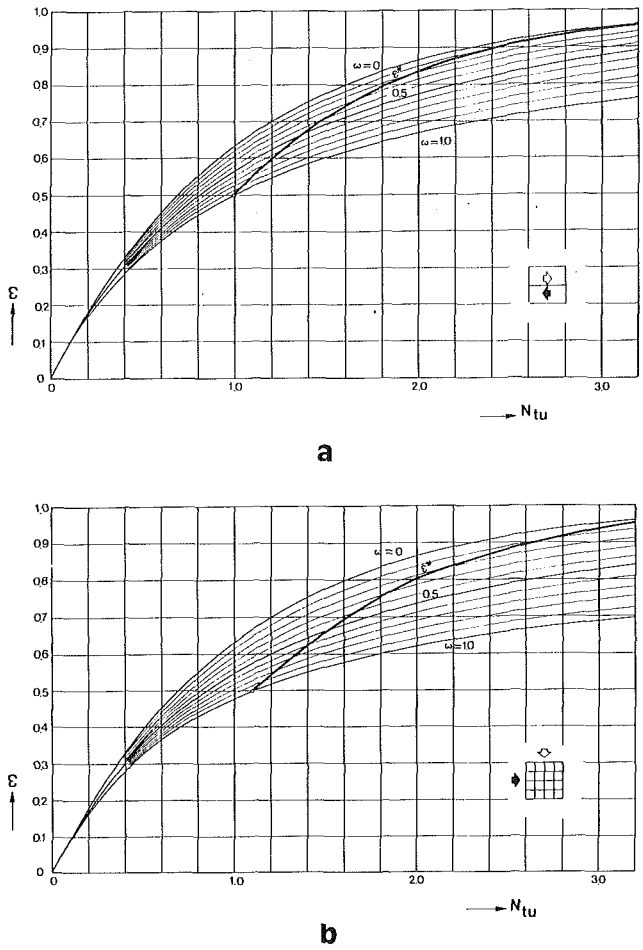

Fig. 9 Operating point charts and irreversibility limits of countercurrent and crossflow heat exchangers (crossflow with both fluids unmixed)

operating point, but that are not recommendable from the standpoint of the second law of thermodynamics? In the limit, the set of operating points corresponding to the minimum of HERN is "prohibited" from the second law standpoint: (N^*_{tu}, ω, ϵ^*). This line can be drawn in an (N_{tu}, ω, ϵ) diagram (for all but cocurrent flow arrangement) as a set of the most inconvenient heat exchanger operating points (from the standpoint of energy transformation quality). Such diagrams are presented in Fig. 9 for two characteristic cases (countercurrent and crossflow flow arrangements).

One must be careful in the interpretation of this presentation. It does not mean that the designer should avoid a priori the region near maximum irreversibilities. In this region the heat exchanger operates in such a way that the outlet temperature difference between the fluids involved almost or totally disappears. Whether the designer should avoid the region near maximum irreversibilities depends on the whole system, in which the heat exchanger is only a component.

The line (N^*_{tu}, ω, ϵ^*) separates the (N_{tu}, ω, ϵ) region into two parts. The first one ($N_{tu} < N^*_{tu}$, i.e., to the left of the ϵ^* line for $\omega = \text{const}$) is characterized by the increase of entropy generation level with increased thermal size of a heat exchanger. In this region, greater thermal size does not mean better quality of energy transformation. For the cocurrent flow arrangement, in the whole region of finite size heat exchangers (complete range of N_{tu} values), an increase of heat exchanger thermal size means an increase of entropy generation level and a decrease of the quality of energy transformation.

It should be noted here that there are some flow arrangements for which the behavior of the HERN curve is more complicated than for countercurrent or cocurrent flow arrangements (for an example of the existence of a local maximum, see Fig. 4 for a crossflow arrangment with both fluids mixed). It is clear that the explanation for the behavior of the quality of energy transformation is somewhat different from the above simpler cases.

In the pragmatic, engineering sense, the full meaning of the concept "quality" includes the thermoeconomic aspect, too. It should be emphasized that thermoeconomic optimization and the concept of entropy generation might be linked together. Depending on the characteristics of a given system and the chosen objective function, various approaches are possible (London, 1982; Zubair et al., 1987). The interrelation between the concept discussed in this paper and the possible thermoeconomic optimization was analyzed recently by Sekulic and Baclic (1987). The thermoeconomic optimum and high quality of energy transformation are related to each other for most operating points under consideration, as had been indicated by Sekulic and Baclic (1987).

Concluding Remarks

The quality of energy transformation in a heat exchanger, expressed in terms of HERN, is a selective criterion in the analysis of a heat exchange process. Linkage of this measure of quality with economic considerations remains to be studied.

Acknowledgments

The author gratefully acknowledges Professor A. Bejan, Duke University, and Professor L. London, Stanford University, for helpful criticism and suggestions. The author's research was supported by the SIZ NR Vojvodina Science Fund, the U.S. Department of Energy (Grant No. DOE-JFP No. 818) and Fulbright Program (Grant No. 11044/88).

References

Bejan, A., 1977, "The Concept of Irreversibility in Heat Exchanger Design: Counterflow Heat Exchangers for Gas-to-Gas Applications," ASME JOURNAL OF HEAT TRANSFER, Vol. 99, pp. 374–380.

Bejan, A., 1982a, "Second-Law Analysis in Heat Transfer and Thermal Design," *Advances in Heat Transfer*, T. F. Irvin and J. P. Hartnett, eds., Vol. 15, p. 28.

Bejan, A., 1982b, *Entropy Generation Through Heat and Fluid Flow*, Wiley, New York, Chap. 2.

Bejan, A., 1987, "The Thermodynamic Design of Heat and Mass Transfer Processes and Devices," *Heat and Fluid Flow*, Vol. 8, pp. 258–276.

Baclic, B. S., 1983, Leeds University, Personal Communication.

Hatsopoulos, G. N., and Keenan, J. H., 1965, *Principles of General Thermodynamics*, Wiley, New York, Chap. 14.

Haywood, R. W., 1980, *Equilibrium Thermodynamics*, Wiley, New York, Chap. 9.

Kays, W. M., and London, L., 1984, *Compact Heat Exchangers*, McGraw-Hill, New York, Chap. 2.

London, A. L., 1982, "Economics and the Second Law: An Engineering View and Methodology," *Int. Journal of Heat and Mass Transfer*, Vol. 25, pp. 743–751.

Sarangi, S., and Chowdhury, K., 1982, "On the Generation of Entropy in a Counterflow Heat Exchanger," *Cryogenics*, Vol. 22, pp. 63–65.

Sekulic, D. P., 1986, "Entropy Generation in a Heat Exchanger," *Heat Transfer Engineering*, Vol. 7, pp. 83–88.

Sekulic, D. P., and Baclic, B. S., 1984, "Enthalpy Exchange Irreversibility," *Proc. of the Faculty of Techn. Sci., University of Novi Sad*, Vol. 15, pp. 113–123.

Sekulic, D. P., and Baclic, B. S., 1987, "The Four E's of a Heat Exchanger," *Second Law Analysis of Thermal Systems*, M. J. Moran and E. Sciubba, eds., ASME, New York, pp. 39–42.

Sekulic, D. P., and Herman, C. V., 1986, "One Approach to Irreversibility Minimization in Compact Crossflow Heat Exchanger Design," *Int. Comm. Heat Mass Transfer*, Vol. 13, pp. 23–32.

Zubair, S. M., Kadaba, P. V., and Evans, R. B., 1987, "Second-Law-Based Thermoeconomic Optimization of Two-Phase Heat Exchangers," ASME JOURNAL OF HEAT TRANSFER, Vol. 109, pp. 287–294.

A. A. Tseng

S. X. Tong

Department of Mechanical Engineering
and Mechanics,
Drexel University,
Philadelphia, PA 19104

S. H. Maslen

J. J. Mills

Martin Marietta Laboratories,
Baltimore, MD 21227

Thermal Behavior of Aluminum Rolling

Proper roll cooling has been identified as a critical factor in the problems of excessive roll spalling and poor thermal crowning in modern, high-speed rolling mills. In this paper, an analytical model has been developed to determine the temperature profiles of the roll and the strip. This model uses basic heat transfer theory and provides the capability of studying the influence of operating parameters on both the work-roll and workpiece temperatures. Examples on cold and hot rolling of aluminum alloys are given to demonstrate the feasibility and capability of the model developed. Previous work on thermal modeling of rolling processes is also briefly reviewed.

Introduction

In metal rolling processes, the roll is used as a tool to deform the workpiece at very high speeds. Heat transfer phenomena of rolling include (1) the heat transferred from the hot strip associated with heat generated by the deformation energy; (2) the heat generated by the interface friction; (3) the heat removed by coolant, ambient air, and the backup roll. The processes occur at extremely high pressure, high velocity, and high temperature. The high temperature, as well as the associated high-temperature gradient, has been observed to cause deterioration of the roll and the rolled product.

Adequate cooling of the roll and strip is of considerable concern to mill designers and oeprators. Improper or insufficient cooling not only can lead to shortened roll life, due to spalling caused by thermal stresses, but can also significantly affect the shape or crown of the roll and result in buckled strips or belled edges. In order to provide adequate cooling of the roll, a good understanding of the roll and strip temperatures is essential. Also, knowledge of the thermomechanical aspects of the process can contribute to insights of the metallurgical structure of the rolled strip and the lubricant behavior, and eventually lead to better control of the material properties and the surface condition of the product.

Considerable work has been done on modeling of the thermal behavior of rolling processes. Johnson and Kudo (1960) used upper bound techniques to predict strip temperatures. Grauer (1961) developed a graphic procedure in an attempt to evaluate the rise in strip temperature during aluminum foil rolling. Based on a Lagrangian formulation, Cermi (1961) provided a transient analytical solution for the temperature distribution in a roll subjected to whole circumferential convective cooling and to a line heat source. Hogshead (1967) simplifed Cerni's approach to provide a convenient analytical expression. Des Ruisseaux and Zerkle (1970) re-examined Cerni's problem by providing an analytical solution for machining applications. Patula (1981), with an Eulerian formulation, attained a steady-state solution for a rotating roll subjected to prescribed surface-heat input over one portion and convective cooling over another portion of the circumference. Yuen (1985) extended Patula's solution to include the effect of a strip scale layer.

Using numerical finite difference approaches, Parke and Baker (1972) developed a two-dimensional (planar) finite difference model to investigate transient roll behavior. By contrast, Wilmotte and Mignon (1973) considered the roll to be axisymmetric. Lahoti et al. (1978) used a similar numerical technique to study the temperatures of the strip and a portion of the roll. Tseng (1984a) investigated both the cold and hot rolling of steel by considering the strip and the roll together. Poplawski and Seccombe (1980) extended a numerical model to include a third dimension.

Mathematically, both the Lagrangian and the Eulerian systems have the capability of describing the rolling process. The coordinates of the former system are fixed on the roll and, in turn, the boundary conditions rotate with respect to the coordinate system. The latter system allows fixed boundary conditions, but gives heat transfer in a moving roll. Since the roll is rapidly rotated, the Lagrangian formulation needs a tremendous number of steps to stimulate the process. According to Parke and Baker (1972), their Lagrangian-model needs 240 steps to simulate one revolution. Hundreds of thousands of steps are necessary for the temperature to reach the steady-state condition. On the other hand, the Eulerian approach may use fewer steps but will result in an elliptical-type governing equation, which will create numerical difficulties at high rotating speed conditions, as indicated by Tseng (1984b). In addition, since all temperature variations in the roll are localized in a very thin layer near the surface, a very fine mesh is required in that layer. Therefore, the numerical simulation can be very costly and time consuming.

In this paper, analytical solutions have been developed to model the thermal behavior of the process. The analytical model considered both the roll and strip. The roll was rotated at a constant speed and the temperature variations were assumed to be cyclically steady state. A Fourier integral technique was used to determine the roll temperatures. The strip temperature was solved by the method of separation of variables. The development of the roll and strip solutions is presented separately. The required compatibility condition to link the roll and strip solutions is also included. The approaches to obtain the convective heat transfer coefficients of cooling and the heat generated by plastic deformation and friction are then discussed. Finally, the heat transfer behavior under typical aluminum rolling conditions is presented to demonstrate the feasibility and capability of the model developed.

Since all the computation can be conducted on a personal computer within a reasonable computing time, the present model enables extensive parametric studies to be performed at a reasonable cost. It also permits on-line simulation, which is

Contributed by the Heat Transfer Division and presented at the 25th National Heat Transfer Conference, Houston, Texas, July 24-27, 1988. Manuscript received by the Heat Transfer Division March 31, 1988; revision received July 5, 1989. Keywords: Conduction, Materials Processing and Manufacturing Processes, Modeling and Scaling.

especially important for automatic process control. The model considers all the major processing parameters and has the capability of studying the influences of cooling practices on both the roll and the workpiece temperatures. Finally, considering that the equivalent heat transfer coefficient for spray cooling and the interface friction behavior remain two of the greatest uncertainties, the analytical model reported here may be the best compromise at present, despite some simplifying assumptions made in the model.

Roll Temperature

In general, the determination of roll temperature is a three-dimensional problem. However, if the effect of axial heat flow is small or the axial temperature variations of the rolls are not significant, the rolling process can be treated as a planar problem. Based on a three-dimensional thermal analysis by Poplawski and Seccombe (1980), the planar condition is indeed a good approximation for flat rolling, especially when considering the region covered by the cooling. In the present analysis, only flat rolling is of interest and no axial variations are considered.

Formulation. With respect to a fixed Eulerian reference frame, the governing equation of the roll temperature (T_r) is

$$\frac{\partial^2 T_r}{\partial r^2} + \frac{1}{r}\frac{\partial T_r}{\partial r} + \frac{1}{r^2}\frac{\partial^2 T_r}{\partial \theta^2} = \frac{\omega}{\alpha_r}\frac{\partial T_r}{\partial \theta} \tag{1}$$

where r and θ are the cylindrical coordinates; ω is the angular velocity; and α_r is the thermal diffusivity. At high rotational speeds, conduction in the circumferential direction is much smaller than conduction in the radial direction or convection in the circumferential direction. Thus, the third term on the left side of equation (1) can be neglected and equation (1) can be reduced to

$$\frac{\partial^2 T_r}{\partial r^2} + \frac{1}{r}\frac{\partial T_r}{\partial r} = \frac{\omega}{\alpha_r}\frac{\partial T_r}{\partial \theta} \tag{2}$$

The roll is subjected to a constant normal heat flux q_r, over the bite angle θ_o, and a uniform convective cooling h_o. The corresponding boundary conditions are

$$k_r\frac{\partial T_r(R,\theta)}{\partial r} = \begin{cases} q_r, & 0 \le \theta \le \theta_o \\ -h_o[T_r(R,\theta) - T_o], & \theta_o \le \theta \le 2\pi \end{cases} \tag{3}$$

$$T_r(0,\theta) = \text{finite} \qquad 0 \le \theta \le 2\pi$$

where k_r is the thermal conductivity; R is the radius of the roll; and T_o is the coolant reference temperature.

Solution. In dimensionless form, equation (2) becomes

$$\frac{\partial^2 t}{\partial \rho^2} + \frac{1}{\rho}\frac{\partial t}{\partial \rho} = \text{Pe}\frac{\partial t}{\partial \theta} \tag{4}$$

where $t = h_o(T_r - T_o)/q_r$ is the dimensionless temperature; ρ is the normalized radius equal to r/R; and Pe, the Peclet number, equals $\omega R^2/\alpha_r$. The corresponding normalized boundary conditions become

$$\frac{\partial t(1,\theta)}{\partial \rho} = \begin{cases} \text{Bi}, & 0 \le \theta \le \theta_o \\ -\text{Bi}\,t(1,\theta), & \theta_o \le \theta \le 2\pi \end{cases}$$
$$t(0,\theta) = \text{finite} \qquad 0 \le \theta \le 2\pi \tag{5}$$

where Bi is the Biot number equal to $h_o R/k_r$.

The roll rotates at a constant speed so that the temperature variations become cyclic steady-state. The Fourier integral technique can be used to determine the cyclic temperature variation. The technique yields a solution to the governing equation (4) and the boundary conditions (5), in an infinite series form:

$$\begin{aligned} t(\theta,\rho) = \theta_0/2\pi + 1/\pi \sum_{n=1}^{\infty} \{ & M_0(A_n)M_0(A_n\rho)/[nD(A_n)] \\ & \times \{\sin[\Theta_0(A_n) - \Theta_0(A_n\rho) - n(\theta-\theta_0)] + \sin[n\theta - \Theta_0(A_n) \\ & + \Theta_0(A_n\rho)]\} + A_n M_1(A_n)M_0(A_n\rho)/[nD(A_n)\text{Bi}] \\ & \times \{\sin[\Theta_1(A_n) - \Theta_0(A_n\rho) - n(\theta-\theta_0) - \pi/4] \\ & + \sin[n\theta - \Theta_1(A_n) + \Theta_0(A_n\rho) + \pi/4]\}\} \end{aligned} \tag{6}$$

where A_n is defined as $\sqrt{n\,\text{Pe}}$; and M_m and Θ_m are, respectively, the modulus and phase of the Kelvin function, and can be defined as

$$M_m^2(A_n) = \text{Ber}_m^2(A_n) + \text{Bei}_m^2(A_n), \qquad m = 0 \text{ or } 1 \tag{7}$$

and

$$\Theta_m(A_n) = \arctan\left[\frac{\text{Bei}_m(A_n)}{\text{Ber}_m(A_n)}\right], \qquad m = 0 \text{ or } 1 \tag{8}$$

Here Ber_m and Bei_m are, respectively, the real and imaginary parts of the Kelvin functions, which relate to Bessel functions with a complex argument (Abramowitz and Stegun, 1964). The function of $D(A_n)$ in equation (6) can be defined as

$$D(A_n) = Z_1^2 + Z_2^2$$

where

$$\begin{aligned} Z_1 &= \text{Ber}_0(A_n) + \sqrt{n\text{Pe}/2}\,[\text{Ber}_1(A_n) + \text{Bei}_1(A_n)]/\text{Bi} \\ Z_2 &= \text{Bei}_0(A_n) - \sqrt{n\,\text{Pe}/2}[\text{Ber}_1(A_n) - \text{Bei}_1(A_n)]/\text{Bi} \end{aligned} \tag{9}$$

The advantage of expressing the normalized temperature as a function of the modulus and the phase is that the solution can be represented by an infinite series. Results with any desired accuracy can be achieved by including the proper number of

Nomenclature

A = constant defined in equation (12)
Bi = Biot number = hR/k
C_i = interface parameter
d = jet diameter
e = heat generation density rate
h = heat transfer coefficient
k = thermal conductivity
K = strength coefficient
n = strain hardening exponent
Pe = Peclet number = $\omega R^2/\alpha$
Pr = Prandtl number of coolant = ν/α
q = heat flux
r, θ = cylindrical coordinates
R = radius of roll
Re = Reynolds number of jet flow = Ud/ν
t = dimensionless temperature = $h_0(T_r - T_0)/q_r$
T = temperature
U = average jet velocity
V_o = average strip velocity
x, y = Cartesian coordinates
α = thermal diffusivity
ν = kinematic viscosity
ρ = dimensionless radial coordinates = r/R
ω = angular velocity

Subscripts

e = entry
n = index
o = average or uniform values
r = quantity related to roll
s = quantity related to strip
∞ = ambient value

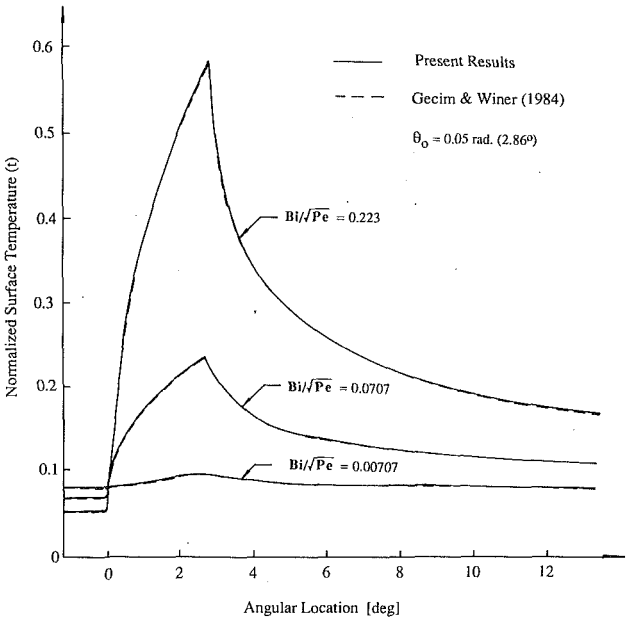

Fig. 1 Normalized roll surface temperature at various conditions

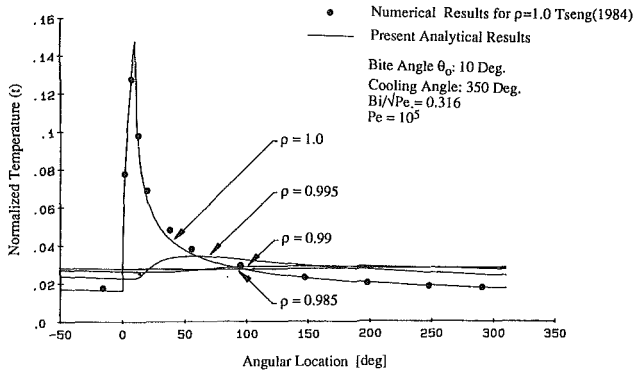

Fig. 2 Normalized roll temperature at several radial locations

terms. If only the first term of the series representation of the modulus, equation (7), and the first two terms of the phase, equation (8), are taken into account, the present solution reduces to the one developed by Gecim and Winer (1984).

The cases considered by Gecim and Winer (1984) are first studied and the results are shown in Fig. 1. In this figure, the normalized surface temperatures of the roll are plotted against the angular location for three values of $\mathrm{Bi}/\sqrt{\mathrm{Pe}}$ for the heating angle, $\theta_o = 0.05$ rad (2.86 deg). As shown, the differences between the present results and those of Gecim and Winer (1984) are insignificant. Since the Peclet number considered is relatively high and the first one or two terms of the infinite series solution are dominant, the solution of Gecim and Winer, as expected, is accurate enough. Also, as shown in the figure and indicated in equation (9), the roll temperature depends strongly on the ratio of $\mathrm{Bi}/\sqrt{\mathrm{Pe}}$ and this ratio plays a significant role in the determination of the roll temperature.

The present solution is also compred with a numerical result for a typical rolling condition: $\theta_0 = 0.175$ rad (10 deg), $\mathrm{Pe} = 10^5$, and $\mathrm{Bi} = 10^2$ (or $\mathrm{Bi}/\sqrt{\mathrm{Pe}} = 0.316$) as shown in Fig. 2. The numerical result was reported by Tseng (1984b) based on a finite difference technique to solve the governing equation including conduction in the circumferential direction, equation (1), instead of equation (2) considered in the present analysis. As shown in Fig. 2, the current surface result agrees very well with the finite difference result with a uniform mesh of 10×144; the maximum difference is about 3 percent near the bite region. The normalized temperatures at other radial locations are also depicted in Fig. 2. As indicated, the temperature variations are limited within a very thin layer. In fact, this thermal layer behavior has been discussed by many investigators [e.g., Patula (1981) and Gecim and Winer (1984)] and has a tremendous influence on the thermal stress pattern (Tseng et al., 1988). Recently, the concept of the thermal layer has also been applied to a numerical analysis by Tseng (1984b) for improving computational accuracy.

Similar to the boundary layer theory, the thermal boundary layer, δ can be defined as the normalized distance from the roll surface ($\rho = 1 - \delta$) at which the temperature difference between the local value and the core temperature reaches 1 percent of the core temperature. Based on the temperature solution of equation (6), the boundary layer thickness can be found as

$$\delta = \frac{2}{\sqrt{2\,\mathrm{Pe}} - 1} \ln \left[\frac{200\mathrm{Bi}(\sqrt{2}\mathrm{Bi}/\sqrt{\mathrm{Pe}} + 2)}{\theta_0 \sqrt{\mathrm{Pe}/2}(\mathrm{Bi}^2/\mathrm{Pe} + \sqrt{2}\mathrm{Bi}/\sqrt{\mathrm{Pe}} + 1)} \right] \tag{10}$$

As indicated in equation (10), the thermal layer thickness depends not only on the Peclet number Pe, but also on the Biot number Bi, and the bite angle θ_0. This improves on the previous layer thickness predictions by Patula (1981) and Tseng (1984b). Their approximations indicate that the thickness is a function of Pe only. For the case considered in Fig. 2, the thermal layer δ is 0.015. In other words, more than 97 percent of the roll is uniformly at the core temperature.

Strip Temperature

In the strip temperature evaluations, as in the roll calculations, the planar simplification was also assumed. The separation of variables method was used to determine the strip temperatures. The technique yields a solution that can accommodate the nonuniformity of the strip entry temperature. The solution is an extension of Cerni's (1961) work in which a uniform entry temperature was assumed.

Formulation. The temperature changes within the strip result from the heat generated by the work of deformation, and the friction between roll and strip in the arc of contact. The deformation work and the frictional dissipation were assumed to be uniformly distributed in the strip and the arc of contact, respectively. It should be noted that the thermal behavior of the friction along the interface is still not fully understood. In addition, when the variation of strip height is compared to the arc length of contact, and the variation of velocity to the velocity itself, the respective ratios are relatively small. As a consequence, a strip problem is postulated whose height $2y_o$ equals an average strip thickness in the bite; whose length x_o equals the length of the bite; and whose sections move at the average strip velocity V_o. This strip temperature (T_S) can be expressed mathematically as

$$\frac{\partial^2 T_s}{\partial y^2} - \frac{V_o}{\alpha_s}\frac{\partial T_s}{\partial x} + \frac{e}{k_s} = 0 \tag{11}$$

where α_s is the thermal diffusivity of the strip; k_s is the strip heat conductivity; and e is the rate of deformation heat generation per unit volume. The implication of equation (11) is that conduction of heat in the x direction is negligible compared to the transport of heat due to the strip motion.

Before entering into the roll bite, the strip loses heat to the ambient air or coolant by convection and radiation, an important effect, especially in hot rolling. The strip entry temperature with a parabolic variation in the thickness direction is often observed and can be expressed as

$$T_s(0, y) = T_e + A(y/y_o)^2 = T_e + (T_\infty - T_e)/[1 + (k_s/h_s y_o)] \tag{12}$$

where T_e is the strip entry temperature at the center; T_∞ is the strip ambient temperature; h_s is the equivalent heat transfer coefficient along the strip including convection and radiation. The other boundary conditions to be satisfied are

$$\frac{\partial T_s(x,0)}{\partial y} = 0, \qquad 0 \le x \le x_o \tag{13}$$

and

$$-k_s \frac{\partial T_s(x,y_o)}{\partial_y} = q_s, \qquad 0 \le x \le x_o \tag{14}$$

where q_s is the uniform surface flux (outward flux is positive).

Solution. The solution of equation (11) subjected to the boundary conditions of equations (12)–(14) can be found from the classical approach of separation of variables associated with the principle of superposition, i.e.,

$$T_s(x,y) - T_e = \frac{A}{3} + \left(e - \frac{q_s}{y_o}\right)\frac{\alpha_s x}{k_s V_o} + \frac{q_s y_o}{2k_s}\left[\frac{1}{3} - \left(\frac{y}{y_o}\right)^2\right] + \frac{4}{\pi^2}\left(\frac{q_s y_o}{2k_s} + A\right)\sum_{n=1}^{\infty}\frac{(-1)^n}{n^2}\exp\left[-\left(\frac{n\pi}{y_o}\right)^2\frac{\alpha_s x}{V_o}\right]\cos\left(\frac{n\pi}{y_o}y\right) \tag{15}$$

If the entry temperature is uniform, i.e., $A = 0$ or $h_s = 0$ in equation (12), the solution of equation (15) is reduced to the one presented by Cerni (1961), derived by a Fourier transformation technique. The values of the heat generation rate e, and uniform heat flux q_s, will be discussed later.

Temperature Compatibility of Roll and Strip. In the rolling process, tremendous pressures build up in the roll/strip interface, and the roll and strip come into intimate contact. However, some coolant film or scale might be also accumulated in the interface and the thermal resistance of this film or scale should be considered. If the interface resistance can be considered as a function of the magnitude of the interface heat flux and if the average assumption is also applied, the interface condition can be expressed as

$$\bar{T}_s|_{y=y_o} / \bar{T}_r|_{r=R} = C_i \tag{16}$$

where $\bar{T}_s|_{y=y_o}$ is the average strip surface temperature in the contact arc; $\bar{T}_r|_{r=R}$ is the average roll bite temperature; and C_i is the thermal resistance parameter. If the interface heat flux is toward the roll or q_s is positive, $C_i > 1$ and vice versa. The magnitude of C_i should be determined experimentally. In the present analysis, the interface thermal resistance is assumed to be insignificant. In other words, the surface temperatures of the roll and the strip approach to the same value, i.e., $C_i = 1$. In a more rigorous approach, Yuan (1985), as mentioned earlier, provided a solution by physically considering the scale layer.

The average temperatures of the roll and the strip can be found by the integration of the surface temperatures at the bite as presented in equations (6) and (15), respectively:

$$\bar{T}_r|_{r=R} = T_o + \frac{q_r\theta_0}{2\pi h_o} + \frac{2q_r}{\pi h_o \theta_0}\sum_{n=1}^{\infty}\frac{1-\cos(n\theta_0)}{n^2 D(A_n)} \{M_o^2(A_n) + A_n M_o(A_n) M_1(A_n) \times \cos[\Theta_o(A_n) - \Theta_1(A_n) + \pi/4]/\mathrm{Bi}\} \tag{17}$$

and

$$\bar{T}_s|_{y=y_o} = T_e + \left(e - \frac{q_s}{y_o}\right)\frac{\alpha_s x_o}{2k_s V_o} - \frac{q_s y_o}{3k_s} + \frac{A}{3} + \frac{4y_o^2}{\pi^4 x_o}\frac{V_o}{\alpha_s}\left(\frac{q_s V_o}{2k_s} + A\right)\sum_{n=1}^{\infty}\frac{1}{n^4}\left\{1 - \exp\left[-\left(\frac{n\pi}{y_o}\right)^2\frac{\alpha_s x_o}{V_o}\right]\right\} \tag{18}$$

where x_o is the length of the bite equal to $R\theta_o$. In addition, the heat flux out of the strip plus the friction energy must be equal to the heat flux into the roll, i.e.,

$$q_s x_o + q_f x_o = q_r R\theta_o$$

or

$$q_s + q_f = q_r \tag{19}$$

where q_f is the friction flux generated by interface friction and will be discussed in the next section. It is to be noted that the heat fluxes q_r and q_s in equations (17) and (18), respectively, are unknown and should be determined by the compatibility conditions of equations (16) and (19).

Heat Generation Input

Information on heat generated by plastic deformation and friction used in the strip and temperature compatibility calculations is obtained from a previously developed force-torque model called ROLLING by Maslen and Tseng (1981). The model is a modified version of that given by Alexander (1972) and is based on work originally done by von Karman. It includes: (1) analysis of the elastic flattening of rolls by Jortner et al. (1960), (2) allowance for variable friction coefficients, and (3) construction such that the variation of the flow stress due to temperature and strain rate can be added as appropriate. It was assumed, based on experimental evidence observed by Farren and Taylor (1925), that 90 percent of the deformation work calculated from the ROLLING program is converted to heat. The friction energy will be entirely converted to heat.

Cooling Heat Transfer Coefficient

Knowledge of the heat transfer coefficient of cooling is essential in evaluating the process numerically. As indicated by Tseng et al. (1987), the heat transfer coefficient is greatly affected by the spray nozzle configuration, spray header arrangement, flow rate, roll speed, roll surface temperature, and other operating factors. Many investigators, including Hill and Gray (1981) of U.S. Steel, and Liu et al. (1987) of Alcoa, have studied the heat transfer coefficient. However, a few qualitative results have been reported from these investigations. It is to be noted that at very high rolling speeds (say, 15 m/s or 3000 fpm), the temperature variation is localized within a very thin layer near the surface as mentioned earlier. As a result, this makes the measurement of heat flux or heat transfer coefficient extremely difficult.

In the present analysis, the heat transfer measurements of spray impinging on stationary surfaces reported by Kadinova and Krivizhenko (1968) have been used. For a round jet with diameter d, the heat transfer coefficient can be approximated by

$$h = 0.42\frac{k_c}{d}\mathrm{Re}^{0.63}\mathrm{Pr}^{0.36}(l/d)^{-0.4} \tag{20}$$

where k_c is the thermal conductivity of coolant; l is the distance from the spray jet to the roll; $\mathrm{Re}(= v/\alpha)$ is the Reynolds number of jet flow; $\mathrm{Pr}(= Ud/v)$ is the Prandtl number of coolant; U is the average of the spray; and v is the kinematic viscosity of the coolant. Equation (20) is an appropriate relationship as long as the value of l/d is in the range of 5 to 60, suitable for most of the water-based cooling systems used in the aluminum industry.

Aluminum Cold Rolling

A cold rolling case studied by Maslen and Tseng (1981) was first selected to illustrate the heat transfer model developed. The parameters used in the present calculations were the actual operating data from an aluminum rolling mill, a Davy-Loewy four-high cold strip mill located in Martin Marietta's Lewisport Plant.

Table 1 Operating data and mechanical properties for cold rolling case

Material	=	1100 Aluminum Alloy
Roll Radius (R)	=	25.4 cm (10 in.)
Annealed Gauge	=	0.259 cm (0.102 in.)
Entry Gauge	=	0.259 cm (0.102 in.)
Exit Gauge	=	0.159 cm (0.0627 in.)
Strip Width	=	91.44 cm (36.0 in.)
Roll Surface Speed (ωR)	=	1091 cm/s (2148 fpm)
Entry Tension	=	1.2065 kN/cm^2 (1750 psi)
Exit Tension	=	1.9677 kN/cm^2 (2854 psi)
Strength Coefficient (K)	=	160 MPa (23.2 ksi)
Strain Hardening Exponent (n)	=	0.26
Yield Strength	=	34.5 MPa (5 ksi)
Friction Coef.	=	0.05

Table 2 Input for heat transfer calculation for cold rolling case

Bite Length (x_o)*	=	1.63 cm (0.64 in.)
Strip Exit Speed (V_o)*	=	1096 cm/sec (2158 fpm)
Deformation Energy*	=	986 kW (1322 hp)
Friction Energy*	=	213 kW (286 hp)
Strip Entry Temperature	=	21 °C (70 °F)
Roll Thermal Conductivity (k_r)	=	0.456W/cm-°C (2.21 Btu/hr-in-°F)
Roll Thermal Diffusivity (α_r)	=	0.1265 cm^2/s (0.0196 in^2/s)
Cooling Heat Transfer Coef. (h_o)	=	0.93 W/cm^2-°C (11.2 Btu/s-in^2-°F)
Strip Thermal Conductivity (k_s)	=	1.82 W/cm-°C (8.75 Btu/hr-in-°F)
Strip Thermal Diffusivity (α_s)	=	0.94 cm^2/s (0.1457 in^2/s)

* Output from the ROLLING program

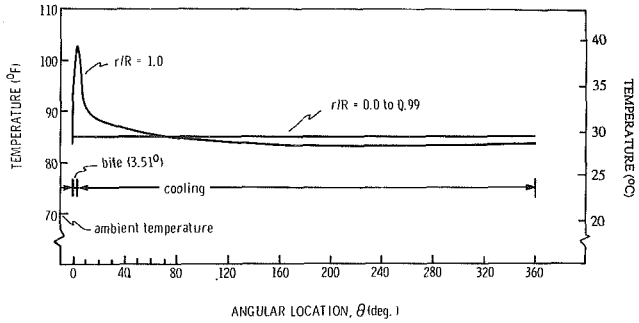

Fig. 3 Roll temperature for cold rolling case

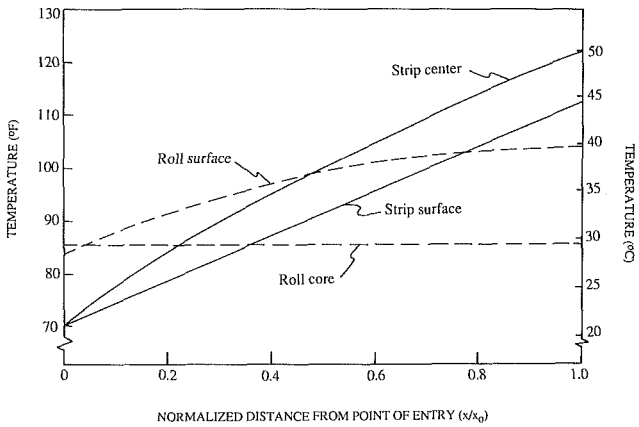

Fig. 4 Temperature near the bite for cold rolling case

The operating data and the material properties used as the input for the ROLLING program are summarized in Table 1. The power curve, $\sigma = K\epsilon^n$, was used to represent the stress (σ)–strain (ϵ) relationship for the annealed aluminum alloy. The values for the parameters K and n in Table 1 were obtained from uniaxial tensile tests and are consistent with the data reported by Anderson (1967). At relatively small strains, if the power curve is followed, the flow stresses can be less than the yield stress. To be consistent with the experimental data, the flow stress is assumed to be the yield stress, if it is less than the yield stress. The friction coefficient was determined by matching the caculated power to the measured value while the measured separating force was used for verification of the calculated force.

The output data obtained from the ROLLING code including the bite length, strip exit speed, deformation energy, and friction energy will be used as input for the heat transfer calculations. These data as well as the thermal properties are summarized in Table 2. The properties used to calculate the heat transfer coefficient are those of a coolant consisting of 94 percent Kensol 50 and 6 percent BT 75 at room temperature, provided by Kendal Refining Co. of Bradford, PA. The initial and cooling ambient temperatures of the strip are 21°C (70°F). The angle for heat input θ_o is estimated from bite length.

The temperature results for the roll are shown in Fig. 3 and the corresponding temperatures near the bite region are depicted in Fig. 4. The temperature variations of the roll essentially are similar to those numerically estimated by Tseng (1984b) or measured by Stevens et al. (1971). Indeed, the temperature varies in a very thin layer near the roll surface. For the case considered, the penetration of the surface temperature variation is less than 1 percent of the radius. Ninety-nine percent of the roll remains at a constant uniform temperature. For any rolling situation involving lower rotational speeds, such as in hot rollng, the penetration would be larger and can be predicted by equation (10).

The strip temperatures shown in Fig. 4 increase almost linearly with respect to the rolling direction. The figure also shows that the surface temperature is higher than that at the centerline. For the case considered, only 1.9 percent of the deformation energy of the strip is transferred to the roll. In other words, more than 90 percent of the heat flux that heats the roll comes from the friction energy. If either the friction coefficient or the lubricant is changed, the temperature of the roll and strip can be affected significantly.

Modification. In general, before entering the bite, the strip and the roll have different surface temperatures. As soon as the strip hits the roll, their surface temperatures will reach about the same value, if the roll and strip come in intimate contact. As reported by Tseng (1984a), this intimate contact generates a steplike temperature change at strip surface. In constant, as shown in Fig. 4, the local temperature difference between the strip and the roll is significant. One way to generate a step temperature change at the strip surface to reduce the temperature difference shown in Fig. 4 is to assume a heat source located at the bite entry. It should be noted that if the initial strip temperature is higher than the roll entering temperature (typical hot rolling conditions), a heat sink or negative heat source should be assumed at the entry contact point.

The heat transfer behavior of a moving heat source or sink has been well studied. The solution developed by Rosenthal (1946), summarized in the Appendix, was adopted in the present study to create the necessary step-type temperature profile by superimposing it on the strip solution developed earlier. In fact, the heat source can be considered as a portion of the deformation energy. Note that the highest strip deformation occurs near the bite entry and diminishes monotonically toward the end of the bite. In the strip solution, a uniform deformation throughout the bite was assumed. Therefore, the heat source might represent the nonuniform part of the deformation energy.

Results—Cold Rolling. Figure 5 shows the results using this modification in the bite region. The difference in the local surface temperature between the strip and the roll almost dis-

Table 3 Operating data and mechanical properties for hot rolling cases

Material	=	5052 Aluminum Alloy
Roll Radius (R)	=	35.56 cm (14 in.)
Anneal Gauge	=	3.81 cm (1.5 in.)
Entry Gauge	=	3.81 cm (1.5 in.)
Exit Gauge	=	1.52-3.05 cm (0.6-1.2 in.)
Roll Speed (ωR)	=	102-152 cm/s (200-300 fpm)
Entry Tension	=	0
Exit Tension	=	0
Strip Entry Temperature	=	371 °C (700 °F)
Strength Coefficient (K)	=	102 MPa (14.8 ksi)
Strain Hardening Exponent (n)	=	0.14
Yield Strength	=	30 MPa (4.4 ksi)
Friction Coef.	=	0.2

appears. The temperature behavior away from the bite region is similar to that in Fig. 3. The computer results indicate that 8.2 percent of the deformation energy is transferred to the roll. At the same time, the heat source contains 59 percent of the deformation energy. Comparing Figs. 5 and 4, the strip surface temperature at the exit of the bite is reduced from 50°C (122°F) to 48°C (119°F) and the hottest roll temperature changes from 39°C (103°F) to 47°C (117°F). It is believed that the interface temperature should be the mean of the modified strip and the roll bite temperatures. In this case, the mean strip exit temperatures is 48°C (118°F).

A noncontact infrared thermometer, Model HR-1PS, manufactured by Capintec Instruments, Inc., Ramsey, NJ, was used to measure the strip exit temperature for further verification of the value predicted by the model. The average exit temperature of the strip was 46°C (116°F), which agrees very well with the model prediction. It is to be noted that during measurement, the strip surface sometimes was flooded with coolant, and the measured temperature varied within a range of 6°C (10°F). It is suspected that the sensor sometimes measured the coolant instead of the strip surface.

Aluminum Hot Rolling

In hot rolling, the strip is normally rolled at elevated temperatures at which recrystallization proceeds faster than work hardening. In addition, the hot strip is generally rolled at a thicker gage and lower speed than that of the cold strip.

The operating data of a 92-in. three-stand mill at the Lewisport Plant were recorded for the study. The 5052 alloy strips with 3.81 cm (1.5 in.) entry gage were heated to 371°C (700°F) and rolled at various reductions and velocities. Since the aluminum alloy is non-hardenable by thermal treatment and the entry temperature is much higher than the recrystallization temperature (=288°C), the strip can be safely assumed to be at the annealed condition. The first stand data were used for deformation and friction energy calculations and reported in Table 3. The average friction coefficient obtained from the hot rolling cases is 0.2.

Since in the hot rolling cases, the objective is parametrically to study the effects of changing reduction and rolling velocity, the stress-strain relationship assumed to be constant can result in better interpretation of the results. The parameters K and n were assumed temperature independent in the hot rolling analysis too; their values in Table 3 were obtained based on the mechanical behavior tested at 300°C. This temperature is close to the mean strip temperature for the cases considered (the calculation of mean strip temperature will be discussed later). As a consequence, the corresponding properties used in the calculation should be accurate enough. The K value in Table 3 is about one third of the data at the room temperature reported by Anderson (1967). This is consistent with the results reported by Wolf et al. (1974) that the strengths of the 2000 and 5000 series alloys are reduced to one third of their room temperature strengths when the testing temperature is increased

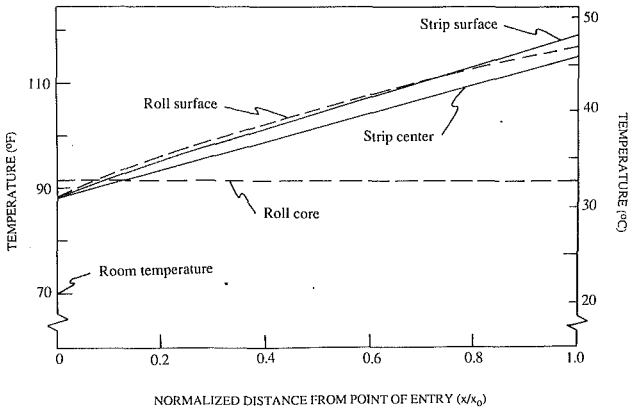

Fig. 5 Modified temperature near the bite for cold rolling case

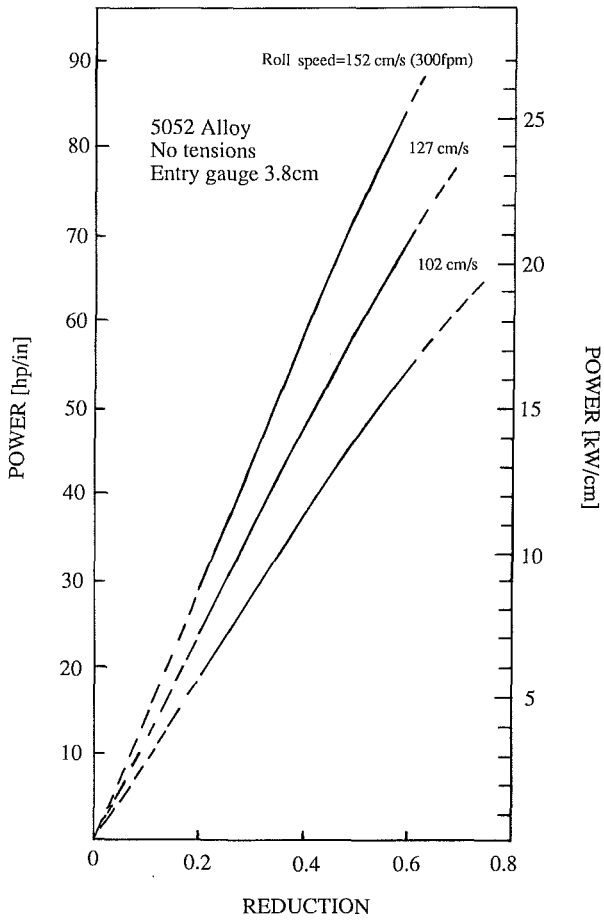

Fig. 6 Power predicted by the ROLLING computer code

from the room temperature to 300°C. The corresponding stress-strain relationship of 5052 at 300°C is about the same as that of Alloy 1100 at the room temperature.

Since the strip width varies, the power consumption estimated by the ROLLING program is reported in kW/cm as shown in Fig. 6. Again, the results from the ROLLING program are input into the thermal model to predict the heat transfer behavior. The thermal properties adopted in the cold rolling case are also used in the hot rolling cases.

The exit temperatures at the locations of strip center, interface, and roll core are shown in Fig. 7 under various hot rolling conditions. As shown, increase of reduction from 0.2 to 0.7 increases the roll core and the interface temperatures

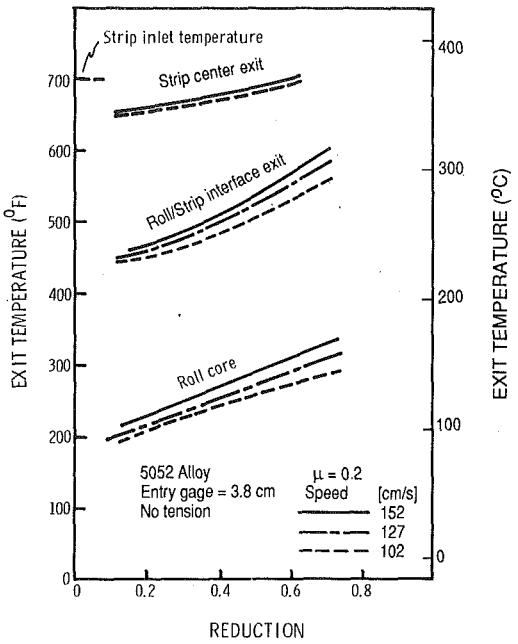

Fig. 7 Roll and strip temperatures for hot rolling cases

by approximately 50°C (90°F). On the other hand, the strip center temperature increases by only 30°C (54°F). The figure also indicates that the faster the rolling speed, the higher the rolling temperature. While the speed changes from 102 to 152 cm/s (200 to 300 fpm), the roll core and the interface temperatures increase by 13°C (23°F) at a 20 percent reduction and 26°C (47°F) at the reduction equal to 0.7. In contrast, with an increase of reduction from 0.2 to 0.7, the temperature change at the strip center is insignificant: about 3°C (5°F). In general these results are consistent with those phenomena observed in the mill operation.

Concluding Remarks

A numerical model has been developed to link two analytical solutions. This model satisfies the required compatibility conditions between the roll and the strip for both heat flux and temperature. Results for typical aluminum cold and hot rolling cases are presented to demonstrate that parametric studies can be performed at a reasonable cost. Thus, the model can be used to explore the effect of changes in geometry and operating parameters on the complex thermal behavior observed in aluminum rolling.

The results also show that under typical rolling conditions, high-temperature gradients occur within a thin surface layer near the bite and, in turn, generate high thermal stress. It is to be noted that the high rolling pressure is also applied at the same location. In the cases considered, this thin surface layer can be as small as 1 percent of the radius, which explains the fact that the thermal crown responds immediately to the changes in cooling conditions. In addition, the results indicate that the roll or strip temperature can be greatly affected by the friction coefficient and the thermal properties of the coolant.

Acknowledgments

This work was partially sponsored by National Science Foundation under Grants No. DMC-8513492 and CBT-8709281 with Drexel University. The authors gratefully acknowledge the support. Thanks are also due to P. F. Sun, A. S. Gunderia, and F. H. Lin of Drexel University for their programming assistance.

References

Abramowitz, M., and Stegun, I. A., 1964, *Handbook of Mathematical Functions*, Applied Mathematics Series No. 55, National Bureau of Standards, Washington, DC.

Alexander, J. M., 1972, "On the Theory of Rolling," *Proc. Royal Soc. London, Ser. A.*, Vol. 326, pp. 535–563.

Anderson, W. A., 1967, "Work Hardening, Recovery, Recrystallization and Grain Growth," in: *Aluminum, Vol. 1, Properties, Physical Metallurgy and Phase Diagrams*, K. R. Van Horn, ed., American Society for Metals, pp. 85–90.

Cerni, S., 1961, "The Temperature and Thermal Stresses in the Rolling of Metal Strip," Ph.D. Thesis, Carnegie-Mellon University, Pittsburgh, PA.

Des Ruisseaux, N. R., and Zerkle, R. D., 1970, "Temperature in Semi-infinite and Cylindrical Bodies Subjected to Moving Heat Sources and Surface Cooling," ASME JOURNAL OF HEAT TRANSFER, Vol. 92, pp. 456–464.

Farren, W. S., and Taylor, G. I., 1925, "The Heat Developed During Plastic Extension of Metal," *Proc. Royal Soc. London, Ser. A.*, Vol. 107, pp. 422–429.

Gecim, B., and Winer, W. O., 1984, "Steady Temperature in a Rotating Cylinder Subject to Surface Heating and Convective Cooling," ASME *J. Tribology*, Vol. 106, pp. 120–127.

Grauer, H. P., 1961, "Grundlagen des Folienwalzen," *Z. Metallk.*, Vol. 53, pp. 633–645.

Hill, D. R., and Gray, L. E., 1981, "Cooling of Work Rolls in Hot Rolling Mills," *Iron Steel Eng.*, Vol. 58, pp. 57–62.

Hogshead, T. H., 1967, "Temperature Distributions in the Rolling of Metal Strip," Ph.D. Thesis, Carnegie-Mellon University, Pittsburgh, PA.

Johnson, W., and Kudo, H., 1960, "The Use of Upper-Bound Solutions for the Determination of Temperature Distributions in Fast Hot Rolling and Axisymmetric Extrusion Processes," *Int. J. Mech. Sci.*, Vol. 1, pp. 175–191.

Jortner, D., Osterle, J. F., and Zorowski, C. F., 1960, "An Analysis of Cold Strip Rolling," *Int. J. Mech. Sci.*, Vol. 2, pp. 179–194.

Kadinova, A. S., and Krivizhenko, V. I., 1960, "Cooling Efficiency of Jets of Various Designs," *Met. Sci. Heat Treat.*, No. 3, pp. 190–193 (translated from *Metallovedenie i Termicheskaya Obrabotka*).

Lahoti, G. D., Shah, S. N., and Altan, T., 1978, "Computer-Aided Analysis of the Deformations and Temperatures in Strip Rolling," ASME *Journal of Engineering for Industry*, Vol. 100, pp. 159–166.

Liu, J. C., Finn, T. L., and Ramser, R. A., 1987, "Average Transfer Coefficient Measurement Technique for Impinging of Spray Jets on a Rotating Cylinder," in: *Measuring and Metering of Unsteady Flows*, ASME FED-Vol. 40, pp. 33–38.

Maslen, S. H., and Tseng, A. A., 1981, "Program-Rolling Users Manual," Rep. No. MML TR 81-8, Martin Marietta Laboratories, Baltimore, MD.

Parke, D. M., and Baker, J. L. L., 1972, "Temperature Effects of Cooling Work Rolls," *Iron Steel Eng.*, Vol. 49, pp. 83–88.

Patula, E. H., 1981, "Steady-State Temperature Distribution in a Rotating Roll Subject to Surface Heat Fluxes and Convective Cooling," ASME JOURNAL OF HEAT TRANSFER, Vol. 103, pp. 36–41.

Poplawski, J. V., and Seccombe, D. A., Jr., 1980, "Bethlehem's Contribution to the Mathematical Modeling of Cold Rolling in Tandem Mills," *Iron Steel Eng.*, Vol. 57, pp. 47–58.

Rosenthal, D., 1946, "The Theory of Moving Sources of Heat and Its Application to Metal Treatments," *Trans. ASME*, Vol. 68, pp. 849–866.

Stevens, P. G., Ivens, K. P., and Harper, P., 1971, "Increasing Work-Roll Life by Improved Roll-Cooling Practice," *J. Iron Steel Inst. London*, Vol. 209, pp. 1–11.

Tseng, A. A., 1984a, "A Numerical Heat Transfer Analysis of Strip Rolling," ASME JOURNAL OF HEAT TRANSFER, Vol. 106, pp. 512–517.

Tseng, A. A., 1984b, "Finite-Difference Solutions for Heat Transfer in a Roll Rotating at High Speed," *Numerical Heat Transfer*, Vol. 7, pp. 113–125.

Tseng, A. A., Chen, S. J., and Westgate, C. R., 1987, "Experiments on Local Heat Transfer Coefficients for Rolling Processes," in: *Modeling of Materials Processing*, ASME MD-Vol. 3, pp. 51–63.

Tseng, A. A., Tong, S., and Lin, F. H., 1989, "Thermal Stresses of a Rotating Roll in Rolling Processes," *J. Thermal Stresses*, Vol. 12, pp. 427–450.

Wilmotte, S., and Mignon, J., 1973, "Thermal Variations of the Camber of the Working Rolls During Hot Rolling," *Metall. Rep. CRM*, No. 34, pp. 17–34.

Wolf, J., et al., 1974, *Aerospace Structural Metals Handbook*, Vol. III, Mechanical Properties Data Center, Traverse City, MI.

Yuen, W. Y. D., 1985, "On the Heat Transfer of a Moving Composite Strip Compressed by Two Rotating Cylinders," ASME JOURNAL OF HEAT TRANSFER, Vol. 107, pp. 541–548.

APPENDIX

Moving Heat Source

Heat transfer in a body resulting from a moving heat source or sink is governed by

$$\frac{d^2T}{dx^2}+\frac{V_o}{\alpha_s}\frac{dT}{dx}-\frac{h_sC}{k_sB}=0 \tag{A.1}$$

where C is the average perimeter of the strip; B is the average cross-sectional area; V_o, α_s, k_s, and h_s have been defined earlier; x is the distance from the entry of the bite; and the rolling directions is negative. The net heat generation in the strip is assumed to be a point source at $x=0$. The other appropriate boundary conditions are

$$T(x)=T_\infty \qquad \text{as } x\to\pm\infty \tag{A.2}$$

The solution, originally studied by Rosenthal (1946), takes two forms, depending on whether x is greater or less than zero: for $x<0$,

$$T(x)-T_\infty=T_{\max}\exp\left\{+x\sqrt{\left[\left(\frac{V_o}{2\alpha_s}\right)^2+\frac{hC}{k_sB}\right]}-\frac{V_o}{2\alpha_s}\right\}, \tag{A.3}$$

for $x>0$,

$$T(x)-T_\infty=T_{\max}\exp\left\{-x\sqrt{\left[\left(\frac{V_o}{2\alpha_s}\right)^2+\frac{hC}{k_sB}\right]}-\frac{V_o}{2\alpha_s}\right\}, \tag{A.4}$$

where

$$T_{\max}=T(0)-T_\infty=\frac{Q}{2k_sB\sqrt{[(V_o/2\alpha_s)^2+hC/k_sB]}} \tag{A.5}$$

and Q is the heat-source rate.

P. S. Wei
Professor.

C. Y. Ho
Graduate Student.

Institute of Mechanical Engineering,
National Sun Yat-Sen University,
Kaohsiung, Taiwan

Axisymmetric Nugget Growth During Resistance Spot Welding

Three-dimensional weld nugget growths for different welding currents, electrode tip shapes, and thickness ratios of workpieces are determined. By providing an effective model to estimate the heat generation at the faying surface between workpieces and taking into account the phase change due to melting, results show that the calculated weld nugget growth, nugget thickness, and shape of the nugget agree well with experimental data. Heat generation at the faying surface in the early stage of welding and joule heating at long weld times dominate the nugget growth. Consideration of radial heat loss is necessary at longer weld times and higher welding currents.

Introduction

Resistance spot welding is a complicated process, which involves interactions of electrical, thermal, mechanical, and metallurgical phenomena. The materials to be joined are brought together under pressure by a pair of electrodes. A high electric current passes through the workpieces between the electrodes. Due to contact resistance and joule heating, a molten weld nugget is formed in the workpieces. The workpieces are joined as solidification of the weld pool occurs. Due to the complexity of the process, a satisfactory analysis of spot welding is still not available at the present time.

As a first step the formation of the weld nugget must be considered. This requires investigation of the thermal process during spot welding. Detailed temperature distributions were first determined numerically by Greenwood (1961). The contact resistance, which decreases rapidly in the first few half cycles of the welding current pulse, was assumed to be negligible at the faying surface. The maximum temperature (due only to joule heating) occurred in a ring around the edge of the electrode-workpiece contact area at initial stages of welding. At longer weld times the maximum temperature was located near the axisymmetric axis and the faying surface. Based on this model, cooling rates were found to be of the order of 1000 K/s, which may lead to a martensitic structure in almost any steel. Later, Bentley et al. (1963) used a metallographic technique to estimate temperature distributions. Comparison with theoretical results revealed that the temperature distributions were strongly affected by contact resistance in the early stage of welding.

Rice and Funk (1967) developed a one-dimensional model to investigate the thermal history for spot welding composite materials. The contact resistance at the faying surface was determined from experimental data. By neglecting the heat of fusion, transient temperatures were predicted for different shapes of the current pulse and duration. Nied (1984) proposed an elaborate axisymmetric finite element model to predict deformation of electrodes and workpieces. More realistic welding conditions including joule heating, variation of the current density and pressure distributions along contact surfaces, and temperature-dependent thermal properties were considered. The computed results for the weld nugget expansion and the nugget diameter as a function of time showed good agreement with experimental data. This study was mainly applied toward understanding the thermal-mechanical interaction during the electrode-squeezing and welding cycles. Nied's computer code offered highly flexible capabilities to model the spot welding process. However, investigation of primary factors affecting the welding process is still lacking from a heat transfer point of view. Crucial effects of the electrical contact resistance, which varies with temperatures, as well as welding current densities on the axial nugget growth have not been discussed.

Recently, Gould (1987) measured the nugget growth by using a metallographic technique. A one-dimensional thermal model, which accounted for heat of fusion, contact resistance, and convection by qualitatively increasing the effective thermal conductivity in the liquid, was developed for comparisons. The difference between predicted and measured nugget thickness and the nuggest growth was suggested to be due to radial heat losses and underestimation of the heat generation at the faying surface. This demonstrates that a quantitatively consistent model is needed to provide insight into the resistance spot welding process.

In this study, an axisymmetric heat conduction model is developed to predict the three-dimensional nugget growth purely from the heat transfer point of view. An effective estimation of the faying surface heat generation is also presented. The enthalpy method described by Crank (1984) is utilized to account for the phase change. The computed nug-

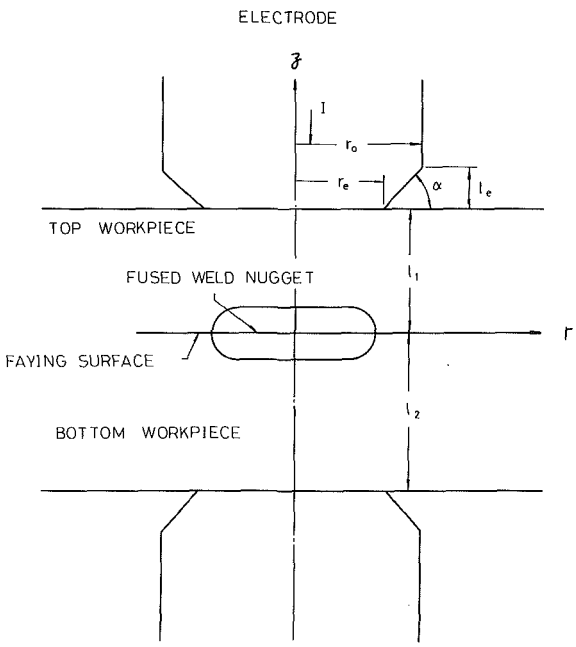

Fig. 1 Resistance spot welding process and coordinate system

Contributed by the Heat Transfer Division for publication in the JOURNAL OF HEAT TRANSFER. Manuscript received by the Heat Transfer Division December 1, 1987; revision received June 25, 1989. Keywords: Materials Processing and Manufacturing Processes, Phase-Change Phenomena, Transient and Unsteady Heat Transfer.

get growth will be compared with the experimental data obtained recently by Gould (1987) to investigate primary factors affecting the resistance spot welding process.

Analysis

The resistance spot welding model considered is shown schematically in Fig. 1. A welding current passes through workpieces and initiates the formation of a weld nugget at the faying surface. In this study, effects of the liquid motion in the fused weld nugget are assumed to be negligible due to the short welding time and the small size of the weld pool in the workpieces. The joule heating, contact resistance, cooling effect of the electrodes, and the phase change of melting are taken into account. In view of limited data available at the temperature involved, thermal and electrical properties of the liquid and the solid are assumed to be constant.

Governing Equations and Boundary Conditions. With the above assumptions, the equations governing the temperature distributions in the electrodes become

$$\rho_e c_e \frac{\partial T_e}{\partial t} = k_e\left[\frac{1}{r}\frac{\partial}{\partial r}\left(r\frac{\partial T_e}{\partial r}\right)+\frac{\partial^2 T_e}{\partial z^2}\right] + \begin{cases} \dfrac{j_e^2}{\sigma_e}, & z > l_1 + l_e \text{ and } z < -(l_2+l_e) \\ \dfrac{R_{te}^4 j_e^2}{\sigma_e}, & l_1 + l_e \geq z \geq l_1 \\ \dfrac{R_{be}^4 j_e^2}{\sigma_e}, & -(l_2+l_e) < z < -l_2 \end{cases} \quad (1)$$

where the last terms on the right-hand side of equation (1) are the joule heating terms, R_{te} and R_{be}, which account for the convergence angle of the electrodes, defined as

$$R_{te} = \frac{l_e r_0}{l_e r_e + (r_0 - r_e)(z - l_1)} \quad (2)$$

$$R_{be} = \frac{l_e r_0}{l_e r_e - (r_0 - r_e)(z + l_2)} \quad (3)$$

To determine the shape change of the weld nugget, the enthalpy method described by Crank (1984) can be used. Instead of working entirely in terms of the temperature, an enthalpy function that represents the total heat content of the material is defined. With a correct enthalpy-temperature relation, the full effect of the phase change can be modeled without needing to know the exact position of the phase change region. This fact makes a numerical solution relatively easy. The heat conduction equation in terms of enthalpy for both the molten and heat-affected zones of the workpieces is given by

$$\frac{\partial h}{\partial t} = \frac{1\partial}{r\partial r}\left(rk\frac{\partial T_i}{\partial r}\right)+\frac{\partial}{\partial z}\left(k\frac{\partial T_i}{\partial z}\right)+\frac{j^2}{\sigma} \quad (4)$$

where $i = 1, 2$ denote the top and the bottom workpieces, respectively. The workpieces are chosen to be of the same material. However, different thermal and electrical properties are specified in the solid and liquid regions. Different enthalpy-temperature relationships have been proposed for the phase change of a pure metal (e.g., Atthey, 1974; Crank, 1984; Bennon and Incropera, 1988). In this study, the en-

Nomenclature

Bi, Bi_e = Biot number; $\mathrm{Bi} = h_a r_0/k_s$, $\mathrm{Bi}_e = h_e r_0/k_s$
Bi_f = $h_f r_0/k_s$
c, C = dimensional and dimensionless specific heat; $C = c/c_l$
F = dependent variable
h, H = dimensional and dimensionless enthalpy; $H = h/\rho_l c_l (T_m - T_\infty)$
h_a, h_e = workpiece to surrounding, and electrode heat transfer coefficient
h_f = faying surface heat transfer coefficient
I = welding current
j, J = dimensional and dimensionless electric current density; $j = I/\pi r_e^2$ in workpiece; $j = I(\sigma R_f/\pi r_e^2 \epsilon_f + 1/\pi^2 r_e^4)^{1/2}$ at workpiece faying surface; $J = jr_0/[k_l \sigma_l (T_m - T_\infty)]^{1/2}$
j_e, J_e = dimensional and dimensionless current density in electrode of radius r_0; $j_e = I/\pi r_0^2$; $J_e = j_e r_0/[k_e \sigma_e (T_{me} - T_\infty)]^{1/2}$
k, K = dimensional and dimensionless workpiece thermal conductivity; $K = k/k_l$
l = workpiece thickness
l_e = length shown in Fig. 1
l_{sl}, L_{sl} = latent heat of melting; $L_{sl} = l_{sl}/\epsilon c_l$
r, R = dimensional and dimensionless radial coordinate; $R = r/r_0$
R_{be} = parameter defined in equation (3)
r_e = electrode radius at contact surface
R_f = faying surface electrical contact resistance
r_0 = electrode radius
R_{te} = parameter defined in equation (2)
R_∞ = static electric contact resistance
t = time
T = temperature
T_{me} = electrode melting temperature
z, Z = dimensional and dimensionless axial coordinate; $Z = z/r_0$
α = electrode convergence angle
β = relaxation factor
δ = l/r_0
δ_e = l_e/r_0
ϵ, ϵ^* = dimensional and dimensionless half temperature range across mushy zone; $\epsilon^* = \epsilon/(T_m - T_\infty)$
ϵ_f = separation between mean surface planes
ζ = Z
θ_e = $(T_e - T_\infty)/(T_{me} - T_\infty)$
θ_i = $(T_i - T_\infty)/(T_m - T_\infty)$
θ_∞ = $T_\infty/(T_m - T_\infty)$
ξ = dimensionless radial coordinate, defined in equation (15)
ρ, ρ^* = dimensional and dimensionless density; $\rho^* = \rho/\rho_l$
σ = electrical conductivity
τ = dimensionless time = $k_l t/r_0^2 \rho_l c_l$
υ = $(T_{me} - T_\infty)/(T_m - T_\infty)$
ϕ = r_e/r_0
ω = $\rho_e c_e k_l/\rho_l c_l k_e$

Subscripts

e = electrode
i = 1 and 2 denoting top and bottom workpiece, respectively
l = liquid
m = melting
s = solid
∞ = ambient

thalpy-temperature relationship used by Voller and Cross (1981) is adopted:

$$h=\begin{cases}\rho_s c_s T_i, & T_i \le T_m-\epsilon \\ h\big|_{T_m-\epsilon}+\dfrac{(\rho_s+\rho_l)l_{sl}(T_i-T_m+\epsilon)}{4\epsilon}, & T_m-\epsilon<T_i<T_m+\epsilon \\ h\big|_{T_m+\epsilon}+\rho_l c_l(T_i-T_m-\epsilon), & T_i\ge T_m+\epsilon\end{cases} \quad (5)$$

Equation (5) was originally proposed by Meyer (1973) for the purpose of smoothing the enthalpy change, which is a discontinuous function across the solid-liquid interface for a pure substance undergoing a change of phase. Hence, a small value of ϵ (e.g., 10 K) is usually assumed for the numerical modeling. Melting or solidification of alloys, unlike that of pure substances, is characterized by the existence of a multiphase or mushy region that separates the pure solid and liquid. The temperature range across the mushy zone can be of the order of 100 K depending on the composition of an alloy. In view of limited data available, properties of the weldments made with AISI 1008 steel (Mn 32 percent, Fe 49.6 percent) are assumed to be the same as those of pure iron in this study. Errors introduced will not be serious. The reason for this is that the temperature range investigated, which is usually around 1500-2000 K, is much larger than that across the mush zone. Besides, the atomic structures of the major constituents, manganese and iron (with atomic numbers of 25 and 26, respectively), are very similar.

The electrodes provide a significant cooling effect during a resistance spot welding process. Heat transfer rates across top and bottom electrode-workpiece contact surfaces yield

$$-k_s\frac{\partial T_1}{\partial z}=h_e(T_1-T_e) \quad \text{at } z=l_1,\quad 0\le r\le r_e \quad (6)$$

$$k_s\frac{\partial T_2}{\partial z}=h_e(T_2-T_e) \quad \text{at } z=-l_2,\quad 0\le r\le r_e \quad (7)$$

Heat transfer losses to the surroundings from workpieces are

$$-k_s\frac{\partial T_1}{\partial z}=h_a(T_1-T_\infty) \quad \text{at } z=l_1,\quad r_e\le r<\infty \quad (8)$$

$$k_s\frac{\partial T_2}{\partial z}=h_a(T_2-T_\infty) \quad \text{at } z=-l_2,\quad r_e\le r<\infty \quad (9)$$

Also, the resistance spot welding process can be affected by the thermal contact resistance at the faying surface. Estimation of the interfacial heat transfer is complicated and uncertain. Hence a heat transfer coefficient is introduced so that the heat transfer rate at the faying surface is determined by

$$k\frac{\partial T_1}{\partial z}=k\frac{\partial T_2}{\partial z}=h_f(T_1-T_2) \quad \text{at } z=0 \quad (10)$$

The heat generation due to the electrical contact resistance between workpieces is an important factor affecting the weld nugget growth (Bentley et al., 1963; Gould, 1987). In this study, the following model is assumed. The interfacial heat generation is modeled by including it in the heat conduction equation governing the material adjacent to the faying surface as additional joule heating. The last term on the right-hand side of equation (4) then becomes

$$\frac{j^2}{\sigma}=I^2\left(\frac{R_f}{\pi r_e^2\epsilon_f}+\frac{1}{\pi^2 r_e^4\sigma}\right) \quad (11)$$

where the first and second terms on the right-hand side of equation (11) represent the heat generation due to electrical contact resistance and joule heating, respectively. Determination of the faying surface electrical resistance R_f is uncertain since it involves complicated interactions of chemical, mechanical, thermal, and metallurgical phenomena. Savage et al. (1978) and Kaiser (1981) measured contact resistances for different welding currents, electrode forces, and initial surface conditions. Results revealed that the faying surface resistance decreases at the location where the weld nugget forms. In lieu of any systematic data, the faying surface contact resistance is assumed to vary as a linear function of temperature (Gould, 1987). The resistance is determined by specifying the static contact resistance, which is the resistance measured at the surrounding temperature during the electrode-squeezing periods, and zero resistance at the melting temperature; that is,

$$R_f=R_\infty\left(\frac{T_m-T}{T_m-T_\infty}\right) \quad (12)$$

The axisymmetric boundary condition at $r=0$ is

$$\frac{\partial T_i}{\partial r}=0 \quad (13)$$

The initial temperature and temperatures of workpieces far from the weld nugget remain at the surrounding temperature T_∞.

Domain Transformation and Dimensionless Equations. Since the electrode shape varies due to the convergence angle, a simple transformation is used to provide a rectangular mesh convenient for finite difference computations. The following new dimensionless independent variables are introduced for this purpose:

$$\zeta=Z \quad (14)$$

$$\xi=\frac{\delta_e R}{\delta_e\phi+(1-\phi)(Z-\delta_1)} \quad \text{for } \delta_1\le Z\le\delta_1+\delta_e$$
$$=R \quad \text{for } Z\ge\delta_e+\delta_1,\ Z\le-(\delta_2+\delta_e) \text{ and } -\delta_2\le Z\le\delta_1$$
$$=\frac{\delta_e R}{\delta_e\phi+(1-\phi)(Z+\delta_2)} \quad \text{for } -(\delta_2+\delta_e)\le Z\le-\delta_2 \quad (15)$$

Equation (1) for the temperature distribution in the electrode then transforms to

$$\omega\frac{\partial\theta_e}{\partial\tau}=\frac{1}{\xi}\frac{\partial}{\partial\xi}\left(\xi\frac{\partial\theta_e}{\partial\xi}\right)+\frac{\partial^2\theta_e}{\partial\zeta^2}+J_e^2 \quad \text{for } \zeta\ge\delta_1+\delta_e \text{ and } \zeta\le-(\delta_2+\delta_e) \quad (16)$$

$$\omega\frac{\partial\theta_e}{\partial\tau}=\frac{M^2\delta_e^2}{\xi(1-\phi)^2}\frac{\partial}{\partial\xi}\left(\xi\frac{\partial\theta_e}{\partial\xi}\right)+M^2\frac{\partial}{\partial\xi}\left(\xi^2\frac{\partial\theta_e}{\partial\xi}\right)$$
$$-2\xi M\frac{\partial^2\theta_e}{\partial\zeta\partial\xi}+\frac{\partial^2\theta_e}{\partial\zeta^2}+R_{te}^4J_e^2 \quad \text{for } \delta_1\le\zeta\le\delta_1+\delta_e \quad (17)$$

$$\omega\frac{\partial\theta_e}{\partial\tau}=\frac{N^2\delta_e^2}{\xi(1-\phi)^2}\frac{\partial}{\partial\xi}\left(\xi\frac{\partial\theta_e}{\partial\xi}\right)+N^2\frac{\partial}{\partial\xi}\left(\xi^2\frac{\partial\theta_e}{\partial\xi}\right)$$
$$-2\xi N\frac{\partial^2\theta_e}{\partial\zeta\partial\xi}+\frac{\partial^2\theta_e}{\partial\zeta^2}+R_{be}^4J_e^2 \quad \text{for } -(\delta_2+\delta_e)\le\zeta\le-\delta_2 \quad (18)$$

where

$$M=\frac{1-\phi}{\delta_e\phi+(\zeta-\delta_1)(1-\phi)},\quad N=\frac{\phi-1}{\delta_e\phi-(\zeta+\delta_2)(1-\phi)} \quad (19)$$

Equation (4) for the workpieces becomes

$$\frac{\partial H}{\partial\tau}=\frac{1}{\xi}\frac{\partial}{\partial\xi}\left(\xi K\frac{\partial\theta_i}{\partial\xi}\right)+\frac{\partial}{\partial\zeta}\left(K\frac{\partial\theta_i}{\partial\zeta}\right)+J^2 \quad (20)$$

in which the enthalpy-temperature relationship is now given by

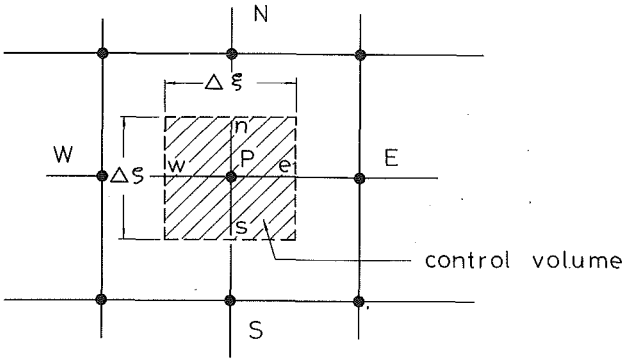

Fig. 2 Grid for control volume formulation

$$H=\begin{cases}\rho^* C(\theta_i+\theta_\infty), & \theta_i \le 1-\epsilon^* \\ H\big|_{1-\epsilon^*}+\dfrac{(1+\rho^*)L_{sl}(\theta_i+\epsilon^*-1)}{4}, & 1-\epsilon^*<\theta_i<1+\epsilon^* \\ H\big|_{1+\epsilon^*}+\theta_i-\epsilon^*-1, & \theta_i \ge 1+\epsilon^*\end{cases} \tag{21}$$

Equations (6)–(9), which represent the heat losses at surfaces of workpieces, become

$$-\frac{\partial\theta_1}{\partial\zeta}=\mathrm{Bi}_e(\theta_1-\theta_e v) \quad \text{at } \zeta=\delta_1, \quad 0\le\xi\le\phi \tag{22}$$

$$\frac{\partial\theta_2}{\partial\zeta}=\mathrm{Bi}_e(\theta_2-\theta_e v) \quad \text{at } \zeta=-\delta_2, \quad 0\le\xi\le\phi \tag{23}$$

$$-\frac{\partial\theta_1}{\partial\zeta}=\mathrm{Bi}\theta_1 \quad \text{at } \zeta=\delta_1, \quad \phi\le\xi\le\infty \tag{24}$$

$$\frac{\partial\theta_2}{\partial\zeta}=\mathrm{Bi}\theta_2 \quad \text{at } \zeta=-\delta_2, \quad \phi\le\xi\le\infty \tag{25}$$

Equation (10) for the heat transfer rate at the faying surface is

$$\frac{\partial\theta_1}{\partial\zeta}=\frac{\partial\theta_2}{\partial\zeta}=\mathrm{Bi}_f(\theta_1-\theta_2) \quad \text{at } \zeta=0 \tag{26}$$

Equation (13) yields

$$\frac{\partial\theta_i}{\partial\xi}=0 \quad \text{at } \xi=0 \tag{27}$$

The temperature far from the weld nugget becomes

$$\theta_i=0 \qquad \text{as } \xi\to\infty \tag{28}$$

and the initial temperature in workpieces gives

$$\theta_i=0 \qquad \text{as } \tau=0 \tag{29}$$

Numerical Procedure. Discrete forms of equations (16)–(18) and (20) with boundary and initial conditions (22)–(29) were developed by using the control volume formulation and the central finite differences developed by Patankar (1980). The governing equations (16)–(18) and (20) can be represented in the following general form:

$$\frac{\partial F}{\partial\tau}=A_1\frac{1\partial}{\xi\partial\xi}\left(A_2\xi\frac{\partial F}{\partial\xi}\right)+A_3\frac{\partial}{\partial\xi}\left(\xi^2\frac{\partial F}{\partial\xi}\right)+\frac{\partial}{\partial\zeta}\left(A_4\frac{\partial F}{\partial\zeta}\right)+S \tag{30}$$

where A_1, A_2, A_3, A_4, and S are functions of ξ and ζ. The source term S represents the terms of joule heating and cross-derivative on the right-hand side of equations (16)–(18), and joule heating in equation (20). A portion of a two-dimensional grid is shown in Fig. 2. Equation (30) can be expressed by the following discrete form:

$$a_P F_P=a_E F_E+a_W F_W+a_N F_N+a_S F_S+b \tag{31}$$

where

$$a_E=\frac{A_{1,P}A_{2,e}\xi_e\Delta\tau}{\xi_p\Delta\xi^2}+\frac{A_{3,P}\xi_e^2\Delta\tau}{\Delta\xi^2}$$

$$a_W=\frac{A_{1,P}A_{2,w}\xi_w\Delta\tau}{\xi_P\Delta\xi^2}+\frac{A_{3,P}\xi_w^2\Delta\tau}{\Delta\xi^2}$$

$$a_N=\frac{A_{4,n}\Delta\tau}{\Delta\zeta^2}$$

$$a_S=\frac{A_{4,s}\Delta\tau}{\Delta\zeta^2}$$

$$a_P=a_E+a_W+a_N+a_S+1$$

$$b=S_P\Delta\tau+F_P^0$$

where S_P denotes the source term S evaluated at grid point P. Joule heating is assumed to prevail throughout the control volume and the cross-derivative term is discretized by the central-difference approximation. The successive overrelaxation (SOR) method was applied to determine dependent variables. Equation (31) can be written as

$$F_P=F_P^*+\beta\left(\frac{\Sigma a_{nb}F_{nb}+b}{a_P}-F_P^*\right) \tag{32}$$

where a_{nb} and F_{nb} denote a_E, a_W, a_N, a_S and F_E, F_W, F_N, F_S, respectively. When the iterative results converge, F_p approaches F_p^*. Equation (32) implies that the converged values of F satisfy equation (31). In the present study, the relaxation factor $\beta=1.25$ was chosen. After the enthalpy was calculated from equation (20), the temperature field could be determined by using equation (21).

The nodal points were uniformly distributed in both the ξ and ζ directions. For sufficient numerical accuracy, a grid of 6×30 nodal points in an electrode and 95×21 nodal points in both the top and the bottom workpieces were used. A grid of 95×42 nodal points in the workpieces was chosen to compare with the experimental data obtained by Gould (1987). Convergence of the numerical solution was checked by examining the temperatures between iterations. The relative error between the two values was always better than 1 percent.

Results and Discussion

The electrodes were chosen to be copper and the workpiece material was AISI 1008 in order to compare with experimental data. In view of limited data available, properties of AISI 1008 steel were assumed to be the same as those of iron. Errors thus introduced would not be serious since atomic structures of the major constituents, Mn and Fe, are very similar as mentioned previously. Properties of iron and copper chosen from Brandes (1983) are listed in Table 1 and Table 2, respectively. The initial effective gap thickness between workpieces was taken to be 5×10^{-5} m (Bentley et al., 1963). Thermal heat transfer coefficients at both the workpiece-electrode interface and the faying surface of workpieces were estimated to be 4×10^4 W/m^2–K (Rohsenow and Hartnett, 1973). Investigation of the separate effect of the electrode pressure and the surface condition of the contact resistance is ignored at the present time. The reason for this is that the electrical contact resistances are affected more markedly by the surface condition than the electrode force (Savage et al., 1977, 1978; Kaiser, 1981). The surface condition, however, is very uncertain and

Table 1 Properties of iron and welding conditions

Solid density ρ_s, kg/m^3	7,870
Liquid density ρ_l, kg/m^3	6,340
Solid specific heat c_s, J/kg-K	456
Liquid specific heat c_l, J/kg-K	791
Solid thermal conductivity k_s, W/m-K	78.2
Liquid thermal conductivity k_l, W/m-K	29.7
Latent heat of melting, l_{sl}, J/kg	2.71 x10^5
Solid electrical conductivity σ_s, mho/m	8.16 x10^6
Liquid electrical conductivity σ_l, mho/m	9.5 x10^5
Static contact resistance R_∞, ohm	2.5 x10^{-4}
Melting temperature T_m, K	1,809
Half temperature range across mushy zone ε, K	10
Separation gap at faying surface ε_f, m	5 x10^{-5}
Heat transfer coefficients:	
workpiece-surroundings h_a, W/m^2-K	50
workpiece-electrode h_e, W/m^2-K	40,000
faying surface h_f, W/m^2-K,	40,000
Surrounding temperature T_∞, K	303

Table 2 Properties of copper

Density ρ_e, kg/m^3	9,000
Specific heat c_e, J/kg-K	390
Thermal conductivity k_e, W/m-K	400
Electrical conductivity σ_e, mho/m	5.9 x10^7
Melting temperature T_{me}, K	1,357

involves complicated interactions of mechanical, chemical, thermal, and metallurgical phenomena.

Variations in the heat generation at the faying surface between workpieces and the joule heating with weld times are shown in Fig. 3. A weld nugget is initiated due to interfacial heat generation, which decreases to zero after the weld nugget develops for weld times larger than 1.6 cycles (1.6/60 s). Joule heating, however, dominates the nugget growth for longer weld times.

The development of a weld nugget at a welding current of 8000 A for welding AISI 1008 sheets of thickness 0.51 mm is shown in Fig. 4. The nugget growth predicted agrees well with experimental data obtained by Gould (1987). Solutions of the one-dimensional model developed by Gould (1987) are also presented for comparison. At early stages of weld times the predicted nugget thickness from the one-dimensional model lies far below the experimental data. Gould (1987) suggested that the heat generation at the faying surface was underestimated. After a weld time of eight cycles the nugget thickness becomes larger than experimental data since the radial heat loss is neglected. The weld nugget is initiated at the welding time of 1.6 cycles and increases abruptly with a growth rate of 3 cm/s to an asymptotic value around 0.58 mm after the welding time of six cycles. The rate of increase of weld nugget thickness is reduced when the weld time becomes

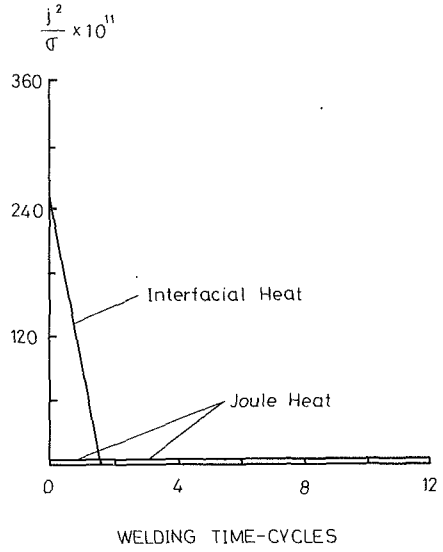

Fig. 3 Variations in interfacial heat generation (J/m^3-s) and joule heating with weld time at center of weld nugget (I = 8000 A, r_0 = 2.4 mm, r_e = 2.04 mm, $l_1 = l_2$ = 0.51 mm, α = 45 deg)

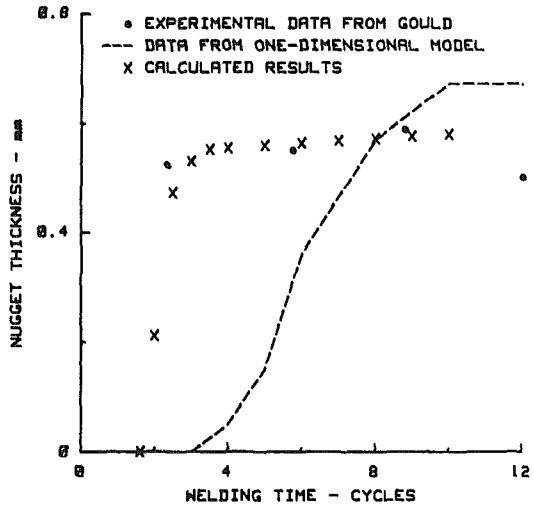

Fig. 4 Calculated and measured nugget growths (I = 8000 A, r_0 = 2.4 mm, r_e = 2.04 mm, $l_1 = l_2$ = 0.51 mm, α = 45 deg)

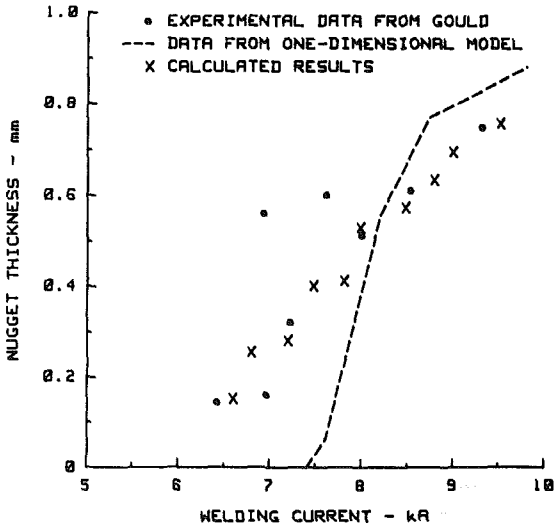

Fig. 5 Calculated and measured nugget thicknesses versus welding currents (t = 6 cycles, r_0 = 2.4 mm, r_e = 2.04 mm, $l_1 = l_2$ = 0.51 mm, α = 45 deg)

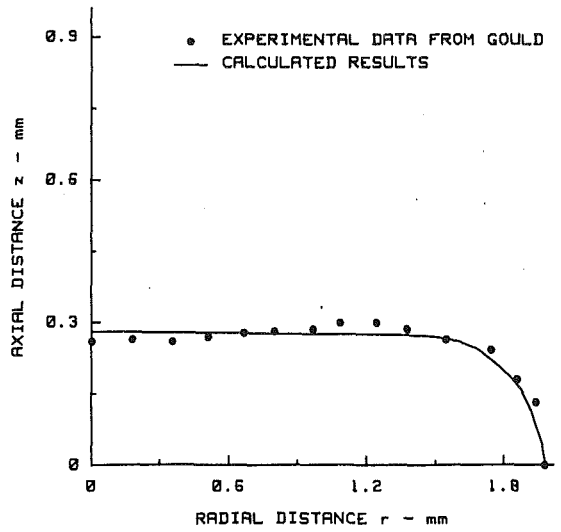

Fig. 6 Calculated and measured shapes of a weld nugget (I = 8100 A, t = 9 cycles, r_0 = 2.4 mm, r_e = 2.04 mm, $l_1 = l_2$ = 0.51 mm, α = 45 deg)

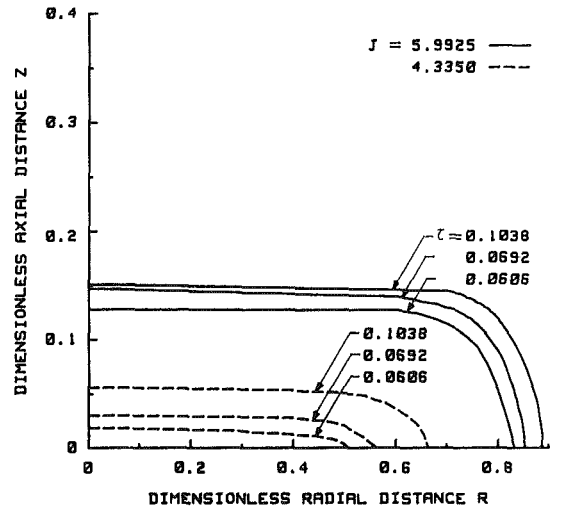

Fig. 7 Dimensionless nugget growth for different welding current densities (ϕ = 0.85, $\delta_1 = \delta_2$ = 0.213, α = 45 deg)

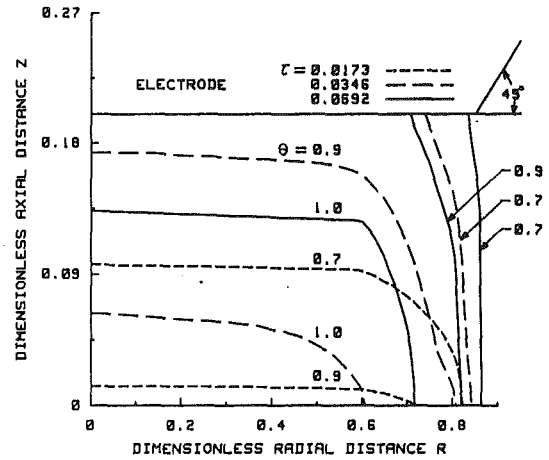

Fig. 8 Dimensionless temperature distributions for different welding times (J = 5.1, ϕ = 0.85, $\delta_1 = \delta_2$ = 0.213, α = 45 deg)

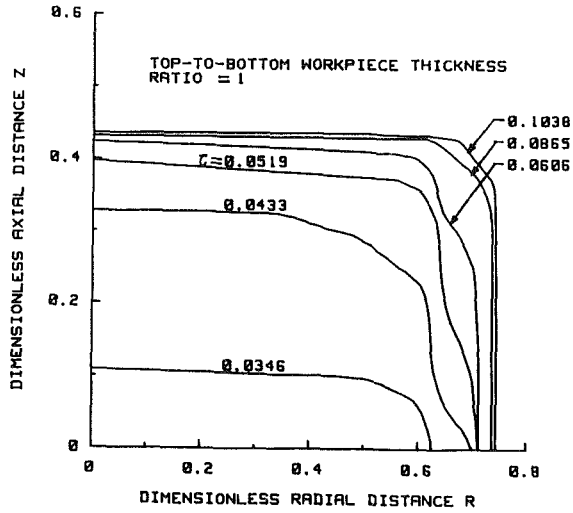

Fig. 9 Dimensionless nugget growths for top-to-bottom workpiece ratio of δ_1/δ_2 = 1 (J = 5.1, ϕ = 0.85, δ_1 = 1.06, α = 45 deg)

large. The importance of joule heating indicates that not only does the welding current have a strong effect on the weld nugget growth, but so also does the bulk electrical resistance with temperature for both the liquid and solid phases for large weld times. Hence detailed investigations of bulk electrical resistance and contact resistance are definitely needed.

The variation of the nugget thickness with the welding current for welding workpieces of thickness 0.51 mm at a welding time of six cycles is shown in Fig. 5. The calculated results agree well with measured data obtained by Gould (1987). The weld nugget forms for a welding current higher than 6 kA. Investigating the difference between one and three dimensional models, where the latter leads to satisfactory results, reveals the importance of an appropriate estimation of the heat generation at the faying surface. A comparison between the calculated and measured shapes of the weld nugget at a welding current of 8100 A and a welding time of nine cycles is shown in Fig. 6. It indicates that good agreement with an accuracy of 7 percent can be obtained.

Transient shape changes of a weld nugget at dimensionless welding current densities J = 5.9925 and 4.335 are shown in Fig. 7. In view of interfacial heat generation and joule heating, a high welding current produces rapid nugget growth. The growth rate decreases as the weld time increases. Temperature distributions for different weld times are presented in Fig. 8. The temperature pattern is similar to that obtained by Bentley et al. (1963). With longer welding times, temperature distributions broaden. The axial temperature gradient is greater than that in the radial direction.

Nugget development of welding workpieces of equal thickness is shown in Fig. 9. The dimensionless thickness and the width of a weld nugget are 0.88 and 1.48, respectively, at a welding time of 0.1038. The nugget growth for the top-to-bottom workpiece thickness ratio of 0.2 is presented in Fig. 10 for comparison. It can be seen that the nugget thickness and the width of the top workpiece decrease to 0.18 and 1.46, respectively, whereas the nugget thickness of the bottom workpiece reduces to 0.43. The explanation is that the top workpiece of lower thickness conducts a larger amount of heat away. Hence energies for raising temperatures and changing phases in both the top and the bottom workpieces are comparatively reduced.

Referring to Fig. 11, the nugget grows at a higher rate for a smaller contact area of the electrode due to a higher current density. The width of the nugget is primarily controlled by the diameter of the contact area. The maximum half-width is 0.6, which is slightly larger than the radius ratio of the electrode ϕ = 0.55. In contrast, the half-width becomes 0.92, which is

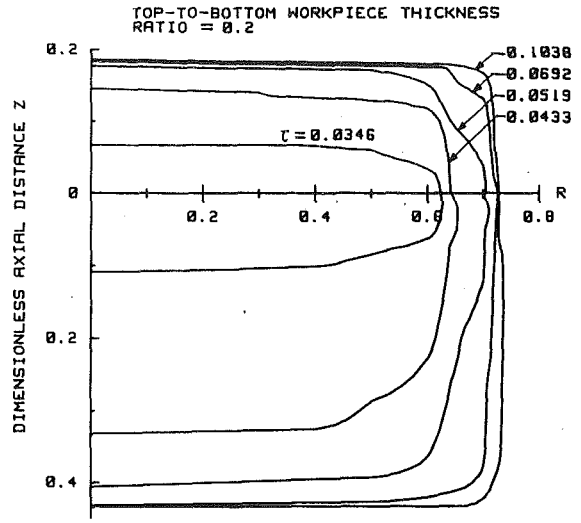

Fig. 10 Dimensionless nugget growths for top-to-bottom workpiece ratio of $\delta_1/\delta_2 = 0.2$ ($J = 5.1$, $\phi = 0.85$, $\delta_1 = 0.213$, $\alpha = 45$ deg)

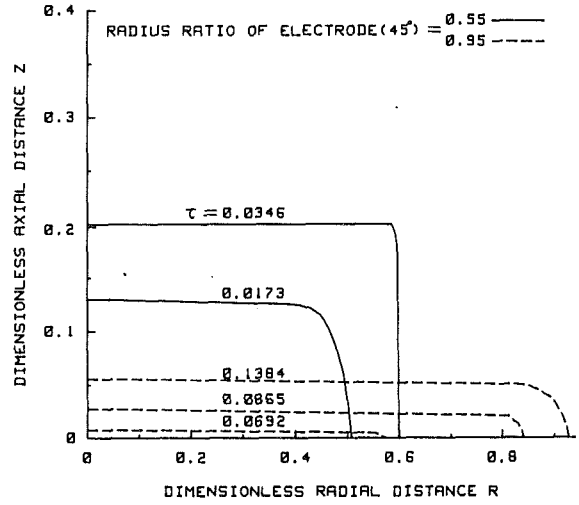

Fig. 11 Dimensionless nugget growth for different electrode radius ratios ($J = 5.1$, $\delta_1 = \delta_2 = 0.213$, $\alpha = 45$ deg)

less than the radius of the contact area for $\phi = 0.95$. This is attributed to an increase of the current density, which increases the heat generation rate and produces a wider weld nugget.

The investigation of transient temperatures is of practical importance since the microstructure of the workpiece is related to the temperature variation. Temperature distributions versus the welding time at different radial distances along the faying surface are plotted in Fig. 12. Three typical points in the weld are considered, namely, one near the center of the weld nugget, one near the edge of the weld spot, and one outside the weld nugget. The temperature increases very rapidly in the weld spot at an initial stage of the weld time. It reaches a value of 1.0, which corresponds to 1809 K at the center of the faying surface. It remains approximately constant due to the energy required for melting. Neglecting the phase change of melting, the temperature will increase and decrease smoothly as illustrated for the curve $R = 1.144$. Similar results were found by Greenwood (1961). The maximum cooling rate is estimated to be around 20,000°C/s, which is of the same order as the estimation made by Gould (1987).

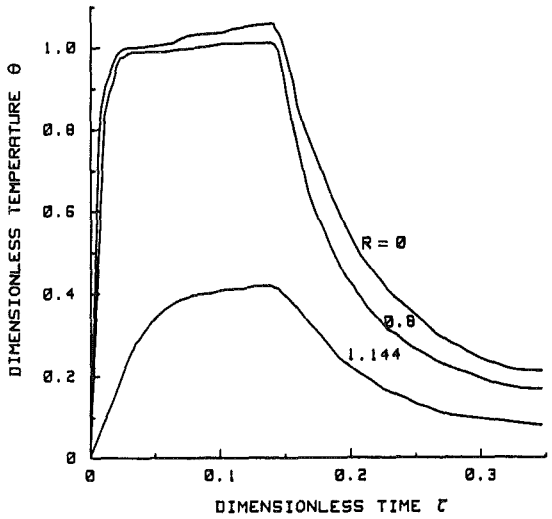

Fig. 12 Transient temperatures at different locations along faying surface of workpieces ($J = 5.1$, $\phi = 0.85$, $\delta_1 = \delta_2 = 0.213$, $\alpha = 45$ deg)

Conclusions

The conclusions drawn are as follows:

1 An unsteady, axisymmetric heat conduction model is proposed to investigate three-dimensional nugget growth for different welding currents, shapes of electrode tip, and workpiece thickness ratios. Results show that the nugget thickness, the nugget growth, and the shape of the weld nugget predicted agree well with experimental data.

2 An appropriate estimation of the heat generation at the faying surface between workpieces is provided. Satisfactory results indicate that this model is useful for very wide ranges of welding currents and weld times. The separate effects of the electrode pressure and the surface condition on the electrical contact resistance are ignored at the present time. The reason for this is that the interfacial resistance is affected more markedly by the surface condition than the electrode pressure. The surface condition, however, involves interactions of thermal, chemical, mechanical, and metallurgical phenomena and is very uncertain.

3 Nugget growth rate is dominated by the interfacial heat generation at initial stages of weld time. Joule heating, however, is responsible for nugget growth at longer weld times. The importance of joule heating indicates that not only does the welding current have a significant effect on the weld nugget growth, but so also does the bulk electrical resistance for both the liquid and solid phases. Hence investigations of factors affecting the contact resistance and the electrical bulk resistance in detail are needed.

4 Consideration of radial heat loss is necessary for longer weld times and higher welding currents.

5 Nugget growth rate and the size of the weld nugget increase with welding current and the thickness of the workpieces. Decreasing the contact area of the electrode increases the rate of nugget growth. The width of the weld nugget is primarily controlled by the electrode contact area.

References

Atthey, D. R., 1974, "A Finite Difference Scheme for Melting Problems," *J. Inst. Math. Applics.*, Vol. 13, pp. 353–366.

Bennon, W. D., and Incropera, F. P., 1988, "Developing Laminar Mixed Convection With Solidification in a Vertical Channel," ASME JOURNAL OF HEAT TRANSFER, Vol. 110, pp. 410–415.

Bentley, K. P., Greenwood, J. A., Knowlson, P. Mck., and Baker, R. G.,

1963, "Temperature Distributions in Spot Welds," *British Welding Journal*, Vol. 10, pp. 613–619.

Brandes, E. A., 1983, *Smithells Metals Reference Book*, Butterworth & Co., Boston, pp. 14-1–14-13.

Crank, J., 1984, *Free and Moving Boundary Problems*, Clarendon Press, Oxford, United Kingdom, Chap. 6.

Gould, J. E., 1987, "An Examination of Nugget Development During Spot Welding, Using Both Experimental and Analytical Techniques," *Welding Journal*, Vol. 66, pp. 1-s–10-s.

Greenwood, J. A., 1961, "Temperatures in Spot Welding," *British Welding Journal*, Vol. 8, pp. 316–322.

Kaiser, J. G., 1981, "The Effect of Electrical Resistance on Nugget Formation During Spot Welding," M.S. thesis, Materials Engineering Department, Massachusetts Institute of Technology, Cambridge, MA.

Meyer, G. H., 1973, "Multidimensional Stefan Problems," *SIAM J. Numer. Anal.*, Vol. 10, pp. 522–538.

Nied, H. A., 1984, "The Finite Element Modeling of the Resistance Spot Welding Process," *Welding Journal*, Vol. 63, pp. 123-s–132-s.

Patankar, S. V., 1980, *Numerical Heat Transfer and Fluid Flow*, Hemisphere Publishing Corp., New York, pp. 59–68.

Rice, W., and Funk, E. J., 1967, "An Analytical Investigation of the Temperature Distributions During Resistance Welding," *Welding Journal*, Vol. 46, pp. 175-s–186-s.

Rohsenow, W. M., and Hartnett, J. P., eds., 1973, *Handbook of Heat Transfer*, McGraw-Hill, New York, pp. 3-14–3-15.

Savage, W. F., Nippes, E. F., and Wassell, F. A., 1977, "Static Contact Resistance of Series Spot Welds," *Welding Journal*, Vol. 56, pp. 365-s–370-s.

Savage, W. F., Nippes, E. F., and Wassell, F. A., 1978, "Dynamic Contact Resistance of Series Spot Welds," *Welding Journal*, Vol. 57, pp. 43-s–50-s.

Voller, V., and Cross, M., 1981, "Accurate Solutions of Moving Boundary Problems Using the Enthalpy Methods," *Int. J. Heat Mass Transfer*, Vol. 24, pp. 545–556.

ERRATA

Errata for the paper "Scaling of Plain and Externally Finned Heat Exchanger Tubes," by R. Sheikholeslami and A. P. Watkinson, JOURNAL OF HEAT TRANSFER, Vol. 108, pp. 147–152, February 1986.

It has come to our attention that the exponent shown on x on the right-hand side of equation (4) is in error. The correct equation is given below:

$$K_1(w/K_R+K_{sp})(w/K_D+y)=4K_2\,x\,(1-w/K_D\,x)(z/2-w/K_D)^2 \tag{4}$$

The error did not enter the model predictions shown in the paper, which used equations (5) and (6).

A Single-Blow Test Procedure for Compact Heat and Mass Exchangers

E. Van den Bulck
Assistant Professor,
Dept. Mechanika,
Katholieke Universiteit Leuven,
Heverlee, Belgium

S. A. Klein
Professor,
Solar Energy Laboratory,
University of Wisconsin—Madison,
Madison, WI 53706

This paper discusses a single-blow test procedure for estimating the overall heat and mass transfer coefficients of compact dehumidifier matrices. The procedure consists of three sequential experimental procedures for obtaining, respectively, the core geometry of the test matrix, the active mass of sorbent within the matrix, and the distributions of the temperature and humidity ratio responses with time and distance in the flow direction. The analysis technique paired to the experimental procedure is based upon the transformation of the model partial differential equations into a set of ordinary differential equations. The temperature and mass-fraction distributions are then modeled by a system of nonstiff ordinary differential equations, which can be easily integrated numerically. The Lewis number, defined as the ratio of the overall heat to mass transfer coefficients, determines the shape of the distributions with a dimensionless flow coordinate x^+. With a curve fit method, the experimental Lewis number can be determined with acceptable accuracy. The procedure is illustrated with selected experimental results for humid air and a silica gel matrix.

1 Introduction

In single-blow experiments, an exchanger test matrix is conditioned at specified initial conditions and a step change is applied to the inlet conditions of the fluid stream passing through the matrix. The distributions in time of the fluid stream outlet conditions form the experimental data that characterize the heat and/or mass transfer performance of the test matrix. Retrieving quantitative information, i.e., the heat and/or mass transfer coefficients, is the objective of the analysis. Whereas the methods for heat transfer alone have evolved into de facto standards, the methods for isothermal or adiabatic mass transfer are less developed.

Single-Blow Methods for Heat Transfer. The single-blow method is widely used for evaluating the performance of compact heat exchanger geometries (Heggs, 1983). Almost all analysis techniques are based upon the *porous-matrix* or *insulated-duct* equations established by Anzelius (1926) and later by Schumann (1929). These equations express an overall energy conservation equation for the adiabatic system {fluid-stream + matrix} and a linear transfer rate equation based upon an overall transfer coefficient.

There exist two classes of solution method for single-blow experiments. In the *point matching solutions* the principle is to match one parameter derived directly from the experimental data with a theoretical curve showing that parameter as a function of the exchanger *Number of Transfer Units* (e.g., Baclic et al., 1986). These parameters can be (Heggs, 1983): the effectiveness at the point of breakthrough, the maximum slope of the breakthrough curve, the initial temperature rise, the second moment of the distribution curve, and the 20–80 percent distribution width. The *curve matching technique* generally employs finite difference solutions of the insulated-duct equations (e.g., Elliot et al., 1986). Curve matching is typically an iterative procedure in which the *NTU* parameter is determined by minimizing the rms error of the experimental distribution data with a theoretical curve. For heat transfer alone, there is usually only one curve-fit parameter.

Single-Blow Methods Involving Mass Transfer. The general classification of the various techniques for heat transfer alone can be used for isothermal mass transfer in adsorbers. However, the mass conservation equation involves a property equlibrium relationship that is generally nonlinear. Eagleton and Bliss (1953) successfully used a maximum-slope point matching technique to obtain the mass transfer coefficient from experimental breakthrough curves with a nonlinear isotherm. Jefferson (1972) discusses the method of moments for dilute (i.e., linear), binary systems. Schneider and Smith (1968) experimentally studied the isothermal mass transfer of hydrocarbons on silica gel in a packed-bed geometry. Their analysis incorporates three dimensionless parameters: the inter- and intraparticle diffusivity and the sorption rate constant. They state that the curve matching procedure is unsatisfactory because good agreement between the experimental data and a theoretical response curve can be obtained with more than one set of these three constants.

Standard techniques for analyzing single-blow, adiabatic sorption experiments are even less developed. Single-blow methods for mass exchangers usually rely on global curve-matching procedures, however; the description of the transient process invariably includes a fair number of adjustable parameters for the transfer rate and equilibrium constants, and the effects of these parameters on the position and shape of the response curves are intermixed. Chi and Wasan (1970) use empirical correlations for the transfer coefficients, developed by Hougen and Marshall (1947), in their numerical model for the adiabatic adsorption of water vapor on silica gel in a packed-bed geometry. They conclude a fair agreement between their theoretical curves and experimental breakthrough curves published by Bullock and Threlkeld (1966).

Clark et al. (1981) report experiments on the adiabatic sorption of water vapor on silica gel-packed beds using a model similar to Chi and Wasan and the Hougen–Marshall correlations. However, the agreement between their theoretical and experimental breakthrough curves is poor and the authors conclude that the discrepancy cannot be explained by experimental

Contributed by the Heat Transfer Division for publication in the JOURNAL OF HEAT TRANSFER. Manuscript received by the Heat Transfer Division December 12, 1988; revision received July 17, 1989. Keywords: Forced Convection, Heat Exchangers, Transient and Unsteady Heat Transfer.

errors. Biswas et al. (1984) and Kim et al. (1985) present a theoretical and experimental investigation of the adiabatic sorption of water vapor on regular density silica gel in a parallel plate geometry. Their model also follows the Anzelius approach. The agreement between experimental and predicted breakthrough curves is only fair, and a sensitivity study shows that several factors can explain the discrepancy.

Pesaran et al. (1986) performed a theoretical and experimental analysis of adiabatic single blow experiments of laminar flow of humid air through a parallel passage silica-gel matrix. The model is based upon the method of moments applied to the two Riemann invariants of the mass and energy conservation equations for infinite transfer coefficients. However, the analysis of the experimental data yields erroneous heat and mass transfer coefficients due to experimental inaccuracies and the inappropriate assumption of linear equations.

Clearly, the conventional single-blow methods developed for exchange processes involving heat transfer alone are limited if mass transfer is occurring. Adsorbers often have nonlinear thermodynamic equilibrium properties. The curve-matching techniques applied to mass transfer involve many parameters, and agreement with experimental data can often be obtained with more than one set of these parameters. Thus it seems that the single-blow technique may not be a useful experimental tool for obtaining the performance characteristics of heat and mass exchangers. This paper introduces a single-blow analysis technique that makes use of the nonlinear character of the conservation equations. Although the technique can be applied to any binary sorption system, it is explained next for the case of humid air flowing through a silica gel matrix because experimental data for this system are available.

2 Model Formulation and Assumptions

The model follows the classical Anzelius model. The situation is that of laminar parallel flow of humid air through a matrix containing a uniform distribution of desiccant material. The equations of change are based upon overall conservation equations for the air stream and test matrix. The transfer-rate equations are linear and expressed in terms of overall heat and mass transfer coefficients. Diffusion equations are not included in the model.

Assumptions

1 The matrix-flow area, the transfer area per unit length, and the distribution of desiccant mass within the test matrix are constant or uniform with respect to position in the flow direction.

2 The axial diffusion of heat and mass in the air stream is negligible compared to the transport by forced convection. Axial diffusion in the desiccant layer is neglected because the layer consists of isolated particles with small dimensions.

3 The pressure drop through the bed is small with respect to absolute pressure and is neglected for evaluating the sorption equilibrium conditions.

4 The rate of heat and mass transfer can be modeled with constant overall heat and mass transfer coefficients.

5 The temperature distributions in the desiccant mass and structural parts of the test matrix are assumed to be uniform, and the average temperatures of both systems are equal at all times.

Assumption 4 converts the model equations from Rosen-type diffusion equations (Rosen, 1954) into Anzelius-type overall rate equations and it simplifies the resulting equations substantially. Van den Bulck (1987) has experimentally investigated the effect of nonuniform, transient distributions of mass and energy fluxes on the air-side and desiccant-side Nusselt and Sherwood numbers. His analysis shows that the effect can be neglected for the distributions that are generally encountered with mass transfer.

With assumptions 1-5, the overall equations of change for the air stream and test matrix can be written as follows.

1 Water vapor conservation

$$\dot{m}_f L \frac{\partial w_f}{\partial x} + \dot{m}_f \theta_d \frac{\partial w_f}{\partial \theta} + M_d \frac{\partial W_d}{\partial \theta} = 0$$

2 Energy conservation

$$\dot{m}_f L \frac{\partial i_f}{\partial x} + \dot{m}_f \theta_d \frac{\partial i_f}{\partial \theta} + M_d \frac{\partial I_m}{\partial \theta} = 0 \qquad (1)$$

3 Rate of water vapor mass transfer

$$M_d \frac{\partial W_d}{\partial \theta} = h_m A (w_f - w_d)$$

4 Rate of thermal energy transfer

$$M_d \frac{\partial I_m}{\partial \theta} = hA (t_f - t_m) + h_m A (w_f - w_d) i_w$$

x measures the distance in the flow direction and θ measures the real time. w_d is the humidity ratio of the air stream in equilibrium with the silica gel at the temperature t_m and water content W_d.

Equations (1) form a system of nonlinear, coupled evolution equations, and the behavior of such systems is well known.

Nomenclature

A = transfer area of exchange matrix
A_c = free flow area of exchange matrix
c_p = fluid thermal capacitance
D_h = hydraulic diameter of flow passage
h = heat transfer coefficient
h_m = mass transfer coefficient
i_f = specific enthalpy of fluid stream (per unit mass of dry air)
i_w = specific enthalpy of water vapor
I_m = specific enthalpy of matrix (per unit mass of dry desiccant)
L = length of flow passage
Le = Lewis number as defined by equation (6)
$\dot{m}_f$ = dry-air mass flow rate
M_d = mass of dry desiccant contained within exchanger
M_f = fluid mass entrained in flow passages
Nu = Nusselt number
Re = passage flow Reynolds number
S = dimensionless wave speed of the breakthrough curves
t_f = fluid stream temperature
t_m = matrix temperature
w_d = humidity ratio of air in equilibrium with desiccant
w_f = humidity ratio of air stream
W_d = water content of dry desiccant
x = coordinate measuring position in the flow direction
x^+ = dimensionless position coordinate
z = flow coordinate
α_f = thermal diffusivity of fluid stream
θ = real-time variable
θ_d = dwell time of fluid within matrix
τ = dimensionless time

Whereas the Anzelius equations model the propagation of the distribution of the air stream temperature, equations (1) model the propagation of two confined property distributions: temperature and humidity. Ruthven (1984) discusses in detail the propagation and dispersion of the distributions, also called waves. There exists a thermal wave, during which most of the sensible energy is exchanged between the air stream and the matrix, and a mass transfer wave, which incorporates the majority of the mass exchange. The thermal wave is narrow and propagates at high speed through the matrix, whereas the mass transfer wave is wider and slower. The respective wave speeds are proportional to the ratio of thermal and mass capacitances of the fluid stream and matrix. The two distributions are usually completely separated, with a well-defined intermediate state between the two transfer zones.

For heat exchangers, the energy conservation equation is linear and as a result the thermal wave is an expansion wave, continuously spreading as it progresses through the exchanger passages. The shape of this wave never becomes *fully developed*, and therefore depends at all times on its initial shape, that is, the change of the inlet conditions with time. For mass transfer, however, the nonlinearity of the sorption isotherm introduces favorable wave patterns, which are not encountered in heat transfer. For selected matrix-initial and fluid-inlet states, the property distributions are *constant-pattern waves*, i.e., the shape of the distributions is preserved as the waves progress through the matrix.

For the system regular-density silica gel and humid air, theoretical analyses by Van den Bulck et al. (1985) experimentally verified by Van den Bulck (1987), show that constant pattern waves occur during regeneration of a wet desiccant with a hot air stream. Constant pattern waves become rapidly fully established after they originate at the inlet face of the matrix. The shape and width of the mass transfer wave in desorption processes are constant, and, for reasonable-quality inlet steps and sufficiently long bed lengths, are independent of the sharpness of the step change in inlet conditions. Furthermore, the wave dispersion is well defined and independent of the air stream mass flow rate.

Michaels (1952) and Garg and Ruthven (1975) successfully used a specific transformation technique introduced by Glueckauf (1947) for analysis of experimental breakthrough curves with constant patterns. This transformation technique is based upon the argument that an observer translating at the speed of the wave will not measure a change of shape of the wave. For the system of equations (1), the physical speed of the second wave is given by

$$\frac{dx}{d\theta} = \frac{\dfrac{\dot{m}_f L}{M_d} S}{1 + \dfrac{\dot{m}_f \theta_d}{M_d} S} \tag{2}$$

where S is a constant dimensionless wave speed dependent only upon the thermodynamic properties of the fluid and matrix system, and the inlet and initial conditions. Based upon equation (2) a new position coordinate z can be defined as

$$z = x - \frac{\dfrac{\dot{m}_f L}{M_d} S}{1 + \dfrac{\dot{m}_f \theta_d}{M_d} S} \theta \tag{3}$$

The partial differential equations expressed in the stationary coordinate system (x, θ) can be written in terms of the moving coordinates (z, θ). The condition for a constant pattern wave translates into $\left(\frac{\partial}{\partial \theta}\right)_z = 0$. Hence, the system of partial differential equations (1) reduces to a system of ordinary differential equations in the z coordinate, moving with the wave. This system can be further simplified by using the time variable τ introduced by Anzelius (1926) for modeling fluid flow through porous matrices

$$\tau = -\left(1 + \frac{\dot{m}_f \theta_d}{M_d} S\right) \frac{hA}{c_p \dot{m}_f} \frac{z}{L} \tag{4}$$

In terms of the dimensionless time τ, the model equations (1) become:

1 *Water vapor conservation*

$$\frac{dw_f}{d\tau} - S \frac{dW_d}{d\tau} = 0$$

2 *Energy conservation*

$$\frac{di_f}{d\tau} - S \frac{dI_m}{d\tau} = 0 \tag{5}$$

3 *Rate of water vapor mass transfer*

$$\frac{dw_f}{d\tau} = \frac{1}{\mathrm{Le}} (w_f - w_d)$$

4 *Rate of energy transfer*

$$\frac{dt_f}{d\tau} = (t_f - t_m)$$

where Le is the effective, overall Lewis number, which is defined for this situation as:

$$\mathrm{Le} = \frac{h}{h_m c_p}, \tag{6}$$

and indicates the magnitude of the resistance for mass transfer relative to that for heat transfer. A compact heat and mass exchanger is characterized by the Nusselt number and Lewis number, i.e., the heat and mass transfer coefficients. The Nusselt number is mainly determined by the geometry of the flow passages, whereas Le is determined by the geometry of the desiccant layer relative to the dimensions of the flow passage. The model equations (5) indicate that the temperature and humidity distributions can be expressed in terms of the new time variable τ, with Le as parameter. Let $\Delta\tau$ measure the width of the wave in dimensionless form. Numerical integration of equations (5) indicates that the breakthrough curves become more asymmetric with increasing Le, and $\Delta\tau$ increases almost linearly with Le. Thus, the Lewis number is a measure of the skewness of the curves.

3 Experimental Results

A full description of a single-blow experimental apparatus and test procedures is given by Van den Bulck (1987). The test loop configuration is that of a conventional single-blow test facility. A humid air stream with controlled properties and mass flow rate is passed through a test matrix arranged as a vertical stack of 74 parallel rectangular passages with hydraulic diameter $D_h = 2.0 \pm 6$ percent mm, a width of 126 ± 0.9 percent mm, and a flow length $L = 0.203 \pm 0.2$ percent m. The walls of the flow passages are coated with regular-density silica gel particles with diameter $D_p = 0.177$–297 mm, yielding a total mass of dry desiccant $M_d = 0.49 \pm 3$ percent kg. The total transfer area $A = 3.65 \pm 4.5$ percent m^2 and the free flow area $A_c = 0.00927 \pm 3$ percent m^2. The $\pm$ values in these and the following statements denote uncertainties.

A series of 14 dynamic desorption experiments is reported by Van den Bulck (1987). The temperature and water content of the desiccant matrix are initialized at selected conditions, and a step change in the inlet temperature of the air stream is introduced. The air stream mass flow rate is varied in a sys-

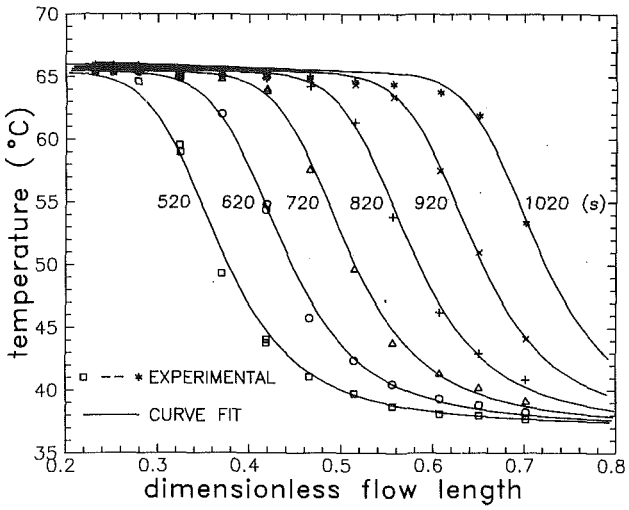

Fig. 1(*a*) Experimental temperature distributions t_f with dimensionless flow length x^+ and measuring time as parameter; each sequence with time corresponds to one single-blow experiment

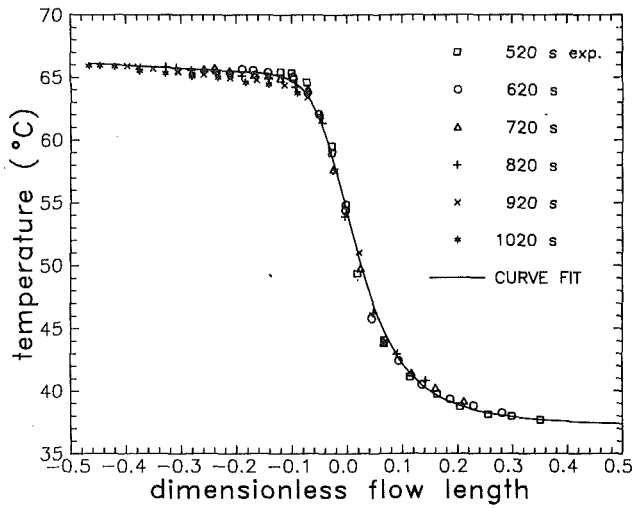

Fig. 2(*a*) Shifted experimental temperature distributions with dimensionless flow length x^+ showing the constant-pattern behavior of the breakthrough curve

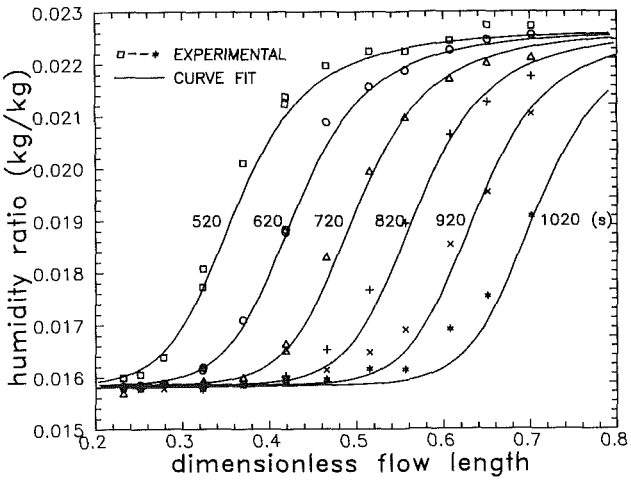

Fig. 1(*b*) Experimental humidity ratio distributions w_f with dimensionless flow length x^+ and measuring time as parameter; the interpolating curves are identical in width and shape

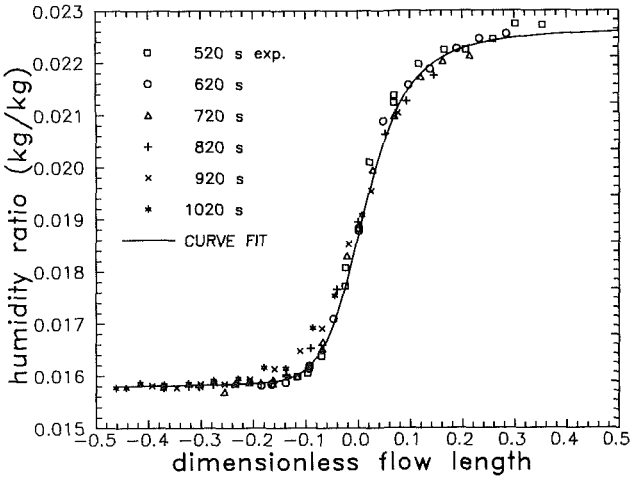

Fig. 2(*b*) Shifted experimental humidity ratio distributions

tematic sequence from $\dot{m}_f = 0.013$ to 0.028 ± 2.5 percent kg/s. Each experiment has the same pair of matrix-initial and air-inlet conditions, ($t_{f,0} = 29.6 \pm 0.8$°C, $w_{f,0} = 0.0141 \pm 0.0006$ kg/kg, $W_{d,0} = 0.228 \pm 0.005$ kg/kg) and ($t_{f,2} = 67.1 \pm 0.2$°C, $w_{f,2} = 0.0157 \pm 0.0004$ kg/kg, $W_{d,2} = 0.047 \pm 0.001$ kg/kg), respectively. For these conditions, the thermal and mass transfer waves are fully separated, and the experimental intermediate state properties are ($t_{f,1} = 37.1 \pm 0.3$°C, $w_{f,1} = 0.0227 \pm 0.0004$ kg/kg, $W_{d,1} = 0.233 \pm 0.005$ kg/kg). The Reynolds number Re based upon the fluid inlet state properties ranges from 140 to 425 for these experiments, providing a passage flow well in the laminar regime.

The experimental results are presented as graphs showing the air stream outlet conditions, i.e., temperature and humidity ratio, versus the dimensionless flow length x^+ defined for each of the experiments as

$$x^+ = \frac{L}{D_h \mathrm{Re}} \tag{7}$$

This dimensionless flow length or Graetz variable x^+ ranges from 0.23 to 0.70 with steps of 0.05 for the alternate experiments. Equations (4) and (7) indicate that τ and x^+ are inversely proportional to $\dot{m}_f$, and thus x^+ is proportional to τ. The constant pattern condition allows the measured fluid outlet property responses with time to be interpreted as the temporal distributions with position in the flow direction. The analysis presented here focuses on the mass transfer wave of the desorption experiments because the property distributions associated with this wave are constant-pattern waves and experimentally well defined.

Figures 1(*a*, *b*) show the experimental air-stream outlet conditions for each of the 14 x^+ values with the real measuring time θ as parameter. The conditions on the left of Figs. 1(*a*, *b*) are those of the inlet state ($t_{f,2}$, $w_{f,2}$), and the conditions on the right are the intermediate state properties ($t_{f,1}$, $w_{f,1}$). Using least-square curve fitting techniques with cubic splines and variable knots, the experimental distributions for the six values of the sampling time θ in Figs. 1(*a*, *b*) can be shifted to the left over a distance x_o proportional to θ to overlap with a single distribution curve. This shift is linear with the wave speed S, and can be determined from the experimental distributions in Fig. 1 with high accuracy. The shifted experimental distributions are shown in Figs. 2(*a*, *b*) and are centered about the point of maximum slope of the curves. The rms scatter of the experimental data about this "best fit" is 0.34°C for temperature and 0.00012 kg/kg for humidity. These values are of the order of the accuracy of the measurements, and therefore show that the distributions satisfy the constant-pattern condition.

The time variable τ in equations (5) is proportional to x^+ and these equations can thus be integrated with respect to x^+, with Le as a parameter. The results of this integration with a

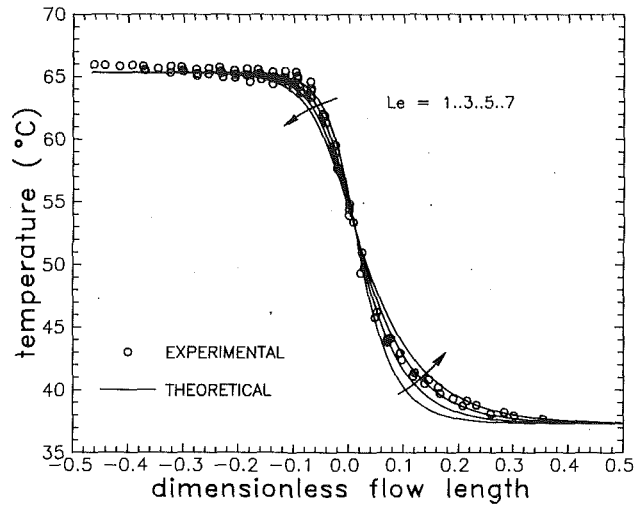

Fig. 3(*a*) Shifted experimental temperature distributions of Fig. 2(*a*) in comparison with theoretical breakthrough curves and Le as parameter

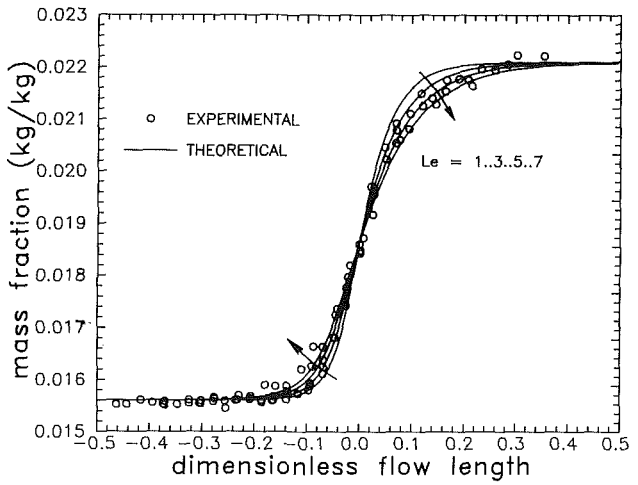

Fig. 3(*b*) Shifted experimental water vapor mass fraction distributions derived from Fig. 2(*b*) in comparison with theoretical breakthrough curves and Le as parameter

fourth-order Runga-Kutta scheme are shown in Figs. 3(*a*, *b*) in comparison with the experimental data of Figs. 2(*a*, *b*).

The alternate curves in Figs. 3(*a*, *b*) illustrate that the Lewis number acts as a skewness parameter for the distributions, whereas the Nusselt number is rather a scale parameter as indicated by equation (9). As a result, it is difficult to extract Le from the experimental results with high accuracy. For the branch connecting the distribution curves with the inlet state, the scatter of the data is larger than the variation caused by varying Lewis numbers, and no conclusion with respect to the magnitude of this parameter can be made. However, for the opposite branch, connecting the curves with the intermediate state, the scatter of the experimental data is confined within a range corresponding to Le = 3. .7 for both temperature and humidity.

The close agreement of the theoretical curves with the experimental breakthrough curves in Figs. 3(*a*, *b*) validate the model based upon overall heat and mass transfer coefficients. A Lewis number greater than unity implies that the mass transfer resistance is predominantly determined by the interparticle transient diffusion process. However, the time scale of the overall transient exchange process is about 600 s, which is much larger than the time constant of the interparticle diffusion process, which is ± 100 s. For these conditions the latter process can be described by a linear transfer rate equation, and the overall transfer rates can thus be modeled with overall transfer coefficients.

The large uncertainty level of the Lewis number is mainly due to the scatter of the experimental data points about average values. This scatter is not as much due to inaccuracies of the model or measurement inaccuracies as it is to the limit with which the initial conditions of the desorption experiments were repeatable with the experimental facility.

4 Discussion

Experimental Procedure and Analysis Technique. The principle of the analysis technique is based upon the transformation of the model partial differential equations into a set of ordinary differential equations for the constant-pattern condition of the desorption wave. The transformation is defined by equation (4). The nature of τ can be shown by relating τ and θ in terms of dimensionless groups. Inserting equation (4) into equation (3) gives

$$\Delta\tau = \frac{hA}{cp_p M_d}(S\Delta\theta) \tag{8}$$

where $\Delta\theta$ measures the elapsed real measuring time at a specified location within the flow channel, e.g., the exit face of the matrix. Using the conventional definition expressions for the Nusselt number Nu and the transfer area A in terms of D_h and the thermal diffusivity of the fluid stream, α_f (Kays and London, 1984), equation (8) can be written as

$$\Delta\tau = \mathrm{Nu}\,\frac{M_f}{M_d}\,\frac{4\alpha_f}{D_h^2}\,S\Delta\theta \tag{9}$$

Nu is a parameter depending upon the geometry of the flow passage. Due to the high thermal conductivity of the solid phase, the heat transfer resistance of the desiccant particles is negligible compared to the convective resistance in the fluid stream. The overall Nusselt number is thus approximately the fluid-side Nusselt number.

All other parameters appearing in the conversion formula (9) can be experimentally determined. The transformation technique requires then the following sequence of experiments.

1 Pressure Drop Experiments. The presence of granular desiccant particles with irregular shape and nonuniform dimensions affects the flow geometry of compact dehumidifiers in such a manner that often this geometry cannot be directly measured or computed. A series of pressure drop experiments should be performed to determine the hydraulic diameter D_h, flow area, transfer area, and porosity of the passages.

2 Sorption Experiments With Varying Matrix-Initial and Fluid-Inlet States. The adhesion of the desiccant particles to the surface of the wall passages may render part of the desiccant mass inactive. A series of dynamic, single-blow adsorption and desorption experiments should be performed to determine the active mass of desiccant M_d within the test matrix. The overall mass balance requires an accurate expression for the isotherm correlation, which should be established preferably by static sorption experiments.

3 Dynamic Sorption Experiments With Varying Mass Flow Rate. A series of repeated desorption experiments should be performed with identical matrix-initial and fluid-inlet conditions, and varying process air-mass flow rates. The choice of the fluid-inlet and matrix-initial conditions is determined by a compromise between the operating range of the experimental facility, the pattern type of the breakthrough wave, and the strength of the outlet response. The accuracy of the analysis of the experimental data increases with the magnitude of the swing in outlet conditions. The range of inlet and initial conditions that produce constant-pattern waves can easily be determined by the equilibrium theory for equations (1) (e.g., Van

den Bulck et al., 1985). The inverses of the sequential mass flow rates should be chosen to form an arithmetic series of numbers because the dimensionless flow length x^+ or τ is inversely proportional to the mass flow rate.

The wave speed S appearing in equation (9) is a semithermodynamic property of the fluid and matrix system, dependent upon the matrix-initial and fluid-inlet conditions. The conservation equations in equations (5) can be readily integrated because S is constant. Along the continuous-property distributions of the wave, the condition for constant pattern translates as

$$\frac{(w_f - w_{f,1})}{(W_d - W_{d,1})} = \frac{(w_{f,2} - w_f)}{(W_{d,2} - W_d)} = \frac{(w_{f,2} - w_{f,1})}{(W_{d,2} - W_{d,1})} = S$$

$$\frac{(i_f - i_{f,1})}{(I_m - I_{m,1})} = \frac{(i_{f,2} - i_f)}{(I_{m,2} - I_m)} = \frac{(i_{f,2} - i_{f,1})}{(I_{m,2} - I_{m,1})} = S \qquad (10)$$

where the subscripts 1 and 2 refer to the conditions at the start and finish of the wave, respectively. For the first (thermal) wave, 1 is the matrix initial state and 2 is the intermediate state. For the second (mass transfer) wave, 1 is the intermediate state and 2 is the fluid stream inlet state. Although equation (10) could be used to compute S from experimental data, S is usually obtained from equation (2). $dx/d\theta$ is the physical wave speed in real-time coordinates. This wave speed can be obtained directly with high accuracy from the series of dynamic sorption experiments with constant matrix-initial and fluid-inlet states and varying fluid mass flow rate. Equation (10) should rather be used as a check on the accuracy of the thermodynamic property relationships and measurements.

Design Criteria for Experimental Facilities. The design criteria for the experimental facility for isothermal or adiabatic mass transfer are different from those for heat transfer alone in the following ways:

1 Of utmost importance is the repeatability of the experimental facility for mass transfer. Repeatability creates the possibility of repeated experiments with identical inlet and initial conditions, and varying process air-mass flow rates. Such a series of experiments is necessary for the analysis technique paired with the experimental procedure, because the wave speed S and the shifted distributions are determined directly from the experimental data. The sample analysis shows that a high-quality experimental apparatus is needed to predict third-order parameters, such as the Lewis number.

2 The squareness of the step change in inlet conditions is less important, because the effect of the inlet step disappears when the wave becomes *fully developed*. The change of inlet conditions with time is determined by the temperature and humidity controllers of the experimental facility. The constant pattern behavior allows the specification requirements for the controllers to be less stringent, and therefore the controllers to be less expensive.

5 Conclusion

The conventional single-blow analysis techniques for compact heat exchangers are reviewed and their limitations for compact heat and mass exchangers are indicated. An alternative single-blow technique for compact dehumidifiers is presented. The governing partial differential equations are reduced to a set of ordinary differential equations by a coordinate transformation. This transformation is based upon the constant-pattern condition, which occurs for selected test conditions with desiccant matrices with nonlinear equilibrium isotherms. The core geometry and effective desiccant capacity of the test matrix are needed to perform the transformation. These specifications can be experimentally determined from conventional pressure drop experiments and dynamic or static sorption experiments.

There are two parameters that determine the width and shape of the temperature and humidity ratio distributions with a dimensionless time coordinate τ. These parameters are the passage Nusselt number and the overall Lewis number. The Nusselt number can be estimated for the core geometry of the matrix with conventional heat transfer tools, and the overall Lewis number can be determined from a curve matching technique applied to experimental distributions. These distributions need to be obtained from a sequence of dynamic sorption experiments with identical initial and inlet conditions, and varying mass flow rates. Repeatability is crucial to achieve accuracy in estimating the Lewis number.

This single-blow technique is easy to perform. The step in inlet conditions does not need to be "near" square. The computations involved are minimal.

References

Anzelius, A., 1926, "Uber Erwarmung vermittels durchstromender Medien," *Ztshr. f. angew. Math. und Mech.*, Vol. 6, No. 4, pp. 291–294.

Baclic, B. S., Heggs, P. J., and Abou Ziyan, H. Z. Z., 1986, "Differential Fluid Enthalpy Method for Predicting Heat Transfer Coefficients in Packed Beds," *Proceedings, 8th International Heat Transfer Conference*, San Francisco, CA, pp. 2617–2622.

Biswas, P., Kim, S., and Mills, A. F., 1984, "A Compact Low-Pressure Drop Desiccant Bed for Solar Air Conditioning Applications: Analysis and Design," ASME *Journal of Solar Energy Engineering*, Vol. 106, pp. 153–158.

Bullock, X. X., and Threlkeld, Y. Y., 1966, "Dehumidification of Moist Air by Adiabatic Adsorption," *Trans. Am. Soc. Heat Refrig. Air-Condit. Engrs.*, Vol. 72, pp. 301–313.

Chi, C. W., and Wasan, D. T., 1970, "Fixed Bed Adsorption Drying," *AIChE Journal*, Vol. 16, No. 1, pp. 23–31.

Clark, J. E., Mills, A. F., and Buchberg, H., 1981, "Design and Testing of Thin Adiabatic Desiccant Beds for Solar Air Conditioning Applications," ASME *Journal of Solar Energy Engineering*, Vol. 103, pp. 89–91.

Eagleton, L. C., and Bliss, H., 1953, "Drying of Air in Fixed Beds," *Chem. Eng. Progress*, Vol. 49, No. 10, pp. 543–548.

Elliot, M. P., Rapley, C. W., and Webb, A. I. C., 1986, "Application of the Single Blow Experimental Method to Square Duct Heat Transfer," *Proceedings, 8th International Heat Transfer Conference*, San Francisco, CA, pp. 981–986.

Garg, D. R., and Ruthven, D. M., 1975, "Performance of Molecular Sieve Adsorption Columns: Combined Effects of Mass Transfer and Longitudinal Diffusion," *Chem. Engng. Sci.*, Vol. 30, pp. 1192–1194.

Glueckauf, E., 1947, *J. Chem. Soc.*, pp. 1302–1329.

Heggs, P. J., 1983, "Experimental Techniques and Correlations for Heat Exchanger Surfacers: Packed Beds," in: *Low Reynolds Number Flow Heat Exchangers*, S. Kakac, R. K. Shah, and A. E. Bergles, eds., Hemisphere Publishing Corp., New York, pp. 341–368.

Hougen, O. A., and Marshall, W. R., Jr., 1947, "Adsorption From a Fluid Stream Flowing Through a Stationary Granular Bed," *Chemical Engineering Progress*, Vol. 43, No. 4, pp. 197–208.

Jefferson, C. P., 1972, "Prediction of Breakthrough Curves in Packed Beds: I. Applicability of Single Parameter Models," *AIChE Journal*, Vol. 18, No. 2, pp. 409–420.

Kays, W. M., and London, A. L., 1984, *Compact Heat Exchangers*, 3rd ed., McGraw-Hill, New York, pp. 79–101.

Kim, S., Biswas, P., and Mills, A. F., 1985, "A Compact Low-Pressure Drop Desiccant Bed for Solar Air Conditioning Applications—II. Bench Scale Tests," ASME *Journal of Solar Energy Engineering*, Vol. 107, pp. 120–127.

Michaels, A. S., 1952, "Simplified Method for Interpreting Kinetic Data in Fixed-Bed Ion Exchange," *Ind. Eng. Chem.*, Vol. 44, No. 8, pp. 1922–1930.

Pesaran, A. A., Maclaine-cross, I. L., and Van den Bulck, E., 1986, "Measurements on Promising Dehumidifier Materials and Geometries," Rep. SERI/TR-252-2898, Solar Energy Research Institute, Golden, CO.

Rosen, J. B., 1954, "General Numerical Solution for Solid Diffusion in Fixed Beds," *Ind. Eng. Chem.*, Vol. 46, No. 8, pp. 1590–1594.

Ruthven, D. M., 1984, *Principles of Adsorption & Adsorption Processes*, Wiley, New York, pp. 124–166.

Schneider, P., and Smith, J. M., 1968, "Chromatographic Study of Surface Diffusion," *AIChE Journal*, Vol. 14, No. 6, pp. 886–895.

Schumann, T. E. W., 1929, "Heat Transfer: A Liquid Flowing Through a Porous Prism," *J. Franklin Inst.*, Vol. 208, pp. 405–416.

Van den Bulck, E., Mitchell, J. W., and Klein, S. A., 1985, "Design Theory for Rotary Heat and Mass Exchangers," *Int. J. Heat Mass Transfer*, Vol. 28, No. 8, pp. 1575–1595.

Van den Bulck, E., 1987, "Convective Heat and Mass Transfer in Compact Regenerative Dehumidifiers," PhD Thesis, University of Wisconsin—Madison, Madison, WI.

The Coupling of Conduction With Forced Convection in Graetz Problems

A. Pozzi

M. Lupo

Istituto di Gasdinamica,
Facolta' di Ingegneria,
University of Naples,
Naples, Italy

This paper presents an analytical solution of the energy equation for a coupled conduction–forced convection heat transfer problem in ducts. In order to compare the thermal field in plane and circular ducts, the solution is obtained in a form describing both flows. The method is based on an asymptotic expansion of the Laplace transform of the temperature and on an application of the stationary-phase method; it enabled us to write the solution, for any value of the coupling parameter p, in terms of confluent hypergeometric functions. Some simple and accurate expressions of the interface temperature, temperature at the axis, bulk temperature, and Nusselt number are given for small and high values of p. The accuracy of the results is proved by a comparison with those obtained through an expansion in terms of 120 eigenfunctions.

1 Introduction

Laminar fluid flow and forced convection heat transfer in plane or circular ducts are important in a large variety of engineering applications, such as heat exchangers and solar collectors. This problem has been solved either with conventional boundary conditions, in which the temperature or the heat flux is prescribed at the solid–fluid interface, or with conjugate boundary conditions treating the solid wall and the fluid as an integral system and specifying that both the temperature and the heat flux be continuous at the interface.

The analysis of the thermal field, either in conventional problems or in conjugated ones, was essentially performed by means of the eigenfunction method.

This method works very well far from the entrance region, when a few terms of the expansion are sufficient to give good accuracy, but many terms are necessary to describe the inlet region. In fact Shah and London (1978) utilized 120 terms to obtain an accurate solution at a nondimensional abscissa (referred to the hydraulic diameter of the duct) of 10^{-3} times Peclet number. Since in many heat transfer problems the Peclet number is greater than 10^4, we consider useful an analytical simple solution that describes the temperature field in the entrance of a duct.

The work up to 1976 was reviewed by Shah and London (1978). Among those papers concerning the coupling of conduction with forced convection in circular ducts are the following. Luikov et al. (1971) gave the exact solution reducing the problem, by the generalized Fourier sine transformation, to a singular integral equation for the unknown temperature at the fluid–solid interface. The solution is presented in terms of complicated functions involving definite integrals and series. This solution, without numerical results, is too complex to permit a comparison with the conventional problem.

Mori et al. (1974) investigated, by using the eigenfunction method, the effects on the Nusselt number of the boundary conditions (constant temperature or constant heat flux) at the outer wall.

Many authors employed the eigenfunction method to study the finite wall thermal resistance case, neglecting the solid axial conduction. Hsu (1971) tabulated the first ten eigenvalues and gave implicit asymptotic formulas to determine higher eigenvalues; the next 110 values were calculated by Shah and London. The literature presents some interesting papers after the Shah and London review. Wijeysundera (1986) developed an analytical method to solve the conjugated problem using Duhamel's superposition technique, also giving a simple procedure for the determination of the eigenvalues of the solution. For the conjugated problem, Barozzi and Pagliarini (1984) used an iterative technique based on Duhamel's superposition technique. They solved the energy equation in the solid by a finite element method, and compared their results with experimental values.

The present solution is obtained by means of an asymptotic expansion of the Laplace transform of the temperature. This technique has been employed successfully by Pozzi and Lupo (1988) for the plane duct.

2 Equations and Boundary Conditions

The equations governing the steady conjugate heat transfer problem in a duct may be written in a form that is valid either for plane or circular ducts.

Figure 1 gives a schematic description of the problem. In this figure h represents the half-height of the duct in the plane case and the radius of the duct in the circular case and b is the thickness of the wall. The velocity at the inlet is assumed to have a fully developed profile with maximum value equal to u_{max}. Fluid is assumed to enter the duct with a uniform temperature T_i and T_b is the constant outer wall temperature.

The temperature field is governed by the energy equations for both the fluid and the wall and the boundary conditions at

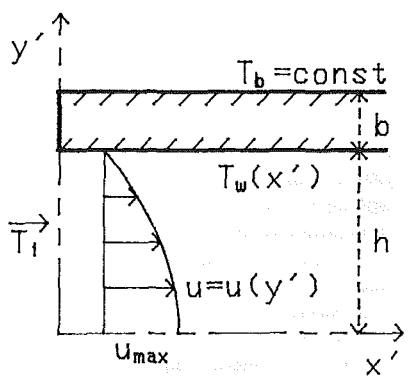

Fig. 1 Schematic diagram of the duct and coordinate system

Contributed by the Heat Transfer Division for publication in the JOURNAL OF HEAT TRANSFER. Manuscript received by the Heat Transfer Division May 24, 1988. Keywords: Conjugate Heat Transfer, Forced Convection.

the interface require that both the temperature and the heat flux be continuous.

In order to determine the temperature T_{so} in the solid we neglect the axial conduction. Such an approximation is acceptable when $b/h\mathrm{Pe} << 1$, where Pe is the Peclet number of the fluid flow. Similar conditions were given by Davis and Gill (1970) and Wijeysundera (1986) for different boundary conditions. Then the temperature T_{so} is given by $T_{so} = T_w + [T_b - T_w](y' - h)/b$ in the plate channel, and by $T_{so} = T_w + [T_b - T_w]\ln(y'/h)/\ln(1 + b/h)$ in the circular duct, where T_w is the unknown temperature at the interface.

For high Peclet numbers the energy equation for fluid phase in a nondimensional form may be written as

$$(1 - y^2)\vartheta_{,x} = (y^n \vartheta_{,y})_{,y}/y^n \tag{1}$$

where $\vartheta = (T - T_i)/(T_b - T_i)$, and $n = 0$ for the plate channel and $n = 1$ for the circular duct. The reference lengths for x' and y' are $h\mathrm{Pe}$ and h, respectively, where the Peclet number Pe is defined as $u_{\max} h\rho c_p/\lambda_f$, with ρ, c_p, and λ_f, being, respectively, density, specific heat at constant pressure, and thermal conductivity of the fluid.

The heat flux continuity condition may be written as

$$\vartheta_w - 1 = -p\vartheta_{,y}(x, 1) \tag{2}$$

where $\vartheta_w = \vartheta(x, 1)$ and the coupling parameter p is given by

$$p = \lambda_f b/\lambda_s h; \qquad p = (\lambda_f/\lambda_s)\ln(1 + b/h) \tag{3}$$

for the plate channel and for the circular duct, respectively, where λ_s is the wall thermal conductivity. Physically the coupling parameter represents the ratio of wall to fluid resistance to conduction heat transfer. As $p \to 0$ the thermal boundary condition approaches an isothermal condition, while as $p \to \infty$, the boundary condition approaches an adiabatic condition.

The remaining boundary conditions for equation (1) are

$$\vartheta(0, y) = \vartheta_{,y}(x, 0) = 0 \tag{4}$$

Equation (1) may be solved by means of Laplace transform technique. Let $F(t, y)$ be the Laplace transform of ϑ. From equations (1), (2), and (4) one has

$$(y^n F_{,y})_{,y}/y^n - t(1 - y^2)F = 0 \tag{5}$$

$$F_{,y}(t, 0) = 0; \qquad F(t, 1) - 1/t = -pF_{,y}(t, 1) \tag{6}$$

The solution of this problem is

$$F(t, y) = \exp[(1 - y^2)is/2]M_1(t, y)F(t, 1)/M_1(t, 1) \tag{7}$$

$$F(t, 1) = M_1(t, 1)/t[(1 - isp)M_1(t, 1) + 2isp(a_n/b_n)M_2(t, 1)] \tag{8}$$

where $s = t^{1/2}$, and $F(t, 1)$ is the Laplace transform of the temperature at the interface with $a_0 = (1 - is)/4$, $b_0 = 1/2$ (plate channel) and $a_1 = (2 - is)/4$, $b_1 = 1$ (circular duct), and

$$M_1(t, y) = M[a_n, b_n, isy^2];$$

$$M_2(t, y) = M[a_n + 1, b_n + 1, isy^2] \tag{9}$$

$M(a, b, x)$ is the confluent hypergeometric function (Abramowitz and Stegun, 1968).

3 Solution for Small Values of x

It is not possible to obtain the inverse Laplace transforms of equations (7) and (8) in terms of elementary functions. In order to determine the solution of the problem holding for small values of x we consider the asymptotic behavior of the confluent hypergeometric function M. By using an integral representation of M (Abramowitz and Stegun, 1968) one has $M_1(t, y) = (\Gamma(b_n)/\Gamma(a_n)\Gamma(b_n - a_n))\, I$, where

$$I = \int_0^1 \exp[isy^2 r + (a_n - 1)\log r + (b_n - a_n - 1)\log(1 - r)]dr \tag{10}$$

A similar formula holds for M_2. The solution for small values of x requires an asymptotic representation of M_1 and M_2: Such a representation may be found by means of the stationary-phase method (Bender and Orsag, 1978). This technique enables one to evaluate an integral of the form (10).

3.1 Interface Temperature, Bulk Temperature, and Nusselt Number. In order to obtain an asymptotic representation of the Laplace transform of the temperature at the interface, given by equation (8), we need to evaluate, for high values of s, the integral

$$\int_0^1 G(r)e^{isf(r)}dr \tag{11}$$

where $f(r) = r - (1/4)\log r + (1/4)\log(1 - r)$ and $G(r) = [r(1 - r)]^{-(3-n)/4}$ for M_1 and $G(r) = r^{(1+n)/4}(1 - r)^{-(3+n)/4}$ for M_2. As $f'(r) = 0$ and $f^{(2k)}(r) = 0$ $(k = 1, 2, \ldots)$ for $r = 1/2$ we consider $f(r)$ given by a Taylor expansion of initial point 1/2.

In these approximations, indefinite integrals of type $I_k = \int_{-\infty}^{\infty} \xi^k e^{-i\xi^3} d\xi$ appear. To calculate I_K the steepest-descent method is used (Bender and Orsag, 1978): It results in $I_K = (2/3)\Gamma[(k + 1)/3]L_k$, where $L_k = \cos[(k + 1)\pi/6]$ for k even and $L_k = -i\sin[(k + 1)\pi/6]$ for k odd. Then from equation (8) one has for the Laplace transform of the temperature at the interface the following expression:

$$F(t, 1) = P_m(\tau)/\mathbf{t}Q_m(\tau) \tag{12}$$

where $\tau = t^{-1/3}$ and P_m and Q_m are two real polynomials given

Nomenclature

A_c = flow cross-sectional area
b = wall thickness
c_p = specific heat at constant fluid pressure
D_h = hydraulic diameter of the duct
D_ν = cylinder parabolic function
F = Laplace transform of dimensionless temperature
h = half-height or radius of the duct
Nu = local Nusselt number $= q_w D_h/\lambda_f(T_w - T_m)$
p = coupling parameter, equations (3*a*) and (3*b*)
Pe = Peclet number $= u_{\max} h\rho c_p/\lambda_f$
q_w = heat flux at interface
T_b = outer wall temperature
T_i = fluid temperature at inlet
T_{so} = temperature in the solid
$u_{\max}$ = maximum velocity of fluid
x = $x'/h\mathrm{Pe}$ = dimensionless axial coordinate
x', y' = dimensional coordinates
$\bar{x}$ = $(u_{\max} h^2/u_m D_h^2)x$
$\tilde{x}$ = $(u_{\max}/u_m)x$
y = y'/h = dimensionless normal coordinate
z = $p^3/\alpha_1^3 x$
Γ = gamma function
ϑ = dimensionless temperature $= (T - T_i)/(T_b - T_i)$
λ_f, λ_s = fluid and wall thermal conductivities

Subscripts

m = mean or bulk
n = index denoting plane $(n = 0)$ or circular case $(n = 1)$
w = refers to solid-fluid interface
$'$ = partial derivative

Table 1 Coefficients of P_m and Q_m defined in equation (12)

n	α_0	α_1	α_2	α_3	γ_0	γ_1	γ_2	γ_3
0	0	1.0887	0.0321	0.1446	1	−0.1089	0.1140	−0.0266
1	0	1.0887	0.1571	0.0629	1	−0.6532	−0.1521	−0.1907

by $P_m = \sum_{k=0}^{m} \alpha_k \tau^k$ and $Q_m = \sum_{k=0}^{m} \beta_k \tau^k$, with $\beta_k = \alpha_k + p\gamma_k$. The coefficients α_k and γ_k are given in Table 1 up to $m=4$ for both the plane and the circular case.

The accuracy of this expansion has been extensively investigated, for the plane case, by Pozzi and Lupo (1988), where equation (12) has been compared with the exact equation (8) in a wide range of the Laplace variable t for several values of p and m. Also in the circular case this expansion gives accurate results.

In order to find the inverse transform of $F(t, 1)$, equation (12) must be rearranged. Let $-\tau_{mk}$ be the m roots of the polynomial Q_m. Then equation (12) becomes

$$F(t, 1) = (1/t^{4/3}) \sum_{k=1}^{m} A_{mk}/(\tau + \tau_{mk}) \tag{13}$$

As $1/(\tau+\tau_{mk}) = (\tau^2 - \tau_{mk}\tau + \tau_{mk}^2)/(\tau^3 + \tau_{mk}^3)$ one has

$$t^{-4/3}/(\tau+\tau_{mk}) = (\tau_{mk}^2 t^{-1/3} - \tau_{mk} t^{-2/3} + t^{-1})/\tau_{mk}^3 (\tau_{mk}^{-3} + t) \tag{14}$$

The inverse transform of this function is

$$H_k(x) = 1 + \exp(-x/\tau_{mk}^3)[3x^{1/3} M(1/3, 4/3, x/\tau_{mk}^3)/\tau_{mk}\Gamma(1/3) - (3/2)x^{2/3} M((2/3, 5/3, x/\tau_{mk}^3)/\tau_{mk}^2 \Gamma(2/3) - 1] \tag{15}$$

Then from equation (13) one has

$$\vartheta_w = \sum_{k=1}^{m} A_{mk} H_k(x) \tag{16}$$

The bulk temperature T_m, defined as $T_m = (1/A_c u_m)\int_{A_c} uT dA$, in dimensionless form is

$$\vartheta_m(x) = (T_m - T_i)/(T_b - T_i) = (u_{\max}/u_m)\, 2^n \int_0^1 y^n (1-y^2)\vartheta(x, y) dy$$

where u_m is the mean velocity of fluid ($u_{\max}/u_m = 3/2$ for the plane case and $u_{\max}/u_m = 2$ for the circular one), and by using equations (1) and (2) it may be written as

$$\vartheta_m(x) = (u_{\max}/u_m)(2^n/p)\int_0^x [1 - \vartheta_w(\bar{x})] d\bar{x} \tag{17}$$

Taking into account equation (16) one obtains for equation (17) the following expression:

$$\vartheta_m = (u_{\max}/u_m)(2^n/p)\left[x - \sum_{k=0}^{m} A_{mk} S_k(x)\right] \tag{18}$$

where

$$S_k(x) = x + \tau_{mk}^3[\exp(-x/\tau_{mk}^3) - 1] + \frac{R(1/3, 1/\tau_{mk}^3, x)}{\tau_{mk}\Gamma(1/3)} - \frac{R(2/3, 1/\tau_{mk}^3, x)}{\tau_{mk}^2\Gamma(2/3)} \tag{19}$$

and

$$R(a, b, x) = (x^a/ab)[1 - \exp(-bx)\, M(a, a+1, bx)] \tag{20}$$

The local Nusselt number $\mathrm{Nu}(x) = q_w D_h/\lambda_f(T_w - T_m)$, D_h being the hydraulic diameter of the duct, is given by

Table 2 Comparion of Nu with the results of Shah and London

	$p=0.1$		$p=0.5$	
$\bar{x}$	Present research	Shah and London	Present research	Shah and London
1×10^{-4}	25.573	25.176	26.823	26.437
6×10^{-4}	13.472	13.453	14.430	14.415
1×10^{-3}	11.231	11.227	12.099	12.096
6×10^{-3}	6.108	6.106	6.674	6.673
1×10^{-2}	5.240	5.236	5.729	5.727
4×10^{-2}	3.976	3.913	4.265	4.222

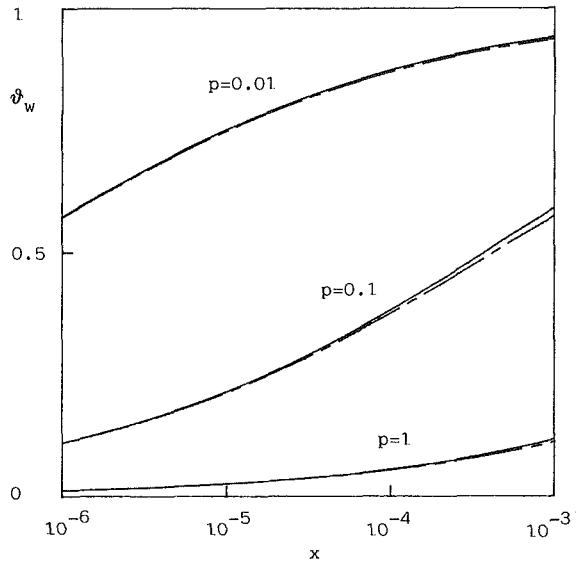

Fig. 2 Interface temperature for the plane (dashed curves) and for the circular case (solid curves) versus x for $p = 0.01$, 0.1, and 1

$$\mathrm{Nu}(x) = (D_h/h)_n\, \vartheta_{,y}(x, 1)/[\vartheta_w(x) - \vartheta_m(x)] \tag{21}$$

where $(D_h/h)_0 = 4$ and $(D_h/h)_1 = 2$, and $\vartheta_{,y}(x, 1)$ is given by equation (2).

The accuracy of equations (16) and (18) is shown in Table 2 where the Nusselt number, calculated from these equations, is compared with the values calculated by using 120 terms of an expansion in eigenfunctions (Shah and London, 1978), for $p=0.1$ and $p=0.5$. This table shows that in the range $10^{-3} \le \bar{x} \le 10^{-2}$ the two methods give nearly the same values with a percent difference less than 0.1. For higher values of $\bar{x}$ the convergence of the eigenfunction method improves and a few terms of this expanion are sufficient to obtain the Nusselt number with high accuracy. On the contrary for $\bar{x} < 10^{-3}$ the values of the Nusselt number calculated through equations (16) and (18) are more accurate than those of the eigenfunction method whose convergence becomes very slow. The dimensionless axial abscissa $\bar{x}$ is that defined by Shah and London (1978) and it is $\bar{x} = (u_{\max} h^2/u_m D_h^2)_n x$ (i.e., $\bar{x} = (3/32)x$ in the plane case and $\bar{x} = x/2$ in the circular one). It has been verified that the accuracy of the Nusselt number found by using equations (16) and (18) is always the same for each value of p listed by Shah and London (1978). In particular for values of p smaller than or equal to 0.1 and higher than or equal to 1 we shall give, in the following sections, simplified representations of equations (16) and (18).

In order to compare the thermal field of the plane duct with the circular one we consider ϑ_w, ϑ_m, and Nu, calculated by mean of equations (16), (18), and (21): ϑ_w is drawn, for several values of p, in Fig. 2, versus x for the plane (dashed curves) and the circular case (solid curves). This figure shows

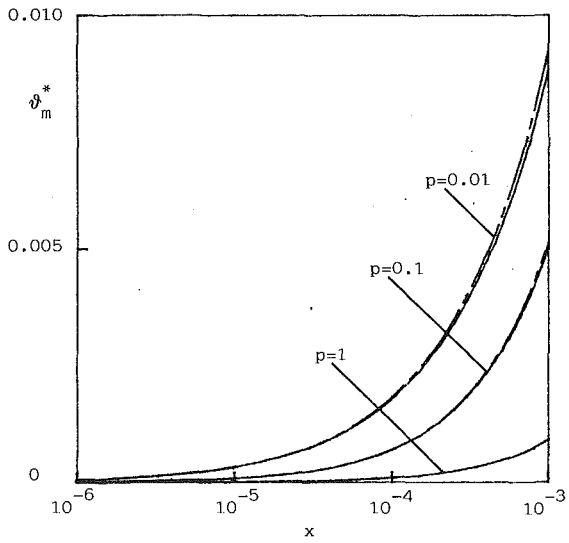

Fig. 3 ϑ_m^* for the plane (dashed curves) and for the circular case (solid curves) versus x for $p = 0.01$, 0.1 and 1

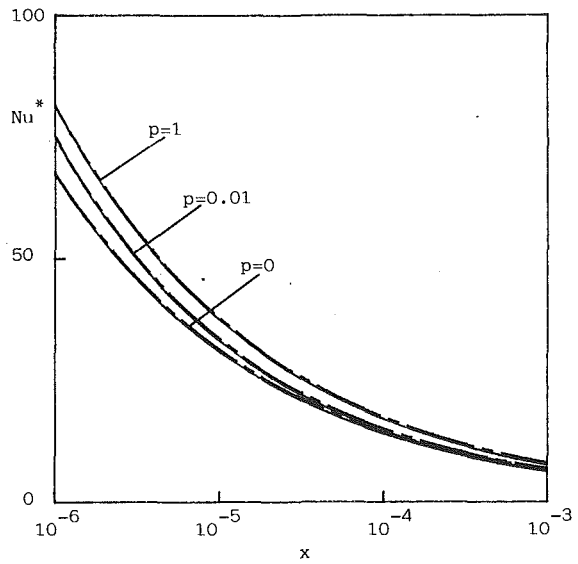

Fig. 4 Nu* for the plane (dashed curves) and for the circular case (solid curves) versus x for $p = 0$, 0.01, and 1

that the curves of ϑ_w for the plane and the circular case are coincident up to $x = 10^{-3}$. Therefore in this range of x the interface temperature, for any value of p, is the same if the velocity profiles have equal maximum velocities (in fact the Peclet number has been defined as $u_{\max} h \rho c_p / \lambda_f$). This behavior can be deduced from equation (12) which, written up to the first term, gives

$$F(t, 1) = \alpha_1 t^{-4/3} / [p + \alpha_1 t^{-1/3} + p\gamma_1 t^{-1/3}] \tag{22}$$

Since the coefficient α_1 is the same for the plane and circular case, and the third term is negligible with respect to the first two for high values of t (i.e., when $x \to 0$) for any value of p, equation (22) shows that in the entrance region the interface temperature does not depend on the geometry if $u_{\max}$ assumes the same value for plane and circular ducts. Since the successive terms of the asymptotic expansion of $F(t, 1)$ are different in the two cases, for x greater than 10^{-3} the curves of ϑ_w for the two geometries separate, as one can see in Fig. 2. Conversely the interface temperature for the two geometries is no longer the same if the velocity profiles have equal mean velocities (in fact the reference length for $\tilde{x}$ is $u_m h^2 \rho c_p / \lambda_f$). Moreover we have that $\vartheta_w \to 1$ as $x \to \infty$ for the temperature boundary condition. ϑ_m and Nu are different in circular and plane ducts. However, letting $\vartheta_m^*(x) = (u_m / 2^n u_{\max}) \vartheta_m(x)$ and $\mathrm{Nu}^*(x) = (h/D_h)_n \vartheta_y(x, 1) / [\vartheta_w(x) - \vartheta_m^*(x)]$, it is possible to have two functions that do not depend on the geometry in the entrance region, as it is shown in Figs. 3 and 4 where ϑ_m^* and Nu* are drawn versus x both for the plane (dashed curves) and the circular case (solid curves) for several values of p.

3.2 ϑ_w, ϑ_m, and Nu for Small Values of p. In this section we shall give some simple and accurate expressions of the interface temperature ϑ_w, of the bulk temperature ϑ_m and of the local Nusselt number, which are valid, in the entrance region of the duct, for small values of the coupling parameter p. By using the asymptotic representation of M, equations (16) and (18) may be written, for $p \le 0.01$, as

$$\vartheta_w = (\alpha_1/\beta_1)[1 - z^{1/3}/\Gamma(2/3) + z^{2/3}/\Gamma(1/3) - z^{4/3}/3\Gamma(2/3) + z^{5/3}2/3\Gamma(1/3)] \tag{23}$$

and

$$\vartheta_m = (u_{\max}/u_m)(2^n/p)x\left\{1 - \frac{\alpha_1}{\beta_1}[1 - z^{1/3}3/2\Gamma(2/3) + z^{2/3}3/\Gamma(1/3) - z + z^{4/3}/\Gamma(2/3) - z^{5/3}/\Gamma(1/3)]\right\} \tag{24}$$

Table 3 Comparison between ϑ_w and ϑ_m obtained from equations (16) and (23) and equations (18) and (24), respectively; $p = 0.01$

$\tilde{x}$	(16)	(23)	(18)	(24)
1×10^{-6}	0.6307	0.6446	3.633E-4	3.735E-4
1×10^{-5}	0.7944	0.7945	2.193E-3	2.194E-3
1×10^{-4}	0.8980	0.8979	1.163E-2	1.164E-2
1×10^{-3}	0.9537	0.9536	5.591E-2	5.601E-2
5×10^{-3}	0.9752	0.9749	1.580E-1	1.591E-1

where

$$z = p^3 / \alpha_1^3 x \tag{25}$$

The accuracy of these representations of ϑ_w and ϑ_m appears from Table 3 where the values obtained from equations (23) and (24) are compared respectively with those obtained from equations (16) and (18), for $p = 0.01$ in the circular case. For $p = 0.01$ equations (23) and (24) gives a percent error less than 0.1 in the range $10^{-5} \le \tilde{x} \le 10^{-3}$, for $\tilde{x} < 10^{-5}$ the precision provided by these equations decreases because the variable z (equation (25)) is not small in spite of small p. However the lower limit of the range of validity of equations (23) and (24) decreases for p decreasing and for $p = 0.001$ it is equal to $\tilde{x} = 10^{-6}$ at least.

Equations (23) and (24) enable us to calculate the Nusselt number. The previous considerations about the range of validity are applicable in the same way.

The limit of the equations (23) and (24) for vanishing p enables us to obtain the representation of the dimensionless wall heat flux $\vartheta_{,y}(x, 1)$, ϑ_m and Nu holding in the isothermal case ($p = 0$). In fact from equation (23) one has

$$\lim_{p \to 0} \vartheta_{,y}(x, 1) = \lim_{p \to 0} (1 - \vartheta_w)/p = \left[\frac{x^{-1/3}}{\Gamma(2/3)} + \gamma_1\right]/\alpha_1 \tag{26}$$

and from equation (24) it is

$$\lim_{p \to 0} \vartheta_m = (u_{\max}/u_m)\ 2^n x\left[\frac{(3/2)x^{-1/3}}{\Gamma(2/3)} + \gamma_1\right]/\alpha_1 \tag{27}$$

so that from equation (21) one obtains

$$\mathrm{Nu} = [1.2326(\tilde{x})^{-1/3} - 0.4]/[1 - 9.8604(\tilde{x})^{2/3} + 2.1333\tilde{x}] \tag{28}$$

in the plane case, and

$$\mathrm{Nu} = [1.0767(\tilde{x})^{-1/3} - 1.2]/[1 - 6.4604(\tilde{x})^{2/3} + 4.8\tilde{x}] \quad (29)$$

in the circular case.

In Table 4 the values of Nu obtained from equation (29) are compared with the values, accurate at least up to the third decimal place, given by Shah and London (1978) calculated through the extended Leveque solution for $\tilde{x} \le 10^{-4}$ and the usual expansion in eigenfunctions with 120 terms for $\tilde{x} > 10^{-4}$. In this table, the values of Nu obtained from the following simplified design formula (Shah and London, 1978) are also shown:

$$\mathrm{Nu} = 1.077(\tilde{x})^{-1/3} - 0.7 \quad (30)$$

Equation (30) is valid for $\tilde{x} \le 0.01$. Table 6 indicates that equation (29) provides values of Nu very close to the exact ones given by Shah and London (1978), with a percent error less than 0.5 up to $\tilde{x} = 10^{-3}$. Although equation (29) is just a little more complicated than equation (30), it is much more accurate than the latter in the whole range of $\tilde{x}$ considered in Table 4.

3.3 ϑ_w, ϑ_m, and Nu for High Values of p. If $p \ge 1$ the polynomial Q_m defined in equation (12), written as $p(1+\epsilon)$, where $\epsilon = (1/p)\sum_{k=1}^{m} b_k \tau^k$, may be expanded in a Taylor series and equation (12) becomes

$$F(t, 1) = P_m \Sigma(-\epsilon)^r / pt$$

The inverse Laplace transform of this function gives the following expression for ϑ_w:

$$\vartheta_w = \frac{1}{p} \sum_{k=0}^{m} c_k \frac{x^{(1+k)/3}}{\Gamma((4+k)/3)} \quad (31)$$

where $c_0 = \alpha_1$; $c_1 = -\alpha_1\beta_1/p$; $c_2 = \alpha_1\beta_1^2/p^2 + \alpha_3$; $c_3 = -\alpha_1(\beta_3 + \beta_1^3/p^2)/p - \alpha_3\beta_1/p + \alpha_4$; $c_4 = \alpha_1(2\beta_1\beta_3/p - \beta_4 + \beta_1^4/p^3)/p + \alpha_3\beta_1^2/p^2 - \alpha_4\beta_1/p$.

The bulk temperature ϑ_m is given by

$$\vartheta_m = (u_{\max}/u_m)(2^n/p)\left[x - \frac{1}{p}\sum_{k=0}^{m} c_k \frac{x^{(4+k)/3}}{\Gamma((4+k)/3)(4+k)/3}\right] \quad (32)$$

Table 5 shows the values of ϑ_w given by equation (31), those of ϑ_m given by equation (32), and those of the Nusselt number obtained from equations (31) and (32) (* column) compared respectively with the values of ϑ_w given by equation (16), those of ϑ_m given by equation (18), and those of the Nusselt number obtained from equations (16) and (18) (0 column), for $p = 1$, in the circular case. This table shows that equations (31) and (32) provide values for ϑ_w and ϑ_m with a percent error less than 0.01 up to $\tilde{x} = 0.01$. For higher values of p the accuracy of equations (31) and (32) is even better. Thus equations (16) and (18) are very accurate up to $\tilde{x} = 0.01$ (see Table 2), and equations (31) and (32) may be used with a high accuracy in this range of $\tilde{x}$ for $p \ge 1$.

Table 4 Nusselt numbers calculated by Shah and London, from equations (29) and (30) for the isothermal case

$\tilde{x}$	Shah and London	(29)	(30)
1×10^{-6}	106.538	106.538	107.000
1×10^{-5}	48.914	48.920	49.290
1×10^{-4}	22.275	22.297	22.503
1×10^{-3}	10.130	10.176	10.070
1×10^{-2}	4.916	5.076	4.299

3.4 Temperature at the Axis of the Duct. From equations (7) and (8) the Laplace transform of the temperature at the axis of the duct $\vartheta(x, 0)$ may be written as

$$F(t, 0) = \exp[is/2]/t[(1 - isp)M_1(t, 1) + 2isp(a_n/b_n)M_2(t, 1)]$$

The asymptotic expansion of $M_2(t, 1)$ gives

$$M_2(t, 1) = (\Gamma(b_n + 1)/\Gamma(a_n + 1)\Gamma(b_n - a_n))e^{is/2}\sum_{k=0} \sigma_k s^{-(1+k)/3}$$

Then the asymptotic representation of the Laplace transfer of $\vartheta(x, 0)$ is

$$F(t, 0) = s^{1/3}\Gamma(a_n)\Gamma(1 - a_n)/[2i\sigma_1\Gamma(b_n)t^{4/3}Q_m(\tau)] \quad (33)$$

where $\sigma_1 = -1.8254i$ for the plane case and $\sigma_1 = -1.2907i$ for the circular case, and $Q_m(\tau)$ is the polynomial defined in Section 3.1.

The asymptotic representation of the gamma function in the leading term gives

$$\Gamma(a_n)\Gamma(1 - a_n) = 2\pi e^{-\pi s/4}(s/4)^{(n-1)/2}$$

and therefore equation (33), taking $m = 1$ (i.e., considering only two terms of the polynomial Q_m), may be written as

$$F(t, 0) = 2^{n-1}\pi t^{(3n-17)/12}\exp(-\pi t^{1/2}/4)/[|\sigma_1|\Gamma(b_n)(p + \beta_1\tau)] \quad (34)$$

The inverse transform of equation (34) is

$$\vartheta(x, 0) = (2^{n-1}\pi/|\sigma_1|\beta_1\Gamma(b_n)\bar{\tau}^3)[\bar{\tau}^2 I(\nu_1, x) - \bar{\tau} I(\nu_2, x) + I(\nu_3, x)] \quad (35)$$

where

$$I_k(\nu, x) = 2^{-\nu}\pi^{-1/2}e^{-\delta x}\int_0^x e^{\delta x}x^{-\nu-1/2} \times \exp[-(\pi/4)^2/8x]D_{2\nu}(\pi/4(2x)^{1/2})dx \quad (36)$$

$\bar{\tau} = (p/\beta_1)$, $\nu_i = (5 - 4i)/12$ for $n = 0$ and $\nu_i = (2 - i)/3$ for $n = 1$, $\delta = (1/\bar{\tau})^3$, and $D_\nu(z)$ is the parabolic cylinder function. Equation (36) may be greatly simplified if $p \le 0.01$, because in this case it is

$$I_k(\nu, x) = 2^{-\nu}\pi^{-1/2}\delta^{-1}x^{-\nu-1/2}\exp[-(\pi/4)^2/8x]D_{2\nu}(\pi/4(2x)^{1/2}) \quad (37)$$

and if x is sufficiently small one has

$$I_k(\nu, x) = 2^{-6\nu}\pi^{2\nu-1/2}\delta^{-1}x^{-2\nu-1/2}\exp[-(\pi/4)^2/4x]$$

In Fig. 5 the curves of $\vartheta(x, 0)$ are drawn, both for the plane (dashed curves) and the circular case (solid lines), versus x, for $p = 0.01$ and $p = 2$. This figure and equation (35) show that the behavior of the temperature at the axis $\vartheta(x, 0)$ is dependent on the duct geometry also if we consider the velocity profiles with the same maximum velocity.

Table 5 Comparison among equations (16) and (31), (18) and (32), and the Nusselt number obtained from these equations (0 and *columns) for $p = 1$

	ϑ_w		ϑ_m		Nu	
$\tilde{x}$	(16)	(31)	(18)	(32)	(0)	(*)
1×10^{-4}	0.0696	0.0696	7.580E-4	7.580E-4	27.040	27.040
1×10^{-3}	0.1460	0.1460	7.116E-3	7.116E-3	12.300	12.300
1×10^{-2}	0.2992	0.2992	6.172E-2	6.172E-2	5.901	5.901

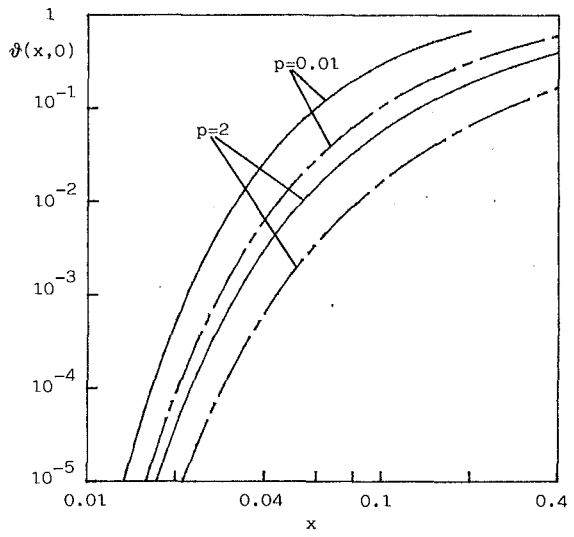

Fig. 5 Temperature at the axis of the duct for the plane (dashed curves) and for the circular case (solid curves) versus x for $p = 0.01$ and 2

4 Concluding Remarks

This work presents an analytical solution of the energy equation, for the problem of coupled laminar convection and wall conduction in a pipe, which holds up to values of the abscissa such that it is possible to represent the thermal field by few terms of the asymptotic solution.

This solution has been obtained, in terms of confluent hypergeometric functions, by means of an asymptotic expansion of the temperature Laplace transform (i.e., for high values of the Laplace variable) and an application of the stationary-phase method. The good accuracy of the results has been shown by a comparison with those found by using an expansion in terms of 120 eigenfunctions. Some simple and accurate formulas for the interface temperature, the bulk temperature, and the Nusselt number have also been presented for cases where the coupling parameter assumes small and high values.

The comparison between the thermal field in plane and circular ducts has shown that in the entrance region the interface temperature does not depend on the duct geometry, for any value of the coupling parameter, if the velocity profiles have equal maximum velocities.

Acknowledgments

This work was sponsored by Ministero Pubblica Istruzione.

References

Abramovitz, M., and Segun, I., 1968, *Handbook of Mathematical Functions*, Dover Publications, New York.

Barozzi, G. S., and Pagliarini, G., 1984, "Conjugated Heat Transfer in a Circular Duct With Uniform and Non-uniform Wall Thickness," *Heat and Technology*, Vol. 2, pp. 72–91.

Bender, C. M., and Orsag, S. A., 1978, *Advanced Mathematical Methods for Scientists and Engineers*, McGraw-Hill, New York.

Davis, E. J., and Gill, W. N., 1970, "The Effect of Axial Conduction in the Wall on Heat Transfer With Laminar Flow," *Int. J. Heat Mass Transfer*, Vol. 13, pp. 459–470.

Hsu, C. J., 1971, "Laminar Flow Heat Transfer in Circular or Parallel Plate Channels With Internal Heat Generation and the Boundary Condition of the Third Kind," *J. Chin. Inst. Chem. Eng.*, Vol. 2, pp. 85–100.

Luikov, A. V., Aleksashenko, V. A., and Aleksashenko, A. A., 1971, "Analytical Methods of Solution of Conjugated Problems in Convective Heat Transfer," *Int. J. Heat Mass Transfer*, Vol. 14, pp. 1047–1056.

Mori, S., Sakaribara, S., and Tanimoto, A., 1974, "Steady Heat Transfer to Laminar Flow in Circular Tube With Conduction in the Tube Wall," *Heat Transfer—Japanese Research*, Vol. 3, pp. 37–46.

Pozzi, A., and Lupo, M., 1988, "The Coupling of Conduction With Forced Convection in Plane Ducts," *Proc. of the Eurotherm Seminar*, No. 3, Bologna, Italy, pp. 73–87.

Shah, R. K., and London, A. L., 1978, *Laminar Flow Forced Convection in Ducts*, Academic Press, New York.

Wijeysundera, N. E., 1986, "Laminar Forced Convection in Circular and Flat Ducts With Wall Axial Conduction and External Convection," *Int. J. Heat Mass Transfer*, Vol. 29, pp. 797–807.

The Influence of a Horseshoe Vortex on Local Convective Heat Transfer

E. M. Fisher
Research Assistant

P. A. Eibeck
Assistant Professor.

Mechanical Engineering Department,
University of California,
Berkeley, CA 94720

The objective of this research program has been to determine experimentally the extent to which horseshoe vortices modify turbulent convective heat transfer along a flat plate downstream of an appendage. The importance of appendage shape on the heat transfer behavior was evaluated by taking Stanton-number measurements downstream of both a cylindrical body and a streamlined body. The results indicate that a region of augmented heat transfer occurs near the centerline downstream of both obstacles, with Stanton numbers 10 to 50 percent over the undisturbed values. The streamlined cylinder produces the strongest modifications in heat transfer.

Introduction

Horseshoe vortices, which are formed at the junction between an appendage and a flat surface, occur naturally within turbomachinery and can have a detrimental effect on device performance. The vortices can have a strong influence on local convective heat transfer characteristics, often leading to localized hot spots, which eventually damage turbomachinery. Designers of turbomachinery devices need to predict this overheating both in the vicinity of the appendage and downstream. However, the effects of the trailing legs of a horseshoe vortex on heat transfer are not well understood.

The physical mechanism responsible for the formation of the vortex is the adverse pressure gradient present at the leading edge of an obstacle. The mean shear within the approaching boundary layer is skewed, or deflected, by the transverse pressure gradient. The boundary layer separates and rolls up to form a spanwise vortex at the leading edge. The fluid away from the junction is undisturbed and tends to wrap the vortex around the obstacle, resulting in two streamwise vortex legs, as shown schematically in Fig. 1. If the vortex legs are not destroyed by the wake behind the obstacle, they should propagate downstream of the obstacle, forming a counterrotating vortex pair that remains immersed in the boundary layer. The fate of the vortex legs downstream of the obstacle is currently not clear due to a lack of sufficient experimental data.

Previous experimental research has illuminated the general characteristics of horseshoe-vortex systems. Flow visualization studies have been performed, primarily focusing on the leading edge of an obstacle, in an effort to understand the formation process. Schwind (1952), Peake and Galway (1965), and Peak et al. (1965) demonstrated that the flow is unsteady and cyclic in the leading edge region under laminar boundary layer conditions. For high-Reynolds-number turbulent boundary layers, Peake and Tobak (1980) state that the leading edge is likely to be steady. Belik (1973) found that the turbulent flow separation region can be characterized by the Reynolds number based on boundary layer thickness. Baker studied the separation region of both laminar (Baker, 1979) and turbulent boundary layers (Baker, 1980) in detail, and postulated that four counterrotating vortices are formed. Goldstein and Karni (1984) present a model of the flow around a cylinder based on their observations of local mass transfer in the separation region. They postulate that a large vortex with a diameter roughly equal to the boundary layer thickness is present, as well as smaller, more vigorous vortices.

Several experimental investigations have shown that the mean velocity profiles of the flow downstream of an obstacle depend on the characteristics of the obstacle generating the horseshoe-vortex system. Sepri (1973) demonstrated that wing incidence has an effect on the relative sizes of the trailing vortex legs. Transverse velocity profiles were made by Love (1963) behind circular cylinders, circular arc profiles, and elliptic profiles, demonstrating the dependence of the downstream flow on obstacle shape. The influence of wing incidence, wing thickness, and boundary layer thickness on the downstream velocity field was investigated by Chu and Young (1975), Barber (1978), and Dickinsen (1984).

The convective heat transfer downstream of an obstacle should depend on the complex interactions of both the horseshoe-vortex trailing legs and the wake with the thermal boundary layer. The horseshoe-vortex legs can potentially both increase and decrease local convective heat transfer coefficients along a flat plate. The gross motion of the vortices sweeps cooler fluid from the outer regions of the thermal boundary layer toward the wall in some areas, locally increasing the heat transfer. By contrast, in regions where the secondary flow is away from the wall, the thermal boundary layer is thickened, resulting in lower heat transfer. In addition to this mixing mechanism, the horseshoe vortex may alter the structure of the turbulence within the boundary layer, which may enhance or lessen heat transfer.

The wake of the obstacle should tend to augment convection as well, except possibly in a stagnant recirculating region.

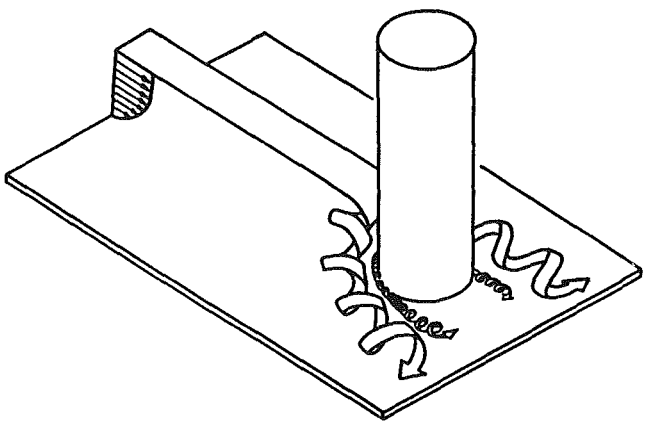

Fig. 1 Schematic of a horseshoe vortex

Contributed by the Heat Transfer Division and presented at the ASME Winter Annual Meeting, Boston, Massachusetts, December 13–18, 1987. Manuscript received by the Heat Transfer Division March 1, 1988. Keywords: Augmentation and Enhancement, Forced Convection, Turbines.

The wake will increase levels of turbulence and mixing, and introduce periodic unsteady motions in the free-stream fluid due to the Karman shedding.

Based on previous investigations, the parameters that should influence convective heat transfer by altering the trailing vortex legs and the behavior of the wake would include the approach-boundary-layer characteristics, the Reynolds number, and the obstacle geometry.

Objective

The objective of this study has been to determine experimentally the extent to which a horseshoe-vortex system modifies turbulent convective heat transfer downstream of two different appendage shapes: a circular cylinder and a tapered cylinder.

Related Work

There have been two investigations that provide detailed flow measurements for the obstacle configurations used in this experiment. Eckerle (1986) obtained aerodynamic measurements in the region of a cylindrical appendage at a Reynolds number based on diameter of 5.5×10^5 and with the boundary-layer-thickness-to-diameter ratio (δ_{99}/D) equal to 0.13. Detailed surface flow visualization and static-pressure measurements, as well as extensive mean-velocity and pressure measurements, were made by Pierce, et al. (1985) upstream of, around, and in a horseshoe vortex generated by a streamlined cylinder normal to a flat plate. The test conditions for this case were $\mathrm{Re}_D = 1.8 \times 10^5$ and $\delta_{99}/D = 0.64$. Both of these studies are restricted to the region of the obstacle and do not illuminate the fluid-dynamics features downstream of the obstacles.

Previous studies have investigated the role that horseshoe vortices play in the heat transfer within turbomachinery. Langston (1980) and Sieverding (1985) present fairly detailed descriptions of the flow within turbine cascades. The flow is complex because the horseshoe vortex that is formed at the junction of the turbine blade and the endwall interacts with the vortices formed by neighboring blades and with the existing pressure gradient between blades. A number of studies have been able to link the heat transfer within a turbine cascade to the flow patterns through flow visualization. Blair (1974) found that Stanton number increased by a factor of three in the leading edge of the turbine blade, and by a factor of four under the vortex farther downstream. Graziani et al. (1980) found that Stanton number increased by only 50 percent under the vortex near the leading edge of the turbine blade. Gaugler and Russell (1984) compared their flow visualization to the heat transfer results of Hylton et al. (1981) and found a correlation between the horseshoe-vortex location and peak endwall heat transfer near the vanes' leading edge.

Local heat and mass-transfer effects of horseshoe vortices produced at a cylinder/wall junction have been studied by Ireland and Jones (1986) for channel flow and by Goldstein et al. (1985) in an external boundary layer. Ireland and Jones studied the heat transfer effects of a circular cylinder spanning a two-dimensional channel in fully developed duct flow. They found that the maximum heat transfer coefficient along the channel wall occurs at the stagnation point upstream of the cylinder, and a double peak in Nusselt number occurs downstream of the cylinder.

Goldstein et al. (1985) present contours of the ratio of local Stanton number to undisturbed Stanton number for circular cylinders in a turbulent boundary layer at a Reynolds number based on cylinder diameter of 4000. Data are reported for two cylinders: a short one, with height on the order of the boundary layer thickness and height-to-diameter ratio of one, and a tall one, with a height-to-diameter ratio of 12. By means of a naphthalene sublimation technique, strongly enhanced mass transfer was observed immediately upstream and to the sides of both cylinders. Locally, the Stanton number was up to 4.5 times the undisturbed value at the leading edge. The experiments indicated that cylinder height influences the local mass transfer distribution in the region downstream of the cylinder. A recirculation zone of relatively low mass transfer was followed by a reattachment region with higher transfer rates. The Stanton number in the reattachment zone was higher for the short cylinder. In the downstream area, the strong central maximum due to reattachment obscures the maxima associated with the two longitudinal vortices of the horseshoe vortex system. The overall enhancement of mass transfer, averaged over the measurement region, is 1.85 for the short cylinder and 1.68 for the tall one.

A related investigation concerning the influence of vortices on heat transfer was made by Eibeck and Eaton (1987). In this study, heat transfer and fluid-dynamics measurements were made within a turbulent boundary layer containing a single longitudinal vortex generated by a half-delta wing. Five different vortex cases were studied. Spanwise profiles of Stanton number showed local increases as large as 24 percent in addition to local decreases of approximately 14 percent. Vortex parameters, such as circulation and location, were measured, and the heat transfer effects tended to increase asymptotically with increasing circulation.

Experimental Procedure

In this experimental study, the influence of horseshoe vortices on local convective heat transfer was determined by mapping the Stanton-number distribution present on a flat plate downstream of two different obstacles. A liquid-crystal technique was used to measure iso-Stanton-number lines at different Reynolds numbers.

The experiments were conducted in an open-circuit, subsonic wind tunnel located in the Fluid Mechanics Research Laboratories at UC Berkeley. The wind tunnel consists of a centrifugal blower and diffuser, a stagnation chamber followed by multiple screens, a contraction section, a test section, and a discharge duct. The test section is 347 cm long, with an 81.3 cm × 81.3 cm square cross section. The boundary layer, which develops along the polished wooden floor of the test section, is tripped by a 0.1-cm-high, 1-cm-wide phenolic strip. Free-stream velocity can be varied between 9 and 25 m/s.

Two different flow obstacles were used for the experiments: a circular cylinder and a tapered cylinder. The tapered cylinder consists of a circular leading edge with two tangential flat sides that terminate in a sharp trailing edge. The tapered cylinder is 19.4 cm long, with the diameter of the circular section identical to that of the cylindrical obstacle, which is 8.3 cm. Both

Nomenclature

C_p = heat capacity
D = obstacle diameter or maximum thickness
h = heat transfer coefficient
Re_D = Reynolds number = UD/ν
St = Stanton number = $h/\rho C_p U_\infty$
U = velocity
U_∞ = free-stream velocity
X = streamwise distance
Y = normal distance
Z = spanwise distance
δ_{99} = boundary-layer thickness
ν = kinematic viscosity
ρ = density

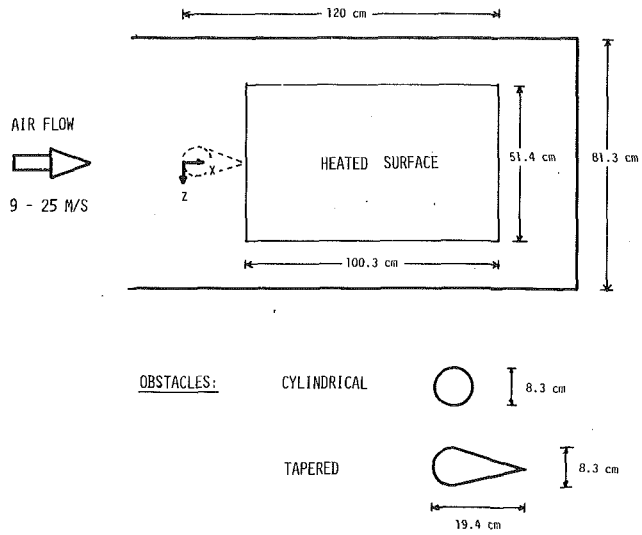

Fig. 2 Experimental test section

obstacles span the height of the tunnel and are positioned on the centerline, with their leading edge 231 cm downstream of the boundary-layer trip. The tapered model was mounted with a zero angle of attack.

Figure 2 is a schematic of the test section, showing the reference coordinate system and the location of the obstacles and the heat transfer test surface. The origin of the streamwise coordinate, i.e., $x=0$, occurs at the leading edge of the obstacle.

Experiments were conducted for Reynolds numbers based on cylinder diameter between 7.7×10^4 and 1.3×10^5. Two-dimensional boundary-layer characteristics were determined by making velocity-profile measurements with a pitot probe at $x=25$ cm with no obstacle in place. Boundary-layer thickness at the centerline varied between 5.7 and 6.4 cm over the Reynolds-number range. The boundary layer was fully turbulent, since the Reynolds number based on momentum thickness ranged from 3000 to 9000, the shape factor varied between 1.32 to 1.35, and the flat-plate velocity profiles matched the familiar law of the wall and law of the wake. Assuming the standard growth rate of a turbulent boundary layer, $\delta/x\sim \mathrm{Re}_x^{-1/7}$, the thickness at $x=0$ was estimated, giving a variation of δ/D from 0.62 to 0.69 at the leading edge of the obstacle.

A slight nonuniformity in the spanwise profile of the boundary layer was observed. In the vicinity of $Z/D=0.5$, a localized momentum deficit was present, with the boundary-layer thickness roughly 25 percent greater than the rest of the boundary layer. This nonuniformity influenced the flat-plate heat transfer less than the measurement uncertainty, although it seems to have led to a slight asymmetry in the two legs of the horseshoe vortex system for the tapered cylinder.

Local convective heat transfer coefficients were measured using liquid crystals and a constant-heat-flux plate. Liquid crystals indicate temperature by undergoing a color change at a specific event temperature. During this color transition, the liquid crystals go through the entire visible spectrum. The isotherm displayed by liquid crystals on a constant-heat-flux surface corresponds to a line of constant heat transfer coefficient. The heat transfer coefficient can be calculated from the wall (i.e., liquid crystal) temperature, the free-stream temperature, and the heat flux.

The constant-heat-flux surface consists of a 0.0051-cm-thick sheet of type 302, annealed stainless steel attached with high-temperature silicone adhesive to a 3.8-cm-thick slab of polystyrene. The surface is 51.4 cm wide and 100.3 cm long, resulting in a width of 6.2 D and a streamwise development length of 12.1 D. A constant heat flux is produced by passing a uniform alternating current across the stainless steel via copper busbars at the two ends. The resistive heating can be determined by measuring the current passing through the foil and the voltage drop across the length of the heated surface. Two-dimensional calculations indicate that less than 1 percent of the heat should escape through the back of the insulating slab. Since the foil is very thin, conduction of heat along the surface is extremely small except at the edges of the surface, where heat is conducted to the unheated surrounding surface. The spanwise uniformity of Stanton number for the flat plate varied within ±1 percent.

The liquid-crystal mixture was airbrushed onto the stainless-steel foil. Two coats of black paint were first applied to the steel to prevent reflections, and then 20 layers of the liquid crystals were applied. The liquid crystals produce a single color band, or isotherm, along the heated surface at a given heat-flux level. To obtain a high resolution of heat transfer coefficients, the magnitude of wall heat flux was changed to alter the spatial positions of the isotherms. The complete spatial distribution of heat transfer coefficients was obtained by taking 35-mm photographs of the heat transfer surface at multiple wall-heat-flux levels. The Stanton numbers corresponding to the isotherms were calculated at each heat-flux level, and then the images were superimposed to produce a final map of Stanton-number distributions. Since physical constraints of the wind tunnel made it impossible to take photographs directly overhead, the camera was angled at the side of the test section. The camera angle and lighting conditions remained constant throughout the data-taking process for each case.

The complete color change of liquid crystals occurs over a relatively large temperature range, and so the liquid crystals were calibrated to match two of the colors in the color band to specific temperatures. The calibrator, described by Chao (1986), consists of an insulated aluminum plate with a hot source and cold sink at the two ends. Embedded thermocouples indicate the temperature distribution along the plate. The liquid-crystal mixture was applied directly to the aluminum plate using the same technique as was used on the heated surface. Photographs were taken of the color bands, replicating the camera angle and lighting conditions of the experiment as closely as possible. Two lines within each color band were selected for quantitative measurements: the dividing line between orange and green, which was calibrated at 31.1°C, and the dividing line between green and blue, which was calibrated at 32.6°C. The calibration procedure indicated the liquid crystals' event temperature within an uncertainty of ±0.2°C.

The tendency of the event temperature to drift with time reduced the reliability of the temperature measurements. Exposure to ultraviolet light caused the event temperature to drift downward by approximately 1.5°C over a period of 6 months following the calibration. New event temperatures were estimated by matching Stanton-number data obtained in a verification test to the original heat transfer data obtained under the same conditions. The different sets of data collapsed on the verification test case with a maximum discrepancy of only 5 percent.

The uncertainty in the Stanton-number measurements is a combination of random experimental errors and the systematic errors introduced when correcting for the drift in event temperature. The uncertainty in the magnitude of the Stanton number accounting for both of these effects was estimated to be 8 percent. However, the uncertainty in comparing relative enhancement levels is slightly lower, at 5 percent.

Experimental Results

The Stanton-number distribution with no obstacle present

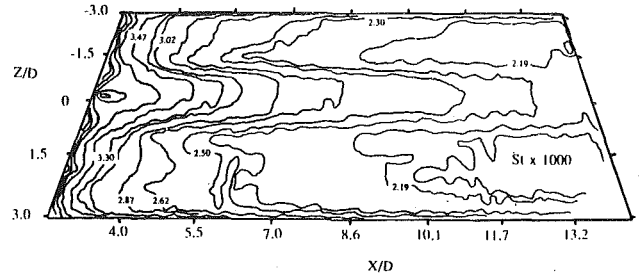

Fig. 3(*a*) Stanton number contours downstream of the tapered cylinder at $Re_D = 7.7 \times 10^4$

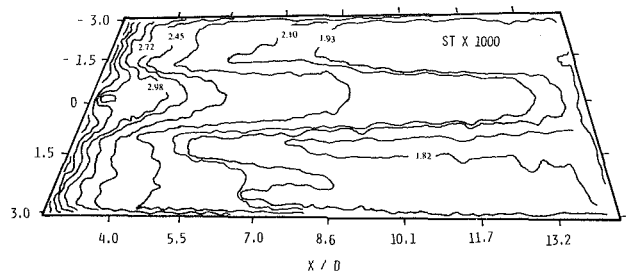

Fig. 3(*b*) Stanton number contours downstream of the tapered cylinder at $Re_D = 1.3 \times 10^5$

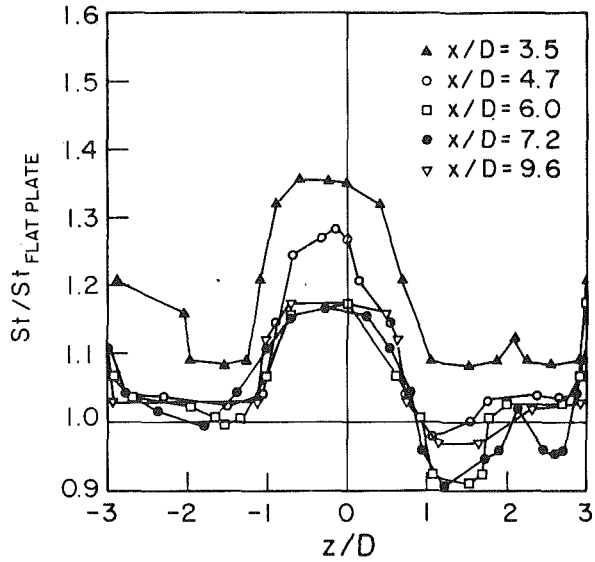

Fig. 4 Spanwise variation of normalized Stanton numbers at different streamwise locations for the tapered cylinder at $Re_D = 1.3 \times 10^5$

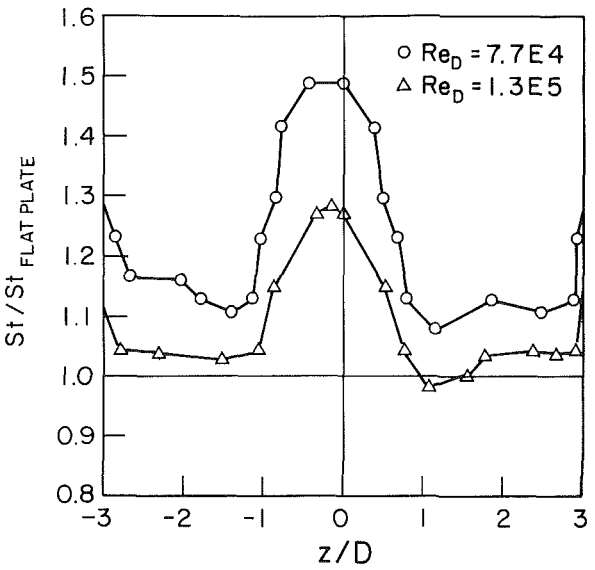

Fig. 5 Spanwise variation of normalized Stanton number at $X/D = 4.7$ for $Re_D = 7.7 \times 10^4$ and 1.3×10^5 behind the tapered cylinder

was measured to determine the two dimensionality of the flat plate boundary layer, and to verify the accuracy of the heat transfer measurements. The spanwise uniformity of the Stanton number measured 20 cm downstream of the flat plate's leading edge remained within the experimental uncertainty, ranging between ± 1 percent at $Re_D = 5.1 \times 10^4$ and ± 3 percent at $Re_D = 1.3 \times 10^5$. The variation of spanwise averaged Stanton number in the streamwise direction was compared to predictions based on the unheated-starting-length correlation presented by Kays and Crawford (1980). The data and the predictions match within the measurement uncertainty except at the leading edge, where conduction is important. The two cases that match theory within ± 1 percent, $Re_D = 7.7 \times 10^4$ and 1.3×10^5, were chosen for presentation in this paper. (Data at the other Reynolds numbers are available from Fisher, 1987.)

Maps of Stanton number distribution along the flat-plate surface downstream of the two different obstacles are presented in Figs. 3(*a*), 3(*b*) and 6(*a*), 6(*b*) for two nominal Reynolds numbers, $Re_D = 7.7 \times 10^4$ and 1.3×10^5. Two features of the figures should be mentioned before discussing the results. Firstly, the shape of the surface is distorted because of the camera angle. Also, the effect of conduction from the edge of the surface to the wind-tunnel floor can be seen in the rapid rise in Stanton number along the edges of the heated plate.

Plots of spanwise Stanton-number distribution were produced by linearly interpolating between neighboring contours on high-resolution Stanton-number maps. These plots, shown in Figs. 4, 5, and 7–9, are presented with Stanton number normalized by the spanwise-averaged Stanton number associated with the two-dimensional boundary layer at the appropriate Reynolds number.

(a) Tapered Cylinder. The Stanton-number contours downstream of the tapered cylinder, shown in Figs. 3(*a*) and 3(*b*), indicate that a considerable variation in Stanton number occurs downstream of the obstacle. An increase in Stanton number is evident along the centerline, and this effect persists in the streamwise direction. A small Stanton-number minimum can be seen at the leading edge of the heat transfer surface. This low-heat-transfer region is associated with the wake of the obstacle, the trailing edge of which is located at the beginning of the heated plate. The spanwise variation in the contours indicates that the Stanton number decreases along the edge of the enhanced region and then approaches a constant value away from the centerline. The spanwise extent of the enhanced-heat-transfer regions seems to be limited, with only a gradual increase with streamwise development. Comparing Figs. 3(*a*) and 3(*b*) shows that Reynolds number has very little qualitative effect on the perturbations induced by a horseshoe-vortex system.

A plot of normalized Stanton number as a function of spanwise distance (Fig. 4) shows the streamwise persistence of the local modifications in heat transfer for the tapered-cylinder case at $Re_D = 1.3 \times 10^5$. The augmentation observed at $X/D = 3.5$ may be a result of both the horseshoe vortex system and the flowpath blockage, since the object diameter is roughly 10 percent of the tunnel width. At X/D greater than 3.5, the blockage effects are not prevalent, and a region of augmentation occurs near the centerline where they drop

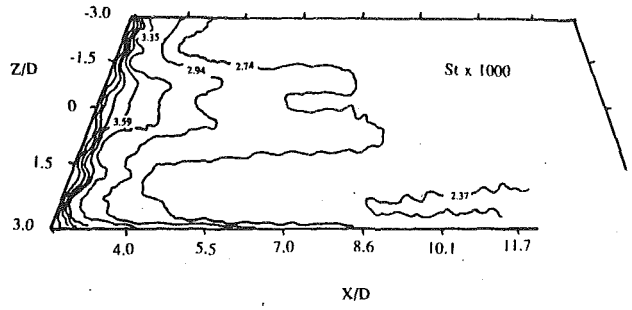

Fig. 6(a) Stanton number contours downstream of the circular cylinder at $Re_D = 7.7 \times 10^4$

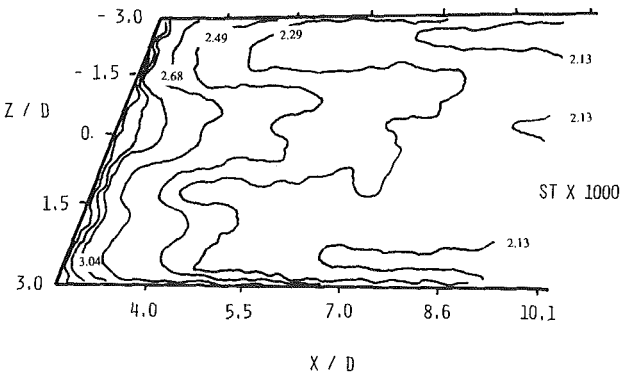

Fig. 6(b) Stanton number contours downstream of the circular cylinder at $Re_D = 1.3 \times 10^5$

down to the flat plate values close to $Z/D = -1.0$. At positive $Z/D > 1.0$, the heat transfer is 10 percent less than the flat plate values. We suspect the asymmetry in the heat transfer is due to asymmetric horseshoe vortex legs caused by the nonuniformity in the upstream boundary layer.

The peak rise in heat transfer along the centerline occurs closest to the leading edge, but the effects do not decrease rapidly with streamwise distance; peak augmentation only varies from 36 to 18 percent between $X/D = 3.5$ and $X/D = 9.6$. In addition, as distances greater than six diameters downstream, the augmentation near the centerline becomes constant, implying a persistent streamwise influence of the vortices.

At all streamwise locations, the region of peak heat transfer occurs over a spanwise extent of roughly 2½ diameters. Outside of the peak augmentation region, the Stanton number approaches the flat-plate value for all cases except $X/D = 3.5$, and in some cases the Stanton number is slightly lower than its undisturbed value.

The sensitivity of the local heat transfer modifications to Reynolds number is demonstrated in Fig. 5, which shows normalized Stanton numbers at $X/D = 4.7$ for two Reynolds numbers, $Re_D = 7.7 \times 10^4$ and 1.3×10^5. The shape of the spanwise Stanton-number curves remains similar, but the level of augmentation is lower at the higher Reynolds number. For example, there is a 50 percent peak augmentation at the centerline behind the tapered cylinder at $Re_D = 7.7 \times 10^4$, contrasted with 28 percent at $Re_D = 1.3 \times 10^5$.

(b) Cylinder. The Stanton-number contours downstream of the circular cylinder are shown in Figs. 6(*a*) and 6(*b*). (Note: The lack of details toward the trailing edge of the heat transfer surface is the result of a lighting problem during data taking.) The modifications imposed by this horseshoe-vortex system are qualitatively different from those imposed by the vortex associated with the tapered cylindrical body. In this

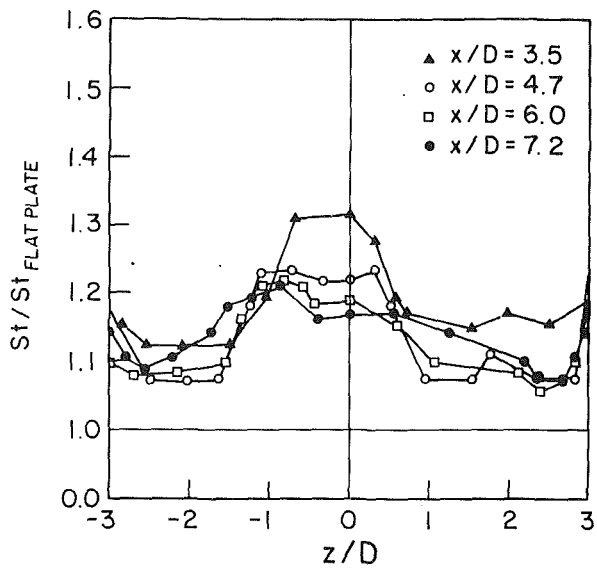

Fig. 7 Spanwise variation of normalized Stanton numbers at different streamwise locations for the circular cylinder at $Re_D = 1.3 \times 10^5$

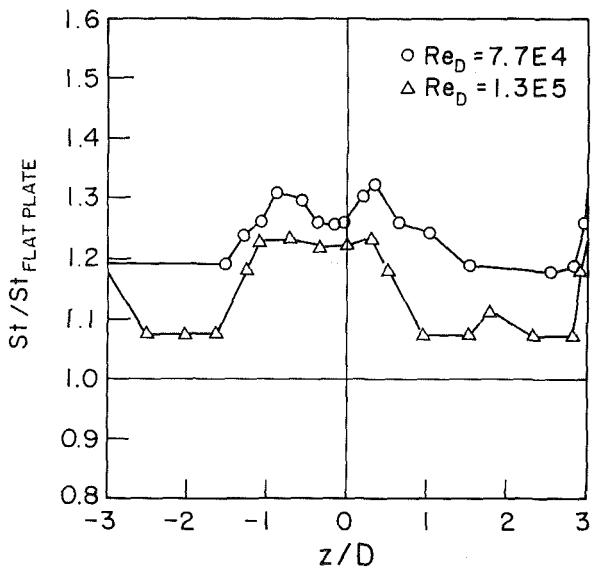

Fig. 8 Normalized Stanton number distribution for the tapered cylinder and the cylindrical obstacle at $X/D = 7.2$ and $Re_D = 1.3 \times 10^5$

case, there are two symmetric peaks in Stanton number, with a lower augmentation of Stanton number at the centerline. As Reynolds number increases, the centerline dip in the Stanton-number curves becomes less pronounced. The Stanton number seems to be approaching a constant value with distance away from the centerline, although at the higher Reynolds numbers this trend is not as apparent.

Figure 7 provides a more quantitative representation of the spanwise Stanton-number distribution at different streamwise locations behind the circular cylinder for $Re_D = 1.3 \times 10^5$. As was the case with the tapered obstacle, the circular cylinder shows a monotonic decrease in the augmentation of heat transfer from a maximum enhancement of 31 percent at $X/D = 3.5$ to 21 percent at $X/D = 7.2$. Unlike the tapered obstacle, the shape of the Stanton-number profiles changes with streamwise distance behind the cylinder. At $X/D = 3.5$, there is a well-defined region of peak enhancement with a spanwise extent of roughly two diameters, and with the maximum level of augmentation occurring at the centerline.

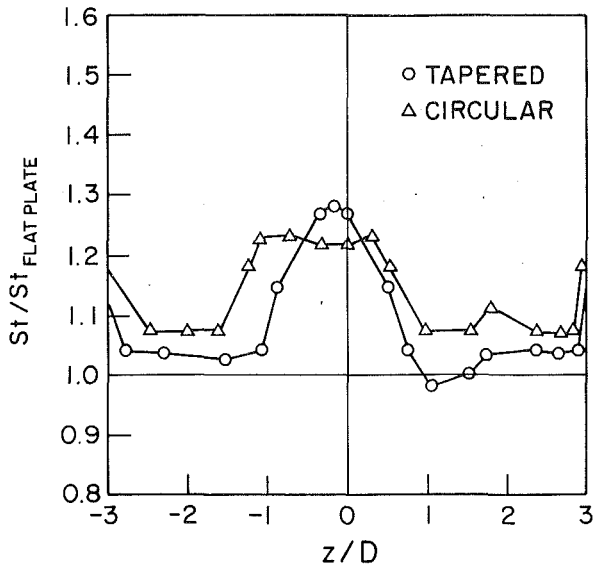

Fig. 9 Spanwise variation of normalized Stanton number at $X/D = 4.7$ for $Re_D = 7.7 \times 10^4$ and $1.3 = 10^5$ behind the circular cylinder

However, with streamwise distance the region of peak enhancement spreads, and the maximum level of augmentation occurs at two symmetric positions about the centerline. A more surprising difference between the two cases is that the Stanton numbers remain at least 7 percent above the flat-plate value away from the centerline at all streamwise locations. This implies that the cylinder enhances the heat transfer over a much greater region than the streamlined obstacle, even though the level of maximum augmentation remains nearly the same. This is demonstrated in Fig. 8, which presents the spanwise distribution of normalized Stanton number for the circular and tapered cylinder at $X/D = 7.2$ and $Re_D = 1.3 \times 10^5$.

The influence of Reynolds number on the heat transfer modifications behind the cylinder is shown in Fig. 9. As was the case for the tapered cylinder, there are stronger effects at the lower Reynolds number with a maximum augmentation of 31 percent at $Re_D = 7.7 \times 10^4$ and a maximum of 23 percent at $Re_D = 1.3 \times 10^5$. In addition, the distinction of the two symmetric peaks is clearer and the enhancement far away from the centerline is greater at the lower Reynolds number.

Discussion

The results of this experiment show that the convective heat transfer on a flat plate downstream of an obstacle is enhanced, with local heat transfer as much as 50 percent greater than the undisturbed value. The magnitude and the spatial distribution of this enhancement vary with obstacle shape, streamwise location, and Reynolds number.

The characteristic shape of the enhanced region behind both obstacles implies that the trailing legs of the horseshoe vortex are influencing the local convection process. The regions of increased heat transfer could be associated with the downwash region of vortices as they sweep cooler fluid toward the wall. The concentration of high heat transfer coefficients along the centerline downstream of the tapered cylinder suggests the vortex legs are close to one another and have a common region of strong downwash flow. The two separate peaks of Stanton number associated with the cylindrical obstacle could be due to trailing legs that are positioned farther apart and have separate downwash regions.

These arguments regarding the high heat transfer assume a strong horseshoe vortex system. While this may be the case for the tapered cylinder (Barber, 1978), the work by Eckerle and Langston (1987) shows that the vortex system associated with a cylinder has greatly diffused as it enters the wake region. This implies that the heat transfer augmentation downstream of the circular cylinder may be due to the vigorous wake behind the cylinder rather than the vortex legs.

The streamwise persistence of the modifications in convection induced by the horseshoe-vortex system is evidenced by the experimental results. The perturbations in Stanton-number extend over 15 obstacle diameters (the length of the heated surface) implying that these effects continue far downstream. In addition, the spanwise enhancement profile doesn't change with streamwise distance after six obstacle diameters. The decrease in enhancement levels over the first six diameters downstream may be caused by a combination of changes in the flow structure, such as decreased mixing in the wake, and the development of the thermal boundary layer.

The sensitivity of the enhancement levels to Reynolds number is a result of changes in flow features, such as the approach boundary-layer thickness, Karman shedding frequency, or wake size, that are affected by Reynolds number. For example, the horseshoe-vortex-formation process is dependent on the approach boundary-layer thickness. As Reynolds number increases, boundary-layer thickness decreases, resulting in a smaller horseshoe vortex. Since augmentation levels downstream are dependent on the interaction of the trailing vortices with the thermal boundary layer, the smaller vortices are likely to cause less modification to the thermal boundary layer. This could lead to lower enhancement levels at higher Reynolds numbers.

From this discussion, it can be seen that the fluid-dynamics features of the horseshoe-vortex system are so complex that, without substantially more detailed fluid-dynamics measurements, we can only postulate about the physical processes that lead to the observed heat transfer perturbations.

Concluding Remarks

In summary, some very interesting qualitative and quantitative features of the Stanton number distribution downstream of a tapered and a cylindrical obstacle were observed. The major conclusions from the experimental results are as follows:

1. The horseshoe-vortex system generated by a tapered cylindrical obstacle induces a region of Stanton number augmented by as much as 50 percent along the centerline downstream of the obstacle.
2. The horseshoe vortex generated by a cylindrical obstacle also leads to a region of higher Stanton numbers downstream of the appendage, with two peaks in heat transfer occurring symmetrically about the centerline. The maximum augmentation level measured was 35 percent.
3. In general, the vortex pair trailing the tapered cylinder results in greater modifications to the Stanton number than the vortex pair trailing the cylindrical body.
4. The modification of local Stanton numbers is persistent with streamwise distance. After six obstacle diameters, the spanwise enhancement profile doesn't change shape with axial distance.
5. Increasing Reynolds number from $Re_D = 7.7 \times 10^4$ to 1.3×10^5 decreases the peak augmentation level from 50 to 29 percent for the tapered obstacle and from 32 to 23 percent for the cylindrical obstacle.

References

Baker, C. J., 1979, "The Laminar Horseshoe Vortex," *Journal of Fluid Mechanics*, Vol. 95, Part 2, pp. 347–368.

Baker, C. J., 1980, "The Turbulent Horseshoe Vortex," *Journal of Wind Engineering and Industrial Aerodynamics*, Vol. 6, Nos. 1–2, pp. 9–23.

Barber, T. J., 1978, "An Investigation of Strut-Wall Intersection Losses," *Journal of Aircraft*, Vol. 15, No. 10, pp. 676–681.

Belik, L., 1973, "The Secondary Flow About Circular Cylinders Mounted Normal to a Flat Plate," *Aeronautical Quarterly*, Vol. 26, pp. 47–54.

Blair, M. F., 1974, "An Experimental Study of Heat Transfer and Film Cooling on Large-Scale Turbine Endwalls," ASME JOURNAL OF HEAT TRANSFER, Vol. 96, pp. 524–529.

Chao, P. T., 1986, "Liquid Crystal Temperature Calibration Technique," Masters Project Report, Department of Mechanical Engineering, University of California, Berkeley.

Chu, J. K., and Young, A. D., 1975, "Further Investigation of Viscous Effects in a Wing-Plate Junction," Queen Mary College Report QMC ER-1003, United Kingdom.

Dickinson, S. C., 1984, "Flow Visualization and Velocity Measurements in the Separated Region of an Appendage-Flat Plate Junction," David Taylor Naval Ship Research and Development Center Report No. 86.

Eckerle, W. A., 1986, "Measurements of a Turbulent Horseshoe Vortex Formed Around a Cylinder," United Technologies Research Center Report UTRC 86-20.

Eibeck, P. A., and Eaton, J. K., 1987, "Heat Transfer Effects on a Longitudinal Vortex Embedded in a Turbulent Boundary Layer," ASME JOURNAL OF HEAT TRANSFER, Vol. 109, No. 1, pp. 16–24.

Fisher, E. M., 1987, "The Influence of a Horseshoe Vortex on Local Convective Heat Transfer Rates," Master's Thesis, Department of Mechanical Engineering, University of California, Berkeley.

Gaugler, R. E., and Russel, L. M., 1984, "Comparison of Visualized Turbine Endwall Secondary Flows and Measured Heat Transfer Patterns," ASME *Journal of Engineering for Gas Turbines and Power*, Vol. 106, pp. 168–172.

Goldstein, R. J., and Karni, J., 1984, "The Effect of a Wall Boundary Layer on Local Mass Transfer From a Cylinder in Crossflow," ASME JOURNAL OF HEAT TRANSFER, Vol. 106, pp. 260–267.

Goldstein, R. J., Chyu, M. K., and Hain, R. C., 1985, "Measurement of Local Mass Transfer on a Surface in the Region of the Base of a Protruding Cylinder With a Computer-Controlled Data Acquisition System," *International Journal of Heat and Mass Transfer*, Vol. 28, No. 5, pp. 977–985.

Graziani, R. A., Blair, M. F., Taylor, J. R., and Mayle, R. E., 1980, "An Experimental Study of Endwall and Airfoil Surface Heat Transfer in a Large Scale Turbine Blade Cascade," ASME *Journal of Engineering for Power*, Vol. 102, p. 257.

Hylton, L. D., Mihelc, M. S., Turner, E. R., and York, R. E., 1981, "Experimental Investigation of Turbine Endwall Heat Transfer," AFWAL-TR-81-2077, three volumes.

Ireland, P. T., and Jones, T. V., 1986, "Detailed Measurements of Heat Transfer on and Around a Pedestal in Fully Developed Passage Flow," *Proceedings, 8th International Heat Transfer Conference*, C. L. Tien et al., eds., Hemisphere Publishing Corp., Washington, DC, Vol. 3, pp. 795–980.

Kays, W. M., and Crawford, M. E., 1980, *Convective Heat and Mass Transfer*, 2nd ed., McGraw-Hill, New York.

Langston, L. S., 1980, "Crossflows in a Turbine Cascade Passage," ASME *Journal of Engineering for Power*, Vol. 102, No. 4, pp. 866–874.

Langston, L. S., and Boyle, M. T., 1982, "A New Surface-Streamline Flow-Visualization Technique," *Journal of Fluid Mechanics*, Vol. 125, pp. 53–57.

Love, R. H., 1963, "An Investigation of the Effect of the Wall Boundary Layer on the Wake of an Obstacle Protruding From the Wall," University of Maryland Technical Note BN-370.

Peake, D. J., and Galway, R. D., 1965, "Three-Dimensional Separation of a Plane Incompressible Laminar Boundary Layer Produced by a Circular Cylinder Mounted Normal to a Flat Plate," *Recent Developments in Boundary Layer Research*, Part II, NATO Agardograph No. 97, pp. 1049–1080.

Peake, D. J., Galway, R. D., and Rainbird, 1965, "The Three-Dimensional Separation of a Plane, Incompressible, Laminar Boundary Layer Produced by a Rankine Oval Mounted Normal to a Flat Plate," Report No. LR-446, National Aeronautical Establishment, Ottawa, Ontario, Canada.

Peake, D. J., and Tobak, M., 1980, "Three-Dimensional Interactions and Vortical Flows With Emphasis on High Speeds," NASA Technical Memorandum TM-81169, NASA-Ames Research Center, Moffett Field, CA.

Pierce, F. J., Harsh, M. D., and Menna, J. D., 1985, "The Mean Flow Structure Around and Within a Turbulent Junction or Horseshoe Vortex," Department of Mechanical Engineering, Virginia Polytechnic Institute and State University, Report No. VPI-E-85-19.

Schwind, R. G., 1952, "The Three-Dimensional Boundary Layer Near a Strut," Gas Turbine Laboratory Report No. 57, Massachussetts Institute of Technology, Cambridge, MA.

Sepri, P., 1973, "An Investigation of the Flow in the Region of the Junction of a Wing and a Flat Surface Normal to the Wing Span," Queen Mary College Report QMC ER-1001, United Kingdom.

Sieverding, C. H., 1985, "Recent Progress in the Understanding of Basic Aspects of Secondary Flows in Turbine Blade Passages," ASME *Journal of Engineering for Gas Turbines and Power*, Vol. 107, pp. 248–257.

Heat Transfer Augmentation Through Wall-Shape-Induced Flow Destabilization

M. Greiner
Assistant Professor.
Assoc. Mem. ASME

R.-F. Chen
Research Assistant.

R. A. Wirtz
Professor.
Mem. ASME

Mechanical Engineering Department,
University of Nevada, Reno,
Reno, NV 89557

Experiments on heat transfer augmentation in a rectangular cross-section water channel are reported. The channel geometry is designed to excite normally damped Tollmien–Schlichting modes in order to enhance mixing. In this experiment, a hydrodynamically fully developed flow encounters a test section where one channel boundary is a series of periodic, saw-tooth, transverse grooves. Free shear layers span the groove openings, separating the main channel flow from the recirculating vortices contained within each cavity. The periodicity length of the grooves is equal to one-half of the expected wavelength of the most unstable mode. The remaining channel walls are flat, and the channel has an aspect ratio of 10:1. Experiments are performed over the Reynolds number range of 300 to 15,000. Streakline flow visualization shows that the flow is steady at the entrance, but becomes oscillatory downstream of an onset location. This location moves upstream with increasing Reynolds numbers. Initially formed traveling waves are two dimensional with a wavelength equal to the predicted most unstable Tollmien–Schlichting mode. Waves become three dimensional with increasing Reynolds number and distance from onset. Some evidence of wave motion persists into the turbulent flow regime. Heat transfer measurements along the smooth channel boundary opposite the grooved wall show augmentation (65 percent) over the equivalent flat channel in the Reynolds number range 1200 to 4800. The degree of enhancement obtained is shown to depend on the channel Reynolds number, and increases with the distance from the onset location.

Introduction and Problem Definition

Practical needs to improve the performance of exchange devices, such as compact heat exchangers (Kays and London, 1984) and blood oxygenators (Bellhouse et al., 1973), and scientific interest in the relation between channel heat transfer and pumping power (Karniadakis et al., 1988) have motivated intense interest in convective transport enhancement (Bergles and Webb, 1985). Much recent attention has been given to passive enhancement techniques in laminar and transitional channel flows by shear destabilization. In these systems, hydrodynamic instability modes, which normally decay in an "unenhanced" flow, are destabilized by careful modification of the system solid boundaries, such as cutting grooves in the channel wall (Greiner et al., 1988; Ghaddar et al., 1986a; Stephanoff, 1986) or adding eddy promoters to the core region of the flow (Kozlu et al., 1988). These modifications lead to the formation of free shear layers, which, at sufficiently large Reynolds numbers, feed energy to the least stable modes. The destabilized systems generally exhibit traveling waves, which augment convective transport normal to the walls. While conventional passive enhancement schemes rely on thermal boundary layer interruption or surface extension, the current technique is based on subtle but important modifications in the flow behavior.

Initial interest in destabilized flows grew from experimental and numerical studies of resonant heat transfer enhancement in grooved channels (Greiner et al., 1986; Ghaddar et al., 1986b; Stephanoff et al., 1980; Sobey, 1980). These studies consider spatially fully developed flows at laminar and transitional Reynolds numbers in transversely grooved channels. By actively modulating the flow rate at frequencies close to the natural frequency of the least stable Tollmien–Schlichting modes, resonant excitation of these modes is observed, even at moderately low Reynolds numbers. The excited flow exhibits greatly enhanced mixing and heat transfer, and a properly tuned 20-percent flow rate modulation has been shown to enhance heat transfer by a factor of two and a half (Greiner et al., 1986; Ghaddar et al., 1986b).

While hydrodynamic resonance is an interesting transport enhancement scheme, its augmentation requires *active* flow modulation, which is inherently less reliable than passive schemes in practical systems. The current study considers *passive* shear destabilized transport enhancement using the grooved channel geometry shown in Fig. 1. A fully developed flow is discharged from a parallel-wall flow development section of height H and width W (normal to the plane of Fig. 1). The upper wall is thermally insulated while the bottom surface is maintained at a uniform temperature T_0. At the position $x = 0$, this flow enters a test section of minimum height H, whose upper surface dissipates a uniform heat flux q'', and whose lower surface is maintained at a constant temperature T_0. Heat transfer is measured at the upper wall under two sets of geometric conditions of the bottom surface: a flat surface, and a saw-toothed profile. The first condition provides a baseline against which enhancement caused by the grooved lower surface can be compared. It also serves to validate the measurement techniques.

Flow visualizations and convective heat transfer measurements are performed for the Reynolds number range, $300 \leq \mathrm{Re} \leq 15{,}000$, where $\mathrm{Re} = VD_h/\nu$, and where $V = Q/HW$ is the average velocity, Q is the fluid volume flow rate, $D_h = 2HW/(H + W)$ is the minimum channel hydraulic diameter, and ν is the fluid kinematic viscosity. The local Nusselt number is defined as $\mathrm{Nu} = hD_h/k$, where h is the local heat transfer coefficient (based on the local bulk fluid temperature) and k

Contributed by the Heat Transfer Division and presented at the National Heat Transfer Conference, Philadelphia, Pennsylvania, August 6–9, 1989. Manuscript received by the Heat Transfer Division January 23, 1989; revision received August 5, 1989. Keywords: Augmentation and Enhancement, Flow Instability, Forced Convection.

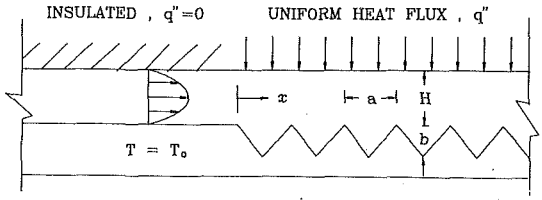

Fig. 1 Geometric and thermal boundary conditions

is the fluid thermal conductivity. Values are reported at six x-locations along the upper flat surface. The Nusselt number dependence on Reynolds number, channel location, and channel geometry is determined experimentally. Several comparisons are made between the flow behavior in the grooved channel shown in Fig. 1 and a flat channel with the same minimum wall-to-wall spacing H, at the same Reynolds number.

The grooved surface is specifically designed to excite the most unstable modes in the unenhanced (flat wall) system. In plane Poiseuille flow, the most unstable modes are two-dimensional Tollmien–Schlichting waves. While these traveling disturbance modes naturally decay with time for Reynolds numbers less than a critical value of $\mathrm{Re}_c = 15{,}400$ (Drazin and Reid, 1981), this value may be drastically reduced by modifying the wall shape. When "open" (deep) grooves are cut into the channel wall, slow-moving recirculating regions fill the cavity, and the groove openings are spanned by free shear layers. A groove aspect ratio of $a/b = 2$ is used so that grooves act as open cavities for the Reynolds number range considered (Yee, 1986). These layers cause inflection points to form in the velocity profile. At sufficiently large Reynolds number, Kelvin–Helmholtz instabilities of these layers have been shown numerically (Ghaddar et al., 1986a) and experimentally (Greiner et al., 1988) to destabilize the normally damped Tollmien–Schlichting waves, effectively reducing the critical Reynolds number. At supercritical conditions, traveling waves, whose amplitude are proportional to $\sqrt{\mathrm{Re}-\mathrm{Re}_c}$, promote transport perpendicular to the channel walls.

In other continuously grooved channels (i.e., no space between grooves) the critical Reynolds number in fully developed flow has been observed to be $\mathrm{Re}_c = 330$ (Greiner et al., 1988), almost 50 times smaller than the flat channel value. To further encourage the onset of instability, the groove periodicity length a of the current design is chosen to be compatible with the wavelength of the most unstable Tollmien–Schlichting mode. Since this wavelength λ is Reynolds number dependent, and the present investigation considers the range $300 \leq \mathrm{Re} \leq 15{,}000$, a representative value at $\mathrm{Re} = 1400$ is selected. At this Reynolds number $\lambda = 2.4\,H$ (Ghaddar et al., 1986a), and the channel periodicity length is chosen so that $a = \lambda/2$.

The current work extends previous numerical and experimental results in several important ways. In past studies, transport is measured from the grooved surface. While this type of measurement is realistic from the practical point of view, it is difficult from a scientific point of view to distinguish the transport enhancement/degradation due to at least three different phenomena: (*a*) the destabilized flow, (*b*) the increase in surface area, and (*c*) the increased thermal resistance between the channel surface and the external flow caused by the slow-moving vortices contained in the cavities. Measurement of heat transfer along the opposite flat surface presumably is a much better measure of the enhancement gained from flow destabilization alone. This type of wall shape induced enhancement evaluation is used by Ichimiya (1987) in the fully turbulent regime.

While previous studies consider only fully developed flows, in the current work heat transfer measurements and flow visualizations are made at several positions along the channel, starting at its inlet and continuing to the fully developed state. These results allow knowledge to be gained about the development length of these flows, which is a matter of great practical interest to common exchange devices. The current wall design, with its continuously grooved sawtooth shape that is compatible with the most unstable Tollmien–Schlichting wavelength, is also a new addition to the base of knowledge in this field.

It can be expected that the enhanced mixing in supercritical grooved channel flows will augment heat transfer relative to that in a flat channel with the same minimum wall-to-wall spacing for the same Reynolds number. It is also to be expected, however, that this favorable augmentation will come at the expense of an increased pumping power requirement relative to a flat channel flow. While other investigators (Karniadakis et al., 1988; Kozlu et al., 1988) and our own recent data indicate that destabilized-flow heat transfer is favorable on an equal pumping power basis when compared to unenhanced systems, this is not the focus of the current study. In the present work, we wish to concentrate on the hydrodynamic conditions for the onset of supercritical flow (Reynolds number, dimensionless development lengths) and the magnitude of the heat transfer enhancement it causes relative to an equivalent flat channel flow. In essence, this paper documents the development, existence and potential usefulness of destabilized flows.

Experimental Apparatus

Measurements are made using the temperature-controlled recirculating water channel shown in Fig. 2. A centrifugal pump delivers distilled water through a bank of rotameters and control valves to the left side of a partitioned reservoir, which contains a cooling coil for temperature control. The right side of the tank is fed via a weir at the top of the partition and can supply up to a 1.2-m head to the test channel. The flow passes two honeycomb sections and enters the channel flow development section through a "soda straw" flow straightener. The flow development section has height $H = 20$ mm and width $W = 203$ mm, giving a hydraulic diameter $D_h = 36.4$ mm. Velocimetry measurements show that the flow development length of 67 hydraulic diameters is sufficient to assure fully developed conditions at the test section inlet ($x = 0$ in Fig. 1). The bottom and side walls of the flow development section are aluminum, and the top surface is Plexiglas. The temperature at $x = -50$ mm is monitored by a digital ther-

Nomenclature

a = groove depth
b = groove length
D_h = minimum hydraulic diameter $= 2HW/(H + W)$
E = enhancement ratio = Nu (grooved)/Nu (flat)
Gz^{-1} = inverse Graetz number $= (x/D_h)/\mathrm{Re\ Pr}$
h = heat transfer coefficient
H = channel height
k = fluid thermal conductivity
Nu = Nusselt number $= hD_h/k$
Pr = fluid Prandtl number
q'' = heat flux
Q = fluid volume flow rate
Re = Reynolds number $= VD_h/\nu$
Re_c = critical Reynolds number
T = temperature
T_m = mixed mean temperature
T_o = lower wall temperature
T_s = heated wall surface temperature
V = average velocity $= Q/HW$
W = channel width
x = axial coordinate
λ = least stable Tollmien–Schlichting wavelength
ν = kinematic viscosity

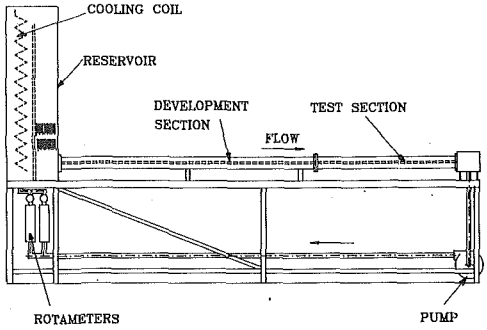

Fig. 2 Closed-loop test apparatus

mometer and maintained at $T_0 = 29.4 \pm 0.6°C$, which is within 3°C of the laboratory room temperature.

The test section is 30.3 hydraulic diameters long, and includes 46 V-shaped grooves, which span the lower surface. These are constructed by mounting right-triangular aluminum ribs, 12 mm high and 24 mm at their base, to a 12-mm-thick aluminum base plate, which is in turn backed by a water jacket for temperature control. The bottom wall is maintained isothermal to within ± 0.2°C while the overall driving temperature difference for experiments ranges from 2 to 10°C. A 12-mm-thick aluminum plate is substituted in place of the triangular elements for the baseline flat channel experiments.

Two different upper surfaces are employed in the test section, one for flow visualization experiments, the other for heat transfer measurements. Both are fabricated from 25-mm-thick Plexiglas. Flow visualizations are performed by injecting colored tracer into the flow field and recording the resulting patterns on video tape. A variable volume flow rate syringe pump is used to inject the pigment at channel center height and midspan through an L-shaped tube (1.0 mm o.d.) inserted through the channel ceiling and bent downstream. For each Reynolds number, the tracer flow rate is adjusted so that its velocity at the injector tip is the same as the average fluid velocity V, thus minimizing disturbances to the channel flow. For the applicable channel Reynolds number range, the injector Reynolds number is less than 40, thus causing negligible flow disturbance. The pigment is a solution of red food coloring, diluted with roughly 17 parts water. While the dye density is slightly greater than that of the working fluid, its settling velocity is much less than that of the center channel speed, even at the lowest Reynolds numbers considered.

The heat transfer surface has six custom heater/thermocouple/heat flux gage assemblies bonded to its surface. The heat flux passing to the fluid from each assembly is monitored by a 102 mm by 102 mm thermopile-type heat flux gage (accuracy ± 1 percent) located at its center. The assemblies contain copper-constantan thermocouple junctions located 0.28 mm beneath the wetted surface at 18 equally spaced points along the channel centerline. These thermocouples are referenced to a junction located at the center of the flow development section, at $x = -50$ mm. After corrections are made for the conduction temperature drop between the wall thermocouples and the wetted wall surface, and the local fluid mixed mean temperature is computed using an approximate energy balance, the local temperature difference between the wall and the mixed mean fluid temperature, $\Delta T = T_s - T_m$, is used with the local heat flux to determine the local heat transfer coefficient h.

Each of the six gage assembly heaters is wired in series with a trimming rheostat, and these subsystems are wired in parallel to a regulated d-c power supply. During an experimental run, the trimming rheostats are adjusted so that the indicated heat flux through each combination gage is the same, resulting in a heat flux uniformity of ± 1 percent of the average heat flux input.

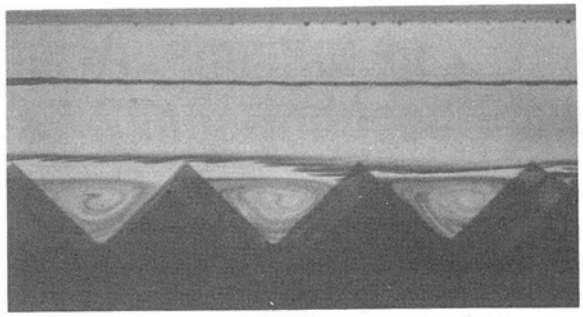

Fig. 3(a)

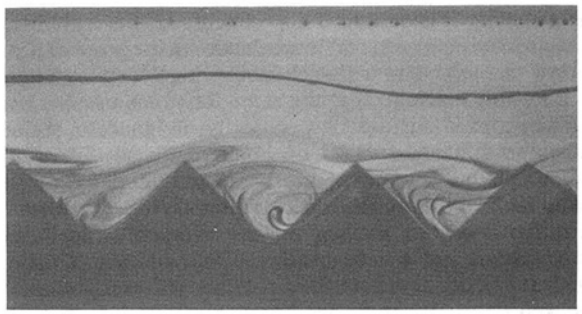

Fig. 3(b)

Fig. 3 Streakline flow visualizations at $x/D_h = 24.4$: (a) Re = 600, steady flow; (b) Re = 700, traveling wave structure

Downstream from the test section the flow passes another "soda straw" flow straightener and enters a small plenum chamber with a return line to the pump. Edge walls of the test section are 6-mm-thick Plexiglas, and all metallic surfaces are coated with baked epoxy paint. The apparatus is covered with 50-mm-thick expanded foam insulation during data collection.

Results

Flow Visualizations. Figures 3 and 4 show a series of streakline patterns, which document the onset of natural flow oscillations and their subsequent breakdown to turbulence. These visualizations are produced by injecting colored tracer at the leading edge of the 38th groove ($x/D_h = 24.4$). The streakline pattern shown for Re = 600 in Fig. 3(*a*) is typical of subcritical flows. The flow is steady and the grooves contain slowly turning vortices. The outer channel streaklines move parallel to the flat wall, much like the flow in ungrooved (flat) channels. At Re = 600 small-amplitude laminar waves are intermittently observed between long periods of steady flow. At a Reynolds number of 700 (Fig. 3*b*) the flow is almost continuously oscillatory, with occasional steady periods. A traveling wave structure develops a regular wavelength, which Fig. 3(*b*) shows to be roughly equal to two groove lengths. The channel geometry is designed so that the wavelength of the most unstable Tollmien–Schlichting mode is equal to two groove lengths, and it is not surprising that this mode is the first to be excited. These streaklines are "smooth" and views from the top of the tank indicate that they are mostly two dimensional. As the Reynolds number increases, however, the patterns become more irregular and three dimensional. Small-scale structures are superimposed on the long-wavelength Tollmien–Schlichting waves in Fig. 4(*a*) for Re = 1000. As the Reynolds number increases, the length scales of the smaller structures decrease and the three dimensionality of the flow increases, as seen in Fig. 4(*b*).

The dye injection visualization technique is not effective at demonstrating the smallest scale motion at higher Reynolds numbers, as the tracer rapidly dissipates. The dye fan envelope does appear to experience periodic large-scale oscillatory mo-

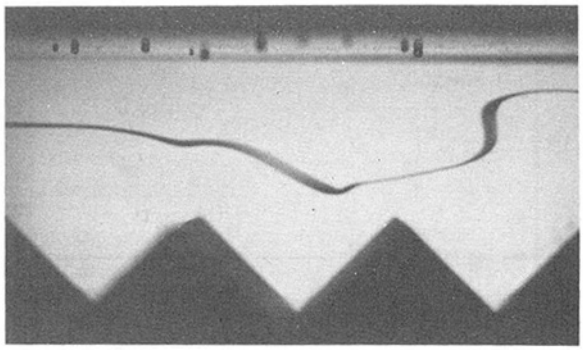

Fig. 4(*a*)

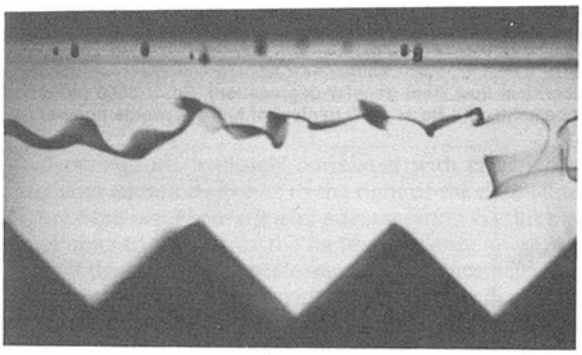

Fig. 4(*b*)

Fig. 4 Streakline flow visualization showing three-dimensional wave structure at x/D_h = 24.4: (*a*) Re = 1000; (*b*) Re = 2000

tion when viewed in real time, suggesting that the groove spanning free shear layers may be capable of effecting turbulent flows in channels. This visualization technique, however, is severely limited at this turbulence level.

A graph showing the fraction of time the flow exhibits an oscillatory behavior, as a function of Reynolds number, is presented in Fig. 5. These data are determined by viewing a flow pattern for a given time period and measuring the fraction of this time the flow is "oscillatory." These measurements are somewhat qualitative because the oscillatory amplitude varies continuously, and does not exhibit an "on/off" behavior. Multiple data points are reported for Reynolds numbers at which more than one observation is made, indicating the imprecision of this technique. Figure 5 shows that the oscillatory flow time-fraction increases sharply in the Reynolds number range 600 to 660. As the Reynolds number increases beyond 700, the flow is observed to become continuously oscillatory.

If the observed critical Reynolds number Re_c is defined (arbitrarily) as the value at which the flow is oscillatory 50 percent of the time, then for this channel location $Re_c = 630 \pm 20$. The dependence of the observed value of Re_c on location is discussed in the following section in connection with the onset of heat transfer enhancement. Reference to Fig. 10 (triangular symbols) shows that Re_c decreases with distance downstream. However, for the present apparatus an asymptotic value is not achieved. Work in progress with a longer test section shows Re_c approaches a value of 350 after about 35 hydraulic diameters, in good agreement with previous predictions (Greiner et al., 1988).

Heat Transfer. For each Reynolds number and axial location, local temperature measurements are made for a range of wall heat fluxes to detect any effect of natural convection and to eliminate the effects of systematic temperature offset errors. A straight line is fit to each q'' versus ΔT data set, and the slope of this line is used to determine the local heat transfer coefficient, $h = dq''/d\Delta T$. The relation is found to be highly linear, indicating the absence of significant buoyancy effects.

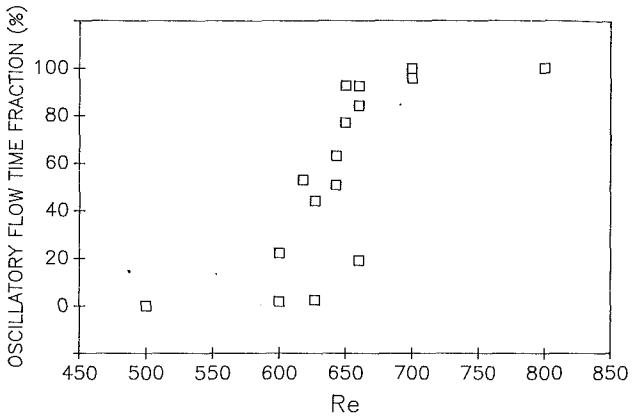

Fig. 5 Oscillatory flow time fraction versus Reynolds number at x/D_h = 24.4; two-dimensional transition occurs in the range 600 < Re < 660

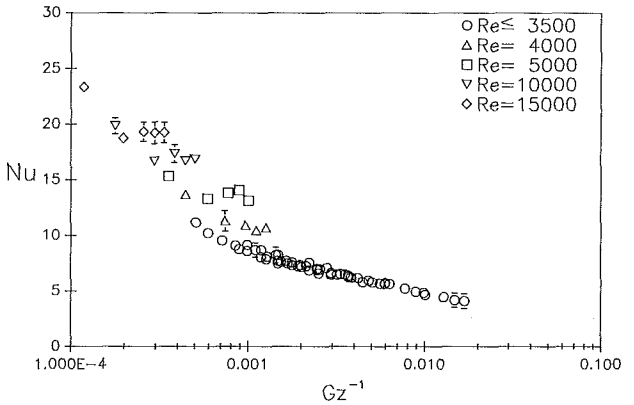

Fig. 6 Measured flat channel Nusselt number versus inverse Graetz number for 300 < Re < 15,000; error bars are used to indicate 99.7 percent confidence band due to random errors when this band is larger than the symbol size

In the following heat transfer plots, error bars representing the 99.7 percent confidence level due to random errors are indicated where the bar size exceeds data point symbol size. In many cases the error bar size is smaller than the symbol size, and is not shown.

Figure 6 shows the local Nusselt number as a function of inverse Graetz number for a flat channel flow. Data for Re < 3500 collapse to a single line, while those for Re ≥ 4000 show the onset of significant turbulent transport. These data are used as the baseline for comparison with grooved channel measurements.

Figure 7 shows the grooved channel Nusselt number as a function of inverse Graetz number for 300 ≤ Re ≤ 15,000. The data are now seen to depart from a single curve at Re ≥ 1200. At Re = 1200, the heat transfer coefficient is seen to increase at $Gz^{-1} \approx 0.003$, and the departure point has moved upstream to $Gz^{-1} \approx 0.0008$ at Re = 2000, with the trend continuing with increasing Reynolds number. The heat transfer coefficient is greater than corresponding flat channel values for Re ≥ 1200, and it is actually less than the flat channel values for Re ≤ 1000, as explained below.

The degree of heat transfer enhancement obtained is more easily interpreted in Fig. 8, which is for a supercritical Reynolds number of 3000. Part (*a*) of the figure compares local Nusselt numbers for the grooved channel flow with that obtained with the flat configuration, and part (*b*) shows the enhancement factor, E = Nu (grooved)/Nu (flat), both plotted against dimensionless axial location. As expected, flat channel values

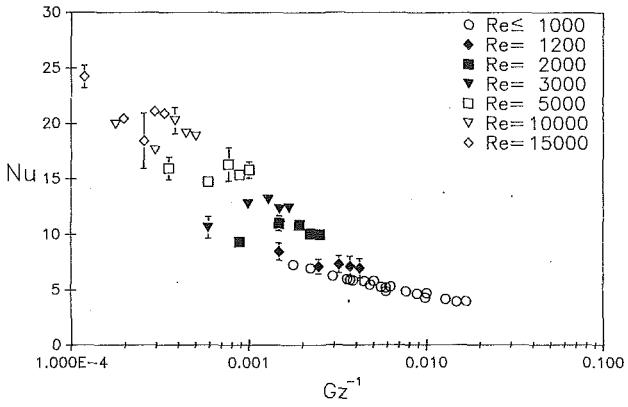

Fig. 7 Measured grooved channel Nusselt number versus inverse Graetz number for 300 < Re < 15,000; error bars are used to indicate 99.7 *percent confidence band due to random errors when this band is larger* than the symbol size

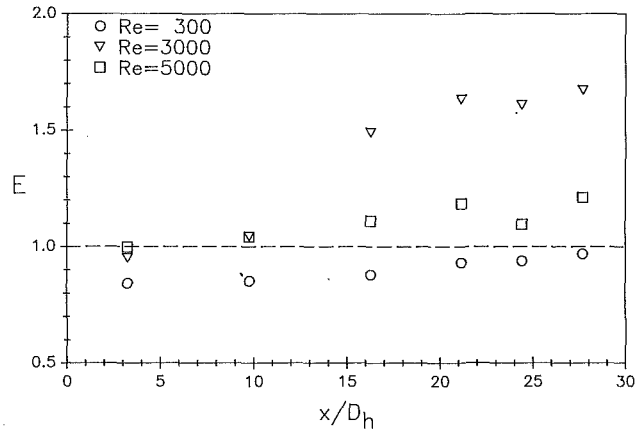

Fig. 9 Local grooved channel heat transfer enhancement for Re = 300 *(subcritical flow, heat transfer degradation), Re = 3000 (maximum enhancement), and Re = 5000 (typical of high Reynolds numbers)*

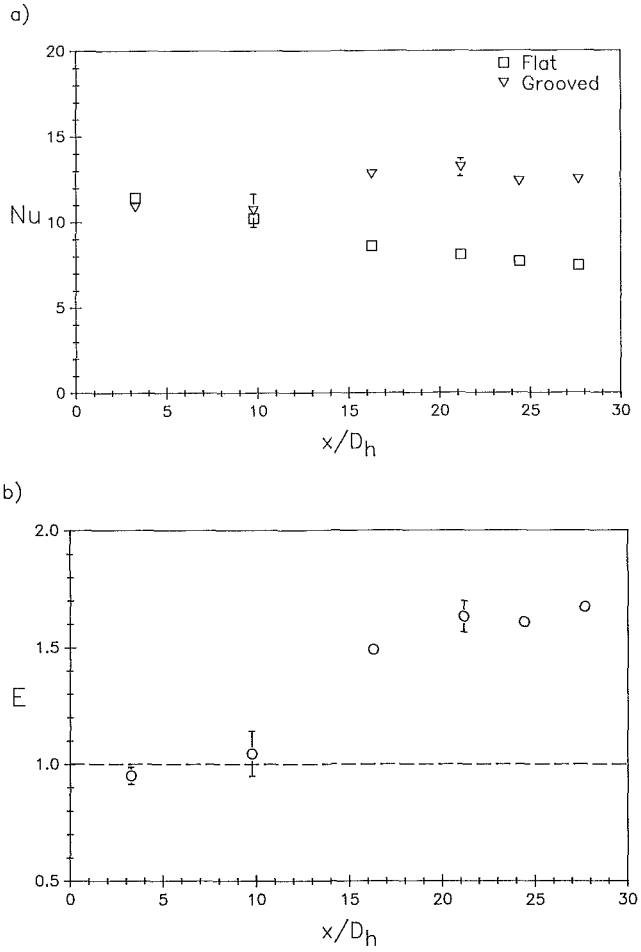

Fig. 8 Local heat transfer measurements at Re = 3000: (*a*) Nusselt number for flat and grooved channels; (*b*) enhancement ratio

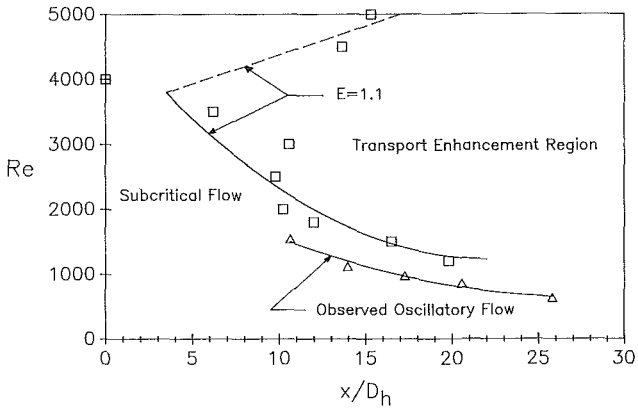

Fig. 10 Location of 10 percent heat transfer enhancement (squares) as a function of Reynolds number ; the onset location of oscillatory flow (triangles) is closely correlated with enhancement

show a steady decrease in the streamwise direction consistent with a thermally developing flow. On the other hand, the grooved channel values show enhancement at $x/D_h \approx 6$, with an augmentation of approximately 65 percent further downstream.

Figure 9 shows typical plots of E as a function of x/D_h for subcritical (Re = 300), supercritical (3000), and turbulent (5000) flows. For a subcritical Reynolds number of 300, the groove geometry is seen to actually decrease the heat transfer coefficient along the upper wall by about 10 percent relative to the ungrooved geometry. The groove-spanning free shear layers relax the no-slip condition along the lower wall, causing the velocity maximum to shift downward, resulting in reduced transport along the upper wall. As a consequence the enhancement ratio is less than unity over the entire length of the channel. For Re = 1200 (not shown in Fig. 9), unsteady structures are visually observed for $x/D_h > 10$. The grooved channel heat transfer exceeds the ungrooved values for $x/D_h > 16$, resulting in enhancement ratios of approximately 1.1

As the Reynolds number is further increased, the break-even point (i.e., the point where $E = 1.0$) rapidly moves upstream, and the magnitude of the local enhancement ratio increases. For Re = 3000, visual observations of the flow show remnants of a traveling wave structure blurred by turbulent mixing. The break-even point shifts to $x/D_h = 7$, and $E > 1.5$ for $x/D_h > 16$ (Figs. 8*b* and 9).

As the Reynolds number is increased beyond 3000, the grooved channel heat transfer coefficient continues to increase. However, the ungrooved heat transfer coefficient increases at a faster rate due to the rapid onset of turbulent mixing. As a consequence, the local enhancement ratio is reduced as shown in the figure for Re = 5000. This result is effectively the same for the upper Reynolds number range, 5000 ≤ Re ≤ 15,000.

Figure 10 includes a Re versus x/D_h map of groove-induced heat transfer enhancement. The figure shows the locus of points (indicated by squares) where the enhancement is 10 percent ($E = 1.1$). Also shown are wave onset locations (triangles) determined from analysis of video records of flow visualization experiments. The figure indicates that the occurrence of groove-

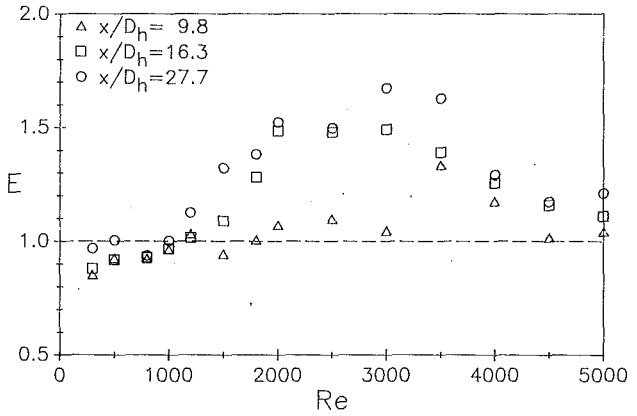

Fig. 11 Local grooved channel enhancement versus Reynolds number for 9.8 ≤ x/D_h ≤ 27.7; enhancement factor is fully developed for x/D_h > 16

induced oscillations is closely correlated with effective heat transfer augmentation. Points to the right of the data band of the figure experience heat transfer augmentation via this mechanism. Points to the left of the band experience no enhancement, or a degradation in performance. Enhancement is seen to move upstream with increasing Reynolds number until Re = 4000, and move downstream for higher Reynolds numbers. It is currently thought that for Re > 4000, turbulent mixing mechanisms become sufficiently strong that they dominate the large-scale wave structures, reducing the difference between grooved and ungrooved channel flows.

Enhancement data as a function of Reynolds number for three measurement stations of the current apparatus are condensed in Fig. 11. For the current channel configuration, the figure shows that significant and spatially constant (i.e., fully developed) enhancement is obtained for $x/D_h > 16$. Maximum heat transfer enhancement of approximately 65 percent is obtained over the range 2000 ≤ Re ≤ 4000. At higher Reynolds numbers turbulence appears to overwhelm the natural oscillations, leading to a reduction in E. Numerical and experimental data presented by Kozlu et al. (1988) for shear destabilized flow using eddy promoters in fully developed air flows show similar enhancement factors in a comparable Reynolds number range.

Conclusions

Groove-induced flow oscillations occur at supercritical Reynolds numbers. The onset location for such oscillations is Reynolds number dependent. With increase in Reynolds number, the oscillation intensity increases and the onset location rapidly move upstream. For the current channel configuration, oscillatory flows are observed for Re ≥ 630, and persist to approximately Re = 4800.

The oscillatory flow mechanism is responsible for augmentation of heat transfer. For the current channel configuration, enhancement in excess of 10 percent extends over the range 1200 ≤ Re ≤ 4800, and $x/D_h > 16$. Maximum enhancement of 65 percent occurs at Re = 3000 ± 1000. Turbulent mixing at higher Reynolds numbers degrades the advantages of the mechanism.

Acknowledgments

This work is supported by the Gas Research Institute under contract number 5087-260-1562. The authors wish to thank Dr. B. Snyder for helpful discussions on this topic.

References

Bergles, A. E., and Webb, R. L., 1985, "A Guide to the Literature on Convective Heat Transfer Augmentation," *Advances in Enhanced Heat Transfer*, S. M. Shenkman et al., eds., ASME HTD-Vol. 43, pp. 81–89.

Bellhouse, B. J., Bellhouse, F. H., Curl, C. J., MacMillan, T. I., Gunning, A. J., Spratt, E. H., MacMurry, S. B., and Nelemes, J. M., 1973, "A High Efficiency Membrane Oxygenator and Pulsatile Pumping System, and Its Application to Animal Trials," *Trans. American Society of Artificial Internal Organs*, Vol. 19, pp. 72–79.

Drazin, P. G., and Reid, W. H., 1981, *Hydrodynamic Stability*, Cambridge University Press, Cambridge, United Kingdom.

Ghaddar, N. K., Korczak, K. Z., Mikic, B. B., and Patera, A. T., 1986a, "Numerical Investigation of Incompressible Flow in Grooved Channels. Part 1. Stability and Self-sustained Oscillations," *J. Fluid Mech.*, Vol. 163, pp. 99–127.

Ghaddar, N. K., Magen, M., Mikic, B. B., and Patera, A. T., 1986B, "Numerical Investigation of Incompressible Flow in Grooved Channels. Part 2. Resonance and Oscillatory Heat-Transfer Enhancement," *J. Fluid Mech.*, Vol. 168, pp. 541–567.

Greiner, M., Ghaddar, N. K., Mikic, B. B., and Patera, A. T., 1986, "Resonant Convective Heat Transfer in Grooved Channels," *Proc. Eighth Int. Heat Trans. Conf.*, Vol. 6, pp. 2867–2872.

Greiner, M., Karniadakis, G. E., Mikic, B. B., and Patera, A. T., 1988, "Heat Transfer Augmentation and Hydrodynamic Stability Theory: Understanding and Exploitation," *Heat Transfer: Korea-US Seminar on Thermal Engineering and High Technology*, J. H. Kim, S. T. Ro, and T. S. Lee, eds., Hemisphere Publishing Corp., New York, pp. 31–50.

Ichimiya, K., 1987, "Effects of Several Roughness Elements on an Insulated Wall for Heat Transfer From the Opposite Smooth Heated Surface in a Parallel Plate Duct," ASME JOURNAL OF HEAT TRANSFER, Vol. 109, pp. 68–73.

Kays, W. M., and London, A. L., 1984, *Compact Heat Exchangers*, 3rd ed., McGraw-Hill, New York.

Karniadakis, G. E., Mikic, B. B., and Patera, A. T., 1988, "Minimum-Dissipation Transport Enhancement by Flow Destabilization: Reynolds' Analogy Revisited," *J. Fluid Mech.*, Vol. 192, pp. 365–391.

Kozlu, H., Mikic, B. B., and Patera, A.T., 1988, "Minimum-Dissipation Heat Removal by Scale-Matched Flow Destabilization," *Int. J. Heat Mass Trans.*, Vol. 31, pp. 2023–2032.

Sobey, I. J., 1980, "On Flow Through Furrowed Channels. Part 1. Calculated Flow Patterns," *J. Fluid Mech.*, Vol. 96, pp. 1–26.

Stephanoff, K. D., Sobey, I. J., and Bellhouse, B. J., 1980, "On Flow Through Furrowed Channels. Part 2. Observed Flow Patterns," *J. Fluid Mech.*, Vol. 96, pp. 27–32.

Stephanoff, K. D., 1986, "Self-excited Shear-Layer Oscillations in a Multicavity Channel With a Steady Mean Velocity," ASME *Journal of Fluids Engineering*, Vol. 108, pp. 338–342.

Yee, E. C., 1986, "The Effect of Geometry on Hydrodynamic Resonance in Grooved Channels," S.B. Thesis, Massachusetts Institute of Technology, Cambridge, MA.

Numerical Prediction of Fluid Flow and Heat Transfer in a Circular Tube With Longitudinal Fins Interrupted in the Streamwise Direction

K. M. Kelkar

S. V. Patankar

Department of Mechanical Engineering,
University of Minnesota,
Minneapolis, MN 55455

Numerical calculations have been made for the performance prediction of laminar flow through circular tubes with longitudinal fins interrupted in the streamwise direction by arranging them either in a staggered or an in-line manner. Calculations are made for three-dimensional parabolic flow. Due to the repetitive nature of the geometry in the axial direction, the flow exhibits periodically repeating behavior after some initial development length. Calculations have been made for various values of the axial length parameter and two Prandtl numbers for two different fin geometries. Results indicate that in the periodic fully developed regime, for a Prandtl number of 0.7, a tube with staggered arrangement of fins produces less heat transfer enhancement than a tube with continuous fins. A tube with in-line arrangement of fins gives about as much heat transfer augmentation as the tubes with either continuous or staggered fins but with a much less pressure drop penalty. Local quantities such as the axial velocity profiles and the variation of centerline axial velocity give a good physical understanding of the governing phenomena.

Introduction

The demand for high-performance heat exchange devices having small spatial dimensions is increasing due to their need in applications such as aerospace and automobile vehicles, cooling of electronic equipment, and so on. This had led to various designs of compact heat exchangers. Offset-fin plate-fin heat exchangers are among the most widely used designs. In an offset-fin heat exchanger, the interruptions of the fin surface prevent the flow from becoming fully developed; the restarting of the boundary layer at each new leading edge gives a higher heat transfer. Also, when longitudinal external fins are used on circular tubes, they are sometimes interrupted in the streamwise direction to improve their performance. It is then conceivable that interrupted fins on the *inner* surface of a circular tube may lead to good heat transfer performance. It is, therefore, of interest to investigate the performance of an internal longitudinally finned circular tube with fin surface interrupted in the axial direction.

Numerical predictions of developing fluid flow and heat transfer in a circular tube with internal longitudinal continuous fins have been reported by Choudhury and Patankar (1985) and Prakash and Liu (1981). A numerical investigation of fluid flow and heat transfer in two-dimensional staggered fin arrays has been presented by Sparrow et al. (1977), while performance comparisons for two-dimensional in-line and staggered fin arrays have been made by Sparrow and Liu (1979). Experimental investigations of offset-fin arrays have been presented in London and Shah (1968) and Joshi and Webb (1982). The effect of plate thickness on heat transfer for two-dimensional staggered fin arrays has been studied numerically by Patankar and Prakash (1981). Three-dimensional flow and heat transfer in offset-fin arrays has been analyzed numerically by Kelkar and Patankar (1985).

The aim of the present study is numerically to predict laminar flow and heat transfer through circular tubes with internal longitudinal fins that are arranged in a staggered or an in-line manner.

Mathematical Formulation

Details of the geometry under consideration are shown in Fig. 1. The thickness of the fins is assumed to be very small. Also, if the axial flow is sufficiently strong, the diffusion in the axial direction can be neglected so that the flow can be assumed to be parabolic in the streamwise direction. Then, to predict the performance numerically, computations for a three-dimensional parabolic flow are sufficient.

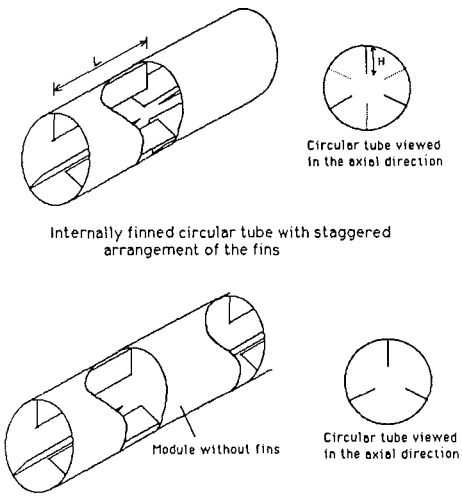

Fig. 1 The geometries considered

Contributed by the Heat Transfer Division and presented at the National Heat Transfer Conference, Pittsburgh, Pennsylvania, August 9–12, 1987. Manuscript received by the Heat Transfer Division June 15, 1988; revision received July 26, 1989. Keywords: Finned Surfaces, Forced Convection.

The equations governing the velocity field for a constant property laminar flow are the Navier–Stokes equations devoid of the axial diffusion terms. These equations in dimensionless form are

Circumferential momentum

$$\frac{U}{R}\frac{\partial U}{\partial \theta} + V\frac{\partial U}{\partial R} + \frac{W}{4}\frac{\partial U}{\partial Z} = \frac{-1\partial P'}{R\,\partial \theta} + \frac{1\partial}{R\partial R}\left(R\frac{\partial U}{\partial R}\right) + \frac{1}{R^2}\frac{\partial^2 U}{\partial \theta^2} - \frac{U}{R^2} + \frac{2}{R^2}\frac{\partial V}{\partial \theta} - \frac{UV}{R} \tag{1}$$

Radial momentum

$$\frac{U}{R}\frac{\partial V}{\partial \theta} + V\frac{\partial V}{\partial R} + \frac{W}{4}\frac{\partial V}{\partial Z} = \frac{\partial P'}{-\partial R} + \frac{1}{R}\frac{\partial}{\partial R}\left(R\frac{\partial V}{\partial R}\right) + \frac{1}{R^2}\frac{\partial^2 V}{\partial \theta^2} - \frac{V}{R^2} - \frac{2}{R^2}\frac{\partial U}{\partial \theta} + \frac{U^2}{R} \tag{2}$$

Axial momentum

$$\frac{U}{R}\frac{\partial W}{\partial \theta} + V\frac{\partial W}{\partial R} + \frac{W}{4}\frac{\partial W}{\partial Z} = \frac{1}{-4}\frac{d\bar{P}}{dZ} + \frac{1}{R}\frac{\partial}{\partial R}\left(R\frac{\partial W}{\partial R}\right) + \frac{1}{R^2}\frac{\partial^2 W}{\partial \theta^2} \tag{3}$$

Continuity

$$\frac{1\partial U}{R\partial \theta} + \frac{1\partial (RV)}{\mathrm{R}\,\partial R} + \frac{1}{4}\frac{\partial W}{\partial Z} = 0 \tag{4}$$

The dimensionless quantities used in the above equations are defined as

$$R = \frac{r}{R_0}, \qquad Z = \frac{(z/D)}{\mathrm{Re}} \tag{5a}$$

$$U = \frac{u}{(\nu/R_0)}, \qquad V = \frac{v}{(\nu/R_0)}, \qquad W = \frac{w}{w_{in}} \tag{5b}$$

$$P' = \frac{p}{\rho(\nu/R_0)^2}, \qquad \bar{P} = \frac{\bar{p}}{\rho w_{in}^2} \text{ with } p = \bar{p} + p' \tag{5c}$$

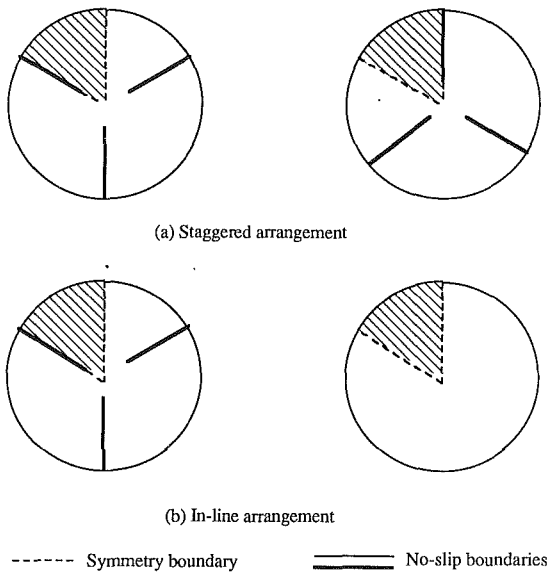

Fig. 2 Computational domains with the corresponding boundary conditions in two successive modules for the staggered and in-line arrangements

$$\mathrm{Re} = \frac{w_{in}D}{\nu}, \qquad D = 2R_0 \tag{5d}$$

By symmetry arguments, the computations at each axial location can be confined to the domain shown in Fig. 2. For a given arrangement of fins in the axial direction, either staggered or in-line, the left and the right boundary conditions depend upon the axial location being considered and are shown in Fig. 2. The no-slip boundary condition is imposed on all the solid surfaces. On the symmetry boundaries, the circumferential velocity vanishes while the gradients of the axial and radial velocities in the circumferential direction are zero. At the inlet, the radial and circumferential velocities are assumed to be zero while the axial velocity is assumed to have a uniform magnitude of w_{in}.

Nomenclature

D = diameter of the tube
f = module-averaged friction factor, equation (8)
$f\mathrm{Re}$ = product of module averaged friction factor and Reynolds number
$f\mathrm{Re}_o$ = value of $f\mathrm{Re}$ for fully developed flow in a circular tube
h = module-averaged heat transfer coefficient, equation (10)
H = height of the fins, Fig. 1
L = length of a module, Fig. 1
LMTD = log mean temperature difference for a module, equation (11)
M = number of modules from the entrance
N = number of fins
Nu = module-averaged Nusselt number, equation (9)
Nu_o = Nusselt number for fully developed flow through a circular tube
p = static pressure
Δp = pressure drop in a module
P' = dimensionless static pressure, equation (5c)
$\bar{p}$ = average static pressure over the cross section
$\bar{P}$ = dimensionless average static pressure over the cross section
r = radial coordinate
R = dimensionless radial coordinate, equation (5a)
R_o = radius of the tube, Fig. 1
Re = Reynolds number, equation (5d)
T = temperature
T_b = bulk temperature of the fluid, equation (12)
T_{bi} = bulk temperature at the inlet of a module
T_{bo} = bulk temperature at the exit of a module
T_w = constant wall temperature
u = circumferential velocity
U = dimensionless circumferential velocity, equation (5b)
v = radial velocity
V = dimensionless radial velocity, equation (5b)
w = axial velocity
w_{in} = uniform inlet axial velocity
W = dimensionless axial velocity, equation (5b)
W_c = dimensionless axial velocity at the centerline
z = axial coordinate
Z = dimensionless axial coordinate, equation (5a)
α = fin height parameter = H/R_0
β = axial length parameter = $(L/D)/\mathrm{Re}$
θ = circumferential coordinate
μ = dynamic viscosity of the fluid
ν = kinematic viscosity of the fluid
ρ = density of the fluid
ϕ = dimensionless temperature, equation (7)
ϕ_b = dimensionless bulk temperature

The governing equation for the temperature field is the energy equation in which the viscous dissipation and axial diffusion terms have been neglected. The dimensionless form of the governing equation is

Temperature field

$$\frac{U\partial\phi}{R\partial\theta} + V\frac{\partial\phi}{\partial R} + \frac{W}{4}\frac{\partial\phi}{\partial Z} = \frac{1}{\mathrm{Pr}}\left(\frac{1}{R}\frac{\partial}{\partial R}\left(R\frac{\partial U}{\partial R}\right) + \frac{1}{R^2}\frac{\partial^2 U}{\partial\theta^2}\right) \tag{6}$$

with

$$\phi = (T - T_w)/(T_{in} - T_w) \tag{7}$$

where T_{in} is the uniform temperature of the fluid at the inlet and T_w is the constant temperature of the tube wall. Further, if the fins are assumed to be highly conducting, the fin surface will also be at T_w. As a consequence of this assumption, the heat transfer results obtained in this study represent the best possible performance of the geometries considered; for fins of moderate conductivity, the performance will be correspondingly lower.

From the dimensionless equations and the boundary conditions, it follows that the governing parameters for the velocity field are the axial length parameter $\beta = (L/D)/\mathrm{Re}$, the fin height parameter $\alpha = H/R_o$, and the number of fins N. The temperature field is governed by an additional parameter, the Prandtl number Pr of the fluid.

Computational Details

As stated earlier, the numerical solution to the problem involves solving the three-dimensional parabolic equations. A general procedure for calculation of three-dimensional parabolic flows is given by Patankar and Spalding (1972). In the present study, the procedure used is basically the same except that the velocity-pressure coupling in the cross section is handled by the SIMPLER algorithm of Patankar (1980) and the axial pressure gradient is calculated by the method given by Raithby and Schneider (1979). Since the fluid properties are assumed to be constant, at each axial location the velocity field is calculated first and the temperature field is then computed using this velocity field. Due to the repetitive nature of the geometry in the axial direction, the flow characteristics exhibit a periodically repeating behavior after some initial development region. Therefore, starting with a uniform velocity and temperature field, the computations are continued until the flow becomes periodically fully developed.

The computations are performed for two different geometric distributions of the fins in the cross section. These are $N = 6$, $H/R_o = 0.5$ and $N = 12$, $H/R_o = 0.3$. For convenience, these will be denoted as geometry 1 and geometry 2, respectively, in the discussion that follows. For the staggered arrangement, the axial length parameter β was varied from 1×10^{-1} to 1×10^{-3} for both geometries. The effect of Prandtl number was studied by calculating the temperature field for Pr = 0.7 and 5 for geometry 1. In order to compare the relative performances of the staggered and the in-line arrangements, computations for the in-line arrangement were done for $\beta = 1 \times 10^{-2}$ for both the geometries with Pr = 0.7.

All the computations have been done using a grid of size 20 × 24 in the computational domain. There were 30 axial steps in each module of length L. The size of the axial step was small at the start of each module, where there is an interruption in the fin surface, and was gradually increased towards the end of the module. Exploratory runs with twice the number of points in each direction indicated a change of 1 percent in the overall results with $\beta = 1 \times 10^{-3}$ and Pr = 0.7. Therefore, the accuracy of the computed results was deemed satisfactory. All the computations were made on the Cray−1 supercomputer. The most expensive case of $\beta = 1 \times 10^{-3}$ and Pr = 5 for geometry 1 required about 5 min of CPU time.

Results and Discussion

To judge the performance of a tube with interrupted fin surfaces, it is useful to average the friction factor and Nusselt number over each module of length L, measured from the start of a discontinuity in the fin surface. The module-averaged friction factor and Nusselt number can be defined as

$$f = \frac{(\Delta p/L)D}{(\rho w_{in}^2/2)} \tag{8}$$

and

$$\mathrm{Nu} = \frac{hD}{k} \tag{9}$$

where h is the heat transfer coefficient based on the nominal tube surface area as defined below:

$$h = \frac{Q}{(2\pi R_0 L)(\mathrm{LMTD})} \tag{10}$$

Here Q is the total heat transferred in the module and LMTD is the log-mean temperature difference defined as

$$\mathrm{LMTD} = \frac{(T_w - T_{bi}) - (T_w - T_{bo})}{\ln((T_w - T_{bi})/(T_w - T_{bo}))} \tag{11}$$

where T_{bi} and T_{bo} are the bulk temperatures at the inlet and the exit of the module, respectively. The bulk temperature is defined as

$$T_b = \frac{\int wTdA}{\int wdA} \tag{12}$$

the integral being taken over the cross section.

Since the natural reference with which the performance of a finned tube can be compared is the circular tube without fins, all the module-averaged $f\mathrm{Re}$ and Nu have been normalized with respect to $f\mathrm{Re}_0 = 64$ and $\mathrm{Nu}_0 = 3.658$, corresponding to the fully developed flow through a circular tube with constant wall temperature. The results for the staggered arrangements are presented first and are followed by a discussion of the results for the in-line arrangement and a comparison of their performances. For each arrangement of the fins, the results for the periodically fully developed region are discussed followed by a discussion of the results for the developing flow.

Staggered Arrangement

Periodic Fully Developed Flow. In the staggered arrangement, each successive module is exactly identical except for the circumferential positions of the fin surfaces, so that the module-averaged $f\mathrm{Re}$ and Nu are identical for successive modules. Figure 3 shows the variation of $f\mathrm{Re}/f\mathrm{Re}_o$ and $\mathrm{Nu}/\mathrm{Nu}_o$ with β for Pr = 0.7 and 5 for geometry 1. The values of $f\mathrm{Re}/f\mathrm{Re}_o$ are always greater than 1 because of the increase in area available for friction. Note that the $f\mathrm{Re}$ for the staggered arrangement of fins is more than the corresponding value for a tube with continuous fins because the staggering of the fins causes extra friction on the fin surfaces at the start of each module. Since at lower values of β, which signify either more frequent interruptions or higher Reynolds number, this extra friction is higher, the $f\mathrm{Re}$ product is higher. At very high values of β, the flow within a module becomes fully developed as if in a tube with continuous fins and the $f\mathrm{Re}$ approaches asymptotically its fully developed value for a tube with continuous fins.

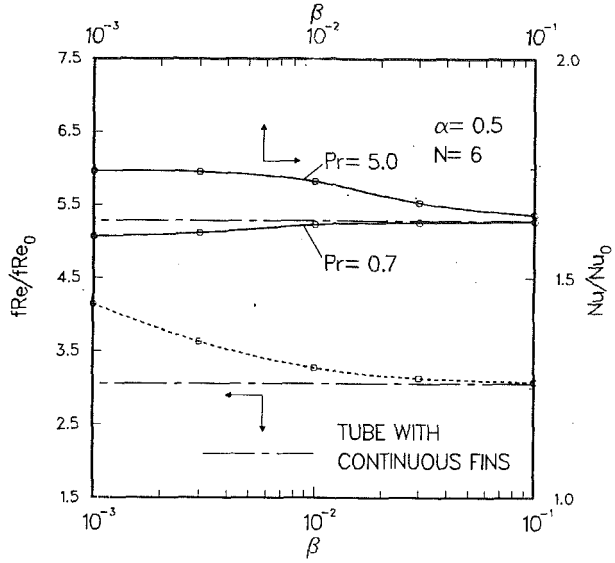

Fig. 3 Variation of the module-averaged friction factor and the module-averaged Nusselt number with the axial length parameter in the periodically fully developed regime for geometry 1 with staggered arrangement of fins

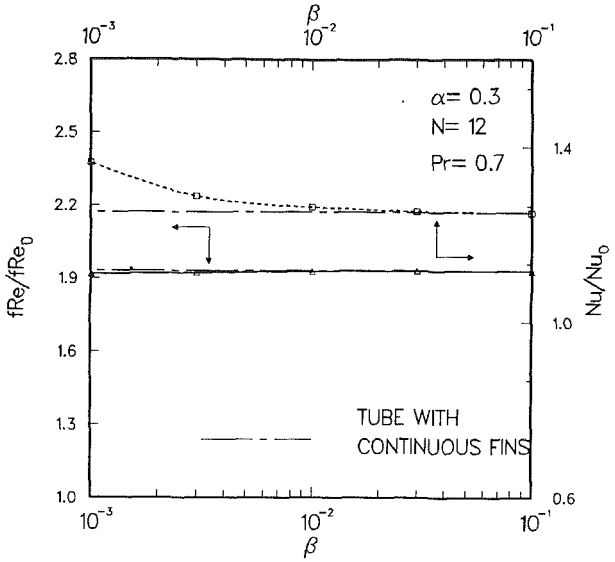

Fig. 5 Variation of the module-averaged friction factor and the module-averaged Nusselt number with the axial length parameter in the periodically fully developed regime for geometry 2 with staggered arrangement of fins

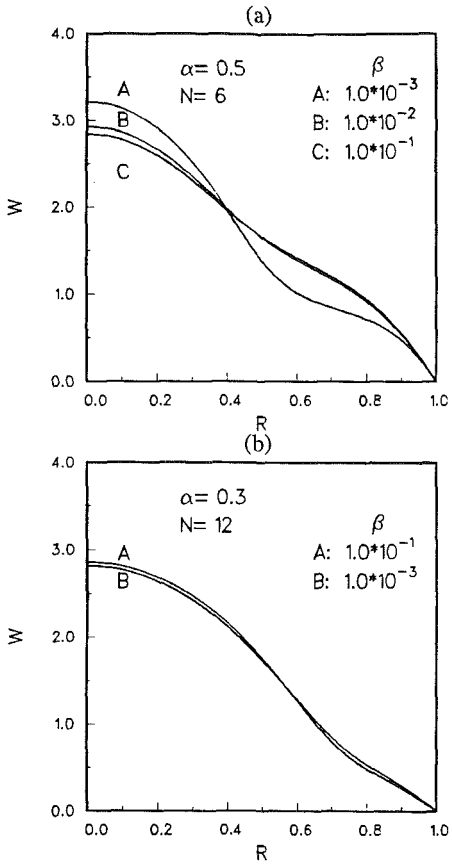

Fig. 4 Effect of the axial length parameter on the axial velocity profile at the symmetry boundary at the exit of a module for both geometries with staggered arrangements of fins

The augmentation of heat transfer caused by the addition of continuous fins on the inside of a circular tube is not very significant. This is because the addition of fins causes the axial flow to move away from the tube and fin surfaces, reducing the washing on these surfaces. A staggered arrangement of fins also affects the axial flow in a similar manner so that the augmentation in heat transfer obtained over a finless circular tube is not very noticeable. Note that for Pr = 0.7, the Nusselt number for the staggered arrangement is always lower than that for the tube with continuous fins, which is rather unexpected. This can be understood by examining Fig. 4(*a*), which gives the plots for normalized axial velocity at the exit of the module at $\theta = \pi/N$ for geometry 1, $\theta = 0$ being the location of the fin surface. The profile of W for $\beta = 1 \times 10^{-1}$ is almost coincident with the corresponding profile for a flow in a tube with continuous fins. Therefore the asymptotic value of Nu at high values of β is the fully developed value for flow in a tube with continuous fins. As β decreases further, the flow escapes through the central core region to circumvent the increased resistance at the leading edges of the fin surfaces. This is indicated by the increase in the magnitude of the centerline velocity with decreasing β in Fig. 4(*a*). This reduces the washing on the tube and the fin surfaces over most of the module. The result is a decrease in the overall Nusselt number with decrease in β for Pr = 0.7. With a high Prandtl number fluid, the thermal boundary layer grows slowly so that the advantage gained by restarting the boundary layer on the fin surfaces at the start of each module persists for a longer length within a module. Thus, with decreasing β, even though more flow escapes through the central core region, the increase in the heat transfer near the leading edges of the fin surfaces causes the Nusselt number to increase for Pr = 5.

Figure 4(*b*) shows the normalized axial velocity profile at the exit of the module at $\theta = \pi/N$, $\theta = 0$ being the location of the fin surface, for geometry 2. Comparing the corresponding profiles in Figs. 4(*a*) and 4(*b*), it can be seen that addition of large number of short fins makes the interfin spaces relatively inaccessible to the throughflow irrespective of whether the fins are continuous or interrupted in the axial direction. Therefore the augmentation of heat transfer with respect to a tube without fins is less in geometry 2 than in geometry 1. For $\beta = 1 \times 10^{-1}$, the exit velocity profile is almost coincident with the corresponding profile for the fully developed flow through a circular tube with continuous fins and the change in this profile caused by decreasing β to 1×10^{-3} is not substantial. This causes the fRe and Nu for geometry 2 with staggered arrangement of fins to be close to the fRe and Nu for a tube with continuous fins as seen in Fig. 5. Again, the slight decrease in Nu for Pr = 0.7 with decreasing β is due to the tendency of the flow to escape through the central core where there are no solid surfaces to provide resistance to the throughflow.

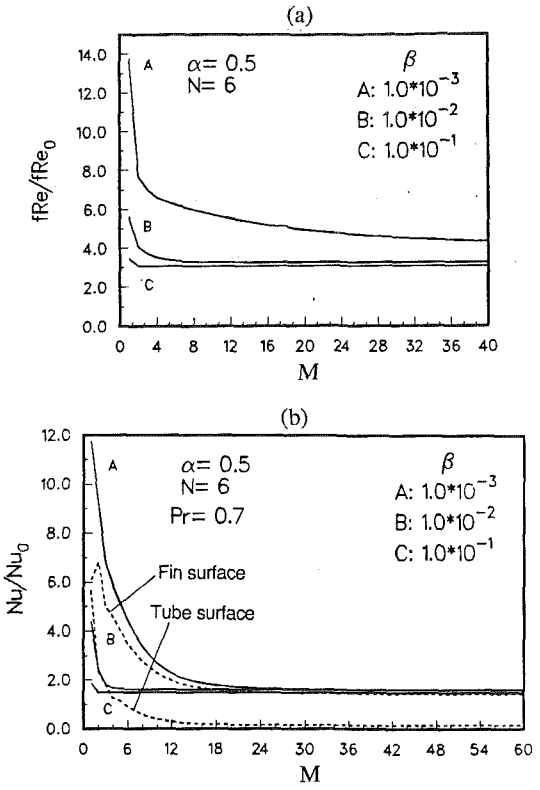

Fig. 6 Variation of the module-averaged friction factor and the module-averaged Nusselt number with the number of modules traveled by the flow for geometry 1 with staggered arrangement of fins

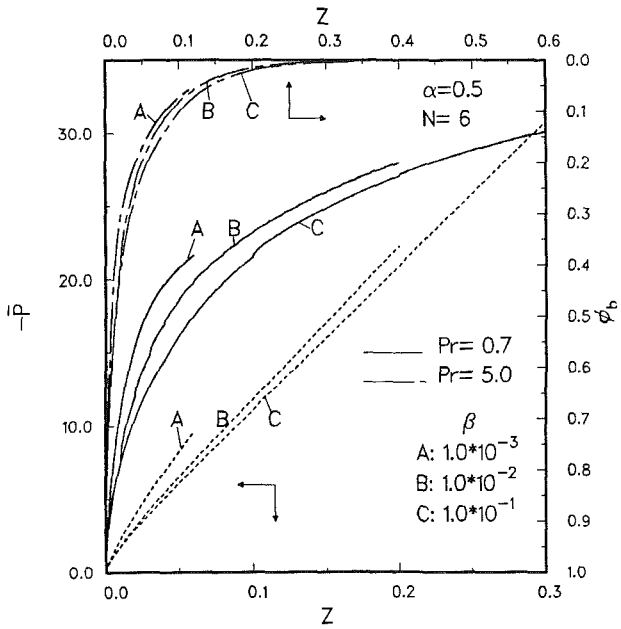

Fig. 7 Axial variation of the total pressure drop and the bulk temperature for geometry 1 with staggered arrangement of fins

Developing Flow. Figure 6 gives the development of $f\mathrm{Re}/f\mathrm{Re}_o$ and $\mathrm{Nu}/\mathrm{Nu}_o$ with the number of modules traveled by the flow for geometry 1. Note that the values of $f\mathrm{Re}$ and Nu represent averages over the entire module. Therefore, in Figs. 6(*a*) and 6(*b*) only the values of $f\mathrm{Re}$ and Nu at integral values of N are meaningful. Successive points in each of these curves are joined by straight lines only to facilitate visualization. For any given β, $f\mathrm{Re}$ starts from a high value and gradually tends to its asymptotic limit corresponding to the periodic fully developed values. The development of Nu follows the same general pattern, the starting value of Nu being higher for higher values of β. For a fixed L/D, a lower β implies a higher Reynolds number. A flow with a higher Reynolds number maintains its initial identity over a larger length because the increased convection in the axial direction causes the boundary effect to be felt less strongly. Therefore the number of modules required for the flow to become periodically fully developed increases with decreasing β. Figure 6(*b*) also shows the development of module-averaged Nusselt numbers on the tube and the fin surfaces of the module. These are calculated using equations (9) through (11), except that the Q in equation (10) is now taken to be the total heat transferred in the module from the surface under consideration so that the overall module-averaged Nu is the sum of the Nu for the tube and the fin surfaces. As the flow travels through the tube, both the tube and the fin Nusselt numbers decrease, indicating the migration of the throughflow away from these surfaces and toward the core region. Figure 7 shows the variation of total pressure drop and the dimensionless bulk temperature with the dimensionless axial distance for geometry 1. Since, with a decrease in β, the average friction increases, the pressure drops more rapidly for lower values of β. Since at low values of β, the flow in the entrance region has a higher heat transfer rate, the dimensionless bulk temperature also drops more rapidly for lower β. Characteristics of the developing flow for geometry 1 and geometry 2 are qualitatively very similar. Therefore the detailed variations of the various quantities are not presented for geometry 2.

Table 1 Results for the periodically fully developed flow for a circular tube with in-line, staggered, and continuous fins for $\beta = 1 \times 10^{-2}$ and Pr = 0.7

	In-line fins		Staggered fins		Continuous fins	
Geometry 1	fRe/fRe0	Nu/Nu0	fRe/fRe0	Nu/Nu0	fRe/fRe0	Nu/Nu0
Averaged over a module with no fins in the in-line arrangement	0.060	0.628	3.273	1.621	3.058	1.630
Averaged over a module with fins	3.497	2.315	3.273	1.621	3.058	1.630
Averaged over two successive modules	1.779	1.472	3.273	1.621	3.058	1.630
Geometry 2	In-line fins		Staggered fins		Continuous fins	
	fRe/fRe0	Nu/Nu0	fRe/fRe0	Nu/Nu0	fRe/fRe0	Nu/Nu0
Averaged over a module with no fins in the in-line arrangement	-0.024	1.035	2.192	1.115	2.172	1.117
Averaged over a module with fins	3.440	1.463	2.192	1.115	2.172	1.117
Averaged over two successive modules	1.708	1.249	2.192	1.115	2.172	1.117

In-Line Arrangement

Fully Developed Flow. Unlike the staggered arrangement, the values of $f\mathrm{Re}$ and Nu for successive modules, each of length L, are not identical for the in-line arrangement because each finned module of length L is followed by a module in which the fins are absent. With this in view, the performance for the in-line arrangement is summarized in Table 1. As the

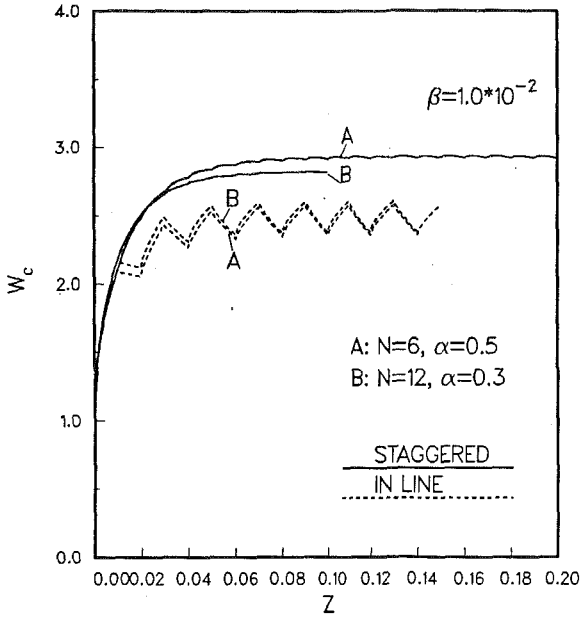

Fig. 8 Axial variation of the centerline velocity for both geometries with staggered and in-line arrangements of fins

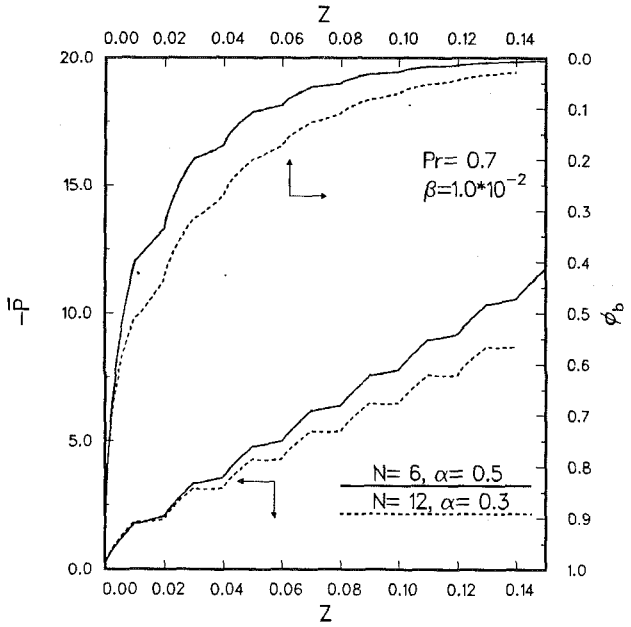

Fig. 10 Axial variation of the total pressure drop and the bulk temperature for geometry 1 with in-line arrangement of fins

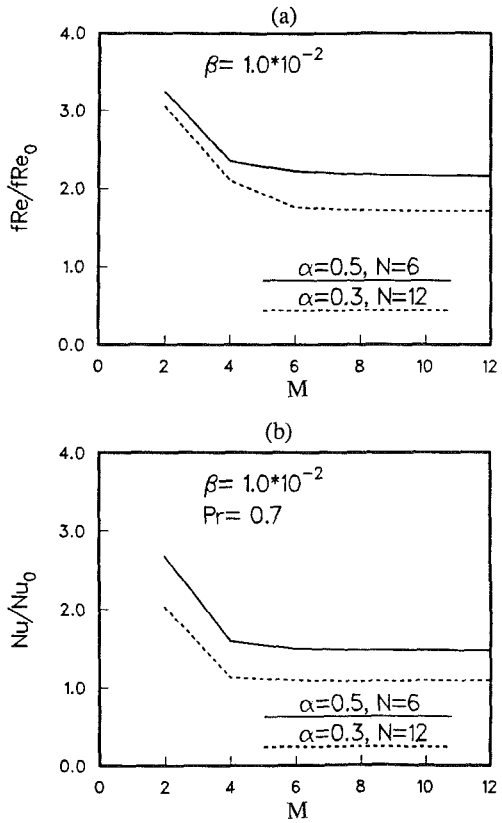

Fig. 9 Variation of the module-averaged friction factor and the module-averaged Nusselt number with the number of modules traveled by the flow for geometry 1 with in-line arrangement of fins

fluid moves through the module without fins, the velocity is redistributed across the cross section with a decrease in the central region and an increase near the tube surface. This causes a net decrease in the momentum efflux over the module, which almost balances the friction on the wall. Thus there is very little pressure drop across such a module. Table 1 shows that the fRe for a module without fins for geometry 1 is very small, whereas for geometry 2 the pressure actually increases across the module, as indicated by a negative value of fRe. (Incidentally, the slight adverse pressure gradient encountered does not cause any reverse flow. Thus, the parabolic calculation procedure is adequate.) In geometry 2, the redistribution is quicker due to a smaller defect in the velocity profile with respect to a parabolic profile, and the Nusselt number for module without fins is closer to Nu_o in geometry 2 than in geometry 1. This cross-sectionally uniform flow, after entering the module with fins, flows over the fin surfaces, which results in higher fRe and Nu than those for a module without fins as well as those for the modules in the staggered arrangement.

It is interesting to compare the performance of a tube with an in-line fin arrangement to that of a tube with staggered or continuous fins. The values of fRe and Nu for a tube with staggered and continuous fins are listed in the table. The effective values of fRe and Nu for the in-line arrangement, which can be compared with the corresponding values for the other arrangements, are obtained by averaging the respective values for modules with and without fins. These values are listed in the last row of the table. To understand clearly the relative performances, the variation of centerline velocity with axial distance for the staggered and the in-line arrangements of fins is presented in Fig. 8. Note that the centerline velocity in the in-line arrangement is always lower than that in the staggered arrangement. This implies a more uniform washing of the heat transfer surfaces. Therefore the heat transfer coefficient, based on the entire available heat transfer area, is highest for the in-line arrangement. The effective value of the Nusselt number is, however, lowest for the in-line arrangement because it is based on the nominal tube area and does not take into account the extra area of the fins in the other two arrangements. Note that, for both geometries, the in-line arrangement, in comparison with the staggered arrangement or the continuous fin case, has significantly less pressure drop penalty with about the same augmentation of heat transfer. Similar relative performance is expected at other values of the Prandtl number or the axial length parameter because there is no fundamental change in the flow pattern.

Developing Flow. Figures 9(*a*) and 9(*b*) give the development of module-averaged fRe and Nu for the in-line arrangement of fins for both the geometries. The values of fRe and Nu are now averaged over two successive modules, each of length L, so that the values of fRe and Nu at even values of N only are

meaningful. The trends are again very similar to those for the staggered arrangement of fins and need no further explanation. Figure 10 gives the variation of dimensionless pressure drop and dimensionless bulk temperature with the normalized axial distance. In the modules without fins, the pressure either remains almost constant or decreases depending upon the geometric distribution of fins. The bulk temperature drops at a slower rate in the modules without fins due to the decrease in the available heat transfer area. Again the geometry with taller and fewer fins has a better heat transfer performance as indicated by the more rapidly falling bulk temperature.

Conclusions

The fluid flow and heat transfer in a circular tube with staggered and in-line arrangement of longitudinal fins on the inside surface of the tube is investigated numerically. Computations are performed assuming the flow to be parabolic in the axial direction. After a certain initial length, the flow characteristics show periodically repeating behavior due to the periodicity in the geometry. Results indicate that for low Prandtl number fluids, the heat transfer performances for a staggered arrangement of fins is actually worse than that for a tube with continuous fins. Calculations for the in-line arrangement indicate that this arrangement gives almost as much heat transfer augmentation as the staggered arrangement or the arrangement with continuous fins, but with a much lower pressure drop penalty. Results for the developing flow show that the module-averaged friction factor and Nusselt number start from a high value and gradually tend toward the asymptotic value corresponding to the periodic fully developed flow with the development length being larger for smaller values of the axial length parameter.

Acknowledgments

This work was supported in part by a grant from the Minnesota Supercomputer Institute.

References

Choudhury, D., and Patankar, S. V., 1985, "Analysis of Laminar Flow Heat Transfer in Tubes With Radial Internal Fins," presented at the 23rd National Heat Transfer Conference, Denver, CO, HTD-Vol. 43, pp. 57–64.

Kelkar, K. M., and Patankar, S. V., 1985, "Numerical Prediction of Heat Transfer and Fluid Flow in Offset-Fin Arrays," presented at the ASME Winter Annual Meeting, Miami, FL, HTD-Vol. 52, pp. 21–28.

London, A. L., and Shah, R. K., 1968, "Offset Rectangular Plate-Fin Surfaces — Heat Transfer and Flow Friction Characteristics," ASME *Journal of Engineering for Power*, Vol. 90, pp. 218–228.

Patankar, S. V., 1980, *Numerical Heat Transfer and Fluid Flow*, Hemisphere, New York.

Patankar, S. V., and Prakash, C., 1981, "An Analysis of the Effect of Plate Thickness on Laminar Flow and Heat Transfer in Interrupted-Plate Passages," *International Journal of Heat and Mass Transfer*, Vol. 24, pp. 1801–1810.

Patankar, S. V., and Spalding, D. B., 1972, "A Calculation Procedure for Heat, Mass and Momentum Transfer in Three-Dimensional Parabolic Flows," *International Journal of Heat and Mass Transfer*, Vol. 15, pp. 1787–1806.

Prakash, C., and Liu, Y. D., 1981, "An Analysis of Laminar Flow and Heat Transfer in the Entrance Region of an Internally Finned Circular Tube," ASME JOURNAL OF HEAT TRANSFER, Vol. 107, pp. 84–91.

Raithby, G. D., and Schneider, G. D., 1979, "Numerical Calculation of Problems in Incompressible Fluid Flow — Treatment of the Velocity Pressure Coupling," *Numerical Heat Transfer*, Vol. 2, pp. 417–440.

Sparrow, E. M., and Liu, C. H., 1979, "Heat Transfer, Pressure Drop and Performance Relationships for In-Line, Staggered and Continuous Plate Heat Exchangers," *International Journal of Heat and Mass Transfer*, Vol. 22, pp. 1613–1625.

Sparrow, E. M., Baliga, B. R., and Patankar, S. V., 1977, "Heat Transfer and Fluid Analysis of Interrupted Wall Channels, With Application to Heat Exchangers," ASME JOURNAL OF HEAT TRANSFER, Vol. 99, pp. 4–11.

Webb, R. L., and Joshi, H. M., 1982, "A Friction Factor Correlation for Offset Strip Fin Matrix," *Proceedings of the Sixth International Heat Transfer Conference*, Vol. 6, pp. 257–262.

The Characteristic Behavior of Finite Length Line Sources of Heat in a Crossflow

P. R. Slawson
Professor.

G. J. Hitchman
Research Engineering.

L. E. Hawker

Department of Mechanical Engineering,
University of Waterloo,
Waterloo, Ontario N2L 3G1, Canada

A modified simple integral model for plume behavior from finite length line sources of heat and momentum is presented that identifies observed trends in plume trajectory data. Experiments on several finite length line sources of heat and momentum in the form of elevated (rows of stacks) and surface (slot) releases were conducted in a water tunnel. Plume behavior was documented through detailed temperature measurements of the plume cross section and by photographing the dyed plume. Results indicate the nature of any plume trajectory and growth enhancement and confirm the empirical relation for the liftoff distance for a buoyant surface plume given by Meroney (1979). In addition to the liftoff distance, the shape of the plume contact zone was measured and related to various regions of plume trajectory and cross-sectional shape. Plume trajectories from elevated line releases are adequately predicted by standard single source formulations; however, plume cross-sectional area is significantly overpredicted.

Introduction

Most of the research conducted to date on the behavior of buoyant plumes released to the air environment has focused on those originating from a single elevated stack. There are of course many situations where the source geometry for buoyant plumes can take the form of area or finite length line sources of heat and momentum. Such sources can be, for example, a cooling pond, a row of similar height closely spaced stacks, exhaust vents, or fan shrouds from mechanical draft cooling towers. The often saturated plume from a cooling pond can move downwind attached to the surface for some distance, after which, given enough buoyancy, it can lift off from the surface. Similarily, the saturated plume from a mechanical draft cooling tower can under suitable downwash conditions attach itself to the surface only to lift off again at some distance from the source (see, for example, Slawson, 1982). Plumes from these sources often result in local fogging of the plant site and adjacent roadways creating a hazard for both plant personnel and the public. One in fact finds that in both the petrochemical and nuclear industries, the behavior of potentially hazardous buoyant releases from surface or near-surface sources, which can be of point, line, or area source geometry, is of interest to safety personnel.

A simple integral model for plume behavior from finite length elevated and surface releases was given by Slawson (1976). In order to test some of the trends of plume behavior predicted by the model, a series of experiments on elevated and surface finite length line sources of heat and momentum in a crossflow were conducted in a water tunnel (Hawker, 1986). The buoyant plume trajectory, growth, and where applicable, liftoff point were documented through detailed measurements of plume cross-sectional temperatures and photographs of the dyed plumes. A summary of some of the experimental results is given here.

Experimental Technique

Water Flume and Instrumentation. The test facility used was a recently constructed water flume in the Fluid Mechanics Laboratory at the University of Waterloo. The test section is 1.22 m × 1.22 m in cross section with a working depth of 1.02 m that is of uniform temperature. The flume length is 12.2 m. The test section has Plexiglas sidewalls over 2.4 m of its length to facilitate visual observation and photography. Various test models are accommodated through a removeable floor plate. Water is heated up to 90°C and pumped to the models from a separate tank where three 9-kW immersion heaters under thermostat control and a recirculation system ensure that the supply temperature is constant. The various supply rates to the models are monitored with a range of rotameters. The source temperature is measured in the model manifold just prior to the exit. In the case of elevated sources, the error included in a nondimensional temperature difference by measuring the exit temperature in the manifold, rather than directly at the exit, was less than 1 percent. A Novar Streamflo propeller-type anemometer was used to document velocities in the flume to within ± 0.2 cm/s with a lower limit of 2.5 cm/s. No attempt was made to simulate the neutral planetary surface layer velocity profile for these specific studies. Two of the velocity profiles used for the present work are illustrated in Fig. 1. All temperatures and velocity data are retrieved and processed through a data acquisition system consisting of a

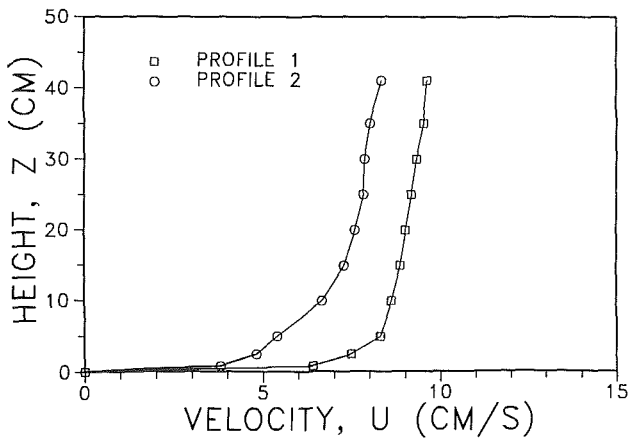

Fig. 1 Velocity profiles in the water flume test section

Contributed by the Heat Transfer Division and presented at the ASME Winter Annual Meeting, Chicago, Illinois, November 28–December 2, 1988. Manuscript received by the Heat Transfer Division November 3, 1988; revision received July 7, 1989.

datalogger, a microcomputer, plotters, printers, and a mainframe computer.

Plume trajectory, growth, and liftoff were documented both from 35 mm color slide film photographs of the dyed plume at 10 s intervals and temperature cross-sectional measurements. Ten individual photographs of visible plume outlines, covering some 100 s were projected and traced onto paper, then digitized to construct a single time-averaged plume trajectory, growth, and liftoff distance. Temperatures were measured with a rake of L-shaped thermistor probes mounted on a permanently installed x-y-z traversing mechanism. Plume cross-sectional isotherms were constructed using time-averages of the nondimensional temperatures defined by

$$N_{ij} = \frac{T_p - T_r}{T_j - T_a} 1000$$

where for each scan i of the rake of probes: T_p is the measured plume temperature of probe j, T_r is the ambient reference temperature of probe j obtained in the ambient flow just prior to the plume measurement, T_j is the jet exit temperature, and T_a is the (upstream) flume water temperature obtained simultaneously with the plume measurements. Between 7 and 11 cross sections were used to define a single plume. Plume trajectory and growth were based on the 25 percent nondimensional isotherm since it is best agreed with the visible boundaries extracted from the dyed plume photographs. For surface line sources, the distance to plume liftoff X_L is measured from the source to the point where the 25 percent nondimensional isotherm detaches from the flume floor. Extra plume cross sections were obtained in this vicinity and the actual liftoff point was linearly interpolated between neighboring cross sections.

The estimated uncertainties for the data extracted from plume photographs are as follows: $z(x)$ (trajectory) ± 10.0 percent; $X_L \pm 0.03$ m. Temperatures are resolved to 0.01°C and the uncertainty in temperature differences is ± 0.02°C. The estimated uncertainties in data extracted from the temperature measurements are: $z(x)$ (trajectory) ± 7.5 percent; $X_L \pm 0.02$ m.

Models. A series of nylon tube stacks 2.5 cm high with an exit diameter of 0.28 cm and separated by 2 cm were used to represent an elevated line source of heat and momentum emitted normal to the crossflow. The length of the line of stacks could easily be changed by fixing more or fewer stacks in predrilled plugged holes in the surface plate of the source manifold. Elevated line lengths of 4, 8, 16, and 20 cm corresponding to 3, 5, 7, 9, and 11 stacks were used in this initial study. The ratio of stack exit velocity to the ambient mean flow velocity at stack height (K) and the exit Froude number (Fr) were varied from 1.4 to 10 and 4.7 to 30, respectively, where

$$\mathrm{Fr} = V_o/(gL(\Delta\rho_o/\rho_o))^{1/2} \quad (1)$$

L is a source length scale, and $g\Delta\rho_o/\rho_o$ is the source buoyant acceleration.

Line lengths of 6.15, 12.15, and 20.35 cm with a slot width of 0.25 cm were used to model the surface line sources and like the elevated sources were oriented normal to the crossflow. Exit Froude numbers (Fr) ranging from 1.8 to 8.6 with velocity ratios (K) ranging from 0.71 to 3.1 were used in the surface line source experiments. Temperature cross sections were typically measured at distances of 2 to 140 cm downstream from the source. Detailed temperature measurements were made near the observed region of liftoff of the dyed plume for the surface releases in order to determine the liftoff point accurately. A similar set of experiments on surface line sources were conducted in a previous water flume; however, interpretation of the liftoff point was made from photographs only.

Theoretical Considerations

Elevated Finite Length Line Sources. The simple integral model for plume rise and growth given by Slawson and Csanady (1967, 1971), Briggs (1969), and many others for a single circular source was modified by Slawson (1976) so that it might apply to finite length elevated and surface line sources of heat and momentum in a crossflow. The essential difference between the single circular model and the finite length line source model is the assumption of a *cigar* or *sausage*-shaped plume cross section for the latter. This *sausage* shape consists of a rectangular midsection with semicircles attached at either end as illustrated in Fig. 2. The area of the plume element is assumed to grow uniformly within the plane of the element, allowing a single entrainment coefficient similar to that found in single source models. The distance L_o might represent the distance between the centers of the outside stacks in a row of

Nomenclature

A = plume cross-sectional area = $\pi R^2 + 2RL_o$, m^2
b = buoyant acceleration = $g\Delta\rho_o/\rho_o$, m/s^2
C = plume circumference = $2\pi R + 2L_o$, m
d = stack diameter or slot width, m
F_o = source buoyant flux = $b_o A_o V_o$, m^4/s^3
Fr = jet densimetric Froude number = $V_o/(gL(\Delta\rho_o/\rho_o))^{1/2}$
g = gravitational acceleration, m/s^2
K = velocity ratio = V_o/U_r
L = exit length scale, m
L_c = plume width in contact with surface, m
L_o = line length, m
l_b = buoyant length scale = $b_o Q_o/U^3$, m
l_{be} = buoyant length scale for an elevated line source = $b_o UQ_o/nU_r^3$, m
l_{bg} = buoyant length scale for a ground-based line source = $d_o b_o Q_o/L_o U^3$, m
l_m = momentum length scale = $(M_o/U^2)^{1/2}$, m
l_{me} = momentum length scale for an elevated line source = $(M_o/nU_r^2)^{1/2}$, m
M = vertical momentum flux = AUw, m^4/s^2
N = nondimensional temperature = $1000(T_p - T_r)/(T_j - T_a)$
n = number of stacks
Q = volumetric flow rate = AV, m^3/s
R = plume radius, m
R_o = stack radius, m
T = temperature
U = an ambient velocity, m/s
V = jet velocity, m/s
v_e = entrainment velocity, m/s
w = plume velocity in z direction, m/s
X_L = plume liftoff distance, m
x = downstream distance, m
y = cross-stream distance, m
z = vertical distance, m
β = entrainment coefficient
$\Delta\rho_o$ = density difference between exit and ambient fluids, kg/m^3
ρ = density, kg/m^3

Subscripts and Superscripts

a = ambient or upstream
j = jet
o = initial or source value
p = plume
r = reference
$\bar{\ }$ = denotes average value over plume rise region

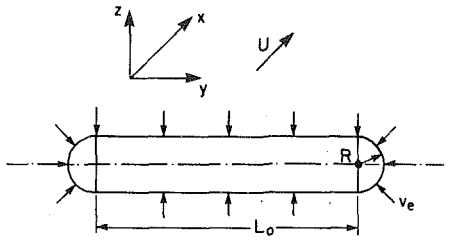

Fig. 2 Assumed cross-sectional shape of the elevated finite length line source plume

stacks normal to the crossflow. At some point downstream of the row of stacks the individual plumes will have merged together to form a shape similar to that of Fig. 2. The model is intended to apply from this point of merging.

The conservation equations of mass, vertical momentum, and density deficiency applied to the above element for a well bent-over plume in a neutral crossflow take the familiar form

$$\frac{d}{dx}(AU) = Cv_e \tag{2}$$

$$U\frac{d}{dx}(M) = F \tag{3}$$

$$\frac{dF}{dx} = 0 \tag{4}$$

where the Boussinesq approximation has been applied, the plume velocity V is assumed approximately equal to the ambient velocity U (low plume angle to the crossflow), and top-hat distributions of all plume parameters are assumed. In these equations v_e is an entrainment velocity ($v_e = \beta w$) where w is the vertical drift velocity of the element and β is an entrainment constant, M is the vertical momentum flux of the plume ($M = AUw$), and F is the flux of buoyancy ($F = AUb$) where b is a buoyant acceleration ($b = g\Delta\rho_o/\rho_o$). The cross sectional area and circumference of the plume element are given respectively by

$$A = \pi R^2 + 2RL_o \tag{5}$$

$$C = 2\pi R + 2L_o \tag{6}$$

The parameters w, U, z, and x are related by the kinematic relation

$$w = U\frac{dz}{dx} \tag{7}$$

Equations (2)–(7) can be solved analytically for uniform or constant crossflow velocity, or numerically integrated for a nonuniform velocity profile, to obtain the plume rise z as a function of downstream distance z. The analytical solution is discussed here as it more readily allows for a physical interpretation of the characteristic behavior of the finite length line sources. The solution is found as follows. Integrating equation (4) yields

$$AUb = F_o = \text{const} \tag{8}$$

Substituting equation (8) into equation (3) and integrating with the initial condition $M = M_o$ at $x = 0$ yields

$$M = \frac{F_o}{U}x + M_o \tag{9}$$

Differentiating equation (5) and substituting the result into equation (6) yields

$$\frac{dA}{dR} = C \tag{10}$$

Table 1 Asymptotic behavior of a bent-over finite length line source of heat and momentum

	$L_o >>> z$		$L_o <<< z$	
bent-over line source (momentum)	z	$\propto x^{1/2}$	z	$\propto x^{1/3}$
	R		R	
bent-over line source (buoyancy)	z	$\propto x$	z	$\propto x^{2/3}$
	R		R	

Substituting equations (7) and (10) into equation (2) and integrating yields

$$R = R_o + \beta z \tag{11}$$

Equation (11) describes the change in plume radius with height above the source and is identical to that found for the single circular source, or by setting $R_o = 0$, the point source. This is not an unexpected result since it is assumed that the plume grows uniformly in all directions within the plane of the cross section, just as in circular cross-sectional plumes. Finally, substituting equations (5), (7), and (11) into $M = AUw$ of equation (9), integrating, and nondimensionalizing with l_b produces a cubic equation for plume rise z as a function of x as given by

$$\left(\frac{z}{l_b}\right)^3 + a_1\left(\frac{z}{l_b}\right)^2 + a_2\left(\frac{z}{l_b}\right) = \frac{3}{\pi\beta^2}\left[\frac{1}{2}\left(\frac{x}{l_b}\right)^2 + \frac{A_o w_o}{l_b^2 U}\left(\frac{x}{l_b}\right)\right] \tag{12}$$

where the coefficients a_1 and a_2 are constants for a given finite length elevated line source and are given by $a_1 = (3C_o)/(2\pi\beta l_b)$ and $a_2 = (3A_o)/(\pi\beta^2 l_b^2)$. In equation (12), l_b is a buoyant length scale defined by $l_b = F_o/U^3$ and represents the total flux of buoyancy divided by the ambient velocity cubed.

For a point source of initial momentum and buoyancy (but no initial radius), a_1 and a_2 become zero and equation (12) reduces to the familiar 1/3, 2/3 law formulation (as given by Briggs, 1975a, for example)

$$z(x) = \left[\frac{3}{2\beta^2}(x^2 l_b + 2x l_m^2)\right]^{1/3} \tag{13}$$

where l_b and l_m are the buoyant and momentum length scales for the point source. The limiting cases of equation (13) are the 1/3 law for bent-over jets ($l_m >>> l_b$) and the 2/3 law for bent-over plumes ($l_b >>> l_m$) given by

$$\frac{z}{l_m} = \left(\frac{3}{\beta^2}\right)^{1/3}\left(\frac{x}{l_m}\right)^{1/3} \tag{14}$$

$$\frac{z}{l_b} = \left(\frac{3}{2\beta^2}\right)^{1/3}\left(\frac{x}{l_b}\right)^{2/3} \tag{15}$$

The corresponding forms of equations (14) and (15) for a finite length line source of zero initial radius are found from equation (12) and are given by

$$\left(\frac{z}{l_m}\right)^3 + \frac{3L_o}{\pi\beta l_m}\left(\frac{z}{l_m}\right)^2 = \frac{3x}{\pi\beta^2 l_m} \tag{16}$$

$$\left(\frac{z}{l_b}\right)^3 + \frac{3L_o}{\pi\beta l_b}\left(\frac{z}{l_b}\right)^2 = \frac{3}{2\pi\beta^2}\left(\frac{x}{l_b}\right)^2 \tag{17}$$

Inspection of equations (16) and (17) for $L_o >>> z$ (long line source of heat or momentum) and $L_o <<< z$ (approaching a point source) produces the asymptotic results given in Table 1. Thus, one would expect to find a parabolic rise region near the source of a bent-over line source of momentum, followed by the familiar 1/3 law region at greater distances from the

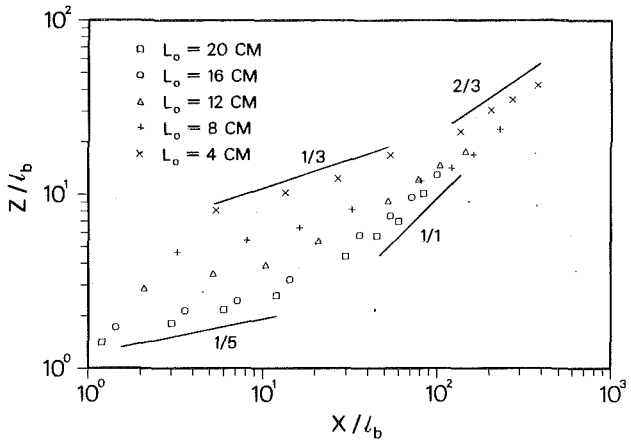

Fig. 3 Elevated line source photographic trajectories with nondimensionalization by l_b based on U_r for varying source lengths at a constant velocity ratio $K = 6.5$

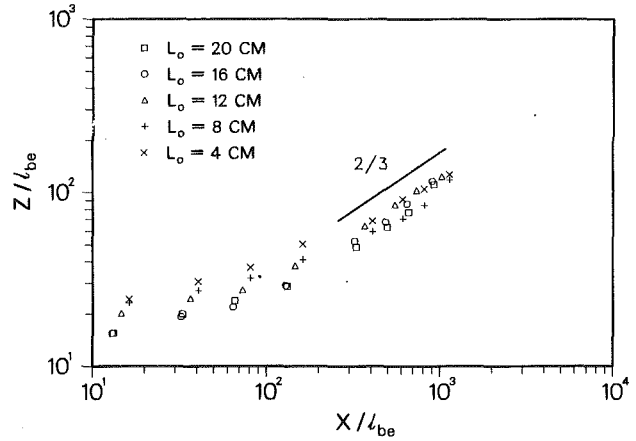

Fig. 4 Elevated line source photographic trajectories with nondimensionalization by l_{be} based on U_r for varying source lengths at a constant velocity ratio $K = 6.5$

source. Similarly, a linear region should exist in the near-field of long sources of heat ultimately reducing to the 2/3 law region far away from the source. A two-dimensional line source of heat at ground level where $L_o \Rightarrow \infty$ should show, according to Table 1, that the depth of the thermal boundary layer (R) grows linearly with distance. Rouse (1947) found that a linear growth adequately describes his data.

Surface Finite Length Line Sources. The surface line source of heat and momentum is modeled using the same equations (2)–(7) as those for the elevated source, except the circumference of the plume cross-sectional element is reduced by an amount L_c in contact with the surface. While the plume is attached to the surface the plume radius is assumed equal to the height of the center of the plume above the surface. As the plume element grows by entrainment of ambient fluid around that part of its circumference not in contact with the surface, the length of the contact zone is assumed to diminish linearly with distance as

$$L_c = L_o(1 - x/X_L) \tag{18}$$

The assumed form of equation (18) requires experimental verification. Also, an empirical formulation for the liftoff distance X_L is required.

Although the model that is presented here is very simplistic in its treatment of the rather complicated physics of the behavior of finite length line sources of heat and momentum in a crossflow, it does serve to indicate some expected trends.

Results and Discussion

Elevated Finite Length Line Sources. The elevated line source (series of stacks) experiments provide a data set with which the present experimental technique could be tested to ensure that observed plume behavior is similar to that found in both field and other laboratory experiments. Also, as many as eleven stacks (20 cm line length) were used to determine to what extent, if any, the plume trajectory was altered due to this source geometry, and to provide data for comparing with the theoretical predictions. Overcamp (1982) suggests, as has Briggs (1975b), that there is little trajectory enhancement for multiple stacks aligned in a row, perpendicular to the mean wind direction. Most industrial stacks are separated by enough stack diameters that blockage to the oncoming flow is minimal and individual plumes or heated jets merge at a point far enough downstream that plume excess temperature has diminished drastically, resulting in little buoyancy enhancement of the merged plumes. The present experiments generally confirm this observation. However, as source line length was increased, reduced rates of rise were observed in the near-field, which can be attributed, in part, to the effects of flow blockage, followed by slightly enhanced rates of rise in the early buoyancy dominated region. Any downwash effects, which might have occurred at K values less than about 1.5, were masked by the effects of flow blockage. Figure 3 illustrates the observed trajectories for the indicated source line lengths of model stacks with the data nondimensionalized by l_b using U_r taken at the model stack height. The source Froude number was essentially constant for these experiments at 21 ± 1 and the ambient reference velocity U_r at 2.5 cm was 7.5 cm/s as given in profile 1 of Fig. 1. From Fig. 3 one can see that the trajectory from the shortest line length of 4 cm (3 stacks) clearly exhibits the familiar 1/3 power law behavior attributed to momentum-dominated heated jets in a crossflow, followed by a 2/3 power law behavior for the buoyancy-dominated region. However, as source line length increased to a maximum of 20 cm (11 stacks), the rate of rise in the momentum dominated near-field diminished to a 1/5 power law, clearly indicating flow blockage effects not accounted for by the theory, which predicts a 1/2 power law as given in Table 1. Careful inspection of the data of Fig. 3 does show some evidence of a 1/2 power law beyond the initial flow blockage region for line lengths of 16 and 20 cm. In the buoyancy-dominated region a linear rate of rise is observed as predicted by the simple integral model. This, of course, is with the data nondimensionalized by the buoyancy length scale l_b, which includes the entire heat flux from all stacks in a given line source. Some increased rate of rise for longer source lengths is expected in the buoyancy-dominated region as the circumference to cross-sectional area ratio of the plume decreases and thus reduces the effective rate of entrainment of ambient air.

The separation of the trajectory data of Fig. 3 can be reduced considerably, as shown in Fig. 4, when the data are nondimensionalized with the buoyancy length scale for a single stack (l_{be}). Figure 4 more clearly defines the 2/3 power law region for this data. Figure 5 illustrates some 22 trajectory experiments with velocity ratios between 1.5 and 20, and source Froude numbers between 5 and 60. The data illustrate the characteristic 1/3 and 2/3 power law behavior of a single plume trajectory when the observations are nondimensionalized by l_{be}. The data of Fig. 5 suggest that any enhanced rate of rise for individual plumes is masked by an rms error band of approximately 15 percent. A best fit of equation (13) to the observed trajectories results in an entrainment coefficient β of 0.6, precisely that found by Briggs (1975a) for full-scale plumes. It would seem that the present physical model results adequately simulate observed plume trajectories from full-scale field observations,

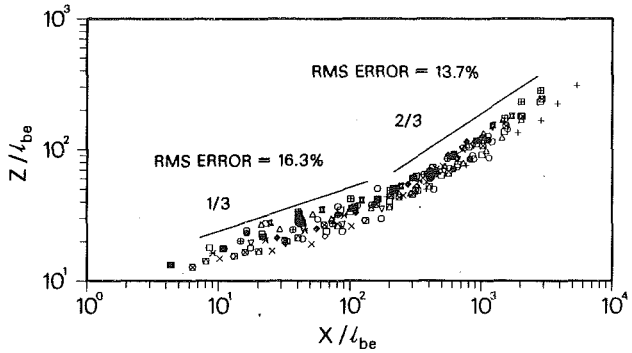

Fig. 5 Elevated line source trajectories with nondimensionalization by l_{be} based on U_r from 22 photographic experiments with varying values for velocity ratio (K) and source Froude number

without necessarily simulating the velocity profile of the atmospheric surface layer.

In the case of fogging problems at relatively short distances from a source one would like to predict the concentration of water vapor or specific humidity within the plume. These calculations require accurate prediction of plume cross-sectional area and sometimes shape, as a function of distance along the plume trajectory in addition to the trajectory itself. Figure 6 illustrates typical plume cross-sectional area and shape at several nondimensional distances (x/l_{be}) downstream of a 12 cm elevated line source for $l_{be}=0.142$. This figure clearly shows the evolution from the *sausage* shape to the typical *kidney-bean* shape at intermediate distances and finally to a nearly circular shape at large distances from the source. The presence of the familiar counter rotating vortex pair is indicated in the last two isotherm plots.

One would expect the 2/3 law for plume trajectory to hold where the plume has approached the assumed circular cross-sectional shape upon which this formulation has been derived. Indeed, upon inspection of some of the elevated plume observations it was found that when the plume cross section achieves a roughly elliptical shape of aspect ratio (major to minor axis) of 2 or less the plume trajectory has entered a 2/3 power-law region.

Preliminary comparisons of observed and predicted plume cross-sectional areas, where the plume edge was assumed to be predicted by the 25 percent nondimensional isotherm, using various forms of the integral model (analytical and numerical integration models) indicates that a numerical integration model is required for best results. The numerical integration model is similar to that given by Slawson (1978) and is required primarily in order to incorporate the effects of mean flow vertical shear. Although the analytical model (equation (12)) adequately predicts plume trajectories, it vastly overpredicts plume cross-sectional area. This is attributed to the use of a single entrainment coefficient that was extracted only from observations of trajectory. Further work on model development and comparison with the rather large data set is in progress.

Surface Finite Length Line Sources. Figure 7 is similar to Fig. 3 except that the observed trajectories are for surface finite length line sources. Here, as in Fig. 3, the individual rates of plume rise for various line lengths are clearly indicated by the different slopes. Also, this figure shows plumes that appear to contain regions with rates of rise that correspond to those predicted by the simple integral model of 1/2, 1/1, and 2/3. However, similar attempts to collapse the observed surface released trajectory data onto a single curve resulted in an unacceptable rms error of approximately 29 percent, as illustrated in Fig. 8. This large error can, in part, be attributed to the very strong shear layer near the surface and the different lift-off points for different sources. Few attempts to describe the observed trajectories of individual plumes using the present integral models have been made so far as further work is warranted.

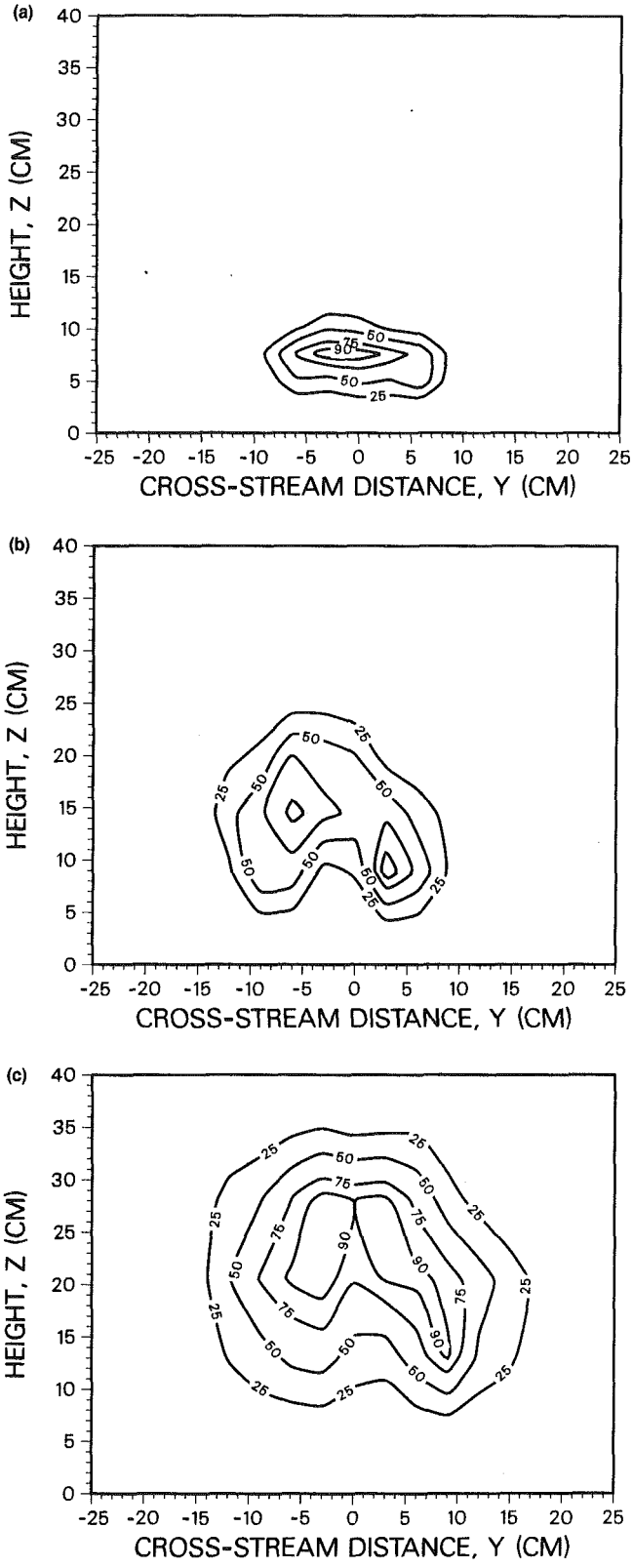

Fig. 6 Measured nondimensional cross-sectional isotherms for a 12-cm elevated line source at a nondimensional distance x/l_{be} = (a) 141, (b) 528, and (c) 985

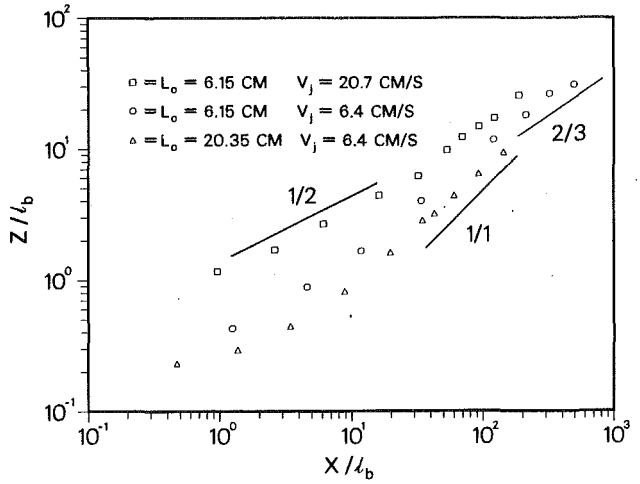

Fig. 7 Ground-based line source temperature trajectories for various values of L_o and K with nondimensionalization by l_b based on $\bar{U}$

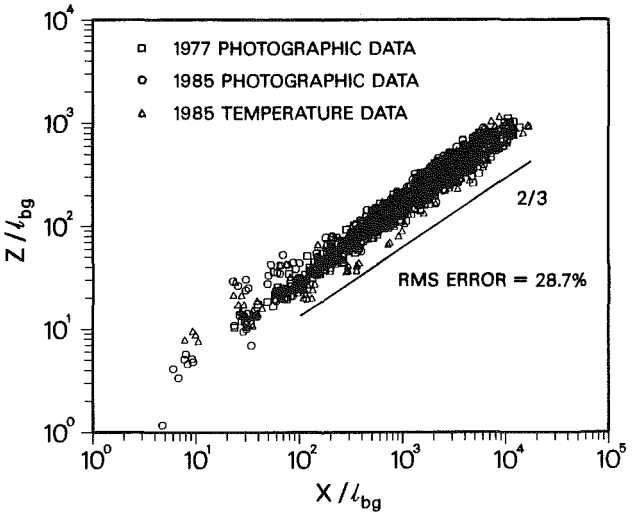

Fig. 8 Ground-based line source trajectories with nondimensionalization by l_{bg} based on $\bar{U}$

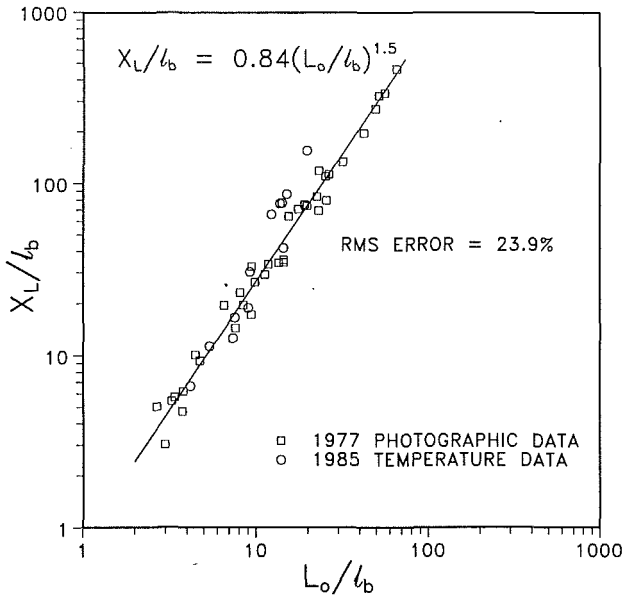

Fig. 9 Ground-based line source liftoff distance with nondimensionalization by l_b based on $\bar{U}_r$ at 10 cm

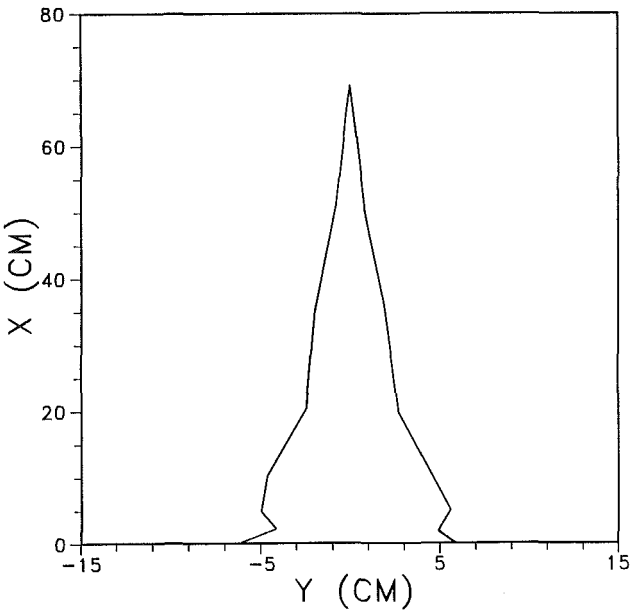

Fig. 10 Typical shape of the plume *footprint* for a 12-cm ground-based line source

Plume Liftoff. Meroney (1979) suggested a formulation for the liftoff distance given by

$$X_L/l_b = a(L_o/l_b)^{3/2} \tag{19}$$

where for his data the constant a equals 0.24. Slawson (1984) obtained a similar result but with the constant a equal to 1.3. The constant a in equation (19) depends on the value of the ambient reference velocity U_r, used in defining $l_b = F_o/\bar{U}_r^3$. The reference velocity depends on the ambient velocity profile and the height at which it is taken within a given profile. An analysis of the present data on liftoff, where three different velocity profiles were used, found that the best choice of reference velocity was that associated with the free-stream flow or region of the flow above which a log-law formulation of the velocity profile was valid. Based on a reference velocity chosen in this way, a fit of the data to equation (19) resulted in a value for the constant a of 0.84. Figure 9 illustrates the resultant formulation. Meroney's data on liftoff were based on effluent emissions in a coflowing stream, whereas the present data are for emissions normal to a crossflow. The ratio $L_o/l_b = (L_o\bar{U}_r^3)/F_o$; thus equation (19) indicates that increased line length or wind speed delays plume liftoff whereas increased source heat flux hastens it, as Meroney (1979) pointed out. He also concluded that liftoff will be delayed by increased mean flow shear. The present data support these logical conclusions.

In determining plume liftoff location, the shape of the so-called plume *footprint*, which defines the plume surface attachment zone, was also documented. Figure 10 illustrates one example of a plume *footprint*. This contact zone is required in order to assess that portion of the plume elemental circumference available for entrainment of ambient fluid in accordance with the simple integral model. On average, over the distance to liftoff, the postulated form of this contact zone given in equation (18) is not an unreasonable representation. The shape of the contact zone can be explained by considering three regions whose characteristics were found in the majority of the data. The first region is characterized by a contraction of the *footprint* immediately downstream of the source. This is caused by the flow of ambient fluid into the low-pressure region immediately downstream of the vertically emitted effluent. The second region, which is characterized by a rapid

decrease in the width of the *footprint*, coincided in most cases with the transition from the 1/2 law of a momentum-dominated plume to the 1/1 trajectory slope region of a buoyancy dominated plume. The third region where the contact zone width is reducing at a much lower rate than that of the second region was most often associated with the transition from a 1/1 to a 2/3 slope of the buoyancy region.

Conclusions

The trends in plume trajectory predicted by the simple closed-form integral model were found in the observations of both elevated and surface line sources of heat and momentum. A plume trajectory formulation, based on a single source, adequately described the plume rise with distance from the source for the elevated line sources (row of stacks). Individual plume rise enhancement subsequently became lost in a 15 percent rms scatter about the single source best fit trajectory line.

A formulation for plume liftoff suggested by Meroney (1979), adequately describes the liftoff distances presented here as a function of source Froude number. Limited observations on the form of the surface contact zone before liftoff of a surface line source suggest that the simple linear formulation given by Slawson (1976) suitably describes the contact zone.

Acknowledgments

The authors gratefully acknowledge the financial support of Atomic Energy of Canada Limited and the National Sciences and Engineering Research Council of Canada.

References

Briggs, G. A., 1969, "Plume Rise," U.S. Atomic Energy Commission, Div. of Tech. Information.

Briggs, G. A., 1975a, "Plume Rise Predictions," *Lectures on Air Pollution and Environmental Impact Analysis*, D. A. Haugen, ed., American Meteorological Society, Boston, MA, pp. 59–111.

Briggs, G. A., 1975b, "Plume Rise From Multiple Sources," *Cooling Tower Environment—1974*, ERDA Symposium Series, CONF-740302, NTIS, Springfield, VA, pp. 161–179.

Hawker, L. E., 1986, "An Experimental Investigation and Integral Model of Buoyant Line and Ring Sources in a Crossflow," MaSc. Thesis, U. of Waterloo, Waterloo, Ontario, Canada.

Meroney, R. N., 1979, "Lift Off of Buoyant Gas Initially on the Ground," *J. of Ind. Aero-dynamics*, Vol. 5, pp. 1–11.

Overcamp, T. J., 1982, "Plume Rise From Two or More Adjacent Stacks," Maryland Power Plant Siting Program, report PPRP-67.

Rouse, H., 1947, "Gravitational Diffusion From a Boundary Source in Two-Dimensional Flow," ASME *Journal of Applied Mechanics*, Vol. 14, pp. 225-228.

Slawson, P. R., and Csanady, G. T., 1967, "On the Mean Path of Buoyant Bent-Over Chimney Plumes," *J. Fluid Mech.*, Vol. 28, pp. 311–322.

Slawson, P. R., and Csanady, G. T., 1971, "The Effect of Atmospheric Conditions on Plume Rise," *J. Fluid Mech.*, Vol. 47, pp. 33–49.

Slawson, P. R., 1976, "On the Behavior of Buoyant Line Sources of Heat Near Ground Level," Envirodyne Ltd. report to Atomic Energy of Canada Ltd., Waterloo, Ontario, Canada.

Slawson, P. R., 1978, "Observations and Predictions of Natural Draft Cooling Tower Plumes at Paradise Steam Plant," *Atmos. Environment*, Vol. 12, pp. 1713–1724.

Slawson, P. R., 1982, "Some Observations on Modeling the Mechanical-Draft Cooling Tower Plume at Plant Gaston," *Atmos. Environment*, Vol. 16, pp. 2089–2094.

Slawson, P. R., 1984, "Laboratory Simulation and Mathematical Modeling to Assist in the Performance Evaluation of a Gas Dispersion System," Envirodyne Ltd. report to Atomic Energy of Canada Ltd., Waterloo, Ontario, Canada.

J. R. Sinclair
Ph. D. Candidate.

P. R. Slawson
Professor.

G. A. Davidson
Associate Professor.

Department of Mechanical Engineering,
University of Waterloo,
Waterloo, Ontario, Canada N2L 3G1

Three-Dimensional Buoyant Wall Jets Released Into a Coflowing Turbulent Boundary Layer

Experiments have been conducted in a water flume to simulate finite-length line sources of heat that issue horizontally at ground level into a coflowing turbulent shear flow. The downstream development of each buoyant jet is documented by detailed mean temperature measurements, which are analyzed to determine the jet trajectory, spread rates, and distance to the point of liftoff from the surface. In addition, a three-dimensional, parabolic, numerical model based on the fundamental conservation equations is developed. Model predictions of several buoyant jets compare reasonably with the experimental data and suggest that the strength of the streamwise vorticity plays an important role in governing liftoff of a buoyant wall jet from the surface.

Introduction

A problem of interest to industry and regulatory authorities entails the prediction of the dispersion of a potentially hazardous continuous plume released at or near the ground. These plumes are observed in the vicinity of low-elevation industrial stacks, cooling towers, ponds, canals, accidental releases from nuclear power plants, or forest fires. For these situations, the nature of the plume rise depends upon how the plume buoyancy interacts with the ambient crossflow. In the case of a surface or very near-surface release, the plume may diffuse like a passive contaminant and remain attached to the surface. This is likely to occur for initially low or moderate plume buoyancy that is quickly diluted by the entrainment of high-velocity ambient fluid. When the plume buoyancy is somewhat greater, the plume rises with enhanced vertical dispersion relative to a nonbuoyant release but still remains attached to the surface. Finally, under high source buoyancy or low ambient velocities, the plume may be expected eventually to lift off from the surface leaving only a trace behind (Fig. 1).

The current study extends the previous work on surface releases of Meroney (1979) and Slawson et al. (1986, 1988), by acquiring mean temperature measurements of buoyant wall jets in a coflowing turbulent boundary layer. Plume liftoff is affected by changing the jet temperature, jet velocity, or jet orifice geometry. In addition, a three-dimensional, parabolic, numerical model based on the fundamental conservation equations is developed and tested against experimental data. The model attempts to evaluate the utility of employing a Prandtl mixing-length hypothesis in the turbulence closure. Model predictions of buoyant jet liftoff distances, trajectories, and spread rates are compared with experimental data. In addition, further insight is gained from analyzing the flow details predicted by the model.

Experimental Techniques

Water Flume. The experiments were conducted in a closed-loop water flume 13 m long, with test section 1.2 m wide by 0.9 m deep. The test section is visible through a Plexiglas sidewall for a length of 2.4 m. A traversing mechanism with three degrees of freedom is used to position probes throughout the test section. Jet-orifice models are installed in a removable floor plate in the test section to which heated water of constant temperature is pumped through a manifold.

Three models were constructed to provide rectangular wall jets with slot length-to-height aspect ratios γ of 1.0, 40.7, and 81.4. Slot I is a low-aspect-ratio model with outflow cross-section dimensions of 0.01 m × 0.01 m. Slot III is a high-aspect-ratio model with dimensions of 0.114 m × 0.0014 m, and slot II was constructed by modifying slot III to a configuration of dimensions 0.057 m × 0.0014 m.

Velocity Measurement. Figure 2 illustrates a vertical profile of the mean streamwise velocity component of the ambient flow measured with a single-component laser-Doppler anemometry system (Sinclair, 1986; Tropea et al., 1986). The equipment consists of an Argon-Ion laser and standard TSI 900 & 9000 optics setup to transmit the two light beams through the Plexiglas side walls of the water flume. Forward scattered light is reflected back by an angled plane mirror located on the opposite side of the water flume. The photomultiplier signal is passed to a countersignal processor, which feeds the Doppler data via DMA to an IBM PC/AT computer where online velocity statistics are computed, data are archived, and plots are generated.

Mean Temperature Measurement. Mean temperature distributions are measured at several stations downstream of the buoyant wall jet source with a horizontal rake of 15 temperature probes. Each **L**-shaped probe is constructed using a YSI 44201 thermistor and 0.0032-m-dia stainless steel tubing. Ambient flume water temperature is monitored with a probe

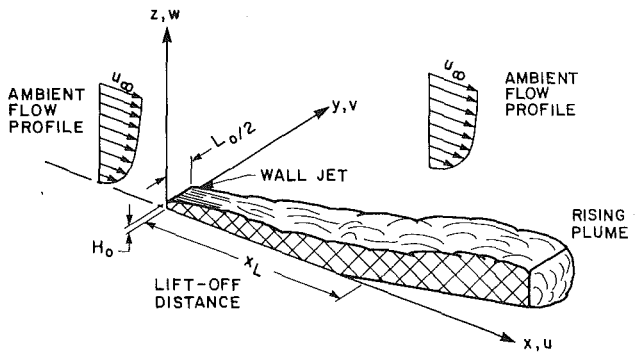

Fig. 1 Plume in a coflow: flow region identification and the coordinate system

Contributed by the Heat Transfer Division and presented at the ASME Winter Annual Meeting, Chicago, Illinois, November 28–December 2, 1988. Manuscript received by the Heat Transfer Division October 31, 1988; revision received June 7, 1989. Keywords: Environmental Heat Transfer, Jets, Plumes.

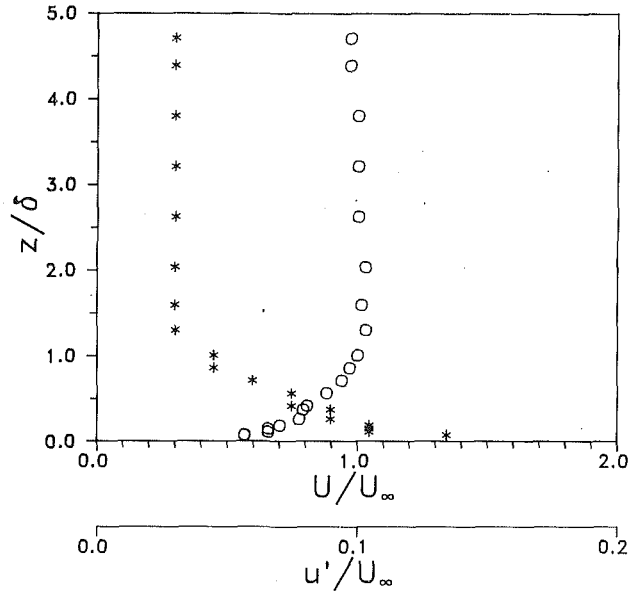

Fig. 2 Vertical profile of the nondimensionalized mean streamwise velocity, U/U_∞, and turbulent intensity, u'/U_∞, measured at the center of the water flume 0.30 m upstream of the jet-orifice model. The vertical distance from the floor of the water flume is nondimensionalized by the boundary layer thickness δ.

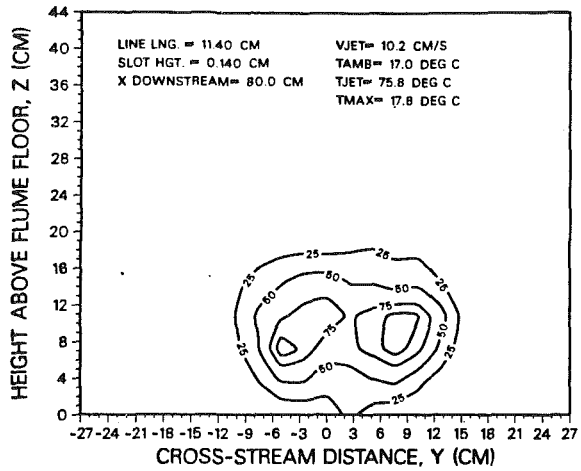

Fig. 3 Measured temperature cross section

mounted upstream of the test section. Jet exit temperature is monitored with a probe mounted in the supply manifold. All thermistor probes are interfaced through an excitation and linearizing circuit to a Fluke 2200B datalogger. Temperatures are resolved to within ± 0.01°C with this system, and uncertainty in calculated temperature differences for a given probe is determined to be ± 0.02°C.

A single experiment or plume is made up of 4 to 7 cross sections. Each cross section is made up of seven vertical positions of the horizontal probe rake. Time-averaged nondimensionalized temperature differences for each probe, $(\overline{T_N})_i$, are accumulated on an HP 85 computer and uploaded to a VAX 11/750 minicomputer where contour plots are prepared of cross-sectional isotherms based on a percentage of the maximum nondimensionalized temperature in the cross section array (e.g., Fig. 3). These plots provide a basis for further reduction of the temperature data to a set of effective plume variables, which describe the position, size, and shape of the plume. This is accomplished by fitting an equivalent area ellipse to the 25 percent isotherm region of each cross section. The 25 percent isotherm is used here to describe the plume geometry because it was found to agree with the mean visible plume boundaries as identified through dye releases.

The following procedure, proposed by Slawson et al. (1986), is used to position the ellipse. The vertical position ($\overline{z}$) is based on the midpoint of the 50 percent isotherm and then the major axis ($L = 2a$) is taken as the width of the 25 percent isotherm. Nominally, the semiminor axis ($b = H/2$) is determined from $A/\pi a$, where A is the measured area of the plume within the 25 percent isotherm. If $\overline{z}$ is less than b a portion of the ellipse is positioned below the flume floor and b is adjusted in order that the above-floor area of the ellipse matches the cross-sectional area of the plume.

Uncertainties in these data are estimated by comparing the values of the effective plume variables abstracted from repeated measurements of the same cross sections taken after a complete restart of an experiment. The estimated total uncertainty (Sinclair, 1986) in the calculated plume trajectories is approximately ± 13 percent and the uncertainties in the spread rates are ± 10 percent.

In a manner consistent with the above definitions, the plume liftoff distance x_L is defined here as the distance from the exit plane of the orifice to the location where the 25 percent isotherm of the nondimensional temperature field separates from the floor of the water flume. Liftoff distances are determined

Nomenclature

a, b = semimajor and semiminor axes of elliptical cross section
a_i = buoyancy parameters in turbulence model
A = cross-sectional area within 25 percent isotherm
B = source buoyancy flux = $(\Delta\rho/\rho_o)gQ_o$
c_p = specific heat at constant pressure
Fr_o = source Froude number = $(U_o^3 L_*/B)^{1/2}$
g = gravitational acceleration acting in the negative z direction
H_o = height of wall jet source orifice
H = plume vertical extent in cross section
L = Monin–Obukhov length scale
l_m = mixing length for turbulence model
L_o = length of plume source orifice
L_* = characteristic length scale = $A_o^{1/2}$
$\dot{M}$ = streamwise mass flux in a given vertical section of the flow
p = pressure
Pr = Prandtl number
P_s = streamwise pressure in decoupling assumption of the parabolic equations
$(q_T^t)_j$ = $-\rho c_p \overline{u_j' T'}$ = turbulent heat flux in j direction
Q_o = source volume flow rate = $U_o H_o L_o$
Ri = gradient Richardson number
R_M = integral mass flux ratio
R_o = source velocity ratio = $U_o/\overline{U}_a$
Re_o = source Reynolds number = $U_o H_o/\nu$
T = mean temperature
$(T_N)_i$ = $= (T_i^{plume} - T_i^{ambient}) / (T_o - T_\infty)$ = nondimensionalized temperature, for $i = 1, 15$ probes
$\overline{U}_a$ = ≈ 0.0468 m/s = integral average ambient velocity over depth of jet (0.03 m in these experiments)
U_τ = friction velocity

by linear interpolation between the neighboring vertical cross sections of the measured temperature field. These locations and the estimated uncertainties are reported in Table 2.

Mathematical Model

In previous studies, prediction of the trajectory and growth of a buoyant jet or plume near a surface has been approached with analytical and integral methods. In this study, a three-dimensional, parabolic, finite-volume model is developed using the time-mean equations for incompressible turbulent flow. One aim of the model is to evaluate the applicability of a Prandtl mixing-length hypothesis in the turbulence closure. The mixing-length function proposed varies continuously through jetlike, plumelike, and boundary-layer-like regions of turbulent diffusion, and tries to account for the local influence of buoyancy in enhancing or suppressing turbulence.

Governing Equations. The predominantly one-way flow in the flume is modeled in a Cartesian coordinate system with time-mean equations formulated for the parabolic streamwise flow. The standard mass, momentum, and energy conservation equations for steady flow are simplified by introducing: the Boussinesq approximations; the parabolic approximations: (*i*) $p_d(x, y, z) = P_s(x) + p(x, y, z)$ where $\partial p/\partial x \ll \partial P_s/\partial x$, (*ii*) $U \gg V, W$, and (*iii*) $\partial/\partial_y, \partial/\partial z \gg \partial/\partial x$; the Boussinesq assumption for turbulent stresses $\sigma^t_{ji} = -\rho \overline{u'_j u'_i}$; and the gradient diffusion hypothesis for turbulent heat flux terms $(q^t_T)_j = \rho c_p \overline{u'_j T'}$. The conservation equations lead to five equations for thirteen unknowns (U, V, W, T, p, $\partial P_s/\partial x$, σ^t_{yx}, σ^t_{zx}, σ^t_{yy}, σ^t_{zy}, σ^t_{zz}, $(q^t_T)_y$, $(q^t_T)_z$). One of the unknowns is eliminated by specifying $\partial P_s/\partial x = 0$. This has been found to be a reasonable approximation based on previous measurements in the water flume (Sinclair, 1986). Closure of the equation set requires a turbulence model parameterization of σ^t_{ji} and $(q^t_T)_j$ and boundary conditions.

Turbulence Model. The unknown correlations in the mean flow equations express transport of momentum, heat, and mass by the turbulent motion. Following the usual Boussinesq turbulent viscosity approach, turbulent stress is modeled by the same type of stress–strain relation as in a laminar Newtonian flow:

$$\sigma^t_{ji} \approx \mu^t \left(\frac{\partial U_i}{\partial x_j} + \frac{\partial U_j}{\partial x_i} \right) \tag{1}$$

where the turbulent viscosity μ^t is a turbulent flow parameter to be determined.

The turbulent heat flux is calculated from

$$(q^t_T)_j \approx \frac{\mu^t}{\mathrm{Pr}^t} \frac{\partial T}{\partial x_j} \tag{2}$$

The gradient diffusion hypothesis used here and the mixing-length closure described below have several limitations in complex flows. However, the attractions to this class of model are its simplicity, the cost advantage in development and operation of the model, compatibility with the generally limited experimental data available, and most importantly, the ease in which the researcher may draw on his understanding of the physics that affect the bulk features of the flow. The performance of this model also will guide future modeling efforts.

Mixing Length. Application of the parabolic approximations reduces the generalized form of the usual mixing-length formula (Patankar, 1975) to

$$\mu^t = \rho \frac{l_m^2}{\phi_M^2} \left\{ \left(\frac{\partial U}{\partial y} \right)^2 + \left(\frac{\partial U}{\partial z} \right)^2 + \left(\frac{\partial V}{\partial z} + \frac{\partial W}{\partial y} \right)^2 \right\}^{1/2} \tag{3}$$

Here, streamwise gradients ($\partial/\partial x$) are ignored in diffusion type terms, and normal-stress gradients ($\partial V/\partial y$), ($\partial W/\partial z$) are ignored since they are likely to be small relative to shear–stress gradients. In addition, the dimensionless wind shear ϕ_M is included to account for enhanced or suppressed turbulent mixing due to buoyancy effects. ϕ_M is traditionally seen in similarity analysis of the temperature stratified, constant stress layer of the atmosphere, although here it is a local parameter that varies throughout the buoyant jet/plume.

Specification of l_m requires careful consideration since it is recognized that many scales are present in this buoyant-jet/plume flow. Figure 4 highlights the main features of the flow, where it is hypothesized that a two-region, flat-plate boundary layer model will provide a basic structure for the mixing length profile. This model follows that of Patankar and Spalding (1970)

$$l_m = \kappa z \, [1 - \exp(-z^+/A^+)] \qquad z < \lambda z_l/\kappa \tag{4}$$

$$l_m = \lambda \, z_l \qquad \lambda z_l/\kappa \le z < z_l \tag{5}$$

where $z^+ = zU_\tau/\nu$ is a nondimensional vertical distance above the wall, U_τ is the friction velocity, ν is the kinematic viscosity of the fluid, $A^+ \approx 26.$ is a profile constant, $\kappa = 0.4 \pm 0.1$ is von Karman's constant, and z_l is the location of the *edge* of the shear layer. Far away from the jet, in the lateral (y) di-

Nomenclature (cont.)

U_∞ = $\approx$0.067 m/s = free-stream velocity
U, V, W = streamwise, lateral, vertical mean velocities
x, y, z = streamwise, lateral, vertical coordinates
x_L = distance from source to separation of 25 percent isotherm from the surface (plume liftoff)
z_l = height of the edge of the shear layer, i.e., outer extent of wall jet
γ = source aspect ratio = L_o/H_o
δ = $\approx$0.068 m = boundary layer thickness; $U(z=\delta) = 0.99U_\infty$
κ = von Karman's constant
λ = mixing length profile parameter
μ, ν = dynamic and kinematic viscosity of fluid
ρ = mass density of fluid
$\sigma^t_{ji} = -\rho \overline{u'_j u'_i}$ = turbulent shear stress (flux of i momentum in j direction)
ϕ_H = dimensionless temperature gradient
ϕ_M = dimensionless wind shear

Subscripts

d = dynamic quantity
i, j = Cartesian tensor notation
o = jet exit condition
∞ = ambient flow condition

Superscripts

t = turbulent quantity

Acronyms

ADI = Alternating Direction Implicit line solver
DMA = Direct Memory Access
SIMPLEC = consistent time-step formulation of the Semi-Implicit Method for Pressure-Linked Equations
TSI = Thermal Systems Incorporated, Minneapolis, MN
YSI = Yellow Springs Inst. Co., OH

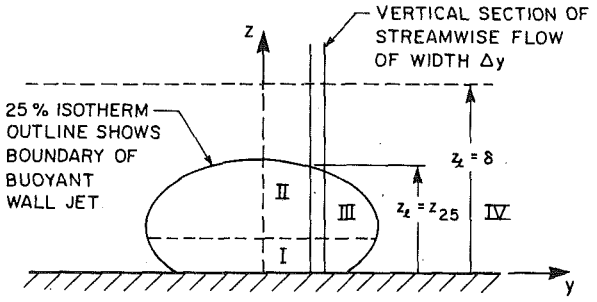

Fig. 4 Jet-boundary layer flow regimes: Region (I) Wall-bounded shear flow: flow momentum is lost to the wall by means of skin friction and fluid viscosity. The presence of the wall damps turbulent fluctuations normal to it. Region (II) and (III) Mixing layer flow: the top and side boundaries of the jet/plume mix with the coflowing ambient boundary layer flow. There is high shear production of turbulence and interaction of jet and boundary layer turbulence fields. Region (IV) Flat plate boundary layer flow far from the jet: the physics is similar to that in the shear layer flow region (I), except that the turbulence is confined to the developing boundary layer of depth δ.

rection, the flow is strictly a flat-plate boundary layer flow where $z_l = \delta$ and $\lambda = \lambda_\infty = 0.09$.

The near-wall profile of equation (4) is the well-known Van Driest profile (White, 1974), which has been used in two-dimensional wall jet flows issuing in a quiescent or uniform moving stream (e.g., Pai and Whitelaw, 1971). In these cases, the edge of the shear layer z_l is well defined. However, in this study, a three-dimensional wall jet issues into a deep boundary layer. Here, z_l is determined using the temperature field as a tracer in which the top boundary of the jet is identified as the height z_{25} where the local nondimensionalized temperature drops to 25 percent of the maximum nondimensionalized temperature in that cross-sectional plane. Since the effective Prandtl number of the flow is ≤ 1, the temperature field can be expected to outline the jet momentum field.

Directly above the jet ($z_{25} < z < \delta$), the flow is treated like the flat-plate boundary layer where the mixing length is determined using $z_l = \delta$.

So far, only vertical segments of the flow have been considered within a crossflow plane (Fig. 4). However, mixing-length profiles must merge smoothly in the lateral (y) direction and also in the streamwise (x) direction as the buoyant wall-jet develops into a plume. To accomplish this the streamwise mass flux in a given vertical section of the flow ($\dot{M}$) is compared to that of the flat-plate boundary layer flow ($\dot{M}_\infty$) observed far away from the jet. For a vertical section of the flow of finite width Δy at a specified downstream location x, the integral mass flux is given by

$$\dot{M} = \int_0^\delta \rho U(x, y, z)\Delta y \, dz \tag{6}$$

The mass flux ratio

$$R_M \equiv \frac{\dot{M} - \dot{M}_\infty}{\dot{M}_\infty} \tag{7}$$

is used to determine if the flow within the vertical section is jetlike or boundary-layer-like. A linear interpolation based on R_M merges the mixing-length profiles between these two regions.

Bridged Singularities. In regions of the flow where velocity maxima or minima occur, the mixing-length hypothesis (equation (3)) erroneously leads to zero μ^t. Within the context of the gradient diffusion hypothesis, this makes little difference to the shear stress, which is zero anyway. However, in modeling scalar transport, say heat, with turbulent Prandtl number Pr^t approximately constant, $\mu^t = 0$ implies that the thermal diffusivity is zero, which is unrealistic. Launder and Spalding (1972) and Pai and Whitelaw (1971) suggest that the μ^t distribution follows the mixing-length hypothesis everywhere except in the regions of zero mean shear. There a suitable value for μ^t is determined by linear interpolation between surrounding peak values.

Buoyancy Effects. The near-field flow of a buoyant wall jet is characterized by shear turbulence, which scales with the velocity ratio R_o. Farther downstream, the initial jet momentum decays and buoyancy body forces cause the plume to rise. However, even in the buoyant-jet transition phase, heated fluid parcels at the top edges of the jet rise and their motion is observed as enhanced vertical dispersion of the jet. In the plume phase the maximum (core) temperature of the plume is located above the flume floor, and fluid parcels at the bottom edge of the plume have their vertical motion retarded due to the stable temperature stratification. The turbulence model described here increases the turbulent viscosity μ^t in unstable temperature stratification and reduces μ^t in stable stratification using empirical relations based on the Monin–Obukhov similarity theory of the surface layer of the atmosphere. Strictly speaking, this theory only applies to the constant stress layer of a temperature stratified atmosphere where the buoyant length and time scales are large. However, for buoyant jets and plumes, the theory will provide the correct tendencies, with values of the constants adjusted for the best agreement between predicted trajectory and spreading and experimental data.

Pasquill and Smith (1983) and Panofsky and Dutton (1984) provide summaries of several empirical forms of ϕ_M. For unstable conditions

$$\phi_M = \left(1 - a_1 \frac{z}{L}\right)^{a_2} \tag{8}$$

where $a_1 \approx 15$ to 28, $a_2 \approx -0.25$, and $-4 < z/L < 0$. For stable conditions

$$\phi_M = 1 + a_3 \frac{z}{L} \tag{9}$$

where $a_3 \approx 4$ to 6 and $0 < z/L < 1$.

In the flume model, the gradient Richardson number Ri is used in place of z/L and the theory predicts the relationship to be $\mathrm{Ri} = z\phi_H/L\phi_M^2$. Here, approximate relationships between these stability parameters are used, as

$$\frac{z}{L} = \mathrm{Ri} = g\beta \frac{\partial T}{\partial z} \Big/ \left(\frac{\partial U}{\partial z}\right)^2 \quad \text{(unstable conditions)} \tag{10}$$

$$\frac{z}{L} = \frac{\mathrm{Ri}}{1 - a_4 \mathrm{Ri}} \quad \text{(stable conditions)} \tag{11}$$

where $a_4 \approx 5.0$ and $\mathrm{Ri} < 1/a_4$. In the lower portion of a freely rising plume, very stable conditions ($\mathrm{Ri} \geq 1/a_4$) are not expected to suppress turbulent mixing completely; therefore, z/L is arbitrarily limited to a maximum value of 2 rather than using equation (11).

Similar empirical relations describe the effect of buoyancy on turbulent heat transfer, as

$$\phi_H = \mathrm{Pr}_N^t \left(1 - a_5 \frac{z}{L}\right)^{a_6} \quad \text{(unstable conditions)} \tag{12}$$

$$\phi_H = \mathrm{Pr}_N^t + a_3 \frac{z}{L} \quad \text{(stable conditions)} \tag{13}$$

where Pr_N^t (≈ 0.74 to 0.9) is the turbulent Prandtl number in neutral conditions, $a_5 \approx 9$ to 16, and $a_6 \approx -0.5$.

In limiting cases $\mathrm{Pr}^t = \phi_H/\phi_M$ attains values: $\mathrm{Pr}^t = \phi_M$ for unstable conditions, $\mathrm{Pr}^t = 1$ for stable conditions, and $\mathrm{Pr}^t = \mathrm{Pr}_N^t$ for neutral conditions.

One difficulty in applying the above relations lies in the determination of Ri. For local mean velocity minima and maxima, $\mathrm{Ri} \to \pm\infty$ and use of ϕ_M in equation (3) leads to incorrect results. Therefore, the denominator of equation (10) is replaced

Table 1 Grid specifications for operational model runs

Grid specifications	Slot I	Slot II
Number of Control Volumes		
(X) Streamwise direction (based on predictions to 0.20 m downstream of slot)	40	40
(Y) Lateral direction	20	20
- in the slot	2	8
(Z) Vertical direction	22	22
- in the slot	4	1
Geometric Expansion Factors		
(X)	1.03	1.03
(Y)	1.05	1.10
(Z)	1.07	1.13

Table 2 Summary of source conditions and liftoff distances for all experiments. Temperature cross section data available for experiments #1-11. Visual observations only for experiments #12-16.

Expt. #	L_o [m]	γ (L_o/H_o)	Q_o [$m^3/s \times 10^6$]	U_o [m/s]	R_o	T_o [C]	T_a [C]	Fr_o	z_L [m]
1	0.01	1.0	9.5	9.5	2.0	34.8	18.8	4.6	0.08±0.02
2	0.01	1.0	0.128	12.8	2.7	35.4	19.2	6.1	0.18±0.02
3	0.01	1.0	0.162	16.2	3.5	35.7	19.0	7.6	0.32±0.02
4	0.01	1.0	0.245	24.5	5.2	85.8	18.5	4.4	0.12±0.02
5	0.01	1.0	0.328	32.8	7.0	75.8	18.3	6.7	0.23±0.02
6	0.053	40.7	0.78	10.6	2.3	63.2	16.6	2.7	0.125±0.02
7	0.053	40.7	0.162	21.8	4.7	74.6	16.6	4.8	0.175±0.02
8	0.053	40.7	0.328	44.3	9.5	75.0	16.8	9.7	0.33±0.02
9	0.114	81.4	0.64	4.0	0.9	70.0	17.1	0.8	> 1.4
10	0.114	81.4	0.162	10.2	2.2	75.9	17.1	1.8	> 1.4
11	0.114	81.4	0.328	20.6	4.4	76.2	17.4	3.7	0.35±0.05
12	0.01	1.0	0.62	6.2	1.3	47.3	18.0	2.0	0.04±0.03
13	0.01	1.0	0.112	11.2	2.4	48.7	18.0	3.6	0.08±0.03
14	0.01	1.0	0.162	16.2	3.5	49.7	18.0	5.1	0.15±0.04
15	0.01	1.0	0.245	24.5	5.2	50.5	18.0	7.5	0.25±0.04
16	0.01	1.0	0.326	32.6	7.0	51.0	18.0	9.9	0.45±0.04

with a spatially averaged form of the bracketed shear terms in equation (3). This eliminates the singularity mentioned above.

Boundary and Initial Conditions. The wall boundary is an adiabatic no-slip boundary impervious to mass transfer. With the assumption that the first interior control volumes normal to the wall are situated in the constant stress region of wall boundary layer flow, a one-dimensional log-law wall function is used to determine the wall shear stresses.

The free-stream (top) boundary is an adiabatic slip boundary and allows vertical mass transfer. The latter is the predicted entrainment of ambient fluid into the plume that satisfies global mass conservation.

The plane of symmetry boundary and the free side boundary are adiabatic slip boundaries impervious to mass transfer. These conditions at the free side boundary are specified as a convenience in the numerical scheme, since, even though the side boundary is necessarily displaced far away from the edge of the plume, the cost of solving the equations is considerably less than when a open boundary is used.

On the inflow boundary, the numerical model requires specification of all dependent variables. Experiments conducted in the water flume provide mean velocity and temperature data that are interpolated to the (y-z) plane grid nodes. The pressure field is set to a constant, based on the one-dimensional nature of the inflow.

Outflow boundary conditions are not required for the parabolic equations.

Solution of the Equations. The governing equations are integrated over the finite control volumes of the discretized Cartesian domain (Sinclair, 1986; Raithby et al., 1986; Patankar, 1980). Piecewise continuous profile approximations of the dependent variables are used to evaluate the required integrals and arrive at an algebraic equation set. The parabolic form of the equations allows crossflow (y-z) planes to be solved elliptically knowing the inflow (streamwise) values and other discrete boundary conditions. The SIMPLEC algorithm (Van Doormaal and Raithby, 1984) is used with an ADI solver for the velocity, pressure, and temperature fields. Predicted outflow conditions from the current crossflow plane act as inflow conditions for the next crossflow plane. In this way, the procedure marches the solution from the inflow boundary of the grid domain to the outflow boundary.

Sinclair (1986) describes numerous code validation experiments in which the model successfully predicts both two- and three-dimensional, internal and external, flows. In particular, predictions of turbulent flat plate boundary layers and two-dimensional wall jets differ from experimental data by only 4–9 percent.

Grid Selection and Values of the Empirical Constants. Model predictions of buoyant jets from slot I and slot II geometries were compared to the experimental data. Grid refinement improved solutions to the point that satisfactory model predictions were achieved with the grid specifications shown in Table 1.

Adjustment or tuning of the turbulence model parameters was carried out on a limited basis using the buoyant jet experiments #4, #6, and #7 (Table 2). Cases #2, #3, #5, and #8 serve as independent test cases.

The parameters a_2, a_4, and a_6 are kept at their suggested values, whereas $a_1 = 4.0$, $a_5 = 4.0$, $a_3 = 5.0$, and $\mathrm{Pr}_N^t = 0.85$ are the adjusted values that improve the agreement of the model predictions with the experimental data. In addition, $\kappa \approx 0.3$ reduces the wall shear stress from that of the more typical value of 0.4. This enhances the near-wall crossflow of the ambient fluid that is responsible for the liftoff of the plume from the surface.

The flow within a vertical section of the grid is considered jetlike if the mass flux ratio $R_M > 0.9$ and boundary-layer-like if $R_M < 0.5$. In between, a linear interpolation of mixing-length scales is used. Within the jet region of the flow the use of $\lambda = 2.0^* \lambda_\infty$ in equation (5) produces a reasonable level of jet spreading.

Results and Discussion

Source conditions and liftoff distances for all experiments are summarized in Table 2. Of the 16 buoyant jet cases available, experiments #2 through #8 are selected for the comparison of the numerical model predictions to the experimental data since these buoyant jets exhibit liftoff in the near-field region of interest, and the data are more detailed for these cases. For each experiment the numerical model predicts the vertical and lateral extents of the 25 and 50 percent isotherms at each crossflow plane. These data are processed using the ellipse-fit procedure described earlier and then compared with the appropriate experimental data.

Figures 5 through 10 illustrate the predicted trajectory, bulk spreading, and vertical spreading of elliptically shaped plumes of experiments #2 through #8. Table 3 summarizes the predictions of plume liftoff distances for these cases.

Discussion of Results. The experimental results indicate that the distance to liftoff is influenced by jet momentum effects. A high jet-to-ambient velocity ratio delays liftoff for low-aspect-ratio slot jets. For high-aspect-ratio slot jets (long line sources), however, these flows are less jetlike and a high efflux velocity increases the buoyancy flux, which enhances liftoff. For low-aspect-ratio buoyant wall jets, lateral spreading is greater than vertical spreading. For high-aspect-ratio slot jets, vertical spreading is generally greater than or equal to lateral spreading since the larger surface area of the jet increases vertical diffusion of the jet momentum by turbulent shear stresses and buoyancy forces.

Numerical model predictions of plume liftoff distance, trajectory, bulk spreading, and vertical spreading are in general

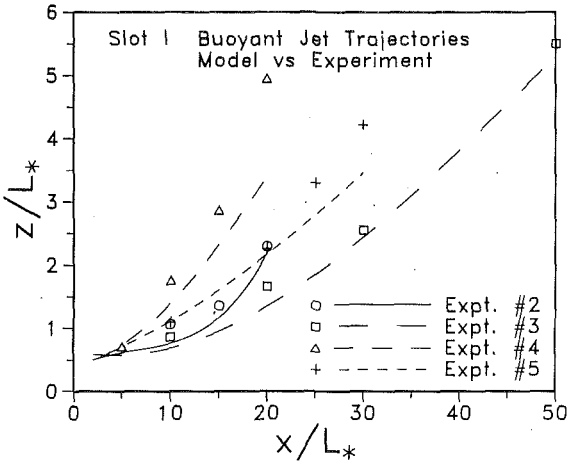

Fig. 5 Model predictions of plume trajectory compared with experiments #2 to #5; $L_* = 0.01$ m

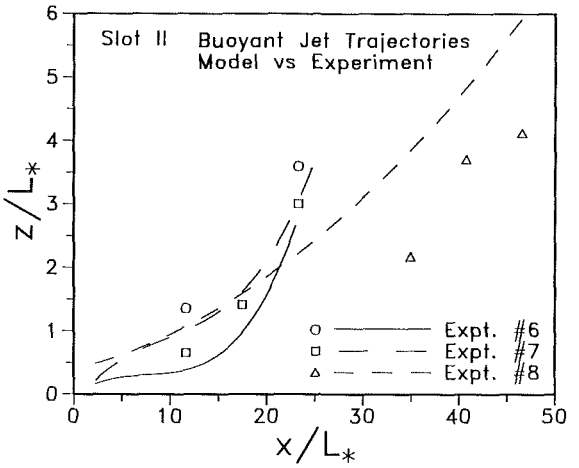

Fig. 6 Model predictions of plume trajectory compared with experiments #6 to #8; $L_* = 0.0086$ m

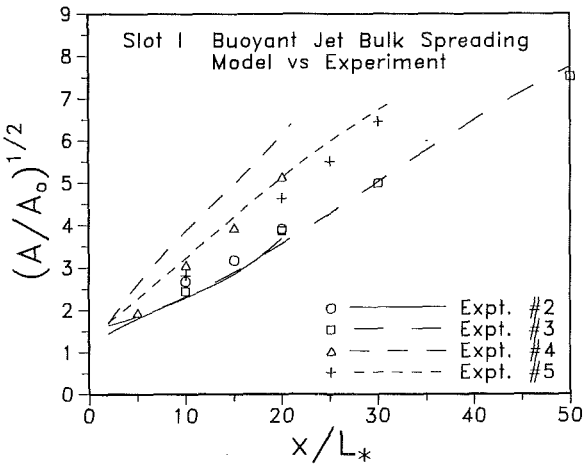

Fig. 7 Model predictions of buoyant jet spreading; cross-sectional area compared with experiments #2 to #5

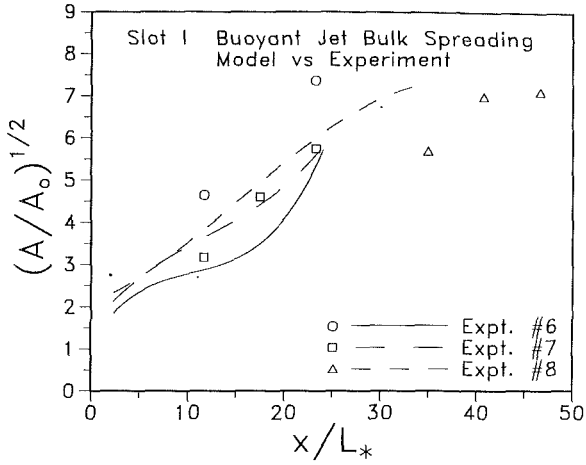

Fig. 8 Model predictions of buoyant jet spreading; cross-sectional area compared with experiments #6 to #8

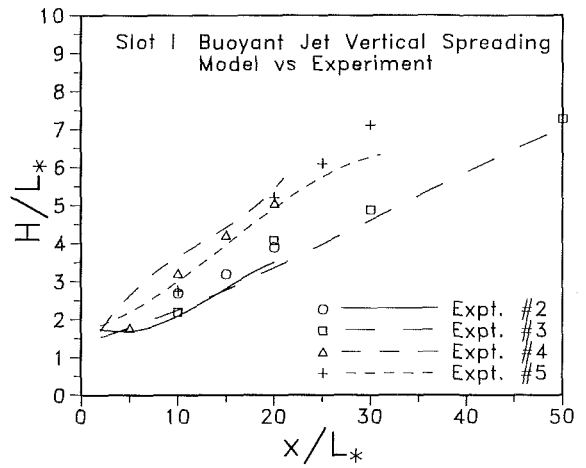

Fig. 9 Model predictions of buoyant jet spreading; vertical extent in cross section compared with experiments #2 to #5

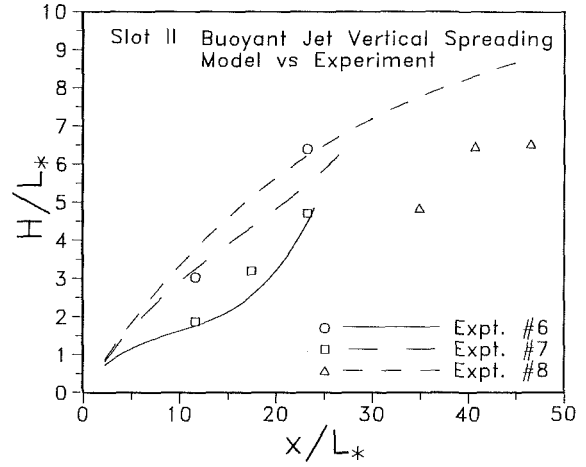

Fig. 10 Model predictions of buoyant jet spreading; vertical extent in cross section compared with experiments #6 to #8

agreement with the experiments. However, there are varying degrees of departure from the observations.

There do not appear to be any systematic deviations in the predicted plume trajectory in comparison to the experimental data. It seems, however, that the bulk spreading of the plume is overpredicted for high velocity ratios (e.g., $R_o > 3.5$) in experiments #4, #5, #7, and #8, and underpredicted for low velocity ratios (e.g., $R_o < 3.5$) in experiments #2 and #4.

Analysis of the vertical spreading predictions indicates satisfactory predictions for slot I experiments (#2 to #5). However,

Table 3 Model predictions of plume liftoff distances from the source, in m

Exp't #	Model Prediction	Experimental Data
2	0.135	0.180
3	0.210	0.320
4	0.155	0.120
5	0.255	0.230
6	0.140	0.125
7	0.178	0.175
8	0.336	0.330

vertical spreading in underpredicted for the low-velocity-ratio case (#6) of slot II and overpredicted for the high-velocity-ratio cases (#7 and #8) of this same slot.

Plume liftoff distance predictions occur too early for the warm slot I jets of experiments #2 and #3 and a little late for the hot jets of experiments #4 and #5. The slot II hot jets of experiments #6, #7, and #8 are predicted quite well.

Predicted Flow Details. Flow details predicted by the numerical model (Fig. 11) highlight the complex behavior of fluid entrained at the edges of the buoyant wall jets and also show the formation of the counter-rotating vortex pair at the upper sides of the jet. This crossflow pattern is initiated by turbulent shear stresses generated in the near-field development of the buoyant wall jet, and receives further support during the plume rise phase, which starts only after sufficient decay of the jet's streamwise momentum. The streamwise vorticity drives the near-wall entrainment flow, which severs the plume from the surface as it rises. In this region where the plume lifts off from the surface, it is likely that a small residual of the plume is left behind near the centerline on the surface (Meroney, 1979). Physically, one could argue that in this region convective transport provided by the entraining crossflow is retarded due to the effects of the no-slip surface, the enhanced near-wall turbulent diffusion, and the local maxima of pressure at the corner of the symmetry plane and surface boundaries. This leaves parcels of the plume on the surface that diffuse and possibly rise slowly, independent of the main body of the plume. Future investigations will attempt to verify this behavior through detailed experiments.

From a square source, the jet immediately takes on a circular cross-sectional shape, which is distorted into an elliptical shape through the buoyant jet and plume phases. The higher lateral spreading predicted by the model is in agreement with experimental results. It is interesting to note that the anisotropic spreading is correctly predicted even though an isotropic mixing process is assumed in the turbulence model. This lends support to the predictions of streamwise vorticity transport effects in promoting lateral spreading.

Conclusions

Numerical model predictions of buoyant jet liftoff distances, trajectories, and spread rates compare reasonably with the experimental data.

The mixing-length turbulence closure employed in the numerical model provides satisfactory predictions of buoyant wall jets. It has the advantages of an easy, cost-effective computer implementation and a readily understood physical interpretation, which aids the modeler in incorporating empirical information. However, the use of mean-velocity shear as a turbulent time scale of the flow leads to difficulties with values of the turbulent viscosity μ^t. The wall jet in a coflow is a complex flow with extrema in the velocity profiles. In regions near maxima and minima in the velocity field, the model would predict unrealistic levels of μ^t without the use of bridging interpolation. Additional difficulties result from determining a local Richardson number based on the mean shear. The level of shear-produced turbulence in not well predicted in complex flows with velocity profile extrema. Therefore, prediction of flow stability effects is approximate and further investigation is required in this area.

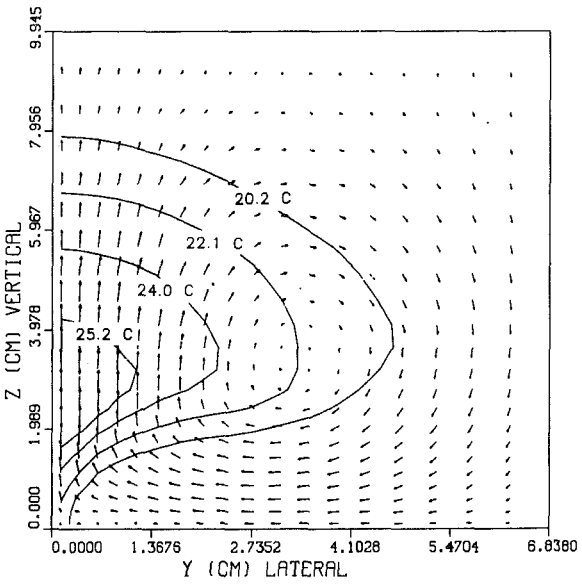

Fig. 11 Model prediction of cross-sectional velocity and temperature fields for the buoyant wall jet experiment #5, at $x/L_s = 30$. The maximum magnitude of crossflow velocity vectors is 0.072 U_o.

Acknowledgments

The authors gratefully acknowledge the financial support of the Natural Sciences and Engineering Research Council of Canada.

References

Launder, B. E., and Spalding, D. B., 1972, *Lectures in Mathematical Models of Turbulence*, Academic Press, New York.

Meroney, R. N., 1979, "Lift Off of Buoyant Gas Initially on the Ground," *J. of Ind. Aerodynamics*, Vol. 5, pp. 1–11.

Pai, B. R., and Whitelaw, J. H., 1971, "The Prediction of Wall Temperature in the Presence of Film Cooling," *Int. Journal of Heat Mass Transfer*, Vol. 14, pp. 409–422.

Panofsky, H. A., and Dutton, J. A., 1984, *Atmospheric Turbulence*, Wiley, New York.

Pasquill, F., and Smith, F. B., 1983, *Atmospheric Diffusion*, 3rd ed., Ellis Horwood Ltd., Wiley, New York.

Patankar, S. V., and Spalding, D. B., 1970, *Heat and Mass Transfer in Boundary Layers*, 2nd ed., Morgan-Grampian, London.

Patankar, S. V., 1975, "Numerical Prediction of Three-Dimensional Flows," *Studies in Convection*, Vol. 1, B. E. Launder, ed., Academic Press, New York.

Patankar, S. V., 1980, *Numerical Heat Transfer and Fluid Flow*, Hemisphere Publishing Corp., New York.

Raithby, G. D., Galpin, P. F., and Van Doormaal, J. P., 1986, "Prediction of Heat and Fluid Flow in Complex Geometries Using General Orthogonal Coordinates," *Numerical Heat Transfer*, Vol. 9, No. 2, pp. 125–142.

Sinclair, J. R., 1986, "An Experimental and Numerical Study of Buoyant Wall Jets Released Into a Co-flowing Turbulent Stream," M.A.Sc. Thesis, U. of Waterloo, Waterloo, Ontario, Canada.

Slawson, P. R., Hitchman, G. J., and Hawker, L. E., 1986, "Laboratory Simulation and Mathematical Modelling to Assist in the Performance Evaluation of a Gas Dispersion System," Envirodyne Ltd., report to Atomic Energy of Canada Ltd.

Slawson, P. R., Hitchman, G. J., and Hawker, L. E, 1988, "The Behavior of Surface and Elevated Finite Length Line Sources of Heat in Crossflows," *Proceedings of the ASME Winter Annual Meeting*, ASME, New York.

Tropea, C., Struthers, D., and Hitchman, G., 1986, "Laser-Doppler Anemometer Measurement System," Mech. Eng. Internal Report, U. of Waterloo, Waterloo, Ontario, Canada.

Van Doormaal, J. P., and Raithby, G. D., 1984, "Enhancements of the SIMPLE Method for Predicting Incompressible Fluid flows," *Numerical Heat Transfer*, Vol. 7, pp. 147–163.

White, F. M., 1974, *Viscous Fluid Flow*, McGraw-Hill, New York.

Thermosolutal Inducement of No-Slip Free Surfaces in Combined Marangoni-Buoyancy Driven Cavity Flows

J. R. Keller

T. L. Bergman
Assistant Professor.
Assoc. Mem. ASME

Department of Mechanical Engineering,
The University of Texas at Austin,
Austin, TX 78712

The presence of a diffusing surfactant in combined surface tension-buoyancy driven convection is studied numerically to examine its influence on the flow structure and heat transfer characteristics of a fluid contained within a cavity. By accounting for the surface tension dependence on both temperature and surfactant concentration, the free surface may become stagnant. As a result, the high local and overall heat transfer rates at the cold wall, which are associated with thermal surface tension-augmented buoyancy driven flows, are decreased.

Introduction

Combined surface tension-buoyancy driven convection is relevant in a variety of engineering systems and manufacturing processes. Oftentimes, this type of convection is present within liquid melts in conjunction with melting and solidification heat transfer during, for example, welding (Kou, 1987), glass making (Stanek and Szekely, 1970; McNeil et al., 1985), metals processing (Camel et al., 1986) and crystal growth (Hurle and Jakeman, 1981). As a result, melting and solidification rates as well as the ultimate product quality may be affected by convection driven by simultaneous buoyancy and surface tension forces.

For a pure fluid, variations in the liquid surface tension occur due to its dependence on the liquid temperature. If the thermally induced surface tension variation occurs along a free surface, the net thermocapillary force will either augment or oppose the buoyancy driven flow within the bulk of the liquid layer. As a result, two distinct thermocapillary flow regimes may exist in, for example, a liquid held within a cavity with heated and cooled side walls.

If thermocapillary forces augment buoyancy forces, free surface velocities increase relative to the pure buoyancy case, advection of thermal energy from the upper hot wall to the upper cold wall is enhanced, and very high local heat transfer rates occur near the top of the cold wall (Schwabe et al., 1978; Villers and Platten, 1985; Bergman and Ramadhyani, 1986). In contrast, if opposing thermocapillary forces are present, a bicellular flow structure may result, leading to decreased heat transfer rates relative to the pure buoyancy case (Legros et al., 1984; Villers and Platten, 1985; Bergman and Ramadhyani, 1986). Most real fluids are susceptible to flow behavior of the first regime while only a few fluids exhibit the second type of flow.

While experimental results and numerical predictions indicate that thermocapillary effects exist and can be significant under certain conditions, it is typical of many systems to possess free surfaces characterized by stagnant conditions (Heiple and Roper, 1982; Kirdyashkin, 1984; Platten and Villers, 1987). This type of behavior constitutes a third flow regime and is superficially identical to the pure buoyancy case with an applied no-slip boundary condition at the free surface. As is evident from a force balance along the free surface, however, surface tension forces must remain in effect, since their absence implies applicability of a no-shear hydrodynamic boundary condition and, in turn, finite velocities at the free surface, which are driven by buoyancy-induced flow in the bulk of the fluid. Thermocapillary forces are not negligible in the third flow regime; they must be counterbalanced by an opposing mechanism.

It is well known that trace concentrations of contaminants such as dust, ionic materials, or other liquids can reduce the surface tension of a host liquid (Shinoda, 1963). If the contaminant is a surfactant, concentration gradients may be induced at the free surface in response to advective mechanisms resulting from other driving forces. In turn, the nonuniform concentration distribution produces surface tension gradients at the free surface, which affect convective transport in the bulk liquid.

Coupling between the solutocapillary convection and bulk fluid motion was initially proposed by Levich in 1948 (1962) to describe behavior of air bubbles rising through a stagnant fluid layer. However, the model could not accurately predict the drag force dependence on particle size and a "stagnant cap" model was developed (Savic, 1953). Here, the insoluble surfactants are advected to the rear of the bubble, creating a stagnant region. Davis and Acrivos (1966) were able to employ the stagnant cap model to predict the rise velocity of air bubbles in a liquid layer. As will become evident, a three-way coupling between buoyancy-induced advection, thermocapillary forces, and solutocapillary forces is responsible for the flow of the third regime.

Analysis

In order to understand the coupling process that induces free surface stagnation, the system of Fig. 1 is considered. A host liquid is contained in a cavity of length L and a free surface is present at $y=H$. Fluid motion is induced by imposing appropriate thermal boundary conditions and is due to the presence of buoyancy and surface tension forces within the bulk fluid and at the free surface, respectively.

By assuming a flat, nondeformable free surface and steady, laminar two-dimensional flow with negligible viscous dissipation, the governing equations for the Boussinesq host liquid are:

$$\frac{\partial u}{\partial x} + \frac{\partial v}{\partial y} = 0 \tag{1}$$

Contributed by the Heat Transfer Division for publication in the JOURNAL OF HEAT TRANSFER. Manuscript received by the Heat Transfer Division November 27, 1988; revision received June 19, 1989. Keywords: Double Diffusion Systems, Enclosure Flows, Thermocapillary Flows.

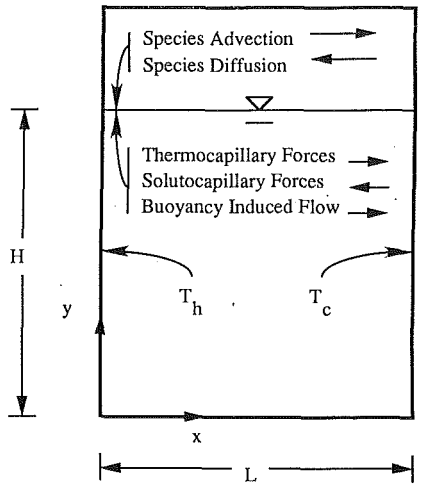

Fig. 1 Schematic of the system showing buoyancy and surface tension forces and surface species diffusion

$$\frac{\partial}{\partial x}(uu)+\frac{\partial}{\partial y}(uv)=\frac{\partial}{\partial x}\left(\nu\frac{\partial u}{\partial x}\right)+\frac{\partial}{\partial y}\left(\nu\frac{\partial u}{\partial y}\right)-\frac{1}{\rho}\frac{\partial P}{\partial x} \tag{2}$$

$$\frac{\partial}{\partial x}(vu)+\frac{\partial}{\partial y}(vv)=\frac{\partial}{\partial x}\left(\nu\frac{\partial v}{\partial x}\right)+\frac{\partial}{\partial y}\left(\nu\frac{\partial v}{\partial y}\right)-\frac{1}{\rho}\frac{\partial P}{\partial y}+g\beta(T-T_o) \tag{3}$$

$$\frac{\partial}{\partial x}(uT)+\frac{\partial}{\partial y}(vT)=\frac{\partial}{\partial x}\left(\alpha\frac{\partial T}{\partial x}\right)+\frac{\partial}{\partial y}\left(\alpha\frac{\partial T}{\partial y}\right) \tag{4}$$

If a surfactant is present along the free surface, it will be subjected to horizontal advection associated with the flow in the host liquid. Horizontal diffusion of the surfactant opposes its advective transport.

$$\frac{\partial}{\partial x}(uc)\Big|_{y=H}=\frac{\partial}{\partial x}\left(D\frac{\partial c}{\partial x}\right)\Big|_{y=H} \tag{5}$$

The hydrodynamic boundary conditions include no-slip conditions at the cavity walls and bottom. The hydrodynamic conditions at $y=H$ result from a force balance at the free surface (Levich and Krylov, 1969)

$$\mu\frac{\partial u}{\partial y}\Big|_{y=H}=\sigma_T'\frac{\partial T}{\partial x}\Big|_{y=H}+\sigma_c'\frac{\partial c}{\partial x}\Big|_{y=H} \tag{6}$$

and

$$v\Big|_{y=H}=0 \tag{7}$$

The thermal boundary conditions considered in this study are

$$T=T_h\Big|_{x=0},\qquad T=T_c\Big|_{x=L} \tag{8}$$

and

$$\frac{\partial T}{\partial y}\Big|_{y=0,H}=0 \tag{9}$$

The surfactant concentration boundary conditions are

$$\frac{\partial c}{\partial x}\Big|_{x=0}=\frac{\partial c}{\partial x}\Big|_{x=L}=0 \tag{10}$$

with the constraint

$$\frac{1}{L}\int_{x=0}^{x=L}c(x)dx=c_{\text{avg}} \tag{11}$$

where c_{avg} is specified a priori.

In writing equations (5) and (11), it is assumed that the contaminant is limited to a thin film, which rides upon the free surface. Inspection of equation (10) reveals that, if a surface velocity exists, the surfactant will be trapped against one of the enclosure walls and its diffusion will induce a concentration gradient along the free surface. The presence of the surfactant eventually influences bulk convective flow and heat transfer in the host liquid through the Marangoni hydrodynamic boundary condition, equation (6).

The following dimensionless parameters govern the system behavior and are identified by appropriate normalization of the governing equations and applied boundary conditions.

Rayleigh number	$\text{Ra}=g\beta\Delta TL^3/\nu\cdot\alpha$	(12)
Prandtl number	$\text{Pr}=\nu/\alpha$	(13)
Schmidt number	$\text{Sc}=\nu/D$	(14)
thermal Marangoni number	$\text{Ma}_T=\sigma_T'\Delta TL/\mu\cdot\alpha$	(15)
solutal Marangoni number	$\text{Ma}_c=\sigma_c'c_{\text{avg}}L/\mu\cdot\alpha$	(16)
liquid layer aspect ratio	$A=H/L$	(17)

It should be noted that the average surfactant concentration is used to normalize the concentration in equations (5), (6), and

Nomenclature

A = liquid layer aspect ratio $=H/L$
Bo = dynamic Bond number $=\text{Ra}/\text{Ma}_T$
c = specific heat, surfactant concentration
D = species diffusion coefficient
E = elasticity number $=\text{Ma}_c/\text{Ma}_T$
g = gravitational acceleration
h = local heat transfer coefficient
H = height of the liquid layer
k = thermal conductivity
L = width of the liquid layer
Le = Lewis number $=\text{Sc}/\text{Pr}$
Ma_c = solutal Marangoni number $=\sigma_c'c_{\text{avg}}L/\mu\cdot\alpha$
Ma_T = thermal Marangoni number $=\sigma_T'\Delta TL/\mu\cdot\alpha$
Nu = local Nusselt number $=hL/k$
$\overline{\text{Nu}}$ = average Nusselt number $=H^{-1}\int_{y=0}^{y=h}\text{Nu}\,dy$
p = pressure
Pr = Prandtl number $=\nu/\alpha$
Ra = Rayleigh number $=g\beta\Delta TL^3/\nu\cdot\alpha$
Sc = Schmidt number $=\nu/D$
T = temperature
u = horizontal velocity
u^* = dimensionless horizontal velocity $=uL/\alpha$
v = vertical velocity
x = horizontal coordinate
y = vertical coordinate
α = thermal diffusivity $=k/\rho\cdot c$
β = thermal expansion coefficient
μ = dynamic viscosity
ν = kinematic viscosity
ρ = mass density
σ' = surface tension variation with temperature or concentration
ψ = dimensionless streamfunction

Subscripts

c = concentration, cold
h = hot
max = maximum
min = minimum
o = reference
T = thermal

(10) due to the absence of a characteristic concentration difference in the system.

Three additional dimensionless parameters may be derived from equations (12)–(17). Although they are not independent they are useful to consider,

Lewis number $\quad \mathrm{Le} = \mathrm{Sc}/\mathrm{Pr} = \alpha/D \quad (18)$

dynamic Bond number $\quad \mathrm{Bo} = \mathrm{Ra}/\mathrm{Ma}_T = g\beta\rho L^2/\sigma_T' \quad (19)$

elasticity number $\quad E = \mathrm{Ma}_c/\mathrm{Ma}_T = c_{\mathrm{avg}}\sigma_c'/\Delta T \cdot \sigma_T' \quad (20)$

The Lewis number is the ratio of thermal to species diffusivities while the dynamic Bond number describes the relative strength of buoyancy to thermal surface tension forces. The elasticity number is a ratio of solutocapillary to thermocapillary forces and has been used previously to describe the influence of a nondiffusing surfactant on surface-tension induced flow (Homsy and Meiburg, 1984; Carpenter and Homsy, 1985).

Solution Technique

The governing equations for the host liquid were discretized using the control volume methodology and the power-law scheme was employed to predict the control surface quantities of the advection-diffusion equations (Patankar, 1980). The SIMPLER algorithm was used to predict the pressure field (Patankar, 1980). The governing equation for the surfactant concentration distribution (5) was solved at every iteration by employing the power law approximation to the exact solution of the one-dimensional advection-diffusion equation.

A grid dependence study has shown that a 40×70 (vertical by horizontal) grid network with packed grids along the free surface and cavity walls is adequate to insure grid independent results for the surfactant concentration and surface velocity distributions, as well as the flow structure in the bulk of the fluid and the local and overall heat transfer rates. The grid packing scheme decreases the dimensions of the control volumes by 10 percent as one progresses from the cneter of the computational domain. The buoyancy portion of the model was validated by comparing the predicted heat transfer rates across a square air-filled cavity with heated endwalls to a benchmark numerical solution (De Vahl Davis, 1983). Average Nusselt numbers were within 2 percent of the benchmark predictions to $\mathrm{Ra} = 10^6$. The surface tension portion of the model was compared to predictions for pure surface tension flow in a square cavity with heated end walls (Zehr et al., 1987). Predicted surface velocities, surface temperatures, and local wall heat fluxes were within 2 percent of the benchmark values for $\mathrm{Ma} \leq 10^3$. It should be noted that the presence of the surfactant significantly reduces the severe grid packing requirements, which are generally necessary to model thermocapillary-induced flow in cavities (Zehr et al., 1987).

Results

Numerical simulations were performed for a range of Ra ($10^2 \leq \mathrm{Ra} \leq 10^6$), Ma_T (250 and 10^3), and E (0.0, 0.1, 0.2, 0.3, ∞). Due to the relative expense of the computations, Pr and A were held at unity while Le values were 1, 10, and 100, which are typical of most host liquids. The value of c_{avg} is 0.001 for all the simulations. The hydrodynamic results are presented in terms of the dimensionless streamfunction, which is defined as

$$\psi(x, y=0) = \psi(x=0, y=0) + \frac{1}{\nu}\int_{x=0}^{x} v\, dx \quad (21)$$

$$\psi(x, y) = \psi(x, y=0) - \frac{1}{\nu}\int_{y=0}^{y} u\, dy \quad (22)$$

with $\psi(x=0, y=0)$ assigned a value of zero.

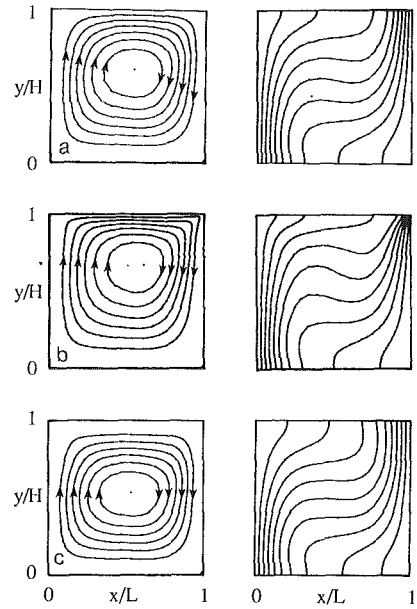

Fig. 2 Predicted streamlines (left) and isotherms (right) for (a) $\mathrm{Ra} = 10^4$, $\mathrm{Ma}_T = 0.0$, $E = 0.0$, $\psi_{\max} = 5990$; (b) $\mathrm{Ra} = 10^4$, $\mathrm{Ma}_T = 10^3$, $E = 0.0$, $\psi_{\max} = 7050$; and (c) $\mathrm{Ra} = 10^4$, $\mathrm{Ma}_T = 10^3$, $E = 0.3$, $\psi_{\max} = 5130$

Predicted Convective Hydrodynamics. Figure 2 shows predicted streamlines and isotherms for no-shear free surface boundary conditions (Fig. 2*a*, $\mathrm{Ra} = 10^4$, $\mathrm{Ma}_T = 0$, $E = 0$), thermocapillary boundary conditions (Fig. 2*b*, $\mathrm{Ra} = 10^4$, $\mathrm{Ma}_T = 10^3$, $E = 0$) and combined thermo-solutocapillary boundary conditions (Fig. 2*c*, $\mathrm{Ra} = 10^4$, $\mathrm{Ma}_T = 10^3$, $E = 0.3$, $\mathrm{Le} = 100$).

Due to the absence of free surface shear in Fig. 2(*a*), surface velocities are nonzero and the center of rotation is slightly above $y/H = 0.5$. Advection of thermal energy is enhanced at $y/H = 1.0$ relative to $y/H = 0.0$ and $\psi_{\max} = 5990$.

Inclusion of buoyancy-augmenting thermocapillary forces at the free surface leads to the flow of the first regime, as shown in Fig. 2(*b*). An effective shear is established at $y/H = 1.0$ by thermally induced surface tension variations at this location, surface velocities are increased substantially, and enhanced advection of warm temperature fluid leads to isotherm compaction at the top of the cold wall. As a result of enhanced free surface velocities, the center of rotation is higher relative to Fig. 2(*a*) and $\psi_{\max}$ is increased to 7050.

Figure 2(*c*) shows the predicted system response as solutocapillary forces, resulting from the presence of the surfactant, counteract thermocapillary forces at the free surface. The streamlines and isotherms bear a remarkable similarity to pure buoyancy flow with imposed no-slip boundary conditions at $y/H = 1.0$. The center of rotation is at $y/H \cong 0.5$, $\psi_{\max}$ is reduced to 5130 and the isotherm distribution is nearly antisymmetric about $x/L = 0.5$.

In order to understand better the coupling responsible for the results of Fig. 2, dimensionless surface velocity and surfactant concentration distributions are presented in Fig. 3.

For the case where no shear exists ($\mathrm{Ma}_T = 0$, $E = 0$, Fig. 2*a*) the dimensionless surface velocity is maximum near $x/L = 0.5$ and the surfactant is pushed to a location adjacent to the cold wall. In contrast, if thermocapillary effects are accounted for ($\mathrm{Ma}_T = 10^3$, $E = 0$, Fig. 2*b*), the free surface velocities are increased everywhere and the isotherm compaction at $x/L \cong 1.0$ leads to substantial thermocapillary-induced velocities near the cold wall. As a result, the surfactant is swept into a very small region adjacent to the cold wall and its distribution has been omitted from Fig. 3 for clarity.

In reality, surfactant concentration gradients resulting from buoyancy and thermocapillarity will induce solutocapillary

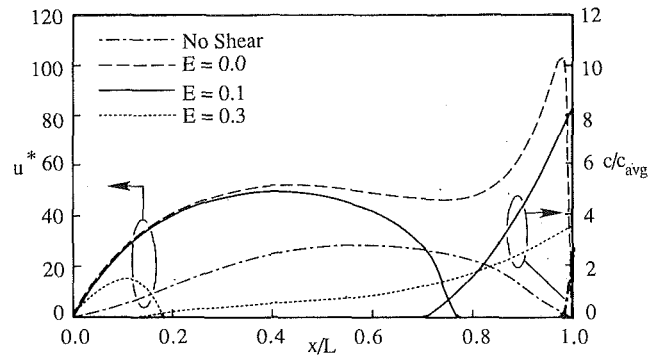

Fig. 3 Dimensionless surface velocity and concentration distributions for the predictions of Fig. 2

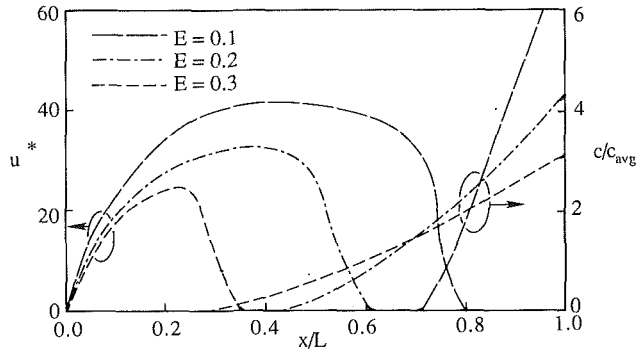

Fig. 5 Dimensionless surface velocity and concentration distributions for the predictions of Fig. 4

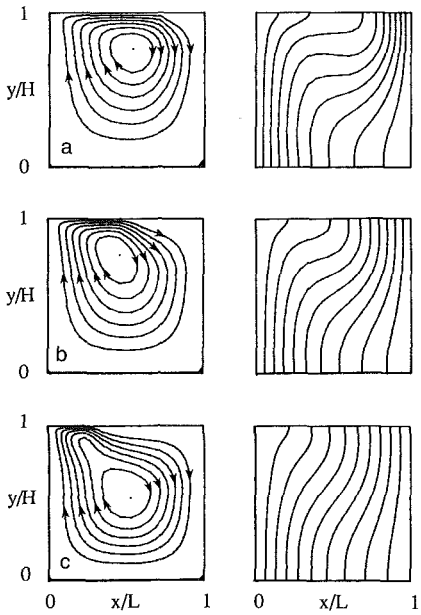

Fig. 4 Predicted streamlines (left) and isotherms (right) for $Ra = 10^3$, $Ma_T = 10^3$, (a) $E = 0.1$, (b) $E = 0.2$, and (c) $E = 0.3$. Values of ψ_{max} are 4100, 2180, and 1300 for $E = 0.1$, 0.2, and 0.3, respectively.

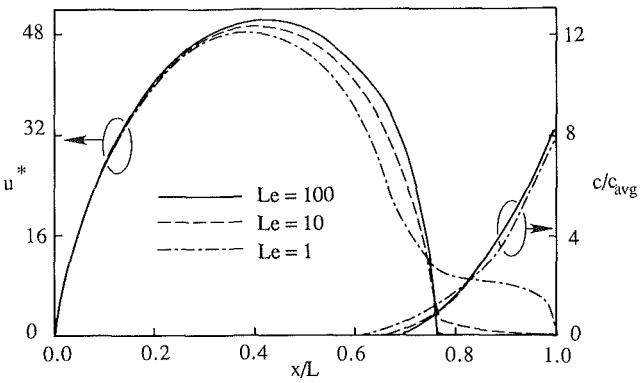

Fig. 6 Dimensionless surface velocity and concentration distributions for various Le; here, $Ra = 10^4$, $Ma_T = 10^3$, and $E = 0.1$

forces that oppose their thermal counterparts (for most liquids). The result is partial or complete surface stagnation. Dimensionless surface velocity and surfactant concentration distributions are included for two nonzero values of E in Fig. 3.

For $Ma_T = 10^3$, $E = 0.1$, the steep concentration gradients resulting from free surface advection induced by buoyancy and/or thermocapillary forces produce surface tension forces at $y/H \cong 1$ as described by equation (6). As a result, surface velocities are decreased near the cold wall, species diffusion extends the surfactants to smaller x/L, and an equilibrium condition is reached where the free surface is stagnant in the range $0.8 \leq x/L \leq 1.0$. Since its magnitude is so small relative to other velocities in the system, the surface velocity distribution in this range is not evident in Fig. 3.

As E is increased further ($Ma_T = 10^3$, $E = 0.3$, Fig. 2c), surfactant concentration gradients wield an even greater influence on the system hydrodynamics and the entire surface is stagnant except for at small x/L. Further increases in E result in an effective free surface no-slip condition at all x/L. The case of total free surface stagnation is typical for many common fluids (see Appendix).

Figure 4 includes predicted streamlines and isotherms that illustrate the role of buoyancy driven flow in the coupling process at the free surface. The dimensionless parameters associated with Fig. 4 are identical to those of Figs. 2 and 3, except Ra is reduced to 10^3 and E values are 0.1, 0.2, and 0.3 for Figs. 4(*a*), 4(*b*), and 4(*c*), respectively. The results show that solutocapillary effects again partially stagnate the free surface. Surprisingly, thermocapillary effects are more pronounced at small x/L than was evident in the results of Fig. 2.

With a reduction in buoyancy forces, circulation rates and, in turn, advection from the hot wall to the cold wall are decreased. As a result, steeper temperature gradients exist along the free surface at small x/L for $Ra = 10^3$, relative to the results associated with $Ra = 10^4$. The locally steep free surface temperature gradients induce strengthened local thermocapillary effects and the host liquid is pulled to the surface near the upper hot wall. It is subsequently returned to smaller y/H as the vicinity of the stagnant free surface is approached. Hence, local thermocapillary forces become more influential in their role of pushing the surfactant to the cold wall.

Figure 5 includes the dimensionless free surface velocity and surfactant distributions associated with Fig. 4. A comparison with Fig. 3 shows that, due to enhanced local thermocapillary forces, a decrease in Ra leads to a reduction in the amount of the free surface stagnated by solutocapillary effects. Specifically, 20 percent reductions in the stagnant free surface length are noted. Again, this reduction is attributed to the enhanced pushing action of the buoyancy-enhanced thermocapillary forces at small x/L.

As evident in the results so far, the diffusing surfactant adjusts its distribution in response to advection induced by buoyancy and thermocapillary forces and stagnates a portion of the liquid's free surface. Hence a variation in Le may lead to a change in the system hydrodynamics (Bergman, 1986).

Figure 6 includes predicted dimensionless velocity and surfactant distributions at the free surface for $Ra = 10^4$, $Ma_T = 10^3$, $E = 0.1$, and Le = 1, 10, and 100. Variations in the

species diffusion rate wield little influence on the system response. The surfactant distribution is similar for all Le (distributions for Le = 10 and 100 coincide in the range $0.8 \le x/L \le 1.0$) and the surface velocity distribution is thermocapillary-dominated in the range $0.0 \le x/L \le 0.8$. Surface velocities in the range $0.8 \le x/L \le 1.0$ are very small and adjust in accordance with the predicted surfactant distribution and equation (5).

The insensitivity of the system response to Le is due to the tendency of the surfactant distribution to adjust in order to promote relative stagnation of the liquid surface adjacent to the cold wall. As long as surface velocities near the cold wall are small relative to the thermocapillary and buoyancy driven velocities throughout the remainder of the system, the temperature distribution remains nearly unchanged. Since the surfactant concentration distribution must continue to satisfy equation (6), it is relatively insensitive to variations in Le. As a result, the hydrodynamic and heat transfer phenomena associated with the host liquid are, for all practical purposes, unaffected by Le. It should be noted that, in the limit of Le = 0 ($D = \infty$), the influence of solutocapillary forces will be negligible. This range of Le was not examined, due to the limited number of real liquids (if any) characterized by $D = \infty$.

Heat Transfer Results. As evident from the previous discussions, inclusion of solutocapillary forces in the analysis leads to significant variations in the hydrodynamics of the system, especially in the vicinity of the free surface. Furthermore, system hydrodynamics are most profoundly influenced near the cold wall, which would correspond to the solid-liquid interface in a solidification or melting application. Hence, a consideration of the resulting impact on local and overall heat transfer rates across the host liquid layer is warranted.

Hot and cold wall Nu distributions associated with the simulations of Figs. 2–5 are presented in Fig. 7. Figure 7 (a) is associated with $Ra = 10^4$ and the free surface conditions of Fig. 3. Local heat transfer rates change as the surface conditions are varied and, as expected, the modifications in Nu are most severe at the upper cold wall. The local heat transfer rates are bracketed by results for the no-slip case and the situation where only thermocapillary forces are included in the analysis. As solutocapillary forces are increased, Nu is decreased at $y/H \cong 1.0$ and slightly increased below $y/H \cong 0.65$. The results for $E = 0.3$ are nearly identical to those associated with incorporation of no-slip boundary conditions.

Figure 7 (b) includes Nu distributions associated with $Ra = 10^3$ and the free surface conditions of Fig. 5 as well as $E = 0.0$ and no-slip cases. Again, the results are bracketed by the extreme cases of imposed no-slip free surface condition and the $E = 0$ results. In contrast to the results of Fig. 7 (a), slight differences exist between the $Ma = 10^3$, $E = 0.3$ and the no-slip results and are traceable to the decreased free surface stagnation length due to decreased buoyancy effects.

Finally, consideration is given to average cavity heat transfer rates in Fig. 8. Figure 8 (a) reports $\overline{Nu}$ for Le = 100 and $Ma_T = 10^3$ while Fig. 8 (b) shows $\overline{Nu}$ for Le = 100 and $Ma_T = 250$ for a range of Ra and E. As expected, the impact of surface tension forces on heat transfer is most severe at small Bo. At larger Bo, the condition of the free surface has little influence upon heat transfer in the system. Within the range of smaller Bo, solutocapillary effects systematically decrease heat transfer rates from the $E = 0$ results to the $E = \infty$ case, which corresponds to the imposition of no-slip boundary conditions at $y/H = 1$. It is noted that Bo values of order unity are common in many materials processing applications involving melting and solidification (Oreper and Szekely, 1984).

Summary and Conclusions

A numerical investigation has been conducted to identify and quantify phenomena that are responsible for the development of no-slip free surfaces in thermocapillary-affected

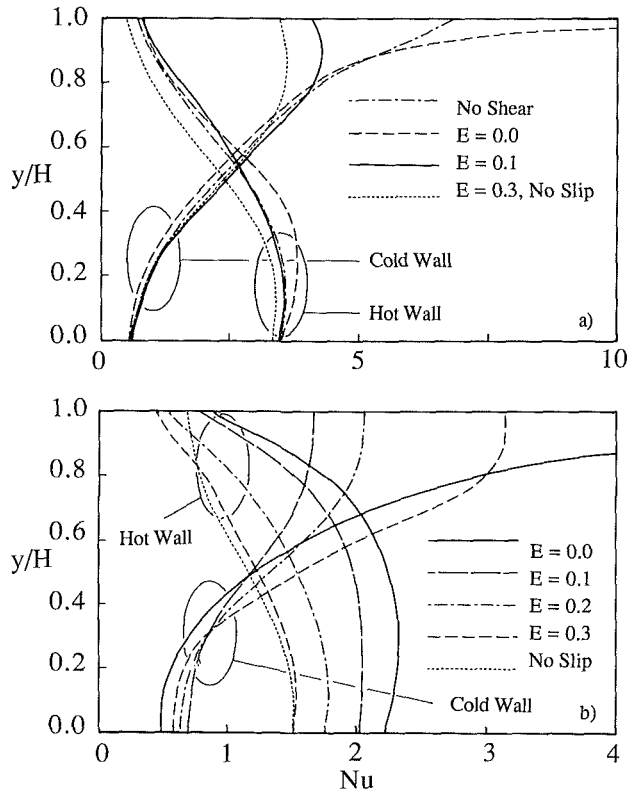

Fig. 7 Local hot and cold wall Nu distributions for (a) the predictions of Fig. 3 and (b) the predictions of Fig. 5

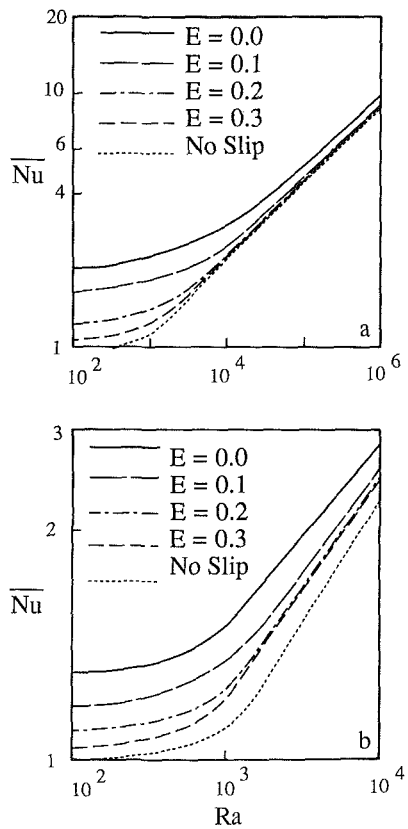

Fig. 8 Average heat transfer for various Ra and (a) $Ma_T = 10^3$ and (b) $Ma_T = 250$

flows. No-slip conditions are considered to be a third flow regime in combined buoyancy-thermocapillary flows and liquids that normally exhibit no slip boundary conditions are identified in the Appendix.

The hypothesis for no-slip boundary condition development is the counteracting role of solutocapillary forces in systems that may otherwise be thermocapillary-dominated. Surfactant concentration gradients develop along the free surface in response to bulk liquid motion and induce solutocapillary forces, which subsequently stagnate the free surface. Results show that variations in buoyancy, thermo-, and solutocapillary forces all affect the amount of free surface stagnation but variations in the species diffusion rate do not play a significant role.

The stagnating action of solutocapillary forces leads to reductions in the local and average heat transfer rates associated with thermocapillary-buoyancy convection. Decreases in the local heat transfer rate are most dramatic at the upper cold wall. Average heat transfer rates are decreased by solutocapillary forces for flows associated with small Bo.

Since the cold wall Nu distribution is most dramatically modified by thermo- and solutocapillary effects, the observed phenomena may be important in melting and solidification heat transfer. Furthermore, the role of solutal effects may be different in melting than in solidification since contaminants are often rejected from the solid phase during freezing, while species rejection is not an issue during melting. However, pure liquid issuing from a melting solid may reduce the surfactant concentration adjacent to the solid–liquid interface, allowing significant thermocapillary induced flow adjacent to the solid–liquid interface. Finally, if solidification of alloys is considered, the surfactant-induced solutocapillary effects may be overwhelmed by surface tension forces due, ultimately, to species rejection from the solid phase. Solutocapillary forces resulting from the presence of multiple species gradients along the free surface may, in fact, be common.

Acknowledgments

Support for this research by the National Science Foundation under grant No. CBT-8552806 is gratefully acknowledged. Computational facilities were provided by the Department of Mechanical Engineering at the University of Texas at Austin.

References

Bergman, T. L., 1986, "Numerical Prediction of Double-Diffusive Marangoni Convection," *Physics of Fluids*, Vol. 29, pp. 2103–2108.

Bergman, T. L., and Ramadhyani, S., 1986, "Combined Buoyancy- and Thermocapillary-Driven Convection in Open Square Cavities," *Numerical Heat Transfer*, Vol. 9, pp. 441–451.

Camel, D., Tison, P., and Favier, J. J., 1986, "Marangoni Flow Regimes in Liquid Metals," *Acta Astronautica*, Vol. 13, pp. 723–726.

Carpenter, B., and Homsy, G. M., 1985, "The Thermocapillary Flow in a Two-Dimensional Slot. Part 2, Partially Contaminated Interfaces," *Journal of Fluid Mechanics*, Vol. 155, pp. 429–439.

Chun, C. H., 1980, "Marangoni Convection in a Floating Zone Under Reduced Gravity," *Journal of Crystal Growth*, Vol. 48, pp. 600–610.

Davis, R. E., and Acrivos, A., 1966, "The Influence of Surfactant on the Creeping Motion of Bubbles," *Chemical Engineering Science*, Vol. 21, pp. 681–685.

De Vahl Davis, G., 1983, "Natural Convection of Air in a Square Cavity: A Bench Mark Numerical Solution," *International Journal of Numerical Methods in Fluids*, Vol. 3, pp. 249–261.

Heiple, C. J., and Roper, J. R., 1982, "Mechanism for Minor Element Effect on GTA Fusion Zone Geometry," *Welding Research*, Vol. 61, pp. 97s–102s.

Homsy, G. M., and Meiburg, E., 1984, "The Effect of Surface Contamination on Thermocapillary Flow in a Two-Dimensional Slot," *Journal of Fluid Mechanics*, Vol. 139, pp. 443–459.

Hurle, D. T. J., and Jakeman, E., 1981, "Introduction to the Techniques of Crystal Growth," *Physico Chemical Hydrodynamics*, Vol. 2, pp. 237–244.

Kirdyashkin, A. G., 1984, "Thermogravitational and Thermocapillary Flows in a Horizontal Liquid Layer Under the Conditions of a Horizontal Temperature Gradient," *International Journal of Heat and Mass Transfer*, Vol. 27, pp. 1205–1218.

Kou, S., 1987, *Welding Metallurgy*, Wiley, New York.

Legros, J. C., Limbourg-Fontaine, M. C., and Petre, G., 1984, "The Influence of a Surface Tension Minimum as a Function of Temperature on the Marangoni Convection," *Acta Astronautica*, Vol. 11, pp. 143–147.

Levich, V. G., 1962, *Physicochemical Hydrodynamics*, Prentice-Hall, Englewood Cliffs, NJ.

Levich, V. G., and Krylov, V. S., 1969, "Surface Tension Driven Phenomena," *Annual Review of Fluid Mechanics*, Vol. 1, pp. 293–316.

McNeil, T. J., Cole, R., and Subramanian, R. S., 1985, "Surface Tension Driven Flow in a Glass Melt," *Journal of the American Ceramics Society*, Vol. 68, pp. 254–259.

Patankar, S. V., 1980, *Numerical Heat Transfer and Fluid Flow*, Hemisphere Publishing Corp., Washington, DC.

Platten, J. K., and Villers, D., 1987, "On Thermocapillary Flows in Containers With Differentially Heated Side Walls," *Proceedings of the NATO Advanced Study Institute at La Rabida*, Plenum Press, New York.

Oreper, G., and Szekely, J., 1984, "Heat- and Fluid-Flow Phenomena in Weld Pools," *Journal of Fluid Mechanics*, Vol. 147, pp. 53–79.

Savic, P., 1953, "Circulation and Distortion of Liquid Drops Falling Through a Viscous Medium," Report No. MT-22, Division of Mechanical Engineering, National Research Council of Canada.

Schwabe, D., Scharmann, A., Presser, F., and Oeder, R., 1978, "Experiments on Surface Tension Driven Flow in Floating Zone Melting," *Journal of Crystal Growth*, Vol. 43, pp. 305–312.

Shinoda, K., 1963, *Colloidal Surfactants*, Academic Press, New York.

Stanek, V., and Szekely, J., 1970, "The Effect of Surface Driven Flows on the Dissolution of a Partially Immersed Solid in a Liquid—Analysis," *Chemical Engineering Science*, Vol. 25, pp. 699–715.

Villers, D., and Platten, J. K., 1985, "Marangoni Convection in Systems Presenting a Minimum in Surface Tension," *Physico Chemical Hydrodynamics*, Vol. 6, pp. 435–451.

Zehr, R. L., Chen, M. M., and Mazumder, J., 1987, "Thermocapillary Convection of a Differentially Heated Cavity at High Marangoni Numbers," presented at the National Heat Transfer Conference, Pittsburgh, Paper No. 87-HT-29.

APPENDIX

Experiments have been performed to visualize the flows of regimes 1 and 3 qualitatively and to categorize the propensity of various fluids to exhibit the flow of a particular regime.

A test cell was constructed using multipass copper heat exchangers to impose isothermal boundary conditions on the sides of the test fluid. The side walls were separated by 10 mm to insure a small Bo and, in turn, induce substantial thermocapillary effects, relative to buoyancy. Two-dimensional flow was approximated by making the test cell deep relative to its width (65 mm). An air gap of approximately 2 mm was placed above the liquid layer to minimize evaporation and convection effects.

The test fluid was seeded with aluminum particles and illuminated with a vertical sheet of laser light. Time exposure photography was used to visualize streamlines.

The surfactant in question is absorbed from the environment or leached from test cell components. As such, its composition and average concentration are unknown. In order to illustrate the tendency of common fluids to exhibit the flow of

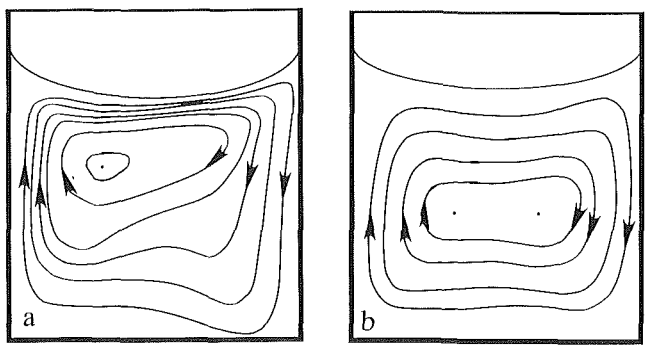

Fig. 9 Experimentally observed streamlines for (*a*) ethanol and (*b*) water

regime 3, precautions were taken to avoid contamination of the host liquid and included: (1) covering all interior surfaces of the test cell with teflon or glass, (2) ultrasonically cleaning the test cell for four hours, and (3) triple rinsing with triple-distilled water prior to each flow visualization experiment.

Figure 9 shows streamlines for ethanol and water, which were sketched from the photographs. (The original photographs are not presented since the free surface curvature causes local overexposure of the film and their quality is poor.) Each condition is characterized by $\mathrm{Ra} = 10^5$ and Ma_T values of 1.4×10^4 and 1.0×10^4 for ethanol and water, respectively. The value of E is unknown.

Ethanol (Fig. 9*a*) clearly exhibits regime 1 flow as the center of rotation is above $y/H = 0.5$, implying relatively large free surface velocities. As is well known, however, water (Fig. 9*b*) exhibits regime 3 flow as the center of rotation is at $y/H = 0.5$.

Table 1 summarizes the tendency of various host liquids to fall into a specific flow regime. Entries in the table without references were identified experimentally and the appearance of a fluid in multiple regimes indicates that extreme precautions (beyond those taken here) are necessary to avoid regime 3 behavior.

Table 1 Regime behavior of various liquids

Regime 1	Regime 2	Regime 3
Water above 4°C[a]	Water below 4°C[a]	Water
Fluorocarbons	Aqueous alcohol solutions[f]	*n*-Octadecane
Sodium nitrate[b]	Binary metal alloys[e]	*n*-Hexadecane
Silicon oil[c]		Decanol
Molten glass[d]		
Molten tin[e]		

[a]Platten and Villers, 1987.
[b]Schwabe et al., 1978.
[c]Chun, 1980.
[d]McNeil et al., 1985.
[e]Camel et al., 1986.
[f]Legros et al., 1984.

Effects of the Heat Transfer at the Side Walls on Natural Convection in Cavities

Y. Le Peutrec

G. Lauriat

Laboratoire de Thermique,
C.N.A.M.,
75141 Paris Cedex 03,
France

Numerical solutions are obtained for fluid flows and heat transfer rates for three-dimensional natural convection in rectangular enclosures. The effects of heat losses at the conducting side walls are investigated. The problem is related to the design of cavities suitable for visualizing the flow field. The computations cover Rayleigh numbers from 10^3 to 10^7 and the thermal conductance of side walls ranging from adiabatic to commonly used glazed walls. The effect of the difference between the ambient temperature and the average temperature of the two isothermal walls is discussed for both air and water-filled enclosures. The results reported in the paper allow quantitative evaluations of the effects of heat losses to the surroundings, which are important considerations in the design of a test cell.

Introduction

Natural convection in rectangular enclosures heated on one vertical wall and cooled on the opposite one has received a great deal of attention in recent years. Numerous numerical results have been presented for the laminar regime and several studies have reported on two- and three-dimensional numerical analysis of the turbulent flow regime using the k–ϵ model (Fraikin et al., 1980; Ozoe et al., 1986). These models contain empirical constants that must be experimentally determined. However, due to the lack of available experimental data for the turbulent quantities, there are differences of opinion on the correct values of these constants. Therefore, additional experimental works on natural convection in enclosures with basic geometries are required to improve the turbulence models, as well as to evaluate the accuracy of numerical solutions at high Rayleigh numbers.

Although natural convection in enclosures is necessarily three dimensional, it is clear that, at a first stage, experiments should be performed in cavities where the time-averaged flows in the central part can be approximated as two dimensional, in order to reduce the complexity of the analysis. Since flow visualization or LDA velocity measurements require the use of glazed side walls, care should be taken to reduce heat losses at the side walls to a negligible level, especially when using gases or low-conductivity fluids as working fluids, since these losses are responsible for a lack of two dimensionality in the flow. In addition to the dimensions of the rectangular box, hot and cold wall temperatures, T_h and T_c, and thermophysical properties of the working fluid, the evaluation of the heat losses requires the specification of two key parameters: the thermal resistance of the walls and the ambient temperature T_a.

However, from an overall view of what has been accomplished experimentally, it appears that such data are generally not reported, although noticeable end effects were mentioned; for example, by Eckert and Carlson (1961), Mynett and Duxbury (1974), Morrison and Tran (1978) and, more recently, by Cheesewright and Zlai (1986). Qualitative discussion of the effect of thermal boundary conditions and measurements of the heat transfer in air-filled cavities with an aspect ratio of 5 and for various bounding walls were also presented by ElSherbiny et al. (1982). Despite the fact that their work has emphasized the need for reporting all the parameters representing the interaction of wall conduction and fluid convection (also including radiative interaction for transparent and semi-transparent fluids), the relevant data have not been specified in the more recent experimental results. As a consequence, difficulties are still encountered when comparing numerical and experimental solutions, especially for gas-filled enclosures of moderate aspect ratio.

The present work is the second part of a numerical study intended to provide data for the design of experimental systems for the basic geometry. We use a three dimensional–finite difference scheme to solve the governing equations with continuity and momentum equations written in terms of vector potential and vorticity. In a previous paper (Le Peutrec and Lauriat, 1987a), computations carried out for air and water, the most commonly used working fluids, have shown that the difference in Prandtl number produces weak effects on both the flow and the heat transfer in the laminar regime for cavities with four adiabatic bounding walls. Also, it has been demonstrated that the flow within a cavity with longitudinal aspect ratio $A_y = 2$ can be assumed as two dimensional provided that the side walls are perfectly insulated; for such a case, the three dimensional motion is negligible in regions away from the side walls in the range of Rayleigh number from 10^3 to 10^7. In the present study, we focus on the effects of heat losses at the vertical side walls on natural convection flow and heat transfer in enclosures with a cross-sectional aspect ratio $A_z = 1$ and adiabatic horizontal walls. The results are for air and water and the interaction between the boundaries and the fluid flow is discussed for a wide range of Rayleigh numbers in the laminar regime.

Mathematical Formulation

A schematic diagram of the physical situation to be investigated is shown in Fig. 1. The vertical walls of height H located at $x = 0$ and $x = D$ are isothermal but at different temperatures, T_h and T_c, respectively. The horizontal walls of width D are insulated while conduction heat losses through the side walls at $y = 0$ and $y = L$ are allowed. The present study is conducted in the framework of the Boussinesq approximation. Therefore, the fluid properties are assumed to be constant except the density in its contribution to the bouyancy force in the momentum equation. The fluid is considered incompressible and the flow is assumed laminar and three dimensional. The dependent variables appearing in the equations governing the conservation of mass, momentum, and energy are normalized by choosing D, the distance between the

Contributed by the Heat Transfer Division for publication in the JOURNAL OF HEAT TRANSFER. Manuscript received by the Heat Transfer Division July 28, 1988; revision received June 6, 1989. Keywords: Conjugate Heat Transfer, Enclosure Flows, Natural Convection.

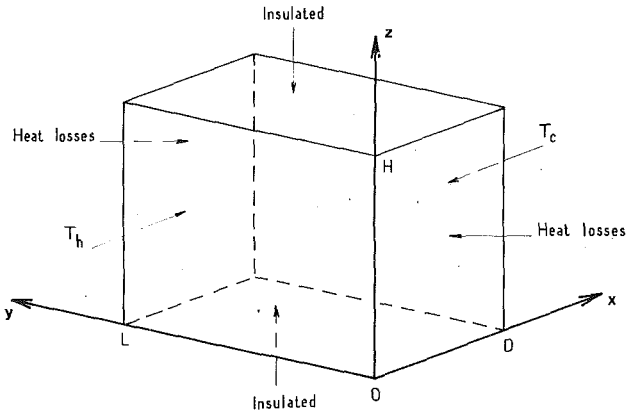

Fig. 1 Schematic diagram of the cavity

isothermal walls, as a scale factor for length, a/D^2 and $\rho_0 a^2/D^2$ as scale factors for time and pressure, respectively. The local temperature difference $(T-T_0)$, where T_0 is the average temperature of the isothermal walls, is scaled by temperature difference, $\Delta T = T_h - T_c$. Then the dimensionless governing equations become

$$\nabla \mathbf{V} = 0 \tag{1}$$

$$\frac{\partial \mathbf{V}}{\partial t} + \mathbf{V} \cdot \nabla \mathbf{V} = -\nabla P + \mathrm{Pr} \nabla^2 \mathbf{V} + \mathrm{RaPr}\theta \mathbf{k} \tag{2}$$

$$\frac{\partial \theta}{\partial t} + \nabla \cdot (\mathbf{V}\theta) = \nabla^2 \theta \tag{3}$$

where $\mathbf{k}$ is the unit vector in the direction opposite to the gravitational force, P is the local pressure minus the hydrostatic component, Ra is the Rayleigh number ($\mathrm{Ra} = g\beta D^3 \Delta T/a\nu$), and Pr is the Prandtl number. Throughout the paper, the dimensionless length and height of the enclosure are denoted A_y and A_z, respectively ($A_y = L/D$, $A_z = H/D$, parallelepiped enclosure $1 \times A_y \times A_z$). The corresponding dimensionless boundary conditions are as follows:

- rigid and impermeable boundaries: $\mathbf{V} = 0$ on all boundaries
- thermal boundary conditions:

$$\theta(0, y, z) = 0.5 \tag{4}$$

$$\theta(1, y, z) = -0.5 \tag{5}$$

$$\frac{\partial \theta}{\partial z} = 0 \qquad \text{at } z = 0, A_z \tag{6}$$

$$\frac{\partial \theta}{\partial z} = \pm C(\theta - \theta_a) \text{ at } y = 0, A_y \tag{7}$$

where C is the thermal conductance of the side walls and θ_a the dimensionless ambient temperature.

The momentum equations were recast in terms of the vorticity vector, $\Omega = \nabla \times \psi$, and a vector ψ, which is a solenoidal potential for velocity, $\mathbf{V} = \nabla \times \psi$. Then equations (1) and (2) may be reformulated into the form

$$\Omega = -\nabla^2 \psi \tag{8}$$

$$\frac{\partial \Omega}{\partial t} + \nabla \times (\Omega + \mathbf{V}) = \mathrm{Pr} \nabla^2 \Omega + \mathrm{RaPr} \nabla \times (\theta \mathbf{k}) \tag{9}$$

Boundary conditions for ψ and Ω were derived from the velocity boundary conditions. The condition of impermeability restated in terms of ψ implies that ψ is normal to the boundaries and that the normal derivative of its normal component is zero (Mallinson and de Vahl Davis, 1977). An example of the form of the boundary condition for ψ is given below:

Nomenclature

a = thermal diffusivity, $m^2 s^{-1}$
A_y = longitudinal aspect ratio = L/D
A_z = vertical aspect ratio = H/D
C = dimensionless thermal conductance of the side walls (equation (23))
C' = dimensional group defined as $C' = D/(R + 1/h_e)$, $Wm^{-1}K^{-1}$
D = enclosure width, m
H = enclosure height, m
h_e = external heat transfer coefficient, $Wm^{-2}K^{-1}$
$\mathbf{k}$ = unit vector in the z direction
L = enclosure length, m
$\bar{\mathrm{Nu}}$ = average Nusselt number
$\bar{\mathrm{Nu}}_{2D}$ = average Nusselt number for two-dimensional flow
$\Delta\bar{\mathrm{Nu}}$ = difference in average Nusselt numbers at the hot and cold walls = $\bar{\mathrm{Nu}}_h - \bar{\mathrm{Nu}}_c$
P = dimensionless pressure
Pr = Prandtl number = ν/a
$\mathbf{q}(M)$ = dimensionless heat flux density
Q = average heat flux
R = thermal resistance of the side walls, m^2KW^{-1}
Ra = Rayleigh number = $g\beta D^3 \Delta T/a\nu$
t = dimensionless time
T = temperature, K
T_o = reference temperature = $(T_h + T_c)/2$, K
ΔT = temperature = $T_h - T_c$, K
$\mathbf{V}$ = dimensionless velocity vector
u, v, w = dimensionless velocity components
x, y, z = dimensionless coordinates, Fig. 1
β = thermal expansion coefficient, K^{-1}
θ = dimensionless temperature = $(T - T_o)/\Delta T$
θ_a = dimensionless ambient temperature
λ_f = thermal conductivity of the fluid, $Wm^{-1}K^{-1}$
ν = kinematic viscosity, $m^2 s^{-1}$
ψ = potential vector
ψ_x, ψ_y, ψ_z = components of the potential vector
Ω = rotational vector
$\Omega_x, \Omega_y, \Omega_z$ = components of the rotational vector

Subscripts

a = ambient
ad = adiabatic
c = cold
h = hot
p = refers to average heat flux at the side walls
w = wall
$\parallel$ = refers to surfaces parallel to the isothermal walls
$\perp$ = refers to surfaces perpendicular to the isothermal walls

$$\frac{\partial \psi_x}{\partial x}=0, \quad \psi_y=\psi z=0 \text{ at } x=0,\ 1 \tag{10}$$

At non-slip surfaces, the tangential derivatives of the velocity components vanish. The boundary conditions on vorticity follow directly and may be exemplified at the wall $x=0$ by

$$\Omega_x=0 \tag{11}$$

$$\Omega_y=-\partial^2\psi_y/\partial_x^2, \quad \Omega_z=-\partial^2\psi_z/\partial_x^2 \tag{12}$$

Following Mallinson and de Vahl Davis (1973), equation (11) and (after integration) equation (12) are used as boundary conditions for solving the vorticity equation.

Heat Transfer

For three-dimensional flows, great attention must be paid to the heat transfer results. As will be discussed in the following section, discrepancies in the heat fluxes at the isothermal walls can be used as a measure of the three dimensionality of the flows for the basic geometries. The nondimensional local heat flux at a given point $M(x, y, z)$ is defined as

$$\mathbf{q}(M)=-\nabla\theta+\mathbf{V}\theta \tag{13}$$

The average heat flux for a surface S with $\mathbf{n}$ as a unit vector normal to the elementary surface ds is

$$Q_S=\frac{1}{S}\int_S(-\nabla\theta+\mathbf{V}\theta)\cdot\mathbf{n}ds \tag{14}$$

In this paper, we discuss the heat transfer rate only on vertical surfaces parallel or perpendicular to the isothermal walls. The nondimensional average heat flux through a section of $x=$ const is written as

$$Q_{\parallel}(x)=\frac{1}{A_yA_z}\int_0^{A_y}\int_0^{A_z}\left(-\frac{\partial\theta}{\partial x}+u\theta\right)dydz \tag{15}$$

At $x=0$ and $x=1$, we define the mean Nusselt number on the isothermal walls as

$$\bar{\mathrm{Nu}}_h=Q_{\parallel}(0) \tag{16a}$$

$$\bar{\mathrm{Nu}}_c=Q_{\parallel}(1) \tag{16b}$$

For adiabatic side walls ($C=0$ in equation (7)), the average heat flux is independent of x at steady state. Therefore

$$Q_{\parallel}(x)=\bar{\mathrm{Nu}}_h=\bar{\mathrm{Nu}}_c=\bar{\mathrm{Nu}}_w \quad 0\le x\le 1 \tag{17}$$

When we want to designate the average heat flux through a vertical section perpendicular to the isothermal walls of $y=$ const, we write

$$Q_{\perp}(y)=\frac{1}{A_z}\int_0^{A_z}\int_0^{1}\left(-\frac{\partial\theta}{\partial y}+v\theta\right)dxdz \tag{18}$$

and

$$Q_{\perp}(y)=0 \quad \text{if} \quad C=0$$

In addition to the thermal conductance, the level of the ambient temperature greatly affects the flow structure and heat transfer rates. Mathematically, the presence of a nonzero constant in equation (7) leads to a loss of the centrosymmetry properties of the solution. For convenience, we can distinguish the two following cases:

(a) $\theta_a=0$: The mean temperature $T_0=(T_h+T_c)/2$ is equal to the ambient temperature and, whatever the C value, the solution is centrosymmetric provided the flow is laminar and stationary. Consequently

$$\bar{\mathrm{Nu}}_h=\bar{\mathrm{Nu}}_c=\bar{\mathrm{Nu}}_w \tag{19}$$

and

$$Q_{\perp}(y)=0 \quad 0\le y\le A_y \tag{20}$$

Indeed, the average heat fluxes through each section of $y=$ const are zero because the heat input in the regions near the cold wall exactly compensates for the heat output near the hot wall. The heat transfer at the side walls influences $Q_{\parallel}(x)$ only. Variations in $Q_{\parallel}$ show the three dimensionality of the flow.

(b) $\theta_a\neq 0$: The difference between the total heat fluxes transferred at the isothermal walls matches the heat losses through the side walls. Consequently, for identical thermal boundary conditions at the side walls, a heat flux balance reads

$$|\bar{\mathrm{Nu}}_h-\bar{\mathrm{Nu}}_c|A_y=2Q_p \tag{21}$$

where

$$Q_p=Q_{\perp}(0)=Q_{\perp}(A_y) \tag{22}$$

Numerical Solution

Various numerical procedures have been used to solve the equations governing natural convection flows in cavities. In many previous papers, it has been shown that the transport terms in the momentum and energy equations must be represented at least with a second-order accuracy in order not to introduce false diffusion. For this purpose, accurate numerical methods such as pseudo-spectral methods (Le Quére and Alziary de Roquefort, 1985; Haldenwang and Labrosse, 1986) or improved finite element and finite difference methods (Upson and al., 1980; Lauriat and Altimir, 1985) were employed. However, comparisons with previously published results show that finite difference methods with a formal second-order accuracy provide extremely good representation of the flows in the whole extent of the laminar regime (Le Peutrec and Lauriat, 1987b).

The discretization of the governing equations can be achieved by using either a control volume finite-difference procedure with staggered grids or Taylor series expansions. No clear consensus has so far emerged about the best method, especially when using nonuniform meshes to increase the resolution near the walls. In this work, coordinate stretching transformations have been applied to the three coordinates. Accordingly, the physical coordinates are transformed using one-dimensional exponential stretch $x=x(p)$, $y=y(q)$, and $z=z(r)$. For example, the x-grid points are determined as a function of the equally divided coordinate p as follows:

$$x=0.5(e^{bp}-1)/(e^{0.5b}-1) \qquad 0\le p\le 0.5 \tag{23}$$

$$x=1.-[0.5(e^{b(1-p)}-1)/(e^{0.5b}-1)] \qquad 0.5\le p\le 1 \tag{24}$$

As an illustrative example, the equation for the x component of the vorticity vector is:

$$\frac{\partial\Omega_p}{\partial t}+A_q\frac{\partial(v\Omega_p)}{\partial q}+A_r\frac{\partial(w\Omega_p)}{\partial r}=\mathrm{Pr}\left[A_p^2\frac{\partial^2\Omega_p}{\partial p^2}+B_p\frac{\partial\Omega_p}{\partial p}+A_q^2\frac{\partial^2\Omega_p}{\partial q^2}+B_q\frac{\partial\Omega_p}{\partial q}+A_r^2\frac{\partial^2\Omega_p}{\partial r^2}+B_r\frac{\partial\Omega_p}{\partial r}\right]+\mathrm{RaPr}A_q\frac{\partial\theta}{\partial q}+A_q\frac{\partial(u\Omega_q)}{\partial q}+A_r\frac{\partial(u\Omega_r)}{\partial r} \tag{25}$$

Then, the vorticity and vector potential equations were discretized using Taylor series expansions. A control volume formulation was employed for the energy equation because it works well with respect to the energy conservation properties. Central difference approximations were used for all the spatial derivatives.

The time integration was performed with a standard ADI scheme. The resulting set of algebraic finite difference equations are tridiagonal and a vectorized version of the Thomas algorithm was employed for the solutions. The convergence

Table 1 Average Nusselt numbers computed with various grids and stretching parameters (Haldenwang and Labrosse, 1986)

Ra	Grid \ b	0	1	2	3	4	5	6	Ref
10^5	21	4.407	4.365	4.361	4.376	4.398	4.422	4.446	.....
	31	4.350	4.344	4.348	4.356	4.366	4.376	4.385	
10^6	31	8.856	8.710	8.667	8.665	8.687	8.710	8.731	8.61
	41	8.704	8.660	8.651	8.657	8.670	8.681	8.693	
10^7	41	17.42	16.86	16.47	16.40	16.40	16.43	16.49	16.12

criterion for steady state was based on the variations of the maximum value of the vorticity components and by monitoring the overall energy balance at each time step.

Computations were carried out on a series of grids in order to determine the minimum number of meshes and the optimum stretching parameter required to obtain accurate enough solution. An example of grid size study is shown in Table 1 for a cubical air-filled enclosure. The same stretching parameters were used in each direction. The value of b should be adjusted so that at least two grid points are located between the walls and the maximum velocity. It should be noted that the stretching parameters should never exceed $b \cong 5$ in order to suppress numerical instabilities in the central part of the cavity. Such effects are closely linked to the size ratio between the largest and the smallest mesh. From the results reported in Table 1, it can be concluded that a grid of $31 \times 31 \times 31$ with $b = 3$ represents a reasonable compromise between accuracy and computing cost for $\mathrm{Ra} = 10^6$ while a $41 \times 41 \times 41$ mesh with $b = 4$ can be employed at $\mathrm{Ra} = 10^7$. For comparison purposes, the results recently computed using a spectral method (Haldenwang and Labrosse, 1986) are also reported in Table 1. As can be seen, a fairly good agreement is obtained for the highest Rayleigh number considered in the present work ($\mathrm{Ra} = 10^7$).

Using a CRAY2 supercomputer, the solution for 41 grid points in each direction took 100 s to accomplish 100 time steps; about 1000 time steps are needed to achieve steady-state results at $\mathrm{Ra} = 10^7$ when the solution obtained at $\mathrm{Ra} = 10^6$ is used as the initial condition. When increasing the longitudinal aspect ratio, initial calculations were carried out for a cubical enclosure and the stretching parameter in the y direction was decreased to insure a sufficient grid fineness over the core of the flow. Therefore, the grid resolution was decreased in that direction and the solutions for large A_y values suffer from the highest inaccuracies.

Results and Discussion

The effects of heat losses through conducting side walls are discussed both for air and water, the most generally used working fluids. In a previous study (Le Peutrec and Lauriat, 1987b), it has been shown that the heat transfer rate was weakly dependent upon the Prandtl number of the fluid in the laminar regime for $0.7 \le \mathrm{Pr} \le 7$ and adiabatic side walls. Therefore, the numerical predictions show that water can be used as the working fluid instead of air to investigate heat transfer by natural convection in cavities of smaller sizes at Rayleigh numbers up to $\mathrm{Ra} = 2 \times 10^7$. However, it should be noted that larger effects of the Prandtl number could be seen on the flow structure at much higher Rayleigh numbers since increases of Pr lead to decreasing influences of the transport terms in the momentum equation. For example, the threshold for oscillatory convection is a function of the Prandtl number, as discussed by Gill and Davey (1969).

The objectives of the present work being to bring quantitative information for the design of test cells, care must be taken when discussing the results in terms of dimensionless parameters. Indeed, their variations should be restricted within the ranges of practical application. In the following sections, special attention will be paid to the dimensionless conductance of the side walls defined as

$$C = \frac{D}{\lambda_f (R + 1/h_e)} \tag{26}$$

where R is the thermal resistance based on the thickness and effective thermal conductivity of the side walls. Heat transferred to the surroundings by convection and radiation is represented by a uniform heat transfer coefficient h_e, whose value is of the order of 5 $\mathrm{W \cdot m^{-2} K^{-1}}$ (Kirkpatrick and Bohn, 1986). Since C is based on the thermal conductivity of the working fluid, its value is much greater for a gas-filled cavity than for a liquid-filled cavity. Therefore, for a designed test cell, the effects of side losses increase when it is filled with a fluid of low thermal conductivity. In addition, from a comparison of the thermophysical properties of air and water, it can be readily shown that enclosures of larger size should be used when using air at atmospheric pressure. By taking these two effects into account, typical C values for air are found to be roughly 50 times greater than for water. Indeed, the thermal conductivity of air is about 20 times smaller and a two to three times wider spacing should be used to obtain the same Rayleigh number at atmospheric pressure and temperature differences compatible with the Boussinesq approximation ($\Delta T < 30$ K for air and $\Delta T < 5$ K for water).

Figure 2 shows the variations in the Nusselt numbers at the hot wall and at the cold wall as a function of C for cubical enclosures filled with air or water. The differences $\Delta \bar{\mathrm{Nu}} = \bar{\mathrm{Nu}}_h - \bar{\mathrm{Nu}}_c$ are also presented ($\Delta \bar{\mathrm{Nu}} = 2Q_p$ for a cubical enclosure, equation (21)). The results are for $\mathrm{Ra} = 10^3$, 10^5, 5×10^6 and the cold wall temperature matches the ambient temperature ($\theta_a = -0.5$), as it was done in the experimental work of Bajorek and Lloyd (1982), for example. For a given set of input parameters, it can be deduced from equation (7) that this θ_a value yields maximum effects of the heat losses through the side walls. For $C = 10^{-2}$, the side walls may be considered as adiabatic. For each Rayleigh number, the predicted $\bar{\mathrm{Nu}}_h$ increases with C while $\bar{\mathrm{Nu}}_c$ decreases, which is expected since the side wall temperatures approach θ_a asymptotically as $C \to \infty$. At the lowest Ra, the effects of C are largest in relative value, but the convective motion has very little influence on the heat transfer rate. In that case, the present results agree very well with calculations performed for two dimensional conductive transfer in a horizontal cross section with two isothermal walls and the boundary conditions given by equation (7) applied at the two other walls. Also, the effect of the difference in Prandtl numbers for air and water is negligibly small for $\mathrm{Ra} < 0^5$. When increasing Ra, $\Delta \bar{\mathrm{Nu}}$ increases dramatically, especially for $C > 10$. It should be noted that opposite though similar variations are shown for $\bar{\mathrm{Nu}}_c$ and $\bar{\mathrm{Nu}}_h$ in the strong convective regime. A week effect of Pr can be seen for $\mathrm{Ra} \ge 10^5$ because the convective terms in the momentum equation become increasingly important. However, it should be noted that the Pr effects remain in the range of experimental uncertainties and have very little influence on $\Delta \bar{\mathrm{Nu}}$ as C increases from 10^{-2} to 10. Therefore, it can be concluded that the effects of variations in Prandtl number in the range [0.7, 7] are similar for adiabatic and conducting side walls. On the other hand, it is evident that the thermal conductivity of the working fluid has a strong effect on $\Delta \bar{\mathrm{Nu}}$.

From these results, it can be concluded that a C value less than about one should be retained in order to maintain the effects of the side losses within acceptable limits. It is also imperative to record both the power supplied to the heaters and the heat flux transferred to the cold plate of an experimental apparatus in order to check the reliability of the

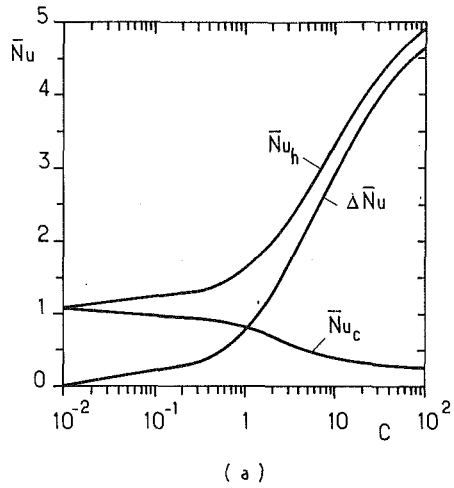

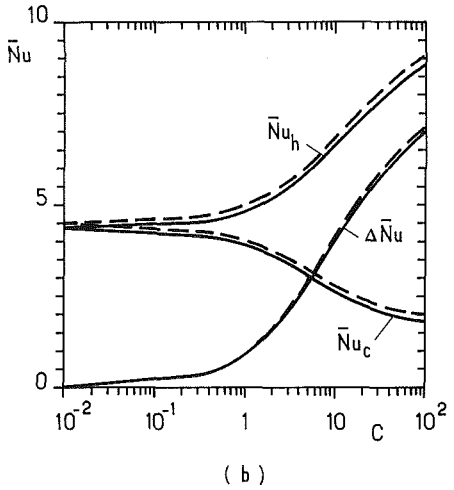

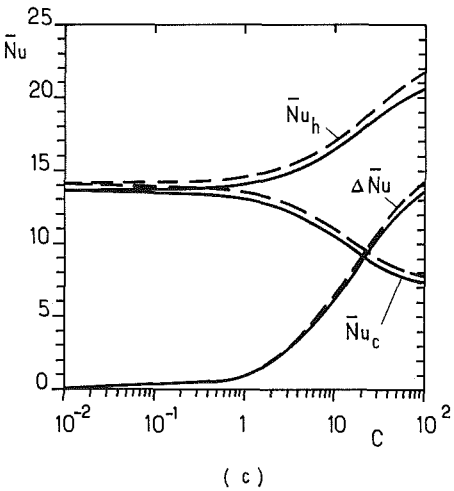

Fig. 2 Variations of the Nusselt numbers at the isothermal walls of a cubical enclosure as a function of the thermal conductance of the side walls at various Ra and $\theta_a = -0.5$ (——— air, ---- water): *(a)* $Ra = 10^3$, *(b)* $Ra = 10^5$, *(c)* $Ra = 5 \times 10^6$

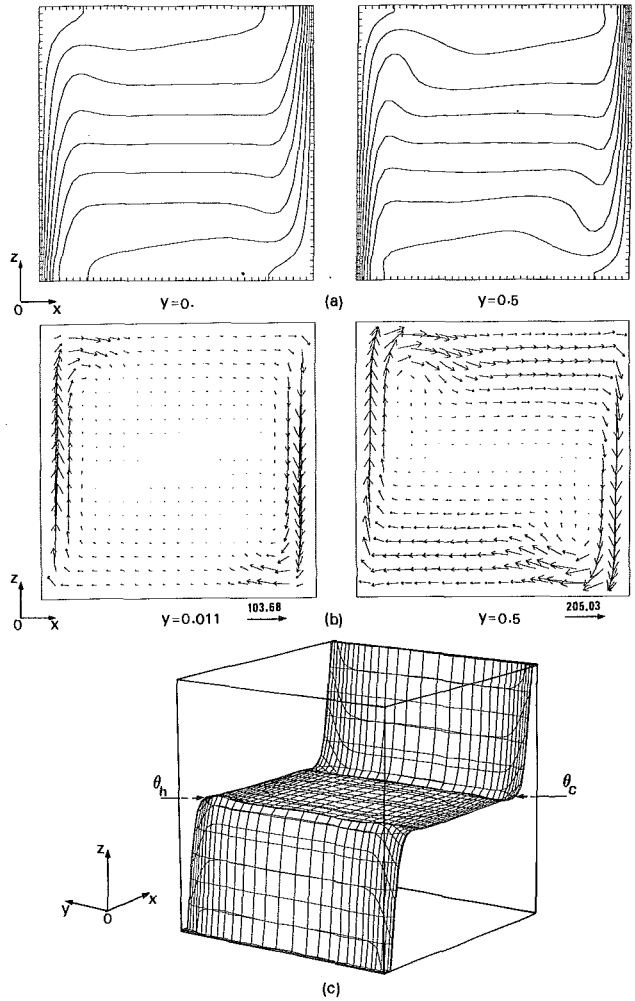

Fig. 3 Temperature distributions *(a)* and velocity vectors projected in vertical cross sections *(b)*. Three-dimensional view of the isotherm $\theta = 0$ *(c)*. Cubical enclosure with adiabatic side walls ($C = 0$) filled with air at $Ra = 10^6$.

measurements. Since the above conclusion has been shown valid independently of the Prandtl number, it follows that the minimum thermal resistance of the side walls should be about $R = 1.5\ D - 0.2$ ($m^2K \cdot W^{-1}$) and $R = 40\ D - 0.2$ ($m^2K \cdot W^{-1}$) for water and air, respectively. It can be deduced that highly thermally insulated side walls should be used for cavities filled with air or with fluids of low thermal conductivity.

The above discussed discrepancies in Nusselt numbers at the isothermal walls can be used as an indication of the strength of the three-dimensional motion produced by the heat losses at the side walls. In Figs. 3–6, we present the contours of isotherms, vertical views of velocity vectors for vertical planes of constant y as well as three-dimensional plots of the isotherm $\theta = 0$ for a cubical enclosure at $Ra = 10^6$. Figure 3 is for an air-filled cavity with adiabatic side walls ($C = 0.$). The plots for water are not shown because no significant differences are found. In the vertical middle plane ($y = 0.5$), the flow is almost the one obtained with two-dimensional simulations. Some changes are seen in the regions adjacent to the isothermal walls, especially for the velocity plots presented for $y = 0.011$. In these plots, the length of the arrows represents the magnitude of the velocity projected in a vertical x–z plane. However, it should be noted that the development of three dimensional flows produced only by no-slip boundary conditions at the side walls appears to be weak, in particular at high Ra numbers. As discussed by Le Peutrec and Lauriat (1987a), such weak three-dimensional effects have little influence on the heat transfer provided that the longitudinal aspect ratio A_y is greater than one and $Ra \geq 10^6$. That conclusion is supported by the plot of the isotherm $\theta = 0$, which shows that the flow is almost two dimensional.

When C is less than one, the effects of the side losses on the velocity plots and isotherms in the vertical middle plane remain negligible. It is evident that three-dimensional motions

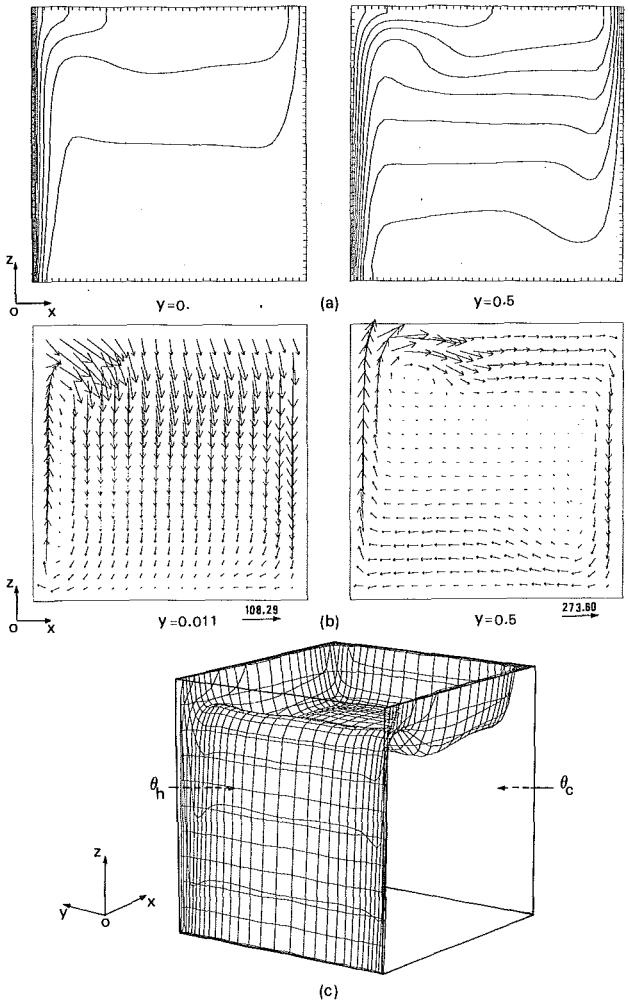

Fig. 4 Temperature distributions *(a)* and velocity vectors projected in vertical cross sections *(b)*. Three-dimensional view of the isotherm $\theta = 0$ *(c)*. Cubical enclosure with conducting side walls ($C = 30$, $\theta_a = -0.5$) filled with air at $Ra = 10^6$.

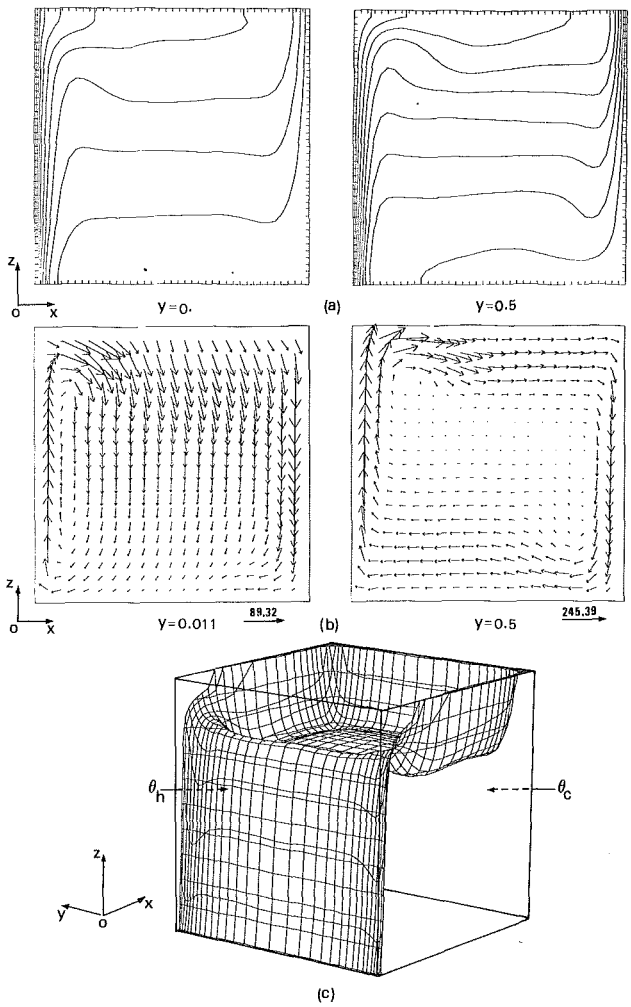

Fig. 5 Temperature distributions *(a)* and velocity vectors projected in vertical cross sections *(b)*. Three-dimensional view of the isotherm $\theta = 0$ *(c)*. Cubical enclosure with conducting side walls ($C' = 0.3$ mK/W, $\theta_a = -0.5$) filled with air at $Ra = 10^6$.

are more pronounced in regions close to the side walls but remain at a low level. These motions increase when C increases and penetrate throughout the cavity, as can be seen in Fig. 4 for $C = 30$. In this case $\Delta\bar{N}u = 8.13$, while the Nusselt number for adiabatic side walls is $\bar{N}u = 8.68$. Here again, the effects of Prandtl number are of minor importance. Therefore, the plots presented in Fig. 4 are for air only. When Fig. 4 is compared with Fig. 3, it can be seen from the isothermal patterns and velocity fields that the central-symmetry property in the vertical section $y = 0.5$ is lost for conducting side walls. In the plane $y = 0.011$, the flow structure is completely modified and the fluid is mostly flowing downward, the upward motion being predicted only in the corner region. From the temperature distributions at the side walls, it is clear that the bottom half is almost kept at the ambient temperature while temperatures greater than $\theta = 0$ are restricted to a narrow strip along the hot wall. The indication is that the heat losses at the side walls have pronounced effects both on flow structure and on average heat fluxes at the isothermal walls.

For practical application, it can be concluded that the thermal resistance of the side walls should be multiplied by about the ratio $\lambda_{water}/\lambda_{air}$ if a cavity is filled with air instead of water in order to confine the side effects to the same level. Therefore, to provide more physical insight into these results, we have re-examined the problem using the dimensional group $C' = D/(R + 1/h_e)$ kept at the same value for the two fluids, i.e., $C' = 0.3$ W•m^{-1}K^{-1}. This value appears to be realistic as can be shown by choosing $h_e = 5$ W•m^{-2}K^{-1}, $0.2 \le D \le 1$ m, which lies in the range of width of the experimental apparatus, and $0.4 \le R \le 3$ m^{2}K•W^{-1}.

Figures 5 and 6 show plots for air and water, respectively. Since the C value for air is then $C \simeq 11.5$, strong entrainment of fluid downward is predicted in dynamic boundary layers adjacent to the side walls. The numerical solutions show that the dimensionless thickness of these boundary layers is of the order of 0.06 at $Ra = 10^6$. At the same time, it can be seen from Fig. 5(*c*) that the flow structure is fully three dimensional. On the other hand, the C value for water being $C \simeq 0.5$, the side walls may be assumed to be adiabatic, at least at a rough estimate. That can be deduced by comparing Figs. 3 and 6. These results suggest that reliable flow visualizations through glazed side walls of gas-filled cavities are highly difficult to achieve if the aspect ratio of the cross section is moderate and for cold wall temperature close to the ambient temperature.

The variations in the differences between the Nusselt numbers at the two isothermal walls are presented in Fig. 7(*a*) versus Ra and for various dimensionless ambient temperatures. Here again, these results are for $C' = 0.3$ W/m•K. It should be noted that opposite values of $\Delta\bar{N}u$ would be obtained for $\theta_a > 0$. As can be seen, little change is obtained for water when increasing Ra whatever the θ_a value investigated. In contrast to these results, increases of $\Delta\bar{N}u$ are shown for air-filled enclosures, which might be expected since

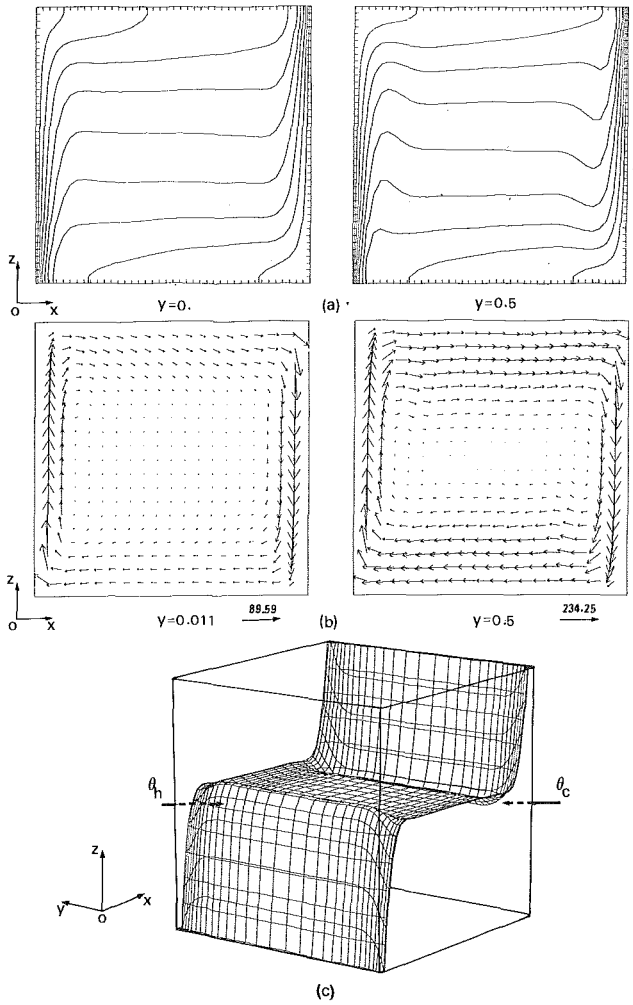

Fig. 6 Temperature distributions *(a)* and velocity vectors projected in vertical cross sections *(b)*. Three-dimensional view of the isotherm $\theta = 0$ *(c)*. Cubical enclosure with conducting side walls ($C' = 0.3$ mK/W, $\theta_a = -0.5$) filled with water at $Ra = 10^6$.

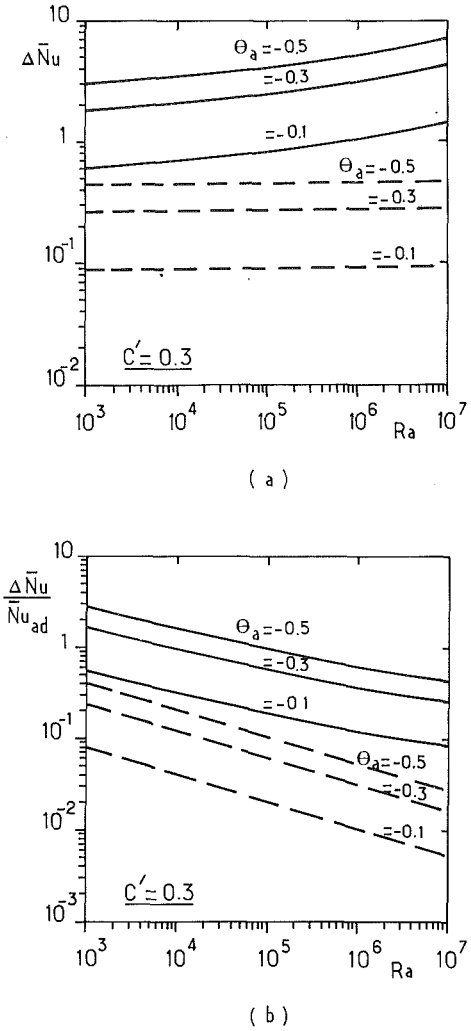

Fig. 7 Variations of the differences in Nusselt numbers at the isothermal walls as a function of Rayleigh number for cubical enclosures (—— *air*, ---- *water*)

large effects of the side losses are reported in Fig. 5 for this C' value. However, the side effects have a decreasing relative influence on the heat transferred between the isothermal walls as Ra is increased from 10^3 to 10^7. That is demonstrated by the variations of $\Delta\bar{N}u$ normalized by the Nusselt number obtained for adiabatic side walls (Fig. 7*b*). According to the θ_a value, the relative discrepancies between $\bar{N}u_h$ and $\bar{N}u_c$ are restricted in the range [0.5 percent, 3 percent] for water at $Ra = 10^7$. Since small temperature differences may be used, it is clear that the side losses have negligible effects both on flow structure and heat transfer rate at high Rayleigh numbers in water-filled enclosures. On the other hand, the discrepancies for air are much larger since the above range is extended from 7 to 30 percent at $Ra = 10^7$. It can be concluded anew that test cells with highly insulated side walls must be employed if low-conductivity fluids are used as working fluids when $\theta_a \neq 0$.

Decreasing effects or reductions of the heat losses at the side walls can be achieved either by increasing the longitudinal aspect ratio or by keeping the average temperature of the isothermal walls close to the ambient temperature. These two possibilities are examined in this section.

The $\bar{N}u$ variations reported in Fig. 8 are for air-filled cavities at $Ra = 10^6$ and $\theta_a = -0.5$. The C value is the one that was used for plotting the velocity fields and isotherms shown in Fig. 5 for a cubical enclosure. Also presented are the asymptotic two dimensional result for a square cavity ($\bar{N}u = 8.80$)

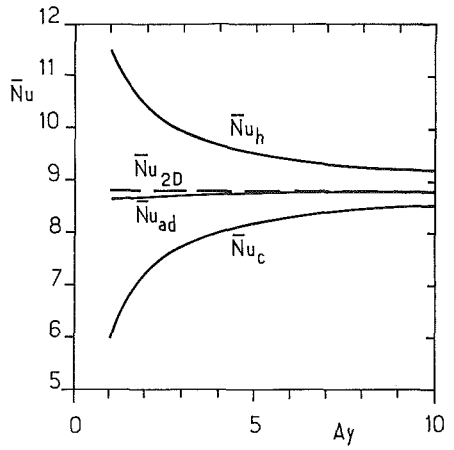

Fig. 8 Variations of the heat transfer rate at the isothermal walls versus longitudinal aspect ratio in air filled enclosures of square cross section ($Ra = 10^6$, $C = 11.5$, $\theta_a = -0.5$)

and the three dimensional results for cavities with perfectly insulated side walls. In the latter cases, the heat transfer rate is seen to be relatively independent of A_y provided $A_y > 2$. For conducting side walls, the calculations show that the values of $\bar{N}u_c$ and $\bar{N}u_h$ tend toward the asymptotic value $\bar{N}u_{2D}$ as A_y in-

Table 2 Nusselt numbers as a function of the longitudinal aspect ratio; Ra = 10^6, A_z = 1, Pr = 0.71, θ_a = − 0.5, C = 11.5

A_y	1	2	3	4	5	6	10
$\bar{Nu}_{ad}$	8.68	8.71	8.73	8.75	8.77	8.78	8.80
$\bar{Nu}_h$	11.48	10.36	9.92	9.68	9.52	9.42	9.19
$\bar{Nu}_c$	5.99	7.26	7.75	8.01	8.18	8.29	8.52

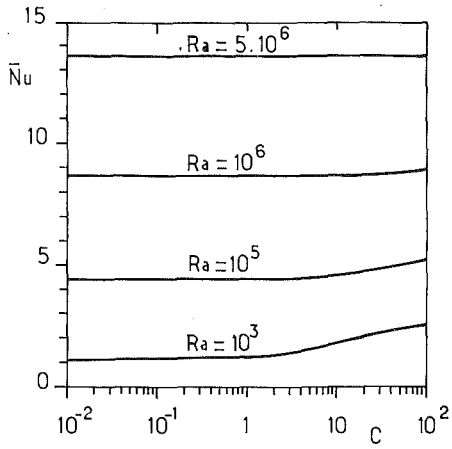

Fig. 9 Average Nusselt number as a function of the dimensionless thermal conductance of the end walls at various Ra for $\theta_a = 0$ (air-filled cubical enclosure)

creases: the relative discrepancies between $\bar{Nu}_h$ and $\bar{Nu}_{2D}$ are 30 percent for $A_y = 1$ and only 4.4 percent for $A_y = 10$. Similar differences are obtained at the cold wall (Table 2).

It should be noted here that the side losses Q_p are almost independent of A_y. Therefore, the above findings could be directly deduced from the energy balance expressed by equation (21). Since $\Delta\bar{Nu} = (2Q_p)/A_y$, decreases in $\Delta\bar{Nu}$ are proportional to A_y^{-1} for constant Ra. When increasing Ra, the data displayed in Fig. 7(a) show that Q_p increases. Hence, it can be concluded that a cavity with a larger longitudinal aspect ratio should be used in order to maintain $\Delta\bar{Nu}$ at the same level. On the other hand, when arguing in terms of the relative differences, i.e., $(\bar{Nu}_h - \bar{Nu}_{2D})/\bar{Nu}_{2D}$ for example, it is clear from Fig. 7(b) that shorter cavities could be used at high Ra to confine the side wall effects to a given relative level. For example, a longitudinal aspect ratio close to 5 should be enough so that $(\bar{Nu}_h - \bar{Nu}_{2D})/\bar{Nu}_{2D}$ is less than 4 percent at Ra = 10^6 while A_y should be of the order of 13 at Ra = 10^5. In other words, if the test cells are designed with rather efficient thermal barriers as side walls (i.e., $R \simeq 0.5$ for $D = 0.2$ m), large longitudinal aspect ratios are not required to produce flows that can be considered as two-dimensional provided the Rayleigh number is large enough.

The average Nusselt numbers at the isothermal walls obtained with $T_o = T_a$ (or, equivalently, $\theta_a = 0$) are presented in Fig. 9 for a cubical enclosure. For these cases, $\bar{Nu}_c = \bar{Nu}_h$ whatever the C value. As can be seen, $\bar{Nu}$ is found to be independent of C for $C < 1$ in the whole range of Ra investigated while increases of $\bar{Nu}$ are shown at low Ra for $C > 1$. For Ra $\geq 5.10^6$, it is rather surprising to notice that the heat transfer rates at the isothermal walls become independent of the thermal conductance of the side walls. In fact, Q_p is negligibly small because the heat output in the top half of the side walls is balanced by the heat input in the bottom half. The isotherms displayed in Fig. 10 for $C = 50$ at $Y = 0$ support this conclusion. Therefore, Fig. 9 shows that the most important parameter to be controlled in experimental runs is the temperature difference between the average temperature of the isothermal walls and the ambient temperature.

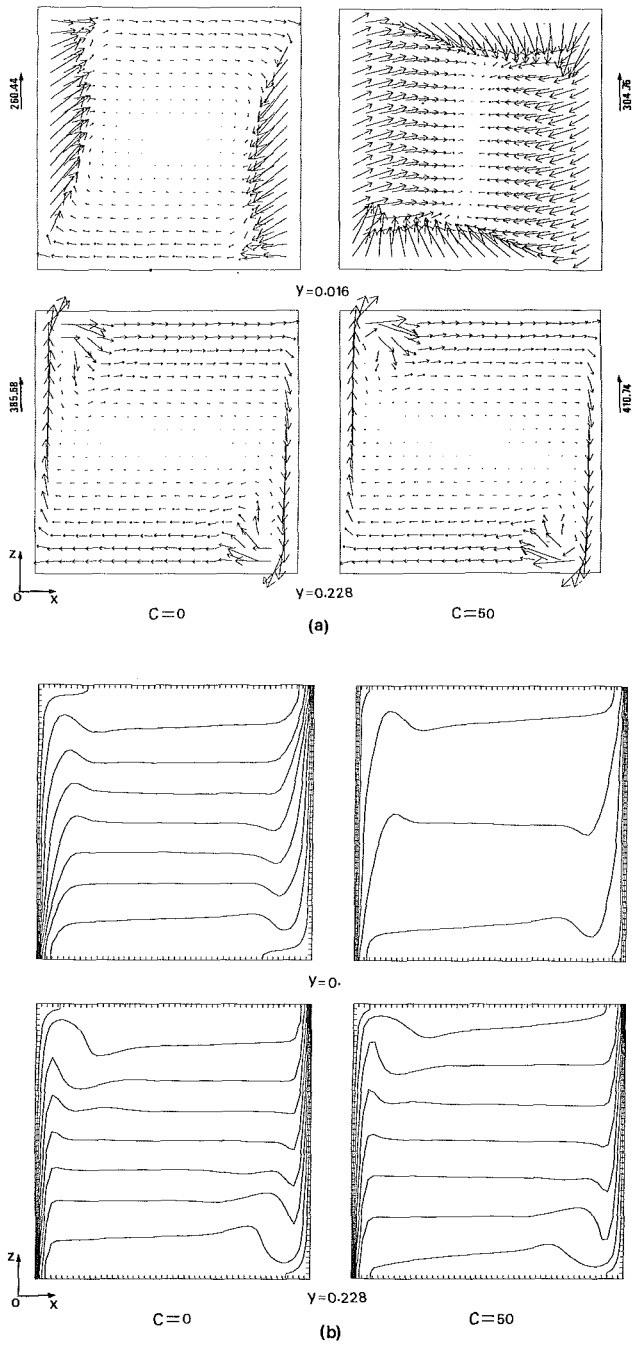

Fig. 10 Temperature distributions and velocity vectors in vertical cross sections for adiabatic ($C = 0$) and conducting side walls ($C = 50$) (Ra = 10^7, Pr = 0.71, A_z = 1, A_y = 2, $\theta_a = 0$)

However, these findings do not imply that the heat fluxes transferred through the side walls have only a marginal effect on the flow structure. This point must be examined since reliable measurements of velocity fields and temperature distributions have to be performed in order to improve the understanding of the transition from steady convection to chaotic flows. To this end, computations were carried out for an air-filled cavity with $A_y = 2$ at Ra = 10^7 and $\theta_a = 0$. From the plots of isotherms and velocity vectors projected in cross-sectional planes presented in Fig. 10, it can be concluded that the longitudinal motion produced at the side walls has a weak effect on the flow structure except in layers adjacent to the side walls, the thickness of which is less than $A_y/10$. Flows in planes $0.2 < y < 1.8$ are essentially two dimensional.

Conclusions

Heat transfer by natural convection in a rectangular box with two vertical walls held at uniform temperature and adiabatic horizontal end walls depends on the thermal boundary conditions applied at the side walls that confine the fluid layer in the spanwise direction. Focused on two important parameters that characterize the heat losses at the side walls, namely the thermal conductance of the walls and the ambient temperature, the present study indicates the following:

1 For enclosures filled with low-conductivity fluids, heat losses have appreciable effects if the average temperature of the hot and cold walls is not kept very close to the ambient temperature.

2 However, their relative influences decrease when increasing both Rayleigh number and the longitudinal aspect ratio.

3 For water-filled enclosures, side walls made of 1-cm-thick perspex are sufficient to confine the effects of the heat losses to an acceptable level.

4 Experiments for two-dimensional flows in air-filled cavities could be conducted at Rayleigh numbers corresponding to the end of steady convection in enclosures with $A_y \geq 2$ provided the mean temperature of the isothermal walls matches the ambient temperature and double-glazed windows with low emissivity coatings are used as side walls.

References

Bajorek, S. M., and Lloyd, J. R., 1982, "Experimental Investigation of Natural Convection in Partitioned Enclosures," ASME JOURNAL OF HEAT TRANSFER, Vol. 104, pp. 527–532.

Cheesewright, R., and Zlai, S., 1986, "Distributions of Temperature and Local Heat-Transfer Rate in Turbulent Natural Convection in a Large Rectangular Cavity," *Proceedings of the 8th Heat Transfer Conference*, San Francisco, CA, NC 03, pp. 1465–1470.

Eckert, E. R. G., and Carlson, W. O., 1961, "Natural Convection in an Air Layer Enclosed Between Two Vertical Plates With Different Temperatures," *Int. J. Heat Mass Transfer*, Vol. 2, pp. 106–120.

ElSherbiny, S. M., Hollands, K. G. T., and Raithby, G. D., 1982, "Effect of Thermal Boundary Conditions on Natural Convection in Vertical and Inclined Air Layers," ASME JOURNAL OF HEAT TRANSFER, Vol. 104, pp. 515–520.

Fraikin, M. P., Portier, J. J., and Fraiken, C. J., 1980, "Application of a k–ϵ Turbulence Model to an Enclosed Buoyancy Driven Recirculating Flow," presented at the 19th ASME–AIChE National Heat Transfer Conference, Paper No. 80-HT-68.

Gill, E., and Davey, A., 1969, "Instabilities of a Buoyancy Driven System," *J. Fluid Mech.*, Vol. 35, Part 4, pp. 775–798.

Haldenwang, P., and Labrosse, G., 1986, "2D and 3D Spectral Chebyshev Solutions for Free Convection at High Rayleigh Numbers," *Proc. 6th Int. Symp. Finite Elements Methods in Flow Problems*.

Kirkpatrick, A. T., and Bohn, M., 1986, "An Experimental Investigation of Mixed Cavity Natural Convection in the High Rayleigh Number Regime," *Int. J. Heat Mass Transfer*, Vol. 29, No. 1, pp. 69–82.

Lauriat, G., and Altimir, I., 1985, "A New Formulation of the SADI Method for the Prediction of Natural Convection Flows in Cavities," *Computers and Fluids*, Vol. 13, pp. 141–155.

Le Peutrec, Y., and Lauriat, G., 1987a, "Three-Dimensional Natural Convection Flows of Air and Water in Vertical Differentially Heated Cavities," in *Natural Circulation*, HTD-Vol. 92/FED-Vol. 61, J. M. Kim and Y. A. Nassan, eds., pp. 351–360.

Le Peutrec, Y., and Lauriat, G., 1987b, "Practical Evaluation of Improved Upwind Finite Difference Schemes for Natural Convection in Enclosures," *Numerical Methods in Thermal Problems*, Vol. 5, Part 1, Pineridge Press, United Kingdom, pp. 344–355.

Le Quéré, P., and Alziary de Roquefort, T., 1985, "Computation of Natural Convection in 2D-Cavities With Chebyshev Polynomials," *J. Comp. Phys.*, Vol. 24, pp. 210–228.

Mallinson, G. D., and de Vahl Davis, G., 1973, "The Method of the False Transient for the Solution of Coupled Elliptic Equations," *J. Comp. Phys.*, Vol. 12, pp. 435–461.

Mallinson, G. D., and de Vahl Davis, G., 1977, "Three-Dimensional Convection in a Box: a Numerical Study," *J. Fluid Mech.*, Vol. 83, Part 1, pp. 1–31.

Morrison, G. L., and Tran, V. Q., 1978, "Laminar Flow Structure in Vertical Free Convective Cavities," *Int. J. Heat Mass Transfer*, Vol. 21, pp. 203–213.

Mynett, J. A., and Duxbury, D., 1974, "Temperature Distributions Within Enclosed Plane Air Cells Associated With Heat Transfer by Natural Convection," *Proc. 5th Int. Heat Transfer Conf.*, Tokyo, Paper No. NC 3.8, pp. 119–123.

Ozoe, H., Mouri, A., Hiramitsu, M., Churchill, S. W., and Lior, N., 1986, "Numerical Calculations of Three-Dimensional Turbulent Natural Convection in a Cubical Enclosure Using a Two-Equation Model for Turbulence," ASME JOURNAL OF HEAT TRANSFER, Vol. 108, pp. 806–813.

Upson, C. D., Gresho, P. M., and Lee, R. L., 1980, "Finite Elements Simulations of Thermally Induced Convection in an Enclosed Cavity," Report UCID-18602, pp. 1–35.

Unsteady Multicellular Natural Convection in a Narrow Horizontal Cylindrical Annulus

D. B. Fant
Air Force Institute of Technology,
Wright-Patterson AFB, OH 45433

J. Prusa

A. P. Rothmayer

Iowa State University
Ames, IA 50011

Numerical and analytical solutions are presented for multicellular flow instability and the subsequent nonlinear development in a horizontal cylindrical annulus. The Boussinesq approximated Navier–Stokes equations are simplified to Cartesian-like boundary layer equations by means of a high Rayleigh number small gap asymptotic expansion. The full numerical problem is explored for the limiting case of zero Prandtl number. At a finite scaled gap spacing, an instability sets in, which results in periodic multicellular flow. The numerical solutions are found to progress through an increasingly complex sequence of periodic solutions, culminating in a very complex unsteady solution that has features normally associated with chaotic systems.

1 Introduction

The need to predict the rate of natural convection heat transfer in the annular region between concentric cylinders constitutes an important engineering problem that occurs in a wide variety of technological applications. Examples of great interest range from latent energy thermal storage systems to nuclear reactor design. Other technological applications may be found in high-voltage electric transmission cables, and in aircraft cabin insulation design.

The basic flowfield induced by buoyancy force consists of two crescent-shaped cells, which are symmetric with respect to the vertical plane containing the axes of the cylinders (Liu et al., 1961; Grigull and Hauf, 1966; Mack and Bishop, 1968; Powe et al., 1969, 1971; among others). While numerous experimental, numerical, and analytical studies all corroborated this picture of the basic flow, peculiar transitions appeared in the flow under various conditions. In particular, a multicellular flow was generally observed in the top portion of a narrow annulus for sufficiently high values of the Grashof number Gr (or the Rayleigh number Ra), suggesting a thermal or Rayleigh–Bénard type of instability (see Liu et al., 1961; Powe et al., 1969, 1971; and more recently, Rao et al., 1985).

Other types of flow instability were also observed when Gr was increased to sufficiently large values. For annular regions that are relatively wide, oscillations of the basic flow convection cells were observed experimentally (Liu et al., 1961; Bishop et al., 1968; Powe et al., 1969). Oscillations of multicells in the top of the annulus were observed numerically (Rao et al., 1985). With annular regions of intermediate width, three-dimensional spiral vortices were found to exist (Powe et al., 1969; Rao et al., 1985). One other type of instability was also reported for low-Pr flows in wide annular regions (Mack and Bishop, 1968). They presented the first four terms of a regular perturbation solution for the problem using Ra as the expansion parameter. The closed-form solution of Mack and Bishop (1968) allowed them to investigate the effect of Pr over the extraordinary range of $[0.02, 6\times 10^6]$. They found that for $\mathrm{Pr}>0.7$, very little qualitative change occurred in their solutions. But for $0.02<\mathrm{Pr}<0.3$, a flow instability consisting of multicells distributed along both the top and bottom of the annulus appeared. (Similar results have since been reported by Huetz and Petit (1974) and Charrier-Mojtabi et al. (1979)). This behavior was never observed in any of the numerical and/or experimental studies mentioned above. Powe et al. (1969) attempted to draw together the several types of flow instability that had been observed to occur, and, with the notable exception of the low-Pr instability observed by Mack and Bishop (1968), they succeeded in developing a flow regime map that neatly categorized all the flow patterns in terms of a critical Gr, which was a function of dimensionless gap width.

Independently of the investigations being carried out on annular geometries, Korpela et al. (1973) and Korpela (1974) used classical linear stability theory to study the growth and decay of disturbances on the natural convection base flow in narrow, vertical, and inclined slots. A later numerical study by Lee and Korpela (1983) supported the earlier results for the vertical slot (Korpela et al., 1973). These studies demonstrated that a critical Gr was a key parameter for low-Pr flows, whereas a critical Ra was a key parameter for high Pr flows, in determining states of neutral stability. But an even more important result was that the *value of Pr* was found to have the dominant influence upon the type of instability that was observed to occur. Two fundamentally different types were recognized:

(i) High-Pr flows: The disturbance energy (kinetic energy for perturbations to base flow) originates from the potential energy associated with the buoyancy force acting on the fluid—the instability is thermal in nature. Counterrotating cells are produced.

(ii) Low-Pr flows: the disturbance energy originates from the kinetic energy of the base flow—the instability is hydrodynamic in nature. Like-rotating cells are produced.

Other related studies of natural convection instabilities in vertical channels can be found in Elder (1965), Vest and Arpaci (1969), Thomas and de Vahl Davis (1970), Pepper and Harris (1977), Seki et al. (1978), Choi and Korpela (1980), and Drummond and Korpela (1987).

For the inclined slot geometry, only a hydrodynamic type of instability can occur for $\mathrm{Pr}<0.24$. This number has great relevance to the present study because locally, a narrow annulus looks like a narrow inclined slot. Walton (1980), using a WKB formulation, confirmed that $\mathrm{Pr}=0.24$ was also a critical value of Prandtl number for the annular geometry. For $\mathrm{Pr}>0.24$, instability first forms at the top of the annulus, indicating that it is thermally dominated. Only for $\mathrm{Pr}<0.24$ can the instability first form elsewhere, indicating a significant

Contributed by the Heat Transfer Division and presented at the First National Fluid Dynamics Conference, Cincinnati, Ohio, September 1988. Manuscript received by the Heat Transfer Division September 7, 1988; revision received September 29, 1989. Keywords: Flow Instability, Natural Convection, Numerical Methods.

hydrodynamic contribution to its origin. The value of Pr is seen to play a fundamental role in characterizing flow instability in (at least narrow) annular regions. The Pr effect is completely missing in the flow regime map of Powe et al. (1969). Most likely, it was never observed because (with the sole exception of the study by Mack and Bishop (1968)) the Pr ranges that had been examined in numerous works never contained sufficiently small values of Pr. Air, for which $Pr = 0.7$, was consistently used as the example of a low-Pr case.

The appearance of the thermal and hydrodynamic instabilities has generally been associated with small-scale radial and azimuthal distances and cells of O(1) aspect ratio (i.e., the same width as length). For example, Walton (1980) concludes that for the small-gap problem, a small portion of the channel can become unstable, presumably leading to cell development in the more nonlinear stages. The actual angular position of this instability is generally a strong function of the annular gap spacing, Rayleigh number, and, perhaps more importantly, the Prandtl number. In this study, a fundamentally different type of instability was encountered, which also appears to be relevant to the hydrodynamic instability problem, and produces qualitative and quantitative behavior, which is seen to be consistent with previous computation and experiment. This instability is believed to be the large gap limit of a high Rayleigh number equivalent of Walton's (1980) problem. A brief analysis of this conjecture has been conducted by one of the authors, A. P. Rothmayer, and is presented in the appendix. In Walton's study the instability was highly localized about a given point in the annulus and was strongly affected by the azimuthal diffusion terms in the governing equations. This result followed from the assumption that the cells were expected to have O(1) aspect ratio. The present study differs from Walton's work in that the Rayleigh number is taken to be large, the Prandtl number small, and the cells have very large aspect ratio. That is, the cells are asymptotically much thinner in the radial coordinate than in the azimuthal coordinate. The cells are therefore spread throughout the entire annulus and are not confined to the neighborhood of a given angle, as in Walton's study. The present study concludes that azimuthal diffusion is not a necessary precursor for hydrodynamic instability. Additional circumstantial evidence and preliminary analysis supporting this view is presented in the appendix.

The equations governing these cells are found to be nonlinear boundary-layer equations with negligible azimuthal diffusion. The boundary-layer equations are driven by a gravitational field that appears periodic from the geometric frame of the annulus. For the small Prandtl number fluids governed by these boundary-layer equations, an unsteady hydrodynamic multicellular flow is found to originate near the vertical section of a two-dimensional narrow horizontal cylindrical annulus.

This unsteadiness is in contrast to the vertical slot studies, for which only steady multicellular flow has been observed in the zero Pr limit. The initial instability behaves in a stationary manner, for values of the scaled gap spacing that are slightly larger than the critical value for instability. Upon slightly increasing the scaled gap spacing, a simple periodic multicellular motion ensues. Further increasing the scaled gap spacing results in more complicated periodic motions. Still further increases of the scaled gap spacing lead to a flow that has no obvious periodic character. The present model also gives evidence of sensitivity to initial conditions—a hallmark of chaotic dynamics—when the solution is in an unsteady, nonperiodic mode. Given the limited nature of the present computations, however, and the lack of theoretical development to determine whether the complicated unsteady flow is chaotic, it is too early to definitely conclude that any sort of a transition to chaos is occurring. Since most of the theory and computational results for transition to a chaotic solution have been derived for low-order systems (i.e., a reasonably small number of ordinary differential equations or a low-order spectral approximation to a partial differential equation), it is noteworthy that the solutions calculated in this study appear to follow a sequence of events that typically characterize the transition to chaos in such low-order systems. The interesting sequence of unsteady solutions observed in the present study were calculated using a relatively simple partial differential equation that is locally parabolic, but rendered globally elliptic due to periodicity and possible flow reversal.

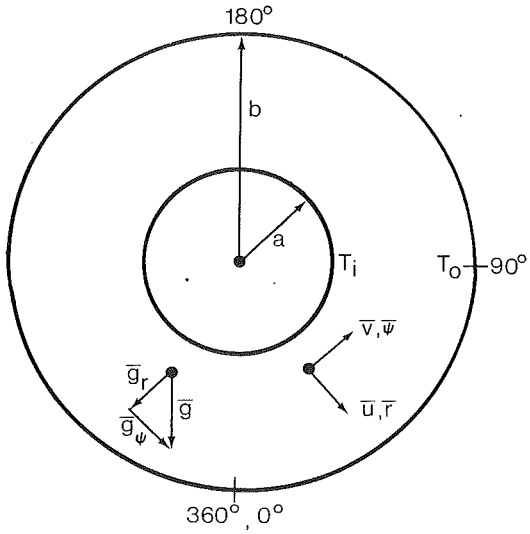

Fig. 1 Two-dimensional concentric cylinder geometry

2 Basic Mathematical Formulation

The Boussinesq-approximated Navier–Stokes equations and the thermal energy equation with negligible viscous dissipation form a starting point for the derivation of the high Rayleigh

Nomenclature

a = inner cylinder radius
b = outer cylinder radius
f^*/ν = dimensionless stream function
G = dimensionless gap spacing
Pr = Prandtl number
r = dimensionless radial coordinate
Ra = Rayleigh number
t = dimensionless time
T = $(T-T_o)/(T_i-T_o)$ = dimensionless temperature
T_i = inner cylinder temperature
T_o = outer cylinder temperature
u = dimensionless radial velocity component
v = dimensionless circumferential velocity component
w = $w^*/(\nu/a^2)$ = dimensionless vorticity
ψ = dimensionless circumferential coordinate

Superscripts

* = dimensional variables
~ = dimensionless variable scaled for large Ra, small G asymptotic limit
^ = dimensionless variable scaled for large Ra, small G, and small Pr asymptotic limit

number small-gap limit. These equations may be used to determine the buoyancy-induced steady or unsteady flow fields between horizontal isothermal concentric cylinders. The vorticity–stream function formulation will be adopted here. The flow is assumed to be laminar, Newtonian, and two dimensional (see Fig. 1). The dimensionless governing equations are (see Fant, 1987)

$$G^2\frac{\partial T}{\partial t}+Gu\frac{\partial T}{\partial r}+\frac{Gv}{r+G^{-1}}\frac{\partial T}{\partial \psi}=$$

(energy) (2.1)

$$=\frac{1}{\mathrm{Pr}}\left\{\frac{\partial^2 T}{\partial r^2}+\frac{1}{r+G^{-1}}\frac{\partial T}{\partial r}+\frac{1}{(r+G^{-1})^2}\frac{\partial^2 T}{\partial \psi^2}\right\}$$

$$\mathrm{Pr}\left\{G^2\frac{\partial w}{\partial t}+Gu\frac{\partial w}{\partial r}+\frac{Gv}{r+G^{-1}}\frac{\partial w}{\partial \psi}\right\}$$

$$=\mathrm{Pr}\left\{\frac{\partial^2 w}{\partial r^2}+\frac{1}{r+G^{-1}}\frac{\partial w}{\partial r}+\frac{1}{(r+G^{-1})^2}\frac{\partial^2 w}{\partial \psi^2}\right\}$$

$$+G\mathrm{Ra}\left\{\sin\psi\frac{\partial T}{\partial r}+\frac{\cos\psi}{r+G^{-1}}\frac{\partial T}{\partial \psi}\right\}$$

(vorticity) (2.2)

$$\frac{\partial^2 f}{\partial r^2}+\frac{1}{r+G^{-1}}\frac{\partial f}{\partial r}+\frac{1}{(r+G^{-1})^2}\frac{\partial^2 f}{\partial \psi^2}=G^2 w$$

(stream function) (2.3)

The stream function is defined by

$$u=\frac{-1}{G(r+G^{-1})}\frac{\partial f}{\partial \psi}\qquad v=\frac{1}{G}\frac{\partial f}{\partial r}\tag{2.4}$$

In the above system of equations, three independent parameters are needed to describe the problem, namely the Rayleigh number, the Prandtl number, and the gap spacing

$$\mathrm{Ra}=\frac{g\beta a^3(T_i-T_0)}{\nu\alpha},\qquad \mathrm{Pr}=\frac{\nu}{\alpha},\qquad G=\frac{b-a}{a}\tag{2.5}$$

The Rayleigh number is based on the temperature difference between the cylinders and the inner cylinder radius. Here g is the local uniform vertical acceleration due to gravity, β is the coefficient of thermal expansion, ν is the kinematic viscosity of the fluid, and α is the thermal diffusivity. T_i and T_o are the inner and outer cylinder temperatures, respectively (see Fig. 1). The radius of the inner cylinder is a, whereas b is the radius of the outer cylinder. The time, the angular coordinate, and especially the radial coordinate have been nondimensionalized as in Prusa and Yao (1983)

$$t=t^*/(a^2)/\nu\qquad \psi=\psi^*\qquad r=\frac{r^*-a}{b-a}\tag{2.6}$$

This means that the nondimensionalized radial coordinate remains O(1) irrespective of the actual physical gap spacing. All of the effects of the gap spacing are incorporated into G. The isothermal and no-slip nondimensional boundary conditions for the above system of equations are

$$T(\psi,0)=1,\qquad f(\psi,0)=0,\ \text{and}\ w(\psi,0)=\frac{1}{G^2}\frac{\partial^2 f}{\partial r^2}(\psi,0)\tag{2.7}$$

on the inner cylinder, as well as

$$T(\psi,1)=0,\qquad f(\psi,1)=0,\ \text{and}\ w(\psi,1)=\frac{1}{G^2}\frac{\partial^2 f}{\partial r^2}(\psi,1)\tag{2.8}$$

on the outer cylinder. The initial condition for this problem is either the state of no flow within the annulus or the solution from the previous numerical calculation.

3 Asymptotic Analysis for the Narrow Annulus

In this section, high Rayleigh number asymptotic expansions will be developed for the narrow-gap limit. A simpler set of equations shall be developed from this intermediate set for the small Prandtl number limit. In both cases, the Navier–Stokes equation are found to reduce to *Cartesian-like boundary-layer equations.*

In the high Rayleigh number limit for finite gap spacing, experience suggests that the annular flowfield can be divided into an inner wall and an outer wall boundary layer with an inviscid core in the center. In fact this type of expansion has been carried out by Jischke and Farshchi (1980), although the correct theory is slightly more complicated than the simple one suggested above. In their study, Jischke and Farshchi (1980) failed to observe multicell development. In addition, many studies, and in particular the study of Walton (1980), suggest that cell development will be found in very narrow cylindrical annuli. Another argument for generating the small gap spacing limit is that the wall boundary layers for finite gap spacing are noninteracting. In general, one might expect the classical boundary-layer singularities to arise in the situation of multicell development. Such a problem can be avoided by letting the gap spacing tend to zero until the boundary layers merge. Once the boundary layers merge, the pressure will not be prescribed and any boundary-layer singularity is avoided; for example see Smith (1983). In either case it seems reasonable to search for multicells in a narrow annulus where viscous effects act across the entire channel.

A preliminary analysis for finite gap spacing boundary-layer theory, and a limit of that solution for small gap spacing, suggests the following expansions for the dependent variables:

$$(u, v, w, f, T)\sim(\mathrm{Ra}^{1/4}\tilde{u}, \mathrm{Ra}^{1/2}\tilde{v}, \mathrm{Ra}^{3/4}\tilde{w}, \mathrm{Ra}^{1/4}\tilde{f}, \tilde{T})+\ldots\tag{3.1}$$

The temperature is maintained at O(1) to satisfy the imposed wall boundary conditions and all the other terms follow from this assumption. The gap spacing in which the boundary layers merge is found to be $O(\mathrm{Ra}^{-1/4})$, provided that the azimuthal coordinate is O(1). The gap spacing is rescaled to this order of magnitude giving

$$G=\mathrm{Ra}^{-1/4}\tilde{G}\tag{3.2}$$

To bring unsteady effects into play at leading order the time is rescaled as follows:

$$t=\mathrm{Ra}^{-1/2}\tilde{t}\tag{3.3}$$

This time scaling produces very high-frequency waves and multicells. Note that the above scaling for the gap spacing implicitly includes the assumption of a small temperature difference between the inner and outer cylinders, which is one of the basic assumptions of the Boussinesq approximation. There is a relatively strong effect of temperature on the critical gap spacing to introduce nonlinearity, which will affect the scaling of the gap spacing if the Boussinesq approximation is abandoned. Substituting the above expansions, equations (3.1), (3.2), and (3.3) into equations (2.1) through (2.3) gives the final governing equations of the small gap limit

$$\tilde{G}^2\frac{\partial \tilde{T}}{\partial \tilde{t}}+\tilde{G}\left\{\frac{\partial \tilde{f}}{\partial r}\frac{\partial \tilde{T}}{\partial \psi}-\frac{\partial \tilde{f}}{\partial \psi}\frac{\partial \tilde{T}}{\partial r}\right\}=\frac{1}{\mathrm{Pr}}\frac{\partial^2 \tilde{T}}{\partial r^2}$$

(energy) (3.4)

$$\tilde{G}^2\frac{\partial \tilde{w}}{\partial \tilde{t}}+\tilde{G}\left\{\frac{\partial \tilde{f}}{\partial r}\frac{\partial \tilde{w}}{\partial \psi}-\frac{\partial \tilde{f}}{\partial \psi}\frac{\partial \tilde{w}}{\partial r}\right\}=\frac{\partial^2 \tilde{w}}{\partial r^2}$$

$$+\frac{\tilde{G}}{\mathrm{Pr}}\sin\psi\frac{\partial \tilde{T}}{\partial r}$$

(vorticity) (3.5)

$$\frac{\partial^2 \tilde{f}}{\partial r^2}=\tilde{G}^2\tilde{w}$$

(stream function) (3.6)

The error introduced by neglecting streamwise diffusion effects in the energy and vorticity equation is, in both cases, on the order of the gap spacing squared, or $O(Ra^{-1/2})$. Note that the radial coordinate r has not been rescaled because of the manner in which it was nondimensionalized. The boundary conditions retain the same form as equations (2.7) and (2.8) but in rescaled variables. (Similar equations have been developed by Bejan (1984) for inclined channels.)

Now, in order to simplify the equations further we consider the small Prandtl number limit. The resulting expansions are found to be

$$(\tilde{w}, \tilde{f}, \tilde{T}) \sim (\mathrm{Pr}^{-3/4} W, \mathrm{Pr}^{-1/4} F, T) + \ldots \tag{3.7}$$

Again to maintain viscosity acting across the entire channel, the channel gap spacing must be reduced still further

$$\tilde{G} = \mathrm{Pr}^{1/4} \hat{G} \tag{3.8}$$

Once again, in order to bring unsteady effects into play at leading order, the time is rescaled as follows:

$$\tilde{t} = \mathrm{Pr}^{1/2} \hat{t} \tag{3.9}$$

This produces an unsteady response at an even higher frequency than the finite Prandtl number equations. In this limit, the temperature equation is found to reduce to a pure conduction equation across the annulus (i.e., $T_{rr} = 0$) giving a temperature field that is independent of the azimuthal coordinate ψ

$$T = 1 - r \tag{3.10}$$

Given this temperature field, the vorticity and stream function equations are found to reduce to

$$\hat{G}^2 \frac{\partial W}{\partial \hat{t}} + \hat{G}\left\{\frac{\partial F}{\partial r}\frac{\partial W}{\partial \psi} - \frac{\partial F}{\partial \psi}\frac{\partial W}{\partial r}\right\} = \frac{\partial^2 W}{\partial r^2} - \hat{G}\sin\psi \tag{3.11}$$

$$\frac{\partial^2 F}{\partial r^2} = \hat{G}^2 W \tag{3.12}$$

The boundary conditions on this system of equations are

$$F(\psi, 0) = F(\psi, 1) = 0,\ W(\psi, 0) = \frac{1}{\hat{G}^2}\frac{\partial^2 F}{\partial r^2}(\psi, 0), \text{ and}$$

$$W(\psi, 1) = \frac{1}{\hat{G}^2}\frac{\partial^2 F}{\partial r^2}(\psi, 1) \tag{3.13}$$

Notice that these equations have the form of incompressible boundary-layer equations, which are being forced by a periodic function—the component of the gravitational field tangent to the annulus. Despite their rather simple form, these equations (3.10)–(3.13) are found to admit a hydrodynamic instability for a critical finite value of the scaled gap spacing (see Appendix), which leads to a sequence of periodic solutions as well as a rather complex aperiodic solution.

4 Viscous-Dominated Flow for Very Small Gap Spacing

As discussed in the introduction, later calculations will show that a steady-state multicellular flow was achieved near the narrow vertical slot portion of the annulus for finite values of $\hat{G}$. In these calculations, the nonlinear solution resulting from the initial instability behaved in a steady-state manner. In view of this, it seems reasonable to look at the very small gap limit (i.e., the limit $\hat{G} \to 0$), partly to verify that the solution is steady and benign for small values of $\hat{G}$, and partly to see whether steady-state multicells might be expected to occur. To do this, the stream function equation (3.12) is substituted into the steady-state version of the vorticity equation (3.11), producing a single fourth-order equation for the stream function. As $\hat{G} \to 0$, the convective terms on the left-hand side of the equation become negligible. The imposed temperature field then drives the remaining viscous term, suggesting the following expansions:

$$F \sim \hat{G}^3 F_1 + \hat{G}^7 F_2 + \hat{G}^{11} F_3 + O(\hat{G}^{15}) \tag{4.1}$$

The solutions to the resulting equations are found to be

$$F_1 = r^2 (r-1)^2 \frac{\sin\psi}{24} \tag{4.2}$$

and

$$F_2 = \left(\frac{r^2}{5040} - \frac{r^3}{1512} + \frac{r^5}{360} - \frac{r^6}{180} + \frac{r^7}{180} - \frac{r^8}{336} + \frac{r^9}{1512}\right)\frac{\sin 2\psi}{96} \tag{4.3}$$

The important feature to notice in the above equations is that the first-order solution is simply two steady-state vertical counterrotating cells, whereas the second-order solution is a four-cell solution. Because of the expansion (4.1), the $\hat{G} \to 0$ limit is expected to be accurate up to relatively large scaled gap spacing $\hat{G}$. However, once $\hat{G}$ becomes large enough, the nonlinear effects will set in. The form of the second-order solution suggests that multicells might be observed in the nonlinear regime. However, it must be stressed that should multicells begin to develop, and nonlinearity to set in, the $\hat{G} \to 0$ limit solution is no longer accurate. The forms of equations (4.2) and (4.3) are similar to those given by Walton (1980), but for a smaller Rayleigh number and finite Prandtl number set of equations. In particular, Walton shows that an instability sets in, but for *much smaller values of the gap spacing parameter and much shorter azimuthal wavelengths*, that is, instabilities that have a small azimuthal wavelength centered about some arbitrary value of ψ (see the appendix for further discussion on this point). The present work contends that another form of instability is possible, and that steady and unsteady multicells can develop directly from equations (3.10)–(3.13) without the presence of azimuthal diffusion. The linear stability issue and its relation to the high Rayleigh number equivalent of Walton's (1980) study is discussed in more detail in Appendix A. The central issue of this study is the nonlinear flow development of equations (3.10)–(3.13) for finite values of the scaled gap spacing $\hat{G}$.

For completeness, the stream function expansion (4.1) and the stream function equation (3.12) suggest the following expansion for the vorticity solution for the $\hat{G} \to 0$ limit:

$$W \sim \hat{G} W_1 + \hat{G}^5 W_2 + \hat{G}^9 W_3 + O(\hat{G}^{13}) \tag{4.4}$$

where W_1 is found to be

$$W_1 = \left(r^2 - r + \frac{1}{6}\right)\frac{\sin\psi}{2} \tag{4.5}$$

5 Computational Method and Details

The two coupled equations (3.11) and (3.12) were solved implicitly in time using a point iterative Gauss–Seidel method with underrelaxation. The dependent variables at a given time level were found by repeated iteration of the governing equations, until a local relative error of $1/10^6$ was reached. The solutions were carried out to steady state whenever possible, and when unsteady flow behavior occurred, sufficiently small time steps (as determine by temporal grid refinements) were used to produce time accurate solutions.

A first-order difference formula was used for the unsteady term in the vorticity equation. All radial spatial derivatives in the governing equations were second-order centrally differenced. This included the radial convective terms, which were represented by a first-order upwind expression, together with

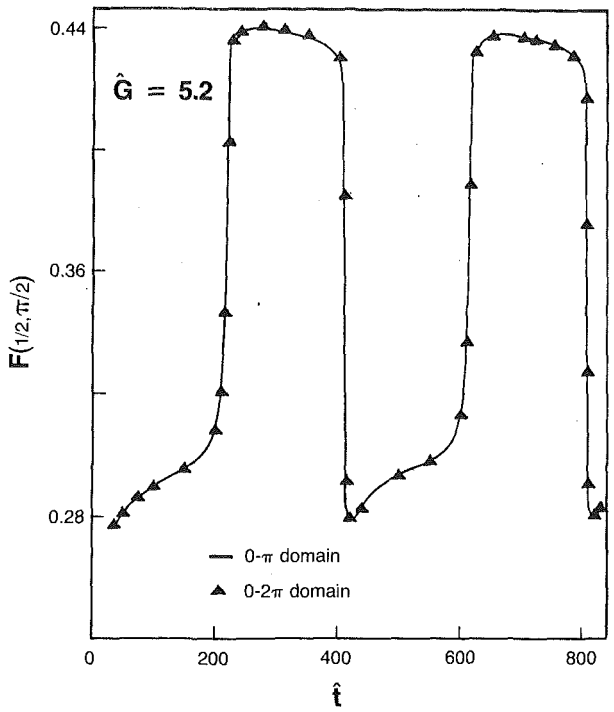

Fig. 2 Comparison of the numerical results with (0-π domain) and without (0-2π domain) symmetric boundary conditions; time dependence of the stream function at $(r, \psi) = (1/2, \pi/2)$

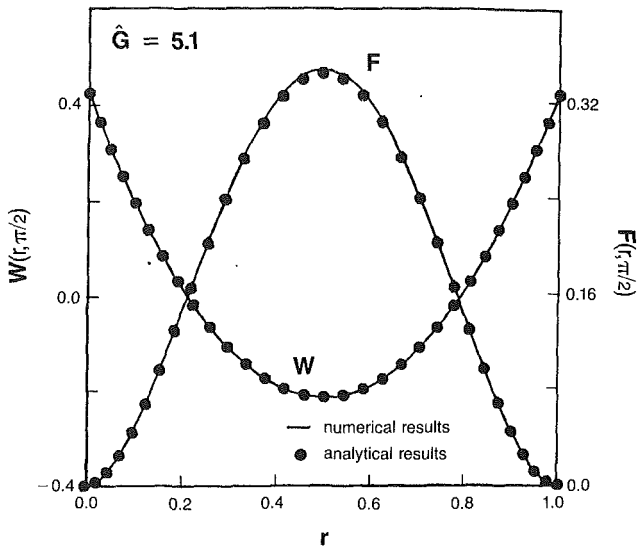

Fig. 3 Radial variation of the vorticity and stream function at $\psi = \pi/2$

the standard correction term, which gives a second-order central difference form in the converged solution. Because of the parabolic nature of equation (3.11), which is first-order in ψ, a corrected second-order upwind difference scheme was employed for the streamwise (azimuthal) convective terms. Variable spatial increments were also used in order to concentrate nodes near the heated and cooled cylinders, and near $\psi = \pi/2$. We evaluated the use of first-order upwind differencing by turning off the second-order correction terms in our numerical algorithm and found that multicellular flow could not be observed in this case, even when using 102 angular nodes. When the correction terms were turned on, the algorithm had no problem capturing multicells. Apparently, *at least second-order accuracy* is required to capture the type of secondary-flow instability examined in this study, a result that was anticipated earlier by Lee and Korpela (1983).

The transitional value of $\hat{G}$ (the value that characterizes the transition from bicellular to multicellular flow) was determined by initially calculating the steady-state bicellular solutions for successively larger pretransitional values of $\hat{G}$. Each successive steady-state calculation was run using the previously converged steady-state solution as an initial guess. This procedure was repeated until at some critical value of $\hat{G}$ a transition to multicells occurred. In the following calculations, the grid spacing set the wavelength of the initial instability (see the appendix for further discussion). The primary aim of this study is to follow the subsequent nonlinear development of the instability as an initial value problem.

For the low Prandtl number boundary-layer equations (3.11) and (3.12), symmetry about the vertical centerline was assumed for a 31×102 mesh (31 radial nodes and 102 angular nodes). This assumption was verified by computing a solution for the full annulus (0-2π) and comparing it with a solution based upon the symmetry assumption (see Fant, 1987, and Fant et al., 1988). The initial time-response behavior of the 0-2π run reproduced that of the 0-π run, up to a dimensionless time of $\tilde{t} = 832$, to within one percent error (see Fig. 2). All the important changes of the cellular pattern with time were also duplicated.

6 Numerical Results and Discussion

Steady-state unicellular results in the half-annulus were obtained up to a $\hat{G}$ value of 5.1. These were found to agree closely with the $\hat{G} \to 0$ steady-state limit solutions even up to a relatively large scaled gap spacing. To verify the $\hat{G} \to 0$ limit solution, the analytical results for F_1 and W_1, given by equations (4.2) and (4.5), respectively, are compared in Fig. 3 to the equivalent numerical results of the boundary-layer equations (3.10) and (3.13) for the pretransitional case of $\hat{G} = 5.1$. In this comparison, the vorticity and stream function were evaluated at $\psi = \pi/2$ and $\hat{G} = 5.1$.

The above results indicate that the pretransitional flow field ($\hat{G} \leq 5.1$) can be adequately represented by the leading-order expansions for $\hat{G} \to 0$. This suggests that the full nonlinear influence only becomes evident just prior to and beyond the point of instability. Note that the expansions of equation (4.1) for the $\hat{G} \to 0$ limit suggest that nonlinearity should become important at about the order of magnitude $\hat{G} \sim 10$. In the present numerical calculations, an instability and the nonlinear effects appear to come into play near $\hat{G} = 5.15$. This transitional gap spacing is a strong function of the azimuthal grid spacing and, in fact, the azimuthal grid spacing sets the wavelength of the initial instability (see Appendix A).

At $\hat{G} = 5.15$, a steady (stationary) seven-cellular flow field was found to develop. The seven cells encompassed an arc of about 80 deg near the vertical portion of the annulus (see Fig. 4). Then at $\hat{G} = 5.2$, an unsteady seven-cell instability set in at time $\hat{t}$ of approximately 35.0. Note that the converged steady-state result for $\hat{G} = 5.1$ was used as an initial condition to start both the $\hat{G} = 5.15$ and 5.2 cases. Also, the initial seven-cell flow field for $\hat{G} = 5.2$ was very similar to that encountered for $\hat{G} = 5.15$.

As previously mentioned, the cellular flow pattern was steady for both the vertical slot geometry of Lee and Korpela (1983) and the $\hat{G} = 5.15$ calculations of the present study. However, the multicellular flow calculated in the present study appears to undergo an unsteady secondary instability at around $\hat{G} = 5.20$, $\hat{t} > 35$, and vacillates periodically about the seven-cell state. The resulting periodic flow is composed of a successive 8-7-8-7 cellular pattern. In the seven-cell formation, the stronger cells appeared near $\psi = 90$ deg (see Fig. 4). The remaining cells successively decreased in strength as they proceeded away from the $\psi = 90$ deg point, in a fashion approximately proportional to $\sin \psi$.

At the start of the unsteady multicell cycle at $\hat{t} \simeq 35$, the

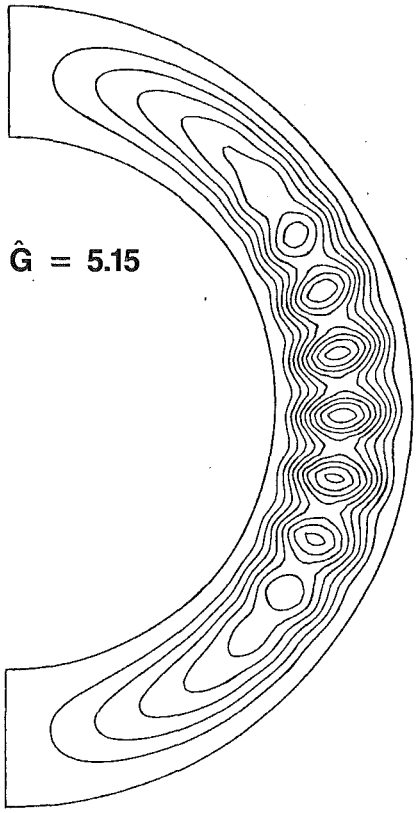

Fig. 4 Streamlines of the steady seven-cellular flow field

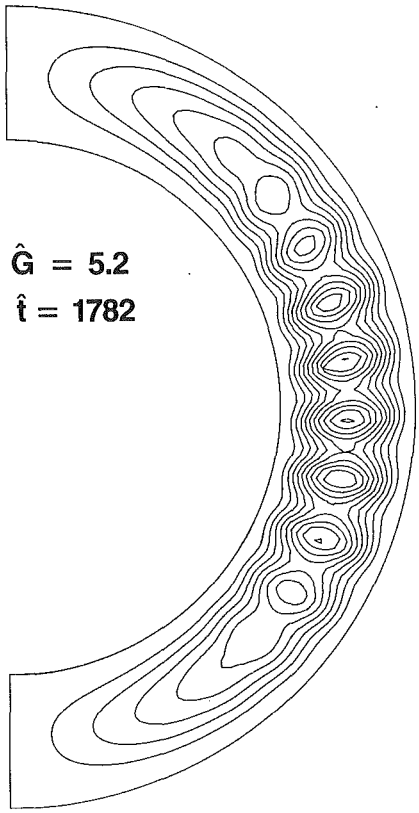

Fig. 5 Streamlines of an upward-shifted eight-cellular flow field (eight cells—top)

seven cells initially present because of primary instability weakened (the maximum stream function decreased) as an eighth cell formed on top (see Fig. 5). Then, the eight-cell pattern grew in strength until the two larger cells near $\psi = 90$ merged into one cell with the maximum stream function shifting upward to about 92 deg, forming an upward-shifted seven-cell flow pattern. Similarly, these seven cells then weakened as an eighth cell formed on the bottom portion of the chain of cells (see Fig. 6). Again, the eight-cell pattern grew in strength until the two larger cells merged into one with the maximum stream function shifting downward to about 87 deg, forming a downward-shifted seven-cell flow pattern and completing the 8–7–8–7 cycle. The strength of the stream function at $\psi = 90$ and $r = 0.5$ behaved in a "square wave" time-periodic fashion, as clearly illustrated in Fig. 7(*a*).

To examine the change in the unsteady cellular behavior as the scaled gap spacing $\hat{G}$ was increased beyond the secondary transition point, solutions were calculated for values of $\hat{G} = 5.3$, 5.4, 5.4841, and 5.5 using the $\hat{G} = 5.2$ seven-cell solution at $\hat{t} = 35.0$ as an initial condition. Figures 7 and 8 display the time variation of the stream function (for $\hat{G} = 5.2$, 5.3, 5.4, 5.4841, and 5.5, respectively) at $\psi = 90$ and $r = 0.5$, with constant time steps $\Delta\hat{t}$ varying from 1.0 to 0.25, respectively. The unsteady flow patterns for $\hat{G} = 5.3$, 5.4, and 5.4841 also appear to be periodic, but the shapes of the wave-form have noticeable differences. For $\hat{G} = 5.2$, the width of the peak is approximately 190 time units, and the maximum stream function is about 0.44. At $\hat{G} = 5.3$ and 5.4, the peak widths are approximately 85 and 70 time units, while the maximum stream functions are about 0.47 and 0.51, respectively. Notice that as $\hat{G}$ increases the unsteady traces of the solution become more involved. Finally, for $\hat{G} = 5.5$. a rather complex unsteady development emerges, with the maximum stream function (for the first 400 time units) near 0.57, and a peak width of approximately 65 time units. Note that the first wave-form shape for

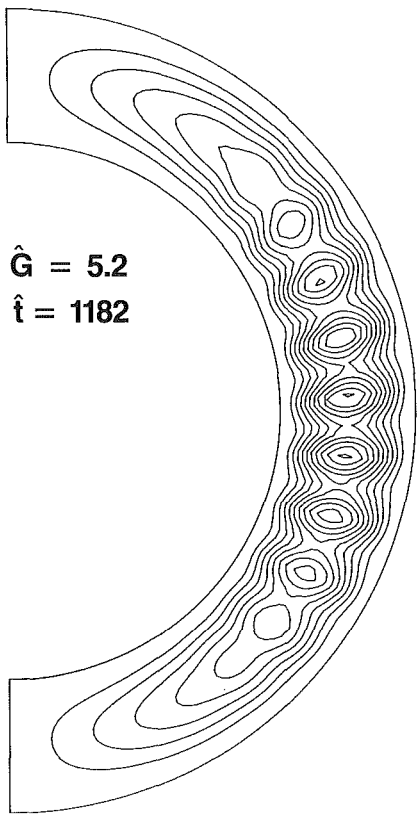

Fig. 6 Streamlines of a downward-shifted eight-cellular flow field (eight cells—bottom)

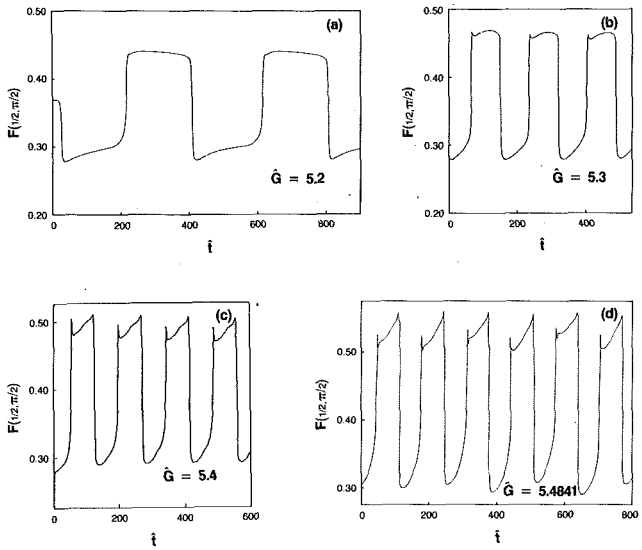

Fig. 7 Periodic time dependencies of the stream function at $(r, \psi) = (1/2, \pi/2)$

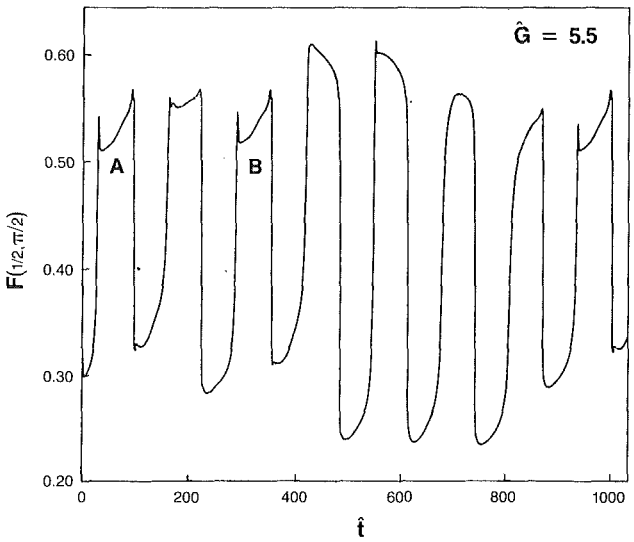

Fig. 8 Nonperiodic time dependence of the stream function at $(r, \psi) = (1/2, \pi/2)$

$\hat{G} = 5.5$ is similar to that for $\hat{G} = 5.4$, and the peak widths are within 5 time units. However, the unsteady solution for $\hat{G} = 5.5$ soon diverges from the behavior observed in the $\hat{G} = 5.4$ solution. The flow for $\hat{G} = 5.5$ appears to become aperiodic fairly soon within the calculations. This last solution has many qualitative features normally associated with chaotic solutions. There is no definite period observed in the solution (although with longer calculations one may yet emerge). In addition very small changes in "initial conditions" may lead to strikingly different unsteady patterns. This claim is supported by the observation that within the same solution, $\hat{G} = 5.5$, the solutions for the first and third peaks (beginning at $\hat{t} = 28$, peak A, and 285, peak B, respectively) are similar and yet the peaks following each of these are quite different. Whether or not a true transition to chaos has occurred in this flow is beyond the scope of this study. The numerical solutions are inconclusive because the relatively small time interval over which the solution has been generated contains too few waveforms for any definite conclusion to be reached (in particular note that near $\hat{t} = 950$ a waveform similar to the starting waveform reappears). Unfortunately, computational constraints did not allow for more extensive calculations (about *200 hours* of CPU time, on a machine equivalent to a VAX 11/780, were required to generate Fig. 7*a* alone). However, it is clear from the $\hat{G} = 5.5$ solution that a very complex unsteady flow pattern is developing. This flow pattern is not only temporally but also spatially complex. It must be remembered that the complexity of the unsteady trace is due to a shifting of the streamline pattern in the physical space. This is an interesting result, given the simplicity of the governing equations (3.10) and (3.13) for the low Prandtl number limit. For all unsteady cases the multicellular flow pattern was similar to that shown previously for $\hat{G} = 5.2$, except the cellular flow seemed to vacillate between nine and ten or ten and eleven cells. Again, the maximum stream function occurred near $\psi = 90$ deg, and was greatest for the nine-cell structure and least for the eleven-cell structure.

7 Conclusion

A high Rayleigh number, small-gap, small Prandtl number asymptotic theory was constructed, which simplified the two-dimensional Navier-Stokes equations into Cartesian-like boundary-layer equations. For these simplified equations, the energy equation decoupled from the vorticity equation and reduced to a simple pure-conduction form. The only nonlinear terms in the governing equations appeared in the vorticity equation.

When the small Prandtl number equations were solved numerically, a steady multicellular instability was found to develop at a scaled gap spacing $\hat{G}$ of 5.15 in the vertical portion of the narrow horizontal annulus.

For $\hat{G} = 5.2$, a secondary instability appeared, which resulted in an unsteady time-periodic multicellular flow, with a simple 8-7-8-7 repetitive cellular behavior. For $\hat{G} = 5.3$ and 5.4 more complicated periodic flow patterns developed. At $\hat{G} = 5.5$ periodicity appeared to be lost, and chaotic cellular behavior may have resulted. Thus, *stationary, time-periodic* and *complex unsteady* multicellular solutions have been calculated from a relatively simple nonlinear parabolic partial differential equation.

The results of this study show that a multicellular hydrodynamic instability is indeed possible in the vertical sections of narrow horizontal annuli, for $\mathrm{Pr} \to 0$. This instability does not need the presence of azimuthal diffusion to occur.

Acknowledgments

The authors would like to thank Dr. Korpela for his many valuable comments on the present paper. Dr. Fant would like to acknowledge the support obtained from the United States Air Force, through the Air Force Institute of Technology, for his studies at Iowa State University and the preparation of this manuscript. This study was supported in part by a National Science Foundation Presidential Young Investigator Award for Dr. Prusa and by a National Science Foundation Presidential Young Investigator Award for Dr. Rothmayer.

References

Arakwa, A., 1966, "Computational Design of a Long-term Numerical Integration of the Equations of Fluid Motion: Two Dimensional Incompressible Flows," *J. Comp. Phys.*, Vol. 1, pp. 119-143.

Bejan, A., 1984, *Convection Heat Transfer*, Wiley Interscience, New York.

Bishop, E. H., Carley, C. T., and Powe, R. E., 1968, "Natural Convective Oscillatory Flow in Cylindrical Annuli," *Int. J. Heat Mass Transfer*, Vol. 11, pp. 1741-1752.

Charrier-Mojtabi, M. C., Mojtabi, A., and Caltagirone, J. P., 1979, "Numerical Solution of a Flow Due to Natural Convection in Horizontal Cylindrical Annulus," ASME JOURNAL OF HEAT TRANSFER, Vol. 101, pp. 171-173.

Choi, I. G., and Korpela, S. A., 1980, "Stability of the Conduction Regime of Natural Convection in a Tall Vertical Annulus," *J. Fluid Mech.*, Vol. 99, pp. 725-738.

Drummond, J. E., and Korpela, S. A., 1987, "Natural Convection in a Shallow Cavity," *J. Fluid Mech.*, Vol. 182, pp. 543-564.

Elder, J. W., 1965, "Laminar Free Convection in a Vertical Slot," *J. Fluid Mech.*, Vol. 23, pp. 77–98.

Fant, D. B., Prusa, J., and Rothmayer, A. P., 1988, "Unsteady Multicellular Natural Convection in a Narrow Horizontal Cylindrical Annulus," *Proceedings of the 1st National Fluid Dynamics Congress*, Cincinnati, OH, July 25–28, pp. 1922–1935.

Fant, D. B., 1987, "The Numerical and Analytical Study of Bifurcation and Multicellular Flow Instability Due to Natural Convection Between Narrow Horizontal Isothermal Cylindrical Annuli at High Rayleigh Numbers," Ph.D. Dissertation, Iowa State University, Ames, IA.

Grigull, U., and Hauf, W., 1966, "Natural Convection in Horizontal Cylindrical Annulli," *Proc. Fluid Int. Heat Transfer Conf.*, Vol. 20, pp. 182–195.

Huetz, J., and Petit, J. P., 1974, "Natural and Mixed Convection in Concentric Annular Spaces—Experiment and Theoretical Results for Liquid Metals," *Proc. of the Fifth Int. Heat Trans. Conf.*, Tokyo, Japan.

Jischke, M. C., and Farshchi, M., 1980, "Boundary Layer Regime for Laminar Free Convection Between Horizontal Circular Cylinders," ASME JOURNAL OF HEAT TRANSFER, Vol. 102, pp. 228–235.

Korpela, S. A., 1983, private communication.

Korpela, S. A., 1974, "A Study of the Effect of Prandtl Number on the Stability of the Conduction Regime of Natural Convection in an Inclined Slot," *Int. J. Heat Mass Trans.*, Vol. 17, pp. 215–222.

Korpela, S. A., Gozum, D., and Baxi, C. B., 1973, "On the Stability of the Conduction Regime of Natural Convection in a Vertical Slot," *Int. J. Heat Mass Transfer*, Vol. 16, pp. 1683–1690.

Lee, Y., and Korpela, S. A., 1983, "Multicellular Natural Convection in a Vertical Slot," *J. Fluid Mech.*, Vol. 126, pp. 91–121.

Liu, C.-Y., Mueller, W. K., and Landis, F., 1961, "Natural Convection Heat Transfer in Long Horizontal Cylindrical Annuli," *Proc. 1961-62 Int. Heat Transfer Conf.*, pp. 976–984.

Mack, L. R., and Bishop, E. H., 1968, "Natural Convection Between Horizontal Concentric Cylinders for Low Rayleigh Numbers," *Q. J. Mech Applied Math*, Vol. 21, pp. 223–241.

Pepper, D. W., and Harris, S. D., 1977, "Numerical Simulation of Natural Convection in Closed Containers by a Fully Implicit Method," *ASME J. Fluids Eng.*, Vol. 99, pp. 649–656.

Powe, R. E., Carley, C. T., and Bishop, E. H., 1969, "Free Convective Flow Patterns in Cylindrical Annuli," ASME JOURNAL OF HEAT TRANSFER, Vol. 91, pp. 310–314.

Powe, R. E., Carley, C. T., and Carruth, S. L., 1971, "A Numerical Solution for Natural Convection in Cylindrical Annulli," ASME JOURNAL OF HEAT TRANSFER, Vol. 93, pp. 210–220.

Prusa, J., and Yao, L. S., 1983, "Natural Convection Heat Transfer Between Eccentric Horizontal Cylinders," ASME JOURNAL OF HEAT TRANSFER, Vol. 105, pp. 108–116.

Rao, Y.-F., Miki, Y., Fukuda, K., Takata, Y., and Hasegawa, S., 1985, "Flow Patterns of Natural Convection in Horizontal Cylindrical Annulli," *Int. J. Heat Mass Transfer*, Vol. 28, pp. 705–714.

Seki, N., Fukusako, S., and Inaba, H., 1978, "Visual Observation of Natural Convective Flow in a Narrow Vertical Cavity," *J. Fluid Mech.*, Vol. 84, pp. 695–704.

Smith, F. T., 1983, "Large-Scale Separation and Wake Closure/Reattachment—The Cascade Problem," United Technologies Report No. UTRC83-13.

Thomas, R. W., and de Vahl Davis, G., 1970, "Natural Convection in Annular and Rectangular Cavities—a Numerical Study," *Proc. of the Fourth Int. Heat Trans. Conf.*, Paris, France, Paper No. NC2.4.

Vest, C. M., and Arpaci, V. S., 1969, "Stability of Natural Convection in a Vertical Slot," *J. Fluid Mech.*, Vol. 36, pp. 1–15.

Walton, I. C., 1980, "The Stability of Free Convection in a Horizontal Cylindrical Annulus," *Q. J. Mech. Appl. Math.*, Vol. 33, pp. 125–139.

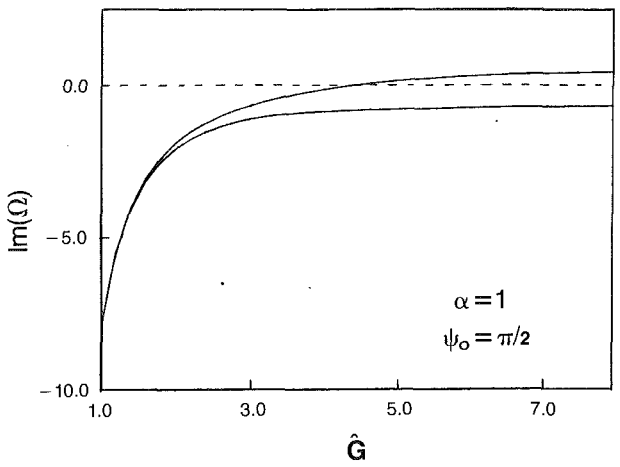

Fig. A1 The imaginary part of Ω as a function of the scaled gap spacing; from equation (A3)

APPENDIX

A Linear Stability Analysis for Inclined Channels

The present study suggests that the low Prandtl number equations undergo an instability for a finite value of the scaled gap spacing $\hat{G}$. In this appendix, a stability analysis will be presented that supports this claim. It should be noted that many prior studies have attributed the hydrodynamic instability to a localized Orr–Sommerfeld problem in which all diffusion effects, and most notably the azimuthal diffusion, are important. The most relevant study as far as the high Rayleigh number small-gap problem is concerned is the study of Walton (1980). The present study contends that instabilities may still be encountered even though streamwise (i.e., azimuthal) diffusion is vanishingly small. The stability analysis for the horizontal annulus is quite complicated because of the angular dependence of the baseline flow. This angular dependence will cause a leading order interplay between all the terms in a spectral decomposition of the disturbance field. To simplify the problem, the simpler inclined slot geometry will be addressed here. The results of this analysis are expected to have qualitative application to the horizontal annulus problem.

The primary simplification for the inclined channel is that the exact baseline solution is

$$F_0 = r^2(r-1)^2\frac{\hat{G}^3 \sin \psi_0}{24} \tag{A1}$$

where ψ_0 is now a fixed channel inclination. This solution is exact for all $\hat{G}$ (i.e., it is not merely the first term of a small $\hat{G}$ limit; also see Bejan, 1984). In addition, the baseline solution of equation (A1) is a function of r only. This solution is perturbed with a small disturbance

$$F \sim F_0 + \epsilon\{f_1(r)e^{i(\alpha\psi - \Omega\hat{t})} + \text{complex conjugate}\} + \ldots \tag{A2}$$

where α is real and $\Omega = \Omega_r + i\Omega_i$. A positive imaginary part of the frequency Ω gives an unstable disturbance, whereas a negative imaginary part of Ω gives a stable disturbance. Substitution of the expansion (A2) and the baseline solution into the governing equation gives an eigenvalue equation, which was solved using the Frobenius series. The convergence of this series was verified numerically for several special cases. Most solutions were found to give stable results. However, one root, starting with $f_1 \sim a_0 r^2 + \ldots$, was found to produce an instability. For example, a low-order truncation of the Frobenius series, to three terms, gives the following dispersion relation:

$$\Omega = \frac{4}{\hat{G}^2}\left[-2i \pm \sqrt{11 - \frac{ia}{24}\hat{G}^4 \sin \psi_0}\,\right] \tag{A3}$$

Note that for $\hat{G} \to 0$ the above equation generates a very large negative value for the imaginary part of Ω (i.e., very stable waves). However, as $\hat{G}$ increases one of the branches produces a positive imaginary part to Ω, giving an unstable wave. This behavior is shown in Fig. (A1) for the vertical channel, $\psi_0 = 90$ deg. Equation (A3) also suggests that unstable waves will be encountered first in the vertical channel, with the inclined channel needing larger values of $\hat{G}$ to generate an instability. Also, if $\psi_0 = 0$ (i.e., a horizontal channel) then no instability is possible. This behavior seems to be consistent with the numerical calculations for the annulus. Although a correction to the low-order truncation may be developed, the above equation appears to be capturing most of the important qualitative behavior. In particular, notice that as α increases (i.e., the wavelength $2\pi/\alpha$ becomes shorter), the neutral $\hat{G}$ is found to decrease as $\hat{G} \sim |\alpha|^{-1/4}$. This suggests a connection

with the equivalent of Walton's (1980) instability for the high Rayleigh number, small Prandtl number theory, on a shorter azimuthal length scale and with a smaller gap spacing. As the wavelength decreases, streamwise diffusion is expected to emerge when the azimuthal length scale is comparable to the radial length scale. This gives an azimuthal length scale of

$$|\alpha|^{-1} \sim O\left(\left[\frac{Ra}{\mathrm{Pr}}\right]^{-1/3}\right) \tag{A4}$$

The above analysis shows that an instability can occur within the context of a boundary-layer set of equations, and the streamwise diffusion effect incorporated by Walton (1980) is not a necessary precursor of instability, although it probably sets the minimum gap spacing for instability. If the above analysis is correct and all disturbances that are linearly unstable eventually emerge as nonlinear disturbances, then the above analysis suggests that multicells will be observed at all gap spacings.

It appears that the multicells observed in the numerical calculations were selected by the grid spacing in the numerical method. A grid size study was conducted to determine the sensitivity to the gap spacing of the initial instability. The results of this study are shown in Fig. (A2). Note that these results for the full annulus produce a transitional gap spacing $\hat{G}$ that varies as $\Delta\psi^{1/4}$, which is consistent with the above predictions. Even though the instability will manifest itself for all gap spacings, the later nonlinear numerical calculations may still be viewed as an initial value problem, with the grid setting the initial condition.

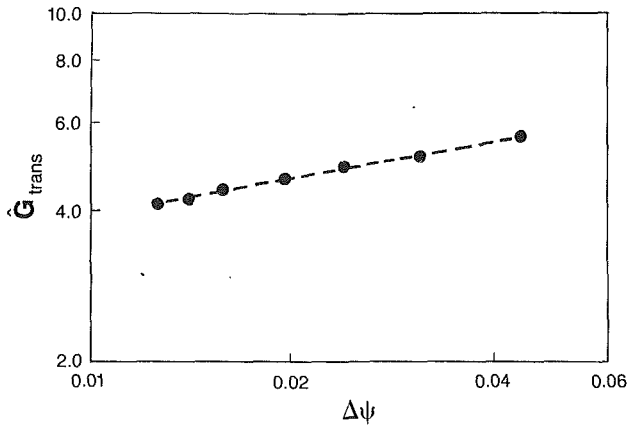

Fig. A2 Numerical result for transitional gap spacing as a function of the azimuthal grid spacing; $\hat{G}_{trans} \propto \Delta\psi^{0.2508}$

Thermal Convection With Large Viscosity Variation in an Enclosure With Localized Heating

T. Y. Chu

C. E. Hickox

Sandia National Laboratories,
Albuquerque, NM 87185

The present study is undertaken in order to gain an understanding of certain aspects of convective transport in a magma chamber. We have chosen to represent the chamber by an enclosure with localized heating from below. Results of both laboratory experiments and computer modeling are reported. The experimental apparatus consists of a transparent enclosure with a square planform. An electrically heated strip, with a width equal to 1/4 of the length of a side of the enclosure, is centered on the lower inside surface of the enclosure. For the experiments reported here, the top of the fluid layer is maintained at a constant temperature and the depth of the layer is equal to the width of the heated strip. The large viscosity variation characteristic of magma convection is simulated by using corn syrup as the working fluid. Measured velocity and temperature distributions as well as overall heat transfer rates are presented. The experiment is numerically simulated through use of a finite element computer program. Numerically predicted steamlines, isotherms, and velocity distributions are presented for the transverse vertical midplane of the enclosure. Good agreement is demonstrated between predictions and measurements.

Introduction

The present study was undertaken in order to gain an understanding of certain aspects of convective transport in a magma chamber and is being pursued in support of the Magma Energy Extraction Program at Sandia National Laboratories (Ortega et al., 1987). The approach taken in our studies is first to characterize the convection in the magma chamber and then to examine the convective heat transfer to an energy extraction device inserted into the magma chamber. Typically, a magma chamber is periodically recharged at a discrete location (Clark et al., 1987). Hence, we elect to represent the magma chamber as an enclosure with localized heating from below. Specifically, the enclosure chosen for study has a square planform with a heated strip centered on the lower inside surface of the enclosure. The large viscosity variation characteristic of magma convection (Clark et al., 1987) is simulated by using corn syrup as a working fluid. Results from laboratory experiments and computer modeling are presented.

Thermal convection is of continuing interest (Globe and Dropkin, 1959; Chu and Goldstein, 1973; Adrian et al., 1986) because of its application in the modeling of flow and energy transfer in geophysics, meterology, and astrophysics as well as in numerous applications to engineering systems. The numerical modeling of Torrance and Turcotte (1971), which treats thermal convection between horizontal free boundaries, appears to be the first such study to consider large viscosity variations. For a Rayleigh number of 3600, the viscosity was found to exert a signficant influence on the flow field. Richter et al. (1983) and Booker (1976) experimentally investigated thermal convection with large viscosity variations in a horizontal fluid layer using a variety of working fluids including a golden syrup. In addition, Richter et al. (1983) also measured horizontally averaged temperatures in the fluid layer. Their results indicate that the Nusselt number Nu for the variable viscosity cases can be approximated by the constant viscosity results if the correlation is cast in a form where the Rayleigh number Ra is normalized with the Rayleigh number at the onset of convection, i.e., $\mathrm{Nu} = C\,(\mathrm{Ra}/\mathrm{Ra}_c)^n$, where C is a constant, the subscript c indicates a critical value, and the viscosity is evaluated at the average of the boundary temperatures. Furthermore, temperature measurements showed the existence of a stagnant conduction zone above the actively convecting part of the layer.

Previous studies of enclosure convection with localized heating from below have been concerned mainly with cases involving a circular heater on the lower surface of an enclosure (Torrance et al., 1969; Kamotuni et al., 1983). Boehm (1977) carried out numerical studies of natural convection in air due to stripwise heating, from below, on a horizontal surface. For a Grashof number of 10^5, a plumelike structure was found to exist above the heated strip.

It appears from the literature review that the combination of large viscosity variation and localized heating in an enclosure has never been studied before. In addition to the fact that localized heating is appropriate for modeling magma chamber flow, this particular geometry produces a convective flow field that is relatively straightforward to model numerically.

Experimental Program

Apparatus. A schematic of the test section is shown in Fig. 1. The enclosure is an open top box with a square planform measuring 55.9 cm on a side and 60 cm high and is constructed from 13-mm-thick Lexan (polycarbonate) sheets. A heater assembly consisting of a centered heated strip measuring 13.6 cm by 55.9 cm is attached to the lower inside surface with silicone adhesive. The heater assembly is a three-layer structure. The top layer is made of a sheet of 13-mm-thick Lexan with a centered recess machined into the sheet to accept the heated strip. This top layer is glued to two 10-mm-thick Lexan glazing sheets. The glazing sheets are extruded sheets with longitudinal cells, providing structural strength and effective insulation. The heated strip consists of a 3-mm-thick copper plate with a thin, flexible, etched foil heater glued on the

Contributed by the Heat Transfer Division and presented at the ASME Winter Annual Meeting, Chicago, Illinois, November 28–December 2, 1988. Manuscript received by the Heat Transfer Division December 23, 1988; revision received July 6, 1989. Keywords: Geophysical Heat Transfer, Natural Convection, Numerical Methods.

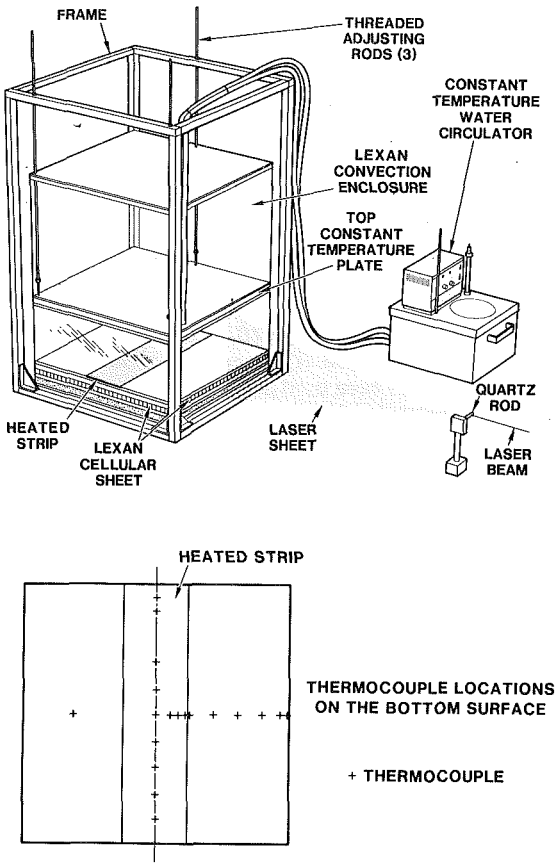

Fig. 1 Schematic of the test section showing thermocouple locations

underside. The resistance of the foil heater is nominally 8 ohms. The temperature of the heated strip is monitored by 12 thermocouples embedded in the copper plate. In addition, there are 7 thermocouples in the unheated portion of the bottom plate. The side wall temperature is similarly monitored with 4 thermocouples. The thermocouples are made of 0.25-mm copper-constantan wires mounted flush with the surface. The thermocouple locations are shown in the schematic.

The fluid layer is bounded from above by a constant temperature plate made of 25.4-mm-thick brass. The temperature of the plate is maintained constant by the circulation of cooling water, from a temperature-controlled bath, in twenty 13 mm by 19 mm parallel channels machined in the back of the plate. The back of the plate is sealed by a 6-mm-thick brass plate. The plate temperature is monitored by thirteen type E (chromel-constantan) thermocouples. During the experiment, the plate temperature was found to be uniform within 0.05°C for plate temperatures ranging from 15 to 50°C and within 0.1°C for plate temperatures below 6°C. The constant-temperature plate is supported from an overhead frame with three threaded adjusting rods, which allow the depth of the fluid layer to be varied. The fluid layer depth for the present series of experiments was fixed at 13.6 cm, the same as the heater width. The horizontal dimension of the layer is thus essentially four times that the layer depth.

Experimental Method. Three types of data are obtained from the experiments: (1) overall heat transfer rates, (2) velocity fields, and (3) temperature profiles. For overall heat transfer measurements, the entire test section is insulated with 13 mm of packing foam and 3.8 cm of urethane insulation. The packing foam forms a conforming seal between the urethane sheet and the Lexan wall to prevent infiltration. For each run, the top surface temperature and the heater power were set to the desired values and a data point was obtained when the heated strip temperature reached a steady state. The average temperature of the central half of the strip is used as the characteristic temperature of the heated strip. The heat transfer coefficient is defined in terms of the temperature difference between the heated strip and upper surface and the area of the heated strip. Typically, the temperature difference varies less than 2 percent over the central region of the heated strip.

The velocity field was made visible by taking time lapse photographs of scattered light from seeded particles in the working fluid. The particles used were glass balloons with typical sizes ranging from 20 to 100 μm. Because of the large viscosity of the fluid and the small size of the particles, the particles can remain in suspension essentially indefinitely (several months). Approximately 0.1 cm^3 of glass balloons were added to each 20 liter bucket of syrup. The resulting particle density was estimated to be in the range of 30–100 particles per cm^3 of fluid. The light source used was a 15 mW He-Ne laser. A 10 mm diameter quartz rod acting as a cylindrical lens was used to create a vertical sheet of laser light cutting through the central plane of the test section. Five-minute time exposures were used to obtain streamline patterns.

Nomenclature

a_o, a_1, a_2 = constants in expression for viscosity
b_o, b_1 = constants in expression for thermal conductivity
C = constant
D = layer depth
c = specific heat
c_o, c_1, c_2 = constants in expression for specific heat
d_o, d_1, d_2 = constants in expression for density
$f(\theta)$ = nondimensional viscosity
$g(\theta)$ = nondimensional thermal conductivity
g = gravitational acceleration
$h(\theta)$ = nondimensional specific heat
k = thermal conductivity
Nu = Nusselt number
Nu(x) = local Nusselt number
P = nondimensional pressure
Pr = Prandtl number
q = mean heat flux
Ra = Rayleigh number
$R(u)_i$ = residual solution vector
T = temperature
u, v = nondimensional velocity components
u_i = solution vector
x, y = nondimensional spatial coordinates
x/W, y/W = nondimensional spatial coordinates
W = width of heated strip
α = thermal diffusivity
β = coefficient of volumetric thermal expansion
ΔT = temperature difference
θ = nondimensional temperature
μ = viscosity
ν = kinematic viscosity
ρ = density

Subscripts

c = critical value
h = heated strip
i = iteration number
L^* = characteristic length
m = mean value
o = reference value

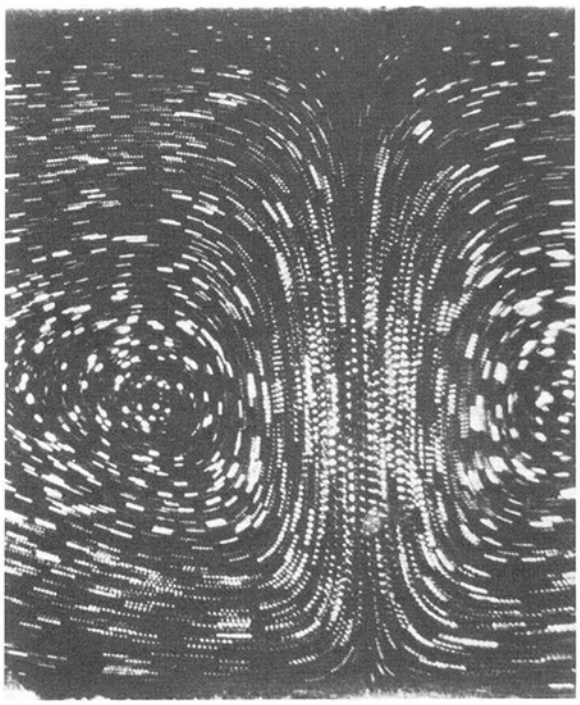

Fig. 2 Example of multiple-exposure particle tracking: Case A (see text for details); exposure interval: 15 s

For velocity determinations, the laser beam is interrupted by a shutter to create a multiple exposure of instantaneous positions of particles at fixed intervals apart. One-second exposures 15 to 30 s apart were found to be satisfactory. A typical example of multiple-exposure particle tracking is shown in Fig. 2. The photograph corresponds to case A (see later section for details) in the present study. Our method is a variation on the time exposure method used by Carey et al. (1981) and is less demanding photographically. It also allows three-dimensional flow effects normal to the illuminated plane detecting region (laser sheet) to be readily detected, which otherwise may be misinterpreted from a time exposure as lower velocities. Shadowgraphs were also used to visualize the temperature field. A 6-mm aperture illuminated with a slide projector was used as the light source. A parallel beam of light was then produced by a 25-cm-dia. f/6 spherical mirror and subsequently directed through the test section onto a screen placed in contact with the test section wall. A double pane window of Lexan was used to minimize the heat loss during photography.

A vertical temperature profile was obtained using a specially made L-shaped probe. The probe body was made of 1.8-mm o.d. stainless steel tubing with 0.13-mm thermocouple wires strung through the center. The vertical leg of the probe passes through a penetration in the upper, constant-temperature plate. The horizontal leg of the probe consists of a stainless steel section approximately 3.5 cm long and a double-bore alumina tube glued inside the stainless steel tube and extending 3 mm beyond it. The two thermocouple wires (copper-constantan) emerging from the alumina tube are welded to form the measuring junction. Because of the large viscosity of the working fluid, the temperature measurement must be accomplished rapidly before the entire flow field adjusts substantially to the presence of the probe. A typical temperature profile measurement requires approximately one hour.

Thermocouples used in the experiment were calibrated in the Standards Laboratory at Sandia National Laboratories using a resistance thermometer, which was calibrated against freezing point standards. The maximum calibration error is ± 0.02°C. The combined errors introduced by the ice-point reference junction and by curve fitting are estimated to be no more than ±0.03°C. Therefore, the maximum error in the measured temperature difference is no more than ±0.1°C. The electrical power input to the heater is determined to an accuracy of ±0.2 percent, based on the known accuracy of the calibrated instruments used in the measurement. The net rate of heat loss or gain between the test section and the surroundings is estimated to be no more than ±2.0 percent of the electrical power input.

Working Fluid. The working fluid used is a commercial corn sweetener commonly known in the food industry as 42/43 corn syrup (*Critical Data Book*, 1975). It has a solid content of 80.3 percent, by weight. Detailed specifications for the material have been published (*Critical Data Book*, 1975). Although this syrup has been used in a number of studies (Olson, 1984), the temperature dependence of some of the thermophysical properties has not previously been available. As a consequence, the temperature dependence of thermal conductivity and viscosity was measured as part of the experimental program. Equations used for the determination of fluid properties are summarized in the appendix.

Since only provisional values of thermal conductivity are available (*Critical Data Book*, 1975), a line heat source probe was used to measure the thermal conductivity of corn syrup as a function of temperature in the range 9–60°C. Details of the experimental method are similar to those described by Hickox et al. (1986). The thermal conductivity probe produced measurements of thermal conductivity that were within ±1.0 percent of those measured with a standard line source probe (Drotning and Tormey, 1984). When used to measure the thermal conductivity of glycerol, the standard probe produced results within ± 1.5 percent of handbook values. Therefore, the accuracy of the thermal conductivity measurements is ±2.5 percent. A total of 27 runs covering five temperatures was made. Thermal conductvity k was found to be a linear function of temperature with an rms deviation of the fit (given in the appendix) from the data of 0.5 percent (Littel et al., 1988).

Since the variation of viscosity with temperature is of prime importance in the present studies, the viscosity of the syrup was measured in a series of falling ball experiments. The experiments were carried out in a 17.3-cm-dia. cylinder at five temperatures ranging from 9 to 51°C. Wall effects were corrected according to the procedure described by Happle and Brenner (1973). Viscosity measurements made with the falling-ball technique are accurate to within ±1.0 percent, with a typical repeatability of ±0.5 percent, and are in excellent agreement with graphic data (*Critical Data Book*, 1975). The experimental data and high-temperature data (*Critical Data Book*, 1975) were combined to fit the viscosity temperature dependence with a superexponential form (Richter et al., 1983) with an rms deviation of the fit from the data in the range of interest of 3.5 percent.

Density and specific heat were obtained from published data (*Detailed Tables. . .*, 1984, *Critical Data Book*, 1975), and the thermal expansion coefficient was calculated by differentiation of the curve of density versus temperature. Typical values, at 25°C, for density, specific heat, thermal expansion coefficient, thermal conductivity, and viscosity are, respectively, 1.423 g/cm^3, 2.30 J/gK, 3.96×10^{-4} K^{-1}, 0.380 W/mK, and 748 poise.

Computational Approach

For computational purposes, a steady, planar flow field was assumed for the vertical midplane of the enclosure. The nondimensional continuity, incompressible Navier–Stokes, and energy equations are

$$\frac{\partial u}{\partial x}+\frac{\partial v}{\partial y}=0 \qquad (1)$$

$$\sqrt{\frac{\mathrm{Ra}_o}{\mathrm{Pr}_o}}\left(u\frac{\partial u}{\partial x}+v\frac{\partial u}{\partial y}\right)= -\frac{\partial P}{\partial x}+\frac{\partial}{\partial x}\left[f(\theta)\frac{\partial u}{\partial x}\right]+\frac{\partial}{\partial y}\left[f(\theta)\frac{\partial u}{\partial y}\right], \quad (2)$$

$$\sqrt{\frac{\mathrm{Ra}_o}{\mathrm{Pr}_o}}\left(u\frac{\partial v}{\partial x}+v\frac{\partial v}{\partial y}\right)= -\frac{\partial P}{\partial y}+\sqrt{\frac{\mathrm{Ra}_o}{\mathrm{Pr}_o}}\,\theta+\frac{\partial}{\partial x}\left[f(\theta)\frac{\partial v}{\partial x}\right]+\frac{\partial}{\partial y}\left[f(\theta)\frac{\partial v}{\partial y}\right], \quad (3)$$

and

$$h(\theta)\sqrt{\mathrm{Ra}_o\mathrm{Pr}_o}\left(u\frac{\partial\theta}{\partial x}+v\frac{\partial\theta}{\partial y}\right)=\frac{\partial}{\partial x}\left[g(\theta)\frac{\partial\theta}{\partial x}\right]+\frac{\partial}{\partial y}\left[g(\theta)\frac{\partial\theta}{\partial y}\right], \quad (4)$$

where the Oberbeck–Boussinesq (OB) approximation (Yih, 1977) has been invoked, the hydrostatic pressure has been absorbed into the pressure term, and all physical properties are treated as temperature dependent. The horizontal and vertical coordinates are denoted by x and y, and the corresponding velocity components by u and v. Gravity g acts in the negative y direction. The nondimensional pressure is P and the nondimensional temperature is $\theta = (T-T_o)/\Delta T$, where T is the temperature, T_o is the temperature of the upper surface of the enclosure, and ΔT is the overall temperature difference between the heated strip and the upper surface. The Rayleigh number is $\mathrm{Ra}_o = g\beta\Delta TW^3/\nu_o\alpha_o$, and $\mathrm{Pr}_o = \nu_o/\alpha$ is the Prandtl number, where the subscript o indicates properties evaluated at T_o. Also, $\nu_o = \mu_o/\rho_o$ and $\alpha_o = k_o/\rho_o c_o$ where μ_o, ρ_o, k_o, and c_o are, respectively, the reference viscosity, density, thermal conductivity, and specific heat. For the nondimensionalization, the reference length is the heated strip width W, the reference velocity is $\sqrt{\mathrm{Ra}_o\mathrm{Pr}_o}\alpha/W$, and the reference pressure is $\mu_o\sqrt{\mathrm{Ra}_o\mathrm{Pr}_o}\alpha_o/W^2$. The variations of physical properties with temperature are given by $\mu/\mu_o = f(\theta)$, $k/k_o = g(\theta)$, and $c/c_o = h(\theta)$, which can be obtained from the expressions presented in the appendix. For computational purposes, the variation of density with temperature is represented in the usual manner by $\rho/\rho_o = 1-\beta\Delta T\theta$, where β is the thermal expansion coefficient, and is assumed constant.

An additional comment is appropriate with regard to the OB approximation. As is well known, this approximation entails the assumption that density changes are important only in the buoyancy term in the equations of motion and are negligible elsewhere. Often, the approximation is invoked along with the additional restriction of constant thermophysical properties. In this "restricted" approximation, the allowable temperature difference is quite small for liquids (approximately 4°C for water at 15°C and 1 atm). However, it can be shown that, if the approximation is "extended" by allowing for the variation of thermophysical properties (other than density) with temperature while retaining the incompressible form of the continuity equation, then the allowable temperature differences can be two to three orders of magnitude larger for liquids (Gartling and Hickox, 1985). This is especially true for liquids that exhibit a strong temperature dependent viscosity. It is thus quite likely that the use of the OB approximation will not introduce any appreciable errors into our analysis.

Numerical solutions to equations (1)–(4) are sought subject to the conditions of no slip on all solid boundaries, $\theta = 1$ on the heated strip, $\theta = 0$ on the upper surface, and zero heat flux on the remaining boundaries. A finite element computer program (FIDAP User's Manual, 1988), based on the Galerkin formulation of the finite element method, was utilized for the numerical simulations. Initial simulations of the entire flow field produced flows that were symmetric about the vertical midplane and in essential agreement with experimental observations. Hence, the numerical simulations described here were performed for a symmetric half of the flow field. The computational domain was discretized using a nonuniform mesh of 600 nine-node, quadrilateral elements, as shown in Fig. 3. A discontinuous pressure discretization was used and a consistent penalty function approach was adopted to enforce the incompressibility constraint. Steady-state solutions were obtained by first using approximately 10 successive substitution iterates with a relaxation factor of 0.5, followed by 10 to 20 Newton–Raphson iterates, with the same relaxation factor. Depending on the particular numerical values of the parameters, it was sometimes necessary to increment the parameters of a converged solution to obtain converged solutions for larger Ra_o, Pr_o, or viscosity variations. Convergence was assumed whenever $\|u_i - u_{i-1}\|/\|u_i\| \le 0.01$ and $\|R(u_i)\|/\|R(u_o)\| \le 0.01$ where $\|\cdot\|$ denotes the Euclidian norm, u_i is the solution vector at iteration i, and $R(u_i)$ is the residual solution vector. Grid refinement studies were performed prior to the selection of the grid geometry used in the simulations in order to assure that the grid spacing was appropriate for the resolution of the flow field to be studied.

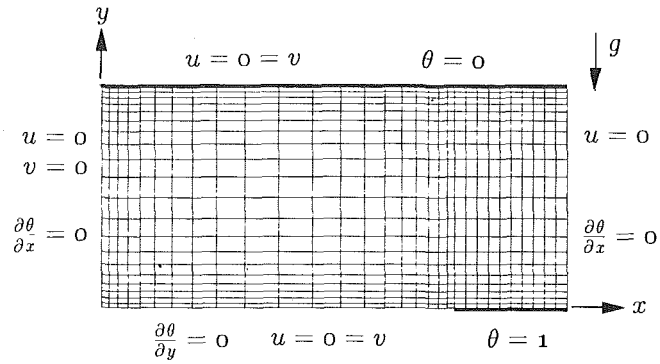

Fig. 3 Computational grid: Nondimensional width and depth are 2.06 and 0.98, and the heated strip half-width is 0.5

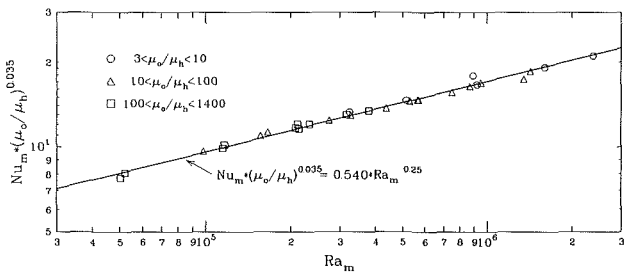

Fig. 4 Overall heat transfer correlation

Results

Heat Transfer. A total of 30 heat transfer runs were made with average heat input ranging from 0.067 to 0.136 W/cm^2, top surface temperature from 4.1 to 50.1°C, and heated strip temperature from 42.7 to 74.6°C. The largest top-to-bottom viscosity ratio across the layer was 1397; the smallest ratio was 3.12. Using the mean of the heater and upper surface temperature as the reference temperature and the layer depth (same as the heater width in the present case) as the characteristic dimension, the Rayleigh number was calculated to vary from 5×10^4 to 2×10^6, and the Prandtl number from 9.2×10^3 to 3.3×10^5. As shown in Fig. 4, the Nusselt number ($\mathrm{Nu}_m = qD/k_m\Delta T$, where q is the mean heat flux) for the heated strip was found to be well correlated with the power law formulation

Table 1 Parameters for the three cases simulated

Case	T_o °C	ΔT, °C	Ra_o $\times 10^{-4}$	Ra_m $\times 10^{-4}$	Pr_o $\times 10^{-5}$	Pr_m $\times 10^{-5}$	μ_o/μ_h	k_o/k_h	c_o/c_h	ρ_o/ρ_h
A	29.2	20.5	6.05	21.7	2.53	0.73	9.9	0.98	0.97	1.01
B	15.6	37.0	1.38	20.1	19.78	1.37	101.3	0.97	0.95	1.02
C	5.3	51.9	0.28	19.4	134.39	1.96	1026.0	0.96	0.92	1.02

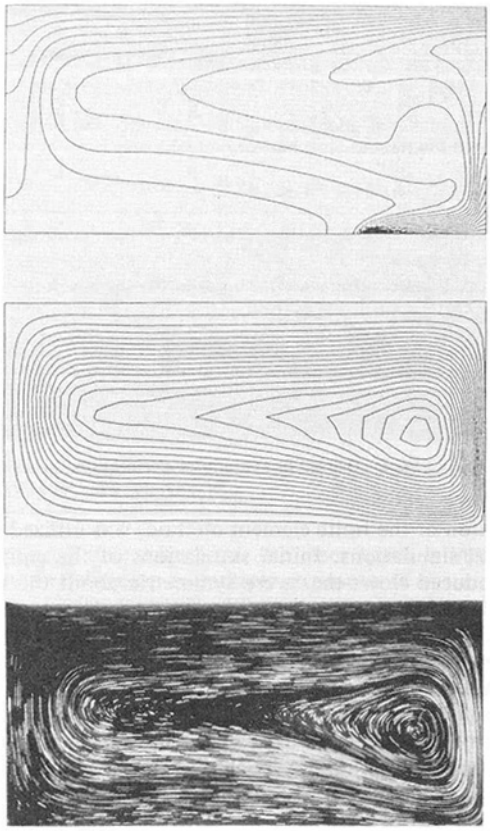

Fig. 5(*a*) Computed isotherms, streamlines, and photographs of particle paths for case A

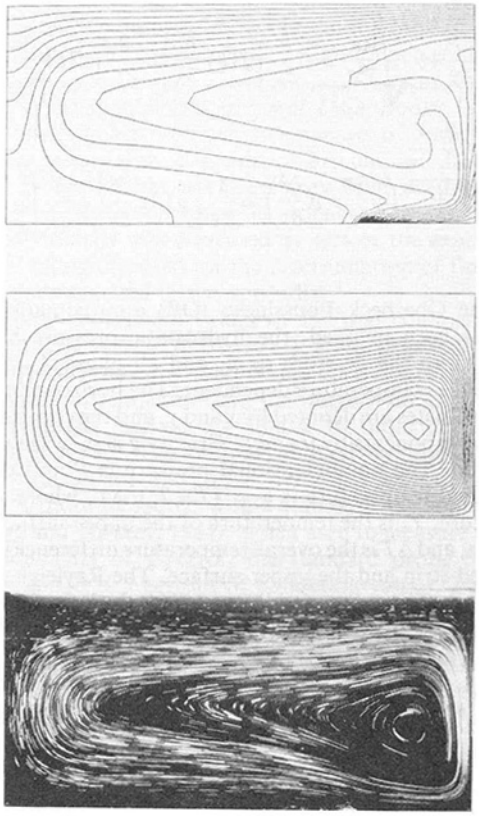

Fig. 5(*b*) Computed isotherms, streamlines, and photographs of particle paths for case C

$$Nu_m = 0.54(Ra_m)^{0.25}\left(\frac{\mu_o}{\mu_h}\right)^{-0.035} \quad (5)$$

where the subscripts m, o, and h indicate that properties are evaluated at the mean, upper surface, or heated strip temperatures. It is interesting to note that the largest effect of property variation is accommodated by evaluating properties at the mean temperature. The additional power law correction based on the viscosity contrast is relatively small. For a viscosity contrast of 1000, the correction is only 21 percent. In this respect, the present result is in agreement with the observations made by Richter et al. (1983) and Carrigan (1987). The rms deviation of the data from the fit is 2.46 percent, and the maximum deviation is 7.7 percent. A quite remarkable result, considering the large viscosity variation involved.

Lloyd and Moran (1974) extended an observation by Goldstein et al. (1973) and proposed a universal correlation for natural convection from arbitrary planforms in an extended medium as

$$Nu = 0.54Ra_{L^*}^{0.25} \quad (6)$$

where the characteristic length L^* is defined as the ratio of surface area to surface perimeter. In the present case, if the perimeter is taken to mean the perimeter available for entrainment, excluding the ends of the heated strip, there is then an exact correspondence between the present result and the Lloyd and Moran correlation. However, this exact correspondence may be somewhat fortuitous since the entrainment mechanism is different for the two cases.

The total error in the determination of the Nusselt number is ±5.9 percent. The individual uncertainties are: ±3.0 percent for the thermal conductivity, ±2.0 percent for the rate of heat transfer with the surroundings, ±0.7 percent for the temperature measurement, and ±0.2 percent for the power measurement. The total error in the determination of the Rayleigh number is ±10.2 percent. The individual uncertainties are: ±6.5 percent for the viscosity (±4.5 percent for the measurement itself and ±2.0 percent for the measurement of temperature), ±3.0 percent for thermal conductivity, and ±0.7 percent for the measurement of temperature difference.

Velocity and Temperature Fields. Comparisons between experimental and computational results were investigated for three cases. Pertinent parameters for the cases studied are summarized in Table 1. The primary distinguishing feature of each of the three cases in the viscosity contrast μ_o/μ_h, which ranges from 10 to 1000. The three cases have essentially the same mean Rayleigh number Ra_m. All simulations were performed for a fluid layer of nondimensional half-width 2.06 and depth 0.98.

In Fig. 5, computed isotherms and streamlines are shown

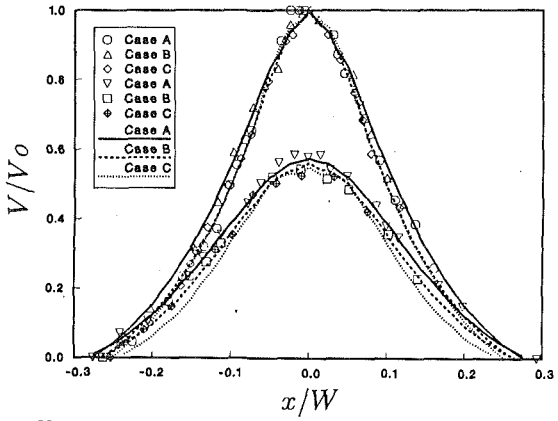

Fig. 6 Measured and computed vertical velocity distributions on the horizontal planes identified in Table 2

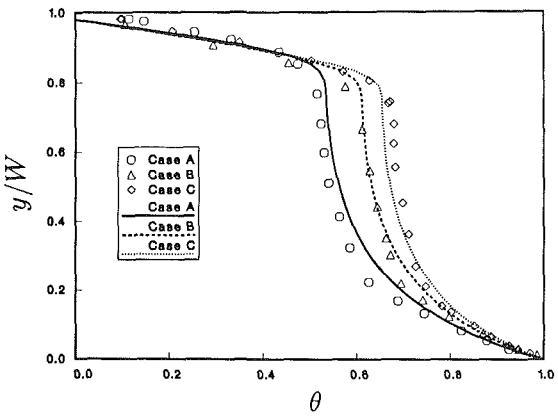

Fig. 7 Measured and computed temperature distributions on the vertical center plane of the enclosure

along with photographs of tracer particle path lines, rendered visible by illumination with a vertical sheet of laser light, for cases A and C. The flow field is laminar, steady, and symmetric with respect to the vertical midplane and consists of two counterrotating cells driven by a plume rising from the heated strip. There is good qualitative agreement between the observed and computed flow structure. For the higher viscosity contrast (case C), it is apparent that the flow is more strongly inhibited in the vicinity of the upper surface when compared with case A, which has a much smaller overall viscosity variation.

Measured and computed vertical velocity distributions on two horizontal planes are compared in Fig. 6 for all three cases. For each case, a vertical velocity profile was determined along a horizontal reference plane passing through the vortex centers of the two cells. The velocity is normalized with respect to the maximum centerline velocity on the reference plane. A second horizotal plane was established for each case at a distance of $W/4$ above the initial reference plane. On this upper plane, the velocities are also normalized by the maximum centerline velocity determined for the original reference plane. Experimental data for these planes are plotted as symbols and the results of the numerical simulations are plotted as continuous curves. The maximum centerline velocities for each case and each horizontal plane are tabulated along with the elevations of the planes in Table 2. The quantitative agreement between measurements and numerically predicted results is good. The magnitudes of the reference velocities differ by as much as 14 percent when experimental data are compared with numerical predictions, as is apparent from an inspection of the information in Table 2. However, when scaled with the reference velocity for each case, the distributions have nearly

Table 2 Comparison of measured and computed maximum centerline velocities

Case	Plane 1 elevation (y/W)	V_1 centerline (cm/min)	Plane 2 elevation (y/W)	V_2 centerline (cm/min)
A (measured)	0.44	1.25	0.69	0.73
A (calculated)	0.42	1.38	0.67	0.79
B (measured)	0.41	1.38	0.66	0.73
B (calculated)	0.39	1.49	0.64	0.84
C (measured)	0.40	1.68	0.65	0.88
C (calculated)	0.39	1.92	0.64	1.05

the same shapes and the experimentally determined distributions are in excellent agreement with predictions.

The nondimensional vertical temperature distribution along the center of the enclosure is plotted in Fig. 7. Experimental data are indicated by symbols and the continuous curves are the computed distributions. Reasonably good agreement is obtained between experimental and computed values. In all cases, a conduction layer is observed to exist adjacent to the upper surface. The layer occupies approximately 15 percent of the depth of the fluid layer. With increasing viscosity contrast, the conduction layer grows progressively thicker and a corresponding larger fraction of the temperature drop occurs in this layer. As a result, the underlying convecting layer grows thinner. This is most likely the reason that the elevation of the vortex centers of the convective cells decreases with an increase in viscosity contrast, as evident from a consideration of the data in Table 2.

It is interesting to note from the isotherm plots in Fig. 5 that the heat flux is a maximum at the center on the top surface where the rising plume impinges on the surface. Correspondingly, the heat flux is a minimum at the center of the heated strip where the plume leaves the surface. The variation of heat flux on the heated strip is demonstrated qualitatively in Fig. 8 by a slit-deflection shadowgraph (Jacob, 1967), for Case C. In this method, a slit of parallel light directed along the heated surface is deflected away from the surface as a result of the temperature-induced gradient in the refractive index of the fluid next to the surface. To first order, the amount of deflection is proportional to the temperature gradient, and is thus an indication of the local heat flux. For comparative purposes, the calculated, nondimensional heat flux distribution is included in the figure. The calculated heat flux exhibits a pronounced peak at the edge of the heated strip, reflecting the singular nature of the computational model at this location. The absence of this peaking phenomenon in the slit-deflection shadowgraph is a result of lateral conduction near the edges of the heated strip, an effect not represented in the computational model. Both the experimental and computed heat flux distributions exhibit a region of near-uniform flux distribution and a significant dip at the base of the rising central plume, a shadowgraph of which is also shown in the figure. The ratios of the computed Nusselt numbers Nu_m, based on the mean temperature, for Cases A, B, and C, to the corresponding Nusselt numbers predicted from equation (5) are 0.98, 0.97, 0.93, respectively, indicating good agreement between computed and experimentally determined values.

Errors in the measurement of the temperature distribution are difficult to assess because the usual methods of bounding the estimate do not provide meaningful results. It is observed that the long term effect due to the presence of the measuring probe is not merely to modify the flow field, but rather to alter completely the geometry of the flow field. For example, the location of the central plume is ultimately displaced by several centimeters in response to the additional resistance to flow associated with the presence of the probe. Therefore, it was necessary to make measurements "quickly" before sig-

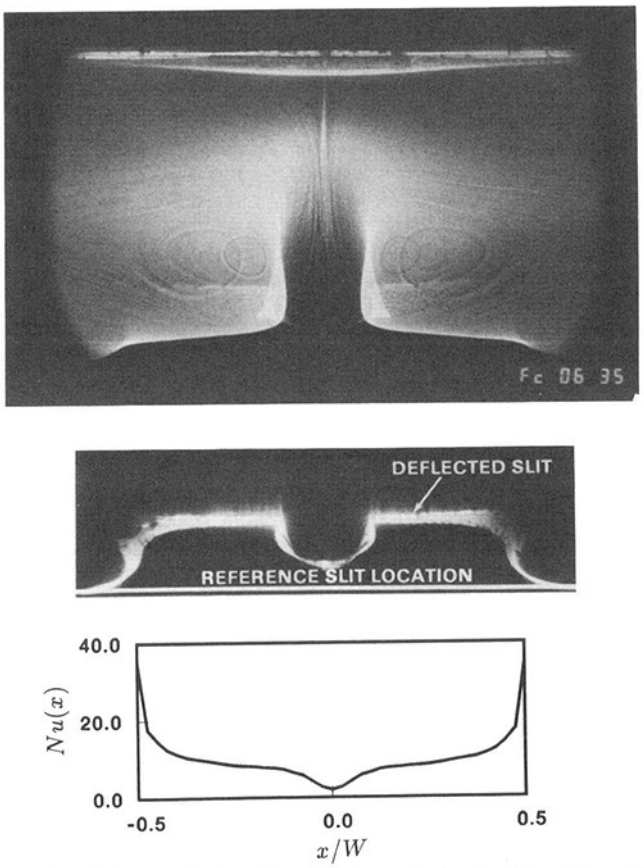

Fig. 8 Shadowgraph of the thermal plume of case C and local Nusselt number Nu(x) distribution on the heated strip by the slit-deflection shadowgraph method (center figure) compared with calculations

nificant alterations in the flow field occurred. The uncertainty in the location of the measurement location associated with the temperature probe is ± 0.5 mm, resulting in a maximum measurement error of $\pm 0.8°C$ within the thermal boundary layer. The overall temperature difference between the heated strip and the upper surface, as predicted from an extrapolation of the measured temperature distribution, is consistently lower than the surface temperature measurement with the largest discrepancy being ± 3.0 percent of the overall temperature difference. Velocity measurements are estimated to have an uncertainty of no more than ± 7.0 percent.

Concluding Remarks

Measurements made in the present series of experiments show that, even with very large viscosity variations, overall heat transfer rates can still be correlated in terms of conventional, constant-viscosity formulations provided that properties are evaluated at the mean temperature. Residual variable viscosity effects can then be represented by a multiplicative power law correction factor involving the viscosity contrast.

Computer modeling and flow visualization showed that the flow field for the present configuration consists of two counterrotating cells driven by a central plume rising from the heated strip. Computed velocity and temperature fields are in good agreement with detailed measurements. It appears that the bulk of the viscosity variation is confined to an essentially stagnant conduction layer next to the cold surface.

The results obtained here are for a specific configuration. However, the observed trends for large viscosity variations are likely to hold for other enclosure configurations involving laminar thermal convection. While by no means complete, the present investigation does provide important insights into the understanding and modeling of magmatic convection. In addition, it has produced useful engineering guidelines for the calculation of energy extraction from magma.

Acknowledgments

We wish to thank Mr. R. D. Jacobson and Mr. R. D. Meyer for their assistance with the construction and operation of the experimental apparatus, and with data acquisition. This work was performed at Sandia National Laboratories, and supported by the U.S. Department of Energy under Contract No. DE-AC04-76DP00789.

References

Adrian, R. J., Ferreira, R. T. D. S., and Boberg, T., 1986, "Turbulent Thermal Convection in Wide Horizontal Fluid Layers," *Experiments in Fluids*, Vol. 4, p. 121.

Boehm, R. F., and Kamyab, D., 1977, "Analysis of Established Natural Convection Due to Stripwise Heating on a Horizontal Surface," ASME JOURNAL OF HEAT TRANSFER, Vol. 99, p. 294.

Booker, J., 1976, "Thermal Convection With Strongly Temperature-Dependent Viscosity," *J. Fluid Mech.*, Vol. 76, p. 741.

Carey, V. P., and Gebhart, B., 1981, "Visualization of the Flow Adjacent to a Vertical Ice Stream Melting in Cold Pure Water," *J. Fluid Mech.*, Vol. 107, p. 37.

Carrigan, C. R., 1987, "The Magmatic Rayleigh Number and Time Dependent Convection in Cooling Lava Lakes," *Geophysical Res. Letters*, Vol. 14, p. 915.

Chu, T. Y., and Goldstein, R. J., 1973, "Turbulent Convection in a Horizontal Layer of Water," *J. Fluid Mech.*, Vol. 60, p. 141.

Clark, S., Spera, F. J., and Yuen, D. A., 1987, "Steady State Double-Diffusive Convection in Magma Chambers Heated From Below," *Magmatic Processes: Physicochemical Principles*, B. O. Mysen, ed., The Geochemical Society.

Critical Data Book, 1975, Corn Refiners Association, Inc., Washington, DC, 3rd ed.

Detailed Tables of Relationship Between Density, Temperature and Dry Substance of Commercial Corn Syrups, High Fructose Corn Syrups, and Blends with Sucrose and Invert Sugar, 1984, Corn Refiner Association, Washington, DC.

Drotning, W. D., and Tormey, T. V., 1984, "Thermal Conductivity Probe Measurement System," SAND83-2057, Sandia National Laboratories, Albuquerque, NM.

FIDAP User's Manual, 1988, Fluid Dynamics International, 1600 Orrington Ave., Evanston, IL, Vols. 1-3.

Gartling, D. K., and Hickox, C. E., 1985, "A Numerical Study of the Applicability of the Boussinesq Approximation for a Fluid-Saturated Porous Medium," *Intl. J. Num. Methods in Fluids*, Vol. 5, pp. 995-1013.

Globe, S., and Dropkin, D., 1959, "Natural Convection Heat Transfer in Liquids Confined by Two Horizontal Plates and Heated From Below," ASME JOURNAL OF HEAT TRANSFER, Vol. 81, p. 24.

Goldstein, R. J., Sparrow, E. M., and Jones, P. C., 1973, "Natural Convection Mass Transfer Adjacent to Horizontal Plates," *Int. J. Heat Mass Transfer*, Vol. 6, 1025.

Happle, J., and Brenner, H., 1973, *Low Reynolds Number Hydrodynamics*, Noordhoff International Publishing, Leyden, The Netherlands.

Hickox, C. E., et al., 1986, "Thermal Conductivity Measurements of Pacific Illite Sediment," *Intl. J. Thermophysics*, Vol. 7, No. 4, p. 755.

Jacob, M., 1967, *Heat Transfer*, 10th printing, Wiley, New York, p. 573.

Kamotuni, Y., Wang, L. W., and Ostrach, S., 1983, "Natural Convection Heat Transfer in a Water Layer With Localized Heating From Below," *Natural Convection in Enclosures—1983*, I. Catton and K. E. Torrance, eds., ASME, New York, p. 43.

Littel, H., Chu, T. Y., and Hickox, C. E., 1988, "Experimental Determination of the Thermal Conductivity of 42/43 Corn Syrup," paper in preparation.

Lloyd, J. R., and Moran, W. R., 1974, "Natural Convection Adjacent to Horizontal Surfaces of Various Planforms," ASME JOURNAL OF HEAT TRANSFER, Vol. 96, p. 443.

Olson, P., 1984, "An Experimental Approach to Thermal Convection in a Two-Layered Mantle," *J. Geophys. Res.*, Vol. 39, p. 11293.

Ortega, A., Dunn, J. C., Chu, T. Y., Wemple, R. T., Hickox, C. E., and Boehm, R. F., 1987, "Recent Progress in Magma Energy Extraction," *Proc. Geothermal Program Review*, D.O.E., Washington, DC.

Richter, F. M., Nataf, H. C., and Daly, S. F., 1983, "Heat Transfer and Horizontally Averaged Temperature of Convection With Large Viscosity Variations," *J. Fluid Mech.*, Vol. 129, p. 173.

Torrance, K. E., Orloft, L., and Rockett, J. A., 1969, "Experiments on Natural Convection in Enclosures With Localized Heating From Below," *J. Fluid Mech.*, Vol. 36, p. 21.

Torrance, K. E., and Turcotte, D. L., 1971, "Thermal Convection With Large Viscosity Variations," *J. Fluid Mech.*, Vol. 47, p. 113.

Yih, C-S, 1977, *Fluid of Mechanics*, West River Press, 3530 West Huron River Drive, Ann Arbor, MI, p. 396.

APPENDIX

Physical Properties of 42/43 Corn Syrup

Viscosity:

$$\mu = a_o \exp[a_1 \exp(-T/a_2)], \ (^\circ\text{C, poise})$$

$$a_o = 0.2412, \quad a_1 = 12.5867, \quad a_2 = 55.7805$$

Thermal conductivity:

$$k = b_o + b_1 T, \ (^\circ\text{C, W/mK})$$

$$b_o = 0.3724, \quad b_1 = 3.034 \times 10^{-4}$$

Specific heat:

$$c = c_o + c_1 T + c_2 T^2, \ (^\circ\text{C, J/gK})$$

$$c_o = 2.2005, \quad c_1 = 3.9532 \times 10^{-3}, \quad c_2 = -6.7883 \times 10^{-6}$$

Density (as used in numerical simulations):

$$\rho = \rho_o[1 - \beta(T - T_o)], \quad (^\circ\text{C, g/cm}^3)$$

$$\rho_o = 1.4314, \quad \beta = 4.1218 \times 10^{-4}$$

Density and thermal expansion coefficient (best estimate):

$$\rho = \rho_o/(1 + \Delta), \ (^\circ\text{C, g/cm}^3)$$

$$\rho_o = 1.4255, \quad \Delta = (d_o + d_1 T + d_2 T^2)/10{,}000$$

$$d_o = -74.5333, \quad d_1 = 3.5691, \quad d_2 = 7.8788 \times 10^{-3}$$

$$\beta \equiv \frac{1}{\rho}\left(\frac{\partial \rho}{\partial T}\right)$$

An Analytical Study on Natural Convection in Isotropic and Anisotropic Porous Channels

T. Nilsen
Department of Mathematics,
University of Bergen,
Bergen, Norway

L. Storesletten
Department of Mathematics,
Agder College,
Kristiansand, Norway

This paper is an analytical study on natural two-dimensional convection in horizontal rectangular channels filled by isotropic and anisotropic porous media. The channel walls, assumed to be impermeable and perfectly heat conducting, are nonuniformly heated to establish a linear temperature distribution in the vertical direction. We derive the critical Rayleigh numbers for the onset of convection and examine the steady flow patterns at moderately supercritical Rayleigh numbers. The stability properties of these flow patterns are examined against two-dimensional perturbations using a weakly nonlinear theory.

1 Introduction

Natural convection in porous media has received increasing interest over the last twenty years due to its numerous applications in geophysics and energy-related systems.

So far, theoretical and experimental investigations have usually been concerned with isotropic porous media. The papers on thermal convection in anisotropic media are not numerous compared to the number of publications on isotropic media; see Kvernvold and Tyvand (1979) and the review article by Bories (1987), and the references quoted therein. However, in several applications the porous materials are anisotropic.

The present paper is an analytical study on natural two-dimensional convection in horizontal rectangular channels filled by isotropic and anisotropic porous media. The channel walls are assumed to be nonuniformly heated to establish a linear temperature distribution in the vertical direction, and the appropriate temperatures are assumed to be maintained on the walls at all times. This is plausible if the walls have a very large thermal conductivity and heat capacity relative to the porous medium. We derive the critical Rayleigh numbers for the onset of convection and examine the steady convective motions existing at moderately supercritical Rayleigh numbers. Moreover, we analyze the stability properties of these flow patterns against two-dimensional perturbations by using a weakly nonlinear theory.

There are two things that distinguish this paper from related work. The boundary conditions involve specified temperatures on the lateral boundaries instead of the more common insulating conditions. In addition, anisotropy in the permeability and thermal diffusivity is considered.

The analogous problem for an isotropic porous channel with perfectly insulating lateral boundaries has been studied by several authors, e.g., Sutton (1970), Riley and Winters (1987), and Impey et al. (1987). Also convection in isotropic porous media confined by rectangular boxes has been investigated in the case of perfectly insulating lateral boundaries (e.g., Beck, 1972; Straus and Schubert, 1978, 1979; Horne, 1979).

Beck (1972) seems to have been the first to carry out a linear stability analysis of convection in a finite three-dimensional box. His results show that near convection onset the fluid motion for thin boxes is always two dimensional in the form of roll-cells. We therefore restrict our problem to short rectangular cylinders assuming, that the end sections are perfectly insulated.

Contributed by the Heat Transfer Division for publication in the JOURNAL OF HEAT TRANSFER. Manuscript received by the Heat Transfer Division October 17, 1988; revision received July 7, 1989. Keywords: Natural Convection, Porous Media.

For an isotropic medium our results differ essentially from the well-studied case with insulating sidewalls; see, e.g., Sutton (1970) and Beck (1972). This is not unexpected since conducting sidewalls change the physical conditions considerably. The heat exchange through the lateral walls increases the critical Rayleigh number and alters the cellular formation at the onset of convection.

We notice the hydraulic analogy between the flow in an isotropic porous medium and flow in a narrow gap between parallel vertical walls, i.e., Hele-Shaw cell; see Hartline and Lister (1977). The present study restricted to isotropic media can therefore be applied to a rectangular Hele-Shaw cell.

2 Mathematical Formulation

We consider two-dimensional free convection in a horizontal porous channel nonuniformly heated. The porous medium is assumed to be anisotropic and saturated by a homogeneous incompressible fluid. The channel is rectangular with height h and width a, and we choose a Cartesian coordinate system with the z axis in the vertical direction and x axis in the horizontal direction perpendicular to the channel axis. The horizontal channel walls are at $z=0$ and $z=h$, and the vertical walls at $x=-a/2$ and $x=a/2$; see Fig. 1.

On assuming that the Prandtl-Darcy number is large so that inertia terms may be neglected and invoking the Boussinesq approximation, the two-dimensional forms of the Darcy-Boussinesq equations become

$$\frac{1}{\rho_0}\frac{\partial p}{\partial x}+\frac{\nu}{k_x}u=0 \tag{2.1}$$

$$\frac{1}{\rho_0}\frac{\partial p}{\partial z}+\frac{\rho}{\rho_0}g+\frac{\nu}{k_z}w=0 \tag{2.2}$$

$$c\frac{\partial T}{\partial t}+\underline{v}\cdot\nabla T=\kappa_x\frac{\partial^2 T}{\partial x^2}+\kappa_z\frac{\partial^2 T}{\partial z^2} \tag{2.3}$$

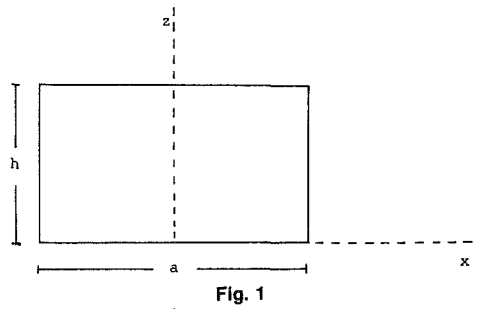

Fig. 1

$$\frac{\partial u}{\partial x}+\frac{\partial w}{\partial z}=0 \tag{2.4}$$

$$\rho=\rho_0(1-\beta(T-T_0)) \tag{2.5}$$

The upper and lower boundaries are at isothermal temperatures T_0 and $T_0+\Delta T$, respectively, where ΔT is a positive temperature difference. All the boundaries are assumed to be impermeable and perfectly heat conducting. From the governing equations (2.1)–(2.5) it follows that a motionless conduction state exists only if the static temperature distribution is independent of x and depends linearly on z. The present study is restricted to this case.

It is convenient to express the temperature in the form

$$T=\left\{T_0+\Delta T\left(1-\frac{z}{h}\right)\right\}+\theta \tag{2.6}$$

where θ is the deviation from the static temperature. Since the flow is two dimensional we introduce the streamfunction ψ by

$$u=\frac{\partial \psi}{\partial z}, \qquad w=-\frac{\partial \psi}{\partial x} \tag{2.7}$$

We also define nondimensional variables denoted by asterisks

$$\left.\begin{aligned} &u=\kappa_z\frac{a}{h^2}u^*, && w=\kappa_z\frac{1}{h}w^* && \\ &t=c\frac{h^2}{\kappa_z}t^*, && x=ax^*, && z=hz^* \\ &T_0=\Delta T\, T_0^*, && \theta=\Delta T\theta^*, && p=\frac{\nu\kappa_z\rho_0}{k_x}p^* \end{aligned}\right\} \tag{2.8}$$

By introducing these expressions into equations (2.1)–(2.5), eliminating the pressure and the density, and deleting the asterisk, we get the governing equations in the following form:

$$\left(\xi\frac{\partial^2}{\partial x^2}+\frac{\partial^2}{\partial z^2}\right)\psi+\xi\mathrm{Ra}\frac{\partial \theta}{\partial x}=0 \tag{2.9}$$

$$\left(\eta\frac{\partial^2}{\partial x^2}+\frac{\partial^2}{\partial z^2}\right)\theta-\frac{\partial \psi}{\partial x}=\frac{\partial \theta}{\partial t}+\underline{v}\cdot\nabla\theta \tag{2.10}$$

where Ra is the Darcy–Rayleigh number (also called the Rayleigh number) defined by

$$\mathrm{Ra}=\frac{\beta g\Delta T k_z h}{\kappa_z \nu} \tag{2.11}$$

and ξ and η are the anisotropy/aspect ratio coefficients defined by

$$\xi=\frac{k_x}{k_z}\left(\frac{h}{a}\right)^2, \qquad \eta=\frac{\kappa_x}{\kappa_z}\left(\frac{h}{a}\right)^2 \tag{2.12}$$

The requirements of perfectly heat-conducting and impermeable boundaries lead to the boundary conditions

$$\psi=\theta=0 \text{ on } \begin{cases} x=-\dfrac{1}{2}, \quad x=\dfrac{1}{2}, \quad 0<z<1 \\ z=0, \quad z=1, \quad -\dfrac{1}{2}<x<\dfrac{1}{2} \end{cases} \tag{2.13}$$

3 Linear Stability and Steady Flow Patterns

The onset of convection is described by the linear versions of equations (2.9) and (2.10). The solutions can be expanded in the Fourier series

$$\psi=e^{\sigma t}\left\{\frac{1}{2}C_0+\sum_{n=1}^{\infty}C_n\cos n\pi z+D_n\sin n\pi z\right\} \tag{3.1}$$

$$\theta=e^{\sigma t}\left\{\frac{1}{2}F_0+\sum_{n=1}^{\infty}F_n\cos n\pi z+G_n\sin n\pi z\right\} \tag{3.2}$$

where C_n, D_n, F_n, and G_n are functions of x and σ is the growth rate. The boundary conditions (2.13) are satisfied if $C_n=F_n=0$ for all x.

By substituting the solutions (3.1) and (3.2) (with $C_n=F_n=0$) into the linearized governing equations and equating terms with same $\sin n\pi z$ dependence, we get the following set of ordinary differential equations:

$$\xi\frac{d^2D_n}{dx^2}-n^2\pi^2D_n+\xi\mathrm{Ra}\frac{dG_n}{dx}=0 \tag{3.3}$$

$$\eta\frac{d^2G_n}{dx^2}-n^2\pi^2G_n-\frac{dD_n}{dx}=\sigma G_n \tag{3.4}$$

The boundary conditions are

$$D_n\left(-\frac{1}{2}\right)=D_n\left(\frac{1}{2}\right)=0, \qquad G_n\left(-\frac{1}{2}\right)=G_n\left(\frac{1}{2}\right)=0 \tag{3.5}$$

The operator on the left-hand side of equations (2.9) and (2.10), with the given boundary conditions (2.13), is shown to be self-adjoint, from which we can conclude that σ is real. Thus, in order to find the critical Rayleigh number Ra_c, giving marginal stability, we put $\sigma=0$ into equation (3.4). The system of equations (3.3)–(3.4) subject to the boundary conditions (3.5) represents a self-adjoint eigenvalue problem with eigenvalues Ra, the smallest of which is Ra_c. The general solution is

$$D_n(x,\mathrm{Ra})=c_1\cos px+c_2\sin px+c_3\cos qx+c_4\sin qx \tag{3.6}$$

Nomenclature

a = width
c = $(\rho c_p)_m/(\rho c_p)_f$; m = mixture; f = fluid
c_p = specific heat capacity
g = acceleration of gravity
h = height
k_x = horizontal permeability
k_z = vertical permeability
p = pressure
Q, S, A = amplitudes
r, s = constants
Ra = Rayleigh number
Ra_c = critical Rayleigh number
$\Delta\mathrm{Ra}$ = $\mathrm{Ra}-\mathrm{Ra}_c$
t = time
T = temperature
T_0 = reference temperature
ΔT = characteristic temperature difference
u, w = horizontal and vertical velocity components, respectively
x, z = horizontal and vertical Cartesian coordinates, respectively
α = constant
β = thermal expansion coefficient
η = $(\kappa_x/\kappa_z)^2(h/a)^2$
θ = deviation from static temperature
κ_x, κ_z = horizontal and vertical components of thermal diffusivity, respectively
ν = kinematic viscosity
ξ = $(k_x/k_z)^2(h/a)^2$
ρ = density
ρ_0 = reference density
σ = growth rate
ψ = streamfunction

$$G_n(x, \mathrm{Ra}) = s\{rc_1 \sin px - rc_2 \cos px + c_3 \sin qx - c_4 \cos qx\} \quad (3.7)$$

where c_1, c_2, c_3, and c_4 are constants and

$$\frac{p}{q} = \frac{\sqrt{\mathrm{Ra}\xi - (n\pi)^2(\sqrt{\xi}-\sqrt{\eta})^2} \pm \sqrt{\mathrm{Ra}\xi - (n\pi)^2(\sqrt{\xi}+\sqrt{\eta})^2}}{2\sqrt{\xi\eta}} \quad (3.8)$$

$$r = \frac{q((n\pi)^2 + \xi p^2)}{p((n\pi)^2 + \xi q^2)} = \frac{q\sqrt{\eta} + p\sqrt{\xi}}{p\sqrt{\eta} + q\sqrt{\xi}}, \qquad s = \frac{(n\pi)^2 + \xi^2 p^2}{\xi \mathrm{Ra} p} \quad (3.9)$$

Here the boundary conditions ensure that $p \neq q$ at $\mathrm{Ra} = \mathrm{Ra}_c$. From the conditions (3.5) we conclude that there exist nontrivial solutions of the boundary value problem when

$$\text{I} \quad (1-r)\sin\frac{p+q}{2} - (1+r)\sin\frac{p-q}{2} = 0 \text{ and } c_2 = c_4 = 0 \quad (3.10)$$

or

$$\text{II} \quad (1-r)\sin\frac{p+q}{2} + (1+r)\sin\frac{p-q}{2} = 0 \text{ and } c_1 = c_3 = 0 \quad (3.11)$$

In the case of $\xi = \eta$, which is satisfied for an isotropic medium, the problem is easily solved analytically and an exact expression for Ra_c is found. When $\xi \neq \eta$ we have to calculate Ra_c numerically.

(a) The Isotropic Case: $\xi = \eta$. In addition to an isotropic medium the condition $\xi = \eta$ is satisfied when $k_x/k_z = \kappa_x/\kappa_z$, i.e., the ratios of the horizontal and vertical components of the permeability and diffusivity, respectively, are equal.

In this case $r = 1$ and cases I and II both lead to the condition

$$p - q = 2m\pi \qquad m = 1, 2, 3, \ldots \quad (3.12)$$

which implies that

$$\mathrm{Ra} = 4\pi^2(n^2 + \xi m^2) \qquad \begin{matrix} n = 1, 2, 3, \ldots \\ m = 1, 2, 3, \ldots \end{matrix} \quad (3.13)$$

The eigenvalues are given by equation (3.13), the smallest of which is the critical Rayleigh number

$$\mathrm{Ra}_c = 4\pi^2(1 + \xi) \quad (3.14)$$

which corresponds to the lowest mode $n = 1$ and $m = 1$. For an isotropic medium relation (3.14) may be written

$$\mathrm{Ra}_c = 4\pi^2\left(1 + \left(\frac{h}{a}\right)^2\right) \quad (3.15)$$

In the limit $(h/a) \to 0$ the channel tends to an infinite horizontal porous layer. In that case $\mathrm{Ra}_c \to 4\pi^2$, which is in accordance with a well-known result for porous layers (Bories, 1987). On the other hand, the critical value from equation (3.15) differs from the result found for a channel with perfectly insulating lateral walls carried out by Sutton (1970). For a square channel equation (3.15) gives $\mathrm{Ra}_c = 8\pi^2$, while the corresponding result when the lateral walls are perfectly insulated is $\mathrm{Ra}_c = 4\pi^2$. A higher critical value with conducting sidewalls was expected, of course, since we in this case have heat exchange through the walls.

The flows for moderately supercritical Rayleigh numbers is usually characterized by the flow at the onset of convection. Since the left-hand-side relations of equations (3.10) and (3.11) coincide when $\xi = \eta$, there exist two linearly independent solutions of the boundary value problem. This is also seen from the stationary linearized version of the governing equations (2.9) and (2.10). If ψ_0, θ_0 is a solution at $\mathrm{Ra} = \mathrm{Ra}_c$, then $\psi_1 = -\xi \mathrm{Ra}\theta_0$, $\theta_1 = \psi_0$ is a linearly independent solution.

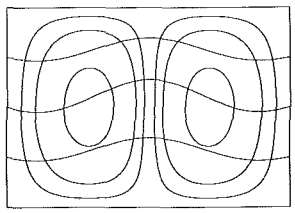

Fig. 2(a)

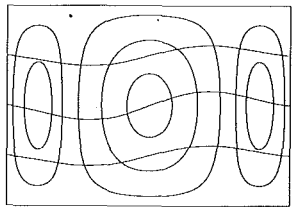

Fig. 2(b)

Fig. 2(a and b) $\xi = 0.5$, $\mathrm{Ra}_c = 59.218$

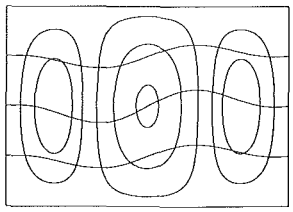

Fig. 2(c)

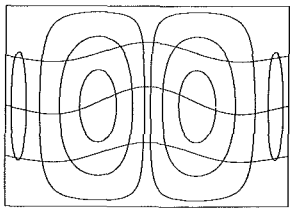

Fig. 2(d)

Fig. 2(c and d) $\xi = 0.2$, $\mathrm{Ra}_c = 47.374$

Two sets of solutions are

$$\psi^{(1)} = Q \sin(\pi\sqrt{1/\xi + 1}x)\cos \pi x \sin \pi z \quad (3.16)$$

$$\theta^{(1)} = -\frac{1}{\sqrt{\xi \mathrm{Ra}_c}} Q \cos(\pi\sqrt{1/\xi + 1}x)\cos \pi x \sin \pi z \quad (3.17)$$

$$\psi^{(2)} = \sqrt{\xi \mathrm{Ra}_c} S \cos(\pi\sqrt{1/\xi + 1}x)\cos \pi x \sin \pi z \quad (3.18)$$

$$\theta^{(2)} = S \sin(\pi\sqrt{1/\xi + 1}x)\cos \pi x \sin \pi z \quad (3.19)$$

where Q and S are amplitude constants. The solution (3.16)-(3.17) yields a symmetric flow pattern consisting of $2n$ cells, where the integer n depends on ξ; the solution (3.18)-(3.19) yields a symmetric flow pattern consisting of $2n \pm 1$ cells. It follows from the analytical form of the solutions that the condition

$1/\xi \leq 3$	yields patterns consisting of 2 and 3 cells
$3 < 1/\xi \leq 8$	yields 3 and 4 cells
$8 < 1/\xi \leq 15$	yields 4 and 5 cells
$(n-1)^2 - 1 < 1/\xi \leq n^2 - 1$	yields n and $n+1$ cells $n = 3, 4, 5, \ldots$.

The computed streamlines and isotherms are shown in Fig. 2 for $\xi = 0.5$ and $\xi = 0.2$, when $(a/h)^2 = 2$.

Table 1 Computed values for Ra_c for various values of ξ and η. The main diagonal corresponds to the isotropic case.

η \ ξ	$\frac{1}{8}$	$\frac{1}{4}$	$\frac{1}{2}$	1	2	4	8
$\frac{1}{8}$	44.42	33.50	26.85	22.90	19.53	17.36	16.14
$\frac{1}{4}$	67.00	49.35	38.55	31.16	26.19	23.19	21.53
$\frac{1}{2}$	107.5	77.11	59.22	47.17	39.39	34.81	32.83
1	183.2	124.6	94.34	78.96	65.75	58.04	53.83
2	312.4	209.5	157.6	131.5	118.4	104.5	96.90
4	555.6	371.0	278.5	232.2	209.0	197.4	183.0
8	1033.8	688.8	516.7	430.6	387.6	366.1	355.3

In the case $1/\xi \le 3$ the results are very similar to those found for convection in a horizontal circular cylinder studied by Storesletten and Tveitereid (1987).

(b) The Anisotropic Case: $\xi \neq \eta$. For $\xi \neq \eta$ there exist nontrivial solutions for D_n, G_n when equations (3.10) or (3.11) are satisfied. In case I the solution has the form

$$D_n = \cos px - \frac{\cos \frac{p}{2}}{\cos \frac{q}{2}} \cos qx$$

(I)

$$G_n = s\left(r \sin px - \frac{\cos \frac{p}{2}}{\cos \frac{q}{2}} \sin qx \right)$$

and in case II

$$D_n = \sin px - \frac{\sin \frac{p}{2}}{\sin \frac{q}{2}} \sin qx$$

(II)

$$G_n = s\left(-r \cos px + \frac{\sin \frac{p}{2}}{\sin \frac{q}{2}} \cos qx \right)$$

There exist solutions (I) and (II) for an infinite set of eigenvalues Ra. Let Ra_I and Ra_{II} be the smallest eigenvalues corresponding to (I) and (II), respectively. These will occur at the lowest mode $n = 1$. For given ξ and η we calculate numerically Ra_I and Ra_{II} from the equations in (3.10) and (3.11), and the critical Rayleigh number $Ra_c = \min(Ra_I, Ra_{II})$. Usually $Ra_I \neq Ra_{II}$, which means that there exists a unique solution, i.e., there is a unique steady flow pattern at the onset of convection. Table 1 shows the computed values of Ra_c for various values of ξ and η. This table possesses a symmetry about the main diagonal according to the relation $\xi Ra_c(\xi, \eta) = \eta Ra_c(\eta, \xi)$, which follows from the governing equations.

We shall also examine the steady motion at the onset of convection, how the number of cells depends on the anisotropy coefficients ξ and η, the uniqueness of solutions, etc. If $\xi \neq \eta$ the left-hand sides of equations (3.10) and (3.11) coincide only when

$$\sin\left(\frac{p+q}{2}\right) = \sin\left(\frac{p-q}{2}\right) = 0 \tag{3.20}$$

which leads to the nonuniqueness condition

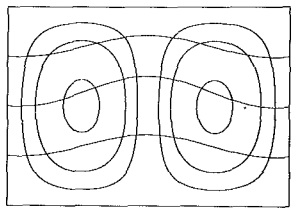

Fig. 3(i)

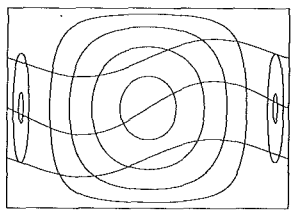

Fig. 3(ii)

Fig. 3 Computed streamlines and isotherms for the anisotropic case when $(a/h)^2 = 2$ and (i) $\xi = 0.5$, $\eta = 2$, $Ra_c = 157.60$; (ii) $\xi = 2$, $\eta = 0.5$, $Ra_c = 39.39$

$$\xi\eta = \frac{1}{(m^2-1)^2}, \qquad m = 2, 3, 4, \ldots \tag{3.21}$$

On the hyperbolas (3.21) in the ξ, η plane the critical Rayleigh number is found analytically as

$$Ra_c = \pi^2[(1+\sqrt{\eta/\xi})^2 + 4\eta] \tag{3.22}$$

Furthermore, on these curves there exist two solutions $D^{(1)}$, $D^{(2)}$ (and $G^{(1)}$, $G^{(2)}$) given by

$$D^{(1)} = 2\cos(\pi\sqrt{1+1/\sqrt{\xi\eta}}x)\cos \pi x \tag{3.23}$$

$$D^{(2)} = 2\sin(\pi\sqrt{1+1/\sqrt{\xi\eta}}x)\cos \pi x \tag{3.24}$$

corresponding to two different flow patterns. However, when equation (3.21) is not satisfied and $\xi \neq \eta$, there exists a unique flow pattern where the number of cells depends on ξ and η in the following way:

$$1/\sqrt{\xi\eta} < 3 \text{ and } \begin{cases} \xi < \eta \text{ yields 2 cells} \\ \xi > \eta \text{ yields 3 cells} \end{cases}$$

$$3 < 1/\sqrt{\xi\eta} < 8 \text{ and } \begin{cases} \xi < \eta \text{ yields 3 cells} \\ \xi > \eta \text{ yields 4 cells} \end{cases}$$

$$8 < 1/\sqrt{\xi\eta} < 15 \text{ and } \begin{cases} \xi < \eta \text{ yields 4 cells} \\ \xi > \eta \text{ yields 5 cells} \end{cases}$$

$$(n-1)^2 - 1 < 1/\sqrt{\xi\eta} < n^2 - 1 \text{ and } \begin{cases} \xi < \eta \text{ yields } n \text{ cells} \\ \xi > \eta \text{ yields } n+1 \text{ cells} \end{cases}$$

$$n = 3, 4, 5, \ldots$$

The computed streamlines and isotherms are displayed in Fig. 3 for $\xi = 0.5$, $\eta = 2$ and $\xi = 2$, $\eta = 0.5$.

4 Nonlinear Stability

It has been revealed from the linear analysis in the preceding section that different kinds of convective motion can be generated for slightly supercritical Rayleigh numbers. If $\xi = \eta$,

two steady flow patterns are found consisting of n and $n+1$ cells, respectively, $n \geq 2$. On the other hand if $\xi \neq \eta$ we found only one flow pattern, consisting of n cells if $\xi < \eta$ and $n+1$ cells if $\xi > \eta$, $n \geq 2$.

In this section we shall examine the stability properties of the steady flow patterns occurring at slightly supercritical Rayleigh numbers. By taking into account the right-hand side of equation (2.10), including the nonlinear term, we derive the so-called Landau equations of the problem. This nonlinear system of equations will be the basis for our stability analysis.

The solution of equations (2.9) and (2.10) can be approximated by the formal expansions

$$\psi = \psi_1 + \psi_2 + \ldots$$

$$\theta = \theta_1 + \theta_2 + \ldots \tag{4.1}$$

$$\mathrm{Ra} = \mathrm{Ra}_c + \mathrm{Ra}_1 + \mathrm{Ra}_2 + \ldots$$

Moreover, we introduce multiple time scales given by

$$\frac{\partial}{\partial t} = \frac{\partial}{\partial t_1} + \frac{\partial}{\partial t_2} + \ldots \tag{4.2}$$

We suppose

$$\psi_i = 0(\epsilon^i) \text{ as } \epsilon \to 0 \tag{4.3}$$

holds uniformly, and similarly for the other quantities θ, Ra, and $\partial/\partial t$. By introducing the expansions (4.1)–(4.2) into equations (2.9) and (2.10) and equating terms of the same order, we find an infinite set of linear equations.

(a) The Isotropic Case: $\xi = \eta$. The solutions of the first-order system are in this case

$$\psi_1 = Q\psi_Q + S\psi_S, \qquad \theta_1 = Q\theta_Q + S\theta_S \tag{4.5}$$

where $\psi_Q = \psi^{(1)}/Q$, $\theta_Q = \theta^{(1)}/Q$ and $\psi_S = \psi^{(2)}/S$, $\theta_S = \theta^{(2)}/S$ are the solutions (3.16)–(3.19) found in the linear analysis, and Q, S are amplitudes of order ϵ.

The solvability condition of the second-order equations implies

$$\mathrm{Ra}_1 = \frac{\partial}{\partial t_1} = 0 \tag{4.5}$$

The Landau equations are now deduced from the solvability condition of the third-order equations. By neglecting the third-order terms of the expressions (4.1) and (4.2) we get

$$A_1 \frac{dQ}{dt} = \Delta \mathrm{Ra} Q - P_1 (Q^2 + 4\pi^2 \xi (1+\xi) S^2) Q \tag{4.6}$$

$$A_2 \frac{dS}{dt} = \Delta \mathrm{Ra} S - P_2 (Q^2 + 4\pi^2 \xi (1+\xi) S^2) S \tag{4.7}$$

where

$$A_1 = 2\left[1 - \frac{\xi}{\pi}\sqrt{\frac{\xi}{1+\xi}} \sin \pi \sqrt{\frac{1+\xi}{\xi}}\right] \tag{4.8}$$

$$A_2 = 2\left[1 + \frac{\xi}{\pi}\sqrt{\frac{\xi}{1+\xi}} \sin \pi \sqrt{\frac{1+\xi}{\xi}}\right] \tag{4.9}$$

$$P_1 = P_2 = P = \frac{3}{16}\pi^2 \left(\frac{1+\xi}{\xi}\right) \tag{4.10}$$

The Landau equations (4.6) and (4.7) describe the evolution of the amplitudes due to nonlinear interactions.

For subcritical Rayleigh numbers, $\Delta \mathrm{Ra} < 0$, it follows that $Q \to 0$, $S \to 0$ as $t \to \infty$. For supercritical Rayleigh numbers, $\Delta \mathrm{Ra} > 0$, the motionless conduction state $Q = S = 0$ is unstable. However, there exist steady nonzero solutions satisfying

$$Q^2 + 4\pi^2 \xi (1+\xi) S^2 = \Delta \mathrm{Ra}/P \tag{4.11}$$

i.e.,

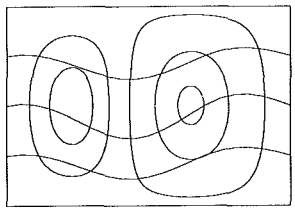

Fig. 4(i)

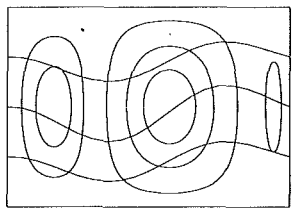

Fig. 4(ii)

Fig. 4 Computed streamlines and isotherms for the composite flow patterns when $(a/h)^2 = 2$ and (i) $\xi = \eta = 0.5$, $\alpha = 0.1$; (ii) $\xi = \eta = 0.5$, $\alpha = 0.32$

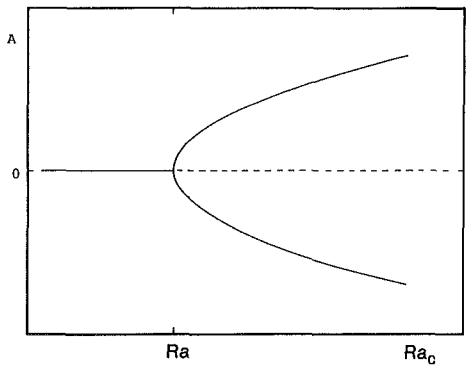

Fig. 5 Sketch of the perfect bifurcation case: ———: stable solution; ------: unstable solution

$$Q = Q_0, \qquad S = \alpha Q_0 \tag{4.12}$$

where α is a constant, $0 \leq \alpha \leq \infty$, and

$$Q_0^2 = \Delta \mathrm{Ra}/P\{1 + 4\pi^2 \xi (1+\xi)\alpha^2\} \tag{4.13}$$

The steady-state solution corresponding to $\alpha = 0$ represents the flow pattern consisting of $2n$ cells, while the $(2n \pm 1)$-cell pattern is obtained when $\alpha \to \infty$. For $0 < \alpha < \infty$ the solution (4.12) is a composition of the $2n$- and $(2n \pm 1)$-cell structures. Composite flow patterns are displayed in Fig. 4 for the case $\xi = 0.5$.

By considering small perturbations superposed on the steady-state solutions, it is proved that solutions (4.12) are stable for all values of α. The stability analysis is similar to that performed in the circular cylinder problem (Storesletten and Tveitereid, 1987) where the Landau equations had exactly the same form. The actual flow pattern, which depends on the constant α, is not uniquely determined by the boundary conditions. The nonlinear analysis therefore fails in selecting a preferred flow pattern. This may be explained by the symmetry of the problem as it appears in the Landau equations ($P_1 = P_2$). Therefore, in order to find a preferred flow one should include other effects, as for example a nonlinear term in the momentum equations (2.1) and (2.2) (non-Darcian fluid). However, in the next section we show that in the anisotropic case we get a unique stable solution.

In order to draw the bifurcation diagram it is convenient to introduce the amplitude A, defined by

$$A^2 = Q^2 + 4\pi^2 \xi (1+\xi) S^2 \tag{4.14}$$

From equation (4.11) we get

$$A = \pm\sqrt{\Delta \mathrm{Ra}/P} \tag{4.15}$$

Thus, according to the nonlinear analysis there is a sharp transition from conduction to convection when the Rayleigh number exceeds the critical value Ra_c. This is a so-called perfect bifurcation, sketched in Fig. 5.

(b) The Anisotropic Case. The first-order system has in this case ($\xi \neq \eta$ and equation (3.21) not satisfied) a unique solution found in the linear analysis. Proceeding as in the isotropic case we derive the Landau equation

$$A_3 \frac{dQ}{dt} = \Delta \mathrm{Ra} Q - P_3 Q^3 \tag{4.16}$$

where Q is the amplitude of order ϵ. The coefficients A_3 and P_3, which depend on ξ and η, have to be calculated numerically. The motionless conduction state is stable when $\Delta \mathrm{Ra} < 0$ and unstable when $\Delta \mathrm{Ra} > 0$. In the supercritical case ($\Delta \mathrm{Ra} > 0$) the nonzero steady-state solution is stable for all ξ and η. As in the isotropic case there is a perfect bifurcation at the critical Rayleigh number Ra_c.

5 Summary

We have examined two-dimensional convection in isotropic and anisotropic porous horizontal channels. The channel walls, assumed to be impermeable and perfectly heat-conducting, are nonuniformly heated to establish a linear temperature distribution in the vertical direction. The main results are:

(*a*) When $\xi = \eta$, which is satisfied for an isotropic medium, the critical Rayleigh number is found to be

$$\mathrm{Ra}_c = 4\pi^2(1+\xi) \tag{5.1}$$

At the onset of convection there exist two different steady flow patterns consisting of n and $n+1$ cells, respectively, where the integer n depends on the aspect ratio a/h. For an isotropic medium, where $1/\xi = (a/h)^2$, the number of cells is given as follows

$$(a/h)^2 \leq 3 \qquad \text{yields 2 and 3 cells} \tag{5.2}$$

$$(n-1)^2 - 1 \leq (a/h)^2 \leq n^2 - 1 \qquad \text{yields } n \text{ and } n+1 \text{ cells} \tag{5.3}$$

$$n = 3, 4, 5, \ldots$$

A nonlinear stability analysis at moderately supercritical Rayleigh numbers shows that both of the flow structures are stable against two-dimensional perturbations. In addition it turns out that any composition of these two flow patterns is a stable nonlinear solution. The actual flow, which will usually be of the composite type, is not uniquely determined by the boundary conditions. According to the nonlinear analysis there exists a sharp transition from conduction to convection when the Rayleigh number exceeds the critical value Ra_c, which is called a perfect bifurcation.

(*b*) In the anisotropic case $\xi \neq \eta$, the critical Rayleigh numbers are calculated numerically; see Table 1. There exists (when equation (3.21) is not satisfied) a unique steady flow pattern at the onset of convection consisting of n cells if $\xi < \eta$, and $n+1$ cells if $\xi > \eta$, where n depends on the product $\xi\eta$ in the following way:

$$1/\sqrt{\xi\eta} < 3 \text{ and } \begin{cases} \xi < \eta \text{ yields 2 cells} \\ \xi > \eta \text{ yields 3 cells} \end{cases} \tag{5.4}$$

$$(n-1)^2 - 1 < 1/\sqrt{\xi\eta} < n^2 - 1 \text{ and } \begin{cases} \xi < \eta \text{ yields } n \text{ cells} \\ \xi > \eta \text{ yields } n+1 \text{ cells} \end{cases} \tag{5.5}$$

$$n = 3, 4, 5, \ldots$$

The stability analysis carried out in section 4 shows that the unique solution is stable against two-dimensional perturbations for all values of the parameters ξ and η. As for the isotropic case there exists a perfect bifurcation at $\mathrm{Ra} = \mathrm{Ra}_c$.

Acknowledgments

This work was carried out during our sabbatical leave at University of California, Santa Barbara 1987/88. The financial support given by the Norwegian Research Council for Science and the Humanities is acknowledged. The authors are grateful to Dr. Peder A. Tyvand, Agricultural University of Norway, for having directed their attention to the problem investigated in this paper.

References

Beck, L. J., 1972, "Convection in a Box of Porous Material Saturated With Fluid," *Phys. Fluids*, Vol. 15, pp. 1377–1388.

Bories, S., 1987, "Natural Convection in Porous Media," *Advances in Transport Phenomena in Porous Media*, NATO ASI series, Nijhoff Publ.

Hartline, B. K., and Lister, C. R. B., 1977, "Thermal Convection in a Hele-Shaw Cell," *J. Fluid Mech.*, Vol. 79, pp. 379–389.

Horne, R. N., 1977, "Three-Dimensional Natural Convection in a Confined Porous Medium Heated From Below," *J. Fluid Mech.*, Vol. 92, pp. 751–766.

Impey, M. D., Riley, D., and Winters, K. H., 1987, "The Effect of Side-Wall Imperfections on Pattern Formation in Lapwood Convection," *Bifurcation Phenomena in Thermal Processes and Convection*, ASME HTD-Vol. 94, pp. 99–107.

Kvernvold, O., and Tyvand, P. A., 1979, "Nonlinear Thermal Convection in Anisotropic Porous Media," *J. Fluid Mech.*, Vol. 90, pp. 609–624.

Riley, D. S., and Winters, K. H., 1987, "A Bifurcation Study of Convection in a Two-Dimensional Saturated Porous Cavity," *Bifurcation Phenomena in Thermal Processes and Convection*, ASME HTD-Vol. 94, pp. 83–89.

Storesletten, L., and Tveitereid, M., 1987, "Thermal Convection in a Porous Medium Confined by a Horizontal Cylinder," *Natural Convection*, ASME HTD-Vol. 92, pp. 223–230.

Straus, J. M., 1974, "Large Amplitudes Convection in Porous Media," *J. Fluid Mech.*, Vol. 64, pp. 51–63.

Straus, J. M., and Schubert, G., 1978, "On the Existence of Three-Dimensional Convection in a Rectangular Box Containing Fluid-Saturated Porous Material," *J. Fluid Mech.*, Vol. 87, pp. 385–394.

Straus, J. M., and Schubert, G., 1979, "Three-Dimensional Convection in a Cubic Box of Fluid-Saturated Porous Material," *J. Fluid Mech.*, Vol. 91, pp. 155–165.

Sutton, F. M., 1970, "Onset of Convection in a Porous Channel With Net Through Flow." *Phys. Fluids*, Vol. 13, pp. 1931–1934.

Y. Ma

V. K. Varadan

V. V. Varadan

Research Center for the Engineering of Electronic and Acoustic Materials, and Department of Engineering Science and Mechanics,
The Pennsylvania State University,
University Park, PA 16802

Enhanced Absorption Due to Dependent Scattering

The role of multiple scattering on dependent scattering as well as on dependent absorption is investigated for heterogeneous media containing a high concentration of particles. The decrease of scattering and increase of absorption for lossy (with intrinsic absorption) particles in a lossless matrix is quantitatively described using a Rayleigh region solution derived from a multiple scattering formalism. For smaller wavelengths, dependent scattering and absorption can be obtained by solving the resulting dispersion equation numerically. Results are shown for lossless particles in a lossy matrix, which models an optical coating system.

1 Introduction

It is well known that when any form of energy propagates through a medium containing scatterers (particles), the entrained energy will be either redistributed in various directions by scattering or absorbed by intrinsic absorption mechanism. Although the importance of multiple scattering is recognized theoretically when the population of scatterers is high, the roles of the accompanying dependent scattering and dependent absorption are not well understood in several applications.

In a recent series of studies on light scattering from pigmented surface coatings (Nelson et al., 1986; Kunitomo et al., 1985) or by radiative heat transfer in powder insulators (Chu, 1988; Tien and Wang, 1984; Tong and Tien, 1983), it has been shown that for densely populated heterogeneous media both dependent scattering and dependent absorption have to be considered. As a result, for paint opacity, the dependent scattering-absorption can greatly affect the diffuse reflectance as it does the overall thermal radiation resistance of the powder insulation composites.

Analogous to the aforementioned applications, chemical and nuclear reactors, fuel combustors, cryogenic insulation, microwave and laser coatings, artificial obscuration materials, and many other commercial and military systems usually involve a high concentration of particles. In order to analyze the energy transport characteristics, the dependent scattering and absorption properties cannot be ignored.

For pure scattering and for the small absorption case, multiple scattering effects have been investigated for acoustic, electromagnetic, and elastic problems for various applications (Ma et al., 1984; Varadan et al., 1983, 1985a, 1985b). Successful comparison with experimental measurements encourages us to extend this approach to the current problem. The multiple scattering formalism employed in the previous study is dynamic in nature and hence considers the response beyond the Rayleigh region. For a small particle, a closed-form solution can always be derived for scattering and absorption efficiencies, which enables one to distinguish the contribution from either the dependent scattering or the dependent absorption. In addition, particles of nonspherical shape with aligned or random orientation can also be handled via the *T*-matrix (Varadan et al., 1980, 1988) with a detailed knowledge of position distribution function (Ma et al., 1987, 1988). Other recent investigation on these problems has either been limited to spherical particles in the Rayleigh region or has been confined to the gas model in approximating the position distribution function (Cartigny et al., 1986; Kumar and Tien, 1987).

Contributed by the Heat Transfer Division for publication in the JOURNAL OF HEAT TRANSFER. Manuscript received by the Heat Transfer Division April 5, 1989; revision received September 25, 1989. Keywords: Modeling and Scaling, Numerical Methods, Radiation Interactions.

The plan of the paper is as follows. Since most details can be found in previous publications, in Section 2 we briefly describe the multiple scattering formalism and use the results to obtain the scattering and absorption efficiencies. Although the formalism can be modified for different radiation forms (acoustic, electromagnetic or optical, elastic), only the electromagnetic case is considered in this paper. The Rayleigh region (long-wavelength limit) results for dependent scattering as well as absorption efficiencies are given in terms of the refractive indices for the optical case in Section 3. In Section 4, we discuss the results based on the multiple scattering formalism and show the quantitative contribution from dependent scattering and dependent absorption for soot deposited on walls in which the particle has absorption and for pigment particles in a vehicle (matrix) in which the vehicle has absorption.

2 Analytical Approach (Multiple Scattering)

Consider the propagation of a plane harmonic electromagnetic wave (the incident radiation) in a medium referred to as the matrix characterized by complex values of the dielectric function $\epsilon_2 = \epsilon_2' + i\epsilon_2''$ and magnetic permeability $\mu_2 = \mu_2' + i\mu_2''$. Embedded in the matrix is a random distribution of uniform size scatterers whose permittivity $\epsilon_1 = \epsilon_1' + i\epsilon_1''$ and permeability $\mu_1 = \mu_1' + i\mu_1''$. The matrix of volume V contains N scatterers such that $N \to \infty$, $V \to \infty$, but the number density n_o $(= N/V)$ is finite.

Let $\mathbf{E}$, $\mathbf{E}^o$, $\mathbf{E}_i^e$, $\mathbf{E}_i^s$ be, respectively, the total electromagnetic field, the incident wave field, the field exciting the ith scatterer; and the field scattered by the ith scatterer. All the fields have implicit $\exp(-i\omega t)$ time dependence and satisfy the vector Helmholtz equation. Let Re ϕ_n and Ou ϕ_n denote the basis of orthogonal functions, which are eigenfunctions of the Helmholtz equation. The qualifiers Re and Ou denote functions that are regular at the origin and outgoing at infinity, which are, respectively, appropriate for expanding the field that is incident on a scatterer and that which it scatters, which in turn must satisfy outgoing or radiation conditions (Varadan and Varadan, 1980). If a spherical coordinate system is employed, the regular and outgoing functions are generally the spherical Bessel and Hankel functions. Thus, we can write the following set of self-consistent equations:

$$\mathbf{E} = \mathbf{E}^o + \sum_{i=1} E_i^s \tag{1}$$

$$\mathbf{E}^o = \sum_n a_n^i \,\mathrm{Re}\,\phi_n(\mathbf{r} - \mathbf{r}_i) \tag{2}$$

$$E_i^e = \sum_n \alpha_n^i \,\mathrm{Re}\,\phi_n(\mathbf{r} - \mathbf{r}_i); \quad a < |\mathbf{r} - \mathbf{r}_i| < 2a \tag{3}$$

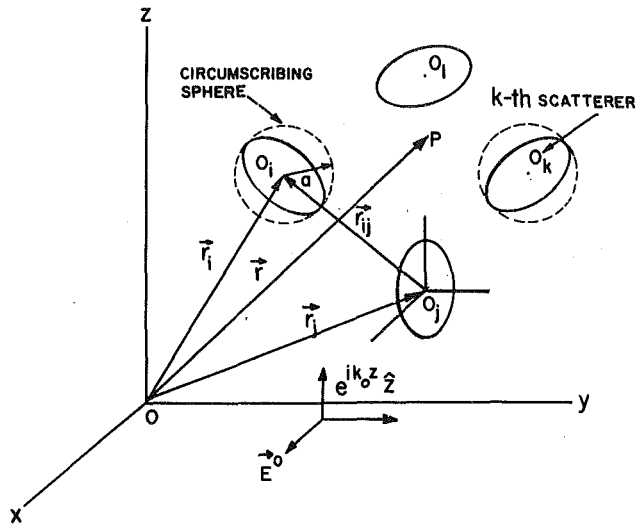

Fig. 1 Geometry of the scattering problem

$$\mathbf{E}_i^s = \sum_n f_n^i \, \mathrm{Ou}\, \phi_n(\mathbf{r}-\mathbf{r}_i); \quad |\mathbf{r}-\mathbf{r}_i| > a \tag{4}$$

In equations (2)–(4), the incident field $\mathbf{E}^o$, the exciting field $\mathbf{E}_i^e$, and the scattered field $\mathbf{E}_i^s$ are all expanded using the orthogonal basis functions. Depending on the incident wavenumber, the subscript n, which is the order of the function, can vary from 1 to infinity. The difference between the incident, exciting, and scattered fields is that the exciting field at one particular scatterer consists of the incident field and the scattered fields from all scatterers except itself. In the equations α_n^i and f_n^i are unknown expansion coefficients and a_n^i are known incident field coefficients. We observe in equations (3) and (4) that a is the radius of the sphere circumscribing the scatterer and that all expansions are with respect to a coordinate origin located in a particular scatterer. The geometry of the scattering problem is depicted in Fig. 1.

The T-matrix by definition simply relates the expansion coefficients of $\mathbf{E}_i^e$ and $\mathbf{E}_i^s$, provided the sum of them is the total field. Thus,

$$f_n^i = \sum_{n'} T_{nn',i}\, \alpha_{n',i} \tag{5}$$

If the addition theorem for the basis functions is invoked, we have

$$\mathrm{Ou}\phi_n(\mathbf{r}-\mathbf{r}_j) = \sum_{n'} \sigma_{nn'}(\mathbf{r}_i-\mathbf{r}_j)\mathrm{Re}\phi_{n'}(\mathbf{r}-\mathbf{r}_i) \tag{6}$$

where $\sigma_{nn'}$ is the translation matrix. Substituting equations (2)–(6) into equation (1), and using the orthogonality of the basis functions, we obtain

$$\alpha^i = a^i + \sum_{j\neq i} T^j \sigma(\mathbf{r}_i-\mathbf{r}_j)\alpha^j \tag{7}$$

This is a set of coupled algebraic equations for the exciting field coefficients, which can be iterated and leads to a multiple scattering series.

For randomly distributed scatterers, an ensemble average can be performed on equation (7), leading to

$$\langle \alpha^i \rangle_i = a^i + \langle \sigma(\mathbf{r}_i-\mathbf{r}_j) T^j \langle \alpha^j \rangle_{ij} \rangle_i \tag{8}$$

where angle brackets and their subscripts i and ij denote conditional averages. Equation (8), when iterated, is an infinite hierarchy involving higher and higher conditional expectations of the exciting field coefficients. In actual engineering applications, a knowledge of higher order correlation functions is difficult to obtain, and usually the hierarchy is truncated so that at most only the two-body positional correlation function is required.

To achieve this simplification the quasi-crystalline approximation (QCA), first introduced by Lax (1952), is invoked, which is stated as

$$\langle \alpha^j \rangle_{ij} \approx \langle \alpha^j \rangle_j \tag{9}$$

Equation (9) is strictly valid in the crystalline case since the neighborhood of every scatterer is the same. By doing this, the fluctuation of the scattered field due to a deviation of a particle i from its average position is eliminated. As mentioned by Hudson (1980), for random distributions, the QCA is accurate to third order (triple scattering). Then, equation (8) simplifies to

$$\langle \alpha^i \rangle_i = a^i + \langle \sigma(\mathbf{r}_i-\mathbf{r}_j) T^j \langle \alpha^j \rangle_j \rangle_i \tag{10}$$

Nomenclature

a = incident field coefficients or size of particle
c = volume fraction of particles
$\mathbf{E}$ = electromagnetic field
f = scattered field coefficients
$g(\,)$ = radial distribution function
Im = imaginary part of a complex number
K = effective propagation constant
k = wavenumber = $2\pi/\lambda$
n = refractive index
n_o = number density
$p(\,)$ = position distribution function
Q = efficiency
Re = real part of a complex number
$\mathbf{r}$ = position vector
T = T-matrix = scattering transfer matrix
V = volume of the heterogeneous medium
w = packing factor = $(1-c)^4/(1+2c)^2$
α = exciting field coefficients
ϵ = relative electric permittivity
λ = wavelength
μ = relative magnetic permeability
σ = translation matrix or cross section
ϕ = basis function, e.g., Bessel or Hankel function
$\langle\ \rangle$ = ensemble average or effective property

Subscripts

ad = dependent absorption
ai = independent absorption
ed = dependent extinction
ei = independent extinction
i or j = referring to particle i or j
n or nn' = modal number
sd = dependent scattering
si = independent scattering
1 = properties pertaining to particle
2 = properties pertaining to matrix

Superscripts

e = pertaining to exciting
o = pertaining to incident
s = pertaining to scattering
$'$ = real part of a complex quantity
$''$ = imaginary part of a complex quantity

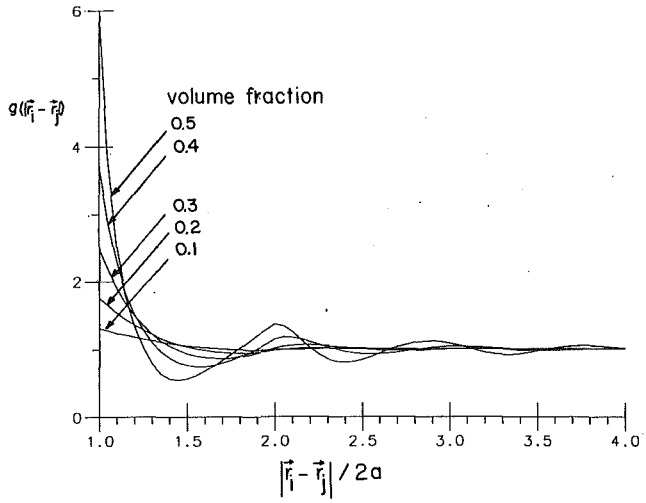

Fig. 2 Radial distribution function versus interparticle distance for different volume fraction

an integral equation for $\langle \alpha^i \rangle_i$, which in principle can be solved. We observe that the ensemble average in equation (10) only requires the joint probability distribution function. In particular, the homogeneous solution of equation (10) leads to a dispersion equation for the effective medium in the quasi-crystalline approximation. Defining the spatial Fourier transform of $\langle \alpha^i \rangle_i$ as

$$\langle \alpha^i \rangle_i = \int e^{i\mathbf{K}\cdot\mathbf{r}_i} X^i(\mathbf{K}) d\mathbf{K} \tag{11}$$

and substituting into equation (10), we obtain for the homogeneous solution

$$X^i(\mathbf{K}) = \sum_{j \neq i} \int \sigma(\mathbf{r}_i - \mathbf{r}_j) T^j p(\mathbf{r}_j | \mathbf{r}_i) e^{i\mathbf{K}\cdot(\mathbf{r}_i - \mathbf{r}_j)} X^j(\mathbf{K}) d\mathbf{r}_j \tag{12}$$

If the scatterers are identical

$$X^i(\mathbf{K}) = X^j(\mathbf{K}) = X(\mathbf{K}) \tag{13}$$

and thus for a nontrivial solution to $\langle \alpha^i \rangle_i$, we require

$$\left| I - \sum_{j \neq i} \int \sigma(\mathbf{r}_i - \mathbf{r}_j) T^j p(\mathbf{r}_j | \mathbf{r}_i) e^{i\mathbf{K}\cdot(\mathbf{r}_i - \mathbf{r}_j)} d\mathbf{r}_j \right| = 0 \tag{14}$$

where I is an identity matrix. In equations (12) and (14), $p(\mathbf{r}_j | \mathbf{r}_i)$ is the joint probability distribution function. For isotropic or spherical statistics,

$$P(\mathbf{r}_j | \mathbf{r}_i) = \begin{cases} 0; & |\mathbf{r}_i - \mathbf{r}_j| < 2a \\ g(|\mathbf{r}_i - \mathbf{r}_j|)/V; & |\mathbf{r}_i - \mathbf{r}_j| > 2a \end{cases} \tag{15}$$

where we have assumed that the scatterers are impenetrable with a minimum separation between the centers, and in equation (15), $2a$ could be the diameter of the circumscribing sphere. For spherical scatterers, the joint probability distribution depends only on the interparticle distance and not on the orientation of the vector joining the centers. The function $g(|\mathbf{r}_i - \mathbf{r}_j|)$ is called the radial distribution function. A discussion of various radial distribution functions and their limitations has been given by Varadan et al. (1985). In Fig. 2, different values of the radial distribution function for different volume fractions are plotted against the normalized radial distance using the Monte Carlo technique (Barker and Henderson, 1971).

From the dispersion equation (14) we can solve for the effective propagation constant $\mathbf{K}$ ($= K\mathbf{k}_o = (K' + iK'')\mathbf{k}_o$, $\mathbf{k}_o$ is the direction of incident radiation) of the heterogeneous medium as a function of frequency, the properties, the shape, size, and orientation of the scatterer via the T-matrix, and the statistics of the distribution via the joint probability distribution function. Although the dispersion equation is exact, the determination of K is computationally involved except in the long wavelength limit.

For dependent scattering, in addition to multiple scattering, another element is the in-phase addition of the far-field scattered radiation, which is, here, through the effective or coherent propagation constant K using the concept of coherent wave (Lax, 1952; Mal and Bose, 1974; Hudson, 1980; Varadan and Varadan, 1980). Most interesting to us is the imaginary part of K, which will be shown later to be related to the extinction efficiency composed of dependent scattering and dependent absorption.

3 Dispersion Equation in the Long Wavelength Limit

The objective of the self-consistent multiple scattering formalism derived for the problem is to obtain an analytical expression for the dispersion equation of radiation propagating in the heterogeneous medium. By solving the dispersion equation, we obtain an effective propagation constant of the heterogeneous medium. If the wavelength in the matrix material is much larger than the size a of the particles and results in a small nondimensional frequency ka in the Rayleigh region, one can solve the dispersion equation in the long wavelength regime and obtain a closed-form solution.

Without considering the magnetic permeability of the matrix and scatterer materials for most optical applications, the dispersion equation can be reduced to the following form (details from Varadan et al., 1986):

$$T(A_o + A_2/2) - 1 = 0 \tag{16}$$

where

$$A_o = 3i\Omega/X_2^3 + w$$

$$A_2 = 3i\Omega(K/k_2)^2/X_2^3$$

$$\Omega = c/[1 - (K/k_2)^2]$$

$$T = i(2X_2^3/3)[(n_1^2 - n_2^2)/(2n_2^2 + n_1^2)]$$

$$w = (1-c)^4/(1+2c)^2$$

$$X_2 = \mathrm{Re}(n_2 k_o)$$

$$n_1 = n_1' + in_1''$$

$$n_2 = n_2' + in_2''$$

$$k_2 = n_2 k_o$$

K = Effective propagation constant = $\langle n \rangle k_o$

$$k_o = 2\pi/\lambda_o$$

λ_o = Wavelength in free space (vacuum)

$\langle n \rangle = \langle n' \rangle + i\langle n'' \rangle$ = Effective refractive index

c = Volume fraction of scatterers

The subscripts 1 and 2 represent the properties pertaining to scatterer and matrix, respectively. The refractive index n is related to the dielectric function ϵ and permeability μ through $n = (\epsilon\mu)^{1/2}$. For randomly distributed lossy/lossless scatterers with a high concentration in a lossy/lossless matrix, the effective propagation constant can be obtained, by solving equation (16),

$$\langle K\rangle/k_2=\langle n\rangle/n_2=\{1-[\beta w-(c\gamma-ci)/(1+\gamma^2)](B+iH)\}$$
$$/\{1-[\beta w+(c\gamma-ci)/2(1+\gamma^2)](B+iH)\}^{1/2} \quad (17)$$

where

$$B=2(C\gamma-D) \qquad H=2(D\gamma+C)$$

$$C=[(n_1'^2-n_1''^2-n_2'^2+n_2''^2)(2n_2'^2-2n_2''^2+n_1'^2-n_1''^2)$$
$$+(2n_1'n_1''-2n_2'n_2'')(4n_2'n_2''+2n_1'n_1'')]/\Delta$$

$$D=[(2n_1'n_1''-2n_2''n_2'')(2n_2'^2-2n_2''^2+n_1'^2-n_1''^2)$$
$$+(n_1'^2-n_1''^2-n_2'^2+n_2''^2)(4n_2'n_2''+2n_1'n_1'')]/\Delta$$

$$\Delta=(2n_2'^2-2n_2''^2+n_1'^2-n_1''^2)^2+(4n_2'n_2''+2n_1'n_1'')^2$$

$$\gamma=(X_2'^3-3X_2^2X_2')/(X_2^3-3X_2X_2'^2)$$

$$\beta=(X_2^3-3X_2X_2'^2)/3$$

$$X_2'=\mathrm{Im}(n_2k_o)$$

Without considering dependent scattering and dependent absorption, the reduced intensity is, from the Lambert–Beer law

$$I=I^o\exp(-n_o\sigma_e z)=I^o\exp[(-n_o\sigma)Q_{ei}z)] \quad (18)$$

where I^o is the intensity of the incident radiation, n_o the number density, σ_{ei} the independent extinction cross section, and z the thickness of the heterogeneous medium. In equation (18), the independent extinction efficiency Q_{ei} is actually the normalized extinction cross section with respect to the physical cross section σ of the particle.

If dependent scattering is considered, the reduced intensity becomes the coherent intensity and has the following expression (Twersky, 1979):

$$I=I^o\exp(-2K''z)=I^o\exp[(-n_o\sigma)Q_{ed}z)] \quad (19)$$

where K'' is the imaginary part of the effective propagation constant K.

Comparing equations (18) and (19), one can show that the dependent extinction efficiency Q_{ed} is related to K'' through the following equation:

$$Q_{ed}=(8/3c)(K''/k_o)(k_oa) \quad (20)$$

Equation (20) is derived specifically for spherical particles in which the volume fraction c is equal to $n_o4\pi a^3/3$.

Because the dependent extinction efficiency is the combination of the dependent absorption efficiency Q_{ad} and the dependent scattering efficiency Q_{sd}, by the use of equation (17), for lossy particles suspended in air ($n_2=1+0i$), we have

$$Q_{ad}=[4D(k_oa)(k_o/K')]/[(1-cC)^2+(2\beta wC+cD)^2] \quad (21)$$

$$Q_{sd}=[8wC^2(k_oa)^4(k_o/K')/3]/[(1-cC)^2+(2\beta wC+cD)^2] \quad (22)$$

In the following, we discuss some limiting cases when equation (17) is applied to compute the effective refractive indices of various systems.

Case 1: Pure Scattering. If neither the scatterers nor the matrix material are lossy, i.e., $n_1''=n_2''=0$, only scattering contributes to the imaginary part of the effective refractive index $\langle n\rangle$.

$$\langle n\rangle/n_2'=[(1+2cT)/(1-cT)+i6\beta wcT^2/(1-cT)^2]^{1/2} \quad (23)$$

where $T=(n_1'^2-n_2'^2)/(n_1'^2+2n_2'^2)$. The effective refractive index $\langle n\rangle$ becomes n_2' and n_1', respectively, when c equal 0 (no scatterer) and 1 (matrix material totally occupied by scatterers). Meanwhile, the imaginary part of $\langle n\rangle$ vanishes due to the disappearance of scatterers.

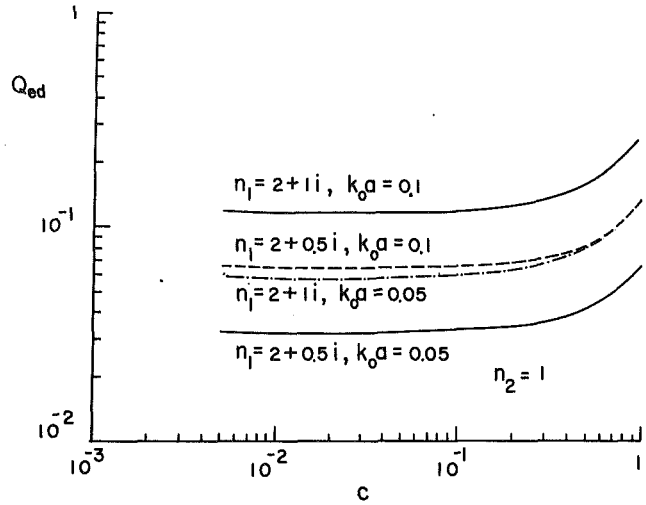

Fig. 3 Dependent extinction efficiency of lossy particles in air

Case 2. Lossy Scatterers in a Lossless Matrix. This is a common occurrence in various problems, e.g., suspensions in fluids and soot in flames. For this case, $n_2''=0$ but n_1'' is not. Equation (17) can be reduced to the following form:

$$\langle n\rangle/n_2'=[\{1+2(\beta w+ci)(D-iC)\}$$
$$/\{1+2[\beta w-ci/2](D-iC)\}]^{1/2} \quad (24)$$

Again, $\langle n\rangle$ becomes n_2' when $c=0$. However, when $c=1$,

$$\langle n\rangle/n_2'=[(1+2C+2iD)/(1-C-iD)]^{1/2}=n_1/n'_2 \quad (25)$$

It is easy to see that the effective refractive index becomes that of the lossy scatterers.

Case 3. Lossless Scatterers in a Lossy Matrix. This problem has been considered for paint films, e.g., absorption-free pigment particles in an absorptive vehicle. For this case, $n_1''=0$ and n_2'' is finite. It is easy to show using equation (17), for $c=0$, $\langle n\rangle=n_2$. For $c=1$, equation (17) reduces to

$$\langle n\rangle/n_2=[(1+2C+2iD)/(1-C-iD)]^{1/2}=n_1'/(n_2'+in_2'') \quad (26)$$

which means the effective refractive index becomes that of the scatterers and is real.

Case 4. Lossy Scatterers in a Lossy Matrix. For this case, the complete form of equation (17) must be considered. As for the relative contribution from scattering and absorption toward $\langle n\rangle$, one can easily show by using Case 2 that

$$\langle n\rangle/n_2'=\{[(1+2cC)(1-cC)-2c^2D^2]/[(1-cC)^2+c^2D^2]$$
$$+i[3cD+6\beta wc(C^2+D^2)]/[(1-cC)^2+c^2D^2]\}^{1/2} \quad (27)$$

4 Results and Discussion

We consider two different problems to show the effects of dependent absorption. The first problem is the application of a long wavelength solution (equation (17)) on small particles with a large index of absorption, such as soot deposited on the wall or ultra-fine powder for heat insulation. In this problem, the absorption of thermal radiation by particles plays an important role in the overall energy transfer (Tien and Wang, 1984; Tong and Tien, 1983; Kumar and Tien, 1987).

The refractive index of soot is chosen to be $n_1=n_1'+in_1''=2+i0.5$ (Kumar and Tien, 1987) in the visible range. Since the absorption index n_1'' is quite large, in the Rayleigh region (i.e., $a/\lambda_o<<1$), one sees from equation (17) that the dependent absorption efficiency Q_{ad} (of the order k_oa) is much larger than the dependent scattering efficiency Q_{sd} (of the order of $k_o^4a^4$). Therefore, the dependent extinction effi-

Table 1 Comparison of the imaginary part of the effective refractive index $\langle n \rangle$ using equation (24) and the Maxwell-Garnett (MG) model

Case 1. $n_1 = 2 + 1\,i$, $n_2 = 1$

No difference between Equation (24) and Maxwell - Garnett model from $k_o a << 1$ to $k_o a = 0.3$

Case 2. $n_1 = 2 + 0.001\,i$, $n_2 = 1$

For $k_o a << 1$

No difference between Equation (24) and Maxwell - Garnett model. Although the difference is small, the magnitude increases as the frequency increases. For example, at $k_o a = 0.1$

volume fraction c	< n" > [Equation (24)]	< n" > [MG model]
0.1	0.63215×10^{-4}	0.51486×10^{-4}
0.2	0.11809×10^{-3}	0.10692×10^{-3}
0.3	0.17575×10^{-3}	0.16788×10^{-3}
0.4	0.24095×10^{-3}	0.23623×10^{-3}
0.5	0.31672×10^{-3}	0.31427×10^{-3}
0.6	0.40603×10^{-3}	0.40496×10^{-3}
0.7	0.51260×10^{-3}	0.51224×10^{-3}
0.8	0.64158×10^{-3}	0.64150×10^{-3}
0.9	0.80038×10^{-3}	0.80037×10^{-3}
1.0	1.00000×10^{-3}	1.00000×10^{-3}

Case 3. $n_1 = 2$, $n_2 = 1$ (pure scattering)

Maxwell - Garnett model does not predict any scattering loss

$k_o a = 0.1$

volume fraction c	< n" > [Equation (23)]	< n" > [MG model]
0.1	0.11729×10^{-4}	0
0.2	0.11172×10^{-4}	0
0.3	0.78725×10^{-5}	0
0.4	0.47246×10^{-5}	0
0.5	0.24552×10^{-5}	0
0.6	0.10710×10^{-5}	0
0.7	0.36017×10^{-6}	0
0.8	0.75917×10^{-7}	0
0.9	0.51004×10^{-8}	0
1.0	0	0

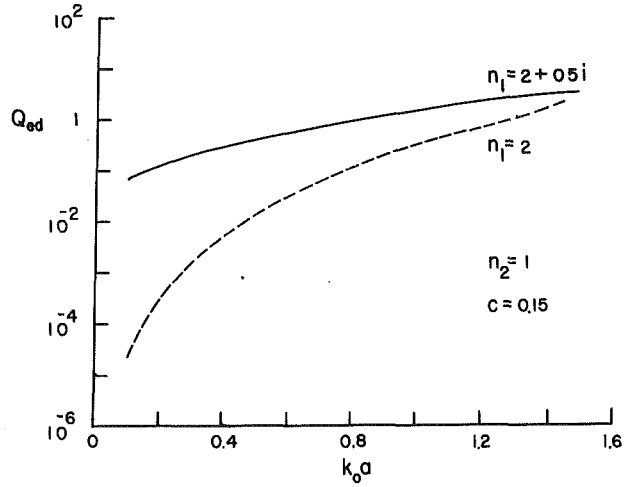

Fig. 4 Frequency-dependent extinction efficiency of particles in air

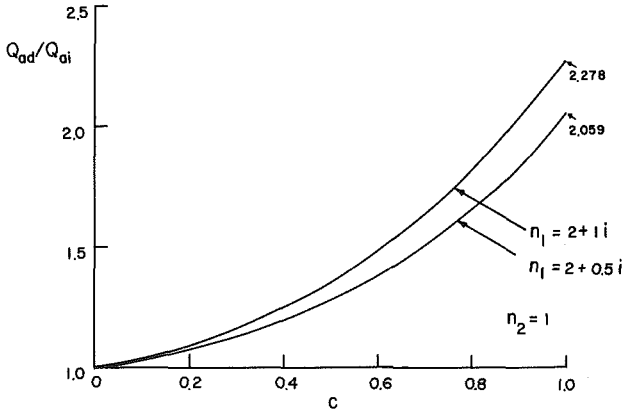

Fig. 5 Ratio of dependent to independent absorption efficiency versus volume fraction c of particles in the Rayleigh region

ciency Q_{ed} is mainly composed of the absorption efficiency Q_{ad} and is plotted against the soot particle volume fraction in Fig. 3. To compare the results of Kumar and Tien (1987), we used the log-log scale. For lossy particles, depending upon the magnitude of the imaginary part of the refractive index n'', there is little or no difference between the present result and that of Kumar and Tien. Nevertheless, the difference can be obvious when lossless particles, i.e., in the pure scattering case, are considered. This is due to the difference in the pair correlation function employed. When the volume fraction is extended to 1, there is no scattering, which is not so in Kumar and Tien's case.

Besides Kumar and Tien's case, for particles with considerable absorption, it can be shown that equation (24) gives virtually the same results as calculated using the Maxwell-Garnett model. Therefore, when the refractive index $n = 2 + 1\,i$ is considered, the results are indistinguishable when plotted against volume fraction. This is not so for small absorption and pure scattering cases. The differences between the current approach and the Maxwell-Garnett model can be found in Table 1.

However, one must realize that when the frequency is increasing, the effect of scattering efficiency becomes more and more important as can be seen in Fig. 4 if the refractive index is frequency independent. In obtaining these results, we considered multipole contributions and rigorously solved the dispersion equation instead of using the long wavelength solution.

For highly absorbent particles in air, the independent absorption efficiency can be found to be

$$Q_{ai} = 4k_o a\{6n_1' n_1''/[2 + n_1'^2 - n_1''^2)^2 + (2n_1' n_1'')^2]\} \qquad (28)$$

The ratio between the dependent absorption efficiency and the independent absorption efficiency can thus be given, also in a closed form

$$Q_{ad}/Q_{ai} = (2/K')/[(1 - cC)^2 + (2\beta wC + cD)^2] \qquad (29)$$

The effect of the particle volume fraction on the ratio of the absorption efficiency is depicted in Fig. 5. It is observed that the absorption is increased when the concentration of particles is increased. Further, it can be proved that for $c = 1$ (air fully replaced by soot), the ratios between Q_{ad} and Q_{ai} become 2.059 and 2.278 for $n_1 = 2 + 0.5i$ and $n_1 = 2 + 1i$, respectively. In Fig. 6, we compare the effective absorption index $\langle n'' \rangle$ from the current formalism with that calculated using the mixture theory in which the absorption is approximated by multiplying the index of absorption with the concentration.

Although a simple equation can be used to predict the dependent absorption as well as scattering efficiencies in the Rayleigh region, a fairly involved computation is required by use of the dispersion equation (14) in the investigation of lossless Mie scatterers in a lossy matrix. This problem, which deals with the reflectance and/or transmittance of a particle layer in the visible region, is very interesting to the paint and paper industries. The essential role of the dependent absorption and scattering efficiencies is to predict correctly the optical distance or the optical density in the associated radiative transfer equation.

The lossless Mie scatterers are titanium dioxide (TiO_2) particles whose properties are well known in the visible range (Kunitomo et al., 1985). In the calculation, we take the parti-

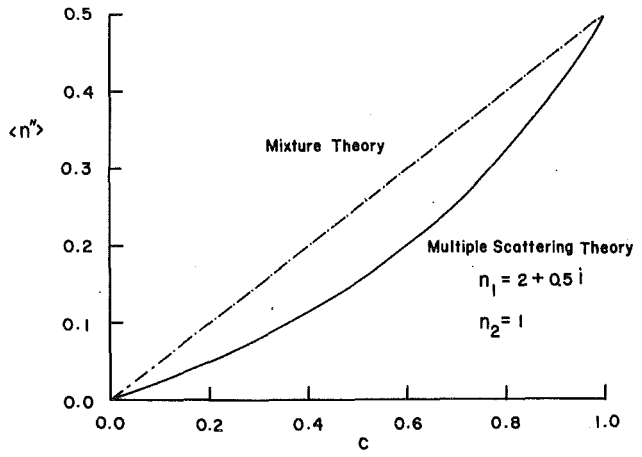

Fig. 6 Effective refractive index (imaginary part) versus volume fraction c from Mixture and Multiple Scattering theories

cle size to be 0.22 μm in diameter and choose the incident wavelength to be 700 nm. The matrix material at this wavelength has the refractive index $n_2 = 1.525 + 0.3 \times 10^{-5} i$. The corresponding nondimensional frequency $k_o a$ is 0.987, which is in any case a non-Rayleigh region. We consider four different concentrations and the results are given in Table 2. As can be seen in the table, this is different from the previous case in which absorption dominates. Nevertheless, the dependent absorption efficiency, though small, is much larger than the independent absorption one. This enhanced absorption greatly affects the diffuse reflectance, as discussed by Kunitomo et al. (1985). The difference is shown quantitatively here but it has remained unclear in the previous investigations (Kunitomo et al., 1985; Chu, 1988). The sensitive change in the absorption efficiency will undoubtedly affect the ratio between the absorption coefficient and the scattering coefficient and the scattering coefficient in the two-flux model (e.g., Kubelka-Munk theory), which has been widely used to calculate the reflectance of a diffuse medium.

Acknowledgments

This research was supported in part by the Office of Naval Research and the Center for Engineering of Electronic and Acoustic Materials at Penn State University.

References

Barker, J. A., and Henderson, D., 1971, "Monte Carlo Values for the Radial Distribution Function of a System of Fluid Hard Spheres," *Molecular Physics*, Vol. 21, pp. 187–191.

Cartigny, J. D., Yamada, Y., and Tien, C. L., 1986, "Radiative Transfer With Dependent Scattering by Particles: Part I — Theoretical Investigation," ASME JOURNAL OF HEAT TRANSFER, Vol. 108, pp. 608–613.

Table 2 Independent and dependent absorption and scattering efficiencies of TiO_2 paint

Volume fraction c	Q_{si}	Q_{ai}	Q_{sd}	Q_{ad}
0.1	1.8932	0.1936×10^{-5}	1.2299	0.7896×10^{-4}
0.2	1.8932	0.1936×10^{-5}	0.6971	0.2632×10^{-4}
0.3	1.8932	0.1936×10^{-5}	0.3711	0.1755×10^{-4}
0.4	1.8932	0.1936×10^{-5}	0.1842	0.1974×10^{-4}

Chu, H. S., 1988, "Analytic Study of Radiative Heat Transfer in Ultra-fine Powder Insulations With Dependent Scattering and Absorption," *Journal of the Chinese Institute of Engineers*, Vol. 11, pp. 327–334.

Hudson, J. A., 1980, "Overall Properties of a Cracked Solid," *Math. Proc. Camb. Phil. Soc.*, Vol. 88, pp. 371–384.

Kumar, S., and Tien, C. L., 1987, "Dependent Scattering and Absorption of Radiation by Small Particles," in: *Fundamentals and Applications of Radiative Heat Transfer*, A. M. Smith and T. F. Smith, eds., pp. 1–7; ASME HTD-Vol. 72, 24th National Heat Transfer Conference, Pittsburgh, PA.

Kunitomo, T., Tsuboi, T. Y., and Shafey, H. M., 1985, "Dependent Scattering and Dependent Absorption of Light in a Fine Particle Dispersed Medium," *Bull. JSME*, Vol. 28, pp. 854–859.

Lax, M., 1952, "Multiple Scattering of Waves II. The Effective Field in Dense Systems," *Physical Review*, Vol. 85, pp. 621–629.

Ma, Y., Varadan, V. K., and Varadan, V. V., 1984, "Application of Twersky's Multiple Scattering Formalism to a Dense Suspension of Elastic Particles in Water," *J. Acoust. Soc. Am.*, Vol. 75, pp. 335–339.

Ma, Y., Varadan, V. V., and Varadan, V. K., 1988, "Wave Propagation in Inhomogeneous Media Containing Randomly Oriented Nonspherical Scatterers," *SPIE Proc.*, Vol. 927, pp. 17–24.

Mal, A. K., and Bose, S. K., 1974, "Dynamic Elastic Moduli of a Suspension of Imperfectly Bonded Spheres," *Proc. Camb. Phil. Soc.*, Vol. 76, pp. 587–600.

Nelson, H. F., Look, D. C., and Crosbie, A. L., 1986, "Two-Dimensional Radiative Backscattering From Optically Thick Media," ASME JOURNAL OF HEAT TRANSFER, Vol. 108, pp. 619–625.

Tien, C. L., and Wang, K. Y., 1984, "Thermal Insulation Heat Transfer," Special Issue for the U.S.-China Binational Heat Transfer Workshop, *Journal of Engineering Thermalphysics*, Vol. 1, pp. 1–11.

Tong, T. W., and Tien, C. L., 1983, "Radiative Heat Transfer in Fibrous Insulations—Part I: Analytic Study," ASME JOURNAL OF HEAT TRANSFER, Vol. 105, pp. 70–75.

Twersky, V., 1979, "Propagation in Pair-Correlated Distributions of Small-Spaced Lossy Scatterers," *J. Opt. Soc. Am.*, Vol. 69, pp. 1567–1572.

Varadan, V. K., and Varadan, V. V., eds., 1980, *Acoustic, Electromagnetic and Elastic Wave Scattering: Focus on the T-Matrix Approach*, Pergamon, New York.

Varadan, V. K., Bringi, V. N., Varadan, V. V., and Ishimaru, A., 1983, "Multiple Scattering Theory for Waves in Discrete Random Media and Comparison With Experiments," *Radio Science*, Vol. 18, pp. 321–327.

Varadan, V. K., Ma, Y., and Varadan, V. V., 1985a, "A Multiple Scattering Theory for Elastic Wave Propagation in Discrete Random Media," *J. Acoust. Soc. Am.*, Vol. 77, pp. 375–385.

Varadan, V. V., Ma, Y., and Varadan, V. K., 1985b, "Propagator Model Including Multiple Fields for Discrete Random Media," *J. Opt Soc. Am.*, Vol. A2, pp. 2195–2201.

Varadan, V. K., Varadan, V. V., Ma, Y., and Hall, W. F., 1986, "Design of Ferrite-Impregnated Plastics (PVC) as Microwave Absorbers," *IEEE Transactions on Microwave Theory and Techniques*, Vol. MIT-34, pp 251–258.

Varadan, V. V., Varadan, V. K., Ma, Y., and Steele, W. A., 1987, "Effects of Nonspherical Statistics on EM Wave Propagation in Discrete Random Media," *Radio Science*, Vol. 22, pp. 491–497.

Varadan, V. V., Lakhtakia, A., and Varadan, V. K., 1988, "Comments on Recent Criticism of the T-Matrix Method," *J. Acoust. Soc. Am.*, Vol. 84, pp. 2280–2283.

Development of a Network Analogy and Evaluation of Mean Beam Lengths for Multidimensional Absorbing/Isotropically Scattering Media

W. W. Yuen
Department of Mechanical and Environmental Engineering, University of California at Santa Barbara, Santa Barbara, CA 93106

Based on Hottel's zonal formulation, a network analogy is developed for the analysis of radiative transfer in general multidimensional absorbing/isotropically scattering media. Applying the analogy to the analysis of an isothermal medium and assuming that the incoming and outgoing flux density is homogeneous within the medium, the effect of scattering on the evaluation of mean beam lengths is illustrated. Two concepts of mean beam length, an absorption mean beam length (AMBL) and an extinction mean beam length (EMBL), are introduced and shown to be important for the analysis of radiative transfer in practical systems. Both mean beam lengths differ significantly from the conventional mean beam length in systems of moderate and large optical thickness. Relations between AMBL and EMBL and their limiting behavior are developed analytically. Numerical results for a sphere radiating to its surface and an infinite parallel slab radiating to one of its surfaces are presented to demonstrate quantitatively the mathematical behavior of the two mean beam lengths.

1 Introduction

Radiative transfer in an absorbing/scattering medium is an important aspect in many practical engineering problems such as the modeling of energy transport in combustion chambers and furnaces. Mathematically, an exact solution to the radiative equation of transfer, coupled with the fluid flow and convective heat transfer occurring inside a furnace, can be extremely complicated and therefore unsuitable for practical engineerirg applications. A great deal of research effort in radiative transfer in the past fifty years has thus been directed toward the development of approximation methods. Sarofim (1986) and Viskanta and Menguc (1987) have given excellent reviews of the various available techniques.

One of the most important concepts utilized in practical radiative transfer calculations, particularly in applications for nongray media, is mean beam length (MBL). Introduced originally by Hottel (1927, 1967), the MBL of a gas volume radiating to a boundary is defined as the radius of an "equivalent" hemisphere that produces a flux to the center of its base equal to the average flux radiated to the area of interest by the actual volume of gas. Since spectral absorption data for all common gaseous species are generally measured in one-dimensional line-of-sight experimental systems, the MBL concept provides an important theoretical link through which the existing one-dimensional spectral absorption data can be applied to radiative transfer calculations in complex multidimensional systems.

In recent years, scattering has been recognized to be important in many particle-laden combustion systems such as fires and pulverized coal furnaces (DeRis, 1978; Wessel, 1985; Menguc and Viskanta, 1986). While it is well known that scattering can have a significant effect on the total radiative heat transfer, its effect on MBL has not yet been established. To the best of the author's knowledge, an approximate expression for the scattering mean beam length in the limit of an optically thin weakly scattering medium (Cartigny, 1986) appears to be the only reported work addressing this important issue. Indeed, the lack of an accurate definition for MBL in an absorbing/scattering medium has led to large uncertainty on the result of many existing furnace calculations (Menguc and Viskanta, 1986; Viskanta and Menguc, 1987).

In this work, a theoretical formulation of MBLs in an absorbing/scattering medium is derived. In section 2, a network analogy for the calculation of radiative transfer in an emitting, absorbing, and isotropically scattering medium is developed. By applying the analogy to an isothermal medium and assuming that the incoming and outgoing flux density is homogeneous, two concepts of MBL, an "absorption" mean beam length (AMBL) and an "extinction" mean beam length (EMBL), are introduced in section 3. Mathematically, AMBL is defined as the radius of a purely absorbing hemisphere with the same absorption coefficient as the medium under consideration, which produces a flux at the center of its base equal to the average heat flux radiated to the area of interest. The concept of AMBL is important in estimating the emission from nongray gaseous species in the presence of scattering particles. EMBL, on the other hand, is defined as the radius of an absorbing/scattering hemisphere with the same extinction coefficient and scattering albedo as the medium under consideration that produces the equivalent heat flux. The concept of EMBL is important in the scaling of scattering/absorbing media. Based on evaluation of AMBL for an absorbing/scattering hemispherical medium radiating to its base, a universal relation between AMBL and EMBL is also presented in section 3. In section 4, exact mathematical expression for the two MBLs are generated for two enclosures, a sphere and an in-

Contributed by the Heat Transfer Division and presented at the National Heat Transfer Conference, Houston, Texas, July 24-27, 1988. Manuscript received by the Heat Transfer Division October 11, 1988. Keywords: Furnaces and Combustors, Modeling and Scaling, Radiation.

finite parallel slab. Numerical results are presented to illustrate parametrically the importance of scattering on the evaluation of MBLs. Finally, a conclusion of the present work and some comments on the future direction of research in this general area are presented in section 5.

2 Network Analogy for an Absorbing/Scattering Medium

The analogy between electrical network and radiative transfer in an enclosure with a nonparticipating medium was first developed by Oppenheim (1956). Bevans and Dunkle (1960) extended the idea to include the effect of an isothermal absorbing medium. The extension, however, is quite complicated mathematically and applicable only for a homogeneous isothermal absorbing medium. The practical application for the Bevans and Dunkle formulation is thus limited. Utilizing results generated by the two-flux model, Tong and Tien (1980) noted that the heat transfer in a planar absorbing/scattering medium can be expressed by a network representation. But they did not consider extension to general multidimensional systems. To the best of the author's knowledge, formulation of the network analogy for a general nonisothermal multidimensional enclosure with an absorbing/scattering medium has not appeared in the literature.

For an isotropically scattering and absorbing medium, the set of radiative exchange relations generated by Hottel's zonal method (Hottel and Sarofim, 1967) is a natural basis for the development of the network analogy. Specifically, in an enclosure with N isothermal surface zones and M gas zones, the energy balance on each zone can be written as

$$A_i H_i = \sum_{j=1}^{N} \overline{s_i s_j} W_j + \sum_{j=1}^{M} \overline{s_i g_j} W_{g,j} \tag{1}$$

$$4KV_i H_{g,i} = \sum_{j=1}^{N} \overline{g_i s_j} W_j + \sum_{j=1}^{M} \overline{g_i g_j} W_{g,j} \tag{2}$$

In the above expressions, H_i and W_i are the irradiation and radiosity (emission plus reflection) of surface A_i while $4H_{g,i}$ and $4KW_{g,i}$ can be interpreted as the incoming and outgoing (emission plus scattering) flux density of a volume element V_i. K is the extinction coefficient. $\overline{s_i s_j}$, $\overline{s_i g_j}$, and $\overline{g_i g_j}$ are the direct exchange factors between A_i and A_j, A_i and V_j, and V_i and V_j, respectively. The mathematical expressions for these exchange factors are given by Hottell and Sarofim (1967) and will not be repeated here. In general, they satisfy the following reciprocity and closure relations:

$$\overline{s_i s_j} = \overline{s_j s_i} \tag{3a}$$

$$\overline{s_i g_j} = \overline{g_j s_i} \tag{3b}$$

$$\overline{g_i g_j} = \overline{g_j g_i} \tag{3c}$$

$$\sum_{i=1}^{N} \overline{s_i s_j} + \sum_{i=1}^{M} \overline{g_i s_j} = A_j \tag{4a}$$

$$\sum_{i=1}^{M} \overline{g_i g_j} + \sum_{i=1}^{N} \overline{s_i g_j} = 4KV_j \tag{4b}$$

The parameters W_i, H_i, $W_{g,i}$, and $H_{g,i}$ are related to the surface emissive power E_i and the gaseous emissive power $E_{g,i}$ by

$$W_i = \epsilon_i E_i + (1-\epsilon_i) H_i \tag{5a}$$

$$W_{g,i} = (1-\omega_0) E_{g,i} + \omega_0 H_{g,i} \tag{5b}$$

Q_i and $Q_{g,i}$, the net heat transfer from surface A_i and volume V_i, respectively, can be written as

$$Q_i = A_i (W_i - H_i) = \frac{A_i \epsilon_i}{1-\epsilon_i} (E_i - W_i) \tag{6a}$$

$$Q_{g,i} = 4V_i (W_{g,i} - H_{g,i}) = 4KV_i \left(\frac{1-\omega_0}{\omega_0}\right) (E_{g,i} - W_{g,i}) \tag{6b}$$

where ϵ_i is the surface emissivity of A_i and ω_0 is the scattering albedo of the medium.

To develop the necessary equation for the network analogy, the first half of equations (6a) and (6b), together with the reciprocity and closure relations, can be readily combined with equations (1) and (2) to yield

$$Q_i = \sum_{j=1}^{N} \overline{s_i s_j} (W_i - W_j) + \sum_{j=1}^{M} \overline{s_i g_j} (W_i - W_{g,j}) \tag{7a}$$

and

$$Q_{g,i} = \sum_{j=1}^{N} \overline{g_i s_j} (W_{g,i} - W_j) + \sum_{j=1}^{M} \overline{g_i g_j} (W_{g,i} - W_{g,j}) \tag{7b}$$

Based on equations (6a), (6b), (7a), and (7b), the analogy

Nomenclature

A_i = ith surface area in an enclosure
D = thickness of the parallel slab system
E_i = blackbody emissive power of surface A_i
$E_{g,i}$ = blackbody emissive power of volume $V_{g,i}$
$E_3(x)$ = exponential integral function
$F(\beta)$ = function defined in equation (A9)
$\overline{g_i g_j}$ = volume–volume direct exchange factor between $V_{g,i}$ and $V_{g,j}$
$\overline{g_i s_j}$ = volume–gas direct exchange factor between $V_{g,i}$ and A_j
H_i = irradiation into surface A_i
$4H_{g,i}$ = incoming flux density into volume $V_{g,i}$
K = extinction coefficient
L_{ab} = absorption mean beam length
L_e = conventional mean beam length (defined for a pure absorption medium)
L_{ex} = extinction mean beam length
q = heat flux
Q_i = total heat transfer from surface A_i
$Q_{g,i}$ = total heat transfer from volume $V_{g,i}$
R = radius
$\overline{s_i s_j}$ = surface–surface direct exchange factor between A_i and A_j
$\overline{s_i g_j}$ = surface–gas direct exchange factor between A_i and V_j
$V_{g,i}$ = ith gas volume in an enclosure
W_i = radiosity from surface A_i
$4KW_{g,i}$ = outgoing flux density from volume $V_{g,i}$
α = angle defined in Fig. A1
β = angle defined in Fig. A1
ϵ_i = emissivity of surface A_i
θ = angle defined in Fig. A1
θ_1 = angle defined by equation (A10a)
θ_2 = angle defined by equation (A10a)
ϕ = azimuthal angle used in equations (A6), (A7), and (A9)
ϕ_m = angle defined by equation (A11)
ω_0 = scattering albedo

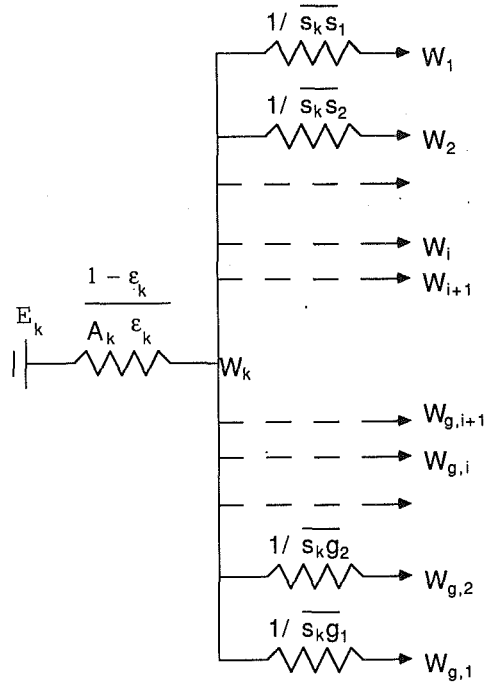

Fig. 1(*a*) Network representation for a surface element A_k

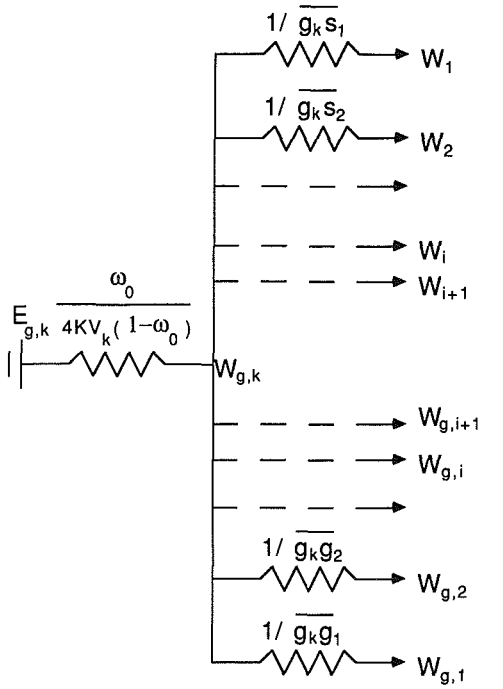

Fig. 1(*b*) Network representation for a volume element V_k

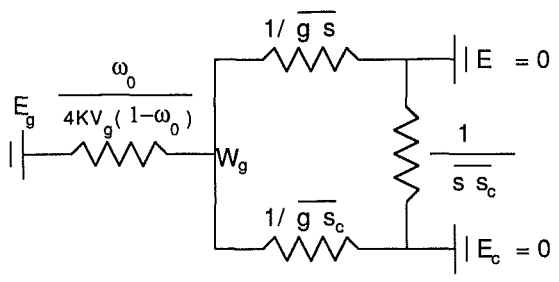

Fig. 2 Network representation for the mean beam length calculation

between electrical network and radiative heat transfer in an absorbing/scattering medium is quite apparent. Specifically

E_i = internal potential of surface A_i

W_i = external potential of surface A_i

$\frac{1-\epsilon_i}{A_i\epsilon_i}$ = internal resistance at surface A_i

$E_{g,i}$ = internal potential of volume V_i

$W_{g,i}$ = external potential of volume V_i

$\frac{\omega_0}{4KV_i(1-\omega_0)}$ = internal resistance at volume V_i

$1/\overline{s_i s_j}$ = resistance between surfaces A_i and A_j

$1/\overline{s_i g_j}$ = resistance between surfaces A_i and V_j

$1/\overline{g_i g_j}$ = resistance between surfaces V_i and V_j

Schematic representations of the network analogy for a surface element A_i and a volume element V_i are shown in Figs. 1(*a*) and 1(*b*), respectively. Note that in contrast to Bevans and Dunkle (1960), the present network analogy does not require the restrictive assumption of an isothermal gas volume. It can be applied to any enclosure containing an absorbing/isotropically scattering medium.

3 Formulation of Mean Beam Lengths

In the formulation of mean beam lengths, the problem of interest is to determine the radiative heat flux incident on an area A from a homogeneous isothermal gas volume (with volume V_g, emissive power E_g, extinction coefficient K, and scattering albedo ω_0). The area A, in general, is a part of the total boundary of the enclosure. Let A_c be the remaining area of the enclosure and assuming that H_g and W_g are uniform in the gas volume, the network analogy is applicable with an equivalent network as shown in Fig. 2. The corresponding network equations can be readily solved to yield the following heat flux expression at surface A:

$$q = \frac{(E_g \overline{sg}/A)(1-\omega_0)}{1-\frac{\omega_0 \overline{gg}}{4KV_g}} \tag{8}$$

3(*a*) Concept of Absorption Mean Length (AMBL). The absorption mean beam length (AMBL), L_{ab}, is defined as the radius of a hemispherical volume of purely absorbing gas (with the same temperature and absorption coefficient as that of the actual mixture), which produces a flux to the center of its base equal to the acutal heat flux. Mathematically, L_{ab} is given by the relation

$$1-e^{-(1-\omega_0)KL_{ab}} = \frac{(1-e^{-KL_e})(1-\omega_0)}{1-\frac{\omega_0 \overline{gg}}{4KV_g}} \tag{9}$$

where the exchange factor $\overline{sg}$ is written in term of the conventional mean beam length L_e as

$$\frac{\overline{sg}}{A} = 1-e^{-KL_e} \tag{10}$$

The concept of AMBL is useful when it is necessary to estimate the effect of scattering particles on the emission of a second species (e.g., the evaluation of the strength of a gaseous absorption band in the presence of scattering particles in furnace calculation). Note that the mean beam length expression considered by Cartigny (1986) is the absorption mean beam length.

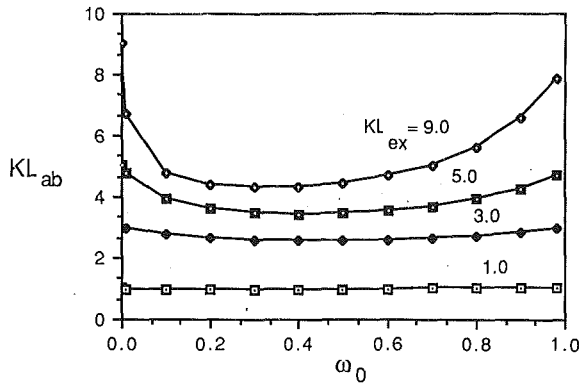

Fig. 3 Universal relation between KL_{ab}, KL_{ex}, and ω_0

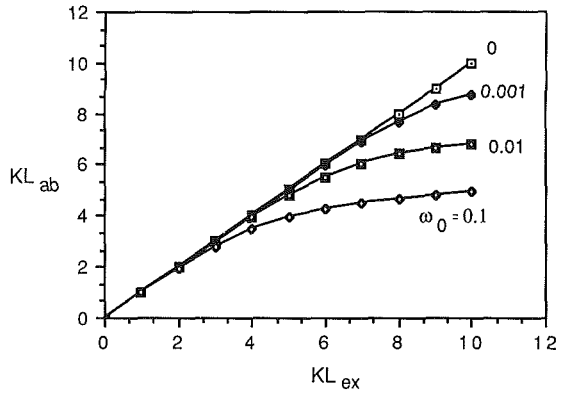

Fig. 4 Relation between KL_{ab} and KL_{ex} in the weak scattering limit

3(*b*) Concept of Extinction Mean Bean Length (EMBL). The extinction mean beam length (EMBL), L_{ex}, is defined as the radius of a hemispherical volume of scattering and absorbing gas (with the same temperature, extinction coefficient, and scattering albedo as that of the actual mixture), which produces a flux to the center of its base equal to the acutal heat flux. This concept is important for the scaling of a mixture in which the effects of absorption and scattering are not readily separable (e.g., the assessment and comparison of optical thicknesses for two geometrically dissimilar sooty flames). Unlike L_e and L_{ab}, a closed-form expression for L_{ex} is not available for an arbitrary enclosure since the heat flux to the center of the base of an absorbing/scattering hemisphere cannot be expressed in closed form. A universal relation between L_{ab} and L_{ex}, however, can be readily generated based on the expression of L_{ab} for a hemispherical volume of gas radiating to the center of its base. Since L_{ex} for a hemisphere radiating to its base is simply its radius, L_{ex} and L_{ab} for an arbitrary enclosure are related by

$$1-e^{-(1-\omega_0)KL_{ab}}=\frac{(1-e^{-KL_{ex}})(1-\omega_0)}{1-\omega_0\left(\dfrac{\overline{gg}}{4KV_g}\right)_{\text{hemisphere}}} \tag{11}$$

where $(\overline{gg}/4KV_g)_{\text{hemisphere}}$ is the self-exchange factor per unit volume for a hemispherical volume of gas with optical radius KL_{ex}. Specifically, the evaluation of EMBL for an arbitrary enclosure requires first the evaluation of AMBL based on equation (9) and then the evaluation of EMBL based on equation (11).

The evaluation of $(\overline{gg}/4KV_g)_{\text{hemisphere}}$, which has not appeared in the literature, is presented in Appendix A. Numerical values for KL_{ab} for different values of KL_{ex} and ω_0 are presented in Fig. 3. It can be readily observed that, in general, $L_{ab} \le L_{ex}$. In a hemispherical geometry, the primary effect of scattering is to reduce heat transfer. A larger absorbing/scattering hemisphere is required to generate the same heat flux to the center of its base as that of a purely absorbing hemisphere.

3(*c*) Limiting Behavior of L_{ex} and L_{ab}. In the optically thin limit ($KL_{ex} \to 0$) and independent of ω_0, equations (9) and (11) are reduced to

$$L_e = L_{ex} = L_{ab} \tag{12}$$

Based on numerical data presented in Fig. 3, L_{ex} and L_{ab} are essentially identical for $KL_{ex} \le 1.0$.

Physically, the three mean beam lengths are also expected to be identical in the limit of no scattering ($\omega_0 = 0$). Numerical data, however, show that the convergence of L_{ab} to L_{ex} is quite slow in the optically thick limit. In Fig. 4, the relation between L_{ab} and L_{ex} in the weak-scattering limit ($\omega_0 \le 0.1$) is presented. Note that even for a "small" scattering albedo (say, $\omega_0 = 0.01$), the difference between L_{ex} and L_{ab} can be quite substantial in systems with moderate and large optical thicknesses. Equation (12), in the more restrictive optically thin weakly scattering limit ($KL_{ab} \to 0$, $\omega_0 \to 0$), is also deduced by Cartigny (1986).

In the strongly scattering limit ($\omega_0 \to 1.0$), equation (9) can be simplified to yield

$$KL_{ab}=\frac{\overline{sg}/A}{1-\dfrac{\overline{gg}}{4KV_g}} \tag{13}$$

and the relation between L_{ab} and L_{ex} becomes

$$KL_{ab}=\frac{(1-e^{-KL_{ex}})}{1-\omega_0\left(\dfrac{\overline{gg}}{4KV_g}\right)_{\text{hemisphere}}} \tag{14}$$

Note that AMBL and EMBL are both nonzero even in the pure scattering limit ($\omega_0 = 1.0$). Similar to the conventional MBL L_e, L_{ab}, and L_{ex} are fundamental geometric parameters of the enclosure.

If A is the total surface to the enclosure (i.e., $A_c = 0$ in Fig. 2), equation (13) can be further simplified (using the reciprocity and closure relations) to yield

$$L_{ab}=\frac{4V_g}{A} \tag{13a}$$

which is identical to the optically thin limiting expression for L_e. Physically, this result is not surprising because from the pure absorption consideration, a pure scattering medium is optically thin. It is important to emphasize that equation (13*a*) holds for all strongly scattering media independent of optical thickness. L_{ex}, in the pure scattering limit, must still be evaluated using equation (14).

4 Numerical Examples

To illustrate quantitatively the effect of scattering on AMBL and EMBL, numerical values are tabulated for two specific geometries, a sphere and an infinite parallel slab. These two cases are selected because many practical furnaces can be approximated by these geometries and closed-form expressions for the necessary exchange factors $\overline{sg}/A$ and $\overline{gg}/(4KV_g)$ are available from standard references (Hottel and Sarofim, 1967).

For an absorbing-scattering spherical medium radiating to its surface, L_{ab} is given by

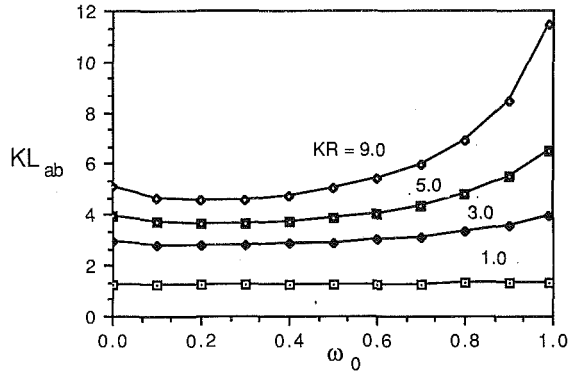

Fig. 5(*a*) Absorption mean beam length for a sphere radiating to its surface for different optical radii (*KR*) and albedos (ω_0)

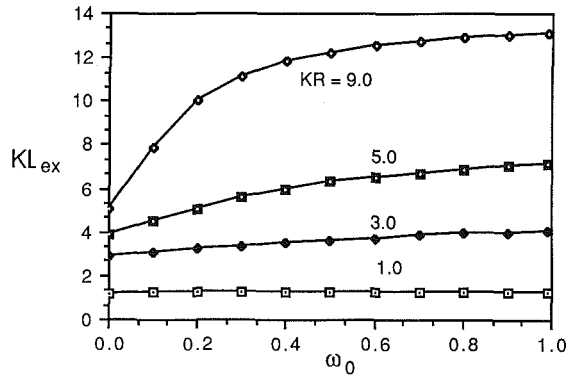

Fig. 5(*b*) Extinction mean beam length for a sphere radiating to its surface for different optical radii (*KR*) and albedos (ω_0)

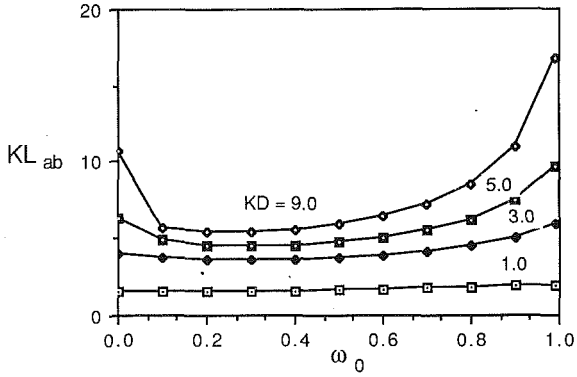

Fig. 6(*a*) Absorption mean beam length for an infinite parallel slab radiating to one of its surfaces for different optical slab thicknesses (*KD*) and albedos (ω_0)

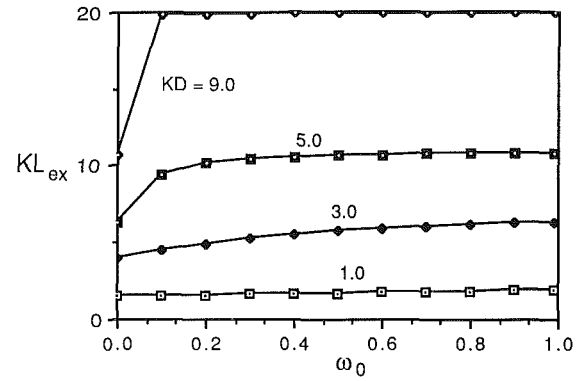

Fig. 6(*b*) Extinction mean beam length for an infinite parallel slab radiating to one of its surfaces for different optical slab thicknesses (*KD*) and albedos (ω_0)

$$1-e^{-(1-\omega_0)KL_{ab}}=\frac{\frac{\overline{sg}}{A}(1-\omega_0)}{1-\omega_0\left(1-\frac{3}{4KR}\frac{\overline{sg}}{A}\right)} \tag{14}$$

where

$$\frac{\overline{sg}}{A}=1-\frac{1}{2(KR)^2}\left(1-(2KR+1)e^{-2KR}\right) \tag{15}$$

with R being the radius of the sphere. Numerical values of AMBL and EMBL for different KR and ω_0 are presented in Figs. 5(*a*) and 5(*b*). While L_{ex}, in general, increases monotonically with ω_0, L_{ab} first decreases and then increases with increasing ω_0. Physically, the slight decrease in L_{ab} with ω_0 at small albedo can be attributed to the slight enhancement of heat transfer by scattering in an optically thick medium. As ω_0 increases, the effect of extinction by scattering becomes dominant and L_{ab} increases. A comparison between Figs. 5(*a*) and 5(*b*) also shows that, in general, L_{ex} is much greater than L_{ab}, particularly in the limit of large albedo.

For a parallel slab of absorbing-scattering medium radiating to one of its two bounding surfaces, L_{ab} is given by

$$1-e^{-(1-\omega_0)KL_{ab}}=\frac{\frac{\overline{sg}}{A}(1-\omega_0)}{1-\omega_0\left(1-\frac{1}{2KD}\frac{\overline{sg}}{A}\right)} \tag{16}$$

where

$$\frac{\overline{sg}}{A}=1-2E_3(KD) \tag{17}$$

with D being the thickness of the slab and $E_3(x)$ the exponential integral function (Hottel and Sarofim, 1967). Numerical results of L_{ex} and L_{ab} for a slab are shown in Figs. 6(*a*) and 6(*b*). Their qualitative behavior is similar to that for the sphere presented in Figs. 5(*a*) and 5(*b*).

5 Conclusions

A network analogy is developed for the analysis of radiative transfer in an absorbing and isotropically scattering medium. Based on a network analysis for an isothermal medium and assuming that the incoming and outgoing flux density are homogeneous, the traditional concept of mean beam length is extended to include the effect of scattering. Two concepts of mean beam length (an absorption mean beam length, AMBL, and an extinction mean beam length, EMBL) are shown to be useful in characterizing the radiative transfer in a scattering medium. Based on an analysis of a hemispherical absorbing/scattering medium, a universal relation between AMBL and EMBL is developed. Numerical values for AMBL and EMBL for two enclosures are presented to show that the two mean beam lengths differ significantly from each other and also from the conventional mean beam length in systems with moderate or large optical thickness. The use of the conventional definition of mean beam length in general absorbing/scattering media can thus lead to significant erorr, except in the optically thin limit.

The general behavior of AMBL and EMBL is illustrated by numerical results generated by two specific systems, a spherical medium radiating to its surface and an infinite parallel slab radiating to one of its surfaces. For a fixed extinction coefficient and physical dimension, EMBL is shown to increase monotonically with scattering albedo while AMBL first decreases and then increases with scattering albedo.

Since an isothermal absorbing/scattering medium can, in general, have nonuniform incoming and outgoing flux density, expressions for AMBL and EMBL developed in the present work are approximate. Additional exact numerical calculations must also be carried out to develop a more precise relation between the two mean beam lengths and their mathematical behavior. Systems with different geometric shapes must be analyzed in order to generate quantitative relations, which are useful for practical applications. These efforts are currently under way and the results will be presented in future publications.

References

Bevans, J. T., and Dunkle, R. V., 1960, "Radiative Exchange Within an Enclosure," ASME JOURNAL OF HEAT TRANSFER, Vol. 82, pp. 1-19.

Cartigny, J. D., 1986, "Mean Beam Length for a Scattering Medium," *Heat Tranfer—1986*, C. L. Tien, V. P. Carey, and J. K. Farrell, eds., Vol. 2, pp. 769-772.

DeRis, J., 1978, "Fire Radiation—A Review," *The Seventeenth Symposium (International) on Combustion*, The Combustion Institute, Pittsburgh, PA, pp. 1003-1016.

Hottel, H. C., 1927, *Transaction American Institute of Chemical Engineers*, Vol. 19, p. 173.

Hottel, H. C., and Sarofim, A. F., 1967, *Radiative Transfer*, McGraw-Hill, New York.

Menguc, M. P., and Viskanta, R., 1986, "An Assessment of Spectral Radiative Transfer Predictions for a Pulverized Coal-Fired Furnace," *Heat Transfer—1986*, C. L. Tien, V. P. Carey, and J. K. Farrell, eds., Vol. 2, pp. 815-820.

Oppenheim, A. K., 1956, "Radiative Analysis by the Network Method," *Trans. ASME*, Vol. 78, pp. 725-735.

Sarofim, A. F., 1986, "Radiative Heat Transfer in Combustion: Friend or Foe," *The Twenty-First Symposium (International) on Combustion*, The Combustion Institute, Pittsburgh, PA, pp. 1-23.

Tong, T. W., and Tien, C. L., 1980, "Resistance-Network Representation of Radiative Heat Transfer With Particulate Scattering," *Journal of Quantitative Spectroscopy and Radiative Transfer*, Vol. 24, pp. 491-503.

Viskanta, R., and Menguc, M. P., 1987, "Radiation Heat Transfer in Combustion Systems," *Progress in Energy and Combustion Science*, Vol. 13, pp. 97-160.

Wessel, R. A., 1985, "Effective Radiative Properties for Particle-Gas Mixtures," *Heat Transfer in Fire and Combustion Systems*, C. K. Law, Y. Jaluria, W. W. Yuen, and K. Miyasaka, eds., pp. 239-249.

APPENDIX

The evaluation of $\overline{gg}/4KV_g$ for a hemispherical volume of gas is presented in this section. Let A_1 and A_2 be the hemispherical surface and the base surface, respectively; equations (4*a*) and (4*b*) can be readily utilized to yield

$$\frac{\overline{gg}}{4KV_g} = 1 - \frac{\overline{gs_1}}{4KV_g} - \frac{\overline{gs_2}}{4KV_g} \tag{A1}$$

where the two surface-gas exchange factors can be written as

$$\frac{\overline{s_1 g}}{A_1} = 1 - \frac{\overline{s_1 s_1}}{A_1} - \frac{\overline{s_1 s_2}}{A_1} \tag{A2}$$

and

$$\frac{\overline{s_2 g}}{A_2} = 1 - \frac{\overline{s_2 s_1}}{A_2} \tag{A3}$$

The evaluation of $\overline{gg}/4KV_g$ thus requires the evaluation of the two surface exchange factors $\overline{s_1 s_1}$ and $\overline{s_1 s_2}$.

The relevant geometry and coordinate system utilized in the evaluation of $\overline{s_1 s_2}$ is shown in Fig. A1. For the differential areas dA_1 and dA_2 as shown, the differential exchange factor $\overline{ds_1 ds_2}$ is given by

$$\overline{ds_1 ds_2} = dA_1 dA_2 \frac{\cos\theta \cos\alpha e^{-Kd}}{\pi d^2} \tag{A4}$$

where d is the distance between dA_1 and dA_2 and θ and α are as defined in Fig. A1.

Mathematically, it can be readily shown that a direct numerical integration based on a Cartesian coordinate is ineffective in the evaluation of $\overline{s_1 s_1}$ and $\overline{s_1 s_2}$ because the integrand becomes singular as $d \to 0$. To overcome this difficulty, equation (A4) is rewritten in terms of a differential solid angle $d\omega_2$ as

$$\overline{ds_1 ds_2} = dA_1 d\omega_2 \frac{\cos\theta e^{-Kd}}{\pi} \tag{A5}$$

where $d\omega_2$ is given by

$$d\omega_2 = \frac{dA_2 \cos\alpha}{d^2} = \sin\theta d\theta d\phi \tag{A6}$$

with ϕ being the azimuthal angle measured on the surface

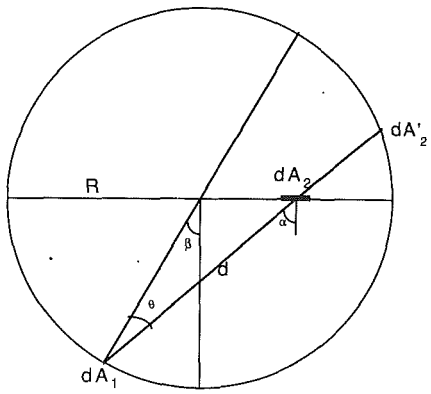

Fig. A1 Geometry and coordinate system for the evaluation of $(\overline{gg}/4KV_g)_{\text{hemisphere}}$

Table 1 Numerical values for the various exchange factors for a hemispherical gas volume

KR	$\overline{s_1 s_1}/A_1$	$\overline{s_1 s_2}/A_1$	$\overline{gg}/4KV_g$
0.00	0.5000e+00	0.5000e+00	0.0000e+00
0.01	0.4944e+00	0.4962e+00	0.7716e-02
0.05	0.4727e+00	0.4813e+00	0.2858e-01
0.10	0.4471e+00	0.4633e+00	0.5266e-01
0.20	0.4006e+00	0.4301e+00	0.1029e+00
0.30	0.3597e+00	0.3999e+00	0.1490e+00
0.40	0.3241e+00	0.3724e+00	0.1917e+00
0.50	0.2920e+00	0.3474e+00	0.2301e+00
0.60	0.2641e+00	0.3245e+00	0.2665e+00
0.70	0.2392e+00	0.3037e+00	0.2998e+00
0.80	0.2171e+00	0.2845e+00	0.3308e+00
0.90	0.1976e+00	0.2670e+00	0.3597e+00
1.00	0.1802e+00	0.2510e+00	0.3867e+00
2.00	0.8044e-01	0.1458e+00	0.5770e+00
5.00	0.1740e-01	0.5283e-01	0.7935e+00
10.00	0.4681e-02	0.2382e-01	0.8914e+00

hemisphere A_2' as shown in Fig. A1. In terms of the angles β, θ, and ϕ, d is given by

$$d=\frac{R\cos\beta}{\cos\theta\cos\beta-\sin\beta\sin\theta\cos\phi} \tag{A7}$$

The integration over dA_2 becomes

$$\overline{ds_1 s_2}=\frac{dA_1}{\pi}F(\beta) \tag{A8}$$

with

$$F(\beta)=\int_0^{2\pi}\int_0^{\theta_1} e^{-Kd}\cos\theta\sin\theta d\theta d\phi + 2\int_{\phi_m(\beta,\theta)}^{\pi}\int_{\theta_1}^{\theta_2} e^{-Kd}\cos\theta\sin\theta d\theta d\phi \tag{A9}$$

where

$$\theta_1=\frac{1}{2}\left(\frac{\pi}{2}-\beta\right) \tag{A10a}$$

$$\theta_2=\frac{1}{2}\left(\frac{\pi}{2}+\beta\right) \tag{A10b}$$

and

$$\phi_m(\beta,\theta)=\cos^{-1}(\cos 2\theta\cot\beta) \qquad \theta\le\frac{\pi}{4} \tag{A11}$$

$$=\pi+\cos^{-1}(\cos 2\theta\cot\beta) \qquad \theta>\frac{\pi}{4}$$

Carrying out the integration over A_1, one obtains

$$\frac{\overline{s_1 s_2}}{R^2}=2\int_0^{\pi/2}F(\beta)\sin\beta d\beta \tag{A12}$$

In a similar manner, the exchange factor $\overline{s_1 s_1}$ can be expressed as

$$\frac{\overline{s_1 s_1}}{R^2}=4\int_0^{\pi/2}\sin\beta d\beta\int_{\theta_1}^{\theta_2}\phi_m(\beta,\theta)e^{-2KR\cos\theta}\cos\theta\sin\theta d\theta + \frac{\pi}{(KR)^2}\left(1-\int_0^{\pi/2}\left[2KR\left(\frac{1-\sin\beta}{2}\right)^{1/2}+1\right] e^{-2KR\left(\frac{1-\sin\beta}{2}\right)^{1/2}}\sin\beta d\beta\right) \tag{A13}$$

Based on equations (A1), (A2), (A3), and (A8) through (A13), numerical values of $gg/4KV_g$ are tabulated for various KR and presented in Table A1. These data, together with equation (11), generate the universal relation between the two mean beam lengths, L_{ab} and L_{ex}, as shown in Fig. 3.

ERRATUM

Erratum for the technical note "Prediction of Heat Transfer in Turbulent Flow Over Rough Surfaces," by R. P. Taylor, H. W. Coleman, and B. K. Hodge, JOURNAL OF HEAT TRANSFER, Vol. 111, pp. 568–572, May 1989:

The constant 1.403 in equation (15) of the referenced technical note was incorrectly published as 1.043 due to a typographical error. The correct expression is

$$\mathrm{Nu}_d = 2.475\ \mathrm{Re}_d^{0.4}\ \mathrm{Pr}^{0.36},\quad \mathrm{Re}_d < 100$$
$$\mathrm{Nu}_d = 1.403\ \mathrm{Re}_d^{0.5}\ \mathrm{Pr}^{0.37},\quad 100 < \mathrm{Re}_d < 1000 \qquad (15)$$

A Finite-Volume Method for Predicting a Radiant Heat Transfer in Enclosures With Participating Media

G. D. Raithby

E. H. Chui

Department of Mechanical Engineering,
University of Waterloo,
Waterloo, Ontario, Canada N2L 3G1

A new "finite-volume" method is proposed to predict radiant heat transfer in enclosures with participating media. The method can conceptually be applied with the same nonorthogonal computational grids used to compute fluid flow and convective heat transfer. A fairly general version of the method is derived, and details are illustrated by applying it to several simple benchmark problems. Test results indicate that good accuracy is obtained on coarse computational grids, and that solution errors diminish rapidly as the grid is refined.

Introduction

Fluid flow and convective heat transfer can now be predicted with reasonable economy and accuracy in very complex geometries. Most methods use finite difference, finite volume, or finite element methods to reduce the continuous equations of motion to a set of coupled algebraic equations that can be solved by computer. For many situations, e.g., flows with combustion, it would be desirable to add a solution for radiant exchange to the code that solves the fluid flow and internal energy equations; it would be convenient if the radiation model were based on the same philosophy and perhaps even used the same computational grid, as the fluid flow solver. Among the solution methods that are currently available, such as the many variations on the Monte Carlo, Zonal, Ray Tracing, Flux, and Discrete Ordinates methods none is fully satisfactory for this purpose except in the limit when the diffusion approximation applies (optically dense medium). Since excellent recent reviews of the state of the art are provided by Viskanta and Mengüç (1984, 1987), the competing methods for predicting radiative heat exchange will not be reviewed here.

According to the finite volume method, a solution domain is subdivided by a computational mesh that defines nodes for each variable and a control volume surrounding each node. To compute flows in complex domains, the flexibility allowed by a nonorthogonal boundary-fitted mesh is desirable. The present paper describes a new method for predicting radiative heat transfer that also uses such a grid. Besides using the same mesh as the flow solver, the method accounts for absorption, emission, and scattering in the medium, permits spectral dependence through a broad-band model (Viskanta and Mengüç, 1987), allows radiation properties to depend on other variables (like local pressure, concentration and temperature), and permits desired reflectivity properties of the wall to be incorporated. The method is also fully conservative in the sense that the global conservation balance for each discrete intensity component, as well as for the radiative flux, is exactly satisfied by the discrete equations.

The model has, until now, only been exercised for simple cases. These include heat transfer in rectangular enclosures, with diffuse gray isothermal walls, that contain gray emitting-absorbing and/or isotropically scattering media. To limit the model description to these cases would, however, make it difficult to appreciate the general applicability of the model. On the other hand, to provide the model in its full generality would result in notational complexity that would encumber the presentation. As a compromise, generality is restricted in those areas where removing the restriction is obvious and simple (e.g., gray medium and diffuse wall). The complexity of a nonisotropically scattering medium and a nonorthogonal grid is retained in the model development, even though these are not used in the test problems.

Finite Volume Approximation

The Volume-Integrated Equation for Intensity. Referring to the definition sketch (Fig. 1A) **r** denotes a location in space, $d\omega$ is a differential solid angle that is centered on the unit vector **s**, and s is distance along a particular pencil of radiation that lies in the **s** direction. Over the path length ds in the direction of the unit vector **s**, the rate of increase of total intensity $I(\mathbf{r}, \mathbf{s})$ is (Siegel, 1981)

$$\frac{dI}{ds} = -(K+\sigma^s)I + (KI_b + \sigma^s \bar{I}) \tag{1}$$

where the first term on the right-hand side is attenuation through absorption and outscattering and the second term is augmentation due to emission and inscattering. Because of the gray-medium approximation, the absorption coefficient K and the scattering coefficient σ^s are appropriate wavelength-averaged quantities. The inscattering term is given by

$$\bar{I}(\mathbf{r}, \mathbf{s}) = \frac{1}{4\pi}\int_{4\pi} I(\mathbf{r}, \mathbf{s}')\Phi(\mathbf{s}, \mathbf{s}')d\omega' \tag{2}$$

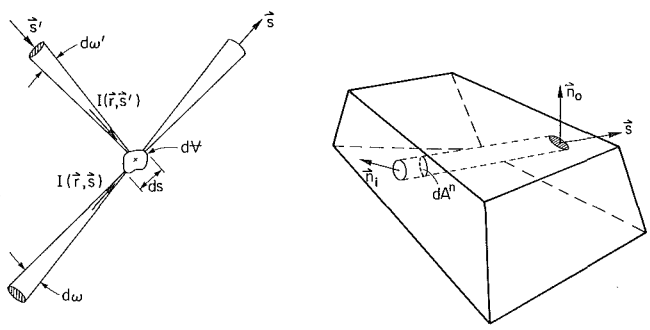

A B

Fig. 1 Part A shows notation used in the model. The control volume, for which the integral equation for intensity is derived, appears in B.

Contributed by the Heat Transfer Division and presented at the National Heat Transfer Conference, Philadelphia, August 6-9, 1989. Manuscript received by the Heat Transfer Division December 8, 1988. Keywords: Numerical Methods, Radiation, Radiation Interactions.

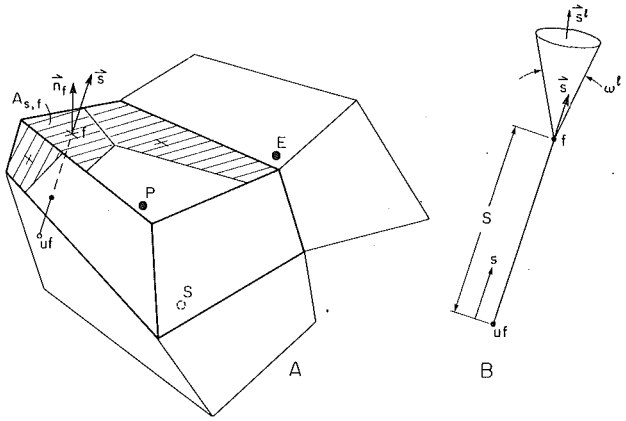

Fig. 2 Discrete surface panels on the discrete volume centered at *P*, and neighbor control volumes. The intensity I^l_f, from which the flux through $A_{s,f}$ is found, is expressed as an "upstream" value I^l_{uf} found by interpolation from nodal values, and a change between *uf* and *f*.

where $I(\mathbf{r}, \mathbf{s}')$ is the intensity at $\mathbf{r}$ within the solid angle $d\omega'$ that lies in the direction of the unit vector $\mathbf{s}'$.

Integration of equation (1) over any specified volume yields the desired integral equation. Choosing the hexahedron in Fig. 1(B) for purposes of illustration, the volume is subdivided into pencils along $\mathbf{s}$ of the cross-sectional area dA^n. Multiplication of equation (1) by the differential volume $d\mathcal{V} = dA^n ds$, carrying out the integration, and multiplying the resulting equation by $d\omega$, yields

$$\int_{A_s} I_S(\mathbf{s}\cdot\mathbf{n})dA_S d\omega = \int_{\mathcal{V}} [-(K+\sigma^s)I + KI_b + \sigma^s \bar{I}]d\mathcal{V}d\omega \qquad (3)$$

where A_s and $\mathcal{V}$ are the surface area and volume of the hexahedron, $\mathbf{n}$ is the unit surface normal, and I_s is the intensity at the surface. This equation demands that the net radiant energy within $d\omega$ that leaves through all surfaces of the volume is exactly balanced by the excess, within the volume, of inscattering and emission over outscattering and absorption.

Discrete Equation, Level 1 Approximation. According to the finite volume method, space within the interior of the domain of interest is subdivided into discrete nonoverlapping volumes, and a single "node" is located centrally within each volume. The control volume in Fig. 1(B) is redrawn in Fig. 2, showing its central node P, and nodes E and S for the neighboring control volumes to the east and south.

Since direction is also an independent variable, it is consistent with the finite volume method to subdivide direction into N^l discrete, nonoverlapping, solid angles of size ω^l, $l = 1, 2, 3, \ldots$, which sum to 4π. The number of angles and their size distribution is, like the discretization of space, at the discretion of the analyst.

The objective of the finite volume method is to find I^l_P, the intensity at each node P associated with each discrete bundle ω^l. An algebraic equation for I^l_P, is obtained by introducing approximations into equation (3).

Choosing the volume in equation (3) to be the control volume associated with node P in Fig. 2, with surface area $A_{S,P}$, and integrating the equation over the discrete solid angle ω^l, (3) becomes

$$\int_{\omega^l}\int_{A_{S,P}} I_S(\mathbf{s}\cdot\mathbf{n})dA_S d\omega =$$

$$\int_{\omega^l}\int_{\mathcal{V}_P} [-(K+\sigma^s)I + KI_b + \sigma^s \bar{I}]d\mathcal{V}d\omega \qquad (4)$$

The simplest approximation of the right-hand side of equation (4) is

$$\int_{\omega^l}\int_{\mathcal{V}_P} [-(K+\sigma^s)I + KI_b + \sigma^s \bar{I}]d\mathcal{V}d\omega$$

$$\approx [-(K_P+\sigma^s_P)I^l_P + K_P I^l_{bP} + \sigma^s_P \bar{I}^l_P]\mathcal{V}_P\omega^l \qquad (5)$$

In carrying out the volume integrations, all variables have been assumed constant over $\mathcal{V}_P$ and ω_l. A more accurate representation, involving, for example some linear distribution between nodes, is possible but is both more complex and may have serious negative computational effects (like a strong coupling between intensities in different directions that is not consistent with equation (1)).

As the first step to approximating the left-hand side of equation (4), the surface of the control volume is subdivided into N_f surface panels of area $A_{S,f}$, a few of which are shown in Fig. 2(A). Denoting the radiant transfer through panel f and within ω^l by Q^l_f, the left-hand side of equation (4) is just the

Nomenclature

A_s = surface area of control volume, m^2
$A_{s,f}$ = surface area of panel f of control volume, m^2
B_P = source term in algebraic equation, e.g., equation (24)
D = depth of one-dimensional plane layer, m
$\mathbf{e}_j$ = unit vector in the j direction
I = radiation intensity, W/m^2Sr
$\bar{I}$ = scattered intensity, W/m^2Sr, see equation (2)
I_a = average intensity, equation (13)
I_b = blackbody intensity $= \sigma T^4/\pi$
I^l_B = discrete intensity at the bottom surface within ω^l
I^l_P = discrete intensity at node P within ω^l
I_S = intensity at surface control volume
I^l_T = discrete intensity at the top surface within ω^l
K = absorption coefficient, m^{-1}
L_x, L_y = dimensions of rectangular cavity in x and y directions, m
m = index denoting the ω^l with boundaries at θ^m_+ and θ^m_- (see Fig. 3(B))
n = index denoting the ω^l with boundaries at ϕ^n_+ and ϕ^n_-
$\mathbf{n}$ = unit vector normal to a control volume surface
N^l = total number of discrete solid angles
N_x, N_y, N_z = number of control volumes in the x, y, and z directions, respectively
N^θ, N^ϕ = number of discrete angles in θ and ϕ directions
q = heat flux, W/m^2
Q = total radiant heat transfer rate, W
Q^l_f = radiant heat transfer across surface panel f
$\mathbf{r}$ = position in space
R = $(KI_b + \sigma^s\bar{I})/\kappa$, W/m^2Sr
$\tilde{R}, \tilde{R}$ = see equation (21)

sum of Q_f^l, $f=1, 2, \ldots, N_f$. The simplest approximation for Q_f^l is

$$Q_f^l = A_{S,f} \int_{\omega^l} I_f(\mathbf{s}\cdot\mathbf{n}_f)d\omega \tag{6}$$

where the intensity and unit normal to the surface have been approximated by their values at the integration point "f," located "centrally" on the panel.

The simplest Level 1 approximation of (3) is therefore

$$\sum_{f=1}^{N_f} Q_f^l = \sum_{f=1}^{N_f} A_{S,f} \int_{\omega^l} I_f(\mathbf{s}\cdot\mathbf{n}_f)d\omega$$
$$= [-(K_P+\sigma_P^s)I_P^l + K_P I_{b,P} + \sigma_P^s \bar{I}_P^l]\mathcal{V}_P\omega^l \tag{7}$$

Discrete Equation, Level 2 Approximation. To close the set of equations, relations are needed between the panel integration-point values I_f and nodal point values I_P, I_E, etc. Since several different closure relations, all starting from equation (7), are possible, these are defined as the Level 2 approximations.

In the present study, I_f was found by tracing back along the path taken by the ray in reaching f (i.e., along the -s direction) until a location was reached at which the intensity can be reasonably found by interpolation between nodes. The location of the interpolation point will be specified later when the grids are generated. For now, it is sufficient to denote its location by uf as shown in Fig. 2 and the intensity (known by the interpolation) by I_{uf}. To estimate the value of I_f from I_{uf} for the given s direction, rewrite equation (1) as

$$\frac{dI}{ds} + \kappa I = \kappa R \tag{8A}$$

where

$$\kappa = K + \sigma^s \text{ and } R = (KI_b + \sigma^s \bar{I})/\kappa \tag{8B}$$

Let R be approximated by the first two terms of a Taylor series expansion about point f, and treat κ as constant at κ_f. Carrying out the integration of equation (8A) over distance S from uf to f, shown in Fig. 2(B), the intensity in direction s at integration point f is

$$I_f = I_{uf}e^{-\kappa_f S} + R_f(1-e^{-\kappa_f S}) - \frac{(\partial R/\partial s)_f}{\kappa_f}(1-e^{-\kappa_f S}(1+\kappa_f S)) \tag{9}$$

$(\partial R/\partial s)_f$, the directional derivative in the s direction, is related to the gradient of R, ∇R, by

$$\left(\frac{\partial R}{\partial s}\right)_f = (\nabla R)_f \cdot \mathbf{s}$$

Introducing equation (9) into equation (6), and carrying out the integration over ω_l, gives the following estimate of the radiant heat transfer within ω^l that crosses surface panel f:

$$Q_f^l \approx A_{S,f} I_{uf}^l e^{-\kappa_f \bar{S}} N_f^l + A_{S,f} R_f^l (1-e^{-\kappa_f \bar{S}})N_f^l$$
$$-\frac{A_{s,f}}{\kappa_f}(1-e^{-\kappa_f \bar{S}}(1+\kappa_f \bar{S}))\sum_{j=1}^{3}\left(\frac{\partial R^l}{\partial x_j}\right)_f D_{jf}^l \tag{10}$$

where R^l is the value of R for the bundle ω^l, where the gradient of R has been arbitrarily written in Cartesian coordinates x_j, defined by the unit vectors $\mathbf{e}_j$, as

$$\nabla R^l = \sum_{j=1}^{3}\left(\frac{\partial R^l}{\partial x_j}\right)\mathbf{e}_j$$

and where N_f^l and D_{jf}^l are integrals that depend only on the panel orientation for a given ω^l

$$N_f^l = \int_{\omega^l} (\mathbf{s}\cdot\mathbf{n}_f)d\omega \qquad D_{jf}^l = \int_{\omega^l} (\mathbf{e}_j\cdot\mathbf{s})(\mathbf{s}\cdot\mathbf{n}_f)d\omega \tag{11}$$

In the integration over ω^l in equation (6) that led to equation (10), I_{uf} was treated as constant, and S was held constant at $\bar{S}$. Their values are evaluated along the ray $\mathbf{s}^l$ that lies in the center of the solid angle ω^l. To include the effect of varying S and I_{uf} over ω^l would dramatically increase complexity. Furthermore, the practice of using constant values is consistent with the other approximations embodied in the discrete equation representation of the continuous equations.

Before continuing, it is of interest to demonstrate that the approximations of the heat flux given by equation (10) is reasonable. For concreteness, consider the case where the surface panel lies in a z plane, with surface normal $\mathbf{e}_3$. For the optically thin limit ($\kappa_f \to 0$), the radiant flux becomes

$$Q_f^l \to A_{S,f} I_{uf}^l \int_{\omega^l} (\mathbf{s}\cdot\mathbf{e}_3)d\omega$$

The intensity in this limit is propagated correctly (i.e., without

Nomenclature (cont.)

s = distance along a beam in the s direction, m
$\mathbf{s}$ = unit vector in the direction for which I is to be calculated
$\mathbf{s}^l$ = unit vector in the center of discrete solid angle ω^l
S = distance from the interpolation point to the integration point (see Fig. 2(B))
$\mathbf{S}$ = average value of S over the solid angle ω^l
T = temperature, K
$\mathcal{V}$ = volume, m^3
x, y, z = Cartesian coordinates, m
x_1, x_2, x_3 = Cartesian coordinates; $x_1 = x$, $x_2 = y$, $x_3 = z$, m
x^* = $(\kappa + K)D$, used for one-dimensional problem
ϵ = surface emissivity
θ = polar angle, measured from the z axis
κ = extinction coefficient $= K + \sigma^s$, m^{-1}
ρ = surface reflectivity
σ = Stefan–Boltzmann constant = 5.729×10^{-8} W/m^{2}K^4
σ^s = scattering coefficient, m^{-1}
ϕ = azimuthal angle in the x–y plane, measured from x axis (Fig. 6)
Φ = phase function for scattering from direction $\mathbf{s}'$ to direction $\mathbf{s}$
ω = solid angle
ω^l = solid angle of the discrete bundle centered at $\mathbf{s}^l$

Subscripts

B = bottom surface
P, N, E, S, W = labels for nodes within control volumes
f = at the integration point f
uf = at the interpolation point (Fig. 2(A))
T = top surface
j = coordinate index = 1, 2, 3

Superscripts

l = in the solid angle ω^l
$*$ = nondimensional

attenuation) from the interpolation point *uf* to the integration point on the panel.

In the optically thick limit ($\kappa_f \to \infty$)

$$Q_f^l \to A_{S,f} R_f^l \int_{\omega^l} (\mathbf{s}\cdot\mathbf{e}_3)d\omega - \frac{A_{S,f}}{\kappa_f} \sum_{j=1}^{3} \left(\frac{\partial R^l}{\partial x_j}\right)_f \int_{\omega^l} (\mathbf{e}_j\cdot\mathbf{s})(\mathbf{s}\cdot\mathbf{e}_3)d\omega$$

Summing over l to obtain the net radiant heat transfer crossing the panel, and for isotropic scattering (so that R becomes independent of angle l)

$$Q_f = \sum_l Q_f^l = A_{S,f}\left(-\frac{4\pi}{3\kappa_f}\right)\left(\frac{\partial R}{\partial x_3}\right)_f$$

This is the correct diffusion approximation for the optically thick limit (Siegel, 1981). Thus the expression for Q_f^l given by equation (10) has retained sufficient generality to capture both the optically thin and thick limits. Note that, had the third term in equation (9) been omitted (which is the usual solution (Siegel, 1981) to (8*A*) for constant κ and R), the radiation heat transfer across the panel would not have recovered the diffusion approximation.

Returning to the development of the discrete equation for I_P^l, equation (10) is substituted into equation (7). The only remaining issues are how to interpolate I_{uf}^l from nodal-point values like I_P^l, and how to find R_f^l. As already mentioned, the interpolation will be illustrated when the method is implemented on a specific mesh. The value of R_f^l is obtained by a straightforward linear interpolation using values of R^l, such as R_P^l, that are calculated and stored at the nodes.

To find R_P^l at the nodes requires an evaluation of both its components (see equation (8*B*)) $\bar{I}_P^l$ and $I_{b,P}$. $\bar{I}_P^l$ is obtained from the following discrete approximations to equation (2):

$$\bar{I}_P^l = \frac{1}{4\pi} \sum_{l'} I_P^{l'} \Phi(l', l)\omega^{l'} \tag{12}$$

where $\Phi(l', l)$ is the phase function for scattering from the solid angle $\omega^{l'}$ to the solid angle ω^l. For isotropic scattering, $\Phi = 1$ and equation (12) becomes

$$\bar{I}_P^l = \frac{1}{4\pi} \sum_{l'} I_P^{l'}\omega^{l'} = I_{aP} \tag{13A}$$

where I_{aP} is the discrete approximation at node P of the average intensity I_a:

$$I_a(\mathbf{r}) = \frac{1}{4\pi}\int_{4\pi} I(\mathbf{r}, \mathbf{s}')d\omega' \tag{13B}$$

The value of the second component of R_p, i.e., $I_{bP} = \sigma T_P^4/\pi$, is found from the thermal energy balance for the P control volume. The increase in internal energy due to radiation crossing the boundaries of the control volume in Fig. 2(*A*) is obtained by replacing the integration limit ω^l in equation (4) by 4π.

$$-\int_{A_{S,P}}\int_{4\pi} I(\mathbf{s}\cdot\mathbf{n})d\omega dA_S = 4\pi\int_{\mathcal{V}_P} K(I_a - I_b)d\mathcal{V} \tag{14A}$$

$$\approx 4\pi K_P(I_{a,P} - I_{b,P})\mathcal{V}_P \tag{14B}$$

The scattering contribution drops out of this energy balance for both isotropic and nonisotropic scattering. The temperature is established, in general, by a complex interaction (Siegel, 1981) of this term with advection and diffusion of energy, and with work done by the pressure and other stresses. For the simplest case of radiative equilibrium, the fluid temperatures adjusts to make the net surface heat transfer in equation (14*A*) zero, so that

$$I_{b,P} = I_{a,P} \tag{15}$$

For the special case of isotropic scattering and radiative equilibrium, combining equations (8*B*), (13), and (15) results in

$$R_P^l = R_P = I_{a,P} = I_{b,P} \tag{16}$$

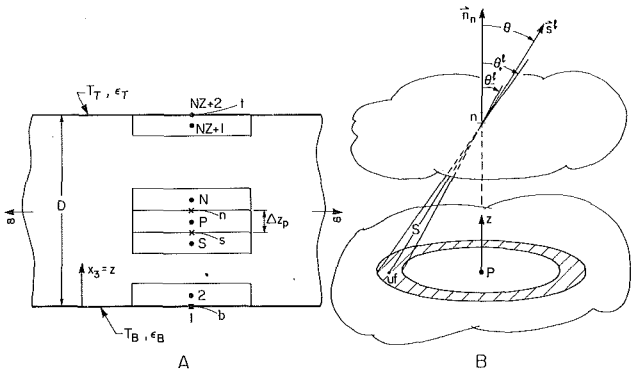

Fig. 3 Geometry and control volumes for radiation in a plane participating medium contained between isothermal gray walls

Summary and Discussion. This section has provided the details of a general finite volume method, except for the interpolation to obtain I_{uf}^l and the application of boundary conditions. These details, and the performance of the method, are illustrated in the following sections by application to some simple problems for which benchmark solutions are available.

One-Dimensional Radiant Heat Transfer in a Plane Medium

Problem Description. Very precise solutions (Heaslet, 1965) (see Viskanta and Mengüç 1987 for other references) have been obtained for radiant heat transfer between two isothermal, diffuse, flat plates, at temperatures T_B and T_T and emissivities ϵ_B and ϵ_T (see Fig. 3), that enclose a gray isotropically scattering or absorbing-emitting medium with constant scattering and absorption coefficients, and that is in radiative equilibrium. The finite volume method is first applied to this problem.

Discrete Equations. The natural control volumes for this problem are shown in Fig. 3(*A*). The depth Δz of each control volume is arbitrary and nodes are located midway between the control volume faces, except for the first and last nodes, which are located on the plates. Integration points, like n and s, which are denoted by $\times$, lie on the volume faces. On the walls, the integration points b and t lie in the medium distance δ from the walls, where $\delta \to 0$.

For this problem, the radiation intensity depends on z and θ (Fig. 3(B)). The discrete solid angle ω^l is defined as the annular cone between θ_-^l and θ_+^l. The interpolation point *uf* that is upstream of the integration point n is taken to lie on the plane of node P, as shown in the figure. From the assumption that the intensity varies spatially only with z, I_{uf}^l in equation (10) can be replaced by I_P^l for $\mathbf{s}\cdot\mathbf{e}_3 > 0$ and by I_N^l for $\mathbf{s}\cdot\mathbf{e}_3 < 0$. For $\mathbf{s}\cdot\mathbf{e}_3 > 0$, the radiant heat transfer within ω^l that travels through the control volume surface n that lies north of node P is, according to equation (10) and Fig. 3(*B*)

$$Q_n^l = F_n^l I_P^l + G_n^l R_n - H_n^l\left(\frac{\partial R}{\partial z}\right)_n \tag{17}$$

where the angular dependence of R has been dropped due to the isotropic scattering approximation. In this equation

$$F_n^l = A_S e^{-\kappa S^l} N^l \qquad G_n^l = A_S(1 - e^{-\kappa S^l})N^l \tag{18A}$$

$$H_n^l = \frac{A_S}{\kappa}(1 - e^{-\kappa S^l}(1 + \kappa S^l))D_3^l \tag{18B}$$

$S^l = (z_n - z_P)/\cos\theta^l$ is defined here as the distance S in Fig.

3(*B*) for the angle $\theta = \theta^l = (\theta^l_- + \theta^l_+)/2$. From equation (11) for this geometry

$$N^l = \int_{\omega^l} (\mathbf{s}\cdot\mathbf{e}_3)d\omega = -\pi[\cos^2\theta^l_+ - \cos^2\theta^l_-] \qquad (18C)$$

$$D^l_3 = \int_{\omega^l} (\mathbf{s}\cdot\mathbf{e}_3)^2 d\omega = -\frac{2\pi}{3}[\cos^3\theta^l_+ - \cos^3\theta^l_-] \qquad (18D)$$

and the solid angle is

$$\omega^l = \int_{\theta^l_-}^{\theta^l_+} 2\pi \sin\theta d\theta = -2\pi[\cos\theta^l_+ - \cos\theta^l_-] \qquad (18E)$$

Substitution of equation (17) for Q^l_n, and a similar equation for the heat transfer through the south face Q^l_s, into equation (7), and collection of all terms involving R into a "source term," b^l_P, results in the following equation for I^l_P (for $\mathbf{s}\cdot\mathbf{e}_3 > 0$):

$$a^l_P I^l_P = a^l_S I^l_S + a^l_N I^l_N + b^l_P \qquad (19A)$$

where

$$a^l_P = F^l_n + \kappa \forall_P \omega^l \qquad a^l_S = F^l_s \qquad a^l_N = 0 \qquad (19B)$$

$$b^l_P = \left[G^l_s R_s - H^l_s\left(\frac{\partial R}{\partial z}\right)_s\right] - \left[G^l_n R_n - H^l_n\left(\frac{\partial R}{\partial z}\right)_n\right] + \kappa R_P \forall_P \omega^l \qquad (19C)$$

The values of R and $(\partial R/\partial z)$ at an integration point (i.e., at a face) are found by linear interpolation of the nodal point values or, at the top and bottom plates, by linear extrapolation from interior nodal values.

For a diffuse top surface, at temperature T_T, the boundary condition for the surface intensity I^l_T for radiation into the medium, $\mathbf{s}^l\cdot\mathbf{e}_3 < 0$, is

$$(1-\epsilon_T)\sum_{\mathbf{s}^{l'}\cdot\mathbf{e}_3>0} Q^{l'}_t + \epsilon_T A_S \sigma T^4_T = \sum_{\mathbf{s}^l\cdot\mathbf{e}_3<0} Q^l_T = A_S \pi I^l_T \qquad (20)$$

The terms on the left-hand side of equation (20) represent reflected and emitted radiation from the T surface, which constitute the total radiation into the medium. The last equality defines the intensity through the gray-surface approximation. A similar equation at the bottom surface relates the intensities into the medium ($\mathbf{s}^l\cdot\mathbf{e}_3 > 0$) to the bottom surface temperature and to intensities incident on the bottom.

Solution Method. For fixed nodal values of R and upward intensities at the bottom surface, I^l_P values are found for a given l by application of equation (19*A*) to each interior node, starting at the bottom and sweeping upward. This is repeated for each l for which $\mathbf{s}^l\cdot\mathbf{e}_3 > 0$. Equation (17) provides the incident fluxes onto the top surface, from which equation (20) gives the downward intensities. Equations similar to equation (19*A*), but with a^l_S rather than a^l_N equal to zero, are then solved for the downward intensities and incident fluxes on the lower surface. The lower surface boundary condition yields the upward boundary intensities to complete one cycle.

If the nodal values of R are fixed, one cycle yields the desired result if $\epsilon_B = \epsilon_T = 1.0$. Several cycles will be required for reflective boundaries.

The determination of R is, of course, part of the solution procedure. The simplest "explicit" method is to obtain the intensities for an assumed R in the manner just described, to substitute these into equation (13*A*) and thus obtain new R values from equation (16). This cycle is repeated until convergence is achieved. Convergence was deemed satisfactory when the change, between successive updates of R, in net heat flux at both surfaces was less than 0.001 percent.

Results. When a fine grid (see below) was used, the non-dimensional heat transfer, $q^* = q/\sigma(T^4_B - T^4_T)$, obtained using the finite volume method agreed to within 1 in the fourth significant figure with the predictions reported by Heaslet and Warming (1965). The gas temperature, and temperature jump at the boundary, were also predicted correctly.

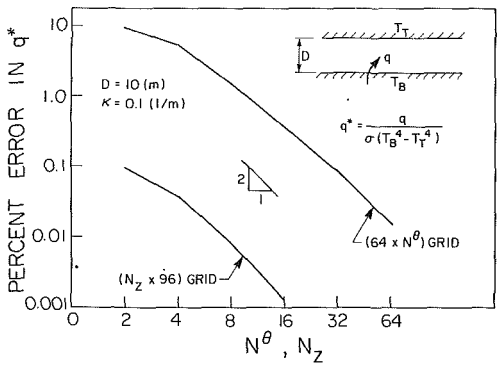

Fig. 4 Results of computational experiments to determine the rate at which the error in heat transfer from the surface decreases with grid refinement. The slope of 2:1 on the figure denotes quadratic convergence.

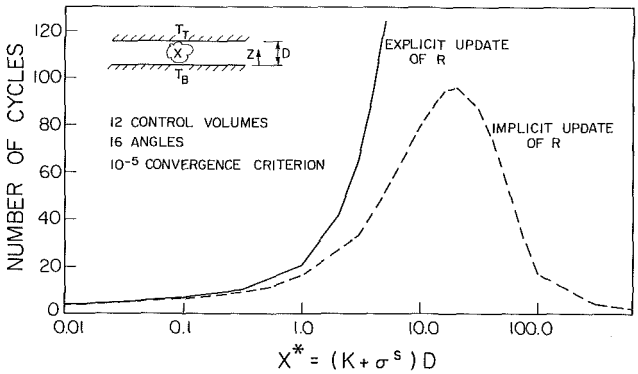

Fig. 5 The number of *R*-update cycles required to obtain a wall heat transfer that changed less than 0.001 percent between cycles

Table 1 Comparison of finite volume results for uniform grid of four control volumes and eight angles with "exact" results (Heaslet and Warming, 1965); $\kappa^* = \kappa D$

	$q^* = q/\sigma(T^4_B - T^4_T)$			
κ^*	Coarse grid finite volume results	Exact results	Percent error	CPU, s
0.0	1.0000	1.0000	0.0	0.1
0.1	0.9125	0.9157	0.3	0.2
0.5	0.6964	0.7040	1.1	0.3
1.0	0.5469	0.5532	1.1	0.4
2.0	0.3865	0.3900	0.9	0.4

Even for a coarse grid (see Fig. 3) of four uniform control volumes in the z direction and with polar angle θ divided into eight equal intervals, the finite volume method predicts the correct heat transfer to within about 1 percent, for a wide range of optical depths, as shown in Table 1. The CPU time required was less than 0.5 s on a MicroVax II computer.

Having established that the finite volume method does yield the correct results as the grid is refined, it is of major interest to establish how quickly the accuracy improves with grid refinement. For $\kappa^* = \kappa D$ of 1.0, the heat transfer was obtained using $N_z = 64$ uniform control volumes and $N^l = N^\theta = 96$ equal angle intervals. To study error reduction with N_z, q^* was recalculated on a sequence of grids of size $(N_z \times 96)$, $N_z = 2$, 4, . . . , 64. The results in Fig. 4 indicate the q^* is obtained to within 0.1 percent with $N_z = 2$, and for $N_z \geq 4$ the error becomes proportional to $(N_z)^{-2}$ (i.e., quadratic convergence).

To study error reduction with angular refinement, q^* was calculated for grids of $(64\times N^\theta)$, $N^\theta = 2, 4, 6, \ldots, 96$. The error decreases from about 10 percent for $N^\theta = 2$, and for $N^\theta \geq 4$, and decreases roughly as $(N^\theta)^{-2}$.

Another issue of major interest is the number of updates of R required to obtain convergence. For black surfaces, and for a change of q^* at the surfaces of less than 0.001 percent between R updates, the number of iterations required by the explicit method is plotted against $\kappa^* = \kappa D$ in Fig. 5. As $\kappa^* \to 0$, the correct solution is obtained without iteration because the intensities become independent of R. The number rises sharply with κ^* but convergence is satisfactory for $\kappa^* < 4.0$, which includes the range of interest for many practical applications. The number of iterations increases sharply with κ^* for $\kappa^* \lesssim 4.0$. A similar behavior, of increasingly difficult convergence with increasing κ^*, has been encountered in the use of the discrete ordinates method (Viskanta and Mengüç, 1987). The next section addresses this issue.

Implicit Solution for Strongly Participating Medium. For applications that involve strongly participating media ($\kappa^* \geq 4$ for a plane layer), the explicit update of R becomes unsatisfactory. This section describes a method that enhances convergence for large κ^*. The method is, for simplicity, presented in the context of the present one-dimensional problem, but the derivation is kept sufficiently general to include nonisotropic scattering.

To re-introduce nonisotropic scattering, R in equation (19C) is replaced by R^l, and the nodal values of R are split as follows:

$$R_P^l = \frac{K_P I_{b,P} + \sigma_P^s I_{a,P}}{\kappa_P} + \frac{\sigma_P^s}{\kappa_P}(\bar{I}_P - I_{a,P}) = \bar{R}_P + \tilde{R}_P^l \qquad (21)$$

For isotropic scattering, $\tilde{R} = 0$. Expressing the integration point values of R_f^l and $(\partial R^l/\partial z)_f$, $f = s$ and n, in equation (19C) in terms of nodal point values using linear interpolation, substituting the resultant b_P^l expression into equation (19A), and dividing by a_P^l, yields an equation for I_P^l of the form

$$I_P^l = \frac{a_S^l}{a_P^l} I_S^l + \frac{a_N^l}{a_P^l} I_N^l - A_P^l \bar{R}_P + A_S^l \bar{R}_S + A_N^l \bar{R}_N + B_P^l \qquad (22)$$

where terms involving $\tilde{R}^l$ have been grouped into B_P^l. Multiplication of equation (22) by ω^l, summation over all ω^l, and division of the resulting equation by 4π yields an equation of the form

$$I_{a,P} = -\hat{A}_P \bar{R}_P + A_S \bar{R}_S + A_N \bar{R}_N + B_P \qquad (23)$$

For the special case of isotropic scattering and radiative equilibrium, $\bar{R}_P = I_{a,P}$ (from equation (16)) so that equation (23) becomes

$$A_P I_{a,P} = A_S I_{a,S} + A_N I_{a,N} + B_P \qquad (24)$$

which is an implicit equation for $I_{a,P} = I_{b,P}$ that is simply solved by application of the Thomas (or tridiagonal) algorithm. This replaces the "explicit" update of R described in the previous section. It is also easily shown that, as $\kappa^* \to \infty$, equation (24) becomes the discrete representation of the diffusion approximation of radiation heat transfer. For large κ^*, therefore, the first solution for $I_{a,P}$ will yield nearly the correct $I_{a,P} = R_P$ values, which, used in the b_P^l term in equation (19A), will yield nearly converged values of I_P^l, so that very few cycles will lead to the converged result.

Figure 5 shows the number of cycles required by this implicit method to obtain surface heat transfers that changed less than 0.001 percent between R-update cycles. The maximum number of cycles is required for $\kappa^* \approx 20$. For $\kappa^* \to 0$ and $\kappa^* \to \infty$, the converged results are obtained in one solution cycle.

Although the method has not yet been applied to problems involving nonisotropic scattering and radiative nonequilibrium, it is interesting to speculate how the implicit method could be used to accelerate convergence. Splitting $\bar{R}$ in equation (23) into its I_a and I_b components results in an equation of the form

$$A_P^{aa} I_{a,P} = A_S^{aa} I_{a,S} + A_N^{aa} I_{a,N} - A_P^{ab} I_{b,P} + A_N^{ab} I_{b,N} + A_S^{ab} I_{b,S} + B_P^a \qquad (25)$$

where the first superscript on the coefficients refers to the equation and the second to the variable it multiplies (either a for the variable I_a or b for the variable I_b).

The thermal energy equation has diffusion and convection terms that are linear in T, and a source term given by equation (14B) that contains I_a and $I_b = \sigma T^4/\pi$. If radiation dominates the internal energy balance, it is appropriate to linearize the discrete energy equation in the form

$$A_P^{bb} I_{b,P} = A_S^{bb} I_{b,S} + A_N^{bb} I_{b,N} + A_P^{ba} I_{a,P} + B_P^b \qquad (26)$$

Equation (25) and (26) can be efficiently solved for $I_{a,P}$ and $I_{b,P}$ (e.g., use a (2×2) block tridiagonal solver). If radiation only weakly affects the medium temperature, it would be more appropriate to linearize the equations such that T instead of I_b appears as the dependent variable in equations (25) and (26). In either case, iteration is required to converge to the solution of the equations in which some terms involve T and others T^4.

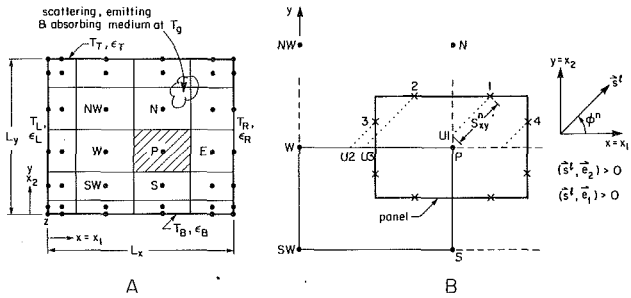

Fig. 6 Schematic of a rectangular cavity with isothermal walls with a Cartesian computational grid. Part B shows details related to determination of the integration point intensities for those intensities that are directed upward and to the right.

Two-Dimensional Exchange in Rectangular Enclosures

Problem Description. The finite volume method will now be applied to a more complex class of problems that involve two-dimensional (2D) radiative heat transfer in rectangular enclosures with isothermal, diffusely reflecting, gray walls. The enclosed medium is also assumed to be gray, and to scatter isotropically. Figure 6(A) shows a typical enclosure. The objective is to predict radiative heat transfer at the boundaries, and the medium temperature under the assumption of radiative equilibrium. To test the finite volume method, several benchmark problems will be solved. To simplify notation in the development that follows, the (x_1, x_2, x_3) coordinates will be used interchangeably with (x, y, z).

Discretization. Space is divided into control volumes of unit depth in the z direction and with boundaries defined by the solid lines in Fig. 6(A). Nodes, also called grid points, are located centrally in each interior volume as well as on the boundary. Each control volume face is divided into two panels with an integration point, such as 1, 2, 3, in Fig. 6(B), located at the center of each panel.

The angular orientation of intensity is defined by a polar angle θ, measured from the $x_3 = z$ axis, and the azimuthal angle ϕ, that lies in the (x, y) plane measured from the x axis. The solid angle ω^l is defined by the range $\theta_-^m \leq \theta \leq \theta_+^m$, $\phi_-^n \leq \phi \leq \phi_+^n$. All results shown are for N^θ equal increments of θ in the range $0 \leq \theta \leq \pi/2$ and for N^ϕ equal increments in ϕ in the range $0 \leq \phi \leq 2\pi$, where, for simplicity, N^ϕ was always chosen to be a multiple of 4.

To apply the general equations of section 2 to the grid system just described, some details must be decided. The central ray within ω^l, i.e., the one along s^l, is defined by (θ^m, ϕ^n), where each angle lies in the middle of its range (e.g., $\phi^n = (\phi^n_+ + \phi^n_-)/2$). The path length $\bar{S}^l$ is taken as the distance from the integration point to the point where the $-s_l$ that passes through the integration point intersects the closest member of the set of surface that join the grid points. For example, in Fig. 6(B), for integration point $f = 1$

$$\bar{S}^l = S^n_{xy}/\sin\theta^m$$

where S^n_{xy} is the projection of $\bar{S}^l$ onto the x–y plane.

Intensities at u_1, u_2, etc. in Fig. 6(B) must be related to the nodal intensities by interpolation functions. This step requires great care. I^l_{u1} could, for example, be found by linear interpolation between I^l_N and I^l_P, but this would cause I^l_N to appear in the I^l_P equation. This is undesirable because the equation for I^l_P can no longer be solved by marching, and because such dependence of "downstream" intensities is inconsistent with the transportive properties of the differential equation for intensity. A better alternative is to find I_{u1} by extrapolation using I^l_P and I^l_S, but applying this practice at each integration point results in a computational molecule that connects I^l_P with as many as six upstream nodal intensities. While this is fairly easily accommodated, a simpler approach was used for the present application. When (for s^l upward and to the right) an interpolation point lies on a solid line in Fig. 6(B), linear interpolation between nodes was used. When it lies on a broken line, the interpolation value was taken as the value at the nearest "upstream" node on the line. According to this scheme I^l_{u1} and I^l_{u4} would be both approximated by I^l_P for $(\mathbf{s}^l \cdot \mathbf{e}_j) \geq 0, j = 1, 2$. I^l_{u2} and I^k_{u3} would both be found by a linear interpolation involving I^l_P and I^l_W.

If linear interpolation or extrapolation were used to find all interpolation-point values, the solution error should decrease quadratically with mesh refinement, as for the one-dimensional problem, but it is well known (from experience in approximating fluid advection) that "wiggles" in the solution can occur. The interpolation practice adopted here is less likely to admit wiggles, but it is expected that errors due to spatial discretization will decrease with grid refinement at a rate that is between a linear and quadratic. These are features that will be examined when the benchmark problems are solved.

Solution Procedure. For intensities in those $\mathbf{s}^l$ directions that are upward to the right, the discrete equation for I^l_P has the form

$$a^l_P I^l_P = a^l_W I^l_W + a^l_S I^l_S + a^l_{SW} I^l_{SW} + b^l_P \qquad (27)$$

Given the boundary values of I^l along the left and bottom surfaces in Fig. 6(A), nodal values of I^l_P are found by direct substitution into equation (27), sweeping the domain in the positive x and y directions. With new incident intensities on the right boundary known, boundary conditions are applied to update the intensities leaving this surface, and an equation similar to equation (27) establishes nodal values for $\mathbf{s}^l$ in the range $(\mathbf{s}\cdot\mathbf{e}_1) < 0$ and $(\mathbf{s}\cdot\mathbf{e}_2) > 0$. Repeating this for all four sectors leads to a new I^l_P solution, for a given R_P distribution. R_P is then explicitly updated by calculating $I_{aP} = R_P$ from equation (13A).

For simplicity, the coefficients of equation (27) were recalculated each time the set of intensities associated with a particular ω^l was updated. The run times for the problems solved could be dramatically reducted by storing coefficients or even by using simple, computationally inexpensive approximations to the exponential terms. The intensities were stored in a four dimensional matrix, also for simplicity. For isotropic scattering, it is only necessary to store the complete I^l_P values at boundary nodes so that four-dimensional storage is not required.

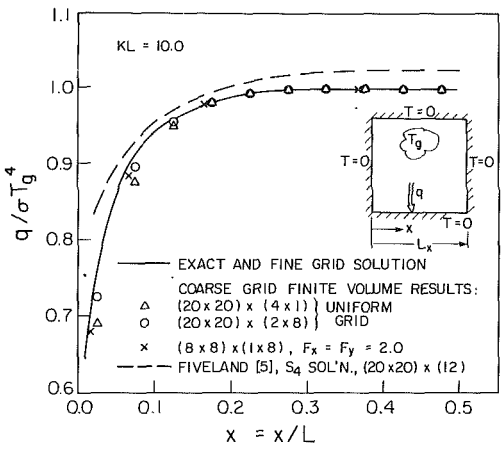

Fig. 7 Nondimensional heat transfer on the wall of a square cavity containing an emitting gas at uniform temperature T_g and with zero wall temperature for an optically thick case ($KL = 10.0$)

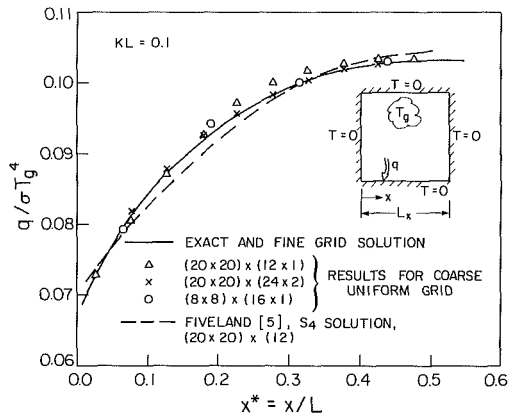

Fig. 8 Nondimensional heat transfer on the wall of a square cavity containing an emitting gas at uniform temperature T_g and with zero wall temperature for an optically thin case ($KL = 0.1$)

Comparison With One-Dimensional Solutions. The two-dimensional solution was applied first to the one-dimensional problem described in the last section, for a range of surface emissivities. As the grid was refined, the two-dimensional model converged to the same result as the one-dimensional model.

Problem 1: Black Enclosure With Emitting Medium. The first benchmark problem is the prediction of surface heat transfer in a square enclosure ($L_x = L_y = L$) with cold walls (at 0 K), which contains a gas at uniform temperature, T_g. The gas does not scatter ($\sigma^s = 0$) but does emit and absorb ($K \neq 0$). With the gas temperature known, the value of R in equation (10) is prescribed.

The local heat flux calculated to fall on the lower wall is plotted in Figs. 7 and 8 for the cases of strongly emitting medium ($KL = 10$) and weakly emitting medium ($KL = 0.1$), respectively. The "exact" solution was obtained by analytically integrating the radiation transfer equation for a given angle to the point of interest on the wall from the "upstream" wall, and then numerically integrating over all angles to find the local heat transfer. The present finite volume model could be made to agree with these exact results to any desired tolerance by refining the spatial and angular grids.

The S_4 discrete ordinates solution by Fiveland (1984) to this problem, using a (20×20) uniform spatial grid and with twelve quadrature points for the angular integrations are shown on Fig. 7 for $KL = 10$. Truelove (1987) was able to improve Fiveland's discrete ordinates solution by changing the

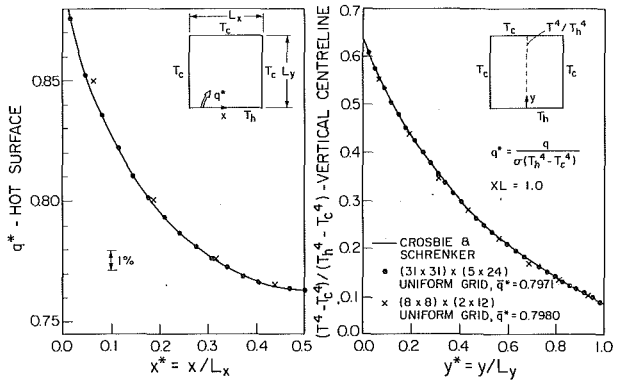

Fig. 9 Nondimensional heat transfer on the bottom, and centerline temperature distribution, in a square cavity with one heated wall enclosing a scattering gas with $\sigma^s L = 1.0$

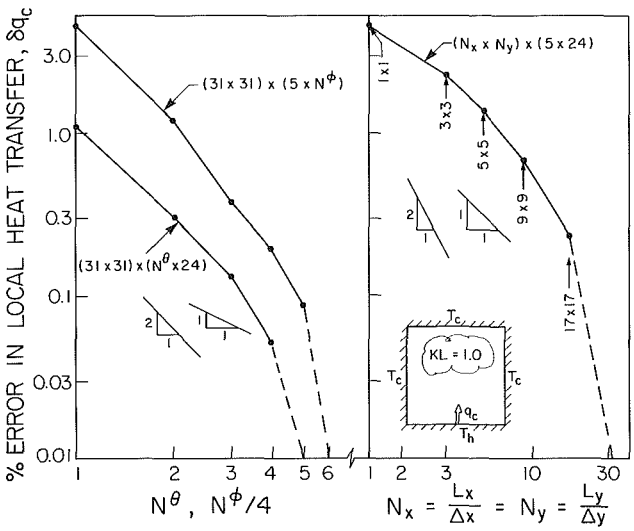

Fig. 10 Reduction in the error in local heat transfer at the center of the heated cavity wall with angle refinement (left side) and spatial refinement (right side)

quadrature points. Comparisons are made here with Fivelands solution, because the quadrature he used was not tuned to this particular class of problem. The present finite volume solutions for 20 uniform control volumes in each direction, $(N_x \times N_y) = (20 \times 20)$, and with a uniform angular discretization of $(N^\theta \times N^\phi) = (1 \times 4)$ and (2×8) are also shown in Fig. 7, and they give reasonable agreement with the exact solution. Reducing the spatial grid to (8×8) but using an expanding mesh that doubles the size of each successive control volume moving from the corners to the centerlines ($F_x = F_y = 2.0$ in Fig. 7), and using a uniform (1×8) angular discretization, results in excellent agreement with the exact solution. The solution time for $(20 \times 20) \times (2 \times 8)$ problem was 15 s on a MicroVax II computer.

Similar results appear in Fig. 8 for the $KL = 0.1$ case. The finite volume results obtained using all the coarse grids shown in Figs. 7 and 8 predict a total heat transfer on the bottom, which agrees with the exact values to within 0.8 percent.

The results for this sample problem illustrate that the finite volume method converges to the exact solution as the angular and spatial grids are refined, and that predictions of good accuracy can be obtained on quite coarse grids.

Problem 2: Two-Dimensional Heat Transfer in an Enclosure With One Hot Wall. The second two-dimensional problem involves radiative exchange in rectangular enclosures with the left, top, and right wall temperatures set to T_c and the bottom wall set a higher temperature T_h. The medium scatters

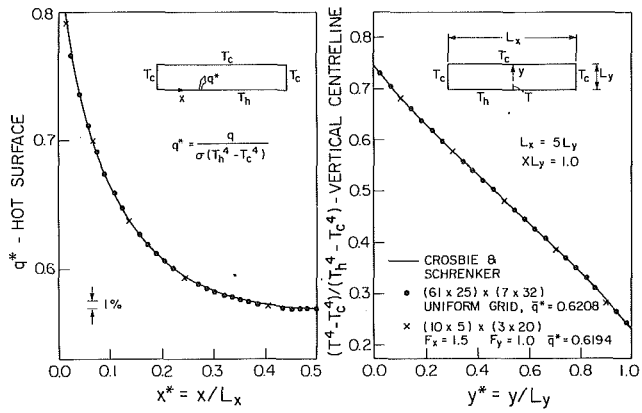

Fig. 11 Nondimensional heat transfer on the bottom, and centerline temperature distribution, in a 5:1 aspect ratio cavity enclosing a scattering gas with $\sigma^s L_y = 1.0$

isotropically and is assumed to be in radiative equilibrium. The objective is to predict the heat transfer that leaves the bottom surface as well as the temperature of the medium. Careful solutions to this problem have been reported by Crosbie and Schrenker (1984) for a range of cavity aspect ratios and scattering coefficients. Comparisons with finite volume predictions are presented here for three cases.

The "exact" (Crosbie and Schrenker, 1984) dimensionless local heat transfer q^* leaving the hot wall and temperature distribution along a vertical line in the center of a square enclosure are plotted as solid lines in Fig. 9 for a medium with $\sigma^s L = 1.0$. Application of the finite volume method with a very fine mesh $(N_x \times N_y) \times (N^\theta \times N^\phi) = (31 \times 31) \times (5 \times 24)$ is shown to give almost exact agreement (local heat fluxes agree to well within 0.1 percent). Use of a coarse $(8 \times 8) \times (2 \times 12)$ grid, such as would be of more practical interest, also yields excellent accuracy, with an average heat transfer $\bar{q}^*$ that is only 0.1 percent too high. To obtain a solution on this grid, in which the absolute value of the heat transfer on all walls changed by less than 0.05 percent between R-updated cycles, required eight cycles and 32 s on a MicroVax II computer.

As previously discussed, it is important to know how quickly the solution error decreases with grid refinement. To perform this evaluation, the error in the local heat transfer at the center of the hot wall ($x/L = 0.5$) was examined. Retaining (32×32) uniform control volumes, fixing N^ϕ at 24, and varying N^θ, Fig. 10 shows that the error diminishes quadratically with N^θ. Similarly, for N^θ fixed at 5, increasing N^ϕ results in a quadratic decrease in error. For a fine angular grid (5×24) and with refinement of a uniform spatial grid, the error is seen in Fig. 10 to decrease somewhere between linear and quadratic with increasing $N_x = N_y$. These results are in agreement with the expectations that were previously discussed.

For an enclosure with an aspect ratio of $L_x/L_y = 5$, the "exact solution" of Crosbie and Schrenker (1984) and a fine-grid $(61 \times 25) \times (7 \times 32)$ finite volume solution are plotted in Fig. 11 for $\sigma^s L_y = 1.0$. The finite volume predictions of heat flux agree with the exact values to within 0.2 percent, and the temperature is also closely predicted. Figure 11 also shows that a much coarser grid $(10 \times 5) \times (3 \times 20)$, where the control volumes widths in the x direction expand by a factor of 1.5 moving from the outer walls toward the center ($F_x = 1.5$), yields virtually identical results, with an average heat transfer ($\bar{q}^*$) just 0.2 percent below the fine grid prediction. The prediction on the $(10 \times 5) \times (3 \times 20)$ grid required five R-update cycles and 17.6 s to achieve a total absolute value of heat transfer on the boundaries that changed less than 0.05 percent between cycles.

The last test problem described in this paper has been specifically chosen to demonstrate that, as mentioned earlier,

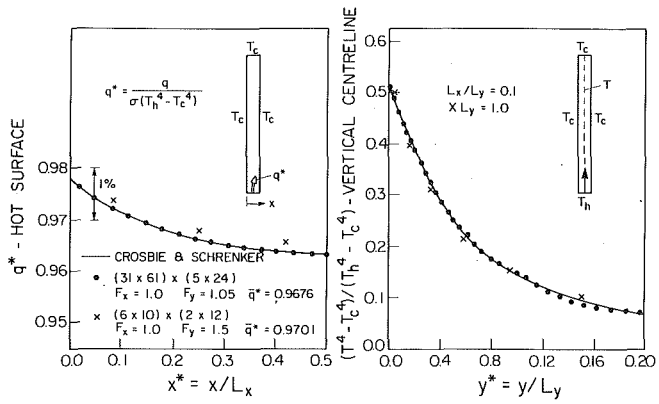

Fig. 12 Nondimensional heat transfer on the bottom, and centerline temperature distribution, in a 1:10 aspect ratio cavity enclosing a scattering gas with $\sigma^S L_y = 1.0$

profile wiggles can occur under adverse conditions. Results for a cavity with $\sigma^s L_y = 1.0$ and $L_y/L_x = 10$ are compared to the predictions of Crosbie and Schrenker in Fig. 12. Calculations on a fine $(31 \times 61) \times (5 \times 24)$ grid, with uniform control volumes in the x direction and with volumes in the y direction that increase by expansion factor of $F_y = 1.05$, yielded local heat transfer predictions that are in excellent agreement with Crosbie and Schrenker (Fig. 12). The predicted centerline temperature near the bottom wall (right side of Fig. 12) is also very accurate but, when the aspect ratio of the control volumes become large in the center to top of the cavity, the predicted temperatures oscillate (or wiggle) slightly about the profile of Crosbie and Schrenker. This "wiggle" is a consequence of the assumed linear profile of I^l between nodes in Fig. 6(B), and is analogous to the wiggles that are often tolerated when a linear profile between nodes is used in the approximation of the advective transport terms in fluid flows. Such wiggles can be overcome (Roache, 1972) at the expense of accuracy by adopting a simple "upwind" approximation, or by using a more elaborate discretization.

Figure 12 also shows predictions using a coarse $(6 \times 10) \times (2 \times 12)$ mesh that has uniform spacing in the x direction and expands rapidly ($F_y = 1.5$) in the y direction away from the heated wall. This grid yields good temperature predictions, and heat transfer rates that are within 0.3 percent of exact values.

Summary and Discussion

A new finite volume method has been proposed for the prediction of radiative heat transfer that can be implemented on nonorthogonal grids of the type employed to predict complex fluid flows. The theory is advanced for an absorbing-emitting and scattering gray medium in an enclosure with gray diffuse walls, but extensions to a broad bandwidth model and to include walls with other reflective properties are straightforward. For strongly participating media, the method captures the diffusion approximation to the radiant heat transfer equations. The method ensures that the intensity in a given direction, as well as the net radiative heat transfer, satisfy the global conservation constraints. The approximations of the solid-angle integrals also prevent any occurrence of the "ray effects" encountered in discrete ordinate methods (Viskanta, 1987). The method also appears to be the first that shares the philosophy of, and can use the same nonorthogonal boundary fitted mesh as, modern methods for computing fluid flows and that also converges with grid refinement to the exact solution of the radiation transport equation.

The authors are indebted to anonymous reviewers for pointing out that it may be undesirable for a radiation grid to be congruent with the fluid flow grid since the need for grid refinement may occur in different regions. Such situations are already encountered when the internal energy equation is solved over extensive regions of the flow in which the temperature is nearly constant, but in these regions a fine grid is needed to compute the fluid flow. It is common practice in such cases to use the same grid for both the fluid flow and heat transfer for the sake of simplicity. Similarly, for fluid flow and radiation different grids could certainly be used, but at the expense of complexity. Even if different grids were used, it is still desirable to use a philosophically consistent method.

The method has been demonstrated for a one-dimensional problem, and several simple two-dimensional problems, for which benchmark solutions and other approximate solutions are available. The method is shown to yield good accuracy on coarse grids, and errors due to the discrete representations of the continuous equations reduce rapidly with grid refinement.

Acknowledgments

This work was supported by a contract, negotiated through the Unsolicited Proposal Program, from the Combustion and Carbonization Research Laboratory of the Energy Resources Laboratory, CANMET, which is part of the Energy Mines and Resources Department of the Canadian Federal Government. The authors gratefully acknowledge the support and assistance of the Scientific Advisor, Mr. Pat Hughes. Our thanks also to Professor K.G.T Hollands of the Mechanical Engineering Department at the University of Waterloo for his encouragement, criticism and enthusiasm. Professor R. Viskanta has also provided valuable comments.

References

Crosbie, A. L., and Schrenker, R. G., 1984, "Radiative Transfer in a Two-Dimensional Rectangular Medium Exposed to Diffuse Radiation," *J. Quant. Spectrosc. Radiat. Transfer*, Vol. 31, pp. 339–372.

Fiveland, W. A., 1984, "Discrete-Ordinates Solutions of the Radiation Transport Equation for Rectangular Enclosures," ASME JOURNAL OF HEAT TRANSFER, Vol. 106, pp. 699–706.

Heaslet, M. A., and Warming, R. F., 1965, "Radiative Transport and Wall Temperature Slip in Absorbing Planar Medium," *Int. J. Heat Mass Transfer*, Vol. 8, pp. 979–994.

Roache, P. J., 1972, *Computational Fluid Dynamics*, Hermosa Publ., Albuquerque, NM.

Siegel, R., and Howell, J. R., 1981, *Thermal Radiation Heat Transfer*, Hemisphere Publishing Corp., New York.

Truelove, J. S., 1987, "Discrete Ordinate Solutions of the Radiation Transport Equation," ASME JOURNAL OF HEAT TRANSFER, Vol. 109, pp. 1048–1051.

Viskanta, R., 1984, "Radiative Heat Transfer," *Fortschrift der Verfahrenstechnik*, Vol. 22A, pp. 51–81.

Viskanta, R., and Mengüç, M. P., 1987, "Radiation Heat Transfer in Combustion Systems," *Prog. Energy Combust. Sci.*, Vol. 13, pp. 97–160.

The Differential-Discrete-Ordinate Method for Solutions of the Equation of Radiative Transfer

S. Kumar
Research Assistant.

A. Majumdar
Research Assistant.

C. L. Tien
A. Martin Berlin Professor.
Fellow ASME

Department of Mechanical Engineering,
University of California,
Berkeley, CA 94720

This paper introduces a powerful but simple methodology for solving the general equation of radiative transfer for scattering and/or absorbing one-dimensional systems. Existing methods, usually designed to handle specific boundary and energy equilibrium conditions, either provide crude estimates or involve intricate mathematical analysis coupled with numerical techniques. In contrast, the present scheme, which uses a discrete-ordinate technique to reduce the integro-differential equation to a system of ordinary differential equations, utilizes readily available software routines to solve the resulting set of coupled first-order ordinary differential equations as a two-point boundary value problem. The advantage of this approach is that the user is freed from having to understand complicated mathematical analysis and perform extensive computer programming. Additionally, the software used is state of the art, which is less prone to numerical instabilities and inaccuracies. Any degree of scattering anisotropy and albedo can be incorporated along with different conditions of energy equilibrium or specified temperature distributions and boundary conditions. Examples are presented where the radiative transfer is computed by using different quadratures such as Gaussian, Lobatto, Fiveland, Chebyshev, and Newton–Cotes. Comparison with benchmark cases shows that in a highly forward scattering medium Gaussian quadrature provides the most accurate and stable solutions.

Introduction

The transport of thermal radiation is an important mechanism of energy transport in numerous engineering applications. The constituent medium in the majority of these systems actively participates in the radiative transfer due to the scattering, absorption, and emission of radiation. Examples are abundant, notably combustion systems such as furnaces containing fly ash, coal particles, and soot agglomerates, spray combustors such as rocket and diesel engines and turbine combustors, packed-bed and fluidized-bed combustors, and large-scale fires. Others include catalytic reactors, microsphere cryogenic insulations, lightweight fibrous insulations, particulate solar collectors, and liquid-droplet radiators used in space applications. Other instances where the participation of particulates is also important is in atmospheres and large bodies of water.

Current literature has a multitude of methods for solving the equation of radiative transfer, as documented in several reviews by Viskanta (1966, 1982, 1984), Mengüç and Viskanta (1983), Viskanta and Mengüç (1987), Vortmeyer (1978), and Sarofim and Hottel (1978), and in standard texts (Özişik, 1973). Existing techniques for solving radiative transfer for scattering-absorbing systems employ either simple and crude approximations or complex mathematical analysis coupled with numerical techniques to obtain the radiative heat fluxes and temperature distributions. Some examples of the first kind are two-flux methods (Viskanta, 1966, 1982, 1984; Viskanta and Mengüç, 1987; Mengüç, 1987; Mengüç and Viskanta, 1983; Özişik, 1973; Brewster and Tien, 1984), whereas the refined and sophisticated ones are quadrature methods (Viskanta, 1966, 1982, 1984; Viskanta and Mengüç, 1987; Mengüç and Viskanta, 1983; Fiveland, 1987, Özişik, 1973; Love and Grosh, 1965), spherical harmonics (Viskanta, 1966, 1982, 1984; Viskanta and Mengüc, 1987; Mengüc and Viskanta, 1983; Özisik, 1973), the F_N method (Mengüc and Viskanta, 1983; Siewert, 1978; Kumar and Felske, 1986), and others. The refined methods require complicated mathematical manipulations to reduce the equations to a form that can be solved by numerical methods. These usually require extensive computer programming effort by the user. In addition, each solution methodology is specific for a geometry of the system, the boundary conditions, and the medium energy equilibrium considerations.

The methodology proposed here uses the quadrature scheme of the discrete-ordinates method (Love and Grosh, 1965) to reduce the radiative transfer equation to a set of differential equations. A previous effort by Anderson et al. (1973), who considered a radiation-conduction problem for a nonscattering medium, solved these equations directly by the method of successive approximations. Fiveland (1987) used a finite difference scheme for isotropically and linearly anisotropically scattering cold media. The present scheme requires the user to be familiar only with simple mathematics to set up the equations and utilizes sophisticated, but readily available, software to solve the resultant system of equations. Commercial software is usually extensively tested for numerical accuracy and stability. This frees the user from tedious programming and having to understand complicated mathematical formulations. Another important advantage is that once formulated any variations in boundary conditions and energy coupling considerations can be incorporated with little effort. The present scheme is so named in order to distinguish it from the conventional discrete ordinates methodology, which converts the system of ordinary differential equations into algebraic ones (Love and Grosh, 1965; Hsia and Love, 1967). Hsia and Love (1967) converted the linear ordinary equations obtained from the quadrature scheme to a complicated system involving eigenvalues and linear algebraic equations for eigenfunctions for media with isothermal and quadratic temperature profiles.

Contributed by the Heat Transfer Division and presented at the 25th National Heat Transfer Conference, Houston, Texas, July 24–27, 1988. Manuscript received by the Heat Transfer Division November 29, 1988; revision received July 26, 1989. Keywords: Numerical Methods, Radiation, Radiation Interactions.

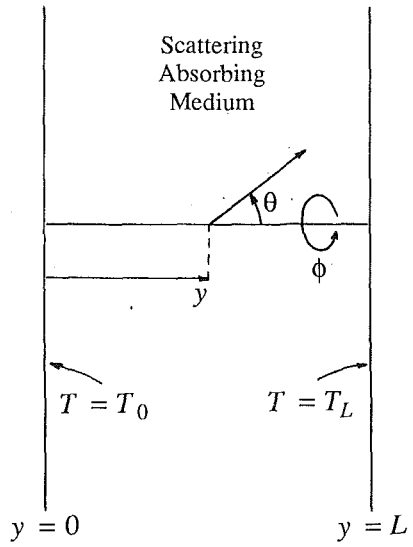

Fig. 1 Coordinate geometry for one-dimensional planar system

Methodology for One-Dimensional Systems

To illustrate the method a plane-parallel gray slab, shown in Fig. 1, is considered. One-dimensional geometry is a good approximation for many physical situations, such as those arising in energy transport through insulations, atmospheres, and large furnaces. It is also a building block for the analysis for other geometries.

Equation of Transfer. The equation of transfer for a one-dimensional medium is expressed by the following (Özişik, 1973):

$$\mu\frac{\partial I(y,\mu,\phi)}{\partial y} = \sigma_a I_b(T(y)) - (\sigma_a+\sigma_s)I(y,\mu,\phi)$$
$$+\frac{\sigma_s}{4\pi}\int_{\mu'=-1}^{1}\int_{\phi'=0}^{2\pi} I(y,\mu',\phi')\Phi(\mu',\phi'\to\mu,\phi)d\mu' d\phi' \quad (1)$$

where I is the intensity, $\mu = \cos\theta$, θ is the polar angle measured from the y axis, ϕ is the azimuthal angle, σ_a and σ_s are the absorption and scattering coefficients, and Φ is the scattering phase function, which can be represented as

$$\Phi(\mu',\phi'\to\mu,\phi) = \sum_{n=0}^{N} a_n P_n(\mu_0), \quad a_0 = 1 \quad (2)$$

where P_n are Legendre polynomials, a_n are coefficients of expansion of phase function, N is the degree of anisotropy of scattering, and μ_0 is the cosine of the angle between directions (μ', ϕ') and (μ, ϕ). Since the azimuthal angle ϕ does not explicitly appear in the equation of transfer, the dependence of intensity on ϕ is introduced only by the azimuthally dependent imposed boundary conditions. For azimuthally independent boundary conditions the intensity in the medium is a function of y and μ only and the phase function is simplified to

$$\Phi(\mu'\to\mu) = \sum_{n=0}^{N} a_n P_n(\mu) P_n(\mu'), \quad a_0 = 1 \quad (3)$$

It has been shown (Kumar and Felske, 1986) that for azimuthally dependent cases where the boundary conditions can be expanded as a Fourier series in the variable ϕ, the intensity $I(y, \mu, \phi)$ can also be similarly expanded, and that the resulting equations are similar to those corresponding to the azimuthally independent case. It is for this reason that the analysis for the azimuthally independent case is considered in depth in the following development. However, for completeness, results for the azimuthally dependent case of collimated incident radiation are also presented.

The first step in the method to analyze the azimuthally independent equation of transfer is to replace the integral over μ' in equation (1) by a quadrature. If μ_i's are the quadrature points between -1 and $+1$ corresponding to a $2M$-order quadrature, and w_i's are the corresponding weights, the above equation is reduced to the following system of ordinary differential equations:

$$\mu_i\frac{dI_i(y)}{dy} = \sigma_a I_b(T(y)) - \sigma_e I_i(y)$$
$$+\frac{\sigma_s}{2}\sum_{\substack{j=-M\\ j\neq 0}}^{M} w_j I_j(y)\Phi(\mu_j\to\mu_i), \quad i=-M,\ldots,M, \quad i\neq 0 \quad (4)$$

where $I_i(y) = I(y, \mu_i)$. The order $2M$ of the quadrature contains an even number of points to avoid the value $\mu = 0$, which

Nomenclature

a_n = coefficients in the expansion of phase function
A = elements of the Jacobian matrix **A**
B = elements of the vector **B**
D = diameter of the particles
i = $\sqrt{-1}$
I = intensity
L = length of the one-dimensional medium
m = complex refractive index $= n + i\kappa$
M = half of the order of quadrature
n = index of refraction
N = degree of scattering anisotropy; order of F_N method
P_n = Legendre polynomials
q = radiative heat flux
Q = nondimensional radiative flux
T = temperature
w = weights for numerical quadrature
x, y, z = Cartesian coordinates
Z = imposed boundary intensities
α = size parameter $= \pi D/\lambda$
ϵ = boundary emissivity
θ = polar angle
κ = index of absorption
λ = wavelength of incident radiation
μ = direction cosine with respect to y direction, $\cos\theta$
μ_0 = cosine of angle between (μ', ϕ') and (μ, ϕ)
ρ = reflectivity
σ = radiative coefficients, $\sigma_e = \sigma_a + \sigma_s$
τ = optical path length
ϕ = azimuthal angle
Φ = scattering phase function
ω = scattering albedo $= \sigma_s/\sigma_e$

Subscripts

a = absorption
b = blackbody
C = collimated
e = extinction
L = length of medium
s = scattering
0 = coordinate origin

Superscripts

d = diffuse
s = specular

has no distinct boundary condition at the two edges of the plane parallel slab. For the sake of simplicity $i=-M, \ldots, -1$, corresponds to the negative μ and $i=1, \ldots, M$, to the positive. Also the μ's are so ordered that $-\mu_j=\mu_{-j}$. The above constitutes a $2M$th-order system of ordinary differential equations. It is a two-point boundary-value where $2M$ boundary conditions are specified. Equation (4) can be rewritten in the matrix form as

$$\frac{d\mathbf{I}}{dy}=[\mathbf{A}]\mathbf{I}+\mathbf{B} \tag{5}$$

where

$$A_{ij}=\frac{1}{\mu_i}\left[-\sigma_e\delta_{ij}+\frac{\sigma_s}{2}w_j\Phi(\mu_i\rightarrow\mu_j)\right],\ B_i=\frac{1}{\mu_i}\sigma_a I_b(T(y)) \tag{6a}$$

Some numerical methods may need the Jacobian of the right side of the differential equation, equation (5), and it is

$$J_{ij}=\frac{\partial}{\partial I_j}\left[\frac{dI_i}{dy}\right]=A_{ij} \tag{6b}$$

Boundary Conditions. The boundary conditions at the reflecting boundaries are expressed as

$$I(0,+\mu,\phi)=Z_0(+\mu,\phi)+I_C\delta(\mu-\mu_C)\delta(\phi-\phi_C)$$
$$+\rho_0^S I(0,-\mu,\phi)+\rho_0^d\frac{1}{\pi}\int_{\mu'=0}^{1}\int_{\phi'=0}^{2\pi}I(0,-\mu',\phi')\phi'd\mu'd\phi',$$
$$\mu>0,$$
$$I(L,-\mu\phi)=Z_L(-\mu,\phi)+\rho_L^s(L,+\mu,\phi)$$
$$+\rho_L^d\frac{1}{\pi}\int_{\mu'=0}^{1}\int_{\phi'=0}^{2\pi}I(L,+\mu',\phi')\mu'd\mu'd\phi',\quad \mu>0 \tag{7}$$

where δ is the Dirac delta function, ρ^s and ρ^d are specular and diffuse reflectivities at the boundaries, and Z_0 and Z_L are the imposed intensity distributions at the $y=0$ and $y=L$ surfaces, respectively, that can be expanded as Fourier series in ϕ. The $I_C\delta(\mu-\mu_C)\delta(\phi-\phi_C)$ term corresponds to an imposed collimated flux at the $y=0$ boundary. For known temperatures at diffuse boundaries

$$Z_0(+\mu,\phi)=\epsilon_0\frac{\sigma T_0^4}{\pi},\quad Z_L(-\mu,\phi)=\epsilon_L\frac{\sigma T_L^4}{\pi},\quad \mu>0 \tag{8}$$

where T_0 and T_L are the temperatures of $y=0$ and $y=L$, respectively, and ϵ is the emissivity of the surfaces.

The corresponding azimuthally independent boundary conditions can be cast in a form that is compatible with the discretized equation of transfer yielding

$$I_{+i}(0)=Z_0(+\mu_i)+\frac{I_C}{2\pi}\delta(\mu-\mu_0)+\rho_0^S I_{-i}(0)$$
$$+2\rho_0^d\sum_{j=1}^{M}w_jI_{-j}(0)\mu_j,\quad i=1,\ldots,M$$
$$I_{-i}(L)=Z_L(-\mu_i)+\rho_L^s I_{+i}(L)+2\rho_L^d\sum_{j=1}^{M}w_jI_{+j}(L)\mu_j,$$
$$i=1,\ldots,M \tag{9}$$

The boundary conditions are thus on $I_i(y=0)$ for all i where μ_i is positive, i.e., for $i=1,\ldots,M$, and $I_j(y=L)$, $j=-M,\ldots,-1$, for which μ_j is negative. If the boundaries are black the reflectivities can be set to zero.

Medium Temperature Conditions. Different energy and/or temperature conditions can apply to the particulate medium for different operating conditions. The commonly encountered ones include (*i*) the case when the emission from the medium can be neglected, such as during the propagation of lasers through a cold medium, (*ii*) the case of an isothermal medium, such as in atmospheric radiative transfer, (*iii*) the medium in radiative equilibrium, such as in soot layers, and (*iv*) the case where the radiative energy is in equilibrium with other modes of energy transport, such as in furnaces and packed-bed combustors. All these conditions can be handled by the present method as indicated in the following.

The cases of the cold medium (*i*) and the isothermal medium (*ii*) are the simplest since the radiative transfer is uncoupled from external influences and can be solved on its own. Equation (4) needs no further simplification since the $I_b(T(y))$ term is specified a priori and the resulting equation is a system of differential equations for the unknown I_j. For the case of radiative equilibrium (*iii*) the following condition holds:

$$0=\nabla\cdot\mathbf{q}(y)=4\pi\sigma_a I_b(T(y))-2\pi\sigma_a\int_{-1}^{1}I(y,\mu)d\mu \tag{10}$$

yielding

$$I_b(T(y))=\frac{1}{2}\int_{-1}^{1}I(y,\mu)d\mu=\frac{1}{2}\sum_{-M}^{M}w_jI_j(y) \tag{11}$$

Substituting the above expression into equation (4) yields a system of equations in which the only unknowns are the I_j, and can be solved as a system of coupled first-order differential equations.

If the radiative energy is coupled with other modes of energy transfer (*iv*) the equation of radiative transfer is coupled to the energy equation via the temperature term $I_b(T(y))$ and can be solved simultaneously. This is achieved by appending the system of first-order ordinary differential equations of radiative transfer to the differential energy and momentum equations and solving the resultant system of equations simultaneously; see Kumar et al. (1988) and Kumar and Tien (1989).

Numerical Quadratures. The present methodology is capable of accommodating different types of quadrature scheme, such as Gaussian, Lobatto, Chebyshev, Newton-Cotes (Kopal, 1961), and Fiveland (Fiveland, 1987). The quadrature schemes are used to approximate an integral of the form

$$\int_{-1}^{1}f(\mu)d\mu=\sum_{j=1}^{n}w_jf(\mu_j) \tag{12}$$

where w_j's are the weight coefficients corresponding to the n discrete points μ_j. The differences between the various quadrature schemes lie in the values of w_j's and μ_j's. Consider $f(\mu)$ to be a polynomial of degree m, having $m+1$ coefficients. For Gaussian quadrature, which considers the $2n$ weights and points to be arbitrary, the maximum value of m for which equation (12) is exact is $m=2n-1$. In the Lobatto quadrature scheme, the boundary points of $\mu=-1$ and $\mu=1$ are fixed, thus reducing the degree of the polynomial to $m=2n-3$. In radiative transfer, fixing these points can be advantageous since the intensities in the forward and the backward direction need evaluation. In both the Chebyshev and Fiveland quadrature schemes, the n weights are held fixed to a value of $2/n$. Therefore, for exact evaluation of the integral, the maximum degree of the polynomial is further reduced to $m=n-1$. For the Chebyshev scheme, the discrete points are determined by solving the set of equations

$$\frac{2}{n}\sum_{j=1}^{n}\mu_j^i=\int_{-1}^{1}\mu^i d\mu\qquad i=1,2,3,\ldots,n \tag{13}$$

This set of equations has real roots for $1\le n\le 7$ and $n=9$,

Table 1 Coefficients of the phase functions I and II: PF I—refractive index $m = 2.20 + i1.12$, and size parameter $\alpha = 1.0$; PF II—refractive index $m = 1.50 + i0.10$ and size parameter $\alpha = 8.0$

PF I		PF II			
a_0	1.000000	a_0	1.000000	a_{13}	4.202631
a_1	0.643833	a_1	2.602844	a_{14}	3.417068
a_2	0.554231	a_2	3.904987	a_{15}	2.441223
a_3	0.103545	a_3	4.951962	a_{16}	1.375775
a_4	0.010498	a_4	5.827835	a_{17}	0.580278
a_5	0.000563	a_5	6.449251	a_{18}	0.240728
a_6	0.000019	a_6	6.857353	a_{19}	0.058807
		a_7	6.986990	a_{20}	0.013133
		a_8	6.876321	a_{21}	0.002492
		a_9	6.564448	a_{22}	0.000410
		a_{10}	6.083206	a_{23}	0.000060
		a_{11}	5.466910	a_{24}	0.000008
		a_{12}	4.874364	a_{25}	0.000001

higher than which this scheme cannot exist (Salzer, 1947). In general, any scheme with equally weighted ordinates has a maximum value of n, corresponding to real roots, beyond which no increase in accuracy is achieved (Kopal, 1961). The points in the Fiveland scheme are obtained from the set of equations (13), by matching the moments over the half range [0, 1], i.e., equation (13) with integration limits from 0 to 1. Since the roots of these equations are found numerically, the existence of complex roots is ignored. The Newton–Cotes scheme fixes the n equally spaced points between the two boundaries and then determines the corresponding weights.

The solution of the radiative transfer in one-dimensional systems involves evaluating the full range moment of intensity in the equation of transfer and the half range for the forward and backward heat fluxes. Any quadrature (Gaussian, Lobatto, Chebyshev, Newton–Cotes, or Fiveland) may be selected since the methodology is extremely general. The user must use a few different quadratures and orders to ascertain which is most suited for the particular problem at hand. Results using different quadratures are presented for a few cases in the following sections.

Method of Solution. After selecting an appropriate quadrature the system of $2M$ first-order ordinary differential equations specified by equation (4) along with the appropriate energy equilibrium condition and boundary conditions are solved by using commercial software available as a standard feature on most mainframe computers. Two such software libraries are the IMSL[1] and the NAG[2] mathematical subroutine libraries written in FORTRAN. Subroutines DVCPR from the IMSL library and D02HAF from NAG are used to solve the two-point boundary value problem. Subroutine DVCPR, which employs the method of finite differences (Pereyra, 1978), is preferred since it is faster and is not too sensitive to the initial guess provided. The initial guess is provided by assuming exponentially decaying intensities characteristic of nonscattering media with the same boundary conditions. The results in this study were obtained by implementing the numerical algorithm in double precision FORTRAN on a VAX 11/8650 operating under the Berkeley UNIX operating system. The subroutine DVCPR from the IMSL library was used throughout. The software allows for nonuniform grid size and thus can handle rapid variations near the boundaries.

Numerical Results. To check the performance and accuracy of the present method with published studies, a scattering medium composed of spherical particles is selected. Two types of particle are considered, I: $\alpha = 1.0$, $m = 2.20 + i1.12$, and II: $\alpha = 8.0$, $m = 1.50 + i0.10$. The coefficients of the corresponding phase functions, which range from semidiffuse to highly forward scattering, are listed in Table 1. These scattering phase functions have also been used by Mengüc and Viskanta (1983) who evaluated the radiative transfer through a one-dimensional geometry for nonreflecting and nonemitting boundaries, and by Kumar and Felske (1986) for collimated incident flux.

Tables 2, 3, 4, and 5 compare the dimensionless fluxes Q, defined as

$$Q(\tau) = \frac{q(y)}{\pi I_0}, \qquad \tau = \int_0^y (\sigma_a + \sigma_s)\, dy \tag{14}$$

evaluated at the two boundaries $\tau = 0$ and $\tau = \tau_L$, to the results from other methods (Mengüc and Viskanta, 1983; Kumar and Felske, 1986). The medium emissivity is neglected and the $y = 0$ boundary is irradiated with diffuse intensity I_0 of unit strength. Benchmark cases correspond to those by the F_9 method.

All the different quadrature schemes give good results for Phase Function I, which is expressible as a polynomial of sixth order and is semidiffuse in nature. The results obtained from the present method by using different quadratures are presented in Table 2. The results of the same case by other methods are presented by Mengüç and Viskanta (1983). It should be noted that for this phase function the Fiveland scheme provides highest accuracy.

Table 3 shows that significant deviations from the exact results are observed for most quadratures when either the scattering is peaked in the forward direction, as specified by Phase Function II, or when the optical thickness is large. Physically unrealistic results are also obtained for some case; Gaussian quadrature seems to be an exception. For $\tau_L = 0.1$ all three schemes provide reasonably accurate results. This is due to the fact that for small path lengths, the uniformity of the intensity due to boundary conditions at $\tau = 0$ is distorted by a small extent giving rise to a polynomial in μ of a low degree, $m < n - 1$. However, at $\tau_L = 10.0$ the highly forward in-scattering term distorts the intensity to high-degree polynomial. It is seen that the Fiveland scheme yields totally unrealistic fluxes, whereas the Gaussian and Lobatto schemes provide accurate results. It should also be noted that at $\tau_L = 10.0$, L_8 gives unrealistic values whereas G_8 provides accurate results.

As observed from Tables 2 and 3, the error reduces to about 0.1 percent for Gaussian quadrature as the number of quadrature points is increased to 20, and to approximately 0.01 percent at a quadrature of 32. It is noted that the error monotonically reduces as the quadrature is increased. By noting the change in the solution as the quadrature $2M$ increases the rate of convergence is easily inferred, and therefore the order of quadrature corresponding to the desired accuracy is obtained. For most practical purposes $2M = 20$ is sufficient since the corresponding relative error is approximately 0.1 percent. Even at 10 quadrature points the error is less than 1.0 percent on the average, which is attractive since the time taken

[1] IMSL, 2500 ParkWest Tower One, 2500 City West Blvd., Houston, TX 77042.

[2] Numerical Algorithms Group, 1131 Warren Ave., Downers Grove, IL 60615.

Table 2 Dimensionless radiative fluxes at boundaries by various methods for phase function PF I, $\tau_L = 1.0$, $\omega = 0.8$

Quadratures	$2M = 4$		$2M = 6$		$2M = 8$		$2M = 10$	
	Q(0)	Q(τ_L)	Q(0)	Q(τ_L)	Q(0)	Q(τ_L)	Q(0)	Q(τ_L)
G	0.77537	0.46260	0.76650	0.45855	0.76390	0.45757	0.76271	0.45704
Nc	0.74405	0.43889	0.77211	0.46251	0.75789	0.45485	0.76616	0.45833
Fv	0.75807	0.45459	0.75974	0.45571	0.76062	0.45609	0.76057	0.45595
L	0.79473	0.47515	0.75974	0.45571	0.76498	0.45799	0.76324	0.45729
Ch	0.74926	0.44949	0.77334	0.46173				
Quadratures	$2M = 12$		$2M = 16$		$2M = 20$		F_9-Benchmark	
	Q(0)	Q(τ_L)	Q(0)	Q(τ_L)	Q(0)	Q(τ_L)	Q(0)	Q(τ_L)
G	0.76206	0.45671	0.76140	0.45634	0.76110	0.45617		
Nc	0.75506	0.45365	0.73817	0.44429			**0.76057**	**0.45588**
Fv	0.76054	0.45582						

G = Gaussian, *Fv* = Fiveland, *L* = Lobatto, *Nc* = Newton-Cotes, *Ch* = Chebychev

Table 3 Dimensionless radiative fluxes at boundaries by various methods for different optical thickness, phase function II, $\omega = 0.8$

Methods	Dimensionless Radiative Flux					
	$\tau_L = 0.1$		$\tau_L = 2.0$		$\tau_L = 10.0$	
	Q(0)	Q(τ_L)	Q(0)	Q(τ_L)	Q(0)	Q(τ_L)
Two-Flux						
SS	0.99404	0.95483	0.94302	0.39844	0.93222	0.01019
M2	0.99481	0.96076	0.94603	0.45057	0.93224	0.01883
Spherical Harmonics						
P_1	0.99718	0.95797	0.97187	0.42409	0.96570	0.01377
P_3	0.98761	0.94865	0.93699	0.41826	0.93336	0.01747
P_5	0.98440	0.94557	0.93345	0.41779	0.92971	0.01740
P_9 9 term P.F.	0.98885	0.95020	0.92660	0.43072	0.91464	0.02456
Discrete Ordinates*						
Approx. P.F.	0.98713	0.94860	0.92482	0.42836	0.91356	0.02370
Full P.F.	0.98797	0.94946	0.92574	0.43048	0.91380	0.02455
F_N-Method						
F_1	0.99293	0.95838	0.93336	0.43903	0.92011	0.02216
F_9-Benchmark	**0.98692**	**0.94856**	**0.92523**	**0.43029**	**0.91332**	**0.02454**
DDO_{2M}-Quadrature						
G_8	1.00161	0.97275	0.93277	0.52564	0.91189	0.06115
Fv_8	0.98450	0.97535	0.89394	0.89882	0.44998	2.14062
L_8	1.00287	1.00081	0.86074	0.85693	0.45128	1.52133
G_{10}	0.99503	0.95633	0.92987	0.43277	0.91775	0.02501
Fv_{10}	0.98547	0.95924	0.91532	0.62132	0.86178	0.38196
L_{10}	0.99821	0.96125	0.93344	0.45203	0.91979	0.03166
G_{12}	0.99186	0.95316	0.92763	0.43094	0.91565	0.02458
Fv_{12}	0.98679	0.96580	0.91288	0.65661	0.85771	0.26588
G_{16}	0.98934	0.95073	0.92639	0.43063	0.91443	0.02456
G_{20}	0.98835	0.94980	0.92592	0.43052	0.91397	0.02456
G_{32}	0.98749	0.94904	0.92549	0.43042	0.91355	0.02455

SS = Schuster-Schwarzchild, M2 = Modified Two-Flux, *G* = Gaussian, *Fv* = Fiveland, *L* = Lobatto

*Quadrature not specified (Mengüç and Viskanta, 1983)

is extremely small. Figure 2 shows the time taken versus increasing quadrature for Phase Function II by using the present scheme. The difference in time taken between different quadrature schemes is probably due to different convergence rates.

Table 4 examines the effect of the different quadratures on the present method, as the albedo ω approaches zero (no scattering) and unity (no absorption). For the case $\omega \to 0$, the intensity at any point is uniform and hence a zero-degree polynomial. Therefore, for this case all methods provide reasonably accurate results. For a nonabsorbing medium, $\omega \to 1$, the Fiveland and the Newton-Cotes quadratures yield unrealistic fluxes when used with the present numerical scheme. However, it can be observed that the Gaussian and Lobatto quadratures consistently gives better results than others. Moreover, the Gaussian scheme for $2M = 32$ gives the

Table 4 Dimensionless radiative fluxes at boundaries by various methods for limiting cases of $\omega \to 0$ and $\omega \to 1$, phase function II, $\tau_L = 2.0$

Quadratures	ω=0.01		ω=0.001		ω=0.0001		ω=0	
	Q(0)	Q(τ_L)	Q(0)	Q(τ_L)	Q(0)	Q(τ_L)	Q(0)	Q(τ_L)
Fv_{10}	0.99973	0.06186	0.99997	0.06033	1.00000	0.06018	1.00000	0.06016
L_{10}	1.00905	0.06170	1.00928	0.06043	1.00931	0.06030	1.00931	0.06029
Nc_{10}	1.01714	0.06303	1.01738	0.06073	1.01741	0.06050	1.01741	0.06048
G_{10}	1.00725	0.06164	1.00749	0.06040	1.00752	0.06028	1.00752	0.06026
G_{32}	*1.00052*	*0.06164*	*1.00075*	*0.06040*	*1.00078*	*0.06028*	*1.00078*	*0.06027*
Exact							**1.00000**	**0.06027**
Quadratures	ω=0.99		ω=0.999		ω=0.9999		ω=1.0	
	Q(0)	Q(τ_L)	Q(0)	Q(τ_L)	Q(0)	Q(τ_L)	Q(0)	Q(τ_L)
Fv_{10}	0.77336	1.16942	0.76002	1.20840	0.75863	1.21240	0.75847	1.21284
L_{10}	0.81645	0.82492	0.80577	0.85196	0.80465	0.85474	0.80453	0.85505
Nc_{10}	-0.61450	6.66016	-0.79475	7.05223	-0.81409	7.09320	-0.81625	7.09777
G_{10}	0.81547	0.77849	0.80527	0.80323	0.80421	0.80577	0.80409	0.80606
G_{32}	0.81190	0.77311	0.80166	0.79768	0.80060	0.80020	**0.80048**	**0.80048**

G = Gaussian, *Fv* = Fiveland, *L* = Lobatto, *Nc* = Newton-Cotes

Table 5 Dimensionless radiative fluxes at boundaries compared with exact results for collimated incidence, phase function I, $\omega = 0.5$, $\tau_L = 1.0$, $\mu_C = 0.0$

ρ_0^s	ρ_L^s	ρ_0^d	ρ_L^d	Method	$q(0)/I_C\mu_C$	$q(\tau_L)/I_C\mu_C$
0.0	0.3	0.0	0.0	DDO_{10}	0.86313	0.28735
				DDO_{16}	0.86368	0.28717
				DDO_{20}	0.86381	0.28712
				DDO_{32}	0.86395	0.28707
				F_9	**0.86404**	**0.28704**
0.0	0.6	0.0	0.0	DDO_{10}	0.81432	0.16934
				DDO_{16}	0.81489	0.16919
				DDO_{20}	0.81503	0.16915
				DDO_{32}	0.81518	0.16911
				F_9	**0.81527**	**0.16908**
0.3	0.0	0.0	0.0	DDO_{10}	0.93436	0.40699
				DDO_{16}	0.93479	0.40683
				DDO_{20}	0.93489	0.40679
				DDO_{32}	0.93500	0.40675
				F_9	**0.93508**	**0.40672**
0.6	0.0	0.0	0.0	DDO_{10}	0.96101	0.41603
				DDO_{16}	0.96129	0.41586
				DDO_{20}	0.96135	0.41582
				DDO_{32}	0.96143	0.41577
				F_9	**0.96148**	**0.41573**
0.0	0.0	0.0	0.3	DDO_{10}	0.86892	0.28792
				DDO_{16}	0.86954	0.28819
				DDO_{20}	0.86969	0.28825
				DDO_{32}	0.86986	0.28832
				F_9	**0.86996**	**0.28836**
0.0	0.0	0.0	0.6	DDO_{10}	0.82519	0.16916
				DDO_{16}	0.82597	0.17004
				DDO_{20}	0.82616	0.17024
				DDO_{32}	0.82637	0.17047
				F_9	**0.82650**	**0.17061**

most accurate result since the fluxes at both boundaries are identical, thereby satisfying conservation of energy in a nonabsorbing medium.

Table 5 is a comparison with the exact results presented by Kumar and Felske (1986) for the case of collimated incidence at $\mu_C = 0.8$ with scattering albedo $\omega = 0.5$ and slab optical thickness $\tau_L = 1.0$ for a variety of surface reflectivities. The phase function is PF I and the quadrature is Gaussian. It is seen that the results of the present approach compare very well with the benchmark cases obtained by the F_9 method. The details of the calculations are presented by Kumar et al. (1988). Since the medium is planar, the results hold for any value of ϕ_C.

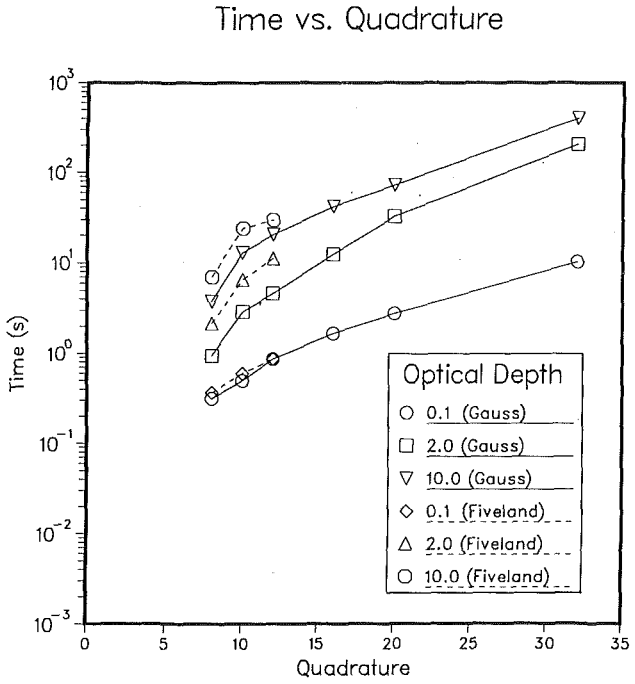

Fig. 2 Time taken for present method, phase function II

Conclusions

The resutls of this method agree well with benchmark cases available in the literature when appropriate quadrature is selected. For highly forward scattering media, the Gaussian quadrature scheme yields the most stable and accurate results when compared to those of the Fiveland, Lobatto, and Newton-Cotes schemes. The merits of the present methodology are summarized as follows: (1) It contains no complicated mathematics that the user needs to understand; (2) the programming effort is negligible; (3) any degree of scattering anisotropy can be considered; (4) it can incorporate the most general boundary conditions; (5) azimuthally asymmetric boundary conditions can be reduced to a form that is tractable by this technique; (6) the computational times are reasonably small; and (7) the method can handle any form of energy equilibrium condition within the medium and may be coupled to the full energy equation. In addition, since the solution is obtained numerically, variations of the absorption and scattering coefficients with position and temperature and of reflectivities with angles can be easily incorporated. Thus this simple scheme retains the generality of the equation of radiative transfer in contrast with the other methods, which are limited to the treatment of only some of the conditions mentioned before.

References

Anderson, E. E., Viskanta, R., and Stevenson, W. H., 1973, "Heat Transfer Through Semitransparent Solids," ASME JOURNAL OF HEAT TRANSFER, Vol. 95, pp. 179–186.

Brewster, M. Q., and Tien, C. L., 1983, "Examination of the Two-Flux Model for Radiative Transfer in Particulate Systems," *International Journal of Heat and Mass Transfer*, Vol. 25, pp. 1905–1907.

Fiveland, W. A., 1987, "Discrete Ordinate Methods for Radiative Heat Transfer in Isotropically and Anisotropically Scattering Media," ASME JOURNAL OF HEAT TRANSFER, Vol. 109, pp. 809–812.

Hsia, H. M., and Love, T. J., 1967, "Radiative Heat Transfer Between Parallel Plates Separated by a Nonisothermal Medium With Anisotropic Scattering," ASME JOURNAL OF HEAT TRANSFER, Vol. 89c, pp. 197–204.

Kopal, Z., 1961, *Numerical Analysis*, Wiley, New York.

Kumar, S., and Felske, J. D., 1986, "Radiative Transport in a Planar Medium Exposed to Azimuthally Unsymmetric Incident Radiation," *Journal of Quantitative Spectroscopy and Radiative Transfer*, Vol. 35, pp. 187–212.

Kumar, S., Majumdar, A., and Tien, C. L., 1988, "The Differential-Discrete-Ordinate Method for Solutions of the Equation of Radiative Transfer," *Proceedings, 25th ASME National Heat Transfer Conference*, H. R. Jacobs, ed., ASME HTD-Vol. 96, pp. 179–185.

Kumar, S., and Tien, C. L., 1989, "Analysis of Combined Radiation and Convection in a Particulate Laden Falling Film," *Proceedings, 26th ASME National Heat Transfer Conference*, Philadelphia, PA, August 6–9.

Love, T. J., and Grosh, R. J., 1965, "Radiative Heat Transfer in Absorbing, Emitting, and Scattering Media," ASME JOURNAL OF HEAT TRANSFER, Vol. 87, pp. 161–166.

Mengüç, M. P., and Viskanta, R., 1983, "Comparison of Radiative Transfer Approximations for Highly Forward Scattering Planar Medium," *Journal of Quantitative Spectroscopy and Radiative Transfer*, Vol. 29, pp. 381–394.

Özişik, M. N., 1973, *Radiative Transfer and Interactions With Conduction and Convection*, Wiley, New York.

Pereyra, V., 1978, "PASVA3: An Adaptive Finite Difference FORTRAN Program for First Order Non-linear Ordinary Boundary Problems," *Lecture Notes in Computer Science*, Springer-Verlag, Berlin, Vol. 76, pp. 67–88.

Salzer, H. E., 1947, "Tables for Facilitating the Use of Chebyshev's Quadrature Formula," *Journal of Mathematics and Physics*, Vol. 26, pp. 191–194.

Sarofim, A. F., and Hottel, H. C., 1978, "Radiative Transfer in Combustion Chambers: Influence of Alternative Fuels," *Proceedings, 6th International Heat Transfer Conference*, Vol. 6, pp. 199–217.

Siewert, C. E., 1978, "The F_N Method for Solving Radiative Transfer Problems in Plane Geometry," *Astrophysics and Space Science*, Vol. 58, pp. 131–137.

Viskanta, R., 1966, "Radiation Transfer and Interaction of Convection With Radiation Heat Transfer," *Advances in Heat Transfer*, T. F. Irvine and J. P. Hartnett, eds., Academic Press, New York, Vol. 3, pp. 176–252.

Viskanta, R., 1982, "Radiation Heat Transfer: Interaction With Conduction and Convection and Approximate Methods in Radiation," *Proceedings, 7th International Heat Transfer Conference*, Vol. 1, pp. 103–121.

Viskanta, R., 1984, "Radiative Heat Transfer," *Progress in Chemical Engineering* (fortschritte der verfahrenstechniks), Section A, Vol. 22, pp. 51–81.

Viskanta, R., and Mengüç, M. P., 1987, "Radiation Heat Transfer in Combustion Systems," *Progress in Energy and Combustion Science*, Vol. 13, pp. 97–160.

Vortmeyer, D., 1978, "Radiation in Packed Solids," *Proceedings, 6th International Heat Transfer Conference*, Vol. 6, pp. 525–539.

A General Correlation for Pool Film Boiling Heat Transfer From a Horizontal Cylinder to Subcooled Liquid: Part 1—A Theoretical Pool Film Boiling Heat Transfer Model Including Radiation Contributions and Its Analytical Solution

A. Sakurai
Professor.
Mem. ASME

M. Shiotsu
Associate Professor.
Mem. ASME

K. Hata
Instructor.

Institute of Atomic Energy,
Kyoto University,
Uji, Kyoto 611, Japan

A rigorous numerical solution of a theoretical model based on laminar boundary layer theory for pool film boiling heat transfer from a horizontal cylinder including the contributions of liquid subcooling and radiation from the cylinder was obtained. The numerical solution predicted accurately the experimental results of pool film boiling heat transfer from a horizontal cylinder in water with high radiation emissivity for a wide range of liquid subcooling in the range of nondimensional cylinder diameters around 1.3, where the numerical solution was applicable to the pool film boiling heat transfer from a cylinder with negligible radiation emissivity. An approximate analytical solution for the theoretical model was also derived. It was given by the sum of the pool film boiling heat transfer coefficient if there were no radiation and the radiation heat transfer coefficient for parallel plates multiplied by a nondimensional radiation parameter similar to the expression for saturated pool film boiling given by Bromley. The approximate analytical solution agreed well with the rigorous numerical solution for various liquids of widely different physical properties under wide ranges of conditions.

1 Introduction

The first systematic theoretical and experimental studies of saturated film boiling heat transfer were made by Bromley (1950). Using a simple theoretical model, he presented a correlation for saturated film boiling heat transfer from a horizontal cylinder in a pool of liquid including the radiation contribution from the cylinder. Breen and Westwater (1962) carried out a series of film boiling experiments on large-diameter cylinders and pointed out that the Bromley correlation was applicable to a limited range of cylinder diameters. They presented a semi-empirical equation of saturated film boiling heat transfer for a wide range of diameters. Siviour and Ede (1970) performed experiments of subcooled film boiling on a horizontal cylinder in water at atmospheric pressure and presented a semi-empirical correlation for subcooled film boiling heat transfer by combining the correlation of saturated film boiling heat transfer with that of natural convection heat transfer in the liquid phase.

On the other hand, there are some works on theoretical analysis according to the laminar boundary layer theory for saturated and subcooled film boiling heat transfer. Koh (1962) presented a solution of saturated film boiling heat transfer from a vertical plate. Sparrow and Cess (1962) carried out an analysis on subcooled film boiling heat transfer from a vertical plate by supposing the tangential velocities of vapor and liquid to be zero at the vapor–liquid interface. Nishikawa and Ito (1966) and Nishikawa et al. (1976) performed a theoretical analysis for subcooled film boiling heat transfer from a vertical plate and a horizontal cylinder introducing continuities of velocity and shear stress at the vapor–liquid interface without such a supposition. In the theoretical analyses mentioned above, the effect of radiation from a plate or a cylinder was not taken into account. Siviour and Ede (1970) reported in their paper that the theoretical values did not agree with their experimental results for saturated and subcooled film boiling heat transfer from horizontal cylinders.

The applicability of these theoretical solutions to real film boiling has not been studied experimentally in a long time. Recently, the authors (Sakurai et al., 1984, 1986) performed systematic experiments on saturated and subcooled film boiling from platinum horizontal cylinders with very low emissivity in a pool of water for wide ranges of system pressure, water subcooling, cylinder diameter, and surface superheat. They first found that their experimental data for a nondimensional cylinder diameter around 1.3 agreed well with the theoretical solution obtained by Nishikawa et al. (1976) for wide ranges of surface superheat, liquid subcooling, and system pressure and also found that, for higher or lower values of the nondimensional diameter, the experimental value gradually became higher than the theoretical value. They presented a correlation for subcooled pool film boiling heat transfer for water based on the theoretical solution and the experimental results, and pointed out that a major mechanism of pool film boiling heat transfer for large subcooling is liquid flow induced by rising vapor at the vapor–liquid interface (Sakurai et al., 1984).

The purpose of the present work is to develop a general correlation of pool film boiling heat transfer from a horizontal cylinder, including the contributions of liquid subcooling and

Contributed by the Heat Transfer Division for publication in the JOURNAL OF HEAT TRANSFER. Manuscript received by the Heat Transfer Division August 1, 1988; revision received July 20, 1989. Keywords: Boiling, Natural Convection, Radiation Interactions.

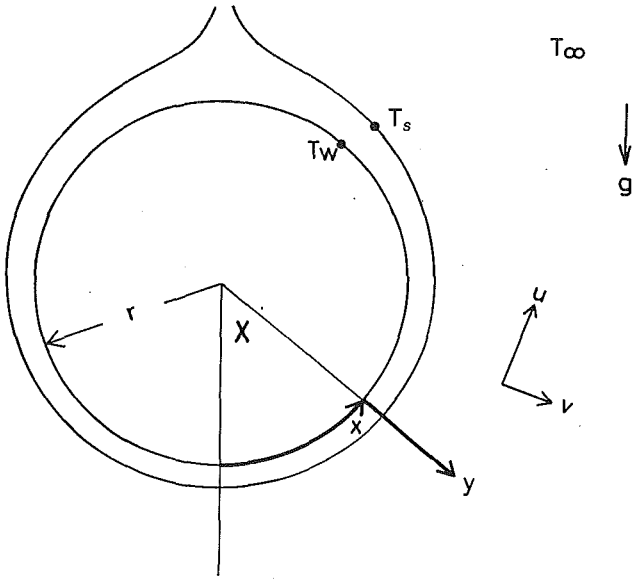

Fig. 1 Physical model and coordinates

radiation from the cylinder under wide ranges of conditions for various kinds of liquid. These liquids include those with low latent heats such as cryogens and freons, and those with Prandtl numbers far higher or lower than unity such as alcohols and liquid metals, respectively. In this first part of the work, a rigorous numerical solution of the theoretical model based on the laminar boundary layer theory for pool film boiling heat transfer from a horizontal cylinder including the effects of liquid subcooling and radiation from the cylinder is derived, and the applicability of the solution is confirmed by comparing it with the experimental data. Then, an approximate analytical solution that can describe the rigorous solution with good accuracy is also derived.

In a subsequent paper, the general correlation is derived by modifying this analytical solution slightly to agree better with the authors' new experimental results of saturated and subcooled pool film boiling heat transfer from horizontal cylinders of various nondimensional diameters in various liquids of widely different physical properties.

2 Rigorous Solution of Theoretical Pool Film Boiling Model With Radiation Effects

2.1 Physical Model. The physical model and coordinates are shown schematically in Fig. 1. It is assumed that the vapor forms a continuous film over the surface of the isothermal horizontal cylinder and that there exists a smooth vapor–liquid interface and laminar boundary layers of vapor and liquid. At the vapor liquid interface, the temperature is at its saturation value T_s, while the bulk of liquid is at a lower temperature T_∞. Radiation from the cylinder to the vapor–liquid interface is postulated to be absorbed in a negligibly small thickness of liquid.

2.2 Basic Equation. The conservation laws for mass, momentum, and energy, separately applied to both vapor and liquid layers, are

$$\frac{\partial}{\partial x}(\rho_v u_v) + \frac{\partial}{\partial y}(\rho_v v_v) = 0 \tag{1}$$

$$\rho_v u_v \frac{\partial u_v}{\partial x} + \rho_v v_v \frac{\partial u_v}{\partial y} = g \sin\left(\frac{x}{r}\right)(\rho_{l\infty} - \rho_v) + \frac{\partial}{\partial y}\left(\mu_v \frac{\partial u_v}{\partial y}\right) \tag{2}$$

$$\rho_v c_{pv}\left(u_v \frac{\partial T_v}{\partial x} + v_v \frac{\partial T_v}{\partial y}\right) = \frac{\partial}{\partial y}\left(k_v \frac{\partial T_v}{\partial y}\right) \tag{3}$$

$$\frac{\partial}{\partial x}(\rho_l u_l) + \frac{\partial}{\partial y}(\rho_l v_l) = 0 \tag{4}$$

Nomenclature

A = nondimensional quantity in equations (70) ~ (73)
B = nondimensional quantity in equations (70) ~ (73)
C = nondimensional quantity in equations (70) ~ (73)
C_{v1} = nondimensional quantity, equation (60)
C_{v2} = nondimensional quantity, equation (61)
C_l = nondimensional quantity, equation (62)
c_p = specific heat capacity, J/(kgK)
D = diameter of cylinder heater, m
D' = $D[g(\rho_l - \rho_v)/\sigma]^{1/2}$ = nondimensional diameter of cylinder heater
E = nondimensional quantity in equations (70) ~ (73)
F = nondimensional quantity in equation (75)
f = nondimensional quantity, equation (58)
f_v, f_l = nondimensional velocity functions, equation (17)
Gr_v = $g(\rho_l - \rho_v)D^3/(\rho_v \nu_v^2)$ = Grashof number
Gr_{vx} = $g(\rho_l - \rho_v)x^3/(\rho_v \nu_v^2)$ = Grashof number
g = acceleration due to gravity, m/s^2
h = heat transfer coefficient, W/(m^{2}K)
h_{co} = heat transfer coefficient if there were no radiation, W/(m^{2}K)
h_r = radiation heat transfer coefficient for parallel plates, W/(m^{2}K)
J = radiation parameter
K = modification factor in equation (74)
K_s = nondimensional quantity, equation (39)
k = thermal conductivity, W/(mK)
L = latent heat of vaporization, J/kg
L' = $L + 0.5c_{pv}\Delta T_{sat}$ = latent heat plus sensible heat content of vapor, J/kg
M = nondimensional quantity in equation (71)
M^* = modified M in equation (73)
M_x = nondimensional quantity in equation (70)
M_v, M_l = nondimensional quantities, equation (19)
N_v, N_l = nondimensional quantities, equation (20)
m_v, m_l = nondimensional quantities, equation (59)
Nu_v = average Nusselt number for cylinder
Nu_{vx} = average Nusselt number for vertical surface
Pr = Prandtl number
q = heat flux, W/m^2
q_{co} = heat flux if there were no radiation, W/m^2
q_x = local heat flux from vertical plate without radiation contribution, W/m^2
$\bar{q}_x$ = average heat flux from vertical plate without radiation contribution, W/m^2
q_{rc} = heat flux due to radiation from cylinder, W/m^2

$$\rho_l u_l \frac{\partial u_l}{\partial x} + \rho_l v_l \frac{\partial u_l}{\partial y} = g \sin\left(\frac{x}{r}\right)(\rho_{l\infty} - \rho_l) + \frac{\partial}{\partial y}\left(\mu_l \frac{\partial u_l}{\partial y}\right) \tag{5}$$

$$\rho_l c_{pl}\left(u_l \frac{\partial T_l}{\partial x} + v_l \frac{\partial T_l}{\partial y}\right) = \frac{\partial}{\partial y}\left(k_l \frac{\partial T_l}{\partial y}\right) \tag{6}$$

The boundary conditions are

$$w_i \equiv \rho_v\left(v_v - u_v \frac{d\delta}{dx}\right)_i = \rho_l\left(v_l - u_l \frac{d\delta}{dx}\right)_i \tag{7}$$

$$(u_v)_i = (u_l)_i \tag{8}$$

$$\left(\mu_v \frac{\partial u_v}{\partial y}\right)_i = \left(\mu_l \frac{\partial u_l}{\partial y}\right)_i \tag{9}$$

$$\left(-k_v \frac{\partial T_v}{\partial y}\right)_i + q_{rc} = \left(-k_l \frac{\partial T_l}{\partial y}\right)_i - w_i L \tag{10}$$

$$(T_v)_i = (T_l)_i = T_s \tag{11}$$

$$y = 0; \quad u_v = v_v = 0, \quad T_v = T_w \tag{12}$$

$$y \to \infty; \quad u_l \to 0, \quad T_l \to T_\infty \tag{13}$$

In pool film boiling heat transfer from a horizontal cylinder, the radiation contribution from the cylinder cannot be ignored generally, especially not for the cylinder of high radiation emissivity, because the cylinder surface temperature needed to realize stable film boiling on the cylinder is high. However, the theoretical pool film boiling heat transfer model based on laminar boundary layer theory has not yet been solved, as far as we know, without ignoring the radiation effect. Here the solution of the theoretical model with radiation effect is derived by the following method.

2.3 Similarity Transformation. It is assumed that the radiation heat flux from the horizontal cylinder q_{rc} in equation (10) is approximately given by a certain function of X described later so that the similarity transformation can be applied to the problem.

A similarity transformation such as that devised by Nishikawa et al. (1976) that considers the temperature-dependent variation in thermophysical properties of liquid and vapor is applied to this problem.

Stream functions Ψ_v and Ψ_l satisfying the following relations are introduced:

$$u_v = \frac{\rho_{vs}}{\rho_v}\frac{\partial \Psi_v}{\partial y}, \qquad v_v = -\frac{\rho_{vs}}{\rho_v}\frac{\partial \Psi_v}{\partial x} \tag{14}$$

$$u_l = \frac{\rho_{ls}}{\rho_l}\frac{\partial \Psi_l}{\partial y}, \qquad v_l = -\frac{\rho_{ls}}{\rho_l}\frac{\partial \Psi_l}{\partial x} \tag{15}$$

where the subscript s denotes the physical properties at the saturation temperature. Next, new independent and dependent variables are introduced as

$$\eta_v = N_v \frac{\gamma(X)}{r}\int_0^y \frac{\rho_v}{\rho_{vs}}\,dy, \qquad \eta_l = N_l \frac{\gamma(X)}{r}\int_\delta^y \frac{\rho_l}{\rho_{ls}}\,dy \tag{16}$$

$$f_v(\eta_v) = \frac{\Psi_v}{M_v \phi(X)}, \qquad f_l(\eta_l) = \frac{\Psi_l}{M_l \phi(X)} \tag{17}$$

$$\theta_v(\eta_v) = \frac{T_v - T_s}{\Delta T_{\text{sat}}}, \qquad \theta_l(\eta_l) = \frac{T_l - T_\infty}{\Delta T_{\text{sub}}} \tag{18}$$

where $X = x/r$. Furthermore, the constants M and N are chosen to be

$$M_v \equiv \nu_{vs}[g(\rho_{l\infty} - \rho_{vs})r^3/(\nu_{vs}^2 \rho_{vs})]^{1/4},$$
$$M_l \equiv \nu_{ls}[g(\rho_{l\infty} - \rho_{ls})r^3/(\nu_{ls}^2 \rho_{ls})]^{1/4} \tag{19}$$

$$N_v \equiv M_v/\nu_{vs}, \qquad N_l \equiv M_l/\nu_{ls} \tag{20}$$

On the other hand, ϕ and γ are assigned to satisfy approximately the following relations as functions of X:

Nomenclature (cont.)

q_{rp} = heat flux due to radiation for parallel plate, W/m^2
R = $[\rho_v \mu_v/(\rho_l \mu_l)]^{1/2}$
R_s = nondimensional quantity, equation (39)
r = radius of cylinder heater, m
Sc = $c_{pl}\Delta T_{\text{sub}}/L' =$ nondimensional subcooling
Sc_r = $c_{pl}\Delta T_{\text{sub}}/L =$ nondimensional subcooling
Sc_s = nondimensional subcooling, equation (38)
Sc^* = modified S_c, equation (74)
Sp = $c_{pv}\Delta T_{\text{sat}}/(L' \text{Pr}_v) =$ nondimensional superheat
Sp_r = $c_{pv}\Delta T_{\text{sat}}/(L \text{Pr}_v) =$ nondimensional superheat
Sp_s = nondimensional superheat, equation (38)
T = temperature, K
U = nondimensional quantity, equation (67)
u = x component velocity, m/s
V = nondimensional quantity, equation (67)
v = y component velocity, m/s
W_1, W_2 = nondimensional quantity in equation (67)
w = mass flux density, kg/(m^2 s)
X = $x/r =$ nondimensional angle measured from bottom of horizontal cylinder
x = coordinate along the heater surface, m
y = coordinate normal to the heater surface, m
z = coordinate measuring distance normal to the heater surface from vapor–liquid interface, m
α = absorptivity of liquid (taken to be unity in this paper)
β = thickness of laminar liquid layer, m
γ = function of X, equation (23)
ΔT_{sat} = heater surface superheat, K
ΔT_{sub} = liquid subcooling, K
δ = thickness of laminar vapor layer, m
ϵ_w = emissivity
ζ = β/δ
ζ_1 = a root of equation (65) given by equation (66)
η = nondimensional similarity variable, equation (16)
θ = nondimensional temperature, equation (18)
μ = viscosity, kg/(m s)
ν = kinematic viscosity, m^2/s
ρ = density, kg/m^3
σ = surface tension, N/m
σ_s = Stefan–Boltzmann constant
ϕ = function of X, equation (23)
Ψ = stream function

Subscripts

i = vapor–liquid interface
l = liquid
r = radiation
s = saturation
v = vapor
w = wall
∞ = bulk

$$\phi\gamma^3 = \sin X, \qquad \phi\gamma^2 \frac{d\phi}{dX} + \phi^2\gamma \frac{d\gamma}{dX} = 2 \sin X,$$

$$\frac{1}{\gamma}\frac{d\phi}{dX} = 3 \tag{21}$$

The following functions ϕ and γ that satisfy the first and third equations, and the second equation at $X = \pi/2$, are assumed to satisfy equation (21) approximately:

$$\phi(X) = \left[4\int_0^X \sin^{1/3} X' dX'\right]^{3/4} \tag{22}$$

$$\gamma(X) = \sin^{1/3} X/\phi^{1/3} \tag{23}$$

The fundamental equations (1) to (6) are transformed into the four ordinary differential equations

$$\left[\frac{(\rho\mu)_v}{(\rho\mu)_{vs}} f_v''\right]' - 2(f_v')^2 + 3f_v f_v'' + \frac{\{(\rho_{l\infty} - \rho)/\rho\}_v}{\{(\rho_{l\infty} - \rho)/\rho\}_{vs}} = 0 \tag{24}$$

$$\left[\frac{(\rho k)_v}{(\rho k)_{vs}} \theta_v'\right]' + 3\mathrm{Pr}_{vs} \frac{c_{pv}}{c_{pvs}} f_v \theta_v' = 0 \tag{25}$$

$$\left[\frac{(\rho\mu)_l}{(\rho\mu)_{ls}} f_l''\right]' - 2(f_l')^2 + 3f_l f_l'' + \frac{\{(\rho_{l\infty} - \rho)/\rho\}_l}{\{(\rho_{l\infty} - \rho)/\rho\}_{ls}} = 0 \tag{26}$$

$$\left[\frac{(\rho k)_l}{(\rho k)_{ls}} \theta_l'\right]' + 3\mathrm{Pr}_{ls} \frac{c_{pl}}{c_{pls}} f_l \theta_l' = 0 \tag{27}$$

where the primes denote differentiation with respect to η. The boundary conditions expressed by equations (7) to (9) are transformed into

$$(f_l)_i = K_s R_s (f_v)_i \tag{28}$$

$$(f_l')_i = K_s^2 (f_v')_i \tag{29}$$

$$(f_l'')_i = K_s^3 R_s (f_v'')_i \tag{30}$$

It is assumed that the radiation heat flux from a horizontal cylinder q_{rc} in equation (10) is approximately given by the function of angle X

$$q_{rc}(X) = q_{rp}\gamma(X)/\bar{\gamma} \tag{31}$$

where q_{rp} is the radiation heat flux for parallel plates

$$q_{rp} = \frac{1}{\pi}\int_0^\pi q_{rc} dX = \frac{\sigma_s}{1/\epsilon_w + 1/\alpha - 1}[T_w^4 - T_s^4] \tag{32}$$

and $\bar{\gamma}$ is the average value given by

$$\bar{\gamma} \equiv \frac{1}{\pi}\int_0^\pi \gamma(X) = 0.6122 \tag{33}$$

The values of $\gamma(X)/\bar{\gamma}$ for each angle from the bottom of the horizontal cylinder are tabulated in Table 1. As shown in the table, the q_{rc} is about 25 percent higher than q_{rp} at $X = 0$ and it gradually decreases with the increase in X to about 75 percent of that at $X = 5\pi/6$. Considering that the radiation contribution averaged over the cylinder surface is of major concern here, the total film boiling heat transfer coefficient including the radiation contribution will be obtained with this approximation.

Then the boundary condition, equation (10), is transformed into

Table 1 Angular variation of $\gamma(X)/\bar{\gamma}$

X	0	$\pi/6$	$\pi/3$	$\pi/2$	$2\pi/3$	$5\pi/6$	$11\pi/12$	π
$\gamma(X)/\bar{\gamma}$	1.24	1.22	1.17	1.08	0.95	0.75	0.59	0

$$Sp_s = -3(f_v/\theta_v')_i + \frac{1}{K_s R_s \mathrm{Pr}_{ls}}(\theta_l'/\theta_v')_i Sc_s + \frac{q_{rp} D}{2LN_v \bar{\gamma}\mu_{vs}(\theta_v')_i} \tag{34}$$

and equations (11) to (13) are transformed into

$$(\theta_v)_i = 0, \qquad (\theta_l)_i = 1 \tag{35}$$

$$f_v(0) = f_v'(0) = 0, \qquad \theta_v(0) = 1 \tag{36}$$

$$\lim_{\eta_l \to \infty} f_l' = \lim_{\eta_l \to \infty} \theta_l' = 0 \tag{37}$$

The nondimensional parameters in the listed equations above are

$$Sp_s \equiv \frac{c_{pvs}\Delta T_{\mathrm{sat}}}{L\mathrm{Pr}_{vs}}, \qquad Sc_s \equiv \frac{c_{pls}\Delta T_{\mathrm{sub}}}{L} \tag{38}$$

$$R_s \equiv \left[\frac{(\rho\mu)_{vs}}{(\rho\mu)_{ls}}\right]^{1/2}, \qquad K_s \equiv \left[\frac{\{(\rho_{l\infty} - \rho)/\rho\}_{vs}}{\{(\rho_{l\infty} - \rho)/\rho\}_{ls}}\right]^{1/4} \tag{39}$$

2.4 Heat Transfer Equation. The film boiling heat transfer coefficient averaged over the cylinder surface, including radiation contribution, is given by the following nondimensional equation:

$$\mathrm{Nu}_v = \frac{hD}{k_{vs}} = -2^{1/4}\bar{\gamma}(\mathrm{Gr}_{vs})^{1/4}\theta_v'(0)\frac{(\rho k)_{vw}}{(\rho k)_{vs}}$$

$$= -0.728(\mathrm{Gr}_{vs})^{1/4}\theta_v'(0)\frac{(\rho k)_{vw}}{(\rho k)_{vs}} \tag{40}$$

where the nondimensional temperature gradient $\theta_v'(0)$ at the cylinder surface is numerically obtained by solving the ordinary differential equations described above with the use of an iteration method.

2.5 Comparison Between the Theoretical Solution and Experimental Results for Horizontal Cylinders With Large Radiation Emissivity. The authors' newly obtained pool film boiling heat transfer data from a horizontal platinum cylinder in various liquids for wide ranges of liquid subcooling, surface superheat, system pressure, and cylinder diameter are compared with the theoretical solutions in detail in part 2 of this work. As the authors have already pointed out in their discussion of the results of their water experiment (Sakurai et al., 1986), the saturated and subcooled film boiling heat transfer coefficients for a horizontal platinum cylinder of nondimensional diameter around 1.3 (the radiation emissivity of which is negligibly small) agree well with the theoretical solution in a comparatively lower superheat region even for various liquids and, for higher superheat and for higher or lower values of the nondimensional diameter, the heat transfer coefficients gradually become higher than the theoretical values.

To verify the applicability of the theoretical solution including the radiation effect obtained here, the theoretical solution is compared with the experimental results obtained by using horizontal cylinders of nondimensional diameter around 1.3 with very low and very high radiation emissivities in water.

The authors' experimental results for the pool film boiling heat transfer coefficients from 3 and 4-mm-dia horizontal platinum cylinders (nondimensional diameters 1.25 and 2 and radiation emissivity around 0.12) in water at pressures of 294 kPa and 1960 kPa, respectively, are shown against surface superheat in Figs. 2 and 3 with the liquid subcooling as a parameter. The theoretical values including the radiation effect are shown in each figure for comparison. The experimental data agree very well with these theoretical values. The theoretical values if there were no radiation are also shown in these figures. These values are almost in agreement with the theoretical values including radiation contribution because of the low emissivity of the platinum. It is confirmed that subcooled pool film boiling heat transfer coefficients including

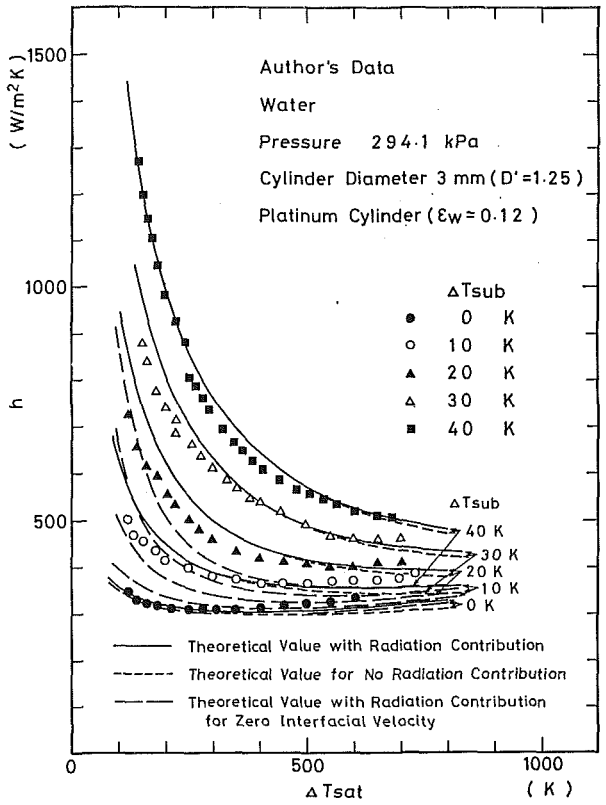

Fig. 2 Comparison of theoretical values including and not including radiation contribution with the authors' data on 3-mm-dia horizontal platinum cylinder ($D' \simeq 1.25$) in water at a pressure of 294 kPa

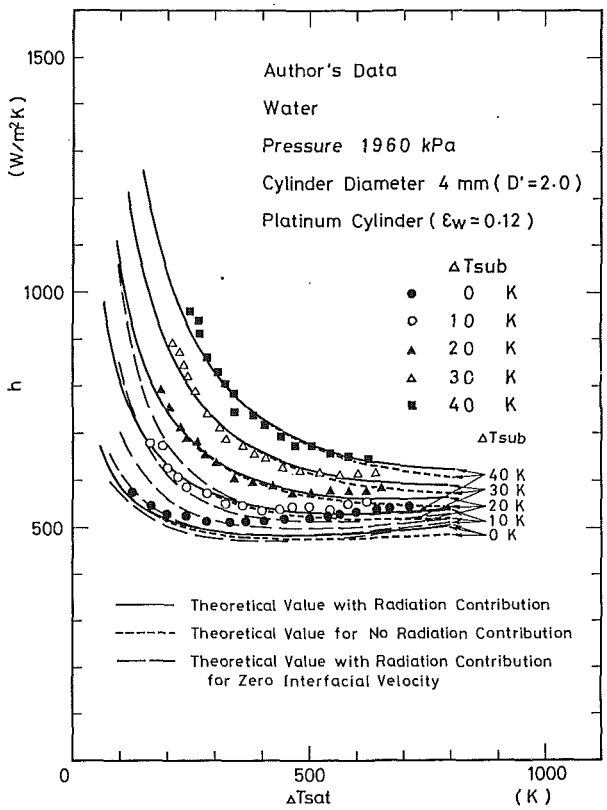

Fig. 3 Comparison of theoretical values including and not including radiation contribution with the authors' data on 4-mm-dia horizontal platinum cylinder ($D' = 2.0$) in water at a pressure of 1960 kPa

little radiation effect (namely, convection contribution) in water for $D' \simeq 1.3$ are predicted well by the theoretical model based on laminar boundary layer theory in a comparatively wide surface superheat region. However, it should be noted that the theoretical solution for the boundary condition of zero tangential vapor and liquid velocities instead of equations (8) and (9) at the vapor–liquid interface, neglecting the flow induced by the action of shear forces similar to that supposed by Sparrow and Cess (1962) in their analysis of film boiling heat transfer from a vertical plate, cannot at all predict the experimental results for subcooled conditions, though it predicts well the results for saturated conditions as shown in these figures. This means that the liquid flow caused by the action of the shear forces at the vapor–liquid interface performs an important role for subcooled film boiling heat transfer in comparison with free convection in the liquid phase.

The experimental results, including a large radiation contribution for $D' \simeq 1.3$ obtained by Siviour and Ede (1970), whose experimental conditions are almost the same except for the large radiation emissivity of the horizontal cylinder, are shown in Figs. 4 and 5. These figures show their data of pool film boiling heat flux versus subcooling for water on 3.2 and 6.4-mm-dia horizontal cylinders (nondimensional diameters 1.28 and 2.6) with a radiation emissivity of 0.75 and the cylinder surface superheat as a parameter. These data are for surface superheats of 444, 611, and 779 K, and for water subcoolings ranging from 0 to 80 K at atmospheric pressure. The theoretical pool film boiling heat fluxes q, including radiation contributions numerically derived from the theoretical model obtained here, are shown in these figures for comparison. The theoretical values, including the radiation contributions, are seen to be in good agreement with the experimental results.

The theoretical pool film boiling heat fluxes q_{co} for no radiation contribution are also shown in these figures. The difference between q and q_{co} at a certain surface superheat becomes smaller with the increase in the liquid subcooling and becomes larger with the increase in the surface superheat. The difference at $\Delta T_{sat} = 779$ K for $\Delta T_{sub} = 80$ K in Fig. 5, as a typical example, corresponds to about 29 percent of the radiation heat flux q_{rp} given by equation (32). The convective heat flux q_c ($q_c = q - q_{rp}$) becomes lower than q_{co} by about 71 percent of the radiation heat flux, because of vapor film thickness due to the radiation heat transfer.

It was postulated to derive the theoretical solution including the radiation contribution that radiation heat transfer from the cylinder to the vapor–liquid interface would be absorbed in a negligibly small distance in the liquid and then produce vapor. If some part of the radiation is assumed to penetrate into the liquid, the difference between q and q_{co} at the same ΔT_{sat} and ΔT_{sub} will increase up to near q_{rp} depending on the increase of the penetration ratio. Judging from the fact that the theoretical solution agreed well with the experimental results as shown in Figs. 4 and 5, the postulation for the theoretical model is considered to be reasonable.

3 Analytical Solution of Theoretical Pool Film Boiling Model With Radiation Effects

Rigorous solution of the theoretical model can only be obtained numerically. In this section, it is intended to derive an approximate analytical solution of the theoretical model, which is necessary as a basic equation for a general correlation for pool film boiling heat transfer.

The pool film boiling heat transfer coefficient h under saturated and subcooled conditions is expressed by the equation, similar to the expression for saturated pool film boiling heat transfer given by Bromley (1950),

$$h = h_{co} + Jh_r \tag{41}$$

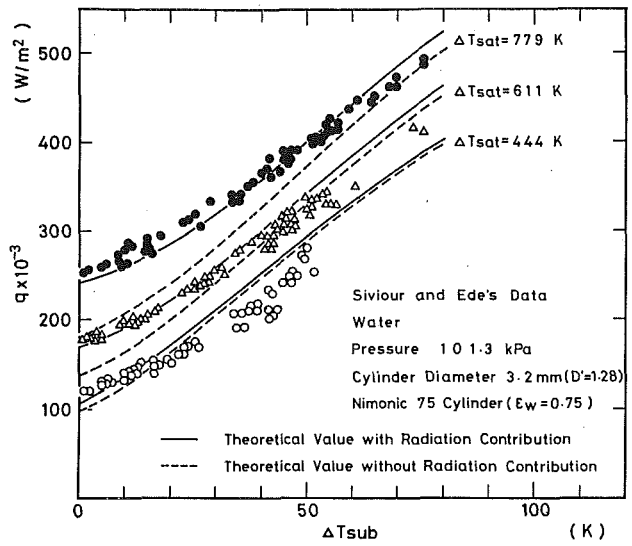

Fig. 4 Comparison of theoretical values including and not including radiation contribution with Siviour and Ede's data on 3.2-mm-dia horizontal cylinder ($D' = 1.28$, $\epsilon_W = 0.75$) in water at atmospheric pressure

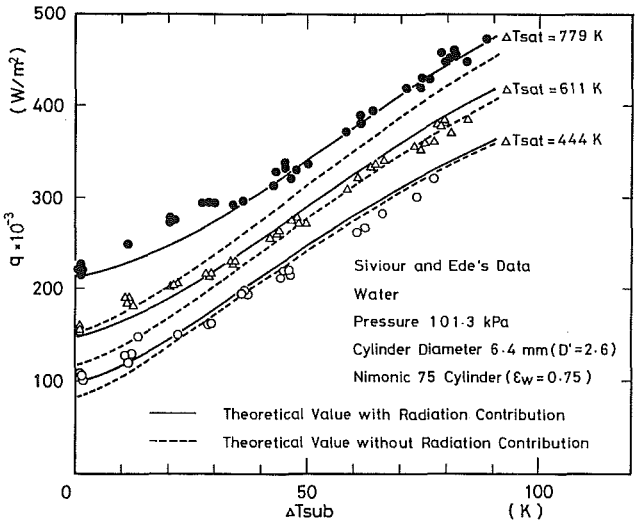

Fig. 5 Comparison of theoretical values including and not including radiation contribution with Siviour and Ede's data on 6.4-mm-dia horizontal cylinder ($D' = 2.6$, $\epsilon_W = 0.75$) in water at atmospheric pressure

$$h_r = \frac{\sigma_s}{1/\epsilon_w + 1/\alpha - 1} \frac{T_w^4 - T_s^4}{\Delta T_{sat}} \tag{42}$$

where h_{co} is the pool film boiling heat transfer coefficient if there were no radiation including an effect of liquid subcooling, J is a radiation parameter, and h_r is a radiation heat transfer coefficient for parallel plates.

3.1 Pool Film Boiling Heat Transfer Coefficient Without Radiation Contribution. To derive the analytical solution of the theoretical model for the pool film boiling heat transfer coefficient without a radiation contribution, the pool film boiling heat transfer coefficient from a vertical plate of uniform temperature is considered first, and then the result for a vertical plate is transformed to that for a horizontal cylinder by using a result for Hermann's transformation.

The following assumptions are made in the theoretical pool film boiling model based on laminar boundary layer theory to obtain the approximate analytical solution in a simple form.

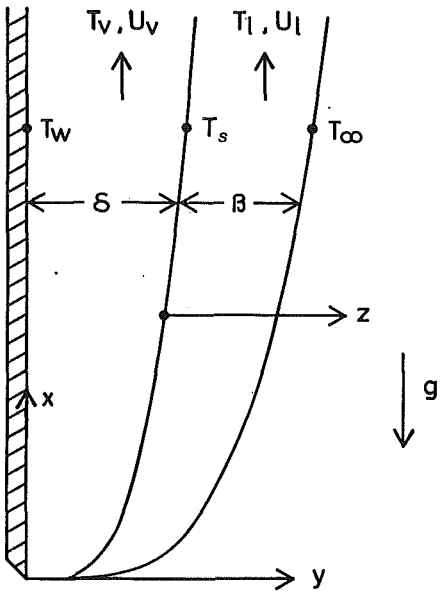

Fig. 6 Physical model and coordinate

The resultant analytical solution will be modified by comparing it with the rigorous solution.

1 As shown in Fig. 6, a laminar liquid sublayer is supposed to exist outside the vapor boundary layer, and outside the liquid layer, the liquid is supposed to be stagnant and at a constant bulk temperature T_∞.

2 The thermophysical properties of vapor and liquid are supposed to be constant at the values for $0.5(T_w + T_s)$ and $T_s - 0.5\Delta T_{sub}$, respectively.

3 Inertia forces and convective energy transports of vapor and liquid, and body force in the liquid are neglected to get the temperature and velocity distributions. Body force in the liquid may be negligible because a major contribution to the pool film boiling heat transfer for large subcooling is liquid flow induced by the action of the shear forces at the vapor-liquid interface. The convective energy transports will be evaluated approximately by integral forms of energy balance equations for vapor and liquid layers described later.

For the vapor boundary layer, momentum and energy conservation, respectively, take the form

$$g(\rho_l - \rho_v) + \mu_v \frac{\partial^2 u_v}{\partial y^2} = 0 \tag{43}$$

$$k_v \frac{\partial^2 T_v}{\partial y^2} = 0 \tag{44}$$

For the liquid boundary layer

$$\mu_l \frac{\partial^2 u_l}{\partial z^2} = 0 \tag{45}$$

$$k_l \frac{\partial^2 T_l}{\partial z^2} = 0 \tag{46}$$

The boundary conditions are as follows:

(*a*) *At the plate interface* ($y = 0$)

$$u_v = 0, \qquad T_v = T_w \tag{47}$$

(*b*) *At the vapor-liquid interface* ($y = \delta$, $z = 0$)

$$u_v = u_l, \qquad T_v = T_l = T_s, \qquad \mu_v \left.\frac{\partial u_v}{\partial y}\right|_{y=\delta} = \mu_l \left.\frac{\partial u_l}{\partial z}\right|_{z=0} \tag{48}$$

(*c*) *At the outer end of the liquid layer* ($z = \beta$)

$$u_l = 0, \qquad T_l = T_\infty \tag{49}$$

The velocity distributions for both layers are

$$u_v = -\frac{g(\rho_l-\rho_v)}{2\mu_v}y^2 + \frac{g(\rho_l-\rho_v)\delta}{2\mu_v}\left[\left(\frac{\mu_l}{\mu_v} + 2\frac{\beta}{\delta}\right)\Big/\left(\frac{\mu_l}{\mu_v}+\frac{\beta}{\delta}\right)\right]y \tag{50}$$

$$u_l = -\frac{g(\rho_l-\rho_v)\delta}{2\mu_l}\frac{\mu_l/\mu_v}{\mu_l/\mu_v+\beta/\delta}z + \frac{g(\rho_l-\rho_v)\delta^2}{2\mu_l}\frac{(\mu_l/\mu_v)(\beta/\delta)}{\mu_l/\mu_v+\beta/\delta} \tag{51}$$

The temperature distributions are

$$T_v = T_w - (y/\delta)(T_w - T_s) \tag{52}$$

$$T_l = T_s - (z/\beta)(T_s - T_\infty) \tag{53}$$

The integral forms of the energy balance equations for both boundary layers are

$$L'\frac{d}{dx}\int_0^\delta \rho_v u_v dy = \frac{k_v(T_w-T_s)}{\delta} - \frac{k_l(T_s-T_\infty)}{\beta} \tag{54}$$

$$c_{pl}\frac{d}{dx}\int_0^\beta \rho_l u_l (T_l - T_\infty)dz = \frac{k_l(T_s-T_\infty)}{\beta} \tag{55}$$

By combining equations (50) and (52) with equation (54), and equations (51) and (53) with equation (55), one obtains

$$\frac{d}{dx}[\delta^3 m_v] = \frac{C_{v1}}{\delta} - \frac{C_{v2}}{\delta\zeta} \tag{56}$$

$$\frac{d}{dx}[\delta^3 m_l] = \frac{C_l}{\delta\zeta} \tag{57}$$

where

$$f=\mu_l/\mu_v, \qquad \zeta=\beta/\delta \tag{58}$$

$$m_v = (f+4\zeta)/(f+\zeta), \qquad m_l = f\zeta^2/(f+\zeta) \tag{59}$$

$$C_{v1} = 12\mu_v k_v(T_w-T_s)/\{L'g\rho_v(\rho_l-\rho_v)\} \tag{60}$$

$$C_{v2} = 12\mu_v k_v(T_s-T_\infty)/\{L'g\rho_v(\rho_l-\rho_v)\} \tag{61}$$

$$C_l = 6\mu_l k_l/\{gc_{pl}\rho_l(\rho_l-\rho_v)\} \tag{62}$$

The only solution that satisfies equations (56) and (57) simultaneously and has practical meaning at $x=0$ is $\zeta=\zeta_1$ (independent of x; β and δ take the same functional forms of x). Integration of equations (56) and (57) leads to

$$\frac{\delta^4}{x} = \frac{4(f+\zeta_1)(C_{v1}\zeta_1 - C_{v2})}{3(f+4\zeta_1)\zeta_1} \tag{63}$$

and

$$\frac{\delta^4}{x} = \frac{4C_l(f+\zeta_1)}{3f\zeta_1^3} \tag{64}$$

Equations (63) and (64) give

$$fC_{v1}\zeta_1^3 - fC_{v2}\zeta_1^2 - 4C_l\zeta_1 - fC_l = 0 \tag{65}$$

The root of equation (65) appropriate for this problem is

$$\zeta_1 = U + V + C_{v2}/(3C_{v1}) \tag{66}$$

where

$$U \equiv (W_1+\sqrt{W_2}), \qquad V \equiv (W_1-\sqrt{W_2}) \tag{67}$$

$$W_1 = (C_{v2}/3C_{v1})^3 + 2C_{v2}C_l/(3fC_{v1}^2) + C_l/(2C_{v1})$$

$$W_2 = [-4C_{v2}^2/(27fC_{v1}) + 2C_{v2}/3 - 64C_l/(27f^2)]\{C_l^2/(fC_{v1}^3)\} + \{C_l/(2C_{v1})\}^2 + (C_l/C_{v1})\{C_{V2}/(3C_{v1})\}^3$$

The local heat flux q_x at $x=x_1$ is given as

$$q_x = k_v(T_w-T_s)/\delta \tag{68}$$

From equation (64)

$$\delta = x_1^{1/4}\{(4/3)C_l(f+\zeta_1)/(f\zeta_1^3)\}^{1/4}$$

The heat flux averaged from $x=0$ to $x=x_1$ is

$$\bar{q}_x = \frac{1}{x_1}\int_0^{x_1} q_x dx = \frac{4}{3}\frac{k_v(T_w-T_s)}{\delta} \tag{69}$$

The pool film boiling heat transfer from a vertical plate averaged from $x=0$ to $x=x_1$ is expressed by the nondimensional equation

$$\mathrm{Nu}_{vx} = \frac{\bar{q}_x x_1}{k_v(T_w-T_s)} = \frac{4x_1}{3\delta} = \frac{4}{3}x_1^{3/4}\left[\frac{3}{4}\frac{f\zeta_1^3}{C_l(f+\zeta_1)}\right]^{1/4} = 0.793M_x^{1/4} \tag{70}$$

The pool film boiling heat transfer from a horizontal cylinder is approximately related to that from a vertical plate by using a result for Hermann's transformation (Nishikawa and Ito, 1966)

$$\mathrm{Nu}_v = \frac{h_{co}D}{k_v} = \frac{3}{4}\cdot 4^{1/4}\cdot 0.728\mathrm{Nu}_{vx}\left(\frac{D}{x_1}\right)^{3/4} = 0.612M^{1/4} \tag{71}$$

The nondimensional parameters in equations (70) and (71) are

$$M_x = [\mathrm{Gr}_{vx}\mathrm{Pr}_v L'/(c_{pv}\Delta T_{\mathrm{sat}})][E^3/\{1 + E/(Sp\mathrm{Pr}_l)\}]/(R\mathrm{Pr}_l Sp)^2$$

$$M = [\mathrm{Gr}_v\mathrm{Pr}_v L'/(c_{pv}\Delta T_{\mathrm{sat}})][E^3/\{1 + E/(Sp\mathrm{Pr}_l)\}]/(R\mathrm{Pr}_l Sp)^2$$

$$E = (A + C\sqrt{B})^{1/3} + (A - C\sqrt{B})^{1/3} + (1/3)Sc$$

$$A = (1/27)Sc^3 + (1/3)R^2 Sp\mathrm{Pr}_l Sc + (1/4)R^2 Sp^2\mathrm{Pr}_l^2$$

$$B = (-4/27)Sc^2 + (2/3)Sp\mathrm{Pr}_l Sc - (32/27)Sp\mathrm{Pr}_l R^2 + (1/4)Sp^2\mathrm{Pr}_l^2 + (2/27)Sc^3/R^2$$

$$C = (1/2)R^2 Sp\mathrm{Pr}_l$$

$$L' = L + 0.5c_{pv}\Delta T_{\mathrm{sat}}, \qquad R = [\rho_v\mu_v/(\rho_l\mu_l)]^{1/2}$$

$$Sc = c_{pl}\Delta T_{\mathrm{sub}}/L', \qquad Sp = c_{pv}\Delta T_{\mathrm{sat}}/(L'\mathrm{Pr}_v)$$

For saturated pool film boiling heat transfer ($Sc=0$) without radiation effects, equation (71) reduces to

$$\mathrm{Nu}_v = 0.612[\{0.5 + 2E/(Sp\mathrm{Pr}_l)\}/\{1 + E/(Sp\mathrm{Pr}_l)\}]^{1/4}[\mathrm{Gr}_v\mathrm{Pr}_v L'/(c_{pv}\Delta T_{\mathrm{sat}})]^{1/4} \tag{72}$$

where $E = (A + C\sqrt{B})^{1/3} + (A - C\sqrt{B})^{1/3}$, $A = (1/4)R^2 Sp^2\mathrm{Pr}_l^2$, $B = -(32/27)Sp\mathrm{Pr}_l R^2 + (1/4)Sp^2\mathrm{Pr}_l^2$, and $C = (1/2)R^2 Sp\mathrm{Pr}_l$.

Bromley (1950) derived the solutions of saturated film boiling heat transfer for two extreme cases based on a simple one-phase film boiling model. These two solutions are the third term of equation (72) multiplied by a constant of 0.512 if the saturated liquid is assumed to be stagnant, and by a constant of 0.724 if it is assumed to move freely with vapor. On the basis of his experimental results, he proposed a correlation of saturated film boiling heat transfer for no radiation effect. This is the third term of equation (72) with the mean value of these constants, 0.62. It is understood that the authors' correlation for the saturation condition given by equation (72) is Bromley's correlation multiplied by a new term (the second term of equation (72)) as a result of more general treatment at the vapor-liquid interface. If the liquid viscosity approaches infinity or zero, which corresponds to the conditions that the saturated liquid is stagnant or move freely with the vapor at the vapor-liquid interface, the value of the combined first and second terms of equation (72) becomes 0.515 or 0.728, respectively. These values agree with those of Bromley, though slight differences exist.

The pool film boiling heat transfer coefficients for no radiation contribution, h_{co}, obtained from the approximate analytical solution, equation (71), for various liquids of widely

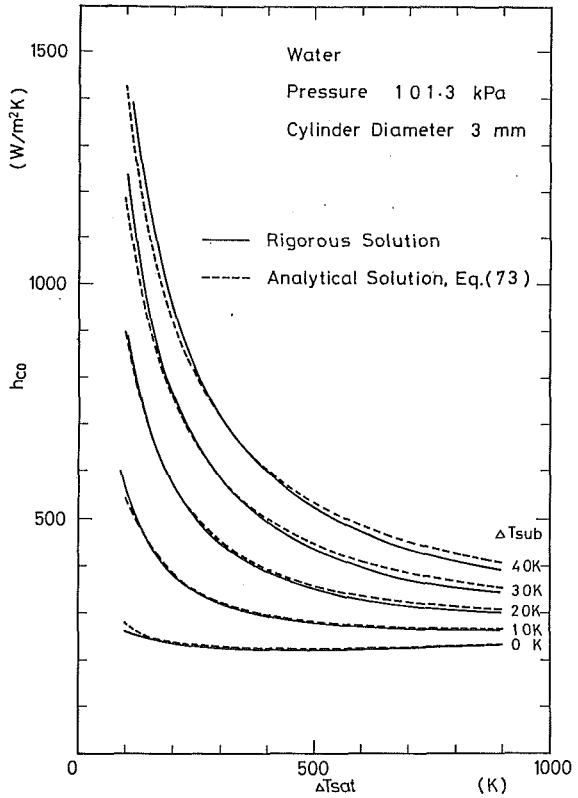

Fig. 7 Values of h_{co} for water from the analytical solution, equation (73), compared with the rigorous solution

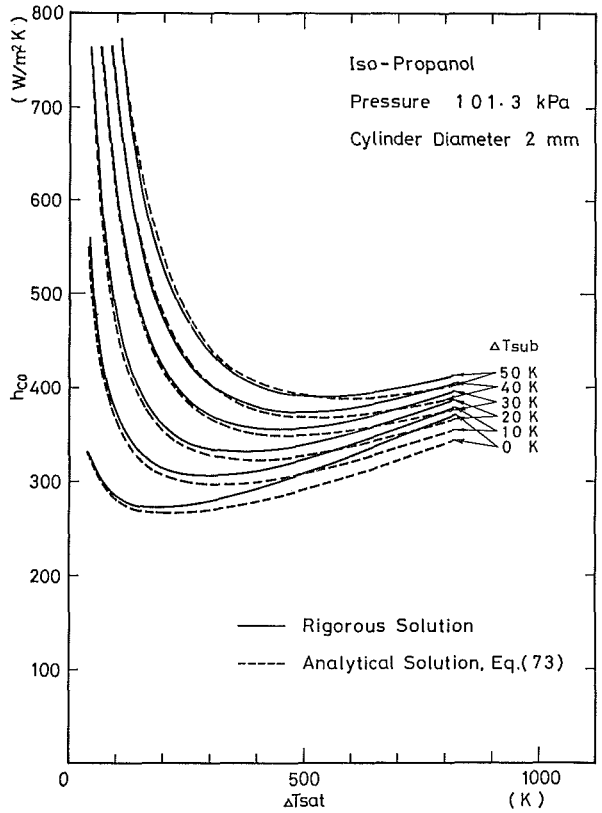

Fig. 8 Values of h_{co} for iso-propanol from the analytical solution, equation (73), compared with the rigorous solution

different physical properties, are compared with those from the rigorous numerical solution of the theoretical model for no radiation effect. For the liquids whose Prandtl numbers are

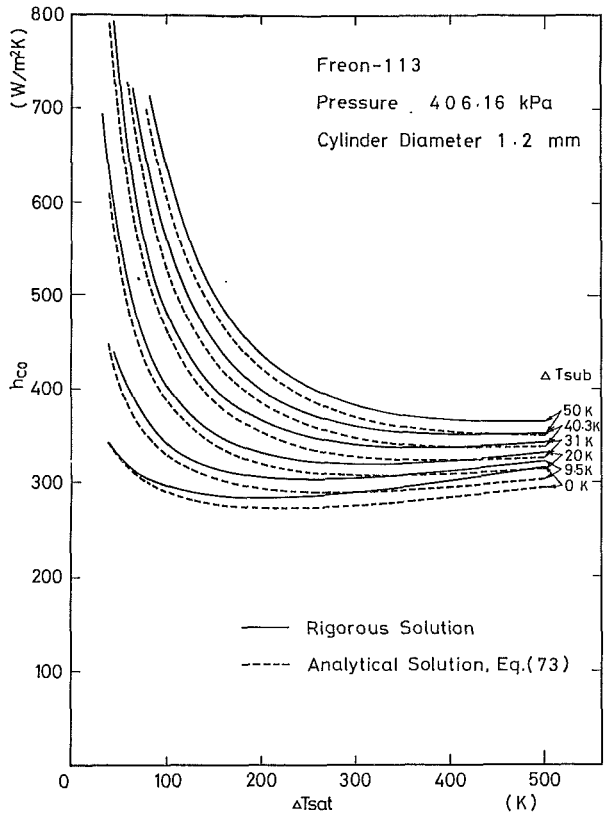

Fig. 9 Values of h_{co} for Freon-113 from the analytical solution, equation (73), compared with the rigorous solution

around unity, such as water, liquid nitrogen, and liquid argon, the values of h_{co} obtained from this approximate analytical solution are in good agreement with those from the rigorous numerical solution within -10 to 3 percent error under saturated and subcooled conditions. This means that the several assumptions made on the derivation of the approximate analytical solution do not cause a serious error for the liquids with the Prandtl numbers around unity.

However, for liquids with higher Prandtl numbers, such as freons and alcohols, the approximate values calculated from equation (71) become lower than the values of the rigorous solution with the increase in subcooling, though they are almost in agreement under the saturated condition. In the case of iso-propanol under atmospheric pressure for instance, the heat transfer coefficients derived from the analytical solution for $\Delta T_{sub} = 50$ K are about 20 percent lower than those from the rigorous one. On the contrary, for the liquids whose Prandtl numbers are far lower than unity such as liquid metals, the approximate values calculated from equation (71) under subcooled condition are higher than the values derived from the rigorous solution, though they are almost in agreement under the saturated condition. In the case of sodium under atmospheric pressure for instance, the appxoximate values from equation (71) for $\Delta T_{sub} = 50$ K at around $\Delta T_{sat} = 1000$ K are about 2 times higher than those from the rigorous solution.

The analytical solution of the theoretical model for no radiation contribution was derived under the supposition that the thermal boundary layer thickness in the liquid was equal to that of the velocity boundary layer as mentioned before. This supposition probably is the major cause of the abovementioned error of the analytical solution for the subcooled liquids whose Prandtl numbers are far higher or lower than unity and it will be valid only for liquids whose Prandtl numbers are around unity. To make the approximate

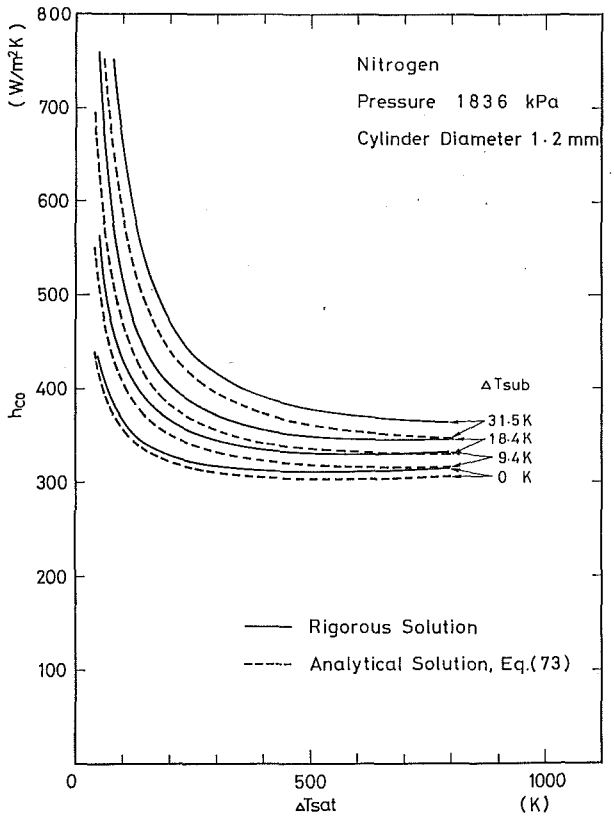

Fig. 10 Values of h_{co} for nitrogen from the analytical solution, equation (73), compared with the rigorous solution

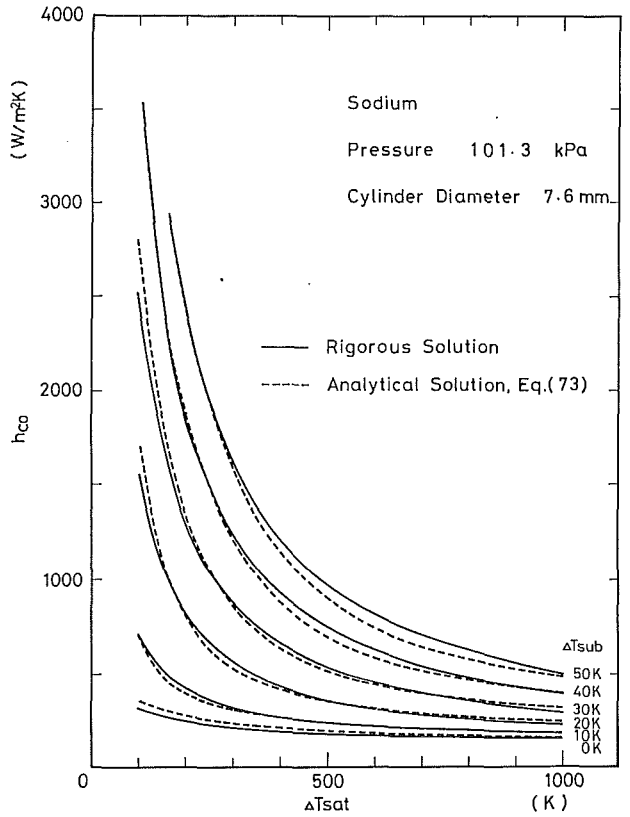

Fig. 11 Values of h_{co} for sodium from the analytical solution, equation (73), compared with the rigorous solution

analytical solution agree with the rigorous numerical solution for various liquids under a wide range of conditions, equation (71) was modified to

$$\mathrm{Nu}_v = 0.612 M^{*0.25} \tag{73}$$

where M^* is given by the same expression as M except that the modified subcooling parameter Sc^* is used instead of Sc as

$$Sc^* = KSc \tag{74}$$

where $K = [0.93\mathrm{Pr}_l^{0.22} + 3.0\exp(-100.0 Sp \mathrm{Pr}_l Sc^{-0.8})]$ $[0.45\times10^5 \mathrm{Pr}_l Sc/(1+0.45\times10^5 \mathrm{Pr}_l Sc)]$. For liquids other than liquid metals, K becomes simpler as

$$K = 0.93\mathrm{Pr}_l^{0.22}$$

This modification was performed by first choosing the functional form of K as functions of nondimensional parameters appeared in the analytical solution of h_{co}, and by least square fitting the coefficient and exponent of each parameter. In Figs. 7 to 11, the values of h_{co} obtained from equation (73) and the values from rigorous numerical solution are shown for comparison against the cylinder surface superheat with the liquid subcooling as a parameter for various liquids of widely different physical properties, such as iso-propanol, which has a large Prandtl number, and liquid sodium, which has a very low Prandtl number. They are in good agreement with each other within -10 to $+5$ percent error as shown in these figures. As for the liquid metals, not only the values for liquid sodium but also for other liquid metals such as potassium, rubidium, and cesium are in good agreement with the values from the rigorous numerical solution.

3.2 Radiation Parameter. Referring to equation (41), the radiation parameter J can be obtained from the difference of two theoretical pool film boiling heat transfer coefficients given as the rigorous numerical solutions of the theoretical model with and without a radiation effect at the same cylinder surface superheat. Relations between J and surface superheat ΔT_{sat} were obtained with liquid subcooling ΔT_{sub} as a parameter for water, ethanol, iso-propanol, Freon-113, Freon-11, liquid nitrogen, liquid argon, liquid helium, and liquid sodium for wide ranges of pressure, subcooling, and cylinder surface superheat. Typical results of J versus ΔT_{sat} curve for the platinum cylinders with negligibly small emissivity are shown in Figs. 12 and 13 for water and liquid nitrogen, respectively. Typical J versus ΔT_{sat} curves for the cylinders made of alloys such as stainless steel and nichrome, whose emissivities at around 1000 K are about 0.75, are shown in Figs. 14 and 15 for water and sodium. The value of J is higher for lower subcooling and it becomes higher with the increase in heater surface superheat. Higher system pressure and higher emissivity of the heater surface material result in a higher value of J for each heater surface superheat at a certain subcooling.

It is assumed that J is a function of h_{co}/h_r and the nondimensional quantities appeared in the analytical solution of h_{co}. The following radiation parameter equation is obtained to express the values of J for various kinds of liquid under wide ranges of pressure, surface superheat, liquid subcooling, and radiation emissivity:

$$J = F + (1-F)/(1+1.4h_{co}/h_r) \tag{75}$$

where

$F =$

$$[1-0.25\exp(-0.13Sp_r)]\exp(-0.64R^{-0.60}\mathrm{Pr}_l^{-0.45}Sp_r^{-0.73}Sc_r^{1.1}) \quad \text{for } F \geq 0.19$$

$$F = 0.19 \quad \text{for } F < 0.19$$

$$Sp_r = c_{pv}\Delta T_{sat}/(L\mathrm{Pr}_v), \qquad Sc_r = c_{pl}\Delta T_{sub}/L$$

It was confirmed that the radiation parameters for large and very small emissivities obtained for the various liquids and for

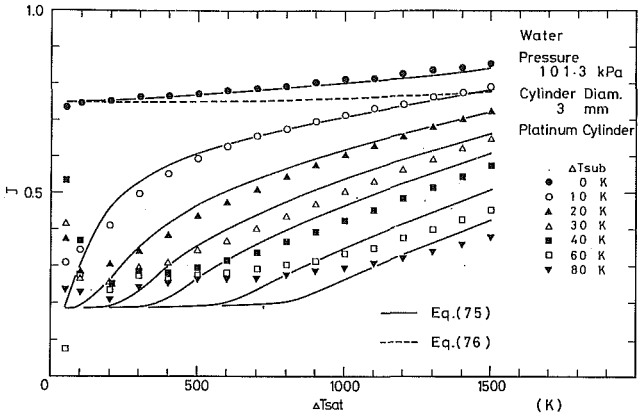

Fig. 12 Radiation parameter J for platinum cylinder in water against surface superheat with liquid subcooling as a parameter

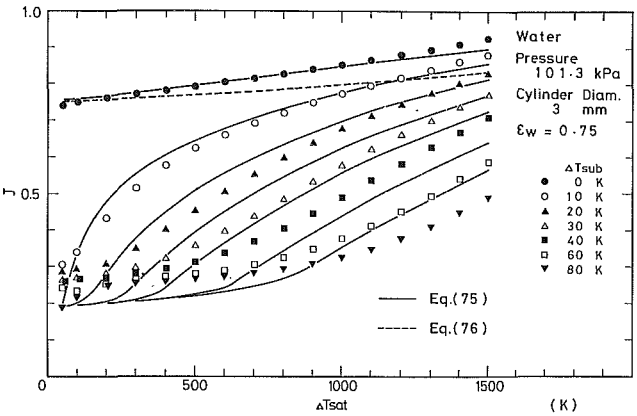

Fig. 14 Radiation parameter J for a cylinder of $\epsilon_w = 0.75$ in water against surface superheat with liquid subcooling as a parameter

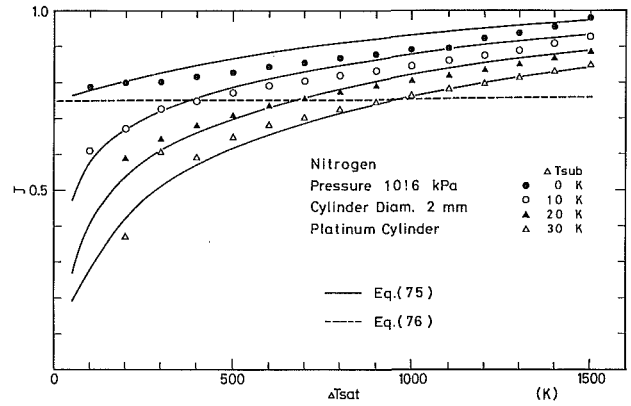

Fig. 13 Radiation parameter J for platinum cylinder in liquid nitrogen against surface superheat with liquid subcooling as a parameter

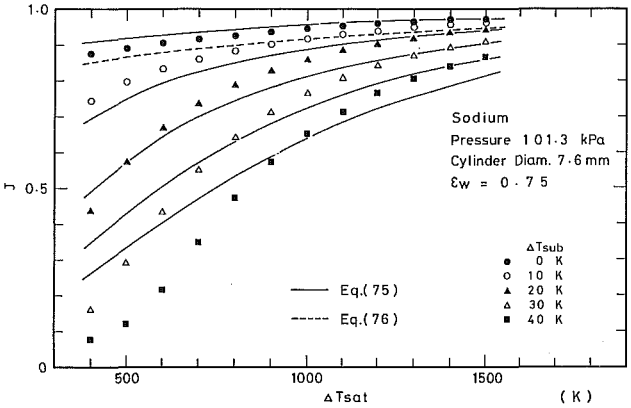

Fig. 15 Radiation parameter J for a cylinder of $\epsilon_w = 0.75$ in liquid sodium against surface superheat with liquid subcooling as a parameter

wide ranges of pressure, subcooling, and cylinder surface superheat are expressed within 20 percent error by equation (75), except for high subcooling and low surface superheat for liquid sodium. The values of J obtained from equation (75) are shown in Figs. 12 to 15 for comparison as typical examples.

Bromley (1950) performed a qualitative study on the effect of radiation and presented the simple radiation parameter equation for saturated pool film boiling

$$J = \frac{3}{4} + \frac{1}{4}\left[\frac{1}{1+2.6h_{co}/h_r}\right] \tag{76}$$

Lubin (1969) analyzed the film boiling from a vertical plate and presented an analytical solution including a radiation effect, which substantiated Bromley's qualitative solution. The values of J obtained from equation (76) are shown in Figs. 12 to 15 for comparison with the authors' values. Although Bromley derived the radiation parameter qualitatively based on the assumption that the temperature distribution in the vapor layer is linear and h_{co} is inversely proportional to the vapor film thickness, the authors' values for various liquids under saturation conditions almost agree with the values given by equation (76) at comparatively lower surface superheats as shown in these figures. The authors' values of J become gradually larger than the values given by equation (76) with the increase in the surface superheat. These increasing rates from the latter values depend on kinds of liquid; they are higher for liquids with lower latent heats, such as alcohols, freons, and cryogenic liquids, than those for the liquids with higher latent heats, such as water and liquid sodium. At 1500 K of the surface superheat, for instance, the authors' values of J are about 10 and 26 percent higher than those from equation (76) for water and for liquid nitrogen, respectively.

Siviour and Ede (1970), and Hamill and Baumeister (1967) assumed that Bromley's equation for the radiation parameter for saturated film boiling is applicable to that in subcooled film boiling. However, the results of this theoretical radiation parameter study do not support this assumption. The difference between q and q_{co} (i.e., Jq_{rp}), for $\Delta T_{sat} = 779$ K and $\Delta T_{sub} = 80$ K on the graph of q versus ΔT_{sub} shown in Fig. 5, corresponds to $0.29q_{rp}$. That is, J is 0.29. This value also can be evaluated from the J versus ΔT_{sat} curve shown in Fig. 12. If the value of J is evaluated by using equation (76) given by Bromley, the value becomes about 0.76, which corresponds to 2.6 times of the value given by the authors. This value will cause overestimation of the total heat flux for pool film boiling by about 12 percent at the conditions mentioned above.

3.3 Comparison Between the Analytical Solution With Radiation Effect and the Rigorous Solution. The approximate analytical solution of the theoretical model with radiation effect thus obtained is given by equation (41) combined with equations (42), (73), and (75). Pool film boiling heat transfer coefficients including a radiation contribution that are calculated from the approximate analytical solution are compared with the rigorous numerical solutions in Fig. 16 for several kinds of liquids. The emissivity of the cylinder was chosen to be 0.75 in this comparison. As shown in this figure, these two coefficients agree with each other within 7 percent error. It was confirmed that the pool film boiling heat transfer coefficients obtained from the rigorous numerical solutions for various liquids of widely different physical properties are predicted with good accuracy by the analytical solutions.

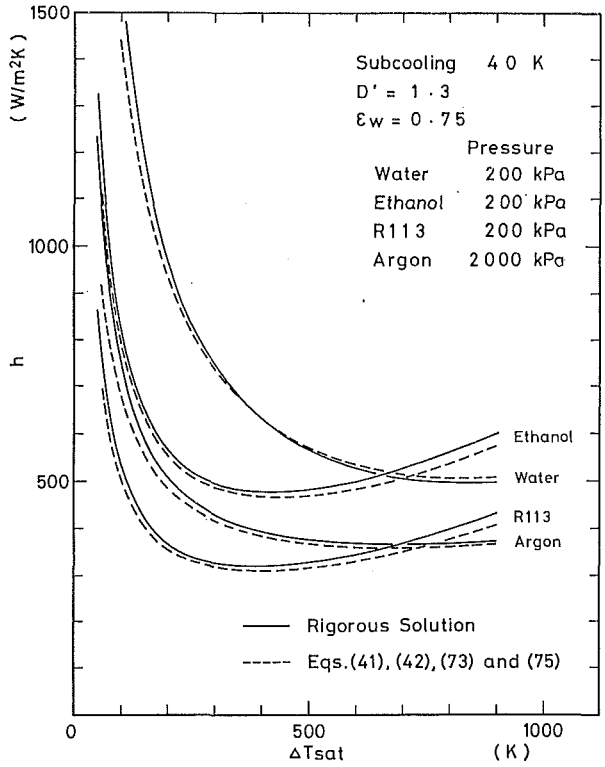

Fig. 16 Pool film boiling heat transfer coefficients including radiation effects for various liquids under subcooled conditions calculated from the analytical solution compared with the rigorous solutions

4 Conclusions

A rigorous numerical solution of the theoretical model for pool film boiling heat transfer from a horizontal cylinder based on laminar boundary layer theory, including the contributions of liquid subcooling and radiation from the cylinder, was derived. It was confirmed that the rigorous solution predicted well the experimental results of pool film boiling heat transfer from a horizontal cylinder with high radiation emissivity for a wide range of water subcooling for nondimensional cylinder diameters around 1.3. There the experimental data of saturated and subcooled pool film boiling heat transfer from the cylinder with negligible radiation emissivity in water agreed well with the values derived from the same theoretical model but excluding radiation contribution for a wide range of the cylinder surface superheat.

An approximate analytical solution of the theoretical model was derived as the sum of the pool film boiling heat transfer coefficient if there were no radiation h_{co} and the radiation heat transfer coefficient for parallel plates h_r, the latter first multiplied by the nondimensional radiation parameter J. The approximate analytical solution accorded very well with the rigorous numerical solution of the theoretical model for various kinds of liquids including both those with low latent heat and those with the Prandtl number far higher or lower than unity.

References

Bromley, L. A., 1950, "Heat Transfer in Stable Film Boiling," *Chem. Eng. Prog.*, Vol. 46, pp. 221–227.

Breen, B. P., and Westwater, J. W., 1962, "Effect of Diameter of Horizontal Tube on Film Boiling Heat Transfer," *Chem. Eng. Prog.*, Vol. 58, pp. 67–72.

Hamill, T. D., and Baumeister, K. J., 1967, "Effect of Subcooling and Radiation on Film Boiling Heat Transfer From a Flat Plate," NASA TN D-3925.

Koh, J. C. Y., 1962, "Analysis of Film Boiling on Vertical Surface," ASME JOURNAL OF HEAT TRANSFER, Vol. 84, pp. 55–62.

Lubin, B. T., 1969, "Analytical Derivation for Total Heat Transfer Coefficient in Stable Film Boiling From Vertical Plate," ASME JOURNAL OF HEAT TRANSFER, Vol. 91, pp. 452–453.

Nishikawa, K., and Ito, T., 1966, "Two-Phase Boundary Layer Treatment of Free Convection Film Boiling," *Int. J. Heat and Mass Transfer*, Vol. 9, pp. 103–115.

Nishikawa, K., Ito, T., and Matsumoto, K., 1976, "Investigation of Variable Thermophysical Property Problem Concerning Pool Film Boiling From Vertical Plate With Prescribed Uniform Temperature," *Int. J. Heat and Mass Transfer*, Vol. 19, pp. 1173–1182.

Sakurai, A., Shiotsu, M., and Hata, K., 1984, "Effect of System Pressure on Film-Boiling Heat Transfer, Minimum Heat Flux, and Minimum Temperature," *Nuclear Science and Engineering*, Vol. 88, pp. 321–330.

Sakurai, A., Shiotsu, M., and Hata, K., 1986, "Effect of Subcooling on Film Boiling Heat Transfer From Horizontal Cylinder in a Pool of Water," *Proceedings, 8th International Heat Transfer Conference*, C. L. Tien et al., eds., Hemisphere Publishing Corp., Washington DC, Vol. 4, pp. 2043–2048.

Siviour, J. B., and Ede, A. J., 1970, "Heat Transfer in Subcooled Pool Film Boiling," *Proceedings, 4th International Heat Transfer Conference*, U. Grigull et al., eds., Elsevier Publishing Co., Amsterdam, Vol. V, B3.12.

Sparrow, E. M., and Cess, R. D., 1962, "The Effect of Subcooled Liquid on Laminar Film Boiling," ASME JOURNAL OF HEAT TRANSFER, Vol. 84, pp. 103–115.

A General Correlation for Pool Film Boiling Heat Transfer From a Horizontal Cylinder to Subcooled Liquid: Part 2—Experimental Data for Various Liquids and Its Correlation

A. Sakurai
Professor.
Mem. ASME

M. Shiotsu
Associate Professor.
Mem. ASME

K. Hata
Instructor.

Institute of Atomic Energy,
Kyoto University,
Uji, Kyoto 611, Japan

Experimental data of pool film boiling heat transfer from horizontal cylinders in various liquids such as water, ethanol, isopropanol, Freon-113, Freon-11, liquid nitrogen, and liquid argon for wide ranges of system pressure, liquid subcooling, surface superheat and cylinder diameter are reported. These experimental data are compared with a rigorous numerical solution and an approximate analytical solution derived from a theoretical model based on laminar boundary layer theory for pool film boiling heat transfer from horizontal cylinders including the effects of liquid subcooling and radiation from the cylinder. A new correlation was developed by slightly modifying the approximate analytical solution to agree better with the experimental data. The values calculated from the correlation agree with the authors' data within ± 10 percent, and also with other researchers' data for various liquids including those with large radiation effects, though these other data were obtained mainly under saturated conditions at atmospheric pressure.

1 Introduction

Even though many experimental data of saturated pool film boiling heat transfer from horizontal cylinders for various conditions have been reported, there are few data for the subcooled case. The effect of liquid subcooling on pool film boiling heat transfer from a cylinder has been studied only under limited conditions, such as in water at atmospheric pressure, by a few investigators (Tachibana and Fukui, 1961; Siviour and Ede, 1970).

The authors (Sakurai et al., 1982, 1984, 1986) carried out, for the first time, systematic experiments concerned with the saturated and subcooled film boiling on a horizontal cylinder in a pool of water for wide ranges of experimental conditions. They presented a correlation for pool film boiling heat transfer from a horizontal cylinder in water by modifying an approximate solution of a theoretical pool film boiling model in light of the experimental data.

The purposes of this work are: first, to obtain the experimental data of pool film boiling heat transfer from a horizontal cylinder in various liquids of widely different physical properties for wide ranges of surface superheat, liquid subcooling, system pressure, and cylinder diameter; second, to compare the data with the values derived from the rigorous numerical and approximate analytical solutions of the theoretical model based on laminar boundary layer theory for pool film boiling heat transfer from a horizontal cylinder including the effects of liquid subcooling and the radiation from the cylinder previously reported (Sakurai et al., 1990); and third, to derive a new correlation applicable to various kinds of liquids by slightly modifying the approximate analytical solution to agree better with the experimental data for various liquids.

Contributed by the Heat Transfer Division for publication in the JOURNAL OF HEAT TRANSFER. Manuscript received by the Heat Transfer Division August 1, 1988; revision received July 20, 1989. Keywords: Boiling, Natural Convection, Radiation Interactions.

2 Apparatus and Method

2.1 Pool Boiling Apparatus. The apparatus used for the experiments in water, ethanol, iso-propanol, Freon-113, and Freon-11 is shown schematically in Fig. 1. It mainly consists of a boiling vessel and a liquid feed tank. The boiling vessel (1) is a cylindrical stainless steel pressure vessel of 20 cm i.d. and 60 cm height capable of operating up to 5 MPa. The vessel has two sight ports and is equipped with a pressure transducer and a sheathed 1-mm-dia CA thermocouple that is used to measure the bulk liquid temperature. A cylinder test heater (2) is horizontally supported in the vessel. The vessel is connected via a valve to a liquid feed tank (8), which is used to adjust the liquid level in the boiling vessel to realize good film boiling conditions, to be described later.

Another apparatus used for the experiments in liquid nitrogen and liquid argon is shown in Fig. 2. The boiling vessel (1) is a vacuum-insulated cylindrical pressure vessel of 20 cm i.d. and 70 cm height capable of working up to 3.5 MPa. The vessel has two sight ports (5) and is equipped with a sheathed 1-mm-dia CC thermocouple that is used to measure the bulk liquid temperature. The vessel is connected via a valve to a liquid feed tank (7). The system pressure in the boiling vessel is automatically controlled within ±1 kPa of a desired value by a pressure control system consisting of a pressure transducer (P.T.), a pressure controller (10), and a control valve (9).

2.2 Test Heater. Platinum cylinder test heaters 0.3, 0.5, 0.7, 1.2, 2, 3, 4, 5, and 6 mm in diameter were bent to a U-shape consisting of horizontal and vertical heater sections as shown in Figs. 1 and 2. Two fine 30-μm-dia platinum wires were spot welded at around 20 mm from each end of the horizontal heater section. The effective lengths of the heaters between the potential taps on which film boiling heat transfer was measured were about 50 mm.

Each heater was annealed and its electrical resistance versus temperature relation was calibrated in liquid nitrogen, water, and glycerin baths before using it in the experiment. The calibration accuracy was estimated to be within ±0.5 K.

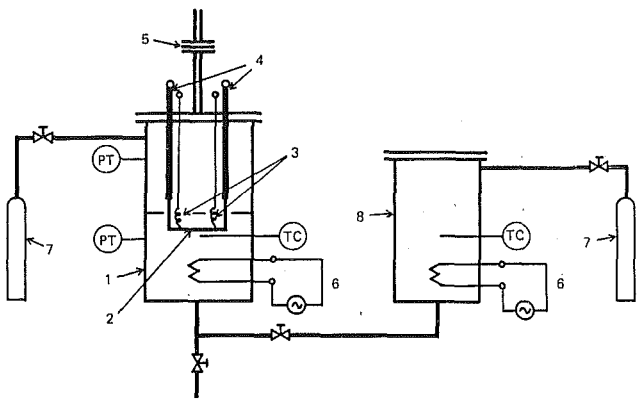

Fig. 1 Schematic of pool boiling apparatus for water, alcohols, and Freons

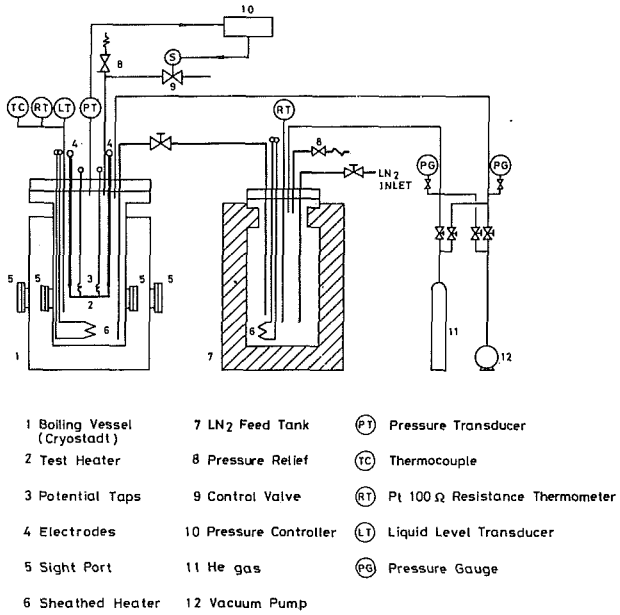

Fig. 2 Schematic of experimental apparatus for liquid nitrogen and liquid argon

2.3 Experimental Method and Procedure. A film boiling state was realized as follows: At first, the cylinder test heater was heated by direct current up to well above the minimum film boiling temperature in the vapor above the saturated liquid at a preselected pressure (the saturation pressure for a desired bulk liquid temperature) in the vessel, and then it was immersed by raising the liquid level to about 20 to 40 mm, depending on the kind of liquid, above the horizontal heater axis. Thereafter the system pressure was set to a desired value to realize a subcooled condition. Nitrogen gas was the pressurizing gas in the subcooled experiments for non-cryogenic liquids, and helium gas for cryogenic liquids. After this pressure setting, the cylinder surface temperature was also set to a desired value by adjusting heater current. In many cases, film boiling heat transfer coefficients were measured by gradually decreasing the heating current from the initial value to that for the minimum film boiling point. However, at higher subcooled condition, the liquid temperature at the level of the test cylinder axis was constant for a while and then began to increase during the experiment; it was impossible to measure for a constant liquid subcooling the heat transfer coefficients on a large diameter cylinder for a wide range of surface superheats in one experimental run. The experimental data for the highly subcooled liquid were obtained by performing several runs for successive short ranges of surface superheat.

The test heater temperature was measured by resistance thermometry. A double bridge circuit including the test heater as a branch was first balanced at the bulk liquid temperature. The output voltages of the bridge circuit together with the voltage drops across the potential taps of the heater and across a standard resistance were amplified and passed to the analog-to-digital converters of a digital computer. The average temperature of the heater was calculated with the aid of the previously calibrated resistance–temperature relation. The heater surface temperature was calculated from the measured average temperature and heat generation rate by solving the conduction equation in the heater.

The experimental error was estimated to be ±1 K in the heater surface temperature and ±2 percent in the heat flux based on the following facts: Platinum cylinders of high purity (99.99 percent) were used and their electrical resistance versus

Nomenclature

c_p = specific heat capacity, J/(kg K)
D = diameter of cylinder heater, m
D' = $D[g(\rho_l-\rho_v)/\sigma]^{1/2}$ = nondimensional diameter of cylinder heater
d = departing bubble diameter, m
g = acceleration due to gravity, m/s^2
Gr_v = $g(\rho_l-\rho_v)D^3/(\rho_v\nu_v^2)$ = Grashof number
h = pool film boiling heat transfer coefficient, W/(m^{2}K)
h_{co} = pool film boiling heat transfer coefficient if there were no radiation, W/(m^{2}K)
h_r = radiation heat transfer coefficient, W/(m^{2}K)
J = radiation parameter
K = nondimensional quantity as a function of D', equation (4)
k = thermal conductivity, W/(m K)
L = latent heat of vaporization, J/kg
L' = $L+0.5\,c_{pv}\Delta T_{sat}$ = latent heat plus sensible heat content of vapor, J/kg
M^* = nondimensional quantity, see Part 1 of this paper
Nu = Nusselt number
Pr = Prandtl number
ΔT_{sat} = heater surface superheat, K
ΔT_{sub} = liquid subcooling, K
λ = wavelength of vapor–liquid interfacial oscillation, m
λ_c = $2\pi[\sigma/\{g(\rho_l-\rho_v)\}]^{1/2}$ = critical wavelength of Taylor instability for horizontal plate, m
λ_m = $2\pi\sqrt{3}[\sigma/\{g(\rho_l-\rho_v)\}]^{1/2}$ = most dangerous wavelength of Taylor instability for horizontal plate, m
μ = viscosity, kg/(s m)
ν = kinematic viscosity, m^2/s
ρ = density, kg/m^3
σ = surface tension, N/m

Subscripts

l = liquid
v = vapor

Table 1

Water	
Cylinder diameter	0.3, 0.5, 0.7, 1,2, 2.0, 3.0, 4.0 mm
System pressure	101.3 kPa–1960 kPa
Liquid subcooling	0 K–40 K
Maximum superheat	700 K
Ethanol	
Cylinder diameter	1.2, 2.0, 4.0 mm
System pressure	101.3 kPa
Liquid subcooling	0 K–50 K
Maximum superheat	600 K
Iso-propanol	
Cylinder diameter	1.2, 2.0, 4.0 mm
System pressure	53.3 kPa, 101.3 kPa
Liquid subcooling	0 K–50 K
Maximum superheat	600 K
Freon-113	
Cylinder diameter	0.7, 1.2, 3.0 mm
System pressure	101.3 kPa–406.2 kPa
Liquid subcooling	0 K–50 K
Maximum superheat	400 K
Freon-11	
Cylinder diameter	0.7, 1.2, 3.0 mm
System pressure	101.3 kPa–783.0 kPa
Liquid subcooling	0 K–50 K
Maximum superheat	400 K
Liquid nitrogen	
Cylinder diameter	0.3, 0.7, 1.2, 3.0, 6.0 mm
System pressure	101.3 kPa–1836 kPa
Liquid subcooling	0 K–30 K
Maximum superheat	700 K
Liquid argon	
Cylinder diameter	1.2, 3.0 mm
System pressure	101.3 kPa–1833 kPa
Liquid subcooling	0 K–37 K
Maximum superheat	700 K

temperature relations were carefully calibrated within ±0.5 K error. For the accurate measurement of film boiling heat transfer, it was required that the temperature be uniform on the horizontal test cylinder before the simultaneous collapse of vapor film on the cylinder at the minimum film boiling point. These conditions were achieved by adjusting the liquid level so as to leave some hot part of the vertical heater section above the liquid level. A high-speed video camera system (200 frames/s with a rotary shutter exposure of 1/2000 s) by which the dynamic behavior of the vapor–liquid interface in film boiling was observed for each experimental run, was also used to assure the simultaneous collapse (within one frame) of the vapor film at the minimum film boiling point, because the simultaneous collapse was realized only for the cylinder with a uniform temperature distribution along its axis. The reproducibility of the data was excellent; all the data for the same experimental conditions, even for cylinders made of other pure materials such as gold, with each other within the estimated experimental error.

3 Results and Discussion

3.1 Experimental Condition for Each Liquid. Experiments of pool film boiling on horizontal cylinders were performed in several kinds of liquid such as water, ethanol, iso-propanol, Freon-113, Freon-11, liquid nitrogen, and liquid argon for wide ranges of cylinder diameter, system pressure, liquid subcooling, and cylinder surface superheat. Experimental conditions for each liquid are tabulated in Table 1.

3.2 Comparison of Experimental Data With the Rigorous Numerical Solution. Experimental results of pool film boiling heat transfer coefficients for various liquids under the wide ranges of conditions shown in Table 1 were compared with the theoretical values derived from the rigorous solution (obtainable only numerically by a digital computer) of the theoretical pool film boiling heat transfer model based on laminar boundary layer theory including the effects of liquid

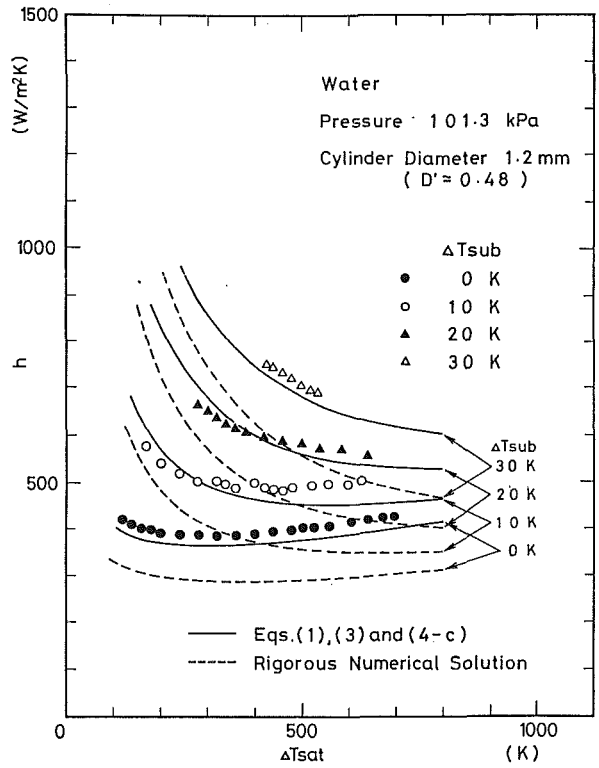

Fig. 3 Film boiling heat transfer coefficients for 1.2-mm-dia cylinder ($D' \simeq 0.48$) in water at atmospheric pressure

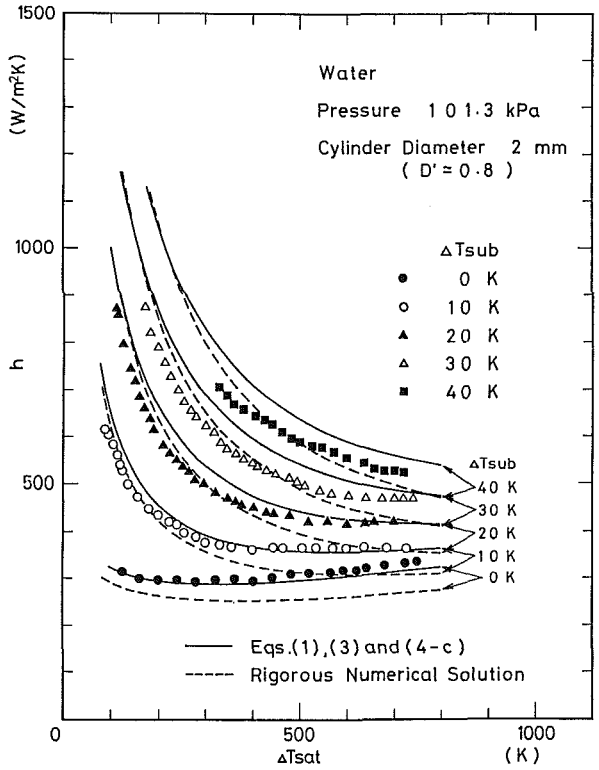

Fig. 4 Film boiling heat transfer coefficients for 2.0-mm-dia cylinder ($D' \simeq 0.8$) in water at atmospheric pressure

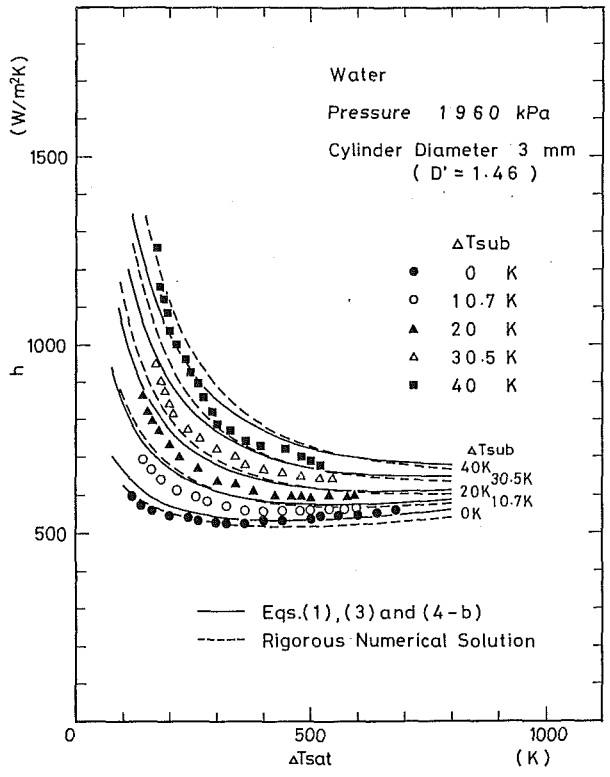

Fig. 5 Film boiling heat transfer coefficients for 3.0-mm-dia cylinder ($D' \simeq 1.46$) in water at pressure of 1960 kPa

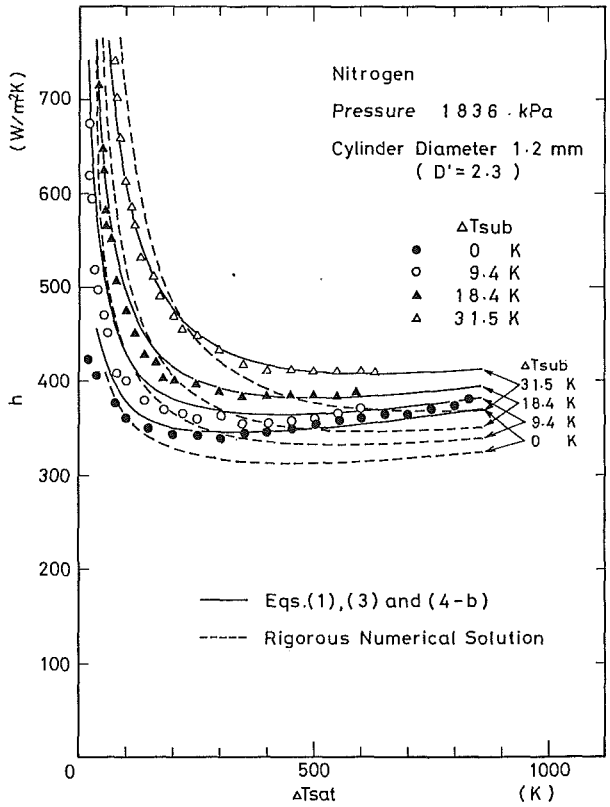

Fig. 7 Film boiling heat transfer coefficients for 1.2-mm-dia cylinder ($D' \simeq 2.3$) in liquid nitrogen at pressure of 1836 kPa

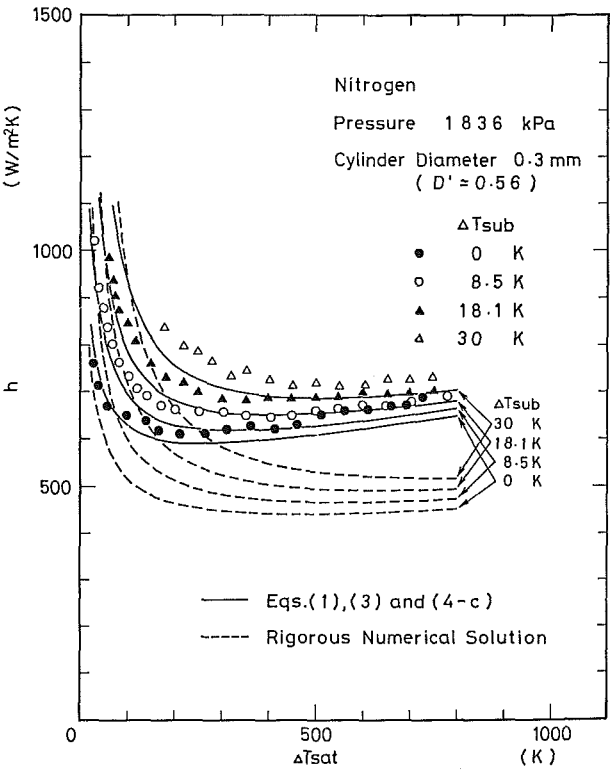

Fig. 6 Film boiling heat transfer coefficients for 0.3-mm-dia cylinder ($D' \simeq 0.56$) in liquid nitrogen at pressure of 1836 kPa

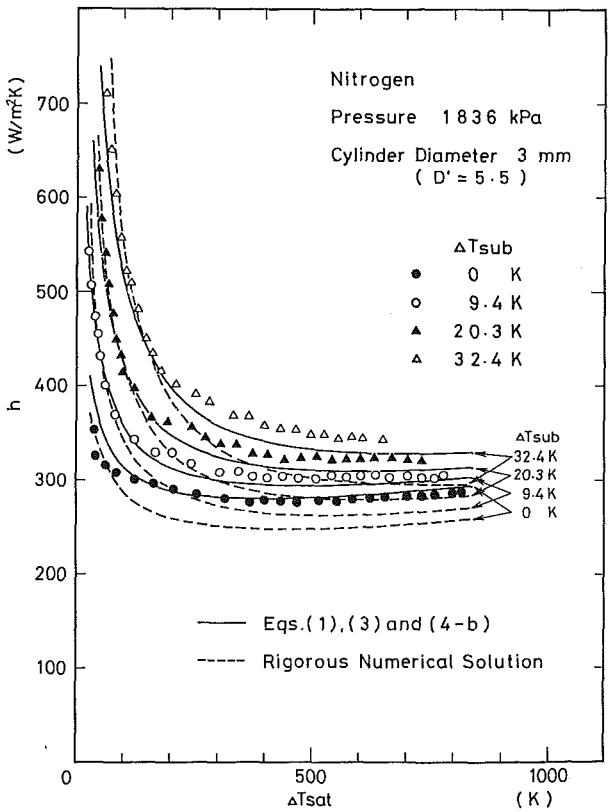

Fig. 8 Film boiling heat transfer coefficients for 3.0-mm-dia cylinder ($D' \simeq 5.5$) in liquid nitrogen at pressure of 1836 kPa

subcooling and radiation from the horizontal cylinder described previously (Sakurai et al., 1990). Comparison of the typical experimental data for various liquids such as water, ethanol, Freon-11, liquid nitrogen, and liquid argon are shown in Figs. 3 to 13.

As shown in Figs. 5, 7, 12, and 13, the experimental data of saturated and subcooled film boiling heat transfer from the horizontal cylinders of nondimensional diameter around 1.3

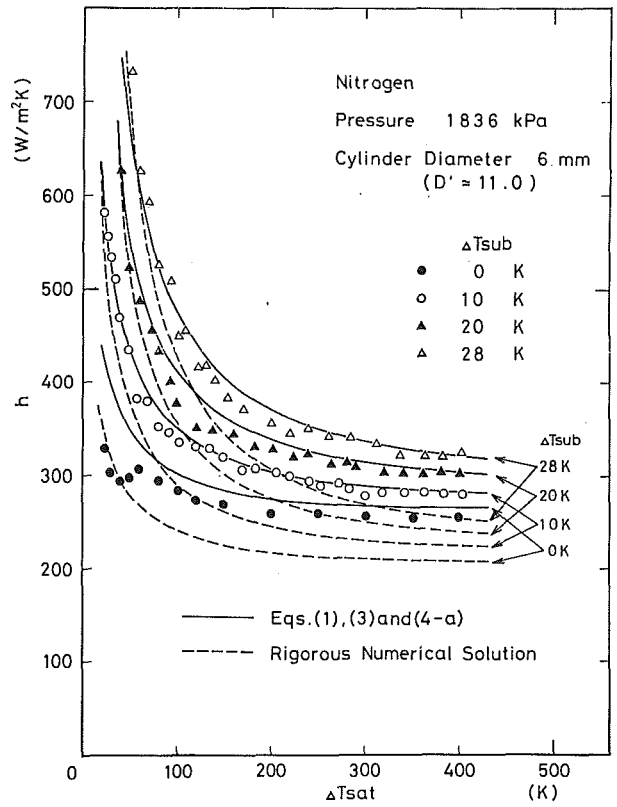

Fig. 9 Film boiling heat transfer coefficients for 6.0-mm-dia cylinder ($D' \simeq 11.0$) in liquid nitrogen at pressure of 1836 kPa

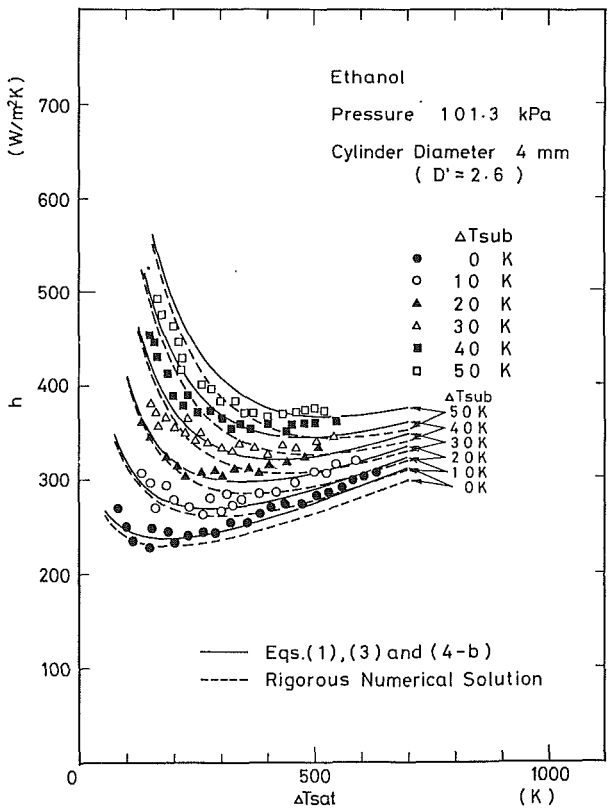

Fig. 11 Film boiling heat transfer coefficients for 4-mm-dia cylinder ($D' \simeq 2.6$) in ethanol at atmospheric pressure

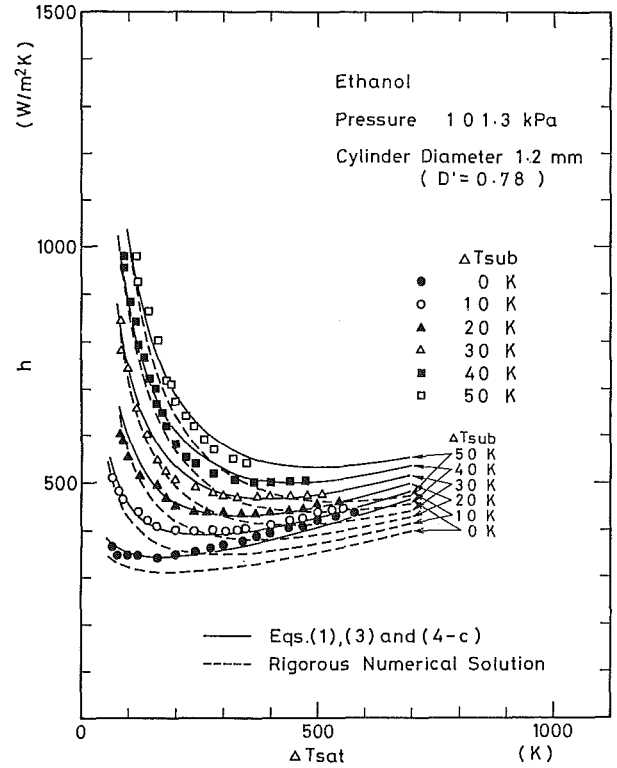

Fig. 10 Film boiling heat transfer coefficients for 1.2-mm-dia cylinder ($D' \simeq 0.78$) in ethanol at atmospheric pressure

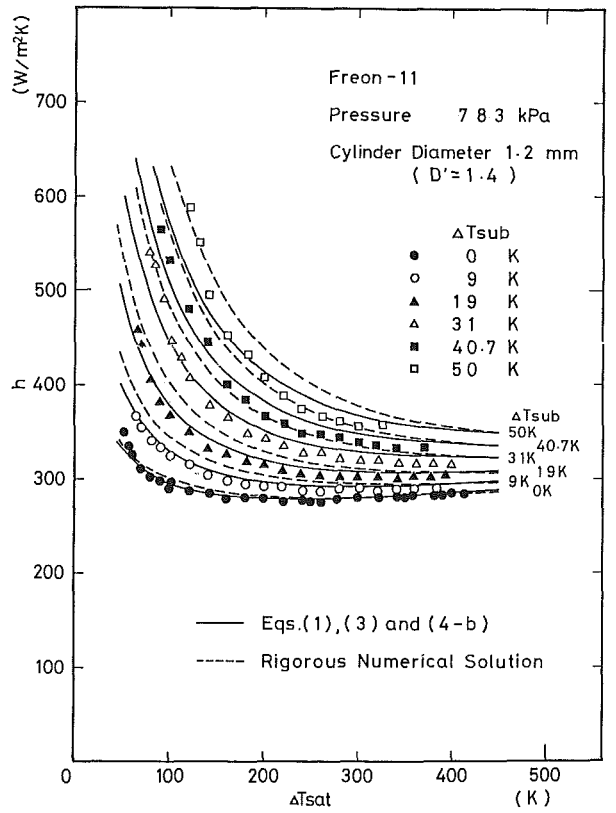

Fig. 12 Film boiling heat transfer coefficients for 1.2-mm-dia cylinder ($D' \simeq 1.4$) in Freon-11 at a pressure of 783 kPa

for water, liquid nitrogen, Freon-11, and liquid argon almost agree with the theoretical value in the lower superheat region comparatively near the minimum film boiling heat flux where the disturbance of the vapor–liquid interface induced by the

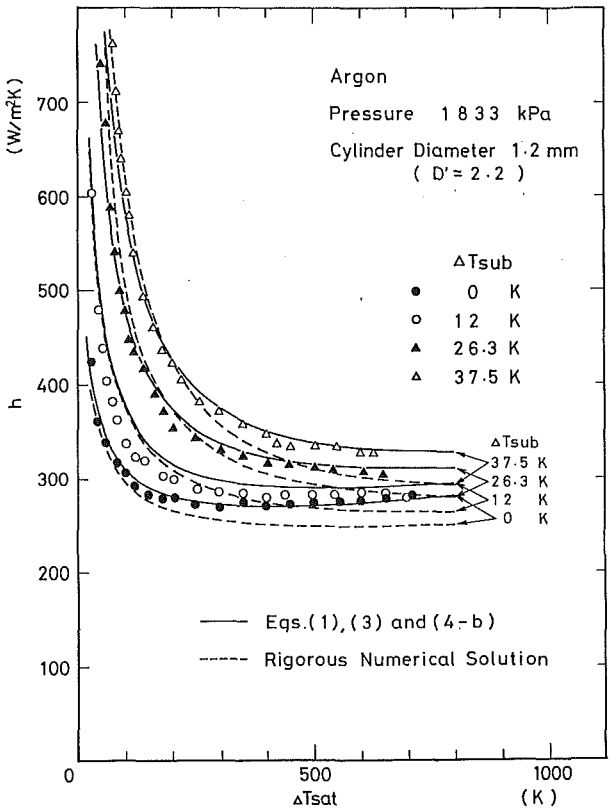

Fig. 13 Film boiling heat transfer coefficients for 1.2-mm-dia cylinder ($D' \simeq 2.2$) in liquid argon at a pressure of 1833 kPa

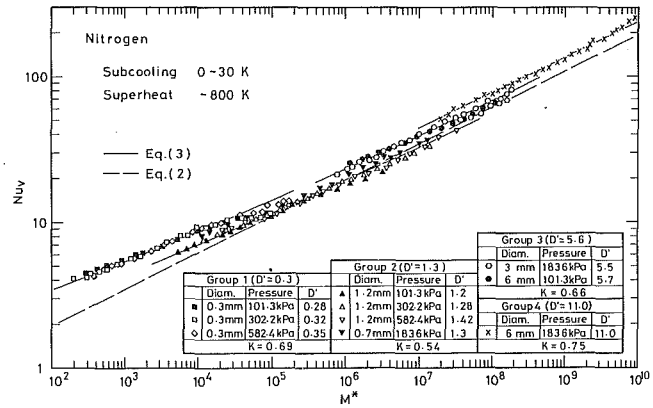

Fig. 14 Saturated and subcooled film boiling heat transfer in liquid nitrogen for several nondimensional cylinder diameters plotted on log Nu_v versus log M^* graph

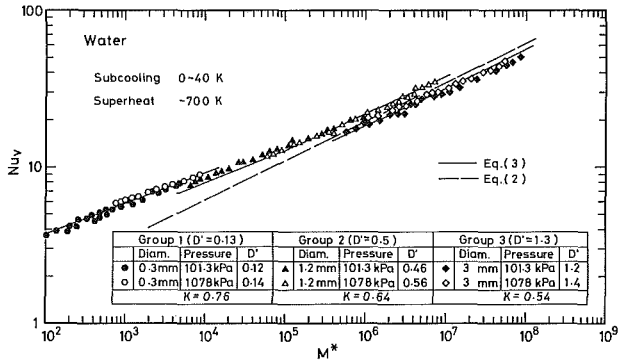

Fig. 15 Saturated and subcooled film boiling heat transfer in water for several nondimensional cylinder diameters plotted on log Nu_v versus log M^* graph

growth and the detachment of vapor bubbles on the horizontal heater caused by Taylor instability is very small because of low heat flux. The region where the experimental data almost agree with the theoretical values is widest when the nondimensional diameter is around 1.3 for each liquid, but its width largely depends on the kind of liquid; it is wider for water and Freon-11, and narrower for liquid nitrogen, ethanol, and liquid argon, as shown in these figures. On the other hand, as shown in Figs. 3, 4, 6, 8, 9, 10, and 11, as the nondimensional diameter increases or decreases from around 1.3, this region becomes shorter and the difference between the experimental results and the theoretical value becomes larger than that for $D' = 1.3$ at the same superheat. Furthermore, the region becomes wider with an increase in liquid subcooling and system pressure.

With careful eyes, we can see in Figs. 5 and 12 that some part of the experimental data under subcooled condition for D' around 1.3 is slightly lower than the theoretical values. Pictures of the film boiling phenomena corresponding to these data taken with a high-speed video camera show that, in saturated and low subcooled film boiling, both the diameter and the frequency of detaching vapor bubbles on the top of the cylinder decrease with a decrease in cylinder surface superheat (Sakurai et al., 1984). Therefore, the supposition of a smooth and continuous vapor-liquid interface for the theoretical model appears to be valid for low surface superheat. However, for a high subcooled condition, vapor bubbles of somewhat large size do not detach but sit on the top of the cylinder and the bubbles become smaller with a decrease in the surface superheat. The bubble behavior on the top of the cylinder may have an effect upon the subcooled film boiling heat transfer, making it sometimes larger and sometimes lower than the theoretical values.

3.3. Comparison of Experimental Data With the Analytical Solution. The following analytical solution of the theoretical model based on laminar boundary layer theory for the pool film boiling heat transfer coefficient h from a horizontal cylinder including the contributions of liquid subcooling and radiation from the cylinder was presented earlier (Sakurai et al., 1990):

$$h = h_{co} + Jh_r \tag{1}$$

where h_{co} is the pool film boiling heat transfer coefficient if there were no radiation, expressed as

$$\mathrm{Nu}_v = h_{co}D/k_v = 0.612M^{*0.25} \tag{2}$$

J and h_r represent the radiation parameter and radiation heat transfer coefficient for parallel plates, respectively.

The experimental data were plotted in the form of log Nu_v versus log M^* to investigate the relation between the data and the analytical solution for the various liquids. The value of h_{co} in Nu_v is obtained by subtracting the value of Jh_r from the experimental data of h, referring to equation (1), though the radiation contribution in pool film boiling heat transfer here obtained by using a platinum cylinder heater is almost negligibly small.

Figures 14 and 15 show typical data for liquid nitrogen and water, respectively, on the graph together with the theoretical curve given by equation (2), which is a straight line with a gradient of 0.25. The data shown are for several groups of nondimensional diameter D', about 0.3, 1.3, 5.6, and 11.0 for nitrogen and about 0.13, 0.5, and 1.3 for water, chosen from the data for the wide ranges of experimental conditions shown in Table 1. The experimental data under the condition of one system pressure and one cylinder diameter for the tested ranges of liquid subcooling and surface superheat are ex-

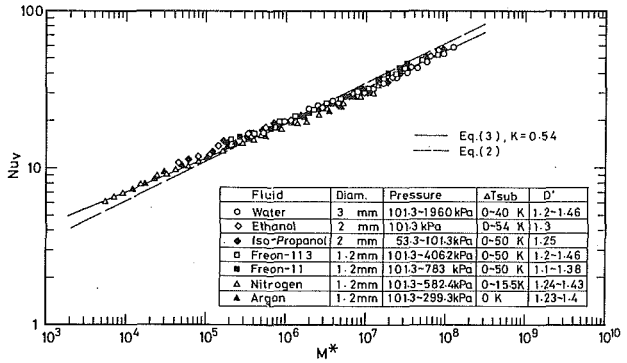

Fig. 16 Saturated and subcooled film boiling heat transfer in various liquids for nondimensional cylinder diameters around 1.3 plotted on log Nu_v versus log M^* graph

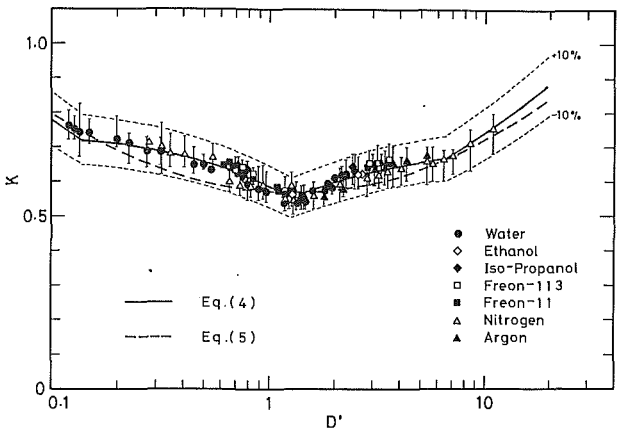

Fig. 17 Values of K derived from the authors' data of saturated and subcooled film boiling heat transfer from horizontal cylinders of various nondimensional diameters, and fitted curves for these values

pressed with the same symbol in these figures. As shown in the columns for Group 2 and Group 3 in the table in Fig. 14, the value of D' depends not only on the cylinder diameter but also on the system pressure. It is possible to have a single value of D' for different combinations of cylinder diameter and system pressure. It seems that the experimental data for each group of D' can be expressed with a single curve on this graph. The experimental data curve for $D' \simeq 1.3$ in each figure lies nearest to the theoretical curve given by equation (2).

As D' varies from around 1.3, the experimental data curve for each D' moves upward almost parallel to that for $D' = 1.3$. As shown in Fig. 14, the gradient of the curve at a value of M^* for $D' \simeq 0.3$ increases from 0.18 to 0.21 with the increase in M^* from 200 to 10^5, that for $D' \simeq 5.6$ from 0.23 to 0.24 with M^* from 10^6 to 10^8, and that for $D' = 11.0$ from 0.24 to 0.25 with the increase in M^* from 2×10^7 to 10^{10}.

Experimental data for water, ethanol, iso-propanol, Freon-113, Freon-11, liquid nitrogen, and liquid argon for the cylinders of $D' \simeq 1.3$ are shown in Fig. 16 on the graph of log Nu_v versus log M^* with the theoretical curve given by equation (2). All the data for $D' \simeq 1.3$ exist in the vicinity of a single curve. The gradient of the curve gradually increases from 0.21 to 0.24 with the increase in the value of M^* from 10^4 to 10^8. The curve intersects the theoretical curve when M^* approximately equals 5×10^5. The value of Nu_v for M^* higher than that of the intersection point is slightly lower than the theoretical value, and it is slightly higher than the theoretical value when M^* is lower than the intersection point.

These figures show that all the data belonging to each group of D' were fitted very well with a single curve on the log Nu_v versus log M^* graph, even though the data are obtained for various liquids of widely different physical properties under wide ranges of experimental conditions. Namely, the pool film boiling heat transfer data are well arranged with the nondimensional diameter as a parameter independent of the system pressure, liquid subcooling, and kind of liquid.

The curves fitted to the data for the values of D' in these figures are expressed by the following equation:

$$Nu_v/(1+2/Nu_v) = KM^{*0.25} \tag{3}$$

The value of K varies depending on the value of D'. The values of K for the values of D' in the figures are 0.76 for $D' \simeq 0.13$, 0.69 for $D' \simeq 0.3$, 0.64 for $D' \simeq 0.5$, 0.54 for $D' \simeq 1.3$, 0.64 for $D' \simeq 5.6$, and 0.75 for $D' = 11.0$. The curves given by equation (3) with these values of K are shown in Figs. 14, 15, and 16.

The Nusselt number can be interpreted to be the ratio of cylinder diameter to average vapor film thickness if the radial temperature distribution in the vapor film is linear. The similarity transformation used to derive the theoretical equation, equation (2), will become less appropriate as the ratio of vapor film thickness to the cylinder diameter increases. It can be considered that the variation of the gradient with the decrease in M^* mentioned above is due to this effect and the term of $(1+2/Nu_v)$ in equation (3) expresses the effect.

It is expected that, if it becomes possible to derive the numerical solution for the previously reported fundamental equations for laminar film boiling heat transfer (Sakurai et al., 1990) without making any approximation such as the similarity transformation, equation (3) with $K = 0.54$, representing the experimental data for $D' \simeq 1.3$, which is slightly higher or lower than equation (2) depending on the value of M^* as shown in Fig. 16, will quantitatively agree with the solution.

3.4 Derivation of a General Correlation. The value of K for each D' is determined by fitting equation (3) to a graph of log Nu_v versus M^* for a series of saturated and subcooled experimental data for a single value of D'. The values of K thus obtained for water, ethanol, iso-propanol, Freon-113, Freon-11, liquid nitrogen, and liquid argon (the experimental conditions for which were already shown in Table 1) are shown against the value of D' in Fig. 17. They are expressed well by the following equations:

$$K(D') = 0.415D'^{0.25} \quad \text{for } D' > 6.6 \tag{4a}$$

$$K(D') = 2.1D'/(1+3.0D') \quad \text{for } 1.25 \le D' \le 6.6 \tag{4b}$$

$$K(D') = 0.75/(1+0.28D') \quad \text{for } 0.14 \le D' < 1.25 \tag{4c}$$

The curves representing the new correlation obtained here, consisting of equations (4*a*), (4*b*), and (4*c*), are shown in the figure. It is seen that the curves are in good agreement, within ± 10 percent, with the values of K derived from experimental data for various liquids for wide ranges of surface superheat, system pressure, liquid subcooling, and nondimensional diameter. These equations can be approximately replaced by a single equation

$$K(D') = 0.57 - 0.041(\log_{10}D') + 0.19(\log_{10}D')^2 \tag{5}$$

for the whole range of D'. The curve representing equation (5) is also shown in Fig. 17.

As shown in Fig. 17, the value of K depends on D' and is minimal at D' around 1.3. It is presumed that the disturbance of the vapor–liquid interface induced by growth and release of vapor bubbles on the top of the cylinder may affect the film boiling heat transfer and make the value of K dependent on D'. This disturbance depending on D' can be explained qualitatively as mentioned below by supposing that the disturbance is proportional to the ratio d/λ_m, where d is the diameter of a bubble departing from the vapor–liquid interface and λ_m is the most dangerous wavelength of the vapor–liquid interface.

The authors have observed the dynamic behavior of vapor

bubbles and of the vapor–liquid interface on the top of the cylinder in the low surface superheat region under saturated conditions. First, the most dangerous wavelength λ_m for large D' is near that of a horizontal plate; it decreases with a decrease in D' due to the effect of surface tension in the transverse direction of the horizontal cylinder on Taylor instability. Second, the diameter of the departing vapor bubble is also affected by surface tension and decreases with a decrease in D'. Third, the departing frequency f is almost independent of D'. They also presented the expressions for λ_m, d, and f (Sakurai et al., 1984).

According to their expressions, the ratio d/λ_m is given by $0.18[1+7.4\times10^{-5}(\rho_l/\rho_v)^{1.15}]D'^{1/3}(1+0.85/D')$, though this expression was confirmed at low superheat near the minimum film boiling point. This ratio is minimal for D' at $D'=1.7$ and increases as D' increases from 1.7.

Although this consideration is based on a simple assumption and experimental facts for limited conditions, it seems that K depends on the value of D' and takes on a minimum value at a certain value of D' because λ_m and d, which participate in the disturbance of the vapor–liquid interface on the top of the cylinder, depend on the value of D' in their special ways as a result of the different restrictions on λ_m and d, respectively, by the horizontal cylinder.

In the region of $D'>6.6$, the heat transfer coefficient h_{co} given by equation (3) with K given by equation (4*a*) becomes almost independent of the cylinder diameter when the value of Nu_v is sufficiently large that the denominator, $(1+2/\mathrm{Nu}_v)$, on the left-hand side of equation (3) can be regarded as unity. Breen and Westwater (1962) pointed out that saturated film boiling heat transfer coefficients for large horizontal cylinder diameters were independent of the diameter. Using λ_c as a characteristic length instead of the cylinder diameter, equation (3) with K given by equation (4*a*) can be approximately expressed by the diameter-independent form

$$(Nu_v)_{D=\lambda_c}=0.415(2\pi)^{1/4}[(M^*)_{D=\lambda_c}]^{0.25}$$
$$=0.66[(M^*)_{D=\lambda_c}]^{0.25} \qquad (6)$$

where λ_c is the critical wavelength of Taylor instability.

The curves given by equations (4*a*) and (4*b*) intersect with each other at $D'=6.6$, which corresponds to a point where the half perimeter of the cylinder almost agrees with the most dangerous wavelength of the Taylor instability ($\pi D/2=\lambda_m$, therefore, $D'=2\pi\sqrt{3}D/\lambda_m=4\sqrt{3}$). In the case of $D'>6.6$, the half perimeter of the cylinder is sufficiently wide to induce an unstable wave in a transverse direction of the cylinder. It is assumed that the unstable wave becomes dominant and the increase in the disturbance due to this unstable wave will increase the value of K and make the heat transfer coefficient no longer dependent on D'. The unstable wave pattern in the transverse direction seems to be similar to that caused by the Helmholz instability at the vapor–liquid interface on a vertical plate. Hsu and Westwater (1960) showed the wavelength data, which were close to the Taylor instability wavelength. The local film boiling heat transfer coefficient on a vertical plate also becomes constant for the distance from the leading edge longer than the wavelength as observed by Bui and Dhir (1985).

3.5 Comparison of Experimental Data With General Correlation. Typical experimental data for the film boiling heat transfer coefficient from horizontal cylinders with widely different nondimensional diameters in water, liquid nitrogen, ethanol, Freon-11, and liquid argon, previously shown in Figs. 3 to 12, are compared with the corresponding values calculated from the correlation consisting of equations (1), (3), and (4) in these figures, respectively. The values from the correlation agree within ±10 percent with the experimental data, in spite of widely different experimental conditions for various liquids.

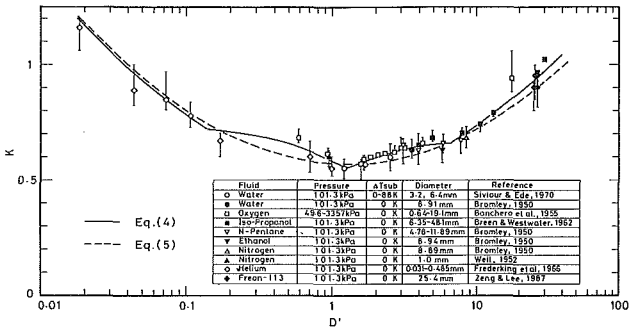

Fig. 18 Other investigators' data of film boiling heat transfer compared with the general correlation

The values of K against D' derived from the experimental data for film boiling heat transfer from horizontal cylinders of other workers (Siviour and Ede, 1970; Bromley, 1950; Banchero et al., 1955; Breen and Westwater, 1962; Weil, 1952; Frederking et al., 1966; Zeng and Lee, 1987) including those with a large radiation contribution from cylinders such as Nimonic 75 alloy (Siviour and Ede, 1970) and carbon (Bromley, 1950) are shown in Fig. 18. These data, except for the data for water at subcoolings ranging from 0 to 80 K from Siviour and Ede, are obtained under saturation conditions for various liquids such as water, oxygen, iso-propanol, *n*-pentane, ethanol, Freon-113, liquid nitrogen, and liquid helium and for a range of cylinder diameters from 0.005 to 48.1 mm. Each experimental condition is shown in a table in the figure. The curves representing the values of K given by equations (4*a*), (4*b*), (4*c*), and equation (5) are also shown in the figure for comparison. They are seen to give a satisfactory fit for the values of K obtained from other researchers' data including those for liquid helium. This means that this new correlation will also be applicable to pool film boiling heat transfer for liquid helium. The values of K for liquid helium under saturated conditions in the range of $D'<0.14$, which is outside the application range of equation (4*c*), become higher than that given by equation (4*c*), in contrast with the range of $D'>6.6$, where the values of K given by equation (4*a*) become higher than that given by equation (4*b*). These values of K for $D'<0.14$ agree well with the curve representing equation (5) as shown in the figure and are well expressed by the following equation:

$$K(D')=0.44D'^{-0.25} \qquad \text{for } D'<0.14 \qquad (4d)$$

The curve expressed by equation (4*d*) is shown in Figs. 17 and 18. Although the correlation for $D'<0.14$ is for academic interest rather than for practical applications, it seems that many reliable experimental data are necessary for various liquids to corroborate the correlation for the D' region. The correlation is dealt with in another work concerning film boiling heat transfer from horizontal cylinders of various D' in liquid helium for various system pressures up to near the critical one (Shiotsu et al., 1990).

3.6 Comparison Between Other Researchers' Correlations and the General Correlation. Other correlations such as that of Siviour and Ede (1970) for a subcooled condition, and those of Bromley (1950) and Breen and Westwater (1962) for saturated conditions are compared with the general correlation obtained here: The values calculated from each correlation are plotted in the form of $K=\mathrm{Nu}_v/\{(1+2/\mathrm{Nu}_v)M^{*0.25}\}$ versus $\log D'$ for several typical cases around the authors' and others' experimental conditions for various liquids shown in Table 1 and in Fig. 18, and compared with the curve derived from equation (4).

Figure 19 shows the values obtained from Siviour and Ede's

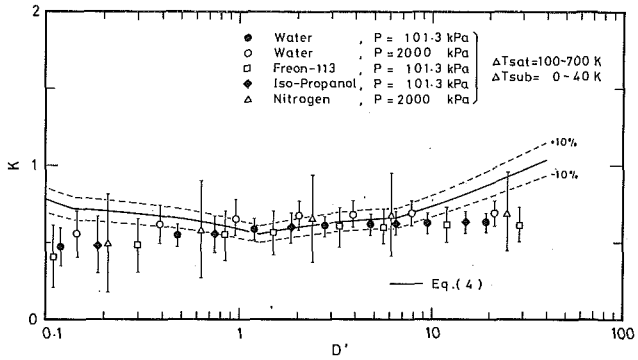

Fig. 19 Values derived from Siviour and Ede's correlation under subcooled conditions compared with the general correlation

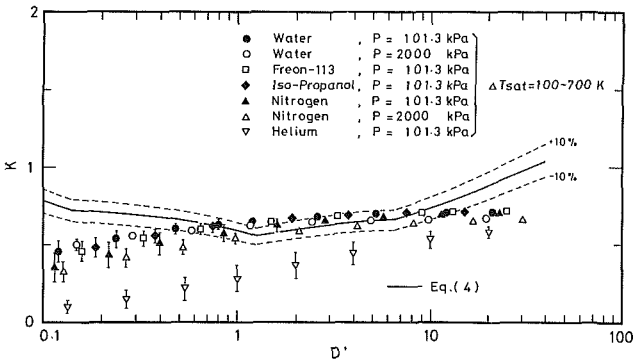

Fig. 20 Values derived from Bromley's correlation under saturated conditions compared with the general correlation

correlation for nondimensional cylinder diameters from 0.1 to 30 in water at pressures of 101.3 and 2000 kPa, in iso-propanol at 101.3 kPa, in nitrogen at 2000 kPa, and in Freon-113 at 101.3 kPa, and for the ranges of surface superheat and liquid subcooling from 100 to 700 K and from 0 to 40 K, respectively. As shown in the figure, the values of their correlation at a constant D' vary significantly on this graph depending on the kind of liquid and system pressure; the maximum deviation from the general correlation is far more than ± 10 percent, which is that of our experimental results for various liquids as mentioned above.

Figure 20 shows the values obtained from the Bromley correlation for nondimensional cylinder diameters from 0.1 to 30 in water at pressures of 101.3 and 2000 kPa, in Freon-113 at 101.3 kPa, in iso-propanol at 101.3 kPa, in liquid nitrogen at 101.3 and 2000 kPa, and in liquid helium at 101.3 kPa, and for the range of surface superheats from 100 to 700 K. The values other than those for liquid helium are around ± 10 percent of the general correlation for the limited range of D' from about 0.6 to 15, except for the liquid helium case where the values are far lower than those derived from the general correlation.

Figure 21 shows the values obtained from Breen and Westwater's correlation for nondimensional cylinder diameters from 0.06 to 30 in water at pressures of 101.3 and 2000 kPa, in Freon-113 at 101.3 kPa, in iso-propanol at 101.3 kPa, in liquid nitrogen at 101.3 and 2000 kPa, and in liquid helium at 101.3 kPa, and for the range of surface superheat from 100 to 700 K. The values for $D' < 1$ become significantly higher than the general correlation with the decrease in D' and arrive at more than double the correlation at the lowest D' here compared. The values for $D' > 1$, except those for liquid helium, are similar in the dependence of D' to that for the general correlation, though the maximum deviations from the general correlation for most of the cases are about 20 percent. The value for liquid helium for a constant D' on this graph in-

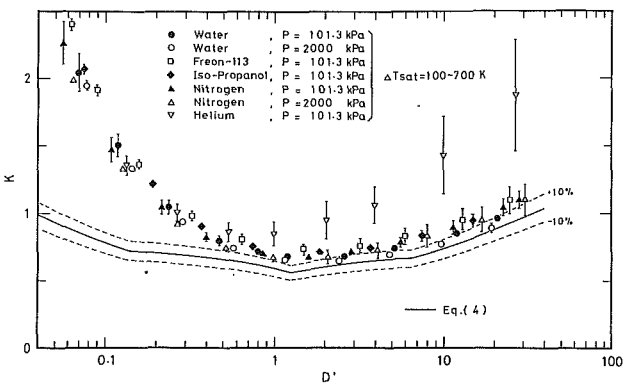

Fig. 21 Values derived from Breen and Westwater's correlation under saturated conditions compared with the general correlation

creases with the increase in surface superheat; the variation range becomes wider and the average value of the range becomes significantly higher than the general correlation with the increase in D'. This is because the modified latent heat expressed by $L' = L(1 + 0.34 c_{pv} \Delta T_{sat}/L)^2$, which is valid only for $c_{pv}\Delta T_{sat}/L$ up to about 3.0 (Bromley, 1952), was used in their correlation.

4 Conclusions

Pool film boiling heat transfer coefficients on horizontal cylinders were experimentally obtained for several kinds of liquid such as water, ethanol, iso-propanol, Freon-113, Freon-11, liquid nitrogen, and liquid argon for wide ranges of cylinder diameter, system pressure, liquid subcooling, and cylinder surface superheat.

The experimental data of saturated and subcooled film boiling heat transfer from horizontal cylinders with nondimensional diameters around 1.3 almost agree with the rigorous numerical solution of the theoretical model based on laminar boundary layer theory in the lower superheat region comparatively near the minimum film boiling heat flux. The region where the experimental data almost agree with the theoretical values is widest when the nondimensional diameter is around 1.3 for each liquid, but its width largely depends on the kind of liquid; it is wider for water and Freon-11, and narrower for liquid nitrogen, ethanol, and liquid argon. As the nondimensional diameter increases or decreases from around 1.3, this region becomes shorter and the difference between the experimental result and the theoretical value becomes larger than that for $D' = 1.3$ at the same superheat. Furthermore, the region becomes wider with an increase in liquid subcooling and system pressure. In the region of $D' > 6.6$, the film boiling heat transfer under saturated and subcooled conditions becomes almost independent of the cylinder diameter.

A new correlation of pool film boiling heat transfer from a horizontal cylinder including the effects of nondimensional diameter, liquid subcooling, and radiation from the cylinder was developed by modifying the approximate analytical solution of the theoretical model based on laminar boundary layer theory to agree better with the experimental data of pool film boiling heat transfer for various liquids of widely different physical properties under wide ranges of experimental conditions.

The values of heat transfer coefficient calculated from the correlation agreed with the authors' data within ± 10 percent, and also with many other researchers' data for various liquids, including those with a large radiation effect, though these others' data were obtained mainly under saturated condition at atmospheric pressure.

It was confirmed that the correlation generally expresses the film boiling heat transfer coefficient on a horizontal cylinder in various kinds of liquid, including the effect of radiation

from the cylinder for wide ranges of surface superheat, liquid subcooling, system pressure, and nondimensional diameter.

References

Banchero, J. T., Barker, G. E., and Boll, R. H., 1955, "Stable Film Boiling of Liquid Oxygen Outside Single Horizontal Tubes and Wires," *Chem. Eng. Progr. Sym. Ser.*, Vol. 51, pp. 21–31.

Breen, B. P., and Westwater, J. W., 1962, "Effect of Diameter of Horizontal Tube on Film Boiling Heat Transfer," *Chem. Eng. Prog.*, Vol. 58, pp. 67–72.

Bromley, L. A., 1950, "Heat Transfer in Stable Film Boiling," *Chem. Eng. Prog.*, Vol. 46, pp. 221–227.

Bromley, L. A., 1952, "Effect of Heat Capacity of Condensate," *Industrial and Engineering Chemistry*, Vol. 44, pp. 2966–2969.

Bui, T. D., and Dhir, V. K., 1985, "Film Boiling Heat Transfer on an Isothermal Vertical Surface," ASME JOURNAL OF HEAT TRANSFER, Vol. 107, pp. 764–771.

Frederking, T. H. K., Wu, Y. C., and Clement, B. W., 1966, "Effects of Interfacial Instability on Film Boiling of Saturated Liquid Helium 1 Above Horizontal Surface," *AIChE Journal*, Vol. 12, pp. 238–244.

Hsu, Y. Y., and Westwater, J. W., 1960, "Approximate Theory for Film Boiling on Vertical Surfaces," *Chem. Eng. Prog. Symp. Ser.*, Vol. 56, pp. 15–24.

Sakurai, A., Shiotsu, M., and Hata, K., 1982, "Steady and Unsteady Film Boiling Heat Transfer at Subatmospheric and Elevated Pressures," *Proceedings, 1980 ICHMT Seminar*, S. G. Bankoff et al., eds., Hemisphere Pub. Corp., Washington, DC, pp. 301–312.

Sakurai, A., Shiotsu, M., and Hata, K., 1984, "Effect of System Pressure on Film-Boiling Heat Transfer, Minimum Heat Flux, and Minimum Temperature," *Nuclear Science and Engineering*, Vol. 88, pp. 321–330.

Sakurai, A., Shiotsu, M., and Hata, K., 1986, "Effect of Subcooling on Film Boiling Heat Transfer From Horizontal Cylinder in a Pool of Water," *Proceedings, 8th International Heat Transfer Conference*, C. L. Tien et al., eds., Hemisphere Pub. Corp., Washington, DC, Vol. 4, pp. 2043–2048.

Sakurai, A., Shiotsu, M., and Hata, K., 1990, "A General Correlation for Pool Film Boiling Heat Transfer From a Horizontal Cylinder to Subcooled Liquid, Part 1: A Theoretical Pool Film Boiling Heat Transfer Model Including Radiation Contribution and Its Analytical Solution," ASME JOURNAL OF HEAT TRANSFER, Vol. 112, this issue.

Shiotzu, M., Hata, K., and Sakurai, A., 1990 "Effect of Pressure on Film Boiling Heat Transfer From Horizontal Cylinder in Saturated Liquid Helium," to be presented at the 9th International Heat Transfer Conference, Israel.

Siviour, J. B., and Ede, A. J., 1970, "Heat Transfer in Subcooled Pool Film Boiling," *Proceedings, 4th International Heat Transfer Conference*, Elsevier Pub. Co., Amsterdam, Vol. V, B3.12.

Tachibana, F., and Fukui, S., 1961, "Heat Transfer in Film Boiling to Subcooled Liquids," *International Development in Heat Transfer—Part 2*, ASME New York, pp. 219–223.

Weil, L., 1952, *Proceedings, IVe Congr. Intern. du Chauf. Industr.*, Paris, No. 210.

Zeng, Y., and Lee, Y., 1987, "The Effect of Peripheral Wall Conduction in Pool Boiling," *Heat Transfer Science and Technology*, Bu-Xuan Wang, ed., Hemisphere Pub. Corp., Washington, DC, pp. 445–452.

ERRATA

In the paper "Natural Convection Along Slender Vertical Cylinders With Variable Surface Heat Flux," by J. J. Heckel, T. S. Chen, and B. F. Armaly, JOURNAL OF HEAT TRANSFER, Vol. 111, pp. 1108–1111, November 1989, the caption for Table 3 should read as follows:

Table 3 The $\overline{Nu}_L\ (Gr_L^*/5)^{-1/5}$ results for power law variation of the surface heat flux

To obtain the $\overline{Nu}_L\ Gr_L^{*-1/5}$ results, the numbers listed in Table 3 should be divided by the factor $5^{1/5}$. The authors would like to thank Prof. B. Grandjean of Laval University, Quebec, Canada for bringing this typographical error to their attention.

Nucleate Boiling With High Gravity and Large Subcooling

M. E. Ulucakli
Department of Mechanical Engineering,
Lafayette College,
Easton, PA 18042

H. Merte, Jr.
Department of Mechanical Engineering
and Applied Mechanics,
University of Michigan,
Ann Arbor, MI 48109

Measurements of the heater surface temperature are presented for pool boiling of distilled water in an accelerating system with various subcoolings and levels of heat flux. The ranges of the experimental variables are: heat flux between 0.19 MW/m² and 1.5 MW/m², accelerations normal to the flat heating surface from 1 to 100 times earth gravity, and liquid subcoolings between 0 K and 89 K. Increasing subcooling first produces an increase and then a decrease in wall superheat, with the eventual cessation of nucleate boiling for certain combinations of conditions. The increase in wall superheat is particularly enhanced at 10g, reaching a maximum value of 9 K at 1.05 MW/m² with 60 K subcooling. This type of behavior is attributed to the interactions between the fluid temperature distribution in the immediate vicinity of the heater surface as it is influenced by natural convection, the activation of nucleation sites, and the influence of increased buoyancy on the heat transfer associated with each departing bubble.

Introduction

Nucleate pool boiling is a complex phenomenon that has been actively studied over the years. The large number of variables involved and the interactions among the elements constituting the process are responsible for its complexity. The following variables have been studied up to this point: (*a*) the thermodynamic and transport properties of the fluid, (*b*) the thermal and surface properties of the heating surface, including the microgeometry, (*c*) the temperature of the heating surface and its distribution in the liquid, (*d*) the macrogeometry of the heating surface-container combination, (*e*) the body force field and orientation relative to the heating surface, (*f*) the history of the surface.

Experimental measurements are presented here showing the combined effects of system acceleration and subcooling on the nucleate boiling driving potential, the heater surface superheat, as a means of disclosing some of the interactions taking place and consequently improving the understanding of the process. The heater surface configuration selected is simple and well defined: a flat horizontal surface.

Literature Survey

Influence of Increased Acceleration. Based on various measurements, opinions as to the influence of increased acceleration on nucleate pool boiling have ranged from little to large. Merte and Clark (1963) varied the gravity fields over the range of 1g to 21g, and their results show a considerable increase in heat transfer with nonboiling convection and low heat flux boiling. At higher heat fluxes the trend was reversed, similar to the observations of Costello and Tuthill (1961). The change from enhancement of the heat transfer at lower levels of heat flux to a degradation at higher levels produces a "crossover" in the boiling curve, also observed by Gray and Marto (1968).

Beckman and Merte (1965) studied the influence of acceleration on the pool boiling of water up to 100g. Using high-speed photography, they observed bubble formation and growth and obtained data on bubble parameters such as growth rate, maximum and departure sizes, departure frequencies, and contact angle. The high-speed motion pictures taken at 3000 to 15,000 frame/s showed remarkable dynamic behavior of the bubbles. Early bubble growth rates are found to be essentially constant and independent of acceleration. Increasing acceleration decreased the number of active nucleation sites, but increased the bubble departure frequency.

Judd and Merte (1970) studied the effects of acceleration and subcooling on nucleate pool boiling of R-113 up to 100g. The test surface was a transparent, electrically conducting glass plate coated with tin oxide. This work demonstrated that increasing acceleration and or/subcooling at constant heat flux enhanced the contribution of natural convection, significantly reducing the contribution of nucleate boiling for a constant imposed heat flux. The temperature of the heating surface and the temperature distribution in the adjacent liquid were measured. High-speed photography was used to determine the active nucleation site density, the average population density, the bubble departure frequency, and the maximum bubble diameter.

Gray and Marto (1968) obtained flow boiling heat transfer coefficients with water in a cylindrical test boiler rotating about its vertical axis. Accelerations up to 200g were applied, and the heat transfer coefficients increased with increasing acceleration at the lower heat flux and decreased at the higher levels of heat flux, producing the crossover effect referred to earlier. However, in a later work by Marto and Gray (1971) with a similar system in which the acceleration and heat flux levels were increased further, no such crossover was observed.

Eschweiler et al. (1967) demonstrated that boiling was suppressed when acceleration was applied. Water was boiled in a small cylinder rotating about its own axis placed vertically with accelerations between 11 and 1280g. Increasing acceleration produced a gradual decrease of slopes in the plot of heat flux versus heater surface superheat, and eventually the slope corresponding to nonboiling natural convection was reached at 620g.

Koerner (1970) also observed a delay in the onset of boiling with increased acceleration. The test apparatus was similar to that of Eschweiler, with a condenser at the rotating axis. Using water as a test fluid, his experiments covered the range from 50 to 1000g. In these results, the slope of the nucleate boiling curve during subcooled boiling was reduced as the acceleration was increased, similar to the results of Eschweiler et al. (1967).

Influence of Subcooling. Liquid subcooling ΔT_{sub} is defined here as the temperature difference between the saturation temperature corresponding to the pressure at the heating surface and the bulk liquid temperature in the vicinity of the

Contributed by the Heat Transfer Division and presented at the National Heat Transfer Conference, Houston, Texas, July 24–27, 1988. Manuscript received by the Heat Transfer Division December 23, 1988; revision received July 18, 1989. Keywords: Boiling, Phase-Change Phenomena.

heating surface. This bulk temperature depends on the temperature distribution in the liquid. With pool boiling this in turn depends on the combination of the system pressure, heat flux, liquid depth above the heating surface, the degree of stirring by the rising bubbles, system geometry and acceleration, and the temperature of the returning condensate.

Early investigations of the influence of subcooling on pool boiling were reported by Gunther and Kreith (1949). Boiling water bubbles were photographed under subcooled conditions at atmospheric pressure in the absence of forced convection. The important characteristics of the bubbles were their small size, large numbers, and rapid collapse. Some bubbles collapsed at the heating surface while others departed from the solid surface and collapsed in the surrounding liquid. It was reported that the decrease in liquid temperature also caused a decrease in bubble life and an increase in the bubble population, although this latter finding was not observed in the experiments of Dew (1948), who found rather that the increase in subcooling decreased the bubble population. Gunther and Kreith (1949) further observed that: (*a*) A given increase in surface superheat resulted in a correspondingly larger increase in heat flux with subcooling than with a saturated liquid, (*b*) the peak heat flux increased by a large amount with subcooling, (*c*) the boiling data were correlated better using the heater surface superheat $T_w - T_{sat}$ as the driving potential.

In a work by Bergles and Rohsenow (1964) dealing primarily with forced-convection surface boiling, measurements of pool boiling of subcooled water on a horizontal cylinder show that increases in subcooling have a significant influence on nucleate boiling, shifting the boiling curve to higher wall superheats as the liquid subcooling was increased at constant heat flux and system pressure. This appears to be contradictory to the findings of Duke and Schrock (1961), who used a flat horizontal heating surface, and Grassman and Hauser (1964), who used a wire heating surface.

The work of Merte and Clark (1961) for pool boiling at high acceleration also included some results with low subcooling. At the lower levels of heat flux, increasing subcooling caused the wall superheat to increase and then to decrease. A plot of wall superheat versus liquid subcooling thus exhibited a maximum. The same trend was observed at higher levels of heat flux and acceleration except that wall temperature increases with subcooling did not reach a maximum, owing to the inability to increase the subcooling further.

Fand and Keswani (1974) describe measurements of the effect of subcooling on nucleate pool boiling heat transfer from a horizontal stainless steel cylinder to water at atmospheric pressure. At constant heat flux the heating surface temperature increased and then decreased as the bulk temperature of the fluid was reduced. This functional relationship had a maximum, which depended on the heat flux: With increasing heat flux, this maximum shifted to lower bulk fluid temperatures. The authors state that the boiling model proposed by Engelberg-Forster and Greif (1959) is substantiated by their experiments. Further they state that the observed effect of subcooling is within the commonly experienced scatter of boiling data, and that in spite of the measured influence of subcooling on boiling, it is of little significance. Shiotsu and Sakurai (1974) pointed out that when plotted on a log q'' versus log T diagram, the data of Fand and Keswani (1974) had a slope of less than 1 at large subcoolings, and therefore must have been in a regime of heat transfer where a transition from natural convection to developed nucleate boiling was taking place. This region of the boiling curve is known to be strongly influenced by subcooling. Bergles (1974) stated that the trends of Fand and Keswani (1974) are in general agreement with his work (1964) discussed earlier and that a "crossover mechanism" was responsible, and opined that the void volume in the vicinity of the heating surface is large with low subcoolings, so that the induced circulation is reduced as subcooling increases. The larger local induced circulation associated with low subcoolings would then reduce the wall temperature at constant heat flux, and the fully established boiling curve therefore would shift to the left as subcooling was reduced. It was further opined that this type of behavior would not be observed on horizontal flat heating surfaces. As will be demonstrated below, this is not the case.

Description of the Experimental Apparatus

A centrifuge, shown in Fig. 1, capable of handling a test vessel of 50 kg with a maximum of 1000 times standard gravitational acceleration, was used, and is described in detail by Ulucakli (1987). The test vessel installed to study nucleate pool boiling of water with high subcooling is shown in Fig. 2. The center of gravity is located so that the vector sum of the centrifugal and gravitational accelerations is normal to the heating surface at all times. The vessel contains the main heater, guard heaters, temperature measurement probes, a heat exchanger to provide subcooling, a condenser, and a water depth control tube above the heating surface. All parts were fabricated from stainless steel, types 316 and 304.

The heater is machined from a 0.05 percent tellurium copper cylinder and provides a heating surface 2.54 cm (1 in.) in diameter. A circular stainless steel foil (type 347) 0.1 mm (0.004 in.) thick and 10.2 cm (4 in.) in diameter was vacuum brazed to the copper cylinder at this end for the actual heating surface. The other end of the copper cylinder was drilled and reamed to insert cartridge heaters. Three radial holes 0.5 mm (0.021 in.) in diameter and 1.3 cm (0.5 in.) deep were drilled in the narrow end to insert calibrated sheathed chromel-constantan thermocouples, which were used to compute the heat flux and to determine the heating surface temperature by extrapolation. These thermocouples were located at the following nominal distances from the boiling surface: 1 mm (0.039 in.); 7.6 mm (0.298 in.); 13.7 mm (0.538 in.). The main heater is surrounded with four guard heaters, radiation

Nomenclature

a = acceleration
a/g = nondimensional acceleration
D = heating surface diameter
g = acceleration due to the earth's gravitational field
h = nonboiling natural convection heat transfer coefficient
k = thermal conductivity of the liquid
Nu_D = Nusselt number based on the heating surface diameter $= hD/k$
P_w = pressure at the heating surface
q'' = heat flux
R = distance between the heating surface and the vertical axis of rotation
Ra_D = Rayleigh number based on the heating surface diameter $= \beta g D^3 (T_w - T_b)/\alpha \nu$
T_b = bulk temperature of the liquid
$T_{sat,w}$ = saturation temperature at the heating surface
T_w = heating surface temperature
ΔT_{sub} = liquid subcooling $= T_{sat,w} - T_b$
ΔT_{sat} = wall superheat $= T_w - T_{sat,w}$
w = angular speed of the centrifuge
α = thermal diffusivity of liquid
β = volumetric thermal expansion of liquid
ν = kinematic viscosity of liquid

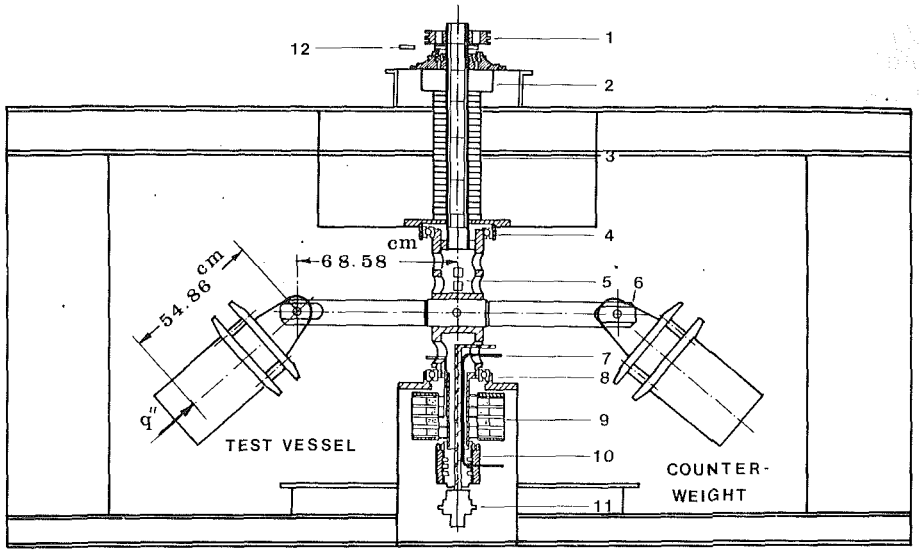

1. Pulley, 2. Kerosene Bath, 3. Mercury Commutators, 4. Upper Main Bearing, 5. Pressure Transducer, 6. Cross-Arm, 7. Cooling Water to Heat Exchangers, 8. Lower Main Bearing, 9. Copper Brushes, 10. Rotating Fluid Coupling, 11. Mercury Commutator for AC Power, 12. Magnetic Pick-up.

Fig. 1 Drawing of the centrifuge

shields, and insulation to minimize heat losses, as shown in Fig. 2.

The hydrostatic pressure at the test surface due to the 2.54 cm (1 in.) liquid depth increased as the acceleration increased from $a/g = 1$ to $a/g = 100$. To maintain a constant pressure at the heating surface at all acceleration levels, the system pressure above the liquid was reduced correspondingly, beginning from initial pressurization of the test vessel at $a/g = 1$ with helium, which has the lowest solubility in water among all gases. A lecture bottle and miniature pressure regulator were mounted on the central part of the centrifuge vertical shaft and connected to the test vessel via a solenoid valve and flexible tubing to pressurize the test vessel under rotation, while the pressure inside the test vessel was measured and controlled using a strain gage type transducer located vertically at the center of rotation, so that centrifugal forces did not influence its output. A large-scale precision pressure gage was connected when the system was stationary, for calibration purposes.

The heat rejection system consists of the following components: two heat exchangers within the test vessel functioning as a subcooling coil and a condensing coil, a rotating union to transfer the cooling water to and from the rotating system, flowmeters for monitoring the volume flow rate through the heat exchangers, needle valves to control the flow rate, and a filter to remove particulates in the cooling water supply.

The temperature measurement system consists of the three heating surface thermocouples, three liquid thermocouples, three differential thermocouples for guard heater control, the reference and constant temperature baths, and the mercury commutators for connecting the rotating system to a precision potentiometer with a minimum of induced electrical noise.

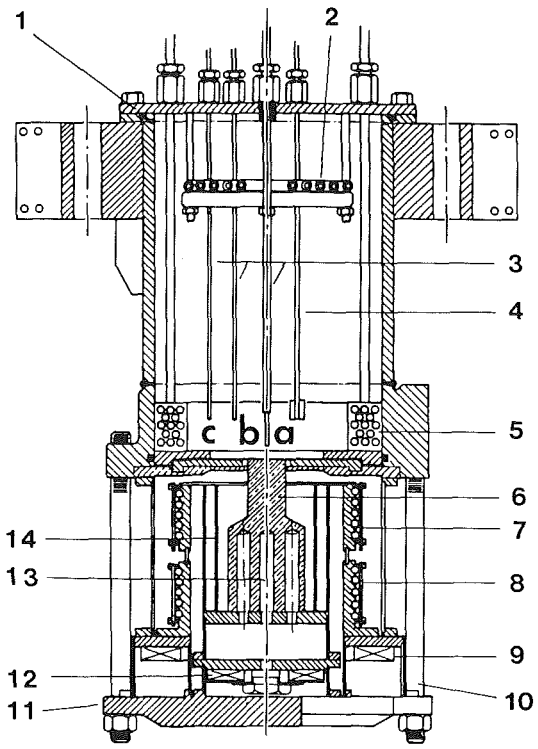

1. Cover Plate, 2. Condensing Heat Exchanger, 3. Liquid Temperature Probes, 4. Liquid Depth Control Tube, 5. Subcooling Heat Exchanger, 6. Copper Cylinder, 7. Upper Cylindrical Guard Heater, 8. Lower Cylindrical Guard Heater, 9. Bottom Ring Guard Heater, 10. Support Bolts, 11. Support Plate, 12. Bottom Disc Guard Heater, 13. Cartridge Heaters, 14. Radiation Shields

Fig. 2 Test vessel schematic

Experimental Procedures

Procedure. All tests were conducted in the steady state. The independent variables were acceleration, liquid subcooling, and heat flux. The tests were conducted in the sequence of accelerations of 1, 10, and 100g, while the heat flux levels were varied between 0.19 and 1.26 MW/m^2. The relatively large lower level of the heat flux was necessary to produce boiling as subcooling or acceleration are increased. As later tests showed, the increased nonboiling natural convection associated with increased acceleration and subcooling can suppress the boiling process. The upper level of heat flux was determined by the approximate critical heat flux at earth gravity. The liquid subcooling was varied between zero and a

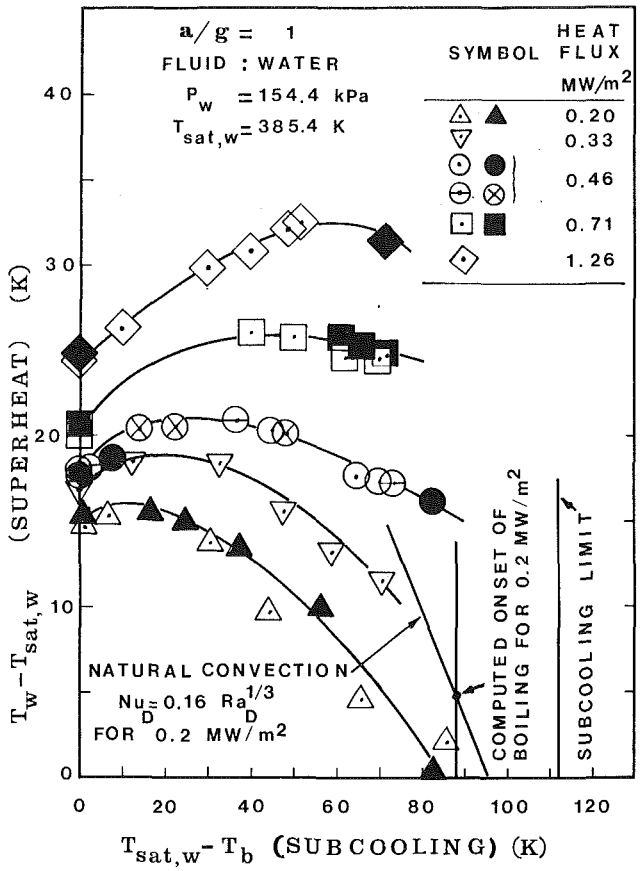

Fig. 3 Superheat versus subcooling results at $a/g = 1$

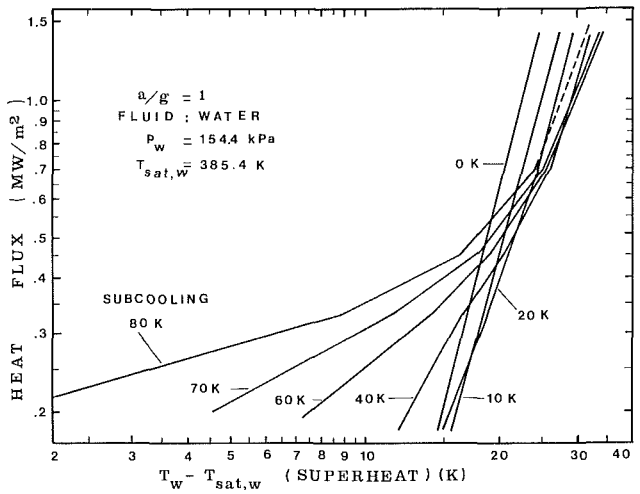

Fig. 4 Heat flux versus wall superheat at $a/g = 1$

maximum of 84 K, determined by the available volume flow rate and temperature of the cooling water and the characteristics of the subcooling coil.

During operation at a given acceleration level, the heat flux was maintained constant while subcooling was varied. The heat flux was then changed to a new level and subcooling varied again. At constant heat flux and acceleration, each test was initiated at or near the saturated state and ended at or near the saturated state. Except for the highest level of heat flux used, which exceeded the normal 1*g* critical heat flux, all elevated acceleration tests started with a 1*g* anchor point at the saturated state and ended with a 1*g* anchor point at the saturated state, which then served as reproducibility checks. It must be noted that due to the increased hydrostatic pressure at the test surface and increased natural convection, the so-called 10*g* and 100*g* saturated data include a certain unavoidable amount of subcooling.

Experiments. Before every test, the test vessel was filled with distilled and deionized water to a depth of 2.54 cm (1 in.). It had been demonstrated that with water the pool boiling process was no longer influenced by the depth when it was more than 2.54 cm (1 in.). Dissolved gases were removed by vigorous boiling and venting over a 3-h period. The electrical resistivity of the water was used as a measure of its purity, with a minimum of 2 M Ω-cm existing at the beginning of each test.

After obtaining data at the saturated liquid state, the cooling water flow rate through the cooling coil was increased, depending on the degree of liquid subcooling desired. Data were taken when the temperatures again reached steady state. The cooling coil flow rate was then increased for another level of subcooling. At a certain flow rate it was not possible to increase the subcooling further, and the cooling coil water was then reduced and time allowed to reach the saturated state again, prior to halting the test.

To determine possible hysteresis effects with subcooled boiling, the procedure described above was modified for the 10*g* test series. After reaching the maximum subcooling, the cooling water flow rate was gradually reduced and data were also taken with decreasing subcooling. The saturated state was eventually reached under rotating conditions, and the centrifuge was then stopped to obtain a 1*g* anchor point at the saturated state. The 100*g* tests were conducted in a similar manner.

Data Reduction. The three temperatures measured axially in the copper near the boiling surface were used to compute the heat flux and surface temperature. The uncertainty of the surface temperature is estimated to be on the order of a maximum of ±0.7°C on an absolute basis, while on a relative basis during a particular test it is considerably less. The uncertainty of the heat flux is ±4 percent.

The centrifugal acceleration is calculated to a reasonable approximation by $a = R * w^2$, where a is the centrifugal acceleration, w is the angular speed of the centrifuge, and R is the radius at which the test surface is located. The radius is 1.234 m (48.6 in.) from the vertical axis of the centrifuge.

Experimental Results

Tests were conducted to determine the maximum subcooling possible with the subcooling heat exchanger shown in Fig. 2, and found to be about 85 K for the saturation temperature of 385.4 K at the test surface, independent of the level of heat flux and acceleration used. A practical maximum limit of 112 K on the subcooling exists, associated with the freezing point of water at 0°C. This subcooling limit is indicated on each of the plots of heater surface superheat versus subcooling on Figs. 3, 5, and 7.

Certain combinations of heat flux, subcooling, and acceleration were found to result in nonboiling natural convection heat transfer. Nonboiling heat transfer was obvious whenever the heater surface temperature was below the local saturation temperature, but also appeared to be present even with significant heater surface superheat, when the measurements were compared with predictions of the appropriate natural convection correlations. The complete nonboiling convection data and their correlation for the geometry used here are presented by Ulucakli (1987). Evaluating the properties at the film temperature, defined as the average of the heater surface and bulk fluid temperatures, the correlation giving the best fit at $a/g = 1$ and $a/g = 10$ is

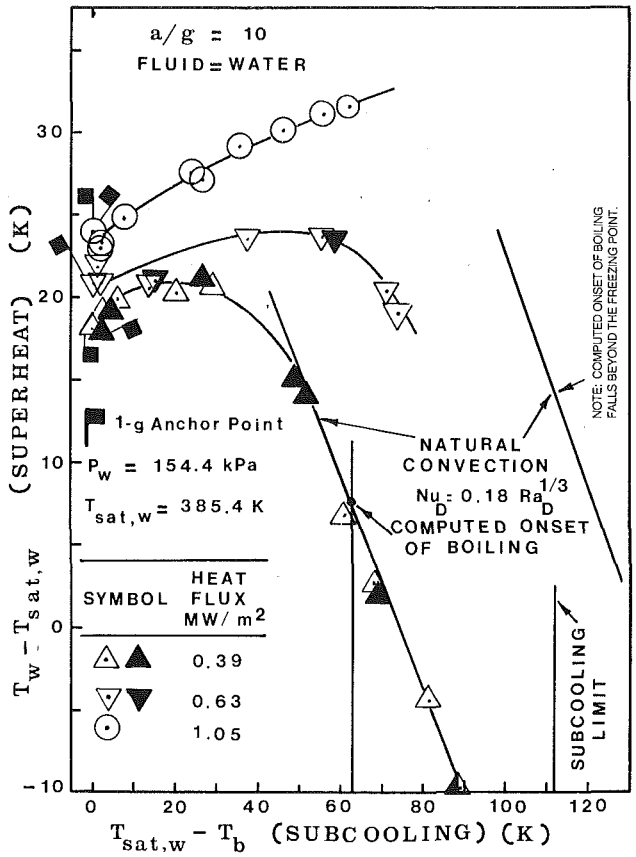

Fig. 5 Superheat versus subcooling results at $a/g = 10$

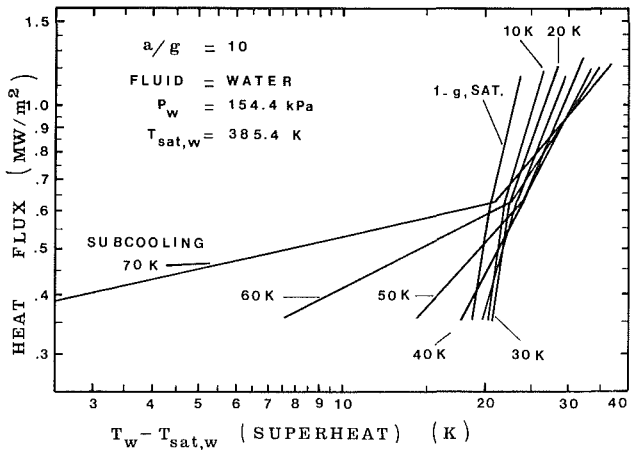

Fig. 6 Heat flux versus wall superheat at $a/g = 10$

$$Nu_D = 0.18\,(Ra_D)^{1/3} \qquad (1)$$

while a coefficient of 0.16 gives a better fit at $a/g = 100$. The experimental data covered the Rayleigh number range of 10^8 to 2×10^{11}. With the wide range of subcooling and associated levels of wall-bulk ΔT's experienced in the present work, the Rayleigh number is quite sensitive to the corresponding property variations, and the form of the "best" correlation remains open to question. For present purposes equation (1) will be used, with the coefficient of 0.16 to be used for $a/g = 100$.

In order to demonstrate the influence of subcooling adequately, the measurements of heater surface superheat are plotted as a function of bulk subcooling with the various levels of heat flux as a parameter in Fig. 3 for $a/g = 1$, in Fig. 5 for $a/g = 10$, and in Fig. 7 for $a/g = 100$. Additional information is included on each of these, described below as appropriate.

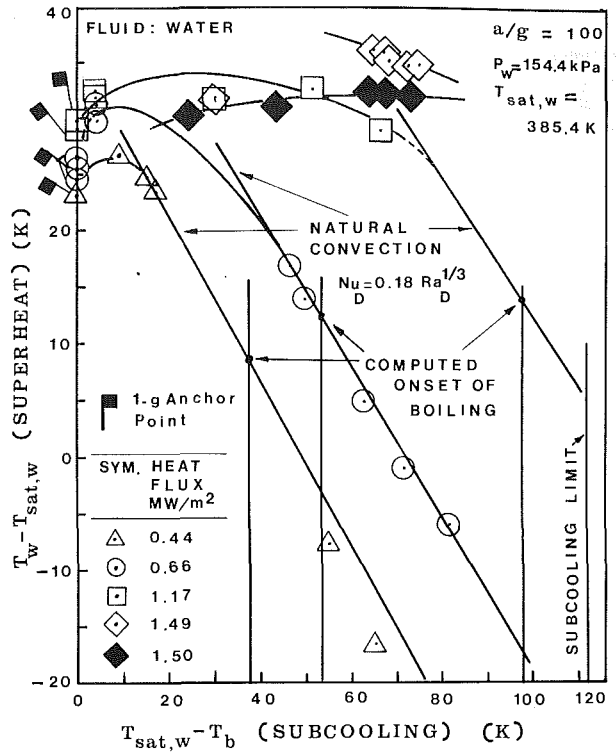

Fig. 7 Superheat versus subcooling results at $a/g = 100$

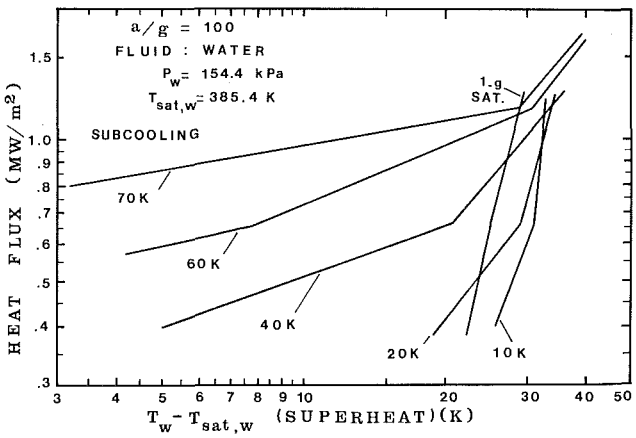

Fig. 8 Heat flux versus wall superheat at $a/g = 100$

The smoothed curves through these data points are then cross-plotted in Figs. 4, 6, and 8 corresponding to the acceleration, in the more traditional boiling heat transfer form of heat flux versus heater surface superheat using bulk subcooling as the parameter. In so doing, the competing and opposite influences of subcooling on the nonboiling and boiling contributions to the heat transfer process become more obvious.

Tests at $a/g = 1$. The lowest heat flux was 0.2 MW/m^2. One test at this heat flux, indicated by the open triangles in Fig. 3, was conducted by increasing the subcooling from zero to the maximum possible. Another, indicated by the darkened triangles, was conducted by decreasing the subcooling to zero from the initial maximum possible. A trend for hysteresis appears to be present, and is intuited to be associated with the activation/deactivation of nucleating sites as the subcooling is decreased or increased, since nonboiling natural convection demonstrates no hysteresis. The other multiple data points included in Fig. 3 attest to a reasonable degree of reproducibility.

It is noted in Fig. 3 that the heater surface superheat at first increases and then decreases as subcooling increases from the saturation state, resulting in a maximum. The increase in superheat with subcooling not only increases with heat flux, but the maximum occurs at larger levels of subcooling for larger levels of heat flux. At the highest heat flux used at $a/g = 1$, 1.26 MW/m^2, the heater surface superheat increases by 8.3 K at a subcooling of 60 K. Using the development of Zuber (1959) the critical heat flux for saturated water at $a/g = 1$ and atmospheric pressure is estimated to be 1.5 MW/m^2, somewhat above the highest level of 1.26 MW/m^2, used here at $a/g = 1$.

The relationship between heater surface superheat and bulk subcooling computed from equation (1) is also included in Fig. 3 for the heat flux of 0.2 MW/m^2. The near tangency with the data for decreasing subcooling, together with the near-zero heater surface superheat at this point, demonstrate that nonboiling natural convection virtually dominates the process here. Another reasonable determination of the onset of nucleate boiling in this region can be made by incorporating equation (1) into the so-called Hsu–Rohsenow–Bergles model of nucleation, presented by Rohsenow (1985). This point is also indicated in Fig. 3.

Although a conjecture at this point, it appears reasonable that the heater surface superheat at the highest level of heat flux in Fig. 3 would also have decreased further were a greater subcooling possible. This limitation exists because of the design of the internal heat exchanger, and the subcooling most likely could be extended were the cooling medium to be refrigerated.

The smoothed data of Fig. 3 are cross-plotted in Fig. 4, and demonstrate that nonboiling convection dominates at the low levels of heat, while as heat flux increases the heater surface superheat increases with subcooling. As will be seen, similar behavior occurs at the higher acceleration levels.

Tests at $a/g = 10$. The next group of tests, conducted at $a/g = 10$, is shown in Fig. 5. Initial tests revealed the extreme sensitivity of the subcooling level to the cooling water flow rate, and modifications to the apparatus were made to provide for fine control. The "anchor" points indicated are obtained for each level of heat flux for the saturated state at $a/g = 1$ immediately prior to and following each test at high acceleration, as a check on reproducibility and/or hysteresis effects as a result of subjecting the boiling system to large body forces. These "anchor" points were found to be repeatable. At the lowest heat flux level shown, the open triangles again correspond to increasing subcooling, while the dark triangles apply to decreasing subcooling, and the reproducibility and lack of hysteresis are evident.

The heater surface superheat versus subcooling relationship for nonboiling natural convection from equation (1) is included for the two lower heat flux levels used. At 0.39 MW/m^2 the predominance of nonboiling is obvious, while at the heat flux of 0.63 MW/m^2 the significant departure from the nonboiling correlation indicates the presence of nucleate boiling even at this large subcooling level. The computed onset of boiling is shown for the lowest heat flux only; the subcooling for the next value used, 0.63 MW/m^2, falls beyond the freezing point of water. Figure 6 is the cross-plot of the smoothed data of Fig. 5, with subcooling as a parameter.

Tests at $a/g = 100$. It was not possible to conduct tests at heat flux levels below 0.3 MW/m^2 with $a/g = 100$ for any degree of subcooling; boiling became completely suppressed. The lowest heat flux used was 0.44 MW/m^2, shown in Fig. 7, and here nucleate boiling appears to be completely suppressed beyond a subcooling of about 17 K. The nonboiling natural convection correlation, with 0.16 as the coefficient, appears to describe the behavior at high heater surface superheats, up to 22 K.

It was not possible to conduct the two anchor point tests at the highest levels of heat flux, 1.49 and 1.50 MW/m^2, with saturated liquid at $a/g = 1$, since this is above the estimated critical heat flux. It is possible that beginning the boiling test with a saturated liquid activates the nucleating sites in a way that is sustained as subcooling varies, thus providing yet another opportunity for the so-called hysteresis to be present. All other testing at the higher acceleration levels except these two was conducted with anchor points, and may explain the apparent discrepancy between these two tests and the others.

At this level of acceleration, it is noted in Fig. 7 that although increases in heater surface superheat with subcooling take place, the changes are now relatively smaller, and a broad plateau is present. From the prior photographic work of Beckman and Merte (1965) and Judd and Merte (1970) it was observed that the maximum departure size of the bubble changes relatively little beyond $a/g = 10$, and it is possible that the associated stirring action induced by the departing bubbles becomes relatively insensitive to the degree of subcooling. In these two cited works, the subcoolings used were relatively small when compared to the present work.

The slopes of the curves in the cross-plots of Fig. 7 presented in Fig. 8 at the heater surface superheats below 20 K show the dominance of nonboiling natural convection with subcoolings greater than 20 K.

Discussion

Understanding and assessing the measurements of nucleate pool boiling with both large system acceleration and large subcooling requires that the symbols and terminology used be quite precise. Figures 3, 5, and 7 are plots of heater surface superheat ($T_w - T_{sat,w}$) versus bulk subcooling ($T_{sat,w} - T_b$). T_w is the heating surface temperature while $T_{sat,w}$ is the saturation temperature corresponding to the pressure at the heater surface. The definition of the latter is normally of no great consequence in research, since pressure variations owing to hydrostatic head changes are negligibly small. With large system accelerations, however, this is no longer the case; the liquid depth of 2.54 cm (1 in.) used here produces a hydrostatic pressure of 254 cm at $a/g = 100$. In the work presented here the hydrostatic pressure at the heating surface and hence $T_{sat,w}$ was maintained constant by reducing the pressure of the helium in the vapor space. Extensive testing conducted both with and without the helium produced no measurable differences. In effect, then, Figs. 3, 5, and 7 are plots of the heater surface temperature T_w versus the bulk temperature T_b measured nearest the heating surface as seen in Fig. 2. A nonboiling natural convection correlation with constant properties, heat flux, and a/g then results in a straight line for T_w versus T_b as indicated. Where the measurements coincide with the correlation over an extended degree of subcooling it can be reasonably deduced that no significant nucleate boiling heat transfer is taking place, even though a significant heater surface superheat exists.

With a saturated liquid, the measurements of Merte and Clark (1961) show that the heater surface superheat increases with acceleration for constant high levels of heat flux, while it decreases for constant low levels. The latter is attributed to the increasing relative contribution of nonboiling convection, even though the liquid bulk is essentially saturated. The degradation of the heat transfer in the former is attributed in part to the action of buoyancy on the growing vapor bubbles, increasing the thickness of the liquid microlayer beneath the bubble and reducing the heat transfer per bubble. For a constant heat flux, then, more nucleation sites are required, resulting in turn in a higher surface temperature. This influence of high acceleration on the microlayer is still somewhat speculative, and remains to be observed directly and described analytically.

As indicated by the measurements presented here, for a constant value of heat flux and acceleration, beginning with an initially saturated or near-saturated bulk liquid state, the heater surface superheat first increases, reaches a maximum, and decreases as the bulk liquid subcooling increases. The explanation for this behavior is as follows: As the bulk liquid subcooling is increased, certain active nucleating sites would tend to become extinguished were the heater surface superheat to be maintained constant, since the superheated thermal boundary layer thickness would be reduced. For a constant imposed heat flux, then, a higher heater surface superheat will be required either to sustain these nucleating sites or to activate others. As the subcooling is increased further, the increasing nonboiling natural convection contribution to the total heat flux begins to outweigh that associated with the active nucleating sites, until a maximum in the heater surface superheat is reached. This indicates that a balance in the rate of change of the effect of subcooling on the nonboiling and the boiling contributions to the total heat flux is present, and further increases in subcooling should then give prominence to the nonboiling natural convection contributions. As the heat flux is increased to higher levels, the natural convection nonboiling contribution requires a significantly larger subcooling before it begins to overshadow the boiling contribution, and hence the rightward shift in the maximum.

The interaction between subcooling, nonboiling natural convection, and the nucleation remains to be described analytically for the case with established boiling. A credible prediction of the onset of nucleate boiling as subcooling is decreased is demonstrated here by the Hsu–Bergles–Rohsenow model, as described by Rohsenow (1973). A reasonable model of the established nucleate boiling process, however, must include a description of the nucleation characteristics of the heater surface–fluid combination. By this is meant those attributes of the surface and fluid necessary to predict both the initial and additional activation of the nucleation sites.

Photographic observations of the nucleation site density with pool boiling of R-113 under high gravity were made through a transparent glass heater surface by Judd and Merte (1970). The maximum acceleration was $a/g = 100$, but the maximum heat flux and subcooling were only 0.1 MW/m^2 and 17 K, respectively. The active site density did not change as subcooling was varied from saturation to 17 K and a/g varied from 1 to 10. The active site density decreased by 1/2 as a/g increased from 10 to 100 for subcoolings between 8 and 17 K. It is surmised that this latter decrease is associated with the increasing role of nonboiling natural convection. Generalizations of these behaviors, even with the limited ranges of heat flux and subcooling, must be made with caution since the glass surface used was quite smooth, relative to metallic surfaces such as that employed here.

Conclusions

For constant heat flux and constant acceleration, increasing the liquid subcooling from saturation results in an increase and then a decrease in heater surface superheat with nucleate pool boiling.

The increase in heater surface superheat increases with heat flux and with acceleration.

For certain combinations of heat flux, subcooling, and acceleration, nucleate boiling is suppressed completely.

The variation in heater surface superheat is a result of the complex interactions between the nonboiling natural convection, the activation of nucleating sites, and the heat transfer associated with each active nucleating site.

References

Beckman, W. A., and Merte, H., Jr., 1965, "A Photographic Study of Boiling in an Accelerating System," ASME JOURNAL OF HEAT TRANSFER, Vol. 87, No. 3, pp. 374–380.

Bergles, A. E., 1974, Discussion of Paper by Fand and Keswani, in: *Heat Transfer 1974*, Vol. IV, p. 98.

Bergles, A. E., and Rohsenow, W. M., 1964, "The Determination of Forced-Convection Surface-Boiling Heat Transfer," ASME JOURNAL OF HEAT TRANSFER, Vol. 86, p. 365.

Clark, J. A., and Merte, H., Jr., 1963, "Boiling Heat Transfer to a Cryogenic Fluid in Both Low and High Gravity Fields," *Proc. 11th Int. Congress of Refrigeration*, Munich, Federal Republic of Germany, p. 27.

Costello, C. P., and Tuthill, W. E., 1961, "Effects of Acceleration on Nucleate Pool Boiling," *Chemical Engineering Progress Symposium Series*, No. 57, Vol. 32, pp. 189–196.

Dew, J. E., 1948, Thesis in Chemical Engineering, M.I.T. (quoted by W. H. McAdams in *Heat Transmission*, 3rd ed., 1954).

Duke, E. E., and Shrock, V. E., 1961, "Void Volume, Site Density and Bubble Size for Subcooled Nucleate Pool Boiling," *Proc. of the 1961 Heat Transfer and Fluid Mechanics Inst.*, pp. 130–145.

Engelberg-Forster, K., and Greif, R., 1959, "Heat Transfer to a Boiling Liquid-Mechanism and Correlations," ASME JOURNAL OF HEAT TRANSFER, Vol. 81, No. 2, pp. 43–53.

Eschweiler, J. C., Benton, A. M., and Preckshot, G. W., 1967, "Boiling and Convective Heat Transfer at High Accelerations," *Chemical Engineering Progress Symposium Series*, No. 79, Vol. 63, pp. 66–72.

Fand, R. M., and Keswani, K. K., 1974, "The Influence of Subcooling on Pool Boiling Heat Transfer From a Horizontal Cylinder to Water," *Heat Transfer 1974*, Vol. 4, pp. 11–14, Paper B 1.3.

Grassman, P., and Hauser, I. J., 1964, "Heat Transfer From Wire to Subcooled and Boiling Water," *Int. J. Heat and Mass Transfer*, Vol. 7, pp. 211–214.

Gray, V. H., and Marto, P. J., 1968, "Boiling Heat Transfer Coefficients, Interface Behavior, and Vapor Quality in Rotating Boiler Operating to 475 G's," NASA Technical Note TN D-4136.

Gunther, F. C., and Kreith, F., 1949, "Photographic Study of Bubble Formation in Heat Transfer to Subcooled Water," *Proc. 1949 Heat Transfer and Fluid Mechanics Institute*, pp. 113–124.

Judd, R. L., and Merte, H., Jr., 1970, "Influence of Acceleration on Subcooled Nucleate Pool Boiling," *Heat Transfer 1970*, Vol. 6, Paper B 8.7.

Judd, R. L., and Merte, H., Jr., 1972, "Evaluation of Nucleate Boiling Heat Flux Predictions at Varying Levels of Subcooling and Acceleration," *Int. J. Heat and Mass Transfer*, Vol. 15, No. 5, pp. 1075–1096.

Koerner, W., 1970, "The Influence of High Acceleration on Boiling Heat Transfer," *Chemie-Ingenieur-Technik*, Vol. 42, No. 6, pp. 409–414 [in German].

Marto, P. J., and Gray, V. H., 1971, "Effects of High Accelerations and Heat Fluxes on Nucleate Boiling of Water in an Axisymmetric Rotating Boiler," NASA Technical Note TN D-6307.

Merte, H., Jr., and Clark, J. A., 1961, "Pool Boiling in an Accelerating System," ASME JOURNAL OF HEAT TRANSFER, Vol. 83, No. 3, pp. 234–242.

Mikic, B. B., and Rohsenow, W. M., 1968, "A New Correlation of Pool Boiling Data Including the Effect of Heating Surface Characteristics," ASME Paper No. 68-WA/HT-22.

Rohsenow, W. M., 1973, "Boiling," *Handbook of Heat Transfer Fundamentals*, McGraw-Hill, Chap. 12, pp. 12-1–12-94.

Shiotsu, M., and Sakurai, A., 1974, Discussion of Paper by Fand and Keswani, *Heat Transfer 1974*, Vol. IV., p. 97.

Ulucakli, M. E., 1987, "Nucleate Pool Boiling With Increased Acceleration and Subcooling," Ph.D. Thesis, University of Michigan, Ann Arbor, MI.

Zuber, N., 1959, "Hydrodynamic Aspects of Boiling Heat Transfer," USAEC Report, AECU-4439.

EHD Enhancement of Nucleate Boiling

P. Cooper
Lecturer,
Department of Mechanical Engineering,
University of Wollongong,
Wollongong, NSW 2500, Australia

This paper describes: (a) an experimental investigation into the effect of an electric field applied to pool boiling of Freon (R114) on a finned tube and (b) a theoretical model of electrically enhanced nucleate boiling applicable to simple surfaces only. Experimental results have shown electrohydrodynamic (EHD) enhancement of heat transfer to be manifest in two ways: (i) elimination of boiling hysteresis, (ii) augmentation of nucleate boiling heat transfer coefficients by up to an order of magnitude. These effects were also observed in electrically enhanced boiling of Freon/oil mixtures. A new analytical model is described whereby EHD nucleate boiling data from previous studies (employing simple apparatus comprising heated wires with concentric cylinder electrodes) have been correlated for the first time using the concept of an electrical influence number. This dimensionless parameter is based upon the relationship between applied electric field intensity and changes in bubble departure diameter at a heat transfer surface.

Introduction

The use of electric fields to enhance convective heat transfer was first reported in a UK patent over seventy years ago (Chubb, 1916). However, this promising enhancement technique has yet to find commercial application despite considerable fundamental research.

One of the first quantitative studies in this field was by Bochirol et al. (1960), which, like many later investigations, was particularly concerned with the dramatic electrohydrodynamic (EHD) enhancement of the film boiling regime and consequent increase in critical heat flux. This particular EHD phenomenon is due to electrical destabilization of the vapor film at a heat transfer surface caused by electrical forces acting on the vapor–liquid interface. These forces arise from the difference between the dielectric permittivity of the liquid and vapor phases and are of the type called "dielectrophoretic."

Since 1960 many further studies of EHD enhanced film boiling have been carried out and these have been reviewed by Jones (1978), along with work on EHD enhanced condensation and single-phase heat transfer. However, most of this research has dealt with situations inappropriate to the needs of heat exchanger manufacturers, not only because film boiling is a mode of heat transfer to be avoided under normal operation conditions but also because the electrode and heat transfer geometries used in experiments have not been applicable to practical evaporators.

EHD enhancement of nucleate boiling involves the application of an intense electric field to the heat transfer surface. Dielectrophoretic electric forces (and possibly "electrophoretic" forces, due to the presence of free charges in the fluid) lead to modified bubble dynamics and enhanced fluid convection in both phases, which in turn promote increased heat transfer.

EHD heat transfer enhancement is thought to be best applied to electrically insulating fluids. Practical implementation of EHD techniques requires the addition of electrodes and a high voltage source to the normal heat exchanger. Thus, large evaporators would appear to provide the most cost-effective application. Of particular interest are systems utilizing small temperature differences across their evaporators where EHD elimination of boiling hysteresis may be advantageous. Thus, plants such as Organic Rankine Cycle (ORC) engines, large-scale heat pumps, Ocean Thermal Energy Conversion (OTEC) plants, etc., would seem to be attractive engineering applications. Indeed work is underway in Japan on the demonstration of a practical EHD evaporator incorporated in a commercial ORC plant. OTEC technology is as yet in its infancy; however, several successful demonstration projects have been realized (e.g., Ito and Seya, 1983). These units rely on a gross temperature difference across the ORC engine of no more than 30°C, giving refrigerant-side evaporating and condensing superheats of less than 5°C.

The work reported here forms part of a continuing research program to develop full-scale shell-and-tube EHD enhanced condensers and evaporators. An earlier stage included optimization of a shell-side electrode system consisting of plates and/or rods (Allen and Cooper, 1985). There followed an experimental and theoretical investigation of EHD enhanced condensation heat transfer, described elsewhere by Cooper and Allen (1984) and Cooper (1986), in which refrigerant-side heat transfer enhancement by up to a factor of three was observed. Although the tenor of previous work by others indicated that condensation heat transfer would be more amenable to EHD enhancement, it has been found, in fact, that EHD techniques have even greater potential when applied to nucleate boiling.

Experimental Apparatus and Procedure

A schematic diagram of the EHD assisted boiling rig is shown in Fig. 1. Full details of the apparatus have been given elsewhere by Cooper (1986) and Allen and Cooper (1987). The evaporator comprised a single, horizontal, integrally finned ("lo-fin") tube within a concentric brass shell. This was designed to model the operation of a tube in the bottom row of a shell-and-tube evaporator with EHD enhancement of shell-side heat transfer only. The experimental tube was chosen as one used commercially in large shell-and-tube evaporators by a major UK manufacturer. The test section of the tube was 514 mm in length and manufactured from brass. Tube fin profile and dimensions are shown in Fig. 2. The evaporator shell was a brass tube of 63.5-mm internal diameter with two 50-mm diameter sight glasses mounted at its mid-section to facilitate visual observation of the EHD phenomena (Fig. 3). The electrode system used for quantitative investigations was made from a copper wire mesh cylinder of 38-mm diameter insulated from the evaporator shell by "Tufnol" (grade 2P/45) inserts, as shown in Fig. 4. Unobstructed visual observation of the experimental tube for

Contributed by the Heat Transfer Division for publication in the JOURNAL OF HEAT TRANSFER. Manuscript received by the Heat Transfer Division September 24, 1987. Keywords: Boiling, Phase-Change Phenomena.

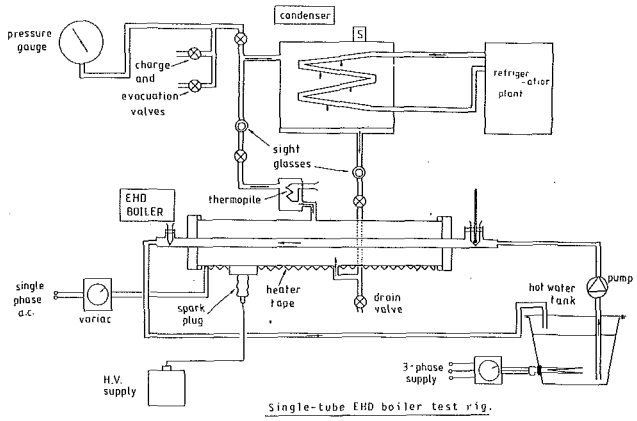

Fig. 1 Schematic diagram of experimental apparatus

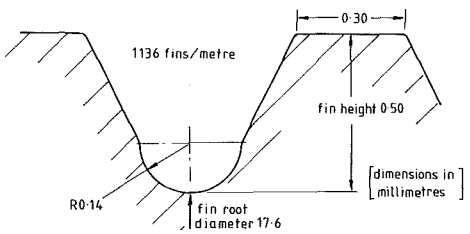

Fig. 2 Cross section of lo-fin tube profile

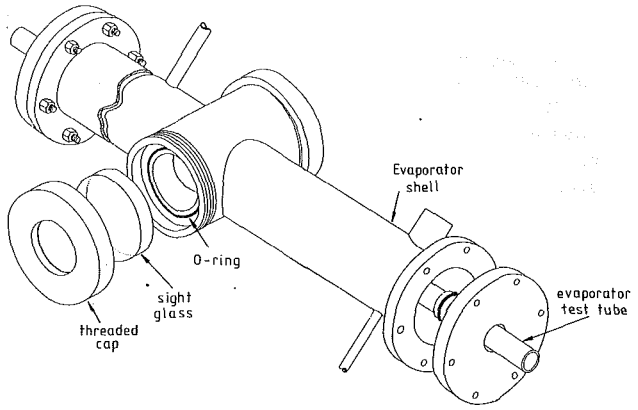

Fig. 3 Evaporator sight-glass arrangement

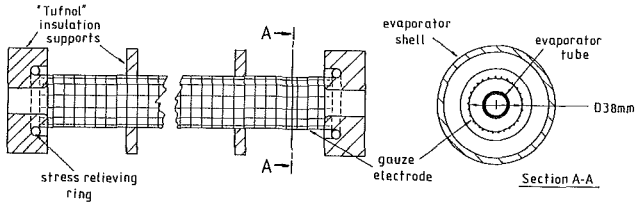

Fig. 4 Cylindrical electrode system

video recording of qualitative experiments was facilitated by a second electrode system with a conductive glass insert.

The high voltage supply (of up to 30 kV) to the electrodes was provided by either one of two electrostatic generators for positive or negative direct current (d.c.) potentials or from a 100-kVA high voltage transformer and regulator for alternating (a.c.) potentials. The electrical supply was fed into the EHD evaporator through a specially modified sparking plug in the shell wall, which made a spring-loaded contact with the electrode. Electrode potentials were monitored using two electrostatic voltmeters (calibrated to BS 358).

The liquid Freon saturation temperature was taken as that of the vapor exiting the EHD boiler and was measured by means of a three-junction thermopile immediately adjacent to (but outside) the evaporator shell. Measurement of the Freon liquid temperature per se was precluded by the intense electric fields within the shell. Fortuitously, other researchers, e.g., Hahne and Muller (1983), have found that the most effective way to characterize wall-to-liquid superheat, for correlating pool boiling data, is to use the system saturation temperature T_s, measured above the liquid surface. This was the situation assumed to pertain in the present study. All data reported below correspond to a system saturation temperature of $T_s = 21.5°C$, which was chosen so as to minimize heat exchange between the apparatus and the surroundings.

The evaporator tube-wall temperature was measured by means of eight copper constantan thermocouples; four were located circumferentially around the tube midsection and the remainder were positioned on one side of the tube, equidistant along the tube length. The thermocouple conductors (0.2-mm diameter with PTFE insulation) were routed through the inside of the evaporator tube to avoid interaction with the intense electric fields in the shell-side fluid. Thermojunctions were soft soldered into holes drilled in the tubewall between tube fins. Local wall-to-liquid saturation superheats were calculated from the measured differential e.m.f.s generated between the thermopile and the individual tube surface thermojunctions concerned. Uncertainty in these measurements was estimated to be approximately $\pm 0.05°C$. Other temperatures were measured by the same means with respect to a thermojunction immersed in an ice/water bath at an estimated uncertainty of $\pm 0.1°C$. Operation of the temperature measurement system was tested under isothermal conditions with and without electric stress applied; no detectable interference between the electric field and temperature measurements was found.

The evaporator test section was heated by hot water pumped from a tank containing a 9-kW immersion heater, its

Nomenclature

A = heat transfer surface area, m^2
a, b = constants in equation (9)
C_1 = constant in equation (1)
D = diameter, m
E = electric field strength, V/m
F_E = electric force on a bubble, N
g = gravitational acceleration, m/s^2
h = heat transfer coefficient, W/m^2K
m, n = constants in equation (1)
Ne = electrical influence number
Nu = Nusselt number
q = heat flux, W/m^2
Re = Reynolds number
T = temperature, K
V = applied electrode potential, V
β = contact angle, rad
Γ = volume, m^3
ϵ = absolute permittivity, F/m
ρ = density, kg/m^3
σ = surface tension, N/m

Subscripts

0 = zero-field condition
b = bubble
E = with applied electric field
L = liquid
m = arithmetic mean value
s = saturation value
v = vapor

output varied by means of a three-phase "variac." Total heat flux through the tube wall was calculated from the heating water bulk temperature drop between inlet and outlet, the water flow rate (measured by a variable-gap flowmeter), and published data for the density and specific heat of water. Bulk inlet and outlet temperatures were measured by means of copper/constantan thermojunctions. The inlet-to-outlet temperature drop of the order of 1–2°C was measured using the differential thermocouple e.m.f. between the inlet and outlet (by means of a digital voltmeter). Thorough mixing of the heating water was ensured by the use of vortex inducing spirals and copper gauze baffles positioned upstream of each thermojunction. Calculated magnitudes of total heat flux and heat transfer coefficients are estimated to be accurate to within ±5 percent and ±10–20 percent, respectively. All experimental results were recorded manually.

The use of water rather than electricity to heat the experimental tube resulted in variation of wall-to-liquid Freon superheat along the tube as the heating water cooled. Thus, all experimental results are quoted with respect to an arithmetic mean wall-to-liquid superheat, ΔT_m. Although not ideal for investigating the fundamental characteristics of EHD enhanced boiling phenomena, this situation was certainly more representative of conditions in a commercial shell-and-tube evaporator than one using electrical heating. Tube midsection surface temperature was measured at the four circumferential thermocouple stations. ΔT_m was then calculated from the arithmetic mean of temperatures at the five side-wall stations along the tube length assuming the circumferential temperature profile to be the same at all cross sections relative to the corresponding tube side wall temperature.

The liquid chosen for the experimental investigation was R114 (dichlorotetrafluoroethylene) because of its excellent dielectric properties, low toxicity, and widespread commercial use in heat pump and Rankine Cycle plants. Several experiments were also conducted to investigate the effect of electric stress on heat transfer to oil-contaminated R114. The oil used was Shell Clavus 68. This was simply mixed on a weight-to-weight (w.w.) basis with the total charge of R114 in the rig. To facilitate degassing and to ensure fully mixed, isothermal, initial conditions, the evaporator was heated before each experiment by means of self-limiting (Freezeguard) heating tape strapped to the underside of the shell. The condenser unit (see Fig. 1) was cooled by water from a thermostatically regulated refrigeration unit. Maximum heat flux obtainable at the heat transfer surface was limited by the capacity of this refrigeration plant. Steady-state conditions were obtained through control of the temperature of the heating and cooling water circuits; the relatively large thermal mass of the system led to long settling times of up to 30 min between data recordings.

Results

Zero-Field Heat Transfer. The first part to the study involved investigation of heat transfer under zero-field conditions. Results for a system saturation temperature T_s of 21.5°C graphed as mean heat transfer coefficient h_{m0} against mean wall-to-liquid superheat ΔT_m are shown in Fig. 5. Results were calculated with respect to the total (developed) external heat transfer surface area of the experimental tube (0.152 m²). As the study of boiling hysteresis was of particular interest, experiments were conducted with both increasing and decreasing ΔT_m. Boiling (or nucleation) hysteresis is manifest as a given threshold ΔT required to activate vapor generation at nucleation sites. Below this critical value of ΔT, heat transfer is by natural convection alone. The actual value of ΔT required to activate nucleation depends on a number of factors, particularly those relating to roughness and contamination of the heat transfer surface. In the present study, the lo-fin tube was installed as received from the manufacturer, with

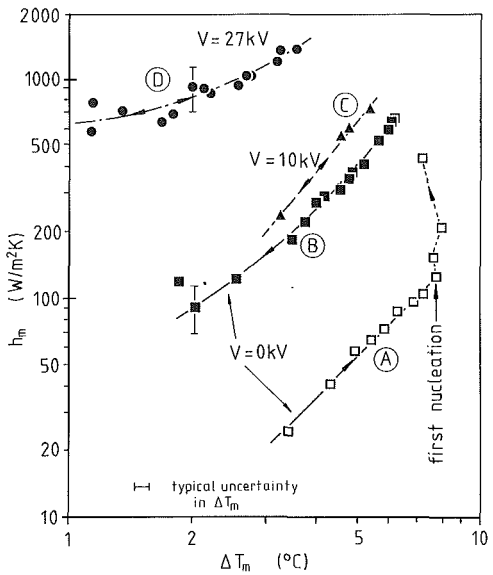

Fig. 5 Boiling hysteresis and EHD heat transfer enhancement of R114 on a horizontal lo-fin tube with cylindrical electrode ($T_s = 21.5°C$)

no special treatment other than cleaning with a wire brush and degreasing with acetone.

Curves A and B of Fig. 5 represent single-phase heat transfer with increasing ΔT_m and nucleate boiling with decreasing ΔT_m, respectively. Experiments were carried out at relatively low heat fluxes, between 200 W/m² and 4000 W/m². At $T_s = 21.5°C$ a local superheat of approximately 7.5°C was required to activate ebullition on the tube surface (this threshold decreased with increasing system saturation temperature). In engineering plants with limited driving temperature differentials across evaporators this may cause problems (e.g., at start-up of vapor recompression equipment).

Effect of Electric Stress on Boiling in Pure R114. Two major EHD phenomena were observed:

(*a*) EHD elimination of boiling hysteresis
(*b*) EHD enhancement of nucleate boiling

EHD elimination of hysteresis resulted from the electrical activation of nucleation sites. Visual observations showed that following zero-field superheating of the experimental tube by a few degrees Centigrade with heat transfer operating in the natural convective mode, application of a modest electrode potential (5–8 kV, say) resulted in immediate activation of ebullition. This electrical stimulation of nucleation sites appeared to be similar to thermal activation since sites remained active after removal of the activation energy source (i.e., the electric field). Moreover, by applying a sufficiently intense field ($V > 10$ kV) for a short duration (less than one second) it was possible to jump from a point on the increasing h_{m0} heat transfer hysteresis loop (curve A) to one for the same superheat on the decreasing h_{m0} curve (curve B) with a dramatic increase in heat transfer coefficient. The vigorous EHD activation of nucleation occurred over the entire heat transfer surface in a manner similar to that reported by Marto and Lepere (1982) for boiling initiation on a "High Flux" enhanced surface.

Continuous application of electric stress to the superheated lo-fin tube produced substantial increases in nucleate boiling heat transfer. Curves C and D in Fig. 5 show EHD enhanced heat transfer for applied electrode potentials of 10 kV and 27

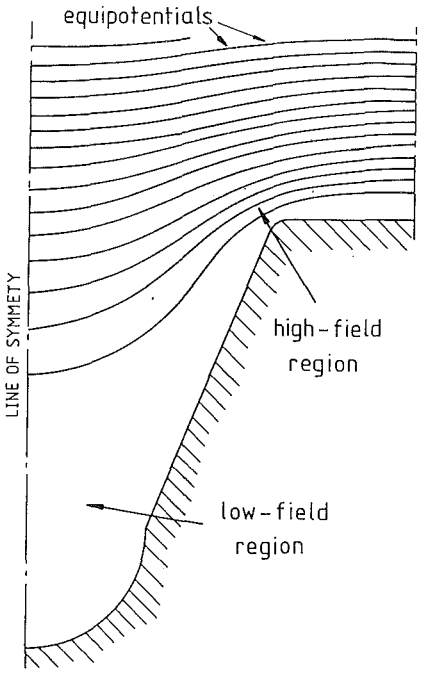

Fig. 6(*a*) Electric field at lo-fin tube surface

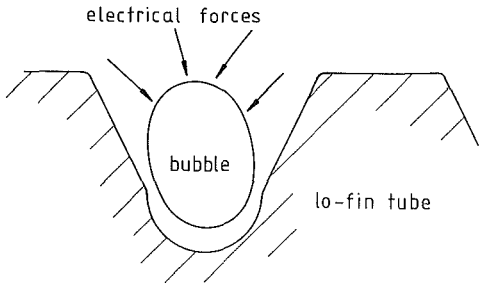

Fig. 6(*b*) Schematic of EHD bubble trapping mechanism

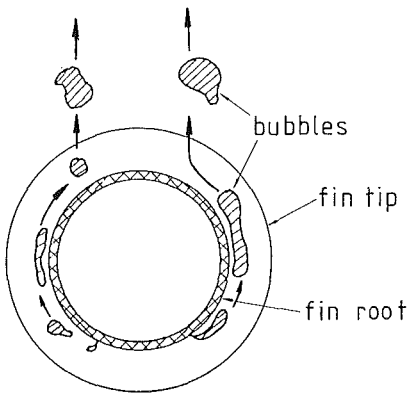

Fig. 6(*c*) Bubble flow paths around lo-fin tube with intense field

kV, respectively. It should be noted that for an electrode potential of 27 kV ebullition was observed for *all* values of tube surface superheat. As with all EHD phenomena observed in the present study, a.c. electric fields and d.c. fields of either polarity were equally effective. It can be seen from Fig. 5 that EHD enhancement of refrigerant-side nucleate boiling heat transfer of up to an order of magnitude was achieved with the complete elimination of hysteresis. This is thought to be due largely to the heat transfer surface geometry utilized, which produced a highly beneficial inhomogeneous electric field.

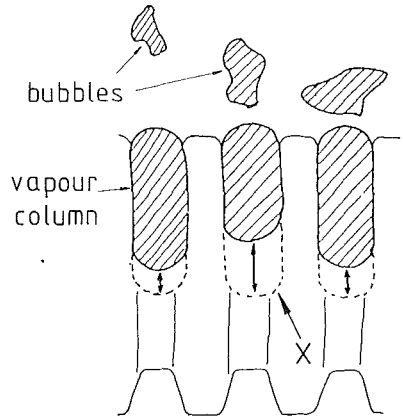

Fig. 7 Vapor columns trapped in lo-fin tube interfin spaces at low heat flux and intense applied field

With electric field strength increasing from zero, visual observations indicated that EHD forces modified the bubble dynamics of the boiling process, so that: (*a*) bubble departure diameter decreased; (*b*) strong electric field inhomogeneities at the surface of the lo-fin tube distorted and trapped bubbles between tube fins at high field strengths.

The electric field on the surface of the lo-fin tube surrounded by a single-phase fluid is shown in Fig. 6(*a*) as calculated by a two-dimensional boundary integral analysis. The action of field inhomogeneities around the lo-fin tube on bubble growth and motion (for $V>20$ kV) is illustrated qualitatively in Figs. 6(*b*) and 6(*c*). Dielectrophoretic forces tend to move matter of low permittivity (i.e., vapor) to areas of low field strength (i.e., to fin roots or away from the immediate tube vicinity). Since the vast majority of active nucleation sites on the lo-fin tube were at the fin roots, where the degree of wall-to-liquid superheat was greatest, bubbles generated there were trapped in the interfin spaces (Fig. 6*b*). Forced to rise by buoyancy forces, these bubbles were compelled to follow the circumference of the tube (Fig. 6*c*). It is suggested that the EHD forces, by keeping the bubbles close to the heat transfer surface, greatly increased local turbulence and mixing and led to the substantial EHD induced increase in heat transfer. This is equivalent to the mechanism by which some enhanced surface tubes, such as the GEWA-T tube, trap bubbles between tube fins by mechanical means, resulting in a liquid–vapor pumping action in the large re-entrant channels (Wanniarachchi et al., 1987; Stephan and Mitrovic, 1982).

An interesting phenomenon was observed at low rates of heat transfer with an intense applied electric field; a column of vapor could be seen trapped on the upper part of the tube in each interfin space (Fig. 7). Each column would grow until buoyancy forces were sufficient to overcome the restraining EHD forces at the top of the tube and a bubble would be released. As a result, the lower liquid–vapor interface of each column would oscillate at a frequency that increased with increasing field strength (point X in Fig. 7). It is not clear what mechanism led to the high EHD enhancement of heat transfer in this situation since the vapor columns may have acted in a manner similar to the vapor blanket in film boiling.

A permanent visual record of the phenomena described above is available from the ASME Film Library (Cooper and Allen, 1987).

The electrical power consumed by the EHD process was extremely small. In fact, no detectable change in the electrode potential versus supply current characteristics for either boiling or isothermal conditions was observed. This observation has been corroborated by the work of Yokoyama et al. (1986). For a positive d.c. electrode potential of 25 kV (at $T_s=21.5°C$) the current supplied to the EHD evaporator was

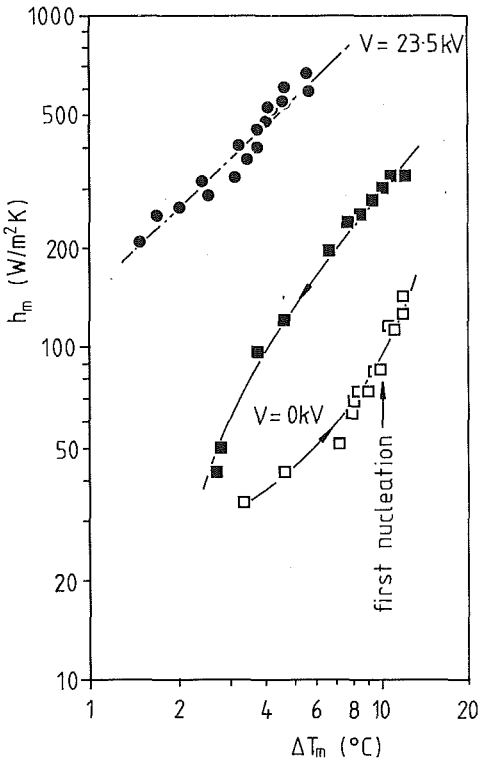

Fig. 8 EHD enhancement of boiling R114 and 10 percent (w.w) oil mixture on horizontal lo-fin tube with cylinder electrode ($T_s = 21.5°C$)

approximately 8.8 μA, representing a power input of 0.22 W. Such an electrode potential could induce an increase in total heat flux through the lo-fin tube of about 200 W for $\Delta T_m = 2.0°C$, giving an "EHD amplification factor" (i.e., the ratio of the EHD induced increase in heat transfer to power input to the electric field) of the order of 10^3.

EHD Enhancement of Boiling in an R114-oil Mixture. Most compressors in vapor recompression systems require a lubricant oil, some of which, by necessity, mixes with the heat transfer fluid. The presence of this less volatile component leads, in general, to a degradation in the thermal performance of the evaporator. At the evaporator heat transfer surfaces, oil concentration increases as the more volatile refrigerant is vaporized. This leads to the formation of a barrier to the diffusion of refrigerant, and therefore heat energy, from the bulk of the fluid to the evaporator tube wall. The behavior of refrigerant/oil mixtures under these conditions is complex (e.g., foaming may occur and, at low oil concentrations, heat transfer may be increased marginally).

The experimental conditions equivalent to those for the results of Fig. 5 were repeated with 5% w.w. Shell Clavus 68 oil added to the R114 refrigerant charge. Almost identical results were obtained as for pure R114. The addition of 10% w.w. oil resulted in very significant heat transfer degradation under zero-field conditions as shown in Fig. 8. This degradation was accompanied by considerable "foaming" of the refrigerant-oil mixture in the evaporator. Similar results have been reported by others (e.g., Wanniarachchi et al., 1987; Dougherty and Sauer, 1974; Henrici and Hess, 1971). Comparison of Figs. 5 and 8 shows that under zero-field conditions for decreasing heat flux 10% w. w. oil contamination reduced heat transfer coefficients by at least 50 percent compared with the case of pure refrigerant.

Application of electric stress resulted in the same EHD effects observed in pure R114. Boiling hysteresis could be completely eliminated with the brief application of an electrode potential of approximately 10 kV. The effect of continuous application of $V = 23.5$ kV is shown in Fig. 8 (note this electrode potential was the maximum permissible due to the reduced electrical insulation properties of the oil-contaminated Freon).

Application of an intense electric field also resulted in a dramatic reduction of "foaming" in the R114/oil mixture.

It should be noted that in the present experiments the oil and refrigerant had almost identical permittivities (by chance). Greater enhancement of heat transfer may occur with oils of significantly different permittivity, which could facilitate EHD dielectrophoretic mixing in regions of inhomogeneous oil concentration.

A Model of EHD Nucleate Boiling

EHD enhanced boiling heat transfer is an extremely complex process. Satisfactory correlation of zero-field boiling has proved difficult and the presence of the electric force field in addition to that due to gravity makes analysis of the EHD situation particularly intractable. Previous treatments of EHD boiling data have been concerned only with the film boiling regime and prediction of the increase in critical heat flux due to application of an electric field. Here the effect of an intense electric field applied across the vapor film is to produce a wavelike instability on the vapor–liquid interface. If the electric field is of sufficient intensity, rewetting of the heat transfer surface occurs. Theoretical analysis of this phenomenon and prediction of the EHD instability wavelength has been carried out by a number of authors (e.g., Berghmans, 1976, and Jones and Hallock, 1978). Linearized perturbation methods were employed similar to those used to model EHD destabilization of condensate films (e.g., see Choi and Reynolds, 1965, or Lee and Choi, 1968).

Theoretical modeling of EHD enhanced nucleate boiling has not been reported until recently due, in part, to: (*a*) lack of experimental data and (*b*) the uncertainty regarding the true nature of the governing EHD mechanisms. However, recent research in Japan and the UK has resulted in two quite different approaches to the modeling of EHD nucleate boiling data. Yokoyama et al. (1986) investigated a horizontal upward-facing flat heated plate in an EHD pool boiling situation (working fluid R11) and developed a method of correlating the experimental results based on the analysis of zero-field flow boiling heat transfer by Chen (1963).

The approach adopted by the present author assumes that the EHD induced change in nucleate boiling heat transfer coefficient is primarily due to the influence of the electric field on bubble growth and separation at the heat transfer surface. The basis of this approach is the zero-field model of nucleate boiling proposed by Rohsenow (1952), which is then modified to account for reduced bubble release radius in an electric field. The Rohsenow model utilizes bubble release radius as a characteristic dimension in both the Nusselt number Nu_0 and the Reynolds number Re_0 and the following equation was proposed as a means of correlating nucleate boiling data:

$$Nu_0 = C_1 \cdot Re_0^{(1-n)} \cdot Pr^{(-m)} \quad (1)$$

From various data of boiling on clean surfaces Rohsenow suggested values of $n = 0.332$, $m = 0.7$, and C_1 is a constant dependent on the fluid/heating surface pair.

Many EHD researchers have noted that the application of an electric field to a zero-field nucleate boiling situation causes a decrease in bubble departure diameter. Research in the Soviet Union by Baboi et al. (1968) quantitatively investigated this phenomenon in a detailed experimental study of EHD pool boiling of benzene on a horizontal heated wire. In their theoretical analysis, which successfully predicted departure diameter of bubbles in an electric field, Baboi et al. assumed that the electric force F_E acting on a bubble is purely dielec-

trophoretic (i.e., bubbles are uncharged). F_E (after conversion to SI units) is given by:

$$\mathbf{F}_E = \left(\frac{1.5\Gamma_b \epsilon_L (\epsilon_V - \epsilon_L)}{(\epsilon_V + 2\epsilon_L)}\right) \nabla E^2 \tag{2}$$

where Γ_b is the volume of a bubble, ϵ is absolute permittivity (the subscripts V and L denote vapor and liquid, respectively) and E is electric field strength at the heat transfer surface. By considering a steady-state balance between electric, buoyancy, and surface tension forces Baboi et al. determined bubble breakaway diameter to be given by:

$$D_b = w(\beta)\left(\frac{\sigma}{g(\rho_L - \rho_V)}\right)^{0.5} \left(1 + \left(\frac{1.5\epsilon_L (\epsilon_V - \epsilon_L)}{(\epsilon_V + 2\epsilon_L) g(\rho_L - \rho_V)}\right) \nabla E^2\right)^{-0.5} \tag{3}$$

where w is a function of contact angle β. The change in bubble departure diameter can be seen as an electrically induced change in the characteristic dimension of Nu_0 and Re_0. Thus, equation (3) may be used to determine the magnitude of electrically modified Reynolds and Nusselt numbers, Re_E and Nu_E, respectively. We may define an electrical influence number Ne such that:

$$\mathrm{Ne} = \left(1 + \left(\frac{1.5\epsilon_L (\epsilon_V - \epsilon_L)}{(\epsilon_V + 2\epsilon_L) g(\rho_L - \rho_V)}\right) \nabla E^2\right)^{-0.5} \tag{4}$$

then

$$\mathrm{Nu}_E = \left(\frac{h_E}{h_0}\right) \mathrm{Nu}_0 (\mathrm{Ne})^{-0.5} \tag{5}$$

and

$$\mathrm{Re}_E = \mathrm{Re}_0 (\mathrm{Ne})^{-0.5} \tag{6}$$

where the subscripts E and 0 indicate finite and zero applied electric field for a given heat flux, respectively. Thus, under conditions of constant heat flux and saturation temperature from equation (1) we have:

$$\left(\frac{\mathrm{Nu}_E}{\mathrm{Nu}_0}\right) = \left(\frac{\mathrm{Re}_E}{\mathrm{Re}_0}\right)^{(1-n)} \tag{7}$$

and combining equations (5), (6), and (7) the degree of EHD enhancement of heat transfer is given by:

$$\left(\frac{h_E}{h_0}\right) = \mathrm{Ne}^{(n/2)} \tag{8}$$

Assumptions held implicitly within the above analysis include:

(*i*) Bubble departure diameter is unaffected by inertial or viscous forces (i.e., the analysis is static).
(*ii*) The electric field strength E at the heat transfer surface is nonuniform and known.
(*iii*) Bubbles do not carry electric charge.
(*iv*) Surface tension and contact angle are not affected by electric field strength.

Assumption (*i*) implies that EHD heat transfer enhancement (h_E/h_0) is independent of heat flux q. This is contrary to available experimental evidence, which indicates that enhancement decreases with increasing zero-field heat flux (reflecting a progressive domination of inertial forces over forces of electrical origin). Therefore, the present author proposes the following model based on both the dimensionless increase in heat transfer from equation (8) and a dimensionless representation of heat flux under zero-field conditions (i.e., Re_0). Thus:

$$\left(\frac{h_E}{h_0}\right) = a\mathrm{Ne}^{(n/2)} (\mathrm{Re}_0)^b \tag{9}$$

where $n = 0.33$ as suggested by Rohsenow and where the constants a and b are determined empirically. Data available from previous studies of EHD enhanced pool boiling on fine horizontal heated wires are shown correlated by equation (9) in Fig. 9. The solid line indicates a least-squares best fit to the data, which has been transcribed from illustrations in the works of Baboi et al. (1968), Choi (1962), and Bonjour et al. (1962). These data result in constants for equation (9) of $a = 0.3$ and $b = -0.16$ (standard deviation = 0.0424).

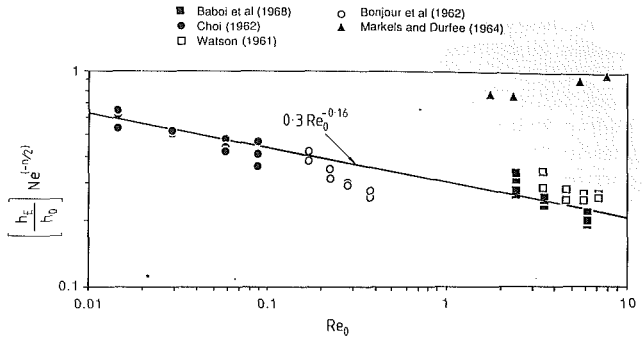

Fig. 9 Correlation of EHD enhanced nucleate boiling on fine horizontal heated wires

[Note: the data of Watson (1961) and Markels and Durfee (1964) are shown in Fig. 9 for completeness, but have not been included in determination of the constants a and b. Experiments by Watson included a substantial degree of subcooling while those of Markels and Durfee involved a significant degree of Joule heating of the working fluid, water.]

The studies of Baboi et al. (1968) and Bonjour et al. (1962) employed thin cylindrical electrodes lying parallel to the heater wire. Calculation of the magnitude of ∇E^2 for evaluation of Ne in these cases was made assuming that the electric field inhomogeneity in the immediate vicinity of the heat transfer surface was similar to that for the co-axial cylinder electrode system (finite element analysis indicated that this approximation was adequate for present purposes).

Equation (9) does not successfully correlate data from the present study or from recent investigations by others (e.g., Yokoyama et al., 1986) as discussed below. However, it does represent the first successful correlation of EHD nucleate boiling data from a number of investigations and the analytical model used may prove to be the basis for development of a more generally applicable correlation method.

Discussion

Elimination of boiling hysteresis by a brief application of a modest electric field to a heat transfer surface may prove to be relatively simple to implement in many engineering heat transfer situations. The required duration of applied electric stress is short and the energy required extremely small. In practice, this has the following implications:

(*a*) A very simple high-voltage generator may be used (e.g., similar to that used in gas ignition spark generators).
(*b*) The need for a sophisticated electrode/insulation system capable of withstanding continuous electric stress is reduced.
(*c*) Relatively conductive working fluids (including water) may be amenable to this technique.

The cost effectiveness of a high-voltage continuous EHD enhancement system in a practical evaporator will be dependent on a number of factors including:

(*i*) the EHD increase in overall heat transfer coefficient obtainable
(*ii*) the influence of the electrode system design on:
- tube bundle packing density
- pressure drop through the equipment
- complexity of the manufacturing process.

The future of practical EHD enhancement is dependent on a realistic assessment of these factors in commercial terms.

Equation (9) successfully models EHD nucleate boiling from heated horizontal wires where conventional nucleate boiling bubble dynamics occur. However, data from the present study and Yokoyama et al. (1986) are not successfully correlated by this method. Several factors may contribute to this lack of agreement, including:

(*i*) The present study for boiling on a "lo-fin" tube involved complex bubble dynamics. The electrical bubble trapping mechanism led to high enhancement of heat transfer for a given value of ∇E^2 compared to experiments using fine horizontal wires. The explanation for this high enhancement may lie in the EHD induced "scouring" effect of bubbles, which disrupt a relatively large proportion of the heat transfer surface boundary layer on the lo-fin tube. This contrasts with the fine wire apparatus where bubbles have relatively little influence on fluid hydrodynamics after release since electric field forces move bubbles radially outward from the heat transfer surface.

(*ii*) The experimental data of Yokoyama et al. (1986) also show high EHD enhancement for the magnitude of ∇E^2 available from the electrode geometry employed. The explanation here may lie in the relatively high degree of charge injection produced from the Yokoyama electrode system, which may have caused considerable disruption of single-phase heat transfer in the thermal boundary layer.

The EHD boiling model described above successfully correlates experimental data, but only for relatively simple apparatus. However, it may yet provide the foundation for the development of a more comprehensive model to correlate all types of EHD nucleate boiling data. Such a correlation must await more detailed experimental data for a variety of heat transfer surfaces and electrode geometries.

Conclusions

EHD enhancement of boiling heat transfer from a lo-fin tube has been shown to improve heat transfer coefficients by up to a factor of ten in pure R114 and in mixtures of R114 and oil.

Boiling hysteresis is completely eliminated through the electrical activation of nucleation sites on the heat transfer surface following a brief application of a modest electric field.

A model of the EHD enhanced nucleate boiling process has been developed, which utilizes the relationship between applied electric stress and bubble departure diameter at a heat transfer surface. This model has successfully correlated data from simple thermal and electrical geometries (i.e., fine horizontal heated wires with co-axial or parallel cylinder electrodes).

Acknowledgments

The author wishes to thank the Science and Engineering Research Council (UK) for funding of the work described above, which was carried out in the laboratories of the Department of Electrical Engineering, Imperial College. He would also like to thank Prof. P. H. G. Allen for advice and support given during and after the study.

References

Allen, P. H. G., and Cooper, P., 1985, "Improvements in or Relating to Heat Exchangers," UK Patent No. 8522680.

Allen, P. H. G., and Cooper, P., 1987, "The Potential of Electrically Enhanced Evaporators," *Proc. 3rd Int. Symp. on the Large Scale Applications of Heat Pumps*, Oxford, UK, pp. 221–229.

Baboi, N. F., Bologa, M. K., and Klykanov, A. A., 1968, "Some Features of Ebullition in an Electric Field," *Appl. Elec. Phenomena (USSR)*, Vol. 20, pp. 57–70.

Berghmans, J., 1976, "Electrostatic Fields and the Maximum Heat Flux," *Int. J. Heat Mass Transfer*, Vol. 19, pp. 791–797.

Bochirol, L., Bonjour, E., and Weil, L., 1960, "Exchanges thermiques-Etude de l'Action de Champs Electriques sur les Transferts de Chaleur dans les Liquides Bouillants," *C. R. Hebd. Seances Acad. Sci. (Paris)*, Vol. 250, pp. 76–78 (in French).

Bonjour, E., Verdier, J., and Weil, L., 1962, "Electroconvection Effects on Heat Transfer," *Chem. Eng. Progress*, Vol. 58, pp. 63–66.

Chen, J. C., 1963, "A Correlation of Boiling Heat Transfer to Saturated Fluid in Convective Flow," ASME Paper No. 63-HT-34.

Choi, H. Y., 1962, "Electrohydrodynamic Boiling Heat Transfer," PhD thesis, Massachusetts Institute of Technology, Cambridge, MA.

Choi, H. Y., and Reynolds, J. M., 1965, "Study of Electrostatic Effects on Condensing Heat Transfer," US Air Force Technical Report No. AFFDL-TR-65-51.

Chubb, L. W., 1916, "Improvements Relating to Methods and Apparatus for Heating Liquids," UK Patent No. 100796.

Cooper, P., 1986, "Electrically Enhanced Heat Transfer in the Shell-and-Tube Heat Exchanger," PhD thesis, University of London.

Cooper, P., and Allen, P. H. G., 1984, "The Potential of Electrically Enhanced Condensors," *Proc. 2nd Int. Symp. on the Large Scale Applications of Heat Pumps*, York, UK, pp. 295–309.

Cooper, P., and Allen, P. H. G., 1987, "Video: Electrohydrodynamic (EHD) Effects on Condensing and Evaporating Freons," ASME Heat Transfer Films Library, ASME, Mechanical and Aerospace Engineering, University of Tennessee, Knoxville, USA.

Dougherty, R. L., and Sauer, H., 1974, "Nucleate Pool Boiling of Refrigerant-Oil Mixtures From Tubes," *ASHRAE Trans.*, Vol. 80, Pt. 2, pp. 175–192.

Hahne, E., and Muller, J., 1983, "Boiling on a Finned Tube and a Finned Tube Bundle," *Int. J. Heat Mass Transfer*, Vol. 26, pp. 849–859.

Ito, F., and Seya, Y., 1983, "Present Situation and Future Outlook for OTEC Power Generation," *Energy Exploration and Exploitation*, Graham and Trotman.

Jones, T. B., 1978, "Electrohydrodynamically Enhanced Heat Transfer in Liquids—A Review," *Advances in Heat Transfer*, Vol. 14, Academic Press, pp. 107–148.

Jones, T. B., and Hallock, K. R., 1978, "Surface Wave Model of Electrohydrodynamically Coupled Minimum Film Boiling," *J. Electrostatics*, Vol. 5, pp. 273–284.

Lee, C., and Choi, H. Y., 1968, "EHD Ridge Instability of a Thin Film Flowing Down an Inclined Plate," ASME JOURNAL OF HEAT TRANSFER, Vol. 90, pp. 135–145.

Markels, M., and Durfee, R. L., 1964, "The Effect of Applied Voltage on Boiling Heat Transfer," *AIChE J.*, Vol. 10, pp. 716–723.

Marto, P. J., and Lepere, V. J., 1982, "Pool Boiling Heat Transfer From Enhanced Surfaces to Dielectric Fluids," ASME JOURNAL OF HEAT TRANSFER, Vol. 104, pp. 292–299.

Rohsenow, W. M., 1952, "A Method of Correlating Heat-Transfer Data for Surface Boiling of Liquids," *Trans. ASME*, Vol. 74, pp. 969–976.

Stephan, K., and Mitnovic, J., 1982, "Heat Transfer in Natural Convective Boiling of Refrigerant-Oil Mixtures," *7th Int. Conf. Heat Trans.*, Munich, Paper No. PB12.

Wanniarachchi, A. S., Sawyer, L. M., and Marto, P. J., 1987, "Effect of Oil on Pool-Boiling Performance of R-114 From Enhanced Surfaces," *2nd ASME-JSME Thermal Engineering Joint Conference*, Honolulu, HI.

Watson, P. K., 1961, "Influence of an Electric Field Upon the Heat Transfer from a Hot Wire to an Insulating Liquid," *Nature*, Vol. 189, No. 4764, pp. 563–564.

Yokoyama, T., Yamazaki, T., Kubo, Y., Ogata, J., Kawada, A., and Ooki, Y., 1986, "The Effect of an Electric Field on Boiling Heat Transfer of Fluorocarbon R-11," *18th Int. Symp. Heat and Mass Transfer in Cryoengineering*, Int. Centre for Heat and Mass Transfer, Dubrovnik, Yugoslavia.

Liquid–Solid Contact During Flow Film Boiling of Subcooled Freon-11

K. H. Chang
Research Assistant.

L. C. Witte
Professor of Mechanical Engineering.
Fellow ASME

Department of Mechanical Engineering,
University of Houston,
Houston, TX 77204

Liquid–solid contacts were measured for flow film boiling of subcooled Freon-11 over an electrically heated cylinder equipped with a surface microthermocouple probe. No systematic variation of the extent of liquid–solid contact with wall superheat, liquid subcooling, or velocity was detected. Only random small-scale contacts that contribute negligibly to overall heat transfer were detected when the surface was above the homogeneous nucleation temperature of the Freon-11. When large-scale contacts were detected, they led to an unexpected intermediate transition from local film boiling to local transition boiling. An explanation is proposed for these unexpected transitions. A comparison of analytical results that used experimentally determined liquid–solid contact parameters to experimental heat fluxes did not show good agreement. It was concluded that the available model for heat transfer accounting for liquid–solid contact is not adequate for flow film boiling.

Introduction

In today's industries film boiling has a role in certain areas of surface–liquid heat transfer. Heat treatment of steels, boiling in rod bundles, rewetting of coolant channels by an emergency core cooling system in a pressurized-water reactor, accidental spills of molten materials into volatile coolants, and cooldown of electrical and superconducting components are only a few examples involving film boiling. A complete understanding of the heat transfer mechanism(s) of film boiling is needed.

Many studies have been done by assuming a continuous vapor film existing between the liquid and the heater surface throughout the film boiling region. But several experimental studies, e.g., Bradfield (1966), Coury and Dukler (1970), Yao and Henry (1978), Lee et al. (1982, 1985), Neti et al. (1986), and Dhuga and Winterton (1986) have shown that brief random contacts between the liquid and the surface occur in some portions of this region. The vapor film might appear to be quite continuous to the naked eye, but small contacts become longer and more numerous as the heating surface superheat approaches the minimum wall superheat. The liquid–solid contacts contribute to the average heat transfer rate during this stage of film boiling, eventually leading to the so-called minimum heat flux.

This paper reports the results of research designed to determine the influence of liquid–solid contact on flow film boiling from a heated cylinder. A liquid–solid contact probe was mounted in the surface of an electrically heated cylinder suspended horizontally in up-flowing Freon-11 (R-11). The probe yielded information concerning the duration of contacts, the frequency of contacts, the temperature depressions caused by contacts, and the fraction of the surface covered by liquid contacts. It also provided boiling curves ($q - \Delta T_w$) for various angular positions on the cylinder. The influence of liquid velocity and subcooling was examined over the ranges allowed by the flow loop in which the experiments were carried out.

Experimental Apparatus

Figure 1 is a schematic diagram of the flow loop in which the experiments were performed. The loop was described in detail by Orozco and Witte (1986). The loop was modified to accommodate a square test section. Figure 2 shows the heater suspended across the test section with the supporting structures and the buses for electrical heating. The heater was a 6.35-mm-o.d. Hastelloy C tube, 0.102-mm wall thickness, with an effective heating length between the walls of the test section of 80 mm.

Figure 3 shows the details of the heater, including a microthermocouple probe for liquid–solid contact measurements. A lava insert gave the heater structural rigidity as well as additional thermal mass to prevent precipitous surface temperature changes because of liquid–solid contacts. A groove was machined into the lava insert in which a 1.6-mm-o.d. Inconel sheathed chromel-alumel thermocouple was laid. Its

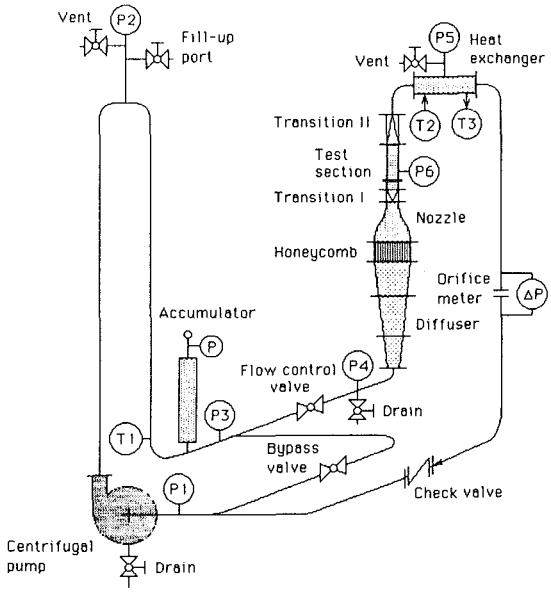

(Tx) represents the temperature measurement at location x.

(Py) represents the pressure measurement at location y.

Fig. 1 Schematic diagram of the flow loop

Contributed by the Heat Transfer Division for publication in the JOURNAL OF HEAT TRANSFER. Manuscript received by the Heat Transfer Division August 29, 1988; revision received June 9, 1989. Keywords: Boiling, Forced Convection, Thin Film Flow.

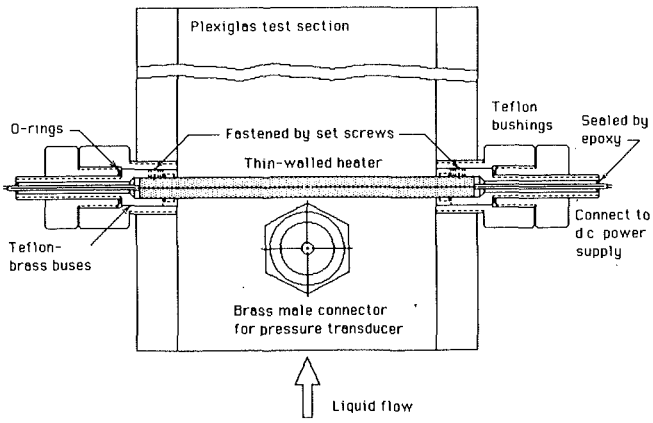

Fig. 2 Cylindrical heater installed in the test section

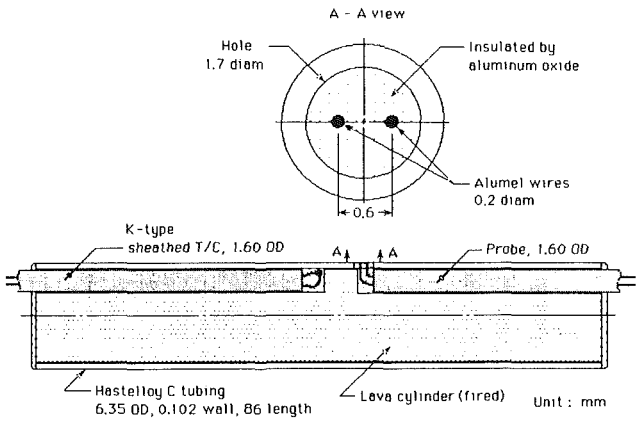

Fig. 3 Microthermocouple installed in the cylindrical heater

wires (0.4 mm in dia.) were brought to the surface through a 1.7-mm hole drilled in the Hastelloy heater. Alumina was packed into the area surrounding the wire. A 0.05-mm-thick, 1-mm circular copper junction was electroplated onto the wires to serve as a sensitive microthermocouple junction. The time constant of the junction was estimated at 0.9 ms.

The area between the junction and the heater was sealed with high-temperature epoxy and polished to be flush with the heater surface. Prior to the probe junction electroplating, the entire assembly was fired in an oven to harden the lava insert. Lava expands permanently upon heating, so a good thermal fit between all the components was assured. After firing in this manner, the lava insert could not be removed from the heater nondestructively.

The heater was powered by a regulated d-c power supply. Probe signals were recorded on a DEC Micro-11 computer equipped with a variable gain A/D board. The details of the data acquisition system are given by Chang (1987).

It was found that the combination of the probe and the data acquisition system could detect temperature depressions of greater than 0.25 deg C at an event frequency up to about 10 contacts/s. The contact event consists of a sharp temperature depression followed by a relatively slow temperature recovery, so that a minimum actual contact time on the order of about 20 ms could be detected.

Liquid–Solid Contact Heat Transfer

Witte et al. (1983) developed an expression for the heat transfer that would occur because of momentary liquid-solid contacts. Their work assumed that the liquid and solid behaved as semi-infinite regions; upon touching, the interface temperature was assumed fixed in time. Chang (1987) investigated a constant flux model in which the surface temperature can change during the duration of the contact. He found that there is little difference between the two models as far as the heat transfer is concerned; indeed the resulting expressions differ only by a constant. Since the constants were both close to unity, he suggested that

$$q_c = \frac{k_s \Delta T_c}{(\alpha_s)^{1/2}} f_c (t_c)^{1/2} \tag{1}$$

be used to represent the influence of liquid–solid contacts on heater transfer. The liquid–solid contact component is added to the film boiling component in the following way:

$$q = q_{fb} + q_l \tag{2}$$

or

$$q = q_v(1 - F_a) + q_c F_a \tag{3}$$

where F_a is the area fraction A_c/A_t, and q_v is computed by the method of Witte and Orozco (1984). Equations (1) and (3) clearly show that to include the influence of liquid–solid contact on the total heat transfer during film boiling, one must know the duration of contact t_c, and the area fraction of contact F_a.

To show the influence of liquid–solid contact on the flow film boiling curve, correlations of the contact parameters described above with the wall superheat are desirable. The experiments described in the following section were directed at obtaining such information.

Flow Boiling Experiments

Extensive testing was carried out to verify that the microthermocouple probe was indeed capable of detecting liquid–solid contact. These tests are described in detail by Chang (1987). Figure 4 shows the data plotted directly from the computer memory for pool boiling tests of the heater/probe. These data show the characteristically steep depression in temperature as contact occurs followed by a relatively slow temperature recovery as the film is re-established.

If the vapor film experiences fluctuations in its thickness

Nomenclature

A = area of heater
f_c = frequency of liquid–solid contact
F_a = area fraction of contact
F_t = time fraction of contact
k_s = thermal conductivity of heater material
q = heat flux density
t_c = duration of liquid–solid contact
T = temperature
T_B = liquid temperature
T_{cr} = critical temperature of liquid
T_{hn} = homogeneous nucleation temperature
T_{sat} = saturation temperature of liquid
T_w = wall temperature
V = liquid velocity
ΔT = temperature difference
ΔT_B = liquid subcooling = $T_{sat} - T_B$
ΔT_c = temperature depression during liquid–solid contact
ΔT_w = wall superheat = $T_W - T_{sat}$
α = thermal diffusivity
θ = angle measured from forward stagnation point

Subscripts

a = alumina
b = bulk solid
c = contact
fb = film boiling
l = liquid, lava
s = solid
t = total
v = film boiling, without liquid–solid contact

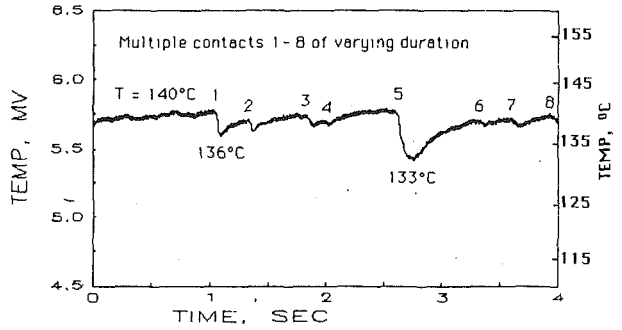

Fig. 4 Probe signals obtained from the tests in pool film boiling of saturated Freon-11: probe position = 180 deg, q = 22 kW/m², ΔT_w = 115°C

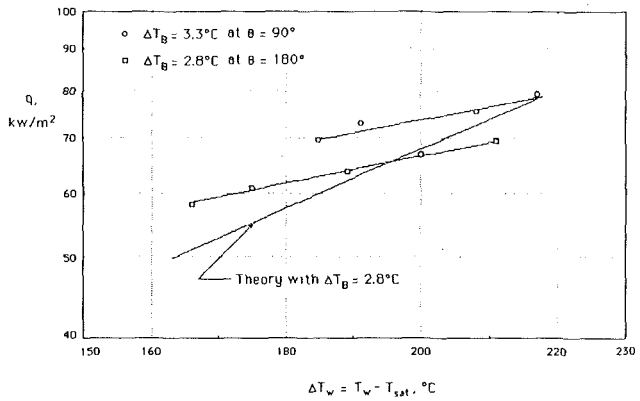

Fig. 5 Boiling curves for V = 0.7 m/s, ΔT_B = 2.8°C or 3.3°C, and θ = 90 or 180 deg with comparisons to theoretical results

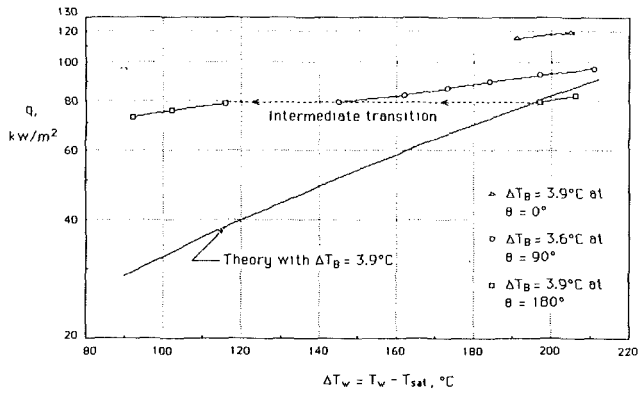

Fig. 6 Boiling curves for V = 1.0 m/s, ΔT_B = 3.6°C or 3.9°C, and θ = 90 or 180 deg with comparisons to theoretical results

without creating liquid–solid contact, it is possible that some fluctuations in the probe output could be caused. Coury and Dukler (1970) observed such fluctuations during film boiling of Freon-113 on a nickel surface. However, these fluctuations would not take on the characteristic "signature" of actual contact, as shown in Fig. 4. In our analysis of contacts, only events that take on the shape characteristic of liquid–solid contact were considered. Flow film boiling experiments were carried out over obtainable ranges of flow velocity and liquid subcooling. Basically, there were three parameters that set apart the experimental runs in this study: flow velocity, liquid subcooling, and probe position in the flow field. The cylinder was rotated so that measurements were made with the probe at 0 deg (the forward stagnation point), 90 deg, and 180 deg. Careful control of the power level, the liquid flow velocity, and the liquid subcooling allowed stable film boiling to be reproduced with only a small difference of wall superheats,

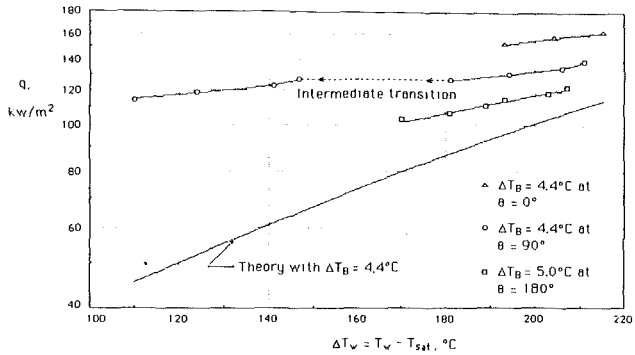

Fig. 7 Boiling curves for V = 1.5 m/s, ΔT_B = 4.4°C or 5.0°C, and θ = 0, 90, or 180 deg with comparisons to theoretical results

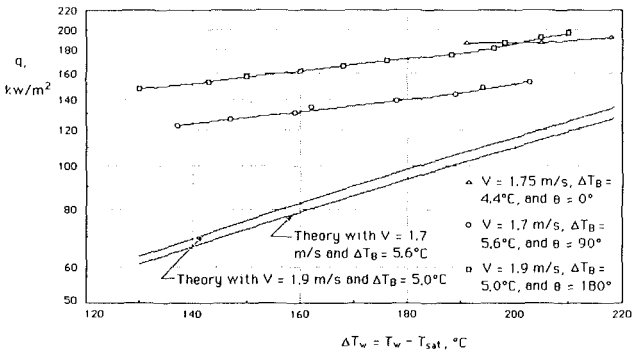

Fig. 8 Boiling curves for V = 1.7 to 1.9 m/s, ΔT_B = 4.4°C to 5.6°C, and θ = 0, 90, or 180 deg with comparisons to theoretical results

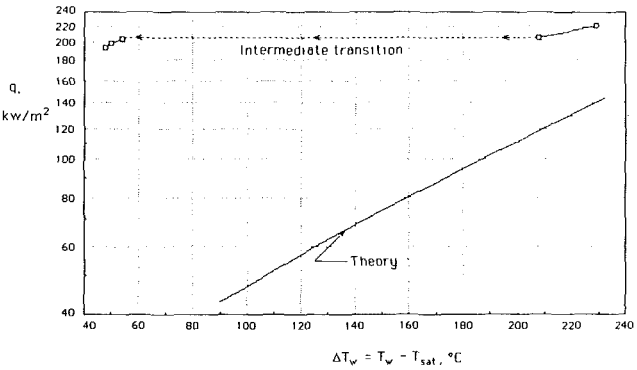

Fig. 9 Boiling curves for V = 1.7 m/s, ΔT_B = 6.7°C, and θ = 180 deg with comparison to theoretical results

about 5°C maximum, between runs. Thus the reproducibility of the data could be considered quite adequate.

Twenty-seven experimental runs, consisting of several steady-state data points for each run, were performed. Some runs ended with premature film collapse or other system malfunctions. Eventually twelve runs that covered the obtainable ranges of subcooling and velocity were selected as representative of the data. Heat transfer and liquid–solid contact information were obtained for these runs. An uncertainty analysis (see Chang, 1987) showed that the heat fluxes could be ascertained with ± 3 percent uncertainty while the corresponding surface temperatures were ± 1 percent accurate.

Heat Transfer Results

Figures 5–9 show the boiling heat transfer data for various liquid subcoolings, velocities, and probe locations. The curves are strongly dependent upon probe position because of the variation of vapor film thickness around the heater as shown by Witte and Orozco (1984). The heat flux is uniform so that

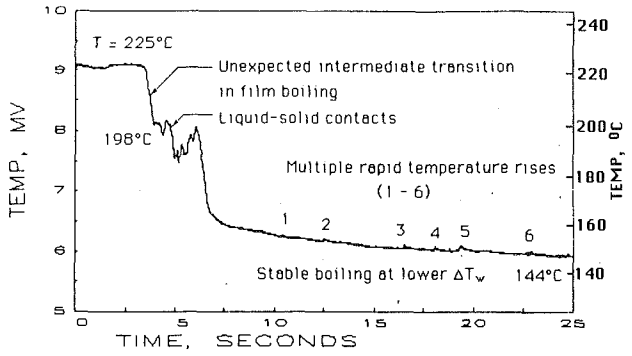

Fig. 10 Probe trace indicating unexpected temperature transition and rapid temperature rises after the transition: V = 1.0 m/s, ΔT_B = 3.9°C, θ = 180 deg, q = 79.3 kW/m²

the surface temperature must adjust itself to accommodate the flux. Thus the wall superheat for the 180-deg position always tends to be higher than the superheat for the 0-deg position at the same q in stable film boiling.

The installation of the probe requires alteration of the thermal environment, leading to the possibility that the probe temperature is not necessarily representative of the surrounding heater temperature. If one assumes that the primary effect is due to the different substrates underlying the heater and the thermocouple, then the influence of the different substrates on the heater and the probe surface temperatures can be estimated.

Using the notion that once liquid–solid contact occurs, a constant heat flux is withdrawn from the surface, one can write using the results of Carslaw and Jaeger (1959)

$$T_c - T_b = \frac{2q_c}{k_s}\sqrt{\frac{\alpha_s t_c}{\pi}} \tag{4}$$

which represents the temperature depression at the surface of the substrate after some contact time t_c. Solving for q_c and assuming that liquid–solid contacts occur simultaneously on the probe and the surrounding heater surface, one finds the following for the ratio of the surface temperature depression for alumina compared to the lava:

$$\frac{(T_c - T_b)_a}{(T_c - T_b)_l} = \frac{k_l}{k_a}\sqrt{\frac{2\alpha_a}{\alpha_l}} \tag{5}$$

Substituting values of k and α typical of our experiments, one finds that this ratio is about 17 percent. This means that at any given time, the surface of the alumina substrate has cooled much less than the surrounding lava substrate. A similar analysis for the copper and Hastelloy surfaces shows just the opposite: The copper probe surface will cool more than the Hastelloy heater surface. In reality, the cooling histories of the two surfaces will depend upon a combination of the cooling characteristics of the metal surfaces and the ceramic substrates. They tend to offset each other, leading us to believe that the probe temperature is representative of the surrounding heater temperature as liquid–solid contact occurs.

Observations and photographs of film boiling over the probe locations showed no sign of disturbances due to the presence of the probe (see Chang, 1987).

Also shown for comparison in the figures are the curves calculated using the technique of Witte and Orozco, which assumes no liquid–solid contact. These curves are based on a uniform wall temperature so that it is expected that some deviation between them and the experimental curves should exist. However, the theoretical curves should compare reasonably well with data at the 90-deg position, since it will

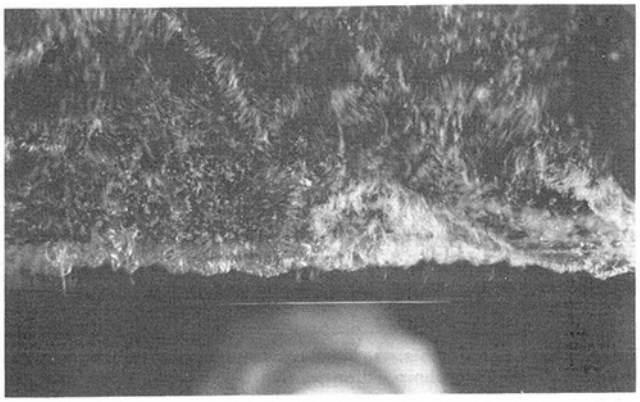

Fig. 11 Photograph of boiling from 6.35-mm heater following an intermediate transition: q = 204.6 kW/m², ΔT_w = 54°C, V = 1.7 m/s, ΔT_B = 6.7°C, θ = 180 deg

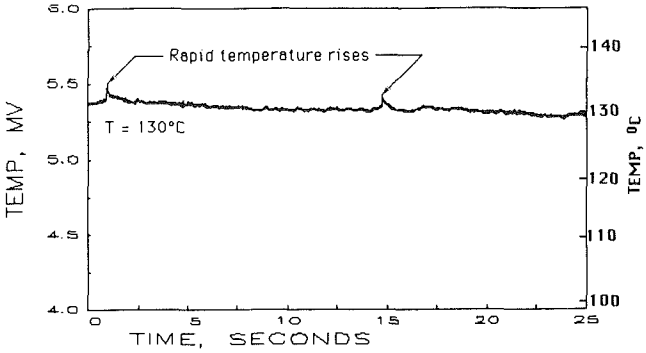

Fig. 12 Probe trace showing rapid temperature rises during stable "intermediate" boiling: V = 1.0 m/s, ΔT_B = 3.9°C, θ = 180 deg, q = 75.7 kW/m², ΔT_w = 102°C

operate at an average temperature between the 0- and 180-deg positions. The lower the wall superheat, the greater is the deviation of the theoretical curves from the experimental ones. Indeed it appears that the no-contact theory is approaching the experimental data as wall temperature is increased. This is to be expected, and indicates that the deviation between the no-contact theory and the experimental values is due to liquid–solid contact.

An Unexpected Boiling Transition

The data showed an unexpected boiling transition in some experimental runs. For example, Figs. 6, 7, and 9 show a very large temperature drop at a fixed heat flux for cases where the probe is at 90 and 180 deg. Figure 10 shows the temperature–time trace that corresponds to the boiling curve that exhibits the transition in Fig. 6. The actual plots in millivolts are shown for authenticity; a temperature coordinate is also shown for convenience.

When such a transition was first observed, we thought this was the transition from film to nucleate boiling. However, visual observations showed that a smooth vapor film still existed over the forward portion of the heater. Figure 11 is a photograph of the heater that has undergone one of these transition events with the probe at 180 deg for the conditions indicated.

Figure 12 shows an excerpt from the probe output recorded after the transition had occurred. The temperature of the probe was stable indefinitely until the heat flux was changed. Figure 13 shows the eventual change to nucleate boiling at a slightly lower heat flux for the same case as Figs. 10 and 12. Thus it is clear that the probe location undergoes two transitions between stable film boiling and stable nucleate boiling.

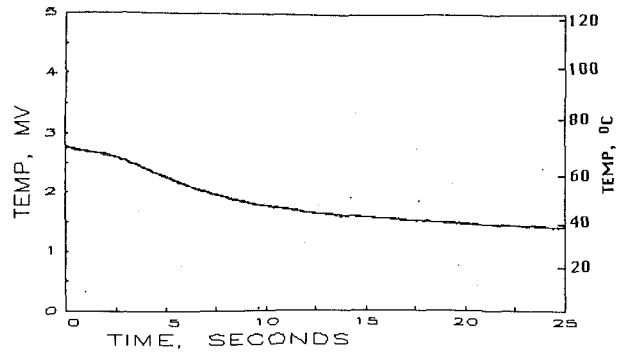

Fig. 13 Probe trace showing eventual transition to nucleate boiling: same conditions as Fig. 10 and 12, and $q = 72.5$ kW/m²

We also found that the first transition was repeatable; that is, by increasing the heat flux after such a transition occurred, the temperature drop could be reversed. A reduction in flux once again led to the large drop in temperature. Since these events were not film-to-nucleate transitions, we called them "intermediate" transitions for want of a better description.

Once the boiling had undergone the final transition to nucleate boiling, the situation could not be reversed by simply increasing the heat flux once again.

Liquid-Solid Contact Measurements

Probe signals revealed that there were two distinct modes of liquid-solid contact in flow film boiling. In the first mode, called the small-scale contact mode, both the temperature depression ΔT_c and the contact duration t_c were small and random. A large-scale mode involved much larger ΔT_c and t_c. However, large-scale contacts were only detected just prior to an intermediate transition.

The peak-to-peak noise of the probe signal was 0.25°C, so only temperature depressions greater than 0.5°C were conservatively identified as contact events from the probe traces. The data from the probe at 0 deg never demonstrated large-scale contacts. The data showed that when the vapor film became unstable there, a total collapse of the vapor film was precipitated, leading immediately to nucleate boiling. This can be explained by the fact that the film thickness is the thinnest and the heater temperature is the least at the forward stagnation point. Contact with the heater apparently caused a cold spot whose energy level could not be replenished and transition always occurred. Consequently, only contact data for the 90- and 180-deg points are reported.

Figures 14 and 15 show averaged contact data for the two extreme cases that we were able to examine in this study. Figure 14 shows data for low velocity/low subcooling, while Fig. 15 contains data for the highest obtainable level of velocity and subcooling. It is clear that there is no discernible trend of contact data with wall superheat, or velocity or subcooling. One would expect that both ΔT_c and t_c should increase as the wall superheat decreases and as velocity and subcooling increase. However, such trends were not present for small-scale contacts. Generally, in the small-scale contact mode, the average contact data were: $\Delta T_c = 0.6$ C, $t_c = 20$ ms, $f_c = 0.2$ contact/s, and $A_c/A_t = 0.004$. Therefore the contact heat flux could not contribute much to the overall heat transfer rate. These values were found by summing over a period of about 50 s.

In the large-scale mode, contacts were much more extensive and led to intermediate transitions. Figure 10 shows the probe trace that corresponds to the intermediate transition of Fig. 6. Large-scale contact of liquid occurred during this event. ΔT_c and t_c were much larger for these cases, ranging up to 20°C and 250 ms, respectively. Such contacts should clearly have a dramatic effect on the total heat transfer from the surface.

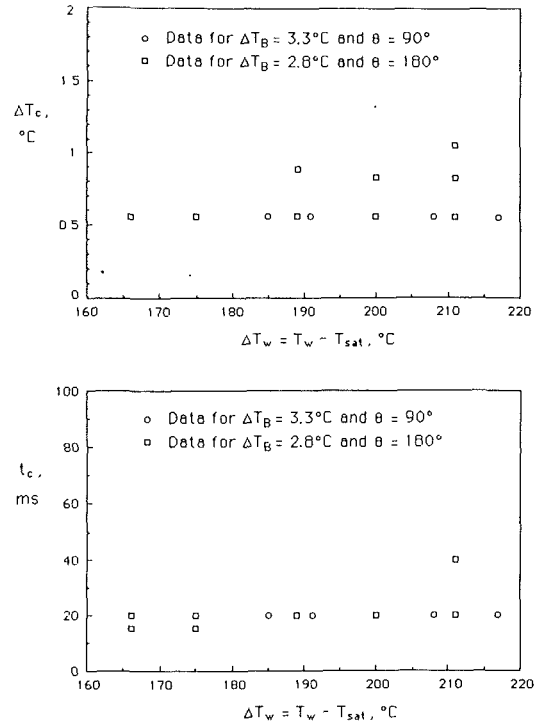

Fig. 14 Liquid-solid contact data for temperature depression ΔT_c and contact duration t_c: $V = 0.7$ m/s, $\Delta T_B = 2.8$°C or 3.3°C, and $\theta = 90$ or 180 deg

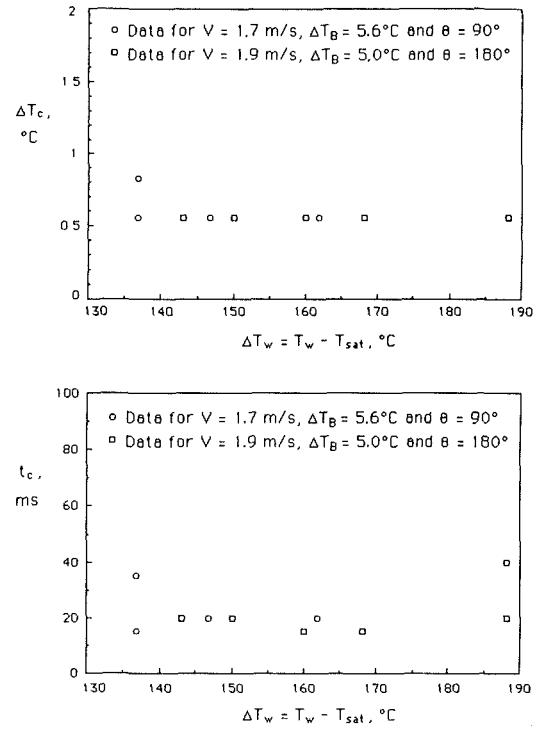

Fig. 15 Liquid-solid contact data for temperature depression ΔT_c and contact duration t_c. $V = 1.7$ m/s or 1.9 m/s, $\Delta T_B = 5.0$°C or 5.6°C, and $\theta = 180$°C

Liquid-solid contact data for two cases where large-scale contact occurred just prior to the intermediate transitions were reduced to a form suitable for the application of equations (1) and (3). Average contact values of $\Delta T_c = 5.2$°C, $t_c = 151$ ms, $f_c = 2.85$ contacts/s, and $F_a = 0.430$ were calculated for $V = 1.0$ m/s, $\Delta T_B = 3.9$°C, and $\theta = 180$ deg (see Fig. 6). The ergodic surmise was used to evaluate F_a; i.e., the time fraction of contact F_t can be set equal to the area fraction if the surface

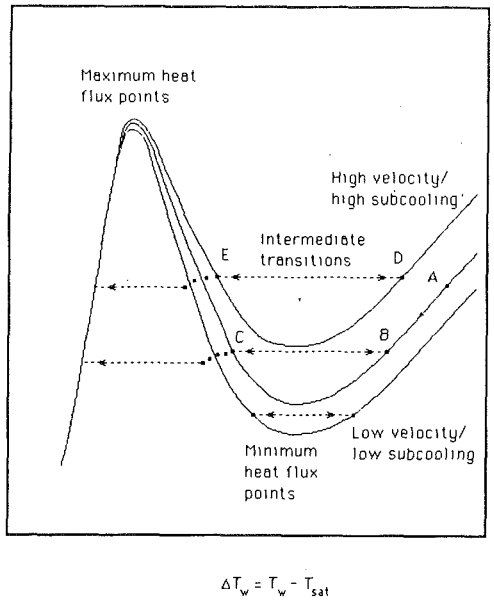

Fig. 16 Qualitative representation of intermediate transition on boiling curves

is large enough to include many contact events per unit time and if the sample time is long enough to include many contact events. These conditions were met in our experiments.

At $\Delta T_w = 195°C$, $q_v = 80$ kW/m^2, while from equation (1) $q_c = 42.3$ kW/m^2. Using the F_a value above yields $q = 63.8$ kW/m^2. While the effect of liquid–solid contact on the calculated heat flux is significant (about 28 percent), the experimental heat flux is about 80kW/m^2. So the prediction is about 20 percent lower than the measured value.

A similar calculation for $V = 1.7$ m/s, $\Delta T_B = 6.7°C$, and $\theta = 180$ deg (see Fig. 9) gives: $\Delta T_c = 6.6°C$, $t_c = 80$ ms, $f_c = 7.08$ contacts/s, and $F_a = 0.566$. For this case, equation (1) gives 97.9 kW/m^2 and q_v is 120 kW/m^2 and $\Delta T_w = 208°C$. Equation (3) gives $q = 107.5$ kW/m^2, which does not compare well with the measured value of 206 kW/m^2.

It is clear that the model for liquid–solid contact of Witte et al. (1983) does not represent an accurate assessment of the influence of liquid–solid contact. Indeed the model for film boiling without liquid–solid contact of Witte and Orozco (1984) predicts higher heat fluxes than do equations (1) and (3) even though there is significant liquid–solid contact at these two data points.

A Proposed Explanation for the Intermediate Transitions

Based on heat transfer and liquid-solid contact data, and on photographic observations, a possible explanation for intermediate transitions can be offered. We believe that intermediate transitions lead to a stable local region of transition boiling in the wake. Generally it is thought that an electrically heated surface cannot achieve a stable transition condition. However, in this study, only a portion of the surface exists in this state while the remainder is in the film boiling state at a significantly higher temperature. Perhaps this heater system distributes energy spatially in such a way as to allow local stable transition boiling. While this cannot be proven, there is substantial evidence that this is what is happening.

Figure 16 shows a qualitative representation of what is speculated to happen as intermediate transitions occur. When the heat flux is lowered along a stable film boiling curve, say from point A to point B on Fig. 16, only small-scale contacts occur without much effect on heat transfer. These points are typified by the heater temperature being greater than the homogeneous nucleation temperature of R-11, so only momentary liquid contact is possible. Lienhard (1982) has shown that for most cases the T_{hn} is well approximated by 0.923 T_{cr}; for our case $T_{hn} = 183°C$.

As the heater temperature approaches T_{hn}, the contact mode becomes large scale as described previously and the surface begins to experience longer and more intense contacts. This drives the heater temperature down to a point where the local cooling of the heater can create temperature depressions that lower the heater temperature below T_{hn}. Then, liquid can remain in contact with the heater surface and a state of transition boiling exists, say point C, where there are alternating liquid and vapor patches over the surface. Both Figs. 10 and 12 show behavior that supports this contention. On Fig. 10, following the large temperature drop that we call the intermediate transition, there are several rapid temperature rises (1-6) typical of vapor being formed over the probe location. Figure 12 shows two such temperature spikes on an expanded temperature scale. Thus the data indicate that superheated liquid is in intimate contact with the heater surface with momentary "flashes" of vapor.

The explanation is supported by the experimental evidence. For the highest velocity, highest subcooling case (see Fig. 9), the tendency for large-scale contacts was to occur at higher heater superheat, as illustrated by Point D on Fig. 16. Thus the transition should begin at a higher ΔT_w. This is indeed the case. Furthermore, if the intermediate state is a stable transition boiling point, the resulting ΔT_w should be less than for lower velocity lower subcooling as shown by point E. Again, the data bear this out.

It is interesting to note that Orozco and Witte (1986) observed a similar transition in R-11 for a spherical heater supplied with heat by circulating Dowtherm. They described a thin-wake regime where it was clear that film boiling was occurring everywhere on the heater, and a thick wake regime that resulted from an uncontrollable temperature drop down to a new stable point. As in the present study using electrical heating, Orozco observed a second transition into nucleate boiling following this intermediate transition. His heater was spherical with a large supporting superstructure in the wake, while the cylindrical heater used in this study had nothing to interfere with the behavior of the wake. It is surprising that two such diverse heaters would display such strikingly similar behavior.

Vapor Wake Behavior

Conventional thinking about how a film boiling wake behaves seems to be substantially incorrect based on the observations and photographs made during this study. Traditionally the wake is pictured as a teardrop-shaped region streaming behind the cylinder with its edges coinciding with the liquid streamlines. For the conditions of this study, the model is not correct. The wake is a relatively thin, irregular patch of vapor with vapor being torn from its edges rather than being diffused out the back of the wake as illustrated in Fig. 11. A stagnant liquid wake region lies above the vapor wake. This suggests that the liquid–vapor interface in this stagnant region should behave much like a pool boiling case. If so, Taylor instability concepts should be used to describe its behavior. The details of the wake behavior have been presented in another paper (Chang and Witte, 1989).

Summary

It was found that liquid–solid contacts occurred in a small-scale mode in most of experiments, where the surface temperature was greater than the homogeneous nucleation temperature of R-11. In contrast, large-scale contacts took place just prior to unexpected intermediate transitions in some cases.

In the large-scale mode, liquid–solid contacts became longer and more intense, causing a cold spot to form. This led to very large temperature drops that shifted the boiling behavior to a significantly lower wall superheat.

An explanation for intermediate transitions was proposed; it assumes that such transitions lead to stable boiling in the wake region of the heater, even though the front portion of the heater can still be covered by a smooth stable vapor film. The last stable film boiling point prior to the transition is at a temperature greater than the homogeneous nucleation temperature while the stable point following the transition is at a temperature less than T_{hn}. Yao and Henry (1978) measured virtually no contact above T_{hn} for pool boiling of saturated ethanol and water. But they measured dramatically increased contact areas as the surface approached T_{hn}. So their observations support our explanation.

Comparison of the experimental data to an analysis that includes the influence of liquid–solid contact on the heat flux did not show good agreement. This indicates that available models accounting for liquid–solid contact during flow boiling are not adequate. The data for liquid–solid contact showed a randomness that prevented the application of the analysis of Witte et al. (1983) over the range of wall superheats covered in this study.

Visual observations of the vapor wake showed that conventional thinking about the shape of the vapor wake during the flow film boiling is incorrect. Rather than a teardrop-shaped wake whose boundaries coincide with liquid streamlines, the wake is a relatively thin irregular patch of vapor. Vapor is torn from its edges rather than being diffused out the back of the wake. Our treatment of the wake region needs to be altered to account for its behavior more accurately.

Acknowledgments

This work was performed under NSF Grant No. MEA-8411894. Thanks are also extended to Mr. Subramanian Sankaran for his help in the experiments.

References

Bradfield, W. S., 1966, "Liquid-Solid Contact in Stable Film Boiling," *Ind. & Eng. Chem Fund*, Vol. 5, No. 2, pp. 22–204.

Carslaw, H. S., and Jaeger, J. C., 1959, *Conduction of Heat in Solids,* 2nd ed., Oxford Press, London, United Kingdom.

Chang, K.-H., 1987, "The Instability of Vapor Films in Flow Boiling From Cylinders," Ph.D. Dissertation, Dept. of Mechanical Engineering, University of Houston, TX.

Chang, K.-H., and Witte, L. C., 1989, "The Hydrodynamics of Film Boiling From a Cylinder in Crossflow," *J. Therm. and Ht. Trans.*, in press.

Coury, G. E., and Dukler, A. E., 1970, "Turbulent Film Boiling on Vertical Surfaces: A Study Including the Influence of Interfacial Waves," *Proc. International Heat Transfer Conference*, Vol. 2, B3.6, pp. 1–13.

Dhuga, D. S., and Winterton, R. H. S., 1986, "Measurement of Liquid-Solid Contact in Boiling," *J. Phys. E. Sci.: Instr.,* Vol. 19, pp. 69–75.

Lee, L. Y. W., Chen, J. C., and Nelson, R. A., 1982, "Surface Probe for Measurement of Liquid Contact in Film and Transition Boiling on High-Temperature Surfaces," *Rev. Sci. Instr.,* Vol. 53, No. 9, pp. 1472–1476.

Lee, L. Y. W., Chen, J. C., and Nelson, R. A., 1985, "Liquid-solid Contact Measurement Using a Surface Thermocouple Probe in Atmospheric Pool Boiling Water," *Int. J. Heat Mass Trans.*, Vol. 28, No. 8, pp. 1415–1423.

Lienhard, J. H., 1982, "Corresponding States Correlations for the Spinodal and Homogeneous Nucleation Temperatures," ASME JOURNAL OF HEAT TRANSFER, Vol. 104, No. 4, pp. 477–482.

Neti, S., Butrie, T. J., and Chen, J. C., 1986, "Fiber-Optic Liquid Contact Measurement in Pool Boiling," *Rev. Sci. Instr.*, Vol. 57, No. 12, pp. 3043–3047.

Orozco, J. A., and Witte, L. C., 1986, "Flow Film Boiling From a Sphere to Subcooled Freon-11," ASME JOURNAL OF HEAT TRANSFER, Vol. 108, pp. 934–938.

Witte, L. C., Chang, K.-H., and Orozco, J. A., 1983, "On the Role of Liquid–Solid Contact in Subcooled Flow Film Boiling From Submerged Bodies," *Symp. on Interfacial Transport Phenomena*, National Heat Transfer Conference, Seattle, pp. 67–74.

Witte, L. C., and Orozco, J. A., 1984, "Vapor Velocity Profile Shape Effects on Subcooled Flow From Submerged Bodies," ASME JOURNAL OF HEAT TRANSFER, Vol. 106, No. 1, pp. 191–197.

Yao, S. C., and Henry , R. E., 1978, "An Investigation on the Minimum Film Boiling Temperature on Horizontal Surfaces," ASME JOURNAL OF HEAT TRANSFER, Vol. 100, pp. 260–267.

T. Aihara
Professor,
Institute of Fluid Science,
Tohoku University,
Sendai 980, Japan

W.-S. Fu
Associate Professor,
Institute of Mechanical Engineering,
National Chiao Tung University,
Hsinchu, Taiwan

Y. Suzuki
Engineer,
Energy and Chemical Plant
Overseas Division,
Mitsui & Company Ltd.,
Tokyo, Japan

Numerical Analysis of Heat and Mass Transfer From Horizontal Cylinders in Downward Flow of Air-Water Mist

A numerical analysis is made of heat and mass transfer from horizontal circular cylinders in a downward flow of air/water mist of polydisperse droplets, taking into account the far-upstream droplet size distribution and the blockage effect of the gas phase flow. The effects of the droplet size distribution, temperatures, and liquid-to-gas mass flow ratio upon the liquid film thickness and wall shear stress, velocity, and temperature of the air-water interface, two-phase Nusselt numbers, etc., are examined.

Introduction

Cooling of heated bodies by water droplets suspended in a gas stream shows a remarkably improved heat transfer performance in comparison with single-phase gas cooling. Accordingly, gas-water mist cooling facilitates a significant reduction in the size and weight of heat exchangers and is useful for emergency cooling at peak loads or in accidents of normally gas-cooled equipment. This simple cooling technique is also suitable for heat transfer control (Aihara, 1988), because a 10-to-30-fold change in the heat transfer performance can easily be accomplished by varying the mass flow rate of droplets to gas by a mere few percent.

Many theoretical and experimental studies of air-water mist cooling have hitherto been carried out; an extensive historical review of 53 papers was made by Aihara (1988). The majority of existing theoretical studies are focused on either the heat transfer from a dry surface or the flow behavior and evaporation of a water film, without considering the droplet trajectories.

Recently, a numerical analysis was made by Lu and Heyt (1980) of heat and mass transfer of double laminar boundary layers, i.e., liquid and outer gas boundary layers. However, the agreement between the predicted and measured values is not good, due to the assumption of nongravity and monodisperse droplets.

On the other hand, Aihara and Fu (1986) made a trajectory analysis of the inertia collection of polydisperse droplets by a circular cylinder and a normal flat plate, taking into account the gas-phase flow separation; they confirmed that the gas flow separation has little influence on the local partial collection efficiency of the cylinder. Furthermore, Aihara et al. (1988) carried out a similar analysis for the case of horizontal cylinders in a vertical downward flow of gas/polydisperse droplets with a blockage ratio of 0–0.4. In the present study, a numerical analysis of the double boundary layers is carried out using the collection efficiencies obtained in these analyses. The effects of the drop size distribution, temperatures, and liquid-to-gas mass flow ratio are examined on the flow behavior and evaporation of a thin liquid film on cylinders with a uniform wall temperature and on the two-phase, local Nusselt number, etc.

Contributed by the Heat Transfer Division for publication in the JOURNAL OF HEAT TRANSFER. Manuscript received by the Heat Transfer Division April 16, 1989; revision received September 8, 1989. Keywords: Evaporation, Forced Convection, Sprays/Droplets.

Mathematical Formulation

Physical Model and Assumptions. We consider heat and mass transfer from the front surfaces of horizontal circular cylinders with a uniform wall temperature T_w in a downward flow of air-water mist. Figure 1 shows the physical model of the near-upstream region for a cylinder placed in the middle of a channel of width b or one of the cylinders in a crossflow array of a pitch b. Water droplets carried by an air stream impinge onto the cylinder and evaporate on its surface. When the mass flow rate of impinging droplets is greater than the mass evaporation rate of droplets on the cylinder surface, a liquid film starts to form in the vicinity of the forward stagnation point. However, farther downstream, less liquid film is formed, because the mass flux of the droplets impinging onto the cylinder decreases progressively on approaching the droplet grazing point. Hereafter, the area where the liquid film

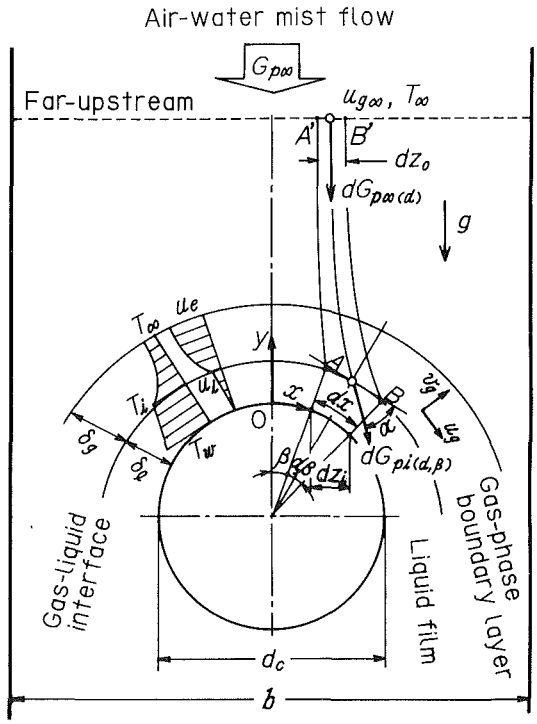

Fig. 1 Physical model of the near-upstream region

forms is referred to as the "liquid film zone," the area with no liquid film as the "dryout zone," and the boundary between both zones as the "starting point of dryout, x_0."

For simplification, the following assumptions are made:

1 The gas–liquid mixture is composed of water droplets and saturated humid air (hereafter referred to as the gas phase); the droplet temperature is the same as the far-upstream gas temperature T_∞.

2 The liquid droplets are uniformly distributed in the gas far upstream and their size distribution can be approximated by the following mass-basis Rosin–Rammler distribution:

$$f_{w(d)} = \frac{n}{d_0}\left(\frac{d_p}{d_0}\right)^{n-1} \exp\left[-\left(\frac{d_p}{d_0}\right)^n\right] \tag{1}$$

where d_p is the droplet diameter, $f_{w(d)}$ the mass-basis size distribution function, d_0 the size parameter, and n the dispersion parameter.

3 The gas velocity at the outer boundary layer, the droplet trajectories, and the local partial collection efficiency on the cylinder surface agree with results obtained in the authors' previous study (Aihara et al., 1988).

4 The cloud of droplets at a low concentration does not affect the gas-phase flow pattern.

5 The thickness of the gas-phase boundary layer is very small compared with the cylinder diameter d_c; the droplets travel in straight paths without heat and mass transfer through the gas boundary layer.

6 Both the gas-phase and liquid-film flows are steady, two dimensional, and laminar.

7 No ripple of liquid film, no re-entrainment due to liquid splashback, and no surface tension are assumed.

8 Within the boundary layers, all fluid physical properties are assumed to be constant and evaluated at a reference temperature $(T_i + T_\infty)/2$ and a reference humidity $(\chi_i + \chi_\infty)/2$.

9 The liquid-to-gas mass flow ratio is small and the liquid film is sufficiently thin to allow the assumption of a linear distribution of velocity and temperature in the liquid film.

Governing Equations. According to Aihara and Fu's (1982) numerical analysis of a heated wedge surface, the term $(d\delta_l/dx)^2$, the inertia and evaporation terms in the liquid-film momentum equation, and the term of enthalpy transport in the liquid-film energy equation are negligible.

Liquid Film Zone $(0 \le x < x_0)$. The gas-phase boundary layer equations are

$$\frac{\partial u_g}{\partial x} + \frac{\partial v_g}{\partial y} = 0 \tag{2}$$

$$u_g \frac{\partial u_g}{\partial x} + v_g \frac{\partial u_g}{\partial y} = u_e \frac{\partial u_e}{\partial x} + \nu_g \frac{\partial^2 u_g}{\partial y^2} \tag{3}$$

$$u_g \frac{\partial T_g}{\partial x} + v_g \frac{\partial T_g}{\partial y} = \frac{\nu_g}{\mathrm{Pr}_g} \frac{\partial^2 T_g}{\partial y^2} \tag{4}$$

$$u_g \frac{\partial \omega_g}{\partial x} + v_g \frac{\partial \omega_g}{\partial y} = D_g \frac{\partial^2 \omega_g}{\partial y^2} \tag{5}$$

Based on the result of a numerical analysis by Aihara and Fu (1982), the term $u_i(d\delta_l/dx)$ can be omitted and the boundary conditions become

for $y = \infty$:

$$u_g = u_e, \quad T_g = T_\infty, \quad \omega_g = \omega_\infty \tag{6a}$$

for $y = \delta_l$:

Nomenclature

b = channel width or transverse pitch of cylinders
c = specific heat at constant pressure
d_c = diameter of circular cylinder
d_p = diameter of droplet
d_0 = size parameter in Rosin–Rammler equation (1)
D_g = binary diffusion coefficient
Fr = Froude number, equation (28)
$f_{w(d)}$ = mass-basis size distribution function, equation (1)
g = gravitational acceleration
G_e = mass evaporation rate of liquid film
$G_{g\infty}$ = mass flow rate of saturated humid air far upstream
$G_{pi(d,\beta)}$ = local partial mass impinging rate for a droplet of diameter d_p at a position of angle β
$G_{pi(\beta)}$ = local total mass impinging rate of droplets at position β
$G_{p\infty}$ = mass flow rate of droplets far upstream
$G_{p\infty(d)}$ = far-upstream mass flow rate for a droplet of diameter d_p
h = local heat transfer coefficient, equation (34)
K = inertia parameter, equation (29)
M = liquid-to-gas mass flow ratio = $G_{p\infty}/G_{g\infty}$
n = dispersion parameter in Rosin–Rammler equation (1)
Nu = local Nusselt number, equation (33)
Pr = Prandtl number
$\dot{q}$ = heat flux
r = latent heat of evaporation
Re_g = gas Reynolds number = $d_c\, u_{g\infty}/\nu_g$
Re_p = droplet free-stream Reynolds number, equation (27)
T, ΔT = temperature and temperature difference = $(T - T_\infty)$
u_e = velocity at the edge of gas-phase boundary layer
u, v = velocities in x and y directions
W_{pi} = impinging velocity of a droplet onto a cylinder, equation (30)
x, y = Cartesian coordinates, as shown in Fig. 1
x_0 = starting point of dryout
α = incidence angle of a droplet onto liquid film (see Fig. 1), equation (30)
β = azimuth angle from the forward-stagnation point
δ_g = thickness of gas-phase boundary-layer
δ_l = thickness of liquid film
$\eta_{(d,\beta)}$ = local partial collection efficiency at a position of angle β, for a droplet of diameter d_p, equation (10)
$\eta_{(\beta)}$ = local total collection efficiency, equation (14)
λ = thermal conductivity
ν = kinematic viscosity
ρ = density
τ = shear stress
χ = saturated absolute humidity
ω = mass fraction of water vapor to humid air = $\chi/(1 + \chi)$

Subscripts

d = droplet of diameter d_p
g = gas phase
i = gas–liquid interface
l = liquid film
p = droplet
w = wall
$(\ )_0$ = stagnation point
∞ = far upstream or free stream

$$u_g = u_i, \quad T_g = T_i, \quad \omega_g = \omega_i, \text{ and } v_g = G_e/\rho_g \tag{6b}$$

for $x = 0$:

$$u_g = \frac{\partial v_g}{\partial x} = \frac{\partial T_g}{\partial x} = \frac{\partial \omega_g}{\partial x} = 0 \tag{6c}$$

with

$$G_e = -\frac{\rho_g D_g}{1-(\omega_g)_i}\left(\frac{\partial \omega_g}{\partial y}\right)_i \tag{7}$$

The liquid-film equations are derived to be solved by the integral method that follows. Denoting the arc AB in Fig. 1 by dx_i, the time-averaged balance of the mass flow rate of droplets in a control volume A′B′AB becomes

$$dG_{p\infty(d)}dz_0 \cong dG_{pi(d,\beta)}(d\chi_i \sin\alpha + d\delta_l \cos\alpha) \tag{8}$$

Referring to the approximate calculation of Hodgson and Sunderland (1968), $2\delta_l/d_c \simeq 10^{-3}$; therefore,

$$dx_i \cong dx = dz_i/\cos\beta \tag{9}$$

Defining the local partial collection efficiency $\eta_{(d,\beta)}$ as

$$\eta_{(d,\beta)} = dz_o/dz_i \tag{10}$$

and substituting these into equation (8), we obtain

$$dG_{p\infty(d)}\eta_{(d,\beta)}\cos\beta = dG_{pi(d,\beta)}[\sin\alpha + \cos\alpha(d\delta_l/dx)] \tag{11}$$

The far-upstream mass flow rate, $dG_{p\infty(d)}$, of droplets with a size interval between d_p and $d_p + dd_p$, is expressed as

$$dG_{p\infty(d)} = G_{p\infty}f_{w(d)}dd_p \tag{12}$$

Substituting equation (12) into equation (11) and then integrating from the minimum drop size $d_{\min}$ to the maximum drop size $d_{\max}$, we obtain

$$\int_{d_{\min}}^{d_{\max}}\left(\sin\alpha + \cos\alpha\frac{d\delta_l}{dx}\right)dG_{pi(d,\beta)} = \int_{d_{\min}}^{d_{\max}}(G_{p\infty}f_{w(d)}\eta_{(d,\beta)}\cos\beta)dd_p \tag{13}$$

Introducing the local total collection efficiency $\eta_{(\beta)}$

$$\eta_{(\beta)} = \int_{d_{\min}}^{d_{\max}} f_{w(d)}\eta_{(d,\beta)}dd_p \tag{14}$$

into equation (13), the following expression is obtained:

$$\int_{d_{\min}}^{d_{\max}}\left(\sin\alpha + \cos\alpha\frac{d\delta_l}{dx}\right)dG_{pi(d,\beta)} = G_{p\infty}\eta_{(\beta)}\cos\beta \tag{15}$$

The mass conservation equation of liquid film is expressed in the integral form as

$$\int_{d_{\min}}^{d_{\max}}\left(\sin\alpha + \cos\alpha\frac{d\delta_l}{dx}\right)dG_{pi(d,\beta)} - \rho_l\frac{d}{dx}\left(\int_0^{\delta_l}u_l\,dy\right) = G_e\left[1+\left(\frac{d\delta_l}{dx}\right)^2\right]^{1/2} \tag{16}$$

where the first and second terms on the left-hand side denote the droplet impingement rate and the net flow rate of the liquid film, respectively, and the right-hand side denotes the evaporation rate. Substituting equation (15) into the first term on the left-hand side of equation (16) and considering $(d\delta_l/dx)^2 \ll 1$, we obtain the final expression for mass conservation as

$$G_{p\infty}\eta_{(\beta)}\cos\beta - \rho_l\frac{d}{dx}\left(\int_0^{\delta_l}u_l\,dy\right) = G_e \tag{17}$$

Similarly, using equation (13), we obtain the following momentum equation for the liquid film:

$$\tau_w = \rho_g\delta_l u_e\frac{du_e}{dx} + g\sin\beta\,\delta_l\rho_l + \tau_{gi} + G_{p\infty}\cos\beta\int_{d_{\min}}^{d_{\max}}[\eta_{(d,\beta)}f_{w(d)}w_{pi}\cos\alpha]dd_p \tag{18}$$

where τ_w is the liquid-film shear stress at the wall, and the first, second, third, and fourth terms on the right-hand side denote the pressure, gravity, gas-phase shear stress at the gas-liquid interface, and droplet impingement force, respectively.

Introducing the relation of equation (15), the energy equation is expressed as

$$\dot{q}_w = -\lambda_g(\partial T_g/\partial y)_i + G_e\,r_i + G_{p\infty}\cos\beta\eta_{(\beta)}c_l(T_i - T_\infty) \tag{19}$$

where the first, second, and third terms on the right-hand side denote the gas-phase convective heat transfer, evaporative cooling, and sensible cooling by droplet impingement, respectively.

Dryout Zone ($x > x_0$). The governing equations for this zone are identical to the gas-phase boundary layer equations (2)–(5) for the liquid film zone, but some modification of equation (6*b*) is required for the boundary conditions as follows:

$$\text{for } y = 0: \quad u_g = 0, \quad v_g = G_{pi(\beta)}/\rho_g, \quad T_g = T_w, \quad \omega_g = \omega_w \tag{20}$$

where

$$G_{pi(\beta)} = G_{p\infty}\eta_{(\beta)}\cos\beta \tag{21}$$

Numerical Solution Procedure

Differential equations (2)–(5) and integral equations (17)–(19) are solved simultaneously with the boundary conditions (6) and (20) by a line-by-line, forward-marching, implicit finite-difference scheme with iteration on each new line. Thus, the values of u_g, v_g, T_g, ω_g, δ_l, u_i, and T_i are obtained as functions of β. Since the finite difference equations and the details of the numerical scheme are given in the authors' previous report (Fu and Aihara, 1985), only the relevant details are described here.

Correlating Equations Used for Numerical Calculation. With regard to the variables u_e, $\eta_{(d,\beta)}$, $\eta_{(\beta)}$, and $w_{pi}\cos\alpha$, the following equations obtained in the authors' numerical analysis (Aihara et al., 1988) are used:

$$\frac{\eta_{(d,\beta)}}{\eta_{(d,0)}} = \left[2\left\{\left(\frac{\tan\beta}{\tan\beta_{\max}}\right)^{m_1}+1\right\}^{-1}-1\right]^{m_2} \tag{22}$$

with

$$m_1 = 2[1 - 0.12\ln K + 0.033\,K^{0.5}] \tag{23a}$$

and

$$m_2 = 0.233\left[1 + 0.024\left(\ln\frac{K}{1.4}\right)^2 - 0.065\ln \mathrm{Re}_g - \frac{0.093}{\mathrm{Fr}}\right]^{-1} \tag{23b}$$

Equations (22) and (23) are applicable for $K = 0.15$–56, $\mathrm{Re}_p = 4.7$–200, $d_c/b = 0$–0.4, $\mathrm{Fr} > 2.8$, and $\mathrm{Re}_g = 4.6 \times 10^3$–$3.4 \times 10^4$ within the maximum error of ± 0.067 in $\eta_{(d,\beta)}$ (within ± 3 percent for the majority of the results). Here $\beta_{\max}$ is the azimuth angle of the grazing point and is approximated by equation (24) within the maximum error of ± 0.045 rad (within ± 3 percent for the majority of the results) for the same range as equation (22)

$$\beta_{\max} = \frac{\pi}{2}\eta_{(d,0)}^{0.86} - 0.047\left[1 + 2.5\left(\frac{d_c}{b}\right) - \frac{2}{\mathrm{Fr}}\right] \tag{24}$$

The partial collection efficiency at the stagnation point, $\eta_{(d,0)}$, is given by the following equations within the maximum error of ± 0.02 for the same range as equation (22):

$$\eta_{(d,0)} = \left(1 - \frac{1}{K^*}\right)\left[1 + \frac{3.8}{\mathrm{Re}_p^{0.88}}\left(\frac{d_c}{b}\right)^{1.5}\right]\left[1 + \frac{0.72}{(\mathrm{Re}_p\mathrm{Fr})^{0.78}}\right] \tag{25}$$

with

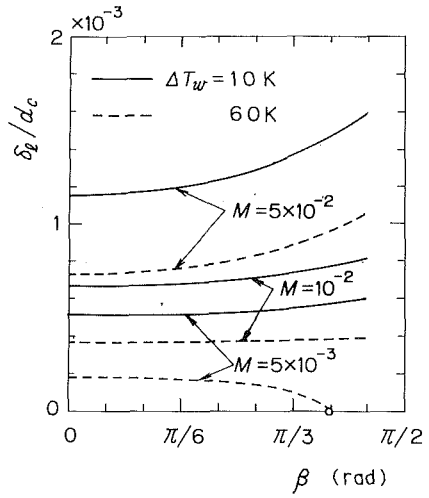

Fig. 2 Effect of mass flow ratio M and temperature difference ($T_w - T_\infty$) on local liquid film thickness δ_l for $Re_g = 1.7 \times 10^4$, $d_0/d_c = 2 \times 10^{-3}$, $n = 3$, and $T_\infty = 283$ K

$$K^* = 2.99 \exp\{0.054(\ln K + 10.2)\ln K\} \tag{26}$$

where Re_p and Fr are the droplet free-stream Reynolds number and Froude number, respectively,

$$Re_p = d_p u_{g\infty}/\nu_g \tag{27}$$

$$Fr = u_{g\infty}/(g d_c)^{1/2} \tag{28}$$

and K is the inertia parameter, defined as

$$K = \frac{1}{18}\left(\frac{d_p}{d_c}\right)\left(\frac{\rho_p}{\rho_g}\right) Re_p \tag{29}$$

The local total collection efficiency $\eta_{(\beta)}$ can be evaluated from equations (1) and (22)–(26). The tangential component, $w_{pi} \cos \alpha$, of the impinging velocity is given by equation (30) within the maximum error of $+0.085$ to -0.011 (within ± 5 percent for the majority of the results) for the same range as equation (22).

$$\frac{w_{pi}}{u_{g\infty}} \cos \alpha = \left[1 + 0.012 \frac{Re_p^2}{Fr^{3.4}} + \frac{0.21}{K^{0.52}}\left\{1 + \frac{\pi}{2}\left(\frac{d_c}{b}\right)^2\left(3 - \frac{1}{K^{0.52}}\right)\right\}\right] \sin \beta \tag{30}$$

Furthermore, according to assumption (9), the velocity and temperature distributions in the liquid film are approximated as

$$u_l = u_i(y/\delta_l) \tag{31}$$

$$T_l = T_w - (T_w - T_i)(y/\delta_l) \tag{32}$$

Therefore, the wall shear stress of the liquid film, τ_w, is expressed as $\tau_w = \mu_l u_i/\delta_l$.

Determination of Stagnation Point Values

Clear Gas Flow. First, the stagnation point values $(u_g)_0$, $(v_g)_0$, $(T_g)_0$, and $(\omega_g)_0$ are determined by Blasius' and Frossling's methods (Schlichting, 1960) for the case of an infinite stream of a viscous fluid past a circular cylinder. Next, employing those as the first starting values, the variables u_g, v_g, T_g, and ω_g for cylinders with flow blockage are numerically calculated progressively up to $\beta \cong \pi/8$. However, unreasonable results arise in heat/mass transfer coefficients near the stagnation point ($\beta \leq \pi/36$), i.e., the stagnation point values are smaller than those downstream.

Accordingly, by extrapolation of these values obtained for $\beta \cong \pi/11$–$\pi/8$, the new stagnation point values are evaluated; then, employing those as the second starting values, the new values of u_g, v_g, T_g, and ω_g are recalculated up to $\beta \cong \pi/8$.

Thereafter, the above iteration process is repeated three to four times until the stagnation point values converge.

Air–Water Mist Flow. First, the liquid film thickness $(\delta_l)_0$ at the stagnation point of a cylinder in an infinite stream is evaluated by the method of Hodgson and Sunderland (1968), assuming straight droplet trajectories and no evaporation of the liquid film. Next, putting $(u_i)_0 = 0$ and $T_i = T_w$, and employing this $(\delta_l)_0$ and the converged values for clear gas flow $(u_g)_0$, $(v_g)_0$, $(T_g)_0$, and $(\omega_g)_0$ as the first starting values, the variables u_g, u_i, v_g, T_g, T_i, and ω_g for the air–water mist stream with flow blockage are numerically calculated progressively up to $\beta \cong \pi/8$.

Thereafter, the iteration process similar to that in the case of the clear gas is repeated three to four times until the stagnation point values converge.

Spatial Grid Sizes and Numerical Errors. The following step sizes are adopted:

Circumferential direction:

$$\Delta x/d_c = 9 \times 10^{-4} \quad \text{for } 0 \leq \beta \leq \pi/180 \text{ rad}$$

$$\Delta x/d_c = 4 \times 10^{-3} \quad \text{for } \pi/180 \leq \beta \leq 80\ \pi/180 \text{ rad}$$

Normal direction:

$$(Re_g)^{1/2} \Delta y/d_c = 7 \times 10^{-3}$$

When the value of δ_l/d_c becomes smaller than 10^{-5}, the liquid film is considered to have vanished.

With regard to fluid physical properties, the correlating equations by Fujii et al. (1977) are used.

Since the possible error due to the numerical scheme is very small, most of the errors in the numerical solutions arise from the physical model and the accuracy of equations (22)–(30). Consequently, the maximum errors in the present solutions for the Nusselt number and shear stress are predicted to be ± 4 percent and ± 6 percent, respectively, excluding those in the vicinity of the droplet grazing point. The present solutions of the local Nusselt number were compared with carefully measured values using a circular cylinder with a blockage ratio of 0.4 in a downward flow of air–water mist; the agreement between them is excellent. The details of this comparison are described in another report of this series (Aihara et al., 1990).

Results and Discussion

The numerical calculations were made for the range of $Re_g = 4.6 \times 10^3$–3.4×10^4, Fr = 2.9–14.3, $d_c/b = 0.4$, $d_0/d_c = 10^{-3}$–6×10^{-3}, n = 2–4, d_{min} = 99.9 percent diameter (oversize), d_{max} = 1 percent diameter, $M = 5 \times 10^{-3}$–5×10^{-2}, T_∞ = 280–350 K, and ΔT_w = 1–70 K. The numerical results beyond those given here are available in the reports by Fu and Aihara (1985) and Aihara (1988).

Figure 2 is a typical plot of the distribution of the liquid film thickness δ_l on the front half surface of a cylinder. When the whole surface of the front half is wetted, the liquid film thickness δ_l increases with distance from the stagnation point; however, in the case where dryout occurs, δ_l decreases in the downstream direction, as shown by the curve for $M = 5 \times 10^{-3}$, ΔT_w = 60 K in the figure.

Figure 3 shows the degree of contribution of the principal force components to the shear stress on the liquid film at a cylinder surface. It is noticeable that the impact force due to droplet impingement ② increases with β; after reaching a maximum in the neighborhood of $\beta \simeq \pi/5$ rad, it decreases sharply to zero. Generally speaking, the dimensionless shear stress $\tau_w/(\rho_l u_{g\infty}^2)$ increases linearly with the mass flow ratio M.

Figure 4 shows the surface velocity of the liquid film, u_i,

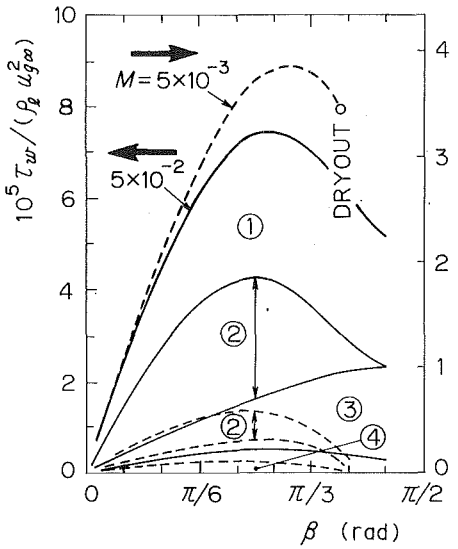

Fig. 3 Contribution of principal force components to shear stress, τ_w, on liquid film at a cylinder surface for $Re_g = 1.7 \times 10^4$, $d_0/d_c = 2 \times 10^{-3}$, $n = 3$, $\Delta T_w = 60$ K, and $T_\infty = 283$ K; ① gas phase shear stress, ② droplet impingement, ③ gravity, ④ pressure gradient

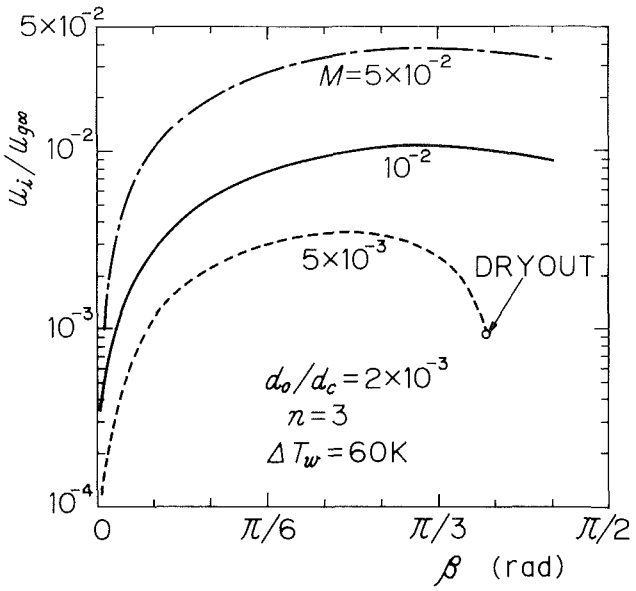

Fig. 4 Effect of mass flow ratio M on local liquid surface velocity u_i for $Re_g = 1.7 \times 10^4$ and $T_\infty = 283$ K

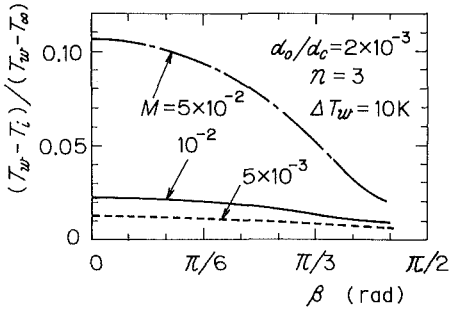

Fig. 5 Typical plot of liquid surface temperature T_l for $Re_g = 1.7 \times 10^4$ and $T_\infty = 283$ K

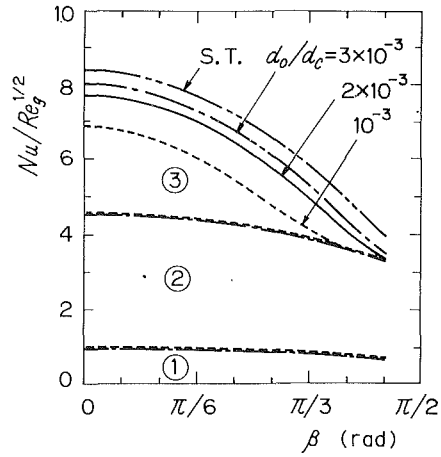

Fig. 6 Contribution of main heat transfer components to local Nusselt number Nu for $Re_g = 1.7 \times 10^4$, $n = 3$, $M = 10^{-2}$, $\Delta T_w = 30$ K, and $T_\infty = 283$ K; ① gas phase convection, ② evaporative cooling, ③ sensible-heat cooling by droplet impingement, and S. T. refers to the straight trajectories of droplets

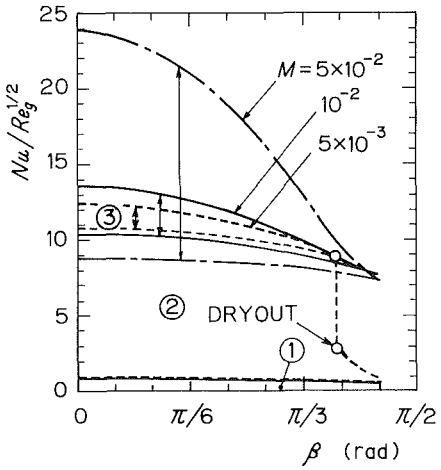

Fig. 7 Effect of mass flow ratio M on contribution of main components to local Nusselt number Nu for $d_0/d_c = 2 \times 10^{-3}$ and $\Delta T_w = 60$ K; other parameters and symbols are the same as in Fig. 6

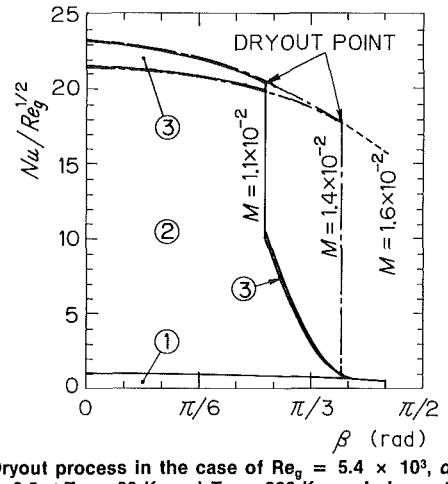

Fig. 8 Dryout process in the case of $Re_g = 5.4 \times 10^3$, $d_0/d_c = 2 \times 10^{-3}$, $n = 3.5$, $\Delta T_w = 30$ K, and $T_\infty = 320$ K; symbols are the same as in Fig. 6

evaluated using the numerical results of Figs. 2 and 3. Generally, the greater the mass flow ratio M and size parameter d_0, the stronger the droplet impact force; consequently, the liquid surface velocity u_i increases with M and d_0.

Figure 5 is a typical plot of the surface temperature of the liquid film T_i. Since the liquid film is very thin, as shown in Fig. 2, the temperature difference between the cylinder and the liquid film, $T_w - T_i$, is only 10 percent or less of $(T_w - T_\infty)$.

Figures 6–8 show the degree of contribution of the main heat transfer components to the local Nusselt number Nu, defined as

$$\mathrm{Nu} = h\, d_c/\lambda_g \tag{33}$$

with

$$h = \dot{q}_w/(T_w - T_\infty) \tag{34}$$

Heat transfer components ①-③ correspond to the respective terms in energy equation (19).

In Fig. 6 for the completely wetted surface, the evaporative component ② is almost the same for every d_0/d_c value. Hence, the effect of increasing the size parameter d_0 appears mainly as an increase in the sensible-heat cooling component ③ due to the enhanced rate of droplet impingement. However, the dispersion parameter n has a weak influence on the Nusselt number when d_0 is specified; only a few percent or less in the range of n = 2–4. This is one of the more important results obtained in the present analysis.

In the case of a completely wetted surface, the effect of the increased mass flow ratio M appears mainly as an increase in the sensible-heat cooling component ③, because of the higher droplet impinging rate, as shown in Fig. 7.

When dryout occurs, the Nu decreases discontinuously as shown by the dashed curve for $M = 5 \times 10^{-3}$ in Fig. 7, where the starting point of dryout is indicated by an open circle. Figure 8 shows the process of dryout in detail. In the liquid film zone near the dryout point x_0, the mass evaporation rate exceeds the mass impinging rate of droplets; the deficiency in liquid mass is compensated for by the liquid film flow from upstream. Therefore, after the occurrence of dryout, the mass evaporation rate depends only upon the mass impinging rate of droplets. This is the reason for the discontinuity in the Nusselt number distribution.

Figures 9 and 10 show the effect of the gas Reynolds number Re_g and temperature difference $T_w - T_\infty$, respectively. The enhancement in Nu produced by increasing Re_g is remarkable in the region of smaller β, i.e., near the stagnation point. In the region of greater β where the droplet impinging rate is lower, the Nu is proportional to $\mathrm{Re}_g^{1/2}$. The effect of temperature difference ΔT_w $(= T_w - T_\infty)$ appears mainly in the evaporative cooling component ②; the Nu increases with ΔT_w. It is noticeable that a family of Nu curves for different ΔT_ws in Fig. 10 have approximately the same shape, and it is especially remarkable that a family of Nu curves for different T_∞s but the same ΔT_w have almost the same shape.

In Fig. 11, the present solutions are compared with some of the experimental results by Hodgson et al. (1968) under identical conditions. According to the authors' previous analyses (Aihara and Fu, 1986; Aihara et al., 1988), the collection efficiency of a cylinder with flow separation is somewhat smaller than that without separation; and the smaller the blockage ratio, the smaller the collection efficiency. Conversely, the higher the gas-phase far-upstream velocity, the better the collection efficiency. These various effects cancel each other out; as a result, the present numerical solutions seem to agree tolerably well with the experimental values of Hodgson et al. (1968).

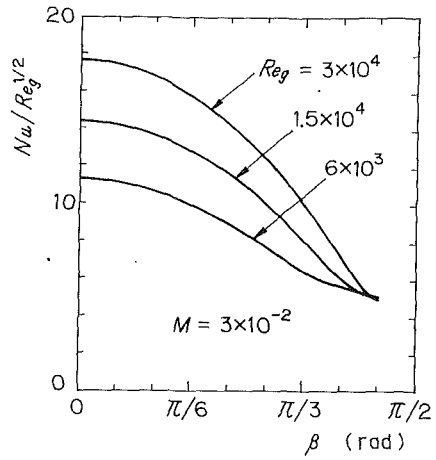

Fig. 9 Effect of gas Reynolds number Re_g on Nusselt number Nu for $d_0/d_c = 2 \times 10^{-3}$, $n = 3.5$, $M = 3 \times 10^{-2}$, $\Delta T_w = 20$ K, and $T_\infty = 300$ K

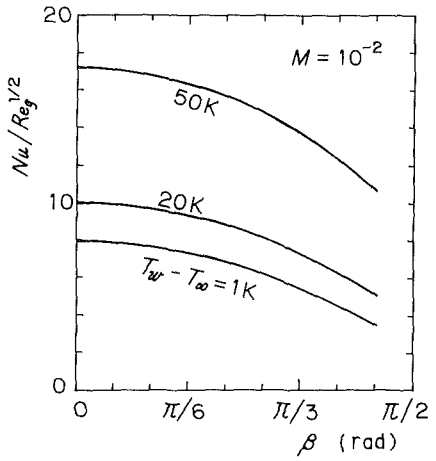

Fig. 10 Effect of temperature difference $T_w - T_\infty$ on Nusselt number Nu for $\mathrm{Re}_g = 1.5 \times 10^4$, $d_0/d_c = 4 \times 10^{-3}$, $n = 3.5$, $M = 10^{-2}$, and $T_\infty = 300$ K

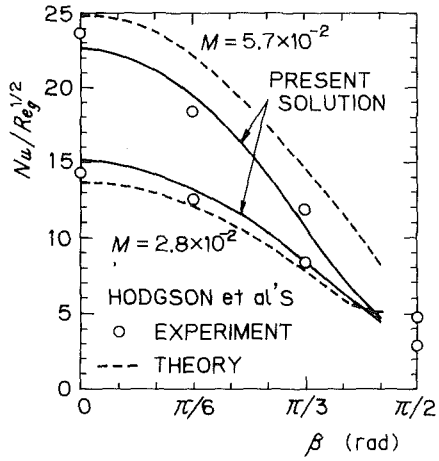

	AUTHORS	HODGSON et al.
d_c	0.05 m	0.076 m
$u_{g\infty}$	5 m/s	6.1 m/s
d_c/b	0.4	0.25
d_o/d_c	2×10^{-3}	2×10^{-3}

Fig. 11 Comparison between the present numerical solution and some of the experimental values by Hodgson et al. (1968) and theoretical values by Hodgson and Sunderland (1968): $\Delta T_w = 17$ K and $T_\infty = 299$ K

Hodgson and Sunderland (1968) carried out a theoretical study based on the assumptions of straight droplet trajectories, constant droplet velocity, and no evaporation of liquid film. In the case of low mass flow ratios, an overestimation of the droplet impinging rate due to the first assumption and neglect of the evaporative cooling effect by the latter assumption cancel each other out. Consequently, their theoretical values seem to show a relatively good agreement with the present numerical solutions. However, in the case of high mass flow ratios with a small temperature difference, the overestimation due to the first assumption is superior, because the sensible-heat cooling by droplet impingement is dominant. Thus the theoretical values of Hodgson and Sunderland (1968) are greater than those of the authors.

Conclusions

A numerical analysis has been carried out on heat and mass transfer from horizontal circular cylinders in a downward flow of air–water mist, approximating the droplet size by the Rosin–Rammler distribution and taking into account the gas-phase flow blockage and gravity.

The following are clarified quantitatively: (1) the effects of the gas Reynolds number, mass flow ratio, temperature difference, and the size and dispersion parameters upon the local Nusselt number distribution; (2) the degree of contribution of the gas-phase shear stress, droplet impact force, gravity, and pressure gradient to the local shear stress of liquid film; and (3) the degree of contribution of the gas phase convection, evaporative cooling, and sensible-heat cooling of impinging droplets to the local Nusselt number.

Furthermore, it has been pointed out that when the size parameter is specified, the dispersion parameter has an influence of only a few percent or less on the Nusselt number, and that dryout occurs from downstream and the local Nusselt number decreases discontinuously at the starting point of dryout.

Acknowledgments

This work is a part of the research carried out with a Grant-in-Aid for Scientific Research B-58460105 from the Ministry of Education, Science, and Culture of Japan.

References

Aihara, T., 1988, "Heat Transfer Augmentation by Gas–Liquid Mist Flow for Thermal Control (Keynote Paper)," *Proceedings, 3rd International Symposium on Transport Phenomena in Thermal Control*, G.-J. Hwang et al., eds., pp. 449–464.

Aihara, T., and Fu, W.-S., 1982, "Heat Transfer From a Wedge in Air–Water Mist Flow (Part 2: Theoretical Study of a Vertical Infinite Wedge of Uniform Wall Temperature)," *Trans. Japan Society of Mechanical Engineers* (Ser. B) [in Japanese], Vol. 48, pp. 2536–2546.

Aihara, T., and Fu, W.-S., 1986, "Effect of Droplet-Size Distribution and Gas-Phase Flow Separation Upon Inertia Collection of Droplets by Bluff-Bodies in Gas–Liquid Mist Flow," *International Journal of Multiphase Flow*, Vol. 12, pp. 389–403.

Aihara, T., Fu, W.-S., Hongoh, M., and Shimoyama, T., 1990, "Experimental Study of Heat and Mass Transfer From a Horizontal Cylinder in Downward Air–Water Mist Flow with Blockage Effect," to be submitted to *Experimental Thermal and Fluid Science*.

Aihara, T., Fu, W.-S., and Suzuki, Y., 1988, "Effects of Droplet-Size Distribution and Flow-Blockage Upon Inertia Collection of Droplets by Horizontal Cylinders in Downward Flow of Gas–Liquid Mist," *Proceedings, 3rd Japan–U. S. Seminar on Two-Phase Flow Dynamics*, X. Ohtsu, I. Michiyoshi, and O. C. Jones, Jr., eds. (to be published by Hemisphere Publishing Corp.)

Fu, W.-S., and Aihara, T., 1985, "Heat Transfer From a Heated Body in Air–Water Mist Flow (3rd Report)," *Trans. Japan Society of Mechanical Engineers* (Ser. B) [in Japanese], Vol. 51, pp. 882–891.

Fujii, T., Kato, Y., and Mihara, K., 1977, "Expressions of Transport and Thermodynamic Properties of Air, Steam and Water," Reports of Research Institute of Industrial Science [in Japanese], Kyushu University, Japan, No. 66, pp. 81–95.

Hodgson, J. W., Saterbak, R. T., and Sunderland, J. E., 1968, "An Experimental Investigation of Heat Transfer From a Spray Cooled Isothermal Cylinder," ASME JOURNAL OF HEAT TRANSFER, Vol. 90, pp. 457–463.

Hodgson, J. W., and Sunderland, J. E., 1968, "Heat Transfer From a Spray-Cooled Isothermal Cylinder," *I&EC Fundamentals*, Vol. 7, pp. 567–572.

Lu, C. C., and Heyt, J. W., 1980, "Heat Transfer From Two-Phase Boundary Layers on Isothermal Cylinder: Influence of Drop Trajectory," *AIChE Journal*, Vol. 26, pp. 762–769.

Schlichting, H., 1960, *Boundary Layer Theory*, translated by J. Kestin, 7th ed., McGraw-Hill, New York.

Practical Fin Shapes for Surface-Tension-Drained Condensation

M. A. Kedzierski
National Institute of Standards and Technology, Gaithersburg, MD 20899

R. L. Webb
The Pennsylvania State University, University Park, PA 16802

This paper introduces a new family of high-performance fin profiles for surface-tension-drained condensation. Previously described profiles for this situation have been defined in terms of the fin curvature and arc length. The existing profiles are generally not suitable for commercial manufacture. The fin profiles presented in this paper are conveniently defined by the fin tip radius, the fin height, and the fin base thickness. Consequently, the designer may easily specify a fin shape with parameters that are compatible with those used by the manufacturing industry. The heat transfer performance of the new profiles provides an improvement over existing, commercial fin shapes. An analysis is presented to show the R-11 condensation performance of the new profiles as a function of the geometric variables. A recommended design practice for fins for surface-tension-drained condensation is given also.

Introduction

This paper introduces a new family of high-performance fin profiles for surface-tension-drained condensation. It is intended that the new profiles be suitable for commercial manufacture. The focus of the paper is on the effect that the fin parameters have on the condensation heat transfer of the fin. The analysis presented here can be used to determine the best fin geometry for a given heat transfer surface. This analysis can also be used with the model of Webb et al. (1985), or the more recent model of Adamek and Webb (1989), to predict the condensation of a total tube.

Gregorig (1954) was the first to propose and design a fin profile that uses surface-tension drainage. Surface-tension forces are the dominant factor in determining the heat transfer for fins with fin heights less than 1.5 mm. The surface-tension enhancement is a result of a variation of the curvature of the liquid–vapor interface of the condensate film on the fin.

Figure 1 is an illustration of a vertical finned plate and the coordinate system used for the convex fin. A condensate film of thickness δ exists on the finned surface. The illustration shows the Gregorig fin profile having an arc length of S_m, and a drainage channel of depth L_s. The coordinate measured along the liquid–vapor interface is s. The coordinate measured along the fin surface is s'. The location $s' = 0$ is the point of symmetry of the fin arc and is referred to as the fin-tip. The angle θ measures the rotation of the liquid–vapor interface from the fin tip to an arbitrary point s. The condensate surface turns through a maximum angle of Θ_m, and a maximum arc length S_m.

Figure 1 shows that surface-tension forces drain the condensate film perpendicular to the direction of gravity (z direction) along the arc length S_m. Then, the condensate is carried by gravity in the channel. The pressure gradient (dP/ds) in the s direction due to surface-tension forces is given by

$$\frac{dP}{ds} = \sigma \frac{d\kappa}{ds} \tag{1}$$

where κ is the curvature of the liquid–vapor interface. Gregorig defined a shape for the convex profile, which would provide a constant film thickness over the entire arc length S_m. The required shape of the liquid–vapor interface is

$$\kappa = \frac{1.5\,\Theta_m}{S_m}\left[1 - \left(\frac{s}{S_m}\right)^2\right] \tag{2}$$

Adamek (1981) defined a family of convex shapes that use surface tension to drain the film. His fin curvature is defined as

$$\kappa = \frac{\Theta_m}{S_m}\left(\frac{\zeta+1}{\zeta}\right)\left[1 - \left(\frac{s}{S_m}\right)^{\zeta}\right] \text{ for } -1 \le \zeta \le \infty \tag{3}$$

where each value of ζ gives a fin profile with a different shape and aspect ratio (e/t_b). Figure 2 shows nine different Adamek profiles for ζ values within the range $-0.9 \le \zeta \le 30$. The profiles of the liquid–vapor interface, as shown in Fig. 2, start at $s = 0$ in the upper left corner and rotate through equal lengths of S_m.

Adamek used equation (3) along with equation (1) to cal-

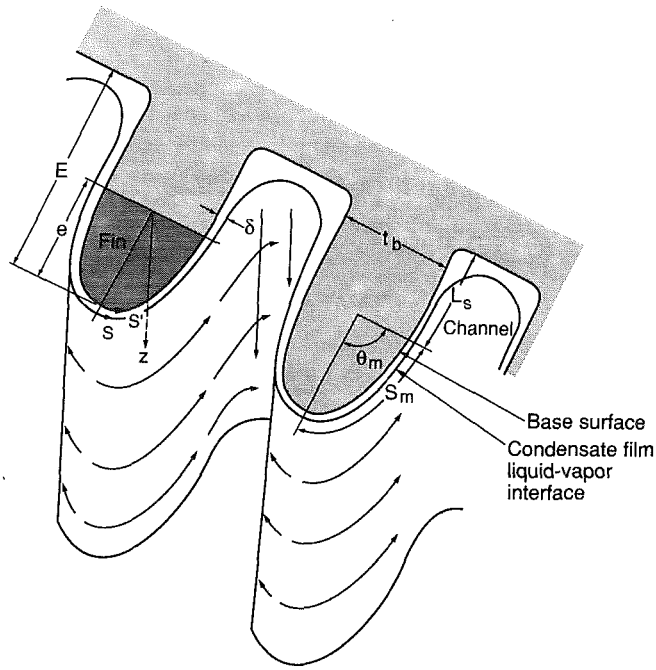

Fig. 1 Finned surface with film, streamlines, and coordinate system

Contributed by the Heat Transfer Division for publication in the JOURNAL OF HEAT TRANSFER. Manuscript received by the Heat Transfer Division December 23, 1988; revision received August 3, 1989. Keywords: Augmentation and Enhancement, Condensation, Finned Surfaces.

culate dP/ds, and paralleled Nusselt's analysis to solve the equation for the film thickness as a function of s ($\delta(s)$), i.e.,

$$\delta = \left(\frac{12\, B\, S_m^{\zeta+1} s^{2-\zeta}}{\Theta_m(\zeta+1)(\zeta+2)} \right)^{1/4} \tag{4}$$

where B is the property group $\nu k \Delta T_s/(\lambda\sigma)$. By integrating $1/\delta$ from equation (4) over $0 \le s \le S_m$, Adamek obtained the average condensate film thickness ($\bar{\delta}$), and using $\bar{h} = k/\bar{\delta}$ obtained the average heat transfer coefficient ($\bar{h}$)

$$\bar{h} = 2.149\, k \left(\frac{\Theta_m(\zeta+1)}{B\, S_m^3 (\zeta+2)^3} \right)^{1/4} \tag{5}$$

The Adamek profile for $\zeta = 2$ is identical to Gregorig's profile. If $\zeta = 1$ one obtains the results for dP/ds = const, a profile that was described by Zener and Lavi (1974).

"Practical" Fin Profiles

There are two primary applications for surface-tension-drained condensation. The first is for a vertical tube with axial fins, on which condensing may occur on the outer surface, and boiling occurs on the inner surface. Such service may be used in water desalination or gas liquefaction equipment. A second application involves horizontal, integral-fin tubes used in shell-and-tube heat exchangers.

Figure 3 shows the cross section of a fin from a commercially available integral-fin tube. The finned tube geometry is typically defined by specifying the tube diameter over the fins (D_o), the fins per meter (fpm), and the fin height (e). The fins of a commercially manufactured finned tube are formed by a thread rolling process. The rolling process uses a series of closely spaced "finning disks," to extrude the base metal from the tube wall into the narrow region between the finning disks. Figure 3 shows that the fins are of a trapezoidal shape, and that the sides are flat. Table 1 shows the dimensions of the fins, as reported by Webb et al. (1985). The fin thickness at the tip and the base are determined by the tooling requirements of the staged finning disks. This typically involves specification of a minimum desirable fin base and fin tip thicknesses, t_b and t_t, respectively. An extrusion process used to produce axial fins on vertical tubes also would establish the minimum desired fin base and tip thickness. Thus, the heat transfer designer typically specifies the D_o, fpm, and e dimensions, while the tooling engineer controls t_t and t_b and the fin shape.

The present analysis seeks to specify the fin shape and thickness dimensions to values that are acceptable to the tooling designer, and which provide favorable condensation performance. Thus, we seek to allow independent specification of the fin base thickness (t_b), the fin-tip radius (r_o), the fin height (e), and the angle Θ_m shown in Fig. 1. Unfortunately, the analyses of Gregorig (1954) and Adamek (1981) do not allow independent specification of e, t_b, r_o, and Θ_m. One may specify only S_m, Θ_m, and ζ. The values of ζ defines the fin aspect ratio, e/t_b. The value of e/t_b increases as ζ becomes smaller; see Fig. 2. This inability to specify e/t_b independently causes two practical problems. First, the Adamek $\zeta \le 1$ profiles all exhibit a zero fin-tip radius, which is physically impossible. Second, with fixed e, the fin thickness increases as ζ is increased ($\zeta > 0$). A large fin thickness will waste material and result in greater condensate retention than would exist with thinner fins. Hence, the Adamek family of fin profiles may not allow specification of the desired fin dimensions.

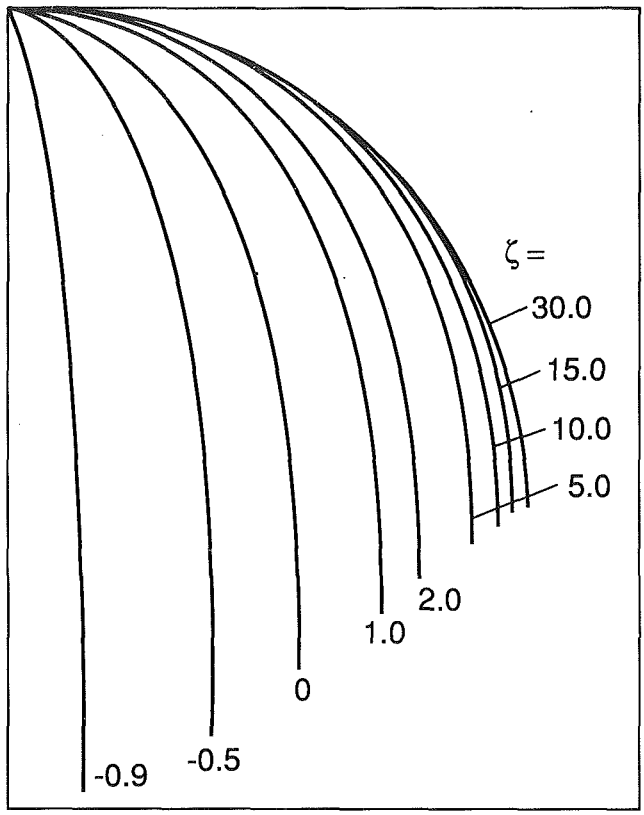

Fig. 2 Family of Adamek liquid-vapor interface profiles

Nomenclature

B = property group = $\nu k\, \Delta T_s/(\sigma\, \lambda)$, m
Bo = Bond number = $-\Delta\rho\, g/(dP/ds)$
D_o = tube diameter over fins, m
e = fin height of convex profile, m
E = total fin height = $e + L_s$, m
fpm = fins per meter, 1/m
g = gravitational acceleration = 9.806 m/s^2
h = heat transfer coefficient, W/(m^2 K)
k = thermal conductivity of condensate, W/(m K)
L_s = depth of drainage channel, m
P = pressure, Pa
r = radius of curvature of fin surface, m
r_o = radius of fin tip, m
S_m = total fin arc length, m
s = coordinate along liquid-vapor interface arc length, m
s' = fin arc length coordinate, m
T_s = saturation temperature of vapor, K
T_w = temperature of fin wall, K
t_b = fin thickness at base, m
t_t = fin thickness at tip, m
x = half fin thickness coordinate, m
y = fin height coordinate, m
z = coordinate perpendicular to x-y plane, m
Z = shape factor in new curvature equation
ΔT_s = $T_s - T_w$, K
$\Delta\rho$ = $\rho - \rho_v$, kg/m^3
δ = condensate film thickness, m
ζ = parameter in Adamek's curvature equation
θ = coordinate of fin, rad
Θ_m = maximum angle through which S_m turns, rad
κ = curvature of fin surface, 1/m
λ = latent heat of condensate, kJ/kg
μ = dynamic viscosity of condensate, kg/(m s)
ν = kinematic viscosity of condensate, m^2/s
ρ = density of condensate, kg/m^3
ρ_v = density of vapor, kg/m^3
σ = surface tension of condensate, N/m

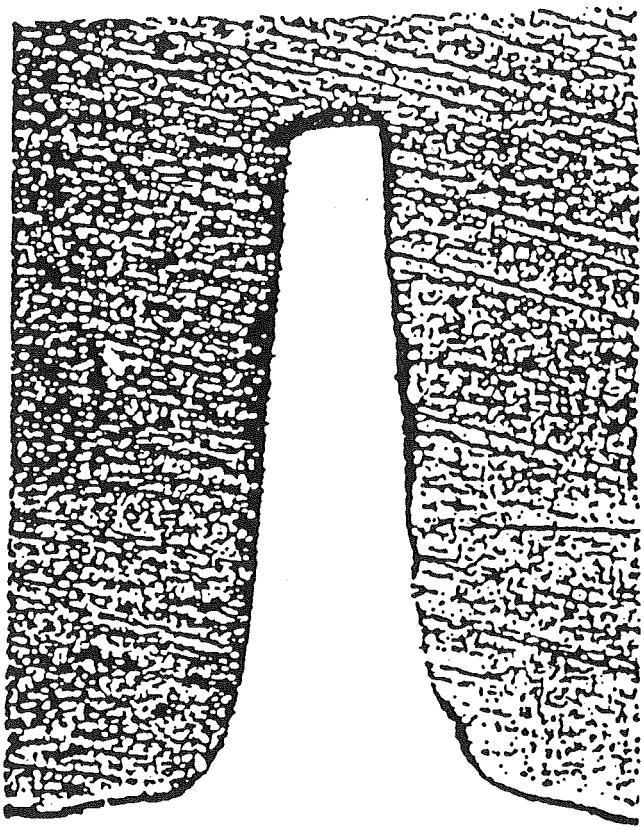

Fig. 3 Cross section of commercial 748-fpm integral fin

The new profiles described here allow specification of r_o and t_b independently of e and Θ_m. Analytical results are presented to show the effect of the several geometric parameters on condensation of R-11. These results are useful to determine the effect of manufacturing tolerances on condensation performance. One may use the analysis to select fin profiles that are manufacturable, and that provide high condensatoin performance. Guidance is provided for selection of the preferred geometric parameters.

Profile Definition

The new profiles, like the profiles of Gregorig and Adamek, are of the liquid–vapor interface. Since the condensate film is thin, the shape of the fin metal closely follows that of the liquid–vapor interface. Therefore, general observations concerning the liquid–vapor interface profile are valid for the solid–liquid profile also.

The new profile describes the fin shape in terms of t_b, r_o, e, Θ_m, and a shape factor parameter Z. The width of the fin tip can be reduced by lowering the value of Z; see Fig. 4. The Z is analogous to the ζ of Adamek that causes a variation in the aspect ratio of the profile. The equation to represent the profile was chosen such that the radius of curvature decreases for increasing θ. A linear combination of an exponential and a linear variation with θ permits an infinite range of functional forms depending on the magnitude of the multiplying constants. The radius of curvature (r) of the new profile is defined by

$$r = C_1 + C_2 \exp(Z\theta) + C_3\theta \tag{6}$$

The constants C_1, C_2, C_3 are given by

$$C_1 = r_o - C_2 \tag{7}$$

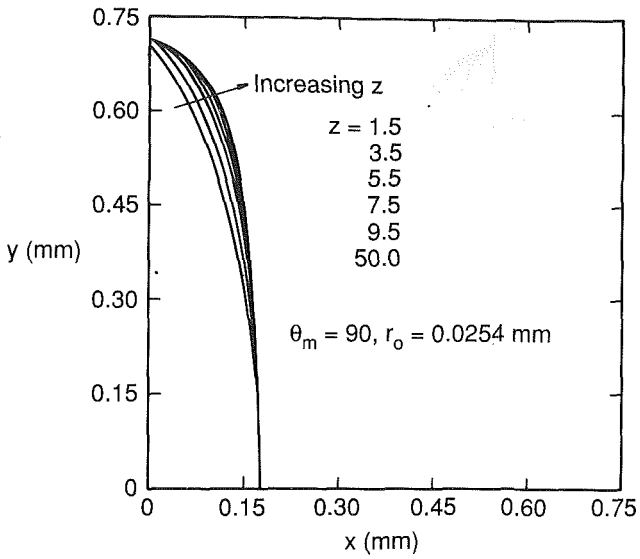

Fig. 4 Cross section of new profile for different values of Z

$$C_2 = \frac{0.5t_b(\sin\Theta_m - \Theta_m\cos\Theta_m) - e(\cos\Theta_m + \Theta_m\sin\Theta_m - 1)}{C_4 - (2(1-\cos\Theta_m) - \Theta_m\sin\Theta_m)} + \frac{r_o(\Theta_m\sin\Theta_m - 2(1-\cos\Theta_m))}{C_4 - (2(1-\cos\Theta_m) - \Theta_m\sin\Theta_m)} \tag{8}$$

$$C_3 = \frac{0.5t_b - C_1\sin\Theta_m - C_2\, Z\exp(Z\Theta_m)\cos\Theta_m/(Z^2+1)}{\cos\Theta_m + \Theta_m\sin\Theta_m - 1} - \frac{C_2(\exp(Z\Theta_m)\sin\Theta_m - Z)/(Z^2+1)}{\cos\Theta_m + \Theta_m\sin\Theta_m - 1} \tag{9}$$

$$C_4 = (\exp(Z\Theta_m)(1-\cos\Theta_m + Z(\sin\Theta_m - \Theta_m)) + (Z\Theta_m - 1)\cos\Theta_m - (Z+\Theta_m)\sin\Theta_m + 1)/(Z^2+1) \tag{10}$$

The constants defined by equations (7)–(9) are obtained by applying the following boundary conditions to equation (6):

$$r = r_o \text{ at } \theta = 0 \tag{11}$$

$$t_b = 2\int_0^{\pi/2} r\cos\theta\, d\theta \tag{12}$$

$$e = \int_0^{\pi/2} r\sin\theta\, d\theta \tag{13}$$

The procedure to solve for the radius of curvature (r) of the new profile is outlined in the following. First, select e, t_b, Θ_m, r_o, and Z. Then evaluate C_4 given by equation (10) and substitute C_4 into equation (8) and solve for C_2. Next use C_2 to solve equation (7) for C_1. The constants C_1 and C_2 can now be used to solve for the remaining constant C_3.

Physically, it is convenient to define the fin in terms of x and y coordinates, where the y coordinate measures the fin height and the x coordinate measures half the fin thickness. Figure 4 shows a plot of six different fin cross sections plotted on x-y coordinates. The origin is at the center of the base of the fin. Equation (6) can be represented in rectangular coordinates (x, y) by integrating the x and y components of r, as done in equation (12) and equation (13). For example, the x coordinate can be obtained by changing the upper limit of integration of equation (12) from $\pi/2$ to θ, obtaining

$$x = \frac{C_2(Z\exp(Z\theta)\cos\theta + \exp(Z\theta)\sin\theta - Z)}{Z^2+1} + C_1\sin\theta + C_3(\cos\theta + \theta\sin\theta - 1) \tag{14}$$

The y coordinate can be obtained similarly by making the same

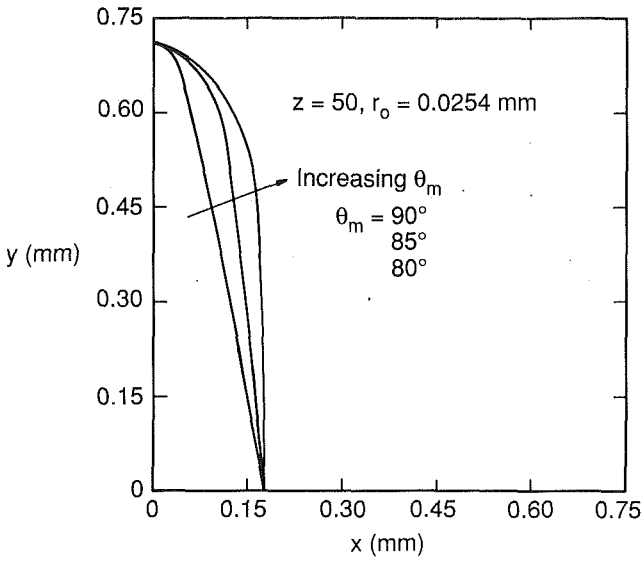

Fig. 5 Cross section of new profile for different values of Θ_m

change to the upper limit of integration of equation (13). The result is

$$y = e - \frac{C_2(Z\exp(Z\theta)\ \sin\theta - \exp(Z\theta)\cos\theta + 1)}{Z^2+1} - C_1(1-\cos\theta) - C_3(\sin\theta - \theta\cos\theta) \quad (15)$$

The above procedure was used to evaluate the constants C_1 through C_4 along with equation (14) and equation (15) to determine the effect of Z and θ_m on the fin shape. Figure 4 shows the shape of the new profile for $t_b = e/2$, $r_o = 0.0254$ mm, and $\Theta_m = 90$ deg for various values of Z. The profile is shown to have wider fin tips for larger values of Z. Figure 5 shows the profile for $t_b = e/2$, $r_o = 0.0254$ mm, and $\Theta_m = 80$, 85, and 90 deg. Notice that a larger portion of the fin side is flat for the smaller Θ_m's.

Since the fin profile is a continuous function, one may proceed to develop an analytical solution for the condensation heat transfer coefficient (h), just as Adamek (1981) and Gregorig (1954) have done for their profiles. The key assumptions used to obtain equation (16) are: (1) laminar condensate flow; (2) surface tension in the s direction is the only driving force; (3) zero interfacial, vapor shear; and (4) constant fin temperature. The assumption that gravity forces are negligible compared to surface-tension forces can be checked by following the procedure given in the "Recommended Design Practice" section of this paper.

The film thickness of the new profile can be obtained by substituting the gradient of equation (6) with respect to θ ($dr/d\theta$) into the following:

$$\delta^4 = 4B\left[\frac{dr}{d\theta}\right]^{-4/3} r^4 \int_0^\theta \left[\frac{dr}{d\theta}\right]^{1/3} d\theta \quad (16)$$

Direct analytical integration of equation (16) proved difficult, so it was solved numerically. The discrete values of δ were used to calculate the average heat transfer coefficient from $h = k/[\int 1/\delta\ ds]/S_m$.

Kedzierski and Webb (1987) have experimentally verified the theories of Gregorig (1954) and Adamek (1981). Equation (16) was the basis of Gregorig's and Adamek's analyses. Therefore, a new theory with the curvature equation given here (equation (6)), substituted into equation (16), also is expected to predict the actual heat transfer. Consequently, no experimental data are given in this paper.

Table 1 Dimensions of fins on commercially available integral fin tubes with D_o = 19.0 mm

Fins/m	748	1024	1378
Fin height, e (mm)	1.53	1.53	0.89
Fin thickness at tip, t_t (mm)	0.20	0.20	0.20
Fin thickness at base, t_b (mm)	0.42	0.52	0.29
Aspect ratio, e/t_b	3.6	2.9	3.1

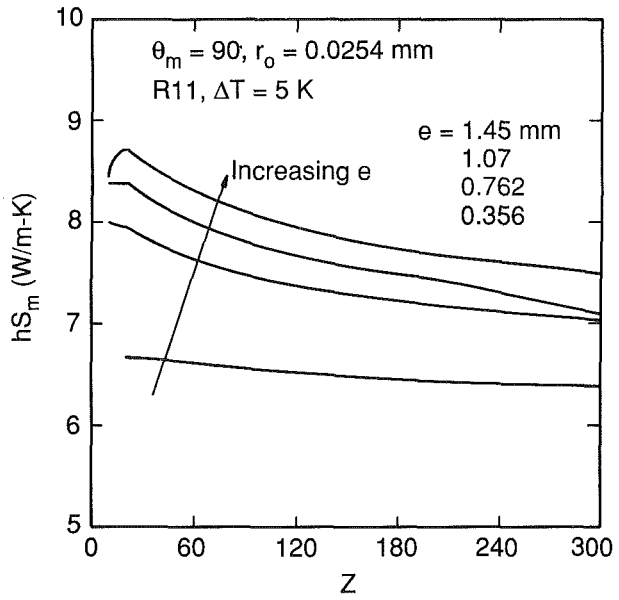

Fig. 6 Influence of Z on R-11 condensation at ΔT_s = 5 K

Condensation Performance of the New Profiles

R-11 condensation at 40°C with ΔT_s = 5 K was selected for illustration of the condensation performance of the new profiles. Four fins with the same t_b (t_b = 0.356 mm) but different fin heights (e = 0.356 mm, 0.762 mm, 1.067 mm, and 1.45 mm) were analyzed. These dimensions encompass the dimensional range of the commercial fin dimensions given in Table 1. The fin heights chosen are slightly lower than those of Table 1 to permit the addition of a 0.13-mm drainage channel, which makes the total fin height (E) compatible with those of Table 1. Thus, the total fin height is $e + L_s \equiv E$, as shown in Fig. 1. Heat transfer calculations for the above fins without drainage channels were done with variations on Z, r_o, and Θ_m to determine which parameters have the greatest influence on the heat transfer.

Figure 6 is a graph of the average overall heat conductance of the fin per unit fin length (hS_m) versus the shape factor (Z) for r_o = 0.0254 mm and Θ_m = 90 deg. Figure 6 demonstrates that the heat transfer is relatively insensitive to a wide range of Z. Recall from Fig. 4 that the shape factor represents the wideness of the fin tip. These results are encouraging since they demonstrate that for a given aspect ratio (e/t_b) a moderate deviation of the fin-tip shape will have little effect on the heat transfer of the fin. Thus, manufacturing tolerances associated with the shaping of the fin tip would tend to have a small effect on the heat transfer.

Figure 7 is a plot of hS_m versus the maximum angle through which the arc length turns (Θ_m) for r_o = 0.0254 mm and Z = 100. In general, Θ_m = 90 deg gives the highest heat transfer for all fin heights (aspect ratios). The Θ_m = 90 deg represents the maximum potential for the surface-tension pressure gradient for a given fin height. Angles less than 90 deg fail to use all of the available drainage force (curvature change) and consequently exhibit reduced heat transfer ability. For example, the hS_m of the e = 1.45 mm fin is reduced by 4 percent for

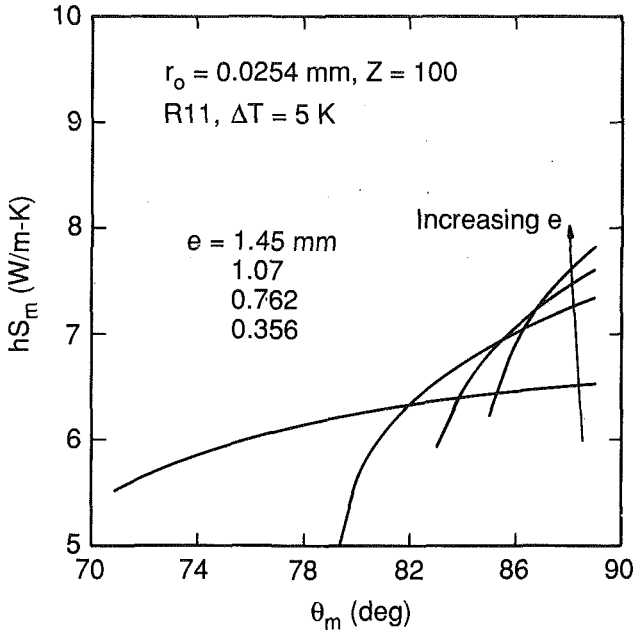

Fig. 7 Influence of Θ_m on R-11 condensation at ΔT_s = 5 K

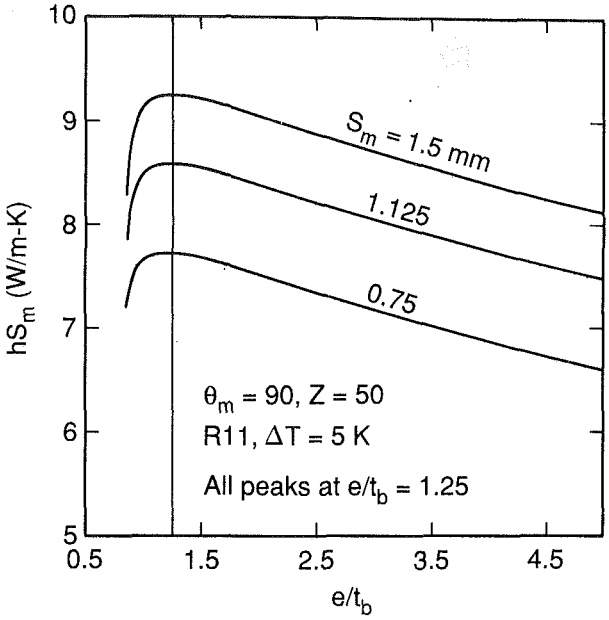

Fig. 9 Influence of aspect ratio and S_m on overall conductance

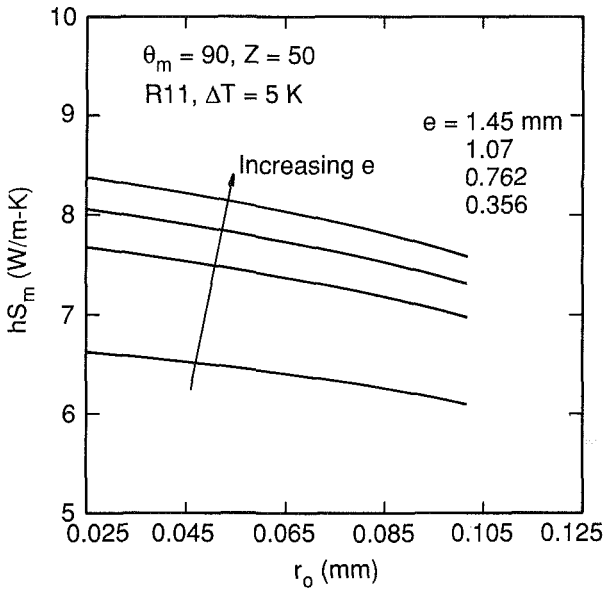

Fig. 8 Influence of r_o on R-11 condensation at ΔT_s = 5 K

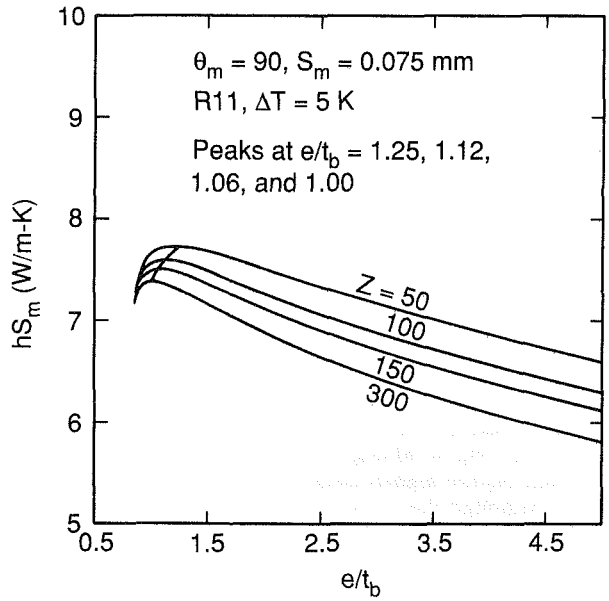

Fig. 10 Influence of aspect ratio and Z on overall conductance

each degree less than 90 deg. Also note that the heat transfer of the e = 0.762 mm fin for Θ_m = 79 deg is 37 percent less than that for Θ_m = 90 deg. Figure 7 demonstrates that the degradation of hS_m due to values of Θ_m less than 90 deg can be significant. Thus, the performance of the integral fin shown in Fig. 3 can be improved by increasing its Θ_m from 85 to 90 deg.

Figure 8 is a plot of hS_m versus the fin-tip radius (r_o) for Θ_m = 90 deg and Z = 50. Surprisingly, a 100 percent increase in r_o has a negligible effect on the heat transfer. As expected, the hS_m is larger for the smaller r_o, since this contributes to a higher average curvature for the fin. However, the above seems to support the observation that the fin-tip shape has a marginal effect on the heat transfer since r_o contributes to the shape of the fin tip.

Figure 9 is a plot of hS_m versus aspect ratio for the new fin geometry for R-11 with ΔT_s = 5 K, Z = 50, and different values of S_m. Figure 9 shows that the fins with larger S_m have higher heat transfer rates. There is a trade-off between increased surface area (S_m) and decrease in the magnitude of the average heat transfer coefficient (h) for higher fin heights. The reduction of h is due to a decrease in the surface-tension drainage force, which may become less than the gravity force if the fin height is too large. The hS_m rapidly decays for increasing e once the gravity force becomes dominant over surface tension. Guidance is given in a later section of this paper on how to determine the optimum value of e. Figure 9 also shows that the maximum hS_m for Z = 50 is at e/t_b = 1.25. The optimum aspect ratio is shown to be independent of S_m for fins of the same Z. The hS_m is shown to decrease by approximately 14 percent when the e/t_b is increased from 1.25 to 5.

Figure 10 illustrates the effect of e/t_b and Z on hS_m for a condensing length of 0.75 mm. The figure shows that for a given aspect ratio, fins with narrower fin tips (smaller Z) have larger hS_m values. For example, approximately a 10 percent

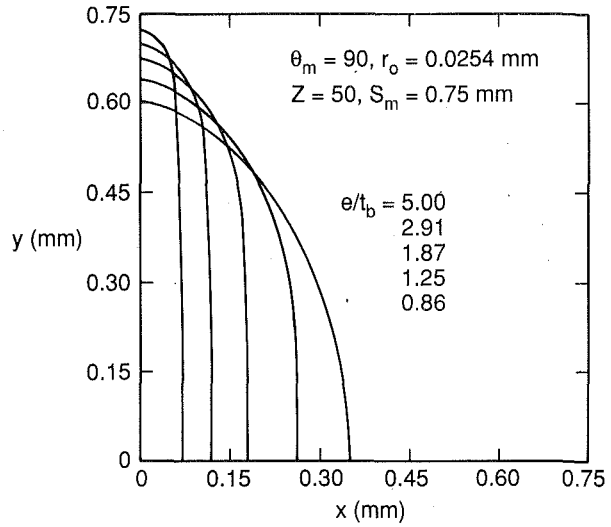

Fig. 11 Cross sections of new profile for different aspect ratios

increase in hS_m is achieved for a reduction of Z from 300 to 50. Consequently, the heat transfer of high-aspect-ratio ($e/t_b > 2$) fins can be increased slightly by reducing the width of the fin tip. Figure 10 also shows that for a given Z, the hS_m becomes smaller with increasing e/t_b for values of e/t_b greater than the optimum value. For example, the hS_m is shown to decrease by approximately 22 percent when e/t_b is increased from the optimum value to $e/t_b = 5$. The value of e/t_b that gives the optimum hS_m is larger for decreasing values of Z. For example, the optimum values of e/t_b for $Z = 50$, 100, 150, and 300 are 1.25, 1.12, 1.06, and 1.0, respectively. The Adamek profile $\zeta = -0.5$, which corresponds to $e/t_b = 2$, gives the optimum hS_m for his family of fins. The fin tip of the Adamek $\zeta = -0.5$ profile is narrower than the $Z = 50$ (narrowest Z). This is consistent with the above generalizations since the optimum e/t_b (2) for the $\zeta = -0.5$ profile (narrower fin tip) is larger than the optimum e/t_b (1.25) for the $Z = 50$ profile (wider fin tip).

Figure 11 shows the half cross section of the fins described by the uppermost curve of Fig. 10, i.e., for $Z = 50$, $r_o = 0.0254$ mm, $\Theta_m = 90$ deg and $S_m = 0.75$ mm. Notice that for the same S_m the higher-aspect-ratio fins contain less fin material. Although the fin with $e/t_b = 1.25$ gives approximately 15 percent higher heat transfer than the $e/t_b = 5.0$ fin for the same arc length, it does so at the expense of three times the fin material. Also note that the t_b of the $e/t_b = 5.0$ fin is less than half that of the $e/t_b = 1.25$ fin. Consequently, at least twice as many of the high-aspect-ratio fins can be used per unit length on a tube than the lower aspect ratio fin. Although $e/t_b = 1.25$ gives the optimum h for a given S_m, a fin with a higher aspect ratio is more economical in terms of fin material and more energy efficient in terms of use with finned tubes.

It is important that the designer know the limitations of the fin parameters Θ_m, r_o, and Z. The maximum value of Θ_m is 90 deg for the fin shape given by equation (6). The smallest value of Θ_m is set by the aspect ratio of the fin, i.e., Θ_m (min) = arctan ($2e/t_b$). The smallest value of Θ_m for a given aspect ratio corresponds to a fin of triangular shape. In order to have a fin of a particular e/t_b with a Θ_m smaller than Θ_m (min), the fin must be concave instead of convex. The largest r_o attempted in this analysis was 0.035 mm. The maximum r_o is directly proportional to S_m. For example, the r_o for a fin of constant radius is $r_o = S_m/\Theta_m$. Consider this to be the upper limit of r_o. However, the maximum r_o for all fins will be less than S_m/θ_m since the radius of curvature decreases as the arc turns through Θ_m. There were certain values of Z that caused the values of the exponential terms encountered in equation (6) to be outside the numerical range permitted by Fortran. Lower limits of Z were found to be around -0.01. Upper limits of Z were found to be around 500. The limitation of Z depends on the aspect ratio of the fin. For example, larger lower limits on Z are associated with larger aspect ratios. Hence, all fins will not necessarily fall within the above limits of Z.

Table 2 Comparison of hS_m on three profile types

Profile	Parameter	e (mm)	t_b (mm)	hS_m (W/m-s)
Gregorig	$\zeta = 2$	1.45	1.88	8.04
Gregorig	$\zeta = 2$	0.28	0.356	5.31
Adamek	$\zeta = -0.78$	1.45	0.356	9.45
New profile ($r_o = 0.025$ mm)	$Z = 10$	1.45	0.356	8.45

Comparison With Adamek and Gregorig Profiles

Table 2 compares the average h over the arc length (S_m) for $S_m = 1.485$ mm and $\Theta_m = 90$ deg for all profiles. For a fin base thickness of $t_b = 0.356$ mm, the value of hS_m of the new profile is within 10 percent of the Adamek profile, which has a zero tip radius. The $r_o = 0$ profile Adamek is not practically attainable. Consequently, the calculated heat transfer coefficient for the Adamek profile is optimistically higher than what can be realistically achieved. However, the authors believe that if the Adamek profile had $r_o \neq 0$, the calculated heat transfer would be only 2–4 percent lower than that for $r_o = 0$. Thus, the actual difference between the heat transfer performance of the new profile and the Adamek profile for the same aspect ratio would be somewhat smaller than the calculated 10 percent.

Table 2 also shows that the $t_b = 0.356$ mm Gregorig profile has a small hS_m, because of its smaller fin height. If the fin height of the Gregorig fin is set at 1.45 mm, hS_m will increase, but the base thickness will be 1.88 mm. A 1.88-mm fin thickness will waste a considerable amount of fin material, and limit the fin density to considerably smaller values than for the $t_b = 0.356$ mm fins. The above discussion illustrates the disadvantage associated with the Gregorig fin by not being able to choose e and t_b independently.

Recommended Design Practice

The sensitivity investigation presented here can be used to provide some general guidelines for good fin design. It can be seen that fins with high aspect ratios result in high hS_m and large fpm, which implies high heat transfer per tube. Fins with $\Theta_m = 90$ deg make better use of the surface-tension enhancement that fins with $\Theta_m < 90$ deg. Therefore, it can be easily decided that the fin should always be designed for $\Theta_m = 90$ deg. But how large can e be? And how small can t_b be?

Care must be taken to ensure that e is not so large that the surface-tension pressure gradient has dissipated over a significant portion of the fin. The Bond number (Bo), which is the ratio of gravity forces to surface-tension forces, can be used to test the strength of the surface-tension pressure gradient. If the surface-tension forces are dominant over gravity forces, then the condensate drainage is determined by surface-tension. The strength of the surface-tension pressure gradient weakens as the film approaches the base of the fin. The Bond number at the base of the fin can be approximated by

$$\text{Bo} = \frac{\Delta\rho\, g\, e^2}{\sigma\, \Theta_m} \tag{17}$$

A Bo of 1 implies that surface-tension forces are equal to the gravity forces at the end of the fin and that surface-tension forces are greater than gravity forces for the remainder of the fin. Equation (17) should always be used to check first whether surface-tension forces are truly dominant (Bo < 1) over gravity

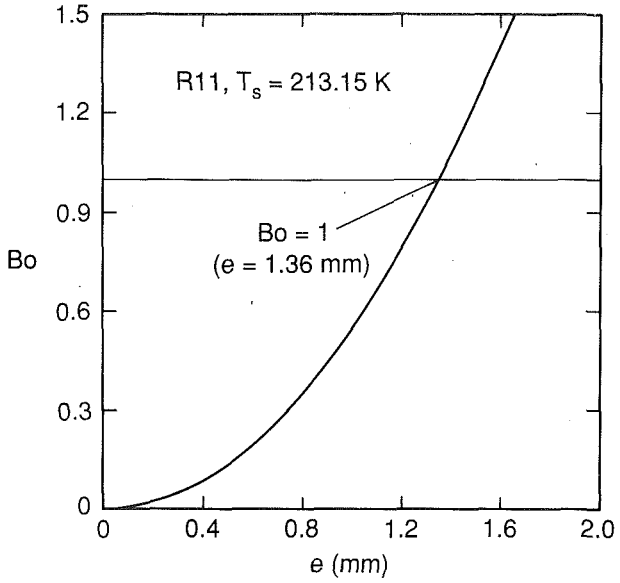

Fig. 12 Bond number as a function of e for R-11 at T_s = 213.15 K

forces before performing an analysis that assumes so. Notice that equation (17) predicts that small fin heights and large Θ_m give strong pressure gradients.

In order to achieve a high hS_m and maintain surface-tension drainage, the authors recommend that fin heights be designed to achieve Bo = 1. Figure 12 is a plot of equation (17) (Bo) for R-11 at T_s = 213.15 K versus e. The Bo becomes 1 at e = 1.36 mm. Consequently, a good fin height design is e = 1.36 mm for condensation of R-11 at T_s = 213.75 K. The Bo = 1 for this fin ensures that surface-tension forces are larger than gravity forces for the entire fin (with the exception of the very end of the fin). The advantage of a high fin height is in that a large hS_m is achieved. Fins larger than 1.36 mm will exhibit surface-tension drainage along the entire fin for higher surface-tension fluids, such as water.

Two other factors to consider when designing the fin height are tube-side pressure drop, and the condensation row effect. Small fin heights are beneficial for applications where low tube-side pressure drop is important. For a constraint on the overall diameter (D_o) of the tube, a large internal diameter is possible if the heights of the fins are small. However, Webb and Murawski (1988) have shown that high fin heights can benefit heat transfer by reducing the row effect caused by condensate inundation.

Two factors to consider when designing the fin thickness are condensate retention and the number of fins per meter. When condensed fluid is retained in the interfin spaces of the lower portion of a horizontal finned tube, the phenomenon is known as condensate retention. The condensed fluid acts as an insulating blanket on the tube. Consequently, severe degradation of heat transfer performance can occur with an increase in condensate retention. For a fixed fpm, one can reduce the condensate retention by reducing the fin thickness. Rudy et al. (1984) have investigated the trade-offs between increased heat transfer for larger fpm and the decrease in heat transfer for increased condensate retention for larger fpm. They have shown that an optimum fpm exists, for each fluid, which is a compromise between the two effects. In general, the optimum fpm is smaller for the higher surface-tension fluids. Also, the fin efficiency can be increased by reducing the fin thickness. Thus, a small t_b is one factor that can lead to finned tubes with high heat tranfser performance. The lower limit of t_b is dictated by the manufacturing process and the desired structural integrity of the fins.

Rudy et al. (1984) used the model of Webb et al. (1985) to predict the relationship between h and fpm for process-industry fluids. The Webb model uses the Adamek fin profiles in their prediction. An iteration for the Adamek fin with the proper aspect ratio is required in the calculation. The iterative procedure will be avoided if the new profiles presented here are used instead of the Adamek profiles in the analysis.

Conclusions

This work has defined fin profile shapes, which are practical for commercial manufacture. The designer may independently specify the fin-tip radius, the fin height, and the fin base thickness. The performance of the new profile with r_o = 0.025 mm is competitive with those of Gregorig and Adamek, for the same fin height. A sensitivity analysis of the parameters Z, r_o, S_m, and Θ_m on the performance of the new profile was presented. Fins with large S_m and Θ_m = 90 deg have large hS_m values. The hS_m decreases for decreasing values of Θ_m, and Θ_m = 90 deg always gives the optimum hS_m. For example, the hS_m of a fin with e = 1.45 mm is reduced by 4 percent for each degree less than 90 deg. The analysis shows that hS_m is moderately sensitive to Z (tip width). Fins with narrower fin tips have marginally higher hS_m values. For example, the heat transfer of high-aspect-ratio ($e/t_b > 2$) fins can be increased approximately 10 percent by reducing Z from 300 to 50. Also, the analysis has shown that a 100 percent increase in r_o has a negligible effect on hS_m. Consequently, the shape of the fin tip (r_o and tip wideness) does not need to be machined precisely. General design guidelines for selection of the geometric parameters are also given. The fin height and the fin thickness are more crucial design parameters than the shape of the fin. The authors suggest that fin heights be designed for Bo = 1 to ensure surface-tension drainage and large hS_m.

References

Adamek, T., 1981, "Bestimmung der Kondensationgroessen auf feingewellten Oberflaechen zur Auslegung optimaler Wandprofile," *Waerme- und Stoffuebertragung*, Vol. 15, pp. 255–270.

Adamek, T., and Webb, R., 1989, "Prediction of Film Condensation on Horizontal Integral-Fin Tubes," submitted to the *Int. J. Heat and Mass Transfer*.

Gregorig, R., 1954, "Hautkondensation an feingewellten Oberflaechen bei Beruecksichtigung der Oberflaechenspannunger," *Zeitschrift fuer angewandte Mathematik und Physik*, Vol. V, pp. 36–49.

Kedzierski, M. A., and Webb, R. L., 1987, "Experimental Measurements of Condensation on Vertical Plates With Enhanced Fins," *Boiling and Condensation in Heat Transfer Equipment*, ASME HTD-Vol. 85, pp. 87–95.

Rudy, T. M., Kedzierski, M. A., and Webb, R. L., 1984, "Investigation of Integral-Fin-Type Condenser Tubes for Process Industry Applications," *First U.K. Natl. Heat Transfer Conf.*, Vol. 86, pp. 633–647.

Webb, R. L., Rudy, T. M., and Kedzierski, M. A., 1985, "Prediction of the Condensation Coefficient on Horizontal Integral-Fin Tubes," ASME JOURNAL OF HEAT TRANSFER, Vol. 107, pp. 369–376.

Webb, R. L., and Murawski, C. G., 1988, "The Row Effect for R-11 Condensation on Enhanced Tubes," The Pennsylvania State University, unpublished.

Zener, C., and Lavi, A., 1974, "Drainage Systems for Condensation," ASME *Journal of Engineering for Power*, Vol. 96, pp. 209–215.

An Instrument for Local Radiative Heat Transfer Measurement Around a Horizontal Tube Immersed in a Fluidized Bed

N. Alavizadeh[1]
Research Assistant.

R. L. Adams[1]
Associate Professor.

J. R. Welty
Professor.

A. Goshayeshi[2]
Research Assistant.

Department of Mechanical Engineering,
Oregon State University,
Corvallis, OR 97331

An instrument for the measurement of the radiative component of total heat transfer in a high-temperature gas fluidized bed is described. The main objective of this paper is to emphasize the design, instrumentation, and calibration of this device. The results are presented and discussed elsewhere (Alavizadeh, 1985; Alavizadeh et al., 1985). The design makes use of a silicon window to transmit the radiative heat flux to a thermopile-type heat flow detector located at the base of a cavity. The window material thermal conductivity is sufficiently large to prevent conduction errors due to the convective component of total heat transfer. Also, its transmission and mechanical hardness are well suited for the fluid bed environment. The device has been calibrated using a blackbody source both before and after exposure to a fluidized bed, indicating the effect of the abrasive bed environment on performance. The instrument has been used to measure local radiative heat transfer around a horizontal tube. Typical results for a particle size of 2.14 mm and a bed temperature of 1050 K are presented and discussed to illustrate instrument performance.

Introduction

In recent years there has been considerable interest in the utilization of fluidized bed combustion of coal for power generation. A fundamental knowledge of heat transfer in high-temperature fluidized beds is essential for proper design and optimization of such a combustor. However, few data regarding the radiative component of heat transfer are reported in the literature. Published data provide mixed assessments of the relative importance of the radiative component of total heat transfer. The present work is an attempt to obtain a direct measurement of local radiative heat transfer around an immersed tube in a fluidized bed by using a carefully designed instrumentation.

There have been limited attempts to measure the radiative component of heat transfer in a gas-fluidized bed. A discussion of different probes employed by other investigators in the measurement of radiative heat transfer in a fluidized bed is appropriate here. Baskakov et al. (1973) measured spatial average radiative heat transfer indirectly in a fluidized bed by recording the transient temperature response of two spheres of low Biot number with different surface emissivities (silver-plated and oxidized). The bed consisted of chamotte particles with mean particle diameters of 0.35, 0.65, and 1.35 mm. The results suggest a radiative heat transfer contribution of about 9 percent for the largest particle size at a bed temperature of 1123 K and wall temperature of 443 K.

Using a similar approach, Yoshida et al. (1974) compared the total heat transfer to two oxidized and polished vertical stainless steel pipes of 1.3 cm o.d. in a bed of fluidized solids of 0.18 mm mean diameter and temperature up to 1273 K. Total heat transfer was calculated indirectly from the heat transfer to the coolant. They concluded that the radiative contribution was insignificant.

Basu (1978) used a 6.5 mm copper tube and a coaxial silica tube with a gap to reduce heat conduction to the copper tube as a result of bed convective heat transfer. He then calculated the spatial average radiation by measuring inlet and outlet water temperature used as a coolant. A correction was made for the conduction error. The bed material in Basu's test was sand of 0.325–0.5 mm diameter. He found the radiative contribution to be about 10 percent of the total heat transfer in a bed at 1173 K.

Vadivel and Vedamurthy (1980) used a "glass quartz" window mounted on top of a cavity within a tube to filter convective heat transfer and to transmit radiation. Transmitted radiation was then detected by a thermistor located at the base of the cavity. The bed temperature was 1023 K and particles up to 6 mm were used. Quartz has low thermal conductivity, which can cause a large conduction errror due to bed convective heat transfer. In the report it is not clear that compensation has been made for this error in the radiative heat transfer calculations. Also, quartz is opaque to incident radiation at wavelengths larger than 5 μm (Touloukian, 1970; Adolf Meller Co., 1981) while the measurements could involve energy spanning over a wide range of wavelengths. They reported that spatial average radiation measured at 30 deg steps around a horizontal tube contributes about 35 percent to the total heat transfer. Their probe is comparable to the present probe in that it is capable of making local measurements around a horizontal tube.

In a study by Ozkaynak et al. (1983), a two-layer flat window of zinc selenide was employed. Although their probe and the one used in the present study have different designs, the authors have appropriately discussed some of the issues involved in the design of the instrumentation. However, their probe is not capable of making local radiative heat transfer measurements around a horizontal tube since it is mounted on a circular flat surface on one end of a brass tube. In addition, it requires circulating air between the windows to minimize the conduction error produced as a result of the bed convective heat transfer. The radiative component was determined to be about 30 percent of the total heat transfer for a mean particle diameter of 1.03 mm and a bed temperature of 1053 K.

[1]Present address: Tektronix Inc, GPID Div., Wilsonville, OR.
[2]Present address: Admiral, Galesburg, IL.

Contributed by the Heat Transfer Division for publication in the JOURNAL OF HEAT TRANSFER. Manuscript received by the Heat Transfer Division March 31, 1988. Keywords: Measurement Techniques, Packed and Fluidized Beds, Radiation.

Zhang and Xie (1985) obtained radiative heat transfer data in a fluidized bed combustion boiler with particles up to 8 mm in diameter and bed temperature between 1073 K and 1313 K. The probe consisted of a Gardon gage (Gardon, 1953) type heat flow sensor with a sheet of monocrystalline silicon placed in front of the sensor, and mounted on a flat end of a tube. The Gardon gage is best suited for an environment where the incident radiative heat flux is uniform over its sensing area. The probe was calibrated in a furnace before and after use in the fluidized bed combustor. They reported the radiative heat transfer to be 20 and 5 percent of the total heat transfer in the main and fine ash bed, respectively, at 1123 K bed temperature.

A round quartz window and a heat flux meter mounted on one end of a 50.8 mm o.d. tube and transversely inserted into a 66.3 mm o.d. pipe were utilized by Mathur and Saxena (1987) to measure radiation in a fluidized bed with 0.56 mm and 0.75 mm particles. In their analysis, theoretical calculations related the heat flux meter reading to radiation at the probe surface by accounting for convective leak and transmissivity of quartz window. They found the radiation to be 12 percent for 0.75 mm particles at 1175 K and about 10 percent for 0.56 mm particles at 985 K.

The present study is an attempt to address some of the issues not adequately discussed in the investigations cited. They include the analysis of radiative heat flux instrumentation probe to assess its performance under the test conditions, tube wall emissivity in determining the radiative heat transfer contribution, and more details regarding the calibration technique.

Instrumentation

Design. Figure 1 illustrates the basic instrument design concept. An infrared transparent window mounted on top of a cavity within a tube transmits the radiative component of the total heat transfer. A heat flow detector located at the base of the cavity detects the transmitted radiation. The following considerations were made in the design of the instrument:

(A) Conductive heat transfer, due to fluid bed convective heat transfer, from the window to heat flow detector should be minimized and instead directed to the sides where the window contacts the tube. This can be achieved without cooling by selecting a window material with high thermal conductivity.

(B) The window should be capable of transmitting radiation in the wavelength range at which maximum emissive power occurs. This range is $2.7 < \lambda < 8.7$ μm for the conditions of operation of the high temperature fluidized bed used in the experiment when behaving similar to a blackbody source. In short, the window should transmit over the widest wavelength range possible.

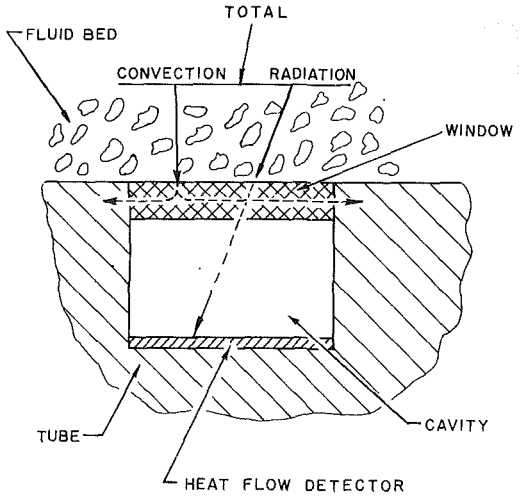

Fig. 1 Schematic of the basic instrumentation design concept

(C) Constant particle motion could cause abrasive damage to the window. This implies that the window material should be mechanically hard to withstand the hostile bed environment.

(D) The nonuniform temperature distribution of the particles, caused by cooling due to contact with the window, will generate a nonuniform heat flux distribution.

(E) The heat flow detector should absorb the largest possible fraction of the radiation transmitted through the window.

(F) The instrumentation should not disturb the flow of gas and particles around the tube.

Analysis. The instrumentation design parameters and performance were established by an analysis that included the following:

Nonuniform Heat Flux. The probability of nonuniform heat flux in a fluidized bed seems to suggest the application of an averaging device such as a thermopile-type (thermocouples in series) heat flow detector formed by a thin low thermal conductivity film with a thermopile on each side. Since this detector measures an average temperature over its sensing area, the nonuniformity in heat flux will have far less effect on the measurement than in the case of a Gardon gage (Gardon, 1953). To assess the performance of this device, a steady-state conduction analysis was completed for a typical model as

Nomenclature

C = heat flow detector thickness
D_p = mean particle diameter
F_{k-j} = view factor, from k to j
$F_{\Delta\lambda}$ = fraction of total emissive power for wavelength interval $\Delta\lambda$
Gr = Grashof number $= \dfrac{gH^3\beta\Delta T}{\nu^2}$
g = acceleration of gravity
H = cavity height
h = heat transfer coefficient
K = thermal conductivity
L = cavity, window, and heat flow detector length
$\dot{q}''$ = heat flux
T = temperature
U_o = gas velocity
W = cavity, window, and heat flow detector width
β = coefficient of thermal expansion
δ = window thickness
δ_{kj} = Kronecker delta, 1 when $j=k$ and 0 when $j\neq k$
Δ = difference
ϵ = emissivity
θ = temperature difference
ν = kinematic viscosity
σ = Stefan-Boltzmann constant
τ = transmissivity

Subscripts and Superscripts

a = air
b = black wall
c = conduction heat transfer
d = heat flow detector
f = fluid bed
i = radiative energy incident
j, k = surface indices
o = radiosity (energy leaving)
r = radiative
s = sensing area of heat flow detector
u = tube wall
w = window

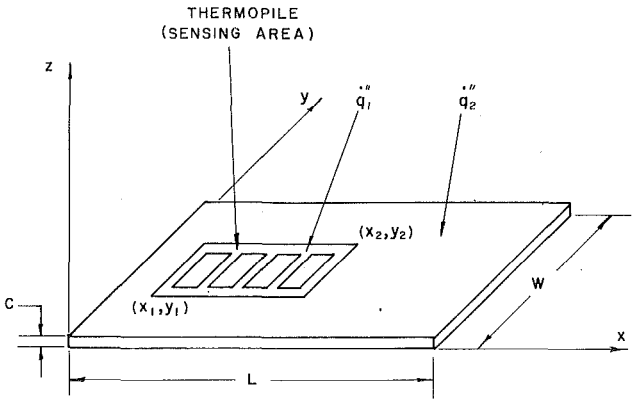

Fig. 2 Schematic of a thermopile-type heat flow detector

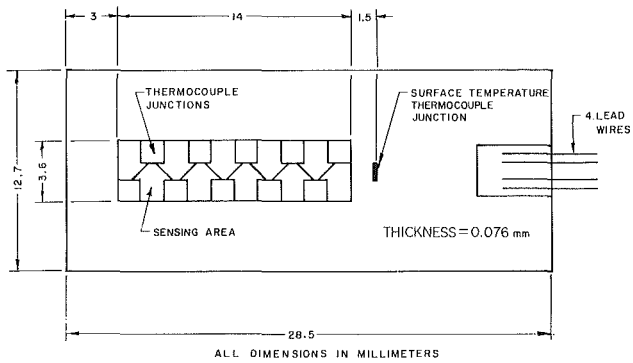

Fig. 3 Geometry of the selected heat flow detector

shown in Fig. 2. The steady temperature distribution within the detector is governed by (Arpaci, 1966)

$$\frac{\partial^2\theta_d}{\partial x^2}+\frac{\partial^2\theta_d}{\partial y^2}+\frac{\partial^2\theta_d}{\partial z^2}=0 \tag{1}$$

where $\theta_d = T_d - T_u$, and the boundary conditions are

$$\theta_d(0, y, z)=0$$

$$\theta_d(L, y, z)=0$$

$$\theta_d(x, 0, z)=0$$

$$\theta_d(x, W, z)=0$$

$$\theta_d(x, y, 0)=0$$

$$\dot{q}'' = -K_d \frac{\partial\theta_d}{\partial z}(x, y, C)=\dot{q}_1'' \qquad \text{sensing area}$$

$$=\dot{q}_2'' \qquad \text{rest of the area}$$

The heat flux detected by the sensing area was analytically calculated from

$$\dot{q}_s''=\frac{K_d}{C}\theta_s \tag{2}$$

where

$$\theta_s=\frac{1}{(x_2-x_1)(y_2-y_1)}\int_{x_1}^{x_2}\int_{y_1}^{y_2}\theta_d(x, y, C)dydx$$

Two cases were compared, one with a uniform heat flux distribution over the entire area of the detector ($\dot{q}_1''=\dot{q}_2''=\dot{q}''$), and the very unlikely case of a nonuniform heat flux distribution of $\dot{q}_1''=\dot{q}''$ and $\dot{q}_2''=0$. A difference of only about 2.5 percent in $\dot{q}_s''$(equation (2)) was calculated for the heat flow detector selected for the instrumentation and shown in Fig. 3.

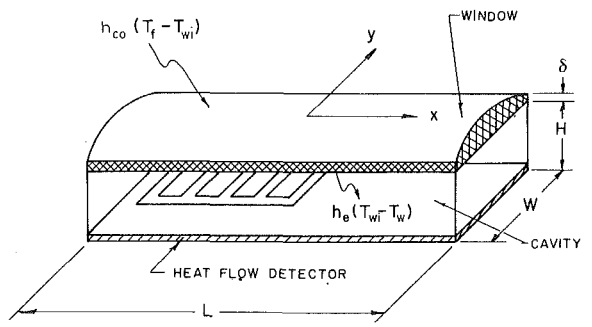

Fig. 4 Cavity with the window on top and the heat flow detector at the bottom

Conduction Error. Of particular concern in the instrumentation design was the error produced by transmission through conduction of the convective component of the total heat transfer to the heat flow detector. Figure 4 illustrates the window with the heat flow detector at the base of the cavity. A two-dimensional heat conduction analysis of the window will yield

$$\frac{\partial^2\theta_w}{\partial x^2}+\frac{\partial^2\theta_w}{\partial y^2}-\lambda^2\theta_w-\lambda^2 T_u+U=0 \tag{3}$$

where

$$\theta_w = T_w - T_u, \quad \lambda^2=\frac{h_f+h_e}{k_w\cdot\delta}, \quad U=\frac{h_f T_f+h_e T_u}{k_w\cdot\delta},$$

$$\text{and } h_e=\frac{K_a}{H}$$

with the boundary conditions

$$\frac{\partial\theta_w}{\partial x}(0, y)=0$$

$$\frac{\partial\theta_w}{\partial y}(x, 0)=0$$

$$\theta_w(L/2, y)=0$$

$$\theta_w(x, W/2)=0$$

The magnitude of conduction error is given by the average heat flux by conduction to the sensing area across the air-filled cavity

$$\dot{q}_{cs}''=\frac{1}{(x_2-x_1)(y_2-y_1)}\int_{x_1}^{x_2}\int_{y_1}^{y_2}h_e\theta_w(x, y)dydx \tag{4}$$

The radiative heat transfer to the sensing area ($\dot{q}_{rs}''$) was estimated by the net radiation method discussed by Siegel and Howell (1972) and spectral characteristics of the window, i.e.,

$$\sum_{j=1}^{N}\left(\frac{\delta_{kj}}{\epsilon_j}-F_{k-j}\frac{1-\epsilon_j}{\epsilon_j}\right)\dot{q}_j''=\sum_{j=1}^{N}(\delta_{kj}-F_{k-j})\sigma T_j^4 F_{\Delta\lambda} \tag{5}$$

The analysis was performed for the enclosure shown in Fig. 4. The radiosity of the window was approximated by

$$\dot{q}_{o,w}''=\tau_w\sigma T_f^4+(1-\tau_w)\dot{q}_{i,w}''$$

Comparison of $\dot{q}_{rs}''$ with the conductive heat transfer estimated according to equation (4), $\dot{q}_{cs}''$, gives an estimate of the relative error in radiative heat transfer measurement. This error is given in Table 1 for four different window materials.

Window Temperature. A substantial temperature difference could arise between a low thermally conducting win-

Table 1 Window material properties with the results of the instrumentation analysis

Window Materials	Transmissivity (waveband, μm)	Thermal conductivity at T_w, W/m K	Hardness (Knoop)	Conduction error, percent	T_w K	Gr
Silicon (Si)	0.50 (1.3–7.0) 0.35 (7.0–12.0)	117.0	1150	1	354	91
Sapphire (Al_2O_3)	0.84 (0.30–5.0)	35.0	1370	3	374	213
Quartz, crystal (SiO_2)	0.92 (0.30–2.2) 0.50 (2.2–3.6)	6.7	741	23	446	555
Quartz, fused (SiO_2)	0.91 (0.30–3.4) 0.40 (3.4–4.7)	1.7	461	28	589	961

dow and the radiation probe wall. The average window temperature can be calculated from

$$T_w = \frac{1}{W \cdot L} \int_{-L/2}^{+L/2} \int_{-W/2}^{+W/2} \theta_w(x, y) dy dx + T_u \qquad (6)$$

where θ_w is the solution of equation (3) and T_u is the probe wall temperature. In the absence of a direct window temperature measurement, care should be exercised in using an appropriate substitute for T_w when computing the radiative heat transfer coefficient, i.e.,

$$h_r = \frac{\dot{q}_r''}{(T_f - T_w)} \qquad (T_f \text{ is fluid bed temperature})$$

T_w as obtained from equation (6) is presented in Table 1 for a bronze tube at 345 K immersed in a bed with the largest total heat transfer coefficient expected in this study.

Natural convection within the cavity was conservatively approximated for a geometry consisting of two infinite plates at temperatures of T_w and T_u and separated by a distance H (Fig. 4). The Grashof number (Gr) was calculated and used to estimate the effect of natural convection. Table 1 shows Grashof numbers for different window materials.

Results. The analysis described above was completed for four window materials: silicon, sapphire, crystal quartz, and fused quartz. Table 1 shows transmissivity, thermal conductivity, and hardness for these materials. The results of the analysis are also shown in Table 1. Test data obtained by George (1981) for the fluid bed used in the present investigation were used to estimate the typical bed conditions at a tube wall temperature of about 345 K.

Of the materials considered, silicon is transparent over the widest waveband (1.3 μm to 12.0 μm). The conduction errors for silicon (1 percent) and sapphire (3 percent) are comparable. Note that this error is considerably greater for quartz. The average window temperature (T_w) is by far larger for crystal quartz when compared to that of silicon and sapphire. The Grashof number is sufficiently small (Gr < 1700) to prevent natural convection in the cavity for all the window materials considered. Based on the wide transmission waveband and small conduction error, silicon (Si) was selected as the window material. Since the transmissivity of silicon drops rapidly with temperature above 573 K, the tube temperature was kept well below this temperature.

Assembly. The radiative heat transfer instrumentation was mounted within the wall of a bronze tube, 51.8 mm in diameter, as shown in Fig. 5. The heat flow detector was bonded to the bottom of the cavity with a high-temperature thermal conducting epoxy and was coated with a high-absorptivity paint (3 M Nextle, $\epsilon = 0.98$) to increase the fraction of transmitted radiation detected. The window was mounted on top of the cavity, using a high thermal conductivity paste to reduce the thermal contact resistance, and was held in position by an overlapping stainless steel shim. To measure the total heat transfer, a gage of the type used in the radiation device was bonded to the tube and was covered with shim. Three such instrumented ports were mounted 90 deg apart. Details of the radiative and total heat transfer measurement instrumentation and assembly have been discussed by Alavizadeh (1985) and George (1981).

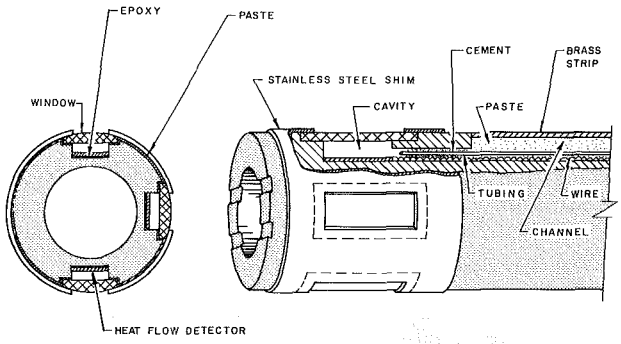

Fig. 5 Radiative heat transfer measurement instrumentation

Calibration

The purpose of the calibration was to relate the radiative heat flux detected by the radiation probe ($\dot{q}_d''$) to the radiation absorbed by a tube with a wall emissivity of unity ($\dot{q}_{ub}''$), i.e., a black wall. The advantage of this method is that the radiation can be estimated for immersed surfaces with different emissivities in a fluidized bed. Further, both the detected and absorbed radiation are directly measured and not calculated. Calibration was carried out employing a blackbody source with a cavity diameter of 2.54 cm and a temperature range of 323 K–1273 K for three different tube temperatures. To measure the detected radiative heat flux by the radiation probe ($\dot{q}_d''$), the window was carefully aligned with the blackbody source and then exposed to it. The radiation absorbed by a black tube wall ($\dot{q}_{ub}''$), used as a reference surface, was determined by aligning and exposing the total heat transfer measurement probe detector to the blackbody source under identical conditions. Natural convection heat losses during calibration were also measured for both probes by blocking the blackbody source and recording the heat flow detector response of each probe.

During each calibration run, enough time was given for the tube and blackbody source to reach their set temperatures. Heat flow detector reading of each probe was recorded with

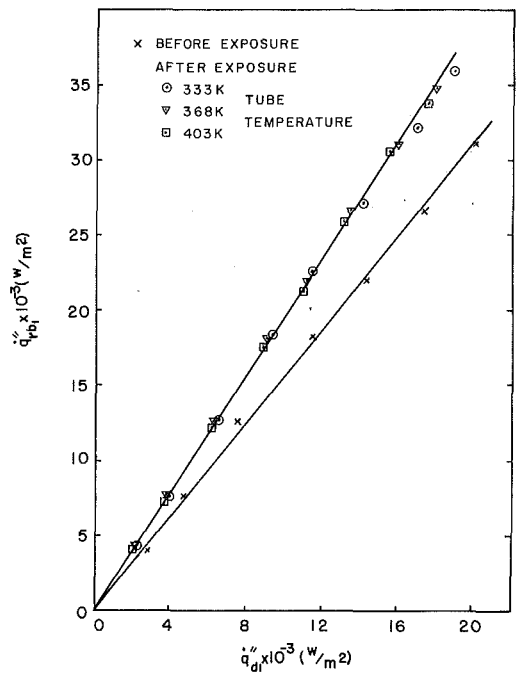

Fig. 6 Radiative heat flux absorbed by a black tube wall versus radiative heat flux detected by the radiation device

the corresponding natural convection losses at the set temperatures. Calibration runs were completed by varying the blackbody source temperature for each fixed tube temperature and repeating the procedure. Finally, subtracting convection losses, the heat flux detected by the radiation probe ($\dot{q}''_d$) and the corresponding radiation absorbed by a black tube wall ($\dot{q}''_{ub}$) were obtained. This calibration procedure was repeated after each exposure to the fluidized bed to account for possible window transmissivity change.

To study the effect of tube wall temperature, calibrations were performed at tube temperatures of 333 K, 368 K, and 403 K. The calibration results were found to be independent of the tube temperature and approximated by the following equation:

$$\dot{q}''_{ub1} = 1.96\dot{q}''_{d1} \tag{7}$$

Figure 6 is a plot of equation (7) and the calibration data for different tube temperatures. Also shown are the calibration results obtained before exposure to the fluidized bed. An average drop of 20 percent in the detected heat flux by the radiation device occurred after the first exposure and no measurable change was observed for the successive runs. The calibration was repeated for the two remaining radiation devices and the following relations were obtained:

$$\dot{q}''_{ub2} = 2.02\,\dot{q}''_{d2} \quad \text{and} \quad \dot{q}''_{ub3} = 1.87\dot{q}''_{d3}$$

The view angle of the radiation probe heat flow detector was wider in the fluid bed than when it was exposed to the blackbody source. This can slightly drop the directional average emissivity (<4 percent), estimated according to Duffie and Beckman (1974), when the probe is immersed in the bed. Also, an overall accuracy of ±11 percent was computed, based on the root-mean-square approach (Doeblin, 1975), for the calibration runs.

Finally, the emissivity of the stainless steel shim covering the total heat transfer detector to protect it from the hostile fluid bed environment was measured by exposing the detector with the shim over it to the blackbody source and comparing the results with those of the black tube wall test ($\dot{q}''_{ub}$). The emissivity was found to be 0.64 (after exposure to the fluidized bed) and was used to adjust the inferred black tube wall radiative heat transfer to obtain the radiative contribution to the total heat transfer.

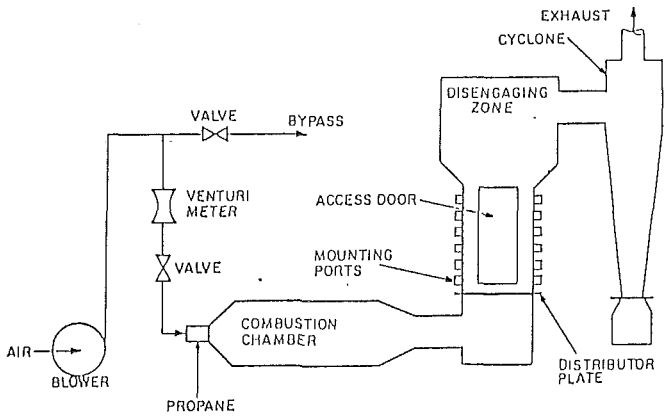

Fig. 7 Schematic of OSU high temperature fluidized bed

Experiments

Measurements were conducted in the Oregon State University high-temperature fluidized bed facility. A schematic of the facility is shown in Fig. 7.

In order to assess the thermal and mechanical performance of the window, one window was exposed to the fluidized bed. To monitor the window temperature, a thin foil thermocouple was inserted between the window and upper base of the cavity and a second thermocouple was located in the wire channel close to the tube surface. The two temperatures did not differ by more than 10 K during 12 hr of operation at 1050 K and lower. This confirmed our earlier predictions that the window temperature should be close to tube temperature (Table 1).

A response time of about 120 ms was measured for the radiation device when the response came to within 5 percent of a step change in the incident heat flux to the window.

Data were taken at 0, 45, 90, 135, and 180 deg from the lower stagnation point using a digital voltmeter. Typical results are presented in Figs. 8 and 9 for the particle mean diameter of 2.14 mm and bed temperature of 1050 K.

Figure 8 shows the local radiative heat transfer coefficient ($h_{rb} = \dot{q}''_{ub}/(T_f - T_u)$) for a black tube wall for gas velocities of 1.56 m/s, 2.8 m/s, and 3.49 m/s. The radiative heat transfer coefficient is seen to be nearly constant over the lower half—0, 45, and 90 deg positions—of the tube. A stagnant stack of more densely packed particles is known to exist on the upper half of the tube at lower gas velocities, resulting in a lower radiative heat flux at the 135 and 180 deg positions for $U_o = 1.56$ m/s. However, this stack collapses when gas velocity is increased and h_{rb} tends to become more uniform around the tube. This is the case for $U_o = 2.18$ m/s and 3.49 m/s as shown in Fig. 8.

The average total and radiative heat transfer coefficients are also shown as a function of gas velocity in Fig. 9. Presented in this figure are the radiative heat transfer coefficient to a black tube wall (curve B) and to the stainless steel shim (measured $\epsilon = 0.64$) covering the heat flow detector used for total heat transfer measurements (curve C). The radiation contribution was found to be about 13 percent for the latter case (curves A, C). The sharp increase in total heat transfer coefficient (curve A) indicates the removal of the particle stack and the slow decrease following is due to larger bed voidage (gas volume/total volume) as gas velocity is increased.

The repeatability of the measurements was ±12 percent and a root square mean (Doeblin, 1975) accuracy of −12 percent,

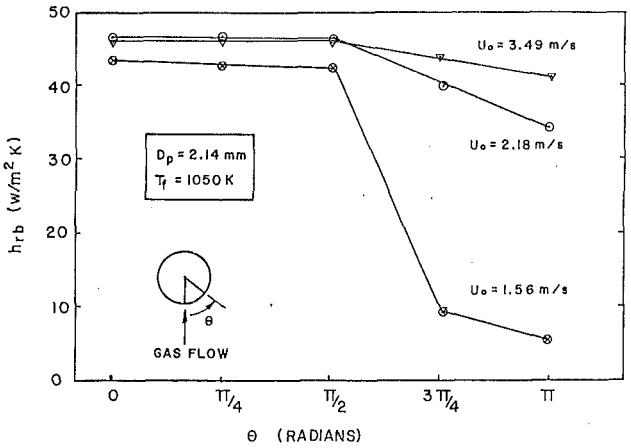

Fig. 8 Local radiative heat transfer coefficient for a black tube wall

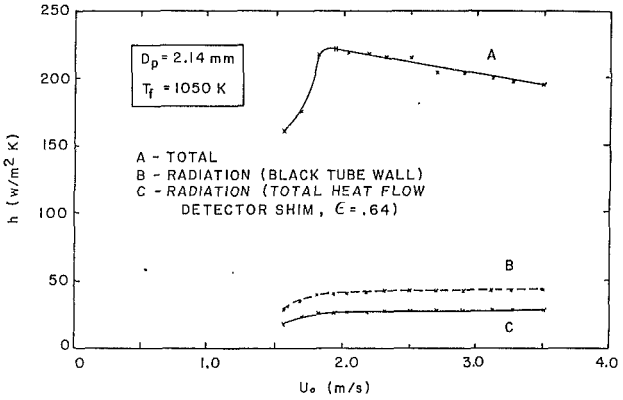

Fig. 9 Total and radiative heat transfer coefficient versus gas velocity

+13 percent was calculated for the conducted tests. A maximum conduction error of 3 percent based on detected heat flux ($\dot{q}''_d$) in the fluidized bed and $\dot{q}''_{cs}$ of equation (4) was recomputed.

Concluding Remarks

The spatial radiative component of the total heat transfer to a horizontal tube was isolated and measured with a carefully designed instrumentation. The conduction error due to convective component of the total heat transfer was found to be negligible.

Calibration of the device revealed the independence of the results from tube temperature. A linear relationship between the radiation absorbed by the tube wall and radiation detected by the device was found. Detected radiation dropped by about 20 percent after the first exposure of the device to the fluidized bed. It remained unchanged for successive runs.

Typical results for a mean particle diameter of 2.14 mm and fluid bed temperature of 1050 K indicate a spatial average radiation contribution of about 13 percent with respect to the surface emissivity of the total heat transfer measurement device ($\epsilon = 0.64$). Spatial average convective and radiative heat transfer coefficients were from 161 to 223 and from 18 to 28 $W/m^2 \cdot K$, respectively, depending on the gas velocity. Little change was observed in the radiative local heat transfer coefficient with gas velocity on the lower half of the tube. However, on the upper half of the tube the radiative heat transfer coefficient was found to rise sharply and then increase at a slower rate.

Acknowledgments

Support of this work by a grant from the National Science Foundation is appreciated. The authors would like to thank the journal referees for their useful comments. Thanks are also due to M. Johansen and H. Merkle for typing the manuscripts.

References

Adolf Meller Company, 1981, General Catalog, Providence, RI.

Alavizadah, N., 1985, "An Experimental Investigation of Radiative and Total Heat Transfer Around a Horizontal Tube Immersed in a High Temperature Gas-Solid Fluidized Bed," Ph.D. Thesis, Oregon State U., Corvallis, OR.

Alavizadah, N., Fu, Z., Adams, R. L., Welty, J. R., and Goshayeshi, A., 1985, "Radiative Heat Transfer Measurement for a Horizontal Tube Immersed in Small and Large Particle Fluidized Beds," *The Proceedings of the International Symposium on Heat Transfer*, Peking, People's Republic of China.

Arpaci, V. S., 1966, *Conduction Heat Transfer*, Addison-Wesley Pub. Co., New York.

Baskakov, A. P., Berg, B. V., Vitt, O. K., Filippovsky, N. F., Kirakosyan, V. A., Goldobin, J. M., and Maskaev, V. K., 1973, "Heat Transfer to Objects Immersed in Fluidized Beds," *Powder Technology*, Vol. 8, pp. 273–282.

Basu, P., 1978, "Bed to Wall Heat Transfer in a Fluidized Bed Coal Combustor," AIChE Symposium Series No. 176, Vol. 74, pp. 187–193.

Doeblin, E. O., 1975, *Measurement Systems Application and Design*, McGraw-Hill, New York.

Duffie, J. A., and Beckman, W. A., 1974, *Solar Energy Thermal Processes*, Wiley, New York.

Gardon, R., 1953, "An Instrument for the Direct Measurement of Intense Thermal Radiation," *Review of Scientific Instruments*, Vol. 24, No. 5, pp. 366–370.

George, A. H., 1981, "An Experimental Study of Heat Transfer to a Horizontal Tube in a Large Particle Fluidized Bed at Elevated Temperature," Ph. D. Thesis, Oregon State University, Corvallis, OR.

Mathur, A., and Saxena, S. C., 1987, "Total and Radioactive Heat Transfer to an Immersed Surface in a Gas-Fluidized Bed," *AIChE Journal*, Vol. 33, No. 7, pp. 1124–1135.

Ozkaynak, T. F., Chen, J. C., and Frankenfield, T. R., 1983, "An Experimental Investigation of Radiation Heat Transfer in a High Temperature Fluidized Bed," *Proceedings of the Fourth International Conference on Fluidization*, Kashikozima, Japan, Paper No. 5-8.

Siegel, R., and Howell, J. R., 1972, *Thermal Radiation Heat Transfer*, McGraw-Hill, New York.

Touloukian, Y. S., Powell, R. W., Ho, C. Y., and Klemens, P. G., 1970, *Thermophysical Properties of Matter*, Vols. 2 and 8, The TRPC Data Series, Plenum, New York.

Vadivel, R., and Vedamurthy, V. N., 1980, "An Investigation of the Influence of Bed Parameters on the Variation of the Local Radiative and Total Heat Transfer Coefficient Around an Embedded Horizontal Tube in a Fluidized Bed Combustor," *Proceedings of the Sixth International Conference on Fluidized Bed Combustion, Vol. III—Technical Session*, NTIS, Springfield, VA, pp. 1159–1172.

Yoshida, K., Ueno, T., and Kunii, D., 1974, "Mechanism of Bed-Wall Heat Transfer in a Fluidized Bed at High Temperatures," *Chem. Eng. Sci.*, Vol. 29, pp. 77–82.

Zhang, H., and Xie, C., 1985, "The Radiative Heat Transfer of the Immersed Tube in a Fluidized Bed at High Temperatures," *Proc. 8th Int. Conf. Fluidized Bed Combustion*, Houston, TX, pp. 142–148.

Journal of Heat Transfer

Technical Notes

This section contains shorter technical papers. These shorter papers will be subjected to the same review process as that for full papers.

Conduction Shape Factor for a Region of Uniform Thickness Surrounding a Three-Dimensional Body of Arbitrary Shape

A. V. Hassani[1] and K. G. T. Hollands[1]

Nomenclature

- A = heat transfer surface area of body, m^2
- a = side dimension of parallelepiped, m
- B = major axis of spheroid, m
- b = side dimension of parallelepiped, m
- C = minor axis of spheroid, m
- c = height of parallelepiped, m
- D_i = base diameter of the inner cone or diameter of the inner cylinder, m
- D_o = base diameter of the outer cone or diameter of the outer cylinder, m
- k = thermal conductivity, W/mK
- L_S = longest straight line passing through the inner body, m
- n = exponent of Churchill–Usagi fit, given as a function of body shape by equation (9)
- Q = heat transfer, W
- $S(\Delta)$ = conduction shape factor of region of thickness Δ surrounding body, m
- $S_o(\Delta)$ = conduction shape factor for small values of Δ, m
- S_∞ = conduction shape factor for large values of Δ, m
- $T_1 - T_2$ = temperature difference across the uniform region, K
- V = volume of inner body, m^3
- Δ = thickness of the uniform layer surrounding the body, m
- γ = body aspect ratio

[1]Department of Mechanical Engineering, University of Waterloo, Waterloo, Ontario, Canada, N2L 3G1.

Contributed by the Heat Transfer Division and presented at the ASME Winter Annual Meeting, Anaheim, California, December 1986. Manuscript received by the Heat Transfer Division July 11, 1988. Keywords: Conduction.

Introduction

Calculation of heat flow through a region of uniform thickness surrounding a body of arbitrary shape is of practical interest, for example, in calculating heat losses from an insulated body. The problem reduces to finding the conduction shape factor S of the bounded region, given by

$$S = \frac{Q}{k(T_1 - T_2)} \tag{1}$$

where Q is the heat transfer, $T_1 - T_2$ is the temperature difference across the region, and k is the thermal conductivity of the bounded region. The existing literature offers very little about this important problem. With the exception of Langmuir et al. (1913) who presented approximate solutions for the shape factor of hollow right rectangular parallelepipeds, researchers in this area have mainly concerned themselves with regions of nonuniform thickness surrounding two-dimensional shapes. Among them are Smith et al. (1958), Balcerzak and Rayner (1961), Lewis (1968), Dungan (1972), Laura and Susemihl (1973), and Laura and Sanchez Sarmienta (1978a, 1978b). Others such as Smythe (1956, 1962), Greenspan (1966), Hahne and Grigull (1975), and Chow and Yovanovich (1982) suggested methods of calculating the shape factor for single bodies in an infinite medium.

Presented here is an approximate method for calculating S for a region of uniform thickness surrounding a three-dimensional body. This method employs the asymptotic solutions

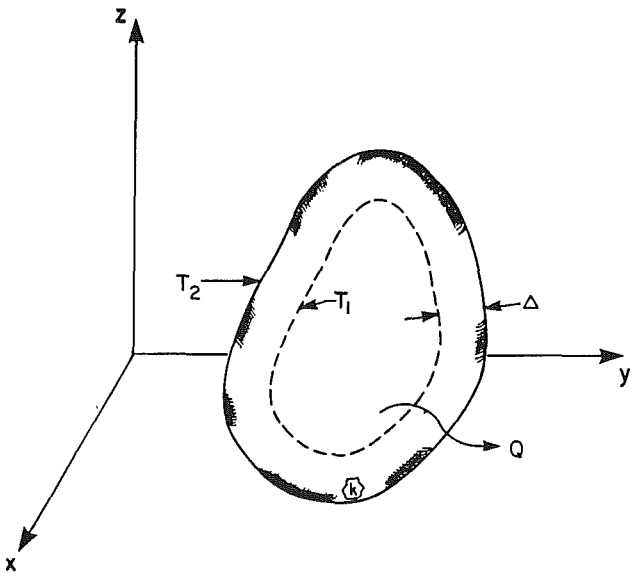

Fig. 1 Heat flow through a region of uniform thickness surrounding a body of arbitrary shape

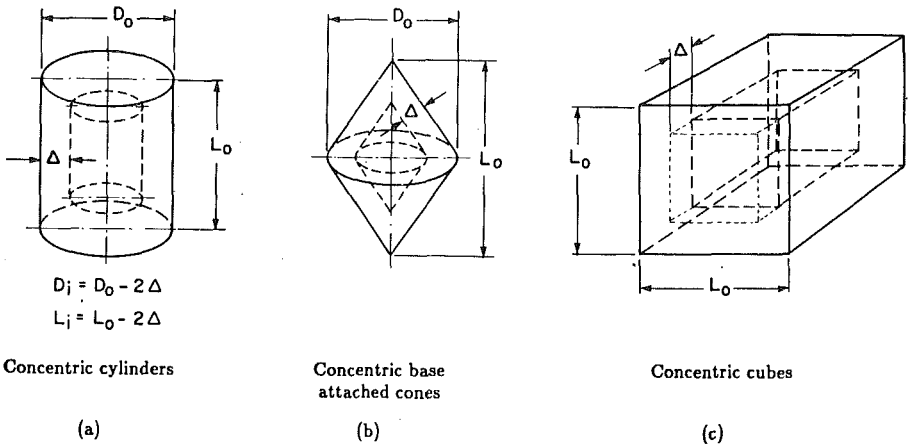

Fig. 2 Three body shapes tested, showing relevant dimensions

for S for large and small values of the thickness Δ of the bounded region. These asymptotic solutions are then used in the interpolation equation suggested by Churchill and Usagi (1972), to give S for any Δ.

Approximate Method

The shape factor S_∞ for a region with very large Δ is equivalent to that of an isothermal body located in an infinite medium. One should obtain S_∞ by analytical or numerical means if possible. Otherwise this asymptote can be closely calculated by the approximate method suggested by Chow and Yovanovich (1982). Their method draws upon the fact that the conduction shape factor of a body of fixed area is a slowly changing function of its shape. Because of this slow change, the conduction shape factor for a body of arbitrary shape and size in an infinite environment can be closely calculated by choosing a similar shape with known conduction shape factor whose area is equal to that of the arbitrary shape. For example the conduction shape factor for a cube can be approximated by that of a sphere whose surface area is equal to the surface area of the cube. The result is $S = 8.682\ L_i$ (where L_i is the side length of the cube), which is 4.6 percent higher than the exact value, $S = 8.298\ L_i$ reported by Greenspan (1966). Thus this asymptote can be closely calculated (within 5 percent) for most three-dimensional shapes by using

$$S_\infty = 3.51\sqrt{A} \tag{2}$$

where A is the surface area of the body.

The other asymptote $S_o(\Delta)$, corresponding to a region of very small thickness, is obtained by assuming one-dimensional heat transfer and ignoring the effects of the corners and the edges. This asymptote can be estimated from

$$S_o(\Delta) = \frac{A}{\Delta} \tag{3}$$

where A is the area of the (inner) body. Applying the Churchill-Usagi technique, the following equation interpolates between two asymptotic solutions, $S_o(\Delta)$ and S_∞:

$$S(\Delta) = (S_o^n(\Delta) + S_\infty^n)^{1/n} \tag{4}$$

where n is a constant that is expected to be a function of the shape of the body. Equation (4), with the appropriate value of n, constitutes the "approximate method."

Several geometries were used to test the appropriateness of the Churchill-Usagi fit and to establish a relationship between n and the body shape. As an example, the case of concentric cylinders, shown in Fig. 2(*a*),[2] with aspect ratio $\gamma = L_i/D_i$ of the inner cylinder equal to unity, is considered here. Application of the method in this case gives

$$S = \left[\left(\frac{3\pi D_i^2}{2\Delta}\right)^n + (7.476\ D_i)^n\right]^{1/n} \tag{5}$$

Equation (5) was compared to a numerical solution for the conduction shape factor obtained using a finite element code. The code was based on the WATSHARE (Waterloo Applied Thermal Science Hydrodynamic software to Aid Research in Engineering) library of subroutines developed at the University of Waterloo, and a grid generation routine developed by Galpin and Raithby (1985). The accuracy of this code was examined by solving some problems with known analytical solutions such as concentric spheres and long concentric cylinders. The difference between the analytical and numerical solutions in either case was found to be less than 0.2 percent. The grid refinement procedure was also performed for each numerical solution until the difference between two successive solutions was less than 0.2 percent. The grid refinement procedure (for a given thickness of the layer surrounding the body) consisted of first solving the conduction problem by using an orthogonal curvilinear mesh, which consisted of 20 × 20 control volumes. Then the problem was solved by increasing the number of control volumes to 25 × 25 and so on up to 35 × 35 control volumes. In each case the solution was compared to the previous case and to the exact solution. As the number of control volumes increased the difference between the exact solution and the numerical solution decreased. The numerical results using a mesh with 35 × 35 control volumes showed only 0.2 percent difference compared to the exact solution. This case also showed only 0.2 percent improvement compared to the numerical results using a mesh with a 30 × 30 control volumes. This indicated that the numerical solution was converging in the right direction. Similar grid refinement studies were applied in numerical solutions for other body shapes described later in the paper. It was concluded that the expected error in the numerically predicted values of S should be less than 0.3 percent.

Through a trial and error procedure, a value of $n = 1.08$ was found to minimize the difference between equation (5) and the numerical solution. The fit was found to be very close; the maximum error was 1.6 percent. This procedure was repeated for several other geometries as well as for cylinders of different aspect ratio. The asymptotic solutions, the n values, and the maximum error in fit for certain geometries are listed in Table 1.

The numerical solution to the above problem was repeated but this time the edges of the outer cylinder were not rounded. The results were compared to the previous numerical solutions listed and differences of less than 1 percent were observed.

[2]For clarity the corners and edges of the outer bodies have not been drawn at uniform distance from those of the inner bodies.

Table 1 Asymptotic solution for various shapes

Shape of The Inner Body	$S_o(\Delta)$	S_∞	n	% Max. Diff.
Cylinder, $\gamma = 1.0$	$\frac{3\pi D_i^2}{2\Delta}$	$2.38\ \pi D_i$	1.08	1.6
Cylinder, $\gamma = 0.4$	$\frac{1.3\pi D_i^2}{2\Delta}$	$1.88\ \pi D_i$	1.12	1.5
Cylinder, $\gamma = 2.2$	$\frac{4.9\pi D_i^2}{2\Delta}$	$3.32\ \pi D_i$	1.03	1.9
Base Attached Cones $\gamma = \frac{\text{height}}{\text{diameter}} = 0.5$	$\frac{1.12\pi D_i^2}{2\Delta}$	$4.67\ D_i$	1.10	1.8
Base Attached Cones $\gamma = \frac{\text{height}}{\text{diameter}} = 2.2$	$\frac{2.42\pi D_i^2}{2\Delta}$	$6.97\ D_i$	1.01	2.0
Parallelpiped with $b = a$ and $\frac{c}{a} = 0.05$	$\frac{2.2a^2}{\Delta}$	$4.88\ a$	1.11	3.2

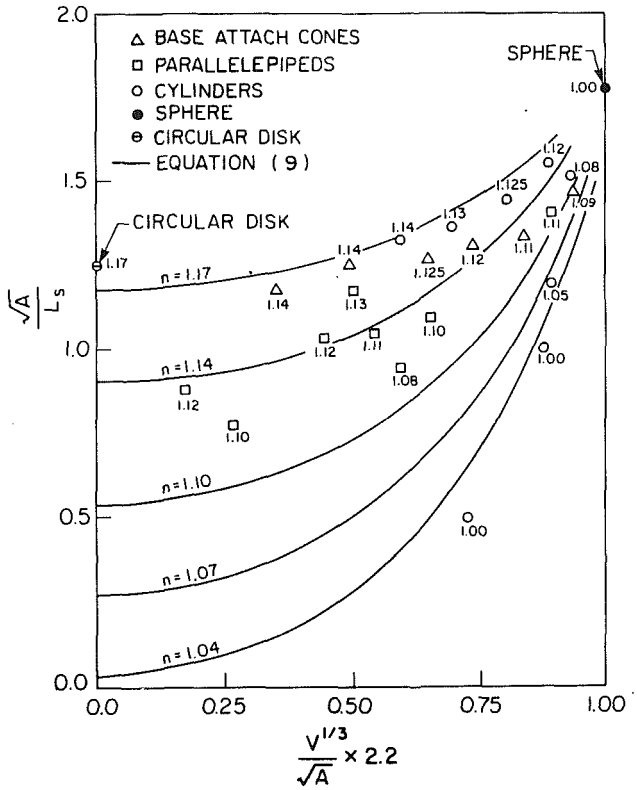

Fig. 3 Exponent n for various shapes

This indicated that rounding of the corners or edges did not substantially alter the solution.

The numerical code could handle only two-dimensional or axisymmetric problems. Therefore for three-dimensional regions such as parallelepiped shells, the results of equation (4) were compared to another source: the approximate solutions given by Langmuir et al. (1913). For example, for a region of uniform thickness Δ surrounding a parallelepiped with dimensions $a = b$, $c/a = 0.05$, and area $A = 2a^2(1 + 2c/a)$, the expression given by Langmuir reduces to the following nondimensional form:

$$\frac{S}{a} = 2.2\frac{a}{\Delta} + 3.72 + 0.35\frac{\Delta}{a} \quad \text{for } \frac{\Delta}{a} < 2.5 \tag{6}$$

There is no analytical solution available for S_∞ of this shape. Therefore S_∞ was approximated by the exact value of S_∞ for an oblate spheroid with aspect ratio $C/B = 0.05$ and surface area equal to that of the inner parallelepiped. This resulted in $S_\infty = 4.88a$. The other asymptote $S_o(\Delta)$ for this shape is

$$S_o(\Delta) = \frac{A}{\Delta} = 2.2\frac{a^2}{\Delta} \tag{7}$$

and equation (4) becomes

$$\frac{S(\Delta)}{a} = \left[\left(\frac{2.2a}{\Delta}\right)^n + (4.88)^n\right]^{1/n} \tag{8}$$

The value $n = 1.11$ was found to give minimum difference between the approximate solution of Langmuir and the predictions of equation (8). This procedure was repeated for parallelepipeds of various dimensions, and the n value that resulted in the best fit was recorded.

In the special case of a sphere the well-known analytical solution gives the shape factor exactly. In this case the error is zero when $n = 1.0$. That is, with the appropriate value of n_1 the approximate method gives the exact result.

As is clear from Table 1, the best value of n is sensitive to the body shape. Being dimensionless, n should correlate with dimensionless measures of body shape. After several tries, two such measures, which seemed to correlate well with n and are readily calculated, were chosen: $\sqrt{A}/L_S$, and $V^{1/3}/\sqrt{A}$, where V and A are the volume and the surface area of the inner body, respectively, and L_S is the longest straight line passing through the inner body. Figure 3 shows the n values obtained for the geometeries tested plotted in parametric form against these two dimensionless measures. The fact that lines of constant n can be constructed in this plot indicates that n is a unique function of these two variables, at least to a reasonable approximation. An empirical formula fitting the lines of constant n has been found to be

$$n = \left[1.26 - \frac{(2 - \sqrt{A}/L_S)}{9\sqrt{1. - 4.79V^{2/3}/A}},\ 1.0\right]_{\max} \tag{9}$$

where $Y = [x_1, x_2]_{\max}$ means that $Y = x_1$ if $x_1 > x_2$ and $Y = x_2$ if $x_2 > x_1$. This formula, plotted in Fig. 3, covers the range for n: $1 \le n \le 1.2$, which includes a very wide range of body shapes.

Equations (4) and (9) were tested for other body shapes, principally the cube (Fig. 2(*c*)) and attached cones (Fig. 2(*b*)) with aspect ratio L_i/D_i equal to unity. For the cones, the maximum error over the full range in Δ was observed to be 3 percent. For the cube, the maximum difference between the present results and those from the method of Langmuir et al. (1913) was 5.8 percent.

A set of tests was performed to examine the sensitivity of the results of the approximate method to the n value obtained from equation (9). It was observed that for $n > 1.11$ a 5 percent error in the n value will cause less than 2.5 percent error in the estimated conduction shape factor. On the other hand for $n < 1.11$ a 5 percent error in the n value will result in less than 1.0 percent error in conduction shape factor. Thus small errors in calculating n from equation (9) will not introduce large errors in conduction shape factor.

Conclusions

A simple approximate method, summarized by equations (3), (4), and (9), has been presented for calculating the conduction shape factor of a region bounded by two concentric bodies with a uniform spacing Δ between them. The results obtained through this method show agreement to within about 5 percent with those obtained from numerical or existing analytical techniques.

References

Balcerzak, M. J., and Raynor, S., 1961, "Steady State Temperature Distribution and Heat Flow in Prismatic Bars With Isothermal Boundary Conditions," *Int. J. Heat Mass Transfer*, Vol. 3, pp. 113–125.

Chow, Y. L., and Yovanovich, M. M., 1982, "The Shape Factor of the Capacitance of a Conductor," *Journal of Applied Mechanics*, Vol. 53, No. 12, pp. 8470–8475.

Churchill, S. W., and Usagi, R., 1972, "A General Expression for the Correlation of Rates of Transfer and Other Phenomena," *AIChE J.*, Vol. 18, pp. 1121–1128.

Dugan, J. P., 1972, "On the Shape Factor for a Hollow, Square Cylinder," *AIChE Journal*, Vol. 18, No. 5, pp. 1082–1083.

Galpin, P. F., and Raithby, G. D., 1988, personal communication.

Greenspan, D., 1966, "Resolution of Classical Capacity Problems by Means of a Digital Computer," *Canadian J. of Physics*, Vol. 44, pp. 2605–2614.

Hahne, E., and Grigull, U., 1975, "Formfaktor und Formwiderstand der Stationaren Mehrdimensionalen Warmeleitung," *Int. J. Heat Mass Transfer*, Vol. 18, pp. 751–767.

Langmuir, I., Adams, E. Q., and Meikle, G. S., 1913, "Flow of Heat Through Furnace Walls: The Shape Factor," *Trans. Am. Electrochem. Soc.*, Vol. 23, p. 299.

Laura, P. A., and Susemihl, E. A., 1973, "Determination of Heat Flow Shape Factors for Hollow, Regular Polygonal Prisms," *Nuclear Eng. and Design*, Vol. 25, pp. 409–412.

Laura, P. A. A., and Sanchez Sarmienta, G., 1978a, "Heat Flow Shape Factors for Circular Rods With Regular Polygonal Concentric Inner Bore," *Nuclear Eng. and Design*, Vol. 47, pp. 227–229.

Laura, P. A. A., and Sanchez Sarmienta, G., 1978b, "Analytical Determination of Heat Flow Shape Factors for Composite, Prismatic Bars of Doubly-Connected Cross Section," *Nuclear Eng. and Design*, Vol. 50, pp. 385–397.

Lewis, G. K., 1968, "Shape Factors in Conduction Heat Flow for Circular Bars and Slabs With Various Internal Geometries," *Int. J. Heat Mass Transfer*, Vol. 11, pp. 985–992.

Morrison, F. A., Jr., and Reed, L. D., 1974, "Low Knudsen Number Heat Tranfser From Two Spheres in Contact," ASME JOURNAL OF HEAT TRANSFER, Vol. 96, pp. 478–482.

Smith, J. C., Lind, J. E., and Lermand, D. S., 1958, "Shape Factors for Conductive Heat Flow," *AIChE Journal*, Sept., pp. 330–331.

Smythe, W. R., 1956, "Charged Right Circular Cylinder," *Journal of Applied Physics*, Vol. 27, No. 8, pp. 917–920.

Smythe, W. R., 1962, "Charged Right Circular Cylinder," *Journal of Applied Physics*, Vol. 33, No. 10, pp. 2966–2967.

A Generalized Laplace Transform Technique for Phase-Change Problems

J. Y. Ku[1] and S. H. Chan[2]

Introduction

Analytical solutions of transient heat transfer problems involving melting or solidification are inherently difficult to obtain because of the nonlinearity associated with the moving boundary condition at the solid–liquid interface. A few exact solutions of phase-change problems are currently available (Ozisik, 1980; Carslaw and Jaeger, 1959). The mathematical approach used to achieve these solutions, however, is quite crude. Instead of solving the problem, a solution is assumed for the temperature profile. The assumed solution satisfies the governing differential equation, one of the boundary conditions and, in some cases, the initial condition as well. The assumed solution depends on the nature of the problem. It could be an error function or a complementary error function with coefficients to be determined by applying the remaining boundary condition. The interface condition is then applied to yield normally a transcendental equation, from which the transient interface location can be determined.

The present note proposes a technique to extend the Laplace Transform method to obtain a closed-form solution for nonlinear phase-change problems. Solutions to a few problems are demonstrated to elucidate the essence of the technique.

Mathematical Formulation and Solutions

To demonstrate how the Laplace transform method can be extended to solve phase-change problems, two melting and two solidification problems are analyzed here. For three of them, the exact solutions are available, which can serve as the benchmark solutions to validate the technique proposed. The remaining problem for which no exact solution is available in the literature is included to illustrate the potential of the technique.

Problem 1—Melting of a Solid. A semi-infinite solid initially at its solidification (or melting) temperature (T_m) is confined to a half-space ($x>0$). At time $t=0$, the temperature of the boundary surface at $x=0$ is raised to T_w, higher than T_m, and maintained at that temperature for time $t>0$.

This is essentially a single-region problem because the temperature throughout the solid phase is T_m. Therefore, only the temperature profile in the liquid phase and the location of the solid–liquid interface $P(t)$ need to be solved for.

The heat conduction equation and the boundary conditions in the liquid phase are

$$\frac{\partial^2 T_l(x,t)}{\partial x^2}=\frac{1}{\alpha_l}\frac{\partial T_l}{\partial t}, \qquad \text{in } 0<x<P(t), \quad t>0 \tag{1}$$

$$T_l=T_w \text{ at } x=0, \quad t>0 \tag{2}$$

$$T_l=T_m \text{ at } x=\mathrm{P}, \quad t>0 \tag{3}$$

$$-k_l\frac{\partial T_l}{\partial x}=\rho L\frac{dP}{dt} \text{ at } x=P, \quad t>0 \tag{4}$$

where L is the latent heat of fusion. The Laplace transforms of equations (1) and (2) yield, respectively,

$$\frac{d^2\bar{T}_l(x,s)}{dx^2}=\frac{1}{\alpha_l}(s\bar{T}_l(x,s)-T_l(x,0)), \qquad \text{in } 0<x<\bar{P}(s) \tag{5}$$

and

$$\bar{T}_l=\frac{T_w}{s} \qquad \text{at } x=0 \tag{6}$$

Before proceeding, it is essential to note that equation (5) calls for an initial temperature profile condition in the newly evolved liquid region, $T_l(x,0)$, which is unspecified, although the one in the solid region is given. As $t\to 0$, the liquid phase region is infinitesimally small and its thickness shrinks to zero, like a line without a thickness. Temperature is discontinuous across this "line" with T_w on one side and T_m on the other. It is therefore reasonable to assume a constant but unspecified value of the initial temperature "profile" in this newly formed liquid phase region, i.e.,

$$T_l(x,t)=T_c \text{ as } t\to 0$$

Then, the solution of equation (5) can be readily obtained as

[1]Graduate Student, Department of Mechanical Engineering, University of Wisconsin—Milwaukee, Milwaukee, WI 53201; current address: Argonne National Laboratory, Argonne, IL.

[2]Wisconsin Distinguished Professor and Chairman, Department of Mechanical Engineering, University of Wisconsin—Milwaukee, Milwaukee, WI 53201.

Contributed by the Heat Transfer Division and presented at the 22nd National Heat Transfer Conference, Niagara Falls, New York, August 5–8, 1984. Manuscript received by the Heat Transfer Division April 27, 1988. Keywords: Conduction, Phase-Change Phenomena.

Conclusions

A simple approximate method, summarized by equations (3), (4), and (9), has been presented for calculating the conduction shape factor of a region bounded by two concentric bodies with a uniform spacing Δ between them. The results obtained through this method show agreement to within about 5 percent with those obtained from numerical or existing analytical techniques.

References

Balcerzak, M. J., and Raynor, S., 1961, "Steady State Temperature Distribution and Heat Flow in Prismatic Bars With Isothermal Boundary Conditions," *Int. J. Heat Mass Transfer*, Vol. 3, pp. 113–125.

Chow, Y. L., and Yovanovich, M. M., 1982, "The Shape Factor of the Capacitance of a Conductor," *Journal of Applied Mechanics*, Vol. 53, No. 12, pp. 8470–8475.

Churchill, S. W., and Usagi, R., 1972, "A General Expression for the Correlation of Rates of Transfer and Other Phenomena," *AIChE J.*, Vol. 18, pp. 1121–1128.

Dugan, J. P., 1972, "On the Shape Factor for a Hollow, Square Cylinder," *AIChE Journal*, Vol. 18, No. 5, pp. 1082–1083.

Galpin, P. F., and Raithby, G. D., 1988, personal communication.

Greenspan, D., 1966, "Resolution of Classical Capacity Problems by Means of a Digital Computer," *Canadian J. of Physics*, Vol. 44, pp. 2605–2614.

Hahne, E., and Grigull, U., 1975, "Formfaktor und Formwiderstand der Stationaren Mehrdimensionalen Warmeleitung," *Int. J. Heat Mass Transfer*, Vol. 18, pp. 751–767.

Langmuir, I., Adams, E. Q., and Meikle, G. S., 1913, "Flow of Heat Through Furnace Walls: The Shape Factor," *Trans. Am. Electrochem. Soc.*, Vol. 23, p. 299.

Laura, P. A., and Susemihl, E. A., 1973, "Determination of Heat Flow Shape Factors for Hollow, Regular Polygonal Prisms," *Nuclear Eng. and Design*, Vol. 25, pp. 409–412.

Laura, P. A. A., and Sanchez Sarmienta, G., 1978a, "Heat Flow Shape Factors for Circular Rods With Regular Polygonal Concentric Inner Bore," *Nuclear Eng. and Design*, Vol. 47, pp. 227–229.

Laura, P. A. A., and Sanchez Sarmienta, G., 1978b, "Analytical Determination of Heat Flow Shape Factors for Composite, Prismatic Bars of Doubly-Connected Cross Section," *Nuclear Eng. and Design*, Vol. 50, pp. 385–397.

Lewis, G. K., 1968, "Shape Factors in Conduction Heat Flow for Circular Bars and Slabs With Various Internal Geometries," *Int. J. Heat Mass Transfer*, Vol. 11, pp. 985–992.

Morrison, F. A., Jr., and Reed, L. D., 1974, "Low Knudsen Number Heat Tranfser From Two Spheres in Contact," ASME JOURNAL OF HEAT TRANSFER, Vol. 96, pp. 478–482.

Smith, J. C., Lind, J. E., and Lermand, D. S., 1958, "Shape Factors for Conductive Heat Flow," *AIChE Journal*, Sept., pp. 330–331.

Smythe, W. R., 1956, "Charged Right Circular Cylinder," *Journal of Applied Physics*, Vol. 27, No. 8, pp. 917–920.

Smythe, W. R., 1962, "Charged Right Circular Cylinder," *Journal of Applied Physics*, Vol. 33, No. 10, pp. 2966–2967.

A Generalized Laplace Transform Technique for Phase-Change Problems

J. Y. Ku[1] and S. H. Chan[2]

Introduction

Analytical solutions of transient heat transfer problems involving melting or solidification are inherently difficult to obtain because of the nonlinearity associated with the moving boundary condition at the solid–liquid interface. A few exact solutions of phase-change problems are currently available (Ozisik, 1980; Carslaw and Jaeger, 1959). The mathematical approach used to achieve these solutions, however, is quite crude. Instead of solving the problem, a solution is assumed for the temperature profile. The assumed solution satisfies the governing differential equation, one of the boundary conditions and, in some cases, the initial condition as well. The assumed solution depends on the nature of the problem. It could be an error function or a complementary error function with coefficients to be determined by applying the remaining boundary condition. The interface condition is then applied to yield normally a transcendental equation, from which the transient interface location can be determined.

The present note proposes a technique to extend the Laplace Transform method to obtain a closed-form solution for nonlinear phase-change problems. Solutions to a few problems are demonstrated to elucidate the essence of the technique.

Mathematical Formulation and Solutions

To demonstrate how the Laplace transform method can be extended to solve phase-change problems, two melting and two solidification problems are analyzed here. For three of them, the exact solutions are available, which can serve as the benchmark solutions to validate the technique proposed. The remaining problem for which no exact solution is available in the literature is included to illustrate the potential of the technique.

Problem 1—Melting of a Solid. A semi-infinite solid initially at its solidification (or melting) temperature (T_m) is confined to a half-space ($x>0$). At time $t=0$, the temperature of the boundary surface at $x=0$ is raised to T_w, higher than T_m, and maintained at that temperature for time $t>0$.

This is essentially a single-region problem because the temperature throughout the solid phase is T_m. Therefore, only the temperature profile in the liquid phase and the location of the solid–liquid interface $P(t)$ need to be solved for.

The heat conduction equation and the boundary conditions in the liquid phase are

$$\frac{\partial^2 T_l(x,t)}{\partial x^2}=\frac{1}{\alpha_l}\frac{\partial T_l}{\partial t}, \qquad \text{in } 0<x<P(t), \quad t>0 \tag{1}$$

$$T_l=T_w \text{ at } x=0, \quad t>0 \tag{2}$$

$$T_l=T_m \text{ at } x=\mathrm{P}, \quad t>0 \tag{3}$$

$$-k_l\frac{\partial T_l}{\partial x}=\rho L\frac{dP}{dt} \text{ at } x=P, \quad t>0 \tag{4}$$

where L is the latent heat of fusion. The Laplace transforms of equations (1) and (2) yield, respectively,

$$\frac{d^2\bar{T}_l(x,s)}{dx^2}=\frac{1}{\alpha_l}(s\bar{T}_l(x,s)-T_l(x,0)), \qquad \text{in } 0<x<\bar{P}(s) \tag{5}$$

and

$$\bar{T}_l=\frac{T_w}{s} \qquad \text{at } x=0 \tag{6}$$

Before proceeding, it is essential to note that equation (5) calls for an initial temperature profile condition in the newly evolved liquid region, $T_l(x,0)$, which is unspecified, although the one in the solid region is given. As $t\to 0$, the liquid phase region is infinitesimally small and its thickness shrinks to zero, like a line without a thickness. Temperature is discontinuous across this "line" with T_w on one side and T_m on the other. It is therefore reasonable to assume a constant but unspecified value of the initial temperature "profile" in this newly formed liquid phase region, i.e.,

$$T_l(x,t)=T_c \text{ as } t\to 0$$

Then, the solution of equation (5) can be readily obtained as

[1]Graduate Student, Department of Mechanical Engineering, University of Wisconsin—Milwaukee, Milwaukee, WI 53201; current address: Argonne National Laboratory, Argonne, IL.

[2]Wisconsin Distinguished Professor and Chairman, Department of Mechanical Engineering, University of Wisconsin—Milwaukee, Milwaukee, WI 53201.

Contributed by the Heat Transfer Division and presented at the 22nd National Heat Transfer Conference, Niagara Falls, New York, August 5–8, 1984. Manuscript received by the Heat Transfer Division April 27, 1988. Keywords: Conduction, Phase-Change Phenomena.

$$\bar{T}_l = C_1 e^{-x(s/\alpha_l)^{1/2}} + C_2 e^{x(s/\alpha_l)^{1/2}} + \frac{T_c}{s} \tag{7}$$

A finite value of the temperature at $x \to \infty$ when $P(t) \to \infty$ requires that $C_2 = 0$. C_1 is determined by applying the boundary condition, given by equation (6). Therefore, taking the inverse of the transformed equation yields

$$(T_l - T_w)/(T_w - T_c) = \text{erf}\left[\frac{x}{2(\alpha_l t)^{1/2}}\right] \tag{8}$$

where T_c is given, after applying equation (3), by

$$T_c = T_w - (T_w - T_m)/\text{erf}(\lambda) \tag{9}$$

with

$$\lambda = P(t)/2(\alpha_l t)^{1/2} \tag{10}$$

The above result is identical to that obtained through the approach described in the introduction (Ozisik, 1980; Carslaw and Jaeger, 1959). Once the temperature profile is found, the value of λ or the interface location, $P(t)$, can be found by applying the interfacial condition, equation (4), in the same manner as the approach mentioned above and will not be reiterated here.

Problem 2—Solidification of a Supercooled Liquid. A semi-infinite supercooled liquid at a uniform temperature (T_i) that is lower than the solidification temperature (T_m) of the solid phase is confined to a half-space ($x > 0$). It is assumed that the solidification starts at the surface $x = 0$ at time $t = 0$ when the surface temperature becomes T_m and the solid–liquid interface moves in the positive x direction.

This is also a single-region problem because one is only concerned with the temperature distribution in the liquid phase and the location of the solid–liquid interface. The heat conduction equation given by equation (1) is equally valid here except it applies to the region in $P(t) < x < \infty$, $t > 0$, and is subject to the boundary and initial conditions

$$T_l = \text{finite as } x \to \infty, \quad t > 0 \tag{11}$$

$$T_l = T_m \qquad \text{at } x = P, \quad t > 0 \tag{12}$$

$$-k_l \frac{\partial T_l}{\partial x} = \rho L \frac{dP}{dt} \text{ at } x = P, \quad t > 0 \tag{13}$$

$$T_l = T_i \text{ for } t = 0, \text{ in } x > 0 \tag{14}$$

Note that the initial condition is known and specified in this case by equation (14). The general solution to the Laplace transformed heat condition equation is simply

$$\bar{T}_l = C_4 e^{-x(s/\alpha_l)^{1/2}} + C_5 e^{x(s/\alpha_l)^{1/2}} + \frac{T_i}{s} \tag{15}$$

By equation (11), $C_5 = 0$. However, in the liquid region of interest, the boundary condition at $x = 0$, as $t \to 0$, suffers a discontinuity, namely, the temperature T_l jumps from T_i to T_m. It is therefore assumed that there exists a constant but unspecified temperature

$$T_l = T_b \text{ as } x \to 0 \text{ and } t \to 0$$

The above can be regarded as a boundary condition, which is used to determine C_4. Thus, the inverse transform of the solution yields

$$(T_l - T_i)/(T_b - T_i) = \text{erfc}\left[\frac{x}{2(\alpha_l t)^{1/2}}\right] \tag{16}$$

By the boundary condition, equation (12), T_b is found as

$$T_b = \frac{T_m - T_i}{\text{erfc}\ (\lambda)} + T_i \tag{17}$$

The final temperature distribution in the liquid phase given by equations (16) and (17) is identical to the exact solution obtained by Ozisik (1980) and Carslaw and Jaeger (1959).

Problem 3—Solidification of a Subcooled Liquid. A semi-infinite liquid at a uniform temperature (T_i), higher than the melting temperature (T_m) of the solid phase, is confined to the half-space ($x > 0$). At time $t = 0$, the temperature of the boundary surface at $x = 0$ is lowered to T_w below T_m and maintained at that temperature for time $t > 0$. This is a two-region problem since the temperatures are unknown in both the solid and liquid phases. Accordingly, for the solid region

$$T_s = T_w \qquad \text{at } x = 0, \quad t > 0 \tag{18}$$

while for the liquid region

$$T_l = \text{finite} \qquad \text{as } x \to 0, \quad t > 0 \tag{19}$$

$$T_l = T_i \qquad \text{at } t = 0, \text{ in } x > 0 \tag{20}$$

The coupling conditions at the interface are

$$T_s = T_l = T_m \quad \text{at } x = P, \quad t > 0 \tag{21}$$

$$k_s \frac{\partial T_s}{\partial x} - k_l \frac{\partial T_l}{\partial x} = \rho L \frac{dP}{dt} \text{ at } x = P, \quad t > 0 \tag{22}$$

The solid phase problem is similar to Problem 1 with an unspecified initial condition in the newly evolved solid region. Therefore, a similar solution is readily obtainable as follows:

$$\frac{T_s - T_w}{T_m - T_w} = \frac{\text{erf}\left[\frac{x}{2(\alpha_s t)^{1/2}}\right]}{\text{erf}\ (\lambda)} \tag{23}$$

where

$$\lambda = P/2(\alpha_s\, t)^{1/2} \tag{24}$$

The liquid region is similar to Problem 2 with a given initial condition, given by equation (20), but with a jump boundary condition as $x \to 0$ and $t \to 0$. The temperature profile can be readily obtained by the present Laplace transform technique as

$$\frac{T_l - T_i}{T_m - T_i} = \text{erfc}\left[\frac{x}{2(\alpha_l t)^{1/2}}\right] / \text{erfc}\left[\lambda(\alpha_s/\alpha_l)^{1/2}\right] \tag{25}$$

where λ is given by equation (24).

The temperature profiles in both phases obtained by the Laplace transform technique are again in agreement with existing solutions (Ozisik, 1980; Carslaw and Jaeger, 1959). Naturally, the use of the interface condition, equation (22), should yield an identical expression for λ.

Problem 4—Solid Melting With Heat Flux Boundary Condition. As a final example, consider a problem for which no prior analytical solution exists. It is the same as Problem 1 above, except subject to a constant heat flux (q_o) condition, namely, $k\, \partial T/\partial x = -q_o$, at $x = 0$.

Following the same procedure one can readily obtain the desired closed form solution. For brevity, only the final temperature profile is given here

$$\theta(\eta, \bar{t}) = 2Q\sqrt{\frac{\bar{t}}{\pi}}\left[\exp(-\eta^2/4\bar{t}) - \exp(-\eta_p^2/4\bar{t})\right]$$

$$- Q\left[\eta\,\text{erfc}(\eta/2\sqrt{\bar{t}}) - \eta_p\,\text{erfc}(\eta_p/2\sqrt{\bar{t}})\right]$$

where $\theta = C(T - T_m)/L$, $\eta = x/L_r$, $\bar{t} = \alpha t/L_r^2$, $Q = CL_r q_o/k\lambda$, $\eta_p = P/L_r$, and L_r is an arbitrary reference length. The interface location is obtainable by the direct integration of the equation

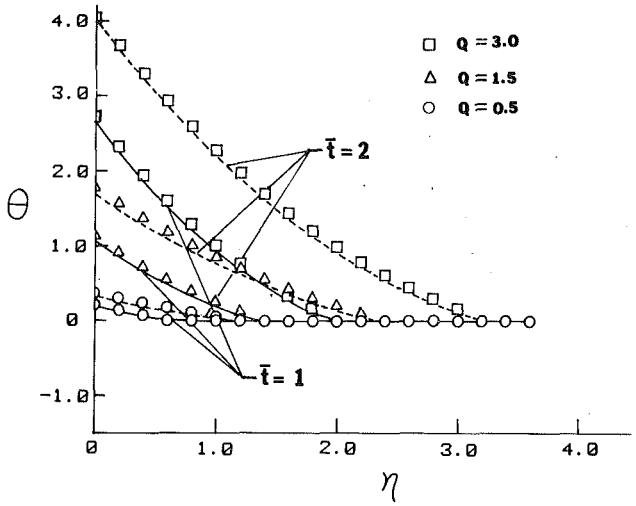

Fig. 1 Analytical and numerical temperature profile comparison with various heat fluxes at two different times

$$d\eta_p/d\bar{t} = Q \operatorname{erfc}(\eta_p/2\sqrt{\bar{t}})$$

with $\eta_p = 0$ at $\bar{t} = 0$.

In the absence of an exact solution in the existing literature, numerical solutions by the standard enthalpy method were carried out and compared with the present analytical solution. Good agreement is shown in Fig. 1 between the analytical (indicated by lines) and the numerical (circles, etc.) results.

Discussion

At the initial state of each problem studied, it is seen that either the temperature is discontinuous at a boundary or the initial temperature is unspecified in the newly evolved phase. In the latter class of problems where the initial temperature profile is unspecified, a constant but undetermined initial temperature T_c is introduced, which makes the Laplace transform method a viable solution technique to these phase-change problems. As shown in Problem 1, the introduced initial temperature T_c, given by equation (9), turns out to be neither the imposed surface temperature T_w nor the initial temperature of the original phase T_m. Had we mistakenly taken T_c as T_m and substituted it into $T_l(x, 0)$ in equation (5), the result would have yielded an erroneous answer. The proposed method is to leave T_c unspecified until the closed-form temperature profile is obtained. Then the proper value of T_c is determined automatically by applying the remaining boundary condition given by equation (3).

In the other class of phase-change problems where the problem of interest lies in the original phase (see Problem 2), one of the boundary conditions suffers a discontinuity initially. To overcome the discontinuity difficulty and to make the Laplace transform technique applicable, we again introduced at the discontinuous boundary a temperature, the value of which is not determined a priori. The introduced temperature allows the Laplace transform technique to proceed to yield the solution, and the solution obtained is in turn used to determine the unspecified value by applying one of the given boundary conditions.

While the proposed technique can systematically derive exact solutions of phase-change problems by the standard Laplace transform method without the need of educated guesses of trial solutions, there are limitations that should be noted. The solution technique obviously does not apply for nonlinearity caused by temperature-dependent thermal properties or by nonlinear boundary conditions. Other limitations may exist, which will be the subjects for future studies. Nevertheless, the technique can reproduce systematically all the existing exact solutions of phase-change problems, including those in cylindrical and spherical coordinates (Chan and Ku, 1984). The potential of the technique has been shown for obtaining the closed-form solution for problems for which no prior closed-form solutions are yet available.

Acknowledgments

The authors are grateful to John Chai for providing the numerical solution.

References

Carslaw, H. S., and Jaeger, J. C., 1959, *Conduction of Heat in Solids*, 2nd ed., Clarendon Press, London, pp. 282–295.

Chan, S. H., and Ku, J. K., 1984, "A Systematic Approach to the Exact Solutions of Some Phase-Change Problems," ASME Paper No. 84-HT-1, presented at the National Heat Transfer Conference, Niagara Falls, NY, Aug. 5–8.

Ozisik, M. H., 1980, *Heat Conduction*, Wiley, New York, pp. 406–423.

A Table of Regenerator Effectiveness

F. E. Romie[1]

Nomenclature

$(hA)_{a,b}$ = thermal conductance, W/K
$t_{a,b}$ = flow period, s
t_t = time for one revolution of rotary regenerator, s
$(wc)_{a,b}$ = capacitance rate of gas, W/K
WC = thermal capacitance of matrix, J/K
$\Lambda_{a,b}$ = $(hA/wc)_{a,b}$
$\Pi_{a,b}$ = $(hAt)_{a,b}/WC$ for stationary regenerators; $(hA)_{a,b}t/_t/WC$ for rotary regenerators

Subscripts

a = assigned such that C^* (Table 1) is not greater than unity

Introduction

This note gives the thermal effectiveness, ϵ_r, of the counterflow regenerator in terms of four parameters, Ntu, C^*, C^*_{rr}, and hA^*, over the range Ntu = 1 to 128, $C^* = 0.8$ to 1, $C^*_{rr} = 0$ to 1, and $hA^* = 0.5$ to 1. These parameters are defined in Table 1 for both rotary and single stationary regenerators. Table 1 also expresses the four parameters in terms of an alternative set of parameters often used in regenerator analysis: Λ_a, Λ_b, Π_a, Π_b.

To provide interpolation accuracy, Table 2 presents ϵ_r in the form

$$\phi = 1 - \epsilon_r/\epsilon_c \tag{1}$$

in which ϵ_c, the thermal effectiveness of the counterflow recuperator, is dependent on Ntu and C^* only

$$\epsilon_c = \text{Ntu}/(1 + \text{Ntu}), \qquad C^* = 1 \tag{2}$$

$$\epsilon_c = [1 - \exp(\text{Ntu}(C^* - 1))]/[1 - C^* \exp(\text{Ntu}(C^* - 1))], \qquad C^* < 1 \tag{3}$$

Note that 100ϕ is the percentage by which ϵ_r is less than ϵ_c and that ϕ goes to zero as C^*_{rr} goes to zero. Also note that Table 2,

[1]Palos Verdes Estates, CA 90274.

Contributed by the Heat Transfer Division for publication in the JOURNAL OF HEAT TRANSFER. Manuscript received by the Heat Transfer Division April 25, 1989; revision received July 7, 1989. Keywords: Heat Exchangers.

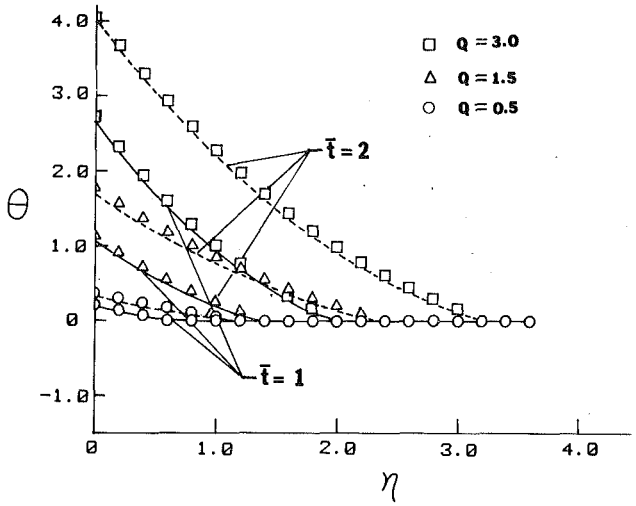

Fig. 1 Analytical and numerical temperature profile comparison with various heat fluxes at two different times

$$d\eta_p/d\bar{t} = Q \operatorname{erfc}(\eta_p/2\sqrt{\bar{t}})$$

with $\eta_p = 0$ at $\bar{t} = 0$.

In the absence of an exact solution in the existing literature, numerical solutions by the standard enthalpy method were carried out and compared with the present analytical solution. Good agreement is shown in Fig. 1 between the analytical (indicated by lines) and the numerical (circles, etc.) results.

Discussion

At the initial state of each problem studied, it is seen that either the temperature is discontinuous at a boundary or the initial temperature is unspecified in the newly evolved phase. In the latter class of problems where the initial temperature profile is unspecified, a constant but undetermined initial temperature T_c is introduced, which makes the Laplace transform method a viable solution technique to these phase-change problems. As shown in Problem 1, the introduced initial temperature T_c, given by equation (9), turns out to be neither the imposed surface temperature T_w nor the initial temperature of the original phase T_m. Had we mistakenly taken T_c as T_m and substituted it into $T_1(x, 0)$ in equation (5), the result would have yielded an erroneous answer. The proposed method is to leave T_c unspecified until the closed-form temperature profile is obtained. Then the proper value of T_c is determined automatically by applying the remaining boundary condition given by equation (3).

In the other class of phase-change problems where the problem of interest lies in the original phase (see Problem 2), one of the boundary conditions suffers a discontinuity initially. To overcome the discontinuity difficulty and to make the Laplace transform technique applicable, we again introduced at the discontinuous boundary a temperature, the value of which is not determined a priori. The introduced temperature allows the Laplace transform technique to proceed to yield the solution, and the solution obtained is in turn used to determine the unspecified value by applying one of the given boundary conditions.

While the proposed technique can systematically derive exact solutions of phase-change problems by the standard Laplace transform method without the need of educated guesses of trial solutions, there are limitations that should be noted. The solution technique obviously does not apply for nonlinearity caused by temperature-dependent thermal properties or by nonlinear boundary conditions. Other limitations may exist, which will be the subjects for future studies. Nevertheless, the technique can reproduce systematically all the existing exact solutions of phase-change problems, including those in cylindrical and spherical coordinates (Chan and Ku, 1984). The potential of the technique has been shown for obtaining the closed-form solution for problems for which no prior closed-form solutions are yet available.

Acknowledgments

The authors are grateful to John Chai for providing the numerical solution.

References

Carslaw, H. S., and Jaeger, J. C., 1959, *Conduction of Heat in Solids*, 2nd ed., Clarendon Press, London, pp. 282-295.

Chan, S. H., and Ku, J. K., 1984, "A Systematic Approach to the Exact Solutions of Some Phase-Change Problems," ASME Paper No. 84-HT-1, presented at the National Heat Transfer Conference, Niagara Falls, NY, Aug. 5-8.

Ozisik, M. H., 1980, *Heat Conduction*, Wiley, New York, pp. 406-423.

A Table of Regenerator Effectiveness

F. E. Romie[1]

Nomenclature

- $(hA)_{a,b}$ = thermal conductance, W/K
- $t_{a,b}$ = flow period, s
- t_t = time for one revolution of rotary regenerator, s
- $(wc)_{a,b}$ = capacitance rate of gas, W/K
- WC = thermal capacitance of matrix, J/K
- $\Lambda_{a,b}$ = $(hA/wc)_{a,b}$
- $\Pi_{a,b}$ = $(hAt)_{a,b}/WC$ for stationary regenerators; $(hA)_{a,b}t/_t/WC$ for rotary regenerators

Subscripts

- a = assigned such that C^* (Table 1) is not greater than unity

Introduction

This note gives the thermal effectiveness, ϵ_r, of the counterflow regenerator in terms of four parameters, Ntu, C^*, C^*_{rr}, and hA^*, over the range Ntu = 1 to 128, $C^* = 0.8$ to 1, $C^*_{rr} = 0$ to 1, and $hA^* = 0.5$ to 1. These parameters are defined in Table 1 for both rotary and single stationary regenerators. Table 1 also expresses the four parameters in terms of an alternative set of parameters often used in regenerator analysis: Λ_a, Λ_b, Π_a, Π_b.

To provide interpolation accuracy, Table 2 presents ϵ_r in the form

$$\phi = 1 - \epsilon_r/\epsilon_c \tag{1}$$

in which ϵ_c, the thermal effectiveness of the counterflow recuperator, is dependent on Ntu and C^* only

$$\epsilon_c = \text{Ntu}/(1 + \text{Ntu}), \qquad C^* = 1 \tag{2}$$

$$\epsilon_c = [1 - \exp(\text{Ntu}(C^* - 1))]/[1 - C^* \exp(\text{Ntu}(C^* - 1))], \qquad C^* < 1 \tag{3}$$

Note that 100ϕ is the percentage by which ϵ_r is less than ϵ_c and that ϕ goes to zero as C^*_{rr} goes to zero. Also note that Table 2,

[1]Palos Verdes Estates, CA 90274.

Contributed by the Heat Transfer Division for publication in the JOURNAL OF HEAT TRANSFER. Manuscript received by the Heat Transfer Division April 25, 1989; revision received July 7, 1989. Keywords: Heat Exchangers.

as indicated in the footnote, gives ϕ for two values of hA^*, 1 and 0.5.

The regenerator described satisfies the usual idealizations. (1) The fluid capacitance rates, $(wc)_a$ and $(wc)_b$, and the thermal conductances, $(hA)_a$ and $(hA)_b$, for transfer of heat between the fluids and matrix are uniform and constant as is the thermal capacitance, WC, of the regenerator matrix. (2) No heat is conducted in the matrix in the direction of fluid flow. (3) The matrix material offers no resistance to heat flow in the direction normal to fluid flow. (Biot's number is very small.) (4) The ratios of the thermal capacitances of the fluids contained, at any instant, in the matrix to the thermal capacitance of the containing matrix are negligibly small and are treated as zero. This latter idealization means, in effect, that the fluids must be gases and that transit times for gas particles to flow through the matrix must be negligibly small compared to the flow periods t_a and t_b.

Table 1 Parameter definitions; A = stationary regenerators, B = rotary regenerators

		A	B
Ntu	$\dfrac{\Lambda_a}{1+\dfrac{\Pi_a}{\Pi_b}}$	$\dfrac{\Lambda_a}{1+hA^*}$	$\dfrac{\Lambda_a}{1+hA^*}$
C^*	$\dfrac{\Pi_a\Lambda_b}{\Pi_b\Lambda_a}$	$\dfrac{(wct)_a}{(wct)_b}$	$\dfrac{(wc)_a}{(wc)_b}$
C^*_{rr}	$\dfrac{\Pi_a}{\Lambda_a}$	$\dfrac{(wct)_a}{WC}$	$\dfrac{(wc)_a t_t}{WC}$
hA^*	$\dfrac{\Pi_a}{\Pi_b}$	$\dfrac{(hAt)_a}{(hAt)_b}$	$\dfrac{(hA)_a}{(hA)_b}$

Discussion

Linear interpolation of ϕ in Table 2 is suitable with respect to Ntu, C^*, and hA^*, but logarithmic interpolation gives bet-

Table 2 ϕ(1)

		C_{rr}*						
Ntu	C*	.1	.2	.4	.6	.8	.9	1
1	1.00	.0007-00	.0029-00	.0114+00	.0253+00	.0440+02	.0551+03	.0671+05
2	1.00	.0011-00	.0043-00	.0171-02	.0376-03	.0652-04	.0814-03	.0990-02
4	1.00	.0013-00	.0052-00	.0197-01	.0424-03	.0737-05	.0928-05	.1142-04
8	1.00	.0014-00	.0053-00	.0183-00	.0382-00	.0678-03	.0876-05	.1112-05
16	1.00	.0014-00	.0045-00	.0143-00	.0294-00	.0540-02	.0725-04	.0971-04
32	1.00	.0011-00	.0033-00	.0098-00	.0202-00	.0386-00	.0546-02	.0791-03
64	1.00	.0008-00	.0022-00	.0061-00	.0127-00	.0256-00	.0383-01	.0616-02
128	1.00	.0005-00	.0013-00	.0036-00	.0076-00	.0160-00	.0253-00	.0466-02
1	.95	.0007+00	.0030+00	.0117+02	.0260+04	.0453+07	.0566+09	.0689+12
2	.95	.0011+00	.0045+00	.0178+01	.0391+02	.0677+05	.0845+07	.1027+10
4	.95	.0014+00	.0054+01	.0205+03	.0443+05	.0772+06	.0972+08	.1196+11
8	.95	.0015+00	.0055+00	.0190+03	.0400+05	.0714+08	.0924+10	.1174+13
16	.95	.0014+00	.0045+01	.0144+02	.0301+05	.0564+09	.0765+11	.1032+15
32	.95	.0010+00	.0029+00	.0088+01	.0190+03	.0384+09	.0561+12	.0834+18
64	.95	.0004+00	.0011+00	.0037+00	.0089+02	.0213+07	.0352+12	.0622+20
128	.95	.0000+00	.0001+00	.0006+00	.0022+00	.0081+04	.0174+11	.0428+21
1	.90	.0008+00	.0030+01	.0121+03	.0267+08	.0465+13	.0582+16	.0708+20
2	.90	.0012+00	.0047+01	.0184+04	.0406+08	.0702+15	.0876+18	.1064+23
4	.90	.0014+01	.0056+02	.0213+06	.0461+12	.0805+18	.1014+22	.1247+27
8	.90	.0015+00	.0055+02	.0193+06	.0410+13	.0740+22	.0962+27	.1227+32
16	.90	.0012+00	.0041+01	.0134+04	.0289+10	.0562+22	.0777+29	.1063+37
32	.90	.0006+00	.0018+00	.0060+02	.0144+07	.0333+20	.0521+29	.0820+40
64	.90	.0001+00	.0002+00	.0010+00	.0035+03	.0130+14	.0269+27	.0567+41
128	.90	.0000+00	.0000+00	.0001+00	.0002+00	.0026+06	.0102+20	.0377+40
1	.85	.0008+00	.0031+02	.0124+05	.0275+11	.0478+19	.0598+23	.0727+28
2	.85	.0012+01	.0049+02	.0191+08	.0421+15	.0728+25	.0907+30	.1101+37
4	.85	.0015+00	.0058+03	.0220+10	.0478+20	.0836+32	.1054+38	.1296+45
8	.85	.0015+00	.0054+03	.0191+10	.0413+22	.0758+36	.0991+45	.1269+52
16	.85	.0010+00	.0034+01	.0115+06	.0261+17	.0540+36	.0767+47	.1072+57
32	.85	.0003+00	.0008+01	.0033+02	.0095+09	.0269+30	.0464+47	.0785+60
64	.85	.0000+00	.0000+00	.0002+00	.0012+02	.0077+19	.0212+40	.0529+58
128	.85	.0000+00	.0000+00	.0000+00	.0000+00	.0010+05	.0072+27	.0359+50
1	.80	.0008+00	.0032+02	.0128+07	.0283+15	.0492+25	.0614+31	.0747+37
2	.80	.0013+00	.0050+03	.0198+11	.0435+23	.0753+37	.0938+44	.1139+51
4	.80	.0015+01	.0059+04	.0226+15	.0492+30	.0865+47	.1091+56	.1343+63
8	.80	.0014+01	.0052+04	.0186+14	.0410+30	.0767+52	.1011+63	.1302+73
16	.80	.0007+01	.0026+02	.0093+07	.0226+22	.0505+51	.0743+67	.1064+79
32	.80	.0001+00	.0003+01	.0016+02	.0058+09	.0214+40	.0414+63	.0752+78
64	.80	.0000+00	.0000+00	.0000+00	.0004+01	.0050+21	.0181+50	.0510+68
128	.80	.0000+00	.0000+00	.0000+00	.0000+00	.0005+05	.0062+31	.0354+53

(1) Example : Ntu=8 , C*=.9 , C_{rr}*=.4 ; Entry=.0193+06
hA*=1.0 ; ϕ = .0193
hA*=0.5 ; ϕ = .0193+.0006=.0199

ter accuracy with respect to C^*_{rr}. For example, to find the thermal effectiveness for Ntu = 11.6, $C^* = 0.873$, $C^*_{rr} = 0.3$, and $hA^* = 0.80$ one uses linear interpolation to find, at Ntu = 11.6, $C^* = 0.873$ and $hA^* = 0.80$; $\phi_1 = 0.0047$ with $C^*_{rr1} = 0.20$ and $\phi_2 = 0.0164$ with $C^*_{rr2} = 0.40$. For logarithmic interpolation let $n = \log(\phi_1/\phi_2)/\log(C^*_{rr1}/C^*_{rr2})$; then $\phi = \phi_1(C^*_{rr}/C^*_{rr1})^n$, from which $\phi = 0.0098$. The thermal effectiveness of the recuperator with Ntu = 11.6 and $C^* = 0.873$ is, from equation (3), 0.9636. Thus the regenerator effectiveness is $\epsilon_r = 0.9636(1 - 0.0098) = 0.9542$. This value is the value given by the computer program so that no error has been introduced by interpolation in this example. If linear interpolation were used with respect to C^*_{rr} the interpolated effectiveness would be 0.9534, which is 0.08 percent less than the correct value.

The maximum errors attributable to interpolation can be expected to be very nearly equal to those at the midpoints of adjacent parameter values listed in Table 2. For example Ntu = 6, $C^* = 0.975$, $C^*_{rr} = 0.3$, and $hA^* = 0.75$ is a midpoint. Comparison of the thermal effectiveness values found by interpolation at the 168 midpoints afforded by Table 2 with values found with the computer program showed an rms error of 0.20 percent with a maximum error of +0.46 percent occurring at Ntu = 3, $C^* = 0.825$, $C^*_{rr} = 0.95$, and $hA^* = 0.75$. The maximum interpolation errors for $C^*_{rr} \le 0.40$ have an rms error of 0.03 percent with a maximum error of −0.10 percent. On average, the errors introduced by interpolation will, of course, be less than these maximum errors.

References

Bahnke, G. D., and Howard, C. P., 1964, "The Effect of Longitudinal Heat Conduction on Periodic-Flow Heat Exchanger Performance," ASME JOURNAL OF HEAT TRANSFER, Vol. 86, pp. 105–119.

Lambertson, T. J., 1958, "Performance Factors of a Periodic-Flow Heat Exchanger," *Transactions of the ASME*, Vol. 80, pp. 586–592.

Romie, F. E., and Baclic, B. S., 1988, "Methods for Rapid Calculation of the Operation of Asymmetric Counterflow Regenerators," ASME JOURNAL OF HEAT TRANSFER, Vol. 110, pp. 785–788.

Exact Solution for Slug Flow Laminar Heat Transfer Development in a Rectangular Duct With Isothermal Walls

G. D. Thiart[1]

Introduction

The transfer of heat to or from a fluid in the entrance region of a straight duct is almost independent of the momentum transfer that is taking place simultaneously if the Prandtl number of the fluid is very low, as is the case with liquid metals. The thermal boundary layer develops much faster than the corresponding hydrodynamic boundary layer; it is therefore a good approximation to assume that a uniform velocity profile (slug flow) exists. The differential equation describing the conservation of energy is then simply

$$U\frac{\partial T}{\partial x} = \frac{k}{\rho c}\left(\frac{\partial^2 T}{\partial x^2} + \frac{\partial^2 T}{\partial y^2} + \frac{\partial^2 T}{\partial z^2}\right) \tag{1}$$

for constant fluid density ρ, heat capacity c, and thermal conductivity k. The solution of equation (1) can be written in a simple closed form for the case of a rectangular duct with isothermal walls, in contrast to the corresponding solutions for other simple geometries, which are usually complicated by the presence of eigenvalues that have to be calculated from so-called eigenfunctions (e.g., zeros of Bessel functions for the circular duct). Nevertheless, this solution (for the rectangular duct) cannot be found in either the extensive compendium of laminar duct flow solutions of Shah and London (1978), nor in the relevant chapter on forced convection heat transfer in ducts in the *Handbook of Heat Transfer Fundamentals* (1985), nor in heat transfer textbooks such as those of Rohsenow and Choi (1961), Kays (1966), Burmeister (1983), or Bejan (1984).

Values of fully developed Nusselt number as function of duct aspect ratio are given by Hartnett and Irvine (1957), but these were apparently calculated from the equation for transient heat conduction without conduction in the axial direction. Now, since the maximum Reynolds number for laminar heat transfer is of the order 2000, while the Prandtl number for liquid metals is of the order 0.001, it follows, as pointed out by Rohsenow (1988), that the maximum Peclet number for the case under discussion is approximately 2. It is clear, therefore, that axial conduction effects are not negligible in practical applications.

Temperature Field Solution

For the configuration shown in Fig. 1, the boundary conditions subject to which equation (1) must be solved are given by

$$T = T_w \text{ at } y = \pm W/2, \quad z = \pm H/2 \tag{2a}$$

$$T = T_i \text{ at } x = 0 \tag{2b}$$

The mathematical problem described by equations (1) and (2) can be written in dimensionless form in terms of the dimensionless variables $\xi = x/D_h\mathrm{Pe}$, $\eta = y/D_h$, $\zeta = z/D_h$, and $\theta = (T_w - T)/(T_w - T_i)$, as well as the Peclet number $\mathrm{Pe} = \rho c U D_h/k$ (with D_h denoting the hydraulic diameter of the duct) as

$$\frac{\partial\theta}{\partial\xi} = \frac{1}{\mathrm{Pe}^2}\frac{\partial^2\theta}{\partial\xi^2} + \frac{\partial^2\theta}{\partial\eta^2} + \frac{\partial^2\theta}{\partial\zeta^2} \tag{3}$$

which have to be solved subject to the boundary conditions

$$\theta = 0 \text{ at } \eta = \pm W/2D_h, \quad \zeta = \pm H/2D_h \tag{3a}$$

$$\theta = 1 \text{ at } \xi = 0 \tag{3b}$$

The solution is obtained by the method of separation of variables, by assuming a product solution of the type $\theta = XYZ$, where X, Y, and Z are functions of ξ, η, and ζ, respectively. It follows that a solution satisfying all the boundary conditions except for (3b) is given by

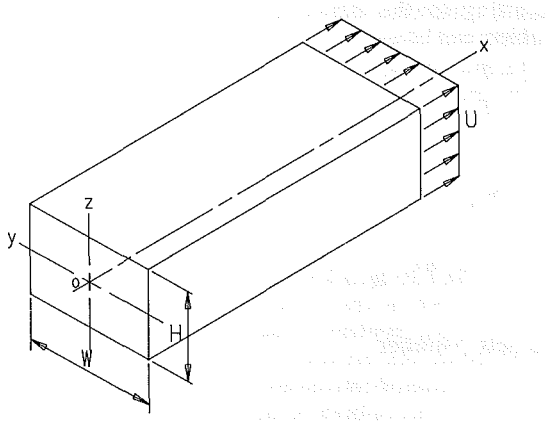

Fig. 1 Coordinate definition

[1]Bureau for Mechanical Engineering, University of Stellenbosch, Stellenbosch 7600, South Africa.

Contributed by the Heat Transfer Division for publication in the JOURNAL OF HEAT TRANSFER. Manuscript received by the Heat Transfer Division April 8, 1988; revision received June 25, 1989. Keywords: Forced Convection.

ter accuracy with respect to C^*_{rr}. For example, to find the thermal effectiveness for Ntu = 11.6, $C^* = 0.873$, $C^*_{rr} = 0.3$, and $hA^* = 0.80$ one uses linear interpolation to find, at Ntu = 11.6, $C^* = 0.873$ and $hA^* = 0.80$; $\phi_1 = 0.0047$ with $C^*_{rr1} = 0.20$ and $\phi_2 = 0.0164$ with $C^*_{rr2} = 0.40$. For logarithmic interpolation let $n = \log(\phi_1/\phi_2)/\log(C^*_{rr1}/C^*_{rr2})$; then $\phi = \phi_1(C^*_{rr}/C^*_{rr1})^n$, from which $\phi = 0.0098$. The thermal effectiveness of the recuperator with Ntu = 11.6 and $C^* = 0.873$ is, from equation (3), 0.9636. Thus the regenerator effectiveness is $\epsilon_r = 0.9636(1 - 0.0098) = 0.9542$. This value is the value given by the computer program so that no error has been introduced by interpolation in this example. If linear interpolation were used with respect to C^*_{rr} the interpolated effectiveness would be 0.9534, which is 0.08 percent less than the correct value.

The maximum errors attributable to interpolation can be expected to be very nearly equal to those at the midpoints of adjacent parameter values listed in Table 2. For example Ntu = 6, $C^* = 0.975$, $C^*_{rr} = 0.3$, and $hA^* = 0.75$ is a midpoint. Comparison of the thermal effectiveness values found by interpolation at the 168 midpoints afforded by Table 2 with values found with the computer program showed an rms error of 0.20 percent with a maximum error of +0.46 percent occurring at Ntu = 3, $C^* = 0.825$, $C^*_{rr} = 0.95$, and $hA^* = 0.75$. The maximum interpolation errors for $C^*_{rr} \le 0.40$ have an rms error of 0.03 percent with a maximum error of −0.10 percent. On average, the errors introduced by interpolation will, of course, be less than these maximum errors.

References

Bahnke, G. D., and Howard, C. P., 1964, "The Effect of Longitudinal Heat Conduction on Periodic-Flow Heat Exchanger Performance," ASME JOURNAL OF HEAT TRANSFER, Vol. 86, pp. 105–119.

Lambertson, T. J., 1958, "Performance Factors of a Periodic-Flow Heat Exchanger," *Transactions of the ASME*, Vol. 80, pp. 586–592.

Romie, F. E., and Baclic, B. S., 1988, "Methods for Rapid Calculation of the Operation of Asymmetric Counterflow Regenerators," ASME JOURNAL OF HEAT TRANSFER, Vol. 110, pp. 785–788.

Exact Solution for Slug Flow Laminar Heat Transfer Development in a Rectangular Duct With Isothermal Walls

G. D. Thiart[1]

Introduction

The transfer of heat to or from a fluid in the entrance region of a straight duct is almost independent of the momentum transfer that is taking place simultaneously if the Prandtl number of the fluid is very low, as is the case with liquid metals. The thermal boundary layer develops much faster than the corresponding hydrodynamic boundary layer; it is therefore a good approximation to assume that a uniform velocity profile (slug flow) exists. The differential equation describing the conservation of energy is then simply

$$U\frac{\partial T}{\partial x} = \frac{k}{\rho c}\left(\frac{\partial^2 T}{\partial x^2} + \frac{\partial^2 T}{\partial y^2} + \frac{\partial^2 T}{\partial z^2}\right) \tag{1}$$

for constant fluid density ρ, heat capacity c, and thermal conductivity k. The solution of equation (1) can be written in a simple closed form for the case of a rectangular duct with isothermal walls, in contrast to the corresponding solutions for other simple geometries, which are usually complicated by the presence of eigenvalues that have to be calculated from so-called eigenfunctions (e.g., zeros of Bessel functions for the circular duct). Nevertheless, this solution (for the rectangular duct) cannot be found in either the extensive compendium of laminar duct flow solutions of Shah and London (1978), nor in the relevant chapter on forced convection heat transfer in ducts in the *Handbook of Heat Transfer Fundamentals* (1985), nor in heat transfer textbooks such as those of Rohsenow and Choi (1961), Kays (1966), Burmeister (1983), or Bejan (1984).

Values of fully developed Nusselt number as function of duct aspect ratio are given by Hartnett and Irvine (1957), but these were apparently calculated from the equation for transient heat conduction without conduction in the axial direction. Now, since the maximum Reynolds number for laminar heat transfer is of the order 2000, while the Prandtl number for liquid metals is of the order 0.001, it follows, as pointed out by Rohsenow (1988), that the maximum Peclet number for the case under discussion is approximately 2. It is clear, therefore, that axial conduction effects are not negligible in practical applications.

Temperature Field Solution

For the configuration shown in Fig. 1, the boundary conditions subject to which equation (1) must be solved are given by

$$T = T_w \text{ at } y = \pm W/2, \quad z = \pm H/2 \tag{2a}$$

$$T = T_i \text{ at } x = 0 \tag{2b}$$

The mathematical problem described by equations (1) and (2) can be written in dimensionless form in terms of the dimensionless variables $\xi = x/D_h\mathrm{Pe}$, $\eta = y/D_h$, $\zeta = z/D_h$, and $\theta = (T_w - T)/(T_w - T_i)$, as well as the Peclet number $\mathrm{Pe} = \rho c U D_h/k$ (with D_h denoting the hydraulic diameter of the duct) as

$$\frac{\partial\theta}{\partial\xi} = \frac{1}{\mathrm{Pe}^2}\frac{\partial^2\theta}{\partial\xi^2} + \frac{\partial^2\theta}{\partial\eta^2} + \frac{\partial^2\theta}{\partial\zeta^2} \tag{3}$$

which have to be solved subject to the boundary conditions

$$\theta = 0 \text{ at } \eta = \pm W/2D_h, \quad \zeta = \pm H/2D_h \tag{3a}$$

$$\theta = 1 \text{ at } \xi = 0 \tag{3b}$$

The solution is obtained by the method of separation of variables, by assuming a product solution of the type $\theta = XYZ$, where X, Y, and Z are functions of ξ, η, and ζ, respectively. It follows that a solution satisfying all the boundary conditions except for (3b) is given by

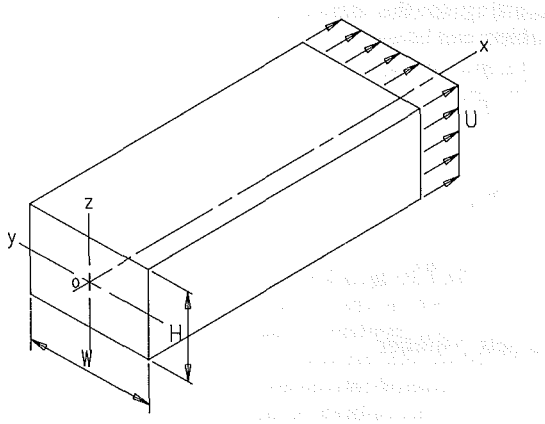

Fig. 1 Coordinate definition

[1]Bureau for Mechanical Engineering, University of Stellenbosch, Stellenbosch 7600, South Africa.

Contributed by the Heat Transfer Division for publication in the JOURNAL OF HEAT TRANSFER. Manuscript received by the Heat Transfer Division April 8, 1988; revision received June 25, 1989. Keywords: Forced Convection.

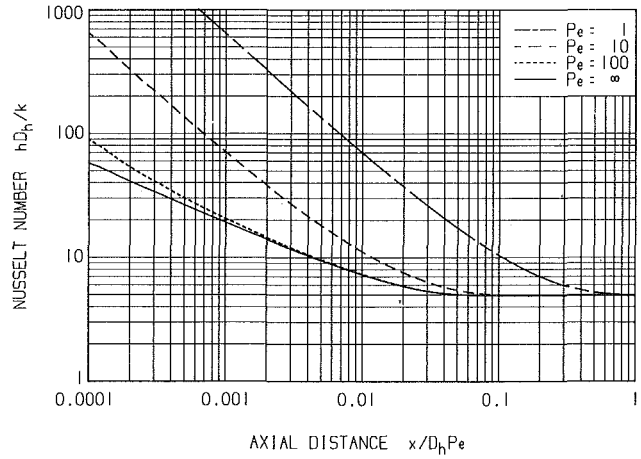

Fig. 2 Nusselt numbers for a square duct

$$\theta_{mn} =$$

$$C_{mn}\exp\left[\tfrac{1}{2}\mathrm{Pe}^2\left\{1-\sqrt{1+\left(\frac{2\pi D_h}{\mathrm{Pe}}\right)^2\left(\frac{m^2}{W^2}+\frac{n^2}{H^2}\right)}\right\}\xi\right]$$

$$\times\cos\left(m\pi\frac{D_h}{W}\eta\right)\cos\left(n\pi\frac{D_h}{H}\zeta\right) \tag{4}$$

Since the governing equation (3) is linear, we can superpose solutions for all m, n to arrive at a possible solution

$$\theta=\sum_m\sum_n C_{mn}\exp$$

$$\left[\tfrac{1}{2}\mathrm{Pe}^2\left\{1-\sqrt{1+\left(\frac{2\pi D_h}{\mathrm{Pe}}\right)^2\left(\frac{m^2}{W^2}+\frac{n^2}{H^2}\right)}\right\}\xi\right]$$

$$\times\cos\left(m\pi\frac{D_h}{W}\eta\right)\cos\left(n\pi\frac{D_h}{H}\zeta\right)\quad\text{for } m,\ n=1,\ 3,\ \ldots \tag{5}$$

The constants C_{mn} are determined from the remaining boundary condition, equation (3*b*), from which we find that

$$C_{mn}=\frac{4D_h^2}{WH}\int_{-H/2D_h}^{H/2D}\int_{-W/2D_h}^{W/2D_h}\cos\left(m\pi\frac{D_h}{W}\eta\right)$$

$$\cos\left(n\pi\frac{D_h}{H}\zeta\right)d\eta d\zeta=\frac{16}{\pi^2 mn}(-1)^{\frac{1}{2}(m+n)+1}$$

$$\text{for } m,\ n=1,\ 3,\ \ldots \tag{6}$$

Reverting to the dimensional form, the solution to the problem can be written as

$$\frac{T_w-T}{T_w-T_i}=\frac{16}{\pi^2}\sum_m\sum_n\frac{1}{mn}(-1)^{\frac{1}{2}(m+n)+1}$$

$$\times\exp\left[\tfrac{1}{2}\mathrm{Pe}\left\{1-\sqrt{1+\left(\frac{2\pi D_h}{\mathrm{Pe}}\right)^2\left(\frac{m^2}{W^2}+\frac{n^2}{H^2}\right)}\right\}\frac{x}{D_h}\right]$$

$$\times\cos\left(m\pi\frac{y}{W}\right)\cos\left(n\pi\frac{z}{H}\right)\quad\text{for } m,\ n=1,\ 3,\ \ldots \tag{7}$$

Nusselt Number

For the sake of convenience, the exponential term in equation (7) will henceforth be denoted by $E(x)$. Now, since the hydraulic diameter for a rectangular duct is equal to $2WH/(H+W)$, it follows, with $\alpha=H/W$ denoting the duct aspect ratio, that $D_h/H=2/(1+\alpha)$. Thus

$$E(x)=\exp\left[\tfrac{1}{2}\mathrm{Pe}\left\{1-\sqrt{1+\left(\frac{4\pi}{\mathrm{Pe}}\right)^2\frac{(\alpha^2m^2+n^2)}{(1+\alpha)^2}}\right\}\frac{x}{D_h}\right] \tag{8}$$

The average or mixing temperature at any axial position can be obtained from the temperature solution in the usual manner:

$$\frac{T_w-T_m}{T_w-T_i}=\frac{1}{HWU}\int_{-H/2}^{H/2}\int_{-W/2}^{W/2}U\frac{T_w-T}{T_w-T_i}\,dydz$$

$$=\frac{64}{\pi^4}\sum_m\sum_n\frac{E(x)}{m^2n^2}\quad\text{for } m,\ n=1,\ 3,\ \ldots \tag{9}$$

The film coefficient for the side $y=W/2$ is

$$h_y=\frac{k\left(\frac{\partial T}{\partial y}\right)_{y=W/2}}{T_w-T_m}$$

$$=\frac{16k}{\pi W}\frac{T_w-T_i}{T_w-T_m}\sum_m\sum_n\frac{1}{n}(-1)^{m+\frac{1}{2}(n+1)}$$

$$\times E(x)\cos\left(n\pi\frac{z}{H}\right)\quad\text{for } m,\ n=1,\ 3,\ \ldots \tag{10}$$

The average film coefficient for the side of the duct under consideration is obtained by integrating this expression over the height of the duct:

$$\bar{h}_y=\frac{1}{H}\int_{-H/2}^{H/2}h_y dz$$

$$=\frac{32k}{\pi^2W}\frac{T_w-T_i}{T_w-T_m}\sum_m\sum_n\frac{1}{n^2}E(x)\quad\text{for } m,\ n=1,\ 3,\ \ldots \tag{11}$$

The average film coefficient $\bar{h}_z$ over the side $z=H/2$ is given by a similar expression. It follows that the average film coefficient over all four sides of the duct is

$$\bar{h}=\frac{H\bar{h}_y+W\bar{h}_z}{H+W}$$

$$=\frac{32k}{\pi^2(H+W)}\frac{T_w-T_i}{T_w-T_m}\sum_m\sum_n\left(\frac{W}{Hm^2}+\frac{H}{Wn^2}\right)E(x)$$

$$\text{for } m,\ n=1,\ 3,\ \ldots \tag{12}$$

The local Nusselt number as function of axial distance is therefore

$$\mathrm{Nu}=\frac{\bar{h}D_h}{k}$$

$$=\frac{64WH}{\pi^2(H+W)^2}\frac{T_w-T_i}{T_w-T_m}\sum_m\sum_n\left(\frac{W}{Hm^2}+\frac{H}{Wn^2}\right)E(x)$$

$$=\frac{\pi^2}{(1+\alpha)^2}\sum_m\sum_n\left(\frac{1}{m^2}+\frac{\alpha^2}{n^2}\right)E(x)\Big/\sum_m\sum_n\frac{1}{m^2n^2}E(x)$$

$$\text{for } m,\ n=1,\ 3,\ \ldots \tag{13}$$

With this expression, values of Nusselt number as functions of duct aspect ratio, Peclet number, and dimensionless axial distance were calculated on the University of Stellenbosch VAX 785 in double precision FORTRAN 77. In summing the series, two suggestions of Kreitzberg and Shneiderman (1972)

were implemented in order to reduce roundoff errors, i.e., summing the series backward and creating subsums. The maximum values of m (m_{max}) and n (n_{max}) were chosen such that the values of the terms for $n=1$, $m=m_{max}$ and $n=n_{max}$, $m=1$ were always less than 10^{-6} times that of the fully summed series. This meant that up to 16 million terms of the series had to be calculated for the lowest Peclet number/lowest axial distance combinations. An indication of the convergence of the numerical summation process is that the difference in Nusselt number calculated with the 10^{-6} limitation always differed by less than 0.005 percent from corresponding values calculated with a 10^{-10} limitation.

Typical results are presented in Fig. 2 for a square duct. The increase in Nusselt number for Peclet numbers of order 10 or less over that for the no-axial-conduction case, represented by the $Pe=\infty$ curve, is clearly evident.

Finally, it was found by numerical computation that the fully developed Nusselt number can be expressed in terms of duct aspect ratio as

$$Nu_\infty = \pi^2 \frac{1+\alpha^2}{(1+\alpha)^2} \tag{14}$$

Although this relationship could not be proved mathematically insofar as it represents the limiting value of Nu (equation (13)) as x tends to infinity, it does exactly reproduce the relationship given in graphic form by Hartnett and Irvine (1957).

References

Bejan, H., 1984, *Convection Heat Transfer*, Wiley, Toronto.

Burmeister, L. C., 1983, *Convective Heat Transfer*, Wiley, New York.

Hartnett, J. P., and Irvine, T. F., 1957, "Nusselt Values for Estimating Turbulent Liquid Metal Heat Transfer in Noncircular Ducts," *AIChE J.*, Vol. 3, pp. 313–317.

Kays, W. M., 1966, *Convective Heat and Mass Transfer*, McGraw-Hill, New York.

Kays, W. M., and Perkins, H. C., 1985, "Forced Convection, Internal Flow in Ducts," *Handbook of Heat Transfer Fundamentals*, 2nd ed., W. M. Rohsenow et al., eds., McGraw-Hill, New York.

Kreitzberg, C. B., and Shneiderman, B., 1972, *The Elements of FORTRAN Style: Techniques for Effective Programming*, Harcourt Brace Jovanovich, New York.

Rohsenow, W. M., and Choi, H. Y., 1961, *Heat, Mass, and Momentum Transfer*, Prentice-Hall, Englewood Cliffs, NJ.

Rohsenow, W. M., 1988, Personal Communication.

Shah, R. K., and London, A. L., 1978, "Laminar Flow Forced Convection in Ducts," Supplement 1 of *Advances in Heat Transfer*, T. F. Irvine and J. P. Hartnett, eds., Academic Press, New York.

Effect of Boundary Conditions on Mass Transfer Near the Base of a Cylinder in Crossflow

R. J. Goldstein,[1] J. Karni,[1,2] and Y. Zhu[1]

Nomenclature

d = diameter of test cylinder
h = local transfer coefficent of heat or mass
h_m = local mass transfer coefficient
h_o = local mass (heat) transfer coefficient on a flat surface without protruding cylinder
L = length of test cylinder (also, height of the wind tunnel) = 305 mm in present study
Re_d = Reynolds number based on U_∞ and d
Sh = local Sherwood number based on cylinder diameter
Sh_o = Sherwood number on a plate without protruding cylinder
U_∞ = mean velocity of mainstream
V1 = a horseshoe vortex; see Fig. 1
V2 = a small vortex located at the base of the cylinder; see Fig. 1
V3 = a small vortex located near the cylinder surface just above V2; see Fig. 1
x = downstream distance along the tunnel test section measured from upstream edge of cylinder; see Fig. 1
y = upward direction along the cylinder front stagnation line measured from the plate; see Fig. 1
z = lateral direction across the tunnel test section; see Fig. 1
δ = mainstream boundary layer thickness
δ^* = displacement thickness of mainstream boundary layer just upstream of the cylinder
θ = angle around the cylinder, measured in degrees from the front stagnation point

Introduction

The mass (heat) transfer pattern near the base of a cylinder in crossflow, at Re_d of 10,000–80,000, was described by Goldstein and Karni (1984) and Karni and Goldstein (1986). Two small, intense vortices within the horseshoe vortex system produce high values and steep gradients of the transport coefficient over a narrow strip extending from the cylinder base to about $0.07d$ above it. The studies also indicate the effects of cylinder diameter and endwall boundary layer thickness on these phenomena.

In those earlier studies an active cylinder and an inactive endwall were used, i.e., the test cylinder was coated with naphthalene, whose local sublimation rate during exposure to air flow was measured, while the endwall was not coated and was impermeable. In the analogous heat transfer case, an active surface corresponds to an isothermal surface, while an inactive or impermeable surface corresponds to an adiabatic one. An active naphthalene plate and inactive cylinders were used by Goldstein et al. (1985) in an investigation of mass (heat) transfer from the endwall near a protruding cylinder. Applications of heated cylinder-endwall components, such as in heat exchangers and gas turbines, generally involve heat transfer from all surfaces. In the present study a portion of the endwall and the test cylinder placed normal to it are coated with naphthalene (Fig. 1). Local mass transfer measurements are conducted on both surfaces and the results are compared to earlier data by Karni and Goldstein (1985) at $Re_d \approx 30{,}000$ and a similar δ^*/d ratio. Thus, the effect of changing the endwall boundary conditions from inactive to active on the mass (heat) transfer pattern is investigated.

Van Dresar and Mayle (1986) used a naphthalene sublimation technique to conduct a similar study at $Re_d = 110{,}000$. Their measurements with an inactive endwall confirmed the main trends reported earlier by Goldstein and Karni (1984) and Karni and Goldstein (1986). At $\theta = 0$ their data obtained with an active endwall are virtually identical to their results with an inactive endwall; but the active endwall diminishes the

[1]Mechanical Engineering Department, University of Minnesota, Minneapolis, MN 55455.

[2]Present address Weizmann Institute of Science, Rehovot 76100 Israel.

Contributed by the Heat Transfer Division for publication in the JOURNAL OF HEAT TRANSFER. Manuscript received by the Heat Transfer Division September 14, 1988. Keywords: Flow Separation, Forced Convection, Mass Transfer.

were implemented in order to reduce roundoff errors, i.e., summing the series backward and creating subsums. The maximum values of m (m_{max}) and n (n_{max}) were chosen such that the values of the terms for $n=1$, $m=m_{max}$ and $n=n_{max}$, $m=1$ were always less than 10^{-6} times that of the fully summed series. This meant that up to 16 million terms of the series had to be calculated for the lowest Peclet number/lowest axial distance combinations. An indication of the convergence of the numerical summation process is that the difference in Nusselt number calculated with the 10^{-6} limitation always differed by less than 0.005 percent from corresponding values calculated with a 10^{-10} limitation.

Typical results are presented in Fig. 2 for a square duct. The increase in Nusselt number for Peclet numbers of order 10 or less over that for the no-axial-conduction case, represented by the $Pe=\infty$ curve, is clearly evident.

Finally, it was found by numerical computation that the fully developed Nusselt number can be expressed in terms of duct aspect ratio as

$$Nu_\infty = \pi^2 \frac{1+\alpha^2}{(1+\alpha)^2} \tag{14}$$

Although this relationship could not be proved mathematically insofar as it represents the limiting value of Nu (equation (13)) as x tends to infinity, it does exactly reproduce the relationship given in graphic form by Hartnett and Irvine (1957).

References

Bejan, H., 1984, *Convection Heat Transfer*, Wiley, Toronto.

Burmeister, L. C., 1983, *Convective Heat Transfer*, Wiley, New York.

Hartnett, J. P., and Irvine, T. F., 1957, "Nusselt Values for Estimating Turbulent Liquid Metal Heat Transfer in Noncircular Ducts," *AIChE J.*, Vol. 3, pp. 313–317.

Kays, W. M., 1966, *Convective Heat and Mass Transfer*, McGraw-Hill, New York.

Kays, W. M., and Perkins, H. C., 1985, "Forced Convection, Internal Flow in Ducts," *Handbook of Heat Transfer Fundamentals*, 2nd ed., W. M. Rohsenow et al., eds., McGraw-Hill, New York.

Kreitzberg, C. B., and Shneiderman, B., 1972, *The Elements of FORTRAN Style: Techniques for Effective Programming*, Harcourt Brace Jovanovich, New York.

Rohsenow, W. M., and Choi, H. Y., 1961, *Heat, Mass, and Momentum Transfer*, Prentice-Hall, Englewood Cliffs, NJ.

Rohsenow, W. M., 1988, Personal Communication.

Shah, R. K., and London, A. L., 1978, "Laminar Flow Forced Convection in Ducts," Supplement 1 of *Advances in Heat Transfer*, T. F. Irvine and J. P. Hartnett, eds., Academic Press, New York.

Effect of Boundary Conditions on Mass Transfer Near the Base of a Cylinder in Crossflow

R. J. Goldstein,[1] J. Karni,[1,2] and Y. Zhu[1]

Nomenclature

d = diameter of test cylinder
h = local transfer coefficent of heat or mass
h_m = local mass transfer coefficient
h_o = local mass (heat) transfer coefficient on a flat surface without protruding cylinder
L = length of test cylinder (also, height of the wind tunnel) = 305 mm in present study
Re_d = Reynolds number based on U_∞ and d
Sh = local Sherwood number based on cylinder diameter
Sh_o = Sherwood number on a plate without protruding cylinder
U_∞ = mean velocity of mainstream
V1 = a horseshoe vortex; see Fig. 1
V2 = a small vortex located at the base of the cylinder; see Fig. 1
V3 = a small vortex located near the cylinder surface just above V2; see Fig. 1
x = downstream distance along the tunnel test section measured from upstream edge of cylinder; see Fig. 1
y = upward direction along the cylinder front stagnation line measured from the plate; see Fig. 1
z = lateral direction across the tunnel test section; see Fig. 1
δ = mainstream boundary layer thickness
δ^* = displacement thickness of mainstream boundary layer just upstream of the cylinder
θ = angle around the cylinder, measured in degrees from the front stagnation point

Introduction

The mass (heat) transfer pattern near the base of a cylinder in crossflow, at Re_d of 10,000–80,000, was described by Goldstein and Karni (1984) and Karni and Goldstein (1986). Two small, intense vortices within the horseshoe vortex system produce high values and steep gradients of the transport coefficient over a narrow strip extending from the cylinder base to about $0.07d$ above it. The studies also indicate the effects of cylinder diameter and endwall boundary layer thickness on these phenomena.

In those earlier studies an active cylinder and an inactive endwall were used, i.e., the test cylinder was coated with naphthalene, whose local sublimation rate during exposure to air flow was measured, while the endwall was not coated and was impermeable. In the analogous heat transfer case, an active surface corresponds to an isothermal surface, while an inactive or impermeable surface corresponds to an adiabatic one. An active naphthalene plate and inactive cylinders were used by Goldstein et al. (1985) in an investigation of mass (heat) transfer from the endwall near a protruding cylinder. Applications of heated cylinder-endwall components, such as in heat exchangers and gas turbines, generally involve heat transfer from all surfaces. In the present study a portion of the endwall and the test cylinder placed normal to it are coated with naphthalene (Fig. 1). Local mass transfer measurements are conducted on both surfaces and the results are compared to earlier data by Karni and Goldstein (1985) at $Re_d \approx 30{,}000$ and a similar δ^*/d ratio. Thus, the effect of changing the endwall boundary conditions from inactive to active on the mass (heat) transfer pattern is investigated.

Van Dresar and Mayle (1986) used a naphthalene sublimation technique to conduct a similar study at $Re_d = 110{,}000$. Their measurements with an inactive endwall confirmed the main trends reported earlier by Goldstein and Karni (1984) and Karni and Goldstein (1986). At $\theta = 0$ their data obtained with an active endwall are virtually identical to their results with an inactive endwall; but the active endwall diminishes the

[1]Mechanical Engineering Department, University of Minnesota, Minneapolis, MN 55455.

[2]Present address Weizmann Institute of Science, Rehovot 76100 Israel.

Contributed by the Heat Transfer Division for publication in the JOURNAL OF HEAT TRANSFER. Manuscript received by the Heat Transfer Division September 14, 1988. Keywords: Flow Separation, Forced Convection, Mass Transfer.

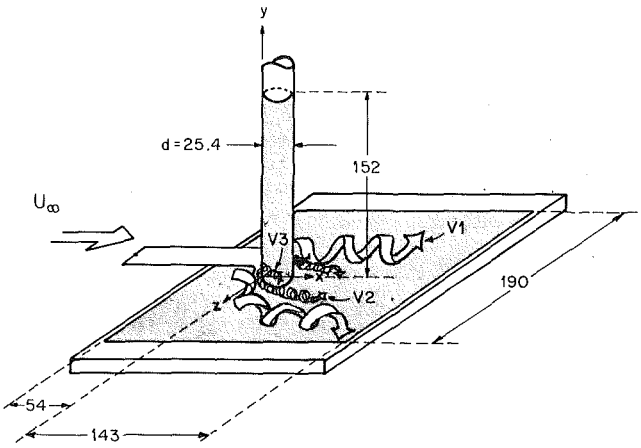

Fig. 1 Schematic view of the experimental setup and the vortex system. The shaded surfaces are covered with naphthalene. Dimensions in mm.

effect of the corner vortex (V2 in Fig. 1) at $\theta = 30$ and 60 deg. They did not report measurements over the endwall. Ireland and Jones (1986) used thermochromic liquid crystals to measure the local heat transfer coefficient on the endwall near a circular cylinder situated in fully developed passage flow, at Re_d of 9000–34,000 and $L/d = 1.0$ and 2.0. Their results are compared herein with the present measurements. Heat and mass transfer studies of narrowly spaced heat exchanger fins also show similar patterns to that presently observed over the endwall [cf. Kruckels (1972)].

Experimental Apparatus and Measurement Technique

The experimental configuration is shown in Fig. 1. The test plate is mounted such that its naphthalene-coated surface is aligned smoothly with the bottom-wall surface of the wind tunnel. The cylinder sits on top of, and perpendicular to, the naphthalene plate, held by a threaded bolt, which is fixed inside it and fitted through a 12.7-mm-dia hole in the plate; the bolt is secured with a nut to the other side of the plate. The naphthalene surface of the cylinder extends to its lower end, matching the naphthalene surface of the plate. The three vortices V1, V2, and V3, which directly affect the mass transfer distribution, are also shown schematically in Fig. 1. The inferred flow pattern is discussed by Goldstein and Karni (1984).

The wind tunnel used and the cylinder position in the tunnel are the same as those described by Karni and Goldstein (1986). The casting process, measurement procedure, and data acquisition and reduction techniques are similar to those described in the earlier papers from this laboratory. The maximum error in measuring the mass transfer coefficient is 6 percent over the cylinder, and 5 percent on the plate.

Results

In Fig. 2, the mass transfer variation along the cylinder, near its base, is shown at various angles around the cylinder. The present results are compared to data obtained with an inactive endwall (Karni and Goldstein, 1986) at similar Re_d, δ^*, and d. Very near the endwall, at $y/d < 0.03$, the Sh values of the present study are consistently lower than those obtained with an inactive endwall. Note that the first peak, detected at $y/d \approx 0.010$ when the endwall is inactive, is now observed at $y/d \approx 0.005$ (Figs. 2*a*, *b*, *c*). This shift is partially accounted for by the sublimation of the endwall, which causes a slight downward shift in the location of the corner vortex V2 (Fig. 1). At θ = 5–10 deg and 50–55 deg (Figs. 2*a* and *b*) the Sh maximum nearest to the endwall is 12–15 percent lower in the

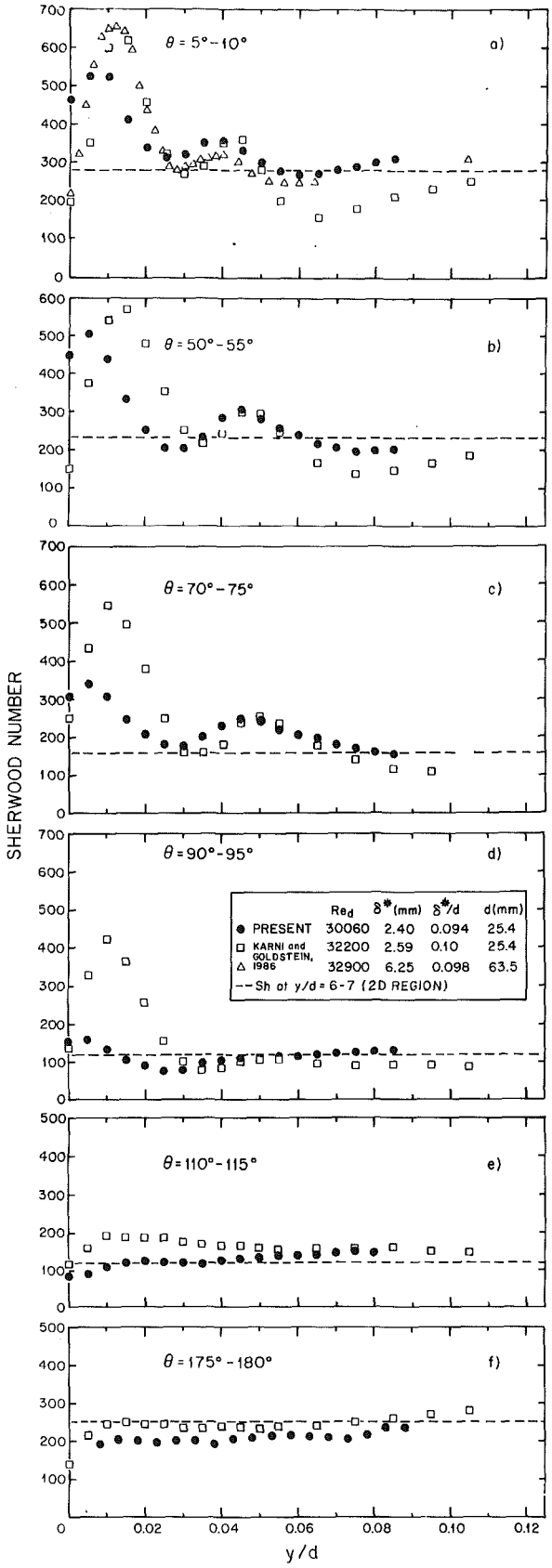

Fig. 2 Variation of Sherwood number along the cylinder near the endwall, at representative angles. Data from Karni and Goldstein (1986) were taken with an inactive endwall.

present measurements than in the earlier ones. The influence of the active endwall increases with θ and at $\theta = 70$–75 deg (Fig.

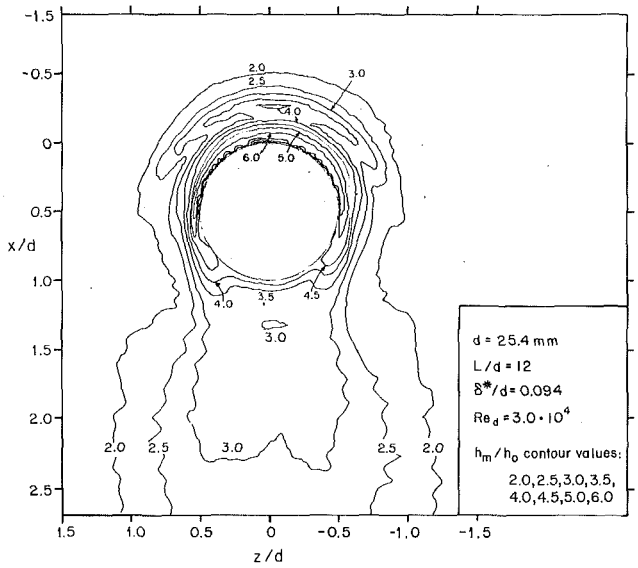

Fig. 3 Contours of h_m/h_o over an active endwall near a protruding active cylinder; $Sh_o \approx 45$

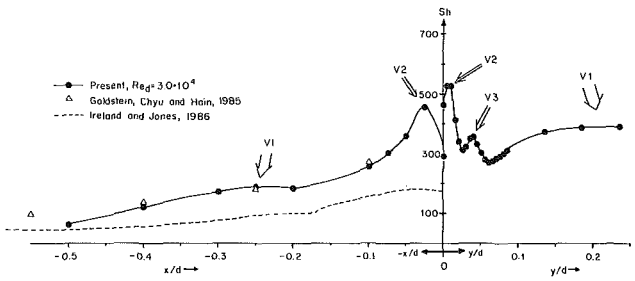

Fig. 4 Sherwood number distribution on the endwall and the cylinder along the upstream line of symmetry ($\theta = 0$ deg, $z = 0$)

2c) the Sh peak is about 40 percent lower than that with an inactive endwall. At $\theta = 90$–95 deg (Fig. 2d) the Sh maximum near the base is still very large when the endwall is inactive but almost disappears when the endwall is active. Note that present results near the cylinder front stagnation line differ somewhat from the data of Van Dresar and Mayle (1986) who found near-perfect agreement between data obtained near $\theta = 0$ deg with active and inactive endwalls. This discrepancy may be due to the different mass transfer boundary conditions, and perhaps somewhat different flow structures in the two studies.

Over the front portion of the cylinder (Figs. 2a, b, c, d), there is little difference between present and earlier values for $y/d > 0.03$. In particular, the second maximum, at $y/d \approx 0.040$–0.045, is nearly unaffected by the change in the endwall boundary conditions. Over the cylinder's rear (Figs. 2e and f) the present results show that Sh remains relatively low up to $y/d \approx 0.08$ when the endwall is active.

Figure 3 is a contour plot of the mass transfer distribution (expressed in terms of h_m/h_o) over the endwall near the cylinder base. The contour lines, which are calculated directly from the measurements, clearly correspond to the pattern of a horseshoe vortex flow as described previously by Goldstein and Karni (1984); mass transfer peaks associated with two different vortices (V1 and V2 in Fig. 1) are observed. The higher peak, which corresponds to V2, is located about $0.025d$ upstream of the cylinder. At this peak $h_m/h_o \approx 10$; this cannot be shown in the contour plot, but is clearly seen in Fig. 4. The second peak (V1), with $h_m/h_o \approx 4.1$, is observed at $x/d \approx -0.25$. A similar pattern, with more moderate gradients, was observed by Ireland and Jones (1986); see Fig. 7 of that study. The existence of two separated mass transfer peaks was not detected by Goldstein et al. (1985) where a relatively small (12.7 mm) cylinder diameter was used, and the distance between measurement points was relatively large. As shown by Karni and Goldstein (1986), the size of the vortices is proportional to d.

Figure 4 combines the Sh distribution along the plate's line of symmetry upstream of the cylinder with that along the cylinder's front stagnation line. The intense corner vortex V2 influences the mass transfer from the cylinder at $0 < y/d < 0.025$, and that from the endwall at $-0.1 < x/d < 0$; thus, the region affected by this vortex is much wider on the plate than on the cylinder. The transport coefficient variations are much steeper on the cylinder than on the plate and the maximum Sh value obtained on the cylinder is about 15 percent higher than that measured on the plate.

Mass and heat transfer results of Goldstein et al. (1985) and Ireland and Jones (1986), along an endwall directly in front of a cylinder, are also shown in Fig. 4. These data could be compared with the present measurements using a correlation for flat plate heat transfer, taking into account the active (heated) length and the total surface length (from the start of the endwall boundary layer), and the ratio between Prandtl and Schmidt numbers. A different and roughly comparable procedure is used wherein Sh values are calculated from the relation

$$\mathrm{Sh} = \frac{h}{h_o}\,\mathrm{Sh}_o \tag{1}$$

The ratio h/h_o is obtained from the original data: Fig. 9 of Goldstein et al. (1985) and Fig. 12 of Ireland and Jones (1986). $\mathrm{Sh}_o = 45$, which is measured in the present study just upstream of the cylinder, is used to correlate the earlier results with the present measurements.

The mass transfer measurements of Goldstein et al. (1985) were taken at $\mathrm{Re}_d \approx 4.0 \times 10^3$; nevertheless, the agreement with present data indicates that the ratio h_m/h_o is not very dependent on Re_d. Compared to present measurements, Ireland and Jones (1986) obtained relatively low increases of the transport coefficient near the cylinder's base (although their h/h_o contour plots indicate a pattern generally similar to that of Fig. 3). However, their study was conducted in a duct flow where a relatively high value of h_o was obtained. Also, conduction in the wall could affect liquid crystal experiments.

Conclusions

Mass transfer measurements conducted over a cylinder and its endwall indicate the following:

(*a*) Similar trends of mass transfer enhancement are observed on the cylinder near its base when either an inactive or active endwall is used. However, the generally high Sh values detected at $y/d < 0.03$ lower when the active wall is used. This reduction in peak values of Sh grows as θ increases from 0 to 90 deg.

(*b*) Two mass transfer maxima, corresponding to two vortices, are observed on the endwall upstream of the cylinder.

(*c*) The region adjacent to the cylinder base where a large mass transfer increase is detected is considerably wider on the plate than on the cylinder, but the Sh peak on the cylinder is about 15 percent higher than that on the plate, and significantly steeper Sh gradients are found on the cylinder.

Acknowledgments

Support for this work was provided by the Air Force Office of Scientific Research.

References

Goldstein, R. J., and Karni, J., 1984, "The Effect of a Wall Boundary Layer

on Local Mass Transfer From a Cylinder in Crossflow," ASME JOURNAL OF HEAT TRANSFER, Vol. 106, pp. 260–267.

Goldstein, R. J., Chyu, M. K., and Hain, R. C., 1985, "Measurement of Local Mass Transfer on a Surface in the Region of the Base of a Protruding Cylinder With a Computer-Controlled Data Acquisition System," *International Journal of Heat and Mass Transfer*, Vol. 28, No. 5, pp. 977–985.

Ireland, P. T., and Jones, T. V., 1986, "Detailed Measurements of Heat Transfer on and Around a Pedestal in Fully Developed Passage Flow," *Heat Transfer 1986, Proceedings of the 8th International Heat Transfer Conference*, San Francisco, CA, Hemisphere Publishing Corp., Vol. 3, pp. 975–980.

Karni, J., and Goldstein, R. J., 1986, "Endwall Effects on Local Mass Transfer From a Cylinder in Crossflow," *Turbulence Measurements and Flow Modeling*, C. J. Chen et al., eds., Hemisphere Publishing Corp., New York, NY, pp. 3–35.

Kruckels, W. W., 1972, "Determination of Local Heat Transfer Coefficients in Forced Convection Air Flow by Aid of Photometric Measurements," *AIChE Symposium Series*, Vol. 68, No. 118, pp. 112–118.

Van Dresar, N., and Mayle, R. E., 1986, "Convection at the Base of a Cylinder With a Horseshoe Vortex," *Heat Transfer 1976, Proceedings of the 8th International Heat Transfer Conference*, San Francisco, CA, Hemisphere Publishing Corp., Vol. 3, pp. 1121–1126.

Analysis of a Free-Convection Micropolar Boundary Layer About a Horizontal Permeable Cylinder at a Nonuniform Thermal Condition

Fue-Sang Lien,[1] Tzer-Ming Chen,[2] and Cha'o-Kuang Chen[3]

Nomenclature

a_1, a_2 = wall temperature or heat flux variation parameters
B = parameter, equation (12)
D = diameter of cylinder
$F(x)$ = prescribed surface function
$\hat{g}$ = gravitational acceleration
Gr, $\tilde{\text{Gr}}$ = Grashof number $= \hat{g}\beta(T_{wo}-T_\infty)R^3/\nu^2$, $\hat{g}\beta q_{wo}R^4/\nu^2 k$, respectively
Gr_D = Grashof number $= \hat{g}\beta(T_{wo}-T_\infty)D^3/\nu^2$
h = local heat transfer coefficient
j = microinertia
k = thermal conductivity
Nu, Nu_D = Nusselt numbers, hR/k, hD/k, respectively
Pr = Prandtl number $= \nu/\alpha$
q = local heat flux
R = radius of cylinder
T = temperature
$\bar{u}, \bar{v}$ = dimensional velocities in $\bar{x}$ and $\bar{y}$ direction
u, v = dimensionless velocities, $u=\bar{u}/(\nu/R)\text{Gr}^{1/2}$, $v=\bar{v}/(\nu/R)\text{Gr}^{1/4}$ (*) $u=\bar{u}/(\nu/R)\tilde{\text{Gr}}^{2/5}$, $v=\bar{v}/(\nu/R)\tilde{\text{Gr}}^{1/5}$ (**)
x, y = dimensionless coordinates, $x=\bar{x}/R$, $y=\bar{y}\text{Gr}^{1/4}/R$(*), $y=\bar{y}\tilde{\text{Gr}}^{1/5}/R$(**)
α = thermal diffusivity
β = coefficient of thermal expansion
γ = spin gradient viscosity
Δ = material parameter, equation (12)
θ = dimensionless temperature, $\theta=(T-T_\infty)/(T_{wo}-T_\infty)F(x)$ (*), $\theta=k(T-T_\infty)\tilde{\text{Gr}}^{1/5}/Rq_{wo}F(x)$ (**)
κ = vortex viscosity
λ = material parameter, equation (12)
μ = dynamic viscosity
ν = kinematic viscosity
ρ = density
$\sigma, \bar{\sigma}$ = angular velocity, $\sigma=\bar{\sigma}/(\nu/R^2)\text{Gr}^{3/4}$(*), $\sigma=\bar{\sigma}/(\nu/R^2)\tilde{\text{Gr}}^{3/5}$ (**)
ϕ = $\bar{x}/R$, deg
ψ = stream function (with $u=\partial\psi/\partial y$, $v=-\partial\psi/\partial x$)

Superscript

$\bar{}$ = dimensional property

Subscripts

w = wall
o = stagnation point

Introduction

The theory of fluids with microstructure has been the subject of a large number of investigations. For an excellent review, see Ariman et al. (1973, 1974).

Latto and Shen (1969) studied the effect of injecting dilute aqueous polymer solutions into a turbulent boundary layer formed on a flat plate. They found that polymer concentration and injection velocity influence the friction drag. This phenomenon cannot be explained on the basis of classical continuum mechanics. The theory of micropolar fluids proposed by Eringen (1964) is capable of explaining this phenomenon. In this theory, the local effects arising from microstructure and intrinsic motion of the fluid element are taken into account. Physically, micropolar fluids represent non-Newtonian fluids consisting of dumbbell molecules or short rigid cylindrical elements, e.g., polymer fluids, fluid suspensions, etc. In addition, it may be possible to use a theory of fluids having microstructure to model turbulent flow. In such an application, the macromotion of the model would correspond to the mean motion of turbulent flow, the micromotion of the model would correspond to the fluctuation motion of the turbulent flow, and the microinertia coefficients would correspond to the characteristic dimensions of eddies.

Recently, jet impingement of a micropolar fluid on a curved surface has been investigated by Ojha et al. (1978). The heat transfer characteristics of a micropolar boundary layer on a nonisothermal circular cylinder have been presented by Gorla (1984). Cooling of the boundaries has numerous applications. Therefore, the purpose of the present paper is to study the heat transfer for free convection flow of micropolar fluid over a horizontal cylinder subjected to constant mass transfer and arbitrary surface temperature or surface heat flux variations. Numerical results were obtained for a Prandtl number of 0.7 and 1, with various values of the dimensionless material parameters Δ and λ. For prescribed surface conditions, the

[1]Lecturer, Department of Mechanical Engineering, National Taipei Institute of Technology, Taiwan; current address: Research Associate, Department of Mechanical Engineering, UMIST, United Kingdom.

[2]Lecturer, Department of Mechanical Engineering, National Kaohsiung Institute of Technology, Taiwan.

[3]Professor, Department of Mechanical Engineering, National Cheng Kung University, Taiwan.

Contributed by the Heat Transfer Division for publication in the JOURNAL OF HEAT TRANSFER. Manuscript received by the Heat Transfer Division January 5, 1988. Keywords: Mass Transfer, Natural Convection, Non-Newtonian Flows and Systems.

on Local Mass Transfer From a Cylinder in Crossflow," ASME JOURNAL OF HEAT TRANSFER, Vol. 106, pp. 260–267.

Goldstein, R. J., Chyu, M. K., and Hain, R. C., 1985, "Measurement of Local Mass Transfer on a Surface in the Region of the Base of a Protruding Cylinder With a Computer-Controlled Data Acquisition System," *International Journal of Heat and Mass Transfer*, Vol. 28, No. 5, pp. 977–985.

Ireland, P. T., and Jones, T. V., 1986, "Detailed Measurements of Heat Transfer on and Around a Pedestal in Fully Developed Passage Flow," *Heat Transfer 1986, Proceedings of the 8th International Heat Transfer Conference*, San Francisco, CA, Hemisphere Publishing Corp., Vol. 3, pp. 975–980.

Karni, J., and Goldstein, R. J., 1986, "Endwall Effects on Local Mass Transfer From a Cylinder in Crossflow," *Turbulence Measurements and Flow Modeling*, C. J. Chen et al., eds., Hemisphere Publishing Corp., New York, NY, pp. 3–35.

Kruckels, W. W., 1972, "Determination of Local Heat Transfer Coefficients in Forced Convection Air Flow by Aid of Photometric Measurements," *AIChE Symposium Series*, Vol. 68, No. 118, pp. 112–118.

Van Dresar, N., and Mayle, R. E., 1986, "Convection at the Base of a Cylinder With a Horseshoe Vortex," *Heat Transfer 1976, Proceedings of the 8th International Heat Transfer Conference*, San Francisco, CA, Hemisphere Publishing Corp., Vol. 3, pp. 1121–1126.

Analysis of a Free-Convection Micropolar Boundary Layer About a Horizontal Permeable Cylinder at a Nonuniform Thermal Condition

Fue-Sang Lien,[1] Tzer-Ming Chen,[2] and Cha'o-Kuang Chen[3]

Nomenclature

a_1, a_2 = wall temperature or heat flux variation parameters
B = parameter, equation (12)
D = diameter of cylinder
$F(x)$ = prescribed surface function
$\hat{g}$ = gravitational acceleration
Gr, $\tilde{\text{Gr}}$ = Grashof number $= \hat{g}\beta(T_{wo}-T_\infty)R^3/\nu^2$, $\hat{g}\beta q_{wo}R^4/\nu^2 k$, respectively
Gr_D = Grashof number $= \hat{g}\beta(T_{wo}-T_\infty)D^3/\nu^2$
h = local heat transfer coefficient
j = microinertia
k = thermal conductivity
Nu, Nu_D = Nusselt numbers, hR/k, hD/k, respectively
Pr = Prandtl number $= \nu/\alpha$
q = local heat flux
R = radius of cylinder
T = temperature
$\bar{u}, \bar{v}$ = dimensional velocities in $\bar{x}$ and $\bar{y}$ direction
u, v = dimensionless velocities, $u=\bar{u}/(\nu/R)\text{Gr}^{1/2}$, $v=\bar{v}/(\nu/R)\text{Gr}^{1/4}$ (*) $u=\bar{u}/(\nu/R)\tilde{\text{Gr}}^{2/5}$, $v=\bar{v}/(\nu/R)\tilde{\text{Gr}}^{1/5}$ (**)
x, y = dimensionless coordinates, $x=\bar{x}/R$, $y=\bar{y}\text{Gr}^{1/4}/R$(*), $y=\bar{y}\tilde{\text{Gr}}^{1/5}/R$(**)
α = thermal diffusivity
β = coefficient of thermal expansion
γ = spin gradient viscosity
Δ = material parameter, equation (12)
θ = dimensionless temperature, $\theta=(T-T_\infty)/(T_{wo}-T_\infty)F(x)$ (*), $\theta=k(T-T_\infty)\tilde{\text{Gr}}^{1/5}/Rq_{wo}F(x)$ (**)
κ = vortex viscosity
λ = material parameter, equation (12)
μ = dynamic viscosity
ν = kinematic viscosity
ρ = density
$\sigma, \bar{\sigma}$ = angular velocity, $\sigma=\bar{\sigma}/(\nu/R^2)\text{Gr}^{3/4}$(*), $\sigma=\bar{\sigma}/(\nu/R^2)\tilde{\text{Gr}}^{3/5}$ (**)
ϕ = $\bar{x}/R$, deg
ψ = stream function (with $u=\partial\psi/\partial y$, $v=-\partial\psi/\partial x$)

Superscript

$\bar{}$ = dimensional property

Subscripts

w = wall
o = stagnation point

Introduction

The theory of fluids with microstructure has been the subject of a large number of investigations. For an excellent review, see Ariman et al. (1973, 1974).

Latto and Shen (1969) studied the effect of injecting dilute aqueous polymer solutions into a turbulent boundary layer formed on a flat plate. They found that polymer concentration and injection velocity influence the friction drag. This phenomenon cannot be explained on the basis of classical continuum mechanics. The theory of micropolar fluids proposed by Eringen (1964) is capable of explaining this phenomenon. In this theory, the local effects arising from microstructure and intrinsic motion of the fluid element are taken into account. Physically, micropolar fluids represent non-Newtonian fluids consisting of dumbbell molecules or short rigid cylindrical elements, e.g., polymer fluids, fluid suspensions, etc. In addition, it may be possible to use a theory of fluids having microstructure to model turbulent flow. In such an application, the macromotion of the model would correspond to the mean motion of turbulent flow, the micromotion of the model would correspond to the fluctuation motion of the turbulent flow, and the microinertia coefficients would correspond to the characteristic dimensions of eddies.

Recently, jet impingement of a micropolar fluid on a curved surface has been investigated by Ojha et al. (1978). The heat transfer characteristics of a micropolar boundary layer on a nonisothermal circular cylinder have been presented by Gorla (1984). Cooling of the boundaries has numerous applications. Therefore, the purpose of the present paper is to study the heat transfer for free convection flow of micropolar fluid over a horizontal cylinder subjected to constant mass transfer and arbitrary surface temperature or surface heat flux variations. Numerical results were obtained for a Prandtl number of 0.7 and 1, with various values of the dimensionless material parameters Δ and λ. For prescribed surface conditions, the

[1]Lecturer, Department of Mechanical Engineering, National Taipei Institute of Technology, Taiwan; current address: Research Associate, Department of Mechanical Engineering, UMIST, United Kingdom.

[2]Lecturer, Department of Mechanical Engineering, National Kaohsiung Institute of Technology, Taiwan.

[3]Professor, Department of Mechanical Engineering, National Cheng Kung University, Taiwan.

Contributed by the Heat Transfer Division for publication in the JOURNAL OF HEAT TRANSFER. Manuscript received by the Heat Transfer Division January 5, 1988. Keywords: Mass Transfer, Natural Convection, Non-Newtonian Flows and Systems.

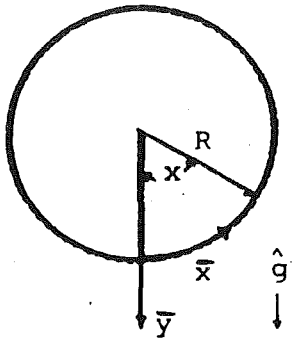

Fig. 1 Coordinate system

solutions covered the range of surface mass transfer parameter v_w from -0.4 to 0.4.

Analysis

The curvilinear orthogonal coordinate system for this analysis, where the wall temperature is assumed to be greater than the ambient temperature, is shown in Fig. 1. By employing the Boussinesq approximation, the conservation equations of the laminar boundary layer for the micropolar fluid can be written as:

Mass

$$\frac{\partial \bar{u}}{\partial \bar{x}} + \frac{\partial \bar{v}}{\partial \bar{y}} = 0 \tag{1}$$

Momentum

$$\bar{u}\frac{\partial \bar{u}}{\partial \bar{x}} + \bar{v}\frac{\partial \bar{u}}{\partial \bar{y}} = \hat{g}\beta(T - T_\infty)\sin(\bar{x}/R) + (\nu + \kappa/\rho)\frac{\partial^2 \bar{u}}{\partial \bar{y}^2} + \frac{\kappa}{\rho}\frac{\partial \bar{\sigma}}{\partial \bar{y}} \tag{2}$$

Angular Momentum

$$\bar{u}\frac{\partial \bar{\sigma}}{\partial \bar{x}} + \bar{v}\frac{\partial \bar{\sigma}}{\partial \bar{y}} = -\frac{\kappa}{\rho j}\left(2\bar{\sigma} + \frac{\partial \bar{u}}{\partial \bar{y}}\right) + \frac{\gamma}{\rho j}\frac{\partial^2 \bar{\sigma}}{\partial \bar{y}^2} \tag{3}$$

Energy

$$\bar{u}\frac{\partial T}{\partial \bar{x}} + \bar{v}\frac{\partial T}{\partial \bar{y}} = \alpha\frac{\partial^2 T}{\partial \bar{y}^2} \tag{4}$$

with the boundary conditions:

$$\bar{u} = 0,\ \bar{v} = \bar{v}_w,\ T = T_w\ (*),\ \bar{\sigma} = -1/2\ \partial \bar{u}/\partial \bar{y}, \quad \text{at } \bar{y} = 0$$
$$\text{or } -k\partial T/\partial \bar{y} = q_w\ (**) \tag{5}$$
$$\bar{u} = 0,\ T = T_\infty,\ \bar{\sigma} = 0 \quad \text{as } \bar{y} \to \infty$$

* :for prescribed surface temperatures

** :for prescribed surface heat fluxes

Equations (1)–(5) are transformed from the $(\bar{x}, \bar{y})$ to (ξ, η) coordinates by a proper choice of transformation variables defined as follows:

$$\xi = 2\int_0^x F(x)dx,\ \eta = yF(x)^{1/2},\ g(\xi, \eta) = \sigma(x, y)/F(x)^{1/2}\xi \tag{6}$$

$$f(\xi, \eta) = F(x)^{1/2}\left[\psi(x, y) + \int_0^x v_w\, dx\right]/\xi$$

The transformed equations are

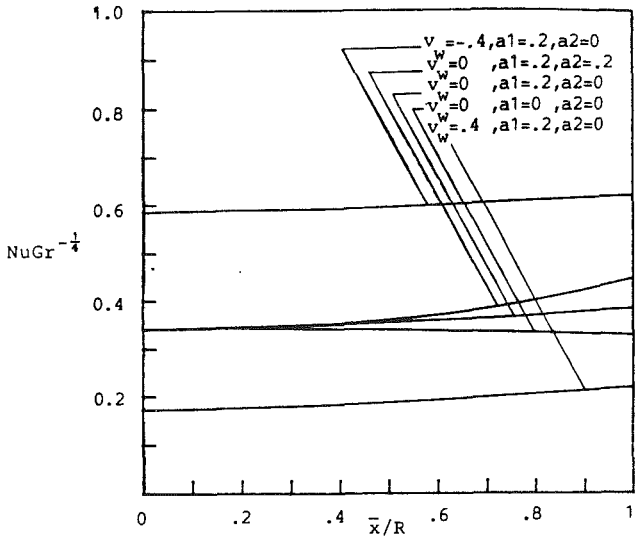

Fig. 2 Angular distributions of the local Nusselt number for the nonisothermal surface case with Pr = 1, B = 1, Δ = 5, and λ = 5

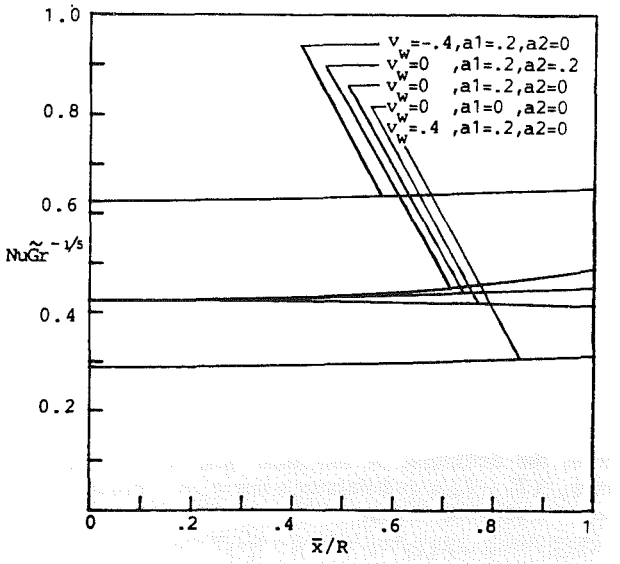

Fig. 3 Angular distributions of the local Nusselt number for the nonuniform heat flux surface case with Pr = 1, B = 1, Δ = 5, and λ = 5

Table 1 Angular distributions of the local Nusselt number $Nu_D Gr_D^{-1/4}$ for Pr = 0.7, $\Delta = 0$, $a_1 = 0$, $a_2 = 0$, and $v_w = 0$

deg	Present method	Gortler series	Merkin numerical	Blasius series	Huang
0	0.4400	0.4402	0.4402	0.4402	0.4402
30	0.4345	0.4351	0.4349	0.4350	0.4349
60	0.4187	0.4187	0.4190	0.4192	0.4191
90	0.3919	0.3898	0.3922	0.3930	0.3922

$$(1+\Delta)f''' + ff''[2-\alpha_1(x)] - f''\alpha_2(x) + \alpha_3(x)\theta - 2(f')^2 + \Delta g' = 2\xi(f'\partial f'/\partial\xi - f''\partial f/\partial\xi) \tag{7}$$

$$\lambda g'' + fg'[2-\alpha_1(x)] - g'\alpha_2(x) - [2+\alpha_1(x)]f'g - \alpha_4(x)[2g+f''] = 2\xi(f'\partial g/\partial\xi - g'\partial f/\partial\xi) \tag{8}$$

$$\mathrm{Pr}^{-1}\theta'' + f\theta'[2-\alpha_1(x)] - \theta'(x)\alpha_2(x) - 2\alpha_1(x)f'\theta = 2\xi(f'\partial\theta/\partial\xi - \theta'\partial f/\partial\xi) \tag{9}$$

Table 2 Angular distributions of the local Nusselt number for Pr = 1, $a_1 = 0.2$, $a_2 = 0$, $B = 1$, and $V_w = 0$

	$\mathrm{NuGr}^{-1/4}$ (nonisothermal)			$\mathrm{NuG\tilde{r}}^{-1/5}$ (nonuniform q_w)		
$\frac{x}{R}$	$\lambda = 5$	$\lambda = 5$	$\lambda = 13.5$	$\lambda = 5$	$\lambda = 5$	$\lambda = 13.5$
	$\Delta = 5$	$\Delta = 13.5$	$\Delta = 5$	$\Delta = 5$	$\Delta = 13.5$	$\Delta = 5$
0.	0.3401	0.2855	0.3391	0.4236	0.3717	0.4224
0.5	0.3557	0.3045	0.3554	0.4337	0.3823	0.4327
1.0	0.3831	0.3274	0.3825	0.4517	0.3988	0.4507
1.5	0.4099	0.3481	0.4086	0.4736	0.4171	0.4723
2.0	0.4221	0.3576	0.4209	0.4892	0.4295	0.4876
2.5	0.4046	0.3389	0.4039	0.4871	0.4255	0.4857
3	0.3256	0.2640	0.3268	0.4443	0.3820	0.4438
π	0.2604	0.1899	0.2621	0.4049	0.3379	0.4055

$$f = f' = 0,\ \theta = 1(*) \text{ or } \theta' = -F(x)^{-1/2}(**),\ g = -1/2\, f'' \quad \text{at } \eta = 0$$

$$f' = g = \theta = 0 \quad \text{as } \eta \to \infty \tag{10}$$

where

$$\alpha_1(x) = 1/2\, F(x)^{-2}\xi dF(x)/dx, \quad \alpha_2(x) = v_w F(x)^{-1/2}$$
$$\alpha_3(x) = \sin(x)/\xi, \quad \alpha_4(x) = \Delta B/F(x) \tag{11}$$

and

$$\Delta = \kappa/\mu,\ \lambda = \gamma/\rho\, j\nu,\ B = R^2/j\mathrm{Gr}^{1/2}(*) \text{ or } B = R^2/j\tilde{\mathrm{G}}\mathrm{r}^{2/5}\ (**) \tag{12}$$

In the foregoing equations, the prime (′) stands for the partial derivative with respect to η. The physical quantity of primary interest is the local Nusselt number, defined by

$$\mathrm{Nu} = hR/k \tag{13}$$

From the definition of the local heat transfer coefficient $h = q_w/(T_w - T_\infty)$, and Fourier's law $q_w = -k(\partial T/\partial y)_{y=0}$, it can be readily shown that

$$\mathrm{NuGr}^{-1/4} = -F(x)^{1/2}\theta'(\xi, 0) \quad (*) \tag{14}$$

$$\mathrm{NuG\tilde{r}}^{-1/5} = 1/\theta(\xi, 0) \quad (**) \tag{15}$$

Results and Discussion

We use an efficient finite difference method to solve equations (7)–(10), from Cebeci and Bradshaw (1977).

Numerical results were obtained for a permeable horizontal cylinder where the wall temperature is assumed to be of the form $T_w = T_\infty + (T_{wo} - T_\infty)(1 + a_1 x + a_2 x^2)$ or the wall heat flux is assumed to be of the form $q_w = q_{wo}(1 + a_1 x + a_2 x^2)$.

In this paper we assumed the microrotation equal to the fluid vorticity at the boundary. This kind of boundary means that in the neighborhood of a rigid boundary the effect of microstructure is negligible since the suspended particles cannot get closer to the boundary than their radius. Hence in the neighborhood of the boundary the only rotation is due to fluid shear, and therefore the gyration vector must be equal to fluid vorticity. This type of boundary condition has been used by Ahmadi (1976) for the solution of micropolar boundary layer flow past a semi-infinite flat plate.

As shown in Figs. 2 and 3, the local Nusselt number increases for suction, while an opposite trend is observed for blowing. By setting $a_1 = a_2 = 0$ in $F(x)$, we obtain the heat transfer rate from cylinders having isothermal or constant-heat-flux surfaces. By varying a_1 and a_2 we obtain heat transfer rates for nonuniform thermal conditions. Positive values of both a_1 and a_2 yield higher heat transfer rates than isothermal or constant-heat-flux surfaces do. This information is very important in the design of industrial equipment where the augmented heat transfer rates may be desirable. By controlling the arbitrary function $F(x)$ properly (i.e., by choosing proper values of a_1 and a_2), it is possible to maintain the desired level of heat transfer rate augmentation.

For comparison of our heat transfer results, Merkin (1977), Huang (1985), the Basius series (1962), and Gortler-type expansion results (1967) were used. The results are included in Table 1 and show excellent agreement with our results.

To illustrate how the dimensionless material parameters Δ and λ affect the local heat transfer rate in the boundary layer of micropolar fluid, representative local Nusselt numbers along the angular positions of the cylinder are shown in Table 2. It is noted in Table 2 that an increase in λ and Δ yields a decrease in $\mathrm{NuGr}^{-1/4}$ and $\mathrm{NuG\tilde{r}}^{-1/5}$.

References

Ahmadi, G., 1976, "Self-Similar Solution of Incompressible Micropolar Boundary Layer Flow Over a Semi-infinite Plate," *Int. J. Engineering Science*, Vol. 14, pp. 639–646.

Ariman, T., Turk, M. A., and Sylvester, N. D., 1973, "Microcontinuum Fluid Mechanics—A Review," *Int. J. Engineering Science*, Vol. 11, pp. 905–930.

Ariman, T., Turk, M. A., and Sylvester, N. D., 1974, "Applications of Microcontinuum Fluid Mechanics," *Int. J. Engineering Science*, Vol. 12, pp. 273–293.

Chiang, T., and Raye, T., 1962, *Proceedings 4th National Congress of Applied Mechanics*, p. 213.

Cebeci, T., and Bradshaw, P., 1977, *Momentum Transfer in Boundary Layers*, Hemisphere Publishing Corp., Washington, DC.

Eringen, A. C., 1964, "Simple Microfluids," *Int. J. Engineering Science*, Vol. 2, pp. 205–217.

Gorla, R. S. R., 1984, "Heat Transfer Characteristics of a Micropolar Boundary Layer in a Cross Flow Over a Nonisothermal Circular Cylinder," *Int. J. Engineering Science*, Vol. 22, pp. 47–55.

Huang, M. J., and Chen, C. K., 1985, *7th Miami International Conference on Alternative Energy Source*, Miami Beach, FL, Dec. 9–11.

Latto, B., and Chi-Hung Shen, 1969, *Proc. Turbulence Measurements in Liquids*, University of Missouri.

Merkin, J. H., 1977, "Free Convection Boundary Layer on Cylinders of Elliptic Cross Section," ASME JOURNAL OF HEAT TRANSFER, Vol. 99, pp. 453–457.

Ojha, S. K., Banerjee, A. K., and Mathur, M. N., 1978, "Micropolar Fluid Jet Impingement on a Curved Surface," *Int. J. Engineering Science*, Vol. 16, pp. 743–764.

Saville, D. A., and Churchill, S. W., 1967, "Laminar Free Convection in Boundary Layers Near Horizontal Cylinders and Vertical Axisymmetric Bodies," *J. Fluid Mechanics*, Vol. 29, pp. 391–399.

Natural Convection in an Inclined Rectangular Porous Slot: the Brinkman-Extended Darcy Model

P. Vasseur,[1] C. H. Wang,[1] and M. Sen[2]

Introduction

Natural convection in porous media is of interest in many applications. Studies have been made of different geometries and heating conditions. For example, a vertical cavity in which a horizontal temperature gradient is induced by side walls maintained at different temperatures was analyzed (Blythe et al., 1983; Daniels, 1983). Others have examined the effect of different types of thermal boundary condition, such as uniform heating on one vertical wall (Prasad and Kulacki, 1984), and constant heat flux on both side walls (Bejan, 1983; Vasseur et al., 1987a, 1987b, 1987c; Sen et al., 1987). In all these studies, use has been made of Darcy's law as a governing equation. In general, it is found to give satisfactory results when the porous medium has a low porosity. However, it has been observed that boundary effects, not included in the Darcy's law model, may become significant for fluid flows in saturated porous media with high permeabilities. For this situation Darcy's model will overpredict the heat transfer (Hong et al., 1985) and flow velocities (Georgiadis and Catton, 1985). Brinkman's extension of Darcy's law should be used, as done by Tong and Subramanian (1985) and Sen (1987), to account for the presence of a rigid boundary. Significant contributions of the viscous diffusion term at high Rayleigh and Darcy numbers have been reported by these authors.

The purpose of this note is to document the flow and heat transfer characteristics in an inclined porous layer with uniform heating and cooling through opposite walls. The model used to describe the flow in the cavity accounts for Brinkman friction. It will be shown that the boundary effect, though not important in low-porosity media, becomes significant in high-porosity media.

Problem Statement and Solution Procedure

A two-dimensional cavity, confined on all sides by an impermeable rectangular box, and filled with an isotropic, homogeneous, fluid-saturated porous medium, is considered. The enclosure is of dimensions L' and H' in the x' and y' directions, with $H' >> L'$, and the direction of the larger dimension is tilted at an angle ϕ counterclockwise with respect to the horizontal plane. An adiabatic condition is imposed on the two end walls, while a uniform heat flux $q' = -k\partial T'/\partial x'$ is applied along both side walls. Here, k is the thermal conductivity of the porous medium, T' the temperature, and the primes denote dimensional variables. It is assumed that the flow is laminar and steady and that the Boussinesq approximation applies.

The Brinkman model is adopted for the porous medium. The governing equations for the nondimensional vorticity ω, stream function ψ, and temperature T are, after scaling length, temperature, and velocity with L', $q'L'/k$, and α/L', respectively

$$\nabla^2\psi = -\omega \tag{1}$$

$$\nabla^2\omega = \mathrm{Da}^{-1}\left\{\omega - R\left(\frac{\partial T}{\partial x}\sin\phi + \frac{\partial T}{\partial y}\cos\phi\right)\right\} \tag{2}$$

$$\nabla^2 T = \frac{\partial\psi}{\partial y}\frac{\partial T}{\partial x} - \frac{\partial\psi}{\partial x}\frac{\partial T}{\partial y} \tag{3}$$

where $\mathrm{Da} = K/L'^2$ is the Darcy number and $R = g\beta KL'^2 q'/k\alpha\nu$ is the Darcy–Rayleigh number. K, g, β, α, and ν are the permeability, gravity, thermal expansion coefficient, thermal diffusivity, and kinematic viscosity, respectively. The boundary conditions are $\psi = 0$, $\partial T/\partial x = 1$ at $x = \pm 1/2$ and $\psi = 0$, $\partial T/\partial y = 0$ at $y = \pm A/2$, where $A = H'/L'$ is the aspect ratio of the cavity. Furthermore, a representative Nusselt number reflecting the convective heat transfer is defined as $\mathrm{Nu} = q'L'/k\Delta T' = 1/\Delta T$, where $\Delta T = T(1/2, 0) - T(-1/2, 0)$ is the wall-to-wall dimensionless temperature difference taken arbitrarily at the position $x = 0$.

Analytical Solution

Following the examples of Vasseur et al. (1987a) and Sen (1987), we proceed to search for an approximate analytical solution for the large aspect ratio of the cavity ($A >> 1$). There is a core region in the center of the cavity in which the flow is essentially parallel ($u = 0$, $v = v(x)$ are the velocity components in the x and y directions) and the temperature distribution is linear in the y direction; there are also two regions near each end wall where the flow turns around. In the core region, we can take $T(x, y) = \theta(x) + Cy$, where C is an unknown constant temperature gradient in the y direction. The value of C can be obtained (Bejan, 1983) from a heat flux balance in the y direction:

$$C = 2\int_0^{1/2} vT dx.$$

With these simplifications the governing equations become

$$\frac{d^2\theta}{dx^2} = -C\frac{d\psi}{dx} \tag{4a}$$

$$\frac{d^5\psi}{dx^5} - \frac{1}{\mathrm{Da}}\frac{d^3\psi}{dx^3} + \frac{RC}{\mathrm{Da}}\sin\phi\frac{d\psi}{dx} = 0 \tag{4b}$$

The solution depends on the sign of $C\sin\phi$; so two cases will be considered.

(a) $C\sin\phi > 0$. This corresponds to a stable temperature gradient in the core region; C is positive (or negative) for $\sin\phi$ positive (or negative). This situation corresponds to "natural flow," being the motion that would start from rest with a conductive temperature field, i.e., counterclockwise (or clockwise) motion for $\sin\phi$ positive (or negative).

Solutions satisfying the boundary conditions are

$$\psi = -\frac{B}{a^2+b^2}(\alpha_1\cosh ax\cos bx + \alpha_2\sinh ax\sin bx - D) \tag{5}$$

$$\theta = B\beta_0(\alpha_0\sinh ax\cos bx + \cosh ax\sin bx) + \frac{v}{2R\sin\phi} - Cx\cot\phi \tag{6}$$

where

$$a = \sqrt{\frac{\gamma+1}{4\mathrm{Da}}}, \qquad b = \sqrt{\frac{\gamma+1}{4\mathrm{Da}}}, \qquad \gamma = \sqrt{4RC\mathrm{Da}\sin\phi}$$

$$B = \frac{\gamma(1 + C\cot\phi)}{2CD\mathrm{Da}},$$

[1]Department of Mechanical Engineering, École Polytechnique de Montréal, Montréal, Quebéc, Canada H3C 3A7.

[2]Department of Aerospace and Mechanical Engineering, University of Notre Dame, Notre Dame, IN 46556.

Contributed by the Heat Transfer Division for publication in the JOURNAL OF HEAT TRANSFER. Manuscript received by the Heat Transfer Division April 28, 1988. Keywords: Enclosure Flows, Natural Convection, Porous Media.

$$D=\alpha_1 \cosh\frac{a}{2}\cos\frac{b}{2}+\alpha_2 \sinh\frac{a}{2}\sin\frac{b}{2}$$

$$\alpha_0=\cot\frac{b}{2}\tanh\frac{a}{2},\qquad \alpha_1=a+b\alpha_0,\qquad \alpha_2=b-a\alpha_0,$$

$$\beta_0=\sqrt{\frac{\gamma^2-1}{2R\sin\phi}}$$

The velocity

$$v=B(\sinh ax\cos bx-\alpha_0\cosh ax\sin bx) \tag{7}$$

The Nusselt number Nu is obtained as

$$\mathrm{Nu}=\frac{1}{2EB\beta_0-C\cot\phi} \tag{8}$$

where $E=\alpha_0\sinh a/2\cos b/2+\cosh a/2\sin b/2$. The temperature gradient C is obtained from

$$\frac{B\cot\phi}{a^2+b^2}\left(D-\frac{4ab}{a^2+b^2}E\right)-\frac{B^2}{8RC}\left[\{G(1+F)+M\}\right.$$

$$\left.+(\alpha_0^2-F)(M+2-G)+\frac{H}{\alpha_0}\{F(1-\alpha_0^2)-2\alpha_0^2\}\right]+1=0 \tag{9}$$

where

$$F=\alpha_0\sqrt{4RC\mathrm{Da}-1},\qquad M=\frac{\sin a}{a}-\frac{\sin b}{b}-1$$

$$G=(b\cosh a\sin b+a\sinh a\cos b)/(a^2+b^2)$$

$$H=(a\cosh a\sin b-b\sinh a\cos b)/(a^2+b^2)$$

Equation (9) can readily be solved numerically to obtain C for given values of R and Da, after which the stream function, temperature, velocity distributions, and Nusselt number are given by equations (5) to (8).

The present analysis, based solely on the assumption of parallel flow, is valid at all Rayleigh numbers for which the flow is stable, including the boundary layer regime. This regime in a vertical cavity with uniform heat flux from the side has been studied by Bejan (1983) for a Darcy porous medium and by Kimura and Bejan (1984) for a viscous fluid, using a modified Oseen linearization method. We can check the results here, since the Brinkman equation reduces to these limits as the permeability $K\to 0$ and ∞ (i.e., $\mathrm{Da}\to 0$ and ∞), respectively. For the boundary layer regime in a vertical cavity, $\phi=90$ deg and $R\to\infty$. If $\mathrm{Da}\to 0$, we get

$$v=-\alpha^{3/2}\exp(-\alpha\bar{x}),\qquad T=\frac{y}{\alpha^{1/2}}-\frac{1}{\alpha}\exp(-\alpha\bar{x}),$$

$$\mathrm{Nu}=\frac{\alpha}{2} \tag{10}$$

where $\alpha=R^{2/5}$ and $\bar{x}=(1/2-x)$. These equations, when translated into corresponding notation, are the same as those obtained by Bejan (1983). But if $\mathrm{Da}\to\infty$, it is found that

$$v=-\frac{\mathrm{Ra}}{2a^3}\exp(-a\bar{x})\sin(a\bar{x}),$$

$$T=\frac{4a^4}{\mathrm{Ra}}y-\frac{1}{a}\exp(-a\bar{x})\cos(a\bar{x}),\qquad \mathrm{Nu}=\frac{a}{2} \tag{11}$$

where $a^9=\mathrm{Ra}^2/32$, $\mathrm{Ra}=R/\mathrm{Da}$, and $\bar{x}=(1/2-x)$. These are similar to the results obtained by Kimura and Bejan (1984).

(b) $C\sin\phi<0$. This corresponds to an unstable temperature gradient in the core region so that C would be negative (or positive) for $\sin\phi$ positive (or negative). For positive inclination the motion is clockwise, while it is counterclockwise for negative inclination. In either case this motion, which cannot be started from rest conditions with a conductive temperature field, will be referred to as "antinatural," since it is opposite in direction to the natural motion (see for instance Moya et al., 1987).

In this case we obtain

$$\psi=-B_1\left\{\left(\frac{\cosh\bar{a}x-\cosh\frac{\bar{a}}{2}}{\bar{a}}\right)\right.$$

$$\left.+\alpha_3\left(\frac{\cos\bar{b}x-\cos\frac{\bar{b}}{2}}{\bar{b}}\right)\right\} \tag{12}$$

$$\theta=B_1C\left(\frac{\sinh\bar{a}x}{\bar{a}^2}+\alpha_3\frac{\sin\bar{b}x}{\bar{b}^2}\right)-Cx\cot\phi \tag{13}$$

$$\mathrm{Nu}=\frac{1}{2B_1CF-C\cot\phi} \tag{14}$$

where

$$\bar{a}=\sqrt{(\beta+1)/2\mathrm{Da}},\qquad \bar{b}=\sqrt{(\beta-1)/2\mathrm{Da}},$$

$$\beta=\sqrt{1-4RC\mathrm{Da}\sin\phi},\qquad \alpha_3=\sinh\frac{\bar{a}}{2}/\sin\frac{\bar{b}}{2} \tag{15}$$

$$F=\frac{\sinh\bar{a}/2}{\bar{a}^2}+\alpha_3\frac{\sin\bar{b}/2}{\bar{b}^2},$$

$$G=\frac{\cosh\bar{a}/2}{\bar{a}}+\alpha_3\frac{\cos\bar{b}/2}{\bar{b}},\qquad B_1=\frac{1+C\cot\phi}{GC}$$

The value of C is obtained from

$$B_1\cot P-B_1^2\left\{Q+\frac{\alpha_3}{\bar{a}^2\bar{b}^2}\left(\frac{\bar{a}^2-\bar{b}^2}{\bar{a}^2+\bar{b}^2}\right)S\right\}+\frac{1}{2}=0 \tag{16}$$

where

$$P=\frac{1}{2\bar{a}^2}(\bar{a}\cosh\bar{a}/2-2\sinh\bar{a}/2)$$

$$+\frac{\alpha_3}{2\bar{b}^2}(\bar{b}\cos\bar{b}/2-2\sin\bar{b}/2)$$

$$Q=\frac{1}{4\bar{a}^3}(\sinh\bar{a}-\bar{a})+\frac{\alpha_3^2}{4\bar{b}^3}(\sin\bar{b}-\bar{b}),$$

$$S=\bar{a}\sin\bar{b}/2\cosh\bar{a}/2-\bar{b}\cos\bar{b}/2\sinh\bar{a}/2 \tag{17}$$

Here again a numerical procedure can be used to solve the simultaneous transcendental equations.

Numerical Solution

The discretized Poisson equation for ψ, equation (1), is solved explicitly with a successive over-relaxation method, whereas the ω and T equations, (2) and (3), are solved using an alternating direction implicit method. The resultant set of finite-difference equations is tridiagonal in form and therefore both easy and economical to solve on a computer. In order to achieve both the desirable accuracy and the dominance of the principal diagonal of the tridiagonal systems of the finite difference equations, very small time steps were used. The solution was assumed to have converged if the relative change in the sum of the unknown variable over all mesh points was less than 10^{-4} for ψ and 10^{-5} for either T or ω. The converged results were stored after each run to be used as initial conditions for the next.

The numerical results shown here were obtained using uniform grids. A grid of 51×51 was found to be sufficient. Increasing the number of grid points further had little discernible effect on the numerical results. For example, for

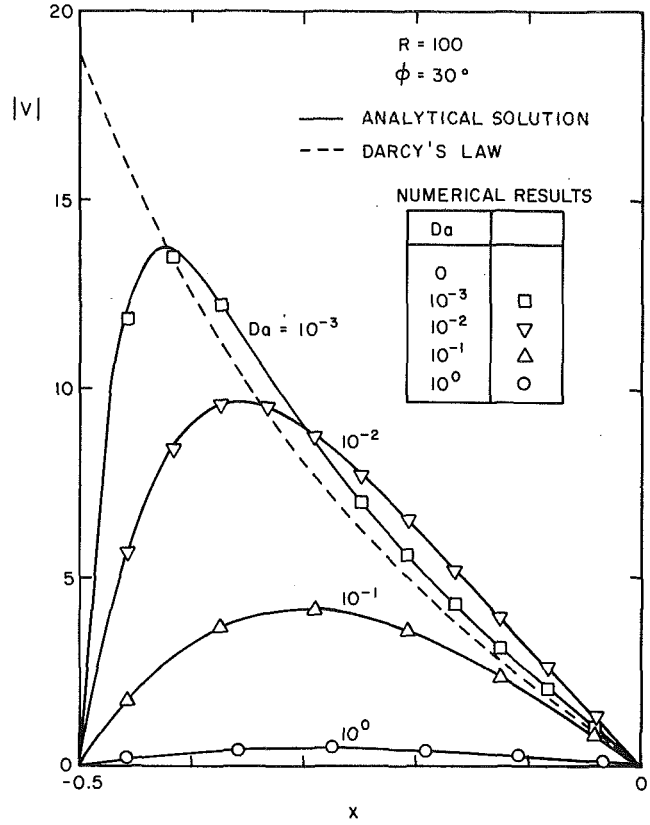

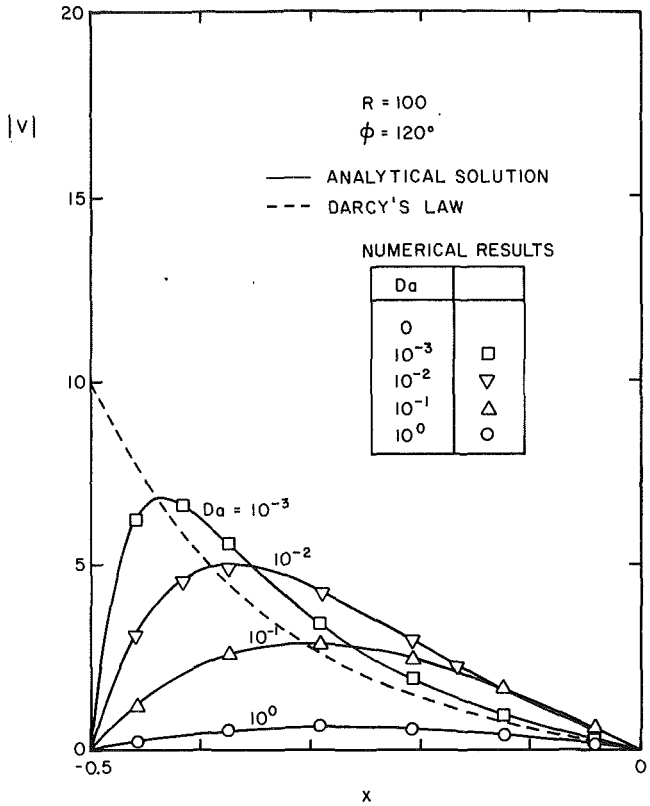

Fig. 1 Velocity profile at midheight of the enclosure, $y = 0$, as a function of Darcy number Da, for $R = 100$ and *(a)* $\phi = 30$ deg, *(b)* $\phi = 90$ deg, *(c)* $\phi = 120$ deg

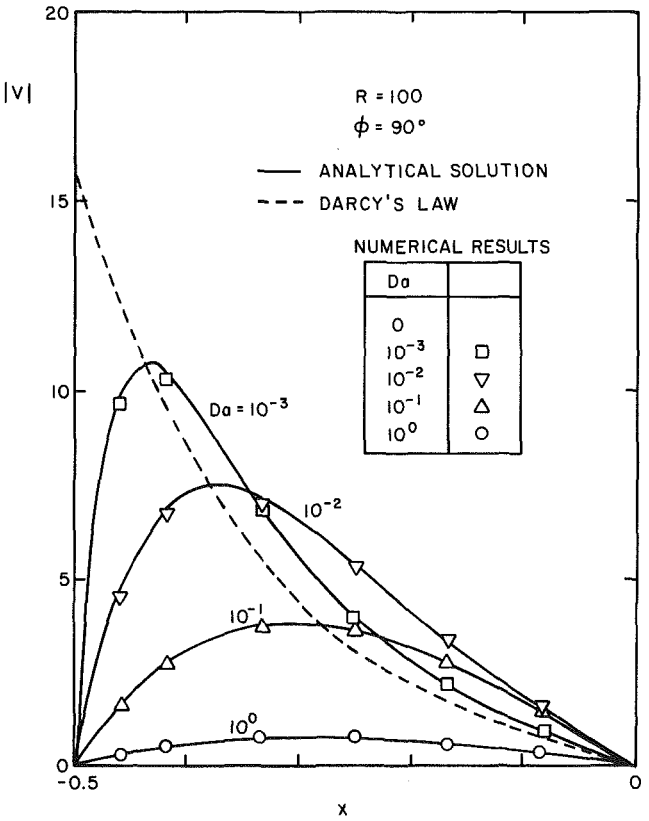

$Da = 10^{-6}$ (Darcy medium) and $R = 250$, increasing the number of grid points from 2601 to 6561 yielded an increase in the value of the Nusselt number of only 1.35 percent. An energy balance was also used to check the accuracy of the results; the heat transfer through each $x = \text{const}$ plane was compared with the heat input at $x = 1/2$, being usually within 1–2 percent.

Results and Discussion

The flow structure over the central part of the cavity is independent of aspect ratio if it is made large enough. With the thermal boundary conditions considered here, parallel flow can be easily established, a fact that was shown by Vasseur et al. (1987a) for an aspect ratio of around 2 for $Da = 0$ and $R \leq 500$. All the numerical results presented in this study were obtained for cavities with $A = 4$.

Analytical results are plotted for a variety of parameters, with numerical solutions of the complete partial differential equations also indicated for confirmation. Figures 1 (*a–c*) show the velocity profiles at midheight of the enclosure for $R = 100$ and various values of Da at $\phi = 30$ deg, 90 deg, and 120 deg, respectively. At a fixed inclination, a significant change is observed in the velocity field with an increase in the Darcy number. The smaller the Darcy number the closer it follows the Darcy medium profile ($Da = 0$), which is shown as a dotted line in the graphs. With Darcy's model the no-slip boundary condition is not satisfied and the velocity is maximum at the wall. In Brinkman's model the velocity is zero at the wall, increasing to a peak value, and then dropping back to zero in the core region of the enclosure. As the value of Da increases, not only does the position of the peak velocity shift away from the wall, but also its magnitude is considerably reduced. It is also noted in Figs. 1 (*a–c*) that, for some values of Da, the velocity in the core of the cavity can be greater than the Darcy velocities. In fact for a given x it is seen that in the core, v goes through a maximum as Da is reduced. A similar trend has been reported recently by Lauriat and Prasad (1987) and was found to be related to the relative magnitudes of the

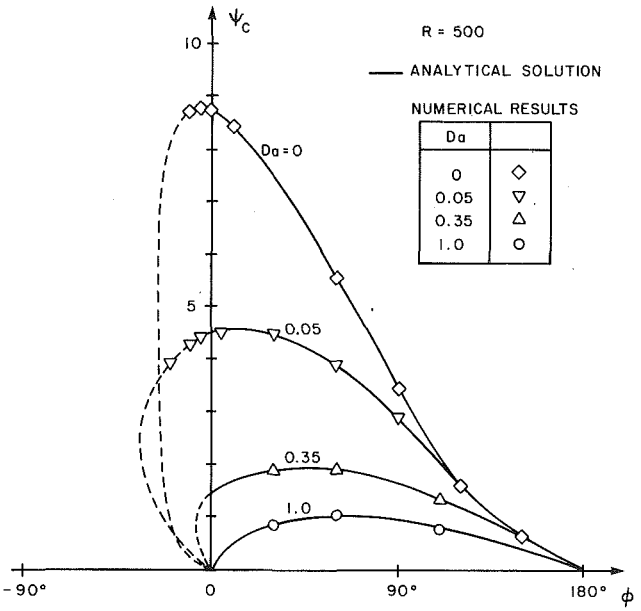

Fig. 2 Variation of stream function at center of layer, ψ_c, as a function of tilt angle ϕ, for various values of Da for $R = 500$

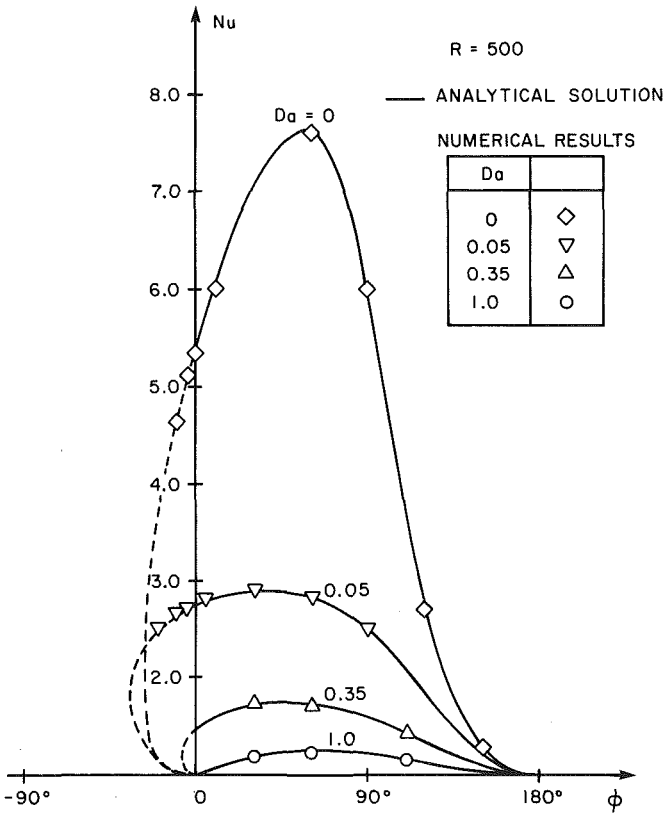

Fig. 3 Variation of Nusselt number Nu, as a function of tilt angle ϕ, for various values of Da for $R = 500$.

diffusion and the buoyancy terms. Thus for a given R, when Da is small enough the viscous forces have no effects in the core. Diffusion effects exist near the walls and the velocity profiles in the core follow Darcy's law. At higher Darcy numbers the viscous and buoyancy terms are of the same magnitude and the vorticity diffuses through the whole cavity. As Da is increased further, viscous effects become more important, the buoyancy-induced convection within the cavity is reduced, and the velocity profiles approach those in a fluid

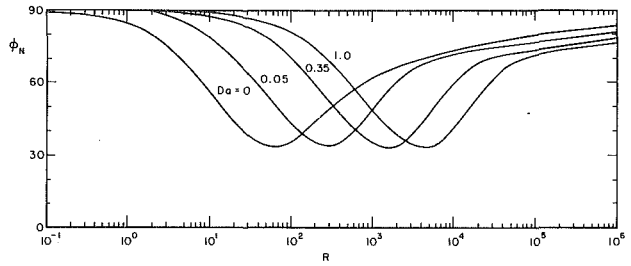

Fig. 4 Tilt angle for maximum Nusselt number, ϕ_N, as a function of Rayleigh number R and Darcy number Da

cavity. Thus the curves for $Da = 10^{-1}$ and $Da = 1$ in Fig. 1(a) are below the Darcy profile. The curves in Figs. 1(a-c) also illustrate the fact that, in general, the convection becomes less vigorous as the inclination of the cavity is increased.

Figures 2 and 3 show the variation of ψ_c, the stream function at the center of the layer, and the Nusselt number Nu, with inclination for various values of Da and a fixed $R = 500$. Since the transformation $\phi \to -\phi$, $\psi \to -\psi$, $T \to T$, $y \to -y$, $x \to -x$ alters neither the governing equations nor the boundary conditions, the flow is symmetric in opposite quadrants; thus only results in quadrants 1 and 4 are presented. The continuous lines in the first quadrant represent natural flow while the dashed lines in the third quadrant represent the anti-natural flow. When $Da = 1$ there is only one steady state for each inclination. However, for $Da = 0.35$ or larger, three values of ψ_c and Nu are possible for inclinations around zero. The range of inclinations for multiple steady states is a function of both the Darcy number and the Rayleigh number.

Figure 4 shows the variation of the angle ϕ_N for maximum heat transfer across the cavity with Rayleigh number for various values of the Darcy number. For small R, i.e., the pseudo-conduction regime, the temperature field is conduction dominated. The largest buoyancy force and circulation take place when the cavity is vertical, i.e., when the temperature gradient is horizontal. Thus all the curves tend toward $\phi_N = 90$ deg when R is small enough. As the Darcy number is increased the effect of the viscous term is enhanced and the pseudo-conduction regime is maintained up to relatively high values of R. For intermediate R, i.e., in the asymptotic regime, the variation of the angle ϕ_N with R is complex. For all the Darcy numbers considered, when R increases, ϕ_N first decreases down to a value of approximately 33.5 deg and then starts to increase again. The smaller the Darcy number, the smaller the Rayleigh number required to reach the minimum value of ϕ_N. Finally, when R is large enough, i.e., in the boundary layer regime, all the curves tend again toward $\phi_N = 90$ deg, i.e., the maximum heat transfer occurs when the cavity is vertical. A similar trend has been reported by other authors while studying numerically the natural convection of a fluid in an inclined cavity with two opposing isothermal walls.

Acknowledgments

This work was supported jointly by the Natural Science and Engineering Research Council of Canada Grant A-9201 and the FACR Government of Quebec Grant EQ-3359.

References

Bejan, A., 1983, "The Boundary Layer Regime in a Porous Layer With Uniform Heat Flux From the Side," *Int. J. Heat Mass Transfer*, Vol. 26, pp. 1339-1346.

Blythe, P. A., Simpkins, P. G., and Daniels, P. G., 1983, "Thermal Convection in a Cavity Filled With a Porous Medium: A Classification of Limiting Behavior," *Int. J. Heat Mass Transfer*, Vol. 26, pp. 701-708.

Daniels, P. G., 1983, "A Numerical Solution of the Vertical Boundary-Layer

Equations in a Horizontally Heated Porous Cavity," *J. Engng. Math.*, Vol. 17, pp. 285–300.

Georgiadis, J., and Catton, I., 1985, "Free Convective Motion in an Infinite Vertical Porous Slot: The Non-Darcian Regime," ASME Paper No. 85-HT-58.

Hong, J. T., Tien, C. L., and Kaviany, M., 1985, "Non-Darcian Effects on Vertical-Plate Natural Convection in Porous Media With High Porosities," *Int. J. Heat Mass Transfer*, Vol. 28, pp. 2149–2157.

Kimura, S., and Bejan, A., 1984, "The Boundary Layer Natural Convection Regime in a Rectangular Cavity With Uniform Heat Flux From the Side," ASME JOURNAL OF HEAT TRANSFER, Vol. 106, pp. 98–103.

Lauriat, G., and Prasad, V., 1987, "Natural Convection in a Vertical Porous Cavity: A Numerical Study of Brinkman-Extended Darcy Formulation," ASME JOURNAL OF HEAT TRANSFER, Vol. 109, pp. 688–696.

Moya, S. L., Ramos, E., and Sen, M., 1987, "Numerical Study of Natural Convection in a Tilted Rectangular Porous Material," *Int. J. Heat Mass Transfer*, Vol. 30, pp. 741–756.

Prasad, V., and Kulacki, F. A., 1984, "Natural Convection in a Rectangular Porous Cavity With Constant Heat Flux on One Vertical Wall," ASME JOURNAL OF HEAT TRANSFER, Vol. 106, pp. 152–157.

Sen, A. K., 1987, "Natural Convection in a Shallow Porous Cavity—The Brinkman Model," *Int. J. Heat Mass Transfer*, Vol. 30, pp. 855–868.

Sen, M., Vasseur, P., and Robillard, L., 1987, "Multiple Steady States for Unicellular Natural Convection in an Inclined Porous Layer," *Int. J. Heat Mass Transfer*, Vol. 30, pp. 2097–2113.

Tong, T. W., and Subramanian, E., 1985, "A Boundary Layer Analysis for Natural Convection in Porous Enclosure—Use of the Brinkman-Extended Darcy Model," *Int. J. Heat Mass Transfer*, Vol. 28, pp. 563–571.

Vasseur, P., Satish, M. G., and Robillard, L., 1987a, "Natural Convection in a Thin Inclined Porous Layer Exposed to a Constant Heat Flux," *Int. J. Heat Mass Transfer*, Vol. 30, pp. 537–549.

Vasseur, P., Robillard, L., and Sen, M., 1987b, "Unicellular Convective Motion in an Inclined Fluid Layer With Uniform Heat Flux," in: *Bifurcation Phenomena in Thermal Processes and Convection*, H. H. Bau et al., eds., ASME HTD-Vol. 94, pp. 23–29.

Vasseur, P., and Robillard, L., 1987c, "The Brinkman Model for Boundary Layer Regime in a Rectangular Cavity With Uniform Heat Flux From the Side," *Int. J. Heat Mass Transfer*, Vol. 30, pp. 717–727.

Forchheimer Free Convection Over a Nonisothermal Body of Arbitrary Shape in a Saturated Porous Medium

A. Nakayama,[1] T. Kokudai,[2] and H. Koyama[1]

Nomenclature

- c = empirical constant associated with porous inertia
- f = dimensionless stream function
- F = general heat transfer function $= \mathrm{Nu}_x/(d\ln\xi/d\ln x)^{1/2}\mathrm{Ra}_x^{1/4}$
- g = acceleration due to gravity
- I = function defined by equation (10c)
- k = effective thermal conductivity of a porous medium
- K = permeability
- L_r = reference length such as a radius and a plate height
- n = exponent associated with wall temperature, defined by equation (14)
- Nu_x = local Nusselt number, defined by equation (21)
- q^* = dimensionless local heat flux defined by equation (22)
- r = function representing a body shape
- r^* = 1 for plane flow and r for axisymmetric flow
- Ra_x = modified Rayleigh number defined by equation (10b)
- T = temperature
- u, v = Darcian velocity components
- x, y = boundary layer coordinates
- α = equivalent thermal diffusivity
- β = coefficient of thermal expansion
- η = similarity variable
- θ = dimensionless temperature
- λ = exponent associated with wall temperature
- ν = kinematic viscosity
- ξ = variable defined by equation (16)
- ϕ = peripheral angle
- ψ = stream function

Subscripts

- e = external
- r = reference
- w = wall

Introduction

Fand et al. (1986) carried out an experimental investigation of free convection from a horizontal circular cylinder embedded in porous media, and reported that deviations from the Darcy law occur when the Reynolds number based on the pore diameter exceeds 1 to 10. Thus, the non-Darcy flow situation is more likely to prevail when the Rayleigh number is sufficiently high that the boundary layer approximations are relevant. Plumb and Huenefeld (1981) considered the non-Darcy flow over a vertical flat plate using the Ergun model (Ergun, 1952), which includes the velocity square term, namely, the Forchheimer term (Forchheimer, 1901). However, the Ergun model permits similarity solutions only for a limited class of boundary conditions. Ingham (1986) argued that the Forchheimer flow may prevail for large Rayleigh number cases, and neglected the Darcy term, which would be small when compared with the non-Darcy term. The experimental data reported by Fand et al. do suggest existence of such a Forchheimer flow regime between the Darcy and post-Forchheimer flow regimes. Ingham extended Merkin's transformation (Merkin, 1979), by dropping the Darcy term, to the Forchheimer free convection on plane and axisymmetric bodies of arbitrary shape. In his analysis, however, the heated bodies were assumed to be isothermal.

In this note, we modify the transformations proposed for the Darcy flows (Nakayama and Koyama, 1987) to attack the problem of Forchheimer free convection. The body may be plane or axisymmetric, and its shape is arbitrary. Furthermore, we allow the surface wall temperature to vary in the streamwise direction. The overall Nusselt numbers on a horizontal circular cylinder estimated by our theory are compared against the experimental data of Fand et al. to examine the validity of the analysis.

Governing Equations and Boundary Conditions

Figure 1 depicts a heated plane or axisymmetric body of arbitrary shape embedded in a fluid-saturated porous medium. The governing equations for the problem, namely, the continuity equation, the Forchheimer-extended-Darcy law (i.e., Ergun model) subjected to the Boussinesq approximation, and the energy equation are written as

$$\frac{\partial r^* u}{\partial x} + \frac{\partial r^* v}{\partial y} = 0 \tag{1}$$

[1]Department of Energy and Mechanical Engineering, Shizuoka University, 3-5-1, Johoku Hamamatsu, 432 Japan.

[2]Suzuki Motor Co. Ltd., Hamamatsu, 432 Japan.

Contributed by the Heat Transfer Division for publication in the JOURNAL OF HEAT TRANSFER. Manuscript received by the Heat Transfer Division May 17, 1988; revision received May 8, 1989. Keywords: Geophysical Heat Transfer, Natural Convection, Porous Media.

Equations in a Horizontally Heated Porous Cavity," *J. Engng. Math.*, Vol. 17, pp. 285–300.

Georgiadis, J., and Catton, I., 1985, "Free Convective Motion in an Infinite Vertical Porous Slot: The Non-Darcian Regime," ASME Paper No. 85-HT-58.

Hong, J. T., Tien, C. L., and Kaviany, M., 1985, "Non-Darcian Effects on Vertical-Plate Natural Convection in Porous Media With High Porosities," *Int. J. Heat Mass Transfer*, Vol. 28, pp. 2149–2157.

Kimura, S., and Bejan, A., 1984, "The Boundary Layer Natural Convection Regime in a Rectangular Cavity With Uniform Heat Flux From the Side," ASME JOURNAL OF HEAT TRANSFER, Vol. 106, pp. 98–103.

Lauriat, G., and Prasad, V., 1987, "Natural Convection in a Vertical Porous Cavity: A Numerical Study of Brinkman-Extended Darcy Formulation," ASME JOURNAL OF HEAT TRANSFER, Vol. 109, pp. 688–696.

Moya, S. L., Ramos, E., and Sen, M., 1987, "Numerical Study of Natural Convection in a Tilted Rectangular Porous Material," *Int. J. Heat Mass Transfer*, Vol. 30, pp. 741–756.

Prasad, V., and Kulacki, F. A., 1984, "Natural Convection in a Rectangular Porous Cavity With Constant Heat Flux on One Vertical Wall," ASME JOURNAL OF HEAT TRANSFER, Vol. 106, pp. 152–157.

Sen, A. K., 1987, "Natural Convection in a Shallow Porous Cavity—The Brinkman Model," *Int. J. Heat Mass Transfer*, Vol. 30, pp. 855–868.

Sen, M., Vasseur, P., and Robillard, L., 1987, "Multiple Steady States for Unicellular Natural Convection in an Inclined Porous Layer," *Int. J. Heat Mass Transfer*, Vol. 30, pp. 2097–2113.

Tong, T. W., and Subramanian, E., 1985, "A Boundary Layer Analysis for Natural Convection in Porous Enclosure—Use of the Brinkman-Extended Darcy Model," *Int. J. Heat Mass Transfer*, Vol. 28, pp. 563–571.

Vasseur, P., Satish, M. G., and Robillard, L., 1987a, "Natural Convection in a Thin Inclined Porous Layer Exposed to a Constant Heat Flux," *Int. J. Heat Mass Transfer*, Vol. 30, pp. 537–549.

Vasseur, P., Robillard, L., and Sen, M., 1987b, "Unicellular Convective Motion in an Inclined Fluid Layer With Uniform Heat Flux," in: *Bifurcation Phenomena in Thermal Processes and Convection*, H. H. Bau et al., eds., ASME HTD-Vol. 94, pp. 23–29.

Vasseur, P., and Robillard, L., 1987c, "The Brinkman Model for Boundary Layer Regime in a Rectangular Cavity With Uniform Heat Flux From the Side," *Int. J. Heat Mass Transfer*, Vol. 30, pp. 717–727.

Forchheimer Free Convection Over a Nonisothermal Body of Arbitrary Shape in a Saturated Porous Medium

A. Nakayama,[1] T. Kokudai,[2] and H. Koyama[1]

Nomenclature

- c = empirical constant associated with porous inertia
- f = dimensionless stream function
- F = general heat transfer function $= \mathrm{Nu}_x/(d\ln\xi/d\ln x)^{1/2}\mathrm{Ra}_x^{1/4}$
- g = acceleration due to gravity
- I = function defined by equation (10*c*)
- k = effective thermal conductivity of a porous medium
- K = permeability
- L_r = reference length such as a radius and a plate height
- n = exponent associated with wall temperature, defined by equation (14)
- Nu_x = local Nusselt number, defined by equation (21)
- q^* = dimensionless local heat flux defined by equation (22)
- r = function representing a body shape
- r^* = 1 for plane flow and r for axisymmetric flow
- Ra_x = modified Rayleigh number defined by equation (10*b*)
- T = temperature
- u, v = Darcian velocity components
- x, y = boundary layer coordinates
- α = equivalent thermal diffusivity
- β = coefficient of thermal expansion
- η = similarity variable
- θ = dimensionless temperature
- λ = exponent associated with wall temperature
- ν = kinematic viscosity
- ξ = variable defined by equation (16)
- ϕ = peripheral angle
- ψ = stream function

Subscripts

- e = external
- r = reference
- w = wall

Introduction

Fand et al. (1986) carried out an experimental investigation of free convection from a horizontal circular cylinder embedded in porous media, and reported that deviations from the Darcy law occur when the Reynolds number based on the pore diameter exceeds 1 to 10. Thus, the non-Darcy flow situation is more likely to prevail when the Rayleigh number is sufficiently high that the boundary layer approximations are relevant. Plumb and Huenefeld (1981) considered the non-Darcy flow over a vertical flat plate using the Ergun model (Ergun, 1952), which includes the velocity square term, namely, the Forchheimer term (Forchheimer, 1901). However, the Ergun model permits similarity solutions only for a limited class of boundary conditions. Ingham (1986) argued that the Forchheimer flow may prevail for large Rayleigh number cases, and neglected the Darcy term, which would be small when compared with the non-Darcy term. The experimental data reported by Fand et al. do suggest existence of such a Forchheimer flow regime between the Darcy and post-Forchheimer flow regimes. Ingham extended Merkin's transformation (Merkin, 1979), by dropping the Darcy term, to the Forchheimer free convection on plane and axisymmetric bodies of arbitrary shape. In his analysis, however, the heated bodies were assumed to be isothermal.

In this note, we modify the transformations proposed for the Darcy flows (Nakayama and Koyama, 1987) to attack the problem of Forchheimer free convection. The body may be plane or axisymmetric, and its shape is arbitrary. Furthermore, we allow the surface wall temperature to vary in the streamwise direction. The overall Nusselt numbers on a horizontal circular cylinder estimated by our theory are compared against the experimental data of Fand et al. to examine the validity of the analysis.

Governing Equations and Boundary Conditions

Figure 1 depicts a heated plane or axisymmetric body of arbitrary shape embedded in a fluid-saturated porous medium. The governing equations for the problem, namely, the continuity equation, the Forchheimer-extended-Darcy law (i.e., Ergun model) subjected to the Boussinesq approximation, and the energy equation are written as

$$\frac{\partial r^* u}{\partial x} + \frac{\partial r^* v}{\partial y} = 0 \tag{1}$$

[1]Department of Energy and Mechanical Engineering, Shizuoka University, 3-5-1, Johoku Hamamatsu, 432 Japan.

[2]Suzuki Motor Co. Ltd., Hamamatsu, 432 Japan.

Contributed by the Heat Transfer Division for publication in the JOURNAL OF HEAT TRANSFER. Manuscript received by the Heat Transfer Division May 17, 1988; revision received May 8, 1989. Keywords: Geophysical Heat Transfer, Natural Convection, Porous Media.

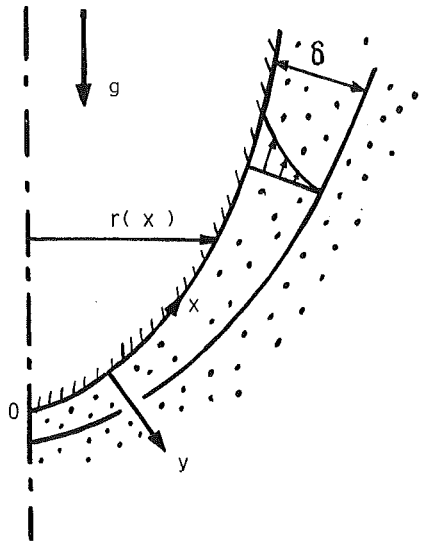

Fig. 1 Physical model and its coordinates

$$u+\frac{C\sqrt{K}}{\nu}u^2=\frac{\beta K}{\nu}(T-T_e)g_x \tag{2}$$

$$u\frac{\partial T}{\partial x}+v\frac{\partial T}{\partial y}=\alpha\frac{\partial^2 T}{\partial y^2} \tag{3}$$

where

$$g_x=g\left(1-\left(\frac{dr}{dx}\right)^2\right)^{1/2} \tag{4}$$

and

$$r^*=\begin{cases}1 & \text{: plane flow}\\ r(x) & \text{: axisymmetric flow}\end{cases} \tag{5}$$

Since the viscous shear stress term (Brinkman term) is neglected, the validity of the present analysis is restricted to comparatively low porosities and permeabilities. For high Rayleigh number flows, the Darcy term (the first left-hand-side term) can be dropped.

$$u^2=\beta\sqrt{K}g_x(T-T_e)/C \tag{6}^3$$

The appropriate boundary conditions for equations (1), (3), and (6) are

$$y=0: \quad v=0 \quad T=T_w(x) \tag{7a, b}$$

$$y\to\infty: \quad u=0, \quad T=T_e \tag{7c, d}$$

Transformation

The continuity equation (1) may automatically be satisfied by introducing the stream function ψ such that

$$u=\frac{\partial\psi}{\partial y}\frac{1}{r^*} \tag{8a}$$

$$v=-\frac{\partial\psi}{\partial x}\frac{1}{r^*} \tag{8b}$$

[3] Strictly speaking, equation (6) is only valid when $CK^{3/2}g_x\beta(T_w-T_e)/\nu^2>>1$. Practically, this requirement can be relaxed, since the experimental data of Fand et al. (against which the present results will be compared) suggest that the assumption is good even when $CK^{3/2}g_x\beta(T_w-T_e)/\nu^2$ is of order unity.

Let us introduce the following transformations similar to those proposed for the Darcy flows (Nakayama and Koyama, 1987):

$$\psi=\alpha r^*(\sqrt{\mathrm{Ra}_x}I)^{1/2}f(x,\eta) \tag{9a}$$

$$\eta=\frac{y}{x}(\sqrt{\mathrm{Ra}_x}/I)^{1/2} \tag{9b}$$

$$T-T_e=\Delta T_w\theta(x,\eta) \tag{9c}$$

where

$$\Delta T_w=T_w-T_e \tag{10a}$$

$$\mathrm{Ra}_x=\sqrt{K}g_x\beta\Delta T_w x^2/C\alpha^2 \tag{10b}$$

and

$$I=\frac{\int_0^x \Delta T_w^{5/2}g_x^{1/2}r^{*2}dx}{\Delta T_w^{5/2}g_x^{1/2}r^{*2}x} \tag{10c}$$

Ra_x is the modified Rayleigh number and η is the proposed similarity variable. Substitution of equations (9) into equations (6) and (3) yields

$$(f')^2=\theta \tag{11a}$$

$$\theta''+\left(\frac{1}{2}-nI\right)f\theta'-nIf'\theta=Ix\left(f'\frac{\partial\theta}{\partial x}-\theta'\frac{\partial f}{\partial x}\right) \tag{11b}$$

which are subjected to the boundary conditions transformed as

$$\eta=0: \quad f=0, \quad \theta=1 \tag{12a, b}$$

$$\eta\to\infty: \quad f'=0, \quad \theta=0 \tag{12c, d}$$

The Darcian velocities are given by

$$u=\frac{\alpha}{x}\sqrt{\mathrm{Ra}_x}f' \tag{13a}$$

and

$$v=\frac{\alpha}{x}(\sqrt{\mathrm{Ra}_x}/I)^{1/2}\left[\left(nI-\frac{1}{2}\right)f+\left(\frac{1}{2}-\frac{3}{2}nI-I\frac{d\ln\sqrt{g_x}r^*}{d\ln x}\right)\eta f'-Ix\frac{\partial f}{\partial x}\right] \tag{13b}$$

where

$$n=\frac{d\ln\Delta T_w}{d\ln x} \tag{14}$$

The primes in the above equations denote differentiation with respect to η.

Similarity Solutions

The exact solutions of equations (11*a*) and (11*b*) are possible when the lumped parameter nI remains constant in the streamwise direction. One such obvious case in an isothermal body of arbitrary shape. The case has been treated by Ingham (1986). Our transformation is more general than his, since it can deal with nonisothermal bodies of arbitrary shape. To seek possible similarity solutions, let us write the lumped parameter nI as

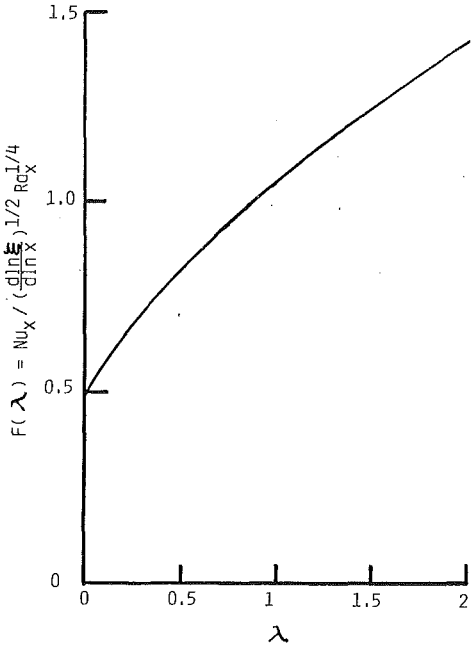

Fig. 2 General heat transfer function $F(\lambda) = \mathrm{Nu}_x/(d\ln\xi/d\ln x)^{1/2}\mathrm{Ra}_x^{1/4}$

$$nI = \frac{d\ln\Delta T_w}{d\ln x}\frac{\int_0^x \Delta T_w^{5/2} g_x^{1/2} r^{*2} dx}{\Delta T_w^{5/2} g_x^{1/2} r^{*2} x}$$

$$= \frac{d\ln\Delta T_w}{d\ln\xi}\frac{\int_0^\xi \Delta T_w^{5/2} d\xi}{\Delta T_w^{5/2}\xi} \tag{15}$$

where

$$\xi = \int_0^x g_x^{1/2} r^{*2} dx \tag{16}$$

The second expression in equation (15) suggests that the similarity solutions are possible when the wall temperature varies according to

$$\Delta T_w \propto \xi^\lambda \tag{17}$$

Upon substituting the foregoing relation into equation (15), we have

$$nI = \frac{\lambda}{1+\frac{5}{2}\lambda} \tag{18}$$

Now, equation (11*a*) may readily be integrated using the boundary condition given by equation (12*a*) as

$$f = \int_0^\eta \sqrt{\bar{\theta}}\, d\eta \tag{19}$$

Upon substituting equations (18) and (19) into equation (11*b*), we obtain

$$\theta'' + \frac{2+\lambda}{2(2+5\lambda)}\theta' \int_0^\eta \sqrt{\bar{\theta}}\, d\eta - \frac{2\lambda}{2+5\lambda}\theta^{3/2} = 0 \tag{20}$$

The foregoing equation, subjected to equtaions (12*b*) and (12*d*), can easily be solved using any standard shooting procedure.

Once the dimensionless temperature distribution $\theta(\eta)$ is known, the local Nusselt number of primary concern may be evaluated from

$$\mathrm{Nu}_x = \frac{q_w x}{\Delta T_w k} = -\theta'(0)\left(1+\frac{5}{2}\lambda\right)^{1/2}\left(\frac{d\ln\xi}{d\ln x}\right)^{1/2}\mathrm{Ra}_x^{1/4} \tag{21}$$

where $q_w = -k(\partial T/\partial y)|_{y=0}$ is the local wall heat flux, and the relation $1/I = (1+(5/2)\lambda)(d\ln\xi/d\ln x)$ is used.

Results and Discussion

The present analysis revealed that a certain class of similarity solutions exists not only for an isothermal body but also for a nonisothermal body of arbitrary shape. The heat transfer results are presented in Fig. 2 in terms of the function $F(\lambda) \equiv \mathrm{Nu}_x/(d\ln\xi/d\ln x)^{1/2}\mathrm{Ra}_x^{1/4}$ once for all plane and axisymmetric bodies.

In order to illustrate the generality acquired in the present similarity transformations, free convection over a vertical flat plate, a vertical cone pointing downward, a horizontal circular cylinder, and a sphere are considered. The transformed variable ξ and its derivative $d\ln\xi/d\ln x$ for each geometric configuration are listed in Appendix A. Similarity solutions exist when the surface wall temperature varies according to equation (17). The local surface heat flux distributions for such cases are listed in Appendix B, where q^* is defined as

$$q^* \equiv \left(\frac{q_w L_r}{\Delta T_w k}\right)\Big/\left(\frac{\sqrt{K}\beta\Delta T_{wr} g L_r^2}{C\alpha^2}\right)^{1/4} \tag{22}$$

where ΔT_{wr} is the wall-ambient temperature difference at a trailing edge or a rear stagnation point. Thus, the local wall heat flux distributions for the vertical flat plate (given by equation (B1)) may readily be translated to those for the vertical cone pointing downward (given by equation (B2)). The heat flux and wall temperature distributions given by equations (B3) to (B6) are plotted in Figs. 3 and 4, for a circular cylinder and a sphere. The heat fluxes at the front stagnation point become infinite when $\lambda < 2/15$ for the circular cylinder and $\lambda < 2/35$ for the sphere. For comparatively large values of λ, on the other hand, the local heat flux vanishes at the front and rear stagnation points, and attains its maximum midway.

Fand et al. (1986) carried out an experimental investigation of free convection from a nearly isothermal circular cylinder, and reduced the experimental data in terms of the overall Nusselt number (based on the diameter $D = 2L_r = 0.0145$ m), which, in our theory, corresponds to

$$\mathrm{Nu} = \left[\left(\frac{4D}{C\sqrt{K}}\right)^{1/4}\frac{1}{\pi}\int^\pi q^* d\phi\right]\left(\frac{Kg\beta\Delta T_{wr} D}{\alpha^2}\right)^{1/4}$$

$$\cong 2.8\left(\frac{Kg\beta\Delta T_{wr} D}{\alpha^2}\right)^{1/4} \tag{23}$$

for the case of water and 3-mm-dia glass spheres ($K = 5.6\times10^{-9}\mathrm{m}^2$ and $C = 0.64$). The empirical constant C in our notation corresponds to $C_2\sqrt{K}$ in their notation. The values based on equation (23) are tabulated in Table 1 with the experimental data and also the values estimated from Darcy's law (Fand et al., 1986), namely,

$$\mathrm{Nu} = 0.565(Kg\beta\Delta T_{wr} D/\alpha\nu)^{1/2} \tag{24}$$

Our theory agrees reasonably well with the experimental data. This substantiates the validity of our analysis.

References

Ergun, S., 1952, "Fluid Flow Through Packed Columns," *Chem. Engng. Prog.*, Vol. 48, pp. 89–94.

Fand, R. M., Steinberger, T. E., and Cheng, P., 1986, "Natural Convection Heat Transfer From a Horizontal Cylinder Embedded in a Porous Medium," *Int. J. Heat and Mass Transfer*, Vol. 29, pp. 119–123.

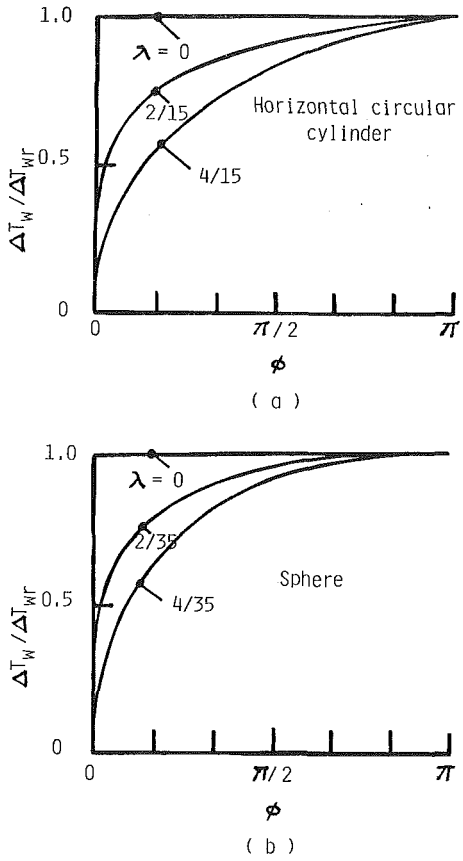

Fig. 3 Wall temperature distributions that permit similarity solutions: (*a*) a horizontal circular cylinder, (*b*) a sphere

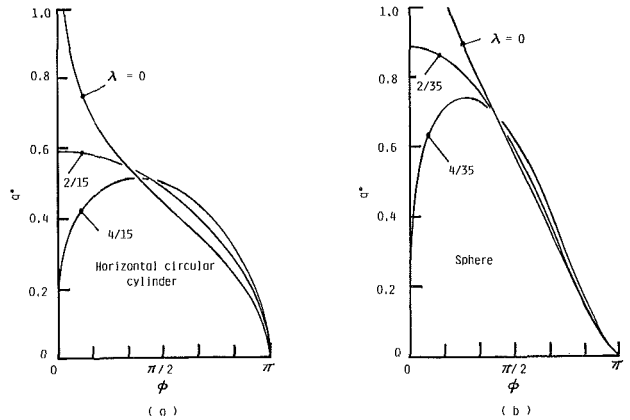

Fig. 4 Effect of wall temperature distributions on local heat fluxes: (*a*) a horizontal circular cylinder, (*b*) a sphere

Table 1 Nu

$Kg\beta\Delta T_{wr}D/\alpha\nu$	(ν/α)	Present results	Experiment	Darcy's law
62.24	(3.029)	10.4	7.30	4.46
125.0	(2.521)	11.8	9.83	6.32
197.9	(2.205)	12.8	11.4	7.95

Forchheimer, P., 1901, "Wasserbewegung durch Boden," *Forschtlft. Ver. D. Ing.*, Vol. 45, pp. 1782–1788.

Ingham, D. B., 1986, "The Non-Darcy Free Convection Boundary Layer on Axisymmetric and Two-Dimensional Bodies of Arbitrary Shape," *Int. J. Heat Mass Transfer*, Vol. 29, pp. 1759–1763.

Merkin, J. H., 1979, "Free Convection Boundary Layers on Axisymmetric and Two-Dimensional Bodies of Arbitrary Shape in a Saturated Porous Medium," *Int. J. Heat Mass Transfer*, Vol. 22, pp. 1461–1462.

Nakayama, A., and Koyama, H., 1987, "Free Convective Heat Transfer Over a Nonisothermal Body of Arbitrary Shape Embedded in a Fluid Saturated Porous Medium," ASME JOURNAL OF HEAT TRANSFER, Vol. 109, pp. 125–130.

Plumb, O. A., and Huenefeld, J. C., 1981, "Non-Darcy Natural Convection From Heated Surfaces in Saturated Porous Media," *Int. J. Heat Mass Transfer*, Vol. 24, pp. 765–768.

APPENDIX A

The similarity variable ξ is given by

$$\xi = \sqrt{g}L_r(x/L_r) \quad (\text{i.e., } \lambda = n)$$

for a vertical flat plate (A1)

$$\xi = (g\cos\gamma)^{1/2}\sin^2\gamma L_r^3(x/L_r)^3/3 \quad (\text{i.e., } \lambda = n/3)$$

for a vertical cone pointing downward (A2)

$$\xi = \sqrt{g}L_r\int_0^{\phi}\sin^{1/2}\phi d\phi$$

for a horizontal circular cylinder (A3)

$$\xi = \sqrt{g}L_r^3\int_0^{\phi}\sin^{5/2}\phi d\phi$$

for a sphere (A4)

The symbol L_r denotes reference lengths such as a plate height, a cone slant height (γ = an apex half-angle), and radii of a cylinder and a sphere, while ϕ is the peripheral angle measured from the lower stagnation point such that $x = L_r\phi$. Correspondingly, $d\ln\xi/d\ln x$ may be given by

$$\frac{d\ln\xi}{d\ln x} = 1$$ for a vertical flat plate (A5)

$$\frac{d\ln\xi}{d\ln x} = 3$$ for a vertical cone pointing downward (A6)

$$\frac{d\ln\xi}{d\ln x} = \phi\sin^{1/2}\phi/\int_0^{\phi}\sin^{1/2}\phi d\phi$$

for a horizontal circular cylinder (A7)

$$\frac{d\ln\xi}{d\ln x} = \phi\sin^{5/2}\phi/\int_0^{\phi}\sin^{5/2}\phi d\phi$$

for a sphere (A8)

APPENDIX B

When $\Delta T_w \propto x^n$, the surface heat flux varies locally as

$$q^* = F(n)(x/L_r)^{-(2-5n)/4}$$ (B1)

for a vertical flat plate

and

$$q^* = \sqrt{3}F(n/3)\cos^{1/4}\gamma(x/L_r)^{-(2-5n)/4}$$ (B2)

for a vertical cone pointing downward.

The surface heat flux on a horizontal circular cylinder varies as

$$q^* = F(\lambda)\left(\frac{\sin\phi}{\int_0^\phi \sin^{1/2}\phi d\phi}\right)^{1/2}\left(\frac{\int_0^\phi \sin^{1/2}\phi d\phi}{\int_0^\pi \sin^{1/2}\phi d\phi}\right)^{\frac{5}{4}\lambda} \quad \text{(B3)}$$

when the wall temperature varies as

$$\Delta T_w/\Delta T_{wr} = \left(\int_0^\phi \sin^{1/2}\phi d\phi / \int_0^\pi \sin^{1/2}\phi d\phi\right)^{\lambda} \quad \text{(B4)}$$

The surface heat flux on a sphere, on the other hand, varies as

$$q^* = F(\lambda)\left(\frac{\sin^3\phi}{\int_0^\phi \sin^{5/2}\phi d\phi}\right)^{1/2}\left(\frac{\int_0^\phi \sin^{5/2}\phi d\phi}{\int_0^\pi \sin^{5/2}\phi d\phi}\right)^{\frac{5}{4}\lambda} \quad \text{(B5)}$$

when the wall temperature varies as

$$\Delta T_w/\Delta T_{wr} = \left(\int_0^\phi \sin^{5/2}\phi d\phi / \int_0^\pi \sin^{5/2}\phi d\phi\right)^{\lambda} \quad \text{(B6)}$$

The Influence of Lateral Mass Flux on Mixed Convection Over Inclined Surfaces in Saturated Porous Media

F. C. Lai[1] and F. A. Kulacki[1]

Nomenclature

A = constant defined in equation (7)
a = constant defined in equation (7)
B = constant defined in equation (8)
f = dimensionless stream function defined by equation (14)
f_w = lateral mass flux parameter defined by equation (16)
g = acceleration due to gravity, m/s^2
g_x, g_y = gravitational acceleration in x and y directions, m/s^2
h = local heat transfer coefficient, W/m^2-K
K = permeability, m^2
k = effective thermal conductivity, W/m-K
m = constant defined in equation (8)
n = constant defined in equation (7)
Nu = local Nusselt number $= hx/k$
p = pressure, Pa
Pe = local Peclet number $= U_\infty x/\alpha$
Ra = modified local Rayleigh number $= Kg\beta\,|T_w - T_\infty\,|x/\nu\alpha$
T = temperature, K
U_∞ = free-stream velocity in x direction, m/s
u = Darcy velocity in the x direction, m/s
v = Darcy velocity in the y direction, m/s
x, y = Cartesian coordinates, m
α = thermal diffusivity of porous medium, m^2/s
β = coefficient of thermal expansion, K^{-1}
γ = angle parameter $= 2m/(m+1)$
η = independent similarity variable
η_T = dimensionless thermal boundary-layer thickness
θ = dimensionless temperature
λ = constant defined in equation (7)
μ = dynamic viscosity of convective fluid, kg/m-s
ν = kinematic viscosity of convective fluid, m^2/s
ψ = stream function

Subscripts

fc = forced convection
mx = mixed convection
nc = natural convection
w = condition at the wall
∞ = condition at infinity

Introduction

For the past decade much work has been done on the study of natural convection in saturated porous media, while mixed convection, although of equal importance in many engineering applications, receives rather less attention. Wooding (1963) made the first attempt to study mixed convection in a porous layer, which was later followed by Prats (1966), Sutton (1970), and Homsy and Sherwood (1976). Experimental results were very limited and reported only by Combarnous and Bia (1971) for flow through a horizontal porous layer, and by Schrock and Laird (1976) for a laboratory model to simulate the geothermal convection loop. By boundary-layer formulation and similarity method, Cheng (1977a, 1977b) has conducted a series of investigations to study mixed convection over vertical, inclined, and horizontal plates. Recently, numerical results on mixed convection in vertical and horizontal porous layers with nonuniform heating on the boundary were reported by Lai et al. (1988a) and Prasad et al. (1988), respectively, while experimental results were reported for the latter case (Lai and Kulacki, 1988b, 1988c).

The purpose of this note is to extend the previous study by Cheng (1977c) to consider the influence of lateral mass flux on mixed convection over inclined surfaces in saturated porous media. As pointed out by Cheng (1977c), problems of this type are very important in applications of geothermal energy. The model, although simple and idealized, does provide some useful informations for the estimation of productionr ate. Similarity solutions are obtained for the special case where the wall temperature, the free-stream velocity, and the injection or withdrawal velocity are prescribed power functions of distance from the leading edge. The limiting cases of free and forced convection are also presented.

Analysis

Consider the problem of injection or withdrawal of fluid along the surface of an inclined wall embedded in a saturated porous medium (Fig. 1). The governing equations based on Darcy's law are given by

$$\frac{\partial u}{\partial x} + \frac{\partial v}{\partial y} = 0 \quad (1)$$

$$u = -\frac{K}{\mu}\left(\frac{\partial p}{\partial x} \pm \rho g_x\right) \quad (2)$$

[1]Department of Mechanical Engineering, Colorado State University, Fort Collins, CO 80523.

Contributed by the Heat Transfer Division for publication in the JOURNAL OF HEAT TRANSFER. Manuscript received by the Heat Transfer Division October 6, 1988; revision received July 3, 1989. Keywords: Mass Transfer, Mixed Convection, Porous Media.

$$q^* = F(\lambda)\left(\frac{\sin\phi}{\int_0^\phi \sin^{1/2}\phi d\phi}\right)^{1/2}\left(\frac{\int_0^\phi \sin^{1/2}\phi d\phi}{\int_0^\pi \sin^{1/2}\phi d\phi}\right)^{\frac{5}{4}\lambda} \quad \text{(B3)}$$

when the wall temperature varies as

$$\Delta T_w/\Delta T_{wr} = \left(\int_0^\phi \sin^{1/2}\phi d\phi / \int_0^\pi \sin^{1/2}\phi d\phi\right)^{\lambda} \quad \text{(B4)}$$

The surface heat flux on a sphere, on the other hand, varies as

$$q^* = F(\lambda)\left(\frac{\sin^3\phi}{\int_0^\phi \sin^{5/2}\phi d\phi}\right)^{1/2}\left(\frac{\int_0^\phi \sin^{5/2}\phi d\phi}{\int_0^\pi \sin^{5/2}\phi d\phi}\right)^{\frac{5}{4}\lambda} \quad \text{(B5)}$$

when the wall temperature varies as

$$\Delta T_w/\Delta T_{wr} = \left(\int_0^\phi \sin^{5/2}\phi d\phi / \int_0^\pi \sin^{5/2}\phi d\phi\right)^{\lambda} \quad \text{(B6)}$$

The Influence of Lateral Mass Flux on Mixed Convection Over Inclined Surfaces in Saturated Porous Media

F. C. Lai[1] and F. A. Kulacki[1]

Nomenclature

- A = constant defined in equation (7)
- a = constant defined in equation (7)
- B = constant defined in equation (8)
- f = dimensionless stream function defined by equation (14)
- f_w = lateral mass flux parameter defined by equation (16)
- g = acceleration due to gravity, m/s^2
- g_x, g_y = gravitational acceleration in x and y directions, m/s^2
- h = local heat transfer coefficient, W/m^2-K
- K = permeability, m^2
- k = effective thermal conductivity, W/m-K
- m = constant defined in equation (8)
- n = constant defined in equation (7)
- Nu = local Nusselt number $= hx/k$
- p = pressure, Pa
- Pe = local Peclet number $= U_\infty x/\alpha$
- Ra = modified local Rayleigh number $= Kg\beta\,|T_w - T_\infty\,|x/\nu\alpha$
- T = temperature, K
- U_∞ = free-stream velocity in x direction, m/s
- u = Darcy velocity in the x direction, m/s
- v = Darcy velocity in the y direction, m/s
- x, y = Cartesian coordinates, m
- α = thermal diffusivity of porous medium, m^2/s
- β = coefficient of thermal expansion, K^{-1}
- γ = angle parameter $= 2m/(m+1)$
- η = independent similarity variable
- η_T = dimensionless thermal boundary-layer thickness
- θ = dimensionless temperature
- λ = constant defined in equation (7)
- μ = dynamic viscosity of convective fluid, kg/m-s
- ν = kinematic viscosity of convective fluid, m^2/s
- ψ = stream function

Subscripts

- fc = forced convection
- mx = mixed convection
- nc = natural convection
- w = condition at the wall
- ∞ = condition at infinity

Introduction

For the past decade much work has been done on the study of natural convection in saturated porous media, while mixed convection, although of equal importance in many engineering applications, receives rather less attention. Wooding (1963) made the first attempt to study mixed convection in a porous layer, which was later followed by Prats (1966), Sutton (1970), and Homsy and Sherwood (1976). Experimental results were very limited and reported only by Combarnous and Bia (1971) for flow through a horizontal porous layer, and by Schrock and Laird (1976) for a laboratory model to simulate the geothermal convection loop. By boundary-layer formulation and similarity method, Cheng (1977a, 1977b) has conducted a series of investigations to study mixed convection over vertical, inclined, and horizontal plates. Recently, numerical results on mixed convection in vertical and horizontal porous layers with nonuniform heating on the boundary were reported by Lai et al. (1988a) and Prasad et al. (1988), respectively, while experimental results were reported for the latter case (Lai and Kulacki, 1988b, 1988c).

The purpose of this note is to extend the previous study by Cheng (1977c) to consider the influence of lateral mass flux on mixed convection over inclined surfaces in saturated porous media. As pointed out by Cheng (1977c), problems of this type are very important in applications of geothermal energy. The model, although simple and idealized, does provide some useful informations for the estimation of productionr ate. Similarity solutions are obtained for the special case where the wall temperature, the free-stream velocity, and the injection or withdrawal velocity are prescribed power functions of distance from the leading edge. The limiting cases of free and forced convection are also presented.

Analysis

Consider the problem of injection or withdrawal of fluid along the surface of an inclined wall embedded in a saturated porous medium (Fig. 1). The governing equations based on Darcy's law are given by

$$\frac{\partial u}{\partial x} + \frac{\partial v}{\partial y} = 0 \quad (1)$$

$$u = -\frac{K}{\mu}\left(\frac{\partial p}{\partial x} \pm \rho g_x\right) \quad (2)$$

[1]Department of Mechanical Engineering, Colorado State University, Fort Collins, CO 80523.

Contributed by the Heat Transfer Division for publication in the JOURNAL OF HEAT TRANSFER. Manuscript received by the Heat Transfer Division October 6, 1988; revision received July 3, 1989. Keywords: Mass Transfer, Mixed Convection, Porous Media.

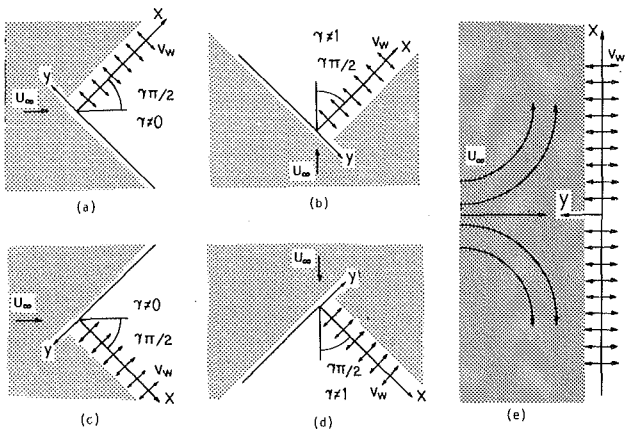

Fig. 1 Coordinate systems for an inclined surface embedded in a saturated porous medium

$$v = -\frac{K}{\mu}\left(\frac{\partial p}{\partial y} \pm \rho g_y\right) \tag{3}$$

$$u\frac{\partial T}{\partial x} + v\frac{\partial T}{\partial y} = \alpha\left(\frac{\partial^2 T}{\partial x^2} + \frac{\partial^2 T}{\partial y^2}\right) \tag{4}$$

where the "+" signs in equations (2) and (3) are for the coordinate systems shown in Figs. 1(*a*) and 1(*b*) while the "−" signs are for Figs. 1(*c*) and 1(*d*).

It is clear that the formulations based on Darcy's law do not take into account viscous effects, flow inertia, or thermal disperison. However, our previous studies (Lai and Kulacki, 1988d, 1989) have shown that these non-Darcy effects, especially the thermal dispersion, are important only when the flow inertia becomes prevalent. The solution of the Darcy formulation always provides a lower bound for the heat tranfser results. Therefore, a first step toward the complete understanding of non-Darcy convection requires the knowledge of basic solutions, i.e., Darcy flow, which is the main concern of the present study.

Having invoked the Boussinesq and boundary-layer approximations, the governing equations in terms of stream function ψ are reduced to

$$\frac{\partial^2 \psi}{\partial y^2} = \pm\frac{Kg_x\beta}{\nu}\frac{\partial T}{\partial y} \tag{5}$$

$$\frac{\partial \psi}{\partial y}\frac{\partial T}{\partial x} - \frac{\partial \psi}{\partial x}\frac{\partial T}{\partial y} = \alpha\frac{\partial^2 T}{\partial y^2} \tag{6}$$

with boundary conditions

$$y=0, \quad T_w = T_\infty \pm Ax^\lambda, \quad v = -\frac{\partial \psi}{\partial x} = ax^n \tag{7}$$

$$y\to\infty, \quad T = T_\infty, \quad u = \frac{\partial \psi}{\partial y} = U_\infty = Bx^m \tag{8}$$

where $A>0$ and $B>0$. It is clear that a is positive for injection of fluid and negative for withdrawal of fluid. For mixed convection, we designate the flow as an "aiding" flow when the buoyancy force has a component in the direction of the free-stream velocity, and likewise, as an "opposing" flow when the buoyancy component is opposite to the free-stream velocity.

It has been shown that similarity solutions exist for the case when there is no injection or withdrawal of fluid (Cheng, 1977a). Similarly, it can be shown that equations (5)–(8) also permit similarity solutions if $\lambda = m$ and $n = (m-1)/2$. Under such a restricted condition, the governing equations are transformed into

$$f'' = \pm\left(\frac{\mathrm{Ra}}{\mathrm{Pe}}\right)\theta' \tag{9}$$

$$\theta'' = -\frac{\lambda+1}{2}f\theta' + \lambda f'\theta \tag{10}$$

with boundary conditions given by

$$\eta=0, \quad \theta=1, \quad f=f_w \tag{11}$$

$$\eta\to\infty, \quad \theta=0, \quad f'=1 \tag{12}$$

where the similarity variables η, f, and θ are defined as

$$\eta = \left(\frac{U_\infty x}{\alpha}\right)^{1/2}\frac{y}{x} \tag{13}$$

$$f = \frac{\psi}{(\alpha U_\infty x)^{1/2}} \tag{14}$$

$$\theta = \frac{T-T_\infty}{T_w - T_\infty} \tag{15}$$

and the lateral mass flux parameter f_w is given by

$$f_w = -\frac{2a}{(\alpha B)^{1/2}} \tag{16}$$

It is clear that f_w is positive for the withdrawal of fluid and negative for injection. With the aid of boundary condition (12), equation (9) can be integrated once to give

$$f' = \pm\left(\frac{\mathrm{Ra}}{\mathrm{Pe}}\right)\theta + 1 \tag{17}$$

For the limiting case of forced convection, it is noted that the governing equations can be readily derived from equations (9) and (10) by simply setting $\mathrm{Ra}/\mathrm{Pa}=0$. Therefore,

$$f = \eta + f_w \tag{18}$$

$$\theta'' = -\frac{\lambda+1}{2}f\theta' + \lambda\theta \tag{19}$$

Results and Discussion

Equations (10) and (17) with the boundary conditions (11) and (12) are solved by numerical integration using the fourth-order Runge–Kutta method and the shooting technique with a systematic guessing of $\theta'(0)$. Integration has been carried out for three cases: (*a*) $\lambda = m = 0$ and $n = -1/2$, which corresponds to a uniform free stream flowing along an isothermal vertical wall with the injection (or withdrawal) rate varying with $x^{-1/2}$; (*b*) $\lambda = m = 1/3$ and $n = -1/3$, which corresponds to a free stream flowing over an inclined wall ($\gamma = 45$ deg) having constant heat flux with the injection (or withdrawal) rate varying with $x^{-1/3}$; and (*c*) $\lambda = m = 1$ and $n = 0$, which corresponds to a stagnation flow normal to a vertical wall with linear temperature variation and a constant injection/withdrawal rate (Fig. 1(*e*)). Selective values of $-\theta'(0)$ and η_T are listed in Table 1. As observed, the injection of fluid tends to thicken the thermal boundary layer while the withdrawal of fluid decreases it, which has a significant influence over the heat transfer results.

The heat transfer coefficient in terms of the Nusselt number can be expressed as

$$\frac{\mathrm{Nu}}{\mathrm{Ra}^{1/2}} = [-\theta'(0)]_{nc} \quad \text{for free convection} \tag{20}$$

$$\frac{\mathrm{Nu}}{\mathrm{Pe}^{1/2}} = [-\theta'(0)]_{mx} \quad \text{for mixed convection} \tag{21}$$

Equation (21) is plotted in Figs. 2–4 as a function of Ra/Pe. The limiting cases of free and forced convection are also

Table 1 Selected values of $\theta'(0)$ and η_T for mixed convection over an inclined surface in a saturated porous medium

$\lambda = 0$

Ra/Pe	$f_w = -1$		$f_w = -0.5$		$f_w = 0$		$f_w = 0.5$		$f_w = 1$	
	$-\theta'(0)$	η_T	$-\theta'(0)$	η_T	$-\theta'(0)$	η_T	$-\theta'(0)$	η_T	$-\theta'(0)$	η_T
					Aiding flows					
0 (fc)	0.2891	4.4119	0.4152	4.0170	0.5642	3.6419	0.7324	3.2972	0.9164	2.9865
0.5	0.3720	3.9379	0.5000	3.6260	0.6474	3.3326	0.8120	3.0538	0.9916	2.7799
1.0	0.4446	3.6011	0.5739	3.3495	0.7206	3.0982	0.8828	2.8656	1.0590	2.6312
3.0	0.6791	2.8267	0.8119	2.6704	0.9575	2.5170	1.1150	2.3701	1.2836	2.2235
10.0	1.2334	1.8643	1.3708	1.7967	1.5152	1.7280	1.6694	1.6568	1.8298	1.5898
20.0	1.7807	1.3873	1.9206	1.3477	2.0663	1.3084	2.2177	1.2687	2.3745	1.2304
					Opposing flows					
0.2	0.2517	4.6730	0.3771	4.2171	0.5270	3.7951	0.6972	3.4184	0.8837	3.0811
0.4	0.2109	4.9815	0.3353	4.4641	0.4866	3.9833	0.6595	3.5563	0.8491	3.1848
0.6	0.1655	5.3316	0.2886	4.7714	0.4421	4.2095	0.6187	3.7135	0.8122	3.3004
0.8	0.1109	6.1689	0.2346	5.1507	0.3919	4.4842	0.5737	3.9071	0.7724	3.4342
1.0	0.0380	7.6964	0.1677	5.6026	0.3326	4.8514	0.5229	4.1501	0.7289	3.5914

$\lambda = 1/3$

Ra/Pe	$f_w = -1$		$f_w = -0.5$		$f_w = 0$		$f_w = 0.5$		$f_w = 1$	
	$-\theta'(0)$	η_T	$-\theta'(0)$	η_T	$-\theta'(0)$	η_T	$-\theta'(0)$	η_T	$-\theta'(0)$	η_T
					Aiding flows					
0 (fc)	0.5160	3.6449	0.6700	3.2930	0.8541	2.9512	1.0649	2.6504	1.2984	2.3831
0.5	0.6459	3.2418	0.8008	2.9786	0.9816	2.7309	1.1867	2.4718	1.4128	2.2444
1.0	0.7587	3.0116	0.9146	2.7803	1.0938	2.5577	1.2951	2.3322	1.5159	2.1361
3.0	1.1211	2.4251	1.2802	2.2652	1.4568	2.1126	1.6503	1.9660	1.8597	1.8271
10.0	1.9724	1.6254	2.1366	1.5525	2.3119	1.4793	2.4981	1.4073	2.6949	1.3373
20.0	2.8102	1.2188	2.9775	1.1736	3.1569	1.0682	3.3362	1.0894	3.5275	1.0480
					Opposing flows					
0.2	0.4572	3.8374	0.6110	3.4377	0.7970	3.0657	1.0112	2.7316	1.2486	2.4473
0.4	0.3926	4.0719	0.5464	3.6184	0.7352	3.1933	0.9536	2.8305	1.1959	2.5175
0.6	0.3196	4.4190	0.4742	3.8337	0.6672	3.3421	0.8913	2.9409	1.1397	2.5962
0.8	0.2332	4.8584	0.3903	4.1363	0.5904	3.5366	0.8228	3.0724	1.0792	2.6852
1.0	0.1151	5.7589	0.2851	4.5688	0.5002	3.7792	0.7458	3.2303	1.0131	2.7892

$\lambda = 1$

Ra/Pe	$f_w = -1$		$f_w = -0.5$		$f_w = 0$		$f_w = 0.5$		$f_w = 1$	
	$-\theta'(0)$	η_T	$-\theta'(0)$	η_T	$-\theta'(0)$	η_T	$-\theta'(0)$	η_T	$-\theta'(0)$	η_T
					Aiding flows					
0 (fc)	0.7766	2.9208	0.9909	2.5759	1.2533	2.2717	1.5599	2.0031	1.9043	1.7722
0.5	0.9696	2.6317	1.1848	2.3631	1.4419	2.1130	1.7387	1.8840	2.0708	1.6827
1.0	1.1373	2.4458	1.3537	2.2137	1.6078	1.9912	1.8981	1.7901	2.2215	1.6089
3.0	1.6747	1.9699	1.8954	1.8165	2.1446	1.6634	2.4217	1.5262	2.7255	1.3990
10.0	2.9332	1.3442	3.1617	1.2609	3.4081	1.1878	3.6726	1.1161	3.9548	1.0492
20.0	4.1706	1.0082	4.4036	0.9621	4.6499	0.9175	4.9096	0.8735	5.1825	0.8317
					Opposing flows					
0.2	0.6890	3.0488	0.9032	2.6818	1.1690	2.3453	1.4811	2.0595	1.8320	1.8139
0.4	0.5925	3.2432	0.8072	2.8048	1.0776	2.4404	1.3968	2.1261	1.7557	1.8582
0.6	0.4835	3.4459	0.6997	2.9655	0.9772	2.5406	1.3058	2.1995	1.6745	1.9099
0.8	0.3538	3.7667	0.5749	3.1627	0.8640	2.6754	1.2062	2.2804	1.5875	1.9664
1.0	0.1759	4.4015	0.4182	3.4776	0.7314	2.8451	1.0947	2.3825	1.4932	2.0300

shown as asymptotes in the same figures. The influence of lateral mass flux on the heat transfer results of mixed convection can be clearly observed from these figures. As is the case for free convection (Cheng, 1977c), the heat transfer rate increases with the mass flux parameter f_w. However, it should be noted that, for opposing flows, an increase in the buoyancy parameter Ra/Pe beyond unity would cause flow to reverse and boundary layer to separate (equation (17)).

For the case of impermeable surfaces, i.e., $[f_w]_{mx} = 0$, the free convection asymptotes are linear and are given by

$$\frac{\mathrm{Nu}}{\mathrm{Pe}^{1/2}} = 0.4445\left(\frac{\mathrm{Re}}{\mathrm{Pe}}\right)^{1/2} \quad \text{for } \lambda = 0$$

$$= 0.6779\left(\frac{\mathrm{Re}}{\mathrm{Pe}}\right)^{1/2} \quad \text{for } \lambda = 1/3$$

$$= 1.0000\left(\frac{\mathrm{Re}}{\mathrm{Pe}}\right)^{1/2} \quad \text{for } \lambda = 1 \tag{22}$$

For $[f_w]_{mx} \neq 0$, the corresponding free convection asymptotes can be obtained by rewriting equation (20) as

$$\frac{\mathrm{Nu}}{\mathrm{Pe}^{1/2}} = \left(\frac{\mathrm{Ra}}{\mathrm{Pe}}\right)^{1/2} [-\theta'(0)]_{nc} \tag{23}$$

and applying the relation between $[f_w]_{mx}$ and $[f_w]_{nc}$

$$[f_w]_{nc} = \frac{[f_w]_{mx}}{\left(\frac{\mathrm{Ra}}{\mathrm{Pe}}\right)^{1/2}(1+\lambda)} \tag{24}$$

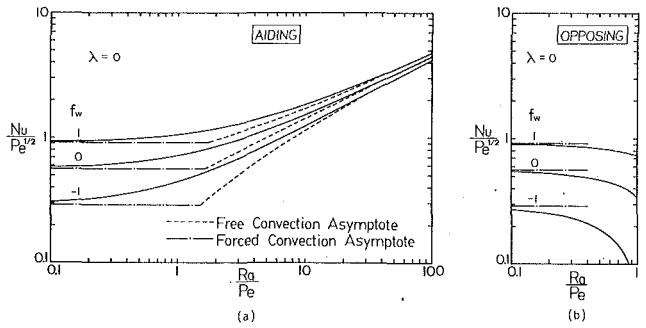

Fig. 2 Effect of lateral mass flux on heat transfer results for mixed convection along a vertical wall in a saturated porous medium, λ = 0: (a) aiding flows, (b) opposing flows

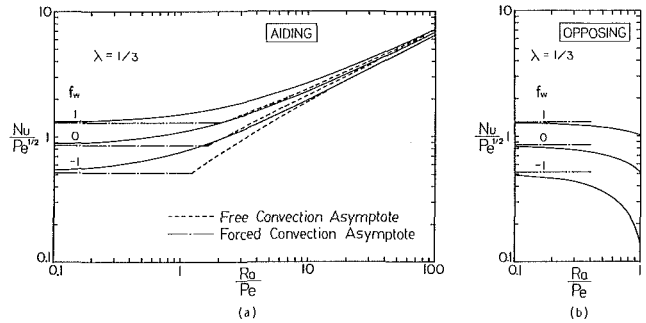

Fig. 3 Effects of lateral mass flux on heat transfer results for mixed convection over an inclined surface in a saturated porous medium, λ = 1/3: (a) aiding flows, (b) opposing flows

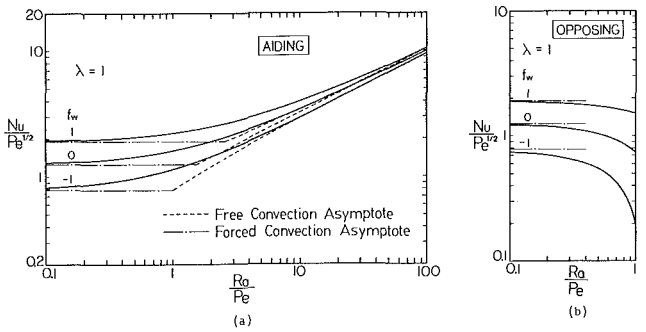

Fig. 4 Effects of lateral mass flux on heat transfer results for mixed convection along a vertical wall in saturated porous medium, λ = 1: (a) aiding flows, (b) opposing flows

With a given $[f_w]_{mx}$ and Ra/Pe, $[f_w]_{nc}$ can be determined through equation (24). Once $[f_w]_{nc}$ is specified, $[-\theta'(0)]_{nc}$ can be solved for by the exact manner described by Cheng (1977b). Therefore, the free convection asymptote is obtained, from equation (23), for each corresponding $[f_w]_{mx}$.

Acknowledgments

The authors would like to express their appreciation for the support from the Computer Center at Colorado State University and the U.S. Nuclear Regulatory Commission under contract No. NRC-04-86-115.

References

Cheng, P., 1977a, "Combined Free and Forced Boundary Layer Flows About Inclined Surfaces in Saturated Porous Media," *International Journal of Heat and Mass Transfer*, Vol. 20, pp. 806–814.

Cheng, P., 1977b, "Similarity Solutions for Mixed Convection From Horizontal Impermeable Surfaces in Saturated Porous Media," *International Journal of Heat and Mass Transfer*, Vol. 20, pp. 893–898.

Cheng, P., 1977c, "The Influence of Lateral Mass Flux on Free Convection Boundary Layers in a Saturated Porous Medium," *International Journal of Heat and Mass Transfer*, Vol. 20, pp. 201–206.

Combarnous, M. A., and Bia, P., 1971, "Combined Free and Forced Convection in Porous Medium," *Society of Petroleum Engineers Journal*, Vol. 11, pp. 399–405.

Homsy, G. M., and Sherwood, A. E., 1976, "Convection Instabilities in Porous Media With Through Flow," *AIChE Journal*, Vol. 22, pp. 168–174.

Lai, F. C., Prasad, V., and Kulacki, F. A., 1988a, "Aiding and Opposing Mixed Convection in a Vertical Porous Layer With a Finite Wall Heat Source," *International Journal of Heat and Mass Transfer*, Vol. 31, pp. 1049–1061.

Lai, F. C., 1988b, "Free and Mixed Convection in Porous Media," Ph.D. Dissertation, Department of Mechanical Engineering, University of Delaware, Newark, DE.

Lai, F. C., and Kulacki, F. A., 1988c, "Experimental Study of Free and Mixed Convection in Porous Media," *International Journal of Heat and Mass Transfer*, in review.

Lai, F. C., and Kulacki, F. A., 1988d, "Effects of Flow Inertia on Mixed Convection Along a Vertical Surface in a Saturated Porous Medium," *Proceedings of the 1988 National Heat Transfer Conference*, Vol. 1, pp. 643–652.

Lai, F. C., and Kulacki, F. A., 1989, "Thermal Dispersion Effects on Non-Darcy Convection Over Horizontal Surfaces in Saturated Porous Media," *International Journal of Heat and Mass Transfer*, Vol. 32, pp. 971–976.

Prasad, V., Lai, F. C., and Kulacki, F. A., 1988, "Mixed Convection in Horizontal Porous Layers Heated From Below," ASME JOURNAL OF HEAT TRANSFER, Vol. 110, pp. 395–402.

Prats, M., 1966, "The Effect of Horizontal Fluid Flow on Thermally Induced Convection Currents in Porous Mediums," *Journal of Geophysical Research*, Vol. 71, pp. 4835–4837.

Schrock, V. E., and Laird, A. D. K., 1976, "Physical Modeling of Combined Forced and Natural Convection in Wet Geothermal Formations," ASME JOURNAL OF HEAT TRANSFER, Vol. 98, pp. 213–220.

Sutton, F. M., 1970, "Onset of Convection in a Porous Channel With Net Through Flow," *Physics of Fluids*, Vol. 18, pp. 1931–1934.

Wooding, R. A., 1963, "Convection in a Saturated Porous Medium at Large Rayleigh Number and Peclet number," *Journal of Fluid Mechanics*, Vol. 15, pp. 527–544.

Non-Darcy Mixed Convection Flow Over a Nonisothermal Cylinder and Sphere Embedded in a Saturated Porous Medium

M. Kumari[1] and G. Nath[2]

Nomenclature

A_n = $A_o = 2$ for cylinder and $A_1 = 3/2$ for sphere
B = non-Darcy parameter
c, c_1 = constants
D_p = particle or pore diameter
f = dimensionless stream function
g = acceleration due to gravity
g_n, h_n = wall temperature functions
G = dimensionless temperature
k, K = thermal conductivity and permeability of the porous medium, respectively
K^* = inertial coefficient in the Ergun model
n = index ($n = 0$ for the cylinder and $n = 1$ for the sphere)
p = pressure
r = radial distance from a surface element to the axis of symmetry
r_0 = radius of the cylinder or the sphere
T = temperature
u, v = velocity components in the x and y directions, respectively

[1]Research Scientist, Department of Applied Mathematics, Indian Institute of Science, Bangalore—560012, India.

[2]Professor, Department of Applied Mathematics, Indian Institute of Science, Bangalore—560012, India.

Contributed by the Heat Transfer Division for publication in the JOURNAL OF HEAT TRANSFER. Manuscript received by the Heat Transfer Division July 12, 1988. Keywords: Mixed Convection, Porous Media.

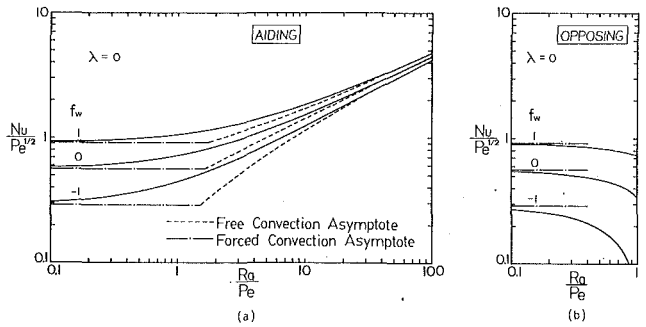

Fig. 2 Effect of lateral mass flux on heat transfer results for mixed convection along a vertical wall in a saturated porous medium, λ = 0: (*a*) aiding flows, (*b*) opposing flows

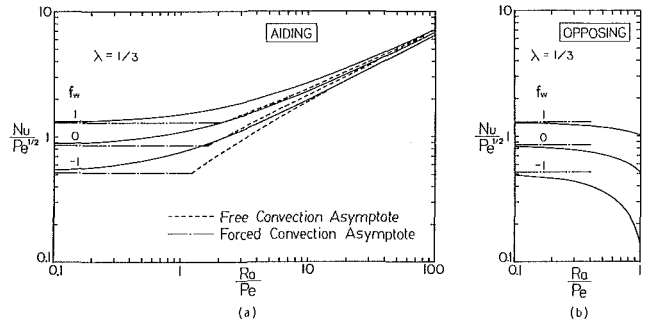

Fig. 3 Effects of lateral mass flux on heat transfer results for mixed convection over an inclined surface in a saturated porous medium, λ = 1/3: (*a*) aiding flows, (*b*) opposing flows

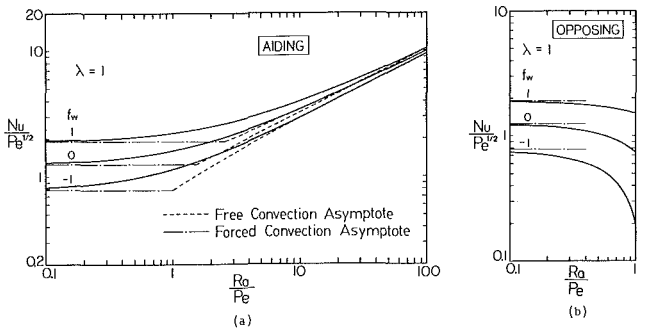

Fig. 4 Effects of lateral mass flux on heat transfer results for mixed convection along a vertical wall in saturated porous medium, λ = 1: (*a*) aiding flows, (*b*) opposing flows

With a given $[f_w]_{mx}$ and Ra/Pe, $[f_w]_{nc}$ can be determined through equation (24). Once $[f_w]_{nc}$ is specified, $[-\theta'(0)]_{nc}$ can be solved for by the exact manner described by Cheng (1977b). Therefore, the free convection asymptote is obtained, from equation (23), for each corresponding $[f_w]_{mx}$.

Acknowledgments

The authors would like to express their appreciation for the support from the Computer Center at Colorado State University and the U.S. Nuclear Regulatory Commission under contract No. NRC-04-86-115.

References

Cheng, P., 1977a, "Combined Free and Forced Boundary Layer Flows About Inclined Surfaces in Saturated Porous Media," *International Journal of Heat and Mass Transfer*, Vol. 20, pp. 806–814.

Cheng, P., 1977b, "Similarity Solutions for Mixed Convection From Horizontal Impermeable Surfaces in Saturated Porous Media," *International Journal of Heat and Mass Transfer*, Vol. 20, pp. 893–898.

Cheng, P., 1977c, "The Influence of Lateral Mass Flux on Free Convection Boundary Layers in a Saturated Porous Medium," *International Journal of Heat and Mass Transfer*, Vol. 20, pp. 201–206.

Combarnous, M. A., and Bia, P., 1971, "Combined Free and Forced Convection in Porous Medium," *Society of Petroleum Engineers Journal*, Vol. 11, pp. 399–405.

Homsy, G. M., and Sherwood, A. E., 1976, "Convection Instabilities in Porous Media With Through Flow," *AIChE Journal*, Vol. 22, pp. 168–174.

Lai, F. C., Prasad, V., and Kulacki, F. A., 1988a, "Aiding and Opposing Mixed Convection in a Vertical Porous Layer With a Finite Wall Heat Source," *International Journal of Heat and Mass Transfer*, Vol. 31, pp. 1049–1061.

Lai, F. C., 1988b, "Free and Mixed Convection in Porous Media," Ph.D. Dissertation, Department of Mechanical Engineering, University of Delaware, Newark, DE.

Lai, F. C., and Kulacki, F. A., 1988c, "Experimental Study of Free and Mixed Convection in Porous Media," *International Journal of Heat and Mass Transfer*, in review.

Lai, F. C., and Kulacki, F. A., 1988d, "Effects of Flow Inertia on Mixed Convection Along a Vertical Surface in a Saturated Porous Medium," *Proceedings of the 1988 National Heat Transfer Conference*, Vol. 1, pp. 643–652.

Lai, F. C., and Kulacki, F. A., 1989, "Thermal Dispersion Effects on Non-Darcy Convection Over Horizontal Surfaces in Saturated Porous Media," *International Journal of Heat and Mass Transfer*, Vol. 32, pp. 971–976.

Prasad, V., Lai, F. C., and Kulacki, F. A., 1988, "Mixed Convection in Horizontal Porous Layers Heated From Below," ASME JOURNAL OF HEAT TRANSFER, Vol. 110, pp. 395–402.

Prats, M., 1966, "The Effect of Horizontal Fluid Flow on Thermally Induced Convection Currents in Porous Mediums," *Journal of Geophysical Research*, Vol. 71, pp. 4835–4837.

Schrock, V. E., and Laird, A. D. K., 1976, "Physical Modeling of Combined Forced and Natural Convection in Wet Geothermal Formations," ASME JOURNAL OF HEAT TRANSFER, Vol. 98, pp. 213–220.

Sutton, F. M., 1970, "Onset of Convection in a Porous Channel With Net Through Flow," *Physics of Fluids*, Vol. 18, pp. 1931–1934.

Wooding, R. A., 1963, "Convection in a Saturated Porous Medium at Large Rayleigh Number and Peclet number," *Journal of Fluid Mechanics*, Vol. 15, pp. 527–544.

Non-Darcy Mixed Convection Flow Over a Nonisothermal Cylinder and Sphere Embedded in a Saturated Porous Medium

M. Kumari[1] and G. Nath[2]

Nomenclature

A_n = $A_o = 2$ for cylinder and $A_1 = 3/2$ for sphere
B = non-Darcy parameter
c, c_1 = constants
D_p = particle or pore diameter
f = dimensionless stream function
g = acceleration due to gravity
g_n, h_n = wall temperature functions
G = dimensionless temperature
k, K = thermal conductivity and permeability of the porous medium, respectively
K^* = inertial coefficient in the Ergun model
n = index ($n = 0$ for the cylinder and $n = 1$ for the sphere)
p = pressure
r = radial distance from a surface element to the axis of symmetry
r_0 = radius of the cylinder or the sphere
T = temperature
u, v = velocity components in the x and y directions, respectively

[1]Research Scientist, Department of Applied Mathematics, Indian Institute of Science, Bangalore—560012, India.

[2]Professor, Department of Applied Mathematics, Indian Institute of Science, Bangalore—560012, India.

Contributed by the Heat Transfer Division for publication in the JOURNAL OF HEAT TRANSFER. Manuscript received by the Heat Transfer Division July 12, 1988. Keywords: Mixed Convection, Porous Media.

x, y = streamwise and transverse coordinates, respectively
α = equivalent thermal diffusivity of the saturated porous medium
β = thermal expansion coefficient of the fluid
ϵ = porosity
λ = exponent defined in equation (4)
μ, ρ = viscosity and density, respectively
ξ, η = transformed coordinates
ϕ = angle of the y axis with respect to the vertical
ψ = stream function

Superscripts

$'$ = denotes derivatives with respect to η

Subscripts

w, ∞ = conditions at the wall and in the free stream, respectively
x, y = derivatives with respect to x and y, respectively

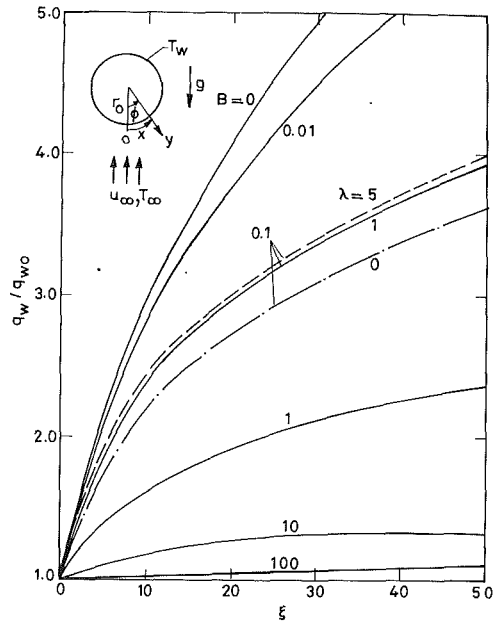

Fig. 1 Heat-flux ratio q_w/q_{w0}: ——·——, $\lambda=0$; ———, $\lambda=1$; — — —, $\lambda=5$

Introduction

In recent years, there has been great interest in the study of fluid flow over a horizontal cylinder and a sphere, because cylindrical and spherical shapes have been proposed for nuclear waste disposal canisters in subseabeds. Also the understanding of the heat transfer process about a horizontal cylinder embedded in a porous medium is relevant in the design of heat exchangers for energy extraction underground, as well as for temperature control of a catalytic bed. The natural convection about two-dimensional and axisymmetric bodies embedded in a saturated porous medium has been studied by Merkin (1979), Nilson (1981), and Nakayama and Koyama (1987a). The analogous mixed convection problem has been investigated by Cheng (1982), Huang et al. (1986), and Nakayama and Koyama (1987b). In the foregoing cases, similarity solutions were obtained. Furthermore, Minkowycz et al. (1985) have considered the mixed convection flow over a nonisothermal cylinder or sphere in a saturated porous medium. They solved the governing partial differential equations using the local nonsimilarity method. Also, Nakayama and Koyama (1987b) have proposed a momentum integral method for the solution of the mixed convection flow over a curved surface of arbitrary shape. Kumari et al. (1987) have studied the mixed convection flow over an isothermal sphere in a saturated porous medium and the partial differential equations governing the flow were solved by Keller box method. In all these studies, the analysis is based on the Darcy model. Plumb and Huenfeld (1981) have found that the Darcy model is valid for low-speed flow; for high-speed flow the non-Darcy model must be used. The non-Darcy free convection flow over two-dimensional and axisymmetric bodies of arbitrary shape has been considered by Ingham (1986).

The aim of the present investigation is to consider the mixed convection flow over a nonisothermal horizontal cylinder and sphere embedded in a saturated porous medium, using the non-Darcy model. Here we have considered the case of an assisting flow only, because that of an opposing flow is more complicated due to the possible flow separation from the body surface. The partial differential equations governing the flow, which are of boundary-layer type, have been solved numerically using the Keller box method. Particular cases of the present results have been compared with those available in the literature.

Governing Equations

We consider a nonisothermal horizontal cylinder and sphere of radius r_0 and wall temperature $T_w(x)$ immersed in a saturated porous medium having temperature T_∞ and velocity $u_e(x)$. The physical model is given in the inset of Fig. 1. We assume that the properties of the fluid and the porous medium are everywhere isotropic and homogeneous, and the convective fluid and the porous medium are everywhere in local thermodynamic equilibrium. The Rayleigh number is considered to be large and the flow is assumed to be described by the Ergun non-Darcy flow model, which is governed by $u+(\rho/\mu)K^*u^2=-(K/\mu)p_x$. The viscous dissipation has been neglected. We also assume that the convection takes place within a thin layer adjacent to the vertical surface. Hence the boundary layer approximation can be used to describe the flow motion in this region. Under the foregoing assumptions, the boundary layer equations with the non-Darcy flow model under the Boussinesq approximation can be expressed as

$$-r^{-n}\psi_{yy}+(K^*/\nu)((r^{-n}\psi_y)^2)_y=(\mu^{-1}K\rho_\infty\beta g\sin\phi)T_y, \tag{1}$$

$$\alpha T_{yy}=r^{-n}(\psi_y T_x-\psi_x T_y), \tag{2}$$

where

$$u=r^{-n}\psi_y, \quad v=-r^{-n}\psi_x \tag{3}$$

The boundary conditions are

$$\left.\begin{aligned} &y=0:\ \psi_x=0,\ T=T_\infty+c(g_n(\phi))^{2\lambda} \\ &y\to\infty:\ r^{-n}\psi_y=A_nU_\infty\sin\phi,\quad T=T_\infty \end{aligned}\right\} \tag{4}$$

Applying the following transformations:

$$\left.\begin{aligned} &\eta=(A_nU_\infty r_0/\alpha)^{1/2}\,(y/r_0)h_n(\phi) \\ &\xi=(c_1/A_n)(g_n(\phi))^{2\lambda}=(A_n\mu U_\infty)^{-1}(K\rho_\infty g\beta)(T_w-T_\infty) \end{aligned}\right\} \tag{5a}$$

$$\left.\begin{aligned} &\psi=\alpha r_0^n(A_nu_\infty r_0/\alpha)^{1/2}g_n(\phi)f(\eta,\xi) \\ &c_1=(K\rho_\infty\beta gc)/(\mu u_\infty),\quad h_n(\phi)=(\sin\phi)^{n+1}/g_n(\phi) \\ &T_w-T_\infty=c(g_n(\phi))^{2\lambda},\quad A_0=2,\quad A_1=3/2 \\ &g_0=(1-\cos\phi)^{1/2},\quad g_1=(1-\cos\phi)[(2+\cos\phi)/3]^{1/2} \end{aligned}\right\} \tag{5b}$$

Table 1 Comparison of heat transfer parameter $-G'(\xi, 0)$ for $B=0$

	Present analysis				Minkowycz et al. (1985)			
ξ	$\lambda=0.1$	$\lambda=1$	$\lambda=2$	$\lambda=10$	$\lambda=0.1$	$\lambda=1$	$\lambda=2$	$\lambda=10$
0.0	0.6389	1.1284	1.5045	3.2020	0.6390	1.129	1.505	3.202
0.5	0.7408	1.3339	1.7834	3.8041	0.7408	1.334	1.784	3.805
1.0	0.8295	1.5107	2.0229	4.3204	0.8296	1.512	2.024	4.324
2.0	0.9824	1.8123	2.4310	5.1997	0.9827	1.815	2.436	5.211
5.0	1.3382	2.5066	3.3695	7.2187	1.339	2.513	3.381	7.248
10.0	1.7785	3.3582	4.5195	9.6899	1.779	3.368	4.537	9.738
15.0	2.1294	4.0340	5.4315	11.6489	2.130	4.045	5.452	11.71
20.0	2.4300	4.6119	6.2114	13.3232	2.431	4.624	6.234	13.39
30.0	2.9404	5.5915	7.5330	16.1595	2.941	5.605	7.560	16.24
50.0	3.7588	7.1596	9.6480	20.6954	3.759	7.175	9.679	20.81

Table 2 Heat transfer parameter $-G'(\xi, 0)$ for different values of B, ξ, and λ

B	$\lambda=0$				$\lambda=1$			
	$\xi=0.5$	$\xi=5$	$\xi=10$	$\xi=20$	$\xi=0.5$	$\xi=5$	$\xi=10$	$\xi=20$
0.00	0.6475	1.1454	1.5161	2.0662	1.3339	2.5066	3.3582	4.6119
0.01	0.6457	1.1229	1.4633	1.9415	1.3295	2.4493	3.2232	4.2931
0.10	0.6328	1.0033	1.2388	1.5422	1.2975	2.1568	2.6797	3.3409
1.00	0.5923	0.7580	0.8705	1.0203	1.1979	1.5871	1.8398	2.1693
10.00	0.5684	0.6025	0.6342	0.6799	1.1390	1.2226	1.2987	1.4041
20.00	0.5664	0.5848	0.6033	0.6405	1.1338	1.1795	1.2245	1.3197
50.00	0.5651	0.5729	0.5811	0.5968	1.1306	1.1500	1.1704	1.2081
100.00	0.5647	0.5686	0.5729	0.5812	1.1295	1.1394	1.1501	1.1706

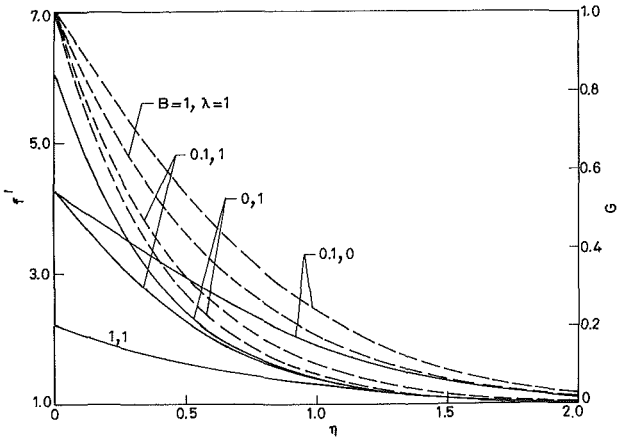

Fig. 2 Velocity and temperature profiles (f', G) for $\xi=5$: ———, f'; — — —, G

$$G(\eta, \xi)=(T-T_\infty)/(T_w-T_\infty)$$
$$B=(K^*/L)\mathrm{Re}, \quad \mathrm{Re}=u_e L/\nu, \quad K=D_p^2\epsilon/[150(1-\epsilon)^2], \quad (5c)$$
$$K^*=1.75D_p/[150(1-\epsilon)],$$

to equations (1) and (2), they reduce to

$$f''+2Bf'f''-\xi G'=0 \quad (6)$$
$$G''+fG'/2-\lambda f'G=\lambda\xi(f'G_\xi-G'f_\xi) \quad (7)$$

The boundary conditions are

$$\eta=0: \lambda\xi f_\xi+f/2=0, \quad G=1, \quad \xi\geq 0$$
$$\eta\to\infty: f'=1, \quad G=0, \quad \xi\geq 0 \quad (8)$$

It may be remarked that equations (6) and (7) for $B=0$ (Darcian flow) reduce to those of Minkowycz et al. (1985) who considered the Darcy flow. Our results are expected to be valid only for small and moderate values of the non-Darcy parameter B. For large values of B (say $B>100$), the transformations may become irrelevant due to the strong dependence of the growth rate of the boundary layer thickness with B. Therefore, we have confined our study to $B\leq 100$. Here ξ is a measure of buoyancy effects in the forced convective flow and $\xi=0$ corresponds to the case of purely forced convective flow. Also, for a given Reynolds number (Re), the non-Darcy parameter B is a constant.

The local surface heat flux can be written as

$$q_w=-k(T_y)_w=k(T_w-T_\infty)(A_n u_\infty/\alpha r_0)^{1/2}h_n(\phi)[-G'(\xi, 0)] \quad (9a)$$

and the ratio of local surface heat flux for the mixed convection flow ($\xi>0$) and the forced convection flow ($\xi=0$) is given by

$$q_w/q_{w0}=[-G'(\xi, 0)]/[-G'(0, 0)] \quad (9b)$$

Results and Discussion

The governing equations (6) and (7) under conditions (8) have been solved numerically using the Keller box method, which is described in great detail by Keller and Cebeci (1971). We have compared our heat transfer results ($-G'(\xi, 0)$) for Darcian flow ($B=0$) with those of Minkowycz et al. (1985), who used the local nonsimilarity method. There is little difference between the two sets of results, which implies that the local nonsimilarity method can also be used for the present problem. The comparison is given in Table 1.

The heat transfer parameter $-G'(\xi, 0)$ for various values of the non-Darcy parameter B, buoyancy parameter ξ, and wall temperature parameter λ is given in Table 2. The heat transfer parameter ($-G'(\xi, 0)$) decreases as B increases, but it increases as ξ or λ increases, because the thermal boundary layer thickness becomes thin due to the increase in ξ or λ. However, the opposite trend is observed when B increases. The heat transfer is rather insensitive to B when $B\geq 50$.

Figure 1 depicts the heat flux ratio q_w/q_{w0} versus ξ for different values of B and λ. It is observed that q_w/q_{w0} increases as ξ or λ increases, but it decreases as B increases. The reason for such behavior has been explained in the previous paragraph. For large $B(B=100)$, q_w/q_{w0} changes very little with the buoyancy parameter ξ.

The velocity and temperature profiles (f', G) for different values of B, ξ, and λ are shown in Fig. 2. It is found that these

parameters strongly influence the velocity profiles near the wall. The effect of wall temperature λ on the temperature profile G is more pronounced than that of ξ or B. The thermal boundary layer thickness grows with B, but it reduces when ξ or λ increases.

Conclusions

It is found that heat transfer is reduced by the non-Darcy parameter, but enhanced by buoyancy forces and wall heating. The heat transfer is rather insensitive to the non-Darcy parameter when it becomes large.

References

Cheng, P., 1982, "Mixed Convection About a Horizontal Cylinder and Sphere in a Fluid Saturated Porous Medium," *Int. J. Heat Mass Transfer*, Vol. 25, 1245-1247.

Huang, M. J., Yih, K. A., Chou, Y. L., and Chen, C. K., 1986, "Mixed Convection Flow Over a Horizontal Cylinder or a Sphere Embedded in a Saturated Porous Medium," ASME JOURNAL OF HEAT TRANSFER, Vol. 108, pp. 469-471.

Ingham, D. B., 1986, "The Non-Darcy Free Convection Boundary Layer on Axisymmetric and Two-Dimensional Bodies of Arbitrary Shape," *Int. J. Heat Mass Transfer*, Vol. 29, pp. 1759-1763.

Keller, H. B., and Cebeci, T., 1971, "Accurate Numerical Methods in Boundary Layers—I. Two-Dimensional Laminar Flows," *Proc. 2nd Int. Conference on Numerical Methods in Fluid Dynamics*, Lecture Notes in Physics, Vol. 8, Springer-Verlag, New York.

Kumari, M., Pop, I., and Nath, G., 1987, "Mixed Convection Boundary Layer Flow Over a Sphere in a Saturated Porous Medium," *ZAMM*, Vol. 67, pp. 569-572.

Merkin, J. H., 1981, "Free Convection Boundary Layers on Axisymmetric and Two-Dimensional Bodies of Arbitrary Shape in a Saturated Porous Medium," *Int. J. Heat Mass Transfer*, Vol. 22, pp. 1461-1462.

Minkowycz, W. J., Cheng, P., and Chang, C. H., 1985, "Mixed Convection About a Nonisothermal Cylinder and Sphere in a Porous Medium," *Num. Heat Transfer*, Vol. 8, pp. 349-359.

Nakayama, A., and Koyama, H., 1987a, "Free Convective Heat Transfer Over a Nonisothermal Body of Arbitrary Shape Embedded in a Fluid-Saturated Porous Medium," ASME JOURNAL OF HEAT TRANSFER, Vol. 109, pp. 1041-1045.

Nakayama, A., and Koyama, H., 1987b, "An Integral Method for Combined Free and Forced Convection Within a Fluid Saturated Porous Medium," *Appl. Sci. Res.*, Vol. 44, pp. 334-340.

Nilson, R. H., 1981, "Natural Convection Boundary Layer on Two-Dimensional and Axisymmetric Surfaces in High-Prandtl Number Fluids or in Fluid Saturated Porous Media," ASME JOURNAL OF HEAT TRANSFER, Vol. 103, pp. 803-807.

Plumb, O. A., and Huenfeld, J. C., 1981, "Non-Darcy Natural Convection From a Heated Surface in Saturated Porous Media," *Int. J. Heat Mass Transfer*, Vol. 24, pp. 765-768.

Solidification on a Chilled Continuous Surface Moving in a Parallel Free Stream

F. B. Cheung[1]

Introduction

The growth of a solidified layer on the surface of a chilled continuous object traveling steadily through an ambient liquid has recently received considerable attention owing to its importance in materials manufacturing. This solidification process, known as freeze coating, finds applications in the chemical and electrical industries involving the casting of insulating coatings on metal wires and electrical cables. Seeniraj and Bose (1981) investigated the freeze-coating problem by assuming the moving object ot be isothermal and the liquid to be saturated at its freezing point. In reality, however, the temperature of the moving object cannot be maintained constant since freezing of the liquid would proceed only at the expense of the sensible heat of the wall. Moreover, the liquid is usually superheated above its freezing point and as a result, there is convective heating of the moving object. Thus the freeze-coating process should be treated as a conjugate heat transfer problem. This was done by Cheung (1985, 1987) and Moutsoglou (1988) for the case of a continuous moving plate and by Cheung and Cha (1987, 1988) for the case of a continuous moving cylinder. The local freeze-coat thickness and the convective heat flux from the warm liquid to the freeze coat were determined simultaneously with the temperature variation within the moving object. All of the above studies, however, were based on the assumption that the ambient liquid is quiescent and the liquid motion is induced entirely by the moving object. In the present work, the effect of free-stream velocity on the freezing-coating process is investigated theoretically by a combined analytical/numerical technique.

Mathematical Formulation

The physical system under consideration is similar to the one described by Cheung (1987) except that the liquid velocity far away from the moving object is not zero but has a positive value. By invoking a similarity transformation, the equations governing the behavior of the liquid, freeze-coat, and wall regions become

(*i*) *Liquid Region* $\eta \geq 1$

$$f''' + \frac{\sigma^2}{2} ff'' = 0 \tag{1}$$

$$\theta'' + \frac{\sigma^2}{2} \Pr f\theta' = 0 \tag{2}$$

$$f'(1) = \theta(1) = 1, \quad f(1) = 1, \quad f'(\infty) = u_\infty/u_s, \quad \theta(\infty) = 0 \tag{3}$$

(*ii*) *Freeze-Coat Region* $0 \leq \eta \leq 1$

$$\phi'' + \frac{\sigma^2}{2}\left(\frac{\alpha_l}{\alpha_s}\right) \Pr \eta\phi' = 0 \tag{4}$$

$$\phi(1) = 1, \quad \phi(0) = \psi(0), \quad \phi'(0) = (k_w/k_s)\psi'(0) \tag{5}$$

(*iii*) *Wall Region* $\eta \leq 0$

$$\psi'' + \frac{\alpha^2}{2}\left(\frac{\alpha_l}{\alpha_w}\right) \Pr \eta\psi' = 0 \tag{6}$$

$$\psi(0) = \phi(0), \quad \psi'(0) = (k_s/k_w)\phi'(0), \quad \psi(-\infty) = 0 \tag{7}$$

where σ is the solidification constant given by

$$\sigma = \left\{2\left(\frac{\alpha_s}{\alpha_l}\right) \Pr^{-1} \mathrm{Ste}[\phi'(1) + \beta\theta'(1)]\right\}^{1/2} \tag{8}$$

In the above equations, η is the independent similarity variable, f the reduced steam function, (θ, ϕ, ψ) the dimensionless liquid, freeze-coat, and wall temperatures, u_s the plate velocity, u_∞ the free-stream velocity, k the thermal conductivity, α the thermal diffusivity, Pr the Prandtl number, Ste the Stefan number, and β the liquid superheat parameter. The primes denote total derivatives with respect to η whereas the subscripts (l, s, w) refer to the liquid, freeze-coat, and wall regions, respectively. In terms of the unknown quantity σ, equations (4)-(7) can be integrated analytically to give

$$\phi'(1) = \frac{\frac{2}{\sqrt{\pi}} Xe^{-X^2}}{\gamma + \mathrm{erf}X}, \quad X = \frac{\sigma}{2} \Pr^{1/2}\left(\frac{\alpha_s}{\alpha_l}\right)^{1/2}, \quad \gamma = \left(\frac{k_s\rho_s Cp_s}{k_w\rho_w Cp_w}\right)^{1/2} \tag{9}$$

where ρ is the density and Cp the specific heat. Equations (1)-(3) need to be solved simultaneously with equations (8) and (9) to determine the values of σ and $\theta'(1)$. Once these values

[1]Department of Mechanical Engineering, The Pennsylvania State University, University Park, PA 16802.

Contributed by the Heat Transfer Division for publication in the JOURNAL OF HEAT TRANSFER. Manuscript received by the Heat Transfer Division December 9, 1988; revision received September 5, 1989. Keywords: Conjugate Heat Transfer, Phase-Change Phenomena.

parameters strongly influence the velocity profiles near the wall. The effect of wall temperature λ on the temperature profile G is more pronounced than that of ξ or B. The thermal boundary layer thickness grows with B, but it reduces when ξ or λ increases.

Conclusions

It is found that heat transfer is reduced by the non-Darcy parameter, but enhanced by buoyancy forces and wall heating. The heat transfer is rather insensitive to the non-Darcy parameter when it becomes large.

References

Cheng, P., 1982, "Mixed Convection About a Horizontal Cylinder and Sphere in a Fluid Saturated Porous Medium," *Int. J. Heat Mass Transfer*, Vol. 25, 1245-1247.

Huang, M. J., Yih, K. A., Chou, Y. L., and Chen, C. K., 1986, "Mixed Convection Flow Over a Horizontal Cylinder or a Sphere Embedded in a Saturated Porous Medium," ASME JOURNAL OF HEAT TRANSFER, Vol. 108, pp. 469-471.

Ingham, D. B., 1986, "The Non-Darcy Free Convection Boundary Layer on Axisymmetric and Two-Dimensional Bodies of Arbitrary Shape," *Int. J. Heat Mass Transfer*, Vol. 29, pp. 1759-1763.

Keller, H. B., and Cebeci, T., 1971, "Accurate Numerical Methods in Boundary Layers—I. Two-Dimensional Laminar Flows," *Proc. 2nd Int. Conference on Numerical Methods in Fluid Dynamics*, Lecture Notes in Physics, Vol. 8, Springer-Verlag, New York.

Kumari, M., Pop, I., and Nath, G., 1987, "Mixed Convection Boundary Layer Flow Over a Sphere in a Saturated Porous Medium," *ZAMM*, Vol. 67, pp. 569-572.

Merkin, J. H., 1981, "Free Convection Boundary Layers on Axisymmetric and Two-Dimensional Bodies of Arbitrary Shape in a Saturated Porous Medium," *Int. J. Heat Mass Transfer*, Vol. 22, pp. 1461-1462.

Minkowycz, W. J., Cheng, P., and Chang, C. H., 1985, "Mixed Convection About a Nonisothermal Cylinder and Sphere in a Porous Medium," *Num. Heat Transfer*, Vol. 8, pp. 349-359.

Nakayama, A., and Koyama, H., 1987a, "Free Convective Heat Transfer Over a Nonisothermal Body of Arbitrary Shape Embedded in a Fluid-Saturated Porous Medium," ASME JOURNAL OF HEAT TRANSFER, Vol. 109, pp. 1041-1045.

Nakayama, A., and Koyama, H., 1987b, "An Integral Method for Combined Free and Forced Convection Within a Fluid Saturated Porous Medium," *Appl. Sci. Res.*, Vol. 44, pp. 334-340.

Nilson, R. H., 1981, "Natural Convection Boundary Layer on Two-Dimensional and Axisymmetric Surfaces in High-Prandtl Number Fluids or in Fluid Saturated Porous Media," ASME JOURNAL OF HEAT TRANSFER, Vol. 103, pp. 803-807.

Plumb, O. A., and Huenfeld, J. C., 1981, "Non-Darcy Natural Convection From a Heated Surface in Saturated Porous Media," *Int. J. Heat Mass Transfer*, Vol. 24, pp. 765-768.

Solidification on a Chilled Continuous Surface Moving in a Parallel Free Stream

F. B. Cheung[1]

Introduction

The growth of a solidified layer on the surface of a chilled continuous object traveling steadily through an ambient liquid has recently received considerable attention owing to its importance in materials manufacturing. This solidification process, known as freeze coating, finds applications in the chemical and electrical industries involving the casting of insulating coatings on metal wires and electrical cables. Seeniraj and Bose (1981) investigated the freeze-coating problem by assuming the moving object ot be isothermal and the liquid to be saturated at its freezing point. In reality, however, the temperature of the moving object cannot be maintained constant since freezing of the liquid would proceed only at the expense of the sensible heat of the wall. Moreover, the liquid is usually superheated above its freezing point and as a result, there is convective heating of the moving object. Thus the freeze-coating process should be treated as a conjugate heat transfer problem. This was done by Cheung (1985, 1987) and Moutsoglou (1988) for the case of a continuous moving plate and by Cheung and Cha (1987, 1988) for the case of a continuous moving cylinder. The local freeze-coat thickness and the convective heat flux from the warm liquid to the freeze coat were determined simultaneously with the temperature variation within the moving object. All of the above studies, however, were based on the assumption that the ambient liquid is quiescent and the liquid motion is induced entirely by the moving object. In the present work, the effect of free-stream velocity on the freezing-coating process is investigated theoretically by a combined analytical/numerical technique.

Mathematical Formulation

The physical system under consideration is similar to the one described by Cheung (1987) except that the liquid velocity far away from the moving object is not zero but has a positive value. By invoking a similarity transformation, the equations governing the behavior of the liquid, freeze-coat, and wall regions become

(*i*) *Liquid Region* $\eta \geq 1$

$$f''' + \frac{\sigma^2}{2} ff'' = 0 \tag{1}$$

$$\theta'' + \frac{\sigma^2}{2} \Pr f\theta' = 0 \tag{2}$$

$$f'(1) = \theta(1) = 1, \quad f(1) = 1, \quad f'(\infty) = u_\infty/u_s, \quad \theta(\infty) = 0 \tag{3}$$

(*ii*) *Freeze-Coat Region* $0 \leq \eta \leq 1$

$$\phi'' + \frac{\sigma^2}{2}\left(\frac{\alpha_l}{\alpha_s}\right) \Pr \eta\phi' = 0 \tag{4}$$

$$\phi(1) = 1, \quad \phi(0) = \psi(0), \quad \phi'(0) = (k_w/k_s)\psi'(0) \tag{5}$$

(*iii*) *Wall Region* $\eta \leq 0$

$$\psi'' + \frac{\alpha^2}{2}\left(\frac{\alpha_l}{\alpha_w}\right) \Pr \eta\psi' = 0 \tag{6}$$

$$\psi(0) = \phi(0), \quad \psi'(0) = (k_s/k_w)\phi'(0), \quad \psi(-\infty) = 0 \tag{7}$$

where σ is the solidification constant given by

$$\sigma = \left\{2\left(\frac{\alpha_s}{\alpha_l}\right) \Pr^{-1} \mathrm{Ste}[\phi'(1) + \beta\theta'(1)]\right\}^{1/2} \tag{8}$$

In the above equations, η is the independent similarity variable, f the reduced steam function, (θ, ϕ, ψ) the dimensionless liquid, freeze-coat, and wall temperatures, u_s the plate velocity, u_∞ the free-stream velocity, k the thermal conductivity, α the thermal diffusivity, Pr the Prandtl number, Ste the Stefan number, and β the liquid superheat parameter. The primes denote total derivatives with respect to η whereas the subscripts (l, s, w) refer to the liquid, freeze-coat, and wall regions, respectively. In terms of the unknown quantity σ, equations (4)-(7) can be integrated analytically to give

$$\phi'(1) = \frac{\frac{2}{\sqrt{\pi}} Xe^{-X^2}}{\gamma + \mathrm{erf}X}, \quad X = \frac{\sigma}{2} \Pr^{1/2}\left(\frac{\alpha_s}{\alpha_l}\right)^{1/2}, \quad \gamma = \left(\frac{k_s\rho_s Cp_s}{k_w\rho_w Cp_w}\right)^{1/2} \tag{9}$$

where ρ is the density and Cp the specific heat. Equations (1)-(3) need to be solved simultaneously with equations (8) and (9) to determine the values of σ and $\theta'(1)$. Once these values

[1]Department of Mechanical Engineering, The Pennsylvania State University, University Park, PA 16802.

Contributed by the Heat Transfer Division for publication in the JOURNAL OF HEAT TRANSFER. Manuscript received by the Heat Transfer Division December 9, 1988; revision received September 5, 1989. Keywords: Conjugate Heat Transfer, Phase-Change Phenomena.

are known, the local freeze-coat thickness and Nusselt number can be obtained respectively as

$$\delta = \sigma\left(\frac{\nu_l x}{u_s}\right)^{1/2} \text{ and } \mathrm{Nu}_x = -\frac{\theta'(1)}{\sigma}\mathrm{Re}_x^{1/2} \tag{10}$$

where $\mathrm{Re}_x = u_s x/\nu_l$ is the local Reynolds number of the flow.

Analytical/Numerical Solutions

For the special case in which the free-stream velocity is the same as the velocity of the moving plate, i.e., $u_\infty = u_s$, equations (1)–(3) can be solved analytically to give

$$f = \eta \text{ and } \theta = [1 - \mathrm{erf}(X\eta)]/(1 - \mathrm{erf}X) \tag{11}$$

Substituting the above solution into equations (8) and (10), implicit expressions can be derived for the solidification constant and the local Nusselt number as

$$\sigma = \frac{1}{\sqrt{\pi}}\left(\frac{\alpha_s}{\alpha_l}\right)^2 \mathrm{Ste}\exp(-X^2)\left[\frac{1}{\gamma + \mathrm{erf}X} - \frac{\beta}{1 - \mathrm{erf}X}\right] \tag{12}$$

$$\mathrm{Nu}_x = \frac{\exp(-X^2)}{\sqrt{\pi}(1 - \mathrm{erf}X)}\left(\frac{\alpha_s}{\alpha_l}\right)^{1/2}\mathrm{Re}_x^{1/2}\mathrm{Pr}^{1/2} \tag{13}$$

In the absence of freezing, the local Nusselt number Nu_{x_o} at the moving surface can be obtained by setting $X = 0$ in equation (13). This gives

$$\mathrm{Nu}_{x_o} = \frac{1}{\sqrt{\pi}}\left(\frac{\alpha_s}{\alpha_l}\right)^{1/2}\mathrm{Re}_x^{1/2}\mathrm{Pr}^{1/2} \text{ for } \sigma = 0 \tag{14}$$

For the general case of $u_\infty \neq u_s$, no analytical solution exists since the velocity and temperature fields are strongly coupled to the solidification process. Equations (1), (2), (3), and (8) are solved numerically using a combination of the fourth-order Runge–Kutta method and the Secant shooting method. For a given set of u_∞/u_s, Pr, Ste, β, γ, and α_s/α_l, equations (1)–(3) are integrated numerically by assuming a trial value for σ. The correct value of σ is determined iteratively using the Secant formula until the condition given by equation (8) is satisfied. The accuracy of the above numerical procedure is examined by comparing the numerical solution obtained for the case of $u_\infty/u_s = 1$ with the special solution determined from equation (12). Over the range of parameters considered in this study, the error involved in the numerical solution is less than 0.01 percent.

Results and Discussion

In actual practice, the free-stream velocity is smaller than the plate velocity. Thus the range of $0 \le u_\infty/u_s \le 1$ is chosen in this study. Figure 1 shows the effect of flow/freezing interaction on the local Nusselt number, where $\mathrm{Nu}_x/\mathrm{Nu}_{x_o}$ is plotted against X for different values of $\mathrm{Pr} \ge 0$ and $0 \le u_\infty/u_s \le 1$. Presenting the results this way weakens the dependence of the Nusselt number on the free-stream velocity and the Prandtl number. Consequently, all the computed values of $\mathrm{Nu}_x/\mathrm{Nu}_{x_o}$ are confined in a thin shaded region as shown in the figure. In the absence of freezing, we have $\sigma = 0$ and $\mathrm{Nu}_x = \mathrm{Nu}_{x_o}$. For all values of Pr and u_∞/u_s, the heat flux ratio approaches unity asymptotically as $\sigma \to 0$. It follows that the deviation of $\mathrm{Nu}_x/\mathrm{Nu}_{x_o}$ from unity can be used to measure the effect of flow/freezing interaction. For a slow freeze-coating process, corresponding to the case of $X < 0.1$, the flow/freezing interaction is small, and Nu_x can be assumed to be the same as Nu_{x_o}. On the other hand, for a fast freeze-coating process, corresponding to the case of $X > 0.1$, the flow-freezing interaction can be quite strong, and Nu_x can be considerably higher than Nu_{x_o}. In this case, the solution of forced convection over a moving plate without freezing cannot be used to calculate the convective heat flux at the solid–liquid interface, since it would greatly underestimate the value of Nu_x and thus substantially overpredict the local freeze-coat thickness. From Fig. 1, it is evident that $\mathrm{Nu}_x/\mathrm{Nu}_{x_o}$ is a weak function of Pr and u_∞/u_s. It depends mainly on the freezing parameter X. For a given value of X, the largest difference in the value of Nu_x occurs between the case of (Pr = 1, $u_\infty/u_s = 0$) and the case of $u_\infty/u_s = 1$. In the latter case, the heat flux ratio is a unique function of X, independent of Pr. Note that the present results for the case of $u_\infty = 0$ are identical to those reported by Cheung (1987).

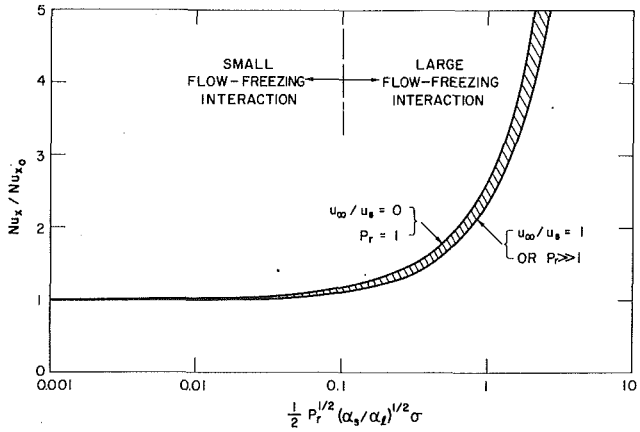

Fig. 1 Effect of flow/freezing interaction on the local Nusselt number for different values of u_∞/u_s and Pr

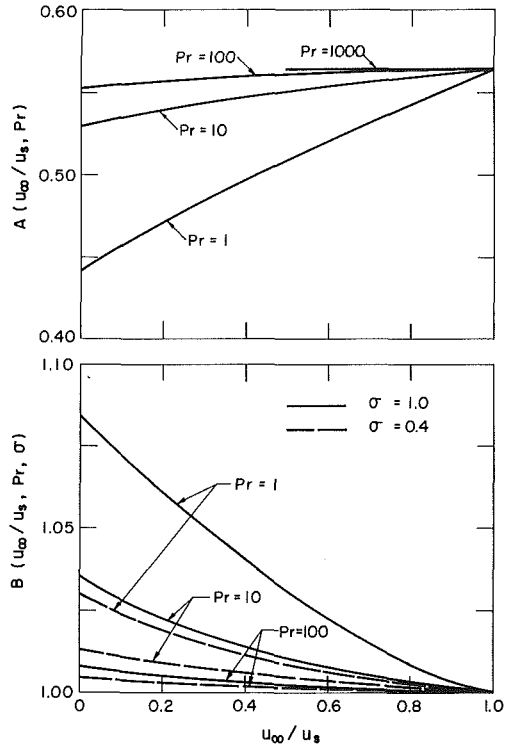

Fig. 2 Variations of the coefficients *A* and *B* with the liquid Prandtl number and the velocity ratio

The relatively weak dependence of $\mathrm{Nu}_x/\mathrm{Nu}_{x_o}$ upon u_∞/u_s and Pr suggests that the heat flux ratio may be correlated with the freezing parameter X in a simple form. To do this, the value of Nu_x for the case without freezing is first correlated with Re_x by

$$\mathrm{Nu}_{x_o} = A(\alpha_s/\alpha_l)^{1/2}\mathrm{Re}_x^{1/2}\mathrm{Pr}^{1/2} \tag{15}$$

where A is a coefficient whose value depends on u_∞/u_s and

Pr, as shown in Fig. 2. For the case of $u_\infty/u_s = 1$, A has a constant value of $1/\sqrt{\pi}$ or 0.5642. For the case of $u_\infty/u_s = 0$, on the other hand, A is a weak function of the Prandtl number having the values of 0.4438, 0.5314, 0.5545, and 0.5642 for Pr = 1, 10, 100, and 1000, respectively. These values are the same as those obtained by Erickson et al. (1966) and Tsou et al. (1967). For a given Prandtl number, a larger value of A is obtained as u_∞/u_s is increased. However, the value of A always approaches asymptotically to 0.5642 as Pr $\rightarrow \infty$. Thus the coefficient A becomes less and less sensitive to the variation of the free-stream velocity as the Prandtl number gets larger and larger. In fact, the special solution for the case of $u_\infty/u_s = 1$ is the same as the infinite-Prandtl-number solution. Physically, the above observation can be explained as follows. Relative to the velocity boundary layer, the thermal boundary layer becomes thinner and thinner as the Prandtl number gets larger and larger. Therefore, with respect to the thermal boundary layer, the liquid velocity approaches the value of u_s when Pr $\rightarrow \infty$. Since the local heat transfer is dictated by the behavior of the thermal boundary layer, the value of Nu_{x_o} for the case of Pr $\rightarrow \infty$ is the same as that for $u_\infty/u_s = 1$.

We may now develop a correlation for the heat flux ratio $\mathrm{Nu}_x/\mathrm{Nu}_{x_o}$. A useful hint can be obtained from equations (12) and (13) for the case of $u_\infty/u_s = 1$. Accordingly, we may write

$$\frac{\mathrm{Nu}_x}{\mathrm{Nu}_{x_o}} = B\,\frac{\exp(-X^2)}{1-\mathrm{erf}X} \tag{16}$$

where B is a coefficient whose value depends on u_∞/u_s, Pr, and σ, as shown in Fig. 2. For the special case of $u_\infty/u_s = 1$, B is equal to unity for all values of Pr and σ. For the case of $u_\infty/u_s \neq 1$, B is always larger than unity, having the maximum value at $u_\infty/u_s = 0$. However, when Pr > 1 and $\sigma < 0.4$, B deviates only slightly from unity. Under these conditions, we may assume $B = 1$. From equations (15) and (16), the local Nusselt number at the solid–liquid interface is

$$\mathrm{Nu}_x = A\,\frac{\exp(-X^2)}{1-\mathrm{erf}X}\left(\frac{\alpha_s}{\alpha_l}\right)^{1/2}\mathrm{Re}_x^{1/2}\mathrm{Pr}^{1/2} \tag{17}$$

where the coefficient $A = A(u_\infty/u_s, \mathrm{Pr})$ can be determined from Fig. 2. The above correlation can be conveniently used as an input quantity and the freeze-coating process can be solved as a heat conduction problem with the solidification constant σ being the only unknown quantity.

References

Cheung, F. B., 1985, "Analysis of Freeze Coating on a Nonisothermal Moving Plate by a Perturbation Method," ASME Journal of Heat Transfer, Vol. 107, pp. 549–556.

Cheung, F. B., 1987, "The Thermal Boundary Layer on a Continuous Moving Plate With Freezing," *AIAA J. Thermophysics and Heat Transfer*, Vol. 1, pp. 335–342.

Cheung, F. B., and Cha, S. W., 1987, "Flow-Freezing Interaction During Freeze-Coating on a Nonisothermal Axially Moving Cylinder," ASME Paper No. 87-HT-4.

Cheung, F. B., and Cha, S. W., 1988, "Numerical Study of Boundary Layer Flow and Heat Transfer on a Continuous Surface With Solidification," AIAA Thermophysics, Plasmadynamics, and Lasers Conf., San Antonio, TX, Paper No. AIAA-88-2642.

Erickson, L. E., Cha, L. C., and Fan, L. T., 1966, "The Cooling of a Moving Continuous Flat Sheet," *Chem. Eng. Prog. Symp. Ser.*, Vol. 52, pp. 157–165.

Moutsoglou, A., 1988, "A Note on the Scale Analysis of Phase Change Problem," ASME Journal of Heat Transfer, Vol. 110, pp. 523–525.

Seeniraj, R. V., and Bose, T. K., 1981, "Freeze-Coating on a Continuous Moving Sheet and on an Axially Moving Cylinder," *Wärme- und Stoffübertragung*, Vol. 15, pp. 239–243.

Tsou, F. K., Sparrow, E. M., and Goldstein, R. J., 1967, "Flow and Heat Transfer in the Boundary Layer on a Continuous Moving Surface," *Int. J. Heat Mass Transfer*, Vol. 10, pp. 219–235.

Preventing Water Hammer in Large Horizontal Pipes Passing Steam and Water

T. J. Swierzawski[1] and P. Griffith[2]

Introduction

In terms of inlet-water flow rate, the region of condensation-induced water hammer in horizontal pipes experiencing the countercurrent flow of steam and subcooled water is bound by the "absolute stability limit" at the lower flow boundary, and by the pipe-full limit at the upper flow boundary. Therefore, one means to prevent condensation-induced water hammer is to ensure that the pipe runs full at all times. Wallis et al. (1977) studied this problem and expressed in terms of a dimensionless Froude number a criterion for the minimum water flow rate necessary to run pipe full

$$\mathrm{Fr} = \frac{4\dot{m}}{\pi\rho g^{1/2}D^{5/2}} = 0.5 \tag{1}$$

where $\dot{m}$ = inlet liquid mass flow rate, ρ = liquid density, g = gravitational acceleration, and D = pipe internal diameter. The "absolute stability limit" at low flow rates was specified by Bjorge and Griffith (1984) and is further analyzed below.

Bjorge and Griffith presented a one-dimensional, stratified flow model that predicts initiation of a water hammer in horizontal and nearly horizontal pipes containing steam and subcooled water. The flow geometry used in this model is shown in Fig. 1. Although the model is appropriate for use in the flow geometry represented by Fig. 1, in practice it is possible to simplify an actual system to this form and obtain significant, albeit less accurate, results.

Equations presented by Bjorge and Griffith to describe a countercurrent flow of water and steam in a pipe are solved by using a finite difference method incorporated into the computer program CHOP (Countercurrent Horizontal Pipe) developed by Bjorge (1982). The condensation-induced water hammer in a pipe is not expected to occur when the filling water flow rate is below the "absolute stability limit," which may be calculated by specifying a very large condensation heat transfer coefficient in the program CHOP. Such a procedure, however, requires extensive trial and error computations in the course of converging on the Taitel-Dukler (1976) stability parameter of one. This technical note presents in brief a numerical solution to the equations developed by Bjorge and Griffith that greatly simplifies the task of determining whether the pipe is prone to water hammer as a result of the countercurrent slug–annular flow regime transition. Additional details are reported by Swierzawski and Griffith (1989).

Results of Analysis

To simplify the procedure outlined by Bjorge and Griffith, a map has been developed for absolute stability and water hammer regions. The map for selected pipe internal diameters and various pipe lengths, based on results generated by CHOP, is presented in Table 1. The following simple equation is recommended to determine safe (i.e., below the "absolute stability limit") inlet-water flow rates to pipes of various diameters (1.5 in. $\leq D \leq$ 40 in.) and L/D (under the conditions pressure (p) = 31.5 psia (2.17 bar); saturation temperature (T_{SAT}) = 253.13°F (396 K); inlet liquid temperature (T_{LO}) = 145.13°F (336 K); $\theta = 0$; and $\dot{m}_{so} = 0$):

[1]Consultant, Mechanical Division, Stone & Webster Engineering Corporation, Boston, MA 02107.

[2]Professor, Department of Mechanical Engineering, Massachusetts Institute of Technology, Cambridge, MA 02139.

Contributed by the Heat Transfer Division for publication in the Journal of Heat Transfer. Manuscript received by the Heat Transfer Division March 13, 1989; revision received June 26, 1989. Keywords: Condensation, Multiphase Flows, Phase-Change Phenomena.

Pr, as shown in Fig. 2. For the case of $u_\infty/u_s = 1$, A has a constant value of $1/\sqrt{\pi}$ or 0.5642. For the case of $u_\infty/u_s = 0$, on the other hand, A is a weak function of the Prandtl number having the values of 0.4438, 0.5314, 0.5545, and 0.5642 for Pr = 1, 10, 100, and 1000, respectively. These values are the same as those obtained by Erickson et al. (1966) and Tsou et al. (1967). For a given Prandtl number, a larger value of A is obtained as u_∞/u_s is increased. However, the value of A always approaches asymptotically to 0.5642 as Pr $\rightarrow \infty$. Thus the coefficient A becomes less and less sensitive to the variation of the free-stream velocity as the Prandtl number gets larger and larger. In fact, the special solution for the case of $u_\infty/u_s = 1$ is the same as the infinite-Prandtl-number solution. Physically, the above observation can be explained as follows. Relative to the velocity boundary layer, the thermal boundary layer becomes thinner and thinner as the Prandtl number gets larger and larger. Therefore, with respect to the thermal boundary layer, the liquid velocity approaches the value of u_s when Pr $\rightarrow \infty$. Since the local heat transfer is dictated by the behavior of the thermal boundary layer, the value of Nu_{x_o} for the case of Pr $\rightarrow \infty$ is the same as that for $u_\infty/u_s = 1$.

We may now develop a correlation for the heat flux ratio $\mathrm{Nu}_x/\mathrm{Nu}_{x_o}$. A useful hint can be obtained from equations (12) and (13) for the case of $u_\infty/u_s = 1$. Accordingly, we may write

$$\frac{\mathrm{Nu}_x}{\mathrm{Nu}_{x_o}} = B\,\frac{\exp(-X^2)}{1-\mathrm{erf}X} \tag{16}$$

where B is a coefficient whose value depends on u_∞/u_s, Pr, and σ, as shown in Fig. 2. For the special case of $u_\infty/u_s = 1$, B is equal to unity for all values of Pr and σ. For the case of $u_\infty/u_s \neq 1$, B is always larger than unity, having the maximum value at $u_\infty/u_s = 0$. However, when Pr > 1 and $\sigma < 0.4$, B deviates only slightly from unity. Under these conditions, we may assume $B = 1$. From equations (15) and (16), the local Nusselt number at the solid–liquid interface is

$$\mathrm{Nu}_x = A\,\frac{\exp(-X^2)}{1-\mathrm{erf}X}\left(\frac{\alpha_s}{\alpha_l}\right)^{1/2}\mathrm{Re}_x^{1/2}\mathrm{Pr}^{1/2} \tag{17}$$

where the coefficient $A = A(u_\infty/u_s, \mathrm{Pr})$ can be determined from Fig. 2. The above correlation can be conveniently used as an input quantity and the freeze-coating process can be solved as a heat conduction problem with the solidification constant σ being the only unknown quantity.

References

Cheung, F. B., 1985, "Analysis of Freeze Coating on a Nonisothermal Moving Plate by a Perturbation Method," ASME JOURNAL OF HEAT TRANSFER, Vol. 107, pp. 549–556.

Cheung, F. B., 1987, "The Thermal Boundary Layer on a Continuous Moving Plate With Freezing," *AIAA J. Thermophysics and Heat Transfer*, Vol. 1, pp. 335–342.

Cheung, F. B., and Cha, S. W., 1987, "Flow-Freezing Interaction During Freeze-Coating on a Nonisothermal Axially Moving Cylinder," ASME Paper No. 87-HT-4.

Cheung, F. B., and Cha, S. W., 1988, "Numerical Study of Boundary Layer Flow and Heat Transfer on a Continuous Surface With Solidification," AIAA Thermophysics, Plasmadynamics, and Lasers Conf., San Antonio, TX, Paper No. AIAA-88-2642.

Erickson, L. E., Cha, L. C., and Fan, L. T., 1966, "The Cooling of a Moving Continuous Flat Sheet," *Chem. Eng. Prog. Symp. Ser.*, Vol. 52, pp. 157–165.

Moutsoglou, A., 1988, "A Note on the Scale Analysis of Phase Change Problem," ASME JOURNAL OF HEAT TRANSFER, Vol. 110, pp. 523–525.

Seeniraj, R. V., and Bose, T. K., 1981, "Freeze-Coating on a Continuous Moving Sheet and on an Axially Moving Cylinder," *Wärme- und Stoffübertragung*, Vol. 15, pp. 239–243.

Tsou, F. K., Sparrow, E. M., and Goldstein, R. J., 1967, "Flow and Heat Transfer in the Boundary Layer on a Continuous Moving Surface," *Int. J. Heat Mass Transfer*, Vol. 10, pp. 219–235.

Preventing Water Hammer in Large Horizontal Pipes Passing Steam and Water

T. J. Swierzawski[1] and P. Griffith[2]

Introduction

In terms of inlet-water flow rate, the region of condensation-induced water hammer in horizontal pipes experiencing the countercurrent flow of steam and subcooled water is bound by the "absolute stability limit" at the lower flow boundary, and by the pipe-full limit at the upper flow boundary. Therefore, one means to prevent condensation-induced water hammer is to ensure that the pipe runs full at all times. Wallis et al. (1977) studied this problem and expressed in terms of a dimensionless Froude number a criterion for the minimum water flow rate necessary to run pipe full

$$\mathrm{Fr} = \frac{4\dot{m}}{\pi\rho g^{1/2}D^{5/2}} = 0.5 \tag{1}$$

where $\dot{m}$ = inlet liquid mass flow rate, ρ = liquid density, g = gravitational acceleration, and D = pipe internal diameter. The "absolute stability limit" at low flow rates was specified by Bjorge and Griffith (1984) and is further analyzed below.

Bjorge and Griffith presented a one-dimensional, stratified flow model that predicts initiation of a water hammer in horizontal and nearly horizontal pipes containing steam and subcooled water. The flow geometry used in this model is shown in Fig. 1. Although the model is appropriate for use in the flow geometry represented by Fig. 1, in practice it is possible to simplify an actual system to this form and obtain significant, albeit less accurate, results.

Equations presented by Bjorge and Griffith to describe a countercurrent flow of water and steam in a pipe are solved by using a finite difference method incorporated into the computer program CHOP (Countercurrent Horizontal Pipe) developed by Bjorge (1982). The condensation-induced water hammer in a pipe is not expected to occur when the filling water flow rate is below the "absolute stability limit," which may be calculated by specifying a very large condensation heat transfer coefficient in the program CHOP. Such a procedure, however, requires extensive trial and error computations in the course of converging on the Taitel-Dukler (1976) stability parameter of one. This technical note presents in brief a numerical solution to the equations developed by Bjorge and Griffith that greatly simplifies the task of determining whether the pipe is prone to water hammer as a result of the countercurrent slug–annular flow regime transition. Additional details are reported by Swierzawski and Griffith (1989).

Results of Analysis

To simplify the procedure outlined by Bjorge and Griffith, a map has been developed for absolute stability and water hammer regions. The map for selected pipe internal diameters and various pipe lengths, based on results generated by CHOP, is presented in Table 1. The following simple equation is recommended to determine safe (i.e., below the "absolute stability limit") inlet-water flow rates to pipes of various diameters (1.5 in. $\leq D \leq$ 40 in.) and L/D (under the conditions pressure $(p) = 31.5$ psia (2.17 bar); saturation temperature $(T_{SAT}) = 253.13$°F (396 K); inlet liquid temperature $(T_{LO}) = 145.13$°F (336 K); $\theta = 0$; and $\dot{m}_{so} = 0$):

[1]Consultant, Mechanical Division, Stone & Webster Engineering Corporation, Boston, MA 02107.

[2]Professor, Department of Mechanical Engineering, Massachusetts Institute of Technology, Cambridge, MA 02139.

Contributed by the Heat Transfer Division for publication in the JOURNAL OF HEAT TRANSFER. Manuscript received by the Heat Transfer Division March 13, 1989; revision received June 26, 1989. Keywords: Condensation, Multiphase Flows, Phase-Change Phenomena.

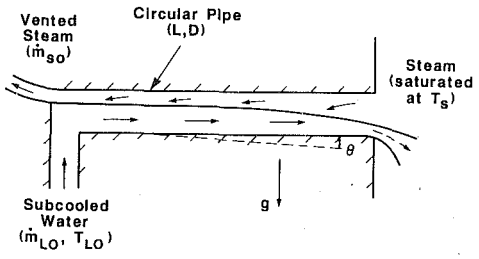

KEY:

L = Pipe length
D = Pipe internal diameter
$\dot{m}_{LO}$ = Inlet liquid mass flow rate
T_{LO} = Inlet liquid temperature
T_S = Steam bulk temperature
$\dot{m}_{SO}$ = Vented steam mass flow rate

Fig. 1 Flow geometry selected for analysis

Table 1 Stable-metastable transition data (absolute stability boundary)

Pipe Diameter (in.)	Pipe L/D	Inlet Water Flow at Stability Limit		
		Calculated by CHOP (kg/s)	Calculated by Proposed Equation (kg/s)	$\Delta = \frac{\text{Col(3)} - \text{Col(4)}}{\text{Col(3)}}$
1	2	3	4	5
1.5 (0.0381 m)	26.25	0.0355	0.0334	0.059
	52.49	0.0294	0.0294	0.000
	78.74	0.0259	0.0259	0.000
5.0 (0.1270 m)	26.22	0.5822	0.5451	0.064
	52.52	0.4797	0.4799	-0.0004
	78.74	0.4250	0.4228	0.005
10.0 (0.2540 m)	26.26	2.650	2.466	0.069
	52.48	2.171	2.172	-0.0005
	78.74	1.920	1.913	0.004
15.0 (0.3810 m)	26.25	6.300	5.828	0.075
	52.49	5.131	5.133	-0.0004
	78.74	4.530	4.521	0.002
20.0 (0.5080 m)	26.26	11.550	10.651	0.078
	52.48	9.375	9.382	-0.0007
	78.72	8.275	8.263	0.001
40.0 (1.0160 m)	26.67	48.420	44.335	0.084
	53.33	39.100	38.968	0.003
	78.74	34.570	34.458	0.003

Table 2 Coefficient C in proposed equation for various internal pipe diameters

D (in.)	C	D (in.)	C
1.50	0.01686	18.00	0.02993
2.00	0.01806	20.00	0.03024
2.50	0.01934	22.00	0.03044
3.00	0.02064	24.00	0.03062
3.50	0.02189	26.00	0.03078
4.00	0.02303	28.00	0.03090
5.00	0.02476	30.00	0.03100
6.00	0.02580	32.00	0.03111
8.00	0.02722	34.00	0.03122
10.00	0.02801	36.00	0.03132
12.00	0.02868	38.00	0.03141
14.00	0.02921	40.00	0.03153
16.00	0.02961		

$$\dot{m}_w = CD^2 \exp\left(-0.00484\frac{L}{D}\right) \qquad (2)$$

where $\dot{m}_w$ is in kg/s, the pipe internal diameter D and the pipe length L are in in. (1 in. = 0.0254 m), and the value of the coefficient C is taken from Table 2, which provides C for various internal pipe diameters.

Because it is difficult to show in a simple way, as required for practical applications, the influence of all system parameters on the "absolute stability limit," the effects on the water hammer region of certain more important parameters should be evaluated. The stable region is that region below the absolute stability boundary. Inspection of Figures V-4 through V-9 in Bjorge's thesis (1982) reveals that after the pipe length L and pipe internal diameter D, the next substantial influence on the "absolute stability limit" is that of inlet-water subcooling, which tends to level out at higher subcoolings. As the proposed equation is derived for the subcooling of 60 K, it is conservative in this respect. Also, the influence of steam pressure may be neglected when using the proposed equation because the lowest inlet-water flows are required at lowest pressures, and the equation is derived for a rather low system pressure of 31.5 psia ($T_{SAT} = 253.13°F = 396$ K).

Conclusion

Appropriate operating procedure, when subcooled water is admitted into an existing steam-filled piping system, is of great importance to plant operators. The inlet-water flow rate is often the only parameter that can be easily controlled to prevent water hammer. A study of filling strategies to prevent water hammer in horizontal pipes containing steam and subcooled water has shown that the critical inlet-water flow rates specified by the Bjorge-Griffith model can be successfully predicted by the proposed equation, which is valid for various pipe diameters and pipe lengths. To avoid operator errors, the installation of a properly sized flow-restricting orifice in the filling system may be considered. The reduction of inlet-water subcooling also helps to decrease the probability of a water hammer.

References

Bjorge, R. W., 1982, "Initiation of Water Hammer in Horizontal or Nearly Horizontal Pipes Containing Steam and Subcooled Water," Ph.D Thesis, Massachusetts Institute of Technology, Cambridge, MA.

Bjorge, R. W., and Griffith, P., 1984, "Initiation of Water Hammer in Horizontal and Nearly Horizontal Pipes Containing Steam and Subcooled Water," ASME JOURNAL OF HEAT TRANSFER, Vol. 106, pp. 835-840.

Swierzawski, T. J., and Griffith, P., 1983, "Preventing Water Hammer in Large Horizontal Pipes Passing Steam and Water," Stone & Webster Engineering Corporation, Boston, MA.

Taitel, Y., and Dukler, A. E., 1976, "A Model for Predicting Flow Regime Transitions in Horizontal and Near Horizontal Gas-Liquid Flow," *AIChE Journal*, Vol. 22, pp. 47-55.

Wallis, G. B., Dobson, J. E., and Hagi, Y., 1977, "Conditions for a Pipe to Run Full When Discharging Liquid Into a Space Filled With Gas," ASME *Journal of Fluids Engineering*, Vol. 99, pp. 405-413.

The Discharge of Two-Phase Flashing Flow From an Inclined Duct

J. C. Leung[1] and M. Epstein[1]

Nomenclature

C_f = liquid phase specific heat at constant pressure
D = hydraulic diameter of duct
f = Fanning friction factor
Fi = flow inclination number, equation (6)
g = gravitational acceleration
G = mass velocity or flux
G^* = normalized mass flux, equation (4)

[1] Fauske & Associates, Inc., 16W070 West 83rd Street, Burr Ridge, IL 60521.

Contributed by the Heat Transfer Division for publication in the JOURNAL OF HEAT TRANSFER. Manuscript received by the Heat Transfer Division March 27, 1989; revision received July 17, 1989. Keywords: Multiphase Flows, Phase-Change Phenomena.

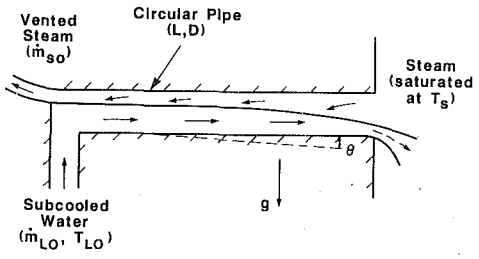

KEY:

L = Pipe length
D = Pipe internal diameter
$\dot{m}_{LO}$ = Inlet liquid mass flow rate
T_{LO} = Inlet liquid temperature
T_S = Steam bulk temperature
$\dot{m}_{SO}$ = Vented steam mass flow rate

Fig. 1 Flow geometry selected for analysis

Table 1 Stable-metastable transition data (absolute stability boundary)

Pipe Diameter (in.)	Pipe L/D	Inlet Water Flow at Stability Limit		
		Calculated by CHOP (kg/s)	Calculated by Proposed Equation (kg/s)	$\Delta = \frac{\text{Col(3)} - \text{Col(4)}}{\text{Col(3)}}$
1	2	3	4	5
1.5 (0.0381 m)	26.25	0.0355	0.0334	0.059
	52.49	0.0294	0.0294	0.000
	78.74	0.0259	0.0259	0.000
5.0 (0.1270 m)	26.22	0.5822	0.5451	0.064
	52.52	0.4797	0.4799	-0.0004
	78.74	0.4250	0.4228	0.005
10.0 (0.2540 m)	26.26	2.650	2.466	0.069
	52.48	2.171	2.172	-0.0005
	78.74	1.920	1.913	0.004
15.0 (0.3810 m)	26.25	6.300	5.828	0.075
	52.49	5.131	5.133	-0.0004
	78.74	4.530	4.521	0.002
20.0 (0.5080 m)	26.26	11.550	10.651	0.078
	52.48	9.375	9.382	-0.0007
	78.72	8.275	8.263	0.001
40.0 (1.0160 m)	26.67	48.420	44.335	0.084
	53.33	39.100	38.968	0.003
	78.74	34.570	34.458	0.003

Table 2 Coefficient C in proposed equation for various internal pipe diameters

D (in.)	C	D (in.)	C
1.50	0.01686	18.00	0.02993
2.00	0.01806	20.00	0.03024
2.50	0.01934	22.00	0.03044
3.00	0.02064	24.00	0.03062
3.50	0.02189	26.00	0.03078
4.00	0.02303	28.00	0.03090
5.00	0.02476	30.00	0.03100
6.00	0.02580	32.00	0.03111
8.00	0.02722	34.00	0.03122
10.00	0.02801	36.00	0.03132
12.00	0.02868	38.00	0.03141
14.00	0.02921	40.00	0.03153
16.00	0.02961		

$$\dot{m}_w = CD^2 \exp\left(-0.00484\frac{L}{D}\right) \qquad (2)$$

where $\dot{m}_w$ is in kg/s, the pipe internal diameter D and the pipe length L are in in. (1 in. = 0.0254 m), and the value of the coefficient C is taken from Table 2, which provides C for various internal pipe diameters.

Because it is difficult to show in a simple way, as required for practical applications, the influence of all system parameters on the "absolute stability limit," the effects on the water hammer region of certain more important parameters should be evaluated. The stable region is that region below the absolute stability boundary. Inspection of Figures V-4 through V-9 in Bjorge's thesis (1982) reveals that after the pipe length L and pipe internal diameter D, the next substantial influence on the "absolute stability limit" is that of inlet-water subcooling, which tends to level out at higher subcoolings. As the proposed equation is derived for the subcooling of 60 K, it is conservative in this respect. Also, the influence of steam pressure may be neglected when using the proposed equation because the lowest inlet-water flows are required at lowest pressures, and the equation is derived for a rather low system pressure of 31.5 psia ($T_{SAT} = 253.13°F = 396$ K).

Conclusion

Appropriate operating procedure, when subcooled water is admitted into an existing steam-filled piping system, is of great importance to plant operators. The inlet-water flow rate is often the only parameter that can be easily controlled to prevent water hammer. A study of filling strategies to prevent water hammer in horizontal pipes containing steam and subcooled water has shown that the critical inlet-water flow rates specified by the Bjorge-Griffith model can be successfully predicted by the proposed equation, which is valid for various pipe diameters and pipe lengths. To avoid operator errors, the installation of a properly sized flow-restricting orifice in the filling system may be considered. The reduction of inlet-water subcooling also helps to decrease the probability of a water hammer.

References

Bjorge, R. W., 1982, "Initiation of Water Hammer in Horizontal or Nearly Horizontal Pipes Containing Steam and Subcooled Water," Ph.D Thesis, Massachusetts Institute of Technology, Cambridge, MA.

Bjorge, R. W., and Griffith, P., 1984, "Initiation of Water Hammer in Horizontal and Nearly Horizontal Pipes Containing Steam and Subcooled Water," ASME JOURNAL OF HEAT TRANSFER, Vol. 106, pp. 835-840.

Swierzawski, T. J., and Griffith, P., 1983, "Preventing Water Hammer in Large Horizontal Pipes Passing Steam and Water," Stone & Webster Engineering Corporation, Boston, MA.

Taitel, Y., and Dukler, A. E., 1976, "A Model for Predicting Flow Regime Transitions in Horizontal and Near Horizontal Gas-Liquid Flow," *AIChE Journal*, Vol. 22, pp. 47-55.

Wallis, G. B., Dobson, J. E., and Hagi, Y., 1977, "Conditions for a Pipe to Run Full When Discharging Liquid Into a Space Filled With Gas," ASME *Journal of Fluids Engineering*, Vol. 99, pp. 405-413.

The Discharge of Two-Phase Flashing Flow From an Inclined Duct

J. C. Leung[1] and M. Epstein[1]

Nomenclature

C_f = liquid phase specific heat at constant pressure
D = hydraulic diameter of duct
f = Fanning friction factor
Fi = flow inclination number, equation (6)
g = gravitational acceleration
G = mass velocity or flux
G^* = normalized mass flux, equation (4)

[1] Fauske & Associates, Inc., 16W070 West 83rd Street, Burr Ridge, IL 60521.

Contributed by the Heat Transfer Division for publication in the JOURNAL OF HEAT TRANSFER. Manuscript received by the Heat Transfer Division March 27, 1989; revision received July 17, 1989. Keywords: Multiphase Flows, Phase-Change Phenomena.

G^* = normalized mass flux, equation (4)
G^{max} = mass flux in a frictionless duct
G^{min} = minimum mass flux in downflow
h = specific enthalpy
L = duct length
P = pressure
v = specific volume
x = quality, vapor mass fraction
ϵ = normalized specific volume, equation (4)
η = pressure ratio, equation (4)
θ = angle of inclination
ρ = density
ω = correlating parameter, equation (8)

Subscripts

c = choked or critical
f = liquid phase
fg = difference between vapor and liquid phase property
0 = stagnation condition
1 = duct inlet
2 = duct exit
3 = outside duct exit

Superscripts

min = minimum flow
max = corresponding to frictionless duct

Introduction

Recently Leung and Grolmes (1987) presented a generalized treatment for correlating flashing flow discharge from a horizontal duct. This paper extends the above methodology to include inclined ducts. Gravity or elevation change takes on a much greater significance in two-phase flow than in single-phase gas flow due to the presence of the liquid phase. Earlier, Bilicki and Kestin (1983) and Bilicki et al. (1987) discussed mathematical solutions for the upward and downward two-phase flow in terms of singular points and turning points as used in geometric–topologic analysis. They found that choking can only occur at the exit end of the flow channel. This paper, instead, presents rather general and complete engineering solutions covering both upflow and downflow discharges. As the inclination angle approaches zero the solutions reduce to the solution for horizontal flow.

Consistent with the earlier treatment on two-phase flashing flow in dusts (Leung and Grolmes, 1987; Bilicki and Kestin, 1983; Bilicki et al., 1987), the basic assumptions employed are homogeneous equilibrium (equal velocity and equal temperature in both phases) flow with negligible heat losses. The governing steady-state conservation equations are (refer to Fig. 1 for usage of subscripts):

Mass

$$G = \text{const} \tag{1}$$

Momentum

$$vdP + G^2\left(vdv + \frac{4fv^2 dL}{2}\right) + g\cos\theta dL = 0 \tag{2}$$

Energy

$$h_0 = h + \frac{G^2 v^2}{2} \tag{3}$$

Here the specific enthalpy and specific volume are expressed in terms of quality (vapor mass fraction) and phasic properties, i.e., $h_0 = h_{f0} + x_0 h_{fg0}$, $h = h_f + x h_{fg}$, and $v = v_f + x v_{fg}$. The third term in equation (2) represents the gravitational component, and the angle of inclination θ is measured from the vertical. It should be noted that the homogeneous equilibrium flow model is not necessarily the most realistic two-phase flow model; however, it offers the design engineer a most simplistic formulation to get on with his task and is certainly a frequently cited reference model. The procedure for solving this set of equations via numerical integration is similar to the horizontal flow case (see Leung and Grolmes, 1987, and Perry, 1984). However, we shall seek a more generalized solution characterized by a minimum number of dimensionless physical parameters.

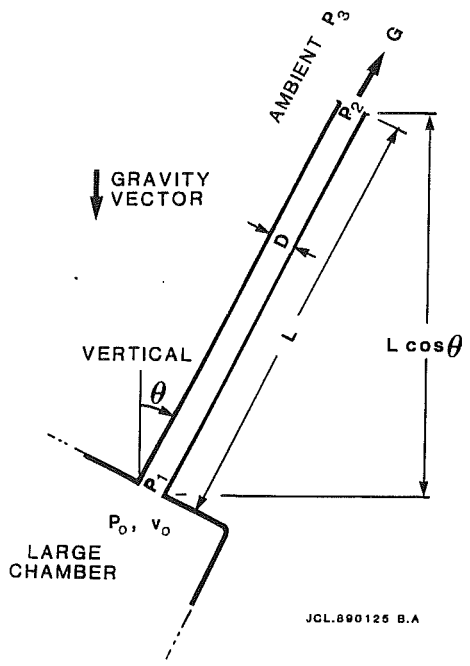

Fig. 1 Discharge through an inclined duct from a larger reservoir

Correlating Parameter for Elevation Changes

The appropriate dimensionless parameter for elevation change is obtained by first nondimensionalizing the momentum equation using the following variables:

$$\eta \equiv \frac{P}{P_o}, \quad \epsilon \equiv \frac{v}{v_0}, \quad G^* \equiv \frac{G}{\sqrt{P_0/v_0}} = \frac{G}{\sqrt{P_0\rho_0}} \tag{4}$$

Then equation (2) can be rearranged to yield

$$4f\frac{dL}{D} = -\frac{\epsilon d\eta + G^{*2}\epsilon d\epsilon}{\frac{1}{2}(G^*\epsilon)^2 + \frac{gD\cos\theta}{4fP_0 v_0}} \tag{5}$$

It is seen that the solution of the momentum equation depends on a dimensionless "flow inclination number," i.e.,[2]

$$Fi \equiv \frac{gD\cos\theta}{4fP_0 v_0} = \frac{gL\cos\theta}{(4fL/D)P_0 v_0} \tag{6}$$

At a constant duct resistance $4fL/D$, the above flow inclination parameter represents the ratio of the potential energy to the flow energy (also known as flow work) and is a measure of the departure from the horizontal flow case.

[2]This parameter was previously suggested by Leung and Fisher (1989).

Approximate Analytical Solution

An approximate analytical solution can be obtained by simply integrating the momentum equation (5) in conjunction with an assumed equation of state, first proposed by Epstein et al. (1983) for steam-water mixtures and subsequently generalized by Leung (1986) for any flashing two-phase mixture, namely

$$\frac{v}{v_0} - 1 = \omega\left(\frac{P_0}{P} - 1\right) \tag{7a}$$

or, in terms of the dimensionless variables

$$\epsilon - 1 = \omega\left(\frac{1}{\eta} - 1\right) \tag{7b}$$

Equation (7*b*) obviates the need to solve the energy equation simultaneously with the momentum equation. By assuming an isenthalpic (constant enthalpy) expansion process, a particularly good approximation for a long duct where the kinetic energy term is necessarily small, the ω can be shown to be given entirely in terms of known inlet stagnation properties (Leung, 1986)

$$\omega = \frac{x_0 v_{fg0}}{v_0} + \frac{C_{f0} T_0 P_0}{v_0}\left(\frac{v_{fg0}}{h_{fg0}}\right)^2 \approx \alpha_0 + \rho_0 C_{f0} T_0 P_0 \left(\frac{v_{fg0}}{h_{fg0}}\right)^2 \tag{8}$$

The parameter ω is made up of two entirely separable terms: the first reflects the compressibility of the mixture due to the existing vapor volume fraction (α_0) and the second reflects the compressibility due to flashing or phase change upon depressurization. As expected the flashing component (second term in equation (8)) is the dominating term until α_0 approaches unity (all-gas inlet). Flashing choked flows of widely differing fluids and inlet conditions have been successfully correlated with this ω parameter (Leung, 1986; Leung and Grolmes, 1987, 1988).

Similar to the classical treatment of gas flow in pipes (Lapple, 1943; Shapiro, 1953; Levenspiel, 1977), the friction factor f is assumed to be constant along the duct so that the left-hand side of equation (5) can be readily integrated. Now, substituting equation (7*b*) into equation (5) to eliminate ϵ in favor of η, and integrating the result over the length of the duct, yields

$$4f\frac{L}{D} = -\int_{\eta_1}^{\eta_2} \frac{[(1-\omega)\eta^2 + \omega\eta]\left(1 - G^{*2}\dfrac{\omega}{\eta^2}\right)d\eta}{\dfrac{G^{*2}}{2}[(1-\omega)\eta + \omega]^2 + \eta^2 Fi} \tag{9}$$

The above integral can be evaluated in closed form, as shown in the Appendix. By treating the inlet to the duct as frictionless flow (see Leung, 1986, equation (3)), the compressible form of the Bernoulli equation is obtained based on the chosen equation of state (Leung and Grolmes, 1987)

$$G^* = \frac{\{-2[\omega \ln \eta_1 + (1-\eta_1)(\omega - 1)\}^{1/2}}{\omega\left(\dfrac{1}{\eta_1} - 1\right) + 1} \tag{10}$$

The exit condition can be either unchoked, in which case $\eta_2 = \eta_3$, or choked where the local choking condition would require (Leung, 1986, equation (10)),

$$G = [-1/(dv/dP)]^{0.5} \tag{11a}$$

or in the normalized form after substituting equation (7*a*)

$$G^* = \frac{\eta_2}{\sqrt{\omega}} \qquad \text{(exit choking)} \tag{11b}$$

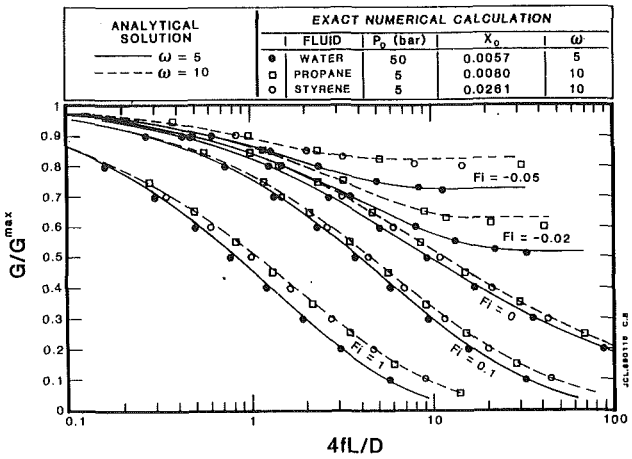

Fig. 2 Comparison between analytical and numerical solutions

Since the exit choking solution is more involved, we shall present its results first. Here given ω, Fi, and $4fL/D$ values, the resulting algebraic equations (A-12), (10), and (11*b*) are solved simultaneously for G^*, η_1, and η_2.

Comparison With Exact Solutions

Exact numerical solutions for the exit choking case (i.e., solving equations (1), (2), and (3) based on finite difference integrations) using detailed thermodynamic properties[3] were obtained for water, propane, and styrene at two selected ω values and for a wide range of flow inclination numbers. The pertinent inlet conditions are summarized in Fig. 2. The results are presented in terms of the flow reduction factor G/G^{max} versus the duct resistance factor $4fL/D$. The quantity G^{max} is the critical mass velocity for frictionless duct (perfect nozzle) flow. For the numerical scheme, G^{max} is evaluated in a rigorous fashion based on the thermodynamic properties. To maintain the same assumption of isenthalpic flow, G^{max} in the analytical scheme is given by equation (11*b*) with $\eta_2 = \eta_1 = \eta$, which in turn satisfies the following transcendental equation (this results from equating the right-hand sides of equations (10) and (11*b*)):

$$\eta^2 + (\omega^2 - 2\omega)(1-\eta)^2 + 2\omega^2 \ln \eta + 2\omega^2(1-\eta) = 0 \tag{12}$$

As can be seen from Fig. 2, the analytical results are found to be in remarkable agreement with the corresponding numerical solutions for a wide range of flow inclination numbers. Apparently the ratio G/G^{max} is not too sensitive to the assumption of the flow process as long as consistent assumptions are applied throughout. Here the usefulness of both ω and Fi number in correlating different fluids, inlet conditions, and duct orientations is amply demonstrated. Such a plot, correlated in terms of the Fi number, clearly displays the conditions under which large flow departures from the horizontal reference case ($Fi = 0$) can be expected.

Minimum Flow Behavior

Figure 2 also illustrates that in downflow situations (negative Fi number), an asymptotic flow behavior is attained at a given $4fL/D$, beyond which adding pipe length does not lead to further reduction in flow. This minimum flow behavior is brought about by a balance between the frictional pressure drop (negative) and the gravitational pressure drop (positive). In many respects, this is similar to the terminal velocity achieved by bodies in free fall when the gravitational (buoyancy) force is balanced by the frictional drag.

[3] Local properties were used at the prevailing pressure along the duct.

Mathematically this minimum flow behavior can be represented by equating the two terms in the denominator of equation (5) and evaluating them at the duct inlet. Accordingly, the minimum mass flux is given by

$$\frac{G^{\min}}{\sqrt{P_0/v_0}} = \frac{\sqrt{2(-Fi)}}{\epsilon_1} \tag{13}$$

This equation together with equation (10) can be used to eliminate $G^{\min}$, yielding

$$\omega \ln \eta_1 + (\omega - 1)(1 - \eta_1) = Fi \tag{14}$$

Expanding the term $\ln \eta_1$ (note that η_1 is typically close to unity) via a two-term Taylor series, solving for η_1, and substituting the result into equation (13), we finally obtain an explicit expression for $G^{\min}$

$$\frac{G^{\min}}{\sqrt{P_0/v_0}} = \sqrt{2(-Fi)}\left[\frac{1+\omega-\sqrt{1+2\omega(-Fi)}}{1+(\omega-1)\sqrt{1+2\omega(-Fi)}}\right] \tag{15}$$

This expression closely reproduces the asymptotic limits predicted with the analytical treatment (to within 1 percent) or the "exact" numerical calculations (to within 5 percent) when $Fi<0$ and $4fL/D$ is large.

Discussion on Choking

Once the exit-choking G or G^* is found from the analytical solution, the exit pressure P_2 (or η_2) is simply obtained by equation (11). If this exit pressure corresponding to choking is less than the downstream back pressure P_3 (or η_3), the flow is said to be unchoked and equation (11), representing the exit choking condition, will no longer apply. The unchoked G is hence obtained by the simultaneous solution of equations (A-12) and (10) only. In most situations, the unchoked case can be approximated by taking η_1 as unity and one can proceed to solve equation (A-12) for G^* directly.

APPENDIX

The integrand in equation (9) is first expanded and rearranged to yield

$$4f\frac{L}{D} = -\int_{\eta_1}^{\eta_2} \frac{(1-\omega)\eta^2 + \omega\eta - \omega(1-\omega)G^{*2} - \omega^2\dfrac{G^{*2}}{\eta}}{\left[\dfrac{G^{*2}}{2}(1-\omega)^2 + Fi\right]\eta^2 + G^{*2}\omega(1-\omega)\eta + \dfrac{G^{*2}\omega^2}{2}}\, d\eta \tag{A-1}$$

Letting $X(\eta)$ denote the denominator of the integrand, we can write out the four pertinent integrals as

$$4f\frac{L}{D} = \underbrace{-\int_{\eta_1}^{\eta_2} \frac{(1-\omega)\eta^2 d\eta}{X(\eta)}}_{I_1} \underbrace{-\int_{\eta_1}^{\eta_2} \frac{\omega\eta d\eta}{X(\eta)}}_{I_2} + \underbrace{\int_{\eta_1}^{\eta_2} \frac{\omega(1-\omega)G^{*2}d\eta}{X(\eta)}}_{I_3} + \underbrace{\int_{\eta_1}^{\eta_2} \frac{\omega^2 G^{*2}d\eta}{\eta X(\eta)}}_{I_4} \tag{A-2}$$

Now making use of the integral table (Abramowitz and Stegun, 1972), and by denoting

$$a \equiv \frac{G^{*2}}{2}\omega^2 \tag{A-3}$$

$$b \equiv G^{*2}\omega(1-\omega) \tag{A-4}$$

$$c \equiv \frac{G^{*2}}{2}(1-\omega)^2 + Fi \tag{A-5}$$

$$q \equiv 4ac - b^2 = 2G^{*2}\omega^2 Fi \tag{A-6}$$

the solution for the fundamental integral, $\int d\eta/X(\eta)$, is given in the following form:

$$I_0(\eta) \equiv \int \frac{d\eta}{X(\eta)}$$

$$= \frac{2}{\sqrt{q}} \tan^{-1}\frac{2c\eta + b}{\sqrt{q}} \qquad (q>0 \text{ or } Fi>0, \text{ upflow}) \tag{A-7a}$$

$$= \frac{1}{\sqrt{-q}} \ln\left|\frac{2c\eta + b - \sqrt{-q}}{2c\eta + b + \sqrt{-q}}\right| \qquad (q<0 \text{ or } Fi<0, \text{ downflow}) \tag{A-7b}$$

$$= -\frac{2}{2c\eta + b} \qquad (q=0 \text{ or } Fi=0, \text{ horizontal flow}) \tag{A-7c}$$

Via integration by parts, the four pertinent integrals can be evaluated as follows:

$$I_1 = (1-\omega)\left[\frac{\eta_2 - \eta_1}{c} - \frac{b}{2c^2}\ln\frac{X(\eta_2)}{X(\eta_1)} + \frac{b^2 - 2ac}{2c^2}(I_0(\eta_2) - I_0(\eta_1))\right] \tag{A-8}$$

$$I_2 = \omega\left[\frac{1}{2c}\ln\frac{X(\eta_2)}{X(\eta_1)} - \frac{b}{2c}(I_0(\eta_2) - I_0(\eta_1))\right] \tag{A-9}$$

References

Abramowitz, M., and Stegun, I. A., 1972, *Handbook of Mathematical Functions*, Dover Publications, New York, Ch. 3.

Bilicki, Z., and Kestin, K., 1983, "Two-Phase Flow in a Vertical Pipe and the Phenomenon of Choking: Homogeneous Diffusion Model—I. Homogeneous Flow Models," *Int. J. Multiphase Flow*, Vol. 9, pp. 269–288.

Bilicki, Z., Kestin, J., and Mikielewicz, J., 1987, "Two-Phase Downflow in a Vertical Pipe and the Phenomenon of Choking: Homogeneous Diffusion Model," *Int. J. Heat Mass Transfer*, Vol. 30, No. 7, pp. 1427–1434.

Epstein, M., Henry, R. E., Midvidy, W., and Pauls, R., 1983, "One-Dimensional Modeling of Two-Phase Jet Expansion and Impingement," *Thermal-Hydraulics of Nuclear Reactors II*, 2nd Int. Topical Meeting on Nuclear Reactor Thermal-Hydraulics, Santa Barbara, CA.

Lapple, C. E., 1943, "Isothermal and Adiabatic Flow of Compressible Fluids," *Trans. Am. Inst. Chem. Eng.*, Vol. 39, pp. 385–432.

Leung, J. C., 1986, "A Generalized Correlation for One-Component Homogeneous Equilibrium Flashing Choked Flow," *AIChE J.*, Vol. 32, pp. 1743–1746.

Leung, J. C., and Grolmes, M. A., 1987, "The Discharge of Two-Phase Flashing Flow in a Horizontal Duct," *AIChE J.*, Vol. 33, pp. 524–527, also errata, 34, pp. 1030 (1988).

Leung, J. C., and Grolmes, M. A., 1988, "A Generalized Correlation for Flashing Choked Flow of Initially Subcooled Liquid," *AIChE J.*, Vol. 34, pp. 688–691.

Leung, J. C., and Fisher, H. G., 1989, "Two-Phases Flow Venting From Reactor Vessels," *J. Loss Prev. Process Ind.*, Vol. 2, pp. 78–86.

Levenspiel, O., 1977, "The Discharge of Gases From a Reservoir Through a Pipe," *AIChE J.*, Vol. 23, pp. 402–403.

Perry, R. H., and Green, D., 1984, *Perry's Chemical Engineers' Handbook*, 6th ed., McGraw-Hill, New York, Ch. 5, p. 44.

Shapiro, A., 1953, *Compressible Fluid Flow*, Ronald Press, New York, Vol. 1, Ch. 6.

$$I_3 = G^{*2}\omega(1-\omega)[I_0(\eta_2) - I_0(\eta_1)] \quad \text{(A-10)}$$

$$I_4 = G^{*2}\omega^2\left[\frac{1}{2a}\ln\frac{\eta_2^2 X(\eta_1)}{\eta_1^2 X(\eta_2)} - \frac{b}{2a}(I_0(\eta_2) - I_0(\eta_1))\right] \quad \text{(A-11)}$$

Finally the desired result is

$$4f\frac{L}{D} = -I_1 - I_2 + I_3 + I_4 \quad \text{(A-12)}$$

For the case when Fi is 0, the above equation reduces exactly to the solution for the horizontal case (Leung and Grolmes, 1987, equation (8); see also the errata).

A Generalized Correlation for Two-Phase Nonflashing Homogeneous Choked Flow

J. C. Leung[1] and M. Epstein[1]

Nomenclature

C_p = specific heat at constant pressure
C_v = specific heat at constant volume
G = mass velocity or flux
G^* = normalized mass velocity
h = specific enthalpy
M_w = gas molecular weight
P = pressure
R = universal gas constant
T = temperature
u = velocity
v = specific volume
x = quality or mass fraction of gas
α_o = stagnation inlet void fraction
γ = gas phase specific heat ratio
Γ = two-phase isentropic exponent
η = pressure ratio
ρ = two-phase density

Subscripts

c = critical or choked
g = gas
l = liquid
o = stagnation condition

Introduction

This paper presents a generalized formulation for evaluating the homogeneous choked flow of a nonflashing two-phase (gas/liquid such as air/water or gas/solid such as air/powder) compressible mixture. The case of interest here is one-dimensional isentropic flow in a frictionless nozzle. The isentropic expansion law for a two-phase nonflashing mixture in thermal equilibrium (rapid heat transfer resulting in equal temperature in both phases) was first obtained by Tangren et al. (1949). They presented the so-called isothermal-limit solutions for the critical pressure ratio as well as the local sonic velocity. Later Starkman et al. (1964) proposed a frozen (thermal insulated or no heat transfer between the two phases) homogeneous model and obtained an expression for the critical mass velocity that was intended for high inlet quality or void fraction conditions by neglecting the liquid-phase acceleration and by assuming the critical pressure ratio to be identical to the all-gas flow case. Henry and Fauske (1971) presented the complete critical pressure ratio solution in transcendental equation form for the frozen flow case, but their approximate solutions were identical to those of Starkman et al. The present study seeks a generalized but exact homogeneous flow formulation for both frozen and thermal equilibrium conditions applicable over the entire range of inlet void fractions. The main focus of this paper is to show that the choked flow rate is expressible in terms of only two parameters and to introduce for the first time an explicit formula for the critical pressure ratio. The present rigorous treatment also allows comparisons to be made against the previously proposed limiting solutions.

Although the present homogeneous flow assumption (i.e., complete momentum exchange between phases) is physically unrealistic in certain applications, it has proved valuable for understanding qualitative features of two-phase discharges, inferring approximate scaling laws, and making order-of-magnitude predictions (Henry, 1979). Moreover, the model can now be found in several textbooks on two-phase flow (see, e.g., Wallis, 1969, and Hsu and Graham, 1976) where it serves as a useful instructional tool and as a reference model against which more elaborate models, such as those incorporating slip, can be compared. Of course, the model correctly represents the flow when the solid or liquid phases are finely dispersed (Altman and Carter, 1956).

Analytical Formulation

Among the various assumptions imbedded in the following treatment of compressible two-phase flow mixtures (see Wallis, 1969, p. 207), the key ones are: (1) There are no mass, heat, or momentum losses from the flow to the nozzle walls; (2) there is no slip between the phases; (3) the gas behaves as a perfect gas; and (4) the liquid or solid (particle cloud) is incompressible.

Using the above assumptions, the equations governing the flow of a nonflashing compressible two-phase mixture are

$$G = \rho u = u/v \quad (1)$$

$$v\,dP + u\,du = 0 \quad (2)$$

$$h_o = h + \frac{1}{2}u^2 \quad (3)$$

$$P = \rho RT/M_w \quad (4)$$

$$h = xh_g + (1-x)h_l \quad (5)$$

$$v = xv_g + (1-x)v_l \text{ or } \frac{1}{\rho} = \frac{x}{\rho_g} + \frac{1-x}{\rho_l} \quad (6)$$

where equations (1)–(3) represent mass velocity, momentum conservation, and energy conservation; and equations (4)–(6) are the expressions of ideal gas behavior, mixture enthalpy, and mixture specific volume or density. In equations (5) and (6), x is the quality or the mass fraction of the gas component and it remains unchanged in a nonflashing flow process ($dx = 0$).

Critical Mass Velocity and Pressure Ratio

Equations (1)–(6) can be combined to obtain the following expression for the mass velocity of a thermally equilibrated two-phase flow as a function of the pressure downstream of the stagnation zone:

[1]Fauske & Associates, Inc., Burr Ridge, IL 60521.

Contributed by the Heat Transfer Division for publication in the JOURNAL OF HEAT TRANSFER. Manuscript received by the Heat Transfer Division March 27, 1989; revision received July 17, 1989. Keywords: Multiphase Flows.

$$I_3 = G^{*2}\omega(1-\omega)[I_0(\eta_2) - I_0(\eta_1)] \quad \text{(A-10)}$$

$$I_4 = G^{*2}\omega^2\left[\frac{1}{2a}\ln\frac{\eta_2^2 X(\eta_1)}{\eta_1^2 X(\eta_2)} - \frac{b}{2a}(I_0(\eta_2) - I_0(\eta_1))\right] \quad \text{(A-11)}$$

Finally the desired result is

$$4f\frac{L}{D} = -I_1 - I_2 + I_3 + I_4 \quad \text{(A-12)}$$

For the case when Fi is 0, the above equation reduces exactly to the solution for the horizontal case (Leung and Grolmes, 1987, equation (8); see also the errata).

A Generalized Correlation for Two-Phase Nonflashing Homogeneous Choked Flow

J. C. Leung[1] and M. Epstein[1]

Nomenclature

C_p = specific heat at constant pressure
C_v = specific heat at constant volume
G = mass velocity or flux
G^* = normalized mass velocity
h = specific enthalpy
M_w = gas molecular weight
P = pressure
R = universal gas constant
T = temperature
u = velocity
v = specific volume
x = quality or mass fraction of gas
α_o = stagnation inlet void fraction
γ = gas phase specific heat ratio
Γ = two-phase isentropic exponent
η = pressure ratio
ρ = two-phase density

Subscripts

c = critical or choked
g = gas
l = liquid
o = stagnation condition

Introduction

This paper presents a generalized formulation for evaluating the homogeneous choked flow of a nonflashing two-phase (gas/liquid such as air/water or gas/solid such as air/powder) compressible mixture. The case of interest here is one-dimensional isentropic flow in a frictionless nozzle. The isentropic expansion law for a two-phase nonflashing mixture in thermal equilibrium (rapid heat transfer resulting in equal temperature in both phases) was first obtained by Tangren et al. (1949). They presented the so-called isothermal-limit solutions for the critical pressure ratio as well as the local sonic velocity. Later Starkman et al. (1964) proposed a frozen (thermal insulated or no heat transfer between the two phases) homogeneous model and obtained an expression for the critical mass velocity that was intended for high inlet quality or void fraction conditions by neglecting the liquid-phase acceleration and by assuming the critical pressure ratio to be identical to the all-gas flow case. Henry and Fauske (1971) presented the complete critical pressure ratio solution in transcendental equation form for the frozen flow case, but their approximate solutions were identical to those of Starkman et al. The present study seeks a generalized but exact homogeneous flow formulation for both frozen and thermal equilibrium conditions applicable over the entire range of inlet void fractions. The main focus of this paper is to show that the choked flow rate is expressible in terms of only two parameters and to introduce for the first time an explicit formula for the critical pressure ratio. The present rigorous treatment also allows comparisons to be made against the previously proposed limiting solutions.

Although the present homogeneous flow assumption (i.e., complete momentum exchange between phases) is physically unrealistic in certain applications, it has proved valuable for understanding qualitative features of two-phase discharges, inferring approximate scaling laws, and making order-of-magnitude predictions (Henry, 1979). Moreover, the model can now be found in several textbooks on two-phase flow (see, e.g., Wallis, 1969, and Hsu and Graham, 1976) where it serves as a useful instructional tool and as a reference model against which more elaborate models, such as those incorporating slip, can be compared. Of course, the model correctly represents the flow when the solid or liquid phases are finely dispersed (Altman and Carter, 1956).

Analytical Formulation

Among the various assumptions imbedded in the following treatment of compressible two-phase flow mixtures (see Wallis, 1969, p. 207), the key ones are: (1) There are no mass, heat, or momentum losses from the flow to the nozzle walls; (2) there is no slip between the phases; (3) the gas behaves as a perfect gas; and (4) the liquid or solid (particle cloud) is incompressible.

Using the above assumptions, the equations governing the flow of a nonflashing compressible two-phase mixture are

$$G = \rho u = u/v \quad (1)$$

$$v\,dP + u\,du = 0 \quad (2)$$

$$h_o = h + \frac{1}{2}u^2 \quad (3)$$

$$P = \rho RT/M_w \quad (4)$$

$$h = xh_g + (1-x)h_l \quad (5)$$

$$v = xv_g + (1-x)v_l \text{ or } \frac{1}{\rho} = \frac{x}{\rho_g} + \frac{1-x}{\rho_l} \quad (6)$$

where equations (1)–(3) represent mass velocity, momentum conservation, and energy conservation; and equations (4)–(6) are the expressions of ideal gas behavior, mixture enthalpy, and mixture specific volume or density. In equations (5) and (6), x is the quality or the mass fraction of the gas component and it remains unchanged in a nonflashing flow process ($dx = 0$).

Critical Mass Velocity and Pressure Ratio

Equations (1)–(6) can be combined to obtain the following expression for the mass velocity of a thermally equilibrated two-phase flow as a function of the pressure downstream of the stagnation zone:

[1]Fauske & Associates, Inc., Burr Ridge, IL 60521.

Contributed by the Heat Transfer Division for publication in the JOURNAL OF HEAT TRANSFER. Manuscript received by the Heat Transfer Division March 27, 1989; revision received July 17, 1989. Keywords: Multiphase Flows.

$$G=\frac{\left\{2xP_o v_{go}\left(\frac{\Gamma}{\Gamma-1}\right)\left[1-\left(\frac{P}{P_o}\right)^{(\Gamma-1)/\Gamma}\right]+2(1-x)v_l(P_o-P)\right\}^{1/2}}{xv_{go}\left(\frac{P}{P_o}\right)^{-1/\Gamma}+(1-x)v_l} \tag{7}$$

where Γ denotes the two-phase isentropic exponent for a thermal equilibrium process as first derived by Tangren et al. (1949)

$$\Gamma=\frac{xC_{pg}+(1-x)C_{pl}}{xC_{vg}+(1-x)C_{pl}} \tag{8}$$

To obtain G for an expansion in which the gas phase is thermally insulated from the liquid or solid phase (frozen flow) one simply replaces Γ with $\gamma=C_{pg}/C_{vg}$ in equation (7). The expression for G can be rewritten in a useful nondimensional form by first noting for homogeneous flow

$$\frac{1-\alpha_o}{\alpha_o}=\frac{v_l}{v_{go}}\left(\frac{1-x}{x}\right) \tag{9}$$

and further defining a normalized mass velocity and a pressure ratio, respectively, as

$$G^*\equiv\frac{G}{\sqrt{P_o/v_o}}=\frac{G}{\sqrt{P_o\rho_o}}, \qquad \eta\equiv P/P_o$$

The desired dimensionless expression is then obtained

$$G^*=\frac{\left\{\frac{2}{\alpha_o}\left[\left(\frac{1-\alpha_o}{\alpha_o}\right)(1-\eta)+\left(\frac{\Gamma}{\Gamma-1}\right)(1-\eta^{(\Gamma-1)/\Gamma})\right]\right\}^{1/2}}{\eta^{-1/\Gamma}+\left(\frac{1-\alpha_o}{\alpha_o}\right)} \tag{10}$$

We note from equation (10) that only two gas properties enter into the mass velocity evaluation: the stagnation void fraction α_o (rather than the quality x) and the isentropic exponent. Examination of the above expression shows that as the downstream pressure is reduced the mass velocity reaches a maximum at the so-called critical pressure ratio η_c (or P_c/P_o). Figure 1 displays the shape of the G^* versus η curves for selected α_o values. As usual, to find the maximum flow condition, we compute the derivative $dG^*/d\eta$ and set it equal to zero. This gives the transcendental formula for η_c, again only a function of α_o and Γ

$$\left(\frac{1-\alpha_o}{\alpha_o}\right)^2\eta_c^{(\Gamma+1)/\Gamma}+\left(\frac{\Gamma+1}{\Gamma-1}\right)\eta_c^{(\Gamma-1)/\Gamma}+2\left(1+\frac{1}{\Gamma}\right)$$
$$\times\left(\frac{1-\alpha_o}{\alpha_o}\right)\eta_c=\frac{2}{\Gamma}\left(\frac{1-\alpha_o}{\alpha_o}\right)+\frac{2}{\Gamma-1} \tag{11}$$

This equation reduces to Henry and Fauskes' (1971) frozen flow result (equation (40) of their paper) by making use of equation (9) and substituting for Γ by γ. Numerical solutions of equation (11) for η_c can be most conveniently presented graphically in terms of the stagnation void fraction and for selected Γ values, as shown in Fig. 2. Also shown are the normalized critical mass velocity G_c^* solutions according to equations (10) and (11).

Explicit Pressure Ratio Formula

An approximate, explicit formula for η_c can be obtained by recognizing the limiting solutions of equation (11) when α_o approaches either 1.0 (all-gas flow) or 0 (near liquid flow). In the limit of all-gas flow we recover the well-known result

$$\eta_c=\left(\frac{2}{\Gamma+1}\right)^{\Gamma/(\Gamma-1)} \quad \text{for } \alpha_o=1 \tag{12}$$

Note that Γ for the thermal equilibrium assumption reduces identically to γ for the gas at this condition. At the other end, as the near liquid flow regime is approached, equation (11) reveals that

$$\eta_c\to\left[\frac{2}{\Gamma}\cdot\frac{\alpha_o}{1-\alpha_o}\right]^{\Gamma/(\Gamma+1)} \quad \text{as } \alpha_o\to 0 \tag{13}$$

However, in most practical situations,as α_o approaches zero the flow would become unchoked since η_c is rapidly converging to zero. In such unchoked flow cases, equation (10)

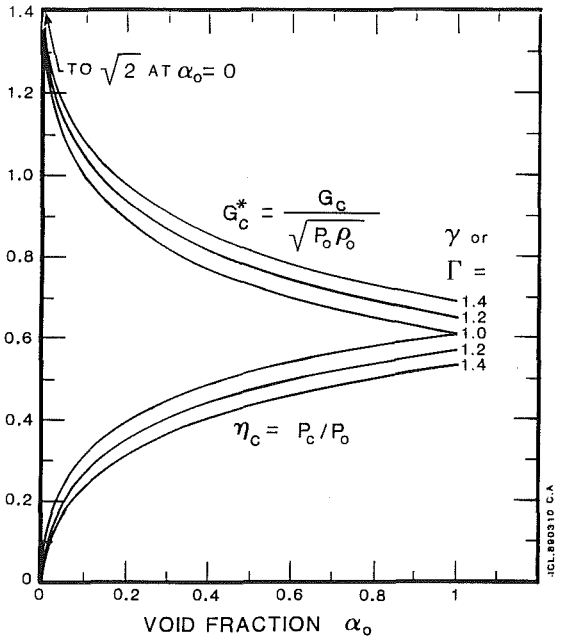

Fig. 1 Normalized mass velocity versus exit pressure ratio

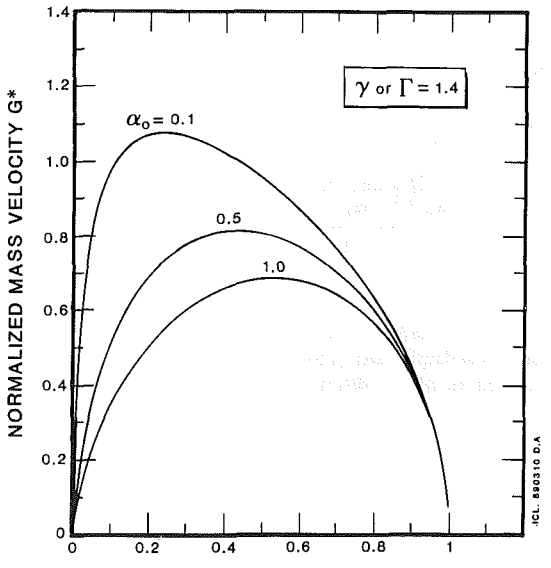

Fig. 2 Graphic plot of exact solutions for G^* and η_c

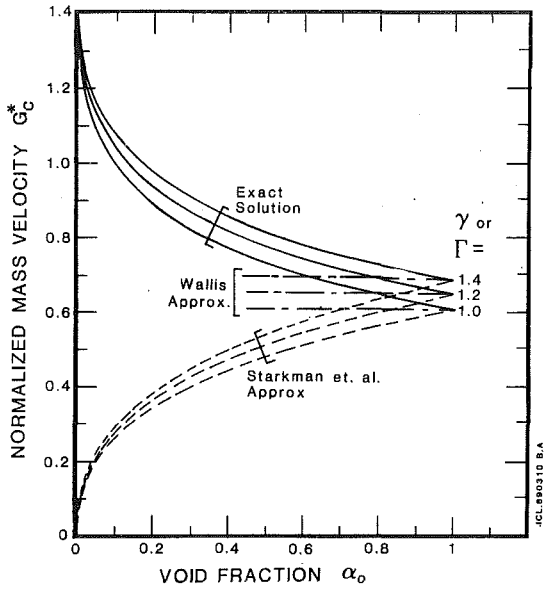

Fig. 3 Comparison of exact solution against the approximate solutions

reduces to the incompressible Bernoulli equation.[2] As for an explicit formula for η_c, the forms of equations (12) and (13) suggest an interpolation formula (Churchill and Usagi, 1972)

$$\eta_c = \left[\left(\frac{\Gamma+1}{2}\right)^{a\Gamma/(\Gamma-1)} + \left(\frac{\Gamma}{2}\cdot\frac{1-\alpha_o}{\alpha_o}\right)^{a\Gamma/(\Gamma+1)}\right]^{-1/a} \tag{14}$$

where the exponent a is chosen to best match the exact solutions. The value $a=4/3$ was found to be very successful in this regard and yields no more than 5 percent deviation from the exact critical pressure ratios from equation (11). Furthermore, the corresponding critical mass velocity is predicted to be well within 0.05 percent using equation (10) together with the above interpolation formula for η_c. The high accuracy achieved with respect to G_c is due to the fact that G_c according to equation (10) is relatively insensitive to the exact values of η_c near its maximum value (see Fig. 1).

Comparison With Previous Work

The exact treatment presented here can be compared with previously obtained solutions. In the isothermal flow limit $\Gamma \to 1.0$ [i.e., thermal equilibrium with $x << 1.0$; see equation (8)], the critical pressure ratio and the critical mass velocity can be deduced from equations (11) and (10), respectively,

$$\ln\eta_c = \left(\frac{1-\alpha_o}{\alpha_o}\right)\left[(1-2\eta_c) - \frac{\eta_c^2}{2}\left(\frac{1-\alpha_o}{\alpha_o}\right)\right] - \frac{1}{2} \tag{15}$$

$$G_c^* = \frac{\left\{\frac{2}{\alpha_o}\left[\left(\frac{1-\alpha_o}{\alpha_o}\right)(1-\eta_c) - \ln\eta_c\right]\right\}^{1/2}}{\frac{1}{\eta_c} + \left(\frac{1-\alpha_o}{\alpha_o}\right)} \tag{16}$$

where use was made of the L'Hopital rule in evaluating the indeterminates. Equation (15) is essentially the result presented by Tangren et al. (1949, i.e., equation (23) in their paper).

[2] At $\alpha_o = 0$, equation (10) yields the limit $G^* = [2(1-\eta)]^{1/2}$ or $G = [2\rho_l(P_o - P)]^{1/2}$.

These solutions are indistinguishable from the curves corresponding to $\Gamma = 1.0$ in Fig. 2 [actually a Γ value of 1.001 was used in Fig. 2 to avoid the numerical difficulty of division by zero in equations (10) and (11)].

The approximate solutions for the frozen flow case as given by Starkman et al. (1964) and later by Henry and Fauske (1971) assume the critical pressure ratio to follow the ideal gas case

$$\eta_c = \left(\frac{2}{\gamma+1}\right)^{\gamma/(\gamma-1)} \tag{17}$$

and the critical mass velocity after being normalized by the present scheme

$$G_c^* = \frac{G_c}{\sqrt{P_o/v_o}} = \frac{\left[\frac{2}{\alpha_o}\left(\frac{\gamma}{\gamma-1}\right)\left(1-\eta_c^{(\gamma-1)/\gamma}\right)\right]^{1/2}}{\eta_c^{-1/\gamma} + \left(\frac{1-\alpha_o}{\alpha_o}\right)} \tag{18}$$

Comparing this to the exact formulation represented by equation (10) indicates that the liquid acceleration term $[(1-\alpha_o)/\alpha_o](1-\eta)$ has been neglected. A more transparent comparison is shown in Fig. 3 where both exact and approximate solutions for G_c^* are plotted. Equation (18) diverges rapidly from the exact solution as α_0 is decreased. The use of equation (18) over the entire quality range has led to the prediction of an artificial maximum in the G_c versus inlet quality curve as the quality approaches zero (see Fig. 5 of Starkman et al., 1964, or Fig. 5 of Henry and Fauske, 1971).

Another approximate solution was suggested by Wallis (1969). His result can be taken directly from the compressible gas flow solution with appropriate substitution for the two-phase specific volume and the modified isentropic exponent Γ. His solution for the frozen case is, therefore,

$$G_c^* = \frac{G_c}{\sqrt{P_o/v_o}} = \left[\gamma\left(\frac{2}{\gamma+1}\right)^{(\gamma+1)/(\gamma-1)}\right]^{1/2} \tag{19}$$

This solution is found to be a better approximation than equation (18) as illustrated in Fig. 3, but again does not exhibit the correct behavior as α_o is reduced. Clearly, the previously reported, approximate solutions should only be used for inlet stagnation void fractions close to unity.

References

Altman, D., and Carter, J. M., 1956, "Expansion Processes," Sec. B, Vol. II of *Combustion Processes*, pp. 52–60. High Speed Aerodynamics and Jet Propulsion, Princeton University Press.

Churchill, S. W., and Usagi, R., 1972, "A General Expression for the Correlation of Rates of Transfer and Other Phenomena," *AIChE J.*, Vol. 18, No. 6, pp. 1121–1128.

Henry, R. E., and Fauske, H. K., 1971, "The Two-Phase Critical Flow of One-Component Mixtures in Nozzles, Orifices, and Short Tubes," ASME JOURNAL OF HEAT TRANSFER, Vol. 93, pp. 179–187.

Henry, R. E., 1979, "Calculational Techniques for Two-Phase Critical Flow," *Proc. Japan-U.S. Seminar on Two-Phase Flow Dynamics*, Kobe, Japan, July 31–Aug. 3, pp. 367–388.

Hsu, Y. Y., and Graham, R. W., 1976, *Transport Processes in Boiling and Two-Phase Systems*, McGraw-Hill, New York.

Starkman, E. S., Schrock, V. E., Neusen, K. F., and Maneely, D. J., 1964, "Expansion of a Very Low Quality Two-Phase Fluid Through a Convergent-Divergent Nozzle," ASME *J. of Basic Engineering*, Vol. 86, pp. 247–256.

Tangren, R. F., Dodge, C. H., and Seifert, H. S., 1949, "Compressibility Effects in Two-Phase Flow," *J. of Applied Physics*, Vol. 20, pp. 637–645.

Wallis, G. B., 1969, *One-Dimensional Two-Phase Flow*, McGraw-Hill, New York.